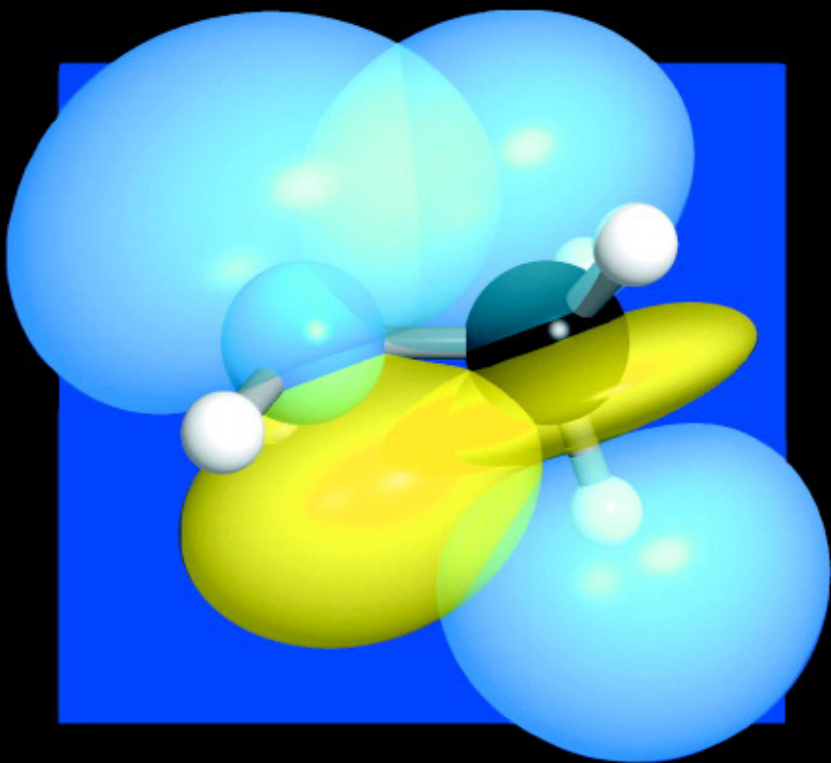


Valency and Bonding

A Natural Bond Orbital Donor-Acceptor Perspective



Frank Weinhold and Clark Landis

CAMBRIDGE

CAMBRIDGE

more information - www.cambridge.org/9780521831284

This page intentionally left blank

VALENCY AND BONDING

This graduate-level text presents the first comprehensive overview of modern chemical valency and bonding theory, written by internationally recognized experts in the field. The authors build on the foundation of Lewis- and Pauling-like localized structural and hybridization concepts to present a book that is directly based on current *ab initio* computational technology.

The presentation is highly visual and intuitive throughout, being based on the recognizable and transferable graphical forms of natural bond orbitals (NBOs) and their spatial overlaps in the molecular environment. The book shows applications to a broad range of molecular and supramolecular species of organic, inorganic, and bioorganic interest. Hundreds of orbital illustrations help to convey the essence of modern NBO concepts in a facile manner for those with no extensive background in the mathematical machinery of the Schrödinger equation. This book will appeal to those studying chemical bonding in relation to chemistry, chemical engineering, biochemistry, and physics.

FRANK A. WEINHOLD is Professor of Physical and Theoretical Chemistry at the University of Wisconsin-Madison. His academic awards include the Alfred P. Sloan Fellowship (1970) and the Camille and Henry Dreyfus Foundation Fellowship (1972) and he has served guest appointments at many prestigious institutes including the Quantum Chemistry Group at the University of Uppsala, Sweden, the Max-Planck-Institut für Physik und Astrophysik in Munich, Germany, and the University of Colorado. He was the 13th Annual Charles A. Coulson lecturer at the Center for Computational Quantum Chemistry, University of Georgia. Professor Weinhold has also served on the Honorary Editorial Advisory Boards of the *International Journal of Quantum Chemistry* and the *Russian Journal of Physical Chemistry* and is the author of over 150 technical publications and software packages.

Following a brief but influential career as an industrial chemist for Monsanto Corporation, CLARK LANDIS began his academic career at the University of Colorado, Boulder, moving to the University of Wisconsin-Madison in 1990, where he is currently a Professor in Inorganic Chemistry. Professor Landis was co-PI of the New Traditions Systemic Reform Project in Chemical Education and is co-author of *Chemistry ConcepTests: A Pathway to Interactive Classrooms* and a companion video tape. He has long served as a consultant to Dow Chemical Company and is a member of its Technical Advisory Board.

VALENCY AND BONDING

A Natural Bond Orbital Donor–Acceptor Perspective

FRANK WEINHOLD AND CLARK R. LANDIS

Department of Chemistry, University of Wisconsin-Madison, Wisconsin 53706



CAMBRIDGE
UNIVERSITY PRESS

CAMBRIDGE UNIVERSITY PRESS

Cambridge, New York, Melbourne, Madrid, Cape Town, Singapore, São Paulo

Cambridge University Press

The Edinburgh Building, Cambridge CB2 2RU, UK

Published in the United States of America by Cambridge University Press, New York

www.cambridge.org

Information on this title: www.cambridge.org/9780521831284

© Cambridge University Press 2005

This book is in copyright. Subject to statutory exception and to the provision of relevant collective licensing agreements, no reproduction of any part may take place without the written permission of Cambridge University Press.

First published in print format 2005

ISBN-13 978-0-511-11548-6 eBook (MyiLibrary)

ISBN-10 0-511-11548-2 eBook (MyiLibrary)

ISBN-13 978-0-521-83128-4 hardback

ISBN-10 0-521-83128-8 hardback

Cambridge University Press has no responsibility for the persistence or accuracy of URLs for external or third-party internet websites referred to in this book, and does not guarantee that any content on such websites is, or will remain, accurate or appropriate.

Contents

<i>Preface</i>	<i>page vii</i>
1 Introduction and theoretical background	1
1.1 The Schrödinger equation and models of chemistry	1
1.2 Hydrogen-atom orbitals	8
1.3 Many-electron systems: Hartree–Fock and correlated treatments	13
1.4 Perturbation theory for orbitals in the Hartree–Fock framework: the donor–acceptor paradigm	16
1.5 Density matrices, natural localized and delocalized orbitals, and the Lewis-structure picture	21
1.6 Natural resonance structures and weightings	32
1.7 Pauli-exchange antisymmetry and steric repulsions	36
1.8 Summary	40
Notes for Chapter 1	41
2 Electrostatic and ionic bonding	45
2.1 Introduction	45
2.2 Atomic and ionic orbitals	47
2.3 Charge transfer and hybridization in ionic bonding	49
2.4 Donor–acceptor theory of hybridization in ionic bonding	55
2.5 Ionic–covalent transitions	60
2.6 Ion–dipole and dipole–dipole bonding	64
2.7 Bent ionic compounds of heavy alkaline earths	73
2.8 Ionic bonding in d-block elements	76
2.9 Summary	86
Notes for Chapter 2	87

3	Molecular bonding in s/p-block elements	89
3.1	Introduction	89
3.2	Covalent and polar covalent bonding	90
3.3	Conjugation and aromaticity	182
3.4	Hyperconjugation	215
3.5	Hypervalency: 3c/4e “ ω bonds”	275
3.6	Hypovalency: 3c/2e bridge bonds	306
3.7	Summary	351
	Notes for Chapter 3	353
4	Molecular bonding in the d-block elements	363
4.1	Introduction	363
4.2	Lewis-like structures for the d-block elements	365
4.3	Hybridization and molecular shape	372
4.4	Covalent and polar-covalent bonding	387
4.5	Coordinative metal–ligand bonding	434
4.6	Beyond sigma bonding: transition-metal hyperbonding and pi back/frontbonding	447
4.7	Hypovalency, agostic interactions, and related aspects of catalytic activation at metal centers	479
4.8	Hyperconjugative effects	519
4.9	Multielectron coordination	522
4.10	Vertical trends in transition-metal bonding	545
4.11	Localized versus delocalized descriptions of transition-metal bonding and hyperbonding	563
4.12	Summary	573
	Notes for Chapter 4	575
5	Supramolecular bonding	579
5.1	An introductory overview of intermolecular forces	579
5.2	Hydrogen bonding	593
5.3	Charge-transfer complexes	661
5.4	Transition-state species	678
5.5	Coupling of intramolecular and intermolecular interactions	693
5.6	Summary	702
	Notes for Chapter 5	704
	Appendix A. Methods and basis sets	710
	Appendix B. Chemical periodicity	715
	Appendix C. Units	723
	<i>Chemical-species index</i>	727
	<i>Author index</i>	732
	<i>Subject index</i>	740

Preface

Two daunting questions face the authors of prospective textbooks. (1) For whom is the book intended? (2) What makes it different from other books intended for the same audience? We first address these questions.

One might think from counting the mathematical equations that the book is intended for a theoretical physicist. This is partially true, for indeed we hope the subject is presented in a way that will satisfy a rigorously inclined mathematical physicist that “valency and bonding” is not just murky chemical voodoo, but authentic science grounded in the deepest tenets of theoretical physics.

Beyond Chapter 1 the reader may be relieved to find few if any equations that would challenge even a moderately gifted high-school student. The emphasis on orbital diagrams and “doing quantum mechanics with pictures” might then suggest that the book is intended for undergraduate chemistry students. This is also partially true. For example, we believe that our treatment of homonuclear diatomic molecules (Section 3.2.9) should be accessible to undergraduates who commonly encounter the topic in introductory chemistry courses.

Our principal goal has been to translate the deepest truths of the Schrödinger equation into a visualizable, intuitive form that “makes sense” even for beginning students, and can help chemistry teachers to present bonding and valency concepts in a manner more consistent with modern chemical research. Chemistry teachers will find here a rather wide selection of elementary topics discussed from a high-level viewpoint. The book includes a considerable amount of previously unpublished material that we believe to be of broad pedagogical interest, such as the novel Lewis-like picture of transition-metal bonding presented in Chapter 4.

Because we are both computational chemistry researchers, we have naturally directed the book also to specialists in this field, particularly those wishing to incorporate natural bond orbital (NBO) and natural resonance theory (NRT) analysis into their methodological and conceptual toolbox. Researchers will find here a

rather broad sampling of NBO/NRT applications to representative chemical problems throughout the periodic table, touching on many areas of modern chemical, biochemical, and materials research.

But, we expect that the majority of readers will be those with only a rudimentary command of quantum chemistry and chemical bonding theory (e.g., at the level of junior-year physical chemistry course) who wish to learn more about the emerging *ab initio* and density-functional view of molecular and supramolecular interactions. While this is not a “textbook in quantum chemistry” per se, we believe that the book can serve as a supplement both in upper-level undergraduate courses and in graduate courses on modern computational chemistry and bonding theory.

In identifying the features that distinguish this book from many predecessors, we do not attempt to conceal the enormous debt of inspiration owed to such classics as Pauling’s *Nature of the Chemical Bond* and Coulson’s *Valence*. We aspire neither to supplant these classics nor to alter substantially the concepts they expounded. Rather, our goal is to take a similarly global view, but develop a more current and quantitative perspective on valency and bonding concepts such as hybridization, electronegativity, and resonance, capitalizing on the many advances in wavefunction calculation and analysis that have subsequently occurred. We hope thereby to sharpen, revitalize, and enhance the usefulness of qualitative bonding concepts by presenting a “twenty-first-century view” of the nature of chemical bonding.

Readers who are accustomed to seeing chemical theorizing buttressed by comparisons with experiments may be surprised to find little of the latter here. Throughout this book, computer solutions of Schrödinger’s equation (rather than experiments) are regarded as the primary “oracle” of chemical information. We specifically assume that high-level calculations (e.g., at the hybrid density-functional B3LYP/6-311++G** level) can be relied upon to describe molecular electronic distributions, geometries, and energetics to a sufficient degree of chemical accuracy for our purposes. (In fact, the accuracy is often comparable to that of the best available experimental data, more than adequate for qualitative pedagogical purposes.) The viewpoint of this book is that modern *ab initio* theory no longer requires extensive experimental comparisons in order for it to be considered seriously, and indeed, theory can be expected to supplant traditional experimental methods in an increasing number of chemical investigations. In the deepest sense, this is a “theory book.”

Dual authorship naturally brings a distinctive blend of perspectives. The book reflects the influence of a “donor–acceptor” perspective based on NBO/NRT wavefunction analysis methods developed in the research group of F. W. (a physical chemist). While NBO analyses are now rather common in the chemical literature, the present work provides the first broad overview of organic and inorganic chemical phenomena from this general viewpoint. The book also incorporates key insights gained from constructing valence-bond-based (VALBOND) molecular-mechanics

potentials for transition metals and hypervalent main-group species, as carried out in the research group of C. R. L. (an inorganic chemist). We both recognize how the constructive synergism of our distinct cultures has added breadth and dimension to this work.

Uppermost in our minds has been a strong concern for chemical pedagogy, which is manifested in several ways. Because we were often prompted by such questions ourselves, we have tended to organize the presentation around “frequently asked questions,” with the emphasis being on individual species that hold special fascination for students of bonding theory. Although leading references for further study are provided, in few if any cases do we attempt a comprehensive survey of the literature; indeed, such a survey would be quite impractical for many of the evergreen bonding topics. Our treatment therefore resembles a textbook rather than a specialist research monograph or review article. We have also taken the opportunity to include numerous examples, including worked-out problems, derivations, and illustrative applications to chemical problems. These often serve as a parallel presentation of important concepts, giving the student a helping hand through rough spots and putting “some flesh on those bones” of abstract text equations.

We are grateful to numerous colleagues who contributed encouragement, advice, criticism, and topics for study. Special thanks are due to Christine Morales for performing the numerical applications of Chapter 4 at higher triple-zeta level, to Mark Wendt for assistance with *NBOView* orbital imagery, and to Bill Jensen for providing photographic portraits from the Oesper Collection at the University of Cincinnati. We benefited from the excellent computing facilities at the University of Wisconsin-Madison under the long-time direction of Brad Spencer. We also wish to acknowledge the patience and support of our families and the kind cooperation of our Cambridge University Press editors, who confronted the many production challenges of the manuscript with skill and good cheer.

1

Introduction and theoretical background

1.1 The Schrödinger equation and models of chemistry

The Schrödinger equation and its elements

As early as 1929, the noted physicist P. A. M. Dirac wrote¹

The underlying physical laws necessary for the mathematical theory of a large part of physics and the whole of chemistry are thus completely known, and the difficulty is only that the exact application of these laws leads to equations much too complicated to be soluble.

A similar view was echoed in a 1944 textbook of quantum chemistry:²

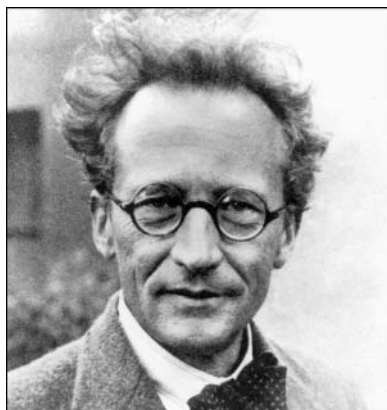
In so far as quantum mechanics is correct, chemical questions are problems in applied mathematics.

The implication is that chemical phenomena are determined by the laws of quantum mechanics, as expressed in the fundamental time-independent Schrödinger equation

$$\hat{H}\Psi = E\Psi \quad (1.1)$$

Exact answers to practically *all* chemical questions are, in principle, obtainable from solutions of this equation.³ Thus, Eq. (1.1) is the ultimate oracle of chemical knowledge.

Equation (1.1) contains three mathematical entities: (i) the *Hamiltonian operator* \hat{H} , determined by the choice of chemical system; (ii) the *wavefunction* Ψ , describing the allowed spatial distribution of electrons and nuclei of the system; and (iii) the *energy* level E associated with Ψ . The Hamiltonian \hat{H} contains terms representing kinetic- and potential-energy contributions, depending only on fixed properties (e.g., mass, charge) of the electrons and nuclei that compose the chosen system of interest. Hence, \hat{H} is the “known” and Ψ and E are the “unknowns” of Eq. (1.1). Mathematically, \hat{H} is an operator that modifies the wavefunction $\Psi(\vec{r}, \vec{R})$ appearing on its right, where we write $\vec{r} = (\vec{r}_1, \vec{r}_2, \dots, \vec{r}_N)$ to denote the collective coordinates of N electrons and $\vec{R} = (\vec{R}_1, \vec{R}_2, \dots, \vec{R}_\nu)$ those of ν nuclei. Only for



Erwin Schrödinger

exceptional choices of Ψ (“eigenstates”) does this operation give a scalar multiple of the original wavefunction, with characteristic multiplier (“eigenvalue”) E . The possible solutions (Ψ_n, E_n) of Eq. (1.1) for a specific \hat{H} are commonly labeled with a quantum-number index n , ordered according to the energy of the ground state and successive excited states of the system. However, in the present work we shall generally restrict attention to the ground solution, so this index can be temporarily omitted.

Perturbation theory of “model chemistry” systems

In practice, the chemist seldom requires numerically exact answers to chemical questions. Answers that are sufficiently accurate *in the context of the chemical investigation* will therefore be considered satisfactory for practical applications. More specifically, this means that energy differences ΔE should be reliable to within a few kcal mol⁻¹ (i.e., a small percentage of a chemical bond energy), but the necessary accuracy may be higher or lower according to context. To achieve this goal, we introduce an approximate *model* Hamiltonian $\hat{H}^{(0)}$ that is somehow simplified (for example, by neglecting some of the potential-energy terms in \hat{H}), but is expected to retain the most important features of the true Hamiltonian for describing chemical phenomena. The Schrödinger-type equation associated with the model $\hat{H}^{(0)}$

$$\hat{H}^{(0)}\psi^{(0)} = E^{(0)}\psi^{(0)} \quad (1.2)$$

may then be said to describe a “model chemistry” (in the terminology introduced by J. A. Pople), just as Eq. (1.1) describes⁴ the true chemistry of \hat{H} . The adequacy or inadequacy of this model chemistry to describe the actual phenomena of chemistry can of course be tested through direct comparisons with experimental results. However, it is also feasible to formulate $\hat{H}^{(0)}$ in a systematically improvable manner, so

that the model chemistry of Eq. (1.2) can be made to approach the exact solutions of Eq. (1.1) as closely as desired (or as far as computational resources permit). From the rate of convergence of these successive corrections, useful estimates of theoretical accuracy that are independent of experimental data can be given. Thus, a central goal of modern computational quantum chemistry is to formulate and improve systematically model $\hat{H}^{(0)}$'s that can predict chemical phenomena at a useful level of accuracy.

For our purposes, the most general way to perform systematic correction of a specified model $\hat{H}^{(0)}$ is by means of *perturbation theory*, as first developed for such problems by Schrödinger himself.⁵ The difference between the true \hat{H} and the model $\hat{H}^{(0)}$ is defined as the perturbation operator $\hat{H}^{(\text{pert})}$,

$$\hat{H}^{(\text{pert})} = \hat{H} - \hat{H}^{(0)} \quad (1.3)$$

The perturbed Schrödinger equation (1.1) is rewritten in terms of the model $\hat{H}^{(0)}$ and $\hat{H}^{(\text{pert})}$ as

$$(\hat{H}^{(0)} + \hat{H}^{(\text{pert})})\Psi = E\Psi \quad (1.4)$$

By systematic perturbation-theoretic procedures,⁶ the exact E can be obtained in terms of successive orders of correction to $E^{(0)}$,

$$E = E^{(0)} + E^{(1)} + E^{(2)} + \dots \quad (1.5a)$$

where $E^{(1)}$ is the first-order correction, $E^{(2)}$ the second-order correction, and so forth; Ψ is similarly expanded as

$$\Psi = \Psi^{(0)} + \Psi^{(1)} + \Psi^{(2)} + \dots \quad (1.5b)$$

For example, the first-order energy correction in Eq. (1.5a) is given by

$$E^{(1)} = \langle \Psi^{(0)} | \hat{H}^{(\text{pert})} | \Psi^{(0)} \rangle \quad (1.5c)$$

where $\langle \rangle$ is the Dirac “bra-ket” symbol⁷

$$\langle \Psi^{(0)} | \hat{H}^{(\text{pert})} | \Psi^{(0)} \rangle = \int \Psi^{(0)*} \hat{H}^{(\text{pert})} \Psi^{(0)} d\tau$$

representing integration over all coordinates, with symbolic differential $d\tau$. (Because Eq. (1.2) remains true when $\Psi^{(0)}$ is multiplied by any number, we assume without loss of generality that $\Psi^{(0)}$ is normalized, $\langle \Psi^{(0)} | \Psi^{(0)} \rangle = 1$.) The second-order correction $E^{(2)}$ can be evaluated from the variational inequality⁸

$$E^{(2)} \leq - \frac{\langle \Psi^{(0)} | \hat{H}^{(\text{pert})} | \tilde{\Psi}^{(1)} \rangle^2}{\langle \tilde{\Psi}^{(1)} | \hat{H}^{(0)} - E^{(0)} | \tilde{\Psi}^{(1)} \rangle} \quad (1.5d)$$

where $\tilde{\Psi}^{(1)}$ is any variational trial function orthogonal to $\Psi^{(0)}$ ($\langle \Psi^{(0)} | \tilde{\Psi}^{(1)} \rangle = 0$) and the inequality becomes *exact* when $\tilde{\Psi}^{(1)} = \Psi^{(1)}$. Note that (1.5d) suggests a numerical method for determining both $\Psi^{(1)}$ (as the $\tilde{\Psi}^{(1)}$ that makes the right-hand side as negative as possible) and $E^{(2)}$ (as the extremal possible value of the right-hand side). The leading corrections $E^{(1)}$ and $E^{(2)}$ will suffice for the applications of this book.

Example 1.1

Exercise: Use the perturbation equations (1.5) to estimate the lowest orbital energy of α spin for a Li atom in a basis of orthogonalized 1s and 2s orbitals, for which the matrix elements of the effective one-electron Hamiltonian operator are⁹ $\langle 1s | \hat{H} | 1s \rangle = -2.3200$, $\langle 1s | \hat{H} | 2s \rangle = -0.3240$, and $\langle 2s | \hat{H} | 2s \rangle = -0.2291$.

Solution: The desired orbital energy is an eigenvalue of a 2×2 matrix, which can be identified as the “ \hat{H} ” for the application of Eqs. (1.1)–(1.5):

$$\hat{H} = \begin{pmatrix} H_{11} & H_{12} \\ H_{12} & H_{22} \end{pmatrix} = \begin{pmatrix} -2.3200 & -0.3240 \\ -0.3240 & -0.2291 \end{pmatrix}$$

To apply the perturbation-theory formalism we can first separate \hat{H} into diagonal (unperturbed) and off-diagonal (perturbation) matrices,

$$\hat{H}^{(0)} = \begin{pmatrix} H_{11} & 0 \\ 0 & H_{22} \end{pmatrix} = \begin{pmatrix} -2.3200 & 0 \\ 0 & -0.2291 \end{pmatrix}$$

$$\hat{H}^{(\text{pert})} = \begin{pmatrix} 0 & H_{12} \\ H_{12} & 0 \end{pmatrix} = \begin{pmatrix} 0 & -0.3240 \\ -0.3240 & 0 \end{pmatrix}$$

The solutions of the eigenvalue equation for $\hat{H}^{(0)}$ are evidently

$$E^{(0)} = H_{11}, \quad \Psi^{(0)} = \begin{pmatrix} 1 \\ 0 \end{pmatrix}$$

and the first-order correction is

$$E^{(1)} = \langle \Psi^{(0)} | \hat{H}^{(\text{pert})} | \Psi^{(0)} \rangle = (1 \ 0) \begin{pmatrix} 0 & H_{12} \\ H_{12} & 0 \end{pmatrix} \begin{pmatrix} 1 \\ 0 \end{pmatrix} = 0$$

For the second-order correction, we can recognize that the only possible normalized trial function $\tilde{\Psi}^{(1)}$ orthogonal to $\Psi^{(0)}$ in this 2×2 case is

$$\tilde{\Psi}^{(1)} = \begin{pmatrix} 0 \\ 1 \end{pmatrix}$$

so that

$$\begin{aligned}\langle \psi^{(0)} | \hat{H}^{(\text{pert})} | \hat{\psi}^{(1)} \rangle &= (1 \ 0) \begin{pmatrix} 0 & H_{12} \\ H_{12} & 0 \end{pmatrix} \begin{pmatrix} 0 \\ 1 \end{pmatrix} = H_{12} \\ \langle \hat{\psi}^{(1)} | \hat{H}^{(0)} - E^{(0)} | \tilde{\psi}^{(1)} \rangle &= (0 \ 1) \begin{pmatrix} 0 & 0 \\ 0 & H_{22} - H_{11} \end{pmatrix} \begin{pmatrix} 0 \\ 1 \end{pmatrix} = H_{22} - H_{11} \\ E^{(2)} &= -\frac{H_{12}^2}{H_{22} - H_{11}}\end{aligned}$$

The lowest eigenvalue (1s orbital energy) is therefore estimated as

$$E = E^{(0)} + E^{(1)} + E^{(2)} = H_{11} - \frac{H_{12}^2}{H_{22} - H_{11}} = -2.3702 \text{ a.u.}$$

The corresponding estimate for the second eigenvalue (2s orbital energy) is -0.1789 . These results are in good agreement with the actual HF/STO-3G (“Hartree–Fock method with a variational basis set of three-term Gaussians for each Slater-type orbital”¹⁰) eigenvalues: $\epsilon_{1s} = -2.3692$ and $\epsilon_{2s} = -0.1801$.

Among various model $\hat{H}^{(0)}$ ’s that could be considered, the best such model is evidently that for which the perturbative corrections are most rapidly convergent, i.e., for which $\hat{H}^{(\text{pert})}$ is in some sense smallest and the model $E^{(0)}$ and $\psi^{(0)}$ are closest to the true E and ψ . Perturbation theory can therefore be used to *guide* selection of the best possible $\hat{H}^{(0)}$ within a class of competing models, as well as to evaluate systematic corrections to this model.

Conceptual constructs in model systems

Perturbation theory also provides the natural mathematical framework for developing chemical concepts and “explanations.” Because the model $\hat{H}^{(0)}$ corresponds to a simpler physical system that is presumably well understood, we can determine how the properties of the more complex system \hat{H} evolve term by term from the perturbative corrections in Eq. (1.5a), and thereby elucidate how these properties originate from the terms contained in $\hat{H}^{(\text{pert})}$. For example, Eq. (1.5c) shows that the first-order correction $E^{(1)}$ is merely the average (quantum-mechanical expectation value) of the perturbation $\hat{H}^{(\text{pert})}$ in the unperturbed eigenstate $\psi^{(0)}$, a highly intuitive result. Most physical explanations in quantum mechanics can be traced back to this kind of perturbative reasoning, wherein the connection is drawn from what is “well understood” to the specific phenomenon of interest.

Perturbative reasoning can be used to justify conceptual models of chemistry that are far from evident in Eq. (1.1) itself. An important example is the concept of *molecular structure* – the notion that nuclei assume a definite equilibrium configuration \vec{R}_0 , which determines the spatial shape and symmetry of the molecule. At first glance, this concept appears to have no intrinsic meaning in Eq. (1.1),

because the true molecular Hamiltonian \hat{H} has *identical* dependence on all identical nuclei,¹¹ and thus could not assign a distinct structural role to a particular nucleus. Indeed, \hat{H} is totally symmetric with respect to all rotation axes, mirror planes, or inversion centers that might be chosen to classify the “structure” of the molecule, and thus could never distinguish between, e.g., *dextro* and *levo* optical isomers, in-plane and out-of-plane H’s of hydrocarbons, carbonyl-type and hydroxyl-type O’s of carboxylic acids, and so forth. This means, for example, that no true eigenstate of Eq. (1.1) can correspond to a chiral molecule of definite handedness,¹² even though the experimental existence of distinct enantiomeric species is well established.

The resolution of this paradox lies in the *Born–Oppenheimer* approximation,¹³ which is based on the fact that nuclei are thousands of times more massive than electrons. The nuclear motions are therefore so sluggish that electrons can be considered to rearrange virtually instantaneously around each static nuclear configuration \vec{R}_0 . In this limit, \hat{H} can be replaced by a model $\hat{H}^{(0)} = \hat{H}(\vec{r}; \vec{R}_0)$ that depends only parametrically on nuclear positions, which are considered fixed at \vec{R}_0 . Solving Eq. (1.2) for the electronic motions alone, while holding \vec{R}_0 fixed, then leads to solutions in which the energy $E^{(0)} = E(\vec{R}_0)$ varies with nuclear configuration, the “potential-energy surface” for subsequent treatment of nuclear motion. The high accuracy of the Born–Oppenheimer model, i.e., the generally negligible values of its higher-order perturbative corrections, amply justifies the chemist’s faith in the existence of well-defined molecular structures. More generally, such considerations validate the direct formulation of Eq. (1.1) as an *electronic* Schrödinger equation in the Born–Oppenheimer framework, as we do throughout this book.

It is also routine to assume the *non-relativistic* approximation¹⁴ in writing Eq. (1.1). This is based on the fact that molecular electronic velocities are generally far less than the speed of light, and the magnetic forces arising from electronic motions can therefore be neglected compared with the dominant electrical forces between charged particles. In this limit, the model Hamiltonian contains only potential-energy terms corresponding to Coulomb’s law of classical electrostatics. However, in reducing \hat{H} from relativistic (Dirac-like) to non-relativistic form, one must recognize the two possible orientations of the intrinsic “spin” angular momentum of each electron (a relativistic effect) and include suitable spin labels in the wavefunction Ψ . Thus, we should generalize the spatial coordinate \vec{r} to include the orientation of each electron in “spin space.” Furthermore, we must insure that the total electronic $\Psi(\vec{r})$ is antisymmetric with respect to exchange of space–spin coordinates of any two electrons i and j , as required by the *Pauli exclusion principle*¹⁵ (Section 1.7),

$$\Psi(\vec{r}_i, \vec{r}_j) = -\Psi(\vec{r}_j, \vec{r}_i) \quad (1.6)$$

However, in other respects spin plays no direct role in construction of the non-relativistic \hat{H} . If higher accuracy is desired, perturbative expressions such as (1.5) can be used to evaluate spin-dependent corrections to the non-relativistic model.

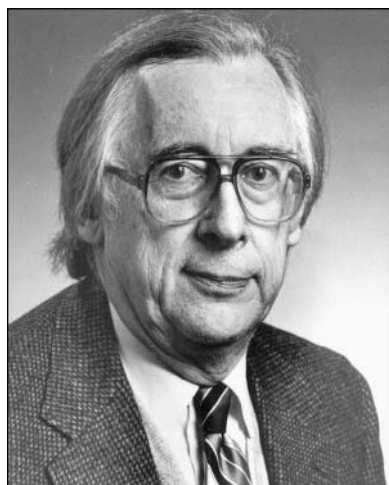
Variational models

Still another useful approximation is introduced by reformulating Eq. (1.1) as a *variational principle*,¹⁶

$$E \leq E^{(0)} = \frac{\langle \psi^{(0)} | \hat{H} | \psi^{(0)} \rangle}{\langle \psi^{(0)} | \psi^{(0)} \rangle} \quad (1.7)$$

The inequality (1.7) is true for any possible variational trial function $\psi^{(0)}$, subject only to the usual antisymmetry and boundary conditions for square-integrable functions of proper symmetry, and the *best* such $\psi^{(0)}$ is that leading to the lowest possible value of $E^{(0)}$, closest to the true E . However, it can be shown¹⁷ that any such trial function $\psi^{(0)}$ and variational energy $E^{(0)}$ are also solutions of a Schrödinger-type equation (1.2) for a suitably defined model Hamiltonian $\hat{H}^{(0)}$. Thus, *any* variational approximation (1.7) can be formulated in terms of a model $\hat{H}^{(0)}$, and the errors of this model can be systematically corrected with perturbative expressions such as Eqs. (1.5).¹⁸ This view of variational calculations, although somewhat unconventional, allows us to treat both variational and perturbative approximation methods in a common “model chemistry” language, along the lines enunciated by Pople.¹⁹

Summing up, we may say that approximation methods in quantum chemistry generally involve (either explicitly or implicitly) a model $\hat{H}^{(0)}$ and associated model chemistry that more or less mimics the true behavior of Eq. (1.1). Such models might be closely patterned after the well-known conceptual models of empirical



John A. Pople

chemistry, such as valence bond or ionic models, or chosen for purely mathematical reasons. Perturbation theory always allows us to choose the best among a family of such proposed models and to calculate systematically the corrections that bring the model into improved agreement with the exact Schrödinger equation (1.1).

The primary goal of a theory of valency and bonding is to find the model $\hat{H}^{(0)}$ that most simply describes the broad panorama of chemical bonding phenomena, or, as Gibbs said,²⁰ “to find the point of view from which the subject appears in its greatest simplicity.” In the past, conceptual models were often cobbled together from diverse empirical patterns, guided only weakly by theory. This resulted in a patchwork of specialized “effects,” with incommensurate seams, indeterminate limits of applicability, and little overall theoretical coherence. However, remarkable advances in computational technology²¹ now make it possible to construct improved conceptual models *directly* from accurate *ab initio* (“first-principles”) wavefunctions.

The fundamental starting point for a rational electronic theory of valency and bonding is the Lewis-structure representation of the shared and unshared electrons in each atomic valence configuration, as formulated by G. N. Lewis. In the present work, we shall focus on a *natural Lewis-structure* model, based on associating the electron pairs of the familiar Lewis-structure diagram with a set of optimal, intrinsic, “natural” bond orbitals (NBOs),²² as outlined in Section 1.5. This viewpoint is deeply tied to traditional chemical bonding concepts – including hybridization, polarization, and bond transferability – and takes advantage of a model $\hat{H}^{(0)}$ that describes localized electron pairs and their interactions in rapidly convergent fashion. By employing a non-empirical theoretical methodology to construct quantitative bonding concepts, we can better achieve the goal of unifying and harmonizing conceptual models of valency and bonding with the deepest principles of chemistry, as expressed by Eq. (1.1).

1.2 Hydrogen-atom orbitals

Orbitals and electron-density distributions

In his first communication²³ on the new wave mechanics, Schrödinger presented and solved his famous Eq. (1.1) for the one-electron hydrogen atom. To this day the H atom is the only atomic or molecular species for which exact solutions of Schrödinger’s equation are known. Hence, these hydrogenic solutions strongly guide the search for accurate solutions of many-electron systems.

The essence of Schrödinger’s treatment was to replace the classical orbit of Bohr’s semi-classical (particle) model of the H-atom by a corresponding wave-like *orbital* (single-electron wavefunction) ψ . Instead of specifying the electron’s

position at a particular point \vec{r} of its orbit (as we should expect classically), the orbital $\Psi(\vec{r})$ determines only the electron *density* $\rho(\vec{r})$ at each spatial point \vec{r} ,

$$\rho(\vec{r}) = |\Psi(\vec{r})|^2 \quad (1.8)$$

The density $\rho(\vec{r})$ might also be described as the fractional *probability* of finding the (entire) electron at point \vec{r} . However, chemical experiments generally do not probe the system in this manner, so it is preferable to picture $\rho(\vec{r})$ as a *continuous* distribution of *fractional* electric charge. This change from a “countable” to a “continuous” picture of electron distribution is one of the most paradoxical (but necessary) conceptual steps to take in visualizing chemical phenomena in orbital terms. Bohr’s “orbits” and the associated “particulate” picture of the electron can serve as a temporary conceptual crutch, but they are ultimately impediments to proper wave-mechanical visualization of chemical phenomena.

Equally paradoxical is the fact that $\rho(\vec{r})$ depends only on the absolute square of the orbital, and is everywhere sensibly non-negative, whereas $\Psi(\vec{r})$ oscillates in “wavy” fashion between positive and negative values.²⁴ The phase patterns corresponding to such sign changes are of utmost importance in chemistry. Solutions of Schrödinger’s equation are generally governed by the *superposition principle*, such that two interacting orbitals may interfere with one another in wave-like constructive (in-phase) or destructive (out-of-phase) patterns²⁵ that strongly alter the form of $\rho(\vec{r})$. Visualizing and understanding the subtle chemical consequences of orbital phase patterns and superposition is a central goal of this book.

Quantum numbers and shapes of atomic orbitals

Let us denote the one-electron hydrogenic Hamiltonian operator by \hat{h} , to distinguish it from the many-electron \hat{H} used elsewhere in this book. This operator contains terms to represent the electronic kinetic energy (\hat{t}_e) and potential energy of attraction to the nucleus (\hat{v}_{nc}),

$$\hat{h} = \hat{t}_e + \hat{v}_{\text{nc}} \quad (1.9)$$

The associated Schrödinger equation for the H atom can then be written as

$$\hat{h}\Psi_{nlm} = \epsilon_n\Psi_{nlm} \quad (1.10)$$

Each orbital eigenstate $\Psi_{nlm} = \Psi_{nlm}(\vec{r})$ is labeled by three quantum numbers:

$$\text{principal: } n = 1, 2, 3, \dots, \infty \quad (1.11a)$$

$$\text{azimuthal: } l = 0, 1, 2, \dots, n - 1 \quad (1.11b)$$

$$\text{magnetic: } m = 0, \pm 1, \pm 2, \dots, \pm l \quad (1.11c)$$

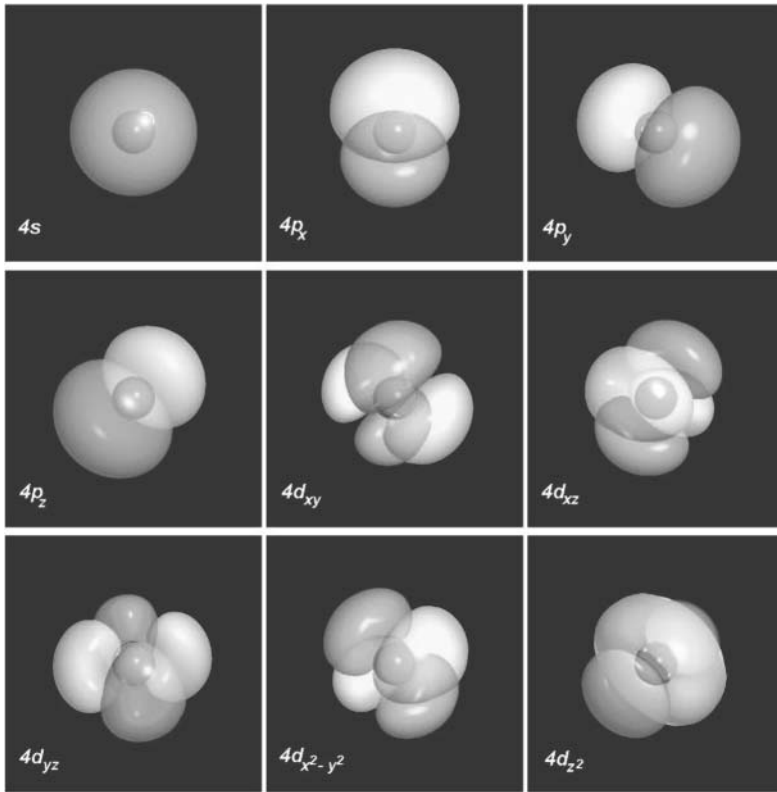


Figure 1.1 Surface plots of representative s, p, and d atomic orbitals (from the Kr valence shell).

The energy eigenvalue ϵ_n depends only on the principal quantum number n ; its value is given (in atomic units; see Appendix C) by

$$\epsilon_n = -\frac{Z^2}{2n^2} \text{ a.u.} \quad (1.12)$$

for atomic number Z ($Z = 1$ for H).

The three quantum numbers may be said to control the size (n), shape (l), and orientation (m) of the orbital Ψ_{nlm} . Most important for orbital visualization are the angular shapes labeled by the azimuthal quantum number l : s-type (spherical, $l = 0$), p-type (“dumbbell,” $l = 1$), d-type (“cloverleaf,” $l = 2$), and so forth. The shapes and orientations of basic s-type, p-type, and d-type hydrogenic orbitals are conventionally visualized as shown in Figs. 1.1 and 1.2. Figure 1.1 depicts a surface of each orbital, corresponding to a chosen electron density near the outer fringes of the orbital. However, a wave-like object intrinsically lacks any definite boundary, and surface plots obviously cannot depict the interesting variations of orbital amplitude *under* the surface. Such variations are better represented by *radial* or *contour*

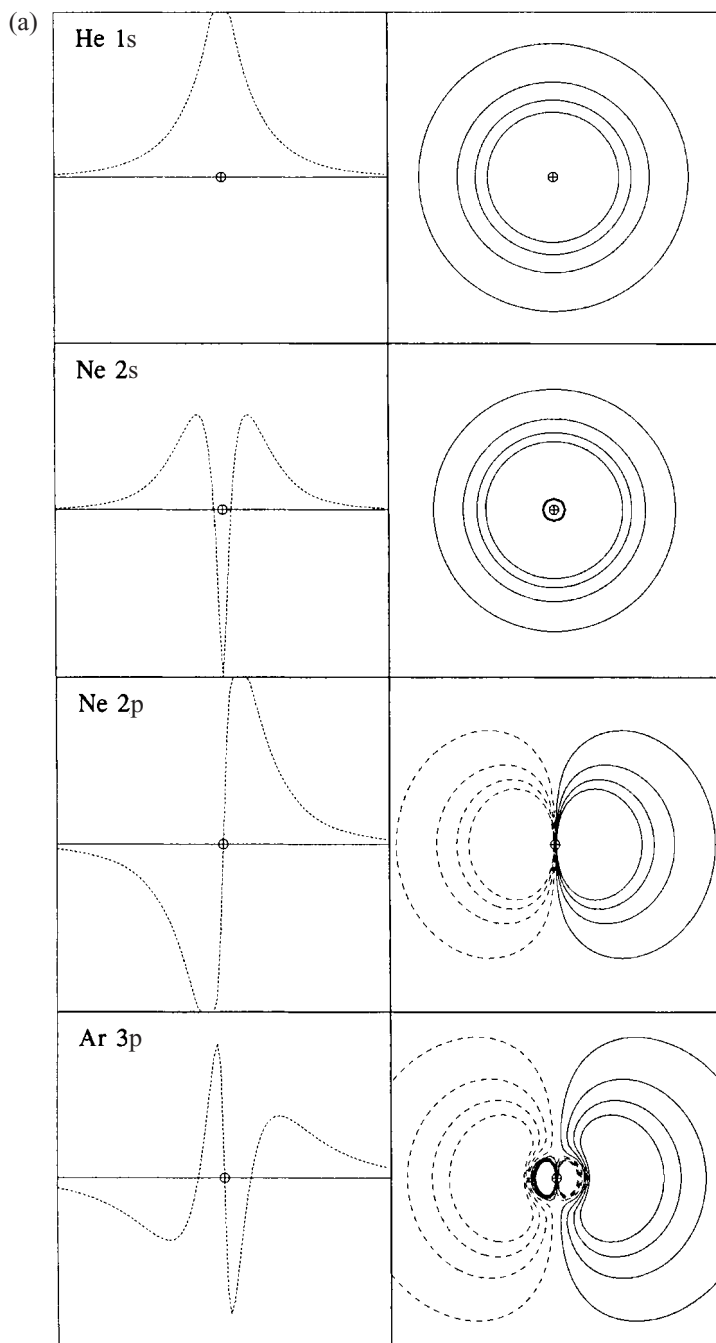


Figure 1.2 (a) Lowest s- and p-type valence atomic orbitals of rare-gas atoms, showing radial profiles (left) and contour plots (right). (Each plot is 3 Å wide, and only the four outermost contours are plotted; see note 26.) (b) Similar to Fig. 1.2(a), for valence 4s, 4p, and 3d atomic orbitals of Kr, corresponding directly to the surface plots of Fig. 1.1.

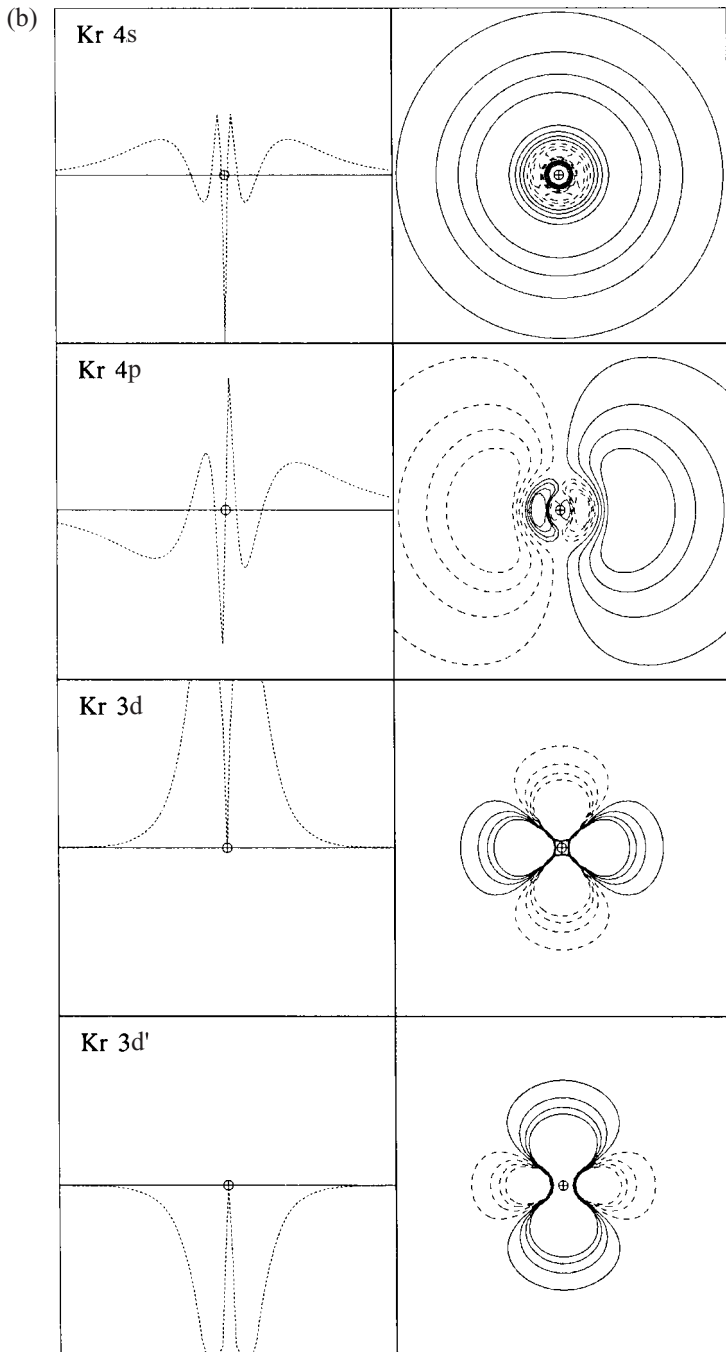


Figure 1.2(b) (Cont.)

plots,²⁶ as shown in Figs. 1.2(a) and (b). Figure 1.2 illustrates representative s, p, and d atomic orbitals for $n = 1 - 4$, showing each orbital in its correct proportionate size to serve as a valence orbital of a rare-gas atom (He, Ne, Ar, or Kr). (The actual plots are of “natural” atomic orbitals, to be described in Section 1.5, but the shapes are practically indistinguishable from those of analytic hydrogenic orbitals, and the diagrams are broadly representative of valence atomic orbitals to be encountered throughout this book.)

Filled and unfilled shells

As one can see from the quantum-number limits in Eqs. (1.11), there is a total of n^2 degenerate (equal-energy) orbitals for each principal quantum number n and energy level ϵ_n . Thus, the orbitals are naturally grouped into *shells*: a single orbital (1s) for $n = 1$, four (2s, 2p_x, 2p_y, and 2p_z) for $n = 2$, and so forth. Only the non-degenerate 1s orbital is occupied in the ground-state H atom, whereas all other solutions are formally vacant.

We are therefore naturally led to ask the following question. What is the physical meaning of such vacant orbitals, which make no contribution to ground-state electron density? The answer is that these orbitals represent the atom’s *capacity for change* in the presence of various *perturbations*. Important examples of such changes include spectral excitations (in the presence of electromagnetic radiation), polarization (in the presence of an external electric field), or chemical transformations (in the presence of other atoms). Indeed, from the viewpoint of valency and chemical reactivity, the vacant (or partially vacant) orbital shells are usually far more important than those of occupied shells. Becoming familiar with the energies and shapes of vacant orbitals is an essential key to understanding the electronic give and take of chemical bonding.

1.3 Many-electron systems: Hartree–Fock and correlated treatments

The Hartree–Fock model

For many-electron atoms, the Schrödinger equation (1.1) cannot be solved exactly. For the carbon atom, for example, the six-electron Hamiltonian operator \hat{H} cannot be written simply as a sum of six one-electron operators $\hat{h}_1, \dots, \hat{h}_6$, due to additional electron–electron repulsion terms (\hat{v}_{ee}). Nevertheless, both theoretical and spectral evidence suggests that the six electrons can be assigned to a *configuration* (1s)²(2s)²(2p)² of hydrogen-like orbitals, each with maximum double occupancy per orbital (one spin “up,” one spin “down”) in accord with the Pauli principle. By choosing the *best possible* orbital product wavefunction $\Psi^{(0)} = \Psi_{\text{HF}}$ corresponding to this single-configuration picture²⁷ we are led to the famous *Hartree–Fock*

approximation, a remarkably simple and successful model of many-electron systems.²⁸

The Hartree–Fock (HF) orbitals ϕ_i can be shown to satisfy a Schrödinger-type eigenvalue equation

$$\hat{F}\phi_i = \epsilon_i\phi_i \quad (1.13a)$$

The Fock operator \hat{F} for an atomic or molecular system is a modified one-electron Hamiltonian (cf. Eq. (1.9b)),

$$\hat{F} = \hat{t}_e + \hat{v}_{ne} + \hat{v}_{ee}^{(av)} \quad (1.13b)$$

that contains a potential-energy term ($\hat{v}_{ee}^{(av)}$) to represent the average (“mean-field”) electron–electron repulsion due to the other $N-1$ electrons. Owing to this mean-field approximation, the motions of a particular electron are not properly “correlated” with the actual dynamical positions of other electrons. The *correlation energy* E_{corr} is defined as the variational energy difference between the true energy and the Hartree–Fock model energy,

$$E_{\text{corr}} = E_{\text{HF}} - E_{\text{true}} \quad (1.14)$$

and serves as a measure of the error due to fluctuations in the true electron–electron repulsions around the mean-field estimate $\hat{v}_{ee}^{(av)}$. E_{corr} is usually of the order of 1% of the total energy, an accuracy sufficient for many chemical purposes. Note that the Hartree–Fock model is a unique and well-defined mathematical construction for any molecular system. Thus, in principle the Fock operator \hat{F} *exists* (as do its eigenfunctions ϕ_i and eigenvalues ϵ_i), even if in practice we obtain only successive numerical approximations to these quantities in any finite-basis calculation.

Electron-correlation corrections

As usual, the Hartree–Fock model can be corrected with perturbation theory (e.g., the Møller–Plesset [MP] method²⁹) and/or variational techniques (e.g., the configuration-interaction [CI] method³⁰) to account for electron-correlation effects. The electron density $\rho(\vec{r}) = N \int |\Psi|^2 d^3\vec{r}_2 \dots d^3\vec{r}_N$ can generally be expressed as

$$\rho(\vec{r}) = \sum_i n_i |\phi_i(\vec{r})|^2 \quad (1.15)$$

where n_i is the number of electrons in orbital ϕ_i ($0 \leq n_i \leq 2$). At the simple HF level, the occupancies n_i are restricted to integer values (0, 1, or 2), but at higher correlated levels these occupancies are non-integer, and the summation includes fractional occupancies of many orbitals that were vacant in the starting HF configuration.

Example 1.2

Let us examine the fluoride ion (F^-), for which variational 6-311++G** calculations give

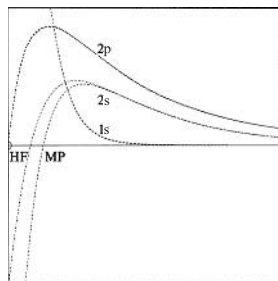
$$E_{\text{HF}} = -99.4457 \text{ a.u.}, \quad E_{\text{MP}} = -99.6976 \text{ a.u.}$$

This leads to the estimated correlation energy

$$E_{\text{corr}}^{(\text{MP})} = 0.2519 \text{ a.u.} \simeq 158 \text{ kcal mol}^{-1}$$

which is only about 0.25% of the total energy (but not negligible on a chemical scale of accuracy!). The table and figure below summarize the effects of electron correlation on the occupancies (n_i) and radial profiles of the F^- occupied orbitals ϕ_i :

ϕ_i	$\epsilon_i(\text{HF})$	$n_i(\text{HF})^a$	$n_i(\text{MP})^a$
1s	-25.8274	2.000	2.000
2s	-1.0702	2.000	1.987
2p	-0.1774	6.000	5.911
3s	—	0.000	0.011
3p	—	0.000	0.079
3d	—	0.000	0.013



^a Sum over m_l sublevels.

The table shows that the HF occupancies are integers that coincide with the formal electron configuration $(1s)^2(2s)^2(2p)^6$, whereas MP occupancies exhibit slight deviations (1%–3% of e) due to electron correlation. For example, the $2s \rightarrow 3s$ configurational excitations needed to describe radial (“in–out”) correlation lead to a shift of about $0.01e$ from the valence $2s$ to the Rydberg $3s$ orbital. The figure displays radial orbital profiles, showing that the HF and MP results are virtually indistinguishable for $1s$ and $2p$ orbitals. However, the MP $2s$ orbital is seen to have stronger (more negative) amplitude at the nucleus as a consequence of radial correlation. We can paraphrase this result by saying that correlated electrons are slightly “smarter” in remaining close to the nucleus, where nuclear attractions are strongest.

The small correlation effects on the n_i 's and ϕ_i 's also lead to slight changes in the electron density $\rho(\vec{r})$ (Eq. (1.15)), which would be perceptible only on a highly expanded plotting scale.

Although HF orbitals are, by definition, the best possible for a single-configuration wavefunction, it is actually possible to find a *better* set of orbitals, called “natural” orbitals,³¹ to describe the correlated $\rho(\vec{r})$. The natural orbitals are maximum-occupancy orbitals, determined from Ψ itself and guaranteed to give fastest possible convergence to $\rho(\vec{r})$, i.e., consistently *higher* occupancies n_i than HF orbitals in Eq. (1.15). For a HF wavefunction the natural orbitals and HF orbitals are equivalent, but for more accurate wavefunctions the natural orbitals allow us to

retain the most HF-like picture of a correlated electron density, leading to the most condensed expression for $\rho(\vec{r})$ in Eq. (1.15). Example 1.2 provides an illustration of how the correlated 2s natural orbital of F^- contracts near the nucleus (compared with the corresponding HF 2s orbital), giving a better description of electron density in this region. Further discussion of natural orbitals is presented in Section 1.5.

Density-functional methods

In recent years *density-functional* methods³² have made it possible to obtain orbitals that mimic correlated natural orbitals *directly* from one-electron eigenvalue equations such as Eq. (1.13a), bypassing the calculation of multi-configurational MP or CI wavefunctions. These methods are based on a modified Kohn–Sham³³ form (\hat{F}_{KS}) of the one-electron effective Hamiltonian in Eq. (1.13a), differing from the HF operator (1.13b) by inclusion of a “correlation potential” (as well as other possible modifications of $(\hat{V}_{ee}^{(av)})$).

The “B3LYP” implementation³⁴ of density-functional theory has proven particularly effective for describing accurate properties of complex chemical systems at practically no increase in computational cost over conventional HF methods. We shall employ the B3LYP version of density-functional theory to obtain the numerical orbitals and electron densities used throughout this book. Note that qualitative valency and bonding concepts are well established even at much simpler levels of theory, so practically no significant changes of our discussion would result from choosing an alternative HF, MP, or CI starting point.

Further details of the underlying computational methods and basis sets to determine the wavefunction and density are described in Appendix A. Unless otherwise noted, all numerical examples of this book employ the B3LYP/6-311++G** level of theory.

1.4 Perturbation theory for orbitals in the Hartree–Fock framework: the donor–acceptor paradigm

The use of the Hartree–Fock model allows the perturbation-theory equations (1.2)–(1.5) to be conveniently recast in terms of underlying orbitals (ϕ_i), orbital energies (ϵ_i), and orbital occupancies (n_i). Such orbital perturbation equations will allow us to treat the complex electronic interactions of the actual many-electron system (described by Fock operator \hat{F}) in terms of a *simpler* non-interacting system (described by unperturbed Fock operator $\hat{F}^{(0)}$). We shall make use of such one-electron perturbation expressions throughout this book to elucidate the origin of chemical bonding effects within the Hartree–Fock model (which can be further refined with post-HF perturbative procedures, if desired).

Hartree–Fock perturbation theory

For the starting HF model, the many-electron $\Psi^{(0)}$ is the antisymmetrized³⁵ product of occupied spin-orbitals $\phi_i^{(0)}(\vec{r}_i)$,

$$\Psi^{(0)}(1, 2, \dots, N) = \hat{\mathcal{A}}[\phi_1^{(0)}(\vec{r}_1)\phi_2^{(0)}(\vec{r}_2)\dots\phi_N^{(0)}(\vec{r}_N)] \quad (1.16a)$$

$E^{(0)}$ is the sum of corresponding orbital energies,

$$E^{(0)} = \epsilon_1^{(0)} + \epsilon_2^{(0)} + \dots + \epsilon_N^{(0)} \quad (1.16b)$$

and $\hat{H}^{(0)}$ is a sum of one-electron unperturbed $\hat{F}_i^{(0)}$ operators,

$$\hat{H}^{(0)} = \hat{F}_1^{(0)} + \hat{F}_2^{(0)} + \dots + \hat{F}_N^{(0)} \quad (1.16c)$$

one for each electron. For example, $\hat{F}^{(0)}$ might be the Fock operator for a hypothetical system of electrons in *non*-interacting H-atom orbitals, whereas \hat{F} is the actual Fock operator for the full system. The many-electron perturbation operator $\hat{H}^{(\text{pert})}$, Eq. (1.3), can therefore be written as a sum of one-electron perturbations,

$$\hat{H}^{(\text{pert})} = \hat{F}_1^{(\text{pert})} + \hat{F}_2^{(\text{pert})} + \dots + \hat{F}_N^{(\text{pert})} \quad (1.17a)$$

where, for electron μ ,

$$\hat{F}_\mu^{(\text{pert})} = \hat{F}_\mu - \hat{F}_\mu^{(0)} \quad (1.17b)$$

Note that the subscript (μ) of $\hat{F}_\mu^{(\text{pert})}$ is the “name” of the electron described by the unperturbed Schrödinger equation,

$$\hat{F}_\mu^{(0)}\phi_i^{(0)}(\vec{r}_\mu) = \epsilon_i^{(0)}\phi_i^{(0)}(\vec{r}_\mu) \quad (1.18)$$

However, the Pauli principle makes all electrons equivalent, so we can generally suppress this subscript in the equations to follow. As usual, the solutions of Eq. (1.18) are mutually orthogonal ($\langle\phi_i^{(0)}|\phi_j^{(0)}\rangle = \delta_{ij}$) and the associated $\epsilon_i^{(0)}$ ’s are real for any physically meaningful (Hermitian) $\hat{F}^{(0)}$.

Example 1.3

We consider again (cf. Example 1.1) the case of Li in the basis of 1s and 2s NAOs, for which the Fock operator of α spin has the 2×2 matrix form

$$\hat{F} = \begin{pmatrix} -2.0294 & 0.0019 \\ 0.0019 & -0.1340 \end{pmatrix}$$

From matrix elements of the operators comprising \hat{F} (cf. Eq. (1.13b)),³⁶ we can decompose $\hat{F} = \hat{F}^{(0)} + \hat{F}^{(\text{pert})}$ into unperturbed ($\hat{F}^{(0)}$) and perturbation ($\hat{F}^{(\text{pert})}$) operators in many possible ways.

(1) *kinetic plus potential energy:*

$$\hat{F}^{(0)} = \hat{t}_e = \begin{pmatrix} 3.0094 & -0.6074 \\ -0.6074 & 0.1678 \end{pmatrix}, \quad \hat{F}^{(\text{pert})} = \hat{v}_{\text{ne}} + \hat{v}_{\text{ee}}^{(\text{av})} = \begin{pmatrix} -5.0388 & 0.6093 \\ 0.6093 & -0.3078 \end{pmatrix}$$

(2) *one-electron plus two-electron terms:*

$$\hat{F}^{(0)} = \hat{t}_e + \hat{v}_{\text{ne}} = \begin{pmatrix} -2.8452 & 0.1659 \\ 0.1659 & -0.9230 \end{pmatrix}, \quad \hat{F}^{(\text{pert})} = \hat{v}_{\text{ee}}^{(\text{av})} = \begin{pmatrix} 0.8158 & -0.1640 \\ -0.1640 & 0.7890 \end{pmatrix}$$

(3) *diagonal plus non-diagonal terms (cf. Example 1.1):*

$$\hat{F}^{(0)} = \begin{pmatrix} -2.0294 & 0 \\ 0 & -0.1340 \end{pmatrix}, \quad \hat{F}^{(\text{pert})} = \begin{pmatrix} 0 & -0.0019 \\ -0.0019 & 0 \end{pmatrix}$$

Although any of these decompositions might be employed in the formal machinery of perturbation theory, one can expect that choices of $\hat{F}^{(0)}$ for which the perturbation elements in $\hat{F}^{(\text{pert})}$ are *small* will lead to more rapid convergence, and thus serve as better models.

By substituting Eqs. (1.16) and (1.17) into the general perturbation expressions (1.5), we can write the total first- and second-order corrections in the form

$$E^{(1)} = \sum_i E_i^{(1)} \quad (1.19a)$$

$$E^{(2)} = \sum_i E_i^{(2)} \quad (1.19b)$$

where

$$E_i^{(1)} = n_i^{(0)} \langle \phi_i^{(0)} | \hat{F}^{(\text{pert})} | \phi_i^{(0)} \rangle \quad (1.20a)$$

$$E_i^{(2)} \leq -n_i^{(0)} \frac{\langle \phi_i^{(0)} | \hat{F}^{(\text{pert})} | \tilde{\phi} \rangle^2}{\langle \tilde{\phi} | \hat{F}^{(0)} - \epsilon_i^{(0)} | \tilde{\phi} \rangle} \quad (1.20b)$$

In these expressions, $n_i^{(0)}$ is the number (0, 1, or 2) of electrons occupying spatial orbital $\phi_i^{(0)}$ in $\Psi^{(0)}$, and $\tilde{\phi}$ is a variational trial function (orthogonal to $\phi_i^{(0)}$) for the first-order orbital correction $\phi_i^{(1)}$. The expressions (1.20) allow us to treat the perturbative effects on an orbital-by-orbital basis, isolating the corrections associated with each HF orbital ϕ_i . Equations (1.18)–(1.20) involve only *single*-electron operators and integrations, and are therefore considerably simpler than (1.5c) and (1.5d).

We can further simplify the treatment by noting that $E^{(1)}$ is merely a constant that can be added to $\hat{H}^{(0)}$ and subtracted from $\hat{H}^{(\text{pert})}$ (leaving the total \hat{H} unmodified), giving a “shift in the zero of the energy scale” for $E^{(0)}$ and making $E^{(1)} = 0$. Thus, we may assume without loss of generality that $\hat{H}^{(0)}$ and $\hat{F}^{(0)}$ are chosen to make the first-order corrections vanish, so that (1.20b) is the leading correction.

We can also simplify (1.20b) by noting that $\hat{F}^{(\text{pert})}$ can be replaced in the numerator by \hat{F} , because $\langle \phi_i^{(0)} | \hat{F}^{(0)} | \tilde{\phi} \rangle = 0$ for any $\tilde{\phi}$ orthogonal to $\phi_i^{(0)}$. We can further

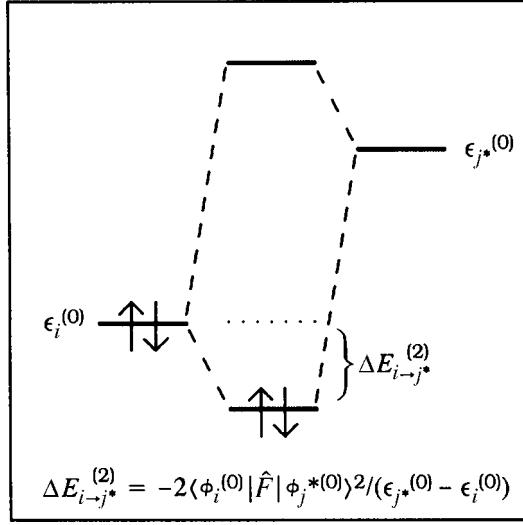


Figure 1.3 The two-electron stabilizing interaction between a filled donor orbital $\phi_i^{(0)}$ and an unfilled acceptor orbital $\phi_{j^*}^{(0)}$, corresponding to perturbation Eq. (1.24).

choose $\tilde{\phi}$ to be a *normalized* trial function, and define

$$\tilde{\epsilon} = \langle \tilde{\phi} | \hat{F}^{(0)} | \tilde{\phi} \rangle \quad (1.21)$$

Then (1.20b) is expressed equivalently as

$$E_i^{(2)} \leq -n_i^{(0)} \frac{\langle \phi_i^{(0)} | \hat{F} | \tilde{\phi} \rangle^2}{\tilde{\epsilon} - \epsilon_i^{(0)}} \quad (1.22)$$

Moreover, it will often occur that the best possible perturbative trial function $\tilde{\phi}$ is dominated by a *single* unperturbed orbital $\phi_{j^*}^{(0)}$ (with $n_{j^*}^{(0)} = 0$, the asterisk denoting an initially unoccupied excited-state orbital), so that we can approximate

$$\tilde{\phi} = \phi_{j^*}^{(0)} \quad (1.23a)$$

$$\tilde{\epsilon} = \epsilon_{j^*}^{(0)} \quad (1.23b)$$

In this case, we can label the second-order correction as an “ $i \rightarrow j^*$ ” correction and write (1.22) as

$$E_{i \rightarrow j^*}^{(2)} = -n_i^{(0)} \frac{\langle \phi_i^{(0)} | \hat{F} | \phi_{j^*}^{(0)} \rangle^2}{\epsilon_{j^*}^{(0)} - \epsilon_i^{(0)}} \quad (1.24)$$

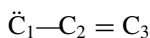
Donor–acceptor stabilization

Equation (1.24) expresses a simple but powerful physical idea, as illustrated (for $n_i^{(0)} = 2$) in Fig. 1.3. This figure shows the unperturbed energy levels for a doubly

occupied “donor” orbital $\phi_i^{(0)}$ and an unoccupied “acceptor” orbital $\phi_{j^*}^{(0)}$, interacting to give the energy lowering $E_{i \rightarrow j^*}^{(2)}$ as expressed by Eq. (1.24). (Figure 1.3 illustrates that there is an equal and opposite *raising* of the perturbed level for $\phi_{j^*}^{(0)}$, but this orbital remains vacant and thus contributes no energy change to the system.) It can be seen from Eq. (1.24) and Fig. 1.3 that the energy shift $E_{i \rightarrow j^*}^{(2)}$ is necessarily *negative*, because $\epsilon_{j^*}^{(0)} \geq \epsilon_i^{(0)}$ for any unoccupied $\phi_{j^*}^{(0)}$, and the interaction is therefore stabilizing (regardless of the form of \hat{F}). The donor–acceptor interaction depicted in Fig. 1.3 is often referred to as a “two-electron stabilizing interaction” to indicate that only the *number* of electrons sharing the two orbitals (rather than, e.g., the energies or shapes of the orbitals) is sufficient to guarantee quantum-mechanical energy lowering. It is a quite remarkable feature of quantum-mechanical superposition that a low-lying filled orbital $\phi_i^{(0)}$ can always further *lower* its energy by mixing with a *higher*-energy unoccupied orbital $\phi_{j^*}^{(0)}$, no matter what the details of the Hamiltonian. The general capacity of atomic and molecular species to make judicious use of available filled and unfilled orbitals is therefore a fundamental guiding principle of chemical valency and bonding.

Example 1.4

For the allyl anion, a localized Lewis structure for the π system is



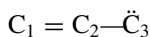
with filled orbitals n_1 and π_{23} and unfilled orbital π_{23}^* , corresponding to the electron configuration

$$(n_1)^2(\pi_{23})^2$$

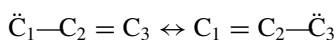
The $n_1 \rightarrow \pi_{23}^*$ donor–acceptor interaction (i.e., $\phi_i^{(0)} = n_1$, $\phi_{j^*}^{(0)} = \pi_{23}^*$ in Eq. (1.24) and Fig. 1.3) represents a partial admixture of the configuration in which two electrons are removed from the lone pair on C_1 and transferred into the $C_2 - C_3$ antibond. This can be represented equivalently as

$$(n_1)^0(\pi_{23})^2(\pi_{23}^*)^2 = (n_1)^0(n_2)^2(n_3)^2 = (\pi_{12})^2(n_3)^2$$

where we rewrite $(n_1)^0(n_2)^2$ as a “polarized π bond” π_{12} . This new configuration evidently represents the alternative



Lewis structure. Thus, the donor–acceptor interaction in this case is equivalent to the “resonance” between Lewis structures



which is known to be intrinsically stabilizing.

1.5 Density matrices, natural localized and delocalized orbitals, and the Lewis-structure picture

We now introduce a set of quantities that are closely related to the electron density $\rho(\vec{r})$, but provide still more detailed information about one-particle subsystems of the N -particle system described by Ψ .

The first-order density operator

The *first-order reduced density operator* $\hat{\gamma}$ can be defined in terms of its kernel function³⁷

$$\gamma(\vec{r}_1|\vec{r}_1') = N \int \Psi(\vec{r}_1, \vec{r}_2, \dots, \vec{r}_N) \Psi^*(\vec{r}_1', \vec{r}_2, \dots, \vec{r}_N) d^3\vec{r}_2 \dots d^3\vec{r}_N \quad (1.25)$$

for any N -electron wavefunction Ψ . (Note that the Pauli principle enforces democracy among all electrons, so we normally drop the label of the preferred electron “1” in Eq. (1.25).) As defined in Eq. (1.25), $\gamma(\vec{r}|\vec{r}')$ is a function of two continuous indices \vec{r} and \vec{r}' and thus can be treated as a type of “continuous matrix.” However, this function is more properly regarded as the kernel of an *integral operator* $\hat{\gamma}$ that operates on a general one-particle (orbital) function $f(\vec{r})$ according to the rule³⁸

$$\hat{\gamma} f(\vec{r}) = g(\vec{r}) = \int \gamma(\vec{r}|\vec{r}') f(\vec{r}') d^3\vec{r}' \quad (1.26)$$

Usually, no confusion is incurred if we treat the kernel $\gamma(\vec{r}|\vec{r}')$ (which defines the operator through Eq. (1.26)) and the operator $\hat{\gamma}$ rather interchangeably. Note that the density operator is as unique and well defined as Ψ itself, although in practice we obtain this operator only in finite numerical approximations.

Example 1.5

For a closed-shell HF wavefunction, with doubly occupied molecular orbitals (MOs) $\phi_1, \phi_2, \dots, \phi_{\text{occ}}$,

$$\Psi_{\text{HF}} = \det|\phi_1^2 \phi_2^2 \dots \phi_{\text{occ}}^2|$$

it can be shown that the density kernel takes the form

$$\begin{aligned} \gamma_{\text{HF}}(\vec{r}_1|\vec{r}_1') &= N \int \Psi_{\text{HF}}(\vec{r}_1, \vec{r}_2, \dots, \vec{r}_N) \Psi_{\text{HF}}^*(\vec{r}_1', \vec{r}_2, \dots, \vec{r}_N) d^3\vec{r}_2 \dots d^3\vec{r}_N \\ &= 2 \sum_i^{\text{occ}} \phi_i(\vec{r}_1) \phi_i^*(\vec{r}_1') \end{aligned}$$

and the corresponding density operator is symbolized as

$$\hat{\gamma}_{\text{HF}} = 2 \sum_{i=1}^{\text{occ}} |\phi_i\rangle \langle \phi_i|$$

i.e., as a sum of projection operators over occupied MOs, each multiplied by its occupancy (2). Let us use these equations to evaluate the matrix elements (γ_{jk}) of $\hat{\gamma}_{\text{HF}}$ in a basis of atomic orbitals $\{\mathcal{X}_j\}$

$$\gamma_{jk} = \langle \mathcal{X}_j | \hat{\gamma}_{\text{HF}} | \mathcal{X}_k \rangle = 2 \sum_{i=1}^{\text{occ}} \langle \mathcal{X}_j | \phi_i \rangle \langle \phi_i | \mathcal{X}_k \rangle$$

Using the familiar LCAO-MO expansion of ϕ_i ,

$$\phi_i = \sum_j c_{ij} \mathcal{X}_j$$

we can recognize that, for an orthonormal basis set,

$$\langle \mathcal{X}_j | \phi_i \rangle = c_{ij}, \quad \langle \phi_i | \mathcal{X}_k \rangle = c_{ik}^*$$

The matrix elements γ_{jk} of the density operator are therefore

$$\gamma_{jk} = (\mathbf{D})_{jk} = 2 \sum_{i=1}^{\text{occ}} c_{ij} c_{ik}^*$$

or, in matrix form,

$$\mathbf{D} = 2 \sum_{i=1}^{\text{occ}} \mathbf{c}_i \mathbf{c}_i^\dagger$$

where \mathbf{c}_i is the column vector of LCAO coefficients of MO ϕ_i . In simple Hückel π -electron theory, the density matrix \mathbf{D} is called the ‘‘Coulson charge and bond-order matrix,’’ because its diagonal element $(\mathbf{D})_{jj}$ is the π charge on atom j , and its off-diagonal element $(\mathbf{D})_{jk}$ is the MO π bond order between atoms j and k .

In any complete, orthonormal basis set of orbitals $\{\mathcal{X}_i\}$, $\gamma(\vec{r}|\vec{r}')$ can be expanded as

$$\gamma(\vec{r}|\vec{r}') = \sum_{i,j} \gamma_{ij} \mathcal{X}_i(\vec{r}) \mathcal{X}_j^*(\vec{r}') \quad (1.27)$$

where $\gamma_{ij} = (\mathbf{D})_{ij}$ are elements of the *density matrix* \mathbf{D} (the representation of $\hat{\gamma}$ as a conventional discrete matrix).³⁹ By setting the ‘‘indices’’ \vec{r} and \vec{r}' equal in $\gamma(\vec{r}|\vec{r}')$ we obtain the local electron density at \vec{r} as a ‘‘diagonal element’’ of $\hat{\gamma}$,

$$\gamma(\vec{r}|\vec{r}) = \rho(\vec{r}) \quad (1.28)$$

However, the more general $\gamma(\vec{r}|\vec{r}')$ allows evaluation of any single-particle property, including non-local operators that do not depend on $\rho(\vec{r})$ alone (e.g., kinetic energy \hat{t}_e). As originally shown by Husimi,³⁷ $\hat{\gamma}$ allows one to address experimental questions pertaining to one-electron *subsystems* of a many-electron system rigorously. At the Hartree–Fock level (cf. Example 1.5), it can be shown that knowledge



Per-Olov Löwdin

of $\hat{\gamma}$ is equivalent to full knowledge of Ψ_{HF} , so the density operator is indeed a formidable alternative oracle of chemical knowledge.

Natural orbitals: NAOs and NBOs

As shown by P.-O. Löwdin,⁴⁰ the complete information content of $\hat{\gamma}$ can be obtained from its eigenorbitals, the “natural” orbitals θ_i , and the corresponding eigenvalues n_i ,

$$\hat{\gamma}\theta_i = n_i\theta_i \quad (1.29)$$

where $n_i = \langle \theta_i | \hat{\gamma} | \theta_i \rangle$ is the occupancy of natural orbital θ_i . General minimum/maximum properties of the eigenvalue equation for $\hat{\gamma}$ guarantee that the θ_i 's are *maximum-occupancy* orbitals (highest possible n_i 's, within the general Pauli restriction $0 \leq n_i \leq 2$), and thus lead to the most rapidly convergent possible expansions of the electron density and other one-electron properties. The exquisite properties of these orbitals amply justify their designation as “natural” orbitals – intrinsic to Ψ itself rather than an arbitrarily chosen basis set.

Example 1.6

Let us consider the simple case of the H atom and its variational approximation at the standard HF/3-21G level, for which we can follow a few of the steps in terms of corresponding density-matrix manipulations. After symmetrically orthogonalizing the two basis orbitals of the 3-21G set to obtain orthonormal basis functions \mathcal{X}_{1s} and \mathcal{X}_{2s} , we obtain the corresponding AO form of the density operator (i.e., the 2×2 matrix representation of $\hat{\gamma}$ in the

basis \mathcal{X}_{1s} and \mathcal{X}_{2s}) as

$$\hat{\gamma}^{(\text{AO})} = \begin{pmatrix} 0.6431 & 0.4791 \\ 0.4791 & 0.3568 \end{pmatrix}$$

From this matrix we see that

$$\gamma_{11} = \langle \mathcal{X}_{1s} | \hat{\gamma} | \mathcal{X}_{1s} \rangle = 0.6431$$

$$\gamma_{22} = \langle \mathcal{X}_{2s} | \hat{\gamma} | \mathcal{X}_{2s} \rangle = 0.3568$$

i.e., that \mathcal{X}_{1s} contains $0.6431e$ and \mathcal{X}_{2s} contains $0.3568e$, far below the expected maximum occupancy of natural orbitals. In this basis set the electron density has the unwieldy form (cf. Eqs. (1.27) and (1.28)),

$$\rho(\vec{r}) = 0.6431 |\mathcal{X}_{1s}(\vec{r})|^2 + 0.3568 |\mathcal{X}_{2s}(\vec{r})|^2 + 2 \cdot 0.4791 \mathcal{X}_{1s}(\vec{r}) \mathcal{X}_{2s}(\vec{r})$$

To find the natural orbitals $\{\theta_i\}$ of this system, we diagonalize the 2×2 matrix $\hat{\gamma}^{(\text{AO})}$ to obtain the eigenvectors and eigenvalues shown below:

	eigenvector	eigenvalue
1.	$\begin{pmatrix} 0.8020 \\ 0.5974 \end{pmatrix}$	1.0000
2.	$\begin{pmatrix} 0.5974 \\ -0.8020 \end{pmatrix}$	0.0000

From the eigenvectors we obtain the natural orbitals in the form

$$\theta_1 = 0.8020 \mathcal{X}_{1s} + 0.5974 \mathcal{X}_{2s},$$

$$\theta_2 = 0.5974 \mathcal{X}_{1s} - 0.8020 \mathcal{X}_{2s},$$

and from the eigenvalues we obtain the corresponding occupancies

$$n_1 = \langle \theta_1 | \hat{\gamma} | \theta_1 \rangle = 1.0000$$

$$n_2 = \langle \theta_2 | \hat{\gamma} | \theta_2 \rangle = 0.0000$$

The occupancy of θ_1 is obviously the maximum possible in this one-electron system, so θ_1 is indeed a natural orbital. In terms of natural orbitals, the density operator takes the form

$$\hat{\gamma}^{(\text{NO})} = \begin{pmatrix} 1.0000 & 0.0000 \\ 0.0000 & 0.0000 \end{pmatrix}$$

and the electron density is condensed to a single term,

$$\rho(\vec{r}) = |\theta_1(\vec{r})|^2$$

The natural orbital θ_1 is equivalent to the variational Hartree–Fock 1s orbital in this case, much closer to the exact hydrogenic solution discussed in Section 1.2.

By restricting the search for maximum-occupancy eigenorbitals to a localized atomic block $\hat{\gamma}$ associated with atom A, one can obtain the optimal set of *natural*

atomic orbitals (NAOs)⁴¹ $\theta_i^{(A)}$, with occupancy $n_i^{(A)}$. The NAOs reduce smoothly to the ordinary natural orbitals of isolated atoms in the dissociation limit, but they retain the maximal-occupancy property *in the molecular environment* and thus continue to serve as “best possible” AOs at all separations. By searching for the highest-occupancy (near-pair) eigenorbitals in each diatomic A—B bonding region, one can similarly obtain the optimal *natural bond orbitals* (NBOs)⁴² $\theta_i^{(AB)}$, with occupancy $n_i^{(AB)}$. The detailed computational algorithms for determining NAOs and NBOs are beyond the scope of this book.⁴³ However, these algorithms are implemented in the general NBO program⁴⁴ and incorporated in a number of popular electronic structure packages (see the NBO website⁴⁵ for current implementations, tutorials, sample output, and other background information), which make it easy to obtain the NAOs and NBOs for any chemical system of practical interest.

Note that the NAOs, NBOs, and associated occupancies are in principle uniquely determined by $\hat{\gamma}$, and thus by Ψ itself. In practice, the NBO-based quantities are found to converge rapidly to well-defined numerical limits, independently of the numerical basis set or other arbitrary details of approximating Ψ . In the present work, the level of describing Ψ will be taken to be sufficiently high that we can generally ignore the small differences that distinguish numerically determined NBOs from the infinite-basis limit.

Like the delocalized natural orbitals $\{\theta_i\}$ of the full system, the localized NAOs $\{\theta_i^{(A)}\}$ and NBOs $\{\theta_i^{(AB)}\}$ have optimal convergence properties for describing localized atomic and bonding regions. Both NAOs and NBOs form a complete, orthonormal set; for example, the NAOs $\{\theta_i^{(A)}\}$ satisfy

$$\langle \theta_i^{(A)} | \theta_j^{(B)} \rangle = \delta_{AB} \delta_{ij} \quad (1.30)$$

Thus, these orbitals can be used to represent *exactly* any property of the system in localized terms. The NAOs divide naturally into a leading high-occupancy set (the “natural minimal basis”) and a residual low-occupancy set (the “natural Rydberg basis”), where the occupancies of the latter orbitals are usually quite negligible for chemical purposes. Thus, even if the underlying variational basis set is of high dimensionality (6-311++G** for the applications of this book), a perturbative analysis couched in NAO terms has the simplicity of an elementary minimal-basis treatment without appreciable loss of chemical accuracy.

Example 1.7

For the H₂ molecule with four basis AOs $\chi_1^{(A)}$, $\chi_2^{(A)}$, $\chi_1^{(B)}$, and $\chi_2^{(B)}$ (non-orthogonal 3-21G basis), the AO density matrix is

$$\hat{\gamma}^{(\text{AO})} = \begin{pmatrix} 1.1540 & 1.3616 & 1.1540 & 1.3616 \\ 1.3616 & 1.6065 & 1.3616 & 1.6065 \\ 1.1540 & 1.3616 & 1.1540 & 1.3616 \\ 1.3616 & 1.6065 & 1.3616 & 1.6065 \end{pmatrix}$$

Diagonalization of the 2×2 atomic subblocks (cf. Example 1.4) leads to NAOs $\theta_1^{(A)}$, $\theta_2^{(A)}$, $\theta_1^{(B)}$, and $\theta_2^{(B)}$ that transform the density operator into

$$\hat{\gamma}^{(\text{NAO})} = \begin{pmatrix} 1 & 0 & 1 & 0 \\ 0 & 0 & 0 & 0 \\ 1 & 0 & 1 & 0 \\ 0 & 0 & 0 & 0 \end{pmatrix}$$

with singly occupied NAOs $\theta_1^{(A)}$ and $\theta_1^{(B)}$ on each atom (i.e., $\langle \theta_1^{(A)} | \hat{\gamma} | \theta_1^{(A)} \rangle = \langle \theta_1^{(B)} | \hat{\gamma} | \theta_1^{(B)} \rangle = 1$). Diagonalization of the two-atom $\hat{\gamma}^{(\text{NAO})}$ matrix leads finally to four NBOs

$$\begin{aligned} \sigma_{\text{AB}} &= 0.7071\theta_1^{(A)} + 0.7071\theta_1^{(B)} \\ \sigma_{\text{AB}}^* &= 0.7071\theta_1^{(A)} - 0.7071\theta_1^{(B)} \\ r_{\text{A}}^* &= \theta_2^{(A)} \\ r_{\text{B}}^* &= \theta_2^{(B)} \end{aligned}$$

that transform the density operator into

$$\hat{\gamma}^{(\text{NBO})} = \begin{pmatrix} 2 & 0 & 0 & 0 \\ 0 & 0 & 0 & 0 \\ 0 & 0 & 0 & 0 \\ 0 & 0 & 0 & 0 \end{pmatrix}$$

with doubly occupied bonding NBO σ_{AB} (i.e., $\langle \sigma_{\text{AB}} | \hat{\gamma} | \sigma_{\text{AB}} \rangle = 2$) and three unoccupied NBOs (antibond σ_{AB}^* , Rydberg orbitals r_{A}^* and r_{B}^*). In this case, $\hat{\gamma}^{(\text{NBO})}$ is identical to the density operator in the MO basis, because the occupied NBO and MO are identical.

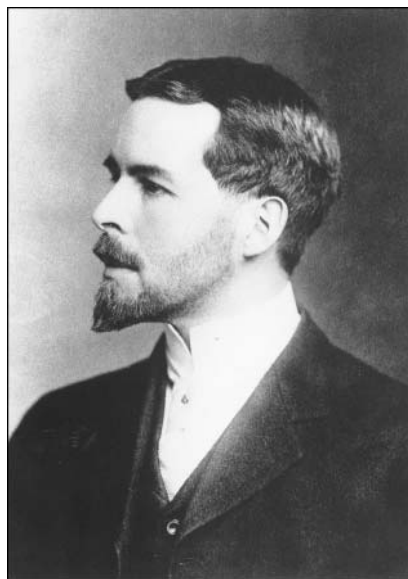
Natural Lewis structures

The $N/2$ ‘‘Lewis-type’’ NBOs of highest occupancy ($n_i^{(\text{AB})} \simeq 2$) can be directly associated with the localized electron pairs of the chemist’s *Lewis-structure* diagram.⁴⁶ Each Lewis-type NBO Ω_{AB} can be decomposed into constituent *natural hybrid orbitals* (NHOs) h_{A} and h_{B} on atoms A and B,

$$\Omega_{\text{AB}} = c_{\text{A}}h_{\text{A}} + c_{\text{B}}h_{\text{B}} \quad (1.31a)$$

with *polarization coefficients* c_{A} and c_{B} satisfying $|c_{\text{A}}|^2 + |c_{\text{B}}|^2 = 1$. The bonding hybrids h_{A} and h_{B} are constructed from NAOs on atoms A and B in a manner that closely resembles the classical Pauling hybridization picture,⁴⁷ but all details of NHO hybridization and polarization are numerically optimized to give the best possible description of electron density. The two valence hybrids h_{A} and h_{B} give rise to two valence-shell NBOs: an *in-phase* Lewis-type NBO (1.31a) and a corresponding *out-of-phase* ‘‘non-Lewis’’ NBO Ω_{AB}^* ,

$$\Omega_{\text{AB}}^* = c_{\text{B}}h_{\text{A}} - c_{\text{A}}h_{\text{B}} \quad (1.31b)$$



Gilbert N. Lewis

(which is unoccupied in the Lewis-structure picture). The set of Lewis-type NBOs typically includes a one-center core (labeled “CR” in the NBO program output) and a valence lone pair (“LP”) as well as two-center bond (“BD”) orbitals. The non-Lewis set includes unoccupied valence nonbonding (“LP*”) and extra-valence-shell Rydberg (“RY*”) orbitals as well as the valence antibonds (“BD*”) of Eq. (1.31b). Thus, the NBOs form a “chemist’s basis set” of Lewis-type (unstarred) and non-Lewis-type (starred) orbitals, each member being closely associated with some aspect of the localized Lewis structure diagram or its capacity for chemical change.

Example 1.8

Let us consider the hydrogen fluoride (HF) molecule as a simple example. The conventional Lewis structure diagram of this molecule



corresponds to a sigma bond (σ_{HF}) and three fluorine lone pairs (n_{F} , n_{F}' , and n_{F}''), as well as the fluorine core pair (K_{F}). A portion of the NBO output (slightly edited) is shown below:

NATURAL BOND ORBITAL ANALYSIS:

(Occupancy) Bond orbital/ Coefficients/ Hybrids

1.	(2.00000)	BD (1)	H 1- F 2		
	(22.39%)	0.4732*	H 1 s(99.89%)	p 0.00 (0.11%)	
	(77.61%)	0.8810*	F 2 s(20.93%)	p 3.77 (78.95%)	d 0.01(0.12%)
2.	(1.99994)	CR (1)	F 2	s (100.00%)	
3.	(1.99940)	LP (1)	F 2	s (79.14%)	p 0.26(20.86%)
4.	(1.99791)	LP (2)	F 2	s (0.00%)	p 1.00(99.97%)
5.	(1.99791)	LP (3)	F 2	s (0.00%)	p 1.00(99.97%)

NBO 1 is the σ_{HF} bond (“BD”), which can be written in the form of Eq. (1.31a) as

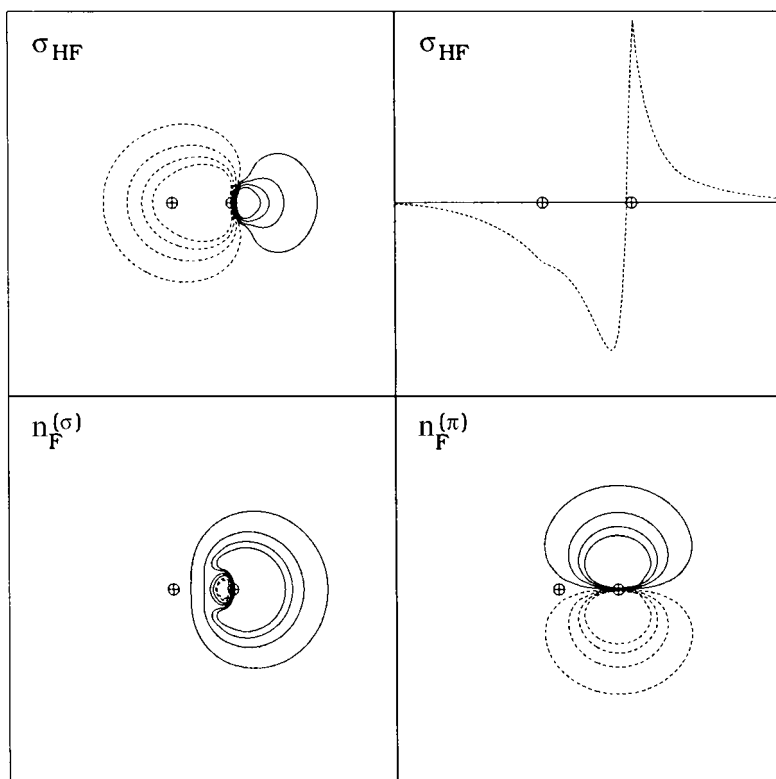
$$\sigma_{\text{HF}} = 0.88(\text{sp}^{3.77})_{\text{F}} + 0.47(1s)_{\text{H}}$$

(The fluorine $\text{sp}^{3.77}$ hybrid [with 78.95% p character; see Example 2.2] also has weak d-orbital contributions [0.12%] that can usually be ignored.) The polarization coefficients indicate that about 77.6% of the electron density is polarized toward the more electronegative F atom.

NBO 2 is the K_{F} core (“CR”) orbital, of 100% s character.

NBOs 3–5 are the three fluorine lone pairs (“LP”). As shown by the occupancies and hybrid composition, these lone pairs are inequivalent. LP(1) is the s-rich sigma-type $\text{sp}^{0.26}$ lone pair ($n_{\text{F}}^{(\sigma)}$; 79% s character), directed along the bond axis. LP(2) and LP(3) are the p-rich pi-type lone pairs ($n_{\text{F}}^{(\pi)}$ and $n_{\text{F}}^{(\pi')}$; 99.97% p-character), perpendicular to the bond axis. The lone “pairs” have occupancies slightly less than 2.000 00 (due to weak delocalization into Rydberg orbitals of the adjacent H), but overall, the correspondence with the elementary Lewis-structure description is excellent.

Contour and amplitude profile plots of the σ_{HF} bond (upper panels) and contour plots of the $n_{\text{F}}^{(\sigma)}$ and $n_{\text{F}}^{(\pi)}$ lone pairs (lower panels) are illustrated below:



The localized wavefunction $\psi^{(L)}$ formed from $N/2$ doubly occupied Lewis-type NBOs,

$$\psi^{(L)} = \hat{A}[(\Omega_{AB})^2(\Omega_{CD})^2 \dots] \quad (1.32)$$

corresponds to an idealized *natural Lewis-structure* picture. As usual, the wavefunction (1.32) can be associated with the Hamiltonian $\hat{H}^{(L)}$ and energy $E^{(L)}$ of a strictly localized Lewis-structure “model chemistry,” with Schrödinger equation

$$\hat{H}^{(L)}\psi^{(L)} = E^{(L)}\psi^{(L)} \quad (1.33)$$

By taking Eq. (1.33) as the starting unperturbed Eq. (1.2), one can analyze delocalization corrections to the localized Lewis structure picture by the perturbative formalism of Eqs. (1.3)–(1.5) and Section 1.4. Valency and bonding phenomena can thereby be dissected into localized and delocalized contributions in a numerically explicit manner. This, in overview, is the strategy to be employed for chemical phenomena throughout this book.

Example 1.9

For hydrogen fluoride, which is well described by a single Lewis structure (cf. Example 1.6), the localized natural Lewis-structure model wavefunction gives

$$E^{(L)} = -100.464\,27 \text{ a.u.}$$

differing by only 0.018 11 a.u. (11.4 kcal mol⁻¹, 0.02%) from the full energy

$$E_{\text{full}} = -100.482\,38 \text{ a.u.}$$

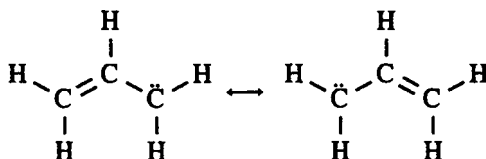
The error of $\psi^{(L)}$ can also be expressed in terms of the “non-Lewis density” $\rho^* = \rho^{(\text{NL})}$, the total occupancy of non-Lewis orbitals in Ψ_{full} . For HF this quantity is

$$\rho^* = 0.004\,77e$$

which is only 0.05% of the total integrated electron density ρ (10e). Thus, by either an energetic or a density criterion, HF is a well-localized molecule.

Example 1.10

An example of a more strongly delocalized species is the allyl anion, which is conventionally described in terms of two resonance structures:



In this case the energy of the natural Lewis-structure model

$$E^{(L)} = -116.965\,62 \text{ a.u.}$$

differs from the full energy

$$E_{\text{full}} = -117.314\,08 \text{ a.u.}$$

by 0.348 46 a.u. (218.7 kcal mol⁻¹, 0.30%), a much larger absolute and relative error, and the non-Lewis density

$$\rho^* = 0.643\,99e$$

is 2.68% of the total ρ . Thus, an idealized single Lewis-structure model requires larger perturbative corrections for the allyl anion than for hydrogen fluoride.

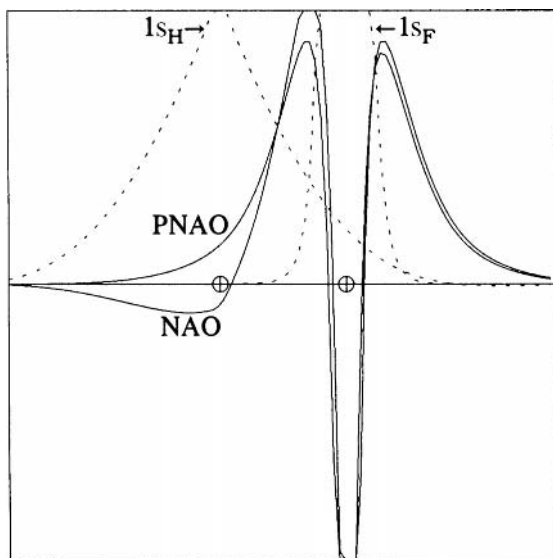
The overlap concept: pre-orthogonal localized orbitals

Although the NAOs and NBOs are strictly orthonormal (as eigenfunctions of any physical Hermitian operator must be), each such orbital is associated with a corresponding “pre-orthogonal” orbital (e.g., PNAO $\tilde{\theta}_i^{(A)}$ for NAO $\theta_i^{(A)}$) that allows one to retain the valuable concept of “overlap.” The PNAOs differ from NAOs only in omission of the final interatomic orthogonalization step⁴⁸ and have the full symmetry of free-atom AOs, so they look like the idealized textbook AOs of pure hydrogenic ψ_{nlm} type, or the natural orbitals of isolated atoms (to which they reduce as the atoms separate to infinity). The PNAOs on a single atom are mutually orthogonal ($\langle \tilde{\theta}_i^{(A)} | \tilde{\theta}_j^{(A)} \rangle = \delta_{ij}$; cf. Eq. (1.30)), but those on distinct atoms have non-vanishing overlaps ($\langle \tilde{\theta}_i^{(A)} | \tilde{\theta}_j^{(B)} \rangle \neq 0$). Similarly, the PNBO $\tilde{\Omega}_{AB}$ has all the same hybridization and polarization coefficients as the NBO Ω_{AB} , but is built from PNAOs rather than NAOs (or, equivalently, from PNHOs \tilde{h}_A and \tilde{h}_B rather than NHOs h_A and h_B).

Example 1.11

The figure below compares the forms of the 2s_F NAO and PNAO in hydrogen fluoride (solid lines), which are shown against the background of the filled 1s_H and 1s_F orbitals (dotted lines).

As seen, the 2s_F PNAO and NAO differ mainly near the adjacent H nucleus, where the NAO exhibits an additional nodal feature and a noticeable contraction of density in the shoulder nearest the (1s_H)² pair. Both the PNAO and the NAO are orthogonal to 1s_F (as required on physical grounds for eigenfunctions of a Hermitian operator), but only the NAO is orthogonal to 1s_H. Thus, the PNAO passes smoothly (and unphysically, as though it were a free-space atom) through the region occupied by the electrons associated with H, without the additional nodal feature (and higher kinetic energy) mandated by the Pauli exclusion principle.



A valuable feature of the overlapping PNHO hybrids \tilde{h}_A and \tilde{h}_B is that they allow the $\langle h_A | \hat{F} | h_B \rangle$ NHO interaction elements to be estimated in terms of the corresponding PNHO *overlap integral* $\langle \tilde{h}_A | \tilde{h}_B \rangle$ by a Mulliken-type approximation⁴⁹ of the form

$$\langle h_A | \hat{F} | h_B \rangle \simeq -k \langle \tilde{h}_A | \tilde{h}_B \rangle \quad (1.34)$$

where k is a constant of order unity in atomic units. Because the qualitative behavior of the overlap $S_{AB} = \langle \tilde{h}_A | \tilde{h}_B \rangle$ can be judged from the hybrid shapes, the bonding interaction elements $F_{AB} = \langle h_A | \hat{F} | h_B \rangle$ between hybrids can often be *visually estimated* by “inspection of the overlap.” Similar Mulliken-type relationships apply to interactions between NAOs or NBOs. Thus, for example, Eq. (1.24) can be replaced by an estimate of the form

$$E_{i \rightarrow j^*}^{(2)} \simeq -n_i^{(0)} \frac{k^2 \langle \tilde{\phi}_i^{(0)} | \tilde{\phi}_{j^*}^{(0)} \rangle^2}{\epsilon_{j^*}^{(0)} - \epsilon_i^{(0)}} = -n_i^{(0)} \frac{k^2 S_{ij^*}^2}{\epsilon_{j^*}^{(0)} - \epsilon_i^{(0)}} \quad (1.35)$$

where $\tilde{\phi}_i^{(0)}$ is the PNBO associated with NBO $\phi_i^{(0)}$, and so forth. Approximations such as Eq. (1.35) allow one to make semi-quantitative estimates of perturbative delocalization effects from the qualitative *shapes* and *energies* of the orbitals. In this manner the elementary “principle of maximum overlap”⁵⁰ is essentially preserved in NBO analysis of chemical interactions.

(For simplicity throughout this text, we shall use the generic term “NBO” to refer both to the orbitals that appear in formulas such as Eq. (1.24) and to those displayed in surface plots and orbital-overlap diagrams. However, in case of confusion, it

should be recalled that the latter are properly identified as “PNBOs” [introduced for visualization purposes only], whereas perturbative equations such as Eqs. (1.15)–(1.18) are formulated in terms of orthonormal NBOs. Similar comments apply to “NAOs” and “NHOs.”)

1.6 Natural resonance structures and weightings

The mathematical criterion for “resonance” description of delocalization effects

The approximation (1.32) of a single Lewis (“resonance”) structure $\psi^{(L)}$ is often inadequate, and the associated model chemistry of Eq. (1.33) cannot accurately describe the system of interest. Because $\psi^{(L)}$ can be expressed in terms of a corresponding density matrix $\mathbf{D}^{(L)}$ (cf. Eqs. (1.25) and (1.27)), we can also say that the localized density matrix $\mathbf{D}^{(L)}$ does not sufficiently approximate the true delocalized density matrix $\mathbf{D}^{(\text{true})}$ associated with ψ .

As suggested by the original *resonance theory* of Pauling and Wheland,⁵¹ such delocalization effects appear to represent some type of average of multiple resonance structures. A general goal of resonance theory is to represent each property $\langle \mathbf{P} \rangle_{\text{true}}$ of the true delocalized system in resonance-averaged form

$$\langle \mathbf{P} \rangle_{\text{true}} = \sum_{\alpha} w_{\alpha} \langle \mathbf{P} \rangle_{\alpha} \quad (1.36)$$

where $\langle \mathbf{P} \rangle_{\alpha}$ is the value of the property for localized resonance structure α and the w_{α} ’s are positive weighting factors, summing to unity, that express the contribution of structure α to the resonance hybrid. We are therefore led to search for additional localized resonance-structure wavefunctions ($\psi_{\alpha}^{(L)}$, $\psi_{\beta}^{(L)}$, ...) and associated density matrices ($\mathbf{D}_{\alpha}^{(L)}$, $\mathbf{D}_{\beta}^{(L)}$, ...) such that a weighted average of $\mathbf{D}_{\alpha}^{(L)}$ ’s can be used to represent $\mathbf{D}^{(\text{true})}$,

$$\mathbf{D}^{(\text{true})} = \sum_{\alpha} w_{\alpha} \mathbf{D}_{\alpha}^{(L)} \quad (1.37)$$

Equation (1.37) is actually the *necessary and sufficient condition* that *any* one-electron property⁵² $\langle \mathbf{P} \rangle$ (such as electron density, dipole moment, kinetic energy, ...) could be written in the resonance-averaged form (1.36). The goal of a quantitative resonance theory is to find the resonance weights w_{α} (if any) for which Eq. (1.37) is most accurately satisfied.

The NRT variational criterion

The *natural resonance theory* (NRT) method⁵³ offers a convenient *ab initio* means to calculate such resonance weights from the “ $\mathbf{D}^{(\text{true})}$ ” density matrix for a ψ of *any*

form. The NRT method begins by calculating the idealized $\mathbf{D}_\alpha^{(L)}$ for each candidate resonance structure by a directed NBO search (analogous to the default NBO search for the leading structure). If we let $\mathbf{D}^{(w)} = \sum_\alpha w_\alpha \mathbf{D}_\alpha^{(L)}$ denote the resonance hybrid on the right-hand side of Eq. (1.37), we can recast this equation as a *variational principle* for optimal weights $\{w_\alpha\}$ that *minimize* the root-mean-squared deviation (δ_w) between $\mathbf{D}^{(\text{true})}$ and $\mathbf{D}^{(w)}$,

$$\delta_w = \min_{\{w_\alpha\}} \|\mathbf{D}^{(\text{true})} - \mathbf{D}^{(w)}\| \geq 0 \quad (1.38)$$

where $\|\dots\|$ denotes the norm (the square root of the trace of the squared matrix) of the enclosed matrix.⁵⁴ The residual error δ_w of the NRT expansion can be compared with the error $\delta_0 = \|\mathbf{D}^{(\text{true})} - \mathbf{D}^{(L)}\|$ of the starting single-structure approximation, expressed in terms of the fractional improvement f_w ,

$$f_w \equiv 1 - \frac{\delta_w}{\delta_0} \quad (1.39)$$

to give an *intrinsic* measure of NRT accuracy ($0 \leq f_w \leq 1$).

Example 1.12

For the case of the allyl anion (cf. Examples 1.4 and 1.10), the density matrix $\mathbf{D}^{(\text{true})}$ for the three 2p_c π -type NAOs is

$$\mathbf{D}^{(\text{true})} = \begin{pmatrix} 1.4694 & 0.7061 & -0.4650 \\ 0.7061 & 0.9927 & 0.7061 \\ -0.4650 & 0.7061 & 1.4694 \end{pmatrix}$$

Let us consider the simplest possible localized density matrices \mathbf{D}_1 and \mathbf{D}_2 for the two resonance structures shown in Example 1.4:

$$\mathbf{D}_1 = \begin{pmatrix} 1 & 1 & 0 \\ 1 & 1 & 0 \\ 0 & 0 & 2 \end{pmatrix}, \quad \mathbf{D}_2 = \begin{pmatrix} 2 & 0 & 0 \\ 0 & 1 & 1 \\ 0 & 1 & 1 \end{pmatrix}$$

For example, \mathbf{D}_1 has coupled singly occupied orbitals on C₁ and C₂ (leading to a C₁–C₂ π bond) and a doubly occupied orbital on C₃, corresponding to the lone pair of the first resonance structure.

For the simplest resonance-weighted density matrix $\mathbf{D}^{(w)} = w_1 \mathbf{D}_1 + w_2 \mathbf{D}_2$ with equal resonance weightings, $w_1 = w_2 = \frac{1}{2}$,

$$\mathbf{D}^{(w)} = \begin{pmatrix} 1.5 & 0.5 & 0 \\ 0.5 & 1 & 0.5 \\ 0 & 0.5 & 1.5 \end{pmatrix}$$

the r.m.s. error δ_w is found to be

$$\delta_w = 0.78$$

This may be compared with the error δ_0 of either \mathbf{D}_1 or \mathbf{D}_2 alone,

$$\delta_0 = 1.45$$

Thus, the fractional improvement of the two-term resonance expansion is

$$f_w = 0.46$$

Natural bond order and valency

From the optimal NRT resonance weights, one can also evaluate the *natural bond order* b_{AB} between atoms A and B as the resonance-weighted average

$$b_{AB} = \sum_{\alpha}^{\text{RS}} w_{\alpha} b_{AB}^{(\alpha)} \quad (1.40)$$

where $b_{AB}^{(\alpha)}$ is the number of A—B bonds in structure α . To distinguish covalent ($b_{AB}^{(\text{cov})}$) and ionic ($b_{AB}^{(\text{ion})}$) contributions to bond order, we define the resonance-averaged “ionic character” i_{AB} of each A—B bond,

$$i_{AB} = \frac{\sum_{\alpha} w_{\alpha} i_{AB}^{(\alpha)}}{b_{AB}} \quad (1.41a)$$

where $i_{AB}^{(\alpha)}$, the ionicity of the A—B bond in resonance structure α , is calculated from NBO polarization coefficients c_A and c_B (Eq. (1.31a)),

$$i_{AB}^{(\alpha)} = \left| \frac{c_A^2 - c_B^2}{c_A^2 + c_B^2} \right| \quad (1.41b)$$

(averaged, if necessary, over multiple bonds). The total NRT bond order b_{AB} is thereby partitioned into fractional ionic and covalent contributions as

$$b_{AB}^{(\text{ion})} = b_{AB} i_{AB} \quad (1.42a)$$

$$b_{AB}^{(\text{cov})} = b_{AB} (1 - i_{AB}) \quad (1.42b)$$

so that $b_{AB} = b_{AB}^{(\text{cov})} + b_{AB}^{(\text{ion})}$ for any A—B pair. (Further aspects of covalent/ionic character in NBO and classical valence-bond descriptions will be discussed in Section 3.2.2.)

Finally, the NRT bond orders about atom A can be summed to give the total *natural atomic valency* V_A as

$$V_A = \sum_{B \neq A} b_{AB} \quad (1.43)$$

Just as the bond order is partitioned into ionic and covalent contributions in Eqs.(1.42a) and (1.42b), so too can the total valency of A be written as the sum of

formal “electrovalency” ($V_A^{(\text{ion})}$) and “covalency” ($V_A^{(\text{cov})}$), evaluated as

$$V_A^{(\text{ion})} = \sum_{B \neq A} b_{AB}^{(\text{ion})} \quad (1.44a)$$

$$V_A^{(\text{cov})} = \sum_{B \neq A} b_{AB}^{(\text{cov})} \quad (1.44b)$$

Unless the bonding about A is of extreme ionic or covalent type, only the *total* V_A is expected to match the empirical valency of an atom as reflected, e.g., in its position in the periodic table (Appendix B).

Example 1.13

For the allyl anion the NRT weightings are found to be 47.5% each for the two leading structures (cf. Example 1.10), plus a smattering of small values (<0.5%) for 16 other structures. These weightings lead to C—C bond orders of 1.511, nearly equal to the classical value 1.5 predicted by the two leading structures alone. The C—H bond orders are 0.972 on the central C and 0.986 and 0.990 on each terminal C. The total valency of the central C is therefore

$$V_C = 2(1.511) + 0.972 = 3.995$$

which is very close to the expected tetravalency. The valency of each terminal C is

$$V_C = 1.511 + 0.972 + 0.986 = 3.488$$

which is close to the average value (3.5) that would be expected from the two classical resonance forms. The valency of each H is equal to the bond order to the attached C, nearly 1 in each case. Thus the NRT bond orders and valencies are in good agreement with the expectations of the standard two-structure resonance model.

Comparison with earlier valence concepts

The NRT resonance weights, bond orders, and valencies are generally comparable to those of the older Pauling–Wheland theory (particularly for species of low ionicity) and can be used to rationalize chemical phenomena in a similar fashion. Pauling’s classic, *The Nature of the Chemical Bond*, brilliantly illustrates such reasoning.

However, we should emphasize that the NBO/NRT concepts of hybridization, Lewis structure, and resonance differ in important respects from previous empirical usage of these terms. In earlier phases of valence theory it was seldom possible to determine, e.g., the atomic “hybridization” by independent theoretical or experimental procedures, and instead this term became a loosely coded synonym for the molecular topology. For example, a trigonally coordinated atom might be categorized as “sp²-hybridized” or an octahedrally coordinated atom as “d²sp³-hybridized,” with no supporting evidence for the accuracy of these labels as descriptors of actual

orbital composition. Similarly, the “Lewis structure” of a molecule was inferred, via the VSEPR logic, merely from its shape, leading to superficial assignments of “valence electron pairs” to each atom without regard to actual electron-density distributions. In a similar fashion, empirical resonance structures and weightings were commonly assigned rather arbitrarily to “explain” geometry features, e.g., to interpret an unusually short bond by increased weighting of double-bonded or triple-bonded resonance structures. In these extreme limits, the assigned hybrids, Lewis structures, or resonance weightings have no independent conceptual content, but merely serve as elaborate codewords for the experimental molecular geometry. Many such empirical usages have deservedly fallen into disrepute.

In contrast, the NBO and NRT methods make *no* use of molecular geometry information (experimental or theoretical), but instead provide optimal descriptions of orbital composition or electron-density distributions based directly on the first-order density operator. For this reason the NBO/NRT indices have predictive utility for a broad range of chemical phenomena, without bias toward geometry or other particular empirical properties.

1.7 Pauli-exchange antisymmetry and steric repulsions

Antisymmetry and indistinguishability

In its most fundamental form the Pauli exclusion principle expresses the mathematical requirement (cf. Eq. (1.6)) that the wavefunction Ψ change sign upon exchange of the space–spin coordinates of any two electrons (or indeed, of any pair of identical fermions). This “exchange antisymmetry” of Ψ represents a subtle but profound difference between classical and quantal concepts of indistinguishability. “Indistinguishable” physical particles necessarily appear symmetrically in the Hamiltonian operator \hat{H} , so that, e.g., $\hat{H}(1, 2)$ and $\hat{H}(2, 1)$ are equivalent if particles “1” and “2” are indistinguishable. This in turn implies that $|\Psi(1, 2)|^2$ and $|\Psi(2, 1)|^2$ are identical probability distributions, leading to identical results in all measurements. However, the physical requirement $|\Psi(2, 1)|^2 = |\Psi(1, 2)|^2$ still allows either of two mathematical possibilities for the wavefunction amplitude under exchange, $\Psi(2, 1) = +\Psi(1, 2)$ (symmetric) or $-\Psi(1, 2)$ (antisymmetric). For deep reasons that we do not discuss further, the + sign is associated with particles of integer spin (bosons) and the – sign with particles of half-integer spin (fermions, including electrons).

The requirement of overall exchange antisymmetry of the N -electron wavefunction $\Psi(1, 2, \dots, N)$ can be expressed more generally in terms of formal invariance under the N -electron antisymmetrizer operator \hat{A}

$$\hat{A}\Psi = \Psi \tag{1.45}$$

As was mentioned previously, simple orbital products (electron configurations) must be converted into antisymmetrized orbital products (Slater determinants) in order to satisfy the Pauli principle. Thus, proper many-electron wavefunctions satisfy constraints of exchange antisymmetry that have no counterpart in pre-quantum theories.

For the chemist, the most important consequence of the exchange antisymmetry is that an allowed electron configuration may have no more than one electron of given spin in a specified spatial orbital, i.e., the spin quantum numbers $m_s = \pm\frac{1}{2}$ of two electrons must be *opposed* if they are assigned to the same spatial orbital (common n, ℓ, m spatial quantum numbers). This occupancy restriction forces successive electron pairs to populate spatially *orthogonal* orbitals as they are brought into a common spatial region. In general, maintenance of spatial orthogonality requires increased oscillatory and nodal structure, corresponding to higher average curvature and thus to higher average *kinetic energy* for electrons forced to occupy these orbitals. As a result, electrons compressed into a restricted spatial volume experience an apparent *destabilizing* (repulsive) “force”⁵⁵ opposing such compression. Weisskopf⁵⁶ has aptly described this general electronic tendency to resist spatial compression as “kinetic-energy pressure.” Chemists call the same effect “steric repulsion.”

Natural steric analysis

Natural steric analysis⁵⁷ allows quantitative evaluation of steric repulsion on the basis of this simple physical picture. Given the converged Fock (or Kohn–Sham) operator \hat{F} , we can evaluate the average energy of each occupied NBO $\Omega_i^{(\text{NBO})}$ and the associated pre-orthogonal PNBO $\Omega_i^{(\text{PNBO})}$ in the usual manner,

$$F_{i,i}^{(\text{NBO})} = \langle \Omega_i^{(\text{NBO})} | \hat{F} | \Omega_i^{(\text{NBO})} \rangle \quad (1.46a)$$

$$F_{i,i}^{(\text{PNBO})} = \langle \Omega_i^{(\text{PNBO})} | \hat{F} | \Omega_i^{(\text{PNBO})} \rangle \quad (1.46b)$$

The PNBO energy $F_{i,i}^{(\text{PNBO})}$ corresponds to a Pauli-violating limit in which each constituent atomic orbital retains its isolated free-atom (PNAO) form, without the additional nodal features required to preserve interatomic orthogonality in the molecular environment. The energy difference between the Pauli-violating $F_{i,i}^{(\text{PNBO})}$ and the actual NBO energy $F_{i,i}^{(\text{NBO})}$ therefore measures the effect of increased steric pressure (for electrons in NBO i) due to proximity of other atoms. The total NBO steric exchange energy ($E_{\text{tot}}^{(\text{st})}$) is evaluated by summing such differences over all occupied NBOs,

$$E_{\text{tot}}^{(\text{st})} = \sum_i^{\text{occ}} (F_{i,i}^{(\text{NBO})} - F_{i,i}^{(\text{PNBO})}) \quad (1.47)$$

Example 1.14

Consider the steric repulsion between two helium atoms at various separations R . In this case, each atom contains only a single doubly occupied 1s-like NBO and Eq. (1.47) reduces to a single term

$$E_{\text{tot}}^{(\text{st})} = 2(F_{1s,1s}^{(\text{NBO})} - F_{1s,1s}^{(\text{PNBO})})$$

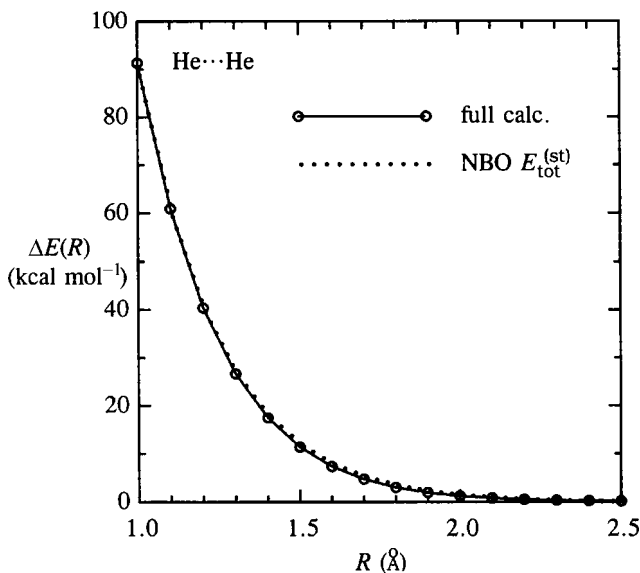
involving the energy difference between 1s-type NBOs and PNBOs on each atom. For example, at $R = 1.5 \text{ \AA}$ the values are

$$F_{1s,1s}^{(\text{NBO})} = -0.6564, \quad F_{1s,1s}^{(\text{PNBO})} = -0.6658$$

leading to steric repulsion

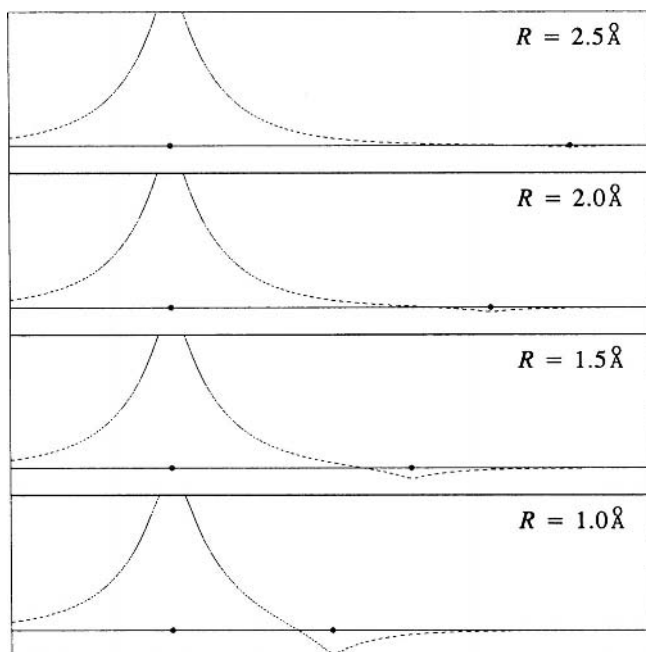
$$E_{\text{tot}}^{(\text{st})} = 2(0.0094) \text{ a.u.} = 11.8 \text{ kcal mol}^{-1}$$

at this distance. The graph below compares $E_{\text{tot}}^{(\text{st})}$ (dotted line) with the full $\Delta E(\text{He} \cdots \text{He})$ (solid line) over a wide range of R , showing the close agreement between the NBO estimate of steric repulsion and the actual potential-energy curve.



We can see the effect of steric repulsions on the form of the He 1s-like NBO. The plot below compares the form of this NBO at $R = 2.5 \text{ \AA}$ (for which the NBO and PNBO are practically identical) with the forms at $R = 2.0, 1.5$ and 1.0 \AA , for which the interatomic nodal structure becomes increasingly apparent.

The increased “choppiness” of the 1s-like waveform is the visual manifestation of increased kinetic energy and stronger He \cdots He repulsion at small R .



Steric repulsions of localized electron pairs

Although Eq. (1.47) gives an evaluation of the *total* steric exchange energy of the N -electron system, it is often desirable to decompose this energy approximately into contributions from the steric interactions of individual electron pairs i, j . For each (i, j) pair, we can form the “partially deorthogonalized” PNBO/2 orbitals $\Omega_i^{(\text{PNBO}/2)}$ and $\Omega_j^{(\text{PNBO}/2)}$ which are non-orthogonal with respect to one another, but remain orthogonal with respect to all other NBOs. (Details of this procedure are beyond the scope of the present work.) The partial i, j contribution $E_{i,j}^{(\text{st})}$ to steric exchange is therefore estimated as

$$E_{i,j}^{(\text{st})} = (F_{i,i}^{(\text{NBO})} - F_{i,i}^{(\text{PNBO}/2)}) + (F_{j,j}^{(\text{NBO})} - F_{j,j}^{(\text{PNBO}/2)}) \quad (1.48)$$

By summing these contributions over all distinct pairs, we obtain an alternative pairwise-additive estimate ($E_{\text{pw}}^{(\text{st})}$) of the steric exchange energy,

$$E_{\text{pw}}^{(\text{st})} = \sum_{i < j} E_{i,j}^{(\text{st})} \quad (1.49)$$

which, however, is only an approximation to the more fundamental expression, Eq. (1.47), for $E_{\text{tot}}^{(\text{st})}$.

The contributions (1.48) for individual NBOs i, j allow one to make direct contact with empirical measures of steric “bulk” or “shape” of individual atoms, atomic shells, or other localized chemical moieties. For example, as two Ne atoms (a and

Table 1.1. *Natural atomic van der Waals radii (Å) for H–Ar*

H							He
1.42							1.07
Li	Be	B	C	N	O	F	Ne
2.76	2.22	1.78	1.62	1.63	1.46	1.27	1.22
Na	Mg	Al	Si	P	S	Cl	Ar
3.07	2.75	2.30	2.21	2.44	2.16	1.89	1.78

b) are brought together, the longest-range steric contribution (1.48) is of $2p_a-2p_b$ type, arising from “collisions” of the outermost valence shells which establish the effective van der Waals radius of the atom. However, at smaller R the successive inner-shell collisions of $2p_a-2s_b$, $2p_a-1s_b$, \dots , $1s_a-2s_b$ type lead to further sharp increases in steric repulsion.

Natural van der Waals radii

By choosing a standard probe species i (e.g., a helium atom) of known van der Waals radius, one can probe the “steric surface” of any doubly occupied NBO j by determining the locus of points for which $E_{i,j}^{(st)}$ achieves a specified energy value (e.g., kT of ambient thermal collisions). *Ab initio* atomic van der Waals radii⁵⁸ determined in this manner are shown in Table 1.1.

The natural van der Waals radii of Table 1.1 are generally found to be in good correspondence to empirical values. However, one can establish that the van der Waals surface of a bonded atom is generally somewhat *ellipsoidal* (rather than spherical), with major and minor axes respectively transverse and longitudinal to the bond direction. One can also evaluate the “hardness” (radial derivative of steric energy), charge dependence, and temperature dependence of van der Waals radii, thereby obtaining many quantitative refinements of empirical steric concepts.

Further examples throughout this book will illustrate the usefulness of quantifying steric repulsions in this manner.

1.8 Summary

“Models” of chemistry can be constructed from sufficiently good approximations to Schrödinger’s equation, the ultimate source of chemical knowledge. Perturbation theory provides a systematic method for choosing the best among competing models, and for systematically correcting a chosen model. The “reality” of a model

chemistry lies in the accuracy of the underlying unperturbed Hamiltonian operator, i.e., its ability to describe the empirical phenomena of chemistry (to the precision required by chemical practitioners) in the most direct and faithful manner, subject to the fewest perturbative corrections. The constructs of the model chemistry must then be as “real” as those employed by chemical practitioners to characterize the empirical phenomena of chemistry. Indeed, the model constructs of an apt theoretical model can be expected to mirror faithfully the experimentally inferred concepts that have been developed to express empirical chemical facts with comparable accuracy.

The Hartree–Fock (molecular-orbital) approximation provides a particularly useful chemical model. The HF model reduces an N -electron system to an effective one-electron Schrödinger-like equation, preserving many features of the exactly soluble H-atom system. Hartree–Fock perturbation theory allows the energy and other properties to be systematically improved on an orbital-by-orbital basis. Particularly important are the perturbative corrections arising from “donor–acceptor” interactions between filled and vacant orbitals, which provide a general stabilizing mechanism promoting chemical affinity between initially non-interacting species.

The first-order reduced density operator succinctly summarizes the chemical information related to electron density and other single-electron properties. Local “natural bond orbital” eigenvectors of this operator describe electron pairs in one- and two-center regions of the molecule, providing a direct orbital realization of the chemist’s Lewis-structure picture. The NBO-based models provide a framework for analyzing chemical phenomena in terms of familiar Lewis-structural concepts, including “resonance” between multiple Lewis structures and repulsive steric interactions between localized filled orbitals. The attractive donor–acceptor interactions between Lewis-type (filled) and non-Lewis-type (vacant) valence NBOs are identified as a unifying theoretical *leitmotif* that governs many valency and bonding phenomena.

Notes for Chapter 1

1. P. A. M. Dirac, *Proc. Roy. Soc.* **123** (1929), 714.
2. H. Eyring, J. Walter, and G. E. Kimball, *Quantum Chemistry* (New York, Wiley, 1944), p. iii.
3. Equation (1.1) is actually the stationary-state version of the more general Schrödinger-like (or Dirac-like) time-dependent wave equation $\hat{H}\Psi = i\hbar\dot{\Psi}$, where i is the unit imaginary number (the square root of -1), \hbar is Planck’s constant, and $\dot{\Psi}$ denotes the time derivative of Ψ . This can be reduced to Eq. (1.1) when the system contains no external time-dependent driving forces, which is the usual case to be considered in this book. The stationary-state solutions of Eq. (1.1) also form the starting point for approximating more general non-stationary systems by time-dependent perturbation theory.
4. The fundamental equivalence between Schrödinger’s wave-mechanical and Heisenberg’s matrix-mechanical representation of quantum theory implies that \hat{H} (or $\hat{H}^{(0)}$) may be viewed as a differential operator *or* a matrix. The latter viewpoint is usually more convenient in the

- present work. In many cases the full Schrödinger equation (1.1) corresponds to a matrix \hat{H} of infinite dimension, whereas the model $\hat{H}^{(0)}$ of (1.2) is of finite dimension.
5. E. Schrödinger, *Ann. Phys.* **80** (1926), 437. The quantal formalism substantially follows the classical method developed by Lord Rayleigh (*Theory of Sound* [1894]) and is commonly referred to as “Rayleigh–Schrödinger perturbation theory.”
 6. Throughout this work, familiarity will be assumed with basic mathematical notation and terminology of quantum chemistry and matrix algebra at the level of a standard text, such as I. N. Levine, *Quantum Chemistry*, 5th edn. (Englewood Cliffs, NJ, Prentice Hall, 2000) or J. R. Barrante, *Applied Mathematics for Physical Chemistry*, 2nd edn. (Upper Saddle River, NJ, Prentice Hall, 1998).
 7. See, e.g., J. O. Hirschfelder, W. Byers Brown, and S. T. Epstein, *Adv. Quantum Chem.* **1** (1964), 255. Formally, Eqs. (1.5a) and (1.5b) originate from expansions of E and Ψ in powers of a perturbation parameter that is set to unity in the final formulas used here.
 8. E. A. Hylleraas, *Z. Phys.* **65** (1930), 209; note 6, p. 279. Note that $E^{(2)}$ can alternatively be expressed as an infinite expansion in the unperturbed eigenfunctions $\Psi_i^{(0)}$, but the Hylleraas variation–perturbation expression (1.5d) is generally more useful for practical numerical applications.
 9. The numerical values were obtained from a simple Hartree–Fock variational treatment, as described in Section 1.3 below. Note that, in this simple case, we could obtain the exact eigenvalues of the 2×2 matrix \hat{H} by solving a quadratic equation. The present use of perturbation theory to approximate these eigenvalues is for illustrative purposes only.
 10. A brief introduction to the cryptic notation designating standard methods and basis sets of modern *ab initio* and density-functional calculations is given in Appendix A. Such designations will be used without further comment throughout this book.
 11. A well-known consequence of the permutational symmetry of the nuclear Hamiltonian is the low-temperature entropy of crystalline hydrogen, which is associated with the spin statistics of *ortho*- and *para*-H₂. See, e.g., N. Davidson, *Statistical Mechanics* (New York, McGraw-Hill, 1962), Chapter 9.
 12. Strictly speaking, a chiral species cannot correspond to a true stationary state of the time-dependent Schrödinger equation $\hat{H}\Psi = i\hbar\dot{\Psi}$, but instead must evolve into a racemic superposition of enantiomers. However, the time scale for such spontaneous racemization is extremely long. The wavefunction of practical interest to the (finite-lived) laboratory chemist is the non-stationary $\Psi(0)$ of a Born–Oppenheimer model Eq. (1.2), rather than the true Ψ of Eq. (1.1).
 13. M. Born and J. R. Oppenheimer, *Ann. Phys.* **84** (1927), 457.
 14. H. A. Bethe and E. E. Salpeter, *The Quantum Mechanics of One- and Two-Electron Atoms* (New York, Academic Press, 1957).
 15. W. Pauli, *Z. Phys.* **31** (1925), 765; and W. Pauli, *Phys. Rev.* **58** (1940), 716.
 16. See, e.g., S. T. Epstein, *The Variation Method in Quantum Chemistry* (New York, Academic Press, 1974).
 17. See, e.g., P.-O. Löwdin, in C. H. Wilcox (ed.), *Perturbation Theory and its Applications in Quantum Mechanics* (New York, Wiley, 1966), p. 255.
 18. Note that every variational approximation corresponds to a model $\hat{H}^{(0)}$, but not every model $\hat{H}^{(0)}$ satisfies the variational principle. Both variational and non-variational models will be employed in the present work.
 19. See, e.g., W. J. Hehre, L. Radom, P. v. R. Schleyer, and J. A. Pople, *Ab Initio Molecular Orbital Theory* (New York, Wiley, 1986), Section 1.1.
 20. J. W. Gibbs (letter of acceptance of the Rumford Medal, January 10, 1881); quoted in L. P. Wheeler, *Josiah Willard Gibbs, The History of a Great Mind* (New Haven, CT, Yale University Press, 1962), p. 88.
 21. See, e.g., J. B. Foresman and A. Frisch, *Exploring Chemistry with Electronic Structure Methods* (Pittsburgh, PA, Gaussian, 1996); and note 19.
 22. A. E. Reed, L. A. Curtiss, and F. Weinhold, *Chem. Rev.* **88** (1988), 899; F. Weinhold, Natural bond orbital methods, in P. v. R. Schleyer (ed.), *Encyclopedia of Computational Chemistry* (New York, Wiley, 1998), and references therein.

23. E. Schrödinger, *Ann. Phys.* **79** (1926), 361.
24. Such sign changes in the orbital are analogous, e.g., to water-wave displacements “above” or “below” the mean surface level. The overall sign of the orbital may be reversed without physical effect, so only sign differences within the orbital are significant.
25. Of course, we have no conceptual difficulty picturing this situation for two impacting water waves, which may mutually reinforce (to give a super wave) or mutually cancel out (to give a strangely quiescent region), but the analogous behavior of electrons in orbitals is, to say the least, conceptually challenging!
26. The outermost contour is consistently chosen as 0.031 62e throughout this book, a value that is roughly consistent with empirical van der Waals radii (R. W. F. Bader *et al.*, *J. Chem. Phys.* **46** [1967], 3341). Successive contours differ by constant 0.05e, and only the four outermost contours are shown. In contour plots the plotting range is usually $\pm 3 \text{ \AA}$ around the center of the diagram, and in radial profile plots the horizontal (spatial) and vertical (orbital amplitude) ranges are usually $\pm 3 \text{ \AA}$ and $\pm 1 \text{ a.u.}$, respectively. However, symmetry considerations, molecular size, or the wish to magnify orbital details will sometimes lead to altered plotting ranges, which can usually be inferred from plotted nuclear positions.
27. $\Psi^{(0)}$ is formally a Slater determinant (antisymmetrized product) of occupied orbitals. Because electronic wavefunctions are always implicitly antisymmetrized to satisfy the Pauli principle, we can treat a configurational product of orbitals $[\phi_1^2 \phi_2^2 \dots]$ and the associated Slater determinant $\det|\phi_1^2 \phi_2^2 \dots| = \hat{A}[\phi_1^2 \phi_2^2 \dots]$ rather interchangeably.
28. D. R. Hartree, *Proc. Camb. Phil. Soc.* **26** (1928), 89; V. Fock, *Z. Phys.* **61** (1930), 126; J. C. Slater, *Phys. Rev.* **35** (1930), 210; and C. C. J. Roothaan, *Rev. Mod. Phys.* **23** (1951), 69. Note that the Hartree–Fock method is often called the “molecular-orbital method” or “self-consistent-field method” for molecules.
29. C. Møller and M. S. Plesset, *Phys. Rev.* **46** (1934), 618; and note 19, pp. 38–40. See also Appendix A.
30. E. A. Hylleraas, *Z. Phys.* **48** (1928), 469; G. R. Taylor and R. G. Parr, *Proc. Nat. Acad. Sci. U.S.A.* **38** (1952), 154; and note 19, pp. 29–38.
31. P.-O. Löwdin, *Phys. Rev.* **97** (1955), 1474.
32. P. Hohenberg and W. Kohn, *Phys. Rev. B* **136** (1964), 864; and note 21, pp. 272–277.
33. W. Kohn and L. J. Sham, *Phys. Rev. A* **140** (1965), 1133.
34. A. Becke, *J. Chem. Phys.* **98** (1993), 1372; and C. Lee, W. Yang, and R. G. Parr, *Phys. Rev. B* **37** (1988), 785.
35. In Eq. (1.16a), \hat{A} is the antisymmetrizer operator that converts the orbital product into a Slater determinant, insuring satisfaction of the Pauli exclusion principle. In this equation (alone), the same spatial orbital might appear twice, with different indices to indicate the change in spin. For example, $\phi_1^{(0)}(\vec{r}_1)\phi_2^{(0)}(\vec{r}_2)$ might be the same as $\phi_1^{(0)}(\vec{r}_1)\bar{\phi}_i^{(0)}(\vec{r}_2)$, a doubly occupied spatial orbital ($n_1^{(0)} = 2$), with a bar denoting opposite spin in the second spin-orbital.
36. The NAO matrix elements of the operators employed in this example can be obtained by standard keywords of the NBO program (FNAO for the Fock operator, KNAO for the kinetic-energy operator, etc.); see note 43.
37. Reduced density operators were first introduced by K. Husimi (*Proc. Phys. Math. Soc. Japan* **22** [1940], 264) to describe *subsets* of the N -electron distribution (first-order for one-particle distributions, second-order for pair distributions, etc.) and are obtained from the full N th-order (von Neumann) density operator $\Psi(\vec{r}_1, \vec{r}_2, \dots, \vec{r}_N)\Psi^*(\vec{r}'_1, \vec{r}'_2, \dots, \vec{r}'_N)$ by integrating (averaging) over successive electronic coordinates; see, e.g., E. R. Davidson, *Reduced Density Matrices in Quantum Chemistry* (New York, Academic Press, 1976) and note 31.
38. The right-hand side of Eq. (1.26) can be seen to be formally similar to the ordinary rule

$$g_i = \sum_j \gamma_{ij} f_j$$

for multiplying a vector by a matrix to form another vector. Other familiar examples of integral operators include Fourier transformations, Dirac delta functions, and projection operators. Only

the fundamental rule of operation (1.26) is needed in order to follow the discussion and equations of this book.

39. In general, we use the symbols for $\hat{\gamma}$ (the operator) and \mathbf{D} (its matrix representation) rather interchangeably when the basis set is clearly specified. However, in some cases we write $\hat{\gamma}^{(\text{basis})}$ (with the basis set identified in parentheses) to identify the specific matrix form of the operator.
40. P.-O. Löwdin, *Phys. Rev.* **97** (1955), 1474.
41. A. E. Reed, R. B. Weinstock, and F. Weinhold, *J. Chem. Phys.* **83** (1985), 735.
42. J. P. Foster and F. Weinhold, *J. Am. Chem. Soc.* **102** (1980), 7211.
43. F. Weinhold, Natural bond orbital methods, in P. v. R. Schleyer, N. L. Allinger, T. Clark *et al.* (eds.), *Encyclopedia of Computational Chemistry*, Vol. 3 (Chichester, John Wiley & Sons, 1998), pp. 1792–1811. See also the NBO Program Manual, note 44.
44. The program NBO 5.0 was developed by E. D. Glendening, J. K. Badenhoop, A. E. Reed, J. E. Carpenter, J. A. Bohmann, C. M. Morales, and F. Weinhold, Theoretical Chemistry Institute, University of Wisconsin, Madison (2001); F. Weinhold, *NBO 5.0 Program Manual: Natural Bond Orbital Analysis Programs* (Madison, WI, Theoretical Chemistry Institute, 2001).
45. The NBO Website URL is <http://www.chem.wisc.edu/~nbo5>.
46. G. N. Lewis, *J. Am. Chem. Soc.* **38** (1916), 762; G. N. Lewis, *Valence and the Structure of Atoms and Molecules* (New York, The Chemical Catalog Co., 1923). As observed by Pauling (in note 51, p. 5), this remarkable work “forms the basis of the modern electronic theory of valence.”
47. L. Pauling, *J. Am. Chem. Soc.* **53** (1931), 1367; and C. A. Coulson, *Valence*, 2nd edn. (London, Oxford University Press, 1961), Chapter 8.
48. A. E. Reed, R. B. Weinstock, and F. Weinhold, *J. Chem. Phys.* **83** (1985), 735.
49. R. S. Mulliken, *Phys. Rev.* **41** (1932), 49; M. Wolfsberg and L. Helmholz, *J. Chem. Phys.* **20** (1952), 837; and R. Hoffmann, *J. Chem. Phys.* **39** (1963), 1397.
50. L. Pauling, *J. Am. Chem. Soc.* **53** (1931), 1367; and Pauling in note 49, pp. 108ff.
51. L. Pauling and G. W. Wheland, *J. Chem. Phys.* **1** (1933), 362; G. W. Wheland and L. Pauling, *J. Am. Chem. Soc.* **57** (1935), 2086; G. W. Wheland, *The Theory of Resonance and its Applications to Organic Chemistry* (New York, Wiley, 1955); and L. Pauling, *The Nature of the Chemical Bond*, 3rd. edn. (Ithaca, NY, Cornell University Press, 1960).
52. At the Hartree–Fock level this statement is true for all properties, not only single-electron properties.
53. E. D. Glendening and F. Weinhold, *J. Comput. Chem.* **19** (1998), 593, 610; and E. D. Glendening, J. K. Badenhoop, and F. Weinhold, *J. Comput. Chem.* **19** (1988), 628.
54. In practice, a simplified single-reference form of Eq. (1.38) is used for the case of a weakly delocalized dominant resonance structure with $w_1 \gg w_2, w_3, \dots$; see note 53.
55. Note that the Hamiltonian \hat{H} contains no explicit potential-energy term giving rise to this force, so the effect is a purely quantal consequence of exchange antisymmetry.
56. V. F. Weisskopf, *Science* **187** (1975), 605.
57. J. K. Badenhoop and F. Weinhold, *J. Chem. Phys.* **107** (1997), 5406.
58. J. K. Badenhoop and F. Weinhold, *J. Chem. Phys.* **107** (1977), 5422, J. K. Badenhoop and F. Weinhold, *Int. J. Quantum Chem.* **72** (1999), 269.

2

Electrostatic and ionic bonding

2.1 Introduction

The close relationship between chemistry and electricity was surmised long before the discovery of quantum mechanics.¹ The inverse-square law for the force between electrically charged objects (“Coulomb’s law”) was established as early as 1766 by the American chemist Joseph Priestley, on the basis of a method suggested by Benjamin Franklin. Galvani’s discoveries of 1780 and the subsequent development of the voltaic pile sparked intensive investigations on the chemical effects of electricity, culminating in Humphry Davy’s electrolytic discoveries of alkali elements and general recognition of the “natural electrical energies of the elements” by about 1806. Within a decade, J. J. Berzelius had formulated his influential “dualistic” electrochemical theory, asserting that “in every chemical combination there is a neutralization of opposite electricities.”

Studies of electrolysis and electromagnetic induction were greatly advanced by Davy’s assistant, Michael Faraday, who also introduced the modern terminology of “cation” and “anion.” Long before the 1897 “discovery” of the electron by J. J. Thomson, strong chemical evidence pointed to the existence of such “corpuscles of electricity,” as could be inferred particularly from Faraday’s studies. Indeed, the word “electron” was coined in 1874 by the chemist J. Stoney, who also estimated the electronic charge from the value of Faraday’s constant. Thus, the essential components of a simple ionic bonding picture, much as presented in current textbooks, were available at least a half-century before the discovery of Schrödinger’s equation and the modern quantal view of electronic behavior.

Although the Berzelius ionic theory achieved successes in interpreting inorganic compounds, it met persistent difficulties in the emerging domain of organic chemistry. By about 1860, E. Frankland, F. A. Kekulé, and others had developed the opposing concept of “valence” (and specifically, the quadrivalence of carbon) to

counter the Berzelius ionic picture. Thus, the stage was set for strongly conflicting views on the nature of chemical affinity and association.

The ionic or electrostatic picture of bonding has an engaging simplicity. According to classical electrostatics, the energy of interaction (E_{es}) of particles with charges Q_1 and Q_2 at separation R is

$$E_{es}(R) = c \frac{Q_1 Q_2}{R} \quad (2.1)$$

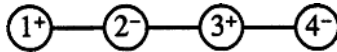
where c is a constant that depends on the chosen units (Appendix C). For oppositely charged particles, this formula leads to an infinitely negative energy at $R \rightarrow 0$, the only stable static solution. Non-static solutions are no better, for Earnshaw's theorem of classical electrostatics establishes that *no* dynamical system of charged particles can achieve stable equilibrium. Hence, electrostatic potentials must be modified by some type of "hard-sphere" potential at chosen R_0 to prevent unphysical collapse.

Example 2.1

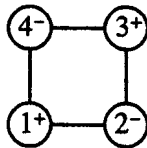
For a system consisting of four ions, with $Q_1 = -Q_2 = Q_3 = -Q_4 = e$, the electrostatic energy is simply a sum of six such Coulombic terms, one for each distinct pair of ions:

$$E = \frac{(+e)(-e)}{R_{12}} + \frac{(+e)(+e)}{R_{13}} + \frac{(+e)(-e)}{R_{14}} + \frac{(-e)(+e)}{R_{23}} + \frac{(-e)(-e)}{R_{24}} + \frac{(+e)(-e)}{R_{34}}$$

Let us compare the energy of linear (E_{lin}) and square (E_{sq}) arrangements, assuming the same nearest-neighbor distance R for each:



$$\begin{aligned} E_{lin}(R) &= \frac{(+e)(-e)}{R} + \frac{(+e)(+e)}{2R} + \frac{(+e)(-e)}{3R} + \frac{(-e)(+e)}{R} + \frac{(-e)(-e)}{2R} + \frac{(+e)(-e)}{R} \\ &= (-7/3)e^2/R = (-2.3333\dots)e^2/R \end{aligned}$$



$$\begin{aligned} E_{sq}(R) &= \frac{(+e)(-e)}{R} + \frac{(+e)(+e)}{2^{1/2}R} + \frac{(+e)(-e)}{R} + \frac{(-e)(+e)}{R} + \frac{(-e)(-e)}{2^{1/2}R} + \frac{(+e)(-e)}{R} \\ &= (-4 + 2^{1/2})e^2/R = (-2.5857\dots)e^2/R \end{aligned}$$

Thus, for any fixed R classical electrostatics favors a square over a linear arrangement by 10.8%, but the only true minimum is $R \rightarrow 0$.

It can be shown² that solution of Schrödinger's equation for a pair of dissociating ions (e.g., $\text{Li}^+ + \text{F}^-$) leads to an energy that agrees with Eq. (2.1) as $R \rightarrow \infty$. In fact, Eq. (2.1) is nearly exact for distances R outside the "exchange region,"³ or roughly speaking, for R values safely larger than the sum of van der Waals radii (R_{vdW}). Thus, Eq. (2.1) and the associated classical ionic picture are in some sense "correct" for sufficiently large R . Nevertheless, chemical bonding and reactivity typically involves separations well *inside* the R_{vdW} contact distance, where corrections to Eq. (2.1) cannot be safely neglected. Thus, this chapter will focus on how the true quantal description of ionic interactions differs from the classical electrostatic description.

2.2 Atomic and ionic orbitals

Charge and configurational variations of atomic orbitals

Although oversimplified treatments commonly speak of "the" atomic orbitals for a given atom, it is clear that AOs must depend on the charge state and specific configuration of the atom. Thus, the (N)AOs of an anionic atom A^- will tend to be markedly more diffuse (i.e., spread out to greater distances from the nucleus) than those of a cationic A^+ .

Figure 2.1. illustrates these differences for the 2s NAOs of Li^- , Li^0 , and Li^+ , showing the strong decrease in the radius of this valence orbital as the net charge increases. It is evident that an attempt to describe, e.g., the valence electron distribution of Li^+ in terms of the fixed 2s AO of Li (or Li^-) would incur a large error,

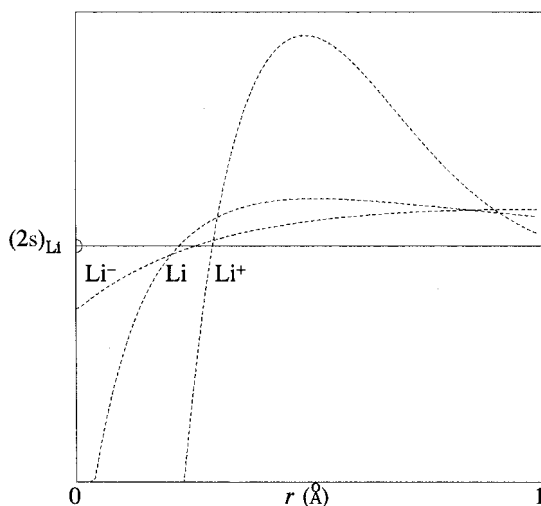


Figure 2.1 Valence 2s NAOs of Li^+ , Li^0 , and Li^- , showing the strong variation of orbital radius with charge state.

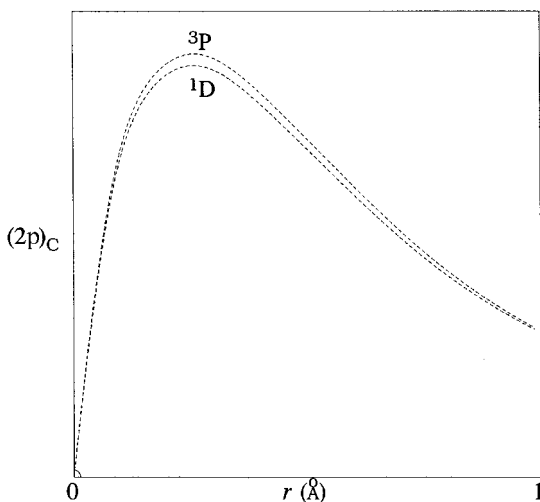


Figure 2.2 Valence 2p NAOs for ground ^3P and first excited ^1D states of the C atom, showing the weak dependence of orbital shape on electron configuration.

due to the inappropriate size of the latter orbitals. In general, we must consider the effective AOs of an atomic species to be *dependent on its charge state*, including the *fractional* variations of charge state involved in chemical bonding.

More subtle variations of NAOs are associated with changes of electron configuration. As a simple example, Fig. 2.2 illustrates the 2p NAOs of an isolated neutral carbon atom for two electronic configurations: the ground triplet state (^3P) and first excited singlet state (^1D). Although these configurations differ only by a single spin flip, the optimal 2p NAO of the excited singlet state is slightly more spatially extended than the corresponding NAO of the ground triplet state. Similar adjustments are expected to accompany valence “promotion” during chemical-bond formation.

The natural minimal basis

The naive concept that a fixed set of valence AOs suffices for all charge states and bonding environments is equivalent to the use of a minimum basis set (e.g., STO-3G), which is known to be quite inadequate for quantitative purposes. Nevertheless, if the AOs are properly allowed to adjust dynamically in the molecular environment, one recovers a minimal-basis description that is surprisingly accurate: the “natural minimal basis.” In the NBO framework the effective *natural* atomic orbitals are continually optimized in the molecular environment, and the number of important NAOs therefore remains close to minimal, greatly simplifying the description of bonding.

In the following sections we shall primarily focus on the linear combinations of NAOs that lead to optimal hybrids and NBOs, rather than on the forms of the NAOs

themselves. Nevertheless, it should be remembered that the disarming simplicity of the NHO/NBO description is largely due to the fact that the underlying NAOs are themselves optimally adapted to the specific charge and bonding state. With such optimized atomic orbitals, the elementary valence-theory assumption of an “effective minimal basis set” is found to be vindicated even at the highest levels of *ab initio* theory.

2.3 Charge transfer and hybridization in ionic bonding

Charge-“leakage” breakdown of the classical ionic picture: lithium fluoride

We shall first examine how the quantal and classical descriptions of ionic bonding deviate for the prototypical example of lithium fluoride ($\text{Li}^+ + \text{F}^-$). Figure 2.3 shows the potential-energy curve for lithium fluoride in the near- R_{eq} region where the bonding is primarily ionic,⁴ comparing the quantum-mechanical⁵ E (solid line) and electrostatic E_{es} (dotted line), both referred to a common zero of energy at $R \rightarrow \infty$. The quantal and classical ionic interaction energies are seen to be in reasonable agreement for larger separations, differing only by the neglected small effects of electric polarization. However, these curves exhibit quite significant differences near R_{eq} (e.g., 0.04 a.u. $\approx 25 \text{ kcal mol}^{-1}$ at $R = 1.6 \text{ \AA}$) and diverge entirely as $R \rightarrow 0$.

Let us examine the quantal energy curve in more detail. On chemical grounds we expect that LiF formation should be reasonably well described by a

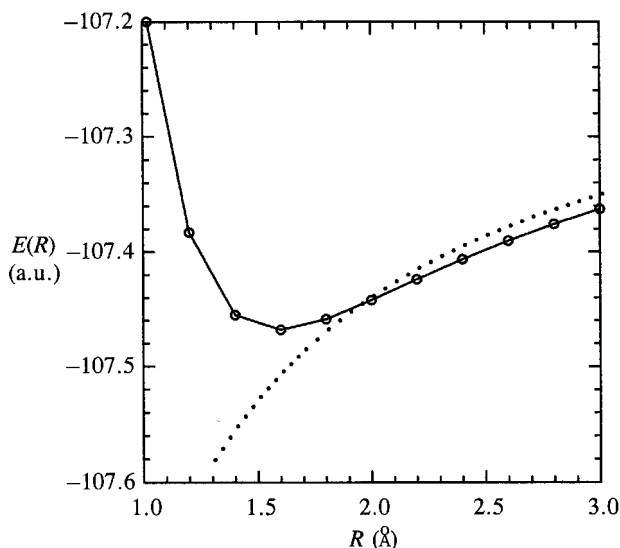


Figure 2.3 The potential-energy curve for $\text{Li}^+ + \text{F}^-$ ionic bond formation according to quantum mechanics (solid line) or classical electrostatics (dotted line).

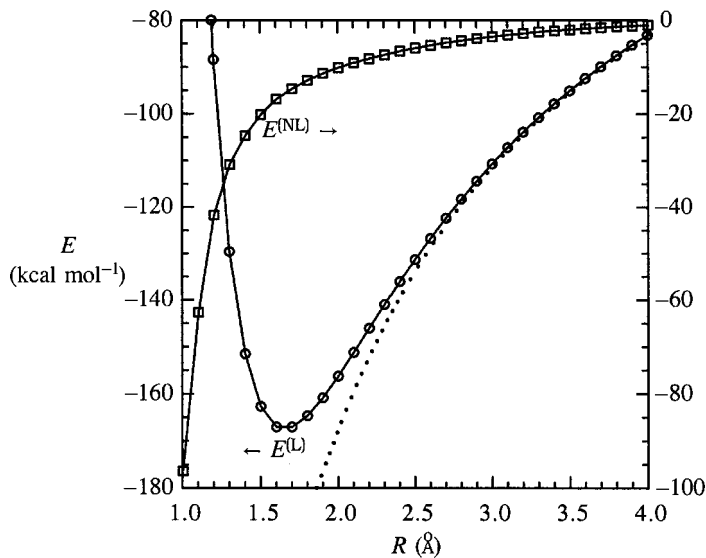


Figure 2.4 Components of the Li–F potential-energy curve $E(R) = E^{(L)}(R) + E^{(NL)}(R)$, showing the localized “natural-Lewis-structure” model energy $E^{(L)}$ (circles, left-hand scale) and delocalized “non-Lewis” correction $E^{(NL)}$ (squares, right-hand scale). The classical electrostatic estimate E_{es} (dotted line) is shown for comparison.

Lewis-structure picture, i.e., by a localized wavefunction of doubly occupied Lewis-type NBOs as given in Eq. (1.32). The energy $E^{(L)}$ of this simple model wavefunction (cf. Eq. (1.33)) is plotted in Fig. 2.4 (circles, left-hand scale). The behavior of the localized Lewis potential $E^{(L)}(R)$ is indeed qualitatively reasonable, leading to an equilibrium bond length and well depth that are both within about 10% of the full optimized values. Moreover, $E^{(L)}(R)$ becomes practically identical to the classical electrostatic limit (dotted curve) beyond $R \simeq 2.5 \text{ \AA}$, as expected for the asymptotic long-range limit. The “error” of the localized Lewis-structure model is the “delocalization energy” (or “non-Lewis energy”) $E^{(NL)}$, which can be obtained as the variational energy difference

$$E^{(NL)}(R) = E^{(L)}(R) - E(R) \quad (2.2)$$

and is also plotted in Fig. 2.4 (squares, right-hand scale). In perturbation-theory language, $E^{(L)} = E^{(0)}$ is the “zeroth-order” energy, corresponding to the unperturbed model Hamiltonian $\hat{H}^{(0)}$, and $E^{(NL)}$ is the sum of perturbative corrections (cf. Eq. (1.5a)). As seen in Fig. 2.4, $E^{(NL)}$ is a relatively small correction to $E^{(L)}$ ($\sim 15\%$ near R_{eq} and less than 1% beyond 3 \AA), which should be well approximated by second-order perturbation theory near R_{eq} . However, at smaller R the magnitude

of the delocalization correction increases strongly (exponentially), necessitating higher-order corrections.

Figure 2.4 shows that a classical electrostatic model provides an accurate description of ionic bonding in the long-range limit. However, this picture cannot be expected to describe the important effects of steric repulsion (included in $E^{(L)}$) and electronic delocalization (included in $E^{(NL)}$) that strongly affect the behavior near R_{eq} . We therefore focus on quantal steric and delocalization corrections that lead to significant deviations from the expected long-range electrostatic behavior.

To understand the behavior shown in Figs. 2.3 and 2.4, we can examine the calculated ionic charge at each R , as shown in Fig. 2.5. This figure displays the “charge transfer” (CT) from anion to cation, expressed as a percentage (% e) of an electron, showing the *continuous “leakage” of charge from anion to cation* as the ions approach. The CT is initially rather small (<0.5% e beyond $R > 5 \text{ \AA}$), but increases steadily to 1%–2% in the region inside R_{vdW} , then much more steeply in the near- R_{eq} region. As will be seen in Section 2.4 below, a donor–acceptor CT interaction that transfers merely 1% of an electron corresponds to an energy lowering of roughly 5–10 kcal mol $^{-1}$ (1% of an atomic unit), so the chemical forces associated with such charge leakage are indeed significant.

The irregular shape of the CT curve near R_{eq} reflects competition of unfavorable donor–donor interactions (steric repulsions) and favorable donor–acceptor

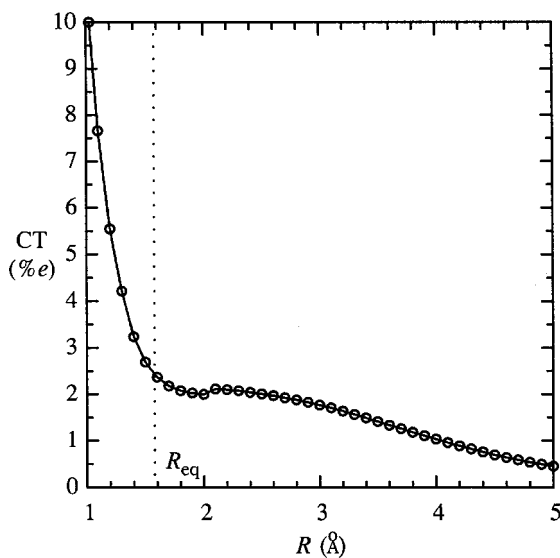


Figure 2.5 Charge transfer (CT; percentage of e charge) from F^- to Li^+ during ionic-bond formation. For reference, a dotted vertical line marks the equilibrium bond length. Note the steep rise corresponding to the onset of the “ionic–covalent transition” near $R = 1 \text{ \AA}$.

interactions as successive unfilled and filled orbital shells begin to overlap strongly. Increasing donor–acceptor overlap in turn confers increasing two-center (covalent) character on the shared electron pair, culminating in the “ionic–covalent transition” to a *dative* covalent bond near $R_c \simeq 0.73 \text{ \AA}$. Further aspects of this short-range behavior are discussed in Section 2.5.

Changes of orbital radii in ionic-bond formation

As would be expected from the charge shifts shown in Fig. 2.5, strong changes in ionic orbital radii accompany ionic-bond formation. Figure 2.6(a) compares the $2s_{\text{Li}}$ valence NAOs of LiF at three separations: $R = 4 \text{ \AA}$ (near the onset of strong ionic orbital overlap), $R = 1.6 \text{ \AA}$ (near R_{eq}), and $R = 1 \text{ \AA}$ (near R_c). Figure 2.6(b) shows a corresponding contour plot for the $2s_{\text{Li}}$ NAO with the incoming donor $2p_{\text{F}}$ orbital at $R = 1.6 \text{ \AA}$, illustrating the adaptation of orbital size to achieve favorable donor–acceptor overlap. The changes in orbital size associated with ionic bonding are related to those shown in Fig. 2.1 but less dramatic, since they involve smaller changes in fractional charge.

Ionic hybridization

Still another aspect of the Li and F valence orbitals is modified by ionic-bond formation. In an isolated ionic or neutral species, each NAO retains the characteristic angular shape of the pure s and p hydrogenic orbitals shown in Fig. 1.1, reflecting the full rotational symmetry of atoms. However, in the presence of another atom or ion this symmetry is *broken*, and the optimal valence orbitals acquire “ sp^λ hybrid” form (assumed for simplicity to include only valence s and p orbitals), as represented mathematically by

$$h = \frac{1}{(1 + \lambda)^{1/2}}(s + \lambda^{1/2}p) \quad (2.3)$$

In this expression, the hybridization parameter λ varies between 0 (pure s) and ∞ (pure p), with any integer or *non-integer* value in this range being physically allowed. The general relationships between λ and percentage s and p characters are given by

$$\%s = 100 \frac{1}{1 + \lambda} \quad (2.4a)$$

$$\%p = 100 \frac{\lambda}{1 + \lambda} \quad (2.4b)$$

or, equivalently,

$$\lambda = \frac{\%p}{\%s} \quad (2.5)$$

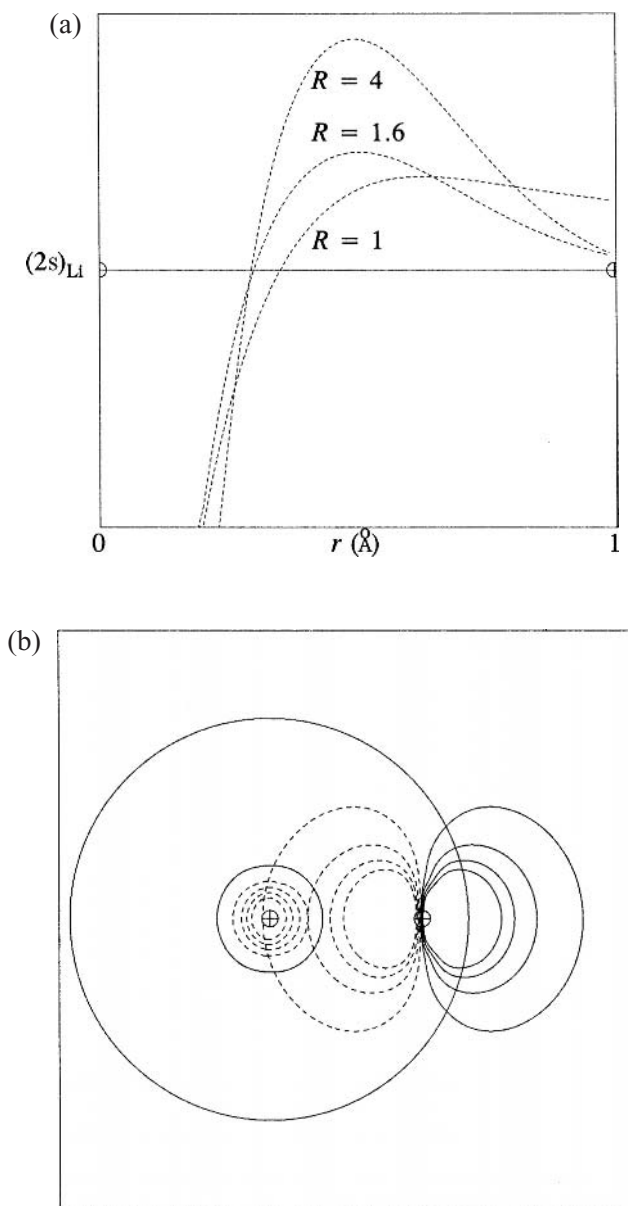


Figure 2.6 (a) Valence 2s NAOs for the Li ion at $R = 4$ Å (near the onset of the strong-overlap region), $R = 1.6$ Å (near equilibrium), and $R = 1$ Å (near the onset of the ionic-covalent transition). (b) Contour plots of unhybridized $2s_{\text{Li}}$ (left) and $2p_{\text{F}}$ (right) valence NAOs of LiF at $R = 1.6$ Å (cf. the middle plot of part (a)).

Example 2.2

An “ $sp^{0.5}$ hybrid” is an s-rich hybrid with

$$\%s = 100 \frac{1}{1 + 0.5} = 66.7\%, \quad \%p = 100 \frac{0.5}{1 + 0.5} = 33.3\%$$

somewhat more spherical (less directional) than a standard digonal sp hybrid (50% s character). Similarly, an “ $sp^{3.5}$ hybrid” is a p-rich hybrid with

$$\%s = 100 \frac{1}{1 + 3.5} = 22.2\%, \quad \%p = 100 \frac{3.5}{1 + 3.5} = 77.8\%$$

rather similar to a standard tetrahedral sp^3 hybrid (75% p character).

How does hybridization vary during ionic-bond formation? Figure 2.7 shows the numerical variation of percentage p character of optimal h_{Li} and h_F NHOs as a function of R in the range 1–5 Å. At large R , the valence NHOs are nearly sp^1 on Li and pure p on F. However, as bond formation proceeds, the hybridization on Li first becomes increasingly s-like ($\sim sp^{0.3}$ at $R \simeq 3$ Å), then sharply more p-like ($\sim sp^7$) in the near- R_{eq} region, and finally again more s-like below $R = 1.0$ Å. The F hybrid remains virtually a pure p orbital both at very long and at very short distances but acquires significant mixed hybrid character in the intermediate bonding region ($1.4 \text{ Å} < R < 3 \text{ Å}$), becoming $\sim sp^5$ -like near R_{eq} . These strong hybridization changes are indicative of important quantal deviations from an elementary electrostatic picture.

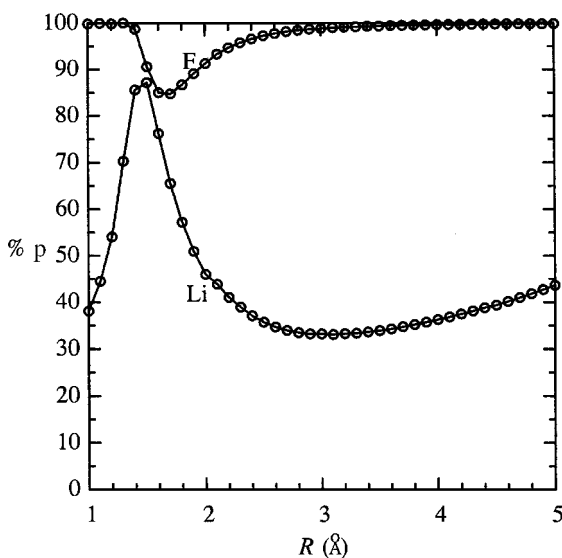


Figure 2.7 Percentage p character of Li and F bonding hybrids in ionic-bond formation.

The physical importance of the h_{Li} hybridization “spike” near $R = 1.45 \text{ \AA}$ can be understood from Fig. 2.8. This figure displays radial (left) and contour (right) plots of the overlapping h_{Li} and h_F hybrids for bond lengths slightly greater than ($R = 1.65 \text{ \AA}$, upper), equal to (middle), and less than ($R = 1.25 \text{ \AA}$, lower) this spike. As Fig. 2.8 shows, the h_{Li} hybrid undergoes an interesting inversion near $R = 1.45 \text{ \AA}$, which serves to maintain high $\langle h_{Li} | h_F \rangle$ bonding overlap, by pointing the hybrid right (toward the ligand) at longer R , but left (*away* from F) at shorter R , thereby avoiding the incoming *node* of the h_F orbital. The hybridized orbitals of Fig. 2.8 are evidently more effective at maintaining good donor–acceptor overlap than the idealized (unhybridized) $2s_{Li}$ and $2p_F$ NAOs of Fig. 2.6(b). Figures 2.7 and 2.8 illustrate the considerable subtlety and intricacy of near- R_{eq} electronic rearrangements, even in this most extreme case of ionic bonding.

The radial orbital profiles of Fig. 2.8 reveal another important aspect of ionic bonding. Whereas the anionic donor h_F orbital remains essentially of $2p$ character at all R , the radial character of the cationic acceptor h_{Li} orbital varies rather strongly with distance. Only at smaller R is h_{Li} composed primarily of $2s$ and $2p$ NAOs, whereas at larger R this hybrid incorporates more diffuse contributions of $3s$, $4s$, . . . type, to maintain bonding overlap with the receding h_F . Properly speaking, no finite R is entirely “outside” the overlap region where quantal CT effects (of *some* scale) could be expected. Nevertheless, vacant Rydberg (extra-valence-shell) NAOs of higher quantum shells are increasingly diffuse and of higher energy, so quantal effects are rapidly quenched as the overlap between *valence*-level shells of the cationic and anionic species diminishes. In this manner the full quantum electrostatics of orbital interactions grades asymptotically into the classical electrostatics picture (described by Coulomb’s law (2.1) and its polarization corrections) at long range. Only in the near- R_{eq} region of *valence* orbital interactions do the differences between classical and quantal pictures of ionic bonding become of critical chemical importance.

2.4 Donor–acceptor theory of hybridization in ionic bonding

An idealized localized picture of ionic bonding

A strictly localized picture of ionic bonding is qualitatively correct at large R , but incurs large errors in the near- R_{eq} region. We can evaluate this error by assuming an idealized localized description $\psi^{(L)}$ of the $Li^+ \cdots F^-$ ion pair, analogous to Eq. (1.32), with the idealized h_F doubly occupied and h_{Li} completely vacant. The model wavefunction $\psi^{(L)}$ is thereby prevented from undergoing charge-transfer (CT) delocalization between ions, and the energy difference $E^{(L)} - E^{(true)}$ measures the error of suppressing CT. At $R = 1.6 \text{ \AA}$, for example, this energy difference is calculated to be $0.0271 \text{ a.u.} \simeq 17 \text{ kcal mol}^{-1}$, a chemically significant error. Obviously, such a flawed “model chemistry” is in serious need of perturbative corrections.

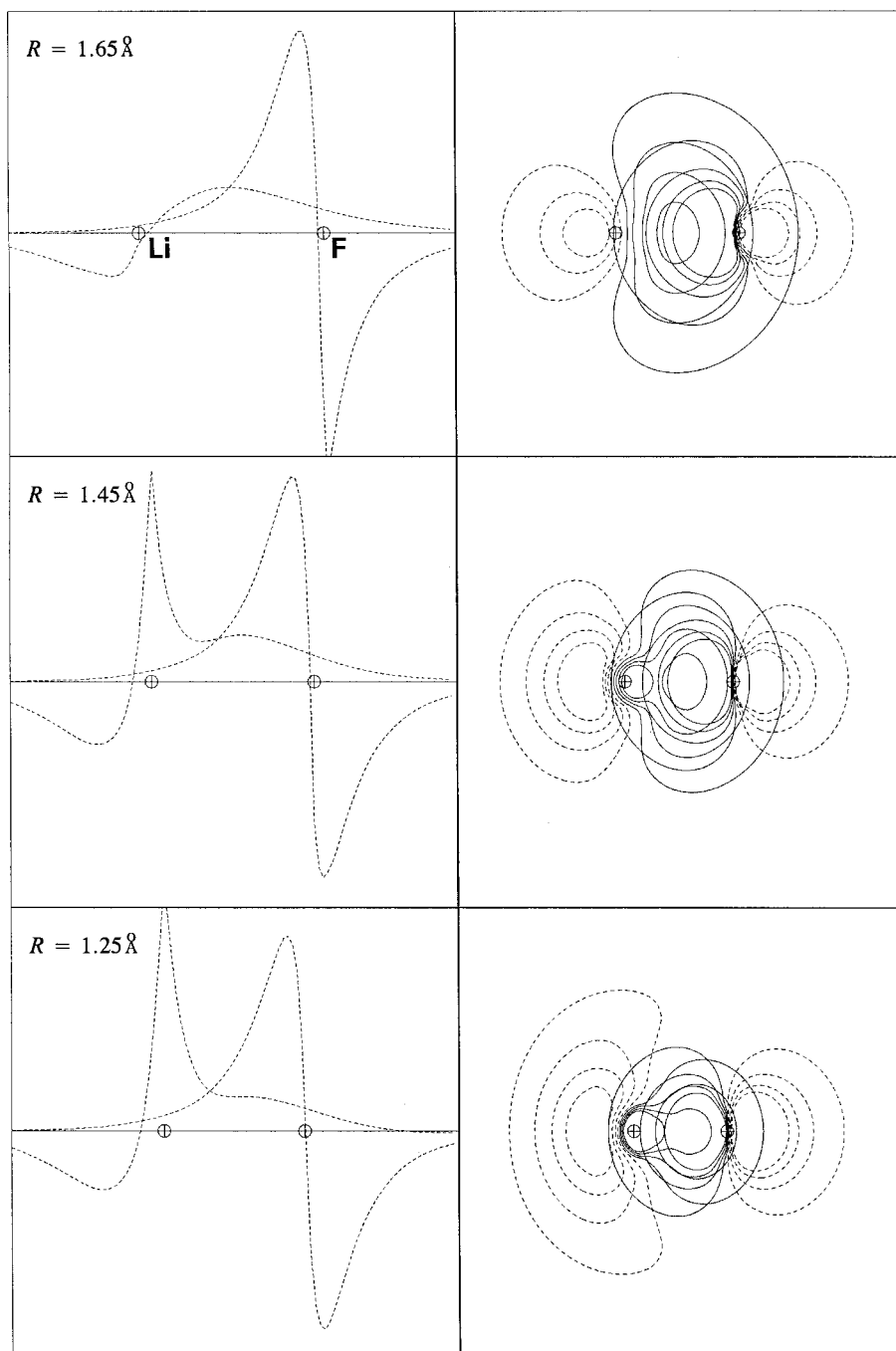


Figure 2.8 Li hybrid "inversion" near 1.45 Å.

Of the 17 kcal mol⁻¹ total error, about half is estimated to arise from the single $h_F \rightarrow h_{Li}$ sigma-type interaction shown in Fig. 2.8, while the remainder arises from weaker pi-type interactions (2–3 kcal mol⁻¹ each). For example, we can carry out a “partially localized” variational calculation, similar to that described above but with *only* h_F prevented from delocalizing into h_{Li} ; this leads to a stabilization energy (at $R = 1.6 \text{ \AA}$)

$$|E(\text{delete } h_F \rightarrow h_{Li}) - E^{(\text{true})}| = 0.0124 \text{ a.u.} \simeq 7.8 \text{ kcal mol}^{-1} \quad (2.6a)$$

The corresponding estimate from NBO second-order perturbative analysis is

$$-E^{(2)}(h_F \rightarrow h_{Li}) = 8.3 \text{ kcal mol}^{-1} \quad (2.6b)$$

in sensibly close agreement. Let us see how an energy lowering of this magnitude arises from the perturbation expressions of Section 1.4.

Theory of ionic donor–acceptor corrections

For the present case, the leading donor–acceptor correction $E_{DA}^{(2)}$, Eq. (1.24), can be rewritten as

$$E_{DA}^{(2)} = -2 \frac{\langle \phi_D | \hat{F} | \phi_A \rangle^2}{\epsilon_A - \epsilon_D} = -2 \frac{\langle h_F | \hat{F} | h_{Li} \rangle^2}{\Delta\epsilon} \quad (2.7)$$

where $\Delta\epsilon = \epsilon(h_{Li}) - \epsilon(h_F)$. Let us approximate the donor orbital $h_F = p_F$ as a pure valence 2p NAO on F, and the acceptor orbital as a variational trial function of the form (cf. Eqs. (1.22) and (2.3))

$$\tilde{\phi} = h(\lambda) = \frac{1}{(1 + \lambda)^{1/2}} (s_{Li} + \lambda^{1/2} p_{Li}) \quad (2.8)$$

where s_{Li} and p_{Li} are pure (unhybridized) valence NAOs of Li, and λ is an unknown hybridization parameter. Since s_{Li} and p_{Li} would have exactly *degenerate* energies in a hydrogenic approximation, and their actual energy difference is always much smaller than $\Delta\epsilon$ ($\sim 500 \text{ kcal mol}^{-1}$), we can see that not much error is incurred if we take $\Delta\epsilon$ to be *independent* of λ . The variational expression for $E_{DA}^{(2)}$ (cf. Eq. (1.22)) then becomes

$$E_{DA}^{(2)} \leq -\frac{2}{1 + \lambda} \frac{\langle p_F | \hat{F} | s_{Li} + \lambda^{1/2} p_{Li} \rangle^2}{\Delta\epsilon} \quad (2.9)$$

If we denote the right-hand side of (2.9) as $\mathcal{E}(\lambda)$, we can variationally *minimize* $\mathcal{E}(\lambda)$ with respect to λ by setting

$$\frac{d\mathcal{E}(\lambda)}{d\lambda} = 0 \quad (2.10)$$

If we further denote

$$f_{ps'} = \langle p_F | \hat{F} | s_{Li} \rangle, \quad f_{pp'} = \langle p_F | \hat{F} | p_{Li} \rangle \quad (2.11a)$$

$$F = f_{ps'} + \lambda^{1/2} f_{pp'} \quad (2.11b)$$

(with the primed index referring to Li acceptor NAOs), Eq. (2.10) is equivalent to

$$2(1 + \lambda) \frac{dF}{d\lambda} = F \quad (2.12)$$

with solution

$$\lambda_{opt} = (f_{pp'}/f_{ps'})^2 \quad (2.13)$$

For example, at $R = 2 \text{ \AA}$ the NAO Fock-matrix elements are⁶

$$f_{ps'} = 0.0348 \text{ a.u.}, \quad f_{pp'} = 0.0650 \text{ a.u.} \quad (2.14a)$$

$$\Delta\epsilon = \epsilon_{2s(Li)} - \epsilon_{2p(F)} = 0.2852 - (-0.5002) = 0.7854 \text{ a.u.} \simeq 493 \text{ kcal mol}^{-1} \quad (2.14b)$$

Equation (2.13) then leads to the estimate

$$\lambda_{opt} = sp^{3.5} \quad (78\% \text{ p character}) \quad (2.15a)$$

in reasonable agreement with the actual $sp^{3.2}$ (76.2% p character). When this λ_{opt} is substituted into Eq. (2.9), one obtains

$$E_{DA}^{(2)} = -0.0138 \text{ a.u.} = -8.7 \text{ kcal mol}^{-1} \quad (2.15b)$$

in reasonable agreement with Eqs. (2.6a) and (2.6b).

Hybridization and charge transfer in ionic bonding

Why do orbitals hybridize? It is apparent from Eq. (2.9) that hybridization ($\lambda \neq 0$) is a *general mechanism* for increasing the bonding strength.⁷ From the variational solution (2.13), one can see that sp^λ hybridization is promoted by stronger $f_{pp'}$ and weaker $f_{ps'}$ coupling, i.e., the p character of the hybrid increases if the donor orbital better “overlaps” the acceptor p' than the s' orbital. As indicated by Mulliken-type approximations (cf. Eq. (1.34)), the spatial overlap can often be used to “visualize” this hybridization propensity as the relative diffuseness of s and p orbitals is varied. Thus, in second-row atoms, where the 3p orbital is relatively larger than 3s, compared with the analogous 2p/2s ratio,⁸ there is a stronger tendency toward p-rich hybridization than in first-row atoms.

Perturbation theory can also be used to estimate the quantity of charge ($Q_{i \rightarrow j^*}$) transferred in a donor–acceptor interaction. From first-order perturbation theory,

it can be shown that the leading correction to the unperturbed orbital $\phi_i^{(0)}$ (cf. Eq. (1.18)) is given by

$$\phi_i^{(1)} = \sum_{j^*} \eta_{i,j^*} \phi_{j^*}^{(0)} \quad (2.16a)$$

where, as before (cf. Eq. (1.24)), $\phi_{j^*}^{(0)}$ is an orbital that is vacant in the initial $\psi^{(0)}$ configuration, and

$$\eta_{i,j^*} = - \frac{\langle \phi_i^{(0)} | \hat{F} | \phi_{j^*}^{(0)} \rangle}{\epsilon_{j^*}^{(0)} - \epsilon_i^{(0)}} \quad (2.16b)$$

In the same limit (cf. Eq. (1.23)) as that in which a single $\phi_{j^*}^{(0)}$ contribution to $E_i^{(2)}$ is dominant, the perturbed orbital ϕ_i becomes

$$\phi_i = \frac{1}{(1 + \eta_{i,j^*}^2)^{1/2}} (\phi_i^{(0)} + \eta_{i,j^*} \phi_{j^*}^{(0)}) \quad (2.17)$$

For small η_{i,j^*} , the electron density transferred from $\phi_i^{(0)}$ (donor) to $\phi_{j^*}^{(0)}$ (acceptor) can therefore be approximated as (cf. Eq. (1.24))

$$Q_{i \rightarrow j^*} = 2|\eta_{i,j^*}|^2 = 2 \left(\frac{\langle \phi_i^{(0)} | \hat{F} | \phi_{j^*}^{(0)} \rangle}{\epsilon_{j^*}^{(0)} - \epsilon_i^{(0)}} \right)^2 = -E_{i \rightarrow j^*}^{(2)} \Delta\epsilon \quad (2.18)$$

With the calculated NBO values (at $R = 1.6 \text{ \AA}$)

$$\langle \phi_i^{(0)} | \hat{F} | \phi_{j^*}^{(0)} \rangle = -0.0982; \quad \epsilon_{j^*}^{(0)} - \epsilon_i^{(0)} = 0.7615 - (-0.6939) = 1.455 \quad (2.19a)$$

Equation (2.18) gives the estimate

$$Q_{i \rightarrow j^*} \simeq 0.0092e \quad (2.19b)$$

which agrees reasonably with the calculated h_{Li} occupancy of $0.0098e$, about half the total CT shown in Fig. 2.5.

Equation (2.18) establishes an important relationship connecting $E_{i \rightarrow j^*}^{(2)}$ (the stabilization energy) and $Q_{i \rightarrow j^*}$ (the charge transferred) in a general donor–acceptor interaction. Since $\Delta\epsilon$ is typically a *large* energy separation (of order *unity* in a.u., $1 \text{ a.u.} = 627.5 \text{ kcal mol}^{-1}$), we can express this relationship in the approximate form

$$E_{i \rightarrow j^*}^{(2)} \simeq Q_{i \rightarrow j^*} \quad (2.20)$$

when both $E_{i \rightarrow j^*}^{(2)}$ and $Q_{i \rightarrow j^*}$ are in atomic units. This means, e.g., that a mere 1% e charge transfer (0.01 a.u. of charge) corresponds to a chemically significant 5–10 kcal mol^{-1} stabilization (~ 0.01 a.u. of energy), as mentioned in Section 2.3. (Note that, for smaller $\Delta\epsilon$, the stabilization associated with a small $Q_{i \rightarrow j^*}$ will be

even *larger* than the estimate suggested by Eq. (2.20).) To understand the subtleties of chemical bonding, we must therefore consider *small fractional changes* of electron density, not merely the “hopping” of full units of electron charge.

2.5 Ionic–covalent transitions

Long-range ionic–covalent “electron-hopping” transitions

The ionic portion of the potential-energy curve (Fig. 2.3) is terminated at both small and large R by strong changes in the wavefunction signaling “transitions” to non-ionic character. Each transition is associated with a characteristic cut-off distance for the short-range (inner $R_c^{(i)}$) or long-range (outer $R_c^{(o)}$) limit of ionic behavior. The nature of these two ionic–covalent transition limits will now be described, with particular emphasis on the short-range limit.

The outer cut-off at $R_c^{(o)}$ is a pure multi-configurational effect. Physically, it can be described as a long-range “electron hopping” from the anion to the cation, which becomes energetically favorable because the electron affinity (EA) of fluorine (0.1249 a.u.) is less than the ionization potential (IP) of lithium (0.1982 a.u.). The neutral $\text{Li} + \text{F}$ limit is therefore asymptotically favored over the ionic $\text{Li}^+ + \text{F}^-$ limit by 0.0732 a.u. as $R \rightarrow \infty$, and the character of the ground-state Born–Oppenheimer wavefunction changes rather abruptly at some intermediate crossing point where ionic and neutral configurations become degenerate. This necessitates a two-term configuration-interaction (CI) treatment in the crossing region, with pronounced change of configurational character near $R_c^{(o)}$. $R_c^{(o)}$ can be estimated as the distance (usually far outside the region where $E(\text{Li} + \text{F})$ varies appreciably) at which the Coulombic interaction of ions, Eq. (2.1), is just sufficient to overcome the asymptotic IP–EA energy difference favoring neutral species,

$$\frac{1}{R} = \text{IP}(\text{Li}) - \text{EA}(\text{F}) = 0.0732 \text{ a.u.} \quad (2.21)$$

leading to the approximate value

$$R_c^{(o)} \simeq \frac{1}{0.0732} \text{ a.u.} \simeq 7.2 \text{ \AA} \quad (2.22)$$

This distance is far beyond the equilibrium region of primary chemical interest, so we do not consider the long-range-hopping process further.

Short-range two-center delocalization

Of much greater chemical significance is the short-range ionic–covalent transition, which marks the inevitable collapse of a purely ionic description at shorter distances. In LiF this transition is centered around $R_c^{(i)} \simeq 0.73 \text{ \AA}$, all but hidden under the

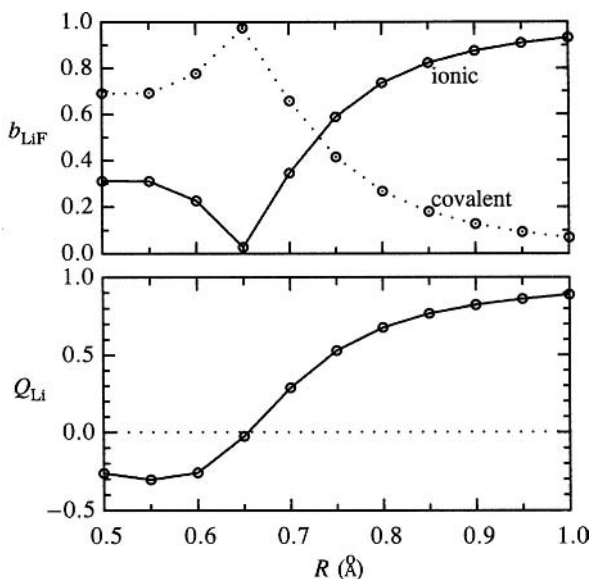


Figure 2.9 Variations of bond order (upper panel) and charge (lower panel) near the short-range ionic-covalent transition.

steeply rising portion of the potential-energy curve associated with the onset of strong steric repulsions. However, the “tail” of this transition significantly affects the near- R_{eq} region even in the present case of highest possible ionicity, and the influence of this transition becomes increasingly prominent in more representative ionic species discussed in this chapter.

The short-range ionic-covalent transition can be described as a continuous shift of the highest-occupied NBO from one-center (lone-pair) to two-center (polar-covalent-bond) form. For a general bonding NBO of the form given by Eq. (1.31a), this shift can be quantified in terms of the ionic and covalent bond orders $b_{\text{LiF}}^{(\text{ion})}$ and $b_{\text{LiF}}^{(\text{cov})}$ (cf. Eq. (1.42)). Figure 2.9 illustrates the calculated R -dependences of $\text{Li} \cdots \text{F}$ ionic and covalent bond orders (upper panel) and lithium charge (lower panel) in the region of the ionic-covalent transition. The ionic character of the $\text{Li} \cdots \text{F}$ bond declines rapidly below $R = 1 \text{ \AA}$, dropping to $\sim 50\%$ at $R \simeq 0.73 \text{ \AA}$ and to virtually pure covalency at $R \simeq 0.65 \text{ \AA}$. Correspondingly, the charge on lithium diminishes to *neutrality* at $R \simeq 0.65 \text{ \AA}$. Figure 2.10 depicts corresponding contour plots of the bonding NBO at three distances in this range ($R = 1.0, 0.73,$ and 0.65 \AA) to illustrate the progressive change from one-center to two-center form.

Of course, there is intrinsically no sharp physical distinction between a strongly delocalized lone pair and a highly polarized dative bond. As shown by Eq. (1.31a), a general NBO allows smooth variations of polarization coefficients between the single-center ionic ($c_A = 0, c_B = 1$) and two-center covalent ($c_A = c_B$) limits.

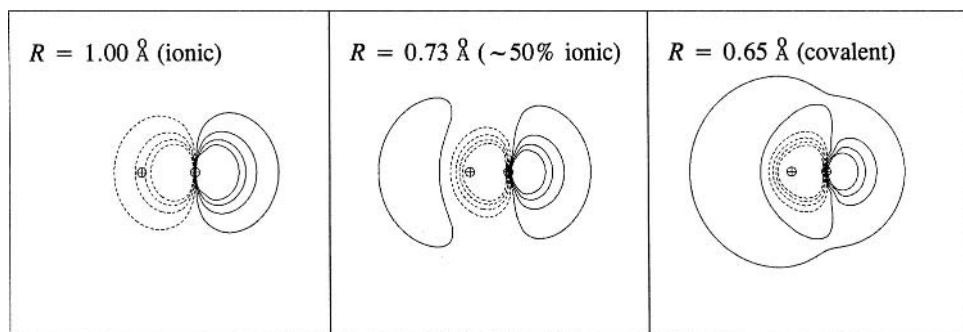


Figure 2.10 The bonding NBO of LiF, showing short-range transition from ionic to covalent form.

In practice, the NBO program labels an electron pair as a “lone pair” (LP) on center B whenever $|c_B|^2 \geq 0.95$, i.e., when more than 95% of the electron density is concentrated on B, with only a weak ($\leq 5\%$) “delocalization tail” on A. Although this numerical threshold produces an apparent discontinuity in program output for the best *single* NBO Lewis structure, the multi-resonance NRT description depicts smooth variations of bond order from $b_{\text{LiF}}^{(\text{ion})} = 1$ (pure ionic one-center) to $b_{\text{LiF}}^{(\text{ion})} = 0$ (covalent two-center). This properly reflects the fact that the ionic–covalent transition is physically a *smooth, continuous variation* of electron-density distribution, rather than abrupt “hopping” from one distinct bond “type” to another.

At still smaller distances, lithium becomes weakly *anionic* and the $\text{Li} \cdots \text{F}$ bond ionicity again increases, but with *opposite* polarity ($\text{Li}^- \text{F}^+$). This can be readily understood from the shapes of unfilled acceptor AOs. At short distances, the $(2p)_{\text{F}}$ orbital becomes an increasingly poor acceptor, because favorable overlap with one lobe is increasingly canceled out by unfavorable overlap with the opposite lobe, as shown in Fig. 2.6(b). Under these circumstances, the unfilled $(2s)_{\text{Li}}$ orbital becomes the best available acceptor orbital, and electron flow is actually reversed toward Li. However, these changes occur far inside the repulsive inner wall of the potential, so their effects will not be considered further here.

Steric effects in ionic bonding

It is also of interest to examine the *steric repulsion* between filled orbitals that dominates the energetics of the short-range region. Figure 2.11 shows the calculated steric exchange energy ΔE_{steric} (from natural steric analysis,⁹ a standard option of the NBO program) in the region $1 \text{ \AA} \leq R \leq 3 \text{ \AA}$. The total repulsion is shown (solid line) together with its individual orbital contributions (dashed lines) as the filled $(1s)_{\text{Li}}$ core successively “collides” with filled orbitals of the fluoride ion, first with the outer sigma-type $(2p_z)_{\text{F}}$ (near 3 Å), then with $(2s)_{\text{F}}$ (near 1.5 Å), and finally

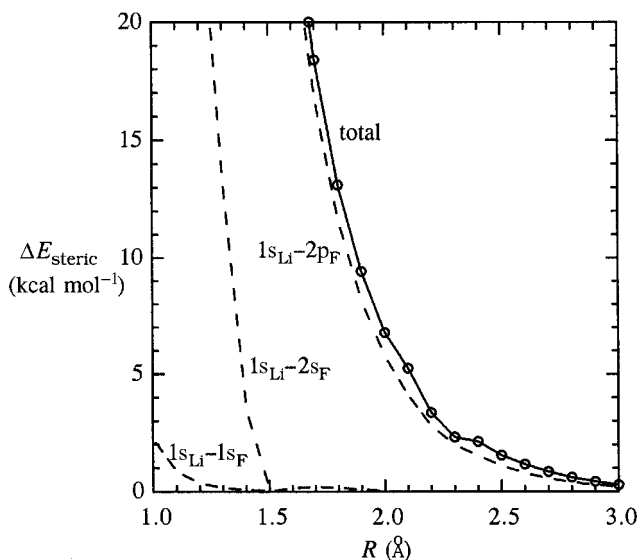


Figure 2.11 $\text{Li}^+ + \text{F}^-$ steric repulsions, showing total (solid) and individual orbital contributions (dashed) for filled-filled orbital interactions near $R_{\text{eq}} \simeq 1.6 \text{ \AA}$.

with the $(1s)_{\text{Li}}$ core pair (near 1 \AA). (Note that the pi-type $(2p_{x,y})_{\text{F}}$ lone pairs, being automatically orthogonal to $(1s)_{\text{Li}}$, pass through the lithium core region without steric disturbance.)

What is the physical origin of steric interactions in orbital terms? Steric repulsions are mandated by the Pauli exclusion principle and can be pictured in terms of the increasing *nodal features* (and hence, increasing oscillations and higher kinetic energy) needed to maintain interatomic orthogonality between occupied orbitals. This leads to a type of “steric pressure”¹⁰ as the electrons occupying a reduced volume are forced into orbitals of higher and higher kinetic energy, as described in Section 1.7. The increasing interatomic nodal features¹¹ are illustrated in Fig. 2.12 for the case of $(1s)_{\text{Li}}$ and $(2s)_{\text{F}}$ NAOs at three distances: $R = 2.0, 1.5,$ and 1.0 \AA . As can be seen in these plots, the NAO wave profiles are relatively smooth and free-atom-like at $R = 2.0 \text{ \AA}$, but become progressively “choppier” (higher kinetic energy) at $R = 1.0 \text{ \AA}$, corresponding to the steep rise in energy seen in the middle dashed curve of Fig. 2.11. The additional “wavelet” that each orbital acquires in the region of the approaching nucleus gives the NAO a rather strange appearance compared with the free-atom forms shown in Fig. 1.2. However, it may be noted that such *interatomic* nodal features are entirely analogous to the *intraatomic* radial oscillation of the $2s$ orbital near its own nucleus, which likewise maintains orthogonality to the $1s$ core and prevents unphysically smooth penetration of electron density into spatial regions that are already occupied by another electron pair (whether on the same or a different nuclear center).

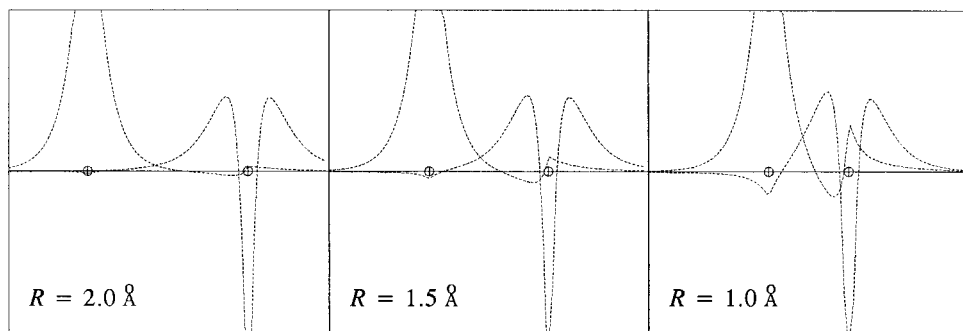


Figure 2.12 Radial profiles of filled $(1s)_{\text{Li}}$ (left) and $(2s)_{\text{F}}$ (right) NAOs, showing the increasing nodal feature at the opposite nucleus in each orbital as R decreases.

It should be emphasized that the ionic–covalent transition is a very *general* quantal phenomenon that terminates the classical-like behavior for *every* ionic interaction. The charge leakage from anion to cation is initially so weak as to be well described by the perturbative approximations of Section 2.4, but this leakage finally swells to an unrestrained flow as the barriers to charge flow collapse and ionic charges are *equalized* (Fig. 2.9). Thus, every ionic interaction culminates in a short-range quantal “phase transition” to a two-center *shared* electron distribution. In favorable cases (such as LiF), opposing steric interactions between filled orbitals (Fig. 2.11) cause this transition to remain *inside* R_{eq} , so the equilibrium species remains primarily ionic. However, as seen in Fig. 2.3, the near- R_{eq} quantal CT corrections are generally quite appreciable, even for ions of the greatest electronegativity difference. Hence, we shall generally need to consider *fractional CT* and the associated hybridization and polarization changes even in the most nearly ideal cases of ionic bonding.

2.6 Ion–dipole and dipole–dipole bonding

Classical electrostatic theory

When the net charge on a species is zero but its electric dipole moment $\vec{\mu}$ is non-zero, classical electrostatics predicts that the interaction with an ion is described by an *ion–dipole interaction* of the form (in atomic units)

$$E_{\text{es}}^{\text{i-d}}(R) = -\frac{Q_1 |\vec{\mu}_2|}{R^2} \cos \theta \quad (2.23)$$

where θ is the angle between $\vec{\mu}_2$ and \vec{R} (the vector from the ion to the dipole center). Equation (2.23) can be derived from a pairwise sum of terms like Eq. (2.1),

including interactions for each pole of the multipole,

$$E_{\text{es}}(R) = \frac{Q_1 Q_2}{R_{12}} + \frac{Q_1 Q_3}{R_{13}} + \frac{Q_2 Q_3}{R_{23}} \quad (2.24)$$

by making the assumption that the fixed dipole length (R_{23}) is much less than the ion–dipole separation ($R = (R_{12} + R_{13})/2$). Under a similar assumption for two fixed dipoles $\vec{\mu}_1$ and $\vec{\mu}_2$ separated by large distance R , one can similarly derive the energy expression for a *dipole–dipole interaction*,

$$E_{\text{es}}^{\text{d-d}}(R) = -\frac{\vec{\mu}_1 \cdot \vec{\mu}_2}{R^3} \quad (2.25)$$

According to Eq. (2.23), the magnitude of the ion–dipole interaction is maximized in collinear arrangements ($|\cos \theta| = 1$), and is attractive or repulsive according to whether the oppositely charged pole of the dipole is aligned toward or away from the ion. Similarly, the dipole–dipole attraction (2.25) is maximized when the dipoles $\vec{\mu}_1$ and $\vec{\mu}_2$ are parallel (attraction) or antiparallel (repulsion).

Like Eq. (2.1), the classical ion–dipole and dipole–dipole energy expressions (2.23) and (2.25) are engagingly simple, and can be rigorously justified at sufficiently large R . However, these approximations can be expected to fail at smaller R where quantal effects become appreciable.

Quantal ion–dipole bonding

To compare the classical and quantal descriptions of ion–dipole bonding, we consider the collinear approach of a lithium ion toward the negative (fluoride) end of a lithium fluoride molecule, with fixed equilibrium bond length 1.583 Å and dipole moment $\mu = 2.50$ a.u. = 6.36 D.¹² Figure 2.13 shows the calculated $\text{Li}^+ + \text{F-Li}$ potential-energy curve in the neighborhood of the equilibrium separation, $R = R_{\text{Li}\cdots\text{F}} = 1.7$ Å, comparing the full quantal calculation (circles, solid line) with the classical ion–dipole approximation (dotted line) of Eq. (2.23). The error of the classical ion–dipole estimate is more than 32 kcal mol⁻¹ (~48% of the well depth) at $R = 1.7$ Å, but much of this error can be attributed to the significant steric repulsions (estimated as ~20 kcal mol⁻¹ from Fig. 2.11) that are present at such short internuclear separations. The classical ion–dipole expression (2.23) also deviates widely from the underlying formula (2.24) from which it was derived,¹³ showing the invalidity of the long-range assumption in the near- R_{eq} region.

Ionic clusters and lattices

As mentioned in Section 2.1, Earnshaw’s theorem establishes that there can be *no* stable static equilibrium arrangement of classical ions and dipoles. Nevertheless, quantum mechanics allows numerous stable arrangements of ions, such as those

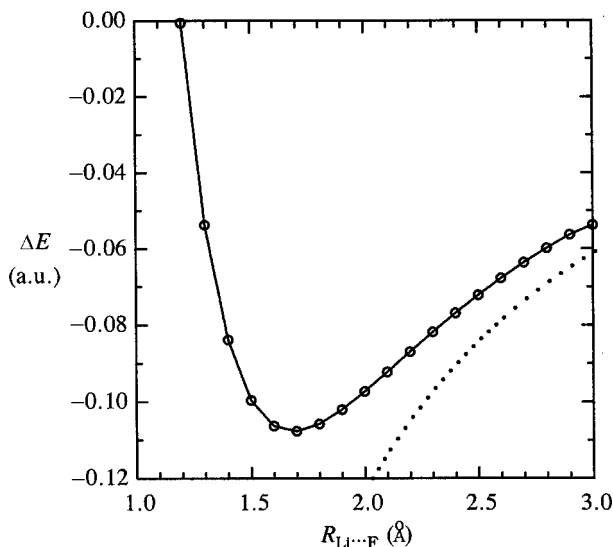


Figure 2.13 The potential-energy curve for collinear $\text{Li}^+ \cdots \text{F-Li}$ ion-dipole interaction, comparing quantal (solid) and classical electrostatic (dotted) values.

illustrated in Fig. 2.14 for various $(\text{Li}^+)_n(\text{F}^-)_m$ ion-dipole and dipole-dipole complexes. Optimized geometrical parameters, binding energies, and ionic charges for these species are summarized in Table 2.1.

The properties of many of these complexes are surprising from a classical electrostatic perspective. For example, no possible *dication* or *dianion* would be expected from classical electrostatics, since the classical energy could always be lowered by removing the “excess” ion to infinity. Yet FLi_3^{2+} and LiF_3^{2-} are both stable equilibrium species of trigonal D_{3h} structure, bound by $\sim 8\text{--}10 \text{ kcal mol}^{-1}$. Furthermore, while Eq. (2.25) would suggest the stability of linear $(\text{LiF})_n$ dipole-dipole complexes, it is quite surprising that the optimal “linear” structures (Figs. 2.14(f)–(h)) are slightly *curved*, and, moreover, these structures are strongly disfavored relative to corresponding *cyclic* complexes (Figs. 2.14(i)–(k)). Whereas a purely ionic picture of the dimer would slightly favor the cyclic over the linear structure by about 10% (cf. Example 2.1), the structure shown in Fig. 2.14(i) is actually favored over that in Fig. 2.14(f) by about 74%. Similarly, the binding energy of the cyclic structure is about 60% stronger than that of the linear for $n = 3$, and about 44% stronger for $n = 4$. The cyclic $(\text{LiF})_4$ complex (Fig. 2.14(k)) is only slightly ($< 1 \text{ kcal mol}^{-1}$) less strongly bound than the cubic structure (Fig. 2.14(l)), which models the actual crystalline ionic lattice of the salt.

Cooperative structural and energetic effects

Closer examination of the charges, distances, and energies in Table 2.1 reveals other subtle departures from classical electrostatic expectations:

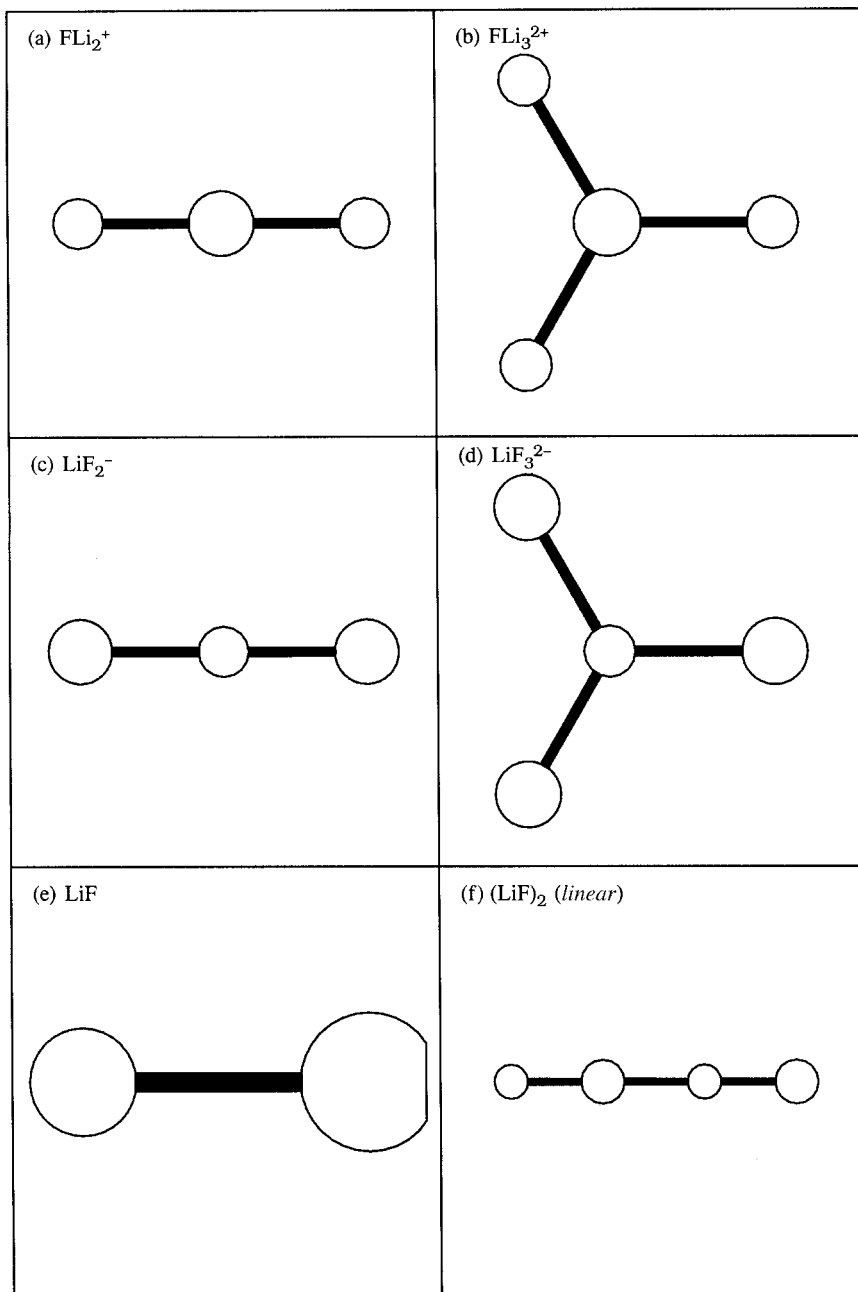


Figure 2.14 $(\text{Li}^+)_n(\text{F}^-)_m$ ion-dipole and dipole-dipole complexes (see Table 2.1).

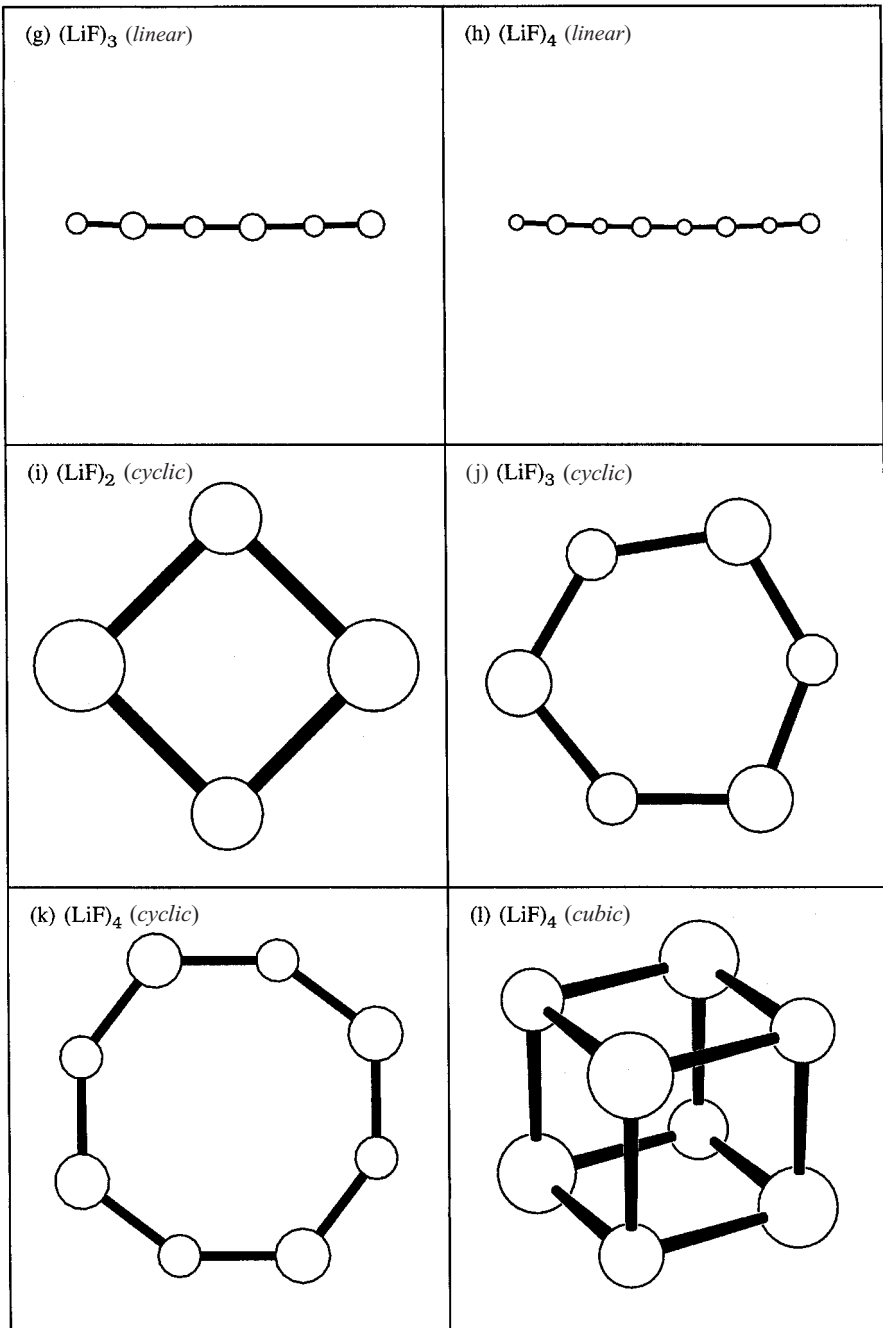


Figure 2.14 (Cont.)

Table 2.1. Selected structural, charge, and energetic properties of ion–dipole and dipole–dipole complexes (see Fig. 2.14); italicized values denote averages in low-symmetry structures

Species	Symmetry	$R_{\text{Li}\cdots\text{F}}$ (Å)	$\langle I_{\text{LiF}} \rangle$ (degrees)	$\langle I_{\text{LiF}} \rangle$ (degrees)	Q_{Li} (e)	E (a.u.)	$-\Delta E^a$ (kcal mol ⁻¹)
Ion–dipole complexes							
Li ⁺	K _h	—	—	—	1.0000	-7.28492	0.0
F ⁻	K _h	—	—	—	—	-99.88869	0.0
FLi ₂ ⁺	D _{∞h}	1.6767	180.0	—	0.9893	-114.86249	68.6
FLi ₃ ²⁺	D _{3h}	1.8735	120.0	—	0.9948	-122.05393	9.9
LiF ₂ ⁻	D _{∞h}	1.6991	—	180.0	0.9470	-207.46941	70.6
LiF ₃ ²⁻	D _{3h}	1.9073	—	120.0	0.9376	-307.25951	8.7
Dipole–dipole complexes							
LiF	C _{∞v}	1.5824	—	—	0.9613	-107.46825	0.0
(LiF) ₂ (linear)	C _{∞v}	<i>1.6750^b</i>	180.0	180.0	<i>0.9681^c</i>	-214.98929	33.1
(LiF) ₃ (linear)	C _s	<i>1.6885^d</i>	<i>178.9</i>	<i>179.1</i>	<i>0.9696^e</i>	-322.52207	73.6
(LiF) ₄ (linear)	C _s	<i>1.6929^f</i>	<i>179.1</i>	<i>178.9</i>	<i>0.9670^g</i>	-430.05867	116.5
(LiF) ₂ (cyclic)	D _{2h}	1.7368	90.0	90.0	0.9660	-215.02835	57.6
(LiF) ₃ (cyclic)	D _{3h}	1.7180	111.1	128.9	0.9646	-322.59244	117.8
(LiF) ₄ (cyclic)	D _{4h}	1.7104	127.3	142.8	0.9653	-430.14123	168.3
(LiF) ₄ (cubic)	T _d	1.8368	90.0	90.0	0.9529	-430.14257	169.2

^a For dipole–dipole complexes, ΔE is the binding energy relative to separated dipoles (isolated LiF molecules at equilibrium); for ion–dipole complexes, ΔE is the binding energy relative to separated dipole and ions (e.g., LiF + 2Li⁺ for FLi₃²⁺).

^b Average of 1.6160, 1.7799, and 1.6294 Å.

^c Average of 0.9792 and 0.9569 (F: -0.9706, -0.9656).

^d Average of 1.6273, 1.7543, 1.6624, 1.7586, and 1.6397 Å.

^e Average of 0.9818, 0.9702, and 0.9569 (F: -0.9719, -0.9697, -0.9673).

^f Average of 1.6319, 1.7452, 1.6743, 1.7267, 1.6752, 1.7499, and 1.6471 Å.

^g Average of 0.9826, 0.9718, 0.9693, and 0.9561 (F: -0.9723, -0.9703, -0.9702, -0.9670).

- (1) In $\text{LiF}_n^{(n-1)-}$ ion–dipole complexes, donor–acceptor charge leakage from F^- to Li^+ is apparent in each member of the series, but the incremental CT, expressed as a percentage of a full electronic charge, is progressively *weakened* with each added F^- ion,

$$3.87\% (n = 1) > 1.43\% (n = 2) > 0.94\% (n = 3)$$

(A similar trend is seen in the $\text{FLi}_n^{(n-1)+}$ series.) This reflects an anticooperative aspect of CT delocalization in the case in which a single acceptor orbital interacts with multiple donor orbitals, or a single donor with multiple acceptors. For example, a F lone pair that donates to one acceptor orbital becomes a *weakened* donor for similar interaction with a second acceptor orbital (a “busy” lone pair), due to the weakening of anionic character with each such donation. This weakening is also reflected in increasing $R_{\text{Li}\cdots\text{F}}$ bond lengths and decreasing binding energies as n increases.

- (2) In linear dipole–dipole clusters, each LiF unit retains its identity along the chain, but the two end units acquire conspicuous *ionic* character (cationic at one end, anionic at the other), whereas interior units are nearly neutral. For example, in $(\text{LiF})_4$ the successive Q_{LiF} charges along the chain are

$$+0.0103, +0.0015, -0.0009, -0.0109$$

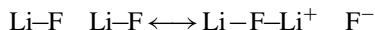
showing that the chain acquires significant *overall* dipolar character, corresponding to transfer of approximately 1% of an electron from one end to the other. This charge pattern is an obvious consequence of the donor–acceptor CT delocalizations discussed in Section 2.4. Each interior LiF serves *both* as a donor and an acceptor (to the adjacent filled $1s_{\text{Li}}-2p_{\text{F}}$ or unfilled $(2s)_{\text{Li}}$ orbital on its immediate left or right, transferring about $0.01e$ in each case, as estimated in Eq. (2.19b)), and therefore remains essentially *electroneutral*. However, end units can delocalize in *one* direction only, and therefore acquire net cationic or anionic character of about $\pm 0.01e$. The net charges (and therefore mutual attraction¹⁴) of the end groups evidently account simply for the tendency of the complex to bend slightly, against the tendency of each interior $(2p)_{\text{F}}-(2s)_{\text{Li}}$ donor–acceptor interaction to remain as linear as possible. The energetic penalty associated with maintaining oppositely charged ends of a linear complex can obviously be avoided by *closing* the two ends to form a *cyclic* complex, and Table 2.1 shows that this is the strongly preferred quantum-mechanical geometry in all cases.

- (3) The $R_{\text{Li}\cdots\text{F}}$ values in Table 2.1 suggest additional quantum subtleties of dipole–dipole interactions. In the linear $(\text{LiF})_n$ complexes, there is still a conspicuous difference (ΔR) between the $R_{\text{Li}\cdots\text{F}}$ distance within the LiF unit (R_{intra}) and that (R_{inter}) between units,

$$\Delta R = |R_{\text{inter}} - R_{\text{intra}}|$$

This difference is particularly strong for end units, but diminishes toward the interior of linear dipole chains. In linear $(\text{LiF})_4$, for example, ΔR is 0.12 and 0.10 Å for the two

end units, but only about half this value for the two middle units. This trend is consistent with the concept that increased CT delocalization tends to *symmetrize* R_{intra} and R_{inter} , in accordance with the resonance-diagram mnemonic,



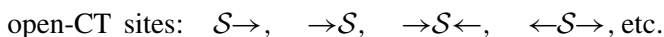
Such symmetrization (reduction of ΔR) is evidently enhanced toward the interior of the linear complexes as CT increases, and becomes *complete* ($\Delta R = 0$, D_{nh} symmetry) in the cyclic complexes, where CT delocalization is strongest.

Open- and closed-CT structures

Generalizing from this simple example, we may say that CT delocalizations are highly cooperative when balanced at each site, so that electron donation in one interaction is countered by electron acceptance in another interaction to preserve electroneutrality. A structure exhibiting such complementary pairing of donor–acceptor interactions may be called a “closed-CT” structure, with equal numbers of donations “in” and “out” of each site S , represented schematically as



Contrarily, an “open-CT” structure contains one or more sites with *unbalanced* donor–acceptor interactions, represented as



In this language, the cyclic $(\text{LiF})_n$ complexes are closed-CT structures (and thus maximally cooperative), whereas the corresponding linear complexes have “reactive” open-CT sites at both ends. As shown in Table 2.1, the energetic consequences of such open-CT versus closed-CT topology are considerable, with cyclic $(\text{LiF})_n$ complexes being stabilized, e.g., by more than 40 kcal mol^{-1} for $n = 3$. Thus, a simple ion–dipole or dipole–dipole picture is clearly inadequate for chemical accuracy.

The weak-dipole limit: the LiCO cation

It might be thought that the breakdown of the classical ion–dipole picture in the $\text{LiF} \cdots \text{Li}^+$ case is due to the unusual strength and ionicity of the Li–F dipole (leading to an unusually short ion–dipole separation that tends to invalidate the long-range assumption). That this is not the case can be seen by examining the interaction of a Li^+ ion with carbon monoxide (CO), a covalent molecule having much *weaker* dipole moment (calculated as 0.0717 D , with $\text{C}^{\delta-}-\text{O}^{\delta+}$ polarity¹⁵) and shorter bond length (1.128 \AA). Figure 2.15 shows the calculated $\text{Li}^+ \cdots \text{CO}$ potential-energy curve (circles, solid line) in comparison with the classical ion–dipole estimate

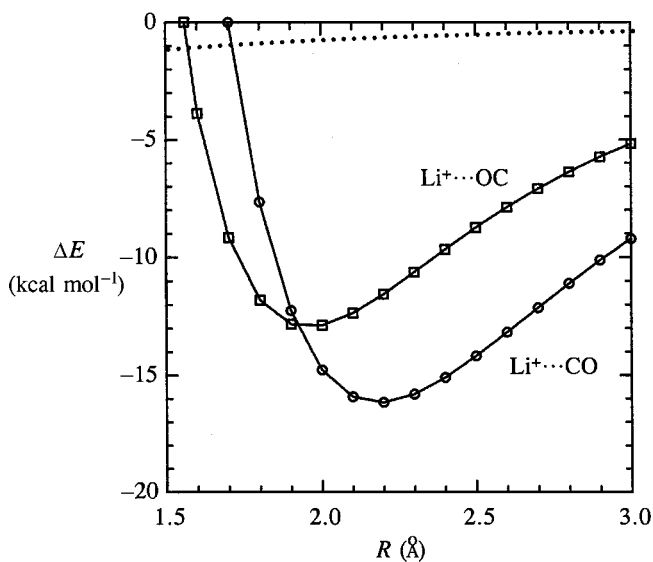


Figure 2.15 Potential-energy curves for linear $\text{Li}^+ \cdots \text{CO}$ (circles) and $\text{Li}^+ \cdots \text{OC}$ (squares) complexes, compared with the classical ion–dipole estimate (dotted line).

(dotted line), demonstrating that the relative errors of the latter are even *larger* than in the $\text{Li}^+ \cdots \text{FLi}$ case. Moreover, Fig. 2.15 also includes the corresponding $\text{Li}^+ \cdots \text{OC}$ potential-energy curve (squares, solid line) in which the dipole direction has been *reversed*. According to Eq. (2.23), such dipole reversal should result in a repulsive ion–dipole interaction, but the actual quantum potential-energy curve is still robustly attractive. Figures 2.13 and 2.15 and Table 2.1 demonstrate that simple classical formulas such as Eq. (2.23) may provide little or no useful guidance regarding the magnitude or angular dependence of the actual quantum-mechanical interactions in the near- R_{eq} region.

The strong $\text{Li}^+ \cdots \text{CO}$ and $\text{Li}^+ \cdots \text{OC}$ bonding (despite the negligible dipole of CO) can be readily understood in donor–acceptor terms. In carbon monoxide, the carbon and oxygen lone pairs (n_{C} and n_{O}) provide suitable donor orbitals for favorable overlap with unfilled $2s_{\text{Li}}$ orbitals approaching either end of the molecule, as shown in Fig. 2.16. Since the n_{C} NBO is somewhat more diffuse than n_{O} (as would be anticipated from the greater electropositivity of carbon), the $n_{\text{C}}-2s_{\text{Li}}$ interaction is somewhat stronger than $n_{\text{O}}-2s_{\text{Li}}$ (as can be judged from Fig. 2.16), and equilibrium is achieved at larger R (see Fig. 2.15). Indeed, the n_{C} and n_{O} orbitals in Fig. 2.16 appear virtually “isolobal” with the two lobes of the $2p_{\text{F}}$ orbital in $\text{Li}^+ \cdots \text{F}^-$ (cf. Fig. 2.6(b)). The donor–acceptor orbital diagrams thereby predict far-reaching similarities between $\text{Li}^+ \cdots \text{CO}$ and $\text{Li}^+ \cdots \text{OC}$ bonding (as is found), as well as parallels to the $2p_{\text{F}}-2s_{\text{Li}}$ bonding discussed in Section 2.4. However, more

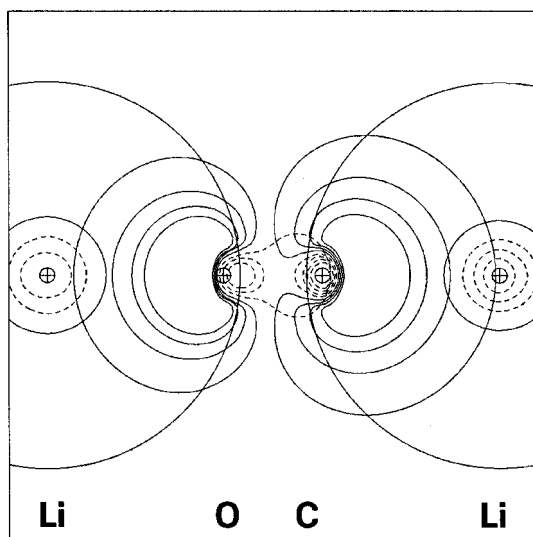


Figure 2.16 Orbital contours comparing $n_{\text{C}} - (2s)_{\text{Li}}$ (right) and $n_{\text{O}} - (2s)_{\text{Li}}$ (left) overlap, with each Li^+ at $R = 2.0 \text{ \AA}$ (cf. Fig. 2.15).

complete discussion of intermolecular interactions involving covalent molecules will be deferred to Chapter 5.

2.7 Bent ionic compounds of heavy alkaline earths

Bent geometry of alkaline earth dihalides

Surprisingly, dihalides and other ionic MX_2 compounds of the heavier alkaline earth metals are found to be *bent*. Klemperer and coworkers¹⁶ first found experimental molecular-beam evidence for nonlinear equilibrium geometries of BaX_2 and SrX_2 dihalides. In contrast, analogous Be and Mg species are known to be linear, and the geometry of CaX_2 species is indeterminate due to the extremely flat character of the potential-energy surface for bending motions. Theoretical calculations generally support such bending, both at Hartree–Fock and at correlated levels.¹⁷ Nonlinear X—M—X geometry conflicts with all simple bonding rationalizations, including models of ionic, valence-shell electron-pair repulsions (VSEPR), MO hybridization, Walsh diagrams, and valence-bond type.

Attempts to account for this bending have emphasized two physical effects, (1) d-orbital participation,¹⁸ and (2) core polarization,¹⁹ but no clear theoretical consensus has been achieved. The calculated bending in BaH_2 , for example, is found to disappear with removal of either d-orbitals or a polarizable-core, suggesting that both aspects are operative. The adequacy of the core-polarization rationale was questioned, and an alternative rationalization based on differences in atomic “softness” between metal and ligand was proposed by Szentpaly and Schwerdtfeger.²⁰

The NBO donor–acceptor picture

The NBO donor–acceptor picture suggests another factor responsible for such bending. Let us first examine an ultrasimplified treatment of the difluorides of strontium and barium, using the LANL2DZ (double zeta with effective core potential) basis set that *lacks* both d-orbitals and core orbitals. Despite omission of both physical effects mentioned above, the B3LYP/LANL2DZ equilibrium geometries of both SrF_2 and BaF_2 are found to be slightly bent (by about $7\text{--}9^\circ$). The NBO analysis shows that the leading metal acceptor orbital is (as usual) an s-rich sp hybrid. However, as shown in Fig. 2.17, this hybrid, denoted $(\text{sp}^\perp)_\text{M}$, has weak directional character oriented *perpendicular* to the near-linear X—M—X axis, so that the metal center appears distinctly “off-center” with respect to the s-like orbital contours. Thus, there is an obvious electronic driving force for each F^- ligand to break the linear symmetry, achieving improved $\langle 2\text{p}_\text{F} | (\text{sp}^\perp)_\text{M} \rangle$ overlap with the “fatter” end of the sp^\perp metal hybrid, as shown in Fig. 2.17. In effect, bending is favored because the metal acceptor orbital is slightly hybridized in pi-type (rather than usual sigma-type) fashion with respect to the incoming fluoride ligands.

The following question remains: “Why are the sigma-type interactions *weaker* than the pi-type interactions in this case?” This is apparently a geometrical effect, enforced by the relative sizes of M and X valence and core orbitals in the ionic bonding environment, and illustrated in the NAO diagrams of Fig. 2.18. We may

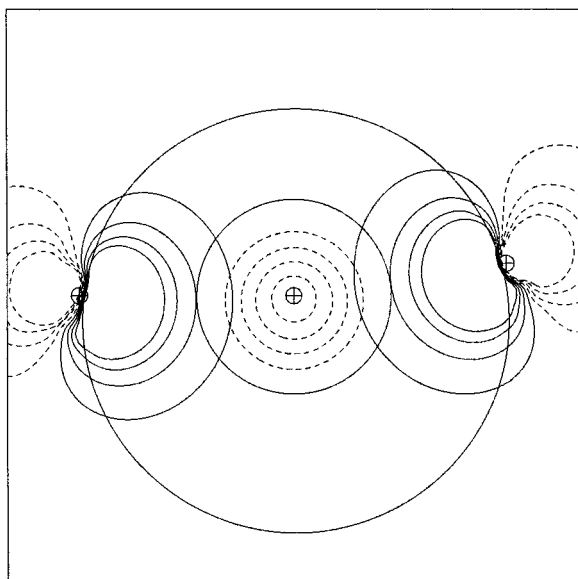


Figure 2.17 Leading $2\text{p}_\text{F} \rightarrow (\text{sp}^\perp)_\text{M}$ donor–acceptor interactions in SrF_2 , showing the sp^\perp acceptor hybrid interacting with the two incoming fluoride lone pairs. Each interaction is estimated as $8.18 \text{ kcal mol}^{-1}$ by second-order perturbation theory.

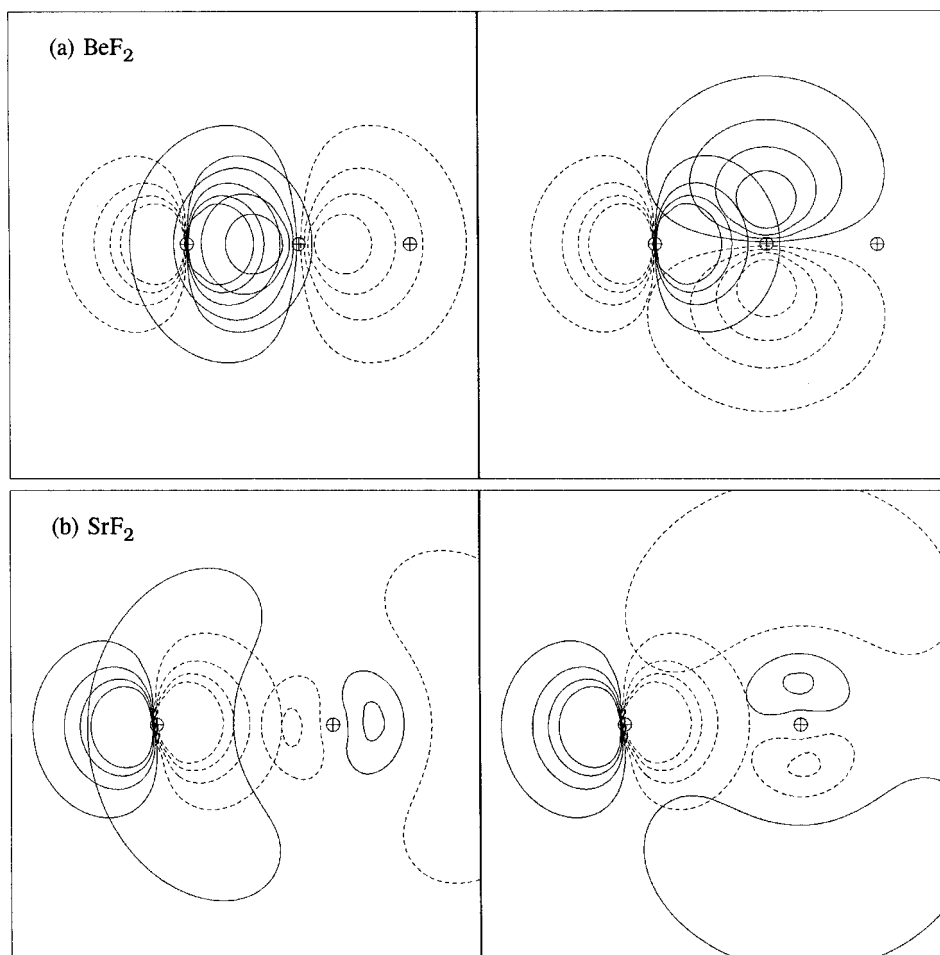


Figure 2.18 (a) BeF_2 σ -type (left) and π -type (right) $(p_F|p_M)$ NAO overlaps. (b) Similar for SrF_2 .

first recall (cf. Fig. 2.4) that the non-Lewis donor–acceptor contributions ($E^{(\text{NL})}$) are generally quite small compared with the dominant Lewis-type contribution ($E^{(\text{L})}$), which in turn is dominated by the strong electrostatic attraction between ions. Thus, if we initially ignore donor–acceptor interactions entirely, we can expect that strong ionic $\text{X}^- \cdots \text{M}^{2+} \cdots \text{X}^-$ interactions will bring each X^- ligand to an equilibrium R_{eq} separation corresponding approximately to the distance of steric “collision” with filled M core orbitals. Looking now at how empty $(p^\sigma)_M$ metal orbitals are spatially distributed, relative to the ligand at fixed distance R_{eq} , we can see that, for $M = \text{Be}$ (Fig. 2.18(a)), the $2p^\sigma$ metal orbital can still overlap favorably with the donor p_F orbital, but for $M = \text{Sr}$ (Figure 2.18(b)) the $5p^\sigma$ orbital has its outermost lobe virtually *centered* on the ligand nucleus, so that overlap with the ligand p_F

is virtually nil. (A very similar situation is seen for $M = \text{Ba}$, where the donor p_F orbital is again virtually centered in the diffuse outer lobe of the $6p^\sigma$ metal orbital, and thus achieves no significant matrix element with this orbital.) In this geometry, the metal p^π orbitals are actually at a more favorable separation to overlap with the incoming donor ligand, but only by bending away from linear symmetry (to break the cancellation between positive and negative lobes of the $(p^\pi)_M$ orbital) can the ligand– p^π interaction become appreciable.

How *far* the $X-M-X$ bending proceeds will of course depend on subtle details of the donor and acceptor orbitals, as well as the size and shape of the metal core that dictates R_{eq} . Thus, both core polarization and basis-set extensions to include d-orbital contributions may affect the equilibrium $X-M-X$ bond angle significantly, since both these factors affect the separation and shapes of donor and acceptor orbitals that dictate the relative strength of pi-type versus sigma-type couplings. Note that, if strong attractive ionic forces were not present, donor–acceptor interactions would naturally increase R_{eq} to maximize the ligand– p^σ overlap. Thus, the strange bending around heavier alkaline earths can be seen as a consequence of their unusually strong ionic attractions and spatially diffuse acceptor orbitals, which force the metal and ligand into unaccustomed proximity such that only pi-type donor–acceptor interactions (promoting bending) remain appreciable.

2.8 Ionic bonding in d-block elements

Ionic bonding in transition metals involves a rich new spectrum of donor–acceptor interactions with the partially filled d-shell. Indeed, the unique optical and magnetic properties of transition metal (TM) ions are directly attributable to the valence-shell reservoir of unpaired d electrons, with near-degenerate orbital energy patterns that are exquisitely “tunable” through interactions with ligands. A characteristic feature of such open-shell systems is that the electrons of spin “up” (α) have quite different spatial distributions than those of spin “down” (β), giving rise to different hybrids and bonding patterns in the two spin sets (“different Lewis structures for different spins”). In the present section we examine aspects of TM bonding to fluorine, the ligand of highest electronegativity.

Atomic and ionic configurations

Let us first consider the charge and spin distributions for atoms and ions of the first transition series ($M = \text{Sc, Ti, V, Cr, Mn, Fe, Co, Ni, Cu, Zn}$). The neutral ground-state TM electron configurations are of generic form s^2d^n , except at $n = 4$ (Cr: s^1d^5) and $n = 9$ (Cu: s^1d^{10}) where the well-known anomalies associated with the special stability of half-filled and filled d shells are manifested. The simplest picture of ionic bonding therefore involves metal ionization from an s orbital to give the

s^1d^n “high-spin” configuration. However, when the d shell is more than half-filled, the alternative s^0d^{n+1} “low-spin” configuration may be energetically preferred. Table 2.2 summarizes basic configurational and energy values for the ground-state

Table 2.2. Calculated B3LYP/6-311++G** energy values and spin properties for ground state configurations of selected atoms and ions

Atom	Experiment ^a	NPA ^b	$2S + 1$	$\langle \hat{S}^2 \rangle^c$	E (a.u.)
F	s^2p^5	$s^{2.00}p^{5.00}$	2	0.7513	-99.760 58
F ⁻	s^2p^6	$s^{2.00}p^{6.00}$	1	0.0000	-99.888 69
Sc	s^2d^1	$s^{1.96}d^{1.04}$	2	0.8150	-760.620 46
Sc ⁺	s^1d^1	$s^{1.00}d^{1.00}$	3	2.0004	-760.382 05
Ti	s^2d^2	$s^{2.00}d^{2.00}$	3	2.0022	-849.352 33
Ti ⁺	s^1d^2	$s^{0.25}d^{2.75}$	4 ^d	3.7505	-849.110 65
V	s^2d^3	$s^{1.85}d^{3.15}$	4	3.9956	-943.892 42
V ⁺	s^0d^4	$s^{0.00}d^{4.00}$	5	6.0004	-943.651 81
Cr	s^1d^5	$s^{1.00}d^{5.00}$	7	12.0002	-1044.423 60
Cr ⁺	s^0d^5	$s^{0.00}d^{5.00}$	6	8.7503	-1044.165 26
Cr ⁶⁺	s^0d^0	$s^{0.00}d^{0.00}$	1	0.0000	-1034.614 10
Mn	s^2d^5	$s^{2.00}d^{5.00}$	6	8.7576	-1150.967 68
Mn ⁺	s^1d^5	$s^{1.00}d^{5.00}$	7	12.0005	-1150.691 29
Fe	s^2d^6	$s^{1.80}d^{6.19}$	5	6.0095	-1263.650 24
Fe ⁺	s^1d^6	$s^{1.00}d^{6.00}$	6 ^e	8.7517	-1263.355 87
Fe ²⁺	s^0d^6	$s^{0.00}d^{6.00}$	5	6.0019	-1262.750 57
Fe ³⁺	s^0d^5	$s^{0.00}d^{5.00}$	6	8.7508	-1261.590 21
Co	s^2d^7	$s^{1.99}d^{7.00}$	4 ^f	3.7549	-1382.687 47
Co ⁺	s^0d^8	$s^{0.00}d^{8.00}$	3	2.0025	-1382.419 74
Ni	s^2d^8	$s^{1.00}d^{9.00}$	3	2.0002	-1508.250 42
Ni ⁺	s^0d^9	$s^{0.00}d^{9.00}$	2	0.7514	-1507.959 46
Cu	s^1d^{10}	$s^{1.00}d^{10.00}$	2	0.7504	-1640.472 26
Cu ⁺	s^0d^{10}	$s^{0.00}d^{10.00}$	1	0.0000	-1640.176 91
Zn	s^2d^{10}	$s^{2.00}d^{10.00}$	1	0.0000	-1779.353 53
Zn ⁺	s^1d^{10}	$s^{1.00}d^{10.00}$	2	0.7504	-1779.007 02

^a C. E. Moore, *Atomic Energy Levels*, National Bureau of Standards Circular 467 (Washington, U.S. Government Printing Office, 1949).

^b Calculated natural population-analysis (NPA) values for the minimum-energy configuration, unless otherwise noted.

^c Deviations from exact value $\langle \hat{S}^2 \rangle = S(S + 1)$ for a spin eigenfunction show the effect of slight spin contamination in UB3LYP wavefunctions.

^d Owing to convergence failures, no wavefunction conforming to a proper s^1d^2 configuration could be determined.

^e The nearly degenerate quadruplet (s^0d^7) state is incorrectly calculated as lower in energy: $E = -1263.363 89$.

^f The s^1d^8 configuration is incorrectly calculated as lower in energy: $E = -1382.703 37$.

atoms and atomic ions to be considered below. The calculated configurational assignments and relative energy values are generally in reasonable agreement with experiment, although Ni is incorrectly calculated to have a ground s^1d^9 configuration, and the results for Ti^+ and Fe^+ suggest an exaggerated preference for s^0d^{n+1} over the nearly degenerate s^1d^n configuration.

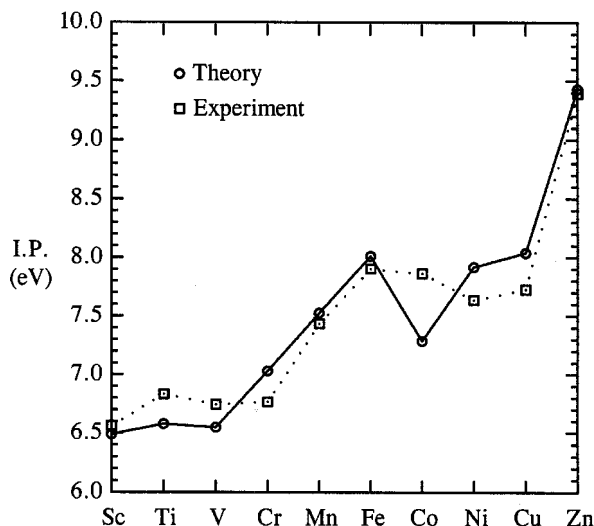
Example 2.3

The electron affinity (EA) of fluorine can be estimated from the first two entries of Table 2.2 as follows:

$$\begin{aligned}
 EA &= E(F) - E(F^-) \\
 &= -99.76058 - (-99.88869) = 0.12811 \text{ a.u.} \\
 &= (0.12811 \text{ a.u.})(627.5 \text{ kcal mol}^{-1} \text{ a.u.}) = 80.39 \text{ kcal mol}^{-1} \\
 &= (0.12811 \text{ a.u.})(27.21 \text{ eV a.u.}^{-1}) = 3.486 \text{ eV}
 \end{aligned}$$

This is within about 2% of the experimental value of 3.40 eV.

Similarly, the energy differences of Table 2.2 can be used to compute the first ionization potential of TM atoms for comparison with experiment, as shown in the plot below:



Since energy differences involving configurational changes are among the most challenging to compute accurately, one may conclude that B3LYP/6-311++G** reproduces the chemical trends fairly satisfactorily (mean absolute deviation 0.22 eV).

Table 2.3. Calculated bond lengths and energies of first-row transition metal monofluorides in low-spin and high-spin configurations (an asterisk marks the spin multiplicity of lowest energy)

Species	Low-spin			High-spin		
	$2S + 1$	R (Å)	E (a.u.)	$2S + 1$	R (Å)	E (a.u.)
ScF	1	1.7971	-860.586 83	3*	1.8584	-860.606 19
TiF	2	1.7741	-949.317 00	4*	1.7912	-949.324 10
VF	3	1.7971	-1043.821 86	5*	1.7997	-1043.864 98
CrF	4	1.7861	-1144.326 30	6*	1.8085	-1144.363 03
MnF	5	1.7971	-1250.844 52	7*	1.8521	-1250.895 18
FeF	4	1.7687	-1363.579 55	6*	1.8000	-1363.580 93
CoF	3*	1.7646	-1482.613 42	5	1.8072	-1482.603 88
NiF	2*	1.7864	-1608.165 43	4	1.7774	-1608.126 86
CuF	1*	1.7828	-1740.378 95	3	1.8399	-1740.270 40
ZnF	2*	1.8142	-1879.218 91			

Monofluorides of the first transition series

Let us first consider the charge and spin distributions in TM monofluorides MF for the first transition series. Calculated geometrical and energetic properties of these species are summarized in Table 2.3.

Natural population analysis of transition-metal-fluoride wavefunctions gives orbital populations that are generally consistent with the expected configurations, but with large departures from an idealized ionic picture. Table 2.4 compares the

Table 2.4. Charge and spin properties of ground-state TM monofluorides, showing the spin multiplicity ($2S + 1$), metal charge (Q_M), and idealized versus NPA configurations (α , β spin)

Species	$2S + 1$	Q_M	Alpha (\uparrow) spin		Beta (\downarrow) spin	
			Ideal	NPA	Ideal	NPA
ScF	3	0.7695	$s^1 d^1$	$s^{0.89} d^{1.17}$	$s^0 d^0$	$s^{0.01} d^{0.11}$
TiF	4	0.6785	$s^1 d^2$	$s^{0.83} d^{2.31}$	$s^0 d^0$	$s^{0.01} d^{0.13}$
VF	5	0.7060	$s^1 d^3$	$s^{0.77} d^{3.33}$	$s^0 d^0$	$s^{0.02} d^{0.13}$
CrF	6	0.7401	$s^1 d^4$	$s^{0.63} d^{4.46}$	$s^0 d^0$	$s^{0.02} d^{0.12}$
MnF	7	0.8376	$s^1 d^5$	$s^{0.92} d^{4.98}$	$s^0 d^0$	$s^{0.03} d^{0.14}$
FeF	6	0.7869	$s^1 d^5$	$s^{0.92} d^{4.98}$	$s^0 d^1$	$s^{0.03} d^{1.19}$
CoF	3	0.7586	$s^0 d^5$	$s^{0.09} d^{4.95}$	$s^0 d^3$	$s^{0.32} d^{2.86}$
NiF	2	0.7871	$s^0 d^5$	$s^{0.10} d^{4.95}$	$s^0 d^4$	$s^{0.26} d^{3.87}$
CuF	1	0.8249	$s^0 d^5$	$s^{0.14} d^{4.88}$	$s^0 d^5$	$s^{0.14} d^{4.88}$
ZnF	2	0.8431	$s^1 d^5$	$s^{0.93} d^{4.99}$	$s^0 d^5$	$s^{0.14} d^{4.99}$

calculated NPA $s^x d^y$ populations with the idealized configurations in each monofluoride. The early members of the sequence all have 11%–14% of an electron in the “empty” $d^{(\beta)}$ shell, as well as significant excess (17%–46% of an electron) over the expected integer value in the $d^{(\alpha)}$ shell. The strong differences between idealized and actual orbital occupancies can also be seen in the tabulated ionic charges (Q_M), which deviate from idealized unit charge by $\sim 30\%$ for early-TM species. Even for the most ionic late-TM species, more than 15% leakage of charge from F^- to M^+ is indicated.

It is noteworthy that the ionic charges do not follow a simple trend with respect to empirical electronegativity values (which increase from Sc to Zn). If anything, the ionicity of late-TM monofluorides tends to be somewhat *higher* than that of early-TM species. Because electronegativity values reflect primarily the sigma-electron-withdrawing strength,²¹ this inverted ordering is indicative of important pi-type interactions with the fluoride ion, as will be discussed below.

We can also examine the R -dependence of charge transfer in metal-fluoride bonding for comparison with the analogous behavior in $Li-F$ (Figs. 2.5 and 2.9). Figure 2.19 illustrates the R -dependent CT curve for $Sc-F$, which is found to terminate in a short-range ionic-covalent transition like that described in Section 2.5. Although the behavior is qualitatively similar to that found earlier for $Li-F$ (e.g., Fig. 2.9), it is evident that the TM species are much *closer* to this transition at their equilibrium geometry, reflecting much *stronger* two-center covalency effects

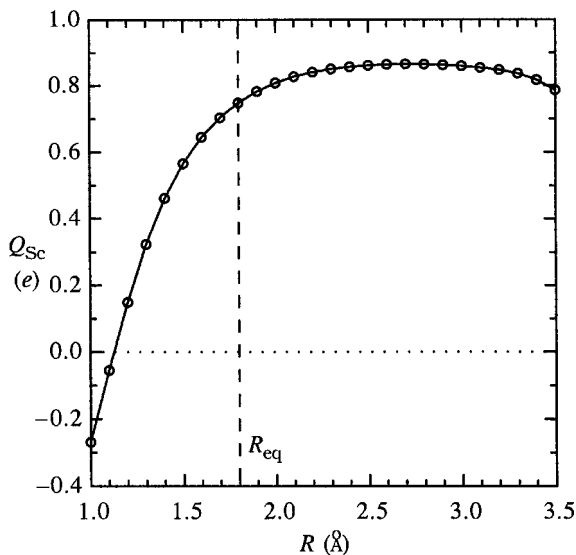


Figure 2.19 R -dependent variation of metal charge (Q_{Sc}) in $Sc-F$, showing R_{eq} (vertical dashed line) and the nearby short-range ionic-covalent transition.

in the near- R_{eq} region. Thus, quantal deviations from a classical ionic picture are systematically more important in TM complexes.

Transition-metal-ion hybridization

What are the expected hybrids for transition-metal bonding? In analogy with the treatment of Section 2.4, we expect that the p_{F} ligand donor orbital can interact with a general $sp^{\lambda}d^{\mu}$ hybrid mixture of valence s, p, d orbitals of the form (cf. Eq. (2.3))

$$h_{\text{M}} = \frac{1}{(1 + \lambda + \mu)^{1/2}} (s_{\text{M}} + \lambda^{1/2} p_{\text{M}} + \mu^{1/2} d_{\text{M}}) \quad (2.26)$$

with

$$\lambda = \frac{\%p}{\%s}, \quad \mu = \frac{\%d}{\%s} \quad (2.27)$$

By following the treatment of Eqs. (2.8)–(2.13), we are led analogously to variational estimates for the optimal metal hybridization,

$$\lambda_{\text{opt}} = (f_{\text{pp}'}/f_{\text{ps}'})^2, \quad \mu_{\text{opt}} = (f_{\text{pd}'}/f_{\text{ps}'})^2 \quad (2.28)$$

where $f_{\text{pd}'} = \langle p_{\text{F}} | \hat{F} | d_{\text{M}} \rangle$ (cf. Eq. (2.11a)). For example, for Sc—F in the empty β shell, these matrix elements are

$$f_{\text{ps}'} = -0.0444 \text{ a.u.}, \quad f_{\text{pp}'} = 0.0092 \text{ a.u.}, \quad f_{\text{pd}'} = -0.1303 \text{ a.u.} \quad (2.29a)$$

leading to

$$\lambda_{\text{opt}} = 0.04, \quad \mu_{\text{opt}} = 8.6 \quad (2.29b)$$

The simple variational estimate (2.29b) compares reasonably with the actual d-rich $sp^{0.01}d^{5.48}$ metal NHO found in this case (i.e., predicted 90% versus actual 84% d character). Similarly, for the mid-series Mn—F species the corresponding β -spin matrix elements have the values

$$f_{\text{ps}'} = -0.0576 \text{ a.u.}, \quad f_{\text{pp}'} = 0.0268 \text{ a.u.}, \quad f_{\text{pd}'} = -0.0908 \text{ a.u.} \quad (2.30a)$$

and lead to the variational estimate

$$\lambda_{\text{opt}} = 0.22, \quad \mu_{\text{opt}} = 2.49 \quad (2.30b)$$

in favorable agreement with the actual $sp^{0.03}d^{2.54}$ NHO.

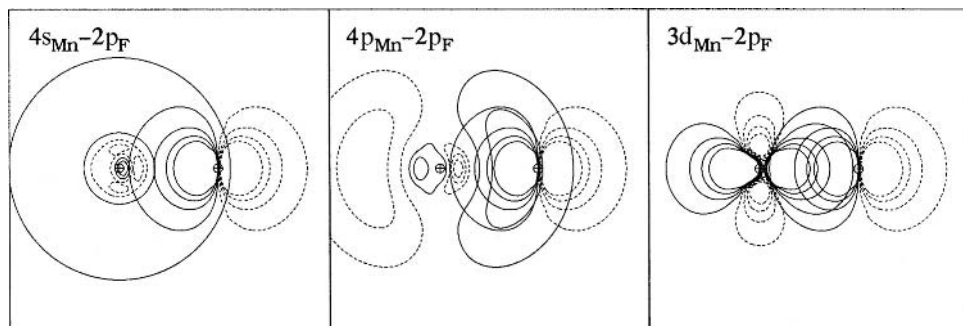


Figure 2.20 NAO contour plots corresponding to hybridization matrix elements (Eq. (2.30)) for Mn—F.

Why are the 3d orbitals so much superior to 4p orbitals at forming $sp^\lambda d^\mu$ hybrids? Figure 2.20 shows the relevant NAO contour plots for Mn—F, corresponding to the $f_{ps'}$, $f_{pp'}$, and $f_{pd'}$ Fock matrix elements in Eq. (2.30). As one can see in the middle panel of Fig. 2.20, the 4p orbital is so diffuse that its outer lobe tends to overlap with the *nodal plane* (rather than the bonding lobe) of the 2p_F orbital. Donor ligand interactions with 4p metal orbitals are therefore greatly weakened compared with those with 4s (left panel) or 3d (right panel). Similar overlap patterns are found throughout the series, which is consistent with the general result $\lambda \ll \mu$ for metal hybrid NBOs. Thus, to a first approximation we can virtually *ignore* the role of p orbitals in the metal “ $sp^\lambda d^\mu$ ” hybrid,²² focussing instead on “ sd^μ hybridization” of the TM atom. The shapes and angular bonding characteristics of general sd^μ hybrids will be discussed in Chapter 4.

Sigma- and pi-type donor–acceptor interactions

Further details of the leading $h_F \rightarrow h_M$ donor–acceptor interactions are gathered in Table 2.5 and Figure 2.21. For each such interaction the table shows the hybrid form of the donor (h_F)²³ and acceptor (h_M) orbitals, the occupancy of the acceptor, and the second-order estimate (cf. Eq. (1.35) or (2.7)) of the donor–acceptor stabilization energy. Let us now discuss some of the trends displayed in Table 2.5.

The preponderance of donor–acceptor interactions naturally arises from the β (minority) spin manifold, which retains unfilled s or d capacity throughout the series. As remarked above, the leading sigma acceptor hybrid is essentially of sd^μ type, varying from nearly pure d in Sc—F to pure s in Zn—F. Consistently with the electronic configurations summarized in Table 2.4, the h_M hybridization changes strongly from d-rich (for Fe—F) to s-rich (for Co—F) as the d-shell occupancy jumps from 20% to 60% of capacity. The sigma-type h_M hybrid participates in a strong (25–40 kcal mol⁻¹) donor–acceptor interaction with the h_M donor orbital

Table 2.5. Leading sigma- and pi-type donor-acceptor ($h_F \rightarrow h_M$) interactions in TM monofluorides, showing ligand donor hybrid h_F (sigma only), metal acceptor hybrid h_M and occupancy, and estimated second-order stabilization energy ($-\Delta E^{(2)}$, with associated degeneracy in parentheses) for each spin set

Species	Sigma				Pi			
	h_F	h_M	Occupancy (e)	$-\Delta E^{(2)}$ (kcal mol $^{-1}$)	h_M^{ν}	Occupancy (e)	$-\Delta E^{(2)}$ (kcal mol $^{-1}$)	
α spin								
ScF	sp ^{6,45}	sd ^{16,7}	0.0697	25.98	pd ^{33,6}	0.0321	7.82(2)	
TiF	sp ^{5,52}	sd ^{5,71}	0.0982	39.50	pd ^{41,3}	0.0443	10.51(2)	
VF	sp ^{6,34}	sd ^{3,14}	0.1019	38.22	pd ^{29,4}	0.0534	11.09(1)	
CrF	sp ^{8,08}	sd ^{1,41}	0.1206 ^b	— ^b	—	—	—	
β spin								
ScF	sp ^{4,57}	sd ^{5,48}	0.0632	26.72	pd ^{42,5}	0.0282	7.20(2)	
TiF	sp ^{4,22}	sd ^{6,12}	0.0774	35.82	pd ^{62,2}	0.0345	8.94(2)	
VF	sp ^{4,63}	sd ^{4,99}	0.0794	35.04	pd ³⁵	0.0337	8.30(2)	
CrF	sp ^{4,94}	sd ^{4,04}	0.0772	32.78	pd ^{25,4}	0.0306	7.49(2)	
MnF	sp ^{6,90}	sd ^{2,54}	0.0905	33.51	pd ^{19,8}	0.0391	7.81(2)	
FeF	sp ^{8,53}	sd ^{3,49}	0.1136 ^b	— ^b	pd ^{24,6}	0.0524	9.88(2)	
CoF	sp ^{7,40}	sd ^{0,33}	0.0957	33.40	pd ^{19,6}	0.0484	9.32(2)	
NiF	sp ^{9,65}	sd ^{0,22}	0.0912	28.74	pd ^{23,6}	0.0537	9.40(1)	
CuF	sp ^{11,6}	sd ^{0,08}	0.1640 ^b	— ^b	—	—	—	
ZnF	sp ^{13,1}	s	0.1332 ^b	— ^b	—	—	—	

^a In analogy with Eq. (2.3), π -type pd^{ν} hybrids of negligible s character are defined such that %p = 100/(1 + ν) and %d = 100 ν /(1 + ν).

^b Two-center σ_{M-F} bond NBO (with h_M occupancy calculated as $|c_M|^2$) in cases of stronger covalency.

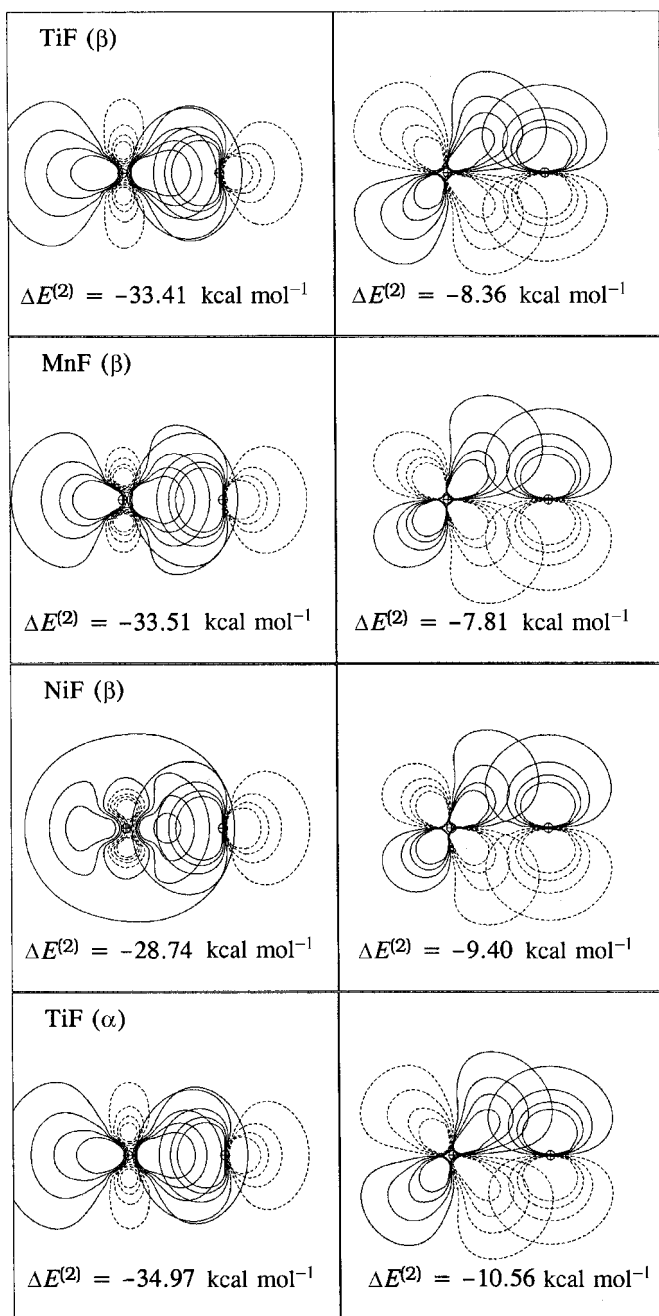


Figure 2.21 Leading sigma- (left) and pi-type (right) donor–acceptor interactions of representative TM monofluorides (see Table 2.5).

which is illustrated in Fig. 2.21 for Ti—F, Mn—F, and Ni—F (representative early-, middle-, and late-TM species). This single interaction transfers $\sim 7\%$ – 15% of an electron to the TM hybrid (generally increasing from left to right, in a manner consistent with the electronegativity trend), and constitutes the leading single contribution to CT shown in Fig. 2.19.²⁴ However, all but the last members of the series also exhibit strong pi-type interactions that transfer another 5% – 10% of e to the TM, as illustrated in the right-hand panels of Fig. 2.21. Such transfers are sequentially quenched in final members of the series as the shell fills to capacity. The right-hand panels of Fig. 2.21 illustrate the superior pi overlap achievable by d orbitals in d_M – p_F interactions, demonstrating why transition metals are much superior to other metals as pi acceptors.

In the α (majority) spin set, similar sigma-type interactions are possible only for the first four TM species, whose valence d orbitals are not completely filled. Two pi-type interactions are also possible for Sc—F and Ti—F, but only one for V—F, and none for later members of the series as the shell continues to fill. Donor–acceptor interactions in the α spin manifold are generally similar in form and magnitude to corresponding interactions in the β manifold, as illustrated in Fig. 2.21 for Ti—F. It is therefore evident that early-TM species (Sc—F, Ti—F) have about *twice* as many strong donor–acceptor interactions as typical mid- or late-TM species. Even if the strength of individual donor–acceptor interactions increases somewhat from left to right (in accordance with the electronegativity trend), early-TM species should generally manifest a *lower* degree of ionicity (higher overall CT), as is observed.

Higher oxidation states

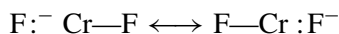
Finally, let us briefly examine some aspects of higher oxidation states in MF_n compounds. Table 2.6 compares geometries, charges, and bond energies of the Fe(II), Fe(III), and Cr(VI) fluorides with corresponding M(I)F species described above. It is apparent that the TM charge (Q_M) bears little relation to the formal “oxidation number” in any of these species, and the discrepancy increases in higher oxidation states (e.g., $Q_{Cr} = 1.59$ in Cr(“VI”)). By all measures, the transition-metal-fluoride ionic bond has *higher* covalent character and *stronger* CT delocalization as TM oxidation state increases. For example, each “F[−]” ion in CrF_6 donates more than 73% of e to the central chromium ion, and the associated sigma- and pi-type delocalization energies $\Delta E_\sigma^{(2)}$, $\Delta E_\pi^{(2)}$ are each about *six times* larger than corresponding estimates for the monofluoride, leading to significant (>0.08 Å) shortening of the Cr—F bond. A purely ionic picture of the bonding thus becomes increasingly unrealistic in these species.²⁵ An interesting aspect of the higher covalency in CrF_6 is the evident importance of linear three-center, four-electron bonding interactions

Table 2.6. *Geometry, metal charge, and bond energy^a of TM fluorides in higher oxidation states: Fe(I)–(III) and Cr(I) and (VI)*

Species	Symmetry	R_e (Å)	Q_M (e)	\bar{E}_{MF} (kcal mol ⁻¹)
FeF	$C_{\infty v}$	1.8000	0.7869	106.8
FeF ₂	$D_{\infty h}$	1.7674	1.4889	119.2
FeF ₃	D_{3h}	1.7693	1.9749	104.3
CrF	$C_{\infty v}$	1.8085	0.7401	112.3
CrF ₆	O_h	1.7244	1.5889	72.0

^a \bar{E}_{MF} is the average metal–fluoride bond energy relative to isolated ground-state atoms.

(“ ω bonds”; see Chapter 3) that can be described in the language of resonance theory as



However, such interactions properly lie in the domain of covalent and coordinate-covalent chemistry, to be discussed in Chapters 3 and 4.

2.9 Summary

A purely classical picture of ionic bonding is generally inadequate to account for the equilibrium structures and binding energies of polar compounds, even for the cases of highest known ionic character such as lithium fluoride. The quantal interactions of ions manifest continuous charge leakage from the anion to the cation. Such inter-ionic delocalization (charge transfer) is initially weak enough to be described by perturbation theory, but eventually leads to a dramatic transformation of the bonding NBO from one-center to two-center character (“ionic–covalent transition”), culminating in full covalency (charge neutralization and equal sharing of electrons) at small R .

For Li—F, the quantal ionic interaction can be qualitatively pictured in terms of the donor–acceptor interaction between a filled $2p_F$ orbital of the anion and the vacant $2s_{Li}$ orbital of the cation. However, ionic-bond formation is accompanied by continuous changes in orbital hybridization and atomic charges whose magnitude can be estimated by the perturbation theory of donor–acceptor interactions. These changes affect not only the attractive interactions between filled and unfilled orbitals, but also the opposing filled–filled orbital interactions (steric repulsions) as the ionic valence shells begin to overlap.

An important consequence of quantal charge transfer between ions and ion pairs (dipoles) is the appearance of *non*-pairwise-additive cooperative or anticooperative contributions that have no counterpart in the classical theory. These nonlinear effects strongly stabilize “closed-CT” systems in which each site is balanced with respect to charge transfers “in” and “out” of the site, and disfavor “open-CT” systems in which one or more sites serves as an uncompensated donor or acceptor. This CT cooperativity accounts for the surprising stability of cyclic $(\text{LiF})_n$ clusters, which are strongly favored compared with linear structures.

Donor–acceptor interactions also lead to strangely bent geometries in heavier F—M—F alkaline earth fluorides. Such bending can occur when strong ionic attractions force a filled fluoride p_z orbital into proximity with an orthogonal metal p_\perp orbital, for in this case symmetry-forbidden $(p_z)_F \rightarrow (p_\perp)_M$ interactions can “turn on” only when the strict σ/π symmetry of a linear F—M—F arrangement is broken.

Ionic bonding in d-block elements involves still more drastic breakdown of the classical ionic picture, due to the powerful sigma- and pi-type acceptor capacity of unfilled metal d shells. For sigma-type interactions, transition metals use pure sd^u hybrids that are fairly analogous to the leading acceptor hybrids of non-TM elements. However for pi-type interactions, transition metals deploy off-axis d_{xz} and d_{yz} orbitals whose d_M – p_F interactions are of much greater strength than analogous p_M – p_F pi-type interactions in non-TM species. Particularly due to this enhanced pi-acceptor capacity, leakage of charge from the donor ligand is much more pronounced for a TM than for a non-TM cation, corresponding to higher covalency in the former case. The degree of covalency is generally enhanced in MF_n polyfluorides of high metal oxidation state, where an increasing number of d_π acceptor orbitals becomes available to ligand pi-donor orbitals. Conversely, covalency tends to diminish in late-TM fluorides as filling of d_π orbitals successively quenches pi-acceptor capacity.

Notes for Chapter 2

1. J. R. Partington, *A Short History of Chemistry*, 3rd edn. (New York, Harper, 1957).
2. See, e.g., J. O. Hirschfelder, C. F. Curtiss, and R. B. Bird, *Molecular Theory of Gases and Liquids*, 2nd corrected printing (New York, Wiley, 1964), pp. 25ff.
3. This is synonymous with the region of significant overlap of orbital charge distributions, where the Pauli restriction (1.6) and quantal superposition effects become important.
4. The ionic portion of the interatomic potential is terminated at both smaller and larger R by covalent–ionic transitions (electron “hopping”), which are described in Section 2.5.
5. The quantum-mechanical energy curve was calculated at the B3LYP/6-311++G** level of hybrid density-functional theory, as described in Appendix A. However, due to B3LYP convergence failures beyond $R \approx 3 \text{ \AA}$, the quantities shown in Figs. 2.4–2.8 were calculated at HF/6-311++G** level.
6. These matrix elements can be obtained by including the FNAO keyword in the \$NBO keylist, to print out the Fock matrix in the NAO basis.

7. Note that, if the donor and acceptor s and p orbitals refer to the *same* atomic center, the coupling matrix elements $f_{ps'}$ and $f_{pp'}$ are identically zero, and hybridization cannot lower the energy. Hence, atomic hybridization is intrinsically a *bonding* effect.
8. The 2p orbital radius may be considered anomalously small (of the same order as the 2s orbital radius) because there is no inner shell of the same angular symmetry that exerts outward steric “pressure” due to the Pauli exclusion principle. (A similar exception causes the first transition series to appear anomalous compared with later lanthanides, since 3d orbitals form the innermost d shell.) The 2p → 3p expansion therefore appears to be relatively more pronounced than 2s → 3s expansion.
9. J. K. Badenhop and F. Weinhold, *J. Chem. Phys.* **107** (1997), 5406, 5422.
10. V. F. Weisskopf, *Science* **187** (1975), 605.
11. Note that Fig. 2.12 depicts NAOs rather than the PNAOs, since the latter do not include interatomic nodal features.
12. The dipole moment of LiF is only about 84% of the value expected for idealized unit point charges $|Q_{\text{Li}}| = |Q_{\text{F}}| = 1$ separated by R_{eq} . This reflects two factors: (1) the actual charges on each ion are reduced by CT; and (2) the actual electronic distributions cannot be represented as point charges, but are spatially distributed around the nuclei in accordance with the shapes of occupied orbitals.
13. The formula (2.24) is actually in far *worse* agreement with the quantal energy curve. At R_{eq} , for example, Eq. (2.24) predicts a binding energy more than four times stronger (and thus, more erroneous) than that predicted by Eq. (2.23).
14. Note that the long-range classical electrostatic limit furnishes an excellent approximation for the electrical attraction of the end groups, since these are separated far outside the range of significant exchange interactions.
15. The experimental value is 0.097 D (with the same surprising polarity).
16. L. Wharton, R. A. Berg, and W. Klemperer, *J. Chem. Phys.* **39** (1963), 2023; A. Büchler, J. L. Stauffer, W. Klemperer, and L. Wharton, *J. Chem. Phys.* **39** (1963), 2299; A. Büchler, J. L. Stauffer, and W. Klemperer, *J. Chem. Phys.* **40** (1964), 3471; and A. Büchler, J. L. Stauffer, and W. Klemperer, *J. Am. Chem. Soc.* **86** (1964), 4544. Subsequent experimental studies include V. Calder, D. E. Mann, K. S. Sheshardri, M. Allavena, and D. White, *J. Chem. Phys.* **51** (1969), 2093; and M. L. Lesiecki and J. W. Nibler, *J. Chem. Phys.* **64** (1976), 871.
17. M. Kaupp, P. v. R. Schleyer, H. Stoll, and H. Preuss, *J. Chem. Phys.* **94** (1991), 1360. Earlier theoretical studies include J. L. Gole, A. K. Q. Siu, and E. F. Hayes, *J. Chem. Phys.* **58** (1973), 857; N. M. Klimenko, D. G. Musaev, and O. P. Charkin, *Russ. J. Inorg. Chem.* **29** (1984), 639; D. R. Yarkony, W. J. Hunt, and H. F. Schaefer, *Mol. Phys.* **26** (1973), 941; U. Salzner and P. v. R. Schleyer, *Chem. Phys. Lett.* **172** (1990), 461, and D. M. Hassett and C. J. Marsden, *J. Chem. Soc., Chem. Commun.* **1953** (1953), 2260.
18. E. F. Hayes, *J. Phys. Chem.* **70** (1970), 3740.
19. M. Guido and G. Gigli, *J. Chem. Phys.* **65** (1976), 1397.
20. L. v. Szentpaly and P. Schwerdtfeger, *Chem. Phys. Lett.* **170** (1990), 555.
21. Thus, fluorine is the strongest sigma-withdrawing element known, but is a mild *donor* (pi base) in pi-type interactions.
22. The hybrids also contain small f-orbital contributions, which are not discussed further.
23. Sigma-type only; for pi-type interactions, h_{F} is a pure 2p orbital.
24. Note that, in several cases (Fe—F, Cu—F, Zn—F in the β spin set; Cr—F in the α spin set), delocalization is so strong that the NBO is of polar covalent (two-center) form.
25. For example, a purely ionic model of CrF_6 predicts a total binding energy (relative to Cr^{6+} plus six F^- isolated ions; cf. Example 2.1) of 7.9832 a.u., more than 1000 kcal mol⁻¹ less than the actual value.

3

Molecular bonding in s/p-block elements

3.1 Introduction

“Covalency” refers to the partial sharing of electrons that leads to mutual attraction of atoms, the profound and characteristic mystery of chemical bonding. The concept of covalency largely evolved from classical organic chemistry (the study of compounds of carbon, hydrogen, and nearby main-group elements) and achieved considerable maturity in the mid nineteenth century, long before Rutherford’s model of atomic structure made it possible to consider the deeper electronic implications of this concept. The latter step was achieved most notably by G. N. Lewis, who showed how the octet rule and shared-electron-pair concepts could provide a comprehensive rationalization of structural bonding principles. The elementary Lewis-structure picture of nonbonding (one-center) and bonding (two-center) valence electron pairs forms the starting point for practically all aspects of molecular bonding in s- and p-block elements, the subject of the present chapter. Extension of covalency concepts to d-block elements will be considered in Chapter 4.

Let us briefly outline the topics to be addressed, which span a rather wide range of covalent and noncovalent “effects” in the bonding of s/p-block elements. The localized Lewis-structure picture of covalent and polar covalent bonding is described in Section 3.2, starting from the simplest diatomic species (e.g., H_2^+ , H_2 , and dialkali analogs) and proceeding through singly and multiply bonded polyatomic species. Inadequacies of the single-Lewis-structure picture (“delocalization effects”) are described in Section 3.3, including conjugative and aromatic “resonance” effects, which are conventionally represented as contributions from additional Lewis structures. Weaker “hyperconjugative” delocalizations are described in Section 3.4, including those responsible for internal rotation barriers, anomeric effects, and other stereoelectronic phenomena. Further departures from the Lewis octet rule are discussed in Section 3.5 (hypervalency) and 3.6 (hypovalency), which respectively describe the important three-center, four-electron (3c/4e) and three-center,

two-electron ($3c/2e$) bonding patterns that augment standard lone-pair ($1c/2e$) and bond ($2c/2e$) elements of the conventional Lewis-structure model.

3.2 Covalent and polar covalent bonding

3.2.1 One- and two-electron covalent bonds in hydrogen and alkali diatomics

Molecular H_2 and related alkali-like diatomic species represent the simplest prototype of covalent bonding. Historically, the quantum theory of covalency was largely conceived and refined in the framework of applications to H_2^+ and H_2 , particularly in the classic works of Heitler and London,¹ Pauling,² James and Coolidge,³ and others.⁴ The one-electron H_2^+ ion is the only molecular species whose Schrödinger equation can be solved *exactly* in the Born-Oppenheimer framework,⁵ and its orbital solutions therefore play a guiding role (comparable to that of the hydrogen atom) in development of methods for describing many-electron molecules. Furthermore, through the remarkable work of Kolos and Wolniewicz,⁶ the low-lying states of H_2 are effectively known “exactly,” i.e., to an accuracy exceeding that of the best available experiments. Thus, these simple species provide the essential foundation for understanding the rich phenomena of covalency in more complex chemical systems.

Figure 3.1 illustrates the potential-energy curves for H_2 and H_2^+ , and analogous Li_2 and Li_2^+ species. As the comparison shows, qualitative differences distinguish

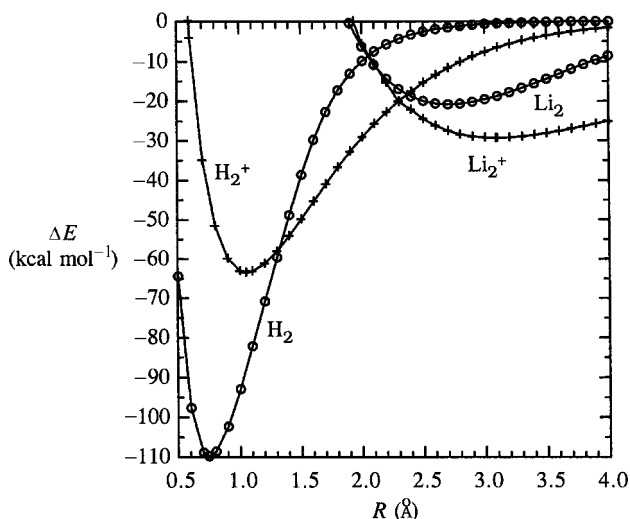
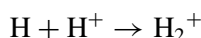


Figure 3.1 Diatomic potential-energy curves for H_2 , Li_2 and their cations. (The one-electron species H_2^+ is calculated at UHF/6-311++G** level; others at B3LYP/6-311++G** level.)

hydrogen from the other alkali diatomics. Li_2 exhibits only a weak, long-range form of bonding (with well depth less than one-fifth that of H_2), and this weakening becomes still more pronounced in Na_2 , K_2 , and heavier alkalis. Surprisingly, the bond of Li_2 is *strengthened* by ionization. This contrasts strongly with the normal behavior manifested by H_2 , whereby ionization leads to a one-electron “half bond” that is about half as strong as (67 versus 110 kcal mol⁻¹) and considerably longer (1.1 versus 0.7 Å) than that of the parent neutral species. Thus, we wish to understand both the normal covalency of dihydrogen and the surprisingly abnormal bonding in Li_2 and other dialkalis.

One-electron covalency: the hydrogen-molecule ion

Let us first consider the hydrogen-molecule ion, H_2^+ . It is evident that formation of this ion from its atomic fragments



can be considered as a *one*-electron donor–acceptor interaction between the filled $1s(\alpha)$ spin-orbital of H and the vacant $1s(\alpha)$ spin-orbital of H^+ . Such a description is analogous to that employed for ion–molecule bonding in Chapter 2, e.g., for the reaction $\text{OC}^+ + \text{Li}^+ \rightarrow \text{OC}—\text{Li}^+$ (cf. Figs. 2.15 and 2.16).

However, perturbation-theoretic expressions such as Eqs. (1.24) and (2.7) are problematic in the degenerate case when donor and acceptor orbitals have equal energies.⁷ In this case we can directly formulate the interaction of orbitals ϕ_A and ϕ_B (with equal energies $\epsilon_A = \epsilon_B = \epsilon$, and $F_{AB} = \langle \phi_A | \hat{F} | \phi_B \rangle$) in terms of a limiting *variational* model with 2×2 secular determinant

$$\begin{vmatrix} \epsilon - E & F_{AB} \\ F_{AB} & \epsilon - E \end{vmatrix} = 0 \quad (3.1)$$

This leads to the well-known variational solutions for the bonding-energy eigenvalues

$$E_{\pm} = \epsilon \pm |F_{AB}| \quad (3.2)$$

as depicted in Fig. 3.2 (cf. the corresponding perturbative Fig. 1.3). Thus, in the degenerate case we can replace Eq. (1.24) with a variational estimate of the form

$$\Delta E_{i \rightarrow j^*} = -n_i^{(0)} |\langle \phi_i^{(0)} | \hat{F} | \phi_{j^*}^{(0)} \rangle| \quad (3.3)$$

with $n_i^{(0)} = 1$ (rather than $n_i^{(0)} = 2$) for a one-electron donor–acceptor interaction such as in H_2^+ .

As discussed in Section 2.5, donor–acceptor interactions generally lead to progressive charge delocalization and “ionic–covalent transition” from one-center to

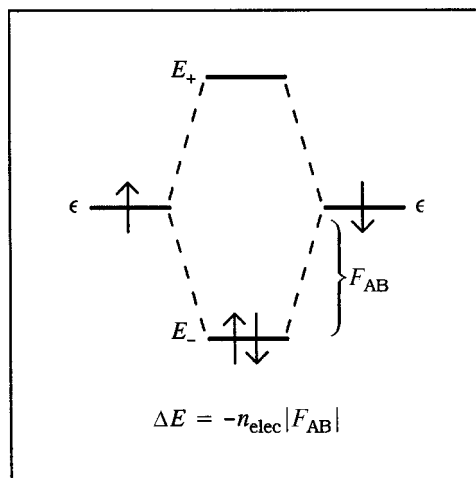


Figure 3.2 An energy-level-splitting diagram (cf. Fig. 1.3) for interaction of orbitals ϕ_A and ϕ_B with degenerate energy ϵ and interaction element $F_{AB} = \langle \phi_A | \hat{F} | \phi_B \rangle$.

two-center form. Thus, interaction of H and H^+ culminates in covalent two-center character ($H^{+1/2} \dots H^{+1/2}$) in which the distinction between “H atom” and “H ion” is completely obliterated. The long-range one-electron donor–acceptor interaction is generally expected to evolve smoothly into the familiar two-center molecular orbital (MO) which can be approximately described as

$$\sigma_{AB} = 2^{-1/2}(1s_A + 1s_B) \quad (3.4)$$

and is singly occupied (half-filled) in H_2^+ .

Two-electron covalency: the hydrogen molecule

In a similar fashion the bonding in H_2 might be formally regarded as a *complementary pair* of one-electron donor–acceptor interactions, one in the α (spin “up”) and the other in the β (spin “down”) spin set.⁸ In the long-range diradical or “spin-polarized” portion of the potential-energy curve, the electrons of α and β spin are localized on opposite atoms (say, α on H_A and β on H_B), in accordance with the asymptotic dissociation into neutral atoms. However as R diminishes, the α electron begins to delocalize into the vacant $1s_B(\alpha)$ spin-orbital on H_B , while β simultaneously delocalizes into $1s_A$ on H_A , until the α and β occupancies on each atom become *equalized* near $R = 1.4 \text{ \AA}$, as shown in Fig. 3.3. These one-electron delocalizations are formally very similar to the two-electron (“dative”) delocalizations discussed in Chapter 2, and they culminate as before (cf. Fig. 2.9) in an ionic–covalent transition to a completely delocalized two-center spin distribution at

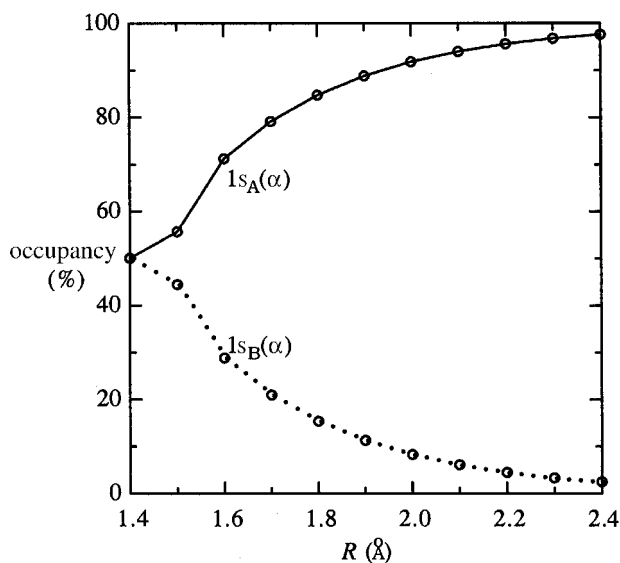


Figure 3.3 Percentage orbital occupancy of $1s_A(\alpha)$ and $1s_B(\alpha)$ spin-orbitals in the spin-polarized (diradical) portion of the potential-energy curve for H_A-H_B covalent-bond formation.

smaller R . Because these complementary delocalizations transfer charge in opposite directions in the two spin sets, each atom remains formally *electroneutral* at all R ($Q_A = Q_B = 0$), although the *spin-charges*⁹ on each atom are strongly varying with R . In this manner the classical electrostatic penalty for creating net dipolar character in mono-directional two-electron CT ($B: + A \rightarrow B:\delta^+ + A:\delta^-$; cf. Chapter 2) is completely avoided. We regard such *strong, complementary, bi-directional charge delocalization* as the essential driving force of covalent-bond formation.

Each of the complementary one-electron CT delocalizations culminates in an equivalent two-center MO (similar to that for H_2^+ ; cf. Eq. (3.4)), one for α and one for β spin. The final result is therefore equivalent to the conventional “doubly occupied MO” description of the H_2 ground state. Figure 3.4 shows the simple second-order estimate (Eq. (1.24)) of the stabilization predicted for two such one-electron donor–acceptor interactions, compared with the actual energy lowering in the long-range region ($R > 2.0$ Å). As expected, the second-order estimate is quite accurate in the long-range limit, but breaks down (reflecting the need for higher-order corrections) as the interaction strength increases at smaller R . Although Eq. (1.24) is quantitatively useful only at large R , and should be replaced by the more accurate variational estimate (3.3) in the near- R_{eq} region, it is clear that the fundamental energy lowering underlying covalent-bond formation can be traced to the same general donor–acceptor principles as those that were employed to describe ionic bonding in Chapter 2.

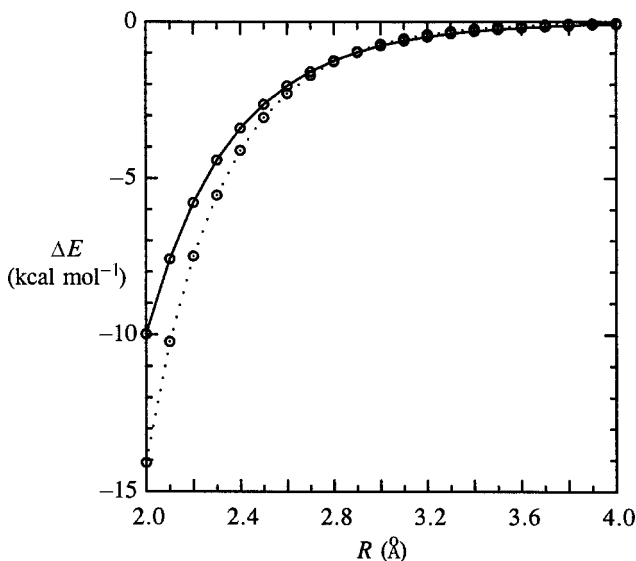


Figure 3.4 The long-range covalent binding energy ΔE (kcal mol^{-1}) of H_2 , comparing the actual value (solid line) with a second-order perturbation estimate for bi-directional donor–acceptor interactions (dotted line).

Comparison with the LCAO-MO description

Let us describe this somewhat unconventional bi-directional-CT picture of covalent bonding in greater detail. We write the spin-polarized NBO pair in terms of component α and β spin-orbitals as

$$(\sigma_{AB})^2 = \sigma_{AB}^{(\alpha)} \sigma_{AB}^{(\beta)} \quad (3.5a)$$

where as usual (cf. Eq. (2.17)) the complementary spin-NBOs can be pictured in terms of contributing donor and acceptor hybrid NHOs, chosen oppositely in the two spin sets,

$$\sigma_{AB}^{(\alpha)} = (1 + \eta^2)^{-1/2} (\mathbf{h}_A + \eta \mathbf{h}_B) \alpha \quad (3.5b)$$

$$\sigma_{AB}^{(\beta)} = (1 + \eta'^2)^{-1/2} (\mathbf{h}_B + \eta' \mathbf{h}_A) \beta \quad (3.5c)$$

Considering the α -spin electron, for example, the hybrid on H_A can be written as

$$\mathbf{h}_A = \mathbf{h}_A(\lambda) = (1 + \lambda^2)^{-1/2} (1s_A + \lambda \cdot 2p_A) \quad (3.6)$$

consisting primarily of the $1s_A$ AO weakly mixed with a polarizing $2p_A$ orbital ($\lambda \ll 1$).

Following a treatment analogous to that leading to Eq. (2.13), we can estimate the hybridization coefficient λ from the equation

$$\lambda \simeq (f_{sp'}/f_{ss'})^2 \quad (3.7)$$

For example, at $R = 1.0 \text{ \AA}$ the relevant NAO Fock-matrix elements are

$$f_{ss'} = \langle 1s_A | \hat{F} | 1s_B \rangle = -0.2472, \quad f_{sp'} = \langle 1s_A | \hat{F} | 2p_B \rangle = -0.0608 \quad (3.8a)$$

leading to the estimate

$$\lambda \simeq 0.06 \quad (3.8b)$$

This shows (as found for the actual NBO) that h_A remains practically a pure $1s$ atomic orbital at all distances, with no appreciable tendency to hybridize. Thus, we incur practically no error by picturing the spin-polarized NBO as a simple normalized linear combination of $1s$ AOs

$$\sigma_{AB} = c_A s_A + c_B s_B \quad (3.9)$$

as suggested by elementary valence theory. Inside $R \simeq 1.4 \text{ \AA}$ the spin-polarized NBO reduces to the unpolarized form given in Eq. (3.4). Thus, the donor–acceptor picture of covalent-bond formation is fully consistent with the usual LCAO-MO description of the H_2 ground state.

We can also verify that the usual LCAO-MO description (3.2) and (3.4) leads to predicted hybridizations that are generally consistent with the donor–acceptor estimates (3.8). Suppose that each H atom is associated with a valence spin-orbital of hybridized form (3.6). According to Eq. (3.2), the optimal electronic energy of bond formation is obtained by choosing the hybridization parameter λ to maximize the magnitude of the interaction element

$$F_{AB}(\lambda) = \langle h_A(\lambda) | \hat{F} | h_B(\lambda) \rangle = f_{ss'} + 2\lambda^{1/2} f_{sp'} + \lambda f_{pp'} \quad (3.10)$$

where $f_{ss'} = \langle 1s_A | \hat{F} | 1s_B \rangle$, $f_{sp'} = \langle 1s_A | \hat{F} | 2p_B \rangle$, and $f_{pp'} = \langle 2p_A | \hat{F} | 2p_B \rangle$. On differentiating this expression with respect to λ , we obtain

$$\frac{dF_{AB}}{d\lambda} = \lambda^{-1/2} f_{sp'} + f_{pp'} = 0 \quad (3.11a)$$

or

$$\lambda_{\text{opt}} = (f_{sp'}/f_{pp'})^2 \quad (3.11b)$$

At $R = 1.0 \text{ \AA}$, these matrix elements are

$$f_{sp'} = -0.0608, \quad f_{pp'} = 0.5375 \quad (3.11c)$$

leading to the estimate

$$\lambda \simeq 0.01 \quad (3.11d)$$

This is again consistent with the essentially pure *s* character of the bonding hybrids in H_2 .¹⁰

The energy expression (3.2) leads to the expectation that electronic bonding increases in proportion to

$$|F_{AB}| = |\langle 1s_A | \hat{F} | 1s_B \rangle| \propto S_{1s,1s} \quad (3.12)$$

that is, in proportion to the overlap of the *1s* orbitals. We might therefore ask “What prevents the *1s* orbitals from simply overlapping *perfectly* ($S_{1s,1s} = 1$) to give the united-atom limit ($R \rightarrow 0$)?” Although electrons might indeed favor such a limit, the Coulombic repulsion between nuclei effectively prevents such collapse. Nevertheless, it is true that the nodeless *1s* orbitals favor unusually small separation (0.74 Å) and high bonding overlap (0.7602), leading to a deep potential well (Fig. 3.1) at R_{eq} .

Inner-shell effects: the dilithium molecule

How does this picture change for Li_2 and other homonuclear dialkali species? Hydrogen is unique in having a valence *s* shell with no underlying core *s* electrons. Thus, if we compare the *2s*–*2s* interaction of Li_2 with the corresponding *1s*–*1s* interaction of H_2 , we can recognize two principal changes.

- (1) The *2s* orbital presents an additional radial *node* that prevents the incoming acceptor orbital from achieving perfect overlap ($S_{2s,2s} = 1$) without traversing an unfavorable intermediate region of phase mismatch, leading to strong reduction of bonding overlap. This is illustrated in Fig. 3.5 (left), which shows the overlapping *2s*-like valence hybrids of Li_2 at various R . As seen in Fig. 3.5(c) (left), the final equilibrium position ($R \simeq 2.7$ Å) occurs near the point where the outer contour of one *2s* orbital begins to penetrate the unfavorable region of opposite phase inside the radial node. Deeper penetration of a *2s* orbital into the core region yields sharply diminished electronic returns.
- (2) The filled (*1s*)² cores lead to additional *steric repulsions* with the incoming donor hybrid. These combine with nuclear Coulomb repulsions to oppose high electronic overlap. Figure 3.6 displays the calculated increase in steric repulsion as each filled *2s* spin-orbital of Li_2 “collides” with the filled core *1s* of the opposite atom. The paired one-electron steric repulsions shown in Fig. 3.6 are similar to the ionic two-electron steric repulsions of Fig. 2.11, and the wave-mechanical origin of the “steric pressure” would be analogous to that described in the discussion surrounding Fig. 2.12.

These two factors combine to create a “nodal barrier” at the boundary of the inner core region, which makes the Li_2 bond much longer and weaker than that of H_2 .

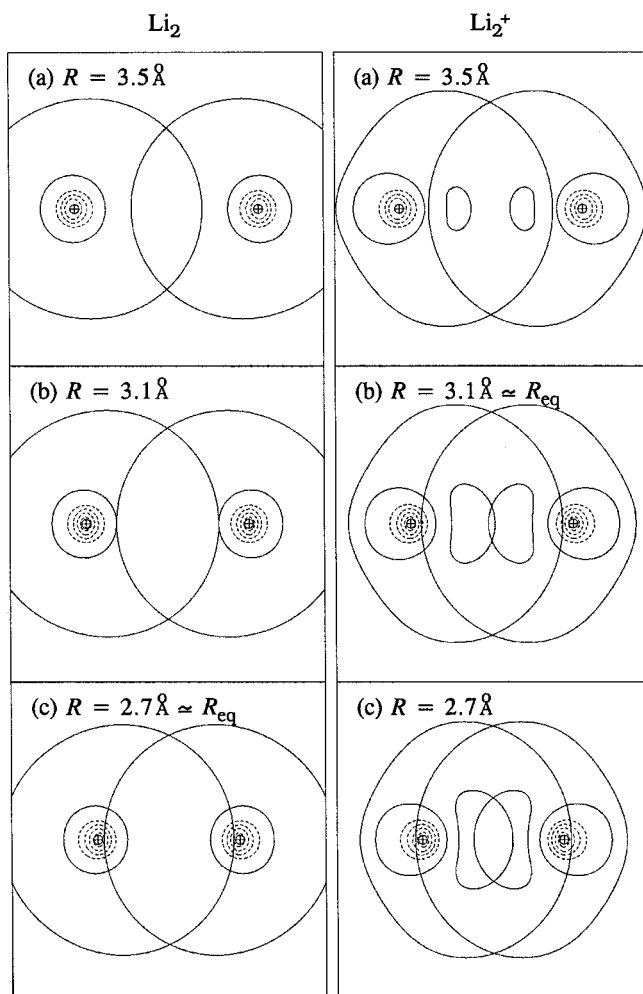


Figure 3.5 Overlapping natural hybrids of Li_2 (left) and Li_2^+ (right) at (a) $R = 3.5 \text{ \AA}$ (upper), (b) $R = 3.1 \text{ \AA}$ (middle, R_{eq} for Li_2^+), and (c) $R = 2.7 \text{ \AA}$ (lower, R_{eq} for Li_2).

In general, pure s-orbital bonding is intrinsically weak due to isotropic dispersal of bonding amplitude in all directions, with no particular bond-directional focus. This is particularly evident when bonding is restricted to the spherical annular region outside the outermost radial node, as occurs in all cases except 1s. Figure 3.7 illustrates the strong contrast in radial amplitude profiles for 1s–1s (upper) and 2s–2s (lower) overlap, each at the respective equilibrium distances in H_2 and Li_2 . From this figure it can be seen that the 2s orbital presents only feeble bonding amplitude to the opposite atom, with practically no radial gradient to promote closer approach of the atoms. Covalent bonding in dialkali species is therefore characterized by elongated

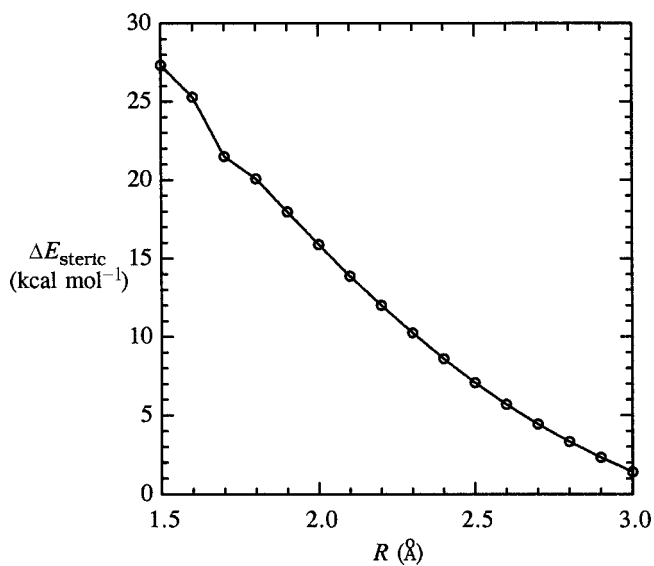


Figure 3.6 Steric repulsion energy in Li_2 (note that $R_{\text{eq}} = 2.70 \text{ \AA}$).

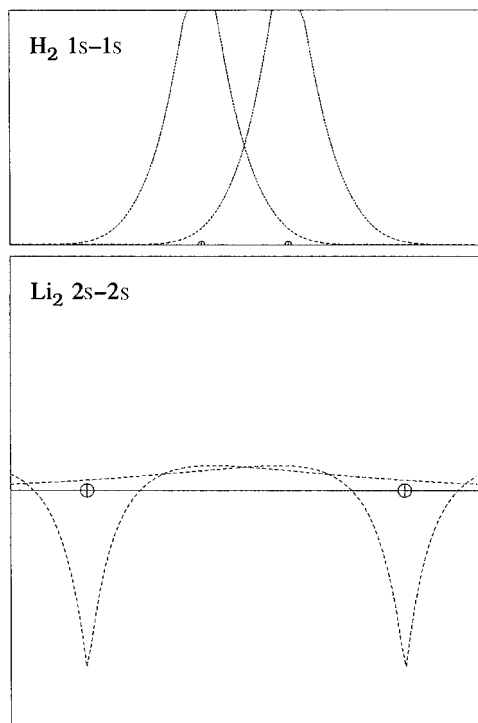


Figure 3.7 Overlapping NAO orbital profiles for 1s-1s (upper) in H_2 and 2s-2s (lower) in Li_2 .

bond distances, diminished bond strengths, and remarkably softened vibrational stretching modes, in sharp contrast to H_2 .

Anomalous bonding of the dilithium cation

We turn now to the paradoxical behavior of Li_2^+ , which manifests a one-electron bond that is *stronger* (but also *longer*) than the weakish two-electron bond of Li_2 . This strongly contradicts the naive bonding notion that the doubly occupied MO of Li_2 contributes *twice* as much bond strength as the singly occupied MO of Li_2^+ , i.e., that net bonding depends only on the number of electrons in the bonding MO, which is presumed to be of the form

$$\sigma_{\text{AB}} = 2^{-1/2}(2s_{\text{A}} + 2s_{\text{B}}) \quad (3.13)$$

in both species. As we shall see, the latter assumption is quite invalid.

The radically altered character of the bonding MO for Li_2^+ is evident from the form of its bonding NHOs, as illustrated in Fig. 3.5 (right). Compared with Li_2 , the bonding hybrids of Li_2^+ are obviously much more directional, corresponding to significant sp-hybrid character. If we choose, for example, the equilibrium bond length of Li_2 , $R = 2.7 \text{ \AA}$, we find the Li_2^+ bonding NHOs to be of $sp^{0.21}$ form (17.6% p character).¹¹ In contrast, the corresponding hybridization in Li_2 is $sp^{0.03}$ (2.7% p character), which is essentially similar to Eq. (3.11d) or (3.13). This difference can be qualitatively understood from comparison plots of the 2s and 2p NAOs for Li_2 and Li_2^+ , as shown in Fig. 3.8. One can see that the valence 2s and (particularly) 2p NAOs of Li_2^+ are favorably contracted to give significantly higher amplitude in the internuclear region of high bonding overlap (due to the stronger attractive nuclear charge), and are thus better adapted to making effective bonding hybrids. The numerical Fock-matrix elements confirm this visual assessment.

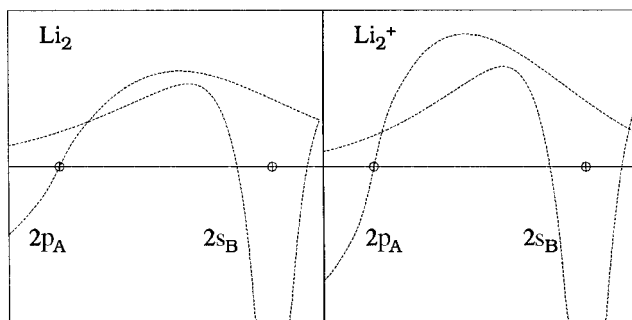


Figure 3.8 Orbital profiles of overlapping $2p_{\text{A}}$ and $2s_{\text{B}}$ NAOs in Li_2 (left) and Li_2^+ (right), both at $R = 2.70 \text{ \AA}$.

Let us now examine the consequences of net charge and enhanced hybridization for the bonding in Li_2^+ . According to Eq. (3.2), the two principal factors that dictate the energy of the lowest bonding MO are the non-interacting hybrid energy (ϵ) and the interaction element (F_{AB}). From general H-atom considerations (see, e.g., Eq. (1.12)) it is apparent¹² that increased net charge *lowers* the value of ϵ , namely -0.2309 in Li_2^+ versus -0.0766 in Li_2 at $R = 2.7 \text{ \AA}$. From variational relationships analogous to Eqs. (3.10) and (3.11), it is also apparent¹³ that increased hybridization *strengthens* the magnitude of the F_{AB} interaction, namely -0.1191 in Li_2^+ versus -0.0658 in Li_2 . From Eq. (3.2) we can therefore estimate that $E_- = -0.2309 - 0.1191 = -0.3500$ for Li_2^+ , *more than twice* as low as the corresponding MO energy estimate for Li_2 (-0.1346). Both estimates are in good agreement with the actual MO energies: -0.3493 for Li_2^+ and -0.1339 for Li_2 . Thus, even a *doubly* occupied MO of Li_2 cannot match the energy of the singly occupied MO of Li_2^+ . At internuclear distances throughout this general range, ionization of an electron from Li_2 to give Li_2^+ is therefore expected to be *exothermic*, as shown in Fig. 3.1. Note that the net charge effect for H_2^+ versus H_2 is expected to be generally similar to that for Li_2^+ versus Li_2 , so the dramatic reversal in relative neutral/cationic stabilities of these species is to be attributed primarily to the increased 2s–2p hybridization (and interaction strength) in Li_2^+ , which has no counterpart in H_2^+ .

We can also understand the anomalous bond-length relation between Li_2^+ and Li_2 in terms of the enhanced hybridization. As shown in Fig. 3.5(b) (right), the equilibrium bond length of Li_2^+ again lies close to where the outer lobe of the bonding hybrid just begins to penetrate the nodal barrier into the core region of the opposite atom. Li_2 and Li_2^+ are therefore similarly prevented from core penetration, but the sp-hybrids of Li_2^+ are noticeably more elongated (by $\sim 0.2 \text{ \AA}$ each) along the bonding axis. It follows that the nuclei in Li_2^+ are held at $\sim 0.4 \text{ \AA}$ greater internuclear separation than those of Li_2 in the equilibrium geometry. This radial elongation of the bonding hybrid seems to account most simply for the increased bond length of Li_2^+ versus Li_2 .

In conclusion, sp-hybrid character differs *strongly* between dialkali neutrals and cations, in sharp distinction to the rather constant s character in H_2 versus H_2^+ . A comparison of bonding in Li_2 and Li_2^+ therefore does not merely depend on the number of electrons in the bonding NBO (change in formal bond order), but rather reflects deep differences in the bonding hybrids themselves, particularly with regard to directional p character.

3.2.2 Polar and apolar covalency: NBO and valence-bond descriptions

In this section we wish to examine the detailed nature of the changes that accompany the gradual transformation from covalent to ionic bonding limits. We previously

discussed LiF as a prototype of ionic bonding (Section 2.3), and we noted the anomalously weak character of the covalent bonding in Li₂ (Section 3.2.1). Let us therefore examine the nature of the electronic changes in various AF fluorides as the bonding varies from pure covalent (A = F) to ionic (A = Li) through a series (A = F, Cl, Br, H, Li) of monovalent bonding partners.

NBO ionicity descriptors

For each member of the series, the molecule is well described by a Lewis-structure diagram of the form



with distinct $n_{\text{F}}^{(\sigma)}$ and $n_{\text{F}}^{(\pi)}$ (2) lone pairs (cf. Example 1.6) and a single σ_{AF} bond that can be written in the usual form (cf. Eq. (1.31a))

$$\sigma_{\text{AF}} = c_{\text{A}}h_{\text{A}} + c_{\text{F}}h_{\text{F}} \quad (3.14)$$

The accuracy of this NBO Lewis-structure description can be quantified in terms of $\% \rho^{(\text{L})}$, the percentage of the total electron density described by Lewis-type NBOs (i.e., $\% \rho^{(\text{L})} = 100 - \% \rho^{(\text{NL})}$; cf. Example 1.7). The polarity of each σ_{AF} bond can be quantified in terms of the *ionicity parameter* (cf. Eq. (1.41b))

$$i_{\text{AF}} = \frac{c_{\text{A}}^2 - c_{\text{F}}^2}{c_{\text{A}}^2 + c_{\text{F}}^2}$$

or the atomic charge (Q_{F}) on F.

Table 3.1 compares key bonding and ionicity descriptors for the NBO Lewis-structure representations of the five AF diatomic fluorides in this series. From this table it can be seen that the single-term natural Lewis-structure description $\psi^{(\text{L})}$ is practically *exact* for all species (with $\% \rho^{(\text{L})} > 99.9\%$ for A = F, Cl, Br, H, and only a

Table 3.1. NBO bonding and ionicity descriptors of AF fluorides (A = F, Cl, Br, H, Li)

A	$\% \rho^{(\text{L})}$	Q_{F}	Fluoride NBOs			
			σ_{AF}	$n_{\text{F}}^{(\sigma)}$	$n_{\text{F}}^{(\pi)}(2)$	$ i_{\text{AF}} $
F	99.99	0.000	$0.71(\text{sp}^{18.9})_{\text{F}} + 0.71(\text{sp}^{18.9})_{\text{F}}$	$\text{sp}^{0.05}$	p	0.000
Cl	99.96	-0.332	$0.82(\text{sp}^{11.9})_{\text{F}} + 0.58(\text{sp}^{18.6})_{\text{Cl}}$	$\text{sp}^{0.08}$	p	0.338
Br	99.98	-0.402	$0.84(\text{sp}^{12.4})_{\text{F}} + 0.54(\text{sp}^{21.8})_{\text{Br}}$	$\text{sp}^{0.08}$	p	0.409
H	99.95	-0.549	$0.88(\text{sp}^{3.90})_{\text{F}} + 0.47(\text{s})_{\text{H}}$	$\text{sp}^{0.25}$	p	0.553
Li ^a	(99.67) ^a	-0.961	$(\text{sp}^{11.1})_{\text{F}}$	$\text{sp}^{0.05}$	p	0.987

^a For ionic (Li⁺F⁻) NBO structure. The i_{AF} parameter is obtained from a corresponding \$CHOOSE structure with highly polarized Li—F bond.

slightly lower value for the completely ionic $\text{Li}^+ + \text{F}^-$ limit). The NBO polarization coefficients c_{F} and c_{A} are seen to vary smoothly from the covalent ($\text{A} = \text{F}$; $c_{\text{A}} = c_{\text{F}} = 2^{-1/2}$) to the ionic ($\text{A} = \text{Li}$; $c_{\text{F}} \simeq 1$, $c_{\text{A}} \simeq 0$) limit. For this single-structure description, the fluoride bond ionicity parameter (i_{AF}) and atomic charge (Q_{F}) serve as practically *equivalent* measures of bond polarity. In all these species, the F is represented as having three similar lone pairs: two pure-p pi-type and one s-rich ($\sim \text{sp}^{0.05}$) sigma-type. The p-rich bonding hybrids on F are also rather similar in all these species, ranging from 95% p character for $\text{A} = \text{F}$ down to 80% p character for $\text{A} = \text{H}$. Thus, all these compounds are well described by a *single* Lewis structure having a localized (σ_{AF}^2) “bonding electron pair” shared between A and F (as freshman chemistry textbooks would suggest), with the only significant difference being the progressive *polarization shift* of the σ_{AF} NBO as the electronegativity of A diminishes.

Comparison with the Heitler–London description

How does this NBO description of A—F bonding compare with the classical valence-bond (VB) picture?¹⁴ Although it is evident that the NBO Lewis-structure description is very “VB-like” in its emphasis on localized, transferable electron-pair bonds and lone pairs of the chemist’s Lewis diagram, there are important differences in mathematical detail.

In the VB picture, each $(\sigma_{\text{AB}})^2$ bond pair is described by a *Heitler–London covalent function* $\psi_{\text{AB}}^{(\text{cov})}$, whose spatial dependence is of the form

$$\psi_{\text{AB}}^{(\text{cov})}(1, 2) = 2^{-1/2}[\text{h}_{\text{A}}(1)\text{h}_{\text{B}}(2) + \text{h}_{\text{B}}(1)\text{h}_{\text{A}}(2)] \quad (3.15)$$

However, $\psi_{\text{AB}}^{(\text{cov})}$ is intrinsically restricted to homopolar bonding. In order to describe $\text{A}^{\delta+}\text{B}^{\delta-}$ polar bond formation, one must therefore append contributions from the Heitler–London *ionic function* $\psi_{\text{AB}}^{(\text{ion})}$,

$$\psi_{\text{AB}}^{(\text{ion})}(1, 2) = \text{h}_{\text{B}}(1)\text{h}_{\text{B}}(2) \quad (3.16)$$

having both electrons in h_{B} . In the classical VB resonance theory of Pauling and Wheland,¹⁵ each polar A—B bond is therefore described as a two-term “resonance hybrid” of the form

$$\psi_{\text{AB}}^{(\text{VB})}(1, 2) = c_{\text{cov}}\psi_{\text{AB}}^{(\text{cov})}(1, 2) + c_{\text{ion}}\psi_{\text{AB}}^{(\text{ion})}(1, 2) \quad (3.17)$$

with relative weightings

$$w_{\text{ion}} = c_{\text{ion}}^2 = i_{\text{AB}} \quad (3.18a)$$

$$w_{\text{cov}} = c_{\text{cov}}^2 = 1 - i_{\text{AB}} \quad (3.18b)$$

where $100i_{\text{AB}}$ is the “percentage ionic character” of the bond.

In contrast, the NBO picture describes $(\sigma_{AB})^2$ in terms of a doubly occupied bond orbital pair function $\psi_{AB}^{(NBO)}$ (cf. Eq. (1.31a)), with spatial dependence (in the closed-shell singlet case)

$$\psi_{AB}^{(NBO)}(1, 2) = [c_A h_A(1) + c_B h_B(1)][c_A h_A(2) + c_B h_B(2)] \quad (3.19)$$

For a normalized bond orbital, the relationship between polarization coefficients c_A and c_B and fractional ionicity i_{AB} can be expressed as (cf. Eq. (1.41a))

$$i_{AB} = c_A^2 - c_B^2 \quad (3.20)$$

for comparison with Eq. (3.18a). Thus, the NBO/NRT formalism describes polar covalency in terms of the *continuously* variable polarity of a *single* NBO function (and NRT resonance structure), whereas the VB formalism employs a resonance-weighted mixture of distinct covalent and ionic bond “types” (with associated resonance structures). However, these inequivalent descriptions can be related through Eqs. (3.18) and (3.20).

Both (3.17) and (3.19) are presumed to be expressed in terms of the same h_A and h_B bonding hybrids,¹⁶ and each function provides only an approximation to the true bond pair wavefunction. In particular, in the closed-shell singlet case $\psi_{AB}^{(NBO)}$ assumes the *same* spatial dependence for each electron of the pair, and thus neglects electron-correlation effects that could better be represented as

$$\begin{aligned} \psi_{AB}^{(better)}(1, 2) = \mathfrak{D}\{[c_A h_A(1) + c_B h_B(1)][c_A' h_A(2) + c_B' h_B(2)] \\ + [c_A' h_A(1) + c_B' h_B(1)][c_A h_A(2) + c_B h_B(2)]\} \end{aligned} \quad (3.21)$$

with $c_A \neq c_A'$ and $c_B \neq c_B'$ (“different polarizations for different spins”). Equation (3.21) is also the spatial form of $\psi_{AB}^{(NBO)}$ for an open-shell (diradical) singlet case, but this is usually not the character of the wavefunction in the near-equilibrium region.

With respect to the improved $\psi_{AB}^{(better)}$, it can be recognized that the normal closed-shell form of $\psi_{AB}^{(NBO)}$ is obtained whenever primed and unprimed spatial functions *coincide*,

$$\psi_{AB}^{(better)} \rightarrow \psi_{AB}^{(NBO)} \quad \text{for } c_A = c_A', c_B = c_B' \quad (3.22a)$$

Correspondingly, $\psi_{AB}^{(cov)}$ is obtained only when these functions *differ* in the most extreme possible fashion,

$$\psi_{AB}^{(better)} \rightarrow \psi_{AB}^{(cov)} \quad \text{for } c_A = c_B' = 1, c_A' = c_B = 0 \quad (3.22b)$$

whereas $\psi_{AB}^{(ion)}$ is obtained when (3.21) and (3.19) coincide at the extreme polarization limit,

$$\psi_{AB}^{(better)} \rightarrow \psi_{AB}^{(ion)} \quad \text{for } c_A = c_A' = 0, c_B = c_B' = 1 \quad (3.22c)$$

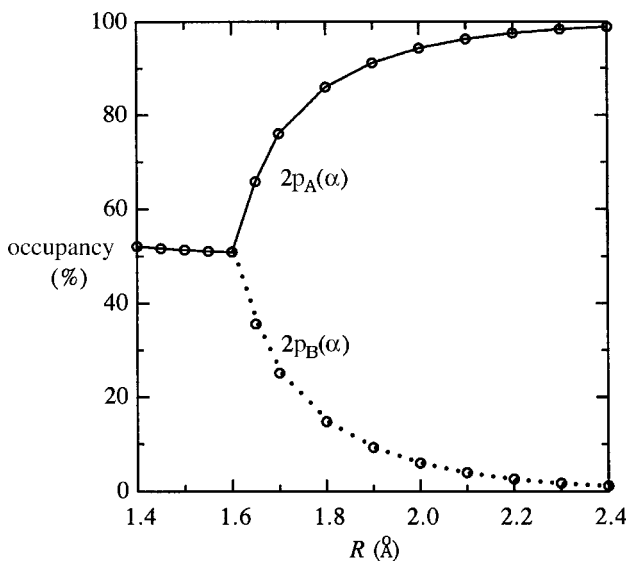


Figure 3.9 Similar to Fig. 3.3, for $2p_A^{(\alpha)}$ and $2p_B^{(\alpha)}$ spin-orbitals in F_A-F_B bonding.

Contrasting “covalent” and “ionic” limits in NBO and VB theory

For simplicity, let us now focus on the apolar case of F_2 , with $c_{\text{ion}} = 0$ in the VB wavefunction (3.17), and with $h_A = h_B = 2p$, in accordance with the p-rich hybridization shown in Table 3.1. For this case it can be recognized that the VB “covalent” function (3.15) is equivalent to the spin-polarized NBO function (3.5) in the limit $\eta = \eta' \rightarrow 0$, i.e., for the long-range limit where donor–acceptor delocalizations are *negligible*. Paradoxically, this corresponds to what was labeled the “ionic” or “one-center” limit in the bi-directional-CT picture of covalent-bond formation (cf. the discussion of Figs. 3.3 and 3.4). It can readily be verified that the assumption of extreme spin-polarized (diradical) character is quite inappropriate near the equilibrium geometry of F_2 . This is illustrated in Fig. 3.9, where we plot the occupancies of $2p_A^{(\alpha)}$ and $2p_B^{(\alpha)}$ spin-orbitals for F_A-F_B covalent-bond formation as a function of R (cf. Fig. 3.3). From Fig. 3.9 it can be judged that spin-polarized diradical character is fully quenched about 0.2 \AA beyond R_{eq} , and that the VB assumption of extreme diradical character cannot be appropriate for distances much smaller than 2.4 \AA , i.e., about 1.0 \AA beyond R_{eq} . Thus, the VB description of covalent bonding in F_2 is literally equivalent to the NBO picture only in the limit of large R , and becomes progressively less realistic in the near-equilibrium region.

Why is the VB description relatively *more* successful for H_2 than for F_2 ? From the nodeless, directionless character of $1s$ orbitals, one can judge that both $1s_A$ and $1s_B$ orbitals of H_2 are approaching a common “united-atom” form as their centers approach, so there is not much change if one switches h_A with h_B for one of the

electrons in $\psi_{AB}^{(\text{cov})}$, Eq. (3.15). That is, $\psi_{AB}^{(\text{cov})}$ for H_2 looks increasingly like a doubly occupied united-atom orbital h_{UA} at small R ,

$$\psi_{AB}^{(\text{cov})}(1, 2) \simeq h_{\text{UA}}(1)h_{\text{UA}}(2), \quad R \rightarrow 0 \quad (3.23)$$

thereby somewhat resembling the MO function (but without the strict constraint of double occupancy) near R_{eq} . In contrast, the two bonding hybrids of F_2 are *oppositely* directed (“in-phase”) $2p_{\text{A}}$ and $2p_{\text{B}}$ orbitals that each become increasingly dissimilar to the united-atom limit for diminishing R , and remain sharply distinguishable from one another when their centers coincide. Thus, $\psi_{AB}^{(\text{cov})}$ for F_2 will have persistent diradical (separated-atom) character that becomes increasingly unsuitable for representing the bonding in the near-equilibrium region.

In practice, the formal mathematical defects of the Heitler–London $\psi_{AB}^{(\text{cov})}$ function can be largely averted by not taking the mathematics too literally! Because actual HLSP-PP-VB calculations were usually too difficult to carry out in rigorous *ab initio* fashion, effective semi-empirical VB treatments were developed by Pauling and others that largely circumvented these formal defects.¹⁷ What strongly persists in such semi-empirical VB formulations is essentially *consistent* with the NBO picture of localized, transferable electron-pair functions that are built from Pauling-type hybrids, mirroring the chemist’s Lewis-structure picture. In this sense, the general NBO description is indeed “VB-like.”

In summary, polar covalency can be viewed in terms of the *continuous* variability of a single localized bond orbital expression (3.14), corresponding to what was described in VB theory as a resonance hybrid (3.17) of two distinct bonding “types.”¹⁸ The inflexible form of the Heitler–London $\psi_{AB}^{(\text{cov})}$ and $\psi_{AB}^{(\text{ion})}$ functions sometimes created an unfortunate impression of dichotomy where none exists physically. Nevertheless, the older valence-bond concepts can be recovered through equations such as (3.18a) and (3.20), which directly relate NBO polarization coefficients to covalent/ionic resonance weightings. Some disadvantages of the Heitler–London mathematical functions were highlighted, but overall, the results of NBO analysis are found to be strongly *supportive* of the underlying localized bonding picture on which classical VB theory rests.

3.2.3 Hybridization and multiple bonding in polyatomic hydrocarbons

We now turn to the bonding in polyatomic molecules, particularly the hydrocarbons and other common species of organic chemistry. The formulation of such important concepts as

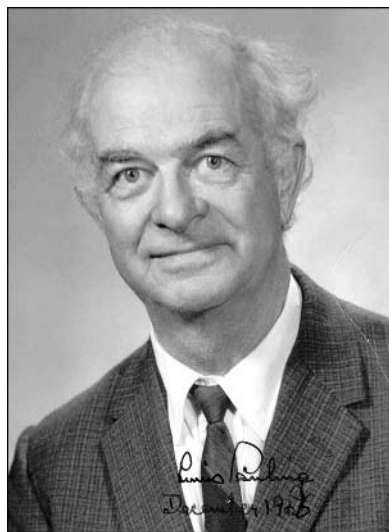
molecular structure

valency

Lewis diagram

*multiple bonding**hybridization**resonance*

originated in the framework of carbon chemistry. Hence, in developing the general NBO perspective on hybridization, valency, and bonding in polyatomic species, we begin with prototype single-, double-, and triple-bonded hydrocarbon species as treated in the classic works of Pauling,¹⁹ Slater,²⁰ Coulson,²¹ and others.



Linus Pauling



John C. Slater



Charles A. Coulson

General NBO theory of directed hybrids

Let us begin by sketching the general polyatomic formulation of hybridization from the NBO viewpoint. A general hybrid $h_i^{(A)}$ on atom A can be expanded in the complete orthonormal set of NAOs $\{\theta_i^{(A)}\}$ on this atom:

$$h_i^{(A)} = \sum_j a_{ij} \theta_j^{(A)} \quad (3.24a)$$

We can divide the NAOs into the “natural minimal basis” (NMB), consisting of only the formal core and valence NAOs of simple bonding theory, and the “natural Rydberg basis” (NRB), consisting of everything else. With this partitioning, Eq. (3.24a) is expressed as

$$h_i^{(A)} = \sum_j^{\text{NMB}} a_{ij} \theta_j^{(A)} + \sum_k^{\text{NRB}} a_{ik} \theta_k^{(A)} \quad (3.24b)$$

In the spirit of elementary bonding theories, we expect that the dominant contributions to $h_i^{(A)}$ come only from the first summation, consisting (for an s/p-block atom) simply of the four contributions (s, p_x , p_y , p_z) from the valence shell. At this level, the hybrid can be written simply as (dropping the atom label throughout)

$$h_i = a_{i0}s + a_{ix}p_x + a_{iy}p_y + a_{iz}p_z \quad (3.25)$$

Example 3.1

How valid is the minimal-basis assumption that leads from (3.24b) to (3.25)? We can examine the accuracy of the NMB restriction (*in the NAO basis!*) by tabulating the percentage of the total electron density associated with the NMB and NRB sets for some common organic molecules, as shown below:

Molecule ^a	n_{NMB}	% $\rho(\text{NMB})$	n_{NRB}	% $\rho(\text{NRB})$
CH ₄	9	99.90	41	0.01
C ₂ H ₄	14	99.73	58	0.27
C ₂ H ₂	12	99.84	46	0.16
C ₆ H ₆	36	99.74	114	0.26

^a Fully optimized B3LYP/6-311++G** level.

Even though the number (n_{NMB}) of NMB functions is much smaller than that (n_{NRB}) of NRB functions, the former are seen to make overwhelmingly greater percentage contributions (>99%) to the total electron density, and thus, to the occupied bonding h_i 's. This conclusion is also confirmed by the accuracy of the "sum rules" to be described below, or by examination of individual hybrids.

If we define the hybridization parameter λ_i as

$$\lambda_i = \frac{a_{ix}^2 + a_{iy}^2 + a_{iz}^2}{a_{i0}^2} \quad (3.26)$$

we can rewrite (3.25) in the standard form (cf. Eq. (2.3))

$$h_i = (1 + \lambda_i)^{1/2}(s + \lambda_i^{1/2}p_i), \quad i = 1-4 \quad (3.27)$$

where p_i is a general directional p orbital (a normalized linear combination of p_x , p_y , and p_z),

$$p_i = d_{ix}p_x + d_{iy}p_y + d_{iz}p_z \quad (3.28)$$

with $d_{ix} = a_{ix}/\lambda_i$, etc.

It is well known that the angular dependence of each Cartesian p orbital is simply a *unit* vector in the corresponding Cartesian direction ($p_x = \hat{u}_x$, etc.). We can therefore associate each p_i with a Cartesian direction vector \mathbf{d}_i ,

$$\mathbf{d}_i = d_{ix}\hat{u}_x + d_{iy}\hat{u}_y + d_{iz}\hat{u}_z \quad (3.29a)$$

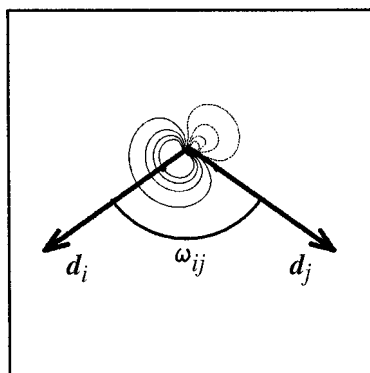


Figure 3.10 The geometry of directional vectors \mathbf{d}_i and \mathbf{d}_j for two directional hybrids (with hybrid h_i shown for reference).

or, in column-matrix form,

$$\mathbf{d}_i = \begin{pmatrix} d_{ix} \\ d_{iy} \\ d_{iz} \end{pmatrix} \quad (3.29b)$$

The components of the direction vector are related in the usual way to the azimuthal (ϕ) and polar (θ) angles of a spherical polar coordinate system,

$$d_{ix} = \sin \theta \cos \phi \quad (3.30a)$$

$$d_{iy} = \sin \theta \sin \phi \quad (3.30b)$$

$$d_{iz} = \cos \theta \quad (3.30c)$$

The vector \mathbf{d}_i conveniently expresses the directionality of hybrid h_i with respect to the chosen molecular axis system. Note that each \mathbf{d}_i is a unit vector ($\mathbf{d}_i \cdot \mathbf{d}_i = 1$), and the scalar product of \mathbf{d}_i and \mathbf{d}_j is related to the angle (ω_{ij}) between these vectors in the usual way (see Fig. 3.10),

$$\mathbf{d}_i \cdot \mathbf{d}_j = \cos \omega_{ij} \quad (3.31)$$

Let us now recall that h_i and h_j are orthonormal, and that an s orbital is orthogonal to every p_i orbital. We can therefore write the hybrid orthogonality relation in the form

$$\begin{aligned} \delta_{ij} &= \langle \mathbf{h}_i | \mathbf{h}_j \rangle \\ &= [(1 + \lambda_i)(1 + \lambda_j)]^{-1/2} \langle (s + \lambda_i^{1/2} p_i | s + \lambda_j^{1/2} p_j) \rangle \\ &= [(1 + \lambda_i)(1 + \lambda_j)]^{-1/2} (\langle s | s \rangle + (\lambda_i \lambda_j)^{1/2} \langle p_i | p_j \rangle) \end{aligned} \quad (3.32)$$

Furthermore, s is normalized ($\langle s | s \rangle = 1$) and

$$\langle p_i | p_j \rangle = \mathbf{d}_i \cdot \mathbf{d}_j = \cos \omega_{ij} \quad (3.33)$$

We therefore see that orthogonality of h_i and h_j is maintained only if

$$\boxed{\cos \omega_{ij} = -\frac{1}{(\lambda_i \lambda_j)^{1/2}}} \quad (3.34)$$

Equation (3.34) is the celebrated directionality theorem of Coulson which governs the bond angles for sp-hybridization.

Example 3.2

Exercise: Show that Eq. (3.34) gives the expected bond angles for standard sp^1 , sp^2 , sp^3 equivalent hybrids.

Solution: For equivalent hybrids, with equal $\lambda_i = \lambda_j = \lambda$, Eq. (3.34) becomes simply

$$\cos \omega_{ij} = -1/\lambda$$

We therefore find

$$\begin{aligned} \lambda = 1 : & \quad \cos \omega_{ij} = -1, \text{ so } \omega_{ij} = 180^\circ \text{ (digonal)} \\ \lambda = 2 : & \quad \cos \omega_{ij} = -\frac{1}{2}, \text{ so } \omega_{ij} = 120^\circ \text{ (trigonal)} \\ \lambda = 3 : & \quad \cos \omega_{ij} = -\frac{1}{3}, \text{ so } \omega_{ij} = 109.47^\circ \text{ (tetrahedral)} \end{aligned}$$

Example 3.3

Exercise: For an ethylene molecule in idealized trigonal geometry (120° bond angles), the carbon NHOs were found to be $sp^{2.33}$ toward hydrogen and $sp^{1.48}$ toward the opposite carbon. Predict how the bond angles will change when the geometry is allowed to optimize fully.

Solution: For the given hybrids, the angle $\omega_{H,H'}$ between the bonding hybrids to H and H' is determined from the directionality theorem

$$\cos \omega_{H,H'} = -\frac{1}{[(2.33)(2.33)]^{1/2}} = -0.429$$

to be $\omega_{H,H'} = 115.4^\circ$. Similarly, the $\omega_{H,C'}$ angle is found from

$$\cos \omega_{H,C'} = -\frac{1}{[(2.33)(1.48)]^{1/2}} = -0.539$$

to be $\omega_{H,C'} = 122.6^\circ$. Thus, in the 120° geometry, the CH bonds are slightly "bent" with respect to the NHO directions. We can expect that geometry optimization will cause the H nuclei to move into better alignment with the NHOs, i.e., that HCH angles will decrease to about 115° , and HCC angles will increase to about 123° . The actual optimized values (116.5° for HCH, 121.7° for HCC) are in rough agreement with these estimates, and the final NHOs (with slightly readjusted hybridizations) are in improved alignment with the nuclei.

Example 3.4

Exercise: For what hybridization λ do equivalent hybrids h_i and h_j achieve the *smallest possible* bond angle?

Solution: For $\lambda_i = \lambda_j = \lambda$, we seek the extremum value for which

$$\frac{d(\cos \omega_{ij})}{d\lambda} = -\frac{d(1/\lambda)}{d\lambda} = 1/\lambda^2 = 0$$

The only solution is $\lambda = \infty$ (pure p orbitals), for which the bond angle $\omega_{ij} = 90^\circ$.

We can see another consequence of the simplified form (3.27) by writing the fractional s and p characters in the form (cf. Example 2.2)

$$f_s^{(i)} = \frac{1}{1 + \lambda_i} \quad (3.35a)$$

$$f_p^{(i)} = \frac{\lambda_i}{1 + \lambda_i} \quad (3.35b)$$

with $f_s^{(i)} + f_p^{(i)} = 1$ for each h_i . If we sum up the fractions $f_s^{(i)}$ for all four valence hybrids, we merely recover the *total* number (1) of valence s orbitals,

$$\sum_i^4 f_s^{(i)} = 1 \quad (3.36a)$$

and the sum of fractional p characters similarly gives the number (3) of valence p orbitals,

$$\sum_i^4 f_p^{(i)} = 3 \quad (3.36b)$$

On combining (3.35) and (3.36), we obtain the “sum rules,”

$$\sum_i^4 \frac{1}{1 + \lambda_i} = 1 \quad (3.37a)$$

$$\sum_i^4 \frac{\lambda_i}{1 + \lambda_i} = 3 \quad (3.37b)$$

which merely express the overall conservation of valence s and p character in the unitary transformation from unhybridized (s, p_x , p_y , p_z) to final hybrid (h_1 , h_2 , h_3 , h_4) orbitals.

Example 3.5

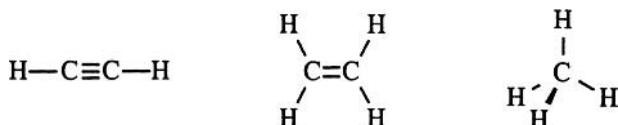
How accurate are the sum rules (3.37a) and (3.37b) for the molecules considered in Example 3.1? The table below summarizes the hybridization parameters λ_i and sum-rule values for C in each species:

Molecule	Hybrids				Sum rules	
	λ_1	λ_2	λ_3	λ_4	$\sum_{i=1}^4 \frac{1}{1+\lambda_i}$	$\sum_{i=1}^4 \frac{\lambda_i}{1+\lambda_i}$
CH ₄	2.99	2.99	2.99	2.99	1.00 ₃	2.99 ₇
C ₂ H ₄	2.37	2.37	1.44	∞	1.00 ₃	2.99 ₇
C ₂ H ₂	1.09	0.91	∞	∞	1.00 ₂	2.99 ₈
C ₆ H ₆	2.35	1.85	1.85	∞	1.00 ₀	3.00 ₀

The final two columns show that the actual NHO values are in nearly exact agreement with the idealized values 1 (column 5) and 3 (column 6), reflecting the high accuracy of the NMB approximation.

Sigma and pi NBOs of hydrocarbons: ethane, ethylene, acetylene

Let us turn now to the actual NBOs for the classical cases of equivalent sp^n hybridization: acetylene ($n = 1$), ethylene ($n = 2$), and methane ($n = 3$). In each case, the NBO results are in excellent agreement with the expected Lewis structures,



with Lewis-type orbitals of near double occupancy conforming generally to the expected bond types, as shown in Table 3.2. Figure 3.11 shows surface and

Table 3.2. *Lewis (L) and non-Lewis (NL) energy contributions and NBO occupancies for sigma and pi bonds of the simplest alkane (CH₄), alkene (C₂H₄), and alkyne (C₂H₂) species, with aromatic benzene (C₆H₆) included for comparison*

Molecule	Lewis accuracy			NBO occupancies (<i>e</i>)		
	$E(\text{L})$ (a.u.)	$E(\text{NL})$ (a.u.)	% $E(\text{L})$	σ_{CH}	σ_{CC}	π_{CC}
CH ₄	-40.5197	-0.0143	99.96	1.9990	—	—
C ₂ H ₄	-78.5207	-0.0949	99.88	1.9849	1.9952	1.9994
C ₂ H ₂	-77.2744	-0.0823	99.89	1.9905	1.9909	1.9996
C ₆ H ₆	-231.6491	-0.6621	99.71	1.9819	1.9820	1.6640

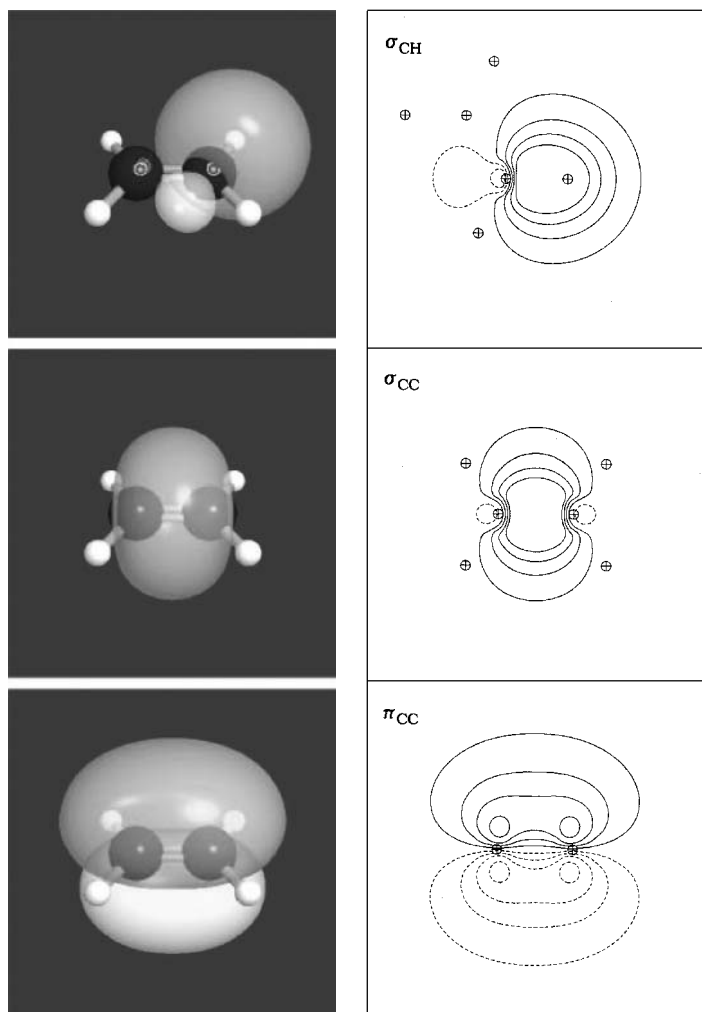


Figure 3.11 Valence NBOs of ethylene, showing σ_{CH} (top), σ_{CC} (middle), and π_{CC} (bottom) bonds in surface (left) and contour (right) views.

contour views of prototype σ_{CH} , σ_{CC} , and π_{CC} bond NBOs for ethylene, which are representative of those found for all these species.

From Example 3.5 one can see that the carbon bonding hybrids to H and C are not perfectly equivalent and the hybridizations differ slightly from integer values. Thus, for C—H bonds, the hybridizations in methane, ethylene, and acetylene are 2.99, 2.37, and 1.09, respectively, rather than the idealized integer values 3, 2, 1. These differences correspond to rather small changes in expected percentage p character²² or bond angles (see Example 3.3). Furthermore, as shown in Table 3.2, the NBO occupancies are generally very close to 2.0000 (except for the π_{CC} bonds of

benzene, which exhibit large “delocalization effects,” to be discussed in Section 3.3). Thus, for example, an elementary Lewis-structure model of ethylene, having each of the NBOs of Fig. 3.11 (plus the C core orbitals, not shown) doubly occupied, would correctly describe the electron density to within 0.42%, and would incur a variational energy error of only 0.12%.²³ Such results (which are representative of those found for many other simple organic species) provide strong evidence for the accuracy of the localized Lewis electron-pair concept.

A more detailed comparison of the various carbon bonding hybrids in these species is presented in Fig. 3.12. This figure shows that the visual changes in hybrid shape, even for rather large changes in λ (e.g., the changes from sp^1 -like to sp^3 -like in the left-hand panels), are rather subtle. Most obvious is the increasing

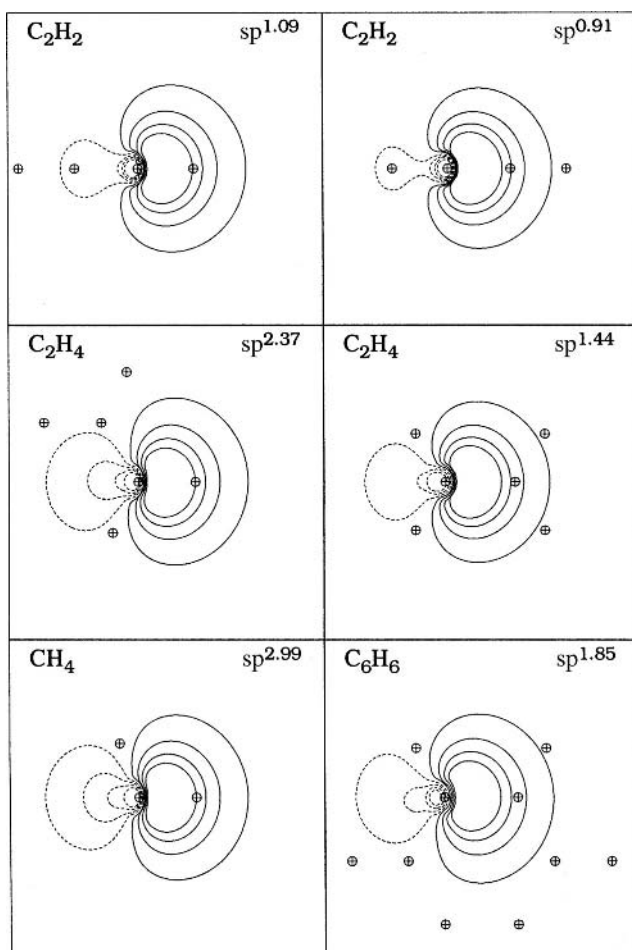


Figure 3.12 Carbon sigma hybrids for σ_{CH} bonds (left-hand panels) and σ_{CC} bonds (right-hand panels) in CH_4 , C_2H_4 , C_2H_2 , and C_6H_6 .

amplitude of the backside lobe of the hybrid as p character increases. Because the 2p orbital lies higher in energy than 2s, the p-rich hybrid also becomes slightly less electronegative, and its polarization coefficient in the σ_{CH} bond NBO diminishes accordingly (e.g., from 0.782 in acetylene to 0.770 in ethylene). Such subtle but chemically important variations can often be better recognized in the numerical hybridization and polarization parameters of the NBOs than in their visual display.

3.2.4 Localized and delocalized MOs in molecules and ions

Canonical versus localized MOs

The natural localized orbitals introduced in Section 1.5 provide a useful alternative to the “canonical” delocalized MOs (CMOs) that are usually employed to analyze chemical bonding. The NAO and NBO basis sets may be regarded as intermediates in a succession of basis transformations that lead from starting AOs $\{\chi_i\}$ to the final canonical MOs $\{\phi_i\}$,

$$\text{AO} \rightarrow \text{NAO} \rightarrow \text{NBO} \rightarrow \text{LMO} \rightarrow \text{CMO} \quad (3.38a)$$

which we shall symbolize as

$$\{\chi_i\} \rightarrow \{\theta_i\} \rightarrow \{\Omega_a\} \rightarrow \{\tilde{\Omega}_a\} \rightarrow \{\phi_j\} \quad (3.38b)$$

Except for the initial $\text{AO} \rightarrow \text{NAO}$ transformation, which starts from non-orthogonal AOs, each step in (3.38) is a unitary transformation from one complete orthonormal set to another. Each localized set gives an *exact* matrix representation of any property or function that can be described by the original AO basis.

The localized molecular orbitals (LMOs) can be defined as the unitary transformation of CMOs that (roughly speaking) makes the transformed functions as much like the localized NBOs as possible,²⁴

$$\tilde{\Omega}_a = \sum_j U_{aj} \phi_j \quad (3.39)$$

Further details of how to obtain the unitary matrix \mathbf{U} are unimportant here. It suffices to recognize²⁵ that *any* unitary transformation of CMOs leaves a determinantal wavefunction and density *unchanged*, and thus has *no* effect on the energy or other properties that could be calculated with this wavefunction or density. Thus, at the HF (or DFT) level we can rigorously write

$$E(\text{LMO}) = E(\text{CMO}) \quad (3.40)$$

This identity has profound consequences for chemical concepts.

How do CMOs and LMOs differ? The CMOs are symmetry-adapted eigenfunctions of the Fock (or Kohn–Sham) operator \hat{F} , necessarily reflecting all the molecular point-group symmetries of \hat{F} itself,²⁶ whereas the LMOs often *lack*

such symmetry. For example, if we consider a diatomic H₂ “molecule” with one H atom on Earth and another on the Moon, the CMOs are always symmetry-adapted functions of the form

$$\phi_1 \simeq 2^{-1/2}(1s_{\text{Earth}} + 1s_{\text{Moon}}) \quad (3.41a)$$

$$\phi_2 \simeq 2^{-1/2}(1s_{\text{Earth}} - 1s_{\text{Moon}}) \quad (3.41b)$$

whereas the LMOs are of the form of localized atomic orbitals

$$\tilde{\Omega}_a \simeq 1s_{\text{Earth}} \quad (3.42a)$$

$$\tilde{\Omega}_b \simeq 1s_{\text{Moon}} \quad (3.42b)$$

Equation (3.40) tells us that the symmetry adaptation (3.39) from LMOs to CMOs is purely *decorative*, with no energetic consequence. As physical intuition suggests, we are perfectly justified in describing the H_{Earth}—H_{Moon} system in terms of localized atom-like functions, each weakly perturbed by its remote “twin,” rather than as a completely delocalized MO of symmetry-adapted form.

How do LMOs differ from NBOs? Each occupied LMO ($\tilde{\Omega}_a$) can be written in terms of a parent Lewis-type NBO (Ω_a) with a weak “delocalization tail” from other non-Lewis NBOs (Ω_b^*),

$$\tilde{\Omega}_a = c_{aa}\Omega_a + \sum_{b^*}^{NL} c_{ab^*}\Omega_{b^*} \quad (3.43)$$

with $|c_{aa}| \gg |c_{ab^*}|$. (The precise form and composition of the non-Lewis delocalization tails will be discussed at length in later sections.) We can therefore separate the total $E(\text{LMO})$ into contributions from the dominant Lewis-type $E(\text{L})$ and residual non-Lewis $E(\text{NL})$ terms²⁷ (see Table 3.2),

$$E(\text{L}) + E(\text{NL}) = E(\text{LMO}) = E(\text{CMO}) \quad (3.44)$$

Unlike the decorative symmetry delocalizations that distinguish LMOs from CMOs, the non-Lewis delocalizations that distinguish LMOs from NBOs have direct physical significance.

Representative well-localized species

Let us now consider the case of well-localized systems for which $E(\text{NL})$ is a negligibly small fraction of the total energy, so that

$$E(\text{CMO}) \simeq E(\text{L}) \quad (3.45)$$

Table 3.3 shows measures of localization ($\% \rho(\text{L})$, $\% E(\text{L})$, and $E(\text{L})$) for four small molecules that can be considered to be well localized: CO, N₂, H₂O, and CH₄.

Table 3.3. *The accuracy of the localized Lewis ($\Psi^{(L)}$) model for CO, N₂, H₂O, and CH₄*

	$\% \rho(L)$	$\% E(L)$	$E(L)$ (a.u.)
CO	99.92	99.97	-113.311 47
N ₂	99.89	99.94	-109.498 05
H ₂ O	99.93	99.97	-76.438 80
CH ₄	99.95	99.96	-40.519 73

Table 3.4 compares the CMO and NBO descriptions of these molecules in terms of the orbital energies

$$\epsilon_i = \langle \phi_i | \hat{F} | \phi_i \rangle \quad (3.46a)$$

$$\epsilon_a^{(L)} = \langle \Omega_a | \hat{F} | \Omega_a \rangle \quad (3.46b)$$

and the orbital compositions, allowing direct comparisons of the forms of CMOs and NBOs. The high values of $\% \rho(L)$ and $\% E(L)$ verify that (3.45) is well satisfied for these molecules, despite the rather wide disparities between the energies of individual NBOs and CMOs that are found in Table 3.4.

How can $E(\text{CMO}) \simeq E(L)$ despite the fact that energies of occupied CMO and NBO differ significantly? The answer is suggested in Fig. 3.13, which depicts the interaction between filled NBOs Ω_a and Ω_b with interaction element

$$F_{ab} = \langle \Omega_a | \hat{F} | \Omega_b \rangle \quad (3.47)$$

to give MOs

$$\phi_{\pm} = 2^{-1/2}(\Omega_a \mp \Omega_b) \quad (3.48)$$

As shown in Fig. 3.13 (cf. Eqs. (3.1) and (3.2)), the energy splittings are *symmetric* about the mean of $\epsilon_a^{(L)}$ and $\epsilon_b^{(L)}$ for *any* F_{ab} , so the sum of orbital energies is *invariant*,

$$\epsilon_+ + \epsilon_- = \epsilon_a^{(L)} + \epsilon_b^{(L)} \quad (3.49)$$

no matter how large the splitting parameter. A similar invariance applies to more complex linear combinations than those in (3.48).

We conclude that Ω_a - Ω_b donor-donor interactions are generally *ineffective* at lowering the total variational energy,²⁸ whereas Ω_a - Ω_b^* donor-acceptor interactions are universally stabilizing. Comparison of Fig. 3.2 (or Fig. 1.3) with Fig. 3.13 shows clearly how this fundamental difference arises from the Pauli restriction on orbital occupancies.

Table 3.4. (a) CMO and (b) NBO descriptions of CO, N₂, H₂O, and CH₄

(a) CMOs and energies

	ϵ_i	CMO composition (as mixture of NBOs)
CO	-0.3875	$0.94n_C - 0.25\sigma_{CO} + 0.20n_O + \dots$
	-0.4868(2)	π_{CO}
	-0.5866	$0.90n_O - 0.33\sigma_{CO} - 0.28n_C + \dots$
	-1.1787	$0.90\sigma_{CO} + 0.38n_O + 0.15n_C + \dots$
	-10.2971	$0.99K_C + \dots$
	-19.2387	$0.99K_O + \dots$
N ₂	-0.4409	$0.67(n_N + n_{N'}) + 0.32\sigma_{NN'} + \dots$
	-0.4768(2)	$\pi_{NN'}$
	-0.5606	$0.70(n_N - n_{N'}) + \dots$
	-1.1406	$0.94\sigma_{NN'} - 0.22(n_N + n_{N'}) + \dots$
	-14.4234	$0.70(K_N - K_{N'}) + \dots$
	-14.4252	$0.70(K_N + K_{N'}) - 0.12\sigma_{NN'} + \dots$
H ₂ O	-0.3230	n_O^π
	-0.3968	$0.86n_O^\sigma - 0.36(\sigma_{OH} - \sigma_{OH'}) + \dots$
	-0.5431	$0.71(\sigma_{OH} + \sigma_{OH'}) + \dots$
	-1.0232	$0.60(\sigma_{OH} - \sigma_{OH'}) + 0.51n_O + \dots$
	-19.1334	$0.99K_O + \dots$
CH ₄	-0.3954(3)	$0.50(\sigma_{CH} + \sigma_{CH'} - \sigma_{CH''} - \sigma_{CH'''}) + \dots$
	-0.6966	$0.50(\sigma_{CH} + \sigma_{CH'} + \sigma_{CH''} + \sigma_{CH'''}) + \dots$
	-10.1531	$0.99K_C + \dots$

(b) NBOs, energies, and occupancies

	$\epsilon_a^{(L)}$	Type	Occupancy	NBO hybrid composition
CO	-0.4957	n_C	1.9984	$(sp^{0.33})_C$
	-0.7961	n_O	1.9913	$(sp^{0.82})_O$
	-0.4868(2)	π_{CO}	2.0000	$0.48(p)_C + 0.88(p)_O$
	-1.2544	σ_{CO}	2.0000	$0.54(sp^{2.59})_C + 0.84(sp^{1.19})_O$
	-10.1609	K_C	1.9998	$(s)_C$
	-18.9661	K_O	1.9997	$(s)_O$
N ₂	-0.6383(2)	n_N	1.9928	$(sp^{0.60})_N$
	-0.4768(2)	$\pi_{NN'}$	2.0000	$0.71(p)_N + 0.71(p)_{N'}$
	-1.2744	$\sigma_{NN'}$	2.0000	$0.71(sp^{1.52})_N + 0.71(sp^{1.52})_{N'}$
	-14.2072	K_N	1.9997	$(s)_N$
H ₂ O	-0.3199	n_O^π	1.9969	$(p)_O$
	-0.6650	n_O^σ	1.9975	$(sp^{0.87})_O$
	-0.7546(2)	σ_{OH}	1.9995	$0.85(sp^{3.30})_O + 0.52(s)_H$
	-18.9169	K_O	1.9998	$(s)_O$
CH ₄	-0.5044(4)	σ_{CH}	1.9990	$0.76(sp^{2.99})_C + 0.63(s)_H$
	-10.0118	K_C	1.9998	$(s)_O$

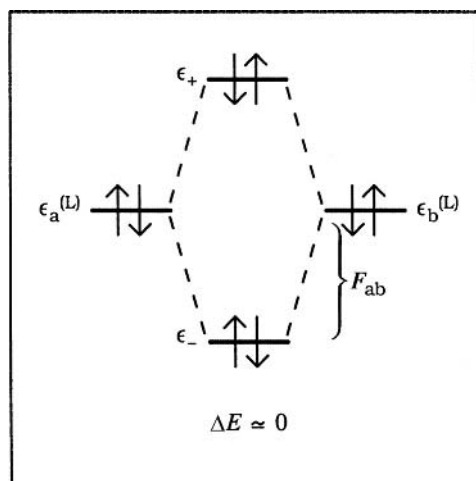


Figure 3.13 The energy-level-splitting diagram (cf. Figs. 1.3 and 3.2) for interaction of filled NBOs Ω_a and Ω_b (with energies $\epsilon_a^{(L)} = \epsilon_b^{(L)}$) and interaction element $F_{ab} = \langle \Omega_a | \hat{F} | \Omega_b \rangle$ to form MO levels ϵ_{\pm} , Eq. (3.48).

Ionization and the Koopmans picture

How can the above conclusions be reconciled with the results of photoelectron spectroscopy, which seem to show that electrons are ionized from CMOs? The latter belief stems from naive acceptance of *Koopmans' theorem*,²⁹ which associates the i th ionization energy (IP_i) with the corresponding CMO orbital energy ϵ_i ,

$$IP_i = -\epsilon_i \quad (3.50)$$

at a very low level of approximation. In particular, Koopmans' theorem neglects orbital relaxation effects that are known to be chemically significant (cf. the Li_2 versus Li_2^+ example in Section 3.2.1). Let us therefore examine this paradox for cations of the small molecules characterized in Table 3.4.

Table 3.5 shows the ground-state energies $E(M)$ for $M = CO, N_2, H_2O,$ and CH_4 , together with the first ionization energy as properly calculated from state-energy differences³⁰

$$IP_1 = E(M^+) - E(M) \quad (3.51)$$

for both adiabatic (geometry relaxed) and vertical ("cation in neutral geometry") processes. We also include Koopmans-type estimates using the MO (KT_{MO}) and NBO (KT_{NBO}) orbital energies, as well as experimental adiabatic ionization energies for comparison. Corresponding optimized geometries of the neutral and cationic species are shown in Table 3.6.

Table 3.5. *Adiabatic and vertical ionization energies of small molecules (cf. Table 3.4), compared with Koopmans'-theorem (KT) estimates using MO or NBO orbital energies, and with experimental adiabatic values*

	E (a.u.)	First ionization energy (a.u.)				Experimental ^a
		Adiabatic	Vertical	KT _{MO}	KT _{NBO}	
CO	-113.349 05	0.5215	0.5222	0.3875	0.4868	0.5150
N ₂	-109.559 70	0.5831	0.5835	0.4409	0.4768	0.5726
H ₂ O	-76.458 53	0.4659	0.4697	0.3230	0.3199	0.4638
CH ₄	-40.534 15	0.4668	0.5247	0.3954	0.5044	0.4636

^a H. M. Rosenstock, K. Draxl, B. W. Steiner, and J. T. Herron, *J. Phys. Chem. Ref. Data* **6** (1977), Supplement 1.

As seen from Table 3.5, the Koopmans-type estimates are quite unrealistic in all cases. Such crude estimates give no real basis for judging whether the delocalized or localized picture is preferable. If anything, the NBO orbital energies give better estimates of this type than do the MO orbital energies!

However, we can judge from even more qualitative considerations that the assumption of unrelaxed NBOs in M^+ must be unfounded. Let us start from a splitting diagram such as Fig. 3.13 for neutral M , considered to have well-localized NBOs Ω_a and Ω_b with strong $F_{ab} = \langle \Omega_a | \hat{F} | \Omega_b \rangle$ interaction. Removal of an electron to form M^+ will now convert the donor-donor (Ω_a - Ω_b) diagram to one of donor-acceptor (Ω_a - Ω_b^*) type for the ionized spin set (cf. Fig. 1.3, or Fig. 3.2 with $n_{\text{elec}} = 1$), with splitting factor F_{ab} that now reflects the strength of $\Omega_a \rightarrow \Omega_b^*$ delocalization. We therefore expect that Ω_a will be strongly mixed with the vacant Ω_b^* in the cation, strongly distorting its form compared with the parent neutral species. For example, if Ω_a and Ω_b were the two equivalent n_N lone pairs of N₂, we would expect from Fig. 3.2 (with $n_{\text{elec}} = 1$) that the final β spin-orbital would be of the form

$$\phi_- \simeq 2^{-1/2}(n_N + n_{N'}) \quad (3.52)$$

Table 3.6. *Optimized geometries of neutral and cationic species*

	Neutral species			Cationic species		
	Symmetry	R (Å)	\angle_{HAH} (degrees)	Symmetry	R (Å)	\angle_{HAH} (degrees)
CO	C _{∞v}	1.1277	—	C _{∞v}	1.1105	—
N ₂	D _{∞h}	1.0956	—	D _{∞h}	1.1087	—
H ₂ O	C _{2v}	0.9621	105.0	C _{2v}	1.0059	109.8
CH ₄	T _d	1.0909	109.5	S ₄	1.2220	96.4, 141.0

resembling a CMO of the parent neutral species. From such considerations we can recognize that the “delocalization” suggested by KT-like behavior pertains to the modified NBOs in the *cation*, not the parent neutral species. Strong mixing of parent NBOs to give CMO-like delocalizations in the cationic species is therefore unsurprising and does not contradict the well-localized character of the parent neutral species.

However, it is entirely possible that the final cation M^+ achieves a well-localized Lewis-structure form, but with *different* NBOs than those of the neutral species. This is the case for three of the four ions considered above (CO^+ , N_2^+ , H_2O^+), which leads to high $\% \rho(L)$ values as shown in Table 3.7. For each of the equilibrium

Table 3.7. Valence-shell NBOs of small cations in equilibrium geometry (cf. Tables 3.4 and 3.6), with percentage Lewis density ($\% \rho(L)$) for each species (an asterisk denotes a formal non-Lewis orbital)

		Cation valence-shell NBOs			
	$\% \rho(L)$	Occupancy	Spin	Type	NBO hybrid composition
CO^+	99.68	1.0000	α	σ_{CO}	$0.54(sp^{1.80})_C + 0.84(sp^{1.51})_O$
		1.0000(2)	α	π_{CO}	$0.56(p)_C + 0.83(p)_O$
		0.9964	α	n_C	$(sp^{0.53})_C$
		0.9973	α	n_O	$(sp^{0.65})_O$
		1.0000	β	σ_{CO}	$0.57(sp^{0.43})_C + 0.82(sp^{2.56})_O$
		1.0000(2)	β	π_{CO}	$0.50(p)_C + 0.87(p)_O$
		0.9662	β	n_O	$(sp^{0.38})_O$
		0.0346	β	n_C^*	$(sp^{2.92})_C$
N_2^+	99.92	1.0000	α	$\sigma_{NN'}$	$0.71(sp^{1.65})_N + 0.71(sp^{1.65})_{N'}$
		1.0000(2)	α	$\pi_{NN'}$	$0.71(p)_N + 0.71(p)_{N'}$
		0.9955(2)	α	n_N	$(sp^{0.59})_N$
		1.0000	β	$\nu_{NN'}$	$0.83(s)_N + 0.56(p)_{N'}$
		1.0000	β	$\bar{\nu}_{NN'}$	$0.56(p)_N + 0.83(s)_{N'}$
1.0000(2)	β	$\pi_{NN'}$	$0.71(p)_N + 0.71(p)_{N'}$		
H_2O^+	99.94	0.9994(2)	α	σ_{OH}	$0.88(sp^{3.64})_O + 0.47(s)_H$
		0.9992	α	n_O^π	$(p)_O$
		0.9990	α	n_O^σ	$(sp^{0.75})_O$
		0.9994(2)	β	σ_{OH}	$0.87(sp^{3.42})_O + 0.49(s)_H$
		0.9989	β	n_O^σ	$(sp^{0.83})_O$
		0.0000	β	$n_O^{\pi*}$	$(p)_O$
CH_4^+	96.43	1.0000(4)	α	σ_{CH}	$0.81(sp^{2.99})_C + 0.59(s)_H$
		0.8943(2)	β	σ_{CH}	$0.84(sp^{1.24})_C + 0.54(s)_H$
		0.8967	β	$\sigma_{CH'}$	$0.84(sp^{8.33})_C + 0.54(s)_{H'}$
		0.2709	β	n_H^*	$(s)_H$

cationic species, this table displays the forms and occupancies of leading valence NBOs in each spin set, for direct comparison with Table 3.4(b). The α (majority-spin) NBOs are generally similar to those of the parent neutral species. However, the β (ionized-spin) NBOs display a number of interesting features that we now discuss in case-by-case fashion.

The carbon monoxide cation

Table 3.7 shows that the photoelectron was indeed removed from the formal n_C NBO (crudely equivalent to the HOMO or “5-sigma” MO of the parent neutral species), whose occupancy has been reduced to 0.0346 in the cation. However, an interesting switch in the hybridization at carbon (from $\sim sp^{2.6}$ to $\sim sp^{0.4}$) has evidently altered the form of the β - σ_{CO} spin-NBO relative to the corresponding σ_{CO} of the parent neutral species (Table 3.4(b)).

To understand this switch, we may first note that the linearly hybridized (nominally sp^1) carbon atom is expected to employ *inequivalent* sigma hybrids, namely an s-rich hybrid ($h^s \simeq sp^{0.3}$) for the nonbonded n_C and a p-rich hybrid ($h^p \simeq sp^{2.6}$) for the bonded σ_{CO} . This propensity is in accord with Bent’s rule (to be discussed in Section 3.2.6), which predicts that electrons will gain low-energy s character when held close to the nucleus (i.e., in nonbonding orbitals), but high-energy p character when shifted toward other atoms (i.e., in polarized bonds to electronegative atoms). If we now consider the ionized case in which the nonbonded electron is removed to infinity, the same type of reasoning would suggest that the vacant n_C^* orbital should become highly p-like (since there is no longer an energy penalty associated with high p character), while the remaining s character should concentrate in the bonding σ_{CO} hybrid. Thus, the switch to an s-rich bonding hybrid h^s in the ion is fully consistent with the elementary Bent’s-rule picture.

Although the β - n_C^* orbital is formally vacant in the cation, Table 3.7 shows that a small residual population (0.0346 e) survives in this orbital. This occupancy can be attributed to a strong donor–acceptor interaction with the filled n_O orbital as depicted in Fig. 3.14. This $n_O \rightarrow n_C^*$ interaction is estimated by second-order perturbation theory (Eq. (1.24)) to stabilize the ion by 19.5 kcal mol⁻¹, a significant delocalization that is primarily responsible for the slightly lower $\% \rho(L)$ value in this ion.

Both orbital reorganization effects described above tend to strengthen the bonding. The s-rich hybrid of the cation σ_{CO} is of smaller radius and lower energy than the corresponding p-rich hybrid of the neutral species, and the attractive $n_O \rightarrow n_C^*$ interaction slightly increases the CO bond order. Thus, although the ionized electron is formally removed from a nonbonding orbital, the internuclear distance is found to decrease significantly (0.017 Å) in the relaxed cation (Table 3.6). This decrease is the more remarkable in view of the increased Coulombic repulsions

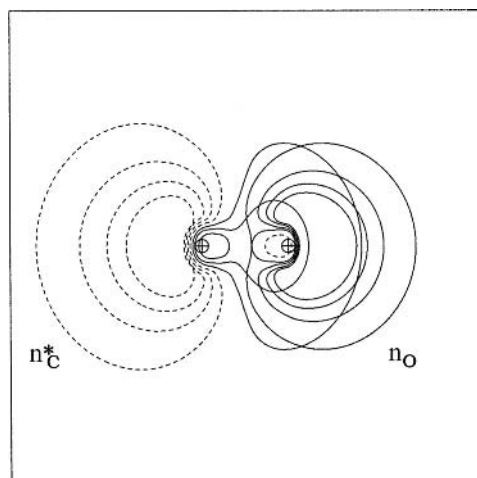


Figure 3.14 The $n_{\text{O}} \rightarrow n_{\text{C}}^*$ donor–acceptor interaction in the CO^+ cation.

between descreened cationic nuclei that must be overcome in order to achieve the reduction.

In other respects, the CO^+ ion exhibits the expected features of its elementary Lewis-structure diagram, including the two polarized π_{CO} bonds which survive virtually unchanged from their form in the parent neutral species.

The dinitrogen cation: nu bonds

The N_2 molecule exhibits the expected s-rich hybridization in n_{N} and p-rich hybridization in $\sigma_{\text{NN}'}$. In other respects its Lewis structure appears quite ordinary, exhibiting the expected similarities to the isoelectronic CO molecule. The α spin set of the cation is also unexceptional.

However, the β spin set of the ion exhibits a quite remarkable transformation to an entirely different mode of *unhybridized* bonding, denoted $\nu_{\text{NN}'}$ and $\bar{\nu}_{\text{NN}'}$ (“nu bonds”) in Table 3.7 and illustrated in Fig. 3.15. Each nu bond is composed of an essentially pure s AO on one atom and pure p AO on the other, asymmetrically *polarized* toward its s end (as Bent’s rule would suggest). A nu bond therefore has strong directional (polar) character, and such bonds necessarily appear in complementary (oppositely directed) *pairs* in a homonuclear diatomic molecule. Accordingly, the β Lewis structure of N_2^+ exhibits a formal *quadruple* bond, with two ordinary pi bonds and two nu bonds (and no nonbonded electrons). The nu bond $\nu_{\text{NN}'}$ may be considered the enhanced analog of the n_{O} (s-rich) \rightarrow n_{C}^* (p-rich) interaction of isoelectronic CO^+ , and the complementary $\bar{\nu}_{\text{NN}'}$ is then the reformed version of the original sigma bond needed to recover D_{2h} symmetry.

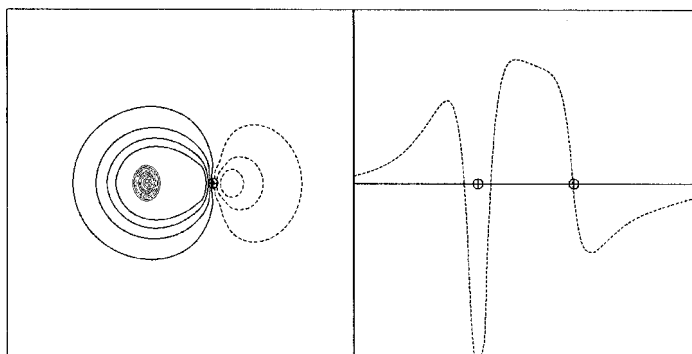


Figure 3.15 The nu bond (ν_{NN}) NBO of N_2^+ in contour (left) and profile (right) plots.

Although our overall goal is to reduce the number of special “effects” or “types” of bonding, it seems evident that the unsymmetric nu bonds warrant a distinctive symbol and nomenclature. Although nu bonds are formally similar to sigma bonds in having cylindrical symmetry about the bonding axis, they violate the parity (inversion) symmetry that is generally associated with sigma orbitals of homonuclear diatomics. Furthermore, unlike ordinary sigma bonds, nu bonds necessarily occur in ν , $\bar{\nu}$ complementary pairs of general form

$$\nu_{\text{AB}} = c_{\text{s}}h_{\text{A}}^{\text{s}} + c_{\text{p}}h_{\text{B}}^{\text{p}} \quad \begin{array}{c} \text{A} \text{---} \text{B} \\ \text{---} \text{---} \end{array} \quad (3.53\text{a})$$

$$\bar{\nu}_{\text{AB}} = c_{\text{p}}h_{\text{A}}^{\text{p}} + c_{\text{s}}h_{\text{B}}^{\text{s}} \quad \begin{array}{c} \text{---} \text{---} \\ \text{A} \text{---} \text{B} \end{array} \quad (3.53\text{b})$$

where h^{s} and h^{p} denote general s-rich and p-rich hybrids, respectively. In subsequent sections we shall investigate the details of how (n, σ) combinations of nonbonded and sigma-bonded hybrids evolve into the curious (ν , $\bar{\nu}$) nu-bond pairs.

The unhybridized $\bar{\nu}_{\text{NN}}$ bond of the cation appears to be weaker than the standard σ_{NN} of the parent neutral species that it replaces. Thus, even though the bond order formally increases in the cation, the added β - ν_{NN} half-bond cannot compensate for the general increase of Coulombic nuclear repulsion and the replacement of σ_{NN} by $\bar{\nu}_{\text{NN}}$ in the cation, so the equilibrium bond distance slightly *increases* (by 0.013 Å). This case illustrates why a general bond-order–bond-length relation cannot be globally linear; the bond length clearly depends on the *types* of bonds (e.g., pi versus sigma versus nu) as well as their number.

Despite the extensive reorganization of individual NBOs, the final cation exhibits a well-localized Lewis structure ($\% \rho(\text{L}) = 99.92\%$), which is even *more* Lewis-like than that of the parent neutral species ($\% \rho(\text{L}) = 99.89\%$).

The water cation

The β NBOs of H_2O^+ show clearly that ionization occurs out of the n_{O}^{π} (not the n_{O}^{σ}) lone pair. The natural atomic charge on O is thereby reduced from its significantly negative value in the neutral species ($Q_{\text{O}} = -0.9164$) to near-neutrality in the cation ($Q_{\text{O}} = -0.0792$). Only slight changes are seen in the occupied NBOs, primarily the increased polarization of σ_{OH} bonds toward oxygen in both spin sets. As a result, the atomic charges on H increase to still more positive values in the cation (from $+0.4582$ to $+0.5396$). The descreened protons move to positions slightly *outside* the centers of the oxygen hybrids, resulting in a slight “bond bending” (about 2.5°) in each OH bond. Thus, as seen in Table 3.6, the H—O—H angle is increased by about 5° in the cation, and the bonding appears slightly weakened as a result of this misalignment and the general increase in Coulombic nuclear repulsions, with each OH bond length increasing by about 0.04 \AA .

The methane cation

In this case, a single-NBO structure depicts the electron as being removed from a particular σ_{CH} bond, but the delocalization effects are obviously severe, with $\% \rho(\text{L})$ reduced to about 96% and each of the three surviving σ_{CH} bonds depleted in occupancy by more than $0.1e$. Each of the four equivalent Lewis structures of this type is severely defective, and one should instead consider a type of “resonance hybrid” to describe the extreme delocalization in this species. The electronic reorganization is also reflected in the severely distorted geometry of the cation, which corresponds to pronounced flattening from T_d to S_4 symmetry (opening two of the H—C—H angles to 141° and closing the others to 96°) and elongation of each C—H bond length by 0.13 \AA . Thus, this species can be discussed only in the framework of strongly delocalized electronic systems, to be considered in Section 3.3.

3.2.5 Hydride bonding and natural electronegativity

The simplicity of the H atom often allows chemical bonding trends to be exposed in their purest form in the A—H bonds of AH_n hydrides. We shall therefore examine the patterns of A—H NBO shape and composition in considerable detail in the present section.

Bonds and antibonds of group 13–17 hydrides

Table 3.8 summarizes the geometries, atomic charges, and σ_{AH} NBO parameters (ionicity and hybridization) for the first three members of each family of elements in groups 13–17. Figures 3.16(a)–(e) show corresponding contour plots of valence bond (σ_{AH} , left) and antibond (σ_{AH}^* , right) NBOs for all these species.

Table 3.8. Geometry (R_{AH} and \angle_{HAH}), atomic charges (Q_{A} and Q_{H}), and NBO ionicity ($i_{\text{AH}} = c_{\text{A}}^2 - c_{\text{H}}^2$) and hybridization (λ) parameters for A—H bonds of group 13–17 AH_n hydrides

AH_n	Geometry		Atomic charge		σ_{AH} NBO	
	R_{AH} (Å)	\angle (degrees)	Q_{A}	Q_{H}	i_{AH}	λ
Group 13						
BH_3	1.1894	120.0	+0.3355	−0.1118	−0.1118	2.00
AlH_3	1.5842	120.0	+1.1663	−0.3888	−0.3985	1.98
GaH_3	1.5600	120.0	+0.9031	−0.3010	−0.3087	2.00
Group 14						
CH_4	1.0909	109.5	−0.8092	+0.2023	+0.2029	2.99
SiH_4	1.4834	109.5	+0.6208	−0.1552	−0.1564	2.97
GeH_4	1.5344	109.5	+0.4731	−0.1183	−0.1187	2.99
Group 15						
NH_3	1.0145	107.9	−1.0534	+0.3511	+0.3527	2.82
PH_3	1.4234	93.5	+0.0538	−0.0179	−0.0167	5.85
AsH_3	1.5253	92.1	+0.1142	−0.0380	−0.0368	7.21
Group 16						
H_2O	0.9621	105.0	−0.9164	+0.4582	+0.4614	3.30
H_2S	1.3480	92.5	−0.2613	+0.1307	+0.1325	5.99
H_2Se	1.4716	91.3	−0.1650	+0.0825	+0.0842	7.30
Group 17						
HF	0.9222	—	−0.5485	+0.5485	+0.5533	3.90
HCl	1.2870	—	−0.2537	+0.2537	+0.2568	6.25
HBr	1.4270	—	−0.1852	+0.1852	+0.1880	7.60

The NBOs of Figs. 3.16(a)–(e) exhibit the expected smooth variations with respect to vertical and horizontal position in the periodic table (Appendix B). One can recognize that NBOs of the first member of each family tend to differ more conspicuously from subsequent family members than the last do from one another, which is consistent with known patterns in chemical behavior on moving down a column of the periodic table. Subtle changes in polarization associated with changes in electronegativity of the central atom A are apparent in the NBOs. These changes are manifested most conspicuously in the “backside” (A-end) lobe of the σ_{AH}^* antibond, which tends to diminish steadily from left to right along a given row, and to increase from top to bottom along a given column (particularly in later groups). As a result, there is often a “diagonal” resemblance pattern in which, e.g., the σ_{AH}^* NBO of a middle family member more nearly resembles that of the element to its lower right than it does those of other elements in its own row and column (cf., for example, σ_{SH}^* with σ_{BrH}^* , or σ_{PH}^* with σ_{SeH}^*). Such variations

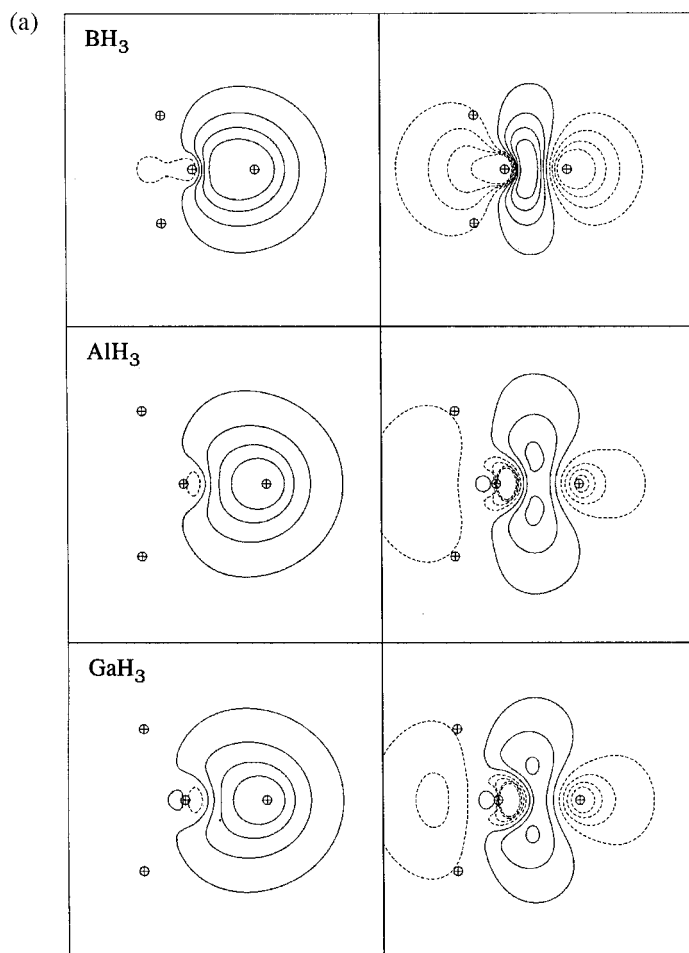


Figure 3.16 Hydride bond (σ_{AH} , left) and antibond (σ_{AH}^* , right) NBOs. (a) Group 13 elements: B, Al, and Ga. (b) Group 14 elements: C, Si, and Ge. (c) Group 15 elements: N, P, and As. (d) Group 16 elements: O, S, and Se. (e) Group 17 elements: F, Cl, and Br.

of electronegativity and A—H bond polarity (manifested most directly in the NBO ionicity values displayed in Table 3.8) are quite consistent with well-known periodic trends in experimental chemical behavior.

Measures of bond ionicity and electronegativity

Let us now discuss the bond polarities and charge distributions in greater detail. For a general hydride bond NBO of the form

$$\sigma_{\text{AH}} = c_{\text{A}}(\text{sp}^{\lambda})_{\text{A}} + c_{\text{H}}(\text{s})_{\text{H}} \quad (3.54)$$

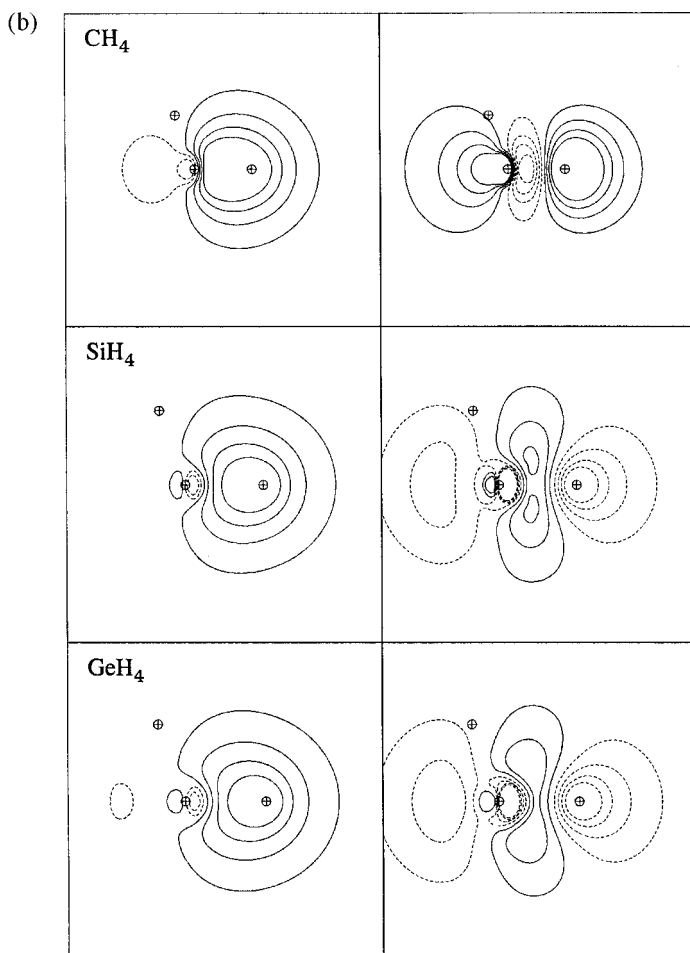


Figure 3.16 (Cont.)

one can see that the net charge (Q_{H}) on H will be approximately given by

$$\begin{aligned}
 Q_{\text{H}} &\simeq Z_{\text{H}} - 2|c_{\text{H}}|^2 = 1 - 2|c_{\text{H}}|^2 \\
 &= (|c_{\text{A}}|^2 + |c_{\text{H}}|^2) - 2|c_{\text{H}}|^2 \\
 &= |c_{\text{A}}|^2 - |c_{\text{H}}|^2
 \end{aligned}
 \tag{3.55a}$$

and thus that

$$Q_{\text{H}} \simeq i_{\text{AH}}
 \tag{3.55b}$$

The accuracy of this approximation is shown in the entries of Table 3.8. Furthermore, the polarization coefficients c_{A} and c_{H} in (3.54) are simply related to the bond

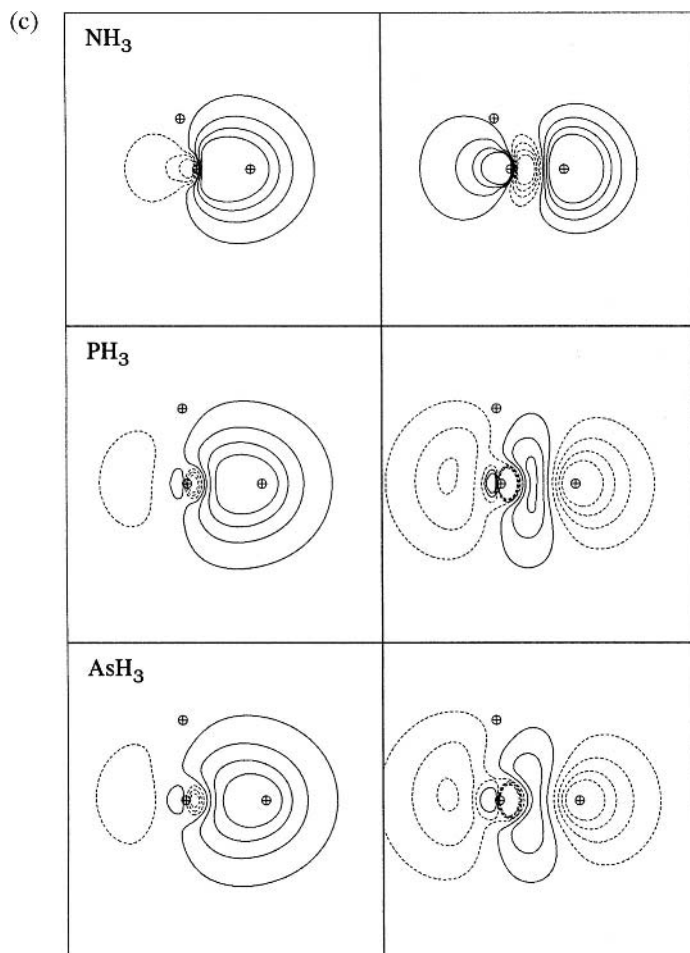


Figure 3.16 (Cont.)

ionicity i_{AH} by

$$c_{\text{A}} = [(1 + i_{\text{AH}})/2]^{1/2} \quad (3.56\text{a})$$

$$c_{\text{H}} = [(1 + i_{\text{AH}})/2]^{1/2} \quad (3.56\text{b})$$

Hence, trends in i_{AH} control both the charge distributions and the NBO compositions of these species.

Now the bond ionicity must be related in some manner to the “electronegativity” x_{A} (the ability of atom A to gain and hold electrons). Pauling originally postulated a relationship of the form³¹

$$i_{\text{AH}} = 1 - \exp[-\frac{1}{4}(x_{\text{A}} - x_{\text{H}})^2] \quad (3.57)$$

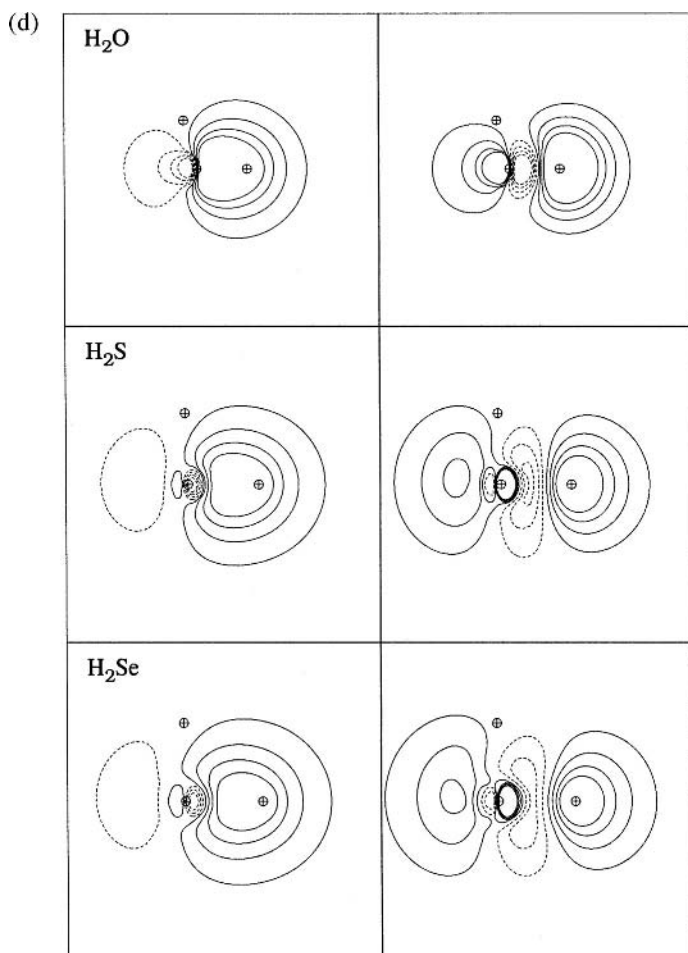


Figure 3.16 (Cont.)

However, Hannay and Smyth³² obtained improved results with a quadratic equation of the form

$$i_{\text{AH}} = 0.035(x_{\text{A}} - x_{\text{H}})^2 + 0.16(x_{\text{A}} - x_{\text{H}}) \quad (3.58)$$

and many alternative relationships have been proposed.³³ Slight differences distinguish the original Pauling electronegativity scale³⁴ from the scale of Allred and Rochow³⁵ and other proposed electronegativity measures.³⁶ Alternative scales of electronegativity generally originate from empirical fits to experimental dipole moments or bond energies. Thus, the conventional electronegativity concept has an inherently vague and empirical character that tends to obscure a simple mathematical relationship to bond ionicity.

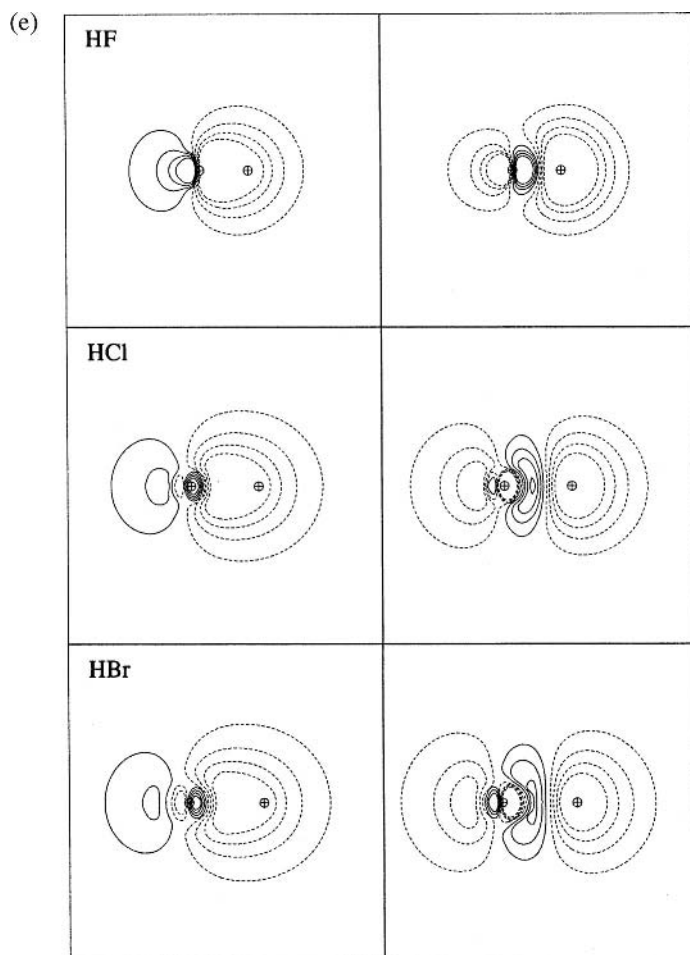


Figure 3.16 (Cont.)

Natural electronegativity

A simple way to bypass the vagaries of empirical fits is to define an alternative, purely theoretical electronegativity scale based on a proposed functional relationship between i_{AH} and x_{A} , analogous, e.g., to Eq. (3.57) or Eq. (3.58). A particularly simple and attractive one-parameter exponential relationship is

$$i_{\text{AH}} = 1 - \exp[-a(x_{\text{A}} - x_{\text{H}})] \quad (3.59)$$

which retains the proper limiting behavior of Pauling's formula (3.57) (i.e., $i_{\text{AH}} \rightarrow 1$ as $x_{\text{A}} \rightarrow \infty$) but includes terms *linearly* proportional to $x_{\text{A}} - x_{\text{H}}$, as in Eq. (3.58). Since $x_{\text{H}} = 2.10$ has a common value on the Pauling and Allred–Rochow scales, we can fix this reference value and choose the “ a ” for which Eq. (3.59) gives x_{A}

values most closely resembling conventional Pauling or Allred–Rochow values. With the choice $a = 0.45$, Eq. (3.59) can be rewritten in a form that defines the “natural” electronegativity scale $x_A^{(N)}$ as

$$x_A^{(N)} \equiv x_H^{(N)} - \ln(1 - i_{AH})/0.45 \quad (3.60)$$

with $x_A^{(N)} = 2.10$ and NBO ionicities i_{AH} taken from Table 3.8.

The definition (3.60) can even be extended to the lone-pair case, in which the “ligand” is nonexistent, by recognizing that this corresponds to the ionicity limit $i = -1$. In this case Eq. (3.60) gives for the formal “lone-pair electronegativity” $x_{nb}^{(N)}$ the value³⁷

$$x_{nb}^{(N)} = 2.1 - \ln(2)/0.45 = 0.56 \quad (3.61)$$

Similarly, the hybridization λ_+ of an empty (ionized) hybrid corresponds to the ionicity limit $i = +1$, which can be formally associated with a ghost (gh) ligand of infinite electronegativity

$$x_{gh}^{(N)} = \infty \quad (3.62)$$

Equation (3.60) leads to $x_A^{(N)}$ electronegativity values that are generally in close agreement with conventional Pauling and Allred–Rochow values, as shown in Table 3.9 and displayed graphically in Fig. 3.17. The r.m.s. deviations of $x_A^{(N)}$ from conventional empirical electronegativities are 0.12 for $x_A^{(N)}$ versus $x_A^{(P)}$ or 0.15 for $x_A^{(N)}$ versus $x_A^{(AR)}$, which are rather similar to the corresponding deviation (0.11) for $x_A^{(P)}$ versus $x_A^{(AR)}$. The small deviations from Pauling values are of the order of the uncertainties in these values, as judged by Pauling.³⁸

As shown in Fig. 3.17, the natural electronegativities $x_A^{(N)}$ generally reproduce qualitative periodic trends of empirical $x_A^{(P)}$ and $x_A^{(AR)}$ values. For all three scales, the maximum individual deviations for any element are about twice the r.m.s. deviation. Comparing $x_A^{(N)}$ and $x_A^{(P)}$ values, for example, the maximum deviation occurs for the heavier halogens (Cl, Br), which are each depicted as being 0.24 units more electropositive on the natural than on the Pauling scale (deviating in the same direction as Allred–Rochow values). The largest deviation between $x_A^{(N)}$ and $x_A^{(AR)}$ occurs for Ga (0.32 units), for which the deviation between Pauling and Allred–Rochow values is also largest (0.22 units). The natural scale agrees with Pauling and Allred–Rochow values that Ga is *more* electronegative than Al (though not so strongly as represented on the Allred–Rochow scale) and that Ge is slightly more electronegative than Si (again, far less than the Allred–Rochow scale would suggest). This reversal of the usual vertical trend (typically exaggerated by

Table 3.9. A comparison of Pauling ($x_A^{(P)}$), Allred–Rochow ($x_A^{(AR)}$), and natural ($x_A^{(N)}$) electronegativity values (B3LYP/6-311++ G^{**} level) for leading alkali metals and group 13–17 elements

	$x_A^{(P)}$	$x_A^{(AR)}$	$x_A^{(N)}$
l.p. ^a	—	—	0.56
H	2.1	2.10	[2.10] ^b
Li	1.0	0.97	0.79
Na	0.9	1.01	0.88
B	2.0	2.01	1.86
Al	1.5	1.47	1.35
Ga	1.6	1.82	1.50
C	2.5	2.50	2.60
Si	1.8	1.74	1.78
Ge	1.8	2.02	1.85
N	3.0	3.07	3.07
P	2.1	2.06	2.06
As	2.0	2.20	2.02
O	3.5	3.50	3.48
S	2.5	2.44	2.42
Se	2.4	2.48	2.30
F	4.0	4.10	3.89
Cl	3.0	2.83	2.76
Br	2.8	2.74	2.56

^a The “lone-pair” (least possible) value.

^b The fixed common point of electronegativity scales.

Allred–Rochow relative to natural or Pauling values) continues toward alkali metals, where Na is found to be slightly more electronegative than Li (which is consistent with the Allred–Rochow scale, but inconsistent with Pauling; cf. Table 3.9). Roughly speaking, we can say that there is only weak vertical electronegativity dependence at the left of the periodic table, but quite strong vertical dependence toward the right, particularly between the first and second members of the family.

We conclude that the theoretical $x_A^{(N)}$ values (3.60) agree satisfactorily with empirical scales, within their inherent uncertainties. However, the natural electronegativity scale offers a considerable conceptual advantage with respect to an intrinsic (defined) association with bond ionicity, reducing the number of independent concepts by one. Equations (3.55), (3.56), and (3.60) show that i_{AH} can be regarded as the key electronic parameter governing bond polarization and atomic charge distributions. This is also the parameter that allows NBO and VB descriptions to be unified in the most direct and satisfying manner.

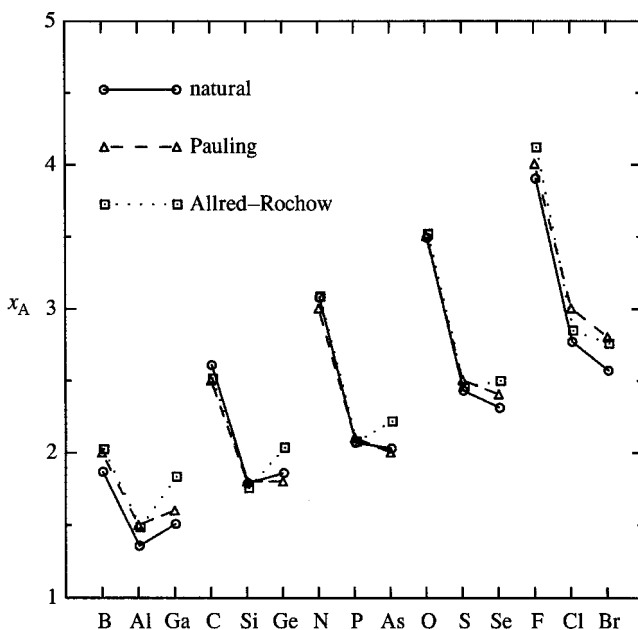


Figure 3.17 Electronegativities x_A for elements of groups 13–17, comparing “natural” values (circles, solid lines) with Pauling (triangles, dashed lines) and Allred–Rochow (squares, dotted lines) values.

Electronegativity and hybridization

Let us return now to the general relationship among AH_n bond ionicity, hybridization, and geometry, as displayed in Table 3.8. It is apparent that the NBO hybridizations are virtually identical to the expected sp^{n-1} types (viz., sp^2 for group 13, sp^3 for group 14) in high-symmetry species with only σ_{AH} bond pairs. However, when one or more lone pairs are present (groups 15–17), the corresponding nonbonding hybrids h_{nb} are generally expected to be of inequivalent form (consistent with Bent’s rule; cf. Section 3.2.6).

To analyze the hybridization in groups 15–17, let n_{bond} denote the number of hydride bonds in the molecule ($n_{\text{bond}} = 3$ for group 15, 2 for group 16, 1 for group 17). As usual, only n_{bond} p orbitals are required, together with the single s orbital, to build the sigma-bonding framework. Hence, only *one* sigma-type lone pair ($n_A^{(\sigma)}$) participates in sp -hybridization, while the remaining $3 - n_{\text{bond}}$ pi-type lone pairs ($n_A^{(\pi)}$) are assigned to unhybridized pure p orbitals (with $\lambda_{nb}^{(\pi)} = \infty$).

To estimate the hybridization of hydride bonds and lone pairs, we first rewrite the sum rule (3.37a) for n_{bond} hydride bonds of hybridization λ_H and one lone pair of hybridization λ_{nb} ,

$$\frac{n_{\text{bond}}}{1 + \lambda_H} + \frac{1}{1 + \lambda_{nb}} = 1 \quad (3.63)$$

This equation can be solved for λ_{nb} to give

$$\lambda_{\text{nb}} = \frac{n_{\text{bond}}}{1 - n_{\text{bond}} + \lambda_{\text{H}}} \quad (3.64)$$

We can also express this conservation condition in terms of the fractional p character of bonding ($f_{\text{p}}^{(\text{AH})}$) and sigma nonbonding ($f_{\text{p}}^{(\text{A:})}$) hybrids,

$$f_{\text{p}}^{(\text{AH})} = 1 - f_{\text{p}}^{(\text{A:})}/n_{\text{bond}} \quad (3.65)$$

which is convenient for the present purpose.

Example 3.6

Exercise: Estimate the hybridization parameters (λ_{nb}) for the sigma lone-pair hybrids h_{nb} of NH_3 , H_2O , and HF .

Solution: On substituting values of $\lambda = \lambda_{\text{H}}$ from Table 3.8 into Eq. (3.64), we find

$$\text{for } \text{NH}_3 \ (n_{\text{bond}} = 3, \lambda_{\text{H}} = 2.82): \quad \lambda_{\text{nb}} = 3.66$$

$$\text{for } \text{H}_2\text{O} \ (n_{\text{bond}} = 2, \lambda_{\text{H}} = 3.30): \quad \lambda_{\text{nb}} = 0.87$$

$$\text{for } \text{HF} \ (n_{\text{bond}} = 1, \lambda_{\text{H}} = 3.90): \quad \lambda_{\text{nb}} = 0.26$$

The actual NBO lone-pair hybridizations are found to be 3.64, 0.87, and 0.25, respectively, nearly identical to the above estimates (within expected roundoff errors).

We can derive an approximate relationship between hybridization and natural electronegativity differences in the following manner. Even cursory inspection of the values in Table 3.8 suggests that λ_{H} increases as the electronegativity of the central atom decreases down a column of the periodic table. Equation (3.64) shows in turn that λ_{nb} must diminish as central-atom electronegativity decreases. Relative to the average fractional p character of the $n_{\text{bond}} + 1$ hybrids,

$$\bar{f}_{\text{p}} = \frac{n_{\text{bond}}}{n_{\text{bond}} + 1} \quad (3.66)$$

we might expect that the fractional p character of bonding ($f_{\text{p}}^{(\text{AH})}$) and nonbonding ($f_{\text{p}}^{(\text{A:})}$) hybrids would vary in simple linear proportionality to the corresponding electronegativity differences,

$$f_{\text{p}}^{(\text{AH})}/\bar{f}_{\text{p}} = a_{\text{H}}(x_{\text{H}} - x_{\text{A}}) + b_{\text{H}} \quad (3.67\text{a})$$

$$f_{\text{p}}^{(\text{A:})}/\bar{f}_{\text{p}} = a_{\text{nb}}(x_{\text{nb}} - x_{\text{A}}) + b_{\text{nb}} \quad (3.67\text{b})$$

where a_{H} , b_{H} , a_{nb} , and b_{nb} , are proportionality constants that depend (at most) on group number (or n_{bond}), but not on the identity of A. Since x_{nb} is the smallest possible electronegativity, we recognize that $f_{\text{p}}^{(\text{A:})}$ must go to zero in the limit

$x_A \rightarrow x_{nb}$, and thus that $b_{nb} = 0$. We can therefore substitute Eqs. (3.67) into (3.65) to obtain

$$a_H(x_H - x_A)\bar{f}_p + b_H\bar{f}_p = 1 - [a_{nb}(x_{nb} - x_A)\bar{f}_p]/n_{\text{bond}} \quad (3.68)$$

Since this equation should be true for *all* A (of the same group), the terms involving x_A must cancel out from this equation, which leads to the condition

$$n_{\text{bond}}a_H = -a_{nb} \quad (3.69)$$

With this substitution, we can rewrite (3.67b) as

$$f_p^{(A:)} = -a_H(x_{nb} - x_A)\frac{n_{\text{bond}}^2}{n_{\text{bond}} + 1} \quad (3.70a)$$

and use Eq. (3.65) to evaluate $f_p^{(AH)}$ from this expression (which is equivalent to finding the b_H that satisfies the sum rule),

$$f_p^{(AH)} = 1 + a_H(x_{nb} - x_A)\frac{n_{\text{bond}}}{n_{\text{bond}} + 1} \quad (3.70b)$$

A single-parameter best fit to the data of Table 3.8 for the remaining unknown a_H gives the value

$$a_H = 0.125 \quad (3.70c)$$

On inserting the value of x_{nb} from Eq. (3.61), we obtain finally

$$f_p^{(A:)} = (0.125x_A - 0.07)n_{\text{bond}}^2/(n_{\text{bond}} + 1) \quad (3.71a)$$

$$f_p^{(AH)} = 1 - (0.125x_A - 0.07)n_{\text{bond}}/(n_{\text{bond}} + 1) \quad (3.71b)$$

The accuracy of the simple approximation (3.71) is illustrated in Fig. 3.18.

Figure 3.18 shows that the simple estimates (3.71) capture the interesting variations of bond and lone-pair p character in a semi-quantitative manner (r.m.s. error <3%) solely on the basis of variations in electronegativity. Since the percentage p characters (or the equivalent λ_{nb} , λ_H hybridization parameters) are intimately connected to molecular geometry through Eq. (3.34), we recognize immediately that variations of central-atom electronegativity (or equivalently, through Eq. (3.60), A—H bond polarity) lead directly to variations of H—A—H bond angles.³⁹ Conversely, we can appreciate that changes of bond angles must be strongly coupled to changes in bond hybridization and polarity. This is the essence of the profound generalization summarized in Bent's rule, which we discuss in the following section.

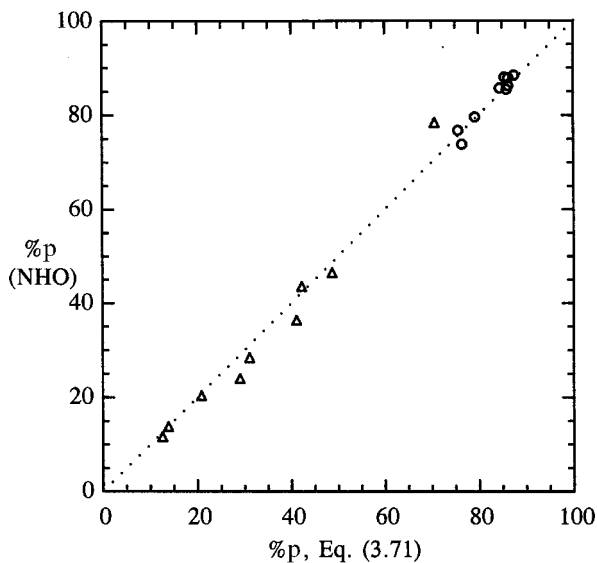


Figure 3.18 Comparison of accurate (%p) and estimated (%p, Eq. (3.71)) percentage p character for hydride bond (circles) and lone-pair (triangle) hybrids of group 15–17 AH_n hydrides (r.m.s. deviation = 2.82%).

Example 3.7

Exercise: Estimate the bond angle of singlet methylene (CH_2).

Solution: From the natural electronegativity of carbon ($x_C = 2.60$; Table 3.9) and Eq. (3.71b), with $n_{\text{bond}} = 2$, we obtain

$$f_p^{(\text{CH})} = 1 - [(0.125 \times 2.60) - 0.07]2/3 = 0.83$$

Relationship (3.35b) gives

$$\lambda = \frac{f_p^{(\text{CH})}}{1 - f_p^{(\text{CH})}} = 4.88$$

and Eq. (3.34) becomes

$$\cos(\angle_{\text{HCH}}) = -\frac{1}{4.88} = -0.20$$

which corresponds to

$$\angle_{\text{HCH}} = 102^\circ$$

This agrees well with the actual optimized value, 101.52° .

3.2.6 Bent's rule: qualitative and quantitative formulations

Nearly four decades ago, American chemist Henry Bent⁴⁰ formulated a remarkable principle that relates atomic hybridization to substituent electronegativity. This principle, now called "Bent's rule," was originally expressed in the following words:

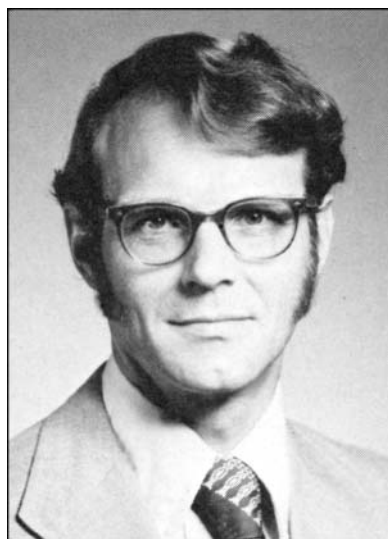
Atomic s character concentrates in orbitals directed toward electropositive substituents

The principle can also be stated in corollary form expressing the enriched p character of hybrids toward electronegative ligands:

A central atom tends to direct hybrids of higher p character toward more electronegative substituents

The importance of Bent's rule is that it suggests how the elementary picture of equivalent hybrids (e.g., the four sp^3 hybrids of methane) must be modified to reflect subtle differences in hybridization to different bonding ligands (e.g., in CH_2ClBr). Thus, Bent's rule provides the first tier of corrections to the elementary sp^n hybrid picture, suggesting the more accurate picture of *inequivalent* sp^λ hybrids with higher λ for ligands of higher electronegativity.

Bent's recognition of this general principle is the more remarkable because it was based primarily on X-ray structural evidence concerning geometry changes (particularly, bond-angle variations) that are only inferentially connected to "hybridization." (It would be several decades before reliable wavefunctions and methods for determining hybrid p character made it possible to confirm the prescience and



Henry A. Bent

accuracy of Bent's rule in a direct manner.) The intimate connection between geometry and hybridization is expressed by the fundamental Eq. (3.34), which relates variations of bond angles B_i-A-B_j to hybridization parameters λ_i and λ_j . Bent showed how such an elementary hybridization picture of angular bending potentials can be used to rationalize a broad variety of puzzling structural phenomena solely on the basis of known electronegativity trends.

Qualitative rationalizations of Bent's rule

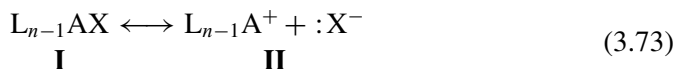
The physical explanation of Bent's rule is usually based on the difference of valence s and p orbital energies ($\epsilon_s < \epsilon_p$) and the variational minimum-energy principle. The overall energy is expected to be lowered if the low-energy s_A orbital is reserved for electron pairs that are more concentrated on A (i.e., a lone pair or polarized bond pair with $|c_A|^2 \gg |c_B|^2$), while the high-energy p_A character is relegated to pairs that have least density on A (i.e., they are strongly polarized toward the opposite atom, $|c_B|^2 \gg |c_A|^2$). This implies that s-rich character will be variationally concentrated in hybrids toward electropositive ligands, while p-rich character is relegated toward electronegative ligands, in accordance with Bent's rule.

In the above picture, the primary factor that dictates allocation of hybrid p character toward electronegative ligands is the "promotion energy" Δ_{sp} , the valence-shell s-p energy separation

$$\Delta_{sp} = \epsilon_p - \epsilon_s \quad (3.72)$$

Figure 3.19 illustrates the dependence of Δ_{sp} on location in the periodic table for each of the first three elements of main groups 13–17. The promotion energy varies with group number in a manner similar to electronegativity (cf. Fig. 3.17). Although Δ_{sp} is doubtless important, other factors (such as differences in orbital radii) appear to play a role in general spd hybridization.

A somewhat different way of rationalizing Bent's rule can be given as follows. Let us initially assume idealized equivalent sp^{n-1} hybrids for a given AL_n species of n ligands. If we now formally replace one L by a highly electronegative X, we can represent the resulting species as a resonance hybrid of neutral and ionic forms



with relative weightings $w_I = 1 - i_{AX}$ and $w_{II} = i_{AX}$, respectively. Assuming that the ionized A orbital in **II** is of pure p character, one can estimate that the fractional p character of the A—X bond ($f_p^{(AX)}$) has the resonance-weighted value

$$f_p^{(AX)} = (1 - i_{AX}) \frac{n-1}{n} + i_{AX}(1) = \frac{n-1}{n} + \frac{i_{AX}}{n} \quad (3.74)$$

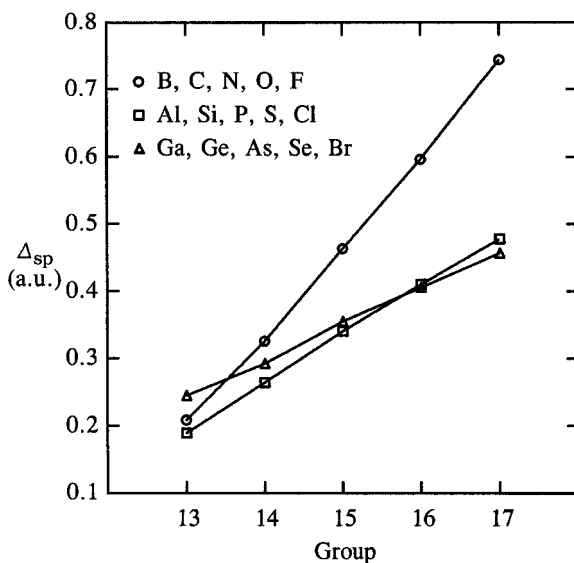
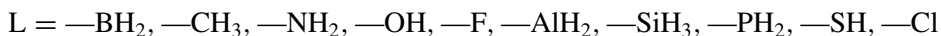


Figure 3.19 The $\Delta_{sp} = \epsilon_{np} - \epsilon_{ns}$ valence-shell promotion energy for group 13–17 elements: $n = 2$ (circles), $n = 3$ (squares), $n = 4$ (triangles). (ϵ_{np} is the average orbital energy of occupied valence p AOs of α spin.)

According to Eq. (3.74) $f_p^{(AX)}$ increases with i_{AX} , and therefore with the electronegativity of X, in accordance with Bent's rule. Note that Eq. (3.74) makes no direct reference to Δ_{sp} and requires only the hybridizations of idealized neutral and ionic structures. Thus, analogous resonance-type reasoning might be used to generalize Bent's rule for more general spd hybridization (Section 4.6).

A generalized NBO version of Bent's rule

Let us now attempt to express Bent's rule in more quantitative form. The dependence of hybrid p character f_p on ligand electronegativity x_L is illustrated in Fig. 3.20 for a series of 40 mono-substituted ALH_n hydrides, where L is chosen from the substituent series of first- and second-row ligands



and A = C, N, O, or F. In each case, x_L is taken as the natural electronegativity of the non-hydride ligand atom directly bonded to A. Values of f_p for second-row ligands ($-\text{AlH}_2, \dots, -\text{Cl}$) are plotted with dotted lines and those for first-row ligands ($-\text{BH}_2, \dots, -\text{F}$) with solid lines to show the trends with increasing substituent electronegativity in each row.

As seen in Fig. 3.20, the general trends along each series of substituents L are consistent with Bent's rule. Thus, with increasing x_L along a row of the periodic table,

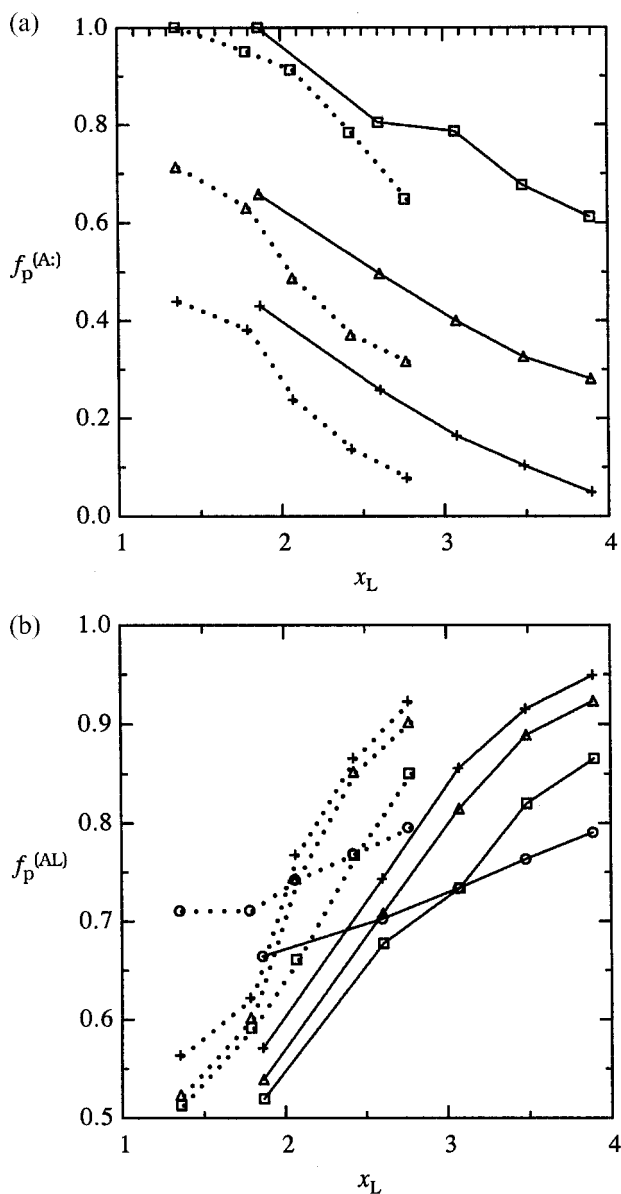


Figure 3.20 Fractional p character (f_p) in mono-substituted first-row ALH_n hydrides for (a) A: lone-pair hybrids (upper), and (b) A—L bond hybrids (lower), showing trends in dependence on the substituent's electronegativity (x_L) for first-row (solid line) and second-row (dotted line) — LH_n substituents of C (circles), N (squares), O (triangles), and F (plus signs) central atoms.

the lone-pair hybrids of the upper panel (Fig. 3.20(a)) generally trend *downward* in p character while the A—L bond hybrids of the lower panel (Fig. 3.20(b)) correspondingly trend *upward*, as Bent's rule suggests. Although Bent's rule successfully predicts the signs of the slopes in Fig. 3.20, it does not provide more quantitative information on the rather complex $f_p(x_L)$ dependence that is evident in this figure.

One can recognize that other factors than ligand electronegativity are important in determining f_p . From the gap between dotted and solid lines, for example, it is apparent that there is systematically higher p character in bonding hybrids toward second-row ligands L than toward corresponding ligands of the same row in the periodic table. This results in numerous apparent inversions with respect to the expectations of Bent's rule. For example, from the lower two curves in Fig. 3.20(a) for fluoride lone pairs of F—L compounds, one can see that the fluorine lone-pair hybrid has *lower* p character in F—Cl ($f_p = 0.0750$) than in F—NH₂ ($f_p = 0.1662$) despite the increase in electronegativity of the ligand ($x_{\text{Cl}} = 2.76$ versus $x_{\text{N}} = 3.07$). It is also apparent that the f_p values depend markedly on the identity of the central atom A. This dependence becomes even more conspicuous if one includes data for corresponding second-row A atoms (not shown), which exhibit systematically higher f_p in bonding hybrids to a given ligand. Thus, Bent's rule provides only a first step in relating hybrid p character to ligand electronegativity.

To develop approximate mathematical expressions for the rather complex behavior depicted in Fig. 3.20, let us begin with the C—L hybridizations $f_p^{(\text{CL})}$ (circles in Fig. 3.20(b)). These follow simple linear behavior that can be approximately represented as

$$f_p^{(\text{CL})} = \begin{cases} \tilde{f}_p & \text{for L} = \text{H} \\ 0.98 - [\tilde{f}_p + 0.26(x_{17} - x_L)]/n_{\text{bond}} & \end{cases} \quad (3.75a)$$

where $\tilde{f}_p = (n_{\text{bond}} - 1)/n_{\text{bond}} = 0.75$, and x_{17} denotes the halogen (group 17) electronegativity of the given period. A similar relationship (with slightly smaller slope and intercept) describes the corresponding hybridizations for silicon

$$f_p^{(\text{SiL})} = 0.96 - [\tilde{f}_p + 0.12(x_{17} - x_L)]/n_{\text{bond}} \quad (3.75b)$$

Equations (3.75a) and (3.75b) satisfactorily reproduce the calculated hybridizations of the mono-substituted methanes and silanes with r.m.s. error of about 0.7%.

For lone-pair-bearing central atoms A, let us next estimate the lone-pair p character in Fig. 3.20(a), taking the solid line for F as a starting point. We can see that there is approximately constant slope ($df_p^{(\text{LF})}/dx_L \simeq -0.23$) for smaller values of x_L , with a slight upward curvature as $f_p^{(\text{LA})}$ approaches the limiting value of zero at the highest possible electronegativity in the period ($x_{17} = x_{\text{F}} = 3.89$). As a first approximation we may assume that the fluorine lone pair has *no* p character in the

Table 3.10. Numerical constants for Eq. (3.75c); r_A denotes the row of atom A and r_L the row of ligand L in the periodic table

a_{1p}	0.23 for $r_A = 1, r_L = 1$ 0.36 for $r_A = 1, r_L = 2$ 0.11 otherwise		
b_{1p}	0.11 for $r_A = 1$ 0 otherwise		
f_A° values:			
	Group 15	Group 16	Group 17
$r_A = 1$	0.54	0.21	-0.04
$r_A = 2$	0.35	0.19	0.05

$x_L = x_{17}$ limit, and that $f_p^{(\text{LF:})}$ thereafter increases linearly as x_L decreases. As a correction to this linear approximation, the slight upward curvature near $x_L = x_{17}$ can be approximated as a small exponential term (amplitude $\simeq 0.11$) that decays rapidly away from $x_L = x_{17}$ within about one electronegativity unit. Thus, for substituted F lone pairs (labeled LF:) we postulate an expression of the form

$$f_p^{(\text{LF:})} \simeq 0.23(x_{17} - x_L) + 0.11 \exp[-3(x_{17} - x_L)]$$

The other two solid curves in Fig. 3.20(a) are of approximately similar form, but shifted upward by an overall constant f_A° for each central atom A. We can therefore approximate each such curve by the general form

$$f_p^{(\text{LA:})} = f_A^\circ + a_{1p}(x_{17} - x_L) + b_{1p} \exp[-3(x_{17} - x_L)] \quad (3.75c)$$

To a crude approximation, Eq. (3.75c) applies to both first- and second-row central atoms and ligands ($r_A, r_L = 1$ or 2) with constants chosen as shown in Table 3.10.

We now assume that hydride bond p character $f_p^{(\text{AH})}$ can be adequately approximated with Eq. (3.71b) (i.e., that L substitution primarily affects $f_p^{(\text{LA:})}$ rather than $f_p^{(\text{AH})}$). The A—L hybridization $f_p^{(\text{AL})}$ of the mono-substituted hydride can then be determined from the sum rule (3.37b) as

$$f_p^{(\text{AL})} = n_{\text{bond}} - (n_{\text{bond}} - 1)f_p^{(\text{AH})} - f_p^{(\text{LA:})} \quad (3.75d)$$

Equations (3.75c) and (3.75d) reproduce the hybridizations of Figs. 3.20(a) and (b) (as well as the corresponding hybridizations of second-row A, not shown) with an r.m.s. error of 3.0%, which is rather similar to the accuracy of Eqs. (3.71) for the pure hydrides (cf. Fig. 3.18).

Let us now turn to the general case of a lone-pair-bearing central atom A with arbitrary substituents L_1, L_2, \dots , labeled \tilde{A} : for short. In the spirit of a

Taylor-series expansion, we can approximate $f_p^{(A\cdot)}$ in terms of the unsubstituted (pure hydride) “reference value” $f_p^{(A\cdot)}$, Eq. (3.71a), and successive corrections $\delta_{L_i}^{(A\cdot)}$ for each substituent

$$f_p^{(\tilde{A}\cdot)} = f_p^{(A\cdot)} + \delta_{L_1}^{(A\cdot)} + \delta_{L_2}^{(A\cdot)} + \dots \quad (3.75e)$$

Each correction $\delta_L^{(A\cdot)}$ can in turn be obtained from the change under mono-substitution,

$$\delta_L^{(A\cdot)} \equiv f_p^{(LA\cdot)} - f_p^{(A\cdot)} \quad (3.75f)$$

as calculated from Eqs. (3.71a) and (3.75c). For the \tilde{A} —L bonding hybrid, we shall assume that

$$f_p^{(\tilde{A}L)} = f_p^{(AL)} \quad (3.75g)$$

(which is similar to the assumption made for $f_p^{(AH)}$ in the previous paragraph). Because direct estimates based on (3.75f) and (3.75g) will generally not satisfy Eq. (3.37b), we normalize these estimates to obtain the final values

$$f_p^{(A\cdot)} = \eta f_p^{(\tilde{A}\cdot)} \quad (3.75h)$$

$$f_p^{(AL)} = \eta f_p^{(\tilde{A}L)} \quad (3.75i)$$

with normalization factor

$$\eta = \frac{n_{\text{bond}}}{f_p^{(\tilde{A}\cdot)} + \sum_L f_p^{(\tilde{A}L)}} \quad (3.75j)$$

to guarantee satisfaction of the sum rule. Corresponding estimates (3.75a) and (3.75b) for a central atom A bearing no lone pairs are renormalized in analogous manner.

Equations (3.75a)–(3.75j) constitute a more quantitative formulation of the relationship between hybrid p character and substituent electronegativity, generalizing Bent’s rule. The accuracy of these approximations is generally of the order of a few percent, sufficient to determine hybrid angles within 1–2° as illustrated in the following examples.

Example 3.8

Exercise: Estimate the interhybrid angles in OF₂.

Solution: From Table 3.10 for A = O we obtain $a_{1p} = 0.23$, $b_{1p} = 0.11$, and $f_A^\circ = 0.21$. For $x_{17} = x_F = x_L$, Eq. (3.75c) then gives

$$f_p^{(FO\cdot)} = 0.21 + 0.11 = 0.32$$

whereas from Eq. (3.71a), with $n_{\text{bond}} = 2$ and $x_{\text{O}} = 3.48$,

$$f_{\text{p}}^{(\text{O}^{\cdot})} = 4/3[(0.125 \times 3.48) - 0.07] = 0.487$$

leading to

$$\delta_{\text{F}}^{(\text{O}^{\cdot})} = -0.167$$

for each ligand. According to Eq. (3.75e), for two F ligands, the lone-pair hybridization is

$$f_{\text{p}}^{(\ddot{\text{O}}^{\cdot})} = 0.487 + 2(-0.167) = 0.153$$

whereas from (3.75d) and (3.75g) the two O—F hybridizations are

$$f_{\text{p}}^{(\ddot{\text{O}}\text{F})} = 2 - 0.757 - 0.32 = 0.923$$

These values are essentially unaltered by normalization ($\eta = 1.000$), so that finally

$$f_{\text{p}}^{(\text{O}^{\cdot})} = 0.153$$

$$f_{\text{p}}^{(\text{OF})} = 0.923$$

leading to the estimated interhybrid angle

$$\angle_{\text{FOF}} = 94.8^{\circ}$$

The corresponding NHO values are

$$f_{\text{p}}^{(\text{O}^{\cdot})} = 0.142$$

$$f_{\text{p}}^{(\text{OF})} = 0.922$$

$$\angle_{\text{FOF}} = 94.8^{\circ}$$

in excellent agreement with the above estimates. (However, the optimized F—O—F angle is 104.2° , corresponding to about 5° bond bending at each O—F bond.)

Example 3.9

Exercise: Estimate the interhybrid angles of $\text{CHF}(\text{OH})(\text{PH}_2)$.

Solution: From the application of Eqs. (3.75a)–(3.75j) and the electronegativities of Table 3.9 we obtain the estimated and actual (NHO) values of $f_{\text{p}}(\text{C—X})$ tabulated below:

	C—H	C—F	C—O	C—P
Estimated	0.7363	0.7935	0.7396	0.7171
NHO	0.7364	0.7781	0.7520	0.7335

These lead to the interhybrid angles shown in the first two columns below, compared with the optimized bond angles in the final column:

Angle	\sphericalangle (degrees)		
	Estimated	NHO	Optimized
H—C—F	108.6	107.5	106.7
H—C—O	110.1	110.6	106.5
H—C—P	111.1	111.9	110.1
F—C—O	107.9	107.3	109.7
F—C—P	108.8	108.4	105.5
O—C—P	110.3	111.7	117.9

Although the estimated and actual interhybrid angles agree well in all cases (within $\sim 1^\circ$), there is evidence of significant bond bending in the actual bond angles (e.g., $\sim 6^\circ$ mismatch in the O—C—P angle).

3.2.7 Angular strain and bond bending

As examples of the previous section have shown, bond hybrids are sometimes misaligned with respect to the line of centers between nuclei, a condition described as “bond bending.” Such bending may be considered to represent the influence of factors other than Bent’s rule. In this section we examine the origin and characteristics of bond bending.

Cyclopropane

Angular strain and bond bending arise most familiarly in small-ring compounds, where the constraints of ring topology require acute bond angles that cannot be matched by any possible orthogonal sp^λ hybrids (Example 3.4). A well-known example is cyclopropane, with 60° C—C—C angles that must deviate by at least 15° along each C—C bond line from minimum-angle bond hybrids (90° , pure p). As recognized by Coulson and Moffitt,⁴¹ the actual C_3H_6 hybrids are closer to the normal $\sim sp^3$ hybrids of acyclic alkanes than to the pure-p hybrids of smallest interhybrid angle, and the bond bending is accordingly greater. Figure 3.21 shows the strained σ_{CC} NBO (left) and corresponding carbon bonding NHO (right) of C_3H_6 . The latter is found to be of $sp^{3.46}$ composition, severely bent by $\sim 24.3^\circ$ outside the line of nuclear centers, in good agreement with the Coulson–Moffitt picture. Owing to the strong bond “kinking,” the NBO bulges far outside the nominal C—C bond line, conferring significant non-cylindrical character to the bonding.

Hyperconjugative interactions (Section 3.4.2) are another factor leading to bond bending. Such interactions are associated with the “stereoelectronic” influence of more remote bonds or lone pairs, particularly those *anti* (trans) to the bond of

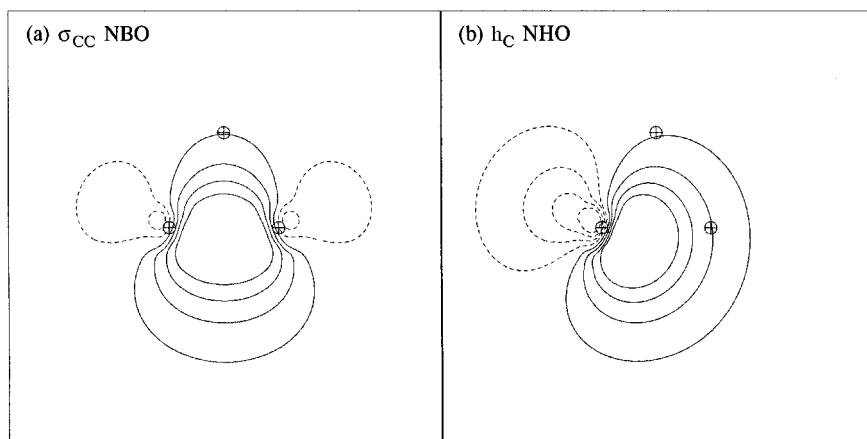


Figure 3.21 The bent C—C bond of cyclopropane, showing (a) the σ_{CC} NBO and (b) the h_C bonding hybrid ($sp^{3.46}$), which is oriented 24.3° outside the line of C—C centers.

interest, and thus can be distinguished from the inductive effects of directly bonded atoms that are described by Bent's rule. A characteristic of hyperconjugative interactions is their pronounced dependence on the relative orientation of the interacting bonds or lone pairs, the bond bending being largest when torsional motions bring the hyperconjugating groups into coplanar alignment. The physical origin of hyperconjugative interactions and the associated torsion–bend coupling will be further described in Section 3.4.2.

Fluoromethylamine

A simple example of hyperconjugative bond bending is provided by the fluoromethylamine molecule (CH_2FNH_2), which exhibits strong stereoelectronic influence of the amine lone pair on the vicinal C—F and C—H bonds of the fluoromethyl group. Figure 3.22 depicts the dependence of C—F, C—H, and C—H' bond bending ($\Delta\theta$) on the torsional angle ϕ (dihedral lp—N—C—F) which controls the orientation of the nitrogen lone pair with respect to C—F. It can be seen that the C—F bond is bent by $\sim 3.1^\circ$ when oriented coplanar to n_N ($\phi = 0^\circ$ or 180°), but the bending falls to less than 1° when these groups are in perpendicular orientation ($\phi = 90^\circ$). Similarly, each C—H bond is bent by $\sim 2.1^\circ$ as it comes into *anti* alignment with n_N (and again by about 0.8° in *syn* alignment), whereas the corresponding bending in the ground conformation is much smaller, $\sim 0.3^\circ$.

Hybrid following in ammonia and phosphine

We might expect that a general displacement from equilibrium nuclear geometry (such as that associated with a normal mode of vibration) could also lead to bond

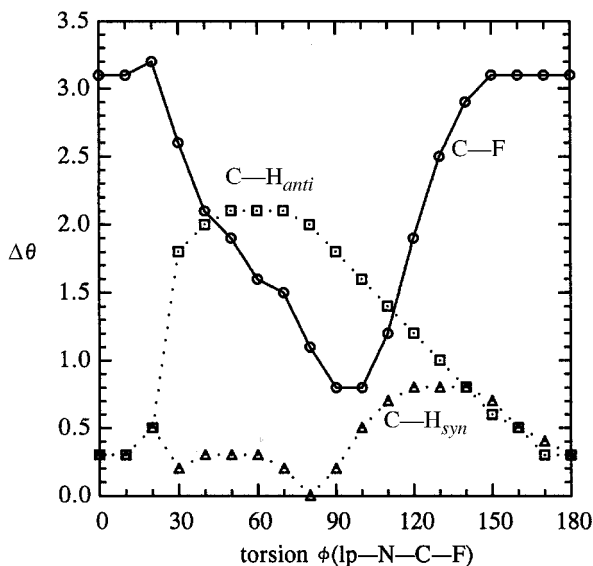


Figure 3.22 Bond bending, $\Delta\theta = \theta_{\text{nuclei}} - \theta_{\text{NHO}}$, in $\text{CH}_2\text{F}-\ddot{\text{N}}\text{H}_2$ for C—F (circles, solid line), C—H_{anti} (squares, dotted line), and C—H_{syn} (triangles, dotted line) bonds as the amine group is twisted from $\phi(\text{lp}-\text{N}-\text{C}-\text{F}) = 0^\circ$ to 180° (“lp” denotes the bisector of the H—N—H angle).

bending. However, Bent’s rule and Eq. (3.34) imply that nuclear geometry and hybrid directionality are bound together in such an intimate manner that changes of nuclear geometry can *cause*, as well as respond to, changes in hybrid geometry. Thus, the degree of bond bending (if any) induced by a change in nuclear geometry depends on how well the hybrid orbitals are able to “follow” the displaced nuclei.

As a specific example, let us consider the umbrella inversion vibration of NH_3 , which carries the molecule from pyramidal C_{3v} equilibrium geometry to the equivalent mirror image through a trigonal-planar D_{3h} transition state that is calculated as $4.1 \text{ kcal mol}^{-1}$ higher in energy. If θ_{nuclei} denotes the lp—N—H umbrella angle for the nuclei, and θ_{NHO} is the corresponding angle for the bonding hybrids, we can examine how well θ_{NHO} follows the nuclei as they move from equilibrium ($\theta_{\text{nuclei}} = 111.0^\circ$) to planar geometry ($\theta_{\text{nuclei}} = 90^\circ$) along the vibrational normal-mode coordinate. For comparison, we also examine the corresponding behavior for PH_3 , which has a much higher inversion barrier ($33.6 \text{ kcal mol}^{-1}$) and a more pyramidal umbrella equilibrium angle (122.7°). Figure 3.23 depicts the θ_{NHO} versus θ_{nuclei} behavior for NH_3 (circles, solid line) and PH_3 (squares, dotted line), compared with the idealized limit ($\theta_{\text{NHO}} = \theta_{\text{nuclei}}$, dashed line) of perfect orbital following.

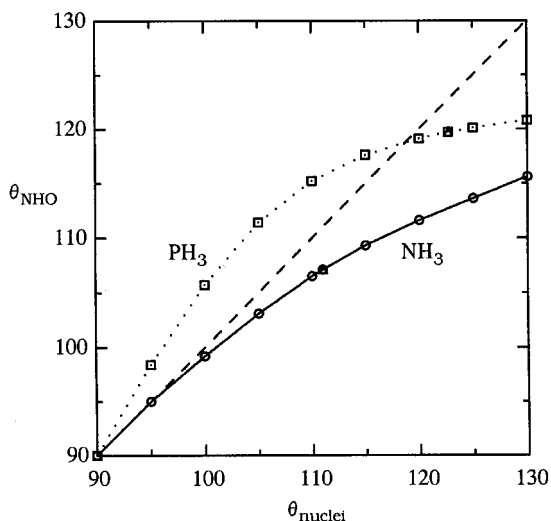


Figure 3.23 Bond bending in umbrella inversion vibration of NH_3 (circles, solid line) and PH_3 (squares, dotted line), comparing the lp—A—H umbrella angle for nuclei (θ_{nuclei}) and hybrids (θ_{NHO}). An inscribed triangle marks the equilibrium geometry for each molecule, and the dashed line marks the limit of perfect orbital following ($\theta_{\text{NHO}} = \theta_{\text{nuclei}}$).

Figure 3.23 shows that NH_3 and PH_3 exhibit quite different patterns of orbital following and bond bending along the inversion coordinate. Both species achieve idealized sp^2 hybridization and 120° hybrid angles at the planar transition state, $\theta_{\text{nuclei}} = 90^\circ$. However, as PH_3 begins to pyramidalize, the h_p hybrids first bend significantly *ahead* of the nuclei ($\theta_{\text{NHO}} > \theta_{\text{nuclei}}$), but later fall back into alignment with the nuclei near $\theta \simeq 120^\circ$ (close to equilibrium) and thereafter lag *behind* the nuclei ($\theta_{\text{NHO}} < \theta_{\text{nuclei}}$) at larger umbrella angles. In contrast, the NH_3 hybrids initially follow the nuclear motion quite closely, but fall increasingly behind the nuclei ($\theta_{\text{NHO}} < \theta_{\text{nuclei}}$) as the displacement increases, with the bond bending growing to $\sim 4^\circ$ at $\theta_{\text{nuclei}} = 111^\circ$ and $\sim 15^\circ$ at $\theta_{\text{nuclei}} = 130^\circ$. Therefore, as the inversion motion proceeds the hybrids of PH_3 must undergo significant bond bending ($\sim 7^\circ$) before coming into alignment with the nuclei in the planar transition state, whereas the hybrids of NH_3 adapt smoothly and monotonically to this transition. This pronounced difference in the ability of the bonding hybrids to accommodate to planarity apparently leads to a large (\sim eight-fold) increase in barrier height on going from NH_3 to PH_3 . Note that, in both species, the bond bending is seen to increase rapidly for pyramidalization angles much beyond the equilibrium value, showing that the hybrids are unable to accommodate to smaller H—A—H angles. Bond bending is therefore closely related to the energy changes associated with vibrational motion, as one expects intuitively.

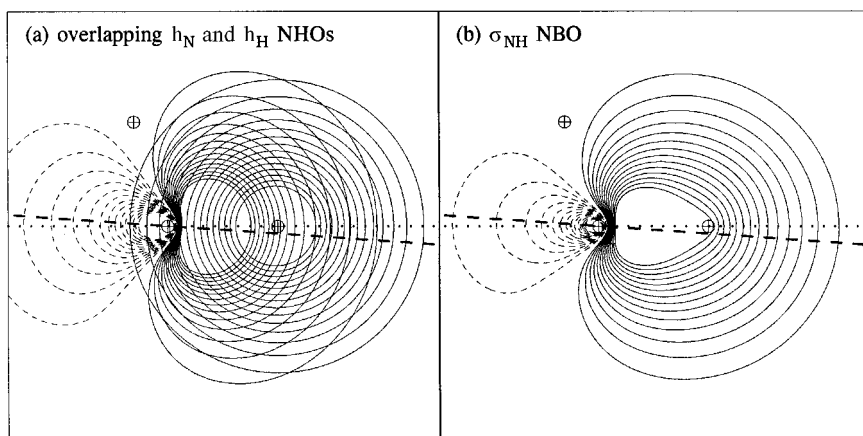


Figure 3.24 The bent N—H bond of NH_3 , showing (a) h_N and h_H NHOs and (b) the σ_{NH} NBO, with the bonding hybrid oriented 3.9° (dashed line) below the line of N—H centers (dotted line).

However, we note from Fig. 3.23 that the equilibrium geometries correspond to residual bond bending in both species, e.g., about 3.9° for NH_3 . To investigate the nature of this residual bending, we plot the contours of the overlapping h_N and h_H NHOs and the σ_{NH} NBO for the equilibrium geometry of NH_3 in greater detail in Fig. 3.24. For this figure we employ a finer grid spacing and larger range of contour values than usual in order to illustrate the inner structure of the bonding h_N hybrid near the position of the H nucleus (marked by a circled plus sign). To assist in visualizing the small degree of bending, we have also plotted a horizontal dotted line through the nuclear centers and a dashed line through the nitrogen nucleus tilted by 3.9° to mark the nominal direction of the h_N hybrid.

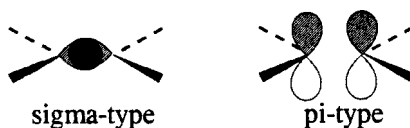
As shown in Fig. 3.24, the outer contours of the h_N NHO and σ_{NH} NBO exhibit the expected cylindrical symmetry about the nominal hybrid direction vector marked by the dashed line. However, the *inner* contours are increasingly directed toward the dotted line of nuclear centers. The lack of overall cylindrical symmetry is best seen in the NBO plot of Fig. 3.24(b), where it can be seen that the H nucleus sits accurately in the “pointy” inner contours which are closely aligned with the dotted line of nuclear centers rather than the dashed line of nominal hybrid direction. This example illustrates that the optimized NHOs are free to adopt complex non-cylindrical shapes in which the apparent “directionality” varies with distance from the nucleus. Thus, the 3.9° bending does not correspond to true misalignment of the hybrid and nuclear directions *at the actual bond distance*, but rather reflects the fact that inner hybrid contours are slightly *skewed* with respect to the nominal average “direction” attributed to the NHO. That is, the hybrid itself (rather than the bond) is slightly bent.

The above example indicates that small degrees of apparent bond bending may be rather endemic in the equilibrium geometries of acyclic molecules. Closer examination will often show that much of the apparent bending originates within the bond hybrid itself, rather than as a result of nuclear “mistakes” in finding the bonding angles of maximum hybrid overlap. Such complex non-cylindrical hybrid shape evidently cannot occur in a primitive minimal basis of *s* and *p* orbitals only, but must reflect the flexibility of polarized double- and triple-zeta basis sets to describe variable “inner” and “outer” directionality. In particular, it has long been recognized that polarized *d*- or *f*-orbital character is important in describing non-cylindrical bonding hybrids.⁴² Extensive computational experience has also shown that polarization basis functions are important for accurately describing inversion potentials.⁴³ Thus, the smaller details of the NHOs and NBOs depicted in Fig. 3.24 correspond to computational refinements that are known to be important for quantitative description of the vibrational potential energy surface, but lie outside the framework of simple Bent’s-rule-type description.

In summary, true angular strain and bond bending can arise from constraints of overall bonding topology and the steric or stereoelectronic influences of neighboring groups. However, apparent bond bending that involves no true angular strain can arise when the hybrids themselves are slightly curved. Such curvature of bonding hybrids might be pictured in terms of an *R*-dependent generalization of Bent’s rule, in which the effective relative electronegativities of central atom and ligand depend somewhat on their separation (this is consistent with the idea that relative bond polarization will change slightly with distance). Such finer details of bond bending, however interesting, lie outside the scope of the present work.

3.2.8 Electronegativity and polarity changes in *pi*-bonding

As predicted by elementary hybrid bonding theory, the multiple bonds of the chemist’s Lewis-structure diagram are usually found to correspond to two distinct types of NBOs: (1) sigma-type, having exact or approximate cylindrical symmetry about the bond axis (as discussed in Sections 3.2.5–3.2.7), and (2) pi-type, having a nodal mirror plane passing through the nuclei.⁴⁴



General relationships between bond polarity and atomic electronegativity, as developed in the two preceding sections for sigma-bonding, will now be extended to pi-bonding.

Table 3.11. Calculated bond lengths (R_{AC}), atomic charges (Q_C and Q_A), and pi-bond ionicity $i_{AC}^{(\pi)}$ for π_{AC} bonds of group 14–16 atoms A in unsaturated $CH_2=AH_n$ hydrides

Molecule	R_{AC} (Å)	Q_C (e)	Q_A (e)	$i_{AC}^{(\pi)}$
Group 14				
$CH_2=CH_2$	1.3288	-0.3667	-0.3667	0.0000
$CH_2=SiH_2$	1.7079	-1.0515	+0.9255	-0.2480
$CH_2=GeH_2$	1.7790	-0.9738	+0.7936	-0.2424
Group 15				
$CH_2=NH$	1.2673	-0.0233	-0.5869	+0.1506
$CH_2=PH$	1.6706	-0.7515	+0.4142	-0.0726
$CH_2=AsH$	1.7861	-0.7625	+0.4568	-0.0770
Group 16				
$CH_2=O$	1.2015	+0.2940	-0.4946	+0.3108
$CH_2=S$	1.6155	-0.4304	+0.0769	+0.1090
$CH_2=Se$	1.7557	-0.5127	+0.1493	+0.0824

Pi bonds and antibonds of group 14–16 hydrides

Analogously to the H atom for sigma-bonding (Section 3.2.5), we can choose the methylene group (CH_2) as the prototype for pi-bonding in group 14–16 hydrides of general formula $H_2C=AH_n$. Table 3.11 summarizes the bond lengths, atomic charges, and π_{CA} NBO ionicity parameters for pi bonds of the first three group members (cf. Table 3.8). Figure 3.25 displays the corresponding contour plots of pi bonds π_{CA} (left) and antibonds π_{CA}^* for all these species, illustrating horizontal and vertical trends in the periodic table.

Natural pi-electronegativity

To describe the polarity of pi-bonding, we can follow a path parallel to that which led to Eqs. (3.59)–(3.60) for sigma-bonding, using CH_2 as the common π -bonding partner. In this manner we are led to define the *pi-electronegativity* $x_A^{(\pi)}$ as being related to pi-bond ionicity $i_{AC}^{(\pi)}$ through the equation

$$i_{AC}^{(\pi)} = 1 - \exp[-a(x_A^{(\pi)} - x_C^{(\pi)})] \quad (3.76)$$

which is analogous to Eq. (3.59). The bond ionicity $i_{AC}^{(\pi)}$ is related to the π_{AC} polarization coefficients $c_A^{(\pi)}$ and $c_C^{(\pi)}$ in the usual way:

$$c_A^{(\pi)} = [(1 + i_{AC}^{(\pi)})/2]^{1/2} \quad (3.77a)$$

$$c_C^{(\pi)} = [(1 - i_{AC}^{(\pi)})/2]^{1/2} \quad (3.77b)$$

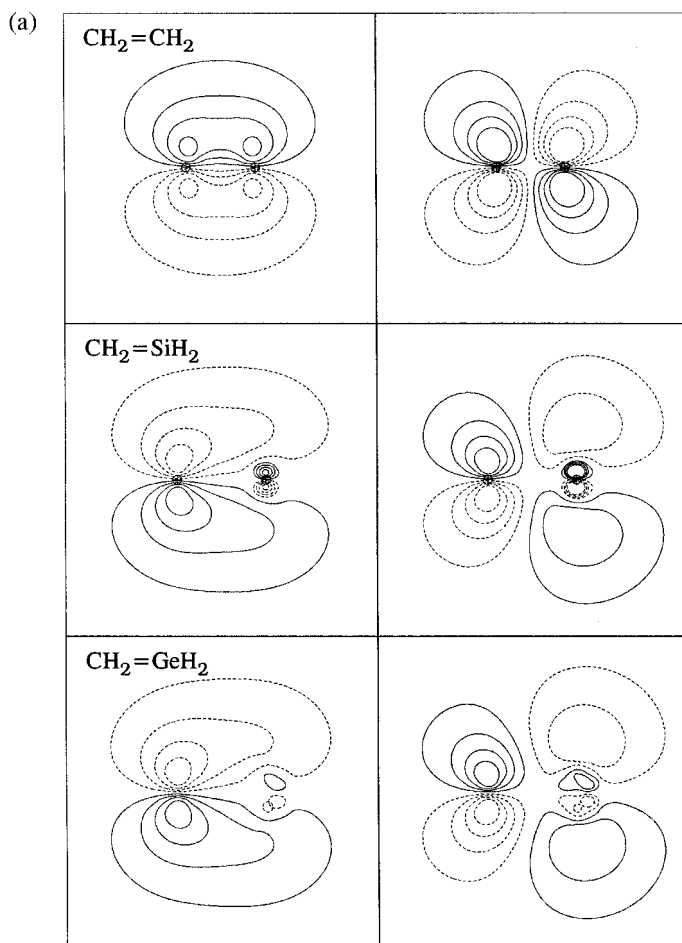


Figure 3.25 Pi-bond (π_{CA} , left) and antibond (π_{CA}^* , right) NBOs in unsaturated $\text{CH}_2=\text{AH}_n$ compounds. (a) Group 14 elements: C, Si, and Ge. (b) Group 15 elements: N, P, and As. (c) Group 16 elements: O, S, and Se.

We again choose the value of the exponential parameter in Eq. (3.76) to be $a = -0.45$ so that sigma- and pi-electronegativity scales have the same “units.” The specification of the scale is then completed by choosing the value of $x_{\text{A}}^{(\pi)}$ for a single atom. For this purpose it is convenient to assign to the carbon atom a *common* value of σ - and π -electronegativity,

$$x_{\text{C}}^{(\sigma)} = x_{\text{C}}^{(\pi)} = 2.60 \quad (3.78)$$

We then obtain the final expression for $x_{\text{A}}^{(\pi)}$ as

$$x_{\text{A}}^{(\pi)} = 2.60 - \ln(1 - i_{\text{AC}}^{(\pi)})/0.45 \quad (3.79)$$

for given bond ionicities from Table 3.11.

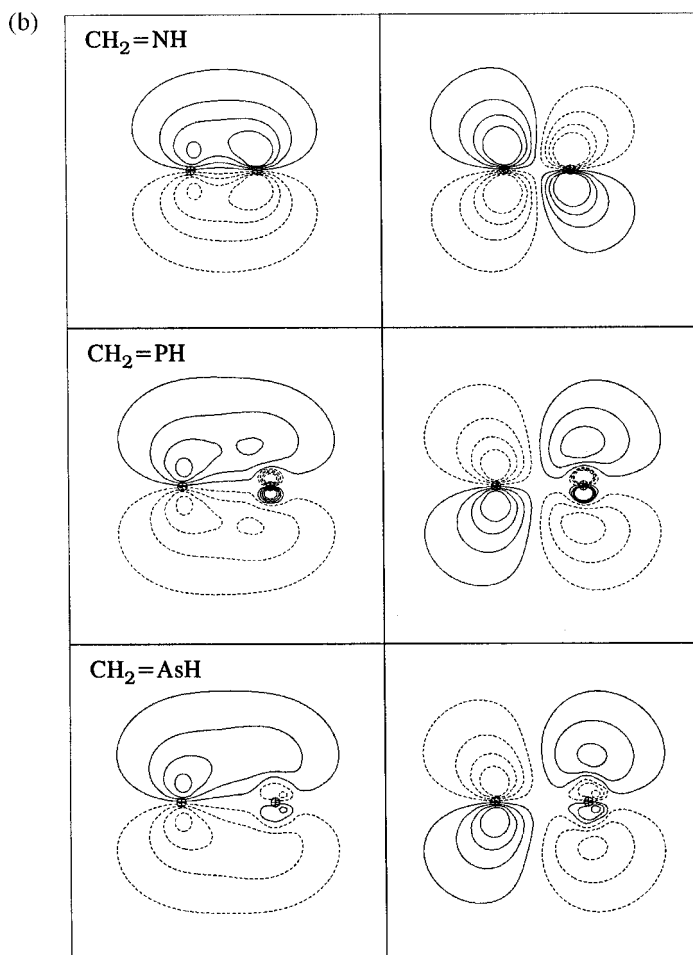


Figure 3.25 (Cont.)

Equation (3.79) leads to the natural π -electronegativity values displayed in Table 3.12. These values are compared with corresponding σ -electronegativities of group 14–16 elements in Fig. 3.26.

Figure 3.26 shows that the π -electronegativity exhibits horizontal and vertical trends similar to those for σ -electronegativity. However, the range of $x_A^{(\pi)}$ values is seen to be significantly smaller than that of $x_A^{(\sigma)}$ values, corresponding to the fact that π_{AB} bonds are usually less polarized than σ_{AB} bonds. As illustrated in Fig. 3.25, the horizontal and vertical periodic variations in pi-bond polarity correspond to rather dramatic variations in the relative lobe sizes of π and π^* orbitals; cf., for example, the $\pi_{\text{C}}-\text{Ge}^*$ antibond of Fig. 3.25(a) with the $\pi_{\text{C}}-\text{O}^*$ antibond

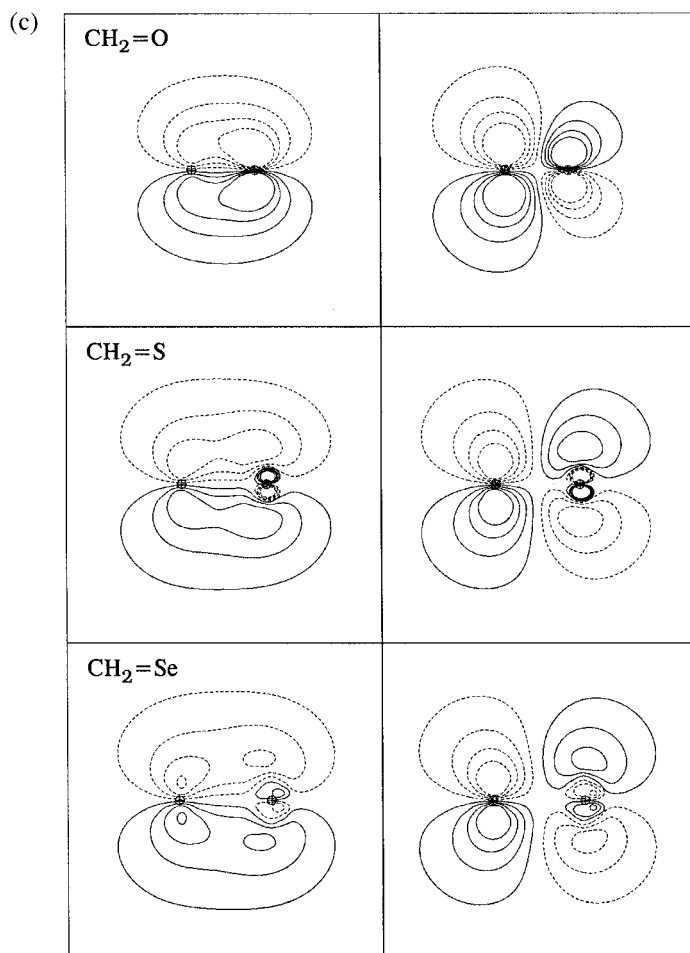


Figure 3.25 (Cont.)

of Fig. 3.25(c). Thus, these variations in pi-electronegativity are expected to correspond to chemically important structural and reactivity differences.

The natural π -electronegativities of Table 3.11 are useful for estimating the bond polarities of pi bonds, as illustrated in the following example.

Table 3.12. *Pi-type natural electronegativities $x_A^{(\pi)}$ of group 14–16 elements*

	C	Si	Ge	N	P	As	O	S	Se
$x_A^{(\pi)}$	[2.60]	2.11	2.12	2.85	2.44	2.43	3.43	2.86	2.79

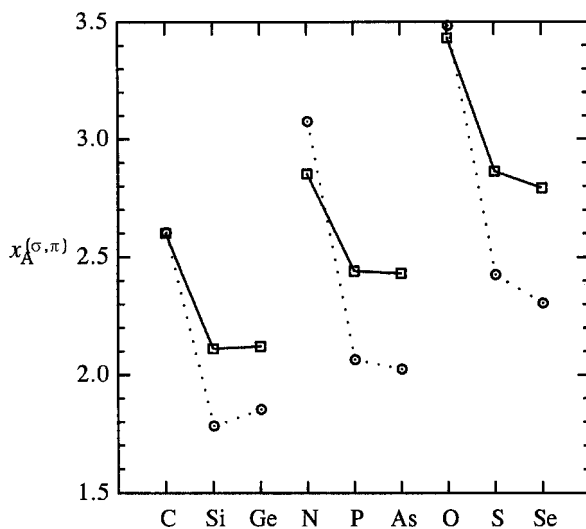


Figure 3.26 Natural electronegativities of group 14–16 elements, comparing pi-type $x_A^{(\pi)}$ (squares, solid line) and sigma-type $x_A^{(\sigma)}$ (circles, dotted line) values. Note that sigma- and pi-electronegativities are *defined* to be equal for C.

Example 3.10

Exercise: Estimate the polarization coefficients of the sigma and pi bonds of $\text{N}\equiv\text{As}$.

Solution: From Table 3.11 the pi-electronegativities of N and As are

$$\begin{aligned}x_N^{(\pi)} &= 2.85 \\x_{\text{As}}^{(\pi)} &= 2.43\end{aligned}$$

and Eq. (3.76) gives

$$i_{\text{NAs}}^{(\pi)} = 1 - \exp[-0.45(2.85 - 2.43)] = 0.172$$

From Eqs. (3.77) we obtain

$$\begin{aligned}c_N^{(\pi)} &= 0.766 \\c_{\text{As}}^{(\pi)} &= 0.643\end{aligned}$$

These estimates compare reasonably with the calculated polarization coefficients in the actual π_{NAs} NBOs of $\text{N}\equiv\text{As}$,

$$\pi_{\text{NAs}} = 0.78_6(\text{p})_N + 0.61_8(\text{p})_{\text{As}}$$

A similar calculation with the sigma-electronegativities of Table 3.9 ($x_N^{(\sigma)} = 3.07$, $x_{\text{As}}^{(\sigma)}$)

= 2.02) gives $i_{\text{NAs}}^{(\sigma)} = 0.377$, which leads to estimated $\sigma_{\text{N}-\text{As}}$ polarization coefficients

$$c_{\text{N}}^{(\sigma)} = 0.83_0 \quad (\text{cf. } 0.82_7)$$

$$c_{\text{As}}^{(\sigma)} = 0.55_8 \quad (\text{cf. } 0.56_2)$$

comparing favorably with the actual NBO values (in parentheses). As these estimates indicate, the sigma bond is found to be polarized significantly more strongly than the pi bond.

What is the nature of pi-electronegativity, and why do its values differ from “ordinary” (sigma) electronegativity? Like its sigma counterpart, the pi-electronegativity $x_{\text{A}}^{(\pi)}$ is a measure of the propensity of A to gain and hold electrons in bonding, and there is no intrinsic reason why this propensity should be equivalent in sigma- and pi-bonding. In fact, the tendency to form pi bonds is itself a distinctive characteristic of group 14–16 elements, and therefore would be expected to be a distinguishing aspect of their “electronegativity.”

Is the natural electronegativity an *atomic* or an *orbital* property? By referring the values of $x_{\text{A}}^{(\sigma,\pi)}$ to prototype sigma- or pi-bonding partners and optimized ground-state geometries, we have reduced the entries of Tables 3.9 and 3.12, as nearly as possible, to generic “atomic” values. However, it is apparent from the way natural electronegativity was defined that it is intrinsically an *orbital* property, related to the bond polarity of a particular sigma- or pi-type NBO. Thus, one can easily generalize Eqs. (3.59) and (3.76) to define *effective* electronegativities for different orbitals, changes in geometry, changes of ionic or electronic state, and so forth. The extent to which the electronegativity concept should be generalized is perhaps a matter of scientific taste. However, we believe that it is heuristically useful to refer to changes in effective electronegativity resulting from changes in hybridization, geometry, attached substituent groups, and so forth (e.g., an sp^2 -hybridized carbon atom is intrinsically more electronegative than an sp^3 -hybridized carbon atom). Generalizations of Eqs. (3.59) and (3.76) make it possible to quantify such “generalized electronegativity” values for a variety of chemical influences, as well as extend the intrinsic atomic values of Tables 3.9 and 3.12 to other atoms or types of bonding.

3.2.9 Homonuclear diatomic molecules

MO and NBO Aufbau

The first-row homonuclear diatomic molecules A_2 of main-group elements ($\text{A} = \text{B}, \text{C}, \text{N}, \text{O}, \text{F}$) exhibit a well-known diversity of ground-state multiplicities, bond lengths, and bond energies. Calculated potential-energy curves for low-lying singlet and triplet states of these species are pictured in Fig. 3.27 and summarized in Table 3.13 (with comparison experimental values). Because these homonuclear

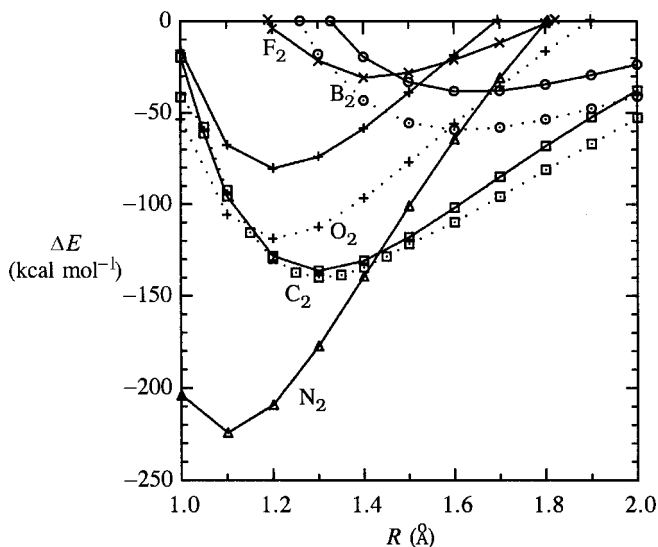


Figure 3.27 Singlet (solid line) and (if lower) triplet (dotted line) potential-energy curves for first-row homonuclear diatomics: B (circles), C (squares), N (triangles), O (plus signs), and F (crosses); cf. Table 3.13.

species eliminate the complicating effects of electronegativity and polarity differences, they provide an important testing ground for concepts of covalent bonding, including the distinction between delocalized MO and localized VB-like descriptions.

Textbook discussions of homonuclear diatomic molecules are commonly based on the familiar type of MO energy diagram shown in Fig. 3.28, which underlies the standard MO *Aufbau* procedure for constructing many-electron molecular configurations (which is analogous to the well-known procedure for atoms). Figure 3.28 purports to represent the energies and compositions of available MOs, which are

Table 3.13. *Calculated spin multiplicity, bond length R_e , and dissociation energy D_e of first-row homonuclear diatomic molecules, with comparison experimental values^a in parentheses*

A_2	State	R_e (Å)	D_e (kcal mol ⁻¹)
B ₂	Triplet	1.6160 (1.59)	59.49 (70)
C ₂	Triplet	1.3060 (1.24)	140.30 (144)
N ₂	Singlet	1.0956 (1.10)	224.80 (225)
O ₂	Triplet	1.2058 (1.21)	119.65 (118)
F ₂	Singlet	1.4083 (1.41)	31.77 (37)

^a K. P. Huber and G. Herzberg, *Molecular Spectra and Molecular Structure. IV. Constants of Diatomic Molecules*. (New York, Van Nostrand, 1979).

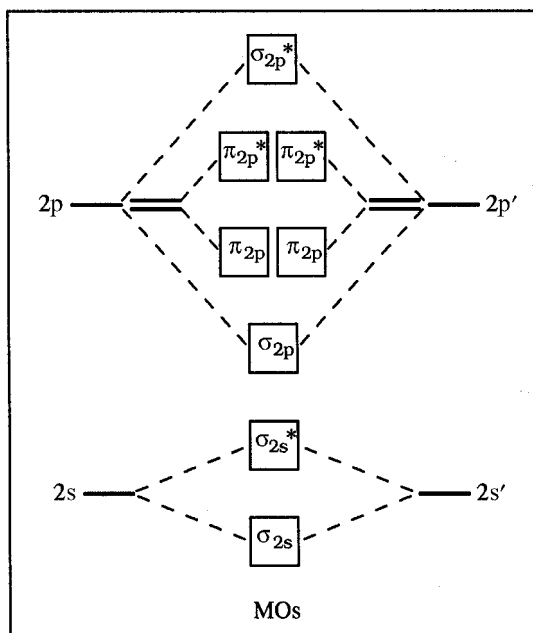


Figure 3.28 A schematic energy diagram for valence MOs of homonuclear diatomic molecules (following Mulliken). The order of σ_{2p} and π_{2p} MOs should be reversed for 14 or fewer electrons.

labeled (in spectroscopic separated-atom notation) as σ_{2s} , σ_{2s}^* , σ_{2p} , ... to designate the in-phase or out-of-phase combinations of degenerate AOs which compose the MO,

$$\sigma_{2s} = 2^{-1/2}(2s + 2s') \quad (3.80a)$$

$$\sigma_{2s}^* = 2^{-1/2}(2s - 2s') \quad (3.80b)$$

and so forth. The available levels are sequentially filled, taking account of the Pauli occupancy restriction and the “Hund’s-rule” tendency of electron spins to remain parallel (and thus avoid double occupancy) in the case of degenerate unfilled orbitals. By adjusting the relative order of MOs as necessary, one can rationalize the fact that certain diatomics (e.g., C_2 and O_2) display triplet spin multiplicities and paramagnetic behavior, whereas others (e.g., N_2 and F_2) display the diamagnetism characteristic of a fully spin-paired ground singlet state. This rationalization is commonly regarded as a notable advantage of the delocalized MO viewpoint over the localized valence-bond viewpoint.

Although the spectroscopic “ σ_{2s} , σ_{2p} , ...” labels are asymptotically accurate as $R \rightarrow \infty$, these labels are seriously misleading in the near-equilibrium region. In N_2 , for example, the bonding molecular orbital (ϕ_3) that most nearly corresponds

to the “ σ_{2s} ” label has the actual LCAO composition near R_c

$$\phi_3 \simeq 0.579(2s) + 0.579(2s') - 0.384(2p_z) + 0.384(2p_z') + \dots \quad (3.81a)$$

and thus corresponds to the strongly mixed description

$$\phi_3 = 0.579\sigma_{2s} + 0.384\sigma_{2p} + \dots \quad (3.81b)$$

Similar mixing, strongly dependent on R and varying from species to species, is found for all the homonuclear diatomics. Because of this mixing, the actual MO splitting pattern often has little relationship to the idealized diagram shown in Fig. 3.28. Rationalizations of the MO splitting patterns and occupancies that are based on this idealized diagram therefore have a somewhat unsatisfactory and ad-hoc character.

Although the most naive form of valence-bond and Lewis-structure theory would not predict the paramagnetism of O_2 , the “VB-like” NBO donor–acceptor perspective allows us to develop an alternative localized picture of general wavefunctions, including those of MO type. Let us therefore seek to develop a general NBO-based configurational picture of homonuclear diatomics to complement the usual MO description.

We first note that a localized NBO description is an equally valid way to view a delocalized molecular-orbital wavefunction. In the case of N_2 , for example, ψ_{MO} is expressed in terms of doubly occupied MOs ϕ_i , $i = 1-7$,

$$\psi_{MO} = (\phi_1)^2(\phi_2)^2(\phi_3)^2(\phi_4)^2(\phi_5)^2(\phi_6)^2(\phi_7)^2 \quad (3.82a)$$

but the same wavefunction is expressed to high accuracy in localized NBO terms as

$$\psi_{MO} = (K_N)^{2.000}(K_{N'})^{2.000}(\sigma_{NN'})^{2.000}(\pi_{NN'}^x)^{2.000}(\pi_{NN'}^y)^{2.000}(\pi_N)^{1.993}(\pi_{N'})^{1.993} \quad (3.82b)$$

i.e., with 99.89% accuracy of the idealized natural Lewis structure. Thus, the NBO description (3.82b) of the wavefunction and density is practically equivalent (in the sense of Fock’s theorem) to the exact MO expression (3.82a), and the MOs themselves appear less strongly mixed in terms of NBOs.⁴⁵ Similarly high accuracy of the natural Lewis-structure representation is found for the other diatomic species. Thus, no significant loss of accuracy will be incurred by describing the results of Fig. 3.27 and Table 3.13 in localized-NBO terms.

Let us now sketch the general LCAO-NBO formation of diatomic NBOs from their constituent (N)AOs, employing the donor–acceptor and hybridization concepts developed in previous sections. If we visualize the starting atomic configurations

in terms of valence s , p_x , p_y , p_z orbitals, general hybridization principles (Section 3.2.3) determine that the s and p_z AOs on each atom will mix to form a p -rich bonding hybrid h_σ and s -rich nonbonding hybrid h_n along the axis of incipient bond formation,

$$s, p_x, p_y, p_z \rightarrow h_n, h_\sigma, p_x, p_y \quad (3.83)$$

leaving unhybridized off-axis p_x and p_y orbitals on each center. As usual, the hybrids h_σ and h_n can be expressed in standard sp^λ notation as

$$h_\sigma = sp^{\lambda_\sigma} \quad (3.84a)$$

$$h_n = sp^{\lambda_n} \quad (3.84b)$$

where, according to the sum rule (3.37a) for this case,

$$\lambda_\sigma \lambda_n = 1 \quad (3.85)$$

Thus, we can choose the hybridization $\lambda = \lambda_\sigma$ as the single independent parameter in this case, with the hybridization of the nonbonding hybrids determined from Eq. (3.85).

Example 3.11

Exercise: Derive Eq. (3.85).

Solution: For the four hybrids (3.83) of the present case,

$$\lambda_1 = \lambda_n, \quad \lambda_2 = \lambda_\sigma, \quad \lambda_3 = \infty, \quad \lambda_4 = \infty$$

the sum rule (3.37a) becomes

$$\begin{aligned} 1 &= \frac{1}{1 + \lambda_n} + \frac{1}{1 + \lambda_\sigma} + 0 + 0 \\ &= \frac{2 + \lambda_\sigma + \lambda_n}{1 + \lambda_\sigma + \lambda_n + \lambda_\sigma \lambda_n} \end{aligned}$$

The solution of this equation is Eq. (3.85).

The hybridization parameter λ can be estimated at each R by expressions such as (3.11b), which in turn are related to visual plots of the s - p_z ' overlap. A procedure for numerically estimating λ will be given at the end of this section. For present purposes, we need only recognize from the percentage s characters that the relative energies of the starting atomic hybrids satisfy

$$\epsilon(h_n) \ll \epsilon(h_\sigma) < \epsilon(p_x) = \epsilon(p_y) \quad (3.86)$$

Table 3.14. *Symmetry-allowed donor–acceptor interactions and NBO labels for homonuclear diatomics*

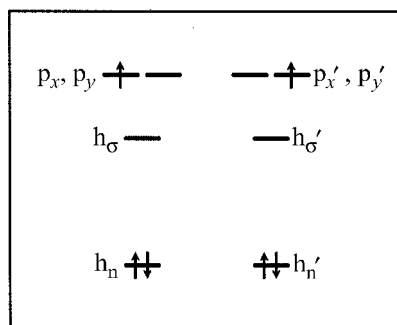
Donor	Acceptor	NBO type	Symbol
p_x	p_x^*	π_x	$\text{A} \curvearrowright \text{A}$
p_y	p_y^*	π_y	$\text{A} \smile \text{A}$
h_σ	h_σ^*	σ	$\text{A} - \text{A}$
h_n (2)	h_σ^* (2)	$\nu(\bar{\nu})$	$\text{A} \rightleftharpoons \text{A}$
$[h_n]$	h_n^*	σ	

These atomic hybrids are the starting point for discussing the donor–acceptor interactions and two-center NBO formation at each R .

The possible donor–acceptor interactions among the valence hybrids are constrained by diatomic symmetry to the five possible combinations shown in Table 3.14. For simplicity, we shall temporarily suppress the subscript atoms in the NBO symbols (which are now simply indicated as σ , π_x , ...). We also introduce a special typographic convention to denote each type of NBO (curved bonds for π_x and π_y , opposed arrows for complementary ν and $\bar{\nu}$, and so forth), as shown in Table 3.14. (The corresponding typographic convention for nonbonded NBOs will consist of a short “bar” on the atomic symbol, $\bar{\text{A}}$ for h_n , $\bar{\text{A}}$ for p_x , and $\underline{\text{A}}$ for p_y .) We also employ the convention of attaching an asterisk (*) to denote an unfilled orbital, i.e., an orbital that is formally serving as an acceptor in a donor–acceptor interaction (the star says “I’m empty”). Thus, the notation $p_x \rightarrow p_x^{*'}$ denotes an interaction from a filled p_x orbital on the first atom to an unfilled p_x' on the second atom.⁴⁶

The first three entries of Table 3.14 correspond to formation of conventional pi and sigma NBOs. The fourth ($h_n \rightarrow h_\sigma^*$, occurring in complementary pairs) corresponds to formation of asymmetric nu bonds (ν , $\bar{\nu}$), as previously discussed in Section 3.2.6 for N_2^+ . (The fifth $[h_n \rightarrow h_n^*]$ cannot occur in the present series, because h_n is never an unfilled acceptor orbital [if h_n' is occupied] in neutral homonuclear diatomics.)

What are the available donor and acceptor NHOs and resulting bond types in each diatomic species? Let us first consider B_2 as an illustrative example. Figure 3.29 exhibits the expected electronic configuration of triplet B_2 in the near- R_e region, showing the ordered NHO energy levels (3.86) and the electrons on each B atom (primed or unprimed). (The systematic *Aufbau* procedure used to determine the NHO bonding configuration of B_2 and other species will be described below.)

Figure 3.29 The 3B_2 bonding configuration.

From Fig. 3.2a and Table 3.14 it can be seen that the only allowed donor–acceptor interactions in the α set of B_2 are



as denoted by $\mathbf{B} \Leftarrow \mathbf{B}$. Similarly, in the β set the allowed interactions are



as denoted by $\mathbf{B} \Rightarrow \mathbf{B}$. The composite NBO configuration from (3.87) and (3.88) is therefore



These results for B_2 are shown as the first row of Table 3.15, which summarizes the expected NBO configurations for the entire series of first-row homonuclear diatomics.

In order to derive the remaining entries of Table 3.15, it suffices to have the starting NHO configuration of each diatomic species. Figure 3.30 summarizes these expected “promoted” bonding configurations, as shown in the right-hand panels. (For example, the upper right-hand panel of Fig. 3.30 is equivalent to Fig. 3.29 for B_2 .) By employing the NHO configurations of Fig. 3.30 in conjunction with Table 3.14 (following the B_2 example given above) one can readily derive the remaining

Table 3.15. Valence-shell NBO configurations of first-row homonuclear diatomics

	α NBOs	β NBOs	Composite configuration(s)
3B_2	$\nu\bar{\nu}\pi_x\pi_y$	$\nu\bar{\nu}$	$(\nu)^2(\bar{\nu})^2(\pi_x)^\dagger(\pi_y)^\dagger$
1C_2	$\sigma nn'/\pi_x$	$\sigma nn'/\pi_x$	$(\sigma)^2(n)^2(n')^2(\pi_x)^2$
3C_2	$\nu\bar{\nu}\pi_x\pi_y$	$\nu\bar{\nu}\pi_x\pi_y$	$(\nu)^2(\bar{\nu})^2(\pi_x)^2(\pi_y)^2$
1N_2	$\sigma nn'/\pi_x\pi_y$	$\sigma nn'$	$(\sigma)^2(n)^2(n')^2(\pi_x)^\dagger(\pi_y)^\dagger$
3O_2	$\sigma nn'/\pi_x\pi_y$	$\sigma nn'\pi_x\pi_y$	$(\sigma)^2(n)^2(n')^2(\pi_x)^2(\pi_y)^2$
1F_2	$\sigma nn'/\pi_x\pi_y\pi_x^*\pi_y^*$	$\sigma nn'/\pi_x\pi_y$	$(\sigma)^2(n)^2(n')^2(\pi_x)^2(\pi_x^*)^\dagger(\pi_y^*)^\dagger$
	$nn'\sigma\pi_x\pi_y\pi_x^*\pi_y^*$	$nn'\sigma\pi_x\pi_y\pi_x^*\pi_y^*$	$(n)^2(n')^2(\sigma)^2(p_x)^2(p_y)^2(p_x')^2(p_y')^2$

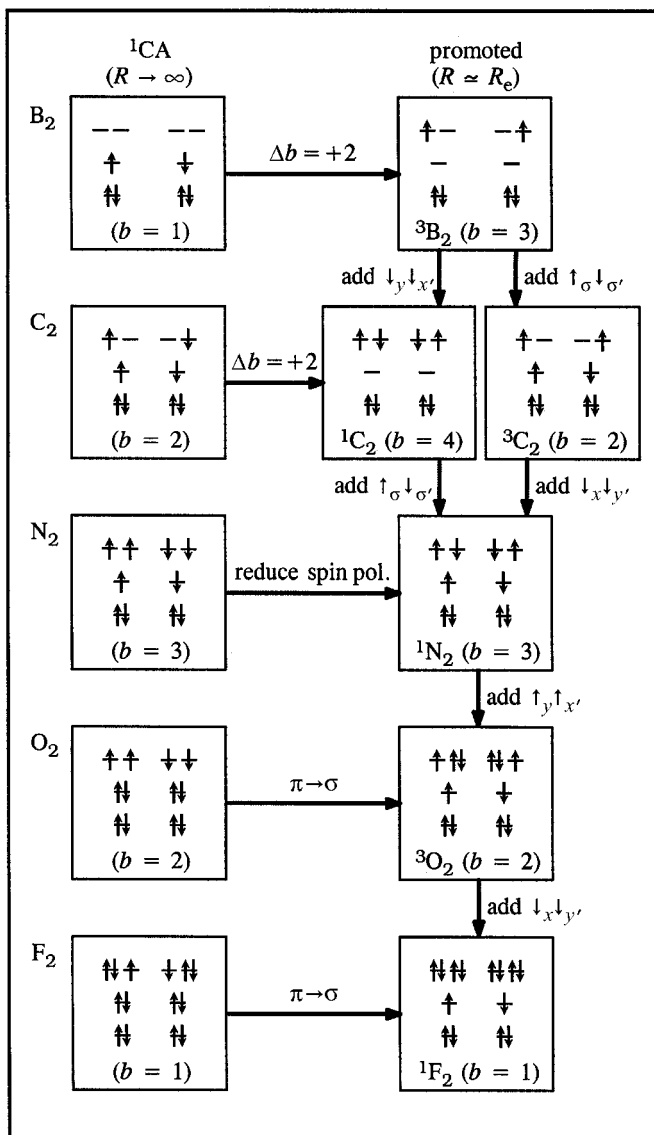


Figure 3.30 The NBO *Aufbau* diagram for first-row homonuclear diatomics, showing expected NHO configurations (right-hand panels) for each species.

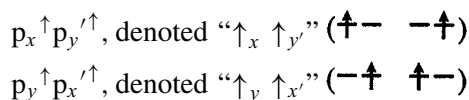
NBO configurations of Table 3.15. Thus, the remaining problem is to assign the preferred NHO configuration of each species, as shown in Fig. 3.30.

Let us now describe the systematic NBO *Aufbau* principles for constructing Fig. 3.30. We formally state these principles as follows.

Molecular NBO Aufbau principles

- I. The preferred configuration is that which achieves the maximum number and strength of bonds, with $\sigma > \pi > \nu$ relative strengths.
- II. The molecular version of Hund's rule: in order to minimize electron repulsions in π -bonding, each added pair of electrons in the degenerate p manifold should be assigned
 - (a) in parallel spin states,
 - (b) in perpendicular spatial planes, and
 - (c) on opposite atoms.
- III. All else being equal, the preferred configuration is that which minimizes the spin polarization (spin-charge) at each atom.

Principle I is rather self-evident, because formation of chemical bonds is the driving force for overall energy lowering. Principle II implies that an added pair of π electrons will prefer to be in configurations such as, for an α pair,



(rather than $\uparrow_x \uparrow_{x'}$, etc.) and analogously for spin β . The physical explanation of IIa–c is again rather evident, being similar to the standard rationalizations of Hund's rule.⁴⁷ Principle III is more subtle, expressing a type of “electroneutrality principle” at the *spin*-charge level. However, this principle is invoked in only a single instance (for N_2 ; see below) and might be seen as a consequence of Principles I and II by following the alternative flowchart path in Fig. 3.30, as will be described.

To construct Fig. 3.30, we first envision an idealized “singlet complementary atom” configuration (denoted 1CA), as shown in the left-hand panels. The 1CA configuration is formed by taking the standard atomic configuration of each atom and “rotating” the second (primed) atom to achieve maximum bonding interactions, where “rotation” involves both spin space (interchanging \uparrow and \downarrow spin) and Cartesian space (interchanging p_x and p_y). This 1CA configuration might be envisioned as the arrangement that maximizes the opportunities for molecular bonding (Principle I), but within the unpromoted configuration that is dictated by Hund's rule for isolated atoms. The formal bond order b of each such configuration is shown in parentheses at the bottom of the panel, and is consistent with the symmetry restrictions of Table 3.14.

As R diminishes into the near-equilibrium region, Principles I–III dictate that the atomic NHO occupancy patterns will be promoted to more favorable bonding

configurations, as shown in the right-hand panels of Fig. 3.30. The formal bond order b of each promoted configuration is again shown in parentheses at the bottom of the panel, alongside the diatomic configurational label of overall singlet or triplet spin symmetry. Let us now examine how Principles I–III dictate the change from ${}^1\text{CA}$ to a promoted configuration (horizontal flowchart arrows) or by two-electron *Aufbau* from one promoted configuration to another (vertical flowchart arrows).

Diboron

The single-bonded ${}^1\text{CA}$ configuration can be improved for bonding by promoting the two h_σ electrons into the degenerate p_x, p_y manifold⁴⁸ in the triplet ($\uparrow_x \uparrow_y$) pattern favored by Principle II. The resulting ${}^3\text{B}_2$ configuration is formally *triple-bonded* (two ν -bonds and two half- π -bonds; cf. Table 3.15) and thus corresponds to a net increase in bond order $\Delta b = +2$. We therefore expect B_2 to be a paramagnetic triplet species with overall NBO configuration (3.89).

The configurational description (3.89) applies over a wide range of R values near equilibrium. However, in the β spin set beyond $R > 2 \text{ \AA}$ the ν and $\bar{\nu}$ bonds “break” to give the nonbonded $\text{B}|\text{B}| \beta$ configuration. Similarly, at much shorter distances $R < 1.2 \text{ \AA}$, the ν and $\bar{\nu}$ are replaced by full σ and π bonds to give the $\text{B}=\text{B} \beta$ configuration. (Similar effects occur in the α spin set at slightly greater distances from R_e .) Thus, the curious ν and $\bar{\nu}$ bonds are seen to be a manifestation of long-range complementary donor–acceptor interactions (partially ionic) that will eventually be replaced by covalent σ and π bonds at shorter range. This behavior is analogous to the short-range ionic–covalent transition discussed in Sections 2.5 (for ionic bonding) and 3.2.2 (for covalent bonding).

Dicarbon

The low-lying states of C_2 have very complex character that is not well described in the single-configuration picture. C_2 was long thought to be a ground-state triplet, but in 1963 the singlet spin state was established to lie slightly lower in energy (by about 2 kcal mol^{-1} !).⁴⁹ Although our goal is to give the best single-configuration description of the bonding, it should be emphasized that such a description is fundamentally less adequate for C_2 than for other homonuclear diatomics.

(Severe computational problems are encountered in describing singlet and triplet C_2 at the single-configuration level [B3LYP/6-311++G**] employed throughout this work. The “default” MOs obtained by the standard self-consistent-field procedure are fairly ordinary, well described by the NBO Lewis-structure picture, but there is a distinct change in the character of the ${}^1\text{C}_2$ configuration near 1.2 \AA , as shown in the two entries of Table 3.15. A more serious complication is that the default configurations prove to be numerically unstable with respect to lower-energy [“stable”] solutions that are shown in Fig. 3.27 and Table 3.13. The stable

solutions incorrectly predict the triplet state to be the ground state and lead to an unusually large error [$\sim 0.07 \text{ \AA}$] for the equilibrium bond length. Moreover, the stable “singlet” solution is found to manifest unphysical spin contamination, which is indicative of the need for higher-level configuration-interaction treatment.⁵⁰ Still another problem is that the lower-energy stable solutions exhibit strange symmetry breaking and are poorly described by NBO configurations. Thus, for the sake of simplicity the present qualitative description will be based on the default B3LYP/6-311++G** configurations for both spin states [using, rather arbitrarily, the second 1C_2 configuration in Table 3.15], but it should be remembered that this description is fundamentally inadequate to describe the actual 1C_2 and 3C_2 wavefunctions.)

Figure 3.30 shows the near-degenerate promoted configurations for both singlet and triplet C_2 . From the starting double-bonded 1CA configuration, the bond order can be increased to *four* by promotion of two singlet-coupled electrons from h_σ to the degenerate p_x, p_y manifold. This promotion allows three donor–acceptor interactions in each spin set,



in effect replacing one sigma bond by two nu bonds and an additional pi bond ($\Delta b = +2$), which is strongly favored by Principle I. Alternatively, the promoted 1C_2 configuration can be seen as the result of adding a $\downarrow_y \downarrow_{x'}$ π -electron pair (consistently with Principle II) to the 3B_2 configuration. The promoted 3C_2 configuration can similarly be seen as the result of adding a $\uparrow_\sigma \downarrow_{\sigma'}$ σ -electron pair to the promoted 3B_2 configuration. The latter alternative replaces two weak nu bonds by a single sigma bond and thus results in formal bond order $b = 2$. Compared with the starting 1CA configuration, this gives no net change in bond order but serves to reduce spin polarization (Principle III).

Which of the two promoted configurations will be preferred for C_2 is unknown, and neither is truly a satisfactory description of the system. However, either configuration can be used to extend the *Aufbau* chain to larger diatomics in the series.

Dinitrogen

Two nitrogen atoms in their ground s^2p^3 quartet configuration would lead to the spin-polarized 1CA configuration shown in the left-hand panel of Fig. 3.30. Principle III then leads to the promoted 1N_2 configuration shown in the right-hand panel.

Alternatively, the promoted 1N_2 configuration is obtained by two-electron *Aufbau* from C_2 if one adds (a) two sigma electrons ($\uparrow_\sigma \downarrow_{\sigma'}$) to 1C_2 , or (b) two

pi electrons ($\downarrow_x\downarrow_{y'}$) to 3C_2 . In other words, starting from the optimal promoted 3B_2 configuration, the same final 1N_2 configuration is obtained by adding a sigma pair ($\uparrow_\sigma\downarrow_{\sigma'}$) and pi pair ($\downarrow_x\downarrow_{y'}$) in either order, passing in one case (first $\downarrow_x\downarrow_{y'}$, then $\uparrow_\sigma\downarrow_{\sigma'}$) through 1C_2 and in the other (first $\uparrow_\sigma\downarrow_{\sigma'}$, then $\downarrow_x\downarrow_{y'}$) through 3C_2 . Thus, the result for N_2 and the remainder of the *Aufbau* sequence is unaffected by uncertainties in assigning the C_2 configuration.

The 1N_2 NHO configuration of Fig. 3.30 leads to three allowed donor–acceptor interactions in each spin set,



corresponding to the standard $\text{||}\overline{\text{N}}\overline{\text{N}}\text{||}$ Lewis structures shown in Table 3.15. This simple NBO configurational picture is extremely stable and prevails over the entire range of the potential curve in Fig. 3.27.

Dioxygen

When the next two electrons are added to the optimal 1N_2 configuration of Fig. 3.30, they perforce quench two of the six donor–acceptor interactions of that configuration. It is clearly advantageous to preserve the strong sigma bond (by keeping h_σ and h_{σ}' half-filled) rather than a weaker pi bond (Principle I). The two additional electrons of O_2 must therefore be added to the p manifold, and Principle II dictates that they be added in $\uparrow_x\uparrow_{y'}$ fashion (parallel spins, perpendicular planes, opposite atoms) to give the uniquely preferred 3O_2 configuration shown in Fig. 3.30.

Alternatively, starting from the 1CA configuration, the promoted 3O_2 configuration can be viewed as the consequence of replacing a pi bond by a sigma bond, which is consistent with Principle I.

The three allowed donor–acceptor interactions of the β spin set are similar to (3.91a)–(3.91c), leading to $\text{||}\overline{\text{O}}\overline{\text{O}}\text{||}$, while the single remaining donor–acceptor interaction of the α set is



leading to $\text{||}\overline{\text{O}}-\overline{\text{O}}\text{||}$, as shown in Table 3.15. (Note that $(p_x)^\uparrow(p_{y'})^\uparrow(p_x)^\uparrow(p_{y'})^\uparrow$ is equivalent to $(\pi_x)^\uparrow(\pi_{y'})^\uparrow(\pi_x^*)^\uparrow(\pi_{y'}^*)^\uparrow$.) The final O_2 configuration is therefore of triplet multiplicity and overall (spin-averaged) bond order 2, and this configurational picture persists over the entire range of bond lengths in Fig. 3.27. Note that the 3O_2 NBO configuration corresponds closely to Pauling’s description of two “three-electron pi bonds” in mutually perpendicular planes.⁵¹

Difluorine

The next two electrons can again be added to the weakly bonding π manifold in the $\downarrow_x \downarrow_{y'}$ pattern favored by Hund's rule (Principle II) to give the 1F_2 configuration shown in Fig. 3.30. Alternatively, this result is obtained from the long-range 1CA configuration by replacing a weak pi bond by a strong sigma bond (Principle I). In the promoted configuration only the sigma-type donor-acceptor interaction (3.92) remains in each spin set, corresponding to the standard $\text{F}=\text{F}$ Lewis structure. This simple configurational picture again persists over the entire range of Fig. 3.27.

Second- and third-row species

Let us also briefly examine the corresponding behavior in second- and third-row homonuclear diatomics. Figures 3.31(a) and (b) display the calculated potential-energy curves for these species (ground-state multiplicities only) and Table 3.16 summarizes the equilibrium bond lengths and bond energies.

As shown in Table 3.16, the calculations appear to reproduce all experimental trends in qualitative or semi-quantitative fashion. A simplifying feature in the second- and third-row series is that the group 14 member (Si_2 , Ge_2) is unambiguously a triplet, with much less evidence of multi-configurational contamination than in the analogous C_2 species. Table 3.17 shows the corresponding NBO configurational assignments of the higher homonuclear diatomics, for comparison with Table 3.15.

As shown in Table 3.17, the NBO configurational assignments are all rather analogous to the corresponding first-row assignments in Table 3.15, with the exception of the group 13 members (B_2 , Al_2 , Ga_2). Even the apparent strong distinction between Al_2 ($\text{Al}=\text{Al}$ in the α set, $\text{Al} \equiv \text{Al}$ in the β set), and B_2 ($\text{B}=\text{B}$ in α , $\text{B} \equiv \text{B}$ in β) is somewhat superficial, reflecting a gradual change from long-range $h_n \rightarrow h_{\sigma^*}$ donor-acceptor interactions (in Al_2) to fully formed ν , $\bar{\nu}$ bonds (in B_2); at distances slightly below R_e the corresponding pairs of nu bonds appear in the Al_2 structures (which become $\text{Al}=\text{Al}$ in the α set below $R \simeq 2.4 \text{ \AA}$ and $\text{Al} \equiv \text{Al}$ in the β set below $R \simeq 2.2 \text{ \AA}$) to match the near- R_e structures of B_2 . However, the distinction between the α structures of Al_2 ($\text{Al}=\text{Al}$) and Ga_2 ($\text{Ga}=\text{Ga}$) is more profound, since Al_2 employs a pair of pi bonds (unsupported by a sigma bond) whereas Ga_2 employs a conventional sigma/pi-bond pair in its α structure. This indicates that there is an interesting near-degeneracy of sigma- and pi-bond strengths for these species, with the usual complications of multi-configurational effects. Nevertheless, the overall configurational patterns are strikingly similar to those discussed previously, and the *Aufbau* construction of Fig. 3.30 can be carried through in a virtually identical manner (following the triplet path through the group 14 member) that we need not describe further.

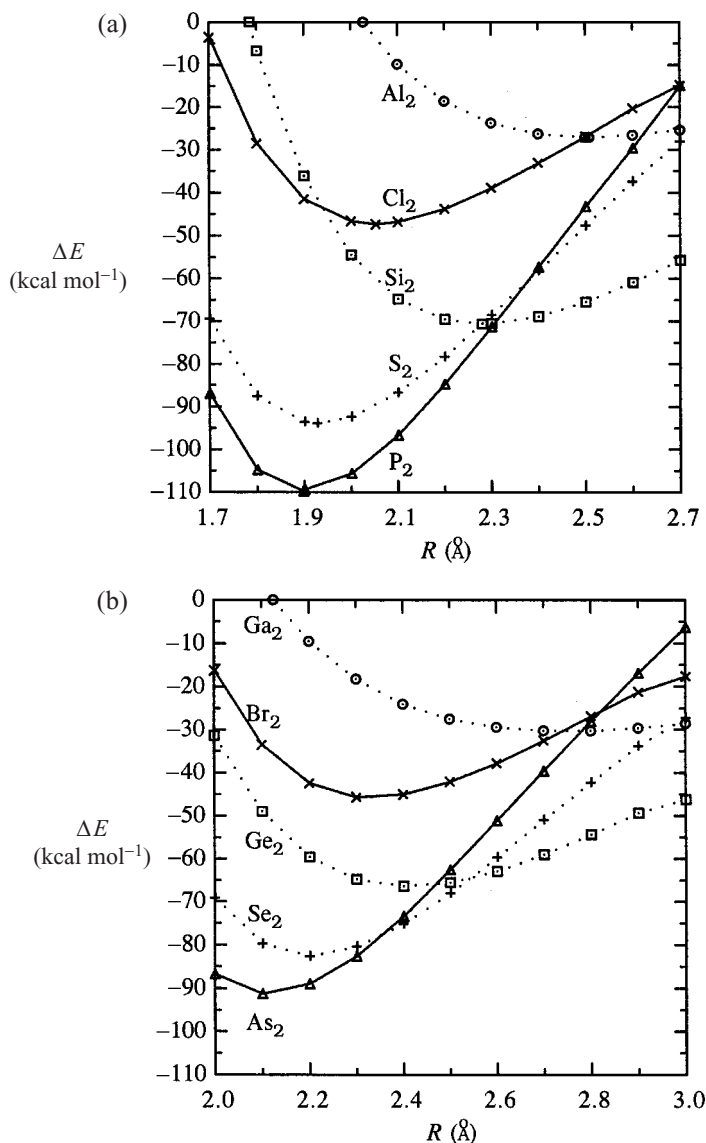


Figure 3.31 (a) Similar to Fig. 3.27, for second-row homonuclear diatomics.
 (b) Similar to Fig. 3.27, for third-row homonuclear diatomics.

A fascinating feature of the Ga_2 species occurs in the excited singlet state. The $^1\text{Ga}_2$ species is bound by $29.0 \text{ kcal mol}^{-1}$ at $R_e = 2.7444 \text{ \AA}$ and has ordinary-looking bond order $b = 1$. However, the bonding character is remarkably *different* in the α and β spin sets, corresponding to bent “banana bonds” of opposite curvature with respect to the internuclear axis. Figure 3.32 displays the form of one of these spin-NBOs, showing the off-axis curvature with respect to the Ga—Ga line of

Table 3.16. *Similar to Table 3.13, for second- and third-row homonuclear diatomics*

A_2	State	R_e (Å)	D_e (kcal mol ⁻¹)
Al ₂	Triplet	2.5078 (2.47)	27.12 (36)
Si ₂	Triplet	2.2803 (2.25)	70.68 (74)
P ₂	Singlet	1.8973 (1.89)	109.55 (116)
S ₂	Triplet	1.9272 (1.89)	94.09 (101)
Cl ₂	Singlet	2.0528 (1.99)	47.61 (57)
Ga ₂	Triplet	2.7435 (—)	31.84 (32)
Ge ₂	Triplet	2.4084 (—)	68.67 (65)
As ₂	Singlet	2.1111 (2.10)	93.42 (91)
Se ₂	Triplet	2.2008 (2.17)	84.11 (79)
Br ₂	Singlet	2.3310 (2.28)	46.93 (45)

centers. Such a formal sigma bond of “mixed” sigma/pi diradical character is highly unusual.

How can such “mixed” sigma/pi bonds occur? In the ¹Ga₂ case the near-degeneracy of sigma and pi bonds evidently allows electron repulsions to be minimized by putting the two bonding electrons into distinct sigma and pi spatial orbitals. This shows that the common tendency of α and β electrons to “pair up” their donor–acceptor interactions in a common spatial orbital (i.e., a “doubly occupied” sigma or pi orbital) is a special consequence of the typical wide energy separation between distinct spatial options. Donor–acceptor bonding is essentially a *single*-electron event; the usual restricted choice of spatial options may force two electrons (of opposite spin) to adopt *common* spatial orbitals for complementary donor–acceptor interactions – the “typical” two-electron covalent bond. However, complementary one-electron donor–acceptor interactions in *different* spatial orbitals are equally easy to envision, and will have an obvious advantage in reducing electron–electron Coulombic repulsions.

Distance-dependent changes in hybridization

Finally, with the diatomic NBO configurations established by Tables 3.15 and 3.17, the only remaining unknown parameter of the NBO Lewis-structure description is the hybridization λ of h_σ , Eq. (3.84a). For values of R around R_e , we can approximate the fractional *s* character of h_σ by

$$f_s \simeq e^{-\xi R^2} \quad (3.93a)$$

or, equivalently,

$$\lambda \simeq e^{\xi R^2} - 1 \quad (3.93b)$$

Table 3.17. Similar to Table 3.15, for second- and third-row homonuclear diatomics

	α NBOs	β NBOs	Composite configuration(s)
$^3\text{Al}_2$	$ \text{Al}\overline{\text{C}}\text{Al} $	$ \text{Al}\text{Al} $	$(n)^2(n')^2(\pi_x)^\dagger(\pi_y)^\dagger$
$^3\text{Si}_2$	$ \text{Si}\overline{\text{S}}\text{Si} $	$ \text{Si}-\text{Si} $	$(\sigma)^2(n)^2(n')^2(\pi_x)^\dagger(\pi_y)^\dagger$
$^1\text{P}_2$	$ \text{P}\overline{\text{P}}\text{P} $	$ \text{P}\overline{\text{P}}\text{P} $	$(\sigma)^2(n)^2(n')^2(\pi_x)^2(\pi_y)^2$
$^3\text{S}_2$	$ \overline{\text{S}}-\overline{\text{S}} $	$ \text{S}\overline{\text{S}}\text{S} $	$(\sigma)^2(n)^2(n')^2(\pi_x)^2(\pi_y)^2(\pi_x^*)^\dagger(\pi_y^*)^\dagger$
$^1\text{Cl}_2$	$ \overline{\text{Cl}}-\overline{\text{Cl}} $	$ \overline{\text{Cl}}-\overline{\text{Cl}} $	$(n)^2(n')^2(\sigma)^2(\text{p}_x)^2(\text{p}_y)^2(\text{p}_x')^2(\text{p}_y')^2$
$^3\text{Ga}_2$	$ \text{Ga}\overline{\text{F}}\text{Ga} $	$ \text{Ga}\text{Ga} $	$(n)^2(n')^2(\sigma)^\dagger(\pi_x)^\dagger$
$^3\text{Ge}_2$	$ \text{Ge}\overline{\text{E}}\text{Ge} $	$ \text{Ge}-\text{Ge} $	$(\sigma)^2(n)^2(n')^2(\pi_x)^\dagger(\pi_y)^\dagger$
$^1\text{As}_2$	$ \text{As}\overline{\text{S}}\text{As} $	$ \text{As}\overline{\text{S}}\text{As} $	$(\sigma)^2(n)^2(n')^2(\pi_x)^2(\pi_y)^2$
$^3\text{Se}_2$	$ \overline{\text{Se}}-\overline{\text{Se}} $	$ \text{Se}\overline{\text{S}}\text{Se} $	$(\sigma)^2(n)^2(n')^2(\pi_x)^2(\pi_y)^2(\pi_x^*)^\dagger(\pi_y^*)^\dagger$
$^1\text{Br}_2$	$ \overline{\text{Br}}-\overline{\text{Br}} $	$ \overline{\text{Br}}-\overline{\text{Br}} $	$(n)^2(n')^2(\sigma)^2(\text{p}_x)^2(\text{p}_y)^2(\text{p}_x')^2(\text{p}_y')^2$

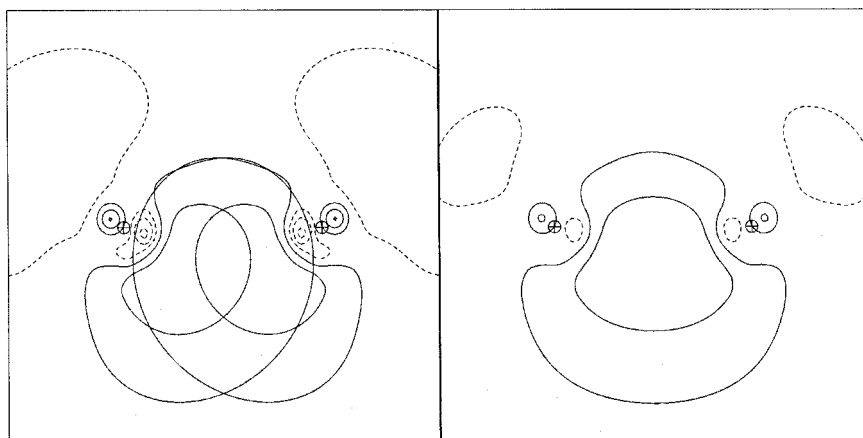


Figure 3.32 Overlapping NHOs (left) and bonding NBO (right) for the α half-bond of singlet Ga_2 ($R = 2.7444 \text{ \AA}$). Each NHO is of $sp^{19.4}$ hybrid composition (94.7% p character), oriented 40.7° from the line of nuclear centers. (The equivalent β half-bond is rotated by 180° about the Ga—Ga axis.)

Table 3.18. Parameters ξ_e and ξ_e' (cf. Eqs. (3.93a)–(3.93c)) for describing hybridization λ of sigma bonds in homonuclear diatomics

Species	α Spin		β Spin	
	ξ_e	ξ_e'	ξ_e	ξ_e'
$^3\text{B}_2$	— ^a	— ^a	— ^a	— ^a
$^1\text{C}_2$	0.684	−0.10	0.684	−0.10
$^3\text{C}_2$	0.725	−0.07	0.646	−0.10
$^1\text{N}_2$	0.768	−0.08	0.768	−0.08
$^1\text{O}_2$	1.074	−0.23	1.074	−0.23
$^3\text{O}_2$	1.112	−0.24	1.031	−0.21
$^1\text{F}_2$	1.496	−0.12	1.496	−0.12
$^3\text{Al}_2$	— ^a	— ^a	— ^a	— ^a
$^3\text{Si}_2$	0.421	−0.04	0.376	−0.04
$^1\text{P}_2$	0.423	−0.03	0.423	−0.03
$^3\text{S}_2$	0.617	0.00	0.588	0.00
$^1\text{Cl}_2$	0.687	−0.01	0.687	−0.01
$^3\text{Ga}_2$	— ^a	— ^a	— ^a	— ^a
$^3\text{Ge}_2$	0.546	−0.14	0.503	−0.13
$^1\text{As}_2$	0.403	0.00	0.403	0.00
$^3\text{Se}_2$	0.485	−0.01	0.472	0.00
$^1\text{Br}_2$	0.570	0.00	0.570	0.00

^a Sigma bond not present in this configuration.

which varies in the expected way from $R = 0$ ($f_s = 1$, $\lambda = 0$) to $R \rightarrow \infty$ ($f_s = 0$, $\lambda = \infty$). Here ξ is a slowly varying function of R that can be approximated by the leading terms of a Taylor-series expansion

$$\xi = \xi_e + \xi_e'(R - R_e) + \dots \quad (3.93c)$$

Numerical values of ξ_e and ξ_e' for low-lying configurations of homonuclear diatomic molecules are displayed in Table 3.18. These values make it possible to estimate the actual diatomic hybridizations $\lambda(R)$ over a fairly wide range of R values around the equilibrium geometry.

Example 3.12

Exercise: Determine the change of hybridization λ of the sigma bond of F_2 as it stretches from $R_e = 1.41 \text{ \AA}$ to 1.5 \AA .

Solution: From the values for F_2 in Table 3.18

$$\xi_e = 1.496, \quad \xi_e' = -0.12$$

we estimate from Eq. (3.93c)

$$\begin{aligned} \xi(R_e) &= 1.496 \\ \xi(1.5) &= 1.496 - 0.12(1.50 - 1.41) = 1.485 \end{aligned}$$

From (3.93b) the hybridizations are therefore

$$\begin{aligned} \lambda(R_e) &= e^{1.496(1.41)^2} - 1 = 18.6 \\ \lambda(1.5) &= e^{1.485(1.50)^2} - 1 = 27.3 \end{aligned}$$

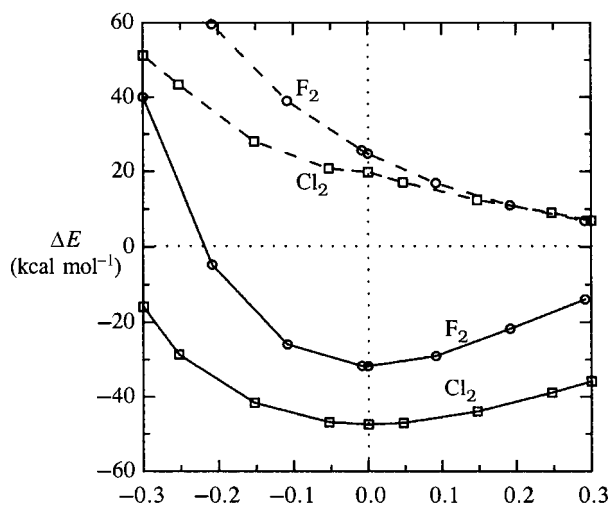
(The actual NHO values are found to be 18.6 and 28.4, respectively.)

Example 3.13

Why is the bond energy of F_2 less than that of Cl_2 ? (This difference runs contrary to the trend between other first- and second-row diatomics.)

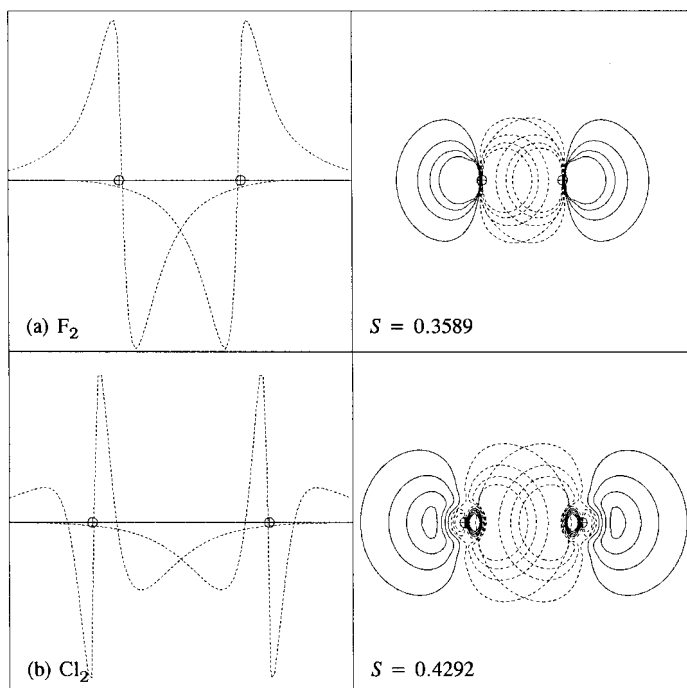
At least two factors appear to be involved, both connected to the high electronegativity of F compared to Cl.

- (1) The steric repulsions between off-axis lone pairs at R_{eq} are stronger in F_2 than in Cl_2 , and the difference increases rapidly at smaller R . This is shown in the plot below, which compares the full potential curves (solid lines) with the pairwise sum of steric repulsions between off-axis lone pairs (dashed lines) for F_2 (circles) and Cl_2 (squares), both shifted to a common origin at R_{eq} (1.4083 and 2.0528 \AA , respectively):



As shown in the plot, the steric repulsions in F_2 are about 5 kcal mol^{-1} stronger at R_{eq} than in Cl_2 , and the steric disadvantage of F_2 becomes rapidly worse at smaller R .

- (2) The second factor arises from the slightly higher *s* character (greater directionality in the bonding direction) in Cl_2 than in F_2 (as can be judged from the ξ_e and ξ_e' values in Table 3.18). This results in somewhat higher bonding overlap at larger R , as shown in the NHO radial profile and overlap contour diagrams below for (a) F_2 and (b) Cl_2 :

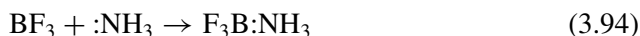


As shown, the bonding overlap is about 20% greater in Cl_2 than in F_2 at R_{eq} , and the advantage is relatively greater at larger R due to higher electronegativity (faster fall-off) of the fluorine bonding hybrid. Thus, poorer hybrid bonding at larger R and greater steric repulsion of off-axis lone pairs at smaller R both appear to play a role in the surprising weakness of F_2 bonding compared with that in Cl_2 and Br_2 .

3.2.10 Lewis-acid–base compounds and dative bonding

Dative versus covalent sigma bonds

It was recognized by G. N. Lewis that the reaction of boron trifluoride plus ammonia



constitutes a generalized acid–base reaction in the donor–acceptor sense. In this reaction, BF_3 plays the role of Lewis acid or electron-pair acceptor through its formally vacant valence $2p$ orbital, while :NH_3 is the Lewis base or electron-pair donor through its valence lone pair. The product $\text{F}_3\text{B:NH}_3$ is a Lewis-acid–base “adduct” with distinctive dative (coordinate–covalent) character of the B–N bond. From this profound insight, Lewis achieved a rich generalization of standard Brønsted (proton-oriented) acid–base chemistry and established the general donor–acceptor bonding paradigm that extends to virtually every aspect of chemical structure and reactivity.⁵²

Reaction (3.94) is an example of general coordinate-covalent-bond formation



in which both members of the shared electron pair originate from the Lewis base B,



rather than one from A and one from B as in standard covalent-bond formation,



The general Lewis-acid–base reaction (3.95) exemplifies the two-electron stabilizing donor–acceptor interaction of Fig. 1.3 (namely the $n_{\text{N}} \rightarrow n_{\text{B}}^*$ interaction for (3.94)), which may be distinguished from the complementary bi-directional donor–acceptor interactions of covalent-bond formation (Section 3.2.1). However, this leaves open the question of whether (or how) the equilibrium bond reflects the formal difference between heterolytic (3.95) and homolytic (3.96) bond formation.

What are the general NBO descriptors that distinguish a dative from a covalent AB bond? Two qualitative criteria may be taken as characteristic of dative bonding.

(DB-1) Formation of a dative bond leads to a change of *formal charge* at each atom (A^-B^+), so the calculated atomic charges $Q_A(\text{dat})$ and $Q_B(\text{dat})$ for a dative-bonded pair deviate markedly from those ($Q_A(\text{sep})$ and $Q_B(\text{sep})$) in the dissociated species by approximately equal and opposite amounts for A and B,

$$Q_{B(\text{dat})} - Q_{B(\text{sep})} \simeq -(Q_{A(\text{dat})} - Q_{A(\text{sep})}) \quad (3.97)$$

(DB-2) Owing to the formal charge difference, the ionicity i_{AB} of a dative bond deviates markedly from the usual relationship to (neutral) electronegativity (cf. Example 3.10),

$$i_{AB}(\text{dat}) \not\approx 1 - \exp[-0.45(x_A - x_B)] \quad (3.98)$$

In general, the R -dependent variations of natural atomic charges in dative bonds are significantly larger than those in covalent bonds. Indeed, the $Q_A(R)$ variations in dative bonds resemble those in ionic bonds (cf. Fig. 2.9), to which they are evidently related by similarities in donor–acceptor character. The strong dQ_A/dR dependence tends to be associated with enhanced infrared vibrational intensity and other spectroscopic signatures characteristic of ionic bonding.

Figure 3.33 displays the σ_{BN} dative bond NBO of $F_3B:NH_3$, comparing it with the nitrogen NHO (basically, the ammonia lone-pair hybrid) of which it is principally composed. Consistently with criterion DB-1, the atomic charges in the equilibrium geometry ($Q_B(R_e) = +1.2843$, $Q_N(R_e) = -0.9175$) differ strongly from the values in the separated BF_3 ($Q_B(\infty) = +1.4071$) and NH_3 ($Q_N(\infty) = -1.0535$).

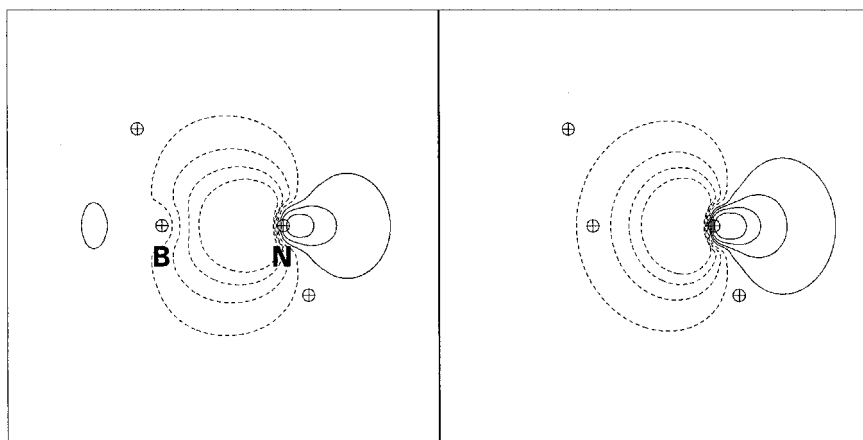


Figure 3.33 The dative sigma bond $\sigma_{B:N}$ of $F_3B:NH_3$, showing the NBO (left) and the donor nitrogen n_N NHO (right).

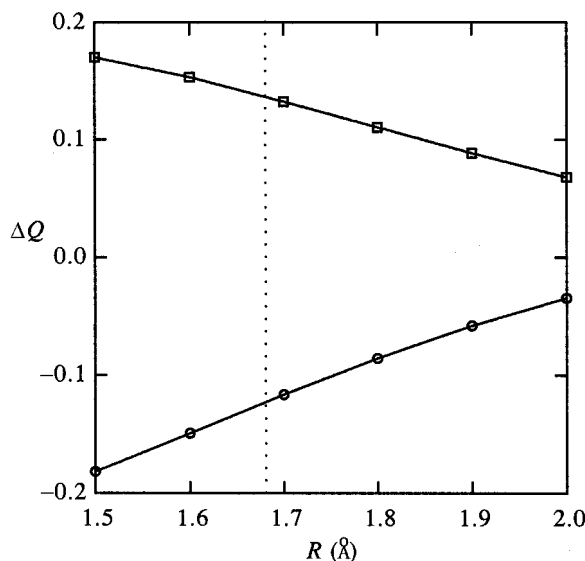


Figure 3.34 Atomic-charge variations $\Delta Q = Q(R) - Q(\infty)$ for boron (circles) and nitrogen (squares) atoms of the σ_{BN} dative bond of the $\text{F}_3\text{B}:\text{NH}_3$ Lewis-acid-base adduct. (A dotted line marks the equilibrium bond length $R_e = 1.6802 \text{ \AA}$.)

Consistently with criterion DB-2, the bond ionicity $i_{\text{BN}} = 0.6572$ also differs appreciably from the expected value 0.7237 calculated from Eq. (3.76).

Figure 3.34 shows the characteristic “mirror-image” variations ΔQ of dative-bond atomic charges with respect to the asymptotic values at $R = \infty$. It can be seen from Fig. 3.34 that the boron and nitrogen atoms have built up a charge difference of $\sim 0.25e$ at R_e (relative to the values in asymptotically separated BF_3 and NH_3 species), and that this “charge splitting” increases rapidly with decreasing separation (by more than $0.5e \text{ \AA}^{-1}$) in the near- R_e region. Thus, intense charge flow from donor n_{N} to acceptor n_{B}^* and rapidly increasing two-center character are indicated in this region, even though the ionic character of the NBO at the equilibrium geometry remains relatively high ($i_{\text{B:N}} = -0.6572$) in this weakly bound complex.

Amine oxides and related species

Even more pronounced examples of dative sigma bonds are obtained by using a stronger, more electronegative Lewis acid. A particularly interesting example involves the singlet oxygen atom in promoted ^1S configuration, where a valence $2p_z$ orbital “hole” is emptied for complexation with a Lewis base. Well-known examples of such dative bonding include amine oxide ($\text{O}:\text{NH}_3$) and analogous $\text{O}:\text{XH}_3$ oxides of group 15 elements. Figure 3.35 displays atomic-charge-variation plots (analogous to Fig. 3.34) for $\sigma_{\text{O:X}}$ bonds of $\text{O}:\text{NH}_3$, $\text{O}:\text{PH}_3$, and $\text{O}:\text{AsH}_3$, showing

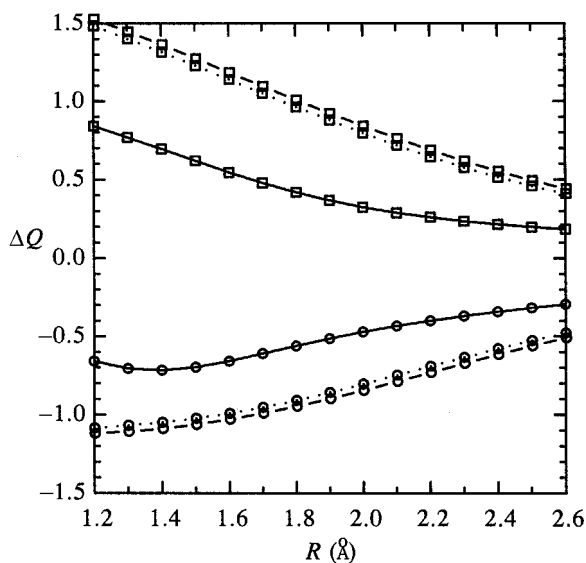


Figure 3.35 Atomic-charge variations $\Delta Q = Q(R) - Q(\infty)$ in dative bonds of H_3NO (solid lines), H_3PO (dotted lines), and H_3AsO (dashed lines). Circles mark oxygen; squares mark A atoms of O:A dative bonds.

the expected mirror-image pattern of strongly varying dipolar character that characterizes dative bonding. In these cases the equilibrium ionic character is further reduced ($|i_{\text{O:N}}| = 0.1244$, $|i_{\text{O:P}}| = 0.4136$, $|i_{\text{O:As}}| = 0.3290$) and the charge splitting is correspondingly increased compared with $\text{F}_3\text{B:NH}_3$.

Owing to their dative character, the O:XH₃ bonds of group 15 oxides differ rather remarkably from ordinary covalent bonds involving the same elements. For example, a “normal” σ_{NO} bond (e.g., in hydroxylamine, HONH_2) would be estimated from Eq. (3.76) to have $i_{\text{NO}} = -0.17$, polarized toward the more electronegative O. However, the dative $\sigma_{\text{N:O}}$ NBO of O:NH₃

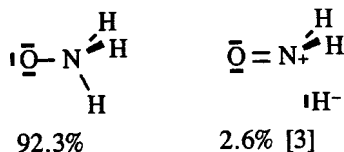
$$\sigma_{\text{N:O}} = 0.7498(\text{sp}^{2.31})_{\text{N}} + 0.6617(\text{sp}^{6.12})_{\text{O}} \quad (3.99)$$

is *oppositely* polarized, with $i_{\text{N:O}} = +0.1244$. Similarly, in O:AsH₃ the ionic character is strongly diminished ($i_{\text{As:O}} = -0.3290$) compared with what would be expected ($\simeq -0.48$) from atomic electronegativity differences. These examples indicate (cf. DB-2) that “normal” relationships between bond polarity and atomic electronegativity will fail dramatically in cases of dative bonding.

Considerable controversy surrounds the nature of the bonding in amine oxides and analogous phosphine and arsine oxides. These species are often depicted in textbooks as double-bonded (O=PH_3 , O=AsH_3) in order to rationalize the unusually short bond lengths. However, both theoretical wavefunction analysis⁵³ and NMR

evidence⁵⁴ indicate that the bonding is better described as a *single* dative bond with anionic $\bar{\text{O}}^-$ character. The usual hyperconjugative interactions (Section 3.4.2) between oxygen lone pairs and vicinal hydride antibonds are expected to confer weak partial double-bond character to this dative bond, but these secondary interactions are insufficient to warrant a double-bonded Lewis-structure representation.

NBO and NRT analysis unequivocally supports this “hyperconjugatively enhanced single-dative-bond” picture of the bonding in group 15 trialkyl oxides. The quantitative NRT resonance weightings in the equilibrium ONH_3 geometry are



leading to NRT bond order $b_{\text{ON}} = 1.077$, only slightly greater than an ordinary single bond. The corresponding NRT bond orders in phosphine oxide ($b_{\text{OP}} = 1.174$) and arsine oxide ($b_{\text{OAs}} = 1.126$) are also in accord with this picture. Thus, it seems clearly preferable to represent the bonding in nitroxides and related species with a special dative-bond symbol (such as $\text{O}:\text{N}$, $\text{O}\leftarrow\text{N}$, O^-N^+ or $\bar{\text{O}}^--\text{N}$) to depict the strong anionic (rather than carbonyl-like) character of the oxygen atom. The same remarks apply to phosphine oxides and higher group 15 congeners.

Dative pi bonds

Dative bonding can also occur in pi-type interactions, particularly involving the BH_2 group. A good example is $\text{H}_2\text{B}=\text{NH}_2$, isoelectronic to ethylene, which is well described by a double-bonded NBO Lewis structure with dative $\pi_{\text{B:N}}$ bond:

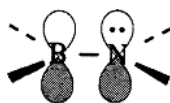


Figure 3.36 shows the form of this dative $\pi_{\text{B:N}}$ bond, comparing the final polarized NBO (left) with the overlapping NHOs (right).

Like their sigma counterparts, dative pi bonds are expected to exhibit strong changes in polarity with bond stretching, but pi-type dipolar “switching” will also occur in response to torsional and pyramidalization changes. In H_2BNH_2 the strength of the dative $\pi_{\text{B:N}}$ bond leads to planar equilibrium geometry both at B and at N, which is indicative of sp^2 -like hybridization⁵⁵ as is actually found in the NBOs,

$$\sigma_{\text{BN}} = 0.4952(\text{sp}^{2.29})_{\text{B}} + 0.8688(\text{sp}^{1.08})_{\text{N}} \quad (3.100\text{a})$$

$$\pi_{\text{B:N}} = 0.3783(\text{p})_{\text{B}} + 0.9257(\text{p})_{\text{N}} \quad (3.100\text{b})$$

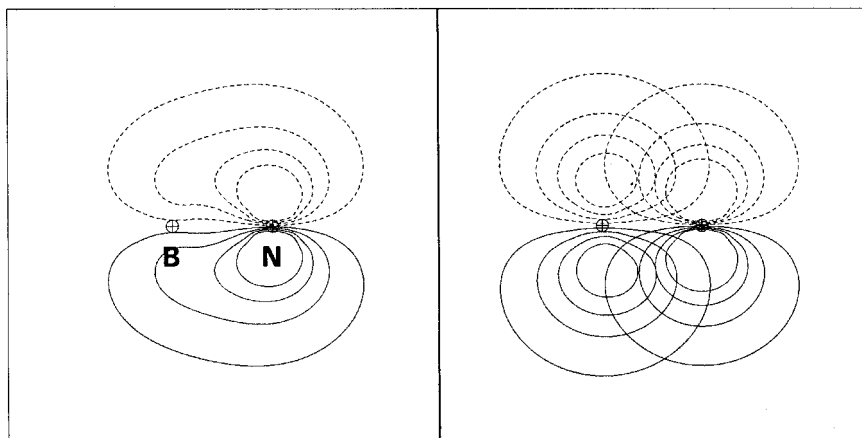


Figure 3.36 The dative pi bond $\pi_{\text{B:N}}$ of H_2BNH_2 , showing the NBO (left) and overlapping NHOs (right).

However, the analogous pi-type interactions in H_2BPH_2 and H_2BASh_2 are significantly weaker, due primarily to the size mismatch in p orbitals from different quantum shells. The latter species can therefore best be described as single-bonded, with pyramidalized sp^3 -like PH_2 and AsH_2 groups, but with strong residual pi-type delocalizations conferring significant partial double-bond character. Owing to the intrinsically weaker character of pi-type interactions, true dative pi-bond NBOs such as (3.100b) are expected to be relatively uncommon in main-group compounds.

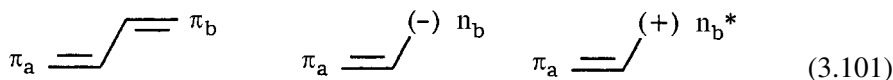
3.3 Conjugation and aromaticity

3.3.1 Conjugation and the resonance concept

Compounds containing multiple bonds often exhibit a characteristic electronic stabilization identified as “conjugation.” In such a case the molecular heat of formation significantly exceeds the predictions of simple bond-energy-additivity schemes, and the actual stability is found to depend sensitively on the *connectivity pattern* of pi (or pi-type) bonds in highly nonlinear fashion. Phenomenologically, the bonds of a conjugated pi network appear much less transferable than those of unconjugated compounds. Indeed, the reactivity at a particular pi-bonding site is found to depend sensitively on changes throughout the conjugated network, with profound consequences for remote chemical control. Conjugation is also associated with characteristic bond-length changes, which can be described in the framework of “resonance” between distinct Lewis structures (see below). In this section we wish to describe the nature of pi-type conjugation in NBO donor–acceptor terms, initially for a pair of conjugated pi bonds and subsequently for complex pi-bonding networks.

The NBO theory of diene conjugation

A characteristic feature of conjugated pi-bond networks is that each pi bond π_a lies adjacent (vicinal, *s-cis* or *s-trans*) to a coplanar pi bond π_b , a pi-type lone pair n_b , or a pi-type vacancy n_b^* (unfilled valence p orbital), e.g.,



The idealized Lewis structures are modified in each case by donor–acceptor interactions involving the filled (Lewis) π_a and unfilled (non-Lewis) π_a^* NBOs of the formal pi bond, $\pi_a \rightarrow \pi_b^*$ and $\pi_b \rightarrow \pi_a^*$, $n_b \rightarrow \pi_a^*$, or $\pi_a \rightarrow n_b^*$ for the three prototypes shown in (3.101).

As described in Sections 1.4 and 1.5, a general $\Omega_a - \Omega_b^*$ donor–acceptor interaction between Lewis (Ω_a) and non-Lewis (Ω_b^*) NBOs leads to perturbative corrections to the zeroth-order natural Lewis-structure wavefunction

$$\psi^{(L)} = \hat{A}[(\Omega_a)^2(\Omega_b)^2 \dots] \quad (3.102)$$

The starting Ω_a NBO is thereby perturbed to a “natural localized molecular orbital” (NLMO), distinguished by a tilde from its parent NBO

$$\tilde{\Omega}_a = \mathfrak{O}(\Omega_a + \lambda \Omega_b^*) \quad (3.103)$$

The associated energy lowering is estimated from perturbation theory as

$$\Delta E(\Omega_a \rightarrow \Omega_b^*) = -2 \frac{\langle \Omega_a | \hat{F} | \Omega_b^* \rangle^2}{\Delta \epsilon} \quad (3.104)$$

where

$$\Delta \epsilon = \langle \Omega_b^* | \hat{F} | \Omega_b^* \rangle - \langle \Omega_a | \hat{F} | \Omega_a \rangle \quad (3.105)$$

is the energy difference of interacting NBOs. The coefficient of the delocalization “tail” in (3.103) can also be perturbatively estimated as

$$\lambda = - \frac{\langle \Omega_a | \hat{F} | \Omega_b^* \rangle}{\Delta \epsilon} \quad (3.106)$$

However, it is more convenient to determine the NLMOs *directly* by a numerical procedure⁵⁶ that incorporates higher perturbation corrections of *all* orders. As mentioned in Section 3.2.4, the Slater determinant of semi-localized NLMOs

$$\psi^{(SL)} = \hat{A}[(\tilde{\Omega}_a)^2(\tilde{\Omega}_a)^2 \dots] \quad (3.107)$$

is completely equivalent to the *exact* Hartree–Fock wavefunction,

$$\psi^{(SL)} = \Psi_{\text{HF}} \quad (3.108)$$

and thus incorporates all physically meaningful delocalization effects of Hartree–Fock theory. In the present treatment we therefore bypass the traditional discussion of conjugation in the canonical MO framework in order to gain the advantages of the simple perturbative expressions (3.103)–(3.106) for localized NBO donor–acceptor interactions.

For the present case of the interactions shown in (3.101), the $\pi_a \rightarrow \pi_b^*$ donor–acceptor interaction, for example, leads to energetic stabilization

$$\Delta E(\pi_a \rightarrow \pi_b^*) = -2 \frac{\langle \pi_a | \hat{F} | \pi_b^* \rangle^2}{\epsilon_{\pi_b^*} - \epsilon_{\pi_a}} \quad (3.109a)$$

while the corresponding $\pi_b \rightarrow \pi_a^*$ interaction leads to

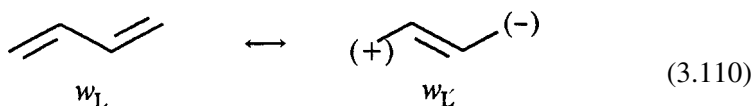
$$\Delta E(\pi_b \rightarrow \pi_a^*) = -2 \frac{\langle \pi_b | \hat{F} | \pi_a^* \rangle^2}{\epsilon_{\pi_a^*} - \epsilon_{\pi_b}} \quad (3.109b)$$

The possible donor–acceptor stabilizations for the two remaining structures in (3.101) are similarly

$$\Delta E(n_b \rightarrow \pi_a^*) = -2 \frac{\langle n_b | \hat{F} | \pi_a^* \rangle^2}{\epsilon_{\pi_a^*} - \epsilon_{n_b}} \quad (3.109c)$$

$$\Delta E(\pi_a \rightarrow n_b^*) = -2 \frac{\langle \pi_a | \hat{F} | n_b^* \rangle^2}{\epsilon_{n_b^*} - \epsilon_{\pi_a}} \quad (3.109d)$$

Consistently with empirical observations, the stabilization $\Delta E(\pi_a \rightarrow \pi_b^*)$, for example, is found to be relatively negligible unless π_a and π_b^* are in a *vicinal* relationship, due to the fact that the $\langle \pi_a | \hat{F} | \pi_b^* \rangle$ matrix element falls off rapidly (exponentially) with distance, and analogously for the other interactions in (3.109). Furthermore (as illustrated in Example 1.4 for the $n_b \rightarrow \pi_a^*$ interaction), the vicinal $\pi_a \rightarrow \pi_b^*$ interaction is equivalent to a partial admixture of the alternative resonance structure:



Consistently with this resonance picture (and with experiment), the $\pi_a \rightarrow \pi_b^*$ donor–acceptor interaction leads to partial bond equalization of the nominal single and double bonds, strengthening and shortening the former while weakening and lengthening the latter. The resonance-weighted bond orders (cf. Eq. (1.40)) thus differ from the parent idealized values, reflecting the relative weightings of the parent Lewis (w_L) and alternative (w_L') structures in (3.110). The conjugative stabilizations (3.109) may also be referred to as “quantum-mechanical resonance energy” (QMRE).

The NBO/NRT description of polyenes and related species

We now wish to describe qualitative trends in pi-conjugated systems in terms of the localized NBO donor–acceptor stabilizations (3.109) and NRT bond orders. For this purpose we consider the representative group of molecules **1–16** shown in Fig. 3.37. Numerical bond orders and conjugative stabilization energies pertaining to these molecules are gathered in Table 3.19.

Let us first inquire whether basic criteria for the validity of low-order perturbation theory are actually satisfied in the present case. As described in Section 1.4, the perturbative starting point is an idealized natural Lewis-structure wavefunction ($\psi^{(L)}$) of doubly occupied NBOs. The accuracy of this Lewis-type starting point may be assessed in terms of the percentage accuracy of the variational energy ($E^{(L)}$) or density ($\rho^{(L)}$), as shown for each molecule in Table 3.20.

As seen in Table 3.20, the unperturbed localized $\psi^{(L)}$ is of high accuracy throughout (>99% in energy, ~98%–99% in density), only slightly lower than that of the parent unconjugated ethylene molecule (99.88% for $E^{(L)}$ and 99.58% for $\rho^{(L)}$). This suggests that the perturbation series should be rapidly convergent for such conjugated species,⁵⁷ and we can therefore expect that simple perturbative expressions such as (3.109) are adequate to describe leading conjugative effects at a useful level of chemical accuracy.

Orientalional and energetic factors in donor–acceptor interactions

Let us next examine the dependence of Eqs. (3.109) on the factors in the numerator and denominator that affect conjugative stabilization, taking Eq. (3.109a) as an example.

On physical grounds we expect that the orbital energy difference in the denominator

$$\Delta\epsilon = \epsilon_{\pi_b^*} - \epsilon_{\pi_a} \quad (3.111a)$$

is rather insensitive to the orientation or separation of the interacting π_a and π_b^* NBOs. Furthermore, this term is typically large (e.g., $\Delta\epsilon = 0.3086$ a.u. $\simeq 200$ kcal mol⁻¹ for **1**) compared with the expected variability of either $\epsilon_{\pi_b^*}$ or ϵ_{π_a} , and therefore has little influence on $\Delta E(\pi_a \rightarrow \pi_b^*)$. (For example, lowering ϵ_{π_a} by 10 kcal mol⁻¹ would decrease $\Delta E(\pi_a \rightarrow \pi_b^*)$ by only about 5%.)

In contrast, the matrix element in the numerator

$$F_{a,b^*} = \langle \pi_a | \hat{F} | \pi_b^* \rangle \quad (3.111b)$$

is smaller in magnitude (e.g., $|F_{a,b^*}| = 0.0608$ a.u. in **1**), but depends *strongly* both on distance and on orientation, and its variations have *much* stronger leverage on $\Delta E(\pi_a \rightarrow \pi_b^*)$. (For example, decreasing F_{a,b^*} by 0.01 alters the stabilization by

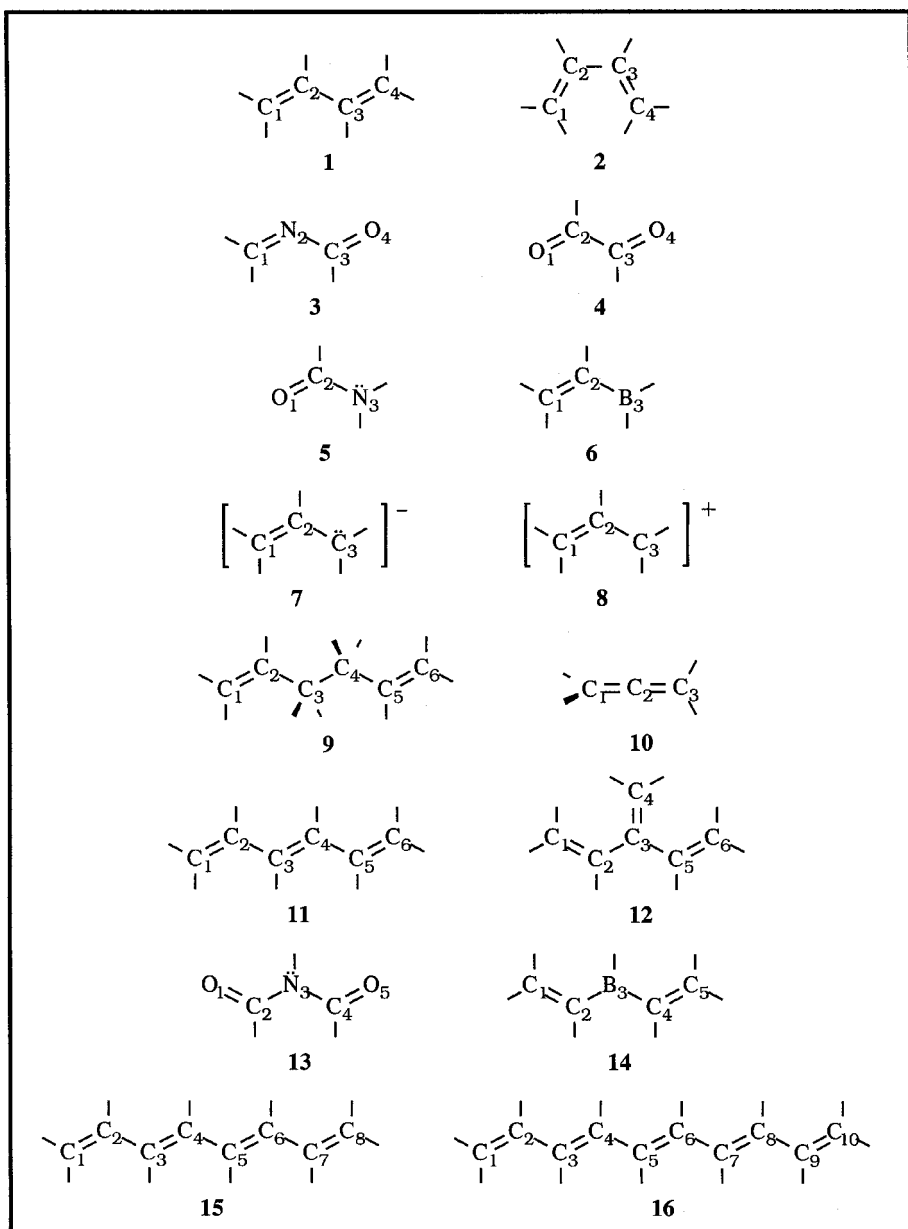


Figure 3.37 Atom numbering and parent Lewis structures for molecules **1–16** (see Table 3.19). Only pi-type lone pairs are shown explicitly.

Table 3.19. Formal π moieties, NRT bond orders of associated atoms, and conjugative stabilization energies for molecules **1–16** (shown in Fig. 3.37)

Molecule	π Moiety		NRT bond order ^a		Stabilization ^b (kcal mol ⁻¹)	
	a	b	a	b	$\Delta E_{a \rightarrow b^*}$	$\Delta E_{b \rightarrow a^*}$
1	$\pi_{C_1C_2}$	$\pi_{C_3C_4}$	1.939	1.939	-15.0	-15.0
2	$\pi_{C_1C_2}$	$\pi_{C_3C_4}$	1.950	1.950	-12.8	-12.8
3	$\pi_{C_1N_2}$	$\pi_{C_3O_4}$	1.977	2.006	-21.2	-5.4
4	$\pi_{O_1C_2}$	$\pi_{C_3O_4}$	2.027	2.027	-7.1	-7.1
5	$\pi_{O_1C_2}$	n_{N_3}	1.732	—	.-	-59.8
6	$\pi_{C_1C_2}$	$n_{B_3}^*$	1.953	—	-26.2	.-
7	$\pi_{C_1C_2}$	n_{C_3}	1.512	—	.-	-112.4
8	$\pi_{C_1C_2}$	$n_{C_3}^*$	1.509	—	-126.7	.-
9	$\pi_{C_1C_2}$	$\pi_{C_5C_6}$	1.983	1.983	.-	.-
10	$\pi_{C_1C_2}$	$\pi_{C_2C_3}$	1.991	1.991	.-	.-
11	$\pi_{C_1C_2}$	$\pi_{C_3C_4}$	1.934	1.841	-14.5	-16.0
12	$\pi_{C_1C_2}$	$\pi_{C_3C_4}$	1.956	1.892	-11.7	-12.0
13	$\pi_{O_1C_2}$	n_{N_3}	1.816	—	.-	-47.9
14	$\pi_{C_1C_2}$	$n_{B_3}^*$	1.952	—	-24.2	.-
15	$\pi_{C_1C_2}$	$\pi_{C_3C_4}$	1.921	1.831	-14.5	-16.2
	$\pi_{C_3C_4}$	$\pi_{C_5C_6}$	1.831	1.831	-16.5	-16.5
16	$\pi_{C_1C_2}$	$\pi_{C_3C_4}$	1.924	1.818	-14.6	-16.3
	$\pi_{C_3C_4}$	$\pi_{C_5C_6}$	1.818	1.818	-16.9	-16.8

^a For reference, the C—C bond order in ethylene is 2.027.

^b Entry “.-” corresponds to the quantity being undefined or negligible (less than the printout threshold of 0.5 kcal mol⁻¹).

Table 3.20. Percentage accuracies of energy ($E^{(L)}$) and density ($\rho^{(L)}$) of the idealized Lewis-type wavefunction $\psi^{(L)}$ for molecules **1–16** (shown in Fig. 3.37)

Molecule	$E^{(L)}$ Accuracy (%)	$\rho^{(L)}$	Molecule	$E^{(L)}$ Accuracy (%)	$\rho^{(L)}$
1	99.82	99.00	2	99.82	99.05
3	99.78	98.68	4	99.81	98.79
5	99.76	98.10	6	99.81	98.96
7	99.70	97.31	8	99.71	97.33
9	99.82	99.21	10	99.78	98.92
11	99.79	98.68	12	99.81	98.99
13	99.73	97.97	14	99.78	98.84
15	99.78	98.49	16	99.77	98.36

about 40%!) Thus, in discussing the factors governing conjugative stabilizations we shall focus primarily on the F_{a,b^*} interaction element.

The strength of the F_{a,b^*} interaction and its variations with distance and orientation can be conveniently visualized in terms of the *overlap* of π_a and π_b^* NBOs, on the basis of a Mulliken-type approximation (cf. Eq. (1.34)). As an example, the top two panels of Fig. 3.38 compare the overlapping π_a - π_b^* orbital contours for *trans* **1** and *cis* **2** isomers of butadiene. As shown in Fig. 3.38, the overlap in the *cis* isomer **2** ($S = 0.2054$) is slightly weaker than that in the *trans* isomer **1** ($S = 0.2209$), due to the unfavorable orientation of the π_a across the nodal plane of the π_b^* in the latter case. Consistently with the weaker π_a - π_b^* overlap, the $\langle \pi_a | \hat{F} | \pi_b^* \rangle$ interaction is less, namely 0.0608 in **1** versus 0.0564 in **2**. The delocalization tail of the $\tilde{\pi}_a$ NLMO is correspondingly less than its value in the *trans* isomer

$$\tilde{\pi}_a(\mathbf{1}) = 0.981\pi_a + 0.191\pi_b^* + \dots \quad (3.112a)$$

$$\tilde{\pi}_a(\mathbf{2}) = 0.984\pi_a + 0.175\pi_b^* + \dots \quad (3.112b)$$

i.e., about 3.65% in **1** versus 3.06% in **2**. (The ellipses denote residual contributions of less than 1%.) As shown in Table 3.19, each of the two possible stabilizations is thereby reduced from 15.0 kcal mol⁻¹ in **1** to 12.8 kcal mol⁻¹ in **2**, so the *trans* isomer **1** is favored by about 4.4 kcal mol⁻¹ overall. Such overlap-based considerations suggest correctly that s-*anti* conformations will be generally preferred over s-*syn* conformations in conjugated dienes. (For similar reasons, synperiplanar and antiperiplanar conformers are strongly preferred over nonplanar conformers that twist the π_a and π_b^* out of conjugation.) In the following discussion we therefore consider only all-*trans* conformers, except (as in **12**) where steric blockage mandates otherwise.

Example 3.14

Exercise: Use perturbation theory to estimate the π_b^* delocalization tail in the $\tilde{\pi}_a$ NLMOs of **1** and **2**.

Solution: From Eq. (3.106) and the values of F_{a,b^*} and $\Delta\epsilon$ quoted above,

$$\lambda(\mathbf{1}) = -\frac{F_{a,b^*}(\mathbf{1})}{\Delta\epsilon} = \frac{0.0608}{0.3086} = 0.197$$

$$\lambda(\mathbf{2}) = -\frac{F_{a,b^*}(\mathbf{2})}{\Delta\epsilon} = \frac{0.0564}{0.3111} = 0.181$$

These estimates compare favorably with the actual values computed from Eqs. (3.112),

$$\lambda(\mathbf{1}) = \frac{0.191}{0.981} = 0.195$$

$$\lambda(\mathbf{2}) = \frac{0.175}{0.984} = 0.178$$

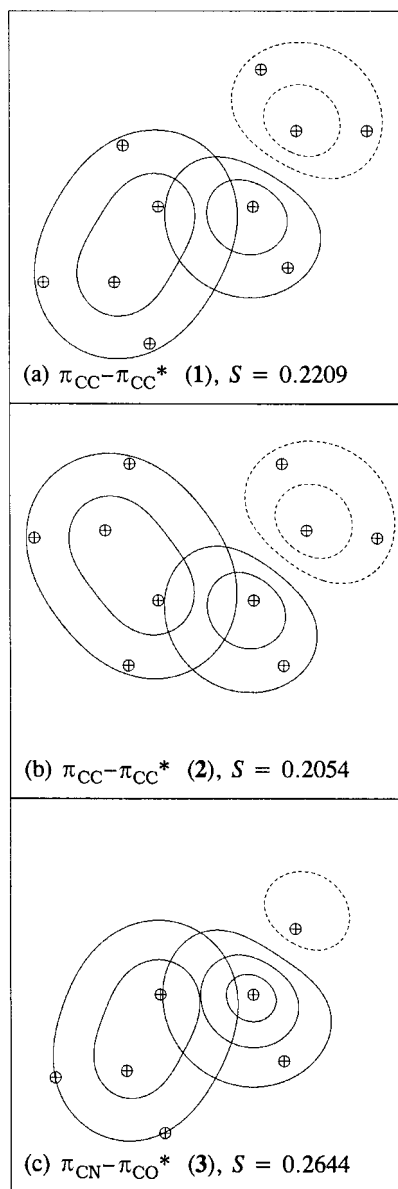


Figure 3.38 Principal conjugative interactions in **1-3** (see Fig. 3.37), showing NBO contours 1 Å above the molecular plane (with projected nuclear positions included for reference).

Let us now consider other factors that are expected to affect the NBO matrix element F_{a,b^*} and conjugative stabilization according to Eq. (3.109).

Bond and antibond polarity

From the manner in which $\pi_a-\pi_b^*$ overlap in **1** arises primarily from the region of the connecting atoms C₂ and C₃, it is apparent that *polarity changes* that amplify the orbitals in this connecting region will enhance the conjugative interaction.

For example, in formylimine **3** the π_{CN} NBO is expected to be more strongly polarized toward the connecting N atom, due to its greater electronegativity. Similarly, the π_{CO} NBO is polarized toward the electronegative O, so the corresponding π_{CO}^* is polarized oppositely toward the connecting C (cf. Eqs. (1.31)). Both polarity changes increase the $\pi_{CN}-\pi_{CO}^*$ overlap (0.2644) and interaction strength (21.2 kcal mol⁻¹) in **3** relative to the apolar $\pi_{CC}-\pi_{CC}^*$ interaction in **1**, as shown in the lower panel of Fig. 3.38. The stronger conjugative mixing is also reflected in the form of the $\tilde{\pi}_{CN}$ NLMO,

$$\tilde{\pi}_{CN}(\mathbf{3}) = 0.975\pi_{CN} + 0.217\pi_{CO}^* + \dots \quad (3.113a)$$

By the same reasoning, the oppositely directed $\pi_{CO}-\pi_{CN}^*$ donor-acceptor pair is *weakened* in overlap (0.0979) and interaction strength (5.4 kcal mol⁻¹), and the $\tilde{\pi}_{CO}$ NLMO is only weakly delocalized:

$$\tilde{\pi}_{CO}(\mathbf{3}) = 0.994\pi_{CO} + 0.107\pi_{CN}^* + \dots \quad (3.113b)$$

Thus, there is net weakening of conjugative stabilization in this case, as well as net delocalization of pi charge from the CN region into the CO region.

We can also see how polarity effects further quench the conjugative interactions in glyoxal **4**, where the symmetry of $a \rightarrow b^*$ and $b \rightarrow a^*$ delocalizations is restored. In this case, the reduced pi-donor strength of the polarized π_{CO} bond leads to overall weakening of $\pi_{CO}-\pi_{CO}^*$ overlap ($S = 0.1838$) and interaction strength (7.1 kcal mol⁻¹) and a relatively well localized NLMO:

$$\tilde{\pi}_{CO}(\mathbf{4}) = 0.992\pi_{CO} + 0.123\pi_{CO}^* + \dots \quad (3.114)$$

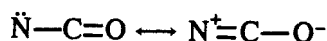
As a result, the CO bond orders in **4** (2.027) are nearly equivalent to those of ethylene, showing that glyoxal is more localized than **1-3** or other molecules to be considered below.

Single-center versus two-center character

To maximize the conjugative interaction with a specified acceptor π_a^* , one could progressively polarize the donor pi moiety until its *entire* amplitude is on the atom adjacent to π_a^* . In this limit, the two-center donor reduces to a one-center *nonbonded* orbital n_b (lone pair), and the donor-acceptor interaction is of $n_b \rightarrow \pi_a^*$ type.

In the limit that nearest-neighbor contributions dominate, such a one-center n_b automatically leads to an approximate $2^{1/2}$ -fold increase in overlap and two-fold increase in interaction energy, compared with a two-center π_b donor. A corresponding enhancement results when the pi-acceptor is reduced from two-center (π_b^*) to one-center (n_b^*) form, i.e., a valence p-type vacancy. Unlike the intrinsically *bi*-directional character of conjugation between two pi bonds ($\pi_a \rightarrow \pi_b^*$, $\pi_b \rightarrow \pi_a^*$), the interactions of a pi bond with a nonbonding center are intrinsically *mono*-directional and lead to uncompensated transfer of pi charge from one moiety to the other.

Such one-center enhancement effects can be illustrated by formamide **5** for $n_b \rightarrow \pi_a^*$ (3.109c) interactions. As shown in Table 3.19, the $n_N \rightarrow \pi_{CO}^*$ interaction of **5** leads to strong conjugative stabilization ($59.8 \text{ kcal mol}^{-1}$) and reduced C—O bond order (1.732), the famous “amide resonance” of peptide chemistry:



The form of the \tilde{n}_N NLMO also reflects the strong conjugative delocalization:

$$\tilde{n}_N(\mathbf{5}) = 0.935n_N + 0.349\pi_{CO}^* + \dots \quad (3.115)$$

As is well known, the intermediate bond orders of such a resonance hybrid correspond to bond lengths (and other bond properties) that are intermediate between the idealized single and double bonds of unconjugated species.

The corresponding enhancements for interactions of $\pi_a \rightarrow n_b^*$ (3.109d) type can be illustrated by vinylborane **6**. The $\pi_{CC} \rightarrow n_B^*$ conjugative stabilization in **6** ($26.2 \text{ kcal mol}^{-1}$) is stronger than corresponding $a \rightarrow b^*$ interactions in **1–3**, but weaker than the $n_N \rightarrow \pi_{CO}^*$ interaction of **5**. Figure 3.39 compares NBO contours of the leading interactions in **5** and **6**, showing the greater strength of conjugation in the former case. The form of the $\tilde{\pi}_{CC}$ NLMO again reflects this conjugation,

$$\tilde{\pi}_{CC}(\mathbf{6}) = 0.967\pi_{CC} + 0.255n_B^* + \dots \quad (3.116)$$

Ionic character

The donor or acceptor strength of a given pi moiety can be further enhanced by giving it net anionic or cationic character. An anionic lone pair, for example, is spatially more diffuse (leading to better overlap and an increased numerator in (3.109c)) and higher in energy (leading to a smaller energy denominator), and is therefore a strongly enhanced Lewis base. A cationic one-center vacancy is correspondingly a greatly strengthened Lewis acid. In either case, the conjugative donor–acceptor interactions will be appreciably stronger than corresponding neutral interactions.

The ionic enhancement effects are illustrated in Table 3.19 by the allyl anion **7** and cation **8** for interaction types (3.102c) and (3.102d), respectively. In both cases

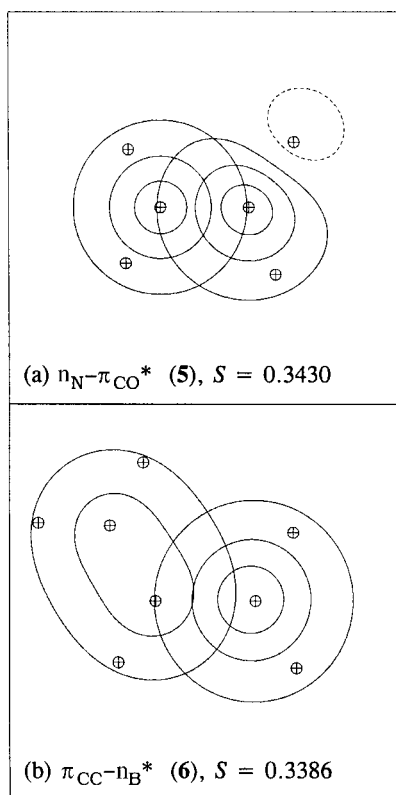


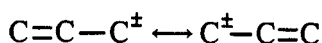
Figure 3.39 Similar to Fig. 3.38, for principal conjugative interactions in (a) formamide, **5**, and (b) vinylborane, **6**.

the conjugative stabilizations are indicated to be extremely large ($>100 \text{ kcal mol}^{-1}$) and the $\tilde{\pi}_{CC}$ NLMOs acquire strong delocalization tails,

$$\tilde{n}_C(\mathbf{7}) = 0.862n_C + 0.497\pi_{CC}^* + \dots \quad (3.117a)$$

$$\tilde{\pi}_{CC}(\mathbf{8}) = 0.865\pi_{CC} + 0.501n_C^* + \dots \quad (3.117b)$$

Indeed, the formal C—C bond orders (~ 1.5) correspond to *equal* weightings of the alternative resonance structures (cf. Example 1.12),



and complete blurring of the distinction between single and double bonds, the characteristic signature of strong resonance. The equilibrium bond lengths and C_{2v} symmetry of these species clearly reflect the strong resonance stabilization.

(We note in passing that open-shell radicals often behave like spin-averaged “hybrids” of corresponding closed-shell anionic and cationic species. For the allyl

radical, for example, the NBOs and NRT weightings for α [majority] spin would resemble those of the allyl anion, whereas those for β [minority] spin resemble those of the allyl cation. Thus, similar NBO overlap-type considerations can be applied separately to α and β spin sets to rationalize qualitative features of radical conjugation.)

Vicinal versus non-vicinal connectivity

To illustrate the importance of vicinal connectivity of conjugating units, we consider two dienes in non-vicinal relationships: 1,5-hexadiene, **9**, and allene, **10**. As shown in Table 3.19, the direct diene conjugations are negligible in both species, on account of spatial separation in **9** and symmetry-imposed orthogonality of the two pi planes in **10**. Consistently with the essential absence of conjugation, the unsaturated C—C bonds of **9** and **10** have calculated bond orders characteristic of ethylene or other unconjugated systems and the $\tilde{\pi}_{CC}$ NLMOs have essentially localized character:

$$\tilde{\pi}_{CC}(\mathbf{9}) = 0.995\pi_{CC} + \dots \quad (3.118a)$$

$$\tilde{\pi}_{CC}(\mathbf{10}) = 0.992\pi_{CC} + \dots \quad (3.118b)$$

Whereas the localized NBO description shows the clear distinction between conjugated and unconjugated double bonds, this distinction is far from obvious in the canonical MO picture. For example, the highest occupied molecular orbitals (HOMOs) are found to have superficially similar “strongly mixed” forms in **1** and **9**:

$$\phi_{\text{HOMO}}(\mathbf{1}) \simeq 0.59p_1 + 0.39p_2 - 0.39p_3 - 0.59p_4 \quad (3.119a)$$

$$\phi_{\text{HOMO}}(\mathbf{9}) \simeq 0.51p_1 + 0.45p_2 + 0.45p_5 + 0.51p_6 \quad (3.119b)$$

whereas the HOMO of **10** appears more localized on the C_1 — C_2 bonding region,

$$\phi_{\text{HOMO}}(\mathbf{10}) \simeq 0.73p_1 + 0.60p_2 \text{ (+ off-axis Hs)} \quad (3.119c)$$

Of course, by suitable comparisons of the energy splittings for higher-lying MOs one can infer that the interactions are actually weaker for **9** than for **1**, and that **9** and **10** are after all the more closely related. However, such qualitative differences in conjugation seem to be displayed much more directly in the localized NBO framework.

Higher networks: cooperative and anticooperative patterns

Even cursory inspection will show that conjugation alters the properties of the participating pi bonds. For example, the vinyl π_{CC} NBO of **6** is not homopolar as in ethylene, but instead becomes rather strongly polarized toward C_2 ,

$$\pi_{CC}(\mathbf{6}) = 0.679p_1 + 0.734p_2 \quad (3.120)$$

so C_2 becomes more nucleophilic while the terminal C_1 gains pi-acceptor capacity (increased π_{CC}^* amplitude). These alterations will in turn affect donor–acceptor interactions with other conjugating groups. Thus, one expects that conjugated pi networks may exhibit strong *nonlinearities*, such that the electronic properties of each pi bond depend sensitively on the number and types of other pi bonds in the network. Depending on the connectivity pattern of the network, the overall stabilization per pi bond may be enhanced (a “cooperative” network) or diminished (an “anticooperative” network) relative to a simple linear (additive) approximation. We now wish to examine larger conjugated network patterns that lead to cooperative or anticooperative stabilization.

Let us first consider the effect of extending the all-*trans* polyene chain from two to five pi bonds in the series **1**, **11**, **15**, **16**. In the chain topology, each interior pi bond participates in *four* donor–acceptor interactions (two each with the pi bonds on the left and right), whereas each terminal pi bond is restricted to *two* such interactions. Thus, each interior pi bond would contribute about *twice* as much conjugative stabilization as a terminal bond, if each donor–acceptor interaction were of equal magnitude. However, as shown in Table 3.19 the individual donor–acceptor interactions actually *increase* toward the interior of the chain (from about 15 kcal mol⁻¹ for terminal sites to ~17 kcal mol⁻¹ for interior sites), so the conjugative stabilization per pi bond is further increased. From the entries in Table 3.19 one can estimate that the conjugative stabilization *per pi bond* increases by 35% for **11**, 57% for **15**, and 72% for **16**, relative to the base diene **1**. The increasing delocalization is also reflected in the form of the most-central $\tilde{\pi}_{CC}$ NLMOs:

$$\tilde{\pi}_{CC}(\mathbf{11}) = 0.959\pi_{CC} + 0.198\pi_{CC'}^* + 0.198\pi_{CC''}^* \quad (3.121a)$$

$$\tilde{\pi}_{CC}(\mathbf{15}) = 0.954\pi_{CC} + 0.200\pi_{CC'}^* + 0.204\pi_{CC''}^* \quad (3.121b)$$

$$\tilde{\pi}_{CC}(\mathbf{16}) = 0.949\pi_{CC} + 0.206\pi_{CC'}^* + 0.206\pi_{CC''}^* \quad (3.121c)$$

(Note that the increment per pi bond approaches constancy for sufficiently long chain length, which is consistent with experimental results.) Such simple counting arguments suggest the considerable thermodynamic advantage of unbranched polyene networks that minimize the number of terminal pi bonds.

Example 3.15

Exercise: Justify the estimate given above for the increased conjugative stabilization (QMRE) in **15** relative to **1**.

Solution: From the entries in Table 3.19 the contributing stabilizations in **1** are (in an obvious notation)

Type	$-\Delta E$ (kcal mol ⁻¹)
$\pi_{1,2} \rightarrow \pi_{3,4}^*$	15.0
$\pi_{3,4} \rightarrow \pi_{1,2}^*$	15.0
Total	30.0

or 15.0 kcal mol⁻¹ per pi bond. For **15** the corresponding stabilizations are

Type	$-\Delta E$ (kcal mol ⁻¹)
$\pi_{1,2} \rightarrow \pi_{3,4}^*$	14.5
$\pi_{3,4} \rightarrow \pi_{1,2}^*$	16.2
$\pi_{3,4} \rightarrow \pi_{5,6}^*$	16.5
$\pi_{5,6} \rightarrow \pi_{3,4}^*$	16.5
$\pi_{5,6} \rightarrow \pi_{7,8}^*$	16.2
$\pi_{7,8} \rightarrow \pi_{5,6}^*$	14.5
Total	94.4

or 23.6 kcal mol⁻¹ per pi bond, 57% greater than the value for **1**.

As a consequence of its asymmetric environment, each terminal π_{CC} NBO is somewhat polarized toward the chain interior, thus building up a slight positive charge at the chain termini. The energetic disadvantage of such polarized end-bonds can be illustrated by comparison of the trienes **11** and **12**. Using the entries of Table 3.19, one can estimate that the conjugative stabilization is 61 kcal mol⁻¹ in **11** but only 47.4 kcal mol⁻¹ in **12**. Only part of this reduction can be attributed to the less favorable *cis*-like vicinal interactions in **1**. The polarized C₃—C₄ bond in **12** must serve as a net donor to both connecting vinyl groups (a “busy donor”), and in this competitive (anticooperative) pattern each donor–acceptor interaction is slightly *weakened* relative to its value in **2**.

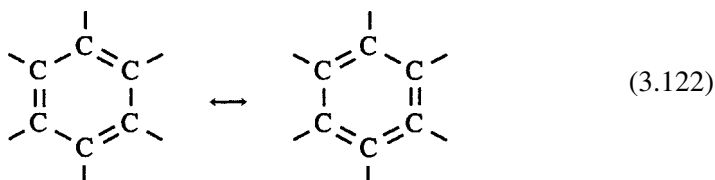
Another such instance of anticooperativity can be seen by comparing **5** with **13**. In the latter case, the two $n \rightarrow \pi_{CO}^*$ interactions make competitive use of the same “busy” nitrogen lone pair, and each such interaction (47.9 kcal mol⁻¹) is thereby weakened relative to the value (59.8 kcal mol⁻¹) in **5**. Similarly, the comparison of vinylborane **6** with divinylborane **14** reveals an anticooperative effect involving competition for the n_B^* pi acceptor, with each $\pi_{CC} \rightarrow n_B^*$ interaction in **14** (24.2 kcal mol⁻¹) being slightly weakened compared with its value in **6** (26.2 kcal mol⁻¹).

We can summarize these considerations by saying that higher-order nonlinear effects generally favor network patterns in which each pi-bond site has balanced or

“closed-CT” character (cf. Section 2.6) with respect to conjugative delocalization in and out of the site. Conversely, end-bonds or other unsymmetric “open-CT” sites that have *unbalanced* donor–acceptor patterns are disfavored by such higher-order nonlinear effects.

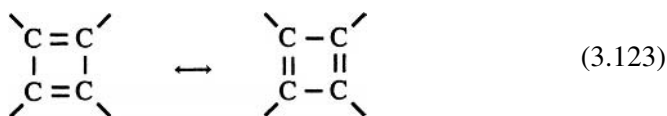
3.3.2 Aromaticity and antiaromaticity

Since its initial discovery by Michael Faraday in 1825,⁵⁸ benzene (C₆H₆) has been recognized as an extraordinary substance. The spectacular properties of benzene and its derivatives (particularly the aniline dyes discovered by W. H. Perkin) initiated dramatic growth of the pharmaceutical, dyestuff, and munitions industries in the mid nineteenth century. The famous puzzle of the chemical structure of benzene was solved in 1865 by August Kekulé in terms of two alternative six-membered-ring formulas:



This “mesomerism” (or “resonance”)⁵⁹ between equivalent Kekulé structures was recognized as the quintessential feature underlying the “aromaticity” of benzene, conferring highly distinctive symmetry, stability, and reactivity patterns.

Superficially, it is also possible to write two equivalent resonance structures for cyclobutadiene (C₄H₄)



and one might suppose that this species is also resonance-stabilized in analogy with (3.122). However, cyclobutadiene appears to be exceptionally *unstable*, and is essentially nonexistent in the high-symmetry D_{4h} form implied by (3.123). The instability of cyclobutadiene is only partially attributable to the angular strain of its sigma-bonding framework, which necessitates considerable bond bending (Section 3.2.7). Rather, the cyclic pi-conjugative pattern in (3.123) appears to be net *destabilizing* even when compared with the non-aromatic *acyclic* species **1** and **2**, and cyclobutadiene is therefore referred to as “antiaromatic.”

Given these surprising experimental facts, it is obviously important to inquire why the cyclic conjugation patterns (3.122) and (3.123) should lead to such diametrically opposite changes in conjugative stability compared with acyclic analogs. A

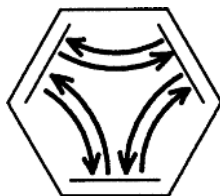
simple answer to this question can be obtained in the framework of Hückel MO theory.⁶⁰ At the Hückel level it can be shown that the highest occupied MOs of a cyclic C_nH_n species are *bonding* (i.e., lower in energy than isolated methynyl fragment pi orbitals) for $4n + 2$ electrons, but degenerate and *nonbonding* for $4n$ electrons. For $n = 1$, this implies that a six-electron species such as (3.122) should be intrinsically favored compared with a four-electron species such as (3.123). The success of the Hückel “ $4n + 2$ Rule” in this case appears to represent a conceptual triumph of MO theory over resonance theory.

In the present section we wish to investigate the differences between aromatic and antiaromatic species from the NBO donor–acceptor perspective. We shall also investigate the “magic of six electrons” by comparing the six-electron cyclopentadienyl anion ($C_5H_5^-$) with the corresponding four-electron cation ($C_5H_5^+$). We also examine other planar six-membered cyclic species such as borazine ($B_3N_3H_6$) and quinone ($C_6O_2H_4$) to determine what (if anything) distinguishes the “degree of aromaticity” in these systems. Direct comparisons with Hückel theory will be presented in the following Section 3.3.3. Figure 3.40 shows the structures and atom numberings for molecules **17–24** to be discussed in this section, while Table 3.21 gives the corresponding NRT bond orders and conjugative stabilizations (cf. Table 3.19).

Benzene

We first consider benzene, **17**, the prototypical aromatic molecule. From the entries in Table 3.21 and comparisons analogous to Example 3.15, one can recognize that conjugative stabilizations in benzene are significantly stronger than those of comparable species in Table 3.19. Thus, on a per-pi-bond basis, the estimated stabilizations in benzene are $40.8 \text{ kcal mol}^{-1}$, more than *three* times those of diene **2** ($12.8 \text{ kcal mol}^{-1}$), *twice* those of the acyclic triene **11** ($20.3 \text{ kcal mol}^{-1}$), and about 58% greater than the most strongly stabilized polyene, **16** ($25.8 \text{ kcal mol}^{-1}$).

The enhanced stabilizations of benzene are apparently due to the unique cyclic conjugative topology in which *all* sites are of closed-CT type. Each site thereby participates in complementary *bi*-directional donor–acceptor interactions,



with no net charge build-up at any site.

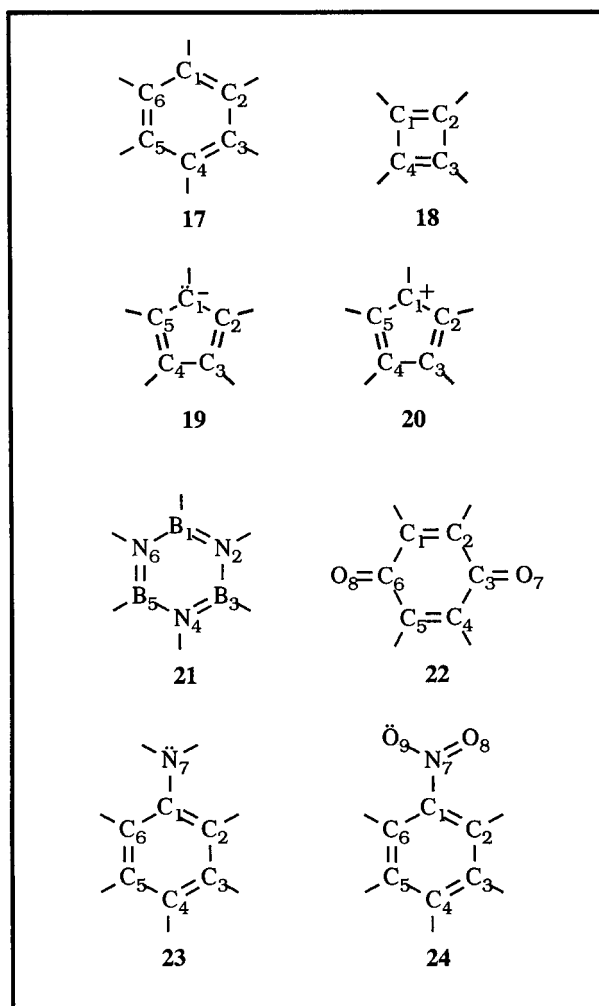


Figure 3.40 Atom numbering and parent Lewis structures for molecules **17–24** (see Table 3.21). Only pi-type lone pairs are shown explicitly.

The vicinal $\pi_a \rightarrow \pi_b^*$ interactions of benzene are depicted in terms of overlapping orbital contours in Fig. 3.41, for comparison with the analogous acyclic diene interaction in Fig. 3.38(b). Unfortunately, for this large change in geometry the overlap integral S does not accurately reflect the increased $|\langle \pi_a | \hat{F} | \pi_b^* \rangle|$ interaction element (from 0.056 a.u. in **2** to 0.067 a.u. in **17**), corresponding to much stronger conjugative stabilization in **17**. However, the greater delocalization of benzene can be clearly seen in the form of its NLMOs,

$$\tilde{\pi}_{CC}(\mathbf{17}) = 0.910\pi_{CC} + 0.288\pi_{CC'}^* + 0.288\pi_{CC''}^* \quad (3.124)$$

compared with those of higher acyclic polyenes (3.121).

Table 3.21. Formal π moieties, NRT bond orders of associated atoms, and conjugative stabilization energies for molecules **17–24** in Fig. 3.40 (B3LYP/6-311++G**//B3LYP/6-31G* level)

Molecule	π Moiety		NRT bond order ^a		Stabilization ^b (kcal mol ⁻¹)	
	a	b	a	b	$\Delta E_{a \rightarrow b^*}$	$\Delta E_{b \rightarrow a^*}$
17	$\pi_{C_1C_2}$	$\pi_{C_3C_4}$	1.498	1.498	-20.4	-20.4
18	$\pi_{C_1C_2}$	$\pi_{C_3C_4}$	1.998	1.998	0.	0.
19	n_{C_1}	$\pi_{C_2C_3}$	—	1.365	-75.9	0.
	$\pi_{C_2C_3}$	$\pi_{C_4C_5}$	1.365	1.365	-17.8	-17.8
20	$n_{C_1}^*$	$\pi_{C_2C_3}$	—	1.886	0.	-78.8
	$\pi_{C_2C_3}$	$\pi_{C_4C_5}$	1.886	1.886	-7.2	-7.2
21	$\pi_{B_1N_2}$	$\pi_{B_3N_4}$	1.380	1.380	-36.8	0. (!)
22	$\pi_{C_1C_2}$	$\pi_{C_3O_7}$	1.891	1.943	-17.8	-6.6
23	n_{N_7}	$\pi_{C_1C_2}$	—	1.429	-24.5	0.
	$\pi_{C_1C_2}$	$\pi_{C_3C_4}$	1.429	1.477	-24.1	-17.3
	$\pi_{C_1C_2}$	$\pi_{C_5C_6}$	1.429	1.480	-16.8	-22.0
	$\pi_{C_3C_4}$	$\pi_{C_5C_6}$	1.477	1.480	-23.1	-16.4
24	n_{O_8}	$\pi_{N_7O_9}$	—	1.511	-162.4	0.
	$\pi_{N_7O_9}$	$\pi_{C_1C_2}$	1.511	1.455	-3.2	-25.5
	$\pi_{C_1C_2}$	$\pi_{C_3C_4}$	1.455	1.482	-17.1	-23.4
	$\pi_{C_1C_2}$	$\pi_{C_5C_6}$	1.455	1.492	-20.7	-20.3
	$\pi_{C_3C_4}$	$\pi_{C_5C_6}$	1.482	1.492	-18.4	-21.3

^a For reference, the C—C bond order in ethylene is 2.027.

^b Entry “0.” corresponds to the quantity being undefined or negligible (less than the printout threshold of 1.0 kcal mol⁻¹).

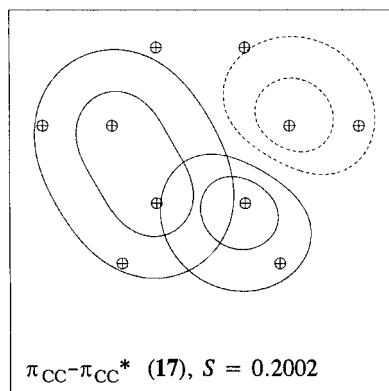


Figure 3.41 Similar to Fig. 3.38, for the principal conjugative interaction in benzene, **17**.

The perturbative estimates of Table 3.21 may be compared with a more direct *variational* estimate of the pi-type non-Lewis correction ($E_{\text{NL}}^{(\pi)}$) to the localized Lewis structure,

$$E_{\text{NL}}^{(\pi)} = E_{\text{total}} - E_{\text{L}}^{(\pi)} \quad (3.125a)$$

where $E_{\text{L}}^{(\pi)}$ is obtained by deleting the nine possible valence pi-type donor–acceptor interactions and thus forcing the three pi bonds to remain doubly occupied and localized.⁶¹ In the equilibrium geometry $E_{\text{NL}}^{(\pi)}$ is found to be

$$E_{\text{NL}}^{(\pi)}/3 = -51.7 \text{ kcal mol}^{-1} \quad (3.125b)$$

which is somewhat greater than the second-order perturbative estimate cited above and indicative of the importance of higher-order perturbative corrections for the strong delocalization effects in this system.

To see the effect of $E_{\text{NL}}^{(\pi)}$ on molecular geometry, we can examine $E_{\text{L}}^{(\pi)}(\Delta R)$ and $E_{\text{total}}(\Delta R)$ along a “distortion coordinate”

$$\Delta R = R_{\text{s}} - R_{\text{d}} = R_{2,3} - R_{1,2} \quad (3.126)$$

which measures the difference between formal single- and double-bond lengths in the distortion toward localized “cyclohexatriene” ($\text{D}_{3\text{h}}$) geometry. (We hold $R_{\text{s}} + R_{\text{d}} = 2.80 \text{ \AA}$, $R_{\text{CH}} = 1.09 \text{ \AA}$, and all bond angles at 120° during this distortion.) Figure 3.42 compares the localized $E_{\text{L}}^{(\pi)}(\Delta R)$ with the full $E_{\text{total}}(\Delta R)$ for distortions up to $|\Delta R| = 0.5 \text{ \AA}$, and Fig. 3.43 shows the behavior of $E_{\text{NL}}^{(\pi)}(\Delta R)$ in the same range. As expected, $E_{\text{total}}(\Delta R)$ is minimized in the undistorted $\text{D}_{6\text{h}}$ geometry at $\Delta R = 0$, whereas the localized $E_{\text{L}}^{(\pi)}(\Delta R)$ exhibits minima at $|\Delta R| \simeq 0.24 \text{ \AA}$, which is close to the value expected for idealized single and double bonds of un-conjugated cyclohexatriene.

The difference in these geometrical preferences is evidently provided by $E_{\text{NL}}^{(\pi)}$, which is most strongly stabilizing in the symmetric $\text{D}_{6\text{h}}$ geometry. Figure 3.43 also includes the corresponding values of $E_{\text{NL}}^{(\pi)}$ for *cis*-butadiene (**2**, “x”), showing that the conjugative delocalization is weaker (but non-zero!) in the acyclic case, insufficient to symmetrize the geometry as in **17**. The behavior shown in Fig. 3.42 is fully in accord with the classic concept of resonance stabilization of the symmetric $\text{D}_{6\text{h}}$ geometry of benzene. However, Fig. 3.43 also emphasizes that conjugative stabilization is appreciable even in highly distorted benzene geometries (e.g., $E_{\text{NL}}^{(\pi)} \simeq -30 \text{ kcal mol}^{-1}$ at $\Delta R = 0.5 \text{ \AA}$).

Cyclobutadiene

In contrast to benzene, the pi-conjugative stabilizations of $\text{D}_{4\text{h}}$ -symmetric cyclobutadiene, **18**, are found to be exactly *zero*. The absence of conjugative stabilization may also be judged from the $\pi_{\text{a}} - \pi_{\text{b}}^*$ orbital contours in Fig. 3.44. Indeed, it is

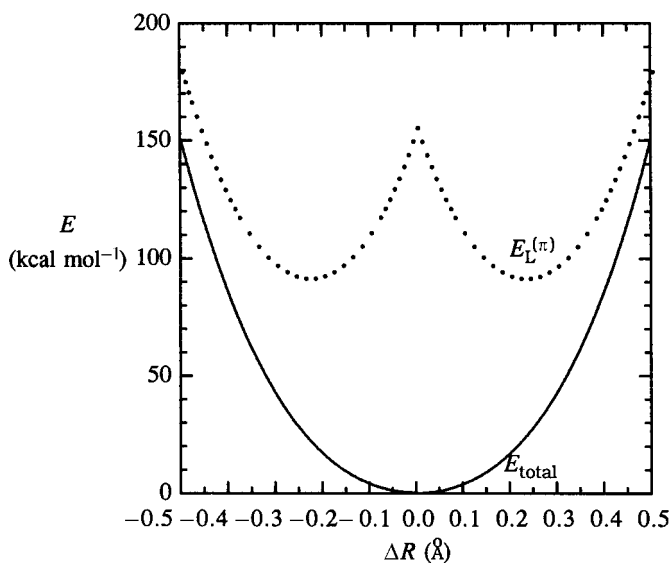


Figure 3.42 Potential-energy curves for benzene (**17**), comparing the total energy (E_{total} , solid curve) with the energy of the idealized single Lewis structure ($E_{\text{L}}^{(\pi)}$, dotted curve) along a D_{3h} distortion coordinate $\Delta R = R_{2,3} - R_{1,2}$ that lowers the D_{6h} symmetry to “cyclohexatriene” form.

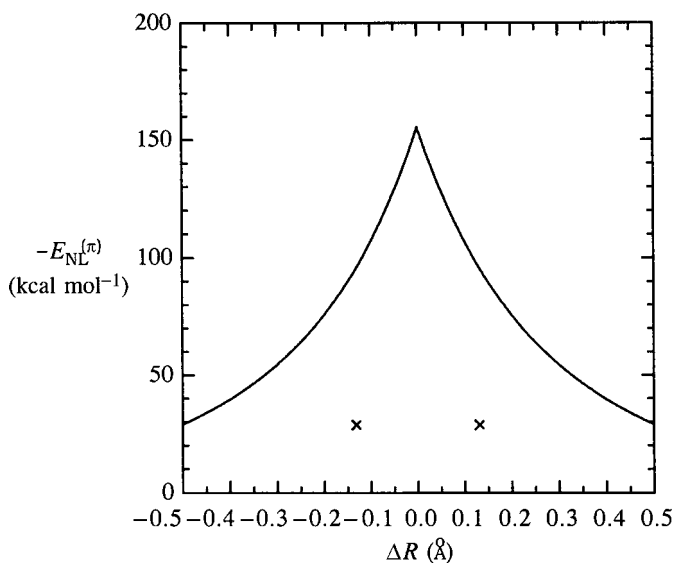


Figure 3.43 The pi-conjugative non-Lewis energy ($E_{\text{NL}}^{(\pi)}$) for benzene (**17**) along a distortion coordinate (cf. Fig. 3.42). Corresponding values for *cis*-butadiene (**2**, crosses) are shown for comparison. (The cusp-like behavior arises because $E_{\text{NL}}^{(\pi)}$ is defined with respect to a different idealized Lewis structure on each side of $\Delta R = 0$.)

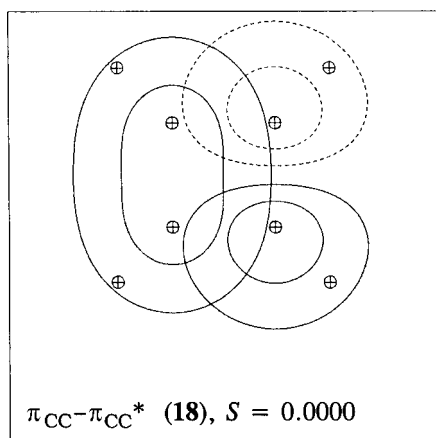


Figure 3.44 Similar to Fig. 3.38, for the principal conjugative interaction in cyclobutadiene, **18**.

obvious by symmetry that apolar π_a and π_b^* NBOs cannot have *any* stabilizing donor–acceptor interactions in the parallel geometry of **18**, and thus **18** is uniquely *disfavored* compared with alternative planar diene geometries. This simple distinction in NBO donor–acceptor interactions accounts quite directly for the unique “anti”aromatic properties of cyclobutadiene **18** compared with benzene **17** and other conjugated species.

To achieve non-zero $\pi_a - \pi_b^*$ conjugation, the pi NBOs of **18** may polarize in opposite directions, leading to a wavefunction of lower symmetry than the nuclear framework. Alternatively, the nuclear framework may distort to diamond-like D_{2h} geometry. However, each such distortion destabilizes what is already a highly unfavorable Lewis-structure wavefunction, so cyclobutadiene is expected to remain highly destabilized relative to other possible polyene topologies.

Whereas the NLMOs of **18** become completely localized (in accordance with the absence of conjugative stabilization), the canonical MOs remain highly mixed, providing no real indication of the dramatic change of conjugation compared with **17**. Thus, the HOMOs of **17** and **18** are

$$\begin{aligned} \phi_{\text{HOMO}}(\mathbf{17}) = & 0.58p_1 + 0.29p_2 - 0.29p_3 - 0.58p_4 \\ & - 0.29p_5 + 0.29p_6 \end{aligned} \quad (3.127a)$$

$$\phi_{\text{HOMO}}(\mathbf{18}) = -0.50p_1 - 0.50p_2 + 0.50p_3 + 0.50p_4 \quad (3.127b)$$

both of which are apparently indicative of the “delocalized” character of the pi-bonding. For **18** such HOMO delocalization is wholly illusory.

The cyclopentadienyl anion and cation

To determine the distinctions (if any) between conjugative donor–acceptor interactions involving six and those involving four pi electrons, we now examine the cyclopentadienyl anion **19** and cation **20**.

As shown in Table 3.21, the leading $n \rightarrow \pi^*$ versus $\pi \rightarrow n^*$ delocalizations of these species are rather similar: 76 versus 79 kcal mol⁻¹. The pi NBOs of **20** are strongly polarized toward the ionic nonbonding center,

$$\pi_{\text{CC}}(\mathbf{20}) = 0.77p_2 + 0.64p_3 \quad (3.128)$$

thus weakening their mutual conjugation across the connecting C₃—C₄ single bond. Owing to the net ionic charge, the conjugative donor–acceptor interactions are relatively strong in *both* species, paralleling the behavior in the acyclic species **7** and **8**. One can also recognize that the conjugative effects in the dienes **19** and **20** are somewhat weakened compared with those in the corresponding allylic species **7** and **8**, due to anticooperative competition for the “busy” n_C or n_C* (as discussed in Section 3.3.1). In all these respects, the six-electron (**19**) and four-electron (**20**) cyclic species exhibit conjugative patterns that are “as expected,” with no sharp distinction to be drawn between the two cases. Certainly, **20** benefits from significant conjugative stabilization and therefore cannot be considered “antiaromatic” in the same sense as cyclobutadiene **18**.

The most conspicuous difference between anionic and cationic species involves their structural symmetry and bond orders. The anion **19** achieves high-symmetry D_{5h} geometry with equal weightings of the five leading resonance structures and equivalent C—C bond orders (1.365), whereas the cation is of C_{2v} symmetry, with relatively high bond order (1.886) in the two formal pi bonds of the leading resonance structure. The dissimilar conjugative effects on geometry can be quantified in terms of variations in $E_{\text{L}}^{(\pi)}(\Delta R)$ and $E_{\text{total}}(\Delta R)$ along a model distortion coordinate for each species, similar to Fig. 3.42 for benzene. Figure 3.45 compares such C_{2v} distortion profiles for the cyclopentadienyl anion and cation,⁶² showing that the $E_{\text{NL}}^{(\pi)}$ delocalization is sufficient to stabilize the undistorted D_{5h} geometry in the former case but not in the latter.

Despite the conspicuously lower symmetry of the four-electron cyclopentadienyl cation, one can judge from comparison of Fig. 3.45(b) with Figs. 3.42 and 3.45(a) that the similarities to the six-electron aromatic species **17** and **19** are more striking than the differences. In each case, strong conjugative stabilizations (>100 kcal mol⁻¹ near equilibrium) reduce the equilibrium distortion from symmetric geometry (e.g., from $\Delta R = 0.24$ to $\Delta R = 0.16$ for **20**, or from 0.24 to 0.00 for **17**). In fact, one can estimate from Fig. 3.45(b) that strengthening the conjugative interactions in C₅H₅⁺ by only 10%–15% would suffice to overcome the small

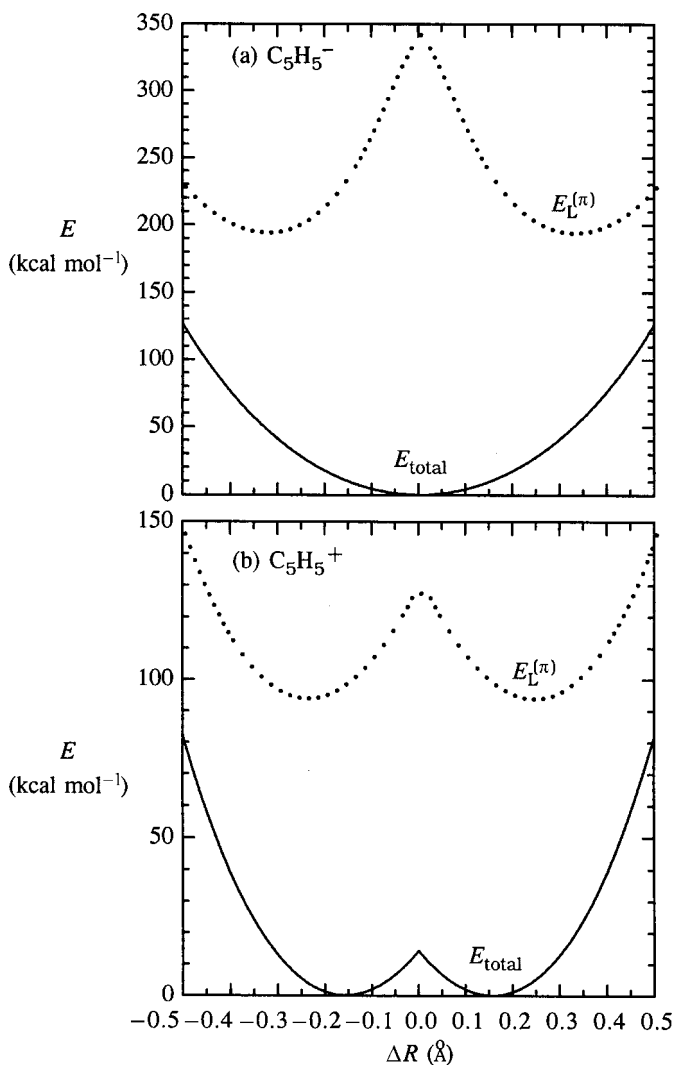


Figure 3.45 Similar to Fig. 3.42, for C_{2v} distortion of cyclopentadienyl (a) anion, **19**, and (b) cation, **20**, from idealized D_{5h} symmetry (note 62).

barrier to symmetric D_{5h} geometry, making $C_5H_5^+$ appear as “aromatic” as **17** or **19**. Thus, the conjugative stabilizations of the four-electron species **20** are only slightly less impressive than those of **17** or **19**, and one sees no real parallel to the antiaromatic species **18**, where such stabilizations are entirely absent.

Borazine

Borazine, **21**, is sometimes called “inorganic benzene.” Like benzene, it achieves a high-symmetry D_{6h} equilibrium structure with equivalent NRT bond orders (1.380)

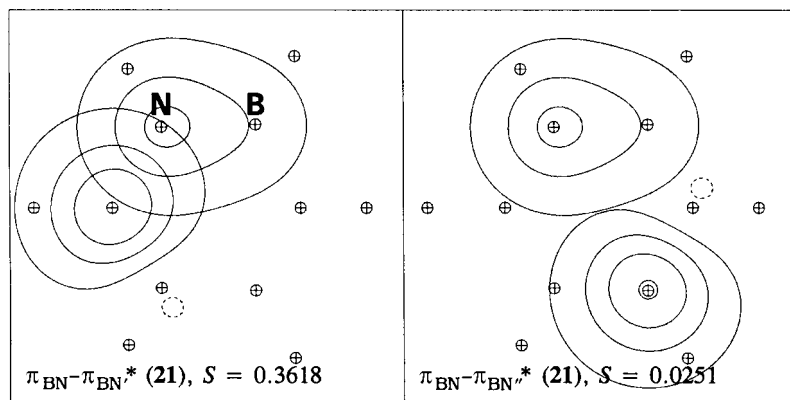


Figure 3.46 Similar to Fig. 3.38, for principal $\pi_{\text{BN}} \rightarrow \pi_{\text{BN}}^*$ conjugative interactions of borazine, **21**, (a) at the N end of π_{BN} and (b) at the B end of π_{BN} .

at each B—N bond. However, unlike benzene the pi NBOs are strongly polarized toward the more electronegative N atom,

$$\pi_{\text{BN}} = 0.49p_{\text{B}} + 0.87p_{\text{N}} \quad (3.129)$$

and the complementary $\pi_{\text{a}} \rightarrow \pi_{\text{b}}^*$ and $\pi_{\text{b}} \rightarrow \pi_{\text{a}}^*$ interactions between any pair of pi bonds are far from equivalent, as shown in the overlap contours of Fig. 3.46.

As shown in Table 3.21, the stabilization corresponding to Fig. 3.46(a) ($36.8 \text{ kcal mol}^{-1}$) is nearly *twice* that of benzene ($20.4 \text{ kcal mol}^{-1}$), but the complementary interaction corresponding to Fig. 3.46(b) is essentially “switched off” (less than 1 kcal mol^{-1}). Thus, borazine has a strong *mono-directional* cyclic pattern of conjugations that is quite unlike that of benzene.

The strong asymmetry of π_{BN} conjugations can also be seen clearly in the form of the borazine NLMOs,

$$\tilde{\pi}_{\text{BN}}(\mathbf{21}) = 0.956\pi_{\text{BN}} + 0.280\pi_{\text{BN}'}^* + 0.080\pi_{\text{BN}''}^* \quad (3.130)$$

compared with (3.124) for benzene. Thus, while the magnitude of total conjugative stabilization in borazine is comparable to that in benzene, the *pattern* of individual donor–acceptor interactions is quite distinct. Borazine therefore deserves to be recognized as having a distinctive “type” of aromaticity compared with benzene, due to the rectified character of its donor–acceptor delocalizations.

Quinone

Quinone, **22**, represents a six-membered carbon ring system with a conjugation pattern quite unlike that of benzene. As shown by its leading Lewis structure (of

high NRT weighting: 59.9%), the two pi bonds of the carbocyclic ring are in unfavorable parallel geometry (cf. cyclobutadiene, **18**) and thus experience *no* mutual conjugative stabilization from one another. Instead, each π_{CC} is strongly conjugated (17.8 kcal mol⁻¹) to the exocyclic carbonyl π_{CO}^* (in a manner somewhat similar to Fig. 3.38(c)), while the complementary $\pi_{CO} \rightarrow \pi_{CC}^*$ interaction is much weaker (6.6 kcal mol⁻¹). Thus, the four strong $\pi_{CC} \rightarrow \pi_{CO}^*$ interactions of quinone all tend to delocalize pi charge *out* of the ring to the exocyclic carbonyl groups, in contrast to a benzene-like pattern. The short C₂—C₃ and C₅—C₆ bond lengths and high NRT bond orders (1.891) confirm that there is no vestige of benzene-like cyclic conjugation in this case.

The two $\tilde{\pi}_{CC}$ NLMOs also exhibit the conjugation to the exocyclic carbonyl groups,

$$\tilde{\pi}_{CC}(\mathbf{22}) = 0.960\pi_{CC} + 0.192\pi_{CO}^* + 0.192\pi_{CO''}^* \quad (3.131)$$

with no trace of conjugation between the two ring C=C bonds. In contrast, the highest π -type canonical MO,

$$\phi_{26}(\mathbf{22}) = -0.50p_2 - 0.50p_3 + 0.50p_5 + 0.50p_6 \quad (3.132)$$

superficially suggests the occurrence of strong mixing of ring p_C orbitals (and no involvement of carbonyl orbitals), a quite misleading picture of the actual conjugative stabilization.

Aniline and nitrobenzene: electrophilic substitution reactivity

We briefly consider the effect of pi-donor or pi-acceptor substituents on aromatic conjugation patterns for two representative examples; aniline (**23**) and nitrobenzene (**24**). The leading NBO interactions between ring and substituent in these species are depicted in Fig. 3.47.

As shown in Table 3.21, the principal conjugative stabilization in aniline, **23**, linking the exocyclic substituent with the ring pi system is the $n_N \rightarrow \pi_{CC}^*$ interaction (24.5 kcal mol⁻¹) depicted in Fig. 3.47(a). This interaction donates pi density from the amine group into the ring pi system (without a compensating donor-acceptor interaction in the opposite direction) and is hence “activating” with respect to electrophilic attack on the aromatic ring system. Furthermore, one can judge from Fig. 3.47(a) that the vicinal C₁—C₂ pi bond *polarizes* slightly from C₁ toward C₂, so that its antibond has higher amplitude at the C₁ position and is thereby better able to conjugate with the exocyclic pi donor. This in turn induces a chain of repolarizations of the remaining pi bonds to maximize their mutual conjugative

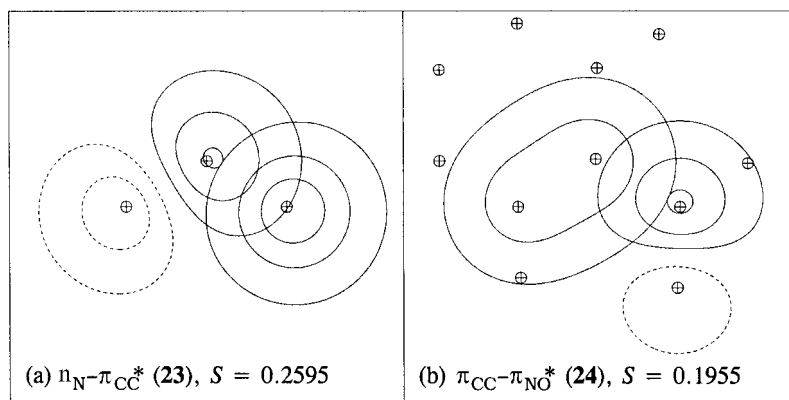


Figure 3.47 Similar to Fig. 3.38, for principal ring-substituent conjugative interactions of (a) aniline, **23**, and (b) nitrobenzene, **24**. The atoms C₁, C₂, and N₇ are in the same relative positions in the two diagrams (note that aniline is nonplanar).

interactions, as can be seen in the forms of the NBOs:

$$\pi_{\text{C}_1\text{C}_2} = 0.678p_1 + 0.735p_2 \quad (3.133a)$$

$$\pi_{\text{C}_3\text{C}_4} = 0.690p_3 + 0.724p_4 \quad (3.133b)$$

$$\pi_{\text{C}_5\text{C}_6} = 0.685p_5 + 0.728p_6 \quad (3.133c)$$

As a result of these substituent-induced polarizations, the complementary conjugative interactions at each ring site become somewhat *imbalanced* (so that, e.g., the donor-acceptor interaction from C₃—C₄ to C₅—C₆ is 23.1 kcal mol⁻¹, but that in the opposite direction is only 16.4 kcal mol⁻¹). From the polarization pattern in (3.133) one can recognize that excess pi density is accumulated at the *ortho* (C₂, C₆) and *para* (C₄) positions, and thus that the reactivity of these sites should *increase* with respect to electrophilic attack. This is in accord with the well-known “*o*, *p*-directing” effect of amino substitution in electrophilic aromatic substitution reactions. Although the localized NBO analysis has been carried out for the specific Kekulé structure of aniline shown in Fig. 3.40, it is easy to verify that exactly the same physical conclusions are drawn if one starts from the alternative Kekulé structure.

Nitrobenzene, **24**, illustrates the opposite case of a strong pi-acceptor substituent. In this case the exocyclic π_{NO} NBO is strongly polarized toward O (away from the ring)

$$\pi_{\text{NO}} = 0.629p_{\text{N}} + 0.778p_{\text{O}} \quad (3.134)$$

As a result, the vicinal $\pi_{\text{NO}} \rightarrow \pi_{\text{CC}}^*$ interaction is relatively weak (3.2 kcal mol⁻¹) whereas the complementary $\pi_{\text{CC}} \rightarrow \pi_{\text{NO}}^*$ interaction depicted in Fig. 3.47(b) is

quite strong ($25.5 \text{ kcal mol}^{-1}$), transferring net pi charge from the ring to the nitro substituent and thus *deactivating* the ring with respect to electrophilic attack. The asymmetry of donor–acceptor interactions with the substituent again induces a chain of polarization changes in the ring pi NBOs, namely

$$\pi_{C_1C_2} = 0.741p_1 + 0.672p_2 \quad (3.134a)$$

$$\pi_{C_3C_4} = 0.716p_3 + 0.698p_4 \quad (3.134b)$$

$$\pi_{C_5C_6} = 0.718p_5 + 0.696p_6 \quad (3.134c)$$

These polarizations are seen to be in the *opposite* direction to those in aniline (3.133), so that higher pi density remains at the C_1 (junction) and C_3 and C_5 (*meta*) positions. These polarity shifts are again consistent with the well-known “*m*-directing” effect of nitro substituents in electrophilic aromatic substitution reactions, and the results are again quite independent of which starting Kekulé structure is selected for the localized analysis.⁶³

The predicted patterns of NBO donor–acceptor interactions can of course be associated (cf. the discussion surrounding (3.110)) with corresponding resonance diagrams for the substituent-induced conjugation. The localized NBO description of substituent directing/activating effects is thus perfectly equivalent to standard textbook discussions in terms of resonance structures (or “electron pushing”), but with considerable additional quantitative detail.

3.3.3 Comparison with the Hückel picture

In the early years of quantum theory, Hückel developed a remarkably simple form of MO theory that retains great influence on the concepts of organic chemistry to this day. The Hückel molecular orbital (HMO) picture for a planar conjugated pi network is based on the assumption of a minimal basis of orthonormal p-type AOs $\{p_r\}$ and an effective pi-Hamiltonian $\hat{h}^{(\text{eff})}$ with matrix elements

$$h_{rs} = \langle p_r | \hat{h}^{(\text{eff})} | p_s \rangle \quad (3.135)$$

between atomic sites r and s . Hückel assumed a constant diagonal value (α) at each site and non-zero coupling (β) only for adjacent sites (i.e., those connected by a sigma bond). This leads to the simple expression for HMO matrix elements

$$h_{rs} = \alpha \delta_{rs} + \beta \tau_{rs} \quad (3.136)$$

where δ_{rs} is the usual Kronecker-delta symbol and τ_{rs} is an analogous “adjacency symbol,”

$$\tau_{rs} = \begin{cases} 1 & \text{if } r \text{ and } s \text{ are bonded} \\ 0 & \text{otherwise} \end{cases} \quad (3.137)$$

With these approximations the secular determinant for the energy eigenvalue ϵ is reduced to sparse banded form; for example, for a linear polyene

$$\begin{vmatrix} \alpha - \epsilon & \beta & 0 & \dots & 0 \\ \beta & \alpha - \epsilon & \beta & \dots & 0 \\ 0 & \beta & \alpha - \epsilon & \dots & 0 \\ \vdots & \vdots & \vdots & & \vdots \\ 0 & 0 & 0 & \dots & \alpha - \epsilon \end{vmatrix} = 0 \quad (3.138)$$

By dividing each matrix element by β (i.e., expressing all matrix elements in units of β) and defining the unknown x as

$$x = \frac{\alpha - \epsilon}{\beta} \quad (3.139)$$

the secular determinantal polynomial can be written as

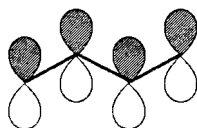
$$D(x) = \begin{vmatrix} x & 1 & 0 & \dots & 0 \\ 1 & x & 1 & \dots & 0 \\ 0 & 1 & x & \dots & 0 \\ \vdots & \vdots & \vdots & & \vdots \\ 0 & 0 & 0 & \dots & x \end{vmatrix} = 0 \quad (3.140)$$

with site diagonals “ x ” and non-vanishing couplings “1” only for connected sites of the network. The ultrasimplified form (3.139) allows exact analytic solutions for x_i and Hückel eigenvalues ϵ_i in many important cases.⁶⁴

Example 3.16

Exercise: Find the Hückel pi-orbital energies ϵ_i for 1,3-butadiene.

Solution: For this linear four-site problem,



the HMO secular determinant (3.140) is

$$D(x) = \begin{vmatrix} x & 1 & 0 & 0 \\ 1 & x & 1 & 0 \\ 0 & 1 & x & 1 \\ 0 & 0 & 1 & x \end{vmatrix} = 0$$

Laplace expansion of the determinant gives

$$D(x) = x \begin{vmatrix} x & 1 & 0 \\ 1 & x & 1 \\ 0 & 1 & x \end{vmatrix} - \begin{vmatrix} 1 & 0 & 0 \\ 1 & x & 1 \\ 0 & 1 & x \end{vmatrix} \\ = x^4 - 3x^2 + 1 = 0$$

Setting $y = x^2$ and solving the quadratic equation

$$y^2 - 3y + 1 = 0$$

leads to

$$y = x^2 = \frac{3 \pm 5^{1/2}}{2}$$

or, from (3.138),

$$\epsilon = \alpha \pm \beta[(3 \pm 5^{-1/2})/2]^{1/2}$$

The HMO orbital energies are therefore

$$\epsilon_1 = \alpha + 1.6180\beta$$

$$\epsilon_2 = \alpha + 0.6180\beta$$

$$\epsilon_3 = \alpha - 0.6180\beta$$

$$\epsilon_4 = \alpha - 1.6180\beta$$

Cyclic polyenes

For the special case of cyclic polyenes, $(\text{CH})_n$, Frost and Musulin⁶⁵ obtained the general “circle mnemonic” for the HMO eigenvalues in the form

$$\epsilon_j = \alpha + 2\beta \cos(2\pi j/n), \quad j = 1, \dots, n \quad (3.141)$$

According to this expression, the eigenvalues ϵ_j can be pictured as lying on the periphery of a circle, centered at α and of radius 2β , such that the lowest level lies at the bottom of the circle, and successive levels are located at successive angular increments $2\pi/n$ (radians) around the circle. This is illustrated in Fig. 3.48 for benzene, $n = 6$.

The LCAO-MO expressions corresponding to the HMO orbital energies (3.141) for the pi MOs ϕ_j can also be obtained, on the basis of symmetry properties of the cyclic C_n topology.⁶⁶ For benzene, for example, the results are (renumbered in

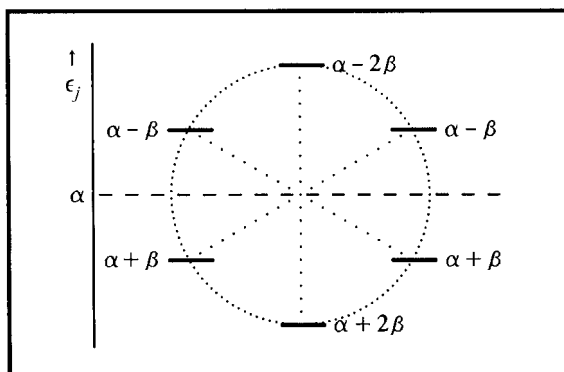


Figure 3.48 The Frost–Musulin circle mnemonic (Eq. (3.141)) for HMO orbital energies ϵ_j of benzene, $n = 6$.

order of ascending energy)

$$\epsilon_1 = \alpha + 2\beta, \quad \phi_1 = 6^{-1/2}(p_1 + p_2 + p_3 + p_4 + p_5 + p_6) \quad (3.142a)$$

$$\epsilon_2 = \alpha + \beta, \quad \phi_2 = 12^{-1/2}(2p_1 + p_2 - p_3 - 2p_4 - p_5 + p_6) \quad (3.142b)$$

$$\epsilon_3 = \alpha + \beta, \quad \phi_3 = 2^{-1}(p_2 + p_3 - p_5 - p_6) \quad (3.142c)$$

$$\epsilon_4 = \alpha - \beta, \quad \phi_4 = 2^{-1}(p_2 - p_3 + p_5 - p_6) \quad (3.142d)$$

$$\epsilon_5 = \alpha - \beta, \quad \phi_5 = 12^{-1/2}(2p_1 - p_2 - p_3 + 2p_4 - p_5 - p_6) \quad (3.142e)$$

$$\epsilon_6 = \alpha - 2\beta, \quad \phi_6 = 6^{-1/2}(p_1 - p_2 + p_3 - p_4 + p_5 - p_6) \quad (3.142f)$$

(Note that, for the degenerate energy levels (3.142b) and (3.142c) or (3.142d) and (3.142e), any linear combination of the chosen ϕ_2 and ϕ_3 or ϕ_4 and ϕ_5 would be equally valid.)

Simple HMO expressions such as (3.142a)–(3.142f) are remarkably effective at representing the qualitative features of conjugated polyenes. Nevertheless, the entire treatment rests on only the two empirical Hückel parameters α and β of (3.136), which cannot be expected to represent subtleties of pi conjugation and dependencies on geometry beyond the level of elementary topology (i.e., atom connectivity). For example, the *ab initio* valence pi-orbital energies of benzene are found to be

$$\begin{aligned} \epsilon_1 &= -0.3725, & \epsilon_2 &= \epsilon_3 = -0.2599, \\ \epsilon_4 &= \epsilon_5 = -0.0180, & \epsilon_6 &= 0.1239 \end{aligned} \quad (3.143)$$

These exhibit the expected degeneracies but not the expected energy splittings of the HMO energy-level pattern in Fig. 3.48. For example, if one takes

$$\alpha = (\epsilon_1 + \epsilon_6)/2 = -0.1243, \quad \beta = (\epsilon_6 - \epsilon_1)/4 = -0.1241 \quad (3.144)$$

to “fit” α and β to the upper and lower non-degenerate levels, one would predict

$$\epsilon_2(\text{predict}) = \alpha + \beta = -0.2484 \quad (\text{cf. } \epsilon_2(\text{actual}) = -0.2599) \quad (3.145a)$$

$$\epsilon_4(\text{predict}) = \alpha - \beta = -0.0002 \quad (\text{cf. } \epsilon_4(\text{actual}) = -0.0180) \quad (3.145b)$$

in appreciable disagreement ($\Delta\epsilon_2 = 7.2 \text{ kcal mol}^{-1}$, $\Delta\epsilon_4 = 11.2 \text{ kcal mol}^{-1}$) with the actual levels. On the other hand, if we fit α and β to the HOMO–LUMO gap

$$\alpha = (\epsilon_4 + \epsilon_2)/2 = -0.1390, \quad \beta = (\epsilon_4 - \epsilon_2)/2 = -0.1210 \quad (3.146)$$

the predicted non-degenerate levels are

$$\epsilon_1(\text{predict}) = \alpha + 2\beta = -0.3810 \quad (\text{cf. } \epsilon_1(\text{actual}) = -0.3725) \quad (3.147a)$$

$$\epsilon_6(\text{predict}) = \alpha - 2\beta = 0.1030 \quad (\text{cf. } \epsilon_6(\text{actual}) = 0.1239) \quad (3.147b)$$

in error by 5.3 and 13.1 kcal mol^{-1} , respectively. Thus, the HMO pattern in Fig. 3.48 is only a qualitatively correct approximation to the actual pi-orbital energy levels.

Ab initio Hückel parameters

We can obtain a more direct comparison of the *ab initio* and Hückel quantities in terms of the valence pi block of the NAO Fock matrix (or Kohn–Sham matrix) $\mathbf{F}^{(\text{NAO})}$, which provides the direct *ab initio* counterpart of (3.155):

$$\mathbf{F}^{(\text{NAO})} = \begin{pmatrix} -0.1102 & -0.1391 & 0.0104 & -0.0031 & 0.0104 & -0.1391 \\ -0.1391 & -0.1102 & -0.1391 & 0.0104 & -0.0031 & 0.0104 \\ 0.0104 & -0.1391 & -0.1102 & -0.1391 & 0.0104 & -0.0031 \\ -0.0031 & 0.0104 & -0.1391 & -0.1102 & -0.1391 & 0.0104 \\ 0.0104 & -0.0031 & 0.0104 & -0.1391 & -0.1102 & -0.1391 \\ -0.1391 & 0.0104 & -0.0031 & 0.0104 & -0.1391 & -0.1102 \end{pmatrix} \quad (3.148)$$

From the diagonal and adjacent off-diagonal elements of $\mathbf{F}^{(\text{NAO})}$ one can see that the *ab initio* α and β values are⁶⁷

$$\begin{aligned} \alpha &= -0.1102 \text{ a.u.} = -69.2 \text{ kcal mol}^{-1} \\ \beta &= -0.1391 \text{ a.u.} = -87.3 \text{ kcal mol}^{-1} \end{aligned} \quad (3.149)$$

Diagonalization of the $6 \times 6 \mathbf{F}^{(\text{NAO})}$ (3.148) leads to orbital energies

$$\mathbf{F}^{(\text{NAO})}: \quad -0.3707, \quad -0.2566 [2], \quad 0.0154 [2], \quad 0.1919 \quad (3.150)$$

that indeed agree closely with the accurate values (3.143) for the occupied levels, namely

$$\Delta\epsilon_1 = 1.1 \text{ kcal mol}^{-1}, \quad \Delta\epsilon_2 = 2.1 \text{ kcal mol}^{-1} \quad (\text{occupied}) \quad (3.151a)$$

but place the virtual levels far too high in energy:

$$\Delta\epsilon_4 = 21.0 \text{ kcal mol}^{-1}, \quad \Delta\epsilon_6 = 42.7 \text{ kcal mol}^{-1} \quad (\text{virtual}) \quad (3.151b)$$

It is evident from (3.15b) that the virtual MOs include important contributions from Rydberg $3p_z, 4p_z, \dots$ NAOs from beyond the formal valence shell. However, these virtual MOs make no contribution to the wavefunction or any physical properties of the molecule. We shall therefore concentrate on the occupied MOs (3.151a) for which the HMO minimal-basis assumption appears rather satisfactory.

It is evident from (3.148) that the *ab initio* valence pi $\mathbf{F}^{(\text{NAO})}$ has the banded structure

$$\mathbf{F}^{(\text{NAO})} = \begin{pmatrix} \alpha & \beta & \beta' & \beta'' & \beta' & \beta \\ \beta & \alpha & \beta & \beta' & \beta'' & \beta' \\ \beta' & \beta & \alpha & \beta & \beta' & \beta'' \\ \beta'' & \beta' & \beta & \alpha & \beta & \beta' \\ \beta' & \beta'' & \beta' & \beta & \alpha & \beta \\ \beta & \beta' & \beta'' & \beta' & \beta & \alpha \end{pmatrix} \quad (3.152)$$

with

$$\beta' = 0.0104 \text{ a.u.} = 6.5 \text{ kcal mol}^{-1}, \quad \beta'' = -0.0031 \text{ a.u.} = -1.9 \text{ kcal mol}^{-1} \quad (3.153)$$

The Hückel approximation (3.136) is equivalent to neglect of β' and β'' (the “tight-binding” approximation), leading to the simpler Hückel-type matrix $\mathbf{h}^{(\text{HMO})}$:

$$\mathbf{h}^{(\text{HMO})} = \begin{pmatrix} -0.1102 & -0.1391 & 0.0000 & 0.0000 & 0.0000 & -0.1391 \\ -0.1391 & -0.1102 & -0.1391 & 0.0000 & 0.0000 & 0.0000 \\ 0.0000 & -0.1391 & -0.1102 & -0.1391 & 0.0000 & 0.0000 \\ 0.0000 & 0.0000 & -0.1391 & -0.1102 & -0.1391 & 0.0000 \\ 0.0000 & 0.0000 & 0.0000 & -0.1391 & -0.1102 & -0.1391 \\ -0.1391 & 0.0000 & 0.0000 & 0.0000 & -0.1391 & -0.1102 \end{pmatrix} \quad (3.154)$$

with eigenvalues

$$\mathbf{h}^{(\text{HMO})}: -0.3884, \quad -0.2493 [2], \quad 0.0289 [2], \quad 0.1680 \quad (3.155)$$

Comparison of these Hückel-type estimates with the full $\mathbf{F}^{(\text{NAO})}$ values of (3.150) shows that neglect of β' and β'' leads to errors in the occupied energy levels,

$$\Delta\epsilon_1 = 11.1 \text{ kcal mol}^{-1}, \quad \Delta\epsilon_2 = 4.6 \text{ kcal mol}^{-1} \quad (3.156)$$

that are 2–10 times larger than those in (3.151a). Thus, the errors inherent in the tight-binding approximation (3.136) are much more severe than those associated with the assumption (3.135) of an effective minimal-basis pi-electron Hamiltonian.

For completeness, we can also consider the corresponding $6 \times 6 \mathbf{F}^{(\text{NBO})}$ in the NBO pi basis (i.e., the basis of $\pi_{12}, \pi_{34}, \pi_{56}, \pi_{12}^*, \pi_{34}^*, \pi_{56}^*$ NBOs),

$$\mathbf{F}^{(\text{NBO})} = \begin{pmatrix} -0.2510 & -0.0601 & -0.0601 & 0.0000 & 0.0674 & 0.0674 \\ -0.0601 & -0.2510 & -0.0601 & 0.0674 & 0.0000 & -0.0674 \\ -0.0601 & -0.0601 & -0.2510 & -0.0674 & -0.0674 & 0.0000 \\ 0.0000 & 0.0674 & -0.0674 & 0.0282 & -0.0814 & 0.0814 \\ 0.0674 & 0.0000 & -0.0674 & -0.0814 & 0.0282 & -0.0814 \\ 0.0674 & -0.0674 & 0.0000 & 0.0814 & -0.0814 & 0.0282 \end{pmatrix} \quad (3.157)$$

This contains only diagonal and vicinal matrix elements of the following types:

$$\langle \pi_a | \hat{F} | \pi_a \rangle = -0.2510 \quad (3.158a)$$

$$\langle \pi_a^* | \hat{F} | \pi_a^* \rangle = 0.0282 \quad (3.158b)$$

$$\langle \pi_a | \hat{F} | \pi_b \rangle = -0.0601 \quad (3.158c)$$

$$\langle \pi_a | \hat{F} | \pi_b^* \rangle = \pm 0.0674 \quad (3.158d)$$

$$\langle \pi_a^* | \hat{F} | \pi_b^* \rangle = \pm 0.0814 \quad (3.158e)$$

Diagonalization of $\mathbf{F}^{(\text{NBO})}$ leads to the eigenvalues

$$\mathbf{F}^{(\text{NBO})}: \quad -0.3712, \quad -0.2576 [2], \quad 0.0135 [2], \quad 0.1910 \quad (3.159)$$

which agree still more closely with the full *ab initio* occupied levels in (3.143),

$$\Delta\epsilon_1 = 0.8 \text{ kcal mol}^{-1}, \quad \Delta\epsilon_2 = 1.4 \text{ kcal mol}^{-1} \quad (3.160)$$

Comparison with (3.156) shows that $\mathbf{F}^{(\text{NBO})}$ is intrinsically of significantly higher accuracy than $\mathbf{h}^{(\text{HMO})}$ for describing the actual pi interactions of benzene. Because $\mathbf{F}^{(\text{NBO})}$ is the fundamental starting point for localized NBO analysis of conjugative interactions, we can conclude that the NBO donor–acceptor picture is inherently more accurate than that based on the Hückel tight-binding approximation.

3.4 Hyperconjugation

3.4.1 Mulliken “primary” hyperconjugation

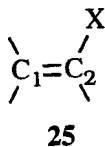
R. S. Mulliken⁶⁸ first recognized that alkyl and other saturated substituents alter a pi-bonded substrate in a manner that suggests “extension of the conjugation chain” into the sigma-bonded moiety (albeit in weakened form). In toluene, for example, the effects of the attached methyl group on spectroscopic $\pi\text{-}\pi^*$ excitations of the aromatic ring are closely analogous to (although weaker than) characteristic conjugative effects of pi-bonded substituents. Mulliken labeled such sigma-extended ($\pi\text{-}\sigma^*$ or $\sigma\text{-}\pi^*$) conjugation as “hyperconjugation” to distinguish it from more familiar conjugative interactions between pi moieties. We may also speak of “primary” hyperconjugation to distinguish this case from the $\sigma\text{-}\sigma^*$ (“secondary”) hyperconjugation to be discussed in Section 3.4.2.

While strict $\pi\text{-}\sigma$ interactions are, of course, forbidden by symmetry, it is convenient to continue to refer to the “pi-like” and “sigma-like” bonds in molecules (such as toluene) that lack strict sigma-pi symmetry. Such informal use of symmetry labels is strongly supported by the NBOs, which clearly retain the effective σ or π symmetry of the local bonding environment even in molecules of low symmetry. Thus, with a slightly relaxed usage of the symmetry labels we can refer to “ $\pi\text{-}\sigma^*$ ” or “ $\sigma\text{-}\pi^*$ ” donor-acceptor interactions without essential ambiguity, and thereby recognize these interactions as hyperconjugative generalizations of the more familiar $\pi\text{-}\pi^*$ conjugative interactions discussed in Section 3.3.

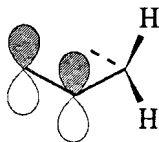


Robert S. Mulliken

A simple example of the effect of an attached saturated group X on a pi bond,



is given by propene (**25**, X=CH₃). In this case the principal hyperconjugative effects are associated with NBO donor–acceptor interactions between the C₁—C₂ pi bond and the two out-of-plane C—H sigma bonds



Because C₁, C₂, C₃, and H do not lie in a common plane, it is more difficult to visualize hyperconjugation ($\sigma\text{-}\pi^*$ or $\sigma^*\text{-}\pi$) involving the sigma-bonded C₃—H and pi-bonded C₁—C₂ NBOs. Figure 3.49 depicts NBO contours of these interactions in two chosen contour planes: (1) a “pi plane” 1 Å above the C₃C₂C₁ skeletal plane, analogous to Fig. 3.38 (on the left); and (2) a perpendicular “sigma plane” passing through C₃—C₂ and bisecting the two out-of-plane C—H bonds (on the right). Although neither view gives a completely satisfactory representation, one can recognize that the $\sigma_{\text{CH}}\rightarrow\pi_{\text{CC}}^*$ interaction (b) is somewhat stronger than the $\pi_{\text{CC}}\rightarrow\sigma_{\text{CH}}^*$ interaction (a). This is confirmed by NBO perturbative analysis, for which the corresponding stabilizations are (a) 2.8 kcal mol⁻¹ and (b) 4.0 kcal mol⁻¹. These hyperconjugative stabilizations are significantly weaker than typical $\pi\rightarrow\pi^*$ conjugative stabilizations of Section 3.3, but nevertheless chemically appreciable.

The characteristic changes in the vinyl group resulting from hyperconjugative interactions with a variety of substituent groups X (X=CH₃, CFH₂, NH₂, OH, F) are summarized in Table 3.22. For each substituent X, the table shows the vinyl C—C bond order and polarization (percentage of π_{CC} on C₁), the form of the $\tilde{\pi}_{\text{CC}}$ and $\tilde{\pi}_{\text{CC}}^*$ NLMOs, and the hyperconjugative stabilizations with available out-of-plane NBOs of X.

We now discuss systematic hyperconjugative effects on orbital composition and stabilization, torsion barriers, and spectroscopic properties, for the CH₂=CHX species summarized in Table 3.22.

Hyperconjugative effects on stabilization and orbital composition

From Table 3.22 one can see that typical hyperconjugative interactions of vinyl pi bonds with hydride bonds are rather weak (2–4 kcal mol⁻¹), but those with lone pairs are considerably stronger (7–30 kcal mol⁻¹). (Of course, a more polar pi bond

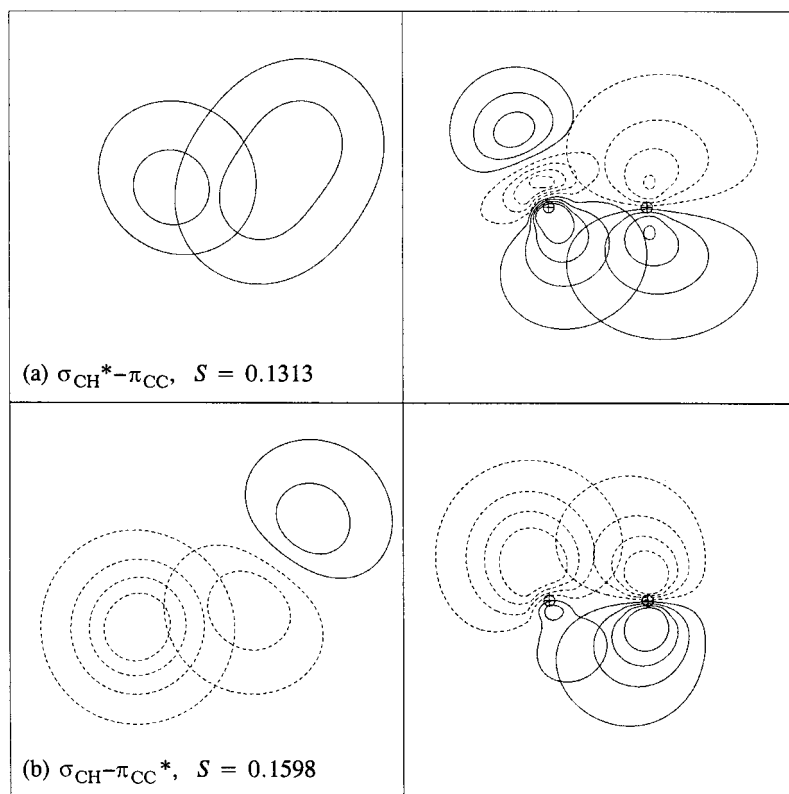


Figure 3.49 Orbital contours for hyperconjugative interactions in propene: (a) $\sigma^* - \pi$ and (b) $\sigma - \pi^*$. The contour plane on the left is chosen 1 Å below (a) or above (b) the $\text{C}_3\text{C}_2\text{C}_1$ plane, while that on the right is perpendicular to the $\text{C}_3\text{C}_2\text{C}_1$ plane, passing through $\text{C}_3 - \text{C}_2$.

would exhibit still stronger effects, for example the $\sim 60 \text{ kcal mol}^{-1} n_{\text{N}} \rightarrow \pi_{\text{CO}}^*$ stabilization of amide **5** in Table 3.19.) These interactions typically polarize the vinyl π_{CC} NBO by 2%–5% (*against* the expected inductive shift due to electronegativity differences), reduce the C—C bond order to 1.95–1.98, and add significant delocalization tails to one or both of the $\tilde{\pi}_{\text{CC}}$ and $\tilde{\pi}_{\text{CC}}^*$ NLMOs (thereby altering the expected character of spectroscopic $\pi \rightarrow \pi^*$ transitions, as discussed below).

The relative strengths of hyperconjugative stabilizations could be rationalized with contour plots similar to Fig. 3.49. The most important features of such plots could be predicted from the transferable forms of the NBOs (cf. Figs. 3.16 and 3.25) and expected variations with electronegativity (Sections 3.2.5 and 3.2.8). As shown in Fig. 3.49, the hyperconjugating σ_{X} and σ_{X}^* NBOs are typically canted away from the pi NBOs, weakening their interactions compared with “ordinary” ($\pi - \pi^*$) conjugative stabilizations in Table 3.19. However, the dependences on bond/antibond

Table 3.22. Some C=C bond orders, π_{CC} polarization, $\tilde{\pi}_{CC}$ and $\tilde{\pi}_{CC}^*$ NLMOs, and hyperconjugative stabilizations between vinyl pi bond and substituent X group in vinyl—X compounds

X	NRT b_{CC}^a	π Polarization (% on C ₁) ^b	$\tilde{\pi}_{CC}, \tilde{\pi}_{CC}^*$ NLMOs	σ_X (n_X) moiety	Stabilization ^c (kcal mol ⁻¹)	
					$\pi_{CC} \rightarrow \sigma_X^*$	$\sigma_X \rightarrow \pi_{CC}^*$
CH ₃	1.985	51.6	$0.995\pi_{CC} + 0.066\sigma_{CH}^* + 0.066\sigma_{CH}^*$ $0.991\pi_{CC}^* + 0.094\sigma_{CH} + 0.094\sigma_{CH}$	σ_{CH}	-2.8	-4.0
CFH ₂	1.985	49.8	$0.991\pi_{CC} + 0.115\sigma_{CF}^* + 0.065\sigma_{CH}^*$ $0.995\pi_{CC}^* + 0.042\sigma_{CF} + 0.076\sigma_{CH}$	σ_{CF} σ_{CH}	-6.5 -2.4	-1.4 -2.9
NH ₂	1.932	52.5	$0.997\pi_{CC} + 0.053\sigma_{NH}^*$ $0.975\pi_{CC}^* + 0.208n_N + 0.068\sigma_{NH}$	n_N σ_{NH}	— -2.3	-7.2 -3.9
OH	1.950	55.3	$0.999\pi_{CC}$ $0.969\pi_{CC}^* + 0.246n_O$	n_O	—	-31.6
F	1.981	52.4	$0.999\pi_{CC}$ $0.981\pi_{CC}^* + 0.193n_F$	n_F	—	-21.5

^a C₁—C₂ NRT bond order.

^b Percentage of π_{CC} NBO on C₁.

^c Second-order perturbative estimate of NBO donor-acceptor stabilization.

polarity, single-center character, ionic character, spatial proximity, and extended conjugation network pattern would closely parallel those discussed in Section 3.3.1.

The conjugative stabilizations in turn are clearly reflected in the forms of the NLMOs. The polar fluoride bond of $X = \text{CFH}_2$ has σ_{CF}^* strongly polarized toward C_3 and is able to act as a relatively strong pi-acceptor to π_{CC} ($6.5 \text{ kcal mol}^{-1}$), which becomes polarized toward the connecting C_2 . The relatively strong mixing of σ_{CF}^* (coefficient 0.115) into the $\tilde{\pi}_{\text{CC}}$ then leads to $\tilde{\pi}_{\text{CC}}$ being more delocalized than π_{CC}^* in this case. For the remaining substituents in Table 3.22, the X group serves as a net pi-donor into π_{CC}^* . The vinyl π_{CC} accordingly polarizes toward C_1 , so π_{CC}^* is polarized toward C_2 and $\tilde{\pi}_{\text{CC}}^*$ acquires the more pronounced delocalization tail, whereas $\tilde{\pi}_{\text{CC}}$ remains relatively well localized.

As shown by the comparison of vinylamine ($X = \text{NH}_2$, Table 3.22) with aniline (**23**, Table 3.21), the hyperconjugative interactions with an aromatic ring can be strongly enhanced compared with those with an isolated vinyl group ($24.5 \text{ kcal mol}^{-1}$ versus $7.2 \text{ kcal mol}^{-1}$ for the $n_{\text{N}} \rightarrow \pi_{\text{CC}}^*$ interaction). This reflects the strong cooperative enhancement of the aromatic conjugation chain, which allows the adjacent π_{CC} bond to polarize more strongly (54% toward C_1 , Eq. (3.133a), which is nearly as strong as the polarization in $\text{CH}_2=\text{CHX}$ for $X = \text{OH}$). In other respects, hyperconjugative interactions with the NBOs of a conjugated ring are qualitatively similar to those with a vinyl pi bond.

A particularly dramatic effect of hyperconjugation on the form of the ethylenic double bond NBOs is shown in Fig. 3.50. This figure depicts one of the two equivalent $\text{C}=\text{C}$ bond and antibond NBOs of vinylamine, twisted slightly out of coplanarity with the nitrogen lone pair with dihedral ϕ ($\text{C}-\text{C}-\text{N}-\text{lp}$) angle 80° (where

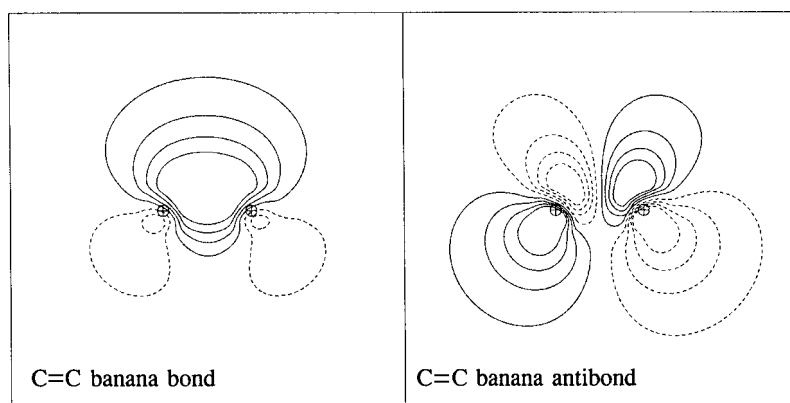
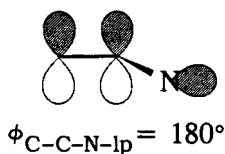


Figure 3.50 Carbon-carbon NBOs of $\text{CH}_2=\text{CHNH}_2$ at ϕ ($\text{C}-\text{C}-\text{N}-\text{lp}$) = 80° , showing the ethylenic “banana bond” (left) and “banana antibond” (right) for this strongly hyperconjugating low-symmetry system. (The second bond and antibond are symmetry-related by reflection through a plane containing the nuclei.)

“lp” denotes the nominal lone-pair direction, in the plane bisecting the two N—H bond vectors). As shown in Fig. 3.50, each of the two ethylenic NBOs is a “banana bond,” deviating strongly from the usual sigma/pi forms for ethylene (Fig. 3.11).

The unusual form of the C=C NBOs in Fig. 3.50 is clearly related to hyperconjugative interactions with the n_N lone pair. In the $\phi = 80^\circ$ geometry, the n_N has comparable delocalizations into *both* “banana antibonds” (stabilization energies of 8.41 and 7.06 kcal mol⁻¹). The C=C NBOs revert rather abruptly to their usual sigma/pi form as n_N is twisted to somewhat smaller ϕ values (e.g., $\phi = 70^\circ$), further away from coplanarity with the formal vinyl π -bond plane, and the same limit is recovered at the $\phi = 180^\circ$ geometry



where only “secondary” $n_N - \sigma_{\text{CC}}^*$ hyperconjugation is allowed by symmetry. Such sigma/pi breakdown suggests (correctly) that the distinction between “primary” ($\pi - \sigma^*$ or $\sigma - \pi^*$) and “secondary” ($\sigma - \sigma^*$, Section 3.4.2) hyperconjugation is only qualitatively valid. While banana bonds blur the distinction between primary and secondary hyperconjugation, they do not appreciably alter the *sum* of such contributions in a general low-symmetry unsaturated species.

Hyperconjugative effects on torsion barriers

The barrier to internal rotation about the C—X single bond of $\text{CH}_2=\text{CHX}$ species reflects a complex interplay of steric, electrostatic, and hyperconjugative factors. The orbital diagrams in Fig. 3.49 suggest why hyperconjugative interactions must be strong contributors to conformational preferences. As shown in Fig. 3.49, each $\langle \pi_{\text{CC}} | \hat{F} | \sigma_{\text{CH}}^* \rangle$ or $\langle \pi_{\text{CC}}^* | \hat{F} | \sigma_{\text{CH}} \rangle$ interaction is maximized when the hyperconjugating orbitals are in a *common* plane. This dependence on geometry is analogous to the well-known case of conjugative $\pi - \pi^*$ interactions, which are maximized when the conjugating pi orbitals are coplanar.

Let us consider the torsional behavior for fluoropropene ($\text{H}_2=\text{CHCFH}_2$) as the —CFH₂ group is twisted about the connecting C—C single bond to the vinyl group (all other geometrical variables being allowed to relax to their optimal values along the torsional coordinate). As shown in the solid curve of Fig. 3.51, two torsional isomers of this molecule are almost equal in energy: the planar skeletal conformer at $\phi_{\text{CCCF}} = 0$, having the C—F bond *eclipsing* the coplanar double bond, and the twisted skeletal conformer at $\phi \simeq 120$, having C—F twisted out of the vinyl plane.

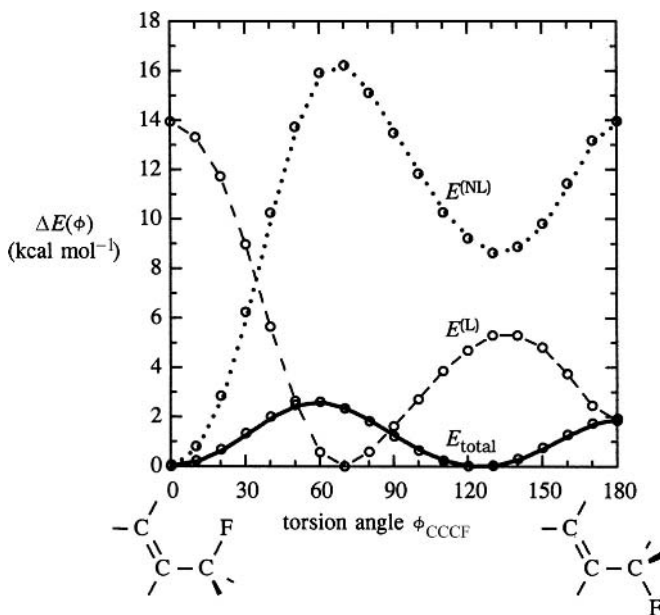


Figure 3.51 The barrier to internal rotation about the C—C single bond of $\text{CH}_2\text{FCH}=\text{CH}_2$, showing the total energy (solid line), localized Lewis component $E^{(L)}$ (dashed line), and delocalized non-Lewis component $E^{(NL)}$ (dotted line) as functions of the dihedral angle ϕ_{CCCF} .

Surprisingly, the coplanar *s-trans* conformer ($\phi = 180^\circ$) having the C—F bond pointed *away* from the vinyl group is a *maximum* of the torsional potential, even though it appears to be the best configuration to alleviate “steric congestion” with the proximal vinyl proton. Similar conformational preferences are found for other X groups, regardless of polarity. This is a simple example of torsional preferences that are “surprising” from a steric or electrostatic viewpoint.

Figure 3.51 also contains a dissection of the total energy (E_{total}) into Lewis ($E^{(L)}$) and non-Lewis ($E^{(NL)}$) components. The localized Lewis component $E^{(L)}$ corresponds to more than 99.3% of the full electron density, and so incorporates steric and classical electrostatic effects in nearly exact fashion. Yet, as shown in Fig. 3.51, this component predicts local minima (at $\phi \simeq 70^\circ$ and 180°) and maxima (at $\phi = 0^\circ$ and $\sim 130^\circ$) that are *opposite* to those of the full potential. In contrast, the non-Lewis component $E^{(NL)}$ exhibits a stronger torsional dependence that is able to “cancel out” the unphysical behavior predicted by $E^{(L)}$, leading to minima correctly located near 0° and 120° . Thus, the hyperconjugative interactions incorporated in $E^{(NL)}$ clearly provide the “surprising” stabilization of 0° and $\sim 120^\circ$ conformers that counter the expected steric and electrostatic effects contained in $E^{(L)}$.

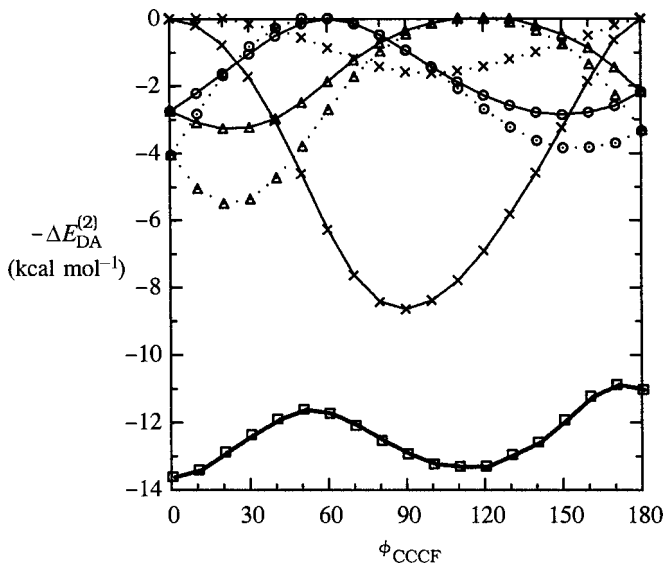


Figure 3.52 Leading hyperconjugative stabilizations in $\text{CFH}_2\text{CH}=\text{CH}_2$, showing the torsional dependence of $\pi-\sigma^*$ (solid lines) and $\sigma-\pi^*$ interactions (dotted lines) for the C—F (crosses) and two C—H bonds (triangles, circles) of the — CFH_2 group. The sum of all six interactions is shown as the heavy solid line (squares), which may be compared with the total barrier potential in Fig. 3.51.

Let us examine the hyperconjugative interactions in greater detail. Figure 3.52 illustrates the torsional dependence of each of the six possible $\pi-\sigma^*$ or $\sigma-\pi^*$ interactions in this case, together with their sum (squares, heavy solid line). One can see, for example, that the $\pi-\sigma_{\text{CF}}^*$ interaction (crosses, solid line) is largest in magnitude ($\sim 8.6 \text{ kcal mol}^{-1}$) and exhibits the expected sine-like dependence that is most stabilizing at $\phi = 90^\circ$ where the orbitals are coplanar. The corresponding $\sigma_{\text{CF}}-\pi^*$ interaction (crosses, dotted line) is also strongest at $\phi = 90^\circ$, but its maximum magnitude is *weakest* of the six interactions (due to the unfavorable polarization of the σ_{CF} donor *away* from the π_{CC}^* acceptor). Thus, the total stabilization at 90° is relatively weaker than at adjacent angles, where the more “balanced” $\pi-\sigma_{\text{CH}}^*$ and $\sigma_{\text{CH}}-\pi^*$ become appreciable. As Fig. 3.52 shows, the *total* stabilization of these six hyperconjugative interactions is strongest at 0° and $\sim 120^\circ$, where the actual minima of $E^{(\text{NL})}$ and E_{total} are found.

The rather confusing conformational dependences in Fig. 3.52 can be rationalized in a simple way. From the total of $\pi-\sigma^*$ and $\sigma-\pi^*$ stabilizations at their respective coplanar alignments with the pi system, one can confirm that C—H bonds are *better* overall hyperconjugating groups than C—F bonds. The most favorable hyperconjugative alignment is therefore to place both C—H bonds maximally out-of-plane (i.e., C—F in-plane) at $\phi = 0^\circ$, whereas a secondary favorable alignment

is to place C—F and C—H symmetrically out-of-plane (i.e., the other C—H in-plane) at $\phi \simeq 120^\circ$, both in *trans*-like relationship to the pi bond. In other words, the favored conformation is that in which the poorest hyperconjugating bond (C—F) *eclipses* the C=C double bond (so that the remaining two C—H bonds are maximally out of plane), while the alternative minima are those in which a C—H bond eclipses C—C, leaving the alternative C—H and C—F bonds maximally out-of-plane.

Still another way to picture the conformational preferences is to visualize the C=C double bond in terms of two equivalent banana bonds (Fig. 3.50). In this picture the preferred conformations are those with C—F in *staggered* orientation with respect to the three bonds (two banana bonds and one C—H bond) of the vinyl moiety, analogous to the preferred conformations of ethane. However, in using this ethane-like mnemonic one should recall that its essential origin lies in the hyperconjugative interactions of $E^{(NL)}$ rather than the steric and electrostatic interactions of $E^{(L)}$.

From comparison of Figs. 3.51 and 3.52 one can judge that $E^{(NL)}$ includes contributions other than the six primary hyperconjugative interactions of Fig. 3.52. These omitted contributions are principally of “secondary” σ – σ^* type, to be discussed in Section 3.4.2. However, these weaker hyperconjugative interactions do not significantly alter the preferred conformational angles established by the dominant six interactions of Fig. 3.52.

It is also interesting to note from Fig. 3.51 that the conformational dependences of $E^{(L)}$ and $E^{(NL)}$ exhibit complementary “mirror-image” shapes (but with larger amplitude of the dominant $E^{(NL)}$ term). This complementarity can be simply rationalized from consideration of the rather similar dihedral dependence of repulsive donor–donor (π – σ) and stabilizing donor–acceptor (π – σ^* or σ – π^*) interactions that dominate $E^{(L)}$ and $E^{(NL)}$, respectively. Thus, any change in the carbon hybrid of the C–F bond will be reflected both in σ_{CF} and in σ_{CF}^* NBOs, leading to respective complementary interactions with π_{CC} that are partly offsetting. The overall torsional potential shown in Fig. 3.51 is therefore the net resultant of opposing interactions (donor–donor versus donor–acceptor) that are inextricably linked through the underlying Lewis and non-Lewis NBOs.

Hyperconjugative effects on spectroscopic excitations

From the repolarizations of π_{CC} NBOs and the modified forms of the $\tilde{\pi}_{CC}$ and $\tilde{\pi}_{CC}^*$ NLMOs shown in Table 3.22, one expects that the spectroscopic properties of the vinyl chromophore will be strongly altered by hyperconjugative interactions. To examine this effect, we consider the lowest allowed valence $\pi \rightarrow \pi^*$ singlet and triplet electronic excitations. Figure 3.53 compares the vertical transition energies

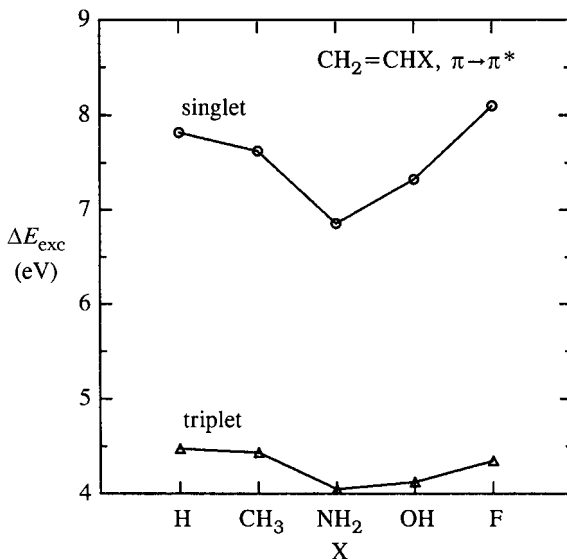


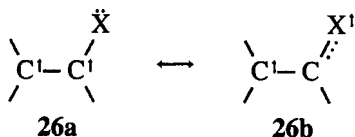
Figure 3.53 Vertical $\pi \rightarrow \pi^*$ excitation energies (ΔE_{exc} for valence singlet (circles) and triplet (triangles) excitations of substituted $\text{CH}_2=\text{CHX}$ compounds. (Singlet states were calculated at CIS/6-311++G**, triplet states at B3LYP/6-311++G** level.)

(ΔE_{exc}) for the various $\text{CH}_2=\text{CHX}$ species, with unsubstituted ethylene included for reference.

As shown in Fig. 3.53, the trends with substitution X are generally similar for singlet and triplet excitations. With the exception of singlet X = F (which is little shifted), the effect of substitution in both spin states is generally to *red*-shift the $\pi \rightarrow \pi^*$ excitation relative to parent propene, showing that hyperconjugative substitution stabilizes the *excited* state even more than the ground state. In each case the spectral shift is greatest for an amino group, with the effect diminishing in the sequence X = NH₂, OH, F. Because $^{1,3}\pi\pi^*$ excited states are expected to exhibit many similarities in a simple Hückel or Koopmans picture, we give primary attention to the lower-lying triplet species, which can be calculated and analyzed by methods parallel to those used for the ground state.

Let us consider the generic case of a lone-pair-bearing substituent \ddot{X} . Formal promotion to the $^3\pi\pi^*$ configuration leads to the triplet excited Lewis structure **26a** shown below, with diradical character on the adjacent carbon nuclei. However, the nonbonded n_X^\downarrow of the substituent is expected to donate strongly into the vacant $n_C^*\downarrow$ of the adjacent carbon, leading to a formal one-electron “half-bond” between C and X with diradical spin density primarily on the terminal C and X atoms, as shown in resonance structure **26b**. The relative weighting (w_{26a} , w_{26b}) of these two resonance structures will be increasingly shifted toward **26b** as X becomes a

stronger pi-donor, resulting in increased b_{CX} bond order (and shorter C—X bond length, if the excited-state geometry is allowed to relax).



The optimal NBO/NRT description of the triplet excited state corresponds most closely to **26b**, with fairly ordinary “single” bond orders for C—H ($b_{CH} = 0.98\text{--}0.99$) and C—C ($1.02\text{--}1.04$), but significant double-bond C—X character for $X = \text{NH}_2$ ($b_{CN} = 1.490$), OH ($b_{OH} = 1.486$), and F ($b_{CF} = 1.739$). Thus, the “singly filled orbitals” in these excited states do *not* resemble the ground-state HOMO and LUMO (as expected in a simple Hückel or Koopmans-like picture), but instead are primarily nonbonding n_C^\uparrow and n_X^\uparrow orbitals on the terminal C and X atoms. The formally vacated valence orbital is a nonbonding $n_C^{*\downarrow}$ on the terminal C, acting as a strong acceptor for the π_{CX}^\downarrow donor. For example, the estimated second-order stabilization energy is $11.47 \text{ kcal mol}^{-1}$ for the $\pi_{CN}^\downarrow \rightarrow n_C^{*\downarrow}$ interaction when $X = \text{NH}_2$.

Figure 3.54 shows the form of two singly occupied spin-NBOs in the vinylamine triplet excited state: the π_{CN}^\downarrow “half-bond” of the β spin set (Fig. 3.54(a)) and the terminal n_C^\uparrow radical orbital of the α spin set (Fig. 3.54(b)). Neither of these orbitals has a true counterpart in the MOs or NBOs of the ground-state molecule. These results emphasize that hyperconjugative reorganization is a *strong* feature of the excited-state orbitals, and the oversimplified HOMO–LUMO (Koopmans-like)

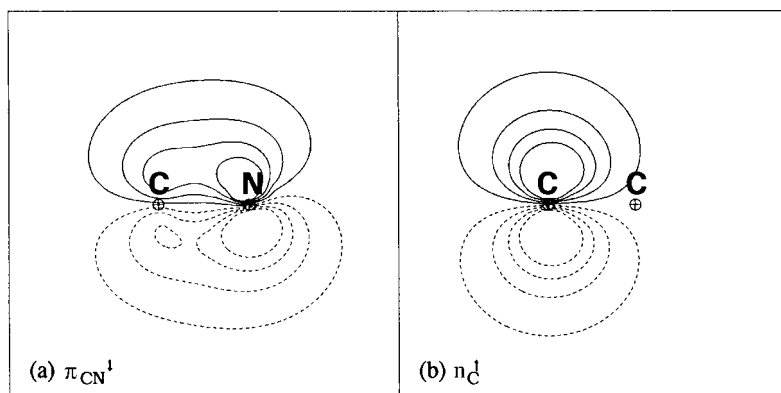


Figure 3.54 Singly occupied spin-NBOs of the lowest triplet $\pi \rightarrow \pi^*$ excited state of vinylamine ($X = \text{NH}_2$): (a) The π_{CN}^\downarrow “half-bond,” β spin; and (b) the n_C^\uparrow radical orbital of the terminal C atom, α spin.

picture may fail to provide even a qualitatively useful description of the electronic distribution of the excited state.

For $X = \text{CH}_3$ the hyperconjugative interactions are expected to be significantly weaker than those with a lone-pair-bearing substituent. In this case the resonance structure corresponding to **26a** is dominant ($w_{26a} = 90.9\%$) and the bond to the methyl carbon has only slight partial double-bond character ($b_{\text{CC}} = 1.050$). The hyperconjugative red-shift induced by the methyl group is therefore weaker and the expected increase in the barrier to internal rotation much smaller than in the C—X cases discussed above. Nevertheless, it is evident that a methyl group has a degree of “conjugative” capacity with respect to other chemical moieties. We are therefore led to investigation of the *mutual* conjugative interactions of methyl groups (or other formally saturated groups), as will be taken up in the following section.

3.4.2 Secondary (σ – σ^*) hyperconjugation

Given the reality of primary (σ – π^* , π – σ^*) hyperconjugative effects in unsaturated systems, it is reasonable to expect that corresponding “secondary” (σ – σ^*) hyperconjugative effects must be present in completely saturated systems, even if weakened in magnitude. The distinction between “sigma” and “pi” moieties is, after all, not rigorously symmetry-based in the vast majority of unsaturated compounds, and sigma–pi separability is found to lose even qualitative validity in certain limits, such as the vinylamine “banana bonds” of Fig. 3.50. From the expected continuity of solutions of Schrödinger’s equation one can therefore conclude that the differences among conjugative (π – π^*), primary hyperconjugative (π – σ^* , σ – π^*), and secondary hyperconjugative (σ – σ^*) interactions must be matters of *degree*, not of principle. In the present section we extend the study of hyperconjugative delocalization effects to fully saturated molecules.

The σ – σ^* delocalization effects tend to be weaker in magnitude and are often well hidden in the complex non-transferable forms of MOs. Older structural and thermochemical methods were often insensitive to subtle effects of long-range electron delocalization, such as are now routinely seen in NMR spin–spin couplings, vibrational shifts, photoelectron splittings, and other sensitive experimental diagnostics. Full recognition of the structural and energetic influence of sigma-conjugative effects was therefore somewhat delayed and subject to controversy, compared with corresponding pi-conjugative effects. However, NBO analysis (which makes no intrinsic distinction between sigma and pi character) now provides a much more direct way to exhibit the many parallels between sigma and pi delocalization in accurate wavefunctions. In the present section we examine various hyperconjugative σ – σ^* effects on torsional barriers, intramolecular vibrational coupling, and chemical reactivity patterns.

The internal rotation barrier of ethane

Why is there a barrier to internal rotation about single bonds? Mulliken⁶⁹ first conjectured that secondary hyperconjugation might play an important role in the internal rotation potential of ethane-like molecules. Early attempts to account for the famous torsion barrier of ~ 3 kcal mol⁻¹ in ethane focussed on classical electrostatics, steric effects, van der Waals (dispersion) forces, and d- and f-orbital participation, with notable lack of predictive success.⁷⁰ Unfortunately, Mulliken's initial estimate of the secondary hyperconjugative effect was very crude, seeming to suggest that such effects were too small to account for observed barriers, and the idea was largely forgotten until the semi-empirical MO studies of Brunck and Weinhold⁷¹ in the 1970s.

By that time a large number of *ab initio* and semi-empirical computational studies⁷² had shown that ethane-like rotation barriers are remarkably *insensitive* to theoretical level, and that the existence of torsion barriers must therefore reflect very qualitative wavefunction features of "low information content."⁷³ Brunck and Weinhold showed how the torsional energy difference arises simply from the qualitative *shapes* of vicinal σ_{CH} and σ_{CH}^* bond orbitals in the characteristic *anti* and *syn* periplanar arrangements of staggered and eclipsed conformers, as illustrated in the two panels of Fig. 3.55. From these panels one can readily judge that the $\sigma_{\text{CH}}-\sigma_{\text{CH}}^*$ donor-acceptor interactions are sharply reduced in the *cis*-like arrangement (Fig. 3.55(b)) compared with the *trans*-like arrangement (Fig. 3.55(a)), due to unfavorable cancellation in the latter case as the nodal plane of the C—H antibond cuts through the main lobe of the C—H bond orbital.⁷⁴ This visual estimate is confirmed by the numerical overlap integrals shown in Fig. 3.55, which differ in magnitude by approximately a factor of *two*, favoring stronger hyperconjugative stabilizations in the staggered conformer.

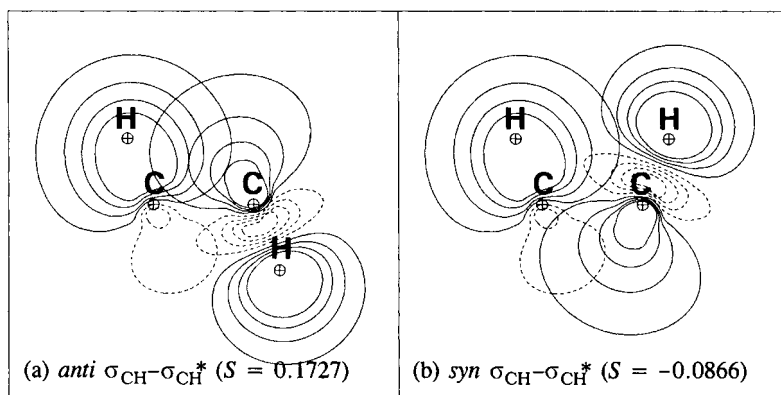


Figure 3.55 Leading $\sigma_{\text{CH}}-\sigma_{\text{CH}}^*$ hyperconjugative donor-acceptor interactions in the staggered (left) and eclipsed (right) conformers of ethane.

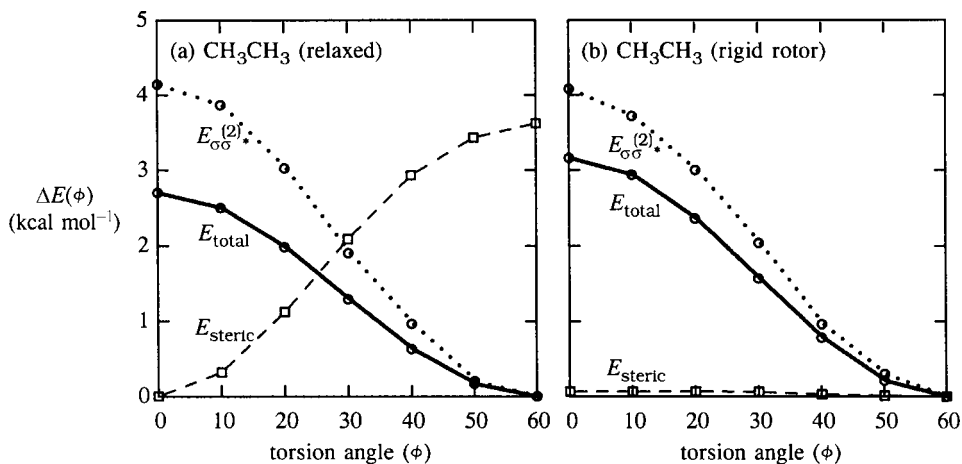


Figure 3.56 The rotation-barrier profile for CH₃CH₃ in (a) fully optimized and (b) idealized rigid-rotor geometry, showing the total energy E_{total} (circles, solid line), vicinal $\sigma_{\text{CH}}-\sigma_{\text{CH}^*}$ stabilization $E_{\sigma\sigma^*}^{(2)}$ (circles, dotted line), and steric energy E_{steric} (squares, dashed line).

Second-order perturbative estimates indicate that each *trans*-like donor–acceptor interaction (Fig. 3.55(a)) stabilizes the molecule by 2.58 kcal mol⁻¹, compared with only 0.89 kcal mol⁻¹ for the *cis*-like interaction (Fig. 3.55(b)). The smaller *gauche*-like stabilizations (0.20 kcal mol⁻¹ at 60° in the staggered conformer, 0.70 kcal mol⁻¹ at 120° in the eclipsed conformer) diminish the difference somewhat, but still preserve a significant hyperconjugative advantage for the staggered conformer.

Figure 3.56(a) shows the calculated torsional potential of ethane with fully relaxed geometry, comparing the full torsional profile (E_{total} , solid line) with the sum of vicinal $\sigma_{\text{CH}}-\sigma_{\text{CH}^*}$ interactions $E_{\sigma\sigma^*}^{(2)}$, dotted line) and the steric energy E_{steric} , dashed line) at each ϕ . As expected, the hyperconjugative $E_{\sigma\sigma^*}^{(2)}$ favors the staggered conformer ($\phi = 60^\circ$) and generally parallels the full E_{total} . Surprisingly, the steric term E_{steric} appears to favor strongly the *eclipsed* conformation! However, this result is somewhat misleading. If we carry out a similar calculation for idealized rigid rotor geometry, with no relaxation of other geometrical variables along the torsional coordinate, we obtain the results shown in Fig. 3.56(b). While the curves for the total barrier E_{total} and hyperconjugative $E_{\sigma\sigma^*}^{(2)}$ are generally similar in the two models, the steric dependence in the “pure” torsion model (b) is found to be entirely negligible (<0.1 kcal mol⁻¹). From comparison of Figs. 3.56(a) and (b) it becomes clear that the steric strain in the equilibrium staggered geometry is largely *induced* by changes in geometry that result from hyperconjugative interactions in the fully relaxed geometry⁷⁵ (as discussed below). The common feature of Figs. 3.56(a) and (b) is the dominance of the hyperconjugative interactions in dictating the overall

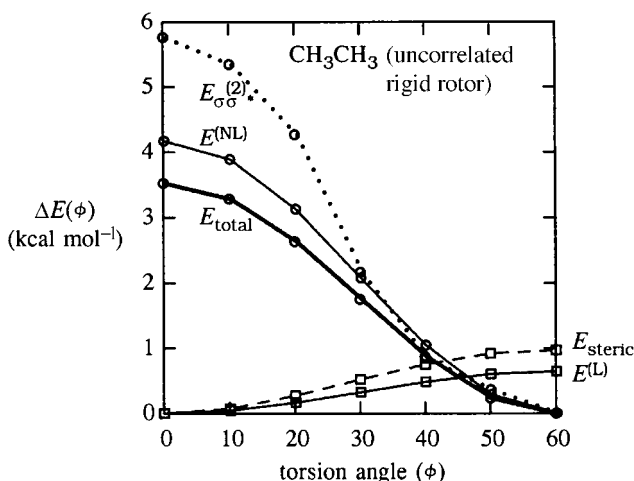


Figure 3.57 Similar to Fig. 3.56(b), for the uncorrelated (RHF) rigid-rotor model. The Lewis ($E^{(L)}$, squares, light solid line) and non-Lewis ($E^{(NL)}$, circles, light solid line) components of $E_{(total)}$ are shown for comparison.

conformational preference, with steric interactions (if significant at all) tending to *oppose* the favored staggered geometry.

To demonstrate further that the picture of hyperconjugative control of ethane torsions is insensitive to theoretical level, we show in Fig. 3.57 a comparison *uncorrelated* calculation (RHF/6-311++G** level) with the same idealized rigid-rotor geometry as that employed in Fig. 3.56(b). The general similarity to Fig. 3.56(b) is evident, showing that electron correlation effects (including van der Waals dispersion interactions) do not appreciably affect the overall barrier profile, or its hyperconjugative and steric contributions. Figure 3.57 also includes the dissection of the total energy into Lewis and non-Lewis components (analogously to Fig. 3.51). The localized Lewis component $E^{(L)}$ incorporates the main steric and electrostatic contributions, whereas the non-Lewis component $E^{(NL)}$ closely corresponds to the hyperconjugative $E_{\sigma\sigma^*(2)}$. The localized $E^{(L)}$ is seen to favor the *eclipsed* conformation (slightly), whereas the non-Lewis $E^{(NL)}$ strongly favors the *staggered* conformation, as expected from consideration of Fig. 3.55. Thus, the hyperconjugative donor–acceptor interactions contained in $E^{(NL)}$, rather than electrostatic and steric interactions in $E^{(L)}$, lead to the observed preference for the staggered conformation by about 3 kcal mol^{-1} .

The “four-electron destabilization” rationale

The rotation barrier of ethane is sometimes “explained” in terms of the mnemonic energy-level-splitting diagram shown in Fig. 3.58. The figure purports to depict how two filled MOs of ethane (ϕ_- and ϕ_+) evolve perturbatively from two

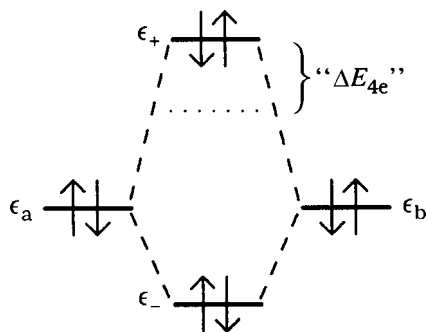


Figure 3.58 The mnemonic energy-level-splitting diagram for the “four-electron destabilizing” interaction of two occupied non-orthogonal orbitals.

non-orthogonal orbitals χ_a and χ_b with overlap $S_{ab} = \langle \chi_a | \chi_b \rangle$. As shown in Fig. 3.58, an asymmetric splitting pattern (with $\Delta E_{4e} \propto S_{ab}^2$) leads to net destabilization of the four-electron system whenever $S_{ab} \neq 0$.

Figure 3.58 originated in Coulson’s remark⁷⁶ concerning the variational 2×2 secular determinant for interacting helium atoms, where $\chi_a = 1s_a$ and $\chi_b = 1s_b$ are the only two significant contributing orbitals. In this case the mnemonic diagram correctly represents the net repulsive character of the variational solutions at small R (cf. Example 1.14). A PMO (perturbative molecular orbital) rationalization of Fig. 3.58 was subsequently developed⁷⁷ and has become deeply entrenched in the research literature of physical organic chemistry.⁷⁸ For the specific case of the ethane barrier, Fig. 3.58 is pictured as describing the interaction of two vicinal C—H bond orbitals σ_{CH} and $\sigma_{C'H'}$ with overlap $S_{\sigma\sigma'} = \langle \sigma_{CH} | \sigma_{C'H'} \rangle$. Because $S_{\sigma\sigma'}$ is envisioned to be larger in the *syn* arrangement, the rotation barrier is “explained” as a four-electron destabilizing steric effect, supposedly similar to He \cdots He repulsion.

However, application of the four-electron destabilizing rationale to the ethane barrier is misleading for three reasons.

- (1) There is no proper perturbative basis for the mnemonic diagram in Fig. 3.58, because the non-orthogonal “unperturbed orbitals” cannot correspond to *any* physical (Hermitian) unperturbed Hamiltonian operator,⁷⁹ as illustrated in Examples 3.17 and 3.18 below. The PMO interpretation of Fig. 3.58 therefore rests on an *unphysical* starting point. Removal of orbital overlap (to restore Hermiticity) eliminates the supposed “effect.”⁸⁰
- (2) The actual Fock-matrix elements between orthogonalized σ_{CH} and $\sigma_{C'H'}$ orbitals are too small to account for appreciable conformational energy differences in the actual geometry of ethane (as can be seen from the small numerical values of E_{steric} in Fig. 3.57).
- (3) The 2×2 PMO treatment *neglects* the numerically *comparable* interactions with acceptor σ_{CH}^* and $\sigma_{C'H'}^*$ orbitals. Thus (unlike He \cdots He), it is numerically *unjustified* to consider the 2×2 ($\sigma_{CH}, \sigma_{C'H'}$) secular determinant as a valid approximation to the full ($\sigma_{CH}, \sigma_{C'H'}, \sigma_{CH}^*, \sigma_{C'H'}^*$) variational problem.

In fact, when the ethane problem is treated properly with inclusion of all four contributing unperturbed NBOs (properly orthogonalized eigenfunctions of a properly Hermitian unperturbed Hamiltonian $\hat{H}^{(L)}$; cf. Section 1.5), the net “ ΔE_{4e} ” energy difference is found to be essentially *equivalent* to the two-electron $\sigma_{\text{CH}} - \sigma_{\text{CH}^*}$ donor–acceptor stabilization depicted in Fig. 1.3 (to within the accuracy of Mulliken-type approximations for the various matrix elements involved).⁸¹ Thus, there is *no* reason to conclude that the “four-electron destabilizing” mnemonic presents a valid perturbative picture of the important barrier-determining interactions in ethane, or that such PMO reasoning can be taken as valid evidence of a steric origin of the rotation barrier of ethane.

Example 3.17

Exercise: For the PMO treatment of interacting non-orthogonal orbitals χ_a and χ_b , what is the “unperturbed Hamiltonian” corresponding to setting $h_{ab} = \langle \chi_a | \hat{H}_{\text{eff}} | \chi_b \rangle$ to zero? Is it the same as the operator whose eigenfunctions are χ_a and χ_b , with corresponding eigenvalues ϵ_a and ϵ_b ?

Solution: Let us first choose a reference orthonormal set $\{\phi_1, \phi_2\}$ to be used consistently in displaying the various matrices and vectors under discussion. For simplicity, we choose $\{\phi_1, \phi_2\}$ to be the (“Löwdin-orthogonalized”) functions that are *closest* to χ_a and χ_b in the mean-squared-deviation sense. The non-orthogonal functions χ_a and χ_b (with $\langle \chi_a | \chi_b \rangle = S$) can then be expressed in terms of reference orthonormal functions as

$$\begin{aligned}\chi_a &= c_1\phi_1 + c_2\phi_2 \\ \chi_b &= c_2\phi_1 + c_1\phi_2\end{aligned}$$

where c_1 and c_2 are found to be

$$\begin{aligned}c_1 &= \frac{(1+S)^{1/2} + (1-S)^{1/2}}{2} \\ c_2 &= \frac{(1+S)^{1/2} - (1-S)^{1/2}}{2}\end{aligned}$$

The equivalent column vectors are

$$\begin{aligned}\chi_a &= \begin{pmatrix} c_1 \\ c_2 \end{pmatrix} \\ \chi_b &= \begin{pmatrix} c_2 \\ c_1 \end{pmatrix}\end{aligned}$$

and can easily be verified to have the desired scalar products

$$\chi_a^\dagger \chi_a = \chi_b^\dagger \chi_b = 1, \quad \chi_a^\dagger \chi_b = S$$

Now suppose that we begin with the full (“perturbed”) secular determinant of the form

$$0 = \begin{vmatrix} \epsilon_a - E & h_{ab} - ES \\ h_{ab} - ES & \epsilon_b - E \end{vmatrix} = \det|\mathbf{H} - E\mathbf{S}|$$

where

$$\mathbf{H} = \begin{pmatrix} \epsilon_a & h_{ab} \\ h_{ab} & \epsilon_b \end{pmatrix}, \quad \mathbf{S} = \begin{pmatrix} 1 & S \\ S & 1 \end{pmatrix}$$

From the rules of determinantal algebra we can write

$$\begin{aligned} 0 &= \det|\mathbf{S}^{-1/2}| \det|\mathbf{H} - E\mathbf{S}| \det|\mathbf{S}^{-1/2}| \\ &= \det|\mathbf{S}^{-1/2} \mathbf{H} \mathbf{S}^{-1/2} - E\mathbf{I}| \\ &= \det|\mathbf{H}' - E\mathbf{I}| \end{aligned}$$

to express the secular determinant equivalently in the orthonormal reference basis. The matrix elements of $\mathbf{H}' = \mathbf{S}^{-1/2} \mathbf{H} \mathbf{S}^{-1/2}$ are found to be

$$\mathbf{H}' = \frac{1}{1-S^2} \times \begin{pmatrix} (\epsilon_a + \epsilon_b)/2 + (1-S^2)^{1/2}(\epsilon_a - \epsilon_b)/2 - Sh_{ab} & h_{ab} - S(\epsilon_a + \epsilon_b)/2 \\ h_{ab} - S(\epsilon_a + \epsilon_b)/2 & (\epsilon_a + \epsilon_b)/2 - (1-S^2)^{1/2}(\epsilon_a - \epsilon_b)/2 - Sh_{ab} \end{pmatrix}$$

The “unperturbed Hamiltonian” ($\mathbf{H}^{(0)}$) corresponding to setting h_{ab} to zero is therefore

$$\mathbf{H}^{(0)} = \frac{1}{1-S^2} \times \begin{pmatrix} (\epsilon_a + \epsilon_b)/2 + (1-S^2)^{1/2}(\epsilon_a - \epsilon_b)/2 & -S(\epsilon_a + \epsilon_b)/2 \\ -S(\epsilon_a + \epsilon_b)/2 & (\epsilon_a + \epsilon_b)/2 - (1-S^2)^{1/2}(\epsilon_a - \epsilon_b)/2 \end{pmatrix}$$

However, it is easy to verify that neither χ_a nor χ_b is an eigenvector of this “unperturbed Hamiltonian,” and neither are ϵ_a and ϵ_b its eigenvalues (see Example 3.18). More generally, since $\mathbf{H}^{(0)}$ is clearly Hermitian, it cannot have *any* non-orthogonal eigenvectors, by virtue of the theorem (note 79) quoted above.

What *is* the “unperturbed Hamiltonian” ($\mathbf{H}^{(0)}$) whose eigenvectors are χ_a and χ_b and whose eigenvalues are ϵ_a and ϵ_b ? We can construct this operator explicitly from the set of *bi*-orthogonal vectors $\tilde{\chi}_a$ and $\tilde{\chi}_b$:

$$\begin{aligned} \tilde{\chi}_a &= \frac{1}{1-S^2} \begin{pmatrix} c_1 - Sc_2 \\ c_2 - Sc_1 \end{pmatrix} \\ \tilde{\chi}_b &= \frac{1}{1-S^2} \begin{pmatrix} c_2 - Sc_1 \\ c_1 - Sc_2 \end{pmatrix} \end{aligned}$$

satisfying

$$\begin{aligned} \tilde{\chi}_a^\dagger \chi_a &= \tilde{\chi}_b^\dagger \chi_b = 1 \\ \tilde{\chi}_a^\dagger \chi_b &= \tilde{\chi}_b^\dagger \chi_a = 0 \end{aligned}$$

The operator satisfying the desired unperturbed eigenvalue equations

$$\mathbf{H}''^{(0)}\chi_a = \epsilon_a\chi_a$$

$$\mathbf{H}''^{(0)}\chi_b = \epsilon_b\chi_b$$

is therefore given by the spectral expansion

$$\mathbf{H}''^{(0)} = \epsilon_a\chi_a\tilde{\chi}_a^\dagger + \epsilon_b\chi_b\tilde{\chi}_b^\dagger$$

or, in more explicit form, by

$$\mathbf{H}''^{(0)} = \frac{1}{1-S^2} \begin{pmatrix} c_1^2\epsilon_a + c_2^2\epsilon_b - Sc_1c_2(\epsilon_a + \epsilon_b) & c_1c_2(\epsilon_a + \epsilon_b) - S(c_1^2\epsilon_a + c_2^2\epsilon_b) \\ c_1c_2(\epsilon_a + \epsilon_b) - S(c_1^2\epsilon_b + c_2^2\epsilon_a) & c_1^2\epsilon_b + c_2^2\epsilon_a - Sc_1c_2(\epsilon_a + \epsilon_b) \end{pmatrix}$$

However, this ‘‘Hamiltonian’’ is manifestly non-Hermitian (unless $S = 0$) and therefore cannot correspond to a physical unperturbed system. Neither of the operators $\mathbf{H}''^{(0)}$ and $\mathbf{H}''^{(0)}$ can serve as a proper unperturbed Hamiltonian for the PMO rationalization (unless $S = 0$, when both are equivalent to a standard $\mathbf{H}^{(0)}$ such as that underlying, e.g., Example 1.1 or Fig. 3.13).

Example 3.18

The equations of Example 3.17 can be illustrated by the simple example of HeH^+ in a minimal basis treatment with $\chi_a = 1s_{\text{He}}$ and $\chi_b = 1s_{\text{H}}$. The numerical matrix elements (B3LYP/STO-3G at $R_{\text{eq}} = 0.80 \text{ \AA}$) are found to be

$$\epsilon_a = -1.5727$$

$$\epsilon_b = -0.8105$$

$$h_{ab} = -1.0258$$

$$S = 0.5208$$

with MO eigenvalues (cf. Fig. 3.58)

$$\epsilon_- = -1.6151$$

$$\epsilon_+ = -0.1891$$

In this case, the PMO unperturbed eigenvectors χ_a and χ_b are

$$\chi_a = \begin{pmatrix} 0.9627 \\ 0.2705 \end{pmatrix}, \quad \chi_b = \begin{pmatrix} 0.2705 \\ 0.9627 \end{pmatrix}$$

and the supposed PMO unperturbed $\mathbf{H}''^{(0)}$ is

$$\mathbf{H}''^{(0)} = \begin{pmatrix} -2.0815 & -0.8516 \\ -0.8516 & -1.1887 \end{pmatrix}$$

However, the actual eigenvalues of this operator are

$$\epsilon_1 = -2.5966, \quad \epsilon_2 = -0.6736$$

and the corresponding eigenvectors are

$$\mathbf{u}_1 = \begin{pmatrix} 0.8556 \\ -0.5176 \end{pmatrix}, \quad \mathbf{u}_2 = \begin{pmatrix} 0.5176 \\ 0.8556 \end{pmatrix}$$

bearing little resemblance to the PMO unperturbed eigenvalues (ϵ_a and ϵ_b) and eigenvectors (χ_a and χ_b) given above. The alternative unperturbed $\mathbf{H}''^{(0)}$ which *does* have these PMO unperturbed eigenvalues and eigenvectors is

$$\mathbf{H}''^{(0)} = \begin{pmatrix} -1.6380 & 0.2325 \\ -0.2325 & -0.7451 \end{pmatrix}$$

but this operator is non-Hermitian and therefore cannot correspond to any physical “unperturbed system.”

Examples 3.17 and 3.18 show clearly that Fig. 3.58 cannot be consistently interpreted in a perturbative framework. Figure 3.58 is a valid mnemonic for numerical diagonalization of a 2×2 matrix, but it cannot be assigned a deeper perturbative significance when $S \neq 0$. Except for visualization purposes (see Example 1.11 and ensuing discussion), the use of non-orthogonal orbitals for interpretive purposes is fraught with danger.⁸²

We conclude that the four-electron stabilization rationalization lacks both physical and numerical relevance to barrier problems and should not be taken as evidence in support of a picture of the rotation barrier of ethane based on steric repulsions.

Other ethane-like barriers

Table 3.23 summarizes the rotation barriers and leading vicinal σ – σ^* interactions for methyl rotors $\text{CH}_3\text{—X}$ ($\text{X} = \text{CH}_3, \text{NH}_2, \text{OH}$) as well as higher group 14 congeners $\text{H}_3\text{M—MH}_3$ ($\text{M} = \text{Si}, \text{Ge}$). Figure 3.59 shows orbital contour diagrams for *syn* and *anti* orientations of selected vicinal donor–acceptor NBOs in these species. We now discuss some qualitative trends of torsion barrier potentials in terms of these examples.

In the series $\text{CH}_3\text{—X}$ ($\text{X} = \text{CH}_3, \text{NH}_2, \text{OH}$), the rotation barrier is systematically reduced in approximate 3 : 2 : 1 ratio (2.70 : 1.93 : 1.05), corresponding to successive replacement of hydride bonds by lone pairs. This reduction might seem surprising, because lone pairs are typically better vicinal donors than hydride bonds (due to their greater amplitude on the axial atom). However, the increased strength of $n_{\text{X}} \rightarrow \sigma_{\text{CH}}^*$ interactions (Table 3.23) is countered primarily by two factors: (1) there is *no* corresponding delocalization in the opposite direction (because there is no valence acceptor orbital corresponding to a lone pair); and (2) the *difference* between *syn* and *anti* $n_{\text{X}} \rightarrow \sigma_{\text{CH}}^*$ interactions is significantly reduced, so the net contribution to the energy difference between staggered and eclipsed rotamers is correspondingly weakened.

Table 3.23. Rotation barriers ($E_{\text{ecl}} - E_{\text{stg}}$) and leading $\sigma\text{-}\sigma^*$ donor–acceptor stabilizations ($-\Delta E_{\sigma\sigma^*}$) in anti and syn orientations for methyl rotors ($\text{CH}_3\text{-X}$, $\text{X} = \text{CH}_3, \text{NH}_2, \text{OH}$) and higher ethane-like congeners

Molecule	Rotation barrier ^a kcal mol ⁻¹	σ	σ^*	$-\Delta E_{\sigma\sigma^*}$ (kcal mol ⁻¹)	
				anti	syn
$\text{H}_3\text{C-CH}_3$	2.70	C—H	C—H	2.58	0.89
$\text{H}_3\text{C-CH}_2$	1.93	C—H	N—H	3.04	1.07
		N—H	C—H	1.97	0.72
		n_{N}	C—H	7.44	6.09
$\text{H}_3\text{C-OH}$	1.05	C—H	O—H	2.42	0.29
		O—H	C—H	1.55	1.19
		n_{O}^{π}	C—H	7.97	7.97
		n_{O}^{σ}	C—H	2.25 ^b	2.57 ^c
$\text{H}_3\text{Si-SiH}_3$	0.94	Si—H	Si—H	0.65	0.38
$\text{H}_3\text{Ge-GeH}_3$	0.63	Ge—H	Ge—H	0.69	0.40

^a Uncorrected for zero-point energy.

^b From the eclipsed conformer.

^c From the staggered conformer.

Figure 3.60 illustrates the second factor, showing the $n_{\text{O}}^{\pi} \rightarrow \sigma_{\text{CH}}^*$ donor–acceptor interaction between the pi-type oxygen lone pair n_{O}^{π} (essentially a pure-p orbital perpendicular to the COH plane) and a vicinal hydride antibond. As one can readily see from Fig. 3.60, the $n_{\text{X}}\text{-}\sigma_{\text{CH}}^*$ overlap only changes sign (but not magnitude) as the orbitals are twisted from “syn” to “anti” alignment, so there can be no net contribution to the rotameric energy difference in this case, even though the hyperconjugative interaction is quite strong (7.97 kcal mol⁻¹ in either rotamer).

Figure 3.59a illustrates the related barrier-weakening effect in methylamine. On comparing the $n_{\text{N}} \rightarrow \sigma_{\text{CH}}^*$ interaction of methylamine with the corresponding $\sigma_{\text{CH}} \rightarrow \sigma_{\text{CH}}^*$ interaction of ethane (Fig. 3.55), one can see that the syn/anti difference is somewhat diminished in the former case because the nodal plane of the σ_{CH}^* only passes through the “edge” of the n_{N} donor NBO. The visual estimate is confirmed by the calculated $n_{\text{N}} \rightarrow \sigma_{\text{CH}}^*$ hyperconjugative stabilization energies (7.44 [anti] versus 6.09 kcal mol⁻¹ [syn]), both of which are much stronger than corresponding $\sigma_{\text{CH}} \rightarrow \sigma_{\text{CH}}^*$ stabilizations in ethane, but with a smaller difference between staggered and eclipsed forms.

From such comparisons one can judge that the syn/anti difference is sensitive to antibond polarity (which shifts the nodal plane relative to the adjacent donor NBO) and to the bond angles at which donor and acceptor NBOs are canted toward one another. Compared with C—H bonds, rotation barriers involving polar A—X bonds

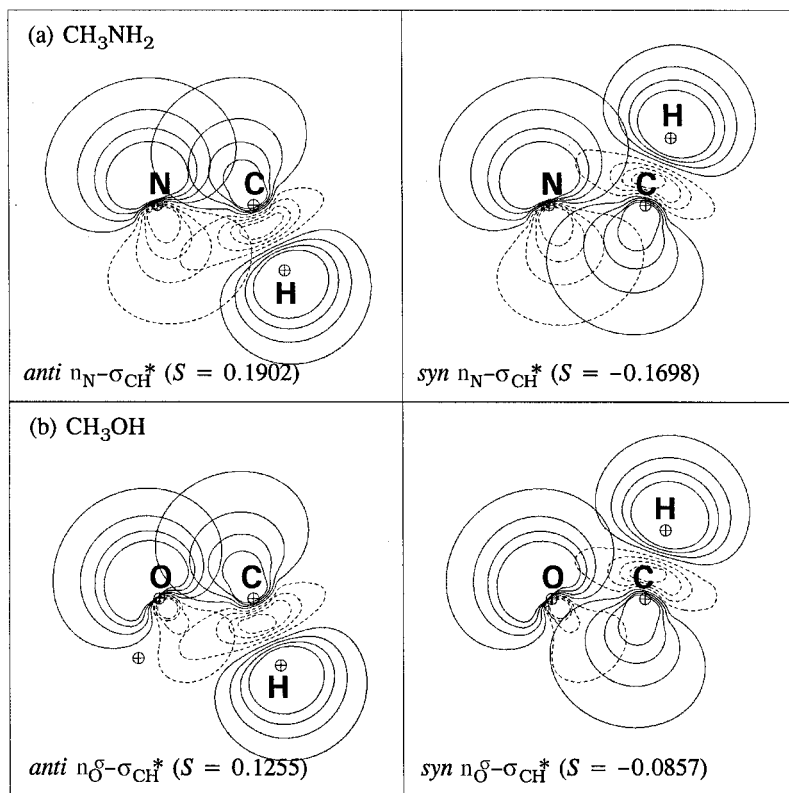


Figure 3.59 Leading vicinal σ - σ^* donor-acceptor interactions for molecules in Table 3.23 (cf. Fig. 3.55 for ethane), comparing orbital contours in *anti* (left) and *syn* (right) orientations of (a) methylamine, (b) methanol, (c) disilane, and (d) digermane.

are often *reduced* because the donor or acceptor NBO is unfavorably polarized away from the torsional axis (i.e., there is an unfavorably polarized donor σ_{AX}^* if X is much more electronegative than A; there is an unfavorable polarized acceptor σ_{AX}^* if A is much more electronegative than X). From general electronegativity and bond-polarity considerations one expects the *donor* NBO strength to decrease in the order

$$\text{lone pair} > \sigma_{\text{OH}} > \sigma_{\text{NH}} > \sigma_{\text{CH}} > \sigma_{\text{CF}} \quad (3.161a)$$

whereas *acceptor* NBO strength decreases in the opposite order,

$$\sigma_{\text{CF}}^* > \sigma_{\text{CH}}^* > \sigma_{\text{NH}}^* > \sigma_{\text{OH}}^* \quad (3.161b)$$

Further examples of the dependence on polarity and geometry will be discussed below.

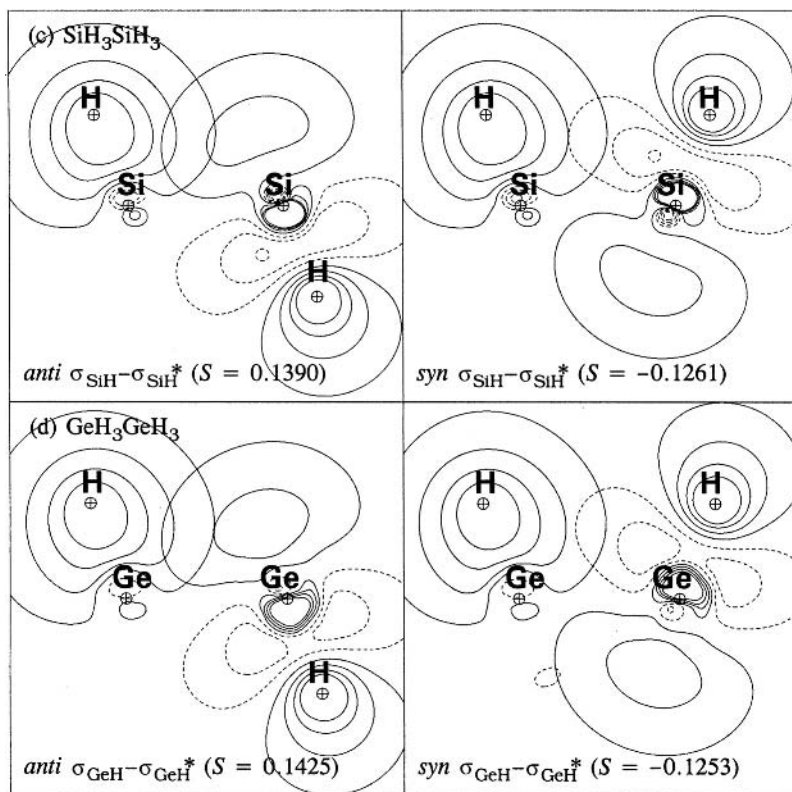
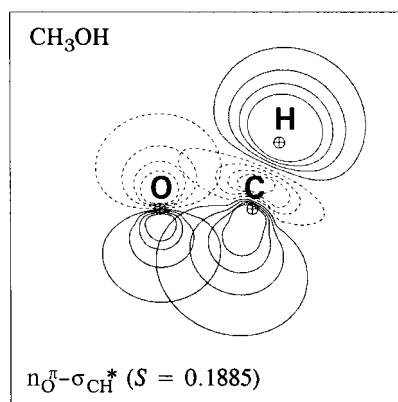


Figure 3.59 (Cont.)

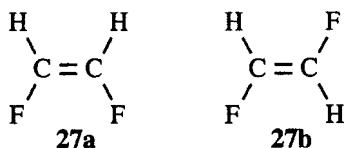
Figure 3.60 Vicinal $n_{\text{O}}^{\pi} \rightarrow \sigma_{\text{CH}}^*$ interaction for the pi-type lone pair of methanol, showing the equivalence of “*syn*” and “*anti*” interactions.

As shown in Table 3.23, the rotation barrier is sharply reduced as one moves from ethane to the later group 14 congeners SiH_3SiH_3 and GeH_3GeH_3 . This is both a distance and a polarity effect, as shown in Figs. 3.59(c) and (d). Owing to the larger Si—Si and Ge—Ge bond lengths (2.36 and 2.44 Å, respectively), the hyperconjugating $\sigma_{\text{MH}} \rightarrow \sigma_{\text{MH}}^*$ orbitals are held much further apart than in the C—C case (1.54 Å), appreciably reducing vicinal overlap. In addition, the lower electronegativity of Si and Ge causes each σ_{MH} donor to be unfavorably polarized toward H, thus reducing its amplitude (and donor strength) near the torsional axis, as shown in Figs. 3.59(c) and (d). (The absence of a significant σ_{MH} “backside lobe” for interaction with the middle lobe of the antibond is a particularly conspicuous aspect of this unfavorable polarity.) These two effects combine to make the $\sigma_{\text{MH}}-\sigma_{\text{MH}}^*$ stabilizations rather feeble in the favored *anti* arrangement (0.65 and 0.69 kcal mol⁻¹ for Si and Ge, respectively), only slightly greater than in the *syn* arrangement (0.38 and 0.40 kcal mol⁻¹, respectively). Thus, the overall barrier falls to a small fraction of its value in ethane, despite qualitative similarities in the vicinal donor and acceptor NBOs that dictate torsional preference in each case.

Of course, by replacing hydride bonds by bulky groups R and R' in $\text{CH}_2\text{R}-\text{CH}_2\text{R}'$ compounds, one can eventually reach the limit in which direct $\text{R} \cdots \text{R}'$ steric contacts become the dominant factor dictating conformational preference. (In a similar manner one can force *cis* $\text{CHR}=\text{CHR}'$ compounds out of their conjugatively preferred planarity by having sufficiently large R and R' groups.) However, gross steric effects are typically less important than hyperconjugative donor–acceptor interactions for controlling conformational preferences in the majority of cases involving monatomic or small-group ligands.

“Steric attraction” in 1, 2-difluoroethylene

A particularly dramatic and interesting example of the dominant role of hyperconjugative interactions over steric and electrostatic interactions is given by *cis* (**27a**) and *trans* (**27b**) isomers of 1,2-difluoroethylene:



Both steric and electrostatic factors appear to favor the *trans* configuration, in which the bulkier and anionically charged F atoms are separated as far as possible. Nevertheless, **27a** is actually found to be the energetically favored isomer by 0.80 kcal mol⁻¹, a counterintuitive result that has been attributed to “steric attraction.”⁸³

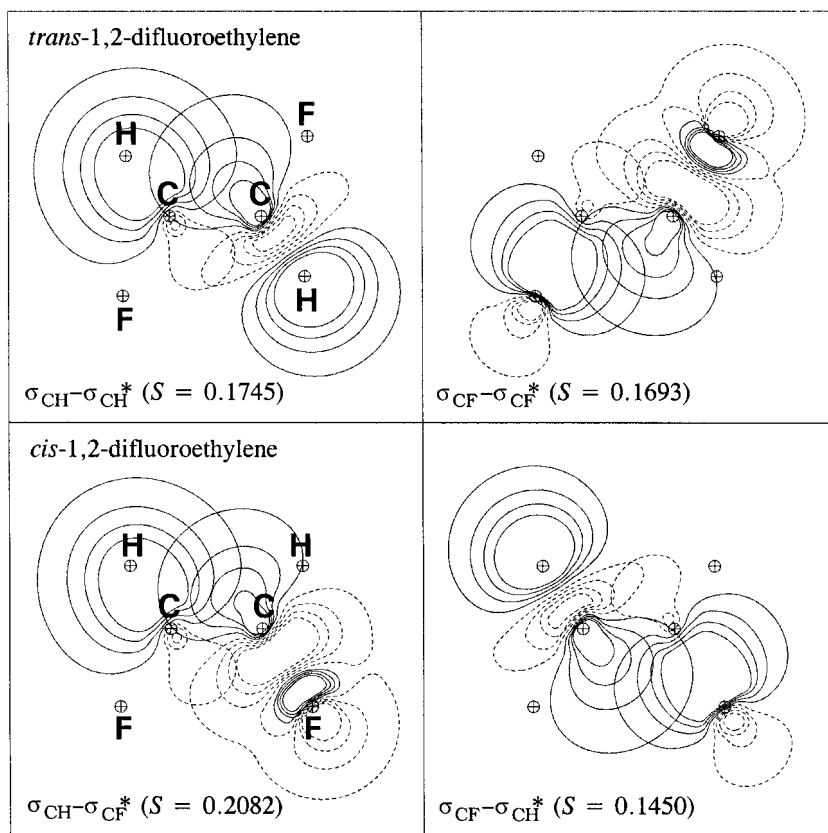


Figure 3.61 Leading hyperconjugative donor–acceptor interactions in *trans* (upper panels) and *cis* (lower panels) 1,2-difluoroethylene.

From the relative strengths of donor and acceptor groups summarized in (3.161), one can recognize that a C—F bond, although an exceedingly good acceptor, is a feeble donor for hyperconjugative interactions. It is therefore advantageous to orient each σ_{CF}^* acceptor *anti* to σ_{CH} (as occurs in the *cis* isomer) rather than to σ_{CF} (as occurs in the *trans* isomer). Figure 3.61 shows NBO overlap diagrams that illustrate the advantageous pattern of donor–acceptor interactions in the *cis* isomer.

According to second-order perturbative estimates, each $\sigma_{\text{CH}} \rightarrow \sigma_{\text{CF}}^*$ interaction of the *cis* isomer (lower left panel of Fig. 3.61) contributes $6.84 \text{ kcal mol}^{-1}$ stabilization, about *twice* that of the $\sigma_{\text{CH}} \rightarrow \sigma_{\text{CH}}^*$ ($3.75 \text{ kcal mol}^{-1}$)⁸⁴ or ($2.29 \text{ kcal mol}^{-1}$) interactions of the *trans* isomer. Even though the remaining $\sigma_{\text{CF}} \rightarrow \sigma_{\text{CH}}^*$ interaction of the *cis* isomer contributes only $1.17 \text{ kcal mol}^{-1}$ stabilization, the sum of the four *anti* donor–acceptor interactions favors the *cis* isomer by almost 4 kcal mol^{-1} . This hyperconjugative advantage of the *cis* isomer is sufficient to overcome the inherent steric and electrostatic advantage of the *trans* isomer.

Numerous small geometrical and energetic differences contribute to the *cis-trans* net energy difference. However, it is evident that ordinary hyperconjugative donor-acceptor interactions (akin to those in ethane-like molecules) can qualitatively account for the surprising stability of the *cis* configuration, without invocation of “steric attraction” or other ad-hoc mechanisms.

The gauche effect, anomeric effect, and related phenomena

The principle that maximum hyperconjugative stabilization results from orienting the best vicinal donors (3.161a) *anti* to the best vicinal acceptors (3.161b) has an immediate corollary.

Each strong donor prefers to orient anti to a strong acceptor (rather than another strong donor). Therefore, two strong donors (such as lone pairs) or two strong acceptors (such as polar bonds) will tend to orient *gauche* to one another.

The general tendency of vicinal lone pairs or highly polar bonds to adopt mutually *gauche* orientation has been called the “*gauche effect*.”⁸⁵ In the special case of carbohydrate chemistry, the characteristic preference for conformations aligning polar bonds in mutually *gauche* arrangements is usually termed the “*anomeric effect*.”⁸⁶ Both “effects” were formerly attributed rather vaguely to steric or electrostatic factors. However, the proper hyperconjugative explanation of the carbohydrate anomeric effect (orienting oxygen lone pairs *anti* to vicinal polar σ_{CO^*} acceptors in a general $\ddot{\text{O}}-\text{C}-\ddot{\text{O}}$ linkage) was pointed out by Havinga and coworkers⁸⁷ and in more quantitative terms by Brunck and Weinhold. The pendulum toward recognition of the hyperconjugative origin of such effects has now swung so far that *all* ethane-like barrier preferences are sometimes referred to as “*anomeric effects*.”⁸⁸ The general importance of anomeric conformational preferences in the chemistry of carbohydrates can hardly be overestimated.

The *gauche* effect is manifested even in the simplest tetraatomic species that could exhibit a rotation barrier, such as hydrogen peroxide (HOOH) and hydrogen disulfide (HSSH).⁸⁹ In both these species the only stable rotameric form is a twisted (C_2) *gauche* conformation with dihedral angle $\phi = 111.3^\circ$ (HOOH) or 91.0° (HSSH). In each case the *anti* arrangement that would be “expected” on steric or electrostatic grounds is found to be an unstable (transition-state) *maximum*, lying $1.23 \text{ kcal mol}^{-1}$ (HOOH) or $5.81 \text{ kcal mol}^{-1}$ (HSSH) above the *gauche* minimum. Figure 3.62 illustrates the leading $n_{\text{O}}-\sigma_{\text{OH}^*}$ (left) and $n_{\text{S}}-\sigma_{\text{SH}^*}$ (right) hyperconjugative interactions that become available in the *gauche* conformer, but are effectively quenched in the unstable planar ($\phi = 0^\circ, 180^\circ$) rotamers. Note how the unfavorable polarization of σ_{OH^*} leads to a greatly weakened interaction with the lone pair in HOOH, whereas the greater electropositivity of S leads to a much more favorable σ_{SH^*} acceptor in the corresponding interaction in HSSH.

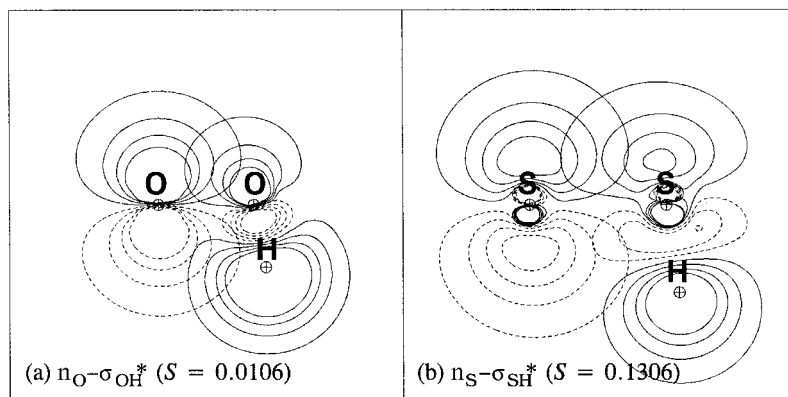


Figure 3.62 Leading $n\text{-}\sigma^*$ hyperconjugative donor-acceptor interactions in *gauche* equilibrium geometries of (a) HOOH and (b) HSSH. The corresponding stabilization energies are estimated as 1.37 and 4.20 kcal mol⁻¹, respectively.

Figure 3.63 illustrates the *gauche* effect for vicinal lone pairs and polar C—F bonds with the examples of (a) hydrazine and (b) 1,2-difluoroethane, respectively. As seen in Fig. 3.63(a), the $\phi = 180^\circ$ conformation in which both hydrazine lone pairs are *anti* to one another (thus squandering their powerful donor strength on vicinal moieties with *no* acceptor capacity) is disfavored by 3.2 kcal mol⁻¹ relative to the preferred $\phi = 93.9^\circ$ conformer in which each n_N hyperconjugates effectively with

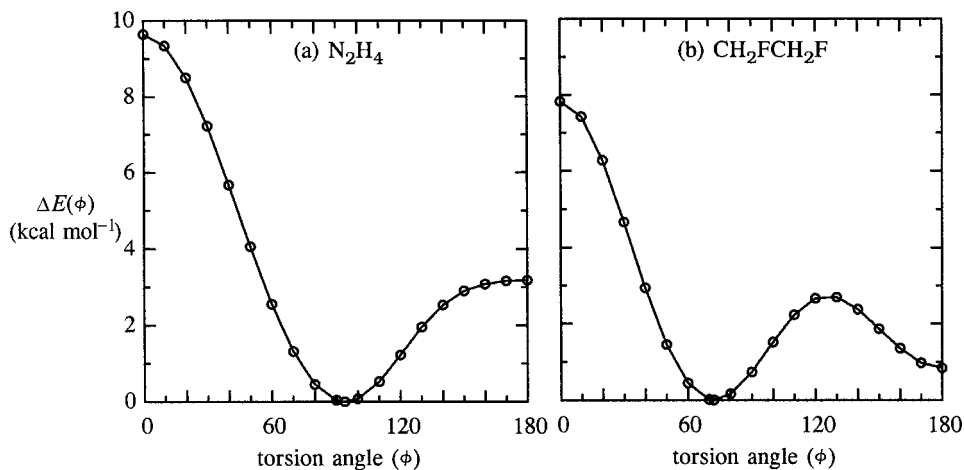


Figure 3.63 Rotation-barrier profiles illustrating the *gauche* effect for (a) lone pairs in hydrazine and (b) polar bonds in 1,2-difluoroethane. (The angle $\phi = 0^\circ$, as ϕ is the dihedral between bisectors of the amine groups in hydrazine, or the FCCF dihedral angle in 1,2-difluoroethane.) The respective torsional minima are at (a) 93.9° and (b) 72.2° .

both out-of-plane σ_{NH}^* acceptors (estimated total stabilization 15.3 kcal mol⁻¹). Similarly, in Fig. 3.63(b), the $\phi = 180^\circ$ conformation that puts the two C—F bonds *anti* to one another is disfavored compared with the $\phi = 72.2^\circ$ conformation in which each strong σ_{CF}^* acceptor lies approximately *anti* to the stronger σ_{CH} donor (as in the analogous 1,2-difluoroethylene case, cf. Fig. 3.61). In both cases the preferred *gauche* conformations appear counterintuitive from a naive steric or electrostatic viewpoint, but they are entirely reasonable to maximize hyperconjugative donor–acceptor interactions.

To exhibit the powerful tendency of a strong donor and strong acceptor to adopt the *anti* orientation, we consider the hypothetical molecule fluoromethylamine (CH₂FNH₂). Favorable *anti* alignment of the n_{N} donor and σ_{CF}^* acceptor results in a deep minimum at $\phi = 0^\circ$,⁹⁰ as shown in Fig. 3.64(a). A corresponding contour diagram of the $n_{\text{N}}-\sigma_{\text{CF}}^*$ interaction (with estimated stabilization energy 21.7 kcal mol⁻¹) is shown in Fig. 3.64(b). In fact, the tendency toward an *anti* $n_{\text{N}}-\sigma_{\text{CF}}^*$ arrangement is so strong that the corresponding *syn*-like arrangement (at $\phi = 180^\circ$) does not *exist* on an adiabatic one-dimensional torsional potential (i.e., with complete optimization of all other coordinates). For dihedral angles $\phi > 150^\circ$, the amine group spontaneously *inverts* (via the umbrella-like pyramidalization motion) to put n_{N} and σ_{CF}^* into a *trans*-like arrangement again. The effect of the $n_{\text{N}}-\sigma_{\text{CF}}^*$ interaction (shown as a dashed line in Fig. 3.64(a)) is so pronounced as to remove the usual three-fold character of the ethane-like barrier potential, replacing it by a two-fold profile that crudely mirrors the $n_{\text{N}}-\sigma_{\text{CF}}^*$ dihedral dependence. Thus,

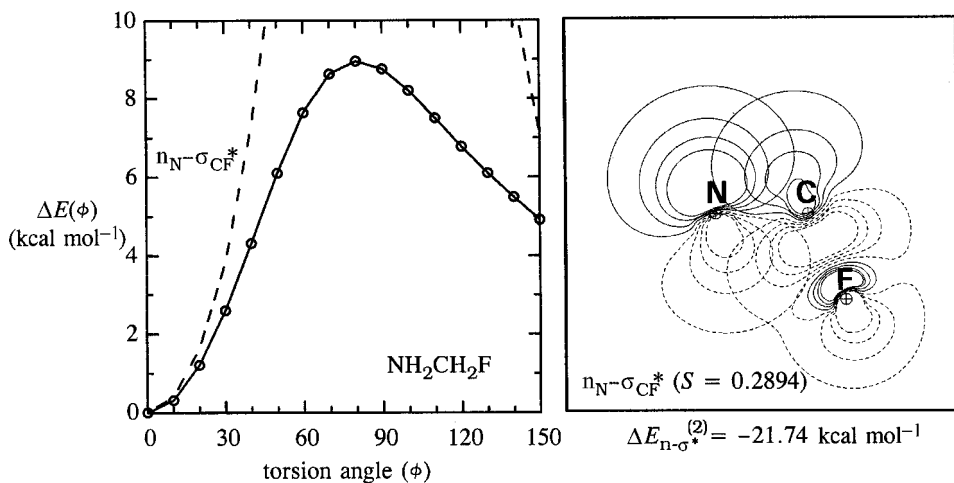


Figure 3.64 Torsion-barrier interactions of NH₂CH₂F. Left panel: the torsional potential (solid line) and leading $n_{\text{N}}-\sigma_{\text{CF}}^*$ stabilization (dashed line) in the range $\phi = 0-150^\circ$, where the amine group does not spontaneously undergo inversion. Right panel: orbital contours of the strong $n_{\text{N}}-\sigma_{\text{CF}}^*$ interaction at $\phi = 0^\circ$.

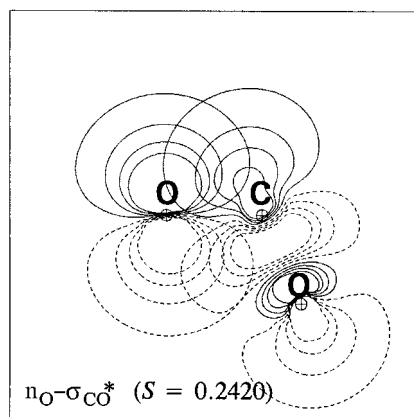


Figure 3.65 The prototypical $n_{\text{O}}-\sigma_{\text{CO}}^*$ “anomeric” donor–acceptor interaction in dihydroxymethane (estimated second-order stabilization energy 14.43 kcal mol⁻¹).

Fig. 3.64 dramatically illustrates how the hyperconjugative preference for strong vicinal donor–acceptor interactions may overcome pyramidalization barriers and other “expected” constraints on a torsion-barrier profile.

As a prototypical example of the anomeric effect we consider the simple case of dihydroxymethane (methanediol). The characteristic *anti* alignment of the pi-type oxygen lone pair n_{O} with the vicinal σ_{CO}^* antibond is illustrated in Fig. 3.65. This strong donor–acceptor interaction is estimated to contribute 14.4 kcal mol⁻¹ stabilization energy, exerting a decisive influence on conformational equilibria in general XO—C—OY linkages. Petillo and Lerner⁹¹ have demonstrated the direct causal connection between the $n_{\text{O}}-\sigma_{\text{CO}}^*$ interaction of Fig. 3.65 and the complete set of characteristic structural and spectroscopic signatures identified as “anomeric effects.”

In comparison with previous plots of this section, the $n_{\text{O}}-\sigma_{\text{CO}}^*$ anomeric interaction of Fig. 3.65 can be seen to be a rather typical example of hyperconjugative donor–acceptor interactions. Consequently, there seems to be no valid reason to invoke a special “effect” for the conformational preferences of sugars, obscuring their essential *conformity* with a unified donor–acceptor picture of ethane-like rotation barriers.

Torsional flexing and related torsion–vibration-coupling effects

At the most elementary level of valence theory, chemical bonds (and the associated NBOs) are expected to retain approximately fixed forms during internal rotations. At this level one can simply visualize torsional interactions in terms of frozen NBOs moving on a frozen “rigid-rotor” geometrical framework, with NBO populations

(and hyperconjugative stabilizations) waxing and waning as vicinal donor and acceptor NBOs rotate in and out of favorable overlap. This viewpoint corresponds closely to the second-order perturbation framework used throughout this book (cf. Eq. (1.24) and Fig. 1.3), with leading energy corrections expressed in terms of fixed “unperturbed” donor and acceptor NBOs. Such an elementary viewpoint allows many *qualitative* aspects of hyperconjugation and torsion-barrier phenomena to be understood satisfactorily.

Nevertheless, at a higher level of approximation one expects that donor–acceptor delocalization can alter the *form* (as well as the occupancies) of strongly interacting donor and acceptor NBOs, leading to higher-order *coupling* effects. These effects include the slight “flexings” of bond lengths and angles that accompany torsional change, as mentioned in previous sections. Owing to such coupling effects, the torsional coordinate can serve as an important “doorway” mode, allowing strong normal-mode mixing and efficient intramolecular vibrational relaxation (IVR) between local modes of the torsion-linked chemical groups. We now wish to describe the leading torsion–vibration coupling effects from the NBO donor–acceptor viewpoint. For this purpose we employ Fig. 3.66, which depicts a generic pair of interacting NBOs σ_{AB} and σ_{CD}^* (actually σ_{CH} and σ_{CH}^*) in a favorable alignment for strong donor–acceptor stabilization.

From the qualitative form of Fig. 3.66 one can predict certain changes in geometry and NBO composition that are promoted by strong σ_{AB} – σ_{CD}^* interaction, and that reciprocally enhance this interaction. We shall use the example of the strong n_N – σ_{CD}^* interaction of $\text{NH}_2\text{CH}_2\text{F}$ (see Fig. 3.64) to illustrate these changes, as summarized in Tables 3.24 (geometry) and 3.25 (NBO composition).

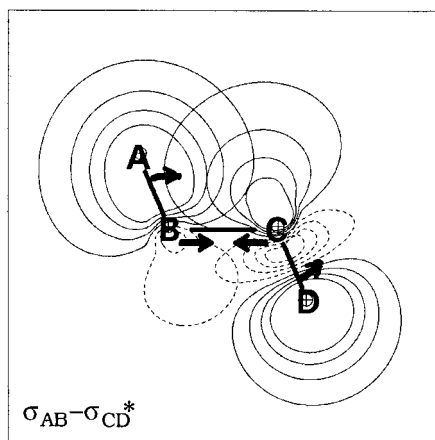


Figure 3.66 Schematic geometrical flexing to maximize the interaction of a strong donor σ_{AB} and a strong acceptor σ_{CD}^* .

Table 3.24. Torsional flexing of $\text{NH}_2\text{CH}_2\text{F}$, showing relaxed R_{NC} and R_{CF} bond lengths and θ_{lpNC} and θ_{NCF} valence angles with variation of the torsion angle ϕ (cf. Fig. 3.64) (θ_{lpNC} denotes the angle between the lone pair and σ_{NC} NHOs at N)

ϕ (degrees)	$R_{\text{NC}}(\text{\AA})$	$R_{\text{CF}}(\text{\AA})$	θ_{lpNC} (degrees)	θ_{NCF} (degrees)
0	1.4070	1.4332	106.3	113.6
30	1.4137	1.4275	106.3	112.9
60	1.4413	1.4064	107.7	110.3
90	1.4512	1.3926	109.4	107.7

Geometry

As depicted by the arrows in Fig. 3.66, the most obvious way to increase $\sigma_{\text{AB}} - \sigma_{\text{CD}}^*$ interaction is by shortening the R_{BC} bond length, bringing the donor and acceptor orbitals into closer proximity. Accordingly, the R_{BC} bond is expected to shorten when σ_{AB} and σ_{CD}^* are in favorable *anti* alignment and lengthen when these orbitals are twisted into unfavorable perpendicular (*perp*) alignment. Thus, in $\text{NH}_2\text{CH}_2\text{F}$ the R_{NC} axial bond lengthens by more than 0.04 Å (from 1.4071 to 1.4512 Å) between *anti* ($\phi = 0^\circ$)⁹¹ and *perp* ($\phi = 90^\circ$) conformations, as shown in Table 3.24. This change is in accordance with the expected reduction in partial double-bond character (see, e.g., Example 1.4 or Fig. 3.78) as the hyperconjugating groups are twisted out of coplanarity.

Because the $\sigma_{\text{AB}} - \sigma_{\text{CD}}^*$ overlap in Fig. 3.66 primarily involves the “shoulder” of the σ_{AB} donor NBO and the “backside lobe” of the σ_{CD}^* acceptor NBO, one can evidently enhance their interaction by the indicated *angular* changes, by *closing* the bond angle θ_{ABC} (to tilt the donor σ_{AB} shoulder toward the backside lobe of the acceptor) or by *opening* the θ_{BCD} angle (to tilt the σ_{CD}^* backside lobe more deeply into the interior of the donor). Table 3.24 shows that the θ_{lpNC} and θ_{NCF} angles of

Table 3.25. Torsional variation of NBO overlap ($S_{\text{n}\sigma^*}$), stabilization energy ($\Delta E_{\text{n}\sigma^*}^{(2)}$), occupancies, and ionicities (i_{AB}) pertaining to $\text{n}_\text{N} - \sigma_{\text{CF}}^*$ interaction in $\text{NH}_2\text{CH}_2\text{F}$

ϕ	$S_{\text{n}\sigma^*}$	$\Delta E_{\text{n}\sigma^*}^{(2)}$ (kcal mol ⁻¹)	Occupancy (e)		Ionicity	
			n_N	σ_{CF}^*	i_{CF}	i_{NC}
0	0.2894	21.74	1.8926	0.0983	0.4656	0.1998
30	0.2664	17.93	1.9016	0.0853	0.4634	0.1998
60	0.1606	5.33	1.9420	0.0416	0.4582	0.1936
90	0.0100	0.00	1.9612	0.0219	0.4542	0.1898

$\text{NH}_2\text{CH}_2\text{F}$ vary strongly in the expected manner, with the donor n_{N} NBO tilting about 3° toward the rotor axis and the acceptor σ_{CD}^* NBO tilting about 6° away from this axis as these orbitals twist from *perp* to *anti* alignment. (The relative magnitudes of bond stretches and bends are in line with known differences in stretching and bending force constants and generally consistent with the relatively small energetic driving forces expected from hyperconjugative donor–acceptor interactions.)

An additional geometrical effect can be expected from the fact that the $n_{\text{N}}-\sigma_{\text{CF}}^*$ interaction transfers electronic population into the C—F antibond, thus significantly lengthening and weakening this bond.⁹² As seen in Table 3.24, the C—F acceptor bond of $\text{NH}_2\text{CH}_2\text{F}$ is lengthened by more than 0.04 \AA in the *perp* \rightarrow *anti* transition, which is consistent with this expectation.

The NBO composition

Table 3.25 shows how the main NBO descriptors vary in the *perp* \rightarrow *anti* transition of $\text{NH}_2\text{CH}_2\text{F}$. As expected, this torsional change leads to strong increases in overlap (from $S_{n\sigma}^* = 0.01$ to $S_{n\sigma} = 0.29$) and hyperconjugative stabilization (from 0 to $21.7 \text{ kcal mol}^{-1}$), as well as significant population shifts ($\sim 0.07e$) from n_{N} to σ_{CD}^* .

Less conspicuous are changes in the *form* of the NBOs themselves, particularly those affecting the *polarity* (ionicity i_{AB}) of the participating NBOs. As shown in Fig. 3.66, the principal contributions to $\sigma_{\text{AB}}-\sigma_{\text{CD}}^*$ overlap arise from the region near the B—C torsional axis. Thus, the $\sigma_{\text{AB}}-\sigma_{\text{CD}}^*$ interaction will be enhanced by polarizing σ_{AB} toward B (to increase i_{AB}) or by polarizing σ_{CD}^* toward C (i.e., polarizing σ_{CD} toward D, to increase i_{CD}); cf. Eqs. (1.41). Consistently with this expectation, the ionicity i_{CF} of the acceptor C—F bond is found to increase from 0.45 to 0.46 as the n_{N} and σ_{CF}^* NBOs are twisted into the *anti* arrangement. In addition, the axial N—C bond becomes more polarized in the staggered conformer (see the final column of Table 3.24), reflecting the tendency to maximize donor and acceptor amplitude near the N—C torsional axis.

Small changes in hybridization are also expected to accompany torsional transitions, in accordance with Bent's rule (Section 3.2.6) and general features of Fig. 3.66. In general, the changes in strong donor and acceptor NBOs are expected to be of opposite character, because these orbitals reflect opposing (complementary) aspects of the donor–acceptor interaction. For the acceptor C—F bond of $\text{NH}_2\text{CH}_2\text{F}$, for example, it can be expected that the amplitude of the backside lobe of σ_{CF}^* is increased by higher percentage p character in the h_{C} hybrid to F, which also promotes C—F lengthening (due to the extended range of p orbitals), and weakened effective h_{C} electronegativity (due to the higher energy of p orbitals). (One could also predict this hybridization shift by extrapolating to $R_{\text{CF}} \rightarrow \infty$, where the radical acceptor orbital on C is expected to be of increasingly high p character.) Consistently with Bent's rule, hyperconjugatively increased percentage p character in the h_{C} hybrid bonding to F leads to increased percentage s character in bonding

hybrids to other atoms. In this manner the various “uninvolved” stretches and bends may also become coupled to the torsional motion. However, such higher-order hyperconjugative effects are generally weaker than those mentioned above and will not be discussed further.

Methyl tilt

The tendency of a strong σ_{CD}^* acceptor to tilt *away* from the connecting axis to a strong hyperconjugating σ_{AB} donor (cf. Fig. 3.66) leads to an interesting symmetry-breaking effect for methyl groups in asymmetric environments. Early microwave measurements on methylamine⁹³ established that the symmetry axis of the methyl rotor does not coincide with the C—N axis, but instead tilts slightly ($\sim 4^\circ$) away from the direction of the adjacent NH_2 triangle, and toward the formal lone-pair position. Similar “methyl-tilt” effects have been observed in methanol, dimethylether, and many other compounds with methyl groups adjacent to lone-pair-bearing atoms. In each case the methyl axis appears to be tilted by approximately $2\text{--}4^\circ$ toward the lone pair(s) of the adjacent atom.⁹⁴ Considerable theoretical and spectroscopic evidence also indicates that the C—H bond is lengthened by a few thousandths of an ångström unit when *anti* to a lone pair.⁹⁵

The donor–acceptor picture readily accounts for the observed methyl tilting and distortion.⁹⁶ Figure 3.67 illustrates the asymmetric bending of each C—H bond of

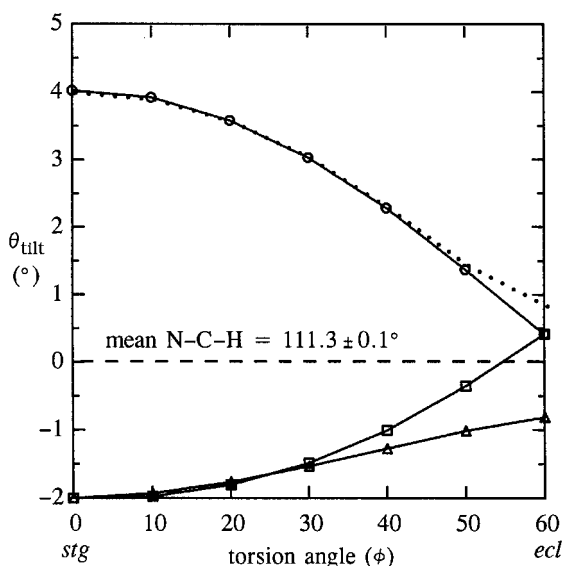


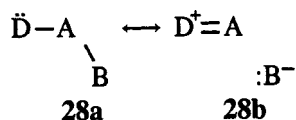
Figure 3.67 Methyl tilt in CH_3NH_2 , showing individual N—C—H angle deviations (solid lines) from the mean value ($111.3 \pm 0.1^\circ$) and the overall tilt angle (dotted line) of the methyl symmetry axis with respect to the C—N bond vector. The *anti* C—H bond (circles) corresponds to Fig. 3.59(a) at $\phi = 0^\circ$.

CH_3NH_2 , showing the $\sim 6^\circ$ variation in N—C—H angle as the H rotates from *gauche* to *anti* alignment with the vicinal n_{N} lone pair. The overall methyl tilt (dotted line) is evidently dominated by the strong outward tilting of the C—H bond *anti* to the lone pair, as discussed above (cf. Fig. 3.66 and Table 3.24).

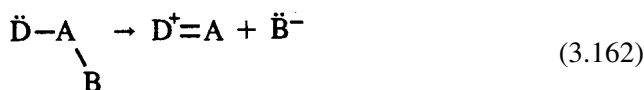
Secondary flexing effects and changes in steric repulsion also affect the detailed energetics of methyl tilting. As mentioned above, the hyperconjugative $n_{\text{N}}-\sigma_{\text{CH}}^*$ interaction lengthens (by about 0.008 Å) and weakens (by about 100 cm^{-1}) the C—H bond *anti* to the lone pair. Such hyperconjugatively induced distortions of idealized methyl geometry are opposed by increases in steric exchange energy (as illustrated in Fig. 3.56). The final geometry therefore reflects a variety of hyperconjugative and steric influences, but the essence of the tilting phenomenon seems to be well captured in the donor–acceptor diagram of Fig. 3.66.

Stereoelectronic effects in chemical reactivity

The bond-lengthening and -weakening influence of an antiperiplanar lone pair leads to strong “stereoelectronic” effects on chemical reactivity.⁹⁷ In molecule **28a** with lone-pair-bearing atom D adjacent to an A—B bond, a vicinal $n_{\text{D}}\rightarrow\sigma_{\text{AB}}^*$ hyperconjugative interaction can be associated (cf. Example 1.4 and Section 3.3.1) with a partial admixture of the alternative resonance structure **28b**,

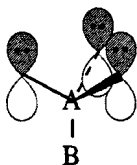


representing virtually a “head-start” toward the heterolytic bond-cleavage reaction

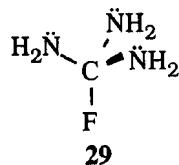


in a polar medium.⁹⁸ Molecules **28a** with n_{D} oriented *anti* to A—B are therefore expected to undergo the dissociative reaction (3.162) with unusual facility. Thus, while a hyperconjugative $n_{\text{D}}\rightarrow\sigma_{\text{AB}}^*$ interaction tends to stabilize the molecule thermodynamically, it may also lower the activation barrier to A—B bond dissociation, sowing the seeds of kinetic instability.

The stereoelectronic bond-weakening effect on A—B can be further promoted by additional vicinal n_{D} donors in molecules of the form



A simple example is provided by triaminomethyl (guanidinium) fluoride, **29**,



in which the C—F bond can lie *anti* to as many as three n_{N} donor lone pairs, each contributing an incremental lengthening and weakening of the bond. The remarkable stability of the guanidinium carbocation provides direct experimental evidence for the strong stereoelectronic enhancement of the ionic resonance form **28b**.

To study the stereoelectronic effect of antiperiplanar $n_{\text{N}} \rightarrow \sigma_{\text{CF}}^*$ interactions on C—F reactivity quantitatively, we consider the four rotameric isomers of **29** shown in Fig. 3.68. These correspond to having zero (**29ggg**), one (**29agg**), two (**29aag**), or all three (**29aaa**) nitrogen lone pairs *anti* (rather than *gauche*) to the target C—F

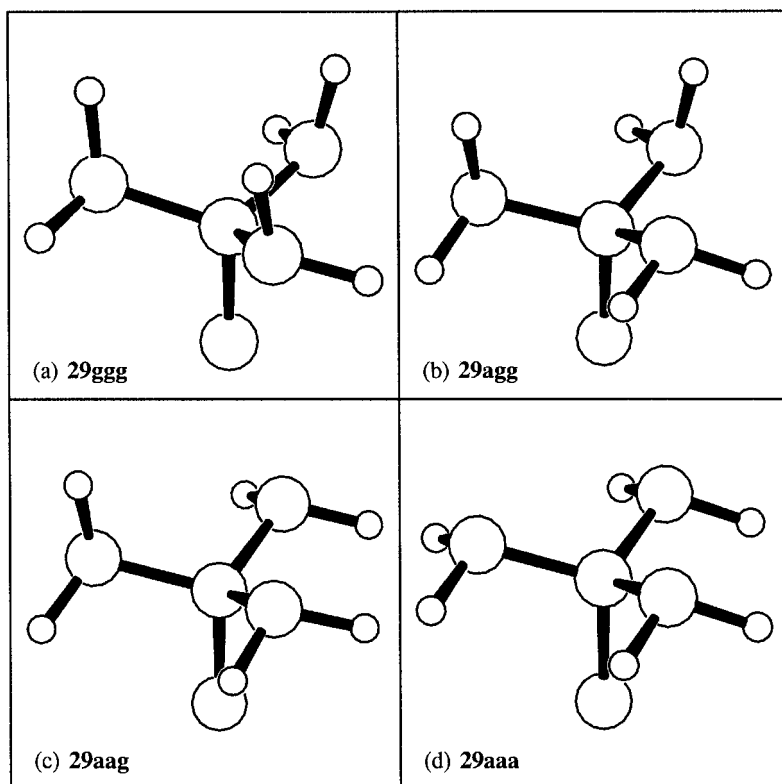


Figure 3.68 Optimized rotamers of triaminomethyl fluoride **29**: (a) *gauche-gauche-gauche*, (b) *anti-gauche-gauche*, (c) *anti-anti-gauche*, and (d) *anti-anti-anti*. (The **aaa** rotamer is a transition state between equivalent **aag** rotamers).

Table 3.26. Relative energies ΔE and other properties of triaminomethyl fluoride rotamers (cf. Fig. 3.68) showing C—F bond length R_{CF} , frequency ν_{CF} , NRT bond order b_{CF} , bond ionicity i_{CF} , fluoride charge q_F , and average second-order stabilization energy for anti-oriented $n_N-\sigma_{CF}^*$ and $n_N-\sigma_{CN}^*$ interactions

Species	ΔE (kcal mol ⁻¹)	R_{CF} (Å)	ν_{CF} (cm ⁻¹)	b_{CF}	i_{CF}	q_F (<i>e</i>)	Stabilization (kcal mol ⁻¹)	
							$n_N-\sigma_{CF}^*$	$n_N-\sigma_{CN}^*$
29ggg	4.90	1.4041	939	0.9630	0.4596	-0.4067	—	10.61
29agg	0.75	1.4262	757	0.9483	0.4702	-0.4289	19.34	11.29
29aag	0.00	1.4650	704	0.9262	0.4830	-0.4610	19.88	11.84
29aaa	2.56	1.5288	477	0.8884	0.5024	-0.5085	20.35	—

bond, with increasing stereoelectronic weakening. Note that inductive and steric effects should play little role in this comparison, so quantitative differences in C—F bond length, ionicity, and dissociation energetics can be taken as direct measures of the pure stereoelectronic (hyperconjugative donor–acceptor) influence.

Successive *anti* $n_N-\sigma_{CF}^*$ interactions lead to dramatic changes in the C—F bond, as summarized in Table 3.26. On average, each *anti* $n_N-\sigma_{CF}^*$ is seen to have the effect of lengthening the C—F bond by ~ 0.04 Å, decreasing its stretching frequency by ~ 150 cm⁻¹, and increasing its ionic charge at F by $\sim 0.03e$, thus appreciably altering the reactivity relative to “normal” C—F bonds (idealized sp^3 $R_{CF} \simeq 1.36$ Å).

Concomitant changes are also evident in the various NBO indices of Table 3.26, including NRT bond order b_{CF} and ionicity i_{CF} . Figure 3.69 illustrates, for example, how changes in bond length R_{CF} are accurately tracked by the variations in NRT bond order over the entire set of rotameric states.

The basic hyperconjugative $n_N \rightarrow \sigma_{CF}^*$ interactions in **29** are essentially similar to that illustrated earlier (cf. Fig. 3.64), and the corresponding stabilization energies shown in Table 3.26 are generally similar in magnitude to the value found previously for NH_2CH_2F (21.7 kcal mol⁻¹). However, it is interesting (and somewhat puzzling) to note that competing donations from three n_N donors to the single σ_{CF}^* acceptor in this case lead to somewhat *increased* stabilization (by about 1 kcal mol⁻¹; see the seventh column of Table 3.26), rather than the expected anticooperative weakening (as shown by $n_N \rightarrow \sigma_{CN}^*$ interactions, final column of Table 3.26). The answer to this puzzle seems to lie in the manner in which the alternative $n_N \rightarrow \sigma_{CN}^*$ *anti* arrangements themselves affect molecular geometry (and thereby $n_N \rightarrow \sigma_{CF}^*$ interaction strength). Each alternative $n_N \rightarrow \sigma_{CN}^*$ *anti* interaction is expected to *lengthen* the C—N acceptor bond, thus *weakening* the vicinal $n_N \rightarrow \sigma_{CF}^*$ interaction along this C—N axis. Thus, replacing *anti* $n_N \rightarrow \sigma_{CN}^*$ by *anti* $n_N \rightarrow \sigma_{CF}^*$ strongly alters the

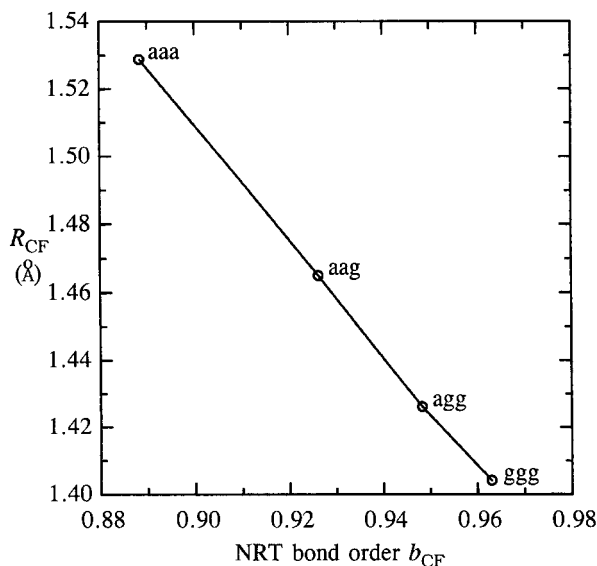
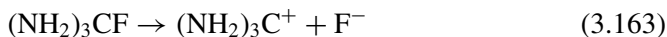


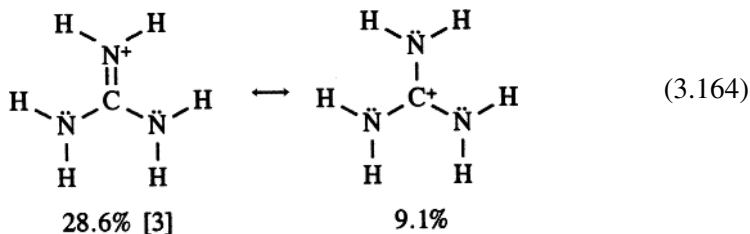
Figure 3.69 C—F bond-order-bond-length correlation for rotamers of triaminomethyl fluoride **29** (cf. Fig. 3.68), showing stereoelectronic bond lengthening and bond-order reduction with each new *anti* $n_N-\sigma_{CF}^*$ interaction. (Points are connected by straight lines to aid visualization.)

geometry in such a way as to promote the strength of *other* $n_N \rightarrow \sigma_{CF}^*$ interactions, despite the increased anticooperative competition for the single σ_{CF}^* acceptor. The overall reduction in average R_{CN} bond length (from 1.4411 Å in **29ggg** to 1.4175 Å in **29aaa**) reflects the more favorable skeletal geometry for $n_N \rightarrow \sigma_{CF}^*$ hyperconjugations in the latter species.

The strong stereoelectronic effect of vicinal n_N donors is also evident in the product guanidinium cation,



whose calculated geometry is shown in Fig. 3.70. In this species, strong hyperconjugative donation from the three nitrogen lone pairs to the formal empty carbocation p orbital leads to three equivalent pi-bonded resonance structures, in addition to the nominal single-bonded structure, with NRT weightings



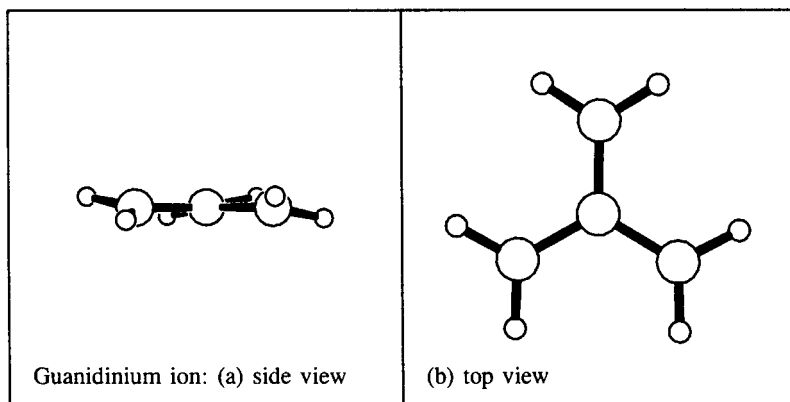


Figure 3.70 The equilibrium guanidinium cation, $(\text{NH}_2)_3\text{C}^+$, (a) side view and (b) top view. Each amino group is feathered by 12.5° with respect to the planar CN_3 skeleton in the propeller-like (C_3) equilibrium geometry.

and overall NRT bond order $b_{\text{CN}} = 1.3000$. This strong partial double-bond character naturally leads to a reduced C—N bond length (1.3349 \AA) as well as to planarized NH_2 groups, which provide a pure p-type n_{N} that is best able to donate to the empty carbon p orbital in pi-type fashion. However, in this tightly pi-bonded skeletal geometry the planar NH_2 groups come into unfavorable steric contact, which is relieved by “feathering” each NH_2 slightly ($\sim 12^\circ$) out of planarity, as shown in Fig. 3.70. The final equilibrium geometry of the ion therefore reflects the balance between stereoelectronic stabilization (favoring planarity and C—N contraction) and $\text{H} \cdots \text{H}$ steric repulsion (favoring nonplanarity and C—N elongation).

In the extreme carbocation limit of (3.163) and (3.164), the stereoelectronic “secondary-hyperconjugation” effects therefore blend seamlessly into ordinary pi-type conjugation phenomena (Section 3.3), the two extremes always being linked by electronic continuity.

3.4.3 Through-bond and through-space interactions

Through-bond coupling in diaminoalkanes

Several lines of evidence suggest that the intramolecular interactions of remote orbitals are often mediated by the connecting bridge of chemical bonds. The characteristics that may distinguish such through-bond (TB) interactions from ordinary through-space (TS) interactions include (1) an “inverted” MO ordering, with the out-of-phase linear combination of orbitals lying *below* the corresponding in-phase combination; and (2) strong dependence of the energy splittings on the conformation

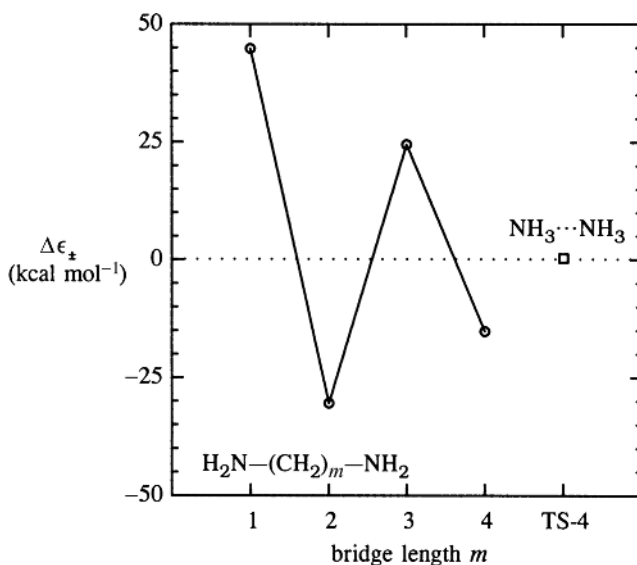
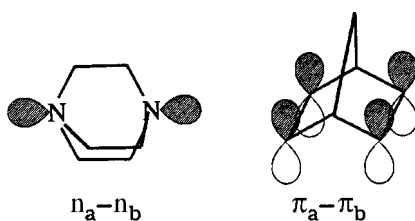


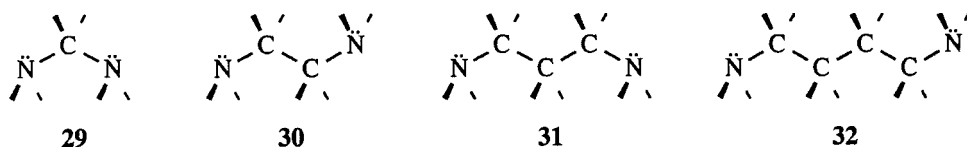
Figure 3.71 Through-bond (TB) splitting $\Delta\epsilon_{\pm} = \epsilon_{-} - \epsilon_{+}$ for idealized all-*trans* diaminoalkanes $\text{NH}_2-(\text{CH}_2)_m-\text{NH}_2$, $m = 1-4$ (**29-32**), compared with through-space $\text{NH}_3 \cdots \text{NH}_3$ interaction in relative geometry of $m = 4$ (TS-4).

of the bridging atoms. Hoffmann and coworkers⁹⁹ first called attention to the importance of TB interactions in species such as [2.2.2]diazabicyclooctane and norbornadiene:



The TB and TS interactions have subsequently been investigated for many systems by a variety of theoretical and experimental methods.¹⁰⁰

Simple examples of TB interactions are shown in Fig. 3.71 for a series of idealized all-*trans* diaminoalkanes $\text{H}_2\text{N}-(\text{CH}_2)_m-\text{NH}_2$, $m = 1-4$ (**29-32**):

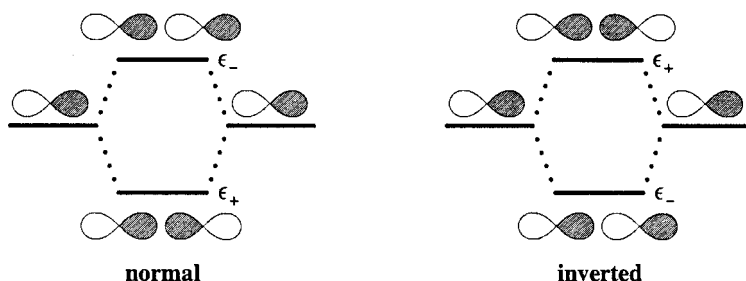


In these compounds the highest occupied MOs are expected to be approximated as in-phase or out-of-phase combinations of the two nitrogen lone pairs n_N and $n_{N'}$:

$$\phi_{\pm} \simeq 2^{-1/2}(n_N \pm n_{N'}) \quad (3.165a)$$

$$\Delta\epsilon_{\pm} = \epsilon_- - \epsilon_+ \quad (3.165b)$$

For TS interactions the in-phase combination is expected to lie lower in energy, leading to a “normal” energy splitting $\Delta\epsilon_{\pm}$ of positive sign:



However, Fig. 3.71 shows that, in the diaminoalkanes, this splitting actually oscillates strongly with the number m of bridging methylene groups, the splitting having the inverted (negative) sign for even $m = 2, 4$, but normal (positive) sign for odd $m = 1, 3$.

Figure 3.71 also compares the TB case $m = 4$ (**32**) with the corresponding TS case of an ammonia dimer ($\text{H}_3\text{N} \cdots \text{NH}_3$) having the two lone pairs at the *same* distance and relative orientation. In the latter case $\Delta\epsilon_{\pm}$ is found to be sharply reduced in magnitude and reversed in sign (from -15.20 to $+0.24$ kcal mol $^{-1}$), showing the dramatic difference between TB and TS patterns in both sign and magnitude of the interaction.

The paradoxical TB splitting patterns can be qualitatively rationalized in terms of the expected Fock-matrix interaction elements between each n_N and the filled and unfilled NBOs of the alkyl bridge. In the all-*trans* conformer, the strongest such interactions are those connecting each n_N with the adjacent vicinal σ_{CC} and σ_{CC}^* NBOs, whereas the direct TS n_N – $n_{N'}$ interaction element is essentially negligible. Within the idealized Lewis-structure picture, the MOs can be pictured as arising from variational mixing of the Lewis-type NBOs alone. According to the variational principle, the highest-occupied (HOMO) level can be shown to correspond to the *most out-of-phase* linear combination of filled NBOs¹⁰¹ (just as the ground level is the most in-phase combination). As a result, the HOMO will have each lone pair mixed out of phase with the vicinal NBO, and therefore in phase with one another, if n_N and $n_{N'}$ share the same vicinal σ_{CC} neighbor. A further contribution to the inverted splitting arises from n_N – σ_{CC}^* donor–acceptor interactions, because the n_N and $n_{N'}$ donors overlap constructively with opposite ends of the bridging σ_{CC}^*

antibond, and thus are coupled with opposite signs to any shared σ_{CC}^* acceptor. Thus, both types of interactions may contribute to the puzzling case in which the out-of-phase combination is stabilized and the in-phase combination is destabilized.

At a more quantitative level, NBO analysis has been employed in a variety of investigations¹⁰² to dissect the detailed pathways of TB interactions. Quantitative theoretical and experimental studies have shown the general unreliability of the older AO-based “superexchange” model¹⁰³ as a guide to TB pathways. The modern NBO-based picture of TB/TS interactions is authoritatively described elsewhere¹⁰⁴ and need not be elaborated here.

The relationship to ionization phenomena

Despite the strong MO mixings indicated by the $\Delta\epsilon_{\pm}$ splittings, one may question to what extent the MO energy variations are reflected in measurable physical properties. As described in Section 3.2.4, the interactions of filled NBOs lead to symmetric second-order energy shifts with no net effect on total energy, wavefunction, and other properties. However, the assumptions of Koopmans’ theorem imply that the vertical ionization potential (IP) is related to HOMO orbital energy by

$$\text{IP} \simeq -\epsilon_{\text{HOMO}} \quad (3.166)$$

and the strong TB-induced variations of ϵ_{HOMO} should therefore be reflected in corresponding variations in IP.

Specifically, if $\Delta(\text{IP})$ denotes the reduction of IP with respect to a chosen reference amine (e.g., isolated ammonia),

$$\Delta(\text{IP}) = \text{IP}(\text{diamine}) - \text{IP}(\text{ref.}) \quad (3.167)$$

one expects from Koopmans’ theorem (3.166) that

$$\Delta(\text{IP}) \simeq |\Delta\epsilon_{\pm}|/2 \quad (3.168a)$$

Furthermore, the singly occupied radical MO (ϕ_{rad}) of the ionized spin set in the cation should closely resemble either ϕ_- or ϕ_+ , according to whether $\Delta\epsilon_{\pm}$ is positive or negative,

$$\phi_{\text{rad}} \simeq \begin{cases} \phi_-, & \text{if } \epsilon_- > \epsilon_+ \\ \phi_+, & \text{otherwise} \end{cases} \quad (3.168b)$$

Perturbations of the neutral molecule that strongly alter TB coupling are therefore expected to alter strongly both $\Delta(\text{IP})$ and the form of ϕ_{rad} , if the Koopmans assumption is valid.

The contrary view of ionization developed in Section 3.2.4 is that strong electronic reorganization of the cation negates the basic assumption of Koopmans’ theorem. Superficial aspects of the Koopmans picture are preserved, however, because

the donor–donor interactions (e.g., $\sigma_{\text{CC}}-\text{n}_{\text{N}}$) leading to CMOs of the neutral parent are converted into corresponding donor–acceptor interactions (e.g., $\sigma_{\text{CC}}-\text{n}_{\text{N}}^*$) in the cation. A neutral amine whose lone pair n_{N} participates in strong $\sigma_{\text{CC}}-\text{n}_{\text{N}}$ TB interactions is therefore expected to give rise to a cationic n_{N}^* orbital that is strongly stabilized by $\sigma_{\text{CC}}-\text{n}_{\text{N}}^*$ donor–acceptor interactions, with a corresponding reduction of IP that somewhat mimics (3.168a). Thus, Eq. (3.168b) is likely to provide the more unique diagnostic of whether a Koopmans-like picture is valid.

To investigate the Koopmans assumptions (3.168) numerically, let us consider the TB-sensitive torsional variations of $\Delta\epsilon_{\pm}$ and $\Delta(\text{IP})$, and other properties of neutral and cationic butyldiamines **32** ($m = 4$). Figure 3.72 shows these variations for two idealized torsional coordinates: (a) twisting a terminal $-\text{NH}_2$ group about the connecting C—N bond, and (b) twisting a terminal $-\text{CH}_2\text{NH}_2$ group about the connecting C—C bond.

As shown in Fig. 3.72, the torsion (a) immediately twists the amine lone pair n_{N} out of favorable coplanarity with bridging σ_{CC} bonds, leading to strong *reversal* of $\Delta\epsilon_{\pm}$ splitting (from -15.2 to $+11.5$ kcal mol $^{-1}$). However, the “crankshaft” torsion (b) retains the favorable *anti* alignment of n_{N} with bridging σ_{CC} bonds (despite bringing n_{N} and $\text{n}_{\text{N}'}$ into much closer proximity). The latter torsion therefore preserves the inverted MO ordering for a much wider range of dihedral variations, until the amine groups are pressed into unrealistically close proximity against the strong steric repulsive forces. As mentioned above, such strong dependence of MO splittings on bridge conformation provides *prima-facie* evidence of TB coupling in the original sense of Hoffmann.

Despite the vivid ~ 27 kcal mol $^{-1}$ variation in TB splitting ($\Delta\epsilon_{\pm}$, dashed line) in Fig. 3.72(a), the total energy (E_{tot} , solid line) exhibits only the typical ± 2 kcal mol $^{-1}$ variations of an ordinary alkyl amine (Table 3.23). Thus, the variations in $\Delta\epsilon_{\pm}$ do not seem to reflect significant variations in stability or localization of the parent neutral species.

However, the vertical ionization energy ($\Delta(\text{IP})$, dotted line) in Fig. 3.72(a) is indeed seen to vary in the manner suggested by Eq. (3.168a). Thus, from the maximum at 90° , the IP is reduced by about 8 kcal mol $^{-1}$ (versus $|\Delta\epsilon_{\pm}|/2 \simeq 7.6$ kcal mol $^{-1}$) as the $\text{n}_{\text{N}}-\sigma_{\text{CC}}$ alignment returns to *anti* (**32**) at 180° . Similarly, for the twist from perpendicular to *syn* alignment, the IP is reduced by about 4.5 kcal mol $^{-1}$ (versus $|\Delta\epsilon_{\pm}|/2 \simeq 6$ kcal mol $^{-1}$). Similar approximate satisfaction of (3.168a) can be seen in Fig. 3.72(b). Thus, the plotted $\Delta(\text{IP})$ curves in Figs. 3.72(a) and (b) do indeed seem to suggest “Koopmans-like” behavior.

Nevertheless, the more direct test (3.168b) of the Koopmans assumption demonstrates the failure of this assumption for a wide range of torsional angles. Specifically, the form of the ionized radical orbital ϕ_{rad} is found to closely resemble ϕ_+ for *all* torsion angles shown in Figs. 3.72(a) and (b). Particularly striking is

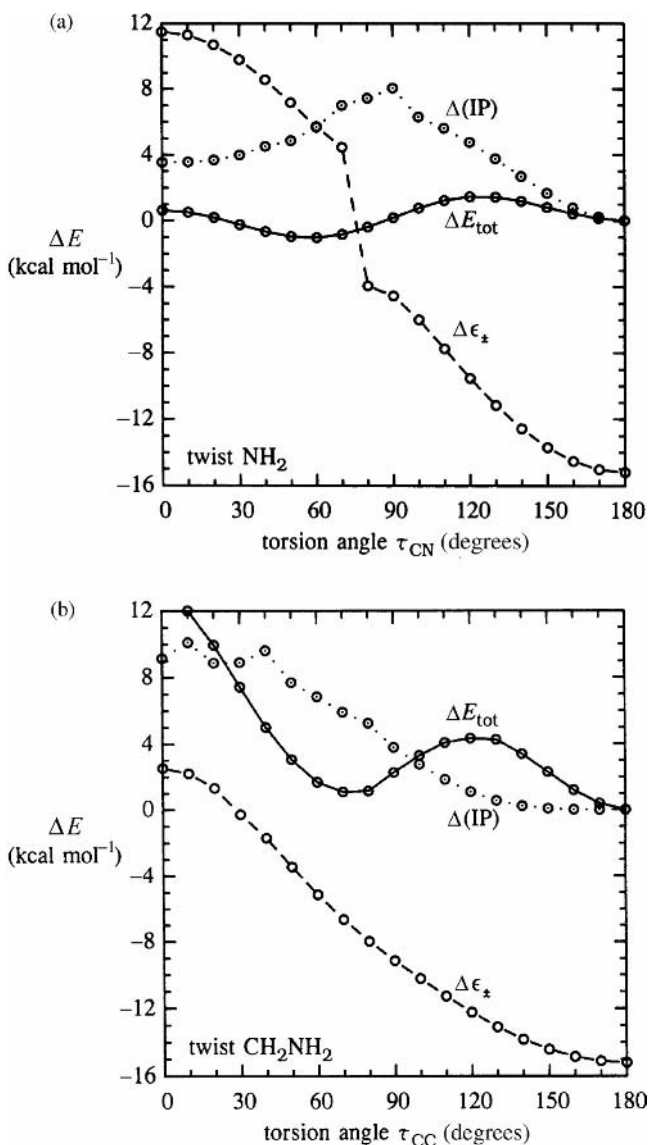


Figure 3.72 (a) Torsional properties of 1,4-diaminobutane, **32**, showing variations of total energy (E_{tot} , solid line), ionization potential (IP, dotted line), and CMO splitting (ϵ_{\pm} , dashed line) for twisting of the terminal -NH_2 group. The all-*trans* conformation **32** ($\phi_{\text{CN}} = 180^\circ$) is the reference zero for ΔE_{tot} and $\Delta(\text{IP})$ variations. (b) Similar to (a), for twisting of the terminal $\text{-CH}_2\text{NH}_2$ group about the C-C bond.

the comparison between the starting **aa** conformer (*anti-anti*, $\tau_{\text{CN}} = 180^\circ$) and the fully twisted **sa** conformer (*syn-anti*, $\tau_{\text{CN}} = 0^\circ$); despite the complete reversal of $\Delta\epsilon_{\pm}$ values in the parent neutral species from $-15.2 \text{ kcal mol}^{-1}$ in **aa** to $+11.5 \text{ kcal mol}^{-1}$ in **sa**, the cation electron configuration is *identical* in the two conformers. The stability of the ionic daughter $(\phi_-)^2(\phi_+)^1$ electron configuration therefore appears to be essentially independent of the TB splitting pattern of the parent neutral species, contrary to a Koopmans-type assumption. An even stronger violation of the Koopmans picture is found in diaminoethane **30** ($m = 2$), where the neutral TB splittings are $-30.05 \text{ kcal mol}^{-1}$ in the **aa** conformer (favoring $\phi_{\text{rad}} = \phi_+$) and $+18.71 \text{ kcal mol}^{-1}$ in the **sa** conformer (favoring $\phi_{\text{rad}} = \phi_-$), but the cationic radical MO is the in-phase ϕ_+ in *both* conformers. Thus, approximate satisfaction of (3.168a) cannot guarantee that Koopmans' theorem provides a correct qualitative picture of cationic electronic structure.

How does the NBO donor–acceptor picture account for the observed cationic $\phi_{\text{rad}} \simeq \phi_+$? If we let $\sigma_{\text{NN}'}^{\text{f}}$ and $\sigma_{\text{NN}'}^{\text{e}}$ respectively denote the “filled” and “empty” NBOs built from the two nitrogen lone pairs of the ionized spin set, one expects that the principal NBO donor–acceptor interactions with the bridge C—C bonds and antibonds are

$$\sigma_{\text{NN}'}^{\text{f}} \rightarrow \sigma_{\text{CC}}^* \quad (3.169\text{a})$$

$$\sigma_{\text{CC}} \rightarrow \sigma_{\text{NN}'}^{\text{e}} \quad (3.169\text{b})$$

By symmetry, one can recognize that $\sigma_{\text{NN}'}^{\text{f}}$ must be taken to be *out* of phase in order for it to interact favorably with the bridge antibond σ_{CC}^* in (3.169a), and similarly $\sigma_{\text{NN}'}^{\text{e}}$ must be *in* phase to serve as an effective acceptor for the bridge bond σ_{CC} in (3.169b). This necessitates that

$$\sigma_{\text{NN}'}^{\text{f}} = \sigma_{\text{NN}'}^* \simeq \phi_- \quad (\text{out of phase}) \quad (3.170\text{a})$$

$$\sigma_{\text{NN}'}^{\text{e}} = \sigma_{\text{NN}'} \simeq \phi_+ \quad (\text{in phase}) \quad (3.170\text{b})$$

Figure 3.73 depicts the leading donor–acceptor interactions (3.169a) and (3.169b) for the **aa** conformer of the diaminoethane cation **30**⁺, where the configuration is $(\phi_-)^2(\phi_+)^1$ (as predicted by Koopmans' theorem). As seen in the figure, the bridging interactions (3.169a) and (3.169b) respectively contribute 13.1 and 7.6 kcal mol⁻¹ stabilization to the cation.

If we now twist an amine group by 180° to the **sa** geometry, the **TB** splitting of the parent neutral species is strongly reversed in sign (from -30.1 to $+18.7 \text{ kcal mol}^{-1}$), suggesting that ionization should now occur out of the ϕ_- MO. However, the actual cation configuration is still $(\phi_-)^2(\phi_+)^1$ and the leading donor–acceptor interactions (3.169) still conform to (3.170), as shown in Fig. 3.74. Compared with **aa** geometry, the interactions (3.169) of the **sa** conformer are somewhat weakened ($9.7 \text{ kcal mol}^{-1}$

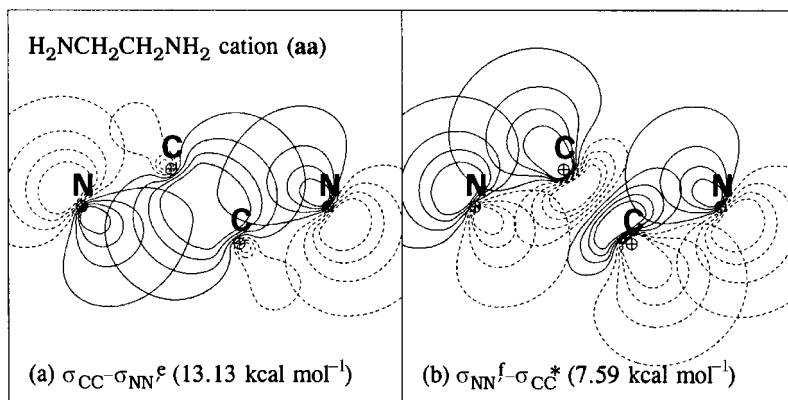


Figure 3.73 Leading NBO donor–acceptor interactions (and second-order stabilization energies) in the **aa** conformer of the 1,2-diaminoethane cation $\mathbf{30}^+$: (a) $\sigma_{\text{CC}} \rightarrow \sigma_{\text{NN}}^{\text{e}}$ and (b) $\sigma_{\text{NN}}^{\text{f}} \rightarrow \sigma_{\text{CC}}^*$. Note that the two N lone-pair hybrids are in phase (ϕ_+) in the acceptor $\sigma_{\text{NN}}^{\text{e}}$ (a), but out of phase (ϕ_-) in the donor $\sigma_{\text{NN}}^{\text{f}}$ (b).

for $\sigma_{\text{NN}}^{\text{f}} \rightarrow \sigma_{\text{CC}}^*$, $6.9 \text{ kcal mol}^{-1}$ for $\sigma_{\text{CC}} \rightarrow \sigma_{\text{NN}}^{\text{e}}$). However, these interactions contribute significant cationic stabilization *provided* that ϕ_{rad} is taken as the in-phase ϕ_+ , contrary to the Koopmans picture.

The *W*-effect and octant-rule interactions

The importance of specific orbital alignments in the TB propagation of remote stereoelectronic influences can be assessed directly by structure-sensitive spectroscopic techniques. The results of many such studies have been summarized as various “effects” or “rules” that express the dependence on geometrical factors, such as the all-*trans* zig-zag or “W” pattern of skeletal bridge bonds. Such a “W-effect”¹⁰⁵

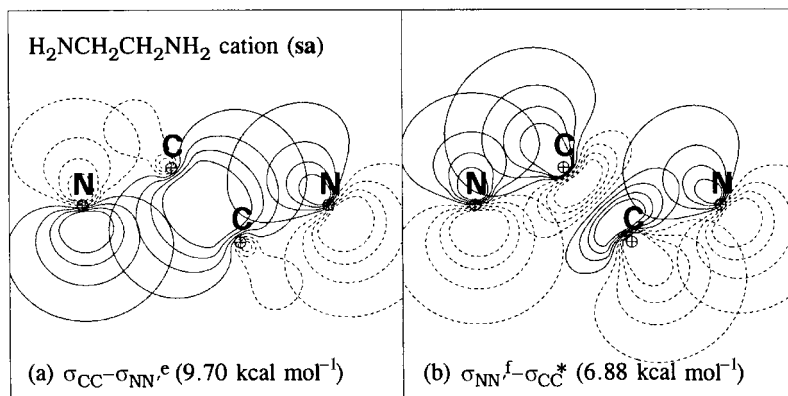


Figure 3.74 Similar to Fig. 3.73, for the **sa** conformer.

can evidently be related to the enhanced NBO donor–acceptor interactions characteristic of vicinal antiperiplanar orbital alignments, as discussed in many examples in this book.

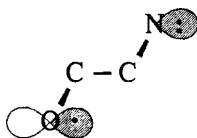
A particularly useful probe of remote-substituent influences is provided by optical rotatory dispersion (ORD),¹⁰⁶ the frequency-dependent optical activity of chiral molecules. The quantum-mechanical theory of optical activity, as developed by Rosenfeld,¹⁰⁷ establishes that the rotatory strength R_{0k} of a $\Psi_0 \rightarrow \Psi_k$ spectroscopic transition is proportional to the scalar product of electric dipole ($\vec{\mu}_{el}$) and magnetic dipole (\vec{m}_{mag}) transition amplitudes,

$$R_{0k} \propto \langle \Psi_0 | \vec{\mu}_{el} | \Psi_k \rangle \cdot \langle \Psi_k | \vec{m}_{mag} | \Psi_0 \rangle \quad (3.170)$$

Owing to the disparate selection rules governing electric- and magnetic-dipole transitions, R_{0k} vanishes (and ORD is quenched) whenever the molecular chromophoric group and associated wavefunctions Ψ_0 and Ψ_k have definite inversion or mirror-reflection symmetry. Such rotatory character would thus be expected to be absent from the famous $n \rightarrow \pi^*$ ($\simeq 290$ nm) transition of ketones, which is associated with the carbonyl chromophore of nominal C_{2v} local symmetry. Nevertheless, detectable optical activity can result from the slight mixing of carbonyl-based orbitals with those of asymmetrically distributed remote substituent groups. A simple one-electron perturbative treatment¹⁰⁸ supports assignment of the *sign* of each substituent's contribution according to its position with respect to symmetry planes of the carbonyl chromophore, as expressed in the octant rule¹⁰⁹ and related sector rules.¹¹⁰ Thus, ORD provides a sensitive measure of *differences* in delocalization pathways to chiral features of the chromophoric environment.

Let us now examine a simple numerical model for the mixing of substituent orbitals into the spectroscopic orbitals of the carbonyl chromophore. For this purpose we consider the triplet ${}^3n \rightarrow \pi^*$ excited state of the model amine derivative of methylethylketone shown in Fig. 3.75.

In the triplet excited state, an electron is formally removed from the oxygen n_O orbital (the in-plane p_y -type nonbonding orbital) of the β manifold and added to the π_{CO}^* antibond of the α manifold (formally “breaking” half the pi bond). From the viewpoint of the amine n_N donor, this excitation makes available a low-lying half-filled n_O acceptor NBO suitable for strong hyperconjugative stabilization. The n_N – n_O interaction



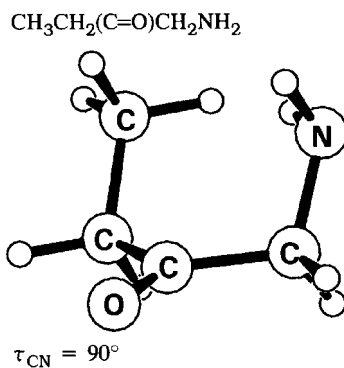


Figure 3.75 A model carbonyl compound with the amine group twisted for maximum delocalization of n_{N} into the half-filled carbonyl n_{O} orbital of the ${}^3n \rightarrow \pi^*$ excited state.

therefore leads to new filled (σ_{ON}^f) and empty (σ_{ON}^e) NLMO orbitals of β spin, mixing the parent n_{N} with the chromophore n_{O} and thus altering the excited-state spin density that enters spectroscopic transition moments. Figure 3.76 depicts the composition of the σ_{ON}^f NLMO, showing the percentages of n_{N} and n_{O} contributions as functions of the dihedral twisting of the amine group about the C—N bond.

As shown in Fig. 3.76, the NLMO composition varies dramatically, from virtually pure localized n_{N} character at $\tau_{\text{CN}} = 180^\circ$ (for which n_{N} and n_{O} are mutually

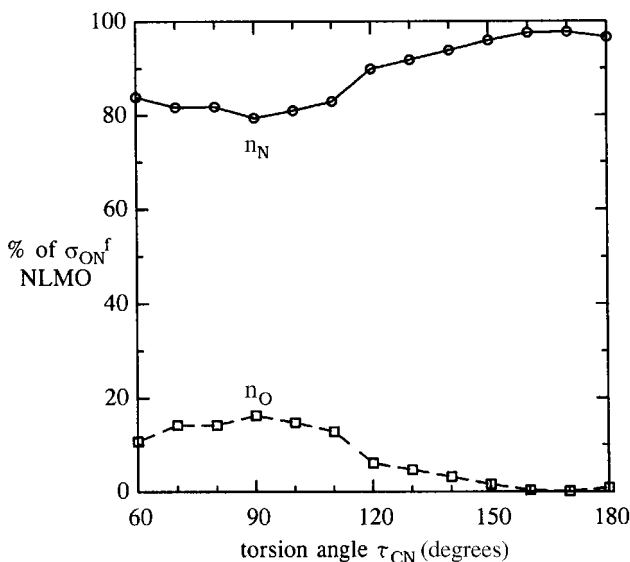


Figure 3.76 The torsion-dependent composition of the σ_{ON}^f NLMO of the ${}^3n \rightarrow \pi^*$ excited state of the model aminoketone shown in Fig. 3.75.

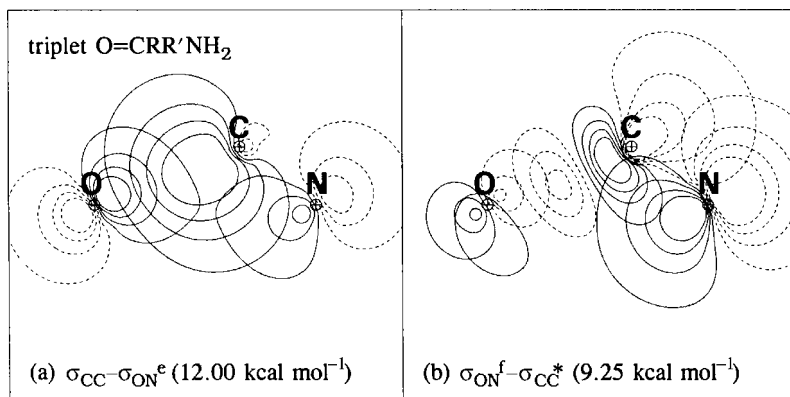


Figure 3.77 Leading donor–acceptor interactions in a $^3n\rightarrow\pi^*$ excited aminodi-alkyl ketone, showing filled ($\sigma_{\text{ON}}^{\text{f}}$) and empty ($\sigma_{\text{ON}}^{\text{e}}$) O—N orbitals of the ionized spin set in TB interactions with bridge σ_{CC} and σ_{CC}^* NBOs. (Note that σ_{CC} and σ_{CC}^* appear truncated because only the C atom directly bonded to N lies in the chosen contour plane.)

perpendicular) to $\sim 17\%$ n_{O} character at $\tau_{\text{CN}} = 90^\circ$ (for which n_{N} and n_{O} are parallel). Interestingly, the low-energy $\sigma_{\text{ON}}^{\text{f}}$ NLMO is the *out-of-phase* mixture, whereas the vacated $\sigma_{\text{ON}}^{\text{e}}$ NLMO from which excitation apparently occurred is the *in-phase* combination,

$$\sigma_{\text{ON}}^{\text{f}} \simeq 0.91n_{\text{N}} - 0.41n_{\text{O}} \quad (3.171\text{a})$$

$$\sigma_{\text{ON}}^{\text{e}} \simeq 0.41n_{\text{N}} + 0.91n_{\text{O}} \quad (3.171\text{b})$$

This surprising inversion shows unequivocally the role of TB coupling involving the bridging σ_{CC} and σ_{CC}^* NBOs that are in favorable antiperiplanar alignments with both n_{N} and n_{O} .

Figure 3.77 depicts contour diagrams of the leading excited-state TB interactions

$$\sigma_{\text{CC}} \rightarrow \sigma_{\text{ON}}^{\text{e}} \quad (3.172\text{a})$$

$$\sigma_{\text{ON}}^{\text{f}} \rightarrow \sigma_{\text{CC}}^* \quad (3.172\text{b})$$

at $\tau_{\text{CN}} = 90^\circ$, showing the portions of these orbitals lying in a plane that contains three of the four $\text{O}=\text{C}-\text{C}-\text{N}$ skeletal atoms. The second-order stabilization energies associated with (3.172a) and (3.172b) are 12.00 and 9.25 kcal mol⁻¹, respectively. The close similarities to Fig. 3.73 are evident, as are the general parallels between the orbital compositions (cf. (3.170) and (3.171)) and donor–acceptor stabilization patterns (cf. (3.169) and (3.172)) involving the radical orbitals. In each case, strong hyperconjugative stabilization and long-range orbital mixing are fostered by the W-like pattern of vicinal antiperiplanar interactions over the extended donor–bridge–acceptor chain.

Thus, electronic promotion to an excited state may be considered in many respects analogous to “partial ionization.” In each case, distinctive opportunities (namely (3.169) and (3.172)) become available for strong NBO donor–acceptor delocalizations.

3.4.4 Geminal hyperconjugation

General characteristics of geminal donor–acceptor interactions

As previous sections have emphasized, the leading contributions to hyperconjugative stabilization and the associated torsional dependences typically arise from NBOs σ_{AB} and σ_{CD}^* in vicinal relationship. Nevertheless, in certain cases significant stabilizations arise from *geminal* interactions between NBOs σ_{AB} and σ_{BC}^* sharing a common apex atom B. We now wish to characterize geminal delocalization effects from the NBO donor–acceptor perspective, comparing and contrasting these effects with the more familiar effects of vicinal hyperconjugation.

Following the procedure for vicinal interactions illustrated in Example 1.4 and Section 3.3.1, we can associate each geminal $\sigma_{AB} \rightarrow \sigma_{BC}^*$ donor–acceptor interaction with an “arrow-pushing” diagram and partial admixture of an alternative resonance diagram, as shown in Fig. 3.78. The formal two-electron transfer from σ_{AB} to σ_{BC}^* results in the NBO configuration

$$(\sigma_{AB})^0(\sigma_{BC})^2(\sigma_{BC}^*)^2 = (n_B)^2(n_C)^2 \quad (3.173)$$

NBO	Arrow diagram	Resonance
vicinal $\sigma_{AB} \rightarrow \sigma_{CD}^*$		A^+ $B = C$ $D:^-$
geminal $\sigma_{AB} \rightarrow \sigma_{BC}^*$		A^+ $C:^-$ $B:$

Figure 3.78 Generic “arrow-pushing” diagrams (left) and secondary resonance structures (right) for vicinal (upper) and geminal (lower) NBO donor–acceptor interactions.

which corresponds to the nonbonded ionic pattern illustrated in the lower-right-hand panel of Fig. 3.78. Compared with the corresponding “double-bond–no-bond” resonance structure of vicinal $\sigma_{AB} \rightarrow \sigma_{CD}^*$ interactions (upper-right-hand panel of Fig. 3.78), geminal delocalization creates formal A^+ , C^- character on atoms that are in close spatial proximity,¹¹¹ with no compensating gain in covalent double-bond character elsewhere. Hence, geminal delocalization corresponds to general loss of covalency and an increasingly ionic picture of the bonding.

As suggested by the resonance diagram in Fig. 3.78, geminal $\sigma_{AB} - \sigma_{BC}^*$ interactions are likely to become appreciable as ionic character increases, i.e., as electronegativity differences among atoms A, B, and C become pronounced. Strong geminal delocalization is rather uncommon in apolar hydrocarbon species, except in cases of strong angular strain (see below). However, geminal effects typically become significant, e.g., in silicon analogs of common organic species, because of electronegativity and size effects to be discussed below.

In the past the sigma-delocalization effects arising from geminal hyperconjugation have been subject to considerable controversy. In particular, Dewar¹¹² judged these effects to be highly important, leading to the “sigma-aromaticity” concept (e.g., in cyclic six-electron sigma skeletons such as C_3H_6 ; see below) that was questioned by other workers.¹¹³ It now appears that Dewar’s assessment of geminal delocalization was exaggerated due to the parameterization of such effects in the Austin-based semi-empirical methods¹¹⁴ leading to large geminal couplings that are not reproduced by *ab initio* wavefunctions. However, geminal delocalization effects are indeed real, and accurate assessment of their structural and energetic consequences is necessary for a comprehensive picture of sigma-delocalization phenomena, as well as for comparison with the better-known vicinal effects. In the following we summarize some leading points of the more complete analysis of geminal delocalization given by Glendening.¹¹⁵

Hybrid contributions

It is inherently surprising that geminal interactions are typically *weaker* than vicinal interactions, because the former involve orbitals that are in closer spatial proximity. The reasons for this counterintuitive distance dependence can be seen by decomposing the geminal Fock-matrix element into individual atomic hybrid contributions.

For this purpose, let us consider a geminal X—A—Y linkage and the associated $\sigma_{AX} - \sigma_{AY}^*$ interaction. This leads to the expected second-order energy lowering

$$\Delta E_{\text{gem}}^{(2)} = -2 \frac{\langle \sigma_{AX} | \hat{F} | \sigma_{AY}^* \rangle^2}{\epsilon_{\sigma^*} - \epsilon_{\sigma}} \quad (3.174)$$

where the variability of the energy difference in the denominator may be neglected. The NBOs can be expressed as usual in terms of hybrids and polarization coefficients,

$$\sigma_{AX} = c_A h_A + c_X h_X \quad (3.175a)$$

$$\sigma_{AY}^* = c_Y h_{A'} - c_A h_Y \quad (3.175b)$$

The geminal Fock-matrix element is therefore written in terms of four contributions,

$$F_{\text{gem}} = \langle \sigma_{AX} | \hat{F} | \sigma_{AY}^* \rangle = c_A c_Y F_{AA'} - c_{A'} c_X F_{XY} + c_X c_Y F_{A'X} - c_A c_{A'} F_{AY} \quad (3.176)$$

which can be respectively identified as the “one-center” term,

$$c_A c_Y F_{AA'} = c_A c_Y \langle h_A | \hat{F} | h_{A'} \rangle \quad (3.177a)$$

the “nonbonded” term,

$$c_X c_{A'} F_{XY} = c_X c_{A'} \langle h_X | \hat{F} | h_Y \rangle \quad (3.177b)$$

and the “cross-bonded” terms

$$c_X c_Y F_{A'X} = c_X c_Y \langle h_{A'} | \hat{F} | h_X \rangle \quad (3.177c)$$

$$c_A c_{A'} F_{AY} = c_A c_{A'} \langle h_A | \hat{F} | h_Y \rangle \quad (3.177d)$$

The overall behavior of $\Delta E_{\text{gem}}^{(2)}$ and $\langle \sigma_{AX} | \hat{F} | \sigma_{AY}^* \rangle$ clearly depends on the strength and degree of cancellation of these terms, which we now consider individually.

The one-center term

The one-center term (3.177a) is often the dominant contributor to the strongest geminal interactions. This may seem surprising, because the contributing hybrids h_A and $h_{A'}$ are mutually orthogonal and the $F_{AA'}$ Fock-matrix element might naively be expected to vanish. However (as emphasized by Dewar), this expectation results from erroneous application of a Mulliken-type approximation (Eq. (1.34)) to hybrids on a single center, and the actual $F_{AA'}$ integral is certainly non-zero.

Indeed, it has been shown by Glendening that $F_{AA'}$ is related to the hybridization parameters λ_A and $\lambda_{A'}$ (Eq. (3.26)) and s/p promotion energy Δ_{sp} (Eq. (3.72)) by the approximate relationship

$$F_{AA'} \simeq [(1 + \lambda_A)(1 + \lambda_{A'})]^{-1/2} \Delta_{\text{sp}} \quad (3.178)$$

In accord with Bent's rule (Section 3.2.6), $F_{AA'}$ is therefore expected to grow with increasing electropositivity of the central atom A or increasing electronegativity of either X or Y.

However, the larger effect of polarity on the one-center term (3.177a) comes from the dependence on the c_{AC_Y} prefactor of $F_{AA'}$. The c_{AC_Y} product is strongest for electropositive X and electronegative Y, corresponding to a concerted (cooperative) polarization pattern of the form



In this pattern, X acquires partial cationic character and Y partial anionic character while the central atom A is little affected, which is consistent with the resonance diagram of Fig. 3.78.

The nonbonded term

The nonbonded term (3.177b) is often pivotal in controlling the final strength of $\langle \sigma_{AX} | \hat{F} | \sigma_{AY}^* \rangle$ and $\Delta E_{\text{gem}}^{(2)}$. Paradoxically, this control usually results from *minimizing* the magnitude of $c_X c_{A'} F_{XY}$, because this term appears with *opposite* algebraic sign to the dominant $c_{AC_Y} F_{AA'}$ one-center term. Thus, geminal delocalization effects are weak when the one-center and nonbonded terms are similar in magnitude (leading to their mutual canceling out), but such effects become appreciable when the one-center term is maximized while the nonbonded term is minimized. (However, an entirely different limit can be achieved when the X–Y separation is so small that (3.177b) becomes dominant compared with (3.177a); in the extreme case of cyclopropane and related three-membered-ring compounds [as discussed below] the “nonbonded” F_{XY} term actually corresponds to chemically bonded atoms.)

From polarity considerations, one can recognize that the prefactor $c_X c_{A'}$ of the nonbonded term is minimized by the *same* concerted polarization pattern as that shown in (3.179), which is consistent with maximization of the one-center term. This is also consistent with higher ionic character and the $X^+ \cdots \ddot{A} \cdots Y^-$ resonance pattern shown in Fig. 3.78.

However, the nonbonded term is more effectively minimized by reducing F_{XY} , i.e., by increasing the separation (reducing the overlap) between X and Y. For fixed bond angles, such a reduction can be brought about most directly by increasing the *size* of the central atom A, reducing the interpenetration of valence orbitals of X and Y. For example, when a carbon atom is replaced by silicon as the central atom, the covalent radius r_A increases from 0.77 to 1.17 Å. Both R_{AX} and R_{AY} are accordingly lengthened by about 0.40 Å and R_{XY} is correspondingly increased by about 0.53 Å (for near-tetrahedral X–A–Y angle). This increase in X \cdots Y separation sharply reduces the nonbonded term, enhancing geminal delocalization as described above. Thus, silicon compounds are generally found to exhibit much stronger geminal delocalization effects than analogous carbon compounds. Similar remarks

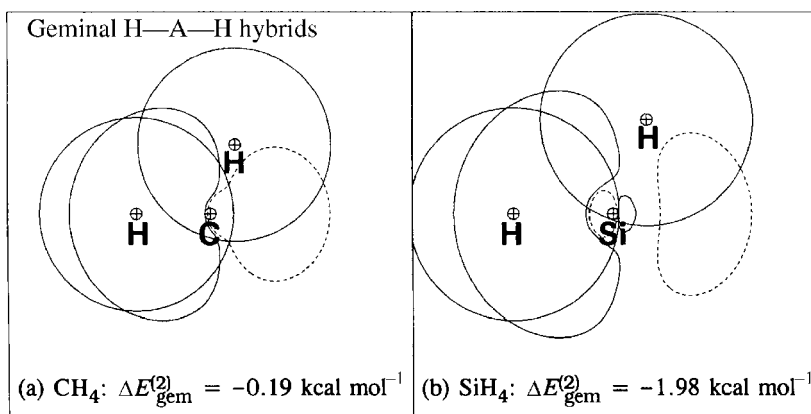


Figure 3.79 Geminal interactions in CH_4 (a) and SiH_4 (b), showing outline contours of three (h_A , h_H , and $h_{H'}$) of the four participating hybrids. Note the lesser nonbonded interaction in SiH_4 ($F_{\text{HH}'} = -0.0105$) compared with CH_4 ($F_{\text{HH}'} = -0.0410$), despite the greater hydridic character in the silane case.

pertain to replacement of first-row central atoms by second-row analogs in other families.

Figure 3.79 illustrates some aspects of the nonbonded and cross-bonded hybrid interactions in CH_4 and SiH_4 , showing the weakened $\text{H} \cdots \text{H}$ nonbonded interaction in the latter case. As a consequence, the geminal $\sigma_{\text{SiH}} - \sigma_{\text{SiH}^*}$ stabilization (1.98 kcal mol^{-1}) of SiH_4 is considerably stronger than the corresponding $\sigma_{\text{CH}} - \sigma_{\text{CH}^*}$ stabilization (0.19 kcal mol^{-1}) of CH_4 .

The cross-bonded terms

The cross-bonded terms $c_{\text{XC}_Y} F_{\text{A}'\text{X}}$ and $c_{\text{AC}_A'} F_{\text{AY}}$ result from interaction of X and Y with the “wrong” bonding hybrids on A. The magnitudes of these terms can usually be judged from simple overlap considerations. Unless X and Y are of quite dissimilar electronic character, the two cross-bonded terms are inherently of similar magnitude and therefore tend to cancel one another out. Thus, cross-bonded terms tend to make only minor contributions to geminal delocalization.

In summary, one can say that geminal hyperconjugation tends to be weak in ordinary organic compounds due to a fortuitous balance of opposing contributions. The picture in these compounds is therefore of individually significant hybrid–hybrid interactions that are prevented by mutual cancellation from giving rise to significant delocalization effects. When this fortuitous balance is broken (e.g., in X—A—Y linkages with more electronegative X and Y or larger central atom A), geminal delocalization effects can emerge as a significant stabilizing factor. “Ordinary” organic compounds may thus be considered to be rather exceptional compared with

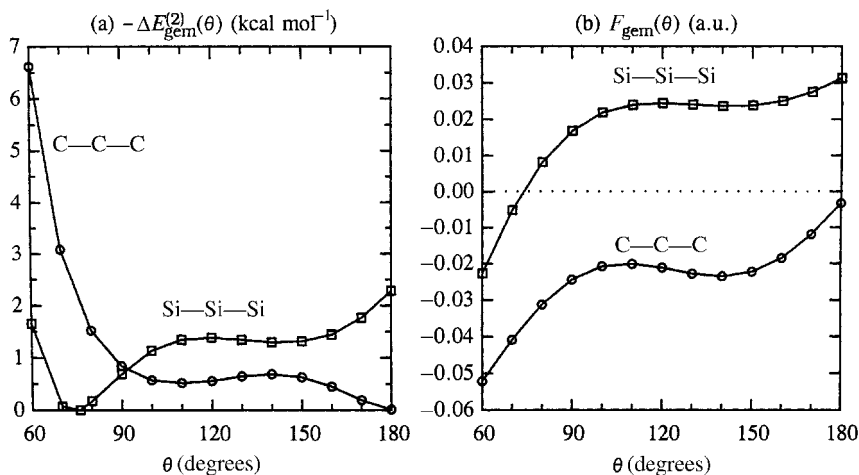


Figure 3.80 Angular dependences of (a) the second-order stabilization energy $-\Delta E_{\text{gem}}^{(2)}$ and (b) the geminal Fock-matrix element F_{gem} for the skeletal bending coordinate θ of propane (circles) and trisilane (squares).

compounds from the remainder of the periodic table, for which geminal delocalization is expected to be a more pervasive phenomenon.

Angular dependence

Compared with the vicinal delocalization effects discussed in Section 3.4.2 (see Fig. 3.66), geminal delocalizations have a more restricted set of geometrical dependences and consequences. In general, a geminal $\sigma_{\text{AX}}-\sigma_{\text{AY}}^*$ interaction can be expected to depend primarily on changes in bond lengths R_{AX} and R_{AY} and bond angle $\theta = \angle_{\text{XAY}}$ of the X—A—Y linkage. The dependence on bond stretches tends to be small, and will be neglected in the present treatment. Much more important is the dependence on geminal bond angle θ , which exhibits many surprising features.

The rather dramatic dependences of $\Delta E_{\text{gem}}^{(2)}$ on θ for geminal skeletal interactions in propane (C_3H_8) and trisilane (Si_3H_8) are illustrated and compared in Fig. 3.80(a). In each case the geminal A—A—A angle ($A = \text{C}, \text{Si}$) is varied in the range $60^\circ \leq \theta \leq 180^\circ$, with all other variables optimized at each θ . As shown in the figure, $\Delta E_{\text{gem}}^{(2)}(\theta)$ for propane is rather weak and featureless in the region ($\theta \simeq 109^\circ$) of normal acyclic bond angles, but it increases steeply near the small-angle limit $\theta = 60^\circ$. The corresponding curve for trisilane is quite different, exhibiting significant geminal stabilization throughout the range of near-tetrahedral valence angles, but dropping to zero near 75° before rising steeply at smaller angles.

How can such differences arise? Figure 3.80(b) shows the dependence of the geminal Fock-matrix element F_{gem} (for $F_{\text{gem}} = \langle \sigma_{\text{CC}} | \hat{F} | \sigma_{\text{CC}}^* \rangle$ or $\langle \sigma_{\text{SiSi}} | \hat{F} | \sigma_{\text{SiSi}}^* \rangle$)

on θ for C_3H_8 and Si_3H_8 . It can be seen that the $F_{gem}(\theta)$ curves have a generally similar shape for these two species, but shifted upward for the silicon compound. The conspicuous feature of both curves is their undulatory character. Each curve necessarily starts from an asymptotic *negative* value at sufficiently small θ (where the “nonbonded” term (3.177b) is dominant), then rises to some maximum value (which may be positive or negative¹¹⁶) before dipping slightly and rising again toward $\theta = 180^\circ$.

That $F_{gem}(\theta)$ can (and must) undergo undulations and sign changes is evident from the numerous mutual cancellations of one-center, nonbonded, and cross-bonded hybrid contributions, as discussed above. For example, at sufficiently small angles the nonbonded term must overcome the single-center term, reversing the usual relationship at larger angles. Similarly, in the cross-bonded terms, each terminal h_X hybrid interacts primarily with the *backside* lobe of the central $h_{A'}$ hybrid at large θ but with the *main* hybrid lobe at sufficiently small θ , so that a sign change in these terms necessarily occurs at some intermediate angle. This can give rise to quite surprising angular variations in which well-localized structures of a narrow angular region are bounded at smaller (and/or larger) angles by delocalized structures evincing strong geminal stabilization. The details of the band-like patterns of geminal stabilization are generally dependent on the particular atoms of the X—A—Y linkage.

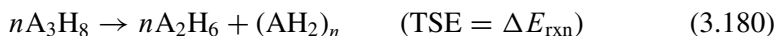
Despite the rather unpredictable angular behavior of geminal donor–acceptor interactions, their effect on molecular shape and reactivity seems to be generally less important than that of vicinal interactions. This is particularly true for common nonpolar organic and biochemical species, for which geminal delocalization effects tend to be rather insignificant in near-equilibrium geometry. Except in specialized cases as described below, geminal hyperconjugation (if significant at all) tends to serve as a background to more chemically interesting vicinal and longer-range donor–acceptor interactions.

Ring strain in small cyclic alkanes and silanes

In the late 1870s, the lack of evidence for the existence of small carbocycles $(CH_2)_n$ persuaded Baeyer and other chemists¹¹⁷ that such structures were intrinsically unstable due to ring strain. Efforts to synthesize three- and four-membered carbon ring systems¹¹⁸ led to Baeyer’s famous ring-strain theory,¹¹⁹ which proposed that ring closure to give five- and six-membered rings is facile due to preservation of near-tetrahedral bond angles, whereas formation of smaller rings requires increasingly large deviations of bond angles from the preferred tetrahedral geometry, corresponding to an increase in destabilizing “strain energy.” Baeyer’s ring-strain hypothesis introduced an important new elasto-mechanical aspect to the emerging concept of molecular structure.

It was therefore a great surprise in the early 1950s when accurate determinations of heats of formation revealed that the strain energies of cyclopropane and cyclobutane are nearly identical.¹²⁰ Thus, from the perspective of Baeyer's strain theory, it appears that cyclopropane is abnormally stabilized or that cyclobutane is abnormally destabilized (or both). Comparison experimental data for corresponding three- and four-membered silicon ring compounds have been more difficult to obtain, because known examples involve protection by bulky substituent groups or other complicating factors. However, available theoretical estimates (see below) suggest that cyclic Si_3H_6 is indeed much less stable than Si_4H_8 , in accord with Baeyer's strain theory. As Schleyer¹²¹ was led to remark, "Perhaps Baeyer should have been a silicon chemist!"

On the theoretical side, theoretical strain energies (TSEs) of cyclic $(\text{AH}_2)_n$ species are usually obtained¹²² as the energy change for the appropriate "homodesmotic" reaction



which conserves the number of bonds and approximate hybrid types with respect to corresponding unstrained acyclic species. Several investigations have shown that such TSEs are in good agreement with strain energies determined experimentally, even at relatively low levels of theory.¹²³ Table 3.27 summarizes calculated TSE values for three- and four-membered C and Si rings. The tabulated values establish

Table 3.27. Symmetry, bond lengths R_{AA} and R_{AH} , bond angle θ_{HAH} and theoretical strain energy (TSE) for small cyclic alkanes ($\text{A} = \text{C}$) and silanes ($\text{A} = \text{Si}$), with corresponding geometrical variables^a of acyclic (C_{2v}) propane and trisilane species for comparison

Species	Symmetry	R_{AA} (Å)	R_{AH} (Å)	θ_{HAH} (degrees)	TSE (kcal mol ⁻¹)
A = C					
C_3H_6	D_{3h}	1.509	1.084	114.2	26.81
C_4H_8	D_{2d}	1.554	1.092	108.5	25.74
C_4H_8^b	D_{4h}	1.557	1.092	107.8	26.52
C_3H_8	C_{2v}	1.532	1.096	106.1	—
A = Si					
Si_3H_6	D_{3h}	2.347	1.484	112.6	34.88
Si_4H_8	D_{4h}	2.385	1.489	108.3	15.22
Si_3H_8	C_{2v}	2.357	1.490	107.6	—

^a Geometrical variables for the central methylene or silylene AH_2 group.

^b Planar ring (D_{4h}) structure, 0.80 kcal mol⁻¹ above equilibrium puckered (D_{2d}) geometry.

that cyclotrisilane is about 8 kcal mol^{-1} more strained and cyclotetrasilane is about 11 kcal mol^{-1} less strained than their carbon analogs. Both computational and experimental results also establish that C_4H_8 adopts a curious *puckered* (D_{2d}) geometry, whereas the other three- and four-membered rings have skeletal mirror planes.

Why is the stability of the cyclopropane ring so much higher than predicted by Baeyer ring-strain theory? An answer is immediately suggested by the angular dependence shown in Fig. 3.80(a). Whereas geminal stabilizations are less than 1 kcal mol^{-1} for larger rings ($n \geq 4$, $\theta_{\text{CCC}} \geq 90^\circ$), these interactions become *strongly* stabilizing at the $\theta = 60^\circ$ geometry of cyclopropane. The visual estimate of Fig. 3.80(a) is confirmed by the actual C_3H_6 geminal interactions depicted in Figs. 3.81(a)–(c). As shown in Fig. 3.81(c), each $\sigma_{\text{CC}}-\sigma_{\text{CC}}^*$ geminal stabilization ($5.5 \text{ kcal mol}^{-1}$) in C_3H_6 is only a little less than the corresponding value

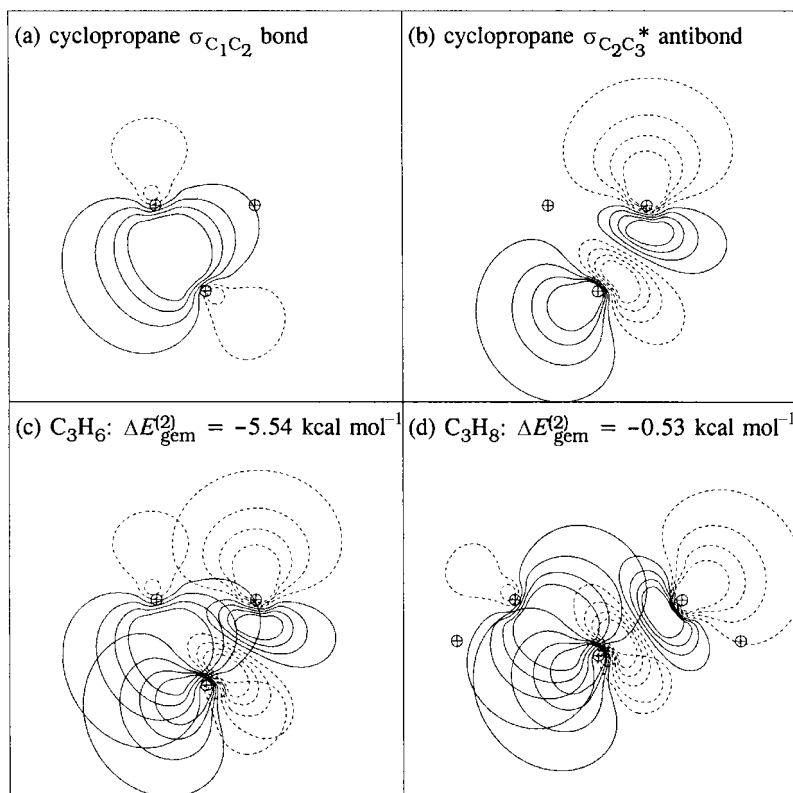


Figure 3.81 Geminal interactions in cyclopropane and propane, showing “bent” cyclopropane (a) bond σ_{CC} and (b) antibond σ_{CC}^* NBOs, with comparison geminal $\sigma_{\text{CC}}-\sigma_{\text{CC}}^*$ overlap contour diagrams for (c) cyclic and (d) acyclic species.

(6.6 kcal mol⁻¹) in the acyclic model of Fig. 3.80(a). The $\Delta E_{\text{gem}}^{(2)}$ values suggest that cyclopropane is stabilized by about 30 kcal mol⁻¹ by the six geminal $\sigma_{\text{CC}}-\sigma_{\text{CC}'}^*$ interactions, each about 5 kcal mol⁻¹ stronger than the corresponding value (0.5 kcal mol⁻¹) in unstrained propane.

The geminal stabilizations of cyclobutane and the silicon three- and four-membered rings can be judged from Fig. 3.80(a) to be *much* smaller than those for cyclopropane. Thus, geminal delocalization becomes a powerful factor in overcoming the intrinsic Baeyer ring strain of the severely bent bonds of cyclopropane, but it plays no corresponding role in C₄H₈, Si₃H₆, and Si₄H₈.

(That the Baeyer strain in silicon rings is generally less than that in carbon rings could be judged from the fact that the Si—Si bonding hybrids are more diffuse and weakly directional [higher *s* character] and the Si—Si bond strengths are significantly weaker than those in carbon analogs [53 versus 83 kcal mol⁻¹ for standard Si—Si versus C—C bond dissociation energies]. Thus, the Si—Si bonds are less affected by a given degree of bending, and Baeyer ring strain is proportionately smaller for silicon than for carbon rings.)

Several other factors play a role in the differential stabilization of three- and four-membered carbon and silicon rings.

- (1) The increased *p* character of the skeletal hybrids in strained ring systems necessitates increased *s* character in the exocyclic bonds to hydrogen, according to Bent's rule (Section 3.2.6.). Such a "rehybridization effect" in C₃H₆ therefore leads to pronounced C—H bond shortening and strengthening that partially compensates for the bending and weakening of C—C bonds.¹²⁴ Such an effect is evident in Table 3.27, where the C—H bond length of cyclic C₃H₆ is seen to be shortened by 0.012 Å (relative to acyclic C₃H₈), whereas the corresponding shortening in cyclobutane is only 0.004 Å. The rehybridization effect is also evident in θ_{HCH} bond angles, which open by more than 8° in C₃H₈, compared with only 1–2° in C₄H₈. The effect is weaker in silicon than in carbon compounds, as can be seen in the weaker variations in R_{SiH} and θ_{HSiH} in Table 3.27. Numerical estimates of the rehybridization effect vary widely¹²⁵ but all suggest that the TSE contributions are smaller than the geminal delocalization cited above.
- (2) Planar ring geometry necessitates the eclipsing of exocyclic C—H (or Si—H) bonds. This "torsional strain effect" involves eight hydride bonds for four-membered rings, but only six for three-membered rings, and thus may contribute to TSE differences. Available estimates¹²⁶ indicate that eclipsing effects reduce the TSE of cyclopropane relative to cyclobutane by about 12 kcal mol⁻¹.
- (3) Repulsive cross-ring interactions in cyclobutane (the "1,3-C—C effect") might in principle increase the TSE of cyclobutane. However, Cremer and Gauss¹²⁷ showed that the effect is actually negligible for cyclobutane, but leads to a small indirect *decrease* in TSE for cyclopropane, due to the way the (small) 1,3-C—C interaction of propane enters the TSE through the homodesmotic reaction (3.180).



Figure 3.82 The puckered (D_{2d}) equilibrium geometry of C_4H_8 , showing canting of methylene units to give alternating “axial” and “equatorial” C—H bonds.

Thus, other possible contributions to TSE appear to be less important than the geminal delocalization effects noted above.

Why does C_4H_8 adopt puckered D_{2d} geometry? As shown in Fig. 3.82, the skeletal carbon atoms twist out of planarity (with dihedral $\phi_{CCCC} = 17.9^\circ$), allowing each methylenic hydrogen to be distinguished as axial (with $\phi_{CCCH(a)} = \pm 94.9^\circ$) or equatorial (with $\phi_{CCCH(e)} = \pm 138.7^\circ$). The puckered equilibrium D_{2d} structure lies only $0.8 \text{ kcal mol}^{-1}$ below the transition-state D_{4h} structure.

The electronic origin of C_4H_8 puckering undoubtedly involves relief of eclipsing strain and gain of *vicinal* hyperconjugation at the expense of somewhat increased C—C bond bending. Investigation reveals that the principal vicinal stabilizations are of $\sigma_{CC} - \sigma_{CH(e)}^*$ type, involving delocalization from strained C—C bonds into equatorial C—H antibonds that are most nearly in favorable *anti*-like alignment. (The corresponding $\sigma_{SiSi} - \sigma_{SiH}^*$ interactions in Si_4H_8 are too weak to support D_{2d} distortion.) Deletion of $\sigma_{CC} - \sigma_{CH}^*$ NBO interactions and reoptimization of C_4H_8 geometry is found to lead back to unpuckered D_{4h} symmetry. Thus, the competition between bond strain and hyperconjugative stabilization is also reflected in more subtle features of the ring structures.

Generally speaking, donor–acceptor delocalizations of both geminal and vicinal types can be expected to increase near bent bonds and antibonds. Covalent bond strain inherently weakens the bond and diminishes bond–antibond splitting, resulting in a higher-energy bond (enhanced donor) and lower-energy antibond (enhanced acceptor) for donor–acceptor interactions. One can therefore expect that hyperconjugative delocalization serves as a general “softening” mechanism to counter the adverse effects of covalent bond strain in polyatomic molecules.

The pi-complex model of cyclopropane

Finally, we briefly compare the NBO donor–acceptor picture of geminal delocalization with Dewar’s “sigma-aromaticity” concept and the associated pi-complex

model¹²⁸ of cyclopropane. This model depicts C_3H_6 as having a strong admixture of $H_2C: + H_2C=C_2H$ character,¹²⁹



with the methylene lone pair forming a pi complex with the ethylene pi bond. Such a picture emphasizes pi-orbital interactions near the ring *center*, rather than sigma bonds bent strongly outside the ring as in the Coulson–Moffitt picture. Wavefunction analysis by Bader’s “atoms-in-molecules” method¹³⁰ seems to support the pi-complex picture, even suggesting that the wavefunction should be described better by the three equivalent resonance structures (3.181) than by the classical single-bonded structural formula.¹³¹

A naive orbital cartoon of “banana bonding,”



might seem to suggest that electron density is concentrated outside the ring periphery. However, the actual electron density in the C_3 plane is plotted in Fig. 3.83(a), showing that the contours along the ring edge bend slightly *inward* toward the ring center, so that the electron density in the ring interior is greater than that around the ring periphery. Thus, the form of the electron density Fig. 3.83(a) may superficially seem to contradict the expectations of (3.182) and support the pi-complex picture (3.81).

However, the orbital cartoon (3.182) presents a very misleading impression of the actual shape of the bent σ_{CC} bond, as shown in Fig. 3.81(a). Although the contours of σ_{CC} indeed “bulge out” asymmetrically toward the outside of the ring, a high proportion of orbital amplitude remains *inside* the ring. This is shown more clearly in Fig. 3.83(b), which represents a cross-section through the midpoint of the σ_{CC} bond both as a contour diagram (solid lines) and amplitude profile (dotted line). From these diagrams one can judge that the σ_{CC} electron density extends significantly into the ring interior, where it adds to the densities from the other two C—C bonds. In fact, the amplitude of each σ_{CC} at the ring center is about 60% of the maximum amplitude outside the ring, and the sum of three such bond densities near the ring center easily exceeds that of a single bond outside the ring. Thus there

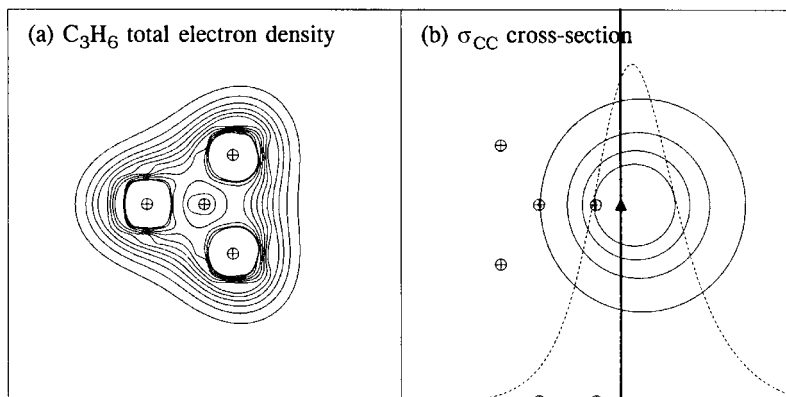
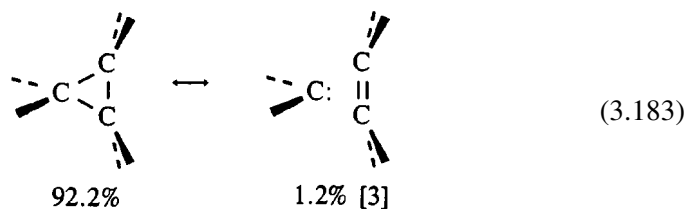


Figure 3.83 (a) Contours of total electron density in the skeletal plane of C_3H_6 . (b) A cross-section of the σ_{CC} NBO in the perpendicular plane passing through one of the CH_2 groups and bisecting the opposite C—C bond (triangle), showing orbital contours (solid lines) and the amplitude profile (dotted line) on either side of the dividing boundary (vertical line) between “inside” and “outside” the C_3H_6 ring. Note that a reference dummy nucleus marks the molecular center in both diagrams.

is no inherent conflict with the bent-bond Coulson–Moffitt picture in finding higher electron density inside, rather than outside, the triangle edges.

The importance of “pi-complex” resonance structures such as (3.181) can also be directly assessed with NRT analysis (Section 1.6). For the equilibrium C_3H_6 structure corresponding to the electron-density map in Fig. 3.81(a), the optimal NRT resonance weightings are found to be



Thus, NBO/NRT analysis generally supports the Coulson–Moffitt picture and indicates that pi-complex character (although present) is a relatively minor feature of the electronic structure of cyclopropane.

3.5 Hypervalency: 3c/4e “ ω bonds”

The conceptual framework and models of hypervalency

The great success of the Lewis-structure concept naturally calls attention to exceptional cases in which Lewis-structural principles appear to be violated. An important

class of such exceptions is constituted by so-called *hypervalent* (“electron-rich”) species containing atoms whose apparent number of nonbonded and bonded electron pairs exceeds the octet-rule limit. (The alternative case of *hypovalent* [“electron-deficient”] species, containing atoms that apparently *lack* the necessary number of nonbonded and bonded electron pairs to complete the valence octet, will be considered in Section 3.6.)

Hypervalency can be defined most simply with respect to purely empirical aspects of chemical periodicity. As beginning chemistry students are taught, each chemical family is associated with a column of the periodic table and associated valence atomic number Z_A^{val} , such that the *empirical valency* V_A^{emp} is the minimum shift of Z_A^{val} to reach the nearest rare gas,

$$V_A^{\text{emp}} = \min\{Z_A^{\text{val}}, |Z_A^{\text{val}} - 8|\} \quad (3.184)$$

For example, atoms of both the alkaline-earth family ($Z_A^{\text{val}} = 2$) and the chalcogen family ($Z_A^{\text{val}} = 6$) correspond to $V_A^{\text{emp}} = 2$, and their stoichiometric proportionality (or coordination number) to monovalent atoms is therefore commonly *two* (AH_2 , ALi_2 , AF_2 , etc.). It is a remarkable and characteristic feature of chemical periodicity that the empirical valency V_A^{emp} applies both to covalent and to ionic limits of bonding, so that, e.g., the monovalency of lithium ($V_{\text{Li}}^{\text{emp}} = 1$) correctly predicts the stoichiometry and coordination number of covalent (e.g., Li_2), polar covalent (e.g., LiH), and extreme ionic (e.g., LiF) molecules. Following Musher,¹³² we can therefore describe *hypervalency* as referring to cases in which the apparent valency V_A exceeds the normal empirical valency (3.184),

$$V_A(\text{hypervalent}) > V_A^{\text{emp}} \quad (3.185)$$

Well-known examples of hypervalency include PF_5 , SF_6 , and other species commonly discussed in the framework of valence-shell electron-pair repulsion (VSEPR) theory (see below).

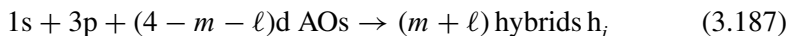
For a general closed-shell AX_m species, the Lewis-type assumption of a shared A:X electron-pair bond for each coordinated monovalent atom X nominally requires m orbitals on A to accommodate the $2m$ bonding electrons, plus additional orbitals for any nonbonded pairs. Thus, for m bonds and ℓ lone pairs, apparent octet-rule violations occur whenever

$$m + \ell > 4 \quad (3.186)$$

requiring more than the four standard valence AOs (s , p_x , p_y , p_z) available to a main-group element. Inequality (3.186) provides an alternative criterion of main-group hypervalency, or apparent octet-rule violation.

Two general conceptual models of hypervalency have been proposed. The first, “d-orbital participation,” is represented in practically every general-chemistry

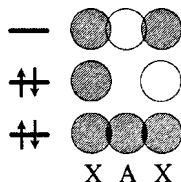
textbook, and is based on the assumption that $4 - m - \ell$ additional d-type AOs are employed to “expand the valence shell” to five, six, or more electron pairs,



leading, e.g., to six d^2sp^3 hybrids for $m + \ell = 6$. The second, “ionic resonance,” is based on the high *ionic* character of the bonding and the importance of resonance delocalization that would be represented in VB language as

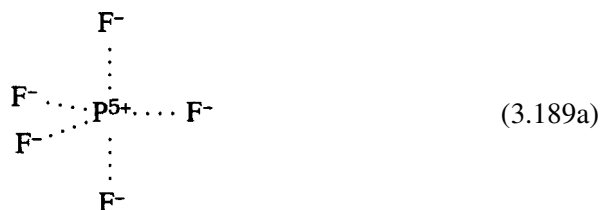


involving ordinary octet-rule-conforming species. As pointed out by Coulson,¹³³ the VB ionic-resonance picture is essentially equivalent to the three-center, four-electron (3c/4e) MO model (described below) in which non-zero bond orders result from filling both the bonding and the nonbonding MOs arising from interaction of three valence AOs; schematically,



The ionic-resonance (or 3c/4e MO) picture implies that d orbitals play only a secondary role as polarization functions (rather than primary components of bonding hybrids), and emphasizes that a *single* acceptor orbital on A may be adequate to form strong donor–acceptor interactions with m ligand donor orbitals. Thus, *no* significant “expansion of the valence shell” or other violations of Lewis-structural principles (beyond resonance delocalization (3.188)) may be needed in order to account for the hypervalency phenomenon. This is consistent with considerable theoretical¹³⁴ and computational¹³⁵ evidence showing that d orbitals play a relatively negligible role in main-group hypervalency phenomena.

A third, more extreme, conceptual model, based on a completely ionic picture of hypervalent bonding, can also be invoked to remove perceived conflicts with Lewis-structural principles. In PF_5 , for example, the completely ionic (“oxidation number”) $P^{5+}(F^-)_5$ representation



describes the bonding in terms of closed-shell [Ne]-like cation and [Ar]-like anions, which is fully consistent with standard Lewis-structure representations of each ion. (The mutual repulsions of anions would, of course, lead to the same D_{3h} geometry as that predicted by the VSEPR logic.) In the ionic limit (3.189a) the *electrovalent* (ionic) bond order of each $F^- \cdots PF_4^+$ ion pair is unity, whereas the covalent bond order is zero,

$$\text{ionic limit: } b_{PF}^{(\text{ion})} = 1, \quad b_{PF}^{(\text{cov})} = 0 \quad (3.189b)$$

The exaggerated ionic picture (3.189) is doubtless unrealistic, but it is interesting to note that the calculated natural atomic charges in PF_5 ,

$$Q_P = +2.63, \quad Q_F = -0.51(\text{eq}), -0.55(\text{ax}) \quad (3.190)$$

are indeed suggestive of high ionic character,¹³⁶ contrary to the “electroneutrality principle” commonly espoused in general-chemistry textbooks.

As the discussion of Chapter 2 and the numerical charges in (3.190) suggest, the extreme ionic picture such as (3.189a) must be modified by donor–acceptor interactions that create partial covalency by delocalizing significant charge ($\sim 0.5e$) from bare fluoride ions into acceptor orbitals of the central cation. Such partial-covalency effects can be represented by resonance delocalization of the form



These resonance corrections to the extreme ionic model correspond to the “ionic-resonance model” symbolized by (3.188).

However, at first sight the ionic-resonance model would not seem applicable to I_3^- and related symmetric hypervalent species, because extreme I^+I^- ionicity differences would not be expected between central and terminal atoms of intrinsically equal electronegativity. Nevertheless, we shall show that the complementary bi-directional resonance stabilization motif (3.188) can lead to effective three-center bonding even if central and terminal atoms are of equal electronegativity.

The Pimentel–Rundle 3c MO model

Pimentel presented a particularly simple and lucid MO model of hypervalency (building on physical concepts that were also recognized by Rundle)¹³⁷ that is applicable to atoms of similar or dissimilar electronegativity. The Pimentel–Rundle model is based on a general triatomic A—B—C species in which each atom contributes only a single basis AO (χ_a, χ_b, χ_c) that interacts strongly with the AO on



George C. Pimentel



Robert E. Rundle

each adjacent atom. From these three AOs one can construct three LCAO-MOs ϕ_i , one each of bonding, nonbonding, and antibonding character,

$$\phi_1 = \frac{1}{2}(\chi_a + 2^{1/2}\chi_b + \chi_c) \quad (3.192a)$$

$$\phi_2 = 2^{-1/2}(\chi_a - \chi_c) \quad (3.192b)$$

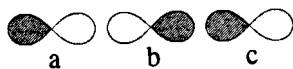
$$\phi_3 = \frac{1}{2}(\chi_a - 2^{1/2}\chi_b + \chi_c) \quad (3.192c)$$

The four electrons involved in bonding can therefore be assigned to the MO configuration

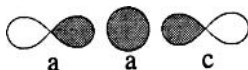
$$\psi_{\text{MO}} = (\phi_1)^2(\phi_2)^2 \quad (3.193)$$

with equal partial MO bond orders for A—B and B—C, which is consistent with the resonance diagram (3.188). Thus, MO theory can account for the fact that the four bonding electrons are accommodated in delocalized three-center MOs, leading to partial bonds from central atom B to both terminal atoms, even though only a single χ_b valence AO participates. Coulson demonstrated the close connection between the 3c MO model and the valence-bond resonance model (3.188).

Pimentel employed this three-center, four-electron (3c/4e) MO model to discuss the bonding in triiodide (I_3^-), bifluoride (FHF^-), and other prototypical hypervalent species. In triiodide and other trihalides, for example, the relevant AOs are the (p_a, p_b, p_c) orbitals along the bonding axis,



whereas in bifluoride the corresponding (p_a, s_b, p_c) valence AOs are employed,



as pictured in Fig. 3.84.

The Pimentel–Rundle 3c/4e MO model can readily be generalized to hybrid orbitals (rather than pure AOs) and more general LCAO-MO mixing coefficients

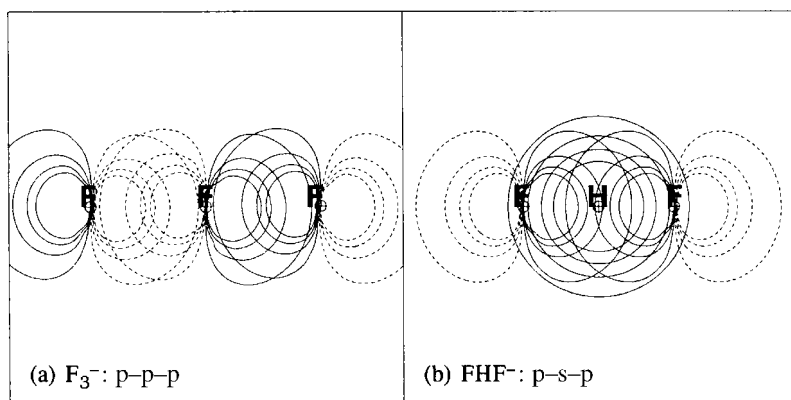


Figure 3.84 An illustration of the Pimentel–Rundle three-center MO model of hypervalency, showing equilibrium valence AO ($\chi_a-\chi_b-\chi_c$) overlap patterns for (a) $2p_{\text{F}}-2p_{\text{F}}-2p_{\text{F}}$ NAOs of the trifluoride ion, F_3^- ; and (b) $2p_{\text{F}}-1s_{\text{F}}-2p_{\text{F}}$ NAOs of the bifluoride ion, FHF^- .

for atoms of unequal electronegativity. The model successfully suggests how ionic resonance (3.188) can arise in the *ab initio* MO framework, employing only orbitals of an octet-rule-conforming valence *sp* description.

The NBO donor–acceptor picture of hypervalency: hyperbonds

Let us re-examine the 3c/4e MO description from the localized NBO perspective. NBO analysis of the MO wavefunction (3.193) may lead to the Lewis structure A: + B—C, with NBOs

$$\text{A: B—C} \begin{cases} n_{\text{A}} = \chi_{\text{a}} \\ \sigma_{\text{BC}} = c_{\text{b}}\chi_{\text{b}} + c_{\text{c}}\chi_{\text{c}} \\ \sigma_{\text{BC}}^* = c_{\text{b}}\chi_{\text{b}} - c_{\text{c}}\chi_{\text{c}} \end{cases} \quad (3.194\text{a})$$

and idealized natural Lewis-structure wavefunction

$$\Psi_{\text{A:BC}}^{(\text{NBO})} = (n_{\text{A}})^2(\sigma_{\text{BC}})^2 \quad (3.194\text{b})$$

Alternatively, one may obtain the A—B + :C structure, with NBOs

$$\text{A—B :C} \begin{cases} n_{\text{C}} = \chi_{\text{c}} \\ \sigma_{\text{AB}} = c_{\text{a}}\chi_{\text{a}} + c_{\text{b}}\chi_{\text{b}} \\ \sigma_{\text{AB}}^* = c_{\text{b}}\chi_{\text{a}} - c_{\text{a}}\chi_{\text{b}} \end{cases} \quad (3.195\text{a})$$

and natural Lewis-structure wavefunction

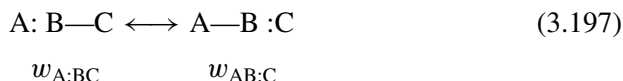
$$\Psi_{\text{AB:C}}^{(\text{NBO})} = (n_{\text{C}})^2(\sigma_{\text{AB}})^2 \quad (3.195\text{b})$$

Perturbative donor–acceptor corrections to the idealized $\Psi_{\text{A:BC}}^{(\text{NBO})}$ and $\Psi_{\text{AB:C}}^{(\text{NBO})}$ Lewis structures are of the respective forms

$$n_{\text{A}} \rightarrow \sigma_{\text{BC}}^*: \quad \Delta E_{\text{A:BC}}^{(2)} = -2 \frac{\langle n_{\text{A}} | \hat{F} | \sigma_{\text{BC}}^* \rangle^2}{\epsilon_{\text{BC}^*} - \epsilon_{\text{A:}}} \quad (3.196\text{a})$$

$$n_{\text{C}} \rightarrow \sigma_{\text{AB}}^*: \quad \Delta E_{\text{AB:C}}^{(2)} = -2 \frac{\langle n_{\text{C}} | \hat{F} | \sigma_{\text{AB}}^* \rangle^2}{\epsilon_{\text{AB}^*} - \epsilon_{\text{C:}}} \quad (3.196\text{b})$$

Each such delocalization corresponds to an admixture of the alternative resonance forms



with respective weightings $w_{\text{A:BC}}$ and $w_{\text{AB:C}}$. These resonance weightings (and those of other contributing resonance structures) can be evaluated with natural

resonance theory (Section 1.6) to obtain the total NRT bond orders and their dissection into ionic and covalent contributions:

$$b_{AB}^{(\text{NRT})} = b_{AB}^{(\text{cov})} + b_{AB}^{(\text{ion})} \quad (3.198\text{a})$$

$$b_{BC}^{(\text{NRT})} = b_{BC}^{(\text{cov})} + b_{BC}^{(\text{ion})} \quad (3.198\text{b})$$

Each member of the coupled pair of resonance structures in (3.197) expresses a semi-localized bonding aspect of the general $3c/4e$ resonance hybrid, a structural motif of considerable generality and importance. We believe that the electronic and structural properties of such $3c/4e$ bonding motifs are so unique and characteristic as to warrant a special nomenclature and symbol that clearly distinguishes them from ordinary $2c/2e$ bonds; indeed, as emphasized by Musher, an intrinsic feature of hypervalency is the appearance of two distinguishable *types* of bonds in the same molecule. We therefore characterize the resonance motif (3.127) as “hyperbonding” or “ ω -bonding” and adopt the symbol ω_{ABC} to denote the $3c/4e$ hyperbonded triad.¹³⁸ The two “precursor” $2c/2e$ bonds A—B and B—C that underlie the ω -bonded triad (in complementary resonance-structure representations) can be identified as “pre- ω bonds” or “ ω prebonds,” which are distinguished by a more specific form of the omega symbol that identifies the particular resonance depiction, namely

$$\omega_{A:BC} \text{ for the } 2c/2e \text{ bond (e.g., } \sigma_{BC}) \text{ of resonance form A: B—C} \quad (3.199\text{a})$$

$$\omega_{AB:C} \text{ for the } 2c/2e \text{ bond (e.g., } \sigma_{AB}) \text{ of resonance form A—B:C} \quad (3.199\text{b})$$

The ω -prebonds $\omega_{A:BC}$ and $\omega_{AB:C}$ might alternatively be denoted by pre-scripted symbols such as ${}^{\omega}\sigma_{AB}$, ${}^{\omega}\pi_{AB}$, etc., to specify further their shape and relationship to conventional $2c/2e$ bonds as well as the implied modification due to hyperbonding. In what follows, we shall generally adopt the more generic symbols (3.199) for the ω prebonds of a given ω_{ABC} hyperbond.

The distinguishing characteristics of ω_{ABC} hyperbonds include the following:

- (HB-1) linear (or near-linear) A—B—C geometry;
- (HB-2) unusually long bond lengths R_{AB} and R_{BC} , corresponding to high populations of σ_{AB}^* and σ_{BC}^* antibonds and strong resonance mixing (3.197);
- (HB-3) pronounced three-center character, with distinctive ${}^2J_{AB}$ geminal spin couplings, IR vibrational couplings, and other spectroscopic signatures;
- (HB-4) equal (or near-equal) resonance weightings $w_{A:BC}$ and $w_{AB:C}$ in (3.197); and
- (HB-5) unusually high cationic character of central atom B and anionic character of terminal atoms A and C, as reflected in natural atomic charges (Q_A , Q_B , Q_C), ionic bond orders ($b_{AB}^{(\text{ion})}$ and $b_{BC}^{(\text{ion})}$), and electrovalencies ($V_A^{(\text{ion})}$, $V_B^{(\text{ion})}$, $V_C^{(\text{ion})}$).

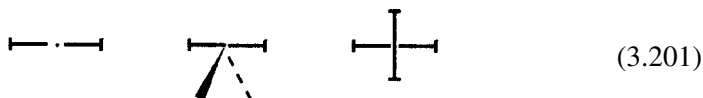
Where appropriate, the ω prebonds in the structure diagram can be indicated by distinctive bond symbols (\vdash , \dashv)



with the terminal vertical stroke toward the terminal atom of the triad. The corresponding symbol for a composite three-center bond is



to suggest the complementarity and linearity of the three-center linkage. The two complementary ω -prebond symbols can also be combined without atomic symbols in combinations such as



Each such ω bond resembles the letter “I” and evokes the “I-bond” nomenclature introduced by Epiotis.¹³⁹

Let us describe the general form of the hyperbonding functions in further detail. For the symmetric $A \vdash B \dashv C$ case in which atoms A and C are of equivalent electronegativity, we can rewrite the antibond NBOs in (3.194) as

$$\sigma_{BC}^* = (1 + \lambda^2)^{-1/2}(\lambda\chi_b - \chi_c) \quad (3.202a)$$

$$\sigma_{AB}^* = (1 + \lambda^2)^{-1/2}(\lambda\chi_b - \chi_a) \quad (3.202b)$$

where λ is related to the bond ionicity $i_{AB} = i_{CB}$ by

$$\lambda = \left(\frac{1 + i_{AB}}{1 - i_{AB}} \right)^{1/2} \quad (3.203)$$

The $n_A \rightarrow \sigma_{BC}^*$ and $n_C \rightarrow \sigma_{AB}^*$ delocalizations lead to semi-localized (NLMO) orbitals $\omega_{AB:C}$ and $\omega_{A:BC}$, which can be written as

$$\omega_{AB:C} = (1 + \mu^2)^{-1/2}(n_A + \mu\sigma_{BC}^*) \quad (3.204a)$$

$$\omega_{A:BC} = (1 + \mu^2)^{-1/2}(n_C + \mu\sigma_{AB}^*) \quad (3.204b)$$

where the mixing coefficient μ is a measure of interaction strength. When expressions (3.202a) and (3.202b) are substituted into (3.204a) and (3.204b), the orthogonality relation $\langle \omega_{AB:C} | \omega_{A:BC} \rangle = 0$ requires that

$$\mu = \frac{2(1 + \lambda^2)^{1/2}}{\lambda^2} \quad (3.205)$$

With this replacement the two hyperbond functions are finally

$$\omega_{AB:C} = \frac{\lambda^2}{\lambda^2 + 2} [\chi_a + (2/\lambda)\chi_b - (2/\lambda^2)\chi_c] \quad (3.206a)$$

$$\omega_{A:BC} = \frac{\lambda^2}{\lambda^2 + 2} [-(2/\lambda^2)\chi_a + (2/\lambda)\chi_b + \chi_c] \quad (3.206b)$$

In addition to the two bonding functions (3.206a) and (3.206b), there remains a third linear combination of (χ_a, χ_b, χ_c) of net *antibonding* character that may be denoted ω_{ABC}^* and written as

$$\omega_{ABC}^* = c_a\chi_a + c_b\chi_b + c_c\chi_c$$

The orthogonality conditions $\langle \omega_{AB:C} | \omega_{ABC}^* \rangle = \langle \omega_{A:BC} | \omega_{ABC}^* \rangle = 0$ allow one to establish that $c_a = c_c$ and $c_b = 2/\lambda - \lambda/2$, and therefore (taking account of the normalization condition) that

$$\omega_{ABC}^* = \frac{2\lambda}{\lambda^2 + 2} \left(\chi_a - \frac{\lambda^2 - 2}{2\lambda} \chi_b + \chi_c \right) \quad (3.206c)$$

Equations (3.206a)–(3.206c) express a one-parameter family of hyperbonding functions (two bonding, one antibonding) that are dependent on bond ionicity through (3.203). The bonding functions (3.206a) and (3.206b) approximate the NLMOs of the hyperbonded triad in the neighborhood of equilibrium.

The electronic configuration $(\omega_{AB:C})^2(\omega_{A:BC})^2$ of the $A \vdash B \dashv C$ hyperbonded unit may equivalently be expressed in terms of any orthogonal linear combination of the two occupied orbitals $\omega_{AB:C}$ and $\omega_{A:BC}$, such as

$$\phi_{\pm} = 2^{-1/2}(\omega_{AB:C} \pm \omega_{A:BC})$$

These are equivalent to

$$\phi_+ = \frac{\lambda^2 - 2}{2^{1/2}(\lambda^2 + 2)} \left(\chi_a + \frac{4\lambda}{\lambda^2 - 2} \chi_b + \chi_c \right) \quad (3.207a)$$

$$\phi_- = 2^{-1/2}(\chi_a - \chi_c) \quad (3.207b)$$

Thus, ϕ_- is equivalent to Pimentel's ϕ_2 (for any λ), while ϕ_+ is equivalent to ϕ_1 (and ω_{ABC}^* to ϕ_3) for the special value

$$\lambda = 2 + 2^{1/2} = 3.414 \quad (3.208)$$

but (3.206a) would differ somewhat from Pimentel's MO (3.192a) in more general cases.

Example 3.19

Exercise: Determine the formal MO bond orders $b_{AB}^{(MO)}$, $b_{BC}^{(MO)}$, and $b_{AC}^{(MO)}$ for the general $(\omega_{AB:C})^2(\omega_{A:BC})^2$ hyperbonded electron configuration.

Solution: As noted above, the NLMO configuration $(\omega_{AB:C})^2(\omega_{A:BC})^2$ is equivalent to the MO configuration $(\phi_+)^2(\phi_-)^2$. The MO bond order $b_{AB}^{(MO)}$ is defined as the coefficient of the cross-term $\chi_a\chi_b$ in the total density $(\phi_+)^2 + (\phi_-)^2 + \dots$.

The $\chi_a\chi_b$ cross-term in $(\phi_+)^2$ is the only contribution to $b_{AB}^{(MO)}$ bond order (and analogously for $b_{BC}^{(MO)}$), so

$$b_{AB}^{(MO)} = \frac{2\lambda(\lambda^2 - 2)}{(\lambda^2 + 2)^2} = b_{BC}^{(MO)}$$

The $\chi_a\chi_c$ cross-term in $(\phi_-)^2$ is $-\frac{1}{2}$, and that in $(\phi_+)^2$ is $\frac{1}{2}[(\lambda^2 - 2)/(\lambda^2 + 2)]^2$, giving the total A—C bond order as

$$b_{AC}^{(MO)} = -\frac{4\lambda^2}{(\lambda^2 + 2)^2}$$

Example 3.20

Exercise: For what ionicity i_{AB} is the *maximum* MO bond order $b_{AB}^{(MO)}$ obtained? How does this maximum value compare with that of the Pimentel MO description?

Solution: By differentiating $b_{AB}^{(MO)}$ (Example 3.19) with respect to λ , we obtain

$$\frac{db_{AB}^{(MO)}}{d\lambda} = \frac{-2\lambda^4 + 24\lambda^2 - 8}{(\lambda^2 + 3)^2} = 0$$

with formal solutions $\lambda^2 = 6 \pm 32^{1/2}$. The allowed solution corresponds exactly to Pimentel’s MO solution (cf. Eq. (3.208))

$$\lambda = 2 + 2^{1/2} = 3.414$$

which is equivalent (through Eq. (3.203)) to the ionicity value

$$i_{AB} = 0.842$$

This leads to the maximum MO bond order

$$b_{AB}^{(MO)} = 8^{-1/2} = 0.354$$

corresponding to Pimentel’s $(\phi_1)^2(\phi_2)^2$ MO description. For this optimal λ , the hyperbond functions are

$$\begin{aligned}\omega_{AB:C} &= 8^{-1/2}[(1 + 2^{1/2})\chi_a + 2^{1/2}\chi_b + (1 - 2^{1/2})\chi_c] \\ \omega_{A:BC} &= 8^{-1/2}[(1 - 2^{1/2})\chi_a + 2^{1/2}\chi_b + (1 + 2^{1/2})\chi_c] \\ \omega_{ABC}^* &= \frac{1}{2}(\chi_a - 2^{1/2}\chi_b + \chi_c)\end{aligned}$$

Linear triatomic anions

The pioneering crystallographic studies of Odd Hassel¹⁴⁰ on trihalides and related donor-acceptor species led to a far-reaching analysis of such "Hassel compounds" by Henry Bent.¹⁴¹ The triiodide ion (I_3^- , stable in aqueous solution) and other known linear trihalide XYZ^- species also served as the prototype for Pimentel's incisive three-center MO analysis of hypervalency. We shall therefore begin with NBO/NRT investigation of a series of hypervalent and non-hypervalent triatomic anions in order to make contact with these classic studies. While *ab initio* studies add many quantitative details to the understanding of these species, the basic picture sketched by Bent and Pimentel is found to be essentially preserved.

Tables 3.28–3.30 summarize the geometry, binding energies, and NBO/NRT descriptors for a variety of linear triatomic XYZ^- species. These include representatives of the p–p–p orbital motif (such as symmetric trihalides [X_3^- , $X = F, Cl, Br$] and the mixed chlorofluorides [$FFCl^-$, $ClFCI^-$, $FCIF^-$, $FCICI^-$]) as well as the p–s–p (FHF^-) and s–s–s ($HLiH^-$, H_3^-) orbital motifs. (Examples of transition metal species manifesting the s–d–s and p–d–p motifs will be considered in Section 4.10.)

Let us summarize the distinguishing characteristics of ω -bonding from the prototype examples of Tables 3.28–3.30. The first eight species exhibit strong ω -bonding that may be contrasted with $HLiH^-$ (a borderline species) and H_3^- (non-hyperbonded).

As shown in Table 3.28, the ω -bond energies typically fall within the range 30–50 kcal mol⁻¹, somewhat weaker than corresponding 2c/2e bond energies (except for F_2), but far stronger than noncovalent ion–dipole (or ion–induced-dipole)

Table 3.28. *Equilibrium bond lengths R_{XY} and R_{YZ} of linear triatomic anions XYZ^- , including binding energy ΔE and bond-length increase ΔR with respect to $X-Y + Z^-$ or $X^- + Y-Z$ precursor species*

XYZ^-	R_{XY}, R_{YZ} (Å)	$X-Y + Z^-$		$X^- + Y-Z$	
		ΔE (kcal mol ⁻¹)	ΔR_{XY} (Å)	ΔE (kcal mol ⁻¹)	ΔR_{YZ} (Å)
FFF^-	1.7454	37.93	0.3371	37.93	0.3371
$ClClCl^-$	2.3936	30.97	0.3678	30.97	0.3678
$BrBrBr^-$	2.6372	33.08	0.3062	33.08	0.3062
$ClFCI^-$	2.0750	16.52	0.3971	16.52	0.3971
$FFCl^-$	1.8359, 1.9816	34.70	0.4276	19.25	0.3037
$FCIF^-$	1.9279	54.21	0.2500	54.21	0.2500
$FCICI^-$	1.9330, 2.3879	36.34	0.2551	46.92	0.3351
FHF^-	1.1472	46.53	0.2250	46.53	0.2250
$HLiH^-$	1.7342	54.75	0.1411	54.75	0.1411
HHH^-	0.7595, 2.4987	1.69	0.0152	1.69	0.0152

Table 3.29. The NBO descriptors of XYZ^- triatomic anions (see Table 3.28), showing natural atomic charges (Q), percentage polarization of σ_{XY} and σ_{YZ} NBOs toward terminal atoms, second-order $n_Z \rightarrow \sigma_{XY}^*$ and $n_X \rightarrow \sigma_{YZ}^*$ stabilizations ($\Delta E^{(2)}$), and occupancies of valence antibonds (σ_{XY}^* and σ_{YZ}^*) and extra-valent Rydberg orbitals (r_Y^*); parenthesized values refer to Lewis structure of lower accuracy

XYZ ⁻	Atomic charge		Bond polarization (%)				$\Delta E^{(2)}$ (kcal mol ⁻¹)		Occupancy (e)	
	Q_X	Q_Y	To X	To Z	X—Y :Z	X: Y—Z	σ_{XY}^*	σ_{YZ}^*	r_Y^*	
FFF ⁻	-0.446	-0.107	62.0	(62.0)	133.7	(133.7)	0.542	(0.542)	0.01	
CIClCl ⁻	-0.444	-0.111	62.0	(62.0)	118.9	(118.9)	0.533	(0.533)	0.02	
BrBrBr ⁻	-0.448	-0.105	62.5	(62.5)	111.1	(111.1)	0.526	(0.526)	0.02	
ClFCl ⁻	-0.305	-0.389	47.5	(47.5)	152.8	(152.8)	0.671	(0.671)	0.02	
FFCl ⁻	-0.499	-0.267	(59.9)	49.2	(290.6)	80.6	(0.751)	0.483	0.01	
FCIF ⁻	-0.607	+0.214	76.2	(76.2)	102.5	(102.5)	0.355	(0.355)	0.03	
FClCl ⁻	-0.573	+0.071	(72.1)	68.6	(101.4)	115.5	(0.470)	0.399	0.03	
FHF ⁻	-0.766	+0.533	87.0	(87.0)	166.2	(166.2)	0.225	(0.225)	0.01	
HLiH ⁻	-0.826	+0.652	93.0	(93.0)	11.1	(11.1)	0.040	(0.040)	0.03	
HHH ⁻	-0.124	+0.075	54.9	(54.9)	6.2	(6.2)	0.039	(0.039)	0.00	

Table 3.30. The NRT descriptors of XYZ^- triatomic anions (see Table 3.28), showing bond orders (b_{XY} and b_{YZ}), central-atom valency (V_Y : total, covalent, and ionic components), and percentage weights of leading resonance structures ($X—Y :Z^-$, $X:^- Y—Z$, $X—Y—Z$, $X:^- Y^+ :Z^-$)

XYZ ⁻	Bond order		Valency V_Y			w_{NRT} (%) ^a			
	b_{XY}	b_{YZ}	Total	Covalent	Ionic	X—Y :Z	X: Y—Z	X—Y—Z	X: Y :Z
FFF ⁻	0.466	0.466	0.932	0.488	0.444	42.7	42.7	3.9	6.7
CIClCl ⁻	0.467	0.467	0.933	0.488	0.445	42.5	42.5	4.2	6.7
BrBrBr ⁻	0.460	0.460	0.921	0.800	0.121	42.2	42.2	3.8	6.8
ClFCl ⁻	0.340	0.340	0.679	0.503	0.176	29.0	29.0	4.9	4.2
FFCl ⁻	0.245	0.565	0.809	0.540	0.269	20.4	52.4	4.1	4.9
FCIF ⁻	0.833	0.833	1.667	0.414	1.253	16.7	16.7	26.6	26.6
FClCl ⁻	0.819	0.848	1.667	0.496	1.171	15.2	18.2	28.3	22.2
FHF ⁻	0.684	0.684	1.368	0.223	1.145	23.6	23.6	39.3	8.0
HLiH ⁻	0.662	0.662	1.323	0.201	1.122	23.1	23.1	43.0	8.9
HHH ⁻	0.945	0.039	0.984	0.832	0.152	94.5	3.9	0.0	1.6

^a For consistency of comparisons, the four tabulated structures were assigned as reference structures (\$NRTSTR keylist) with full density-matrix averaging (NRTFDM keyword) for each species.

intermolecular interactions. Indeed, the slightly weaker $\omega_{\text{Cl:FCl}}$ prebond of ClFCl^- (16.5 kcal mol $^{-1}$) and $\omega_{\text{FF:Cl}}$ prebond of FFCl^- (19.3 kcal mol $^{-1}$) constitute examples of unfavorable binding of the anion X^- to the *negative* (fluoride) end of the $Y-Z$ (F—Cl) dipole. This shows that classical ion–dipole forces, although present, exert only a secondary modulating effect on hyperbonding, which remains primarily covalent in character. The much weaker H_3^- bond energy (1.7 kcal mol $^{-1}$) is indicative of a non-hyperbonded species retaining $\text{H}_2 \cdots \text{H}^-$ “ion–dipole-complex” character.

A characteristic of hyperbonding is the symmetric (or near-symmetric) linear geometry in which the possible distinction between intramolecular and intermolecular bond lengths R_{XY} and R_{YZ} is erased. The ω -bond lengths fall within a distinctive range, approximately 0.2–0.4 Å beyond normal single-bond lengths. Weaker elongation (0.14 Å) is found for HLiH^- , where the central Li atom is indicated (see below) to have only weak hyperbond character.

Distinctive characteristics of ω bonds can also be recognized in the NBO descriptors of Table 3.29. The natural atomic charges and NBO bond polarizations reveal a typical ionicity pattern with the central atom significantly less anionic than the terminal atoms, i.e., with Q_Y exceeding Q_X by 0.3e or more (except when the difference in electronegativity becomes too severe in the opposite direction). This is particularly striking in the elemental trihalides X_3^- , where the distribution of charge between “inner” and “outer” X atoms is far from democratic (e.g., $\text{F}^{-0.45}\text{F}^{-0.11}\text{F}^{-0.45}$). The σ_{XY}^* and σ_{YZ}^* occupancies for each idealized Lewis structure are also quite large ((0.2–0.5)e), and the corresponding second-order energies $\Delta E^{(2)}$ are 80–120 kcal mol $^{-1}$ or larger. Hyperbonded species thus manifest strong hyperconjugative delocalizations associated with unusually strong polarization of each bond *away* from Y (thereby increasing Q_Y) in order to maximize simultaneously *both* $n_X \rightarrow \sigma_{YZ}^*$ and $n_Z \rightarrow \sigma_{XY}^*$ donor–acceptor interactions. In contrast, the species HLiH^- and H_3^- manifest much weaker antibond occupancies ($\sim 0.04e$) and delocalization energies (~ 6 –11 kcal mol $^{-1}$), which are indicative of reasonably localized Lewis structures.

It is noteworthy that Rydberg orbital occupancies on the central atom (r_Y^* , final column of Table 3.29) are relatively negligible (0.01–0.03e), showing that “d-orbital participation” or other “expansion of the valence shell” is a relatively insignificant feature of hyperbonded species. However, the case of HLiH^- is somewhat paradoxical in this respect. The cationic central Li is found to use conventional sp linear hybrids to form the hydride bonds, and thus seems to represent a genuine case of “expansion of the valence shell” (i.e., to the 2p subshell) to form two bonding hybrids. However, the two hydride “bonds” are both so strongly polarized toward H (93%) as to have practically no contribution from Li orbitals, so the actual occupancy of extra-valent $2p_{\text{Li}}$ orbitals ($\sim 0.03e$) remains quite small in this case.

Although HLiH^- exhibits certain structural signatures of hyperbonding, it appears more to exemplify normal *hybridized* bonding (with extra-valent $2p_{\text{Li}}$ character) and the limit of complete ionic $\text{H}^- \text{Li}^+ \text{H}^-$ character, rather than true ω -bonding.

Finally, the NRT descriptors of Table 3.30 also reflect the strong $\text{X}^- \text{Y}-\text{Z} \longleftrightarrow \text{X}-\text{Y} : \text{Z}^-$ resonance mixing, leading to equal (or near-equal) bond orders b_{XY} and b_{YZ} and high ionic character.¹⁴² Although the total valency V_{Y} of the central atom sometimes exceeds unity, the *covalency* is always significantly smaller (0.2–0.8), indicating that there is no real need for orbitals outside the valence shell. Thus, a formal coordination number of two is entirely consistent with the single unfilled valence orbital of the parent central atom.

We conclude that the first eight triatomic anions of Table 3.28 exhibit the properties (HB-1)–(HB-5) expected of hyperbonding and can be described by modified Lewis-structural formulas employing 3c/4e ω bonds of the form



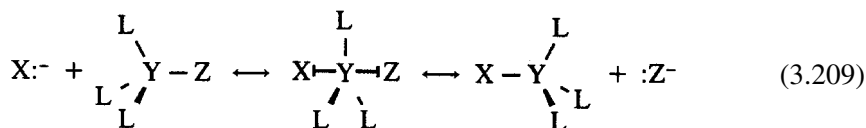
whereas the final two species are adequately described by conventional Lewis structures,



employing only ionic or conventional 2c/2e bonding.

Trigonal-bipyramidal species and nucleophilic displacement reactivity

The 3c/4e ω -bonding motif can also be achieved in nonlinear polyatomics by “backside” attack of a nucleophile X^- on a polar $\text{Y}-\text{Z}$ bond of a conventional Lewis-structure molecule,

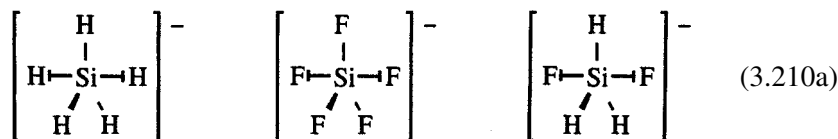


The complementary bi-directional resonance (3.209) leading to $\text{X}\vdash\text{Y}\dashv\text{Z}$ ω -bonding may be considered as the “frustrated” (interrupted) limit of a conventional $\text{S}_{\text{N}}2$ nucleophilic displacement reaction, in which the usual activation barrier has progressively been lowered until a binding *well* is formed at the symmetric trigonal-bipyramidal geometry that separates the two limits in (3.209). Thus, the electronic factors that stabilize $\text{S}_{\text{N}}2$ transition states and catalyze $\text{S}_{\text{N}}2$ reactivity are closely related to (i.e., weaker forms of) factors that promote axial ω -bonding in trigonal-bipyramidal geometry.

Table 3.31. Trigonal bipyramidal anions, comparing central-atom valency V_M (and percentage ionic character), *d*-orbital occupancy d_M^* , bond lengths R_{MX} , bond orders b_{MX} (and percentage ionic character), and ligand atomic charges Q_X for ω -bonded (SiH_5^- , SiF_5^- , and SiH_3F_2^-) versus non- ω -bonded (CH_3F_2^-) species

Species	Symmetry	V_M (% ion.)	$d_M^*(e)$	M—X	R_{MX} (Å)	b_{MX} (% ion.)	Q_X
SiH_5^-	D_{3h}	3.829 (26%)	0.03	Si—H(ax)	1.624	0.517 (40%)	-0.362
				Si—H(eq)	1.535	0.932 (21%)	-0.231
SiF_5^-	D_{3h}	4.083 (78%)	0.07	Si—F(ax)	1.686	0.593 (81%)	-0.702
				Si—F(eq)	1.652	0.966 (76%)	-0.678
SiH_3F_2^-	D_{3h}	3.959 (42%)	0.04	Si—F(ax)	1.780	0.543 (81%)	-0.741
				Si—H(eq)	1.501	0.956 (27%)	-0.271
CH_3F_2^-	C_{3v}	4.064 (30%)	0.01	C—F	1.454	0.833 (52%)	-0.472
				C...F	2.569	0.275 (99%)	-0.957
				C—H	1.084	0.985 (18%)	+0.172

Table 3.31 displays geometrical and NBO/NRT indices for three ω -bonded representatives of resonance motif (3.209),



as well as a comparison non- ω -bonded “ion-dipole complex”



The five-coordinate anions SiH_5^- , SiF_5^- , and SiH_3F_2^- are seen to exhibit the characteristic trigonal-bipyramidal (D_{3h}) geometry and NBO/NRT indices expected of ω -bonding. Particularly striking is the contrast between strong, short equatorial bonds (ordinary $2c/2e$; $b \simeq 0.93$ – 0.97 ; lower polarity) and weak, elongated axial bonds (ω -bonded; $b \simeq 0.52$ – 0.59 ; higher polarity).¹⁴³ Despite the pentacoordinate D_{3h} geometry, the central Si atom displays rather unexceptional tetravalency ($V_M \simeq 3.8$ – 4.1) and negligible *d*-orbital participation (0.04 – 0.07). The contrasting $\text{F}^- \cdots \text{CH}_3\text{F}$ complex (3.210b) exhibits strongly inequivalent C—F bond orders (0.83 and 0.28), corresponding to incomplete ω -bond formation, but the

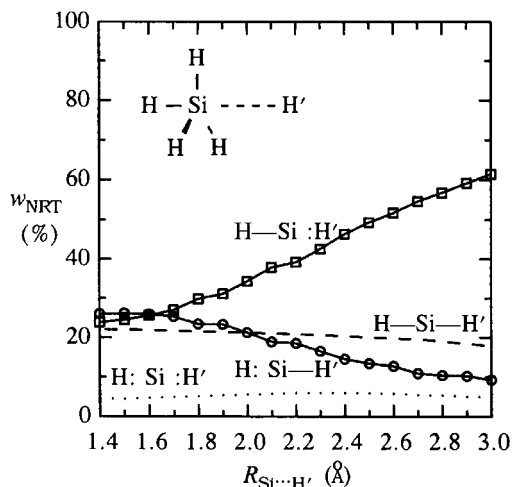


Figure 3.85 The NRT resonance weights for the approach of H^- to SiH_4 along the C_{3v} axis (“ $\text{S}_{\text{N}}2$ -like” reaction coordinate), showing weightings of one-bond $\text{H-Si:H}'$ and $\text{H:Si-H}'$ (solid lines), two-bond $\text{H-Si-H}'$ (dashed line), and no-bond $\text{H:Si:H}'$ (dotted line) resonance structures. The equilibrium D_{3h} structure corresponds to $R_{\text{Si}\cdots\text{H}'} = 1.6236 \text{ \AA}$.

“four-coordinate” central atom displays valency and d-orbital occupancy that are rather similar to those of the five-coordinate species (3.210a).

Figure 3.85 illustrates the representative changes in NRT resonance weightings for barrierless formation of pentacoordinate SiH_5^- from the long-range $\text{H}^- + \text{SiH}_4$ complex in $\text{S}_{\text{N}}2$ -like approach geometry. At large $R_{\text{Si}\cdots\text{H}'}$, the resonance weights of $\text{H-Si:H}'$ and $\text{H:Si-H}'$ structures are strongly inequivalent (as in the equilibrium CH_3F_2^- species), but these structures become equivalent at $R_{\text{Si}\cdots\text{H}'} = 1.624 \text{ \AA}$, the ω -bonded equilibrium geometry.

The distinctive features of ω -bonded $\text{H-Si}\rightarrow\text{H}$ linkages can be illustrated with reference to the unusual IR vibrational and NMR spin-coupling properties of SiH_5^- , compared with those of the parent SiH_4 . A characteristic measure of hydride bond coupling is the difference in IR frequency between asymmetric and symmetric stretch frequencies,

$$\delta\nu_{\text{str}} = \nu_{\text{str}}(\text{asym.}) - \nu_{\text{str}}(\text{sym.}) \quad (3.211a)$$

which is calculated to differ dramatically between normal-valent SiH_4 and hypervalent SiH_5^- :

$$\delta\nu_{\text{str}}(\text{SiH}_4) = 9 \text{ cm}^{-1}, \quad \delta\nu_{\text{str}}(\text{SiH}_5^-) = 176 \text{ cm}^{-1} \quad (3.211b)$$

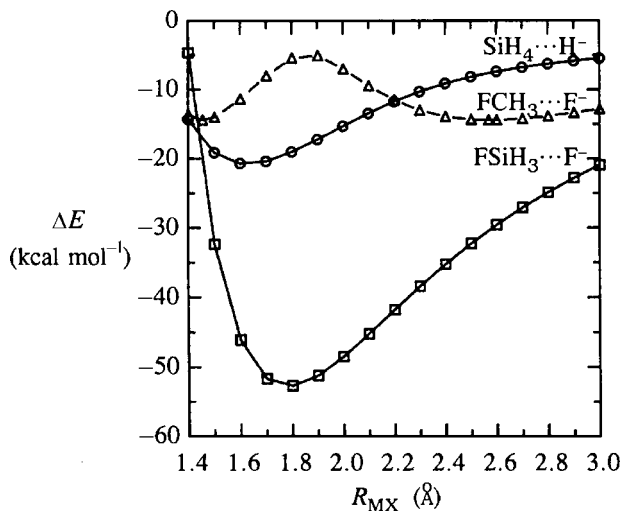


Figure 3.86 Potential-energy profiles for $\text{XMH}_3 \cdots \text{X}$ dissociation along an adiabatic $\text{S}_{\text{N}}2$ -like reaction coordinate for $\text{SiH}_4 + \text{H}^-$ ($\text{M} = \text{Si}$, $\text{X} = \text{H}$; circles, solid line), $\text{FSiH}_3 + \text{F}^-$ ($\text{M} = \text{Si}$, $\text{X} = \text{F}$; squares, solid line), and $\text{FCH}_3 + \text{F}^-$ ($\text{M} = \text{C}$, $\text{X} = \text{F}$; triangles, dashed line), showing ω -bonded equilibrium behavior in the first two cases and transition-state behavior in the last case.

Similarly, the calculated geminal ${}^2J_{\text{HH}}$ spin couplings in SiH_5^- (${}^2J_{\text{H}(\text{eq})\text{H}(\text{eq})} = 18.1 \text{ Hz}$, ${}^2J_{\text{H}(\text{ax})\text{H}(\text{eq})} = -4.8 \text{ Hz}$, ${}^2J_{\text{H}(\text{ax})\text{H}(\text{ax})} = 1.5 \text{ Hz}$) display the marked inequivalences between bond types and the shift from normal-valent behavior (e.g., ${}^2J_{\text{HH}} = 3.8 \text{ Hz}$ for SiH_4).

The similarities and contrasts between ω -bonded species (3.210a) and $\text{S}_{\text{N}}2$ -precursor species (3.210b) are further illustrated in Fig. 3.86. This figure shows the potential energy ΔE relative to $R \rightarrow \infty$ along the $\text{S}_{\text{N}}2$ -like reaction coordinate for the hyperbonded species SiH_5^- (cf. Fig. 3.85) and $\text{FSiH}_3 \cdots \text{F}^-$, compared with that for the corresponding $\text{FCH}_3 \cdots \text{F}^-$ species.

As seen in Fig. 3.86, the potential-energy profiles for the first two cases lead to a *well*, corresponding to equilibrium ω -bonding, whereas that for the last case leads to a *barrier*, corresponding to the transition state for an activated $\text{S}_{\text{N}}2$ displacement reaction. Particularly interesting is the comparison of FMH_3F^- ($\text{M} = \text{C}, \text{Si}$) species, where replacement of C by Si converts the pentacoordinate species from an unstable $\text{S}_{\text{N}}2$ transition-state intermediate into a stable ω -bonded molecular anion. As Fig. 3.86 suggests, a rather modest percentage increase in the $n_{\text{F}} - \sigma_{\text{CF}}^*$ stabilization of the $\text{F}^- \cdots \text{CH}_3\text{F}$ complex (i.e., from 72 to 82 kcal mol $^{-1}$ in the transition-state geometry) would apparently suffice to convert a reactive transition-state complex into an equilibrium species! Thus, the conditions for catalyzing $\text{S}_{\text{N}}2$ reactivity are intimately connected to those for promoting ω -bonding.

Table 3.32. *Symmetry, bond lengths, and bond angles for ordinary covalent (M—F) and ω -bonded (M—F $_{\omega}$) fluoride bonds of normal-valent and hypervalent second-row main-group fluorides MF $_n$ (M = P, S, Cl); see Fig. 3.87*

Species	Symmetry	Bond lengths R (Å)		Bond angles θ (degrees)		
		M—F (no.)	M—F $_{\omega}$ (no.)	$\theta_{\sigma\sigma'}$	$\theta_{\sigma\omega}$	$\theta_{\omega\omega'}$
PF $_3$	C $_{3v}$	1.605 (3)	—	97.4	—	—
PF $_5$	D $_{3h}$	1.571 (3)	1.605 (2)	120.0	90.0	180.0
SF $_2$	C $_{2v}$	1.639 (2)	—	99.0	—	—
SF $_4$	C $_{2v}$	1.597 (2)	1.705 (2)	101.5	87.7	172.8
SF $_6$	O $_h$	—	1.607 (6)	—	—	90.0
ClF	C $_{\infty v}$	1.678 (1)	—	—	—	—
ClF $_3$	C $_{2v}$	1.663 (1)	1.768 (2)	—	87.5	175.0
ClF $_5$	C $_{4v}$	1.672 (1)	1.737 (4)	—	86.0	172.0

Hyperbonding and the VSEPR picture

The ω -bonding model provides a more complete and fundamental description of hypervalent molecules that are often interpreted in terms of the VSEPR model.¹⁴⁴ In the present section we examine some MX $_n$ species that are commonly used to illustrate VSEPR principles, comparing and contrasting the VSEPR mnemonic with general Bent's rule, hybridization, and donor–acceptor concepts for rationalizing molecular geometry. Tables 3.32 and 3.33 summarize geometrical and NBO/NRT descriptors for a variety of normal-valent and hypervalent second-row fluorides to be discussed below, and Fig. 3.87 shows optimized structures of the hypervalent MF $_n$ species (M = P, S, Cl; $n = 3$ –6).

Table 3.33. *NBO/NRT descriptors of molecules in Table 3.32, including atomic charges (Q), central atom d -orbital occupancy (d_M^*), NRT bond orders, and central-atom valency (with percentage ionic character)*

Species	Charge			Bond order		
	$Q_{F(\sigma)}$	$Q_{F(\omega)}$	d_M^*	M—F	M—F $_{\omega}$	V_M (% ion.)
PF $_3$	−0.560	—	0.06	0.998	—	2.994 (67%)
PF $_5$	−0.510	−0.547	0.12	0.797	0.835	4.098 (65%)
SF $_2$	−0.444	—	0.04	1.000	—	2.000 (51%)
SF $_4$	−0.414	−0.523	0.10	0.833	0.748	3.161 (58%)
SF $_6$	−0.421	−0.421	0.17	0.882	0.882	5.293 (56%)
ClF	−0.332	—	0.01	1.000	—	1.000 (34%)
ClF $_3$	−0.295	−0.457	0.05	0.817	0.681	2.178 (47%)
ClF $_5$	−0.289	−0.398	0.11	0.813	0.828	4.126 (53%)

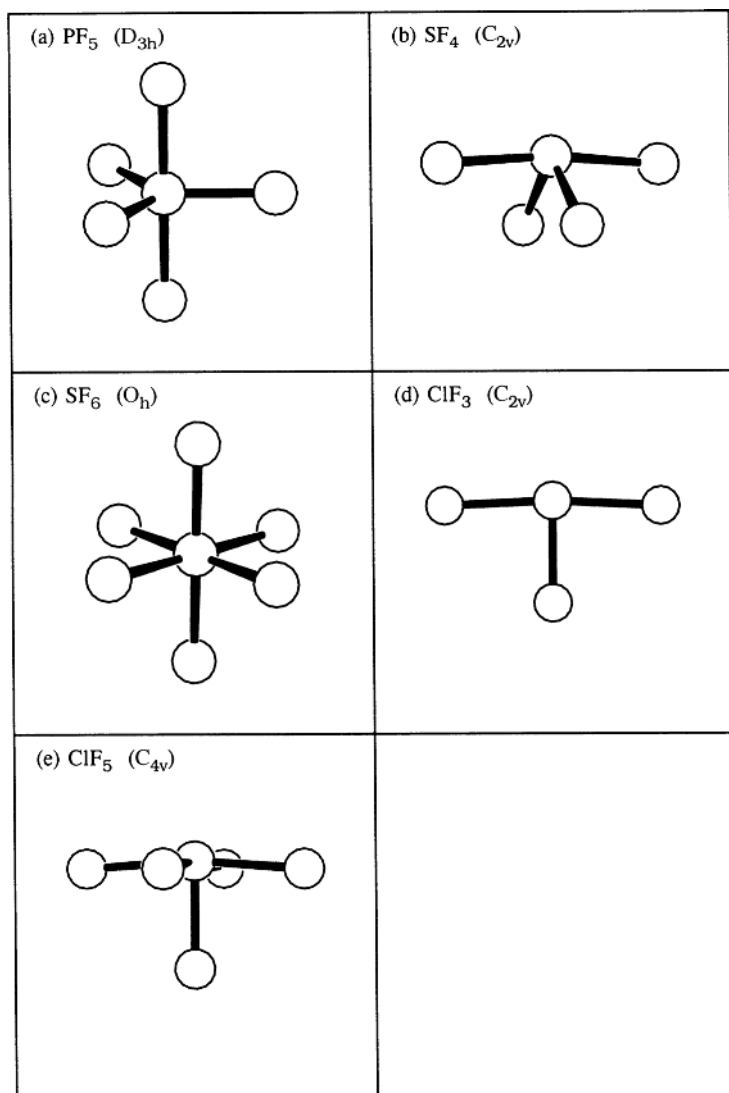


Figure 3.87 Structural depictions of hypervalent molecules (see Tables 3.32 and 3.33).

In analogy with (3.209), we can picture each hypervalent MF_m species as being formed from a precursor *normal*-valent cation $\text{M}^{n+}\text{F}_{m-n}$ by n successive “ ω -additions” of fluoride ions,

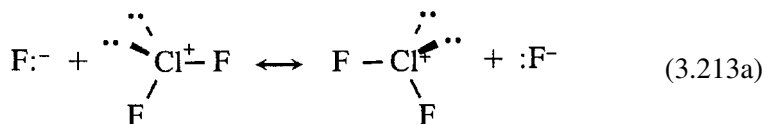


provided that $m - n \geq n$, or

$$m \geq 2n \quad (3.212b)$$

Because the resonance stabilization of the ω bond is always maximized in linear geometry (for which $n_F - \sigma_{MF}^*$ overlap is highest), each ω -addition characteristically results in an additional linear $F \leftarrow M \rightarrow F$ linkage.

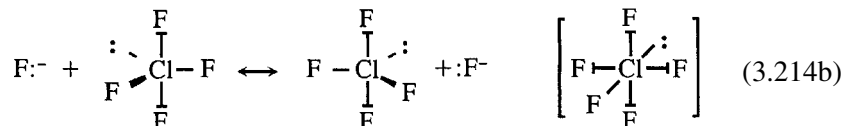
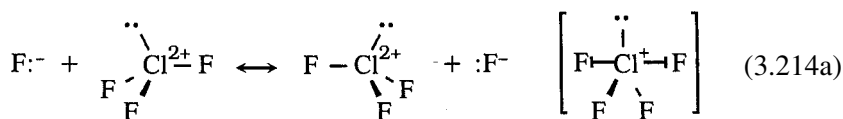
For example, ClF_3 may be considered to derive from a single F^- ω -addition to normal-valent Cl^+F_2 (which is isoelectronic to SF_2), and can be represented in analogy to (3.209) as



or in ω -bonded form as

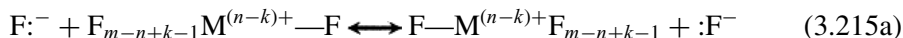


Similarly, ClF_5 may be considered to derive from two fluoride ω -additions to normal-valent $Cl^{2+}F_3$ (which is isoelectronic to PF_3)

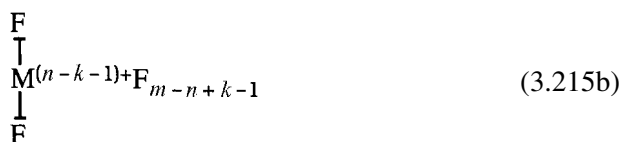


and so forth.

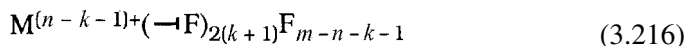
Equivalently (but more formally), each recursive step in sequence (3.212) can be written as (for $k = 0, 1, \dots, n - 1$)



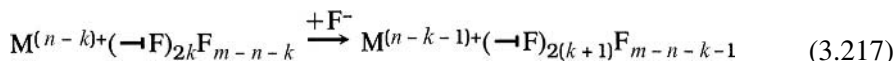
equivalent to the ω -bonded product



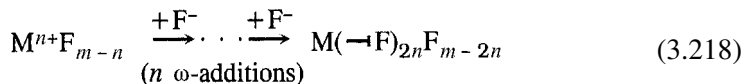
Because ω prebonds are always created in *pairs*, the species (3.215b) can be written more explicitly as



to distinguish the $2(k+1) \omega_{\text{F:MF}}$ prebonds from the remaining $m-n-k-1 \sigma_{\text{MF}}$ bonds. The general k th step in (3.212) can therefore be written as

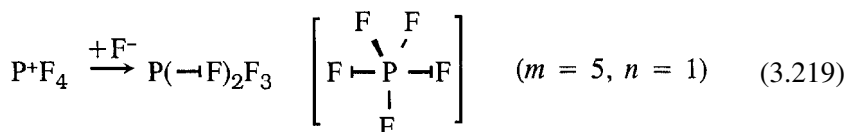


for $k = 0, 1, 2, \dots, n-1$, and the overall sequence is

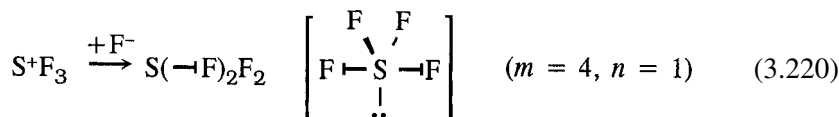


By construction, each step in (3.218) requires only the normal-valent orbitals on the central atom M, and maximum use of $n = 4$ such valence orbitals (i.e., for a normal-valent precursor M^{4+}F_4 with four σ_{MF} bonds) allows coordination numbers up to $m = 8$, which is consistent with (3.212).

Further examples of scheme (3.218) may be given for the species in Fig. 3.87. PF_5 can be formed from precursor P^+F_4 (which is isoelectronic to SiF_4) by a single ω -addition,



Similarly, SF_4 is formed from S^+F_3 (which is isoelectronic to PF_3) by a single ω -addition,



and SF_6 can be formed from S^{2+}F_4 (which is isoelectronic to SiF_4) by two ω -additions,

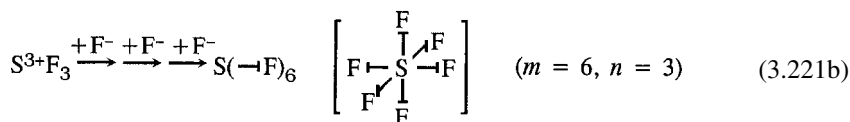


However, the case (3.221a) seems to distinguish the two sets of ω bonds (along the x and y directions) from the σ bonds (along the z direction), whereas no such distinction exists in SF_6 . We can rationalize this case in two ways.

- (1) Consistently with the Pimentel–Rundle $3c/4e$ MO model, the central atom is expected to use a single p orbital to form each ω -bonded pair (i.e., p_x for the ω bonds in the x direction and p_y for the ω bonds in the y direction), which leaves only s and p_z orbitals for forming the two bonds along the z direction. As a result of the inherent symmetry of the three spatial directions and equivalence of the available orbitals for bonding in each

direction, the σ bonds along z are thus expected to become equivalent to the ω bonds along x and y in this limit (cf. note 143). In effect, formation of the two sets of linear ω bonds forces the near-linearity of the remaining two bonds, which switches on the characteristic resonance stabilization of ω -bonding.

- (2) We can alternatively begin the recursion (3.218) with $S^{3+}F_3$ (which is isoelectronic to hypovalent AlF_3), leading thereby to



This scheme suggests (correctly) that the six-coordinate SF_6 geometry can actually be achieved using only *three* of the four sulfur valence orbitals (i.e., without “s-orbital participation”). Thus, while digonal sp -hybridization can be employed along any direction to describe vibrational displacements from idealized O_h geometry, the high equilibrium symmetry of SF_6 actually works *against* s-orbital character in the bonding σ or ω hybrids. Although ω prebonds and σ bonds are *usually* inequivalent, their close relationship (i.e., through reciprocal pairs of resonance structures) implies that they *can* become equivalent, and they *do* so in the high-symmetry limit of SF_6 .

What is the origin of the slight nonlinearities in ω -bonding seen (cf. Table 3.32, final column) in SF_4 , ClF_3 , ClF_5 , and related species? Although ionic-resonance delocalization is maximized in linear geometry, slight departures from this maximum incur only a small (second-order) energy penalty. Thus, asymmetries of the ω -bonding environment can be readily accommodated by small deviations from linearity, particularly those arising from asymmetric steric congestion with the sigma system (i.e., axially non-symmetric arrangements of sigma bonds and lone pairs in SF_4 or ClF_3). Rationalizations of these nonlinearities would thus be essentially similar to those invoked in VSEPR-like models, which are couched in terms of differential steric pressure due to surrounding bonds and lone pairs (particularly, the higher s character and angular volume demanded for lone pairs by Bent’s rule; see below).

The final ω -bonded formulas (3.213), (3.214), and (3.219)–(3.221) bear an obvious resemblance to the usual VSEPR representations of these hypervalent species. Indeed, each ω -bonded structure has the same number of formal bond pairs (bp) and lone pairs (lp) as the VSEPR representation. Furthermore, the predicted angular geometries of the two models are essentially identical, with the linear (or near-linear) ω -bonded ligands occupying axial positions in the S_N2 -like trigonal bipyramidal motif.

However, the implications (HB-1)–(HB-5) of the ω -bonded model go far beyond those of the VSEPR model. The VSEPR model addresses only the angular geometry about the central atom, and provides no clear basis for judging the length, strength,

polarity, or other properties of symmetry-inequivalent bonds. In contrast, the ω -bonded model provides a clear electronic rationale for distinguishing the weaker, longer, and more polar and reactive hyperbond pairs from ordinary covalent bonds. More importantly, the ω -bonding model helps to explain the *existence* of model VSEPR compounds, and why many apparently isovalent ML_n “analogs” have no comparable stability; because ω -bonding originates from strong ionic resonance, this phenomenon is essentially restricted to highly electronegative fluoride ligands and/or relatively electropositive central atoms.

For the covalent bonds of hypervalent species, the valence angles (bp–bp, bp–lp, lp–lp) are expected to be governed by the usual Bent’s rule relationships between central-atom hybrid *p* character and ligand electronegativity. Thus, as in normal-valent main-group species, it is expected that lone-pair hybrids will have higher *s* character (and, by virtue of Eq. (3.34), larger bond angles) than bond hybrids, leading to greater apparent “volume” of the former. Indeed, the approximation methods of Section 3.2.6 could be adapted to make qualitative estimates of the bond angles in hypervalent species (parallel to those for non-hypervalent species), going significantly beyond the VSEPR model in this respect. Thus, both for hypervalent and for non-hypervalent main-group species, the general hybridization/Bent’s rule/ ω -bonding model seems to provide a more comprehensive and satisfactory picture of molecular geometry and electronic distribution than the VSEPR model.

An interesting consequence of the ω -bonded structures of hypervalent species can be recognized in the pattern of bond-dissociation energies (BDEs), as displayed in Fig. 3.88 for SF_6 . Strong oscillations of S—F bond strength are evident, reflecting the strongly coupled three-center character of each ω -bond pair. The integrity

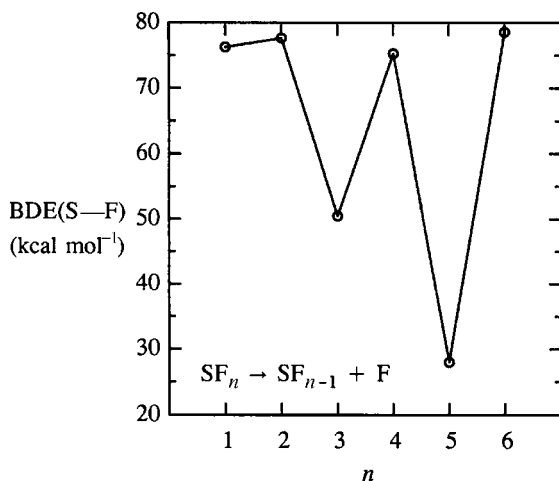


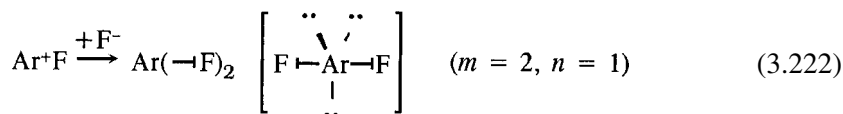
Figure 3.88 Successive bond-dissociation energies (BDEs) for S—F bonds of SF_n , showing the alternation associated with breaking of strongly coupled ω -bond pairs.

of each $F \leftarrow S \rightarrow F$ hyperbond pair is critically dependent on maintenance of the cooperative three-center resonance coupling, as reflected in the high BDE for the first member of the ω -bond pair. However, the “smoke-and-mirrors” nature of the bonding is exposed as soon as the triad is disrupted, and the remaining weak $2c/3e$ bond ($(\sigma_{SF})^2(\sigma_{SF}^*)^1$) dissociates with much lower BDE. This pattern is repeated for each ω -bonded pair until only the two covalent bonds of normal-valent SF_2 remain, with BDE values exhibiting only the (weak) degree of interdependence typical of two-center covalent bonds.

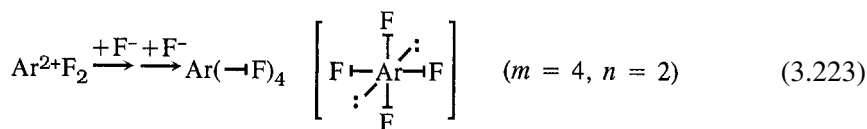
Rare-gas compounds

The ultimate extension of the hypervalency concept involves bonding to group 18 rare-gas elements. The rare gases were long considered to be chemically “inert” until Neil Bartlett and coworkers synthesized XeF_2 , XeF_4 , and other RgF_n compounds (particularly for $Rg = Xe, Kr$) in the 1960s.¹⁴⁵ Many more such compounds are now known.¹⁴⁶

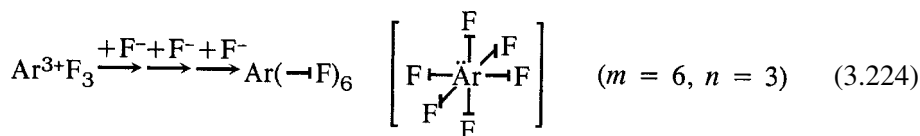
The ω -bonding model (3.218) can readily be extended to rare-gas central atoms by considering the limit $m = 2n$. Taking $M = Ar$, for example, we can envision formation of the molecule ArF_2 from the normal-valent precursor Ar^+F (which is isoelectronic to ClF) through a single ω -addition:



Similarly, ArF_4 is formed from $Ar^{2+}F_2$ (which is isoelectronic to SF_2) by two ω -additions,



while ArF_6 is formed from $Ar^{3+}F_3$ (which is isoelectronic to PF_3) by three ω -additions,



Each $F \leftarrow Ar \rightarrow F$ ω -bond pair in (3.222)–(3.224) is constructed from one of the three orthogonal $3p_{Ar}$ AOs in the usual manner,

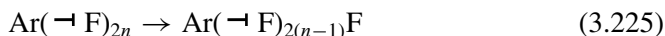


Table 3.34. The Ar—F bond lengths *R*, average Ar—F bond-dissociation energies ⟨BDE⟩, and vibrational frequencies of ArF_{*n*} species

Species	Symmetry	<i>R</i> (Å)	⟨BDE⟩ (kcal mol ⁻¹)	IR frequency (cm ⁻¹)
ArF	C _{∞v}	2.578	0.97	111
ArF ₂	D _{∞h}	1.878	6.72	224(2), 404, 616
ArF ₄	D _{4h}	1.883	22.87	133, 185(2), 202, 291, 326, 385, 618(2)
ArF ₆	O _h	1.895	17.48	145(3), 190(3), 204(3), 302(2), 367, 607(3)

and the remaining Ar lone pairs are accommodated in residual unhybridized valence AOs,¹⁴⁷ namely three (*s*²*p*_{*x*}²*p*_{*y*}²) in ArF₂, two (*s*²*p*_{*x*}²) in ArF₄, and one (*s*²) in ArF₆. All these species are therefore perfectly consistent with the octet rule.

Each parent closed-shell species ArF_{2*n*} can be envisioned to give rise to a daughter open-shell ArF_{2*n*-1} species by breaking one of the F—Ar—F triads (with high BDE),



leaving a weakened 2*c*/3*e* Ar—F bond [(σ_{ArF})²(σ_{ArF*})⁻¹]. However, the latter bond is actually *unstable* except in ArF, and other odd-membered species (ArF₅, ArF₃) apparently do not form true equilibrium structures. Such even–odd alternation of stability for ArF_{*n*} is clearly related to the zig-zag pattern of bond energies in SF₆ (Fig. 3.88).

Table 3.34 summarizes the calculated geometries and energetics of various ArF_{*n*} species and Table 3.35 shows corresponding NBO/NRT descriptors.

The results of Tables 3.34 and 3.35 are in full accord with the ω-bonded representations (3.222)—(3.225). The sole open-shell species, ArF, exhibits a very weak (BDE < 1 kcal mol⁻¹, ν ≈ 100 cm⁻¹) and long (*R* ≈ 2.58 Å) Ar—F bond,

Table 3.35. Natural atomic charges (*Q*), *d*-orbital occupancies (*d*_{Ar*}), and NRT bond orders and valencies (with percentage ionic character) for ArF_{*n*} species

Species	Charge			Bond order (% ionic)		Valency (% ionic)	
	<i>Q</i> _{Ar}	<i>Q</i> _F	<i>d</i> _{Ar*}	Ar—F	F—F	Ar	F
ArF	+0.060	-0.060	0.00	0.031 (90%)	—	0.031 (90%)	0.031 (90%)
ArF ₂	+0.756	-0.378	0.02	0.408 (46%)	0.138 (0%)	0.816 (46%)	0.546 (35%)
ArF ₄	+1.228	-0.307	0.04	0.271 (20%)	0.459 (44%)	1.082 (20%)	0.730 (35%)
ArF ₆	+1.512	-0.252	0.06	0.320 (33%)	0.342 (40%)	1.922 (33%)	0.677 (37%)

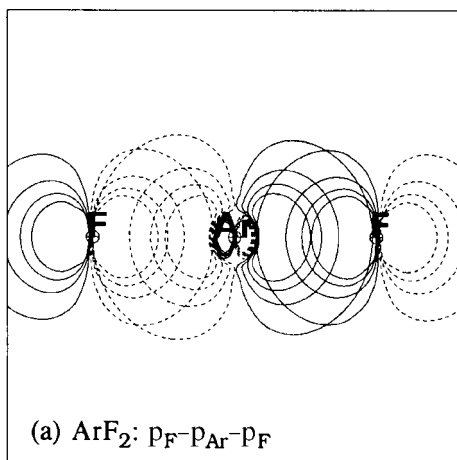


Figure 3.89 Hyperbonding AOs of ArF_2 ($\text{F} \leftarrow \text{Ar} \rightarrow \text{F}$), showing the similarity to Fig. 3.84(a).

whereas the closed-shell ArF_{2n} members exhibit the symmetries and short, strong $\text{Ar} \rightarrow \text{F}$ bonds ($R \simeq 1.88 \text{ \AA}$, $\text{BDE} \simeq 6\text{--}23 \text{ kcal mol}^{-1}$, $\nu \simeq 600 \text{ cm}^{-1}$), high polarities, and strong vibrational couplings (e.g., $\delta\nu_{\text{str}} = 212 \text{ cm}^{-1}$ for ArF_2) expected in the ω -bonding model. Figure 3.89 illustrates the three hyperbonding $p_{\text{F}}-p_{\text{Ar}}-p_{\text{F}}$ AOs of ArF_2 , showing the essential similarity to other hyperbonded species (cf. Fig. 3.84(a)). As usual, the d-orbital occupancies on Ar are rather negligible (0.06e or less), and the high bond ionicity is conspicuous (with $Q_{\text{F}} \simeq -0.3$, ionic character $\simeq 20\%\text{--}50\%$), which is consistent with achievement of strong ω -bonding *within* the constraints of the octet rule.

It is noteworthy that the ω -bonded structure for ArF_6 differs from that predicted by VSEPR theory. ArF_6 is predicted to be of octahedral (O_{h}) symmetry, with three mutually perpendicular $\text{F} \leftarrow \text{Ar} \rightarrow \text{F}$ triads and an s-type lone pair. In contrast, VSEPR predicts a pentagonal bipyramid (or other seven-vertex polyhedron) with some or all $\text{F}-\text{Ar}-\text{F}$ angles less than 90° . The calculated equilibrium structure is in agreement with the ω -bonding model.

In principle, the ω -bonding sequence (3.218) could be further extended to $m = 8$, $n = 4$, leading to ArF_8 species. This corresponds to four ω -additions to Ar^{4+}F_4 (which is isoelectronic to SiF_4) and can be pictured in terms of four successive $\text{S}_{\text{N}}2$ -like attacks of fluoride on the Ar^{4+}F_4 tetrahedral faces. This would lead to overall body-centered cubic structure (O_{h} symmetry) with each $\text{F} \leftarrow \text{Ar} \rightarrow \text{F}$ triad spanning one of the four body diagonals. However, it appears that such a structure remains a transition state on the ArF_8 (or KrF_8) surface, failing to achieve a stable equilibrium geometry. This failure may be attributed both to extreme steric congestion and to the difficulty of achieving the Ar^{4+}F_4 precursor species (due

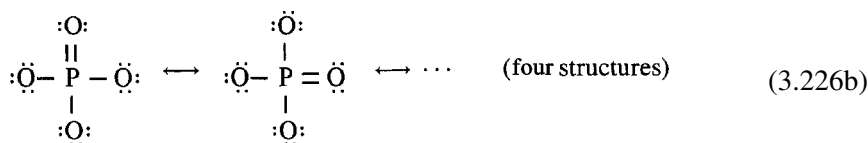
to the high electronegativity of cationic argon), as well as to forced use of the low-energy *s*-orbital in the tetrahedral bonding hybrids, which further increases the effective electronegativity of the central rare-gas atom to a deleterious degree. Whether such a cubic RgF_8 equilibrium structure could be achieved for the heavier rare-gas elements remains unknown.

Anions of common laboratory oxyacids

Another type of “hypervalency” is encountered in textbook descriptions of the oxyanions of common laboratory acids. Generations of chemistry students have been taught that the “correct” representations of these species are in terms of resonance-delocalized hypervalent Lewis-structure diagrams, such as sulfate (SO_4^{2-}),



phosphate (PO_4^{3-}),



and perchlorate (ClO_4^-),



Structure (3.226c), for example, depicts a central *heptavalent* Cl atom ($V_{\text{Cl}} = 7$), exceeding the normal valence octet by *six* electrons! (These excess electrons are assumed to be accommodated in chlorine 3d orbitals, whereas “d-orbital participation” is prevented in first-row compounds.) Hypervalent structures such as (3.226a)–(3.226c) are claimed to be justified by the “electroneutrality principle,” which stipulates that second-row central atoms have zero formal charge (whereas first-row oxyanion Lewis structures commonly violate this principle).¹⁴⁸

Although such textbook diagrams are called “Lewis structures,” they are *not* the electron-dot diagrams that G. N. Lewis originally wrote for such species. Lewis’s depiction of SO_4^{2-} , for example, is reproduced in Fig. 3.90. This shows a normal-valent S^{2+} ion with shared-pair bonds to four O^- ions, which is fully consistent with the octet rule, with no intrinsic need for multiple resonance structures to account for the observed T_d symmetry. According to Lewis’s original concept, each ion is

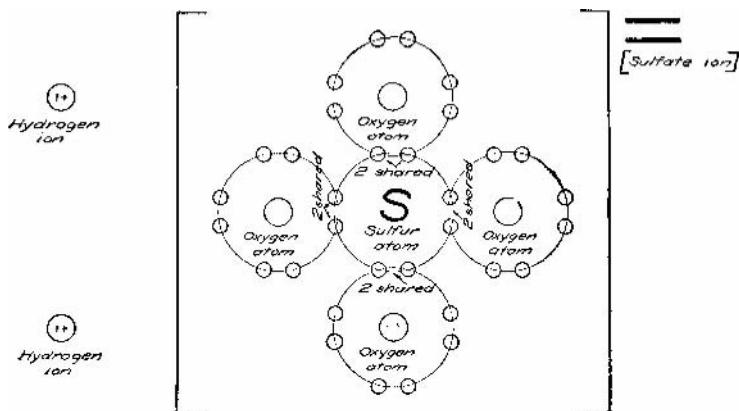
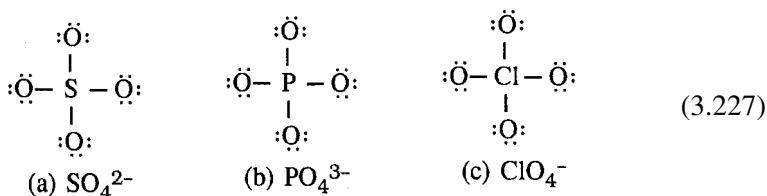


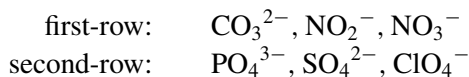
Figure 3.90 A reproduction (p. 134) from C. W. Gray, C. W. Sandifur, and H. J. Hanna, *Fundamentals of Chemistry*, revised and enlarged edition (Boston, Houghton Mifflin, 1929), showing how the “original” Lewis structure for the sulfate anion was first presented in general chemistry textbooks. As the authors note (p. 132), “Dr. G. N. Lewis, of the University of California, has advanced an explanation that is now generally accepted (1928–1929).”

therefore expected to be described as a *single* localized (but highly ionic) octet-conforming dot diagram,



Thus, neither hypervalency nor strong resonance delocalization is implied by Lewis’s original electron-dot picture, which rests on a distinctly ionic (not “electronneutral”) picture of the bonding.

Natural resonance theory (NRT) allows these conflicting pictures of the oxyanion electron distributions to be tested quantitatively.¹⁴⁹ Table 3.36 compares the geometries, NRT bond orders, atomic charges, and d-orbital occupancies for a representative variety of first- and second-row XO_m^{n+} species,



and Table 3.37 summarizes the leading terms of the NRT resonance expansion for each species.

The results in Tables 3.36 and 3.37 establish that Lewis’s original diagrams (3.227) are far more accurate than the modern textbook diagrams (3.226). In all cases the most highly weighted NRT structure conforms to the original (3.227),

Table 3.36. Geometries and NBO/NRT descriptors of common oxyanions XO_m^{n-} (see Fig. 3.91), showing symmetry, bond length R_{XO} , NRT bond order b_{XO} and central-atom valency V_{X} , atomic charges Q_{X} and Q_{O} , and *d*-orbital occupancy d_{X}^* for representative first- and second-row species

Species	Symmetry	R_{XO} (Å)	b_{XO}	V_{X}	Q_{X}	Q_{O}	d_{X}^*
First row							
CO_3^{2-}	$\text{D}_{3\text{h}}$	1.308	1.333	4.000	+0.929	-0.976	0.02
NO_2^-	$\text{C}_{2\text{v}}$	1.258	1.500	3.000	+0.180	-0.590	0.02
NO_3^-	$\text{D}_{3\text{h}}$	1.260	1.333	4.000	+0.679	-0.560	0.02
Second row							
PO_4^{3-}	T_d	1.602	1.000	4.000	+2.363	-1.341	0.11
SO_4^{2-}	T_d	1.527	1.000	4.000	+2.445	-1.111	0.18
ClO_4^-	T_d	1.501	1.000	4.000	+2.370	-0.843	0.24

whereas the modern structures (3.226) gain *no* weighting in the NRT expansion. The leading resonance corrections to (3.227) are the many structures of still more ionic form (with individual weighting 1%–2%). The NRT bond orders and valencies are also in essential agreement with the Lewis diagrams (3.227), showing *no* discernible evidence of hypervalency (e.g., $V_{\text{Cl}} = 4.000$, not “7”). Furthermore, the large positive charges on the central atom ($Q_{\text{X}} \simeq +2.4$) confirm that the second-row species are highly ionic (not “electroneutral”). (This increased ionicity would, of course, be expected from the general electronegativity differences between first- and second-row atoms [Section 3.2.5].) One can also see from Table 3.36 that the low *d*-orbital occupancy ($\sim (0.1\text{--}0.2)e$) is *far* less than would be necessary for structures such as (3.226). Thus, the “hypervalent” representations (3.226) provide a completely misleading picture of the actual electronic distributions and should be abandoned.

In contrast, for the first-row XO_m^{n-} species the NRT results are completely consistent with the usual textbook descriptions, namely

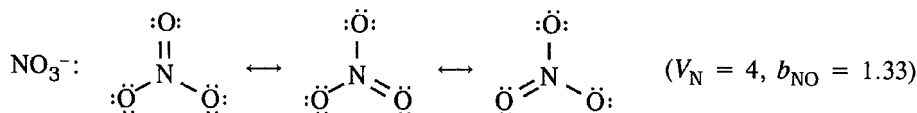
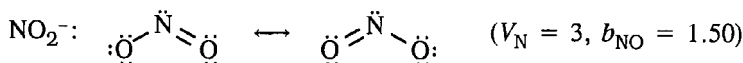
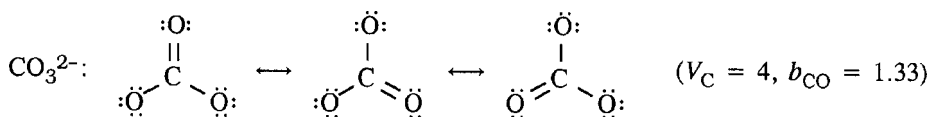


Table 3.37. Leading NRT resonance structures and weightings (with numbers of symmetry-equivalent resonance structures in brackets) for anions of common laboratory oxyacids

Species	NRT resonance structures and weightings		
1. CO_3^{2-}	$\begin{array}{c} \text{:}\ddot{\text{O}}\text{:} \\ \\ \text{:}\ddot{\text{O}}\text{=C=}\ddot{\text{O}}\text{:} \\ \text{a. 30.5\% [3]} \end{array}$	$\begin{array}{c} \text{:}\ddot{\text{O}}\text{:} \\ // \\ \text{:}\ddot{\text{O}}\text{=C=}\ddot{\text{O}}\text{:} \\ \text{b. 1.4\% [3]} \end{array}$	(remainder) 4.3%
2. NO_2^-	$\begin{array}{c} \text{:}\ddot{\text{O}}\text{:} \\ \backslash \\ \text{:}\ddot{\text{N}}\text{=}\ddot{\text{O}}\text{:} \\ \text{a. 48.5\% [2]} \end{array}$	$\begin{array}{c} \text{:}\ddot{\text{O}}\text{:} \\ \backslash \\ \text{:}\text{N}\equiv\ddot{\text{O}} \\ \text{b. 1.5\% [2]} \end{array}$	
3. NO_3^-	$\begin{array}{c} \text{:}\text{O}\text{:} \\ \\ \text{:}\ddot{\text{O}}\text{-N-}\ddot{\text{O}}\text{:} \\ \text{a. 30.4\% [3]} \end{array}$	$\begin{array}{c} \text{:}\text{O}\text{:} \\ \\ \text{:}\ddot{\text{O}}\text{:N=}\ddot{\text{O}}\text{:} \\ \text{b. 1.5\% [3]} \end{array}$	(remainder) 4.4%
4. PO_4^-	$\begin{array}{c} \text{:}\ddot{\text{O}}\text{:} \\ / \\ \text{:}\ddot{\text{O}}\text{-P} \\ \backslash \quad \backslash \\ \quad \quad \text{:}\ddot{\text{O}}\text{:} \\ \quad \quad \text{:}\ddot{\text{O}}\text{:} \end{array}$	$\begin{array}{c} \text{:}\ddot{\text{O}}\text{:} \\ // \\ \ddot{\text{O}}\text{=P} \\ \backslash \quad \backslash \\ \quad \quad \text{:}\ddot{\text{O}}\text{:} \\ \quad \quad \text{:}\ddot{\text{O}}\text{:} \end{array}$	(remainder) $0.5 \times 10^{-1}\%$
5. SO_4^-	$\begin{array}{c} \text{:}\ddot{\text{O}}\text{:} \\ / \\ \text{:}\ddot{\text{O}}\text{-S} \\ \backslash \quad \backslash \\ \quad \quad \text{:}\ddot{\text{O}}\text{:} \\ \quad \quad \text{:}\ddot{\text{O}}\text{:} \end{array}$	$\begin{array}{c} \text{:}\ddot{\text{O}}\text{:} \\ // \\ \text{:}\ddot{\text{O}}\text{:S} \\ \backslash \quad \backslash \\ \quad \quad \text{:}\ddot{\text{O}}\text{:} \\ \quad \quad \text{:}\ddot{\text{O}}\text{:} \end{array}$	(remainder) 10.5%
6. ClO_4^-	$\begin{array}{c} \text{:}\ddot{\text{O}}\text{:} \\ / \\ \text{:}\ddot{\text{O}}\text{-Cl} \\ \backslash \quad \backslash \\ \quad \quad \text{:}\ddot{\text{O}}\text{:} \\ \quad \quad \text{:}\ddot{\text{O}}\text{:} \end{array}$	$\begin{array}{c} \text{:}\ddot{\text{O}}\text{:} \\ // \\ \ddot{\text{O}}\text{=Cl} \\ \backslash \quad \backslash \\ \quad \quad \text{:}\ddot{\text{O}}\text{:} \\ \quad \quad \text{:}\ddot{\text{O}}\text{:} \end{array}$	

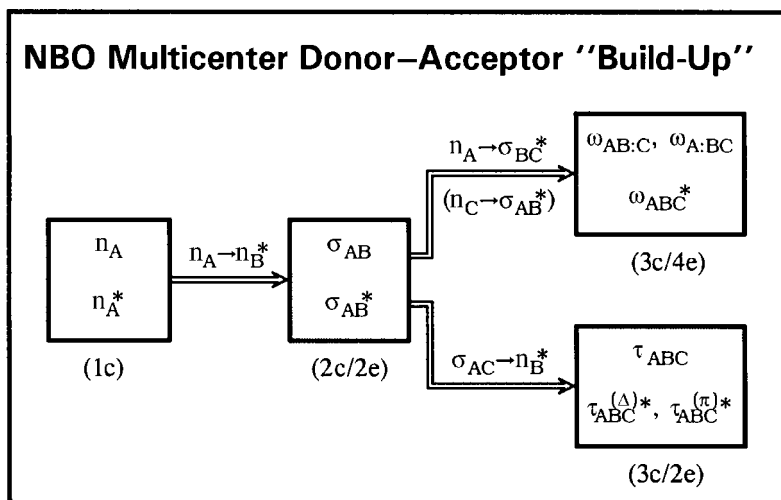


Figure 3.91 A schematic depiction of NBO donor–acceptor relationships connecting one-center (n), two-center (σ), and three-center (ω and τ) orbital “types.”

However, these involve only normal-valent Lewis structures, and hence present no conceptual difficulties akin to those for second-row species.

3.6 Hypovalency: 3c/2e bridge bonds

The NBO donor–acceptor theory of hypovalency: three-center bridge bonds

As described in Section 3.5, the 3c/4e ω -bonding motif can be considered as the limit of a strong donor–acceptor interaction between a one-center donor and a two-center acceptor (e.g., $n_A \rightarrow \sigma_{BC}^*$). However, three-center character can alternatively be achieved by a two-center donor interacting with a one-center acceptor (e.g., $\sigma_{AC} \rightarrow n_B^*$). In this case the three starting valence hybrids (h_A , h_B , and h_C) are occupied only by the two electrons of the two-center donor. The resulting 3c/2e orbitals (which will be denoted τ_{ABC} , $\tau_{ABC}^{(\Delta)*}$, and $\tau_{ABC}^{(\pi)*}$) are therefore adapted to describe “electron-deficient” (hypovalent) systems having a surplus of valence orbitals compared with available electrons. Figure 3.91 depicts the schematic “genealogical construction” by which the two distinct types of three-centre orbitals (ω and τ) can be built up from donor–acceptor interactions of underlying one- and two-center orbitals.

The NBO picture of 3c/2e τ -bonding may be developed along lines parallel to those for 3c/4e ω -bonding in Eqs. (3.194) *et seq.* Let us first consider the special case of a homopolar two-center bond $\sigma_{AC} = 2^{-1/2}(h_A + h_B)$ interacting with a vacant one-center orbital $n_B^* = h_B$ to form a three-center bond τ_{ABC} of the form

$$\tau_{ABC} = (1 + \lambda^2)^{-1/2}(\sigma_{AC} + \lambda n_B^*) \quad (3.228)$$

where λ is a measure of $\sigma_{AC} \rightarrow n_B^*$ interaction strength. In terms of starting hybrids h_A , h_B , and h_C , this bonding function can be rewritten as

$$\tau_{ABC} = (2 + 2\lambda^2)^{-1/2}[h_A + (2^{1/2}\lambda)h_B + h_C] \quad (3.229a)$$

There remain two other (net antibonding) linear combinations of h_A , h_B , and h_C orthogonal to τ_{ABC} ; these may be taken, e.g., as the unmodified σ_{AC}^* antibond,

$$\tau_{ABC}^{(\pi)*} = \sigma_{AC}^* = 2^{-1/2}(h_A - h_C) \quad (3.229b)$$

and the true three-center antibond

$$\tau_{ABC}^{(\Delta)*} = \lambda(2 + 2\lambda^2)^{-1/2}[h_A - (2^{1/2}/\lambda)h_B + h_C] \quad (3.229c)$$

but any orthogonal transforms of (3.229b) and (3.229c) are equally valid. The two antibonding NBOs associated with each τ_{ABC} remain available to interact with (delocalize) other filled NBOs of the Lewis-structure diagram.

The three-center orbitals (3.229a)–(3.229c) can also be considered to arise from the 3×3 secular determinant for interaction of the three hybrids, with Fock-matrix elements

$$\langle h_A | \hat{F} | h_B \rangle = \langle h_B | \hat{F} | h_C \rangle = \beta, \quad \langle h_A | \hat{F} | h_C \rangle = \gamma \quad (3.230)$$

As shown originally by Eberhardt, Crawford, and Lipscomb,¹⁵⁰ three limits can be distinguished for these matrix elements, leading to three distinct forms of the lowest (occupied) MO ϕ_+ :

$$\gamma/\beta = 0: \quad \phi_+ = \frac{1}{2}(h_A + 2^{1/2}h_B + h_C) \quad (\text{“open”}) \quad (3.231a)$$

$$\gamma/\beta = 1: \quad \phi_+ = 3^{-1/2}(h_A + h_B + h_C) \quad (\text{“central”}) \quad (3.231b)$$

$$\gamma/\beta = \infty: \quad \phi_+ = 2^{-1/2}(h_A + h_C) = \sigma_{AC} \quad (\text{“ordinary two-center”}) \quad (3.231c)$$

These correspond, respectively, to the values $\lambda = 1$ (“open”), $\lambda = 2^{-1/2}$ (“central”), and $\lambda = 0$ (“ordinary two-center”), in the general expression (3.229a) for τ_{ABC} of a homopolar $\sigma_{AC} \rightarrow n_B^*$ interaction.

More generally, each τ_{ABC} NBO can be expressed as a general linear combination of NHOs,

$$\tau_{ABC} = c_A h_A + c_B h_B + c_C h_C \quad (3.232a)$$

with optimal coefficients and hybrids chosen for maximal occupancy. Possible choices of the associated antibonds are the idealized two-center $\tau_{ABC}^{(\pi)*}$,

$$\tau_{ABC}^{(\pi)*} = \mathfrak{A}(c_C h_A - c_A h_C) \quad (3.232b)$$

and three-center $\tau_{ABC}^{(\Delta)*}$,

$$\tau_{ABC}^{(\Delta)*} = \mathfrak{N}[c_B c_A h_A - (c_A^2 + c_B^2) h_B + c_B c_C h_C] \quad (3.232c)$$

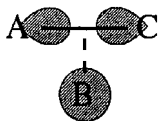
However, the two antibonding NBOs (ordered by occupancy) are more generally expressed as

$$\tau'_{ABC}{}^* = c'_A h_A + c'_B h_B + c'_C h_C \quad (3.233a)$$

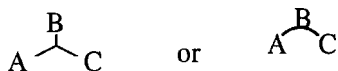
$$\tau''_{ABC}{}^* = c'_A h_A + c'_B h_B + c'_C h_C \quad (3.233b)$$

to optimize the description of electron density.

Because the amplitude of a two-center donor orbital σ_{AC} is generally maximal near the bond midpoint (rather than at the ends, where only one of the two hybrids contributes), the preferred $\sigma_{BC} \rightarrow n_B^*$ geometry is generally T-shaped,



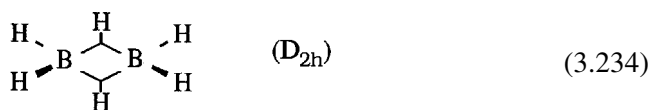
Moreover, the strong loss of occupancy from the σ_{AC} NBO weakens and lengthens this bond, so that B has the appearance of “bridging” the weakened $A \cdots C$ linkage. Thus, the τ_{ABC} bond is often represented with a distinctive trigonal symbol (“Y-bond” \lrcorner) or arc segment,



to depict this bridging $A-(B)-C$ relationship.

Diborane

The structure of diborane (B_2H_6) and other boron hydrides presented a famous challenge to valence theorists. Although a hydrogen-bridged structure for diborane was proposed as early as 1921,¹⁵¹ conflicting structural evidence delayed general acceptance of this concept until about 1947,¹⁵² when the now-familiar τ -bridged representation



was definitively established.¹⁵³ Subsequently, the general theory of three-center bonding has been strongly advanced (particularly through the work of W. N.



William N. Lipscomb Jr.

Lipscomb and coworkers¹⁵⁴) and various qualitative schemes for rationalizing the bonding in boranes and other electron-deficient compounds have been developed.¹⁵⁵

Each three-center BHB unit in (3.234) can be described by a bonding NBO τ_{BHB} (with occupancy 1.9846)

$$\tau_{\text{BHB}} = 0.52(\text{sp}^{4.59})_{\text{B}} + 0.67(\text{s})_{\text{H}} + 0.52(\text{sp}^{4.59})_{\text{B}} \quad (3.235\text{a})$$

and two antibond NBOs τ'_{BHB}^* and τ''_{BHB}^* (with occupancies 0.0152 and 0.0005, respectively),

$$\tau'_{\text{BHB}}^* = 0.48(\text{sp}^{4.59})_{\text{B}} - 0.74(\text{s})_{\text{H}} + 0.48(\text{sp}^{4.59})_{\text{B}} \quad (3.235\text{b})$$

$$\tau''_{\text{BHB}}^* = 0.71(\text{sp}^{4.59})_{\text{B}} - 0.71(\text{sp}^{4.59})_{\text{B}} \quad (3.235\text{c})$$

Figure 3.92 shows a ball-and-stick model of the equilibrium geometry (left) and overlapping pattern of hybrid orbitals associated with τ_{BHB} formation (right), while Fig. 3.93 displays the forms of the boron bonding hybrid and three-center BHB bonds and antibonds in both contour and surface plots, illustrating classic representatives of the “open” τ -bonding motif (3.231a).

It must be emphasized that the formulation of three-center τ -bonds provides a *qualitative* (not merely incremental) improvement in the accuracy of the natural Lewis-structure description of diborane. Because a three-center orbital is intrinsically more mathematically flexible than a two-center orbital, the description of *any* molecule is seemingly “improved” by employing three-center in place of two-center NBOs. However, for most non-boron molecules this improvement would be quite negligible (e.g., less than 0.1% for ethane, whose two-center Lewis-structure

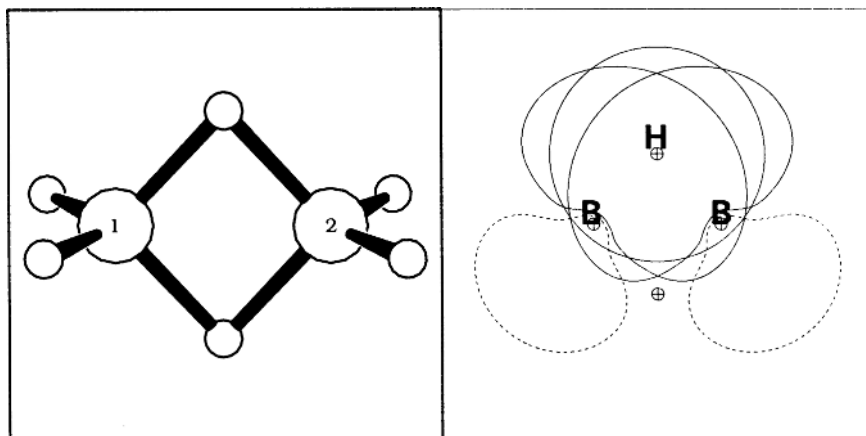


Figure 3.92 The structure of diborane B₂H₆ (left) and shapes of the overlapping (sp^{4.59})_B and (s)_H natural hybrids contributing to the three-center τ_{BHB} bridge bond (right). (Only the outermost hybrid contours are shown, in order to reduce congestion on the diagram.)

description is already >99.9% accurate), in no way justifying the extra complexity introduced. For diborane, in contrast, the accuracy of the two-center Lewis-structure description is barely 86% (with more than 2.22e unaccounted for!), whereas that of the three-center Lewis structure (3.234) is >99.6%. Thus, three-center bonds provide a genuinely new and necessary “building block” of the Lewis-structure concept, if the accustomed accuracy of this concept is to be preserved for electron-deficient compounds.

The two antibond NBOs $\tau^{(\Delta)*}$ and $\tau^{(\pi)*}$ have distinctive shapes and nodal characteristics that may be characterized as follows.

- (1) The $\tau^{(\Delta)*}$ antibond (Fig. 3.93(c)) is concentrated near the B···B midpoint and has contributions from all three atoms. The inner region, of trilobate form, protrudes across each edge of the bonding triangle, while the outer regions, of opposite sign, extend outward from each vertex. The NBO label “ $\tau^{(\Delta)*}$ ” suggests its distinctive triangular form in the midpoint of the B···B region and its true three-center character;
- (2) The $\tau^{(\pi)*}$ antibond (Fig. 3.93(d)) has the form of a “bent π^* ” (or banana antibond) orbital, with nodal planes approximating those of an ordinary π_{BB}^* orbital. Because the boron bonding hybrids are canted about 45° between idealized sigma- and pi-bonding directions, this NBO also resembles a d_{xy} orbital centered at the molecular midpoint (with slight vertical asymmetry to preserve orthogonality with the corresponding NBO of the opposite bridge bond). The NBO label “ $\tau^{(\pi)*}$ ” suggests its distinctive π^* -like form and quasi-two-center character.

The appreciable occupancy of the $\tau_{\text{BHB}}^{(\Delta)*}$ antibond NBO indicates that the idealized τ -bonded Lewis structure (3.324) is stabilized by significant additional

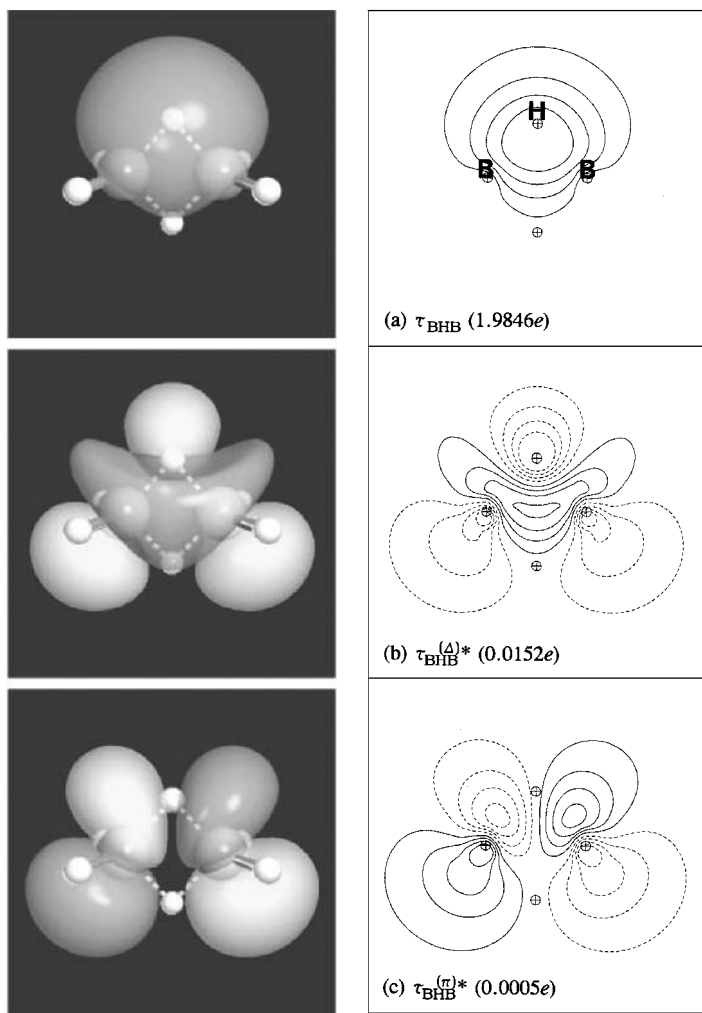
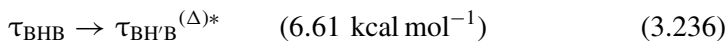


Figure 3.93 Three-center BHB orbitals (and occupancies) in diborane, showing (a) the three-center bond τ_{BHB} , (b) the three-center antibond $\tau_{\text{BHB}}^{(\Delta)*}$, and (c) the three-center antibond $\tau_{\text{BHB}}^{(\pi)*}$.

donor–acceptor delocalizations involving this orbital. From NBO second-order perturbative analysis, the most important of these is



involving the mutual delocalization of the two τ bonds. The two τ bonds in mutual conjugation are therefore considerably stronger than the corresponding bonds in isolation. Contour diagrams of interaction (3.236) are shown in Fig. 3.94, displaying the favorable orbital overlap near the molecular midpoint.

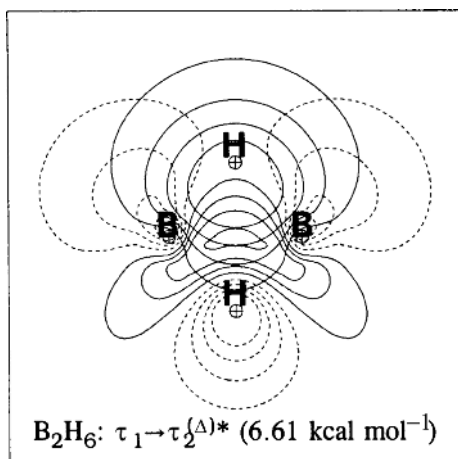
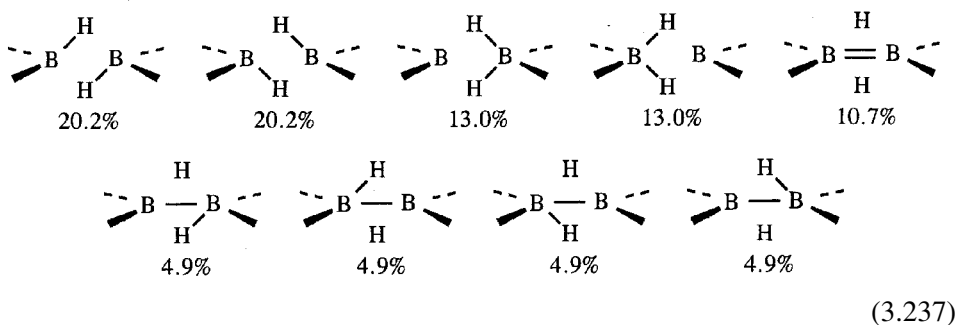


Figure 3.94 The NBO $\tau_1 \rightarrow \tau_2^{(\Delta)*}$ three-center donor–acceptor interaction in B_2H_6 .

As a result of the strong complementary $\tau_1 \rightarrow \tau_2^{(\Delta)*}$ delocalizations (3.236), τ bonds may be expected to appear in *pairs* in stable bridge-bonded structures. (This structural principle will be further elaborated in connection with central-type τ_{BBB} bonds, to be discussed below.)

As suggested by Pauling (note 14) one can also describe diborane bonding in terms of multiple resonance structures of conventional one- and two-center type. The difficulty is that such a description leads to a large number of structures of similar weighting, complicating both numerical determination and physical interpretation. For diborane, natural resonance theory (NRT) leads to *nine* structures of non-negligible weighting,



The corresponding NRT bond orders are

$$b_{BB} = 0.432, \quad b_{BH(\mu)} = 0.391, \quad b_{BH(t)} = 0.993 \quad (3.238)$$

where $H(\mu)$ and $H(t)$ respectively denote bridged and terminal protons. The practical difficulty of determining resonance weights increases rapidly as the number of

resonance structures proliferates in more complex boron hydrides. Hence, the three-center description will be given primary attention in this book.

*Protonated ethylene and other three-center τ-bonding motifs:
agostic interactions*

Results of early studies¹⁵⁶ suggested the aptness of a "protonated-ethylene" picture of bridge bonding. The qualitative orbital-splitting diagram for interaction of an unfilled $H^+ s^*$ orbital with the π and π^* orbitals of ethylene is shown in Fig. 3.95. The parent π^* orbital is scarcely affected by τ -bond formation, and this orbital therefore correlates with the quasi-two-center $\tau_{\text{CHC}}^{(\pi)*}$ NBO in the τ -bonded product. However, the filled π and unfilled s^* orbitals interact strongly to give the final τ -bonded NBOs $\tau_{\text{CHC}} \simeq \mathfrak{N}(\pi_{\text{CC}} + s_{\text{H}}^*)$ and $\tau_{\text{CHC}}^{(\Delta)*} \simeq \mathfrak{N}(\pi_{\text{CC}} - s_{\text{H}}^*)$.

Figure 3.96 shows the actual NBO orbital energy correlation diagram for T-shaped approach of a proton to ethylene (along the C_2 axis). It can be seen that, inside $R \simeq 1.5 \text{ \AA}$, the energy ordering of the $\tau_{\text{CHC}}^{(\Delta)*}$ and $\tau_{\text{CHC}}^{(\pi)*}$ antibond NBOs is inverted with respect to that shown in Fig. 3.95 by the strong $\pi_{\text{CC}}-s_{\text{H}}^*$ splitting.

The equilibrium geometry and three-center NBOs of the protonated ethylene model are displayed in Fig 3.97. The qualitative similarities to the diborane bridge bond (Fig. 3.93) are evident. Thus, the $\pi-s^*$ model (cf. Fig. 3.91) may be considered a useful descriptive picture of three-center τ -bond formation in diborane.

In a similar manner, many other types of $2c \rightarrow 1c^*$ donor-acceptor interactions may be considered as precursors to $3c/2e$ τ -bonds. As simple examples, let us

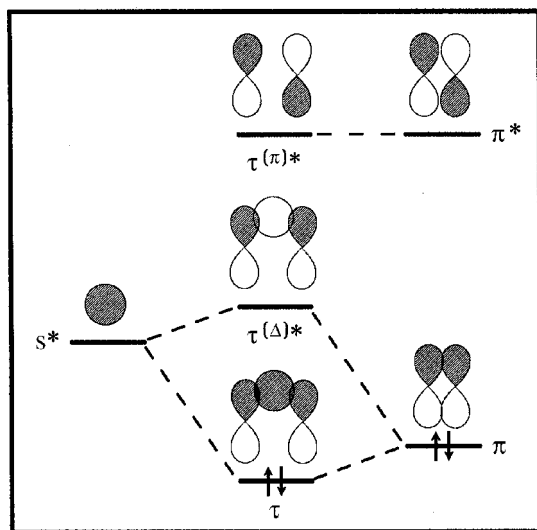


Figure 3.95 A schematic NBO interaction diagram for τ -bonding.

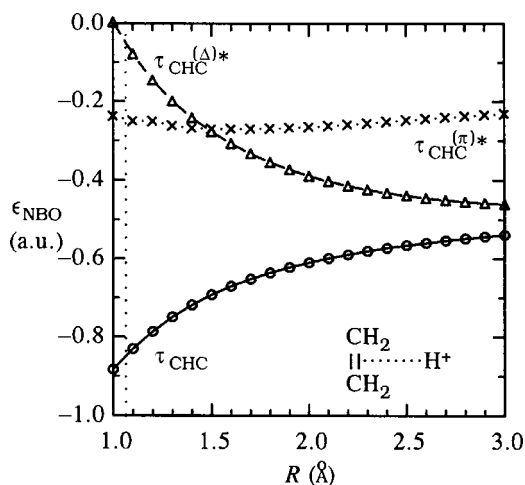
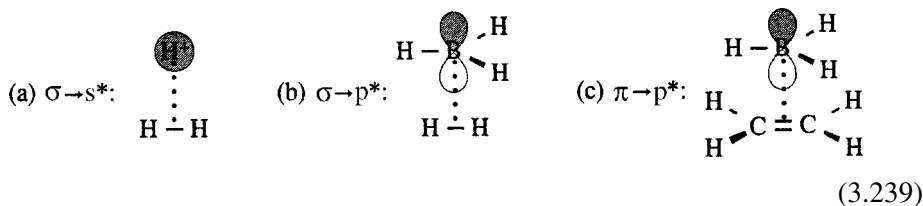


Figure 3.96 The NBO orbital energy variations for the three-center τ_{CHC} (circles), $\tau_{\text{CHC}}^{(\Delta)*}$ (triangles), and $\tau_{\text{CHC}}^{(\pi)*}$ (crosses) NBOs of protonated ethylene (cf. Fig. 3.95). R is the distance from the proton to the C=C midpoint, with the vertical dotted line marking equilibrium ($R_e = 1.064 \text{ \AA}$).

consider only the prototypes involving elementary σ - and π -type donors such as H_2 (σ) and C_2H_4 (π), and s^* - and p^* -type acceptors such as H^+ (s^*) and BH_3 (p^*). Any possible donor–acceptor combination arising from these precursors can be considered a candidate for three-center τ -bond formation, including (beyond the protonated-ethylene case already considered)



(Examples involving d^* -type acceptor orbitals or δ -type donor orbitals will be considered in Chapter 4.) Figures 3.98–3.100 show the three-center NBOs and occupancies for each of the prototype species (3.239a)–(3.239c).

Although the forms of the three-center NBOs in Figs. 3.97–3.100 vary widely, these orbitals share several common features. The filled (Lewis-type) τ -bond NBO in each case has an almost spherical region of high amplitude concentrated near the center of the bonding triangle. The “true” (Δ -type) $\tau^{(\Delta)*}$ antibond NBO has contributions from all three of the triangle nuclei, and has the rough appearance of a p_y orbital in H_3^+ (Fig. 3.98) or a d -like lobal pattern in C_2H_5^+ (Fig. 3.97)

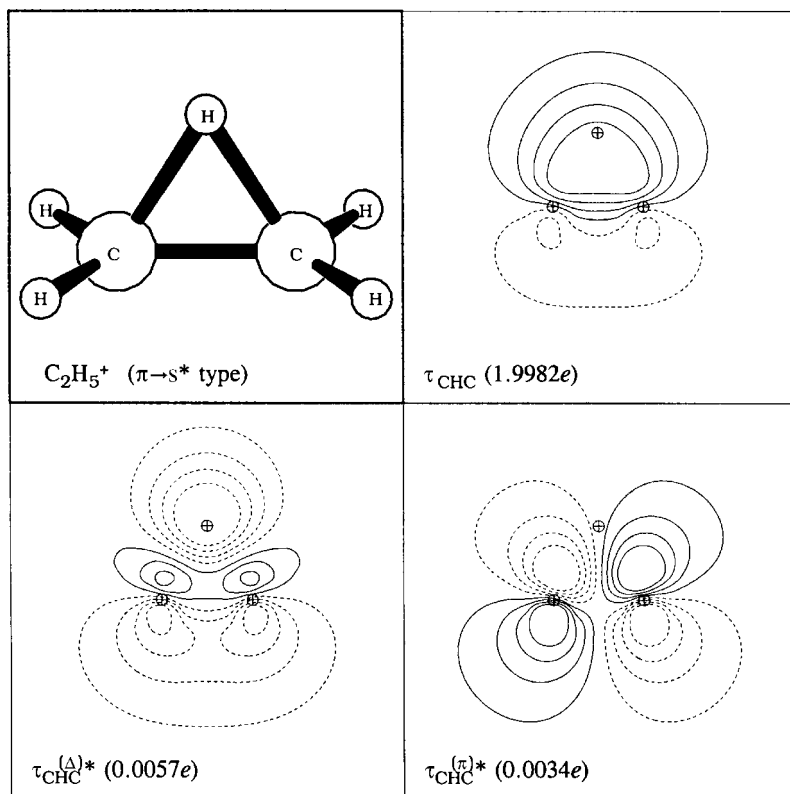


Figure 3.97 The equilibrium geometry and three-center NBOs τ_{CHC} , $\tau_{CHC}^{(\Delta)*}$, and $\tau_{CHC}^{(\pi)*}$ for protonated ethylene $C_2H_5^+$ ($\pi \rightarrow s^*$ type), showing the general similarity to the diborane bridge bond (cf. Fig. 3.93).

and BH_5 (Fig. 3.99). This NBO therefore appears to be vertically oriented, and is particularly suitable for delocalizations above the apex and below the base of the triangle. The remaining $\tau^{(\pi)*}$ NBO has a node passing through the apex atom and strongly resembles a p_x orbital in H_3^+ (Fig. 3.98) and BH_5 (Fig. 3.99), or a d_{xy} orbital in $C_2H_5^+$ (Fig. 3.97) and $H_3BC_2H_4$ (Fig. 3.100), centered at the midpoint of the triangle base. The $\tau^{(\pi)*}$ NBO is therefore somewhat more horizontally oriented, making it suitable for delocalizations along either edge of the triangle. Particularly striking in Fig. 3.100 is the *strong* delocalization (estimated at $34.7 \text{ kcal mol}^{-1}$) involving interaction of $\tau_{CBC}^{(\pi)*}$ with the in-plane σ_{BH} bond, which is conspicuously lengthened and canted downward as a result of this interaction. The contour diagram for this strong $\sigma_{BH} \rightarrow \tau_{CBC}^{(\pi)*}$ interaction is shown in Fig. 3.101.

As a result of the interaction in Fig. 3.101, the in-plane B—H bond elongates significantly (by 0.025 \AA compared with the two out-of-plane B—H bonds) and

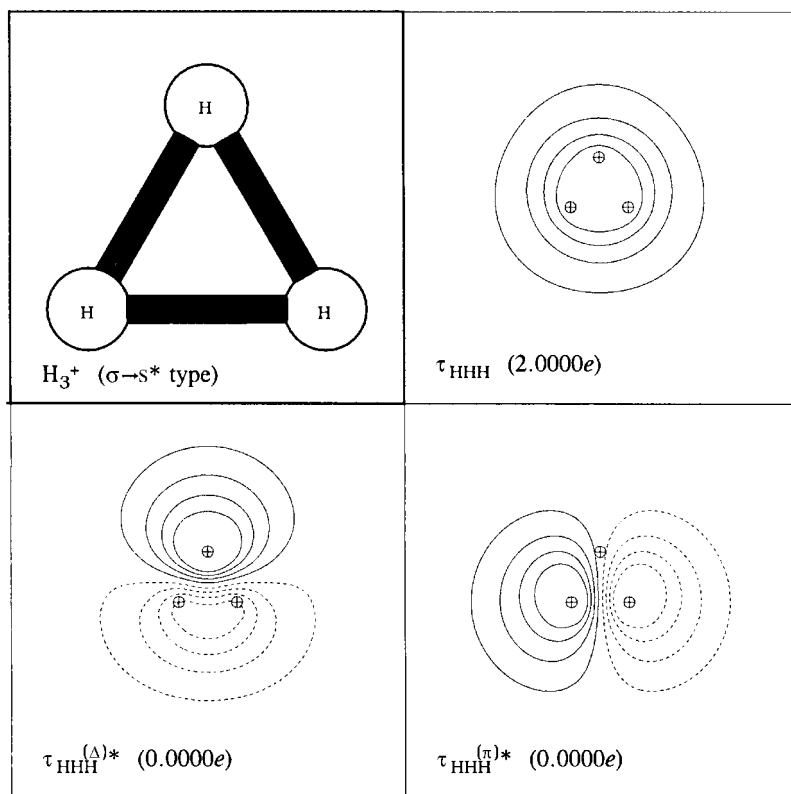


Figure 3.98 Three-center NBOs and occupancies for H_3^+ ($\sigma \rightarrow s^*$ type).

the *p* character of the boron hybrid increases (to $sp^{3.57}$ for in-plane B—H, versus $sp^{2.32}$ for out-of-plane B—H) to strengthen $\sigma_{\text{BH}} \rightarrow \tau_{\text{CBC}}^{(\pi)*}$ delocalization. Indeed, one can see that the orbital relationships are approaching those for C—(H)—C bridge-bond formation (cf. Fig. 3.92(b)). Thus, one can recognize in this strong $\sigma_{\text{BH}} \rightarrow \tau_{\text{CBC}}^{(\pi)*}$ interaction a connection to the mutual reinforcement of facing τ bonds (cf. Eq. (3.236)) and the strong tendency for bridging τ bonds to be formed in *pairs*.

Formation of the three-center τ_{CBC} bond also has a profound effect on the residual “ σ_{CC} ” bond NBO of the starting ethylene unit. As shown in Fig. 3.102, this NBO acquires pronounced “banana-bond” character, with each bonding hybrid directed about 23° from the line of C—C centers. Indeed, the disposition of the bonding hybrids resembles that in fully formed three-center bonds (cf., e.g., the right-hand panel of Fig. 3.92), showing that this C—C bond has been virtually “prepared” for formation of *another* three-center bond across the opposite face of the original ethylene moiety. This again emphasizes the synergistic character of three-center bond formation which favors their formation in *pairs*.

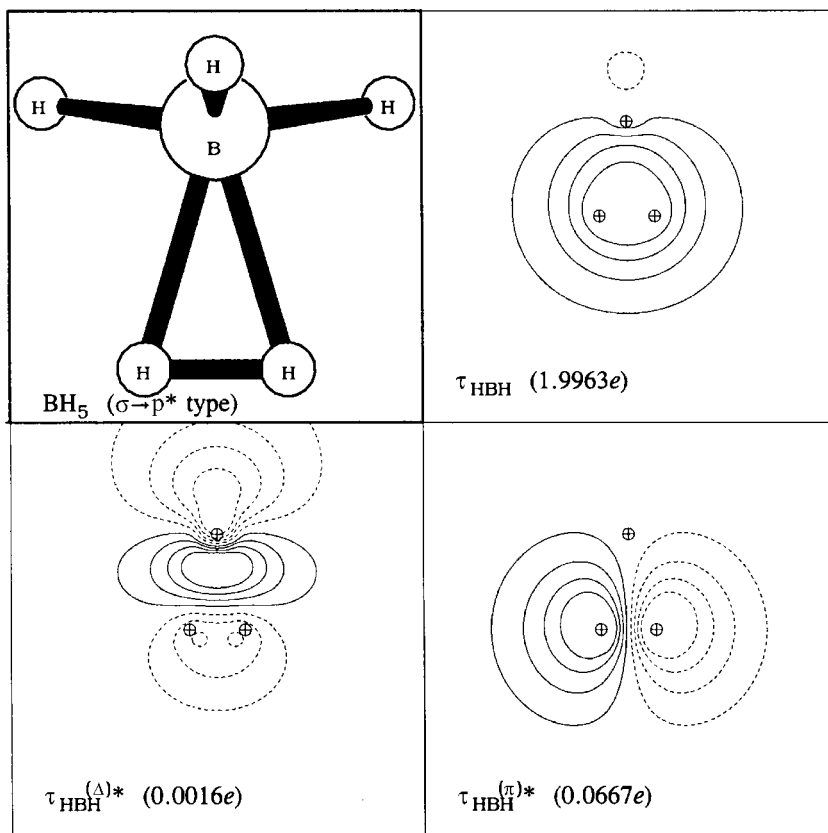


Figure 3.99 Three-center NBOs and occupancies for BH_5 ($\sigma \rightarrow p^*$ type).

Each of the $2c \rightarrow 1c^*$ donor–acceptor interactions in Figs. 3.97–3.100 exemplifies what are also termed *agostic* interactions. Such interactions are generally characterized by T-shaped (near-perpendicular) attack of an electrophile A on a filled B—C bond (σ_{BC} or π_{BC}):



to give partial or complete three-center “insertion.” In general, agostic attack may result in

- a long-range donor–acceptor complex;
- a stable three-center τ -bonded compound; or
- reactive displacement of an alternative (e.g., C or A) electrophile,

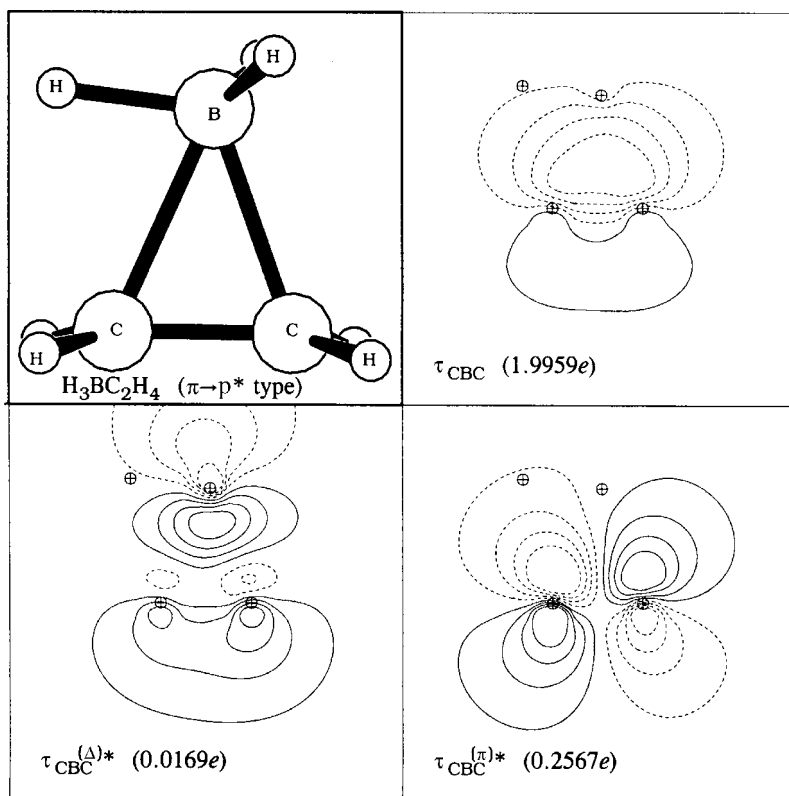


Figure 3.100 Three-center NBOs and occupancies for $\text{H}_3\text{BC}_2\text{H}_4$ ($\pi \rightarrow p^*$ type). Note the high occupancy ($0.2567e$) of $\tau_{\text{CBC}}^{(\pi)*}$, largely as a result of its strong interaction (estimated second-order stabilization $34.69 \text{ kcal mol}^{-1}$) with the in-plane B—H bond, which is thereby weakened and lengthened.

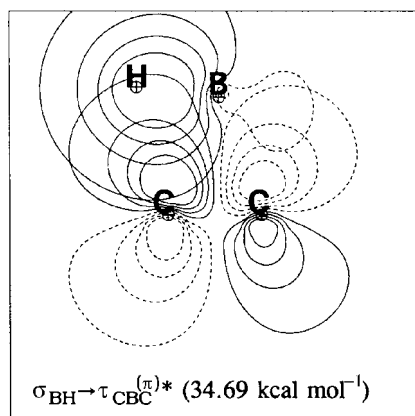


Figure 3.101 The NBO $\sigma_{\text{BH}} \rightarrow \tau_{\text{CBC}}^{(\pi)*}$ donor–acceptor interaction in $\text{H}_3\text{BC}_2\text{H}_4$ (cf. Fig. 3.100).

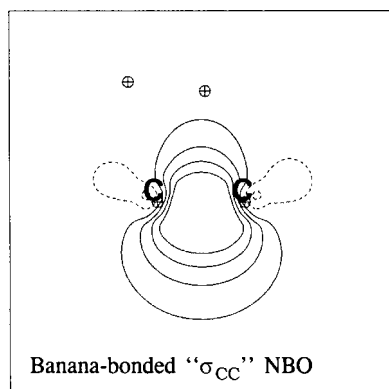
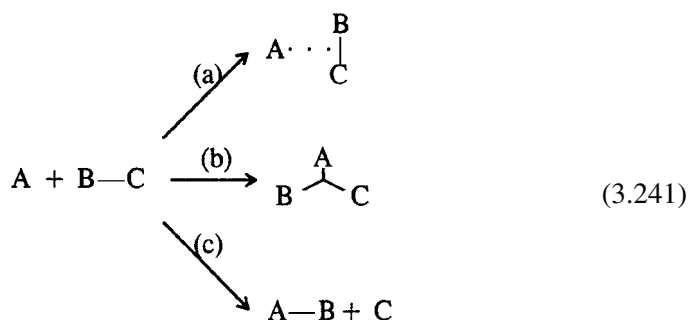


Figure 3.102 The residual "σ_{CC}" NBO in H₃BC₂H₄, showing the strong banana-bond shape of the NBO and the effective "preparation" for forming a second three-center bond (or agostic interaction) with an empty orbital approaching from the opposite face of the original ethylene moiety.

namely



In complete parallel to the discussion in Section 3.5, the conditions for forming a stable 2c→1c* complex or τ-bonded compound are intimately related to those for catalyzing the corresponding electrophilic displacement reaction. Thus, the implications of 3c/2e τ-bonding go far beyond the chemistry of boron compounds.

Boron hydrides

The classic cases of 3c/2e τ-bonding are exemplified by the boron hydrides B_pH_q and their ions. Many of these species were first prepared by Stock and coworkers¹⁵⁷ and subsequently characterized crystallographically and theoretically by Lipscomb and coworkers. Figure 3.103 shows representative examples of the boron hydrides (B₄H₁₀, B₅H₉, B₅H₁₁, B₆H₁₀), all of which were prepared originally by Stock and are among the best studied species of this type. Corresponding comparisons of theoretical and experimental geometries for these species are summarized in Table 3.38.

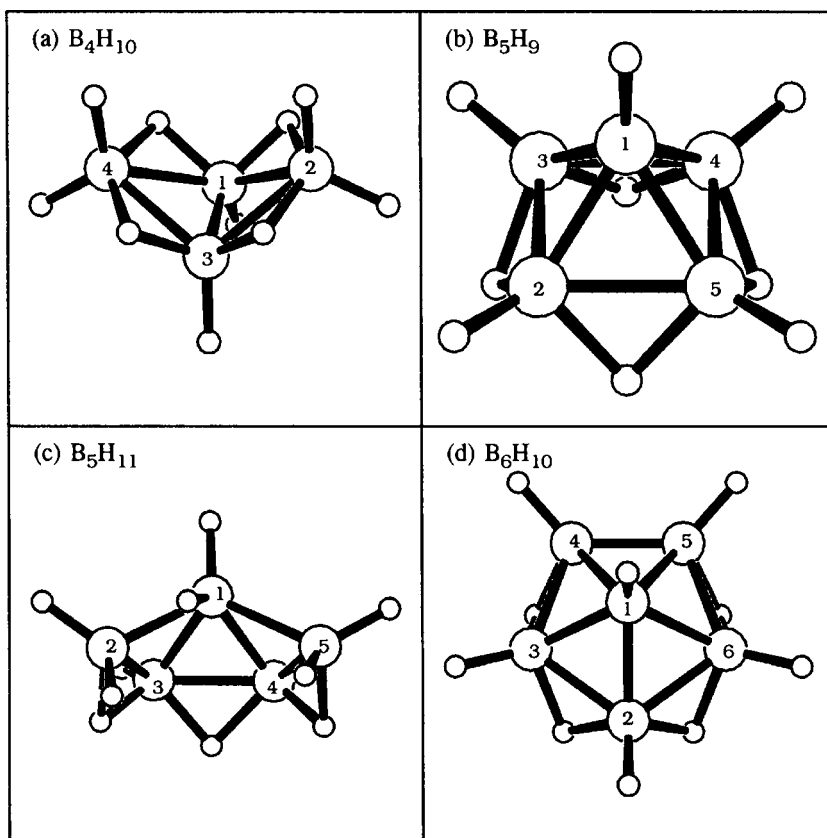


Figure 3.103 Boron hydrides (see Table 3.33), with views chosen approximately to match Figs. 1.2–1.5 of note 154.

The comparisons of Table 3.38 establish that standard computational methods can account quite successfully for the surprising borohydride geometries.

Some common characteristics of these species are apparent from the structures shown in Fig. 3.103. The molecular structure tends to be a lattice-work of triangular facets, with each near-neighbor B—B pair typically bridged by *two* B—(B)—B or B—(H)—B triangles (an exception being the B₄—B₅ bond of B₆H₁₀, which has only one such bridging triangle). The boron skeleton thus tends to form a trigonal surface mesh that can wrap around to form a closed polygon (as in the icosahedral B₁₂H₁₂²⁻ anion, to be discussed below) or can have its outer edges “stitched” with hydridic B—(H)—B triangles. Each B atom of the mesh ordinarily has a protruding B—H bond of ordinary $2c/2e$ covalent type, and any left-over “end” atoms along an unclosed edge must have an extra B—H bond (i.e., a —BH₂ group) as terminus.

Table 3.38. Comparison of calculated (B3LYP/6-311++G**) and experimental (note 154) bond lengths and bond angles for boron hydrides (see Fig. 3.103).

“H_(μ)” denotes a bridge hydrogen

Species	Variable	Theory	Experiment
B ₂ H ₆	B ₁ —B ₂ (Å)	1.767	1.77
	B—H (Å)	1.187	1.19
	B—H _(μ) (Å)	1.316	1.33
	H—B—H (degrees)	121.9	121.5
B ₄ H ₁₀	B ₁ —B ₂ (Å)	1.860	1.84
	B ₁ —B ₃ (Å)	1.720	1.71
	B—H (Å)	1.187	1.19
	B ₁ —H _(μ) (Å)	1.257	1.33
	B ₂ —H _(μ) (Å)	1.414	1.43
	B ₂ —B ₁ —B ₄ (degrees)	98.8	98
B ₅ H ₉	B ₁ —B ₂ (Å)	1.695	1.69
	B ₂ —B ₃ (Å)	1.798	1.80
B ₅ H ₁₁	B ₁ —B ₂ (Å)	1.881	1.87
	B ₁ —B ₃ (Å)	1.747	1.73
	B ₁ —B ₄ (Å)	1.733	1.70
	B ₁ —B ₅ (Å)	1.903	1.87
	B ₂ —B ₃ (Å)	1.835	(1.77) ^a
	B ₃ —B ₄ (Å)	1.796	1.77
	B ₄ —B ₅ (Å)	1.740	(1.75) ^a
B ₆ H ₁₀	B ₁ —B ₂ (Å)	1.748	1.74
	B ₁ —B ₃ (Å)	1.757	1.75
	B ₁ —B ₄ (Å)	1.818	1.80
	B ₂ —B ₃ (Å)	1.801	1.79
	B ₃ —B ₄ (Å)	1.741	1.74
	B ₄ —B ₅ (Å)	1.637	1.60
B ₁₂ H ₁₂ ²⁻	B ₁ —B ₂ (Å)	1.787	1.77

^a Assigned for consistency with the lowered symmetry of the theoretical structure.

The number (x) of such end groups (or “extra” B—H bonds) can be combined with the numbers (s) of τ_{BHB} bonds and (t) of τ_{BBB} bonds, as well as the number (y) of *singly* bridged B—B pairs, to give the well-known *styx* code:

$$\left. \begin{array}{l}
 s = \text{number of } \tau_{\text{BHB}} \text{ bonds} \\
 t = \text{number of } \tau_{\text{BBB}} \text{ bonds} \\
 y = \text{number of singly bridged B—B pairs (} \sigma_{\text{BB}} \text{ bonds)} \\
 x = \text{number of “extra” } \sigma_{\text{BH}} \text{ bonds (one per “end” B)}
 \end{array} \right\} \textit{styx} \text{ code}$$

When added to the p additional terminal B—H bonds (one per B), the sum of *styx* values accounts for all two-electron bonds in the molecule, which must therefore correspond to all $3p + q$ valence electrons of the B_pH_q molecule, if no lone pairs or other bond types are present,

$$2(p + s + t + y + x) = 3p + q \quad (3.243a)$$

or equivalently

$$2(s + t + y + x) = p + q \quad (3.243b)$$

Furthermore, by virtue of atomic balance the total number (q) of H atoms must sum to

$$q = s + x + p \quad (3.244)$$

and the total number (p) of B atoms (if each is assumed to be four-coordinate) must satisfy

$$p = s + t \quad (3.245)$$

These constraints lead to the standard *styx* codes shown in Table 3.39.

Let us now consider some general aspects of the atomic charge distributions. For the H atoms, the calculated natural atomic charges Q_H are found to depend most strongly on whether the atom appears at a bridging H(μ), terminal H(t), or BH₂ “extra” H(x) position. Typical Q_H values fall within the disjoint ranges

$$+0.14 \leq Q_{H(\mu)} \leq +0.16 \quad (3.246a)$$

$$+0.06 \leq Q_{H(t)} \leq +0.07 \quad (3.246b)$$

$$0.00 \leq Q_{H(x)} \leq +0.03 \quad (3.246c)$$

with bridging H(μ) protons significantly more acidic than non-bridging protons. The only values falling outside the narrow ranges (3.246a)–(3.246c) occur in diborane, where the bridging protons are somewhat less acidic ($Q_H = +0.09$), and in B₅H₁₁, where the oddly asymmetric proton bridging B₁ and B₂ is more acidic

Table 3.39. *Standard allowed styx codes for some boron hydrides B_pH_q (see Fig. 3.103)*

	B ₂ H ₆	B ₄ H ₁₀	B ₅ H ₉	B ₅ H ₁₁	B ₆ H ₁₀
<i>styx</i> code(s)	2002	4012 3103	4120 3211 2302	5021 4112 3202	4220 3311 2402

Table 3.40. Boron atomic charge distributions in boron hydrides (see Fig. 3.103 for atom numberings), comparing Lipscomb’s “zeroth-order” (ZO) estimates (note 154) with NPA atomic charges

Species	Atom	Atomic charge Q_B	
		ZO	NPA
B_2H_6	B ₁	0.00	−0.092
B_4H_{10}	B ₁	0.00	−0.312
	B ₂	0.00	−0.138
B_5H_9	B ₁	−1.00	−0.344
	B ₂	+0.25	−0.122
B_5H_{11}	B ₁	−0.33 ^a	−0.363
	B ₂	−0.17 ^b	−0.142
	B ₃	+0.33	−0.196
	B ₄	+0.33	−0.138
	B ₅	−0.17	−0.095
B_6H_{10}	B ₁	−0.33	−0.286
	B ₂	0.00	−0.188
	B ₃	+0.33	−0.062
	B ₄	−0.17	−0.153

^a Estimate from alternative three-center structure: −0.67.

^b Estimate from alternative three-center structure: 0.00.

($Q_H = +0.22$) than normal. The boron atomic charges are found to fall within the general range

$$-0.36 \leq Q_B \leq -0.06 \quad (3.247)$$

Table 3.40 displays the calculated Q_B charges from natural population analysis (NPA) for all unique B atoms. This table also includes comparison of the NPA charges with corresponding “zeroth-order” (ZO) estimates given by Lipscomb, which are based essentially on the formal charges for conjectured three-center bond and *styx*-code assignments for each species (to be discussed below).

As seen in Table 3.40, the ZO estimates tend to fall within crudely the same order as the NPA charges, but the quantitative correlation is rather poor. The ZO estimates evidently fail to make adequate distinction between sites that NPA finds to have strongly inequivalent charges (e.g., B₁ and B₂ in B_4H_{10}), and they suggest a much more extreme range of variations ($-1.00 \leq Q_B^{(ZO)} \leq +0.33$, about four times the range in (3.247)). It is noteworthy that NPA represents all B atoms as somewhat anionic and all H atoms (except the borderline bridging protons of B_2H_6) as somewhat cationic. One can also recognize from Table 3.40 that an apex B atom

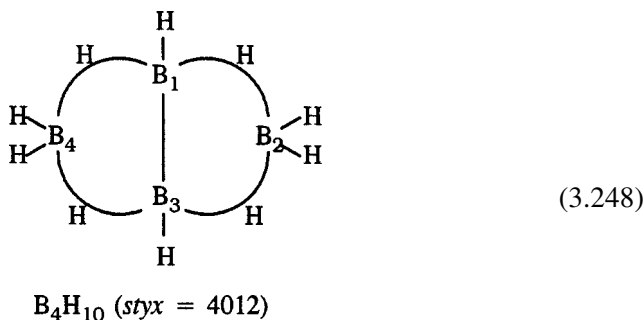
is the likely site for electrophilic addition, whereas an “end” ($-\text{BH}_2$ -bonded) B atom is the likely site of nucleophilic addition.

We now describe the individual molecules in Fig. 3.103 (as well as the limiting icosahedral $\text{B}_{12}\text{H}_{12}^{2-}$ species to be introduced below), giving details of the NBOs, relative weightings of alternative *styx* structures, and NRT bond orders for each species.

B_4H_{10}

Dihydrotetraborane, B_4H_{10} , is a high-symmetry (C_{2v}) species for which both boron and hydrogen positions have been determined by X-ray diffraction, as summarized in Table 3.38. In accordance with the X-ray structure, the four B—(H)—B bridges are found to be slightly asymmetric, with the proton lying closer (1.257 versus 1.414 Å) to the B_1/B_3 end of the bridge. The B—H—B angle is opened to a somewhat larger value than in B_2H_6 (88.1° versus 84.3°) and the two basal B—B—H angles are distinctly unequal (42.5° for $\text{B}_1-\text{B}_2-\text{H}$ versus 49.4° for $\text{B}_2-\text{B}_1-\text{H}$). However, in other respects the τ_{BHB} bonds are qualitatively similar to those described previously for diborane.

The bonding in B_4H_{10} can best be represented as shown in the structure diagram below, with $s = 4 \tau_{\text{BHB}}$ bridge bonds (depicted as arcs), six terminal σ_{BH} bonds (one for each B atom plus $x = 2$ “extra” at B_2 and B_4), and $y = 1$ single B_1-B_3 σ_{BB} bond:



This structure corresponds to the *styx* = 4012 bond pattern (cf. Table 3.39), with the detailed list of bond types shown in Table 3.41(a). Other NBO/NRT descriptors to be discussed below are also summarized in Table 3.41.

As indicated in Table 3.39, an alternative *styx* = 3103 structure can be envisioned. This can be achieved, e.g., by replacing a chosen τ_{BHB} , σ_{BB} bond pair with a new τ_{BBB} , σ_{BH} bond pattern, as shown in the *styx* = 3103 entry of Table 3.41(a). The asymmetrical 3103 structure seems much less suitable to describe the actual bonding features of B_4H_{10} , and the 4012 structure is therefore usually considered to be “preferred” on intuitive grounds.

Table 3.41. NBO/NRT descriptors for B_4H_{10} (see Fig. 3.103(a)), showing (a) alternative styx codes (with specific bond types) and associated non-Lewis density “error” ρ_{NL} ; (b) NHO h_B and percentage polarization for NBOs of the most accurate styx structure; and (c) approximate b_{BB} and b_{BH} bond orders from a non-converged NRT procedure (see the text)

(a) Alternative styx structures

styx code	ρ_{NL} (e)	Bond types			
		τ_{BHB}	τ_{BBB}	σ_{BB}	$\sigma_{BH(x)}$
4012	0.6072	B_1HB_2 B_2HB_3 B_3HB_4 B_4HB_1		B_1B_3	B_2H B_4H
3103	0.8760	B_1HB_2 B_2HB_3 B_3HB_4	$B_1B_3B_4$		B_1H B_2H B_4H

(b) NBO boron hybridization and percentage polarization (for styx = 4012)

Atom	τ_{BHB}		σ_{BB}		$\sigma_{BH(t)}$		$\sigma_{BH(x)}$	
	h_B	Pol.	h_B	Pol.	h_B	Pol.	h_B	Pol.
B_1	$sp^{3.00}$	35%	$sp^{4.60}$	50%	$sp^{2.12}$	53%		
B_2	$sp^{3.69}$	24%			$sp^{2.39}$	51%	$sp^{2.60}$	51%

(c) Natural resonance theory

Atom	Bond order					
	B_2	B_3	B_4	$H_{(\mu)}$	$H(t)$	$H(x)$
B_1	0.13	0.89	0.13	0.51	1.00	0.00
B_2	0.00	0.13	0.00	0.33	0.00	1.00

However, the relative accuracies of the two possible structural bond patterns can be assessed more quantitatively with NBO analysis. The NBO procedure allows one to specify alternative Lewis structure patterns of two- and three-center bonds¹⁵⁸ and determine the non-Lewis density “error” ρ_{NL} of each such structure. As shown in Table 3.41(a), the non-Lewis density of the 4012 structure (0.6072e) is smaller than that of the 3103 structure (0.8760e), which confirms that the 4012 structure (3.248) is indeed the superior bonding description in this case.

Table 3.41(b) shows details of the NBO compositions in the optimal 4012 structure. The τ_{BHB} bridge bonds are found to be noticeably polarized toward the B_1/B_3

end (35% versus 24% at the B_2/B_4 end), where the hybrids are also of noticeably lower p character ($sp^{3.00}$ versus $sp^{3.69}$ at the B_2/B_4 end). The hybrids of highest s character ($sp^{2.1} - sp^{2.6}$) are used for forming the various terminal σ_{BH} bonds, while those of highest p character ($sp^{4.60}$) form the σ_{BB} bond.

All these features are consistent with Bent's rule (Section 3.2.6) and with the geometrical features noted above. Specifically, the B_2/B_4 atoms bearing "extra" σ_{BH} bonds must commit higher s character to the terminal B—H bonds, and hence higher p character to the two bridge bonds, leading to smaller H—B—H interbridge angles at B_2/B_4 than at B_1/B_3 . Similarly, the polarization of τ_{BHB} toward the B_1/B_3 boron hybrid of higher s character (greater effective electronegativity) is in accord with the expectations of Bent's rule. Thus, it appears that many of the qualitative Bent's rule/electronegativity/geometry relationships developed in Sections 3.2.5–3.2.7 can be extended to three-center bonding in a fairly straightforward manner.

The localized structure (3.248) is subject to strong delocalization corrections from residual donor–acceptor interactions. By far the strongest of these are the four equivalent interactions of the form



depicted in Fig. 3.104, involving delocalization from the B_1 — B_3 bond NBO σ_{BB} into, e.g., the B_1 —(H)— B_2 three-center antibond NBO $\tau_{BHB}^{(\Delta)*}$, each with estimated second-order stabilization $28.9 \text{ kcal mol}^{-1}$. As seen in the diagram, the relevant three-center τ^* for the B_1 —(H)— B_2 bridge in this case resembles an ordinary two-center σ_{BH}^* for the B_2 —(H) portion of the bridge (because the H is shared quite unsymmetrically between the two B atoms, in contrast to τ_{BHB}^* orbitals seen in other examples). The orbital interaction in Fig. 3.104 thus bears some resemblance to vicinal $\sigma_{BB} \rightarrow \sigma_{BH}^*$ interactions of the type seen elsewhere in this book

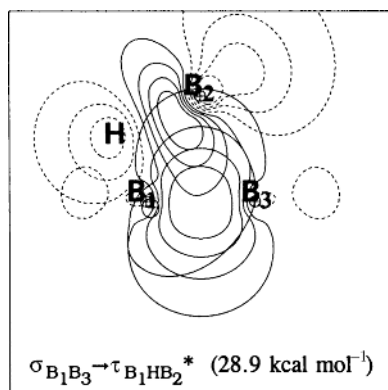


Figure 3.104 One of the four equivalent strong $\sigma_{BB} \rightarrow \tau_{BHB}^*$ donor–acceptor interactions in B_4H_{10} (estimated second-order stabilization: $28.9 \text{ kcal mol}^{-1}$). Note the resemblance to a canted *cis*-like vicinal $\sigma_{B_1B_3} \rightarrow \sigma_{B_2H}^*$ interaction.

(Sections 3.3 and 3.4). The strong interactions (3.249) emphasize that the localized structural representation (3.248), although “optimal,” fails to depict important details of the actual electron distribution in this highly delocalized species.

As mentioned above, it is also possible in principle to describe three-center bonding in terms of highly delocalized one- and two-center resonance structures, using natural resonance theory (NRT, Section 1.6) to compute the relative weightings (cf. Eq. (3.237)). In practice the limit of many strongly interacting resonance structures leads to NRT numerical instability, symmetry breaking, and failure to converge to a unique leading set of resonance structures. However, by averaging the calculated bond orders over equivalent positions¹⁵⁹ one can achieve a degree of convergence in the overall bonding patterns that is adequate for qualitative purposes. Table 3.41(c) summarizes the estimated b_{BB} and b_{BH} bond orders for B_4H_{10} . As suggested by the *styx* structure (3.248), the B_1 — B_3 bond is of high bond order (0.89), and each of these atoms is weakly bonded (0.13) to each of the adjacent B_2/B_4 atoms, which themselves are essentially nonbonded. The terminal B—H bonds are normal single bonds ($b_{BH} = 1.00$), while the bridging B—(H) bonds have significantly lower bond orders, somewhat stronger toward B_1/B_3 (0.5) than toward B_2/B_4 (0.3). These results are generally in line with the geometrical features noted above as well as with NBO dissection of the leading three-center *styx* structure shown in (3.248).

B_5H_9

Pentaborane, B_5H_9 , is unusual in having a tetragonal C_{4v} skeleton, rather than the icosahedral fragment geometry that is typical of other boron hydrides. The unique apex atom B_1 makes four short B—B bonds to the base (1.695 Å), whereas the four basal B—B bonds are of more typical length (1.798 Å).

No single three-center structure can adequately represent this molecule. As shown below, the best localized structural representation is one of the four equivalent structures shown in (3.250),

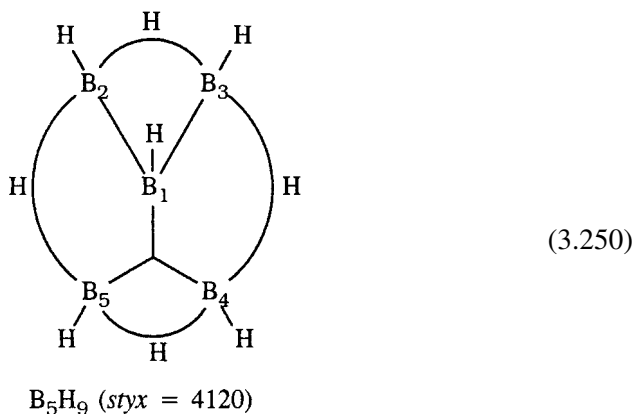


Table 3.42. Similar to Table 3.41, for B₅H₉

(a) Alternative styx structures

styx code	$\rho_{\text{NL}} (e)$	Bond types			
		τ_{BHB}	τ_{BBB}	σ_{BB}	$\sigma_{\text{BH(x)}}$
4120	1.2625	B ₂ HB ₃ B ₃ HB ₄ B ₄ HB ₅ B ₂ HB ₅	B ₁ B ₄ B ₅	B ₁ B ₂ B ₁ B ₃	
“4210” ^a	1.3705	B ₂ HB ₃ B ₃ HB ₄ B ₄ HB ₅ B ₂ HB ₅	B ₁ B ₂ B ₅ B ₁ B ₅ B ₄	B ₁ B ₃	
4120'	1.3902	B ₂ HB ₃ B ₃ HB ₄ B ₄ HB ₅ B ₂ HB ₅	B ₃ B ₁ B ₅	B ₁ B ₂ B ₁ B ₄	
“4200” ^b	1.6477	B ₂ HB ₃ B ₃ HB ₄ B ₄ HB ₅ B ₂ HB ₅	B ₁ B ₂ B ₃ B ₁ B ₄ B ₅		
3211	1.9201	B ₂ HB ₃ B ₃ HB ₄ B ₂ HB ₅	B ₁ B ₂ B ₅ B ₁ B ₃ B ₄	B ₁ B ₄	B ₅ H
2302	2.3085	B ₃ HB ₄ B ₂ HB ₅	B ₁ B ₂ B ₃ B ₁ B ₂ B ₅ B ₁ B ₃ B ₄		B ₂ H B ₄ H

^aNon-standard styx code: pentacoordinate B(5).^bNon-standard styx code: tricoordinate B(1).

(b) NBO boron hybridization and percentage polarization (for styx = 4120)

Atom	τ_{BHB}^a		τ_{BBB}		σ_{BB}		$\sigma_{\text{BH(t)}}$	
	h _B	Pol.	h _B	Pol.	h _B	Pol.	h _B	Pol.
B ₁			sp ^{2.39}	39%	sp ^{4.39}	49%	sp ^{2.08}	53%
B ₂	sp ^{4.27}	29%			sp ^{2.37}	51%	sp ^{2.10}	53%
	sp ^{4.32}	30%						
B ₅	sp ^{3.03}	29%	sp ^{2.19}	31%			sp ^{2.05}	53%

^aFor two entries, the second denotes the bond to the later-numbered B atom.

Table 3.42. (Cont.)

(c) Natural resonance theory

Atom	Bond order					
	B ₂	B ₃	B ₄	H _(μ)	H(t)	H(x)
B ₁	0.58	0.58	0.58	—	1.00	—
B ₂	—	0.07	0.07	0.40	1.00	—

with four three-center τ_{BHB} bonds ($s = 4$), one three-center τ_{BBB} bond ($t = 1$), and two two-center σ_{BB} bonds ($y = 2$), corresponding to $styx$ code 4120. Various NBO/NRT descriptors pertaining to B_5H_9 are summarized in Table 3.42.

As shown in Table 3.39, three standard $styx$ codes (4120, 3211, and 2302) are possible for B_5H_9 . Table 3.42(a) specifies representatives of each of these structures, including two *distinct* structures (labeled 4120 and 4120') corresponding to the 4120 motif. In addition, one may consider various non-standard $styx$ motifs such as the structures labeled “4210” and “4200” in Table 3.42(a), which correspond to one or more B atoms lacking the usual tetracoordinate pattern. Table 3.42(a) summarizes the NBO ρ_{NL} density errors associated with the six listed structures, showing that the 4120 structure (3.250) has the smallest ρ_{NL} value and is indeed the “best” single NBO structure.

The 4120' structure was formerly considered “best” (note 154, Fig. 2-11), but is seen to be markedly inferior to the structure shown in (3.250). Indeed, 4120' is also found to be slightly inferior to the *non*-standard 4210 structure in which one of the basal B atoms is pentacoordinate. The two alternative standard $styx$ structures 3211 and 2302 are also seen to be significantly inferior to *either* of the non-standard structures 4210 and 4200. Thus, one should always give consideration to non-standard $styx$ bonding topologies in attempting to judge the best single localized structural formula. The general superiority of 4120 to 4120' has also been recognized from a general bond-localization criterion based on improved MO wavefunctions.¹⁶⁰

In addition to the usual three-center τ_{BHB} bonds, B_5H_9 exhibits a three-center τ_{BBB} bond of “central” type, as shown in Fig. 3.105. In this case the three boron hybrids are mutually oriented toward the midpoint of the triangle $\text{B}_1\text{B}_4\text{B}_5$ (Fig. 3.105(a)), leading to a bonding NBO of trilobate form (Fig. 3.105(b)) that somewhat resembles the corresponding τ_{CBC} NBO in $\text{H}_3\text{BC}_2\text{H}_4$ (Fig. 3.100). The two associated antibonds (Figs. 3.105(c) and (d)) also resemble those of Fig. 3.100, and may be analogously labeled $\tau_{\text{BBB}}^{(\Delta)*}$ and $\tau_{\text{BBB}}^{(\pi)*}$ to denote their distinctive shapes.

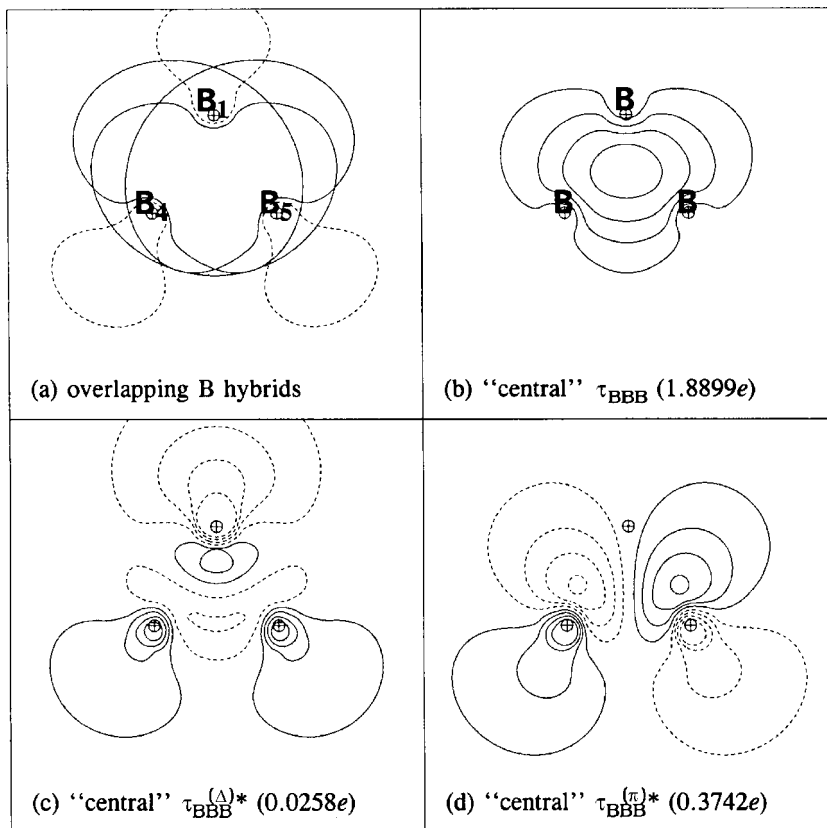


Figure 3.105 Overlapping $(sp^{2.19})_B - (sp^{2.39})_B - (sp^{2.19})_B$ NHO shapes (a) and the final τ_{BBB} bond (b) and $\tau_{BBB}^{(\Delta)*}$ and $\tau_{BBB}^{(\pi)*}$ antibond (c) and (d) NBOs and occupancies for “central” three-center $B_4B_1B_5$ bond in B_5H_9 ($styx = 4120$). Only the outermost contour is shown in the NHO plot, in order to reduce congestion on the plot.

The alternative “open” form of τ_{BBB} bond is found in the alternative 4120' structure, which involves a single $B_5B_1B_3$ τ -bond diagonally spanning the tetragonal pyramid. Figure 3.106 illustrates the τ bonds and antibonds found in this case.

Comparison of Figs. 3.105(a) and 3.106(a) shows that the role of the apical B_1 atom differs markedly in the two cases. In the central case (Fig. 3.105(a)), B_1 has no privileged role but merely contributes one of the three near-equivalent hybrids directed into the midpoint of the triangle. However, in the open case (Fig. 3.106(a)) B_1 uniquely contributes a pure p orbital whose two lobes are overlapped by the end borons, forming an open chain with distinct center (B_1) and end (B_3 and B_5) links. Whereas the central-type $\tau_{BBB}^{(c)}$ bond resists breaking up the triangular

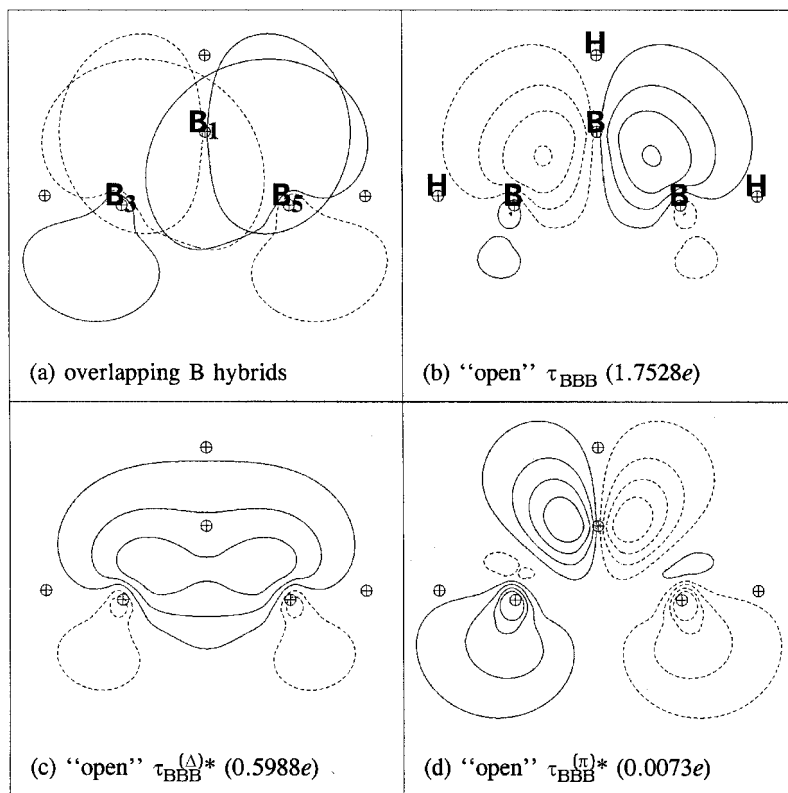
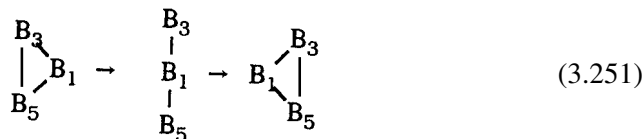


Figure 3.106 Overlapping $(sp^{2.60})_B-(p)_B-(sp^{2.60})_B$ NHO shapes (a) and the final τ_{BBB} bond (b) and $\tau_{BBB}^{(\Delta)*}$ and $\tau_{BBB}^{(\pi)*}$ antibond (c) and (d) NBOs and occupancies for the “open” three-center $B_3B_1B_5$ bond in B_5H_9 ($stylx = 4120'$). Only the outermost contour is shown in the NHO plot, in order to reduce congestion on the plot.

arrangement, the open-type $\tau_{BBB}^{(0)}$ allows easy rearrangements of the form



involving B_3-B_5 bond-breaking and linear intermediates. Thus, the two types of τ_{BBB} bonds are adapted to different geometrical limits.

The dominant feature of the NBO description of B_5H_9 is the *large* delocalization that remains even for the best possible three-center Lewis structure (3.250). The non-Lewis density for this structure is found to be $1.2625e$, or fully 3.71% of the total of 34 electrons, even higher (on a percentage basis) than in such “highly

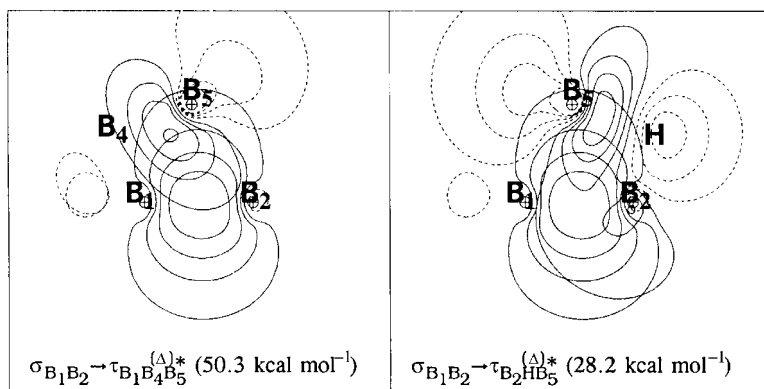


Figure 3.107 Leading donor–acceptor interactions of $\sigma_{BB} \rightarrow \tau_{BBB}^{(\Delta)*}$ (left) and $\sigma_{BB} \rightarrow \tau_{BBB}^{(\Delta)*}$ (right) type in B_5H_9 ; see Eqs. (3.252a) and (3.252b) in the text.

delocalized” systems as benzene and the cyclopentadienyl anion (Section 3.3.2). The leading donor–acceptor delocalizations are found to involve donation from either of the two σ_{BB} bonds into antibonds of the three connecting three-center bonds (one τ_{BBB} and two τ_{BHB}),

$$\sigma_{BB} \rightarrow \tau_{BBB}^{(\pi)*} \quad (50.3 \text{ kcal mol}^{-1}) \quad (3.252a)$$

$$\sigma_{BB} \rightarrow \tau_{BHB}^{(\Delta)*} \quad (B_1-B_2 \rightarrow B_2-H-B_5^*) \quad (28.2 \text{ kcal mol}^{-1}) \quad (3.252b)$$

$$\sigma_{BB} \rightarrow \tau_{BHB}^{(\Delta)*'} \quad (B_1-B_2 \rightarrow B_2-H-B_3^*) \quad (13.4 \text{ kcal mol}^{-1}) \quad (3.252c)$$

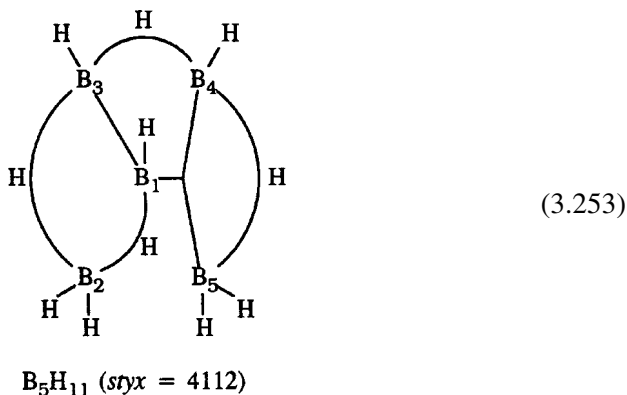
These large values emphasize that strong resonance mixing is needed to describe the bonding even after an optimal three-center starting structure has been found. Figure 3.107 illustrates the two leading interactions (3.252a) and (3.252b), showing the similarity to the corresponding interaction in B_4H_{10} (cf. Fig. 3.104).

Finally, Table 3.42(c) summarizes the qualitative NRT results, confirming that (except for terminal $\sigma_{BH(t)}$ bonds) the B–B and B–H bond orders all involve strong resonance mixing.

B_5H_{11}

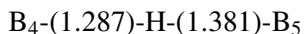
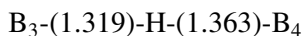
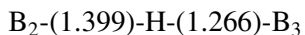
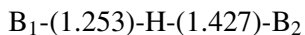
Dihydropentaborane, B_5H_{11} , presents stronger disagreements between theory and experiment than do the other boron hydrides (Table 3.38). As shown in Fig. 3.103(c), theory depicts one of the B_1-H bonds as strongly bent out of the approximate vertical symmetry plane to form a bridge bond to B_2 . Such symmetry breaking may lead to significant fluxional disorder in the X-ray pattern, complicating the extraction of reliable experimental geometrical parameters.

What can be considered to be the “best” localized structural representation of B_5H_{11} is shown in (3.253), corresponding to *styx* code 4112



What were earlier (note 154, Fig. 2–7) considered “best” three-center structures for this molecule were of 3203 bond topology, both having a symmetric pattern of two τ_{BBB} bridge bonds around the B_1 apex atom ($B_2B_3B_1$ and $B_1B_4B_5$ in 3203; $B_3B_1B_4$ and $B_2B_1B_5$ in 3203'). However, as shown in Table 3.43(a), both these structures have significantly larger ρ_{NL} errors than either the 4112 structure (3.253) or a non-standard 4202 structure with five-coordinate B_2 . Although 3203 and 3203' were thought to be of similar accuracy, the alternative 3203' structure is actually *far* inferior to 3203 (with ρ_{NL} 2–3 *times* as large). The NBO/NRT descriptors for this molecule are summarized in Table 3.43.

The τ_{BHB} bridges are all rather asymmetric, as reflected in the polarizations and hybridizations of the NBOs. The bridging proton generally lies further from the $-BH_2$ group (i.e., B_2 and B_5) than from the opposite end of the bridge, and only $B_3-(H)-B_4$ resembles the symmetric bridge of diborane. The separations (in ångström units) in each bridged triad are calculated to be



and the nearer boron commonly employs a hybrid of higher s character in the bridge bond, as might have been predicted from Bent's rule. The τ_{BBB} bond also has a significantly higher percentage at the apex B_1 (39%) than at the basal B_4 and B_5 (32% and 29%) atoms.

The nominal localized 4112 structure (3.253) again manifests *large* delocalization corrections, of which the most important involve donation from the $B_1-B_3\sigma_{BB}$

Table 3.43. Similar to Table 3.41, for B₅H₁₁

(a) Alternative styx structures

styx code	$\rho_{\text{NL}}(e)$	Bond types			
		τ_{BHB}	τ_{BBB}	σ_{BB}	$\sigma_{\text{BH}(x)}$
4112	0.8343	B ₂ HB ₃ B ₃ HB ₄ B ₄ HB ₅ B ₁ HB ₂	B ₁ B ₄ B ₅	B ₁ B ₃	B ₂ H B ₅ H
“4202” ^a	0.9711	B ₂ HB ₃ B ₃ HB ₄ B ₄ HB ₅ B ₁ HB ₂	B ₁ B ₂ B ₃ B ₁ B ₄ B ₅		B ₂ H B ₅ H
3203	1.0581	B ₂ HB ₃ B ₃ HB ₄ B ₄ HB ₅	B ₁ B ₂ B ₃ B ₁ B ₄ B ₅		B ₁ H B ₂ H B ₅ H
“4022” ^b	1.3906	B ₂ HB ₃ B ₃ HB ₄ B ₄ HB ₅ B ₁ HB ₂		B ₁ B ₃ B ₁ B ₅	B ₂ H B ₅ H
3203'	2.8878	B ₂ HB ₃ B ₃ HB ₄ B ₄ HB ₅	B ₁ B ₃ B ₄ B ₂ B ₁ B ₅		B ₁ H B ₂ H B ₅ H

^a Non-standard styx: pentacoordinate B(2).^b Non-standard styx: tricoordinate B(4).

(b) NBO boron hybridization and percentage polarization (for styx = 4112)

Atom	τ_{BHB}^a		τ_{BBB}		σ_{BB}		σ_{BH}^b	
	h_{B}	Pol.	h_{B}	Pol.	h_{B}	Pol.	h_{B}	Pol.
B ₁	sp ^{3.14}	37%	sp ^{2.56}	39%	sp ^{4.43}	50%	sp ^{2.45}	53%
B ₂	sp ^{3.39}	25%					sp ^{2.31}	51%
	sp ^{3.84}	24%					sp ^{2.80}	51%
B ₃	sp ^{3.15}	24%			sp ^{2.96}	50%	sp ^{2.31}	53%
	sp ^{3.93}	30%						
B ₄	sp ^{3.08}	28%	sp ^{2.44}	32%			sp ^{2.37}	53%
	sp ^{4.98}	35%						
B ₅	sp ^{6.97}	23%	sp ^{2.77}	29%			sp ^{2.33}	50%
							sp ^{2.24}	50%

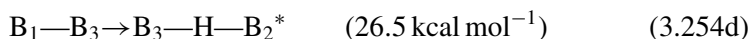
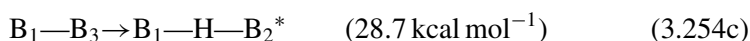
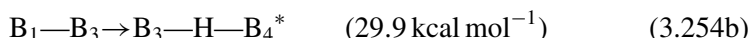
^a For two entries, the second denotes the bond to the later-numbered B atom.^b For two entries, the first denotes $\sigma_{\text{BH}(1)}$, the second $\sigma_{\text{BH}(x)}$.

Table 3.43. (Cont.)

(c) Natural resonance theory

Atom	Bond order					
	B ₂	B ₃	B ₄	H(μ)	H(t)	H(x)
B ₁	0.12	0.90	0.81	0.85	1.00	—
B ₂	—	0.17	0.00	0.05	1.00	1.00
B ₃	0.17	—	0.12	0.62	1.00	—
B ₄	0.00	0.12	—	0.66	1.00	—
B ₅	0.00	0.00	0.19	0.05	1.00	1.00

bond NBO into τ^* antibond NBOs of the four adjacent BHB and BBB groups,



The NRT bond orders also reflect the strong resonance delocalization involving all but the terminal $\sigma_{\text{BH}(t)}$ and $\sigma_{\text{BH}(x)}$ bonds. Figure 3.108 depicts the two leading donor–acceptor interactions (3.254a) and (3.254b) as representative of the strong $\sigma_{\text{BB}} \rightarrow \tau_{\text{BBB}}^{(\Delta)*}$ and $\sigma_{\text{BB}} \rightarrow \tau_{\text{BHB}}^{(\Delta)*}$ delocalizations in this molecule.

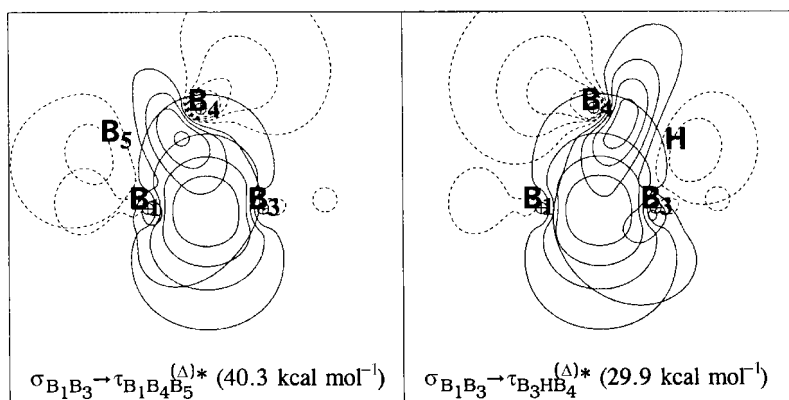
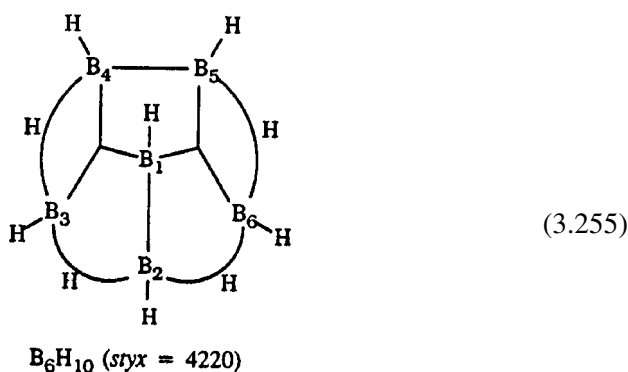


Figure 3.108 Leading donor–acceptor interactions of $\sigma_{\text{BB}} \rightarrow \tau_{\text{BBB}}^{(\Delta)*}$ (left) and $\sigma_{\text{BB}} \rightarrow \tau_{\text{BHB}}^{(\Delta)*}$ (right) type in B_5H_{11} ; see Eqs. (3.254a) and (3.254b) in the text.

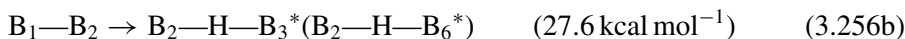
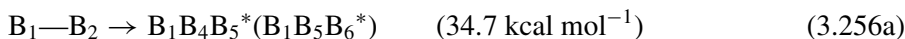
B_6H_{10}

Hexaborane, B_6H_{10} , has the form of an icosahedral cap of reduced (C_{2v}) symmetry, with a vertical symmetry plane bisecting B_4-B_5 and passing through B_1 and B_2 . The unbridged B_4-B_5 bond has the smallest known B—B bond length ($<1.64 \text{ \AA}$). As surmised by Lipscomb (note 154, Fig. 2-8), the optimal localized representation has four τ_{BHB} bonds around the cap edges and two central τ_{BBB} bonds emanating symmetrically from the apex atom to give the *styx* = 4220 structure shown in (3.255). The other two standard *styx* codes (3311 and 2402) lead to much higher ρ_{NL} values, as shown in Table 3.44(a), and hence play no significant role in describing the electronic distribution. Table 3.44 summarizes the NBO/NRT descriptors of B_6H_{10} for direct comparison with those of other boron hydrides.



The $B_1B_3B_4$ and $B_1B_5B_6$ bridge bonds are of characteristic central form (similar to that shown in Fig. 3.105), with somewhat higher amplitude and hybrid *s* character at the apex B_1 atom. Although B_1-B_2 and B_4-B_5 are both nominal σ_{BB} single bonds, the latter employs hybrids of much higher *s* character ($sp^{1.97}$ at B_4 and B_5 versus $sp^{2.79}$ at B_2 and $sp^{6.73}$ at B_1), leading to stronger and shorter bonding (due to the low energy and smaller radius of valence *s* orbitals). Thus, B_1-B_2 is better adapted to be a donor in subsequent donor–acceptor delocalizations.

While the 4220 structure (3.255) is the uniquely best localized representation, *strong* delocalization is again evident in the strength of intramolecular donor–acceptor interactions. Most important by far are the four interactions involving donation from the B_1-B_2 bond into each pair of adjacent $\tau_{BBB}^{(\Delta)*}$ and $\tau_{BHB}^{(\Delta)*}$ antibonds,



as shown in Fig. 3.109. The similarities to Figs. 3.107 and 3.108 are evident, both in form and in general magnitude. The NRT bond orders in Table 3.44(c) also reflect the strong resonance delocalization involving all but the terminal $\sigma_{BH(t)}$ bonds.

Table 3.44. Similar to Table 3.41, for B_6H_{10}

(a) Alternative styx structures

styx code	ρ_{NL} (e)	Bond types			
		τ_{BHB}	τ_{BBB}	σ_{BB}	$\sigma_{BH(x)}$
4220	1.2187	B ₂ HB ₃ B ₃ HB ₄ B ₅ HB ₆ B ₂ HB ₆	B ₁ B ₄ B ₃ B ₁ B ₅ B ₆	B ₁ B ₂ B ₄ B ₅	
3311	3.0610	B ₂ HB ₃ B ₃ HB ₄ B ₅ HB ₆	B ₁ B ₄ B ₅ B ₁ B ₃ B ₄ B ₁ B ₅ B ₆	B ₂ B ₆	B ₂ H
2402	3.7522	B ₂ HB ₃ B ₂ HB ₆	B ₃ B ₂ B ₆ B ₁ B ₃ B ₄ B ₁ B ₅ B ₆ B ₁ B ₄ B ₅		B ₄ H B ₅ H

(b) NBO boron hybridization and percentage polarization (for styx = 4220)

Atom	τ_{BHB}^a		τ_{BBB}		σ_{BB}		$\sigma_{BH(t)}$	
	h_B	Pol.	h_B	Pol.	h_B	Pol.	h_B	Pol.
B ₁			sp ^{2.46}	39%	sp ^{6.73}	50%	sp ^{2.49}	54%
B ₂	sp ^{3.65}	32%			sp ^{2.79}	50%	sp ^{2.29}	53%
B ₃	sp ^{4.03} sp ^{4.07}	27% 27%	sp ^{2.50}	34%			sp ^{2.16}	53%
B ₄	sp ^{4.49}	27%	sp ^{4.86}	27%	sp ^{1.97}	50%	sp ^{2.25}	52%

^a For two entries, the second denotes the bond to the later-numbered B atom.

(c) Natural resonance theory

Atom	Bond order					
	B ₂	B ₃	B ₄	B ₅	H _(μ)	H(t)
B ₁	0.80	0.84	0.10	0.10	—	1.00
B ₂	—	0.10	0.00	0.00	0.79	1.00
B ₃	0.10	—	0.16	0.08	0.12	1.00
B ₄	0.00	0.16	—	1.04	0.73	1.00

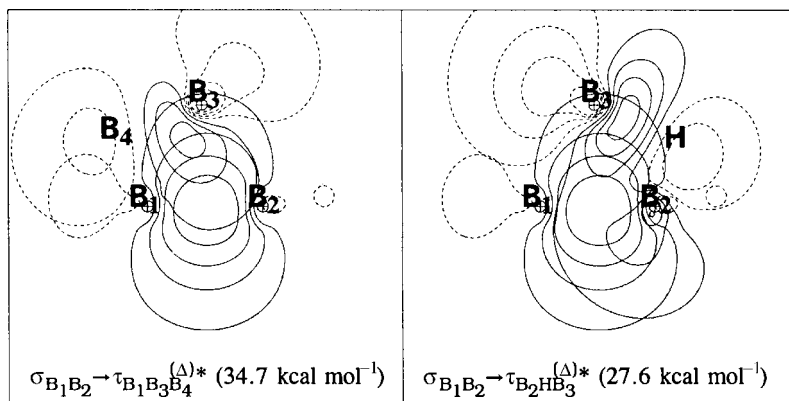
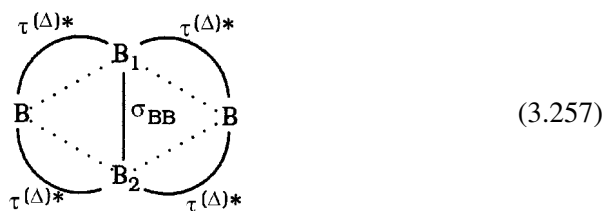


Figure 3.109 Leading donor–acceptor interactions of $\sigma_{BB} \rightarrow \tau_{BBB}^{(\Delta)*}$ (left) and $\sigma_{BB} \rightarrow \tau_{BBB}^{(\Delta)*}$ (right) type in B_6H_{10} ; see Eqs. (3.256a) and (3.256b) in the text.

$B_{12}H_{12}^{2-}$

As a final example we consider the icosahedral $B_{12}H_{12}^{2-}$ dianion, whose relevance to higher extended boron structures may be motivated in the following terms.

Looking back at the four previous examples, we can recognize that a common motif of successful *styx* structures is a central σ_{BB} bond with as many as four attached bridge bonds, each providing a strong $\sigma_{BB} \rightarrow \tau^{(\Delta)*}$ delocalization. (The σ_{BB} bonds are the best available donors, due to their high *p* character and concentration on two nuclei, while the low-lying three-center $\tau^{(\Delta)*}$ antibonds are the best available acceptors.) The favored motif can be represented schematically as



where each arc represents a three-center τ_{BBB} or τ_{BHB} bridging one edge of the B_4 “diamond” spanned by the σ_{BB} donor. As found in the examples above, each such adjacent $\sigma_{BB} \rightarrow \tau^{(\Delta)*}$ delocalization contributes significant stabilization (about 30 kcal mol^{-1} for τ_{BHB} , $40\text{--}50 \text{ kcal mol}^{-1}$ for τ_{BBB}) that strongly favors such bridged-diamond *styx* patterns. Thus, *styx* patterns in which the number of bridge bonds is in approximate 4 : 1 proportion to the number of donor σ_{BB} bonds can be expected to be particularly stable.

As the number of boron atoms increases, the favored motif (3.257) is specifically of the form



involving four central-type τ_{BBB} bonds clustered around σ_{BB} . Each such unit can be connected to other such units in a hexagonal pattern. Of course, this “hexagonal” aspect refers only to topological connectivity, since the local coordination at each B (actually, BH(t)) apex is approximately tetrahedral. Thus, an extended mesh of such hexagonal units (3.258) necessarily forms a curved surface in three dimensions. The edges of this mesh may be “hemmed” by τ_{BHB} bridges, or at “corners” by an extra hydrogen, to complete the local octet at each B. However, such truncation and hemming of the hexagonal mesh pattern typically involves departures from the optimal bond pattern (3.258).

A particularly elegant and stable solution is to close the hexagonal pattern in a three-dimensional icosahedron of $p = 12$ apices, as shown schematically in Fig. 3.110. (Apices labeled with small numbers must be connected to the corresponding boldface-numbered apex to form the correct three-dimensional

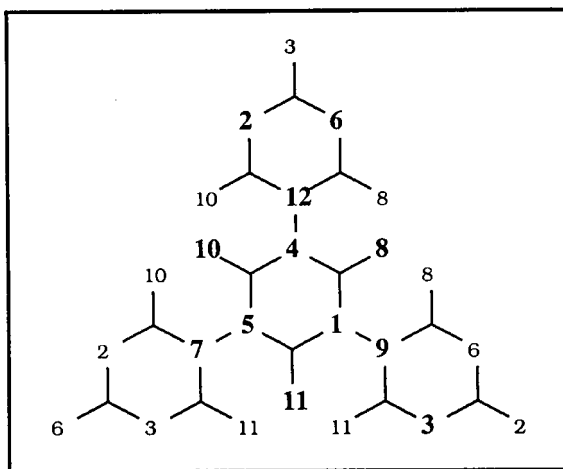


Figure 3.110 Boron-atom numbering and the two-dimensional hexagonal grid pattern of two two-center and ten three-center bonds in the 0.10.3.0 *styx* structure for icosahedral $\text{B}_{12}\text{H}_{12}^{2-}$.

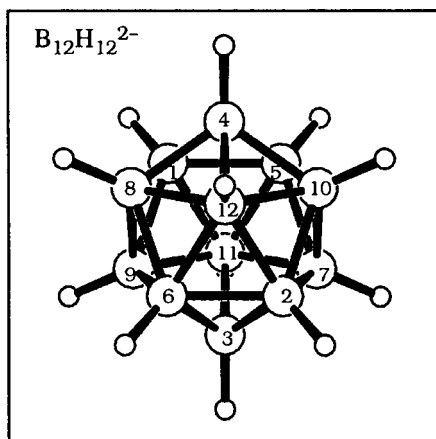


Figure 3.111 Icosahedral $B_{12}H_{12}^{2-}$ (with the atom numbering of note 154).

polygon.) As is easily verified from the diagram, the resulting $(BH)_{12}$ bond pattern ($styx = 0.10.3.0$) contains $y = 3 \sigma_{BB}$ bonds,

$$\sigma_{BB} : \quad 1-9, 4-12, 5-7 \quad (3.259a)$$

and $t = 10 \tau_{BBB}$ bonds,

$$\tau_{BBB} \begin{cases} 1-4-8, 1-5-11, 2-3-6, 2-7-10, 2-10-12, \\ 3-7-11, 3-9-11, 4-5-10, 6-8-9, 6-8-12 \end{cases} \quad (3.259b)$$

The optimal $styx$ pattern of three σ_{BB} , ten τ_{BBB} , and twelve $\sigma_{BH(t)}$ bonds requires a total of $2(3 + 10 + 12) = 50$ electrons, whereas a neutral $(BH)_{12}$ framework provides only $12(3 + 1) = 48$ valence electrons. Hence, two additional electrons must be added to form the $B_{12}H_{12}^{2-}$ anion that achieves the idealized icosahedral bonding pattern (3.259). Figure 3.111 depicts the computed structure of $B_{12}H_{12}^{2-}$, which indeed optimizes to perfect icosahedral symmetry with each $B-B = 1.787 \text{ \AA}$ (experimental 1.77 \AA) and $B-H = 1.202 \text{ \AA}$.

The specific realization (3.259) of the favored $0.10.3.0$ $styx$ pattern is only one of many equivalent localized representations. The “central” $1-4-5$ triangle of Fig. 3.110 could equivalently be chosen as any of the 20 possible triangular facets in Fig. 3.111, leading to 20 equivalent three-center Lewis structures that contribute to the overall resonance delocalization of $B_{12}H_{12}^{2-}$. The non-Lewis density of any such structure is found to be

$$\rho_{NL} = 3.706e \quad (5.01\%) \quad (3.260)$$

which significantly exceeds corresponding values in benzene, cyclopentadiene, and other “highly delocalized” species. Thus, by any criterion of delocalization density

or number of strongly contributing resonance structures, $B_{12}H_{12}^{2-}$ exhibits a more impressive degree of electronic delocalization than benzene and other “aromatic” prototypes of organic chemistry.

Icosahedral $B_{12}H_{12}^{2-}$ is evidently the structural “parent” of many of the smaller known boron hydrides, as well as a fundamental building block of more extended boron structures. Indeed, by systematically removing terminal hydrogens and re-connecting the dangling hybrids of adjacent B_{12} clusters through two- or three-center intercluster bonds (sometimes with a connecting “interstitial” boron atom, as in the tetragonal crystalline form), one recovers various solid forms of pure boron. The known metallic polymorphs of boron all seem to be built from such icosahedral boron clusters, varying only in the details of intercluster connections that bind these units into an extended three-dimensional network. Thus, the electronic properties of the boron skeleton in the prototypical icosahedral $B_{12}H_{12}^{2-}$ species appear to underlie the behavior of extended metallic phases of boron.

The natural atomic charges of $B_{12}H_{12}^{2-}$ are found to be

$$Q_B = -0.1703, \quad Q_H = +0.0036 \quad (3.261)$$

For the two-center B—H(t) and B—B bonds the optimal NBOs and occupancies are

$$\sigma_{BH(t)} = 0.710(sp^{2.83})_B + 0.705(s)_H \quad (1.9876e) \quad (3.262)$$

$$\sigma_{BB} = 0.707(sp^{5.95})_B + 0.707(sp^{5.95})_B \quad (1.3954e) \quad (3.263)$$

The severe depletion of the donor σ_{BB} bonds (due to $\sim 0.15e$ delocalization into each of the four adjacent three-center acceptor antibonds) is particularly to be noted.

The three-center τ_{BBB} bonds are of three types, depending on whether they lie adjacent to two σ_{BB} bonds (1—4—8, 1—5—11, 4—5—10), one σ_{BB} bond (2—7—10, 2—10—12, 3—7—11, 3—9—11, 6—8—9, 6—8—12), or no σ_{BB} bond (2—3—6). Those of the first type (illustrated in Fig. 3.112, left-hand panels) have bond and antibond NBOs and occupancies of the form (e.g., for 1—4—8)

$$\begin{aligned} \tau_{B_1B_4B_8} &= 0.584(sp^{2.42})_1 + 0.564(sp^{1.96})_8 \\ &\quad + 0.584(sp^{2.42})_4 \quad (1.8527e) \end{aligned} \quad (3.264a)$$

$$\begin{aligned} \tau_{B_1B_4B_8}^{(\Delta)*} &= 0.399(sp^{2.42})_1 - 0.826(sp^{1.96})_8 \\ &\quad + 0.399(sp^{2.42})_4 \quad (0.1589e) \end{aligned} \quad (3.264b)$$

$$\tau_{B_1B_4B_8}^{(\tau)*} = 0.707(sp^{2.42})_1 - 0.707(sp^{2.42})_4 \quad (0.1013e) \quad (3.264c)$$

For the second type (e.g., 6—8—12, illustrated in the right-hand panels of Fig. 3.112) the corresponding NBOs are

$$\tau_{B_6B_8B_{12}} = 0.571(sp^{4.15})_6 + 0.606(sp^{2.42})_8 + 0.555(sp^{4.15})_{12} \quad (1.8296e) \quad (3.265a)$$

$$\tau_{B_6B_8B_{12}}^{(\Delta)*} = 0.502(sp^{4.15})_6 - 0.720(sp^{2.42})_8 + 0.348(sp^{4.15})_{12} \quad (0.0556e) \quad (3.265b)$$

$$\tau_{B_6B_8B_{12}}^{(\pi)*} = 0.650(sp^{4.15})_6 - 0.756(sp^{4.15})_{12} \quad (0.2753e) \quad (3.265c)$$

and for the third type (2—3—6) the corresponding NBOs are

$$\tau_{B_2B_3B_6} = 0.577(sp^{1.96})_2 + 0.577(sp^{1.96})_3 + 0.577(sp^{1.96})_6 \quad (1.8456e) \quad (3.266a)$$

$$\tau_{B_2B_3B_6}^{(\Delta)*} = 0.500(sp^{1.96})_2 - 0.707(sp^{1.96})_3 + 0.500(sp^{1.96})_6 \quad (0.1247e) \quad (3.266b)$$

$$\tau_{B_2B_3B_6}^{(\pi)*} = 0.707(sp^{1.96})_2 - 0.707(sp^{1.96})_6 \quad (0.1247e) \quad (3.266c)$$

As expected, the strongest delocalizations are the four $\sigma \rightarrow \tau^*$ donor–acceptor interactions around each σ_{BB} bond, including two strong interactions with $\tau^{(\pi)*}$ antibonds of the second type (see Fig. 3.113, left)

$$\tau_{B_4B_{12}} \rightarrow \tau_{B_6B_8B_{12}}^{(\pi)*} \quad (37.50 \text{ kcal mol}^{-1}) \quad (3.267a)$$

and two weaker interactions with $\tau^{(\Delta)*}$ antibonds of the first type (see Fig. 3.113, right)

$$\tau_{B_4B_{12}} \rightarrow \tau_{B_1B_4B_8}^{(\Delta)*} \quad (21.15 \text{ kcal mol}^{-1}) \quad (3.267b)$$

(The weaker delocalization in the latter case would be expected from the anticooperative nature of competitive interactions with two donors.) These interactions thus exhibit forms and magnitudes that are generally similar to those found in smaller boron hydrides.

In summary, we can say that all these boron hydrides exhibit a consistent pattern of recognizable, transferable three-center NBOs and interactions. Bond patterns that maximize the clustering of three-center τ_{BBB} bonds adjacent to donor σ_{BB} bonds can be expected to be a rather general feature of the most stable species of this type. Strong resonance mixing among the many equivalent structures of this form is a characteristic of icosahedral $B_{12}H_{12}^{2-}$, in which the favorable pattern of interlinked three-center bonding extends seamlessly and symmetrically over a closed three-dimensional surface. Compared with ordinary $2c/2e$ or electron-rich $3c/4e$ motifs, one can recognize that the $3c/2e$ τ -bonding motif offers a much richer

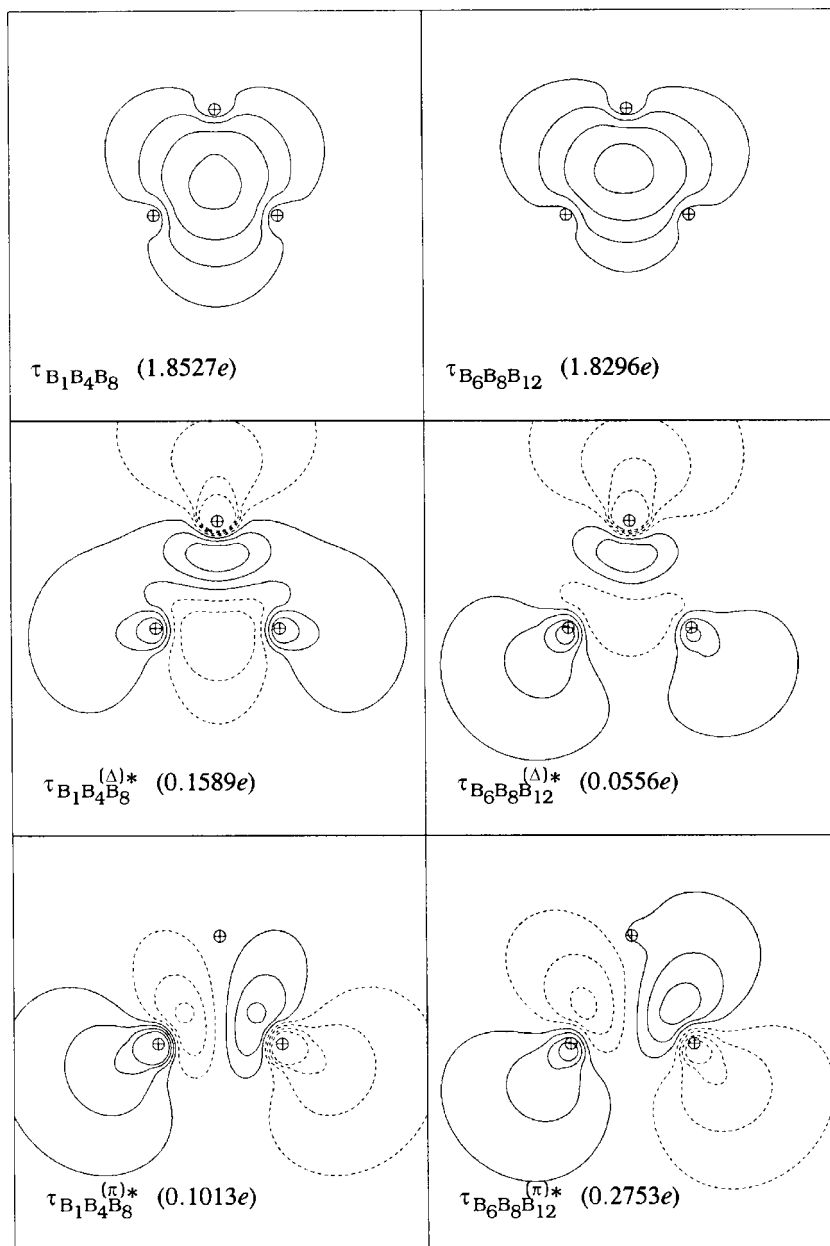


Figure 3.112 The three-center τ_{BBB} bond and antibond NBOs of type 1 (left; cf. Eqs. (3.264)) and type 2 (right; cf. Eqs. (3.265)) in $B_{12} H_{12}^{2-}$.

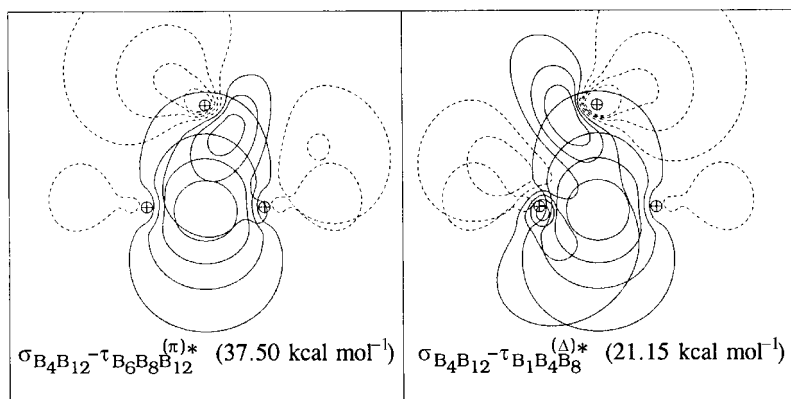


Figure 3.113 Leading σ - τ^* donor-acceptor interactions in $B_{12}H_{12}^{2-}$. Note that both τ^* orbitals appear truncated in this view (cf. Fig. 3.112) because atoms 1 and 6 fall below the chosen (4—8—12) contour plane.

choice of delocalizing acceptor orbitals (without the conflicting steric exchange interactions among filled orbitals) with which to achieve highly favorable patterns of donor-acceptor stabilization.

Carboranes and other aspects of the boron/carbon connection

The concept that carbon atoms and BH(t) groups are “isovalent” leads naturally to the conjecture that many $(BH)_pH_q$ boranes are related to analogous *carboranes* of formula $C_n(BH)_{p-n}H_q$. As one such example, $C_2B_4H_8$ is a close structural and electronic analog of hexaborane B_6H_{10} (3.255), in which the BH groups at positions 4 and 5 in Fig. 3.103(d) have been substituted by C atoms. Because C is somewhat smaller and more electronegative than B, this substitution leads to expected small changes in geometry and electronic distribution.¹⁶¹ However, the general similarities in Lewis structures, NBOs, and delocalization patterns of the borane and carborane compounds suggest that these species are indeed “isostructural” (except for the obvious replacement of two hydride bonds by carbon lone pairs), and should manifest many analogous chemical properties.

The borane/carborane connection is illustrated in Table 3.45, which shows details of the NBOs of $C_2B_4H_8$ for direct comparison with corresponding data for B_6H_{10} in Table 3.44. The slight shifts in NBO hybridization and polarization are in accord with differences in electronegativity between B and C, but the overall similarities are apparent. As further evidence of the near-transferability of NBOs from borane to carborane, we show direct comparisons of three-center borane τ_{BHB} and carborane τ_{BHC} NBOs in Fig. 3.114, and we illustrate in Fig. 3.115 the leading donor-acceptor delocalizations of $C_2B_4H_8$ in a form that can be directly compared with the analogous interactions of B_6H_{10} in Fig. 3.109:

Table 3.45. Similar to Table 3.44(b), for $C_2B_4H_8$.

NBO X(= B,C) hybridization and percentage polarization (for styx = 4220)								
Atom X	τ_{BHX}^a		τ_{BBX}		σ_{XX}		$\sigma_{BH(t)}$	
	$h_{B/C}$	Pol.	$h_{B/C}$	Pol.	$h_{B/C}$	Pol.	h_B	Pol.
B ₁			$sp^{3.08}$	31%	$sp^{4.35}$	49%	$sp^{2.15}$	53%
B ₂	$sp^{3.61}$	33%			$sp^{2.86}$	51%	$sp^{2.27}$	54%
B ₃	$sp^{3.19}$	26%	$sp^{2.41}$	30%			$sp^{1.93}$	53%
	$sp^{6.94}$	29%						
C ₄	$sp^{7.01}$	33%	$sp^{2.49}$	39%	$sp^{0.96}$	50%		

^aFor two entries, the second denotes the bond to the later-numbered X atom.

As a second illustrative aspect of the boron/carbon connection, we consider the dicarbollide ion, $C_2B_9H_{11}^{2-}$, which can be pictured as derived from $B_{12}H_{12}^{2-}$ by removing one BH(t) vertex and replacing two adjacent borons of the exposed pentagonal face by carbon atoms, as shown in Fig. 3.116. This ion exhibits remarkable electronic “mimicry” of the cyclopentadienyl ion ($C_5H_5^-$, Section 3.3.2), forming similar coordination and sandwich complexes with many metallic species.¹⁶²

The NBO analysis reveals the strong electronic similarities between $C_2B_9H_{11}^{2-}$ and $C_5H_5^-$. The optimal NBO Lewis structure representations, (3.268a)–(3.268c), all have two-center single bonds connecting the B₇, B₈, B₉, C₁₀, and C₁₁ “rim” atoms, with the familiar motif of a two-center B—B bond flanked by four

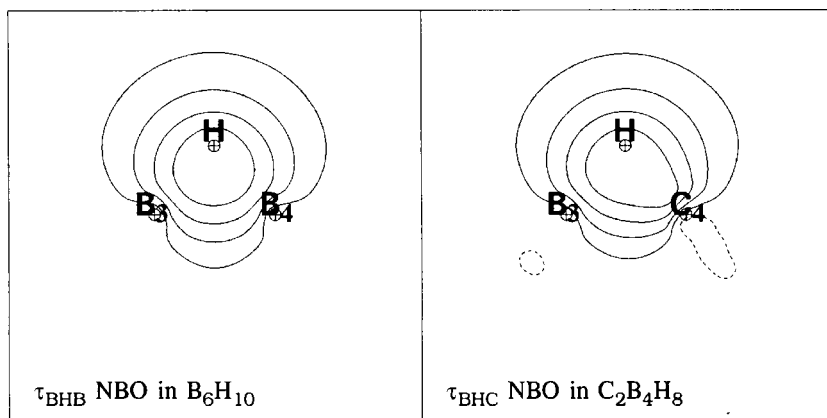


Figure 3.114 A comparison of the three-center τ_{BHB} of B_6H_{10} (left) with the corresponding τ_{BHC} of $C_2B_4H_8$ (right).

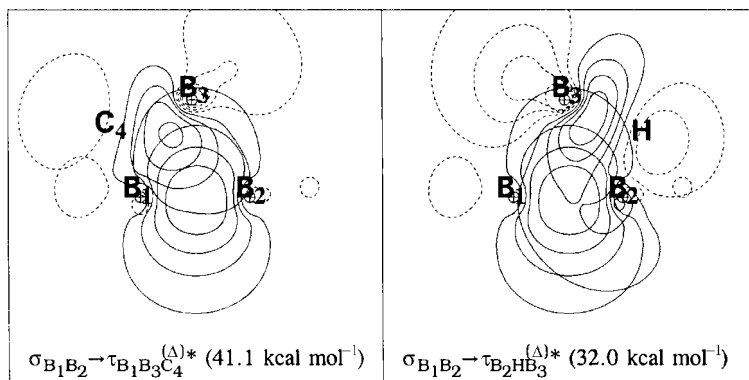
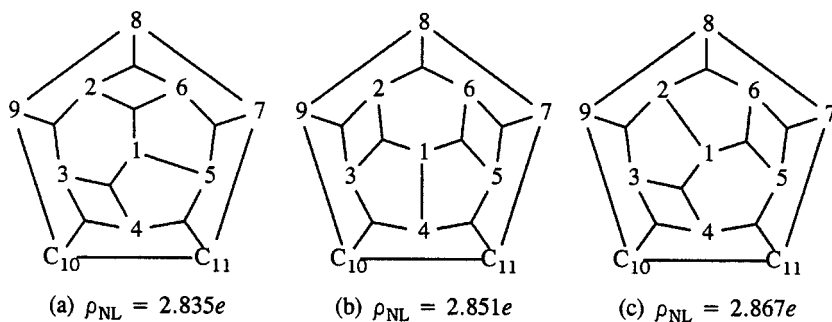


Figure 3.115 Leading donor–acceptor interactions of $\sigma_{BB} \rightarrow \tau_{BBC}^{(\Delta)*}$ (left) and $\sigma_{BB} \rightarrow \tau_{BHB}^{(\Delta)*}$ (right) type in $C_2B_4H_8$, showing the general similarity to B_6H_{10} (Fig. 3.109).

three-center bonds forming the main “cup”:



(3.268)

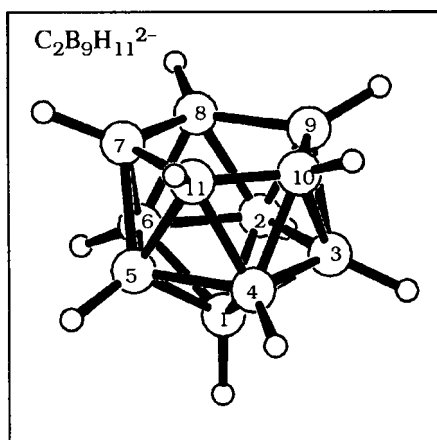


Figure 3.116 The optimized structure of the dicarbollide anion, $C_2B_9H_{11}^{2-}$, with the atom numbering employed herein.

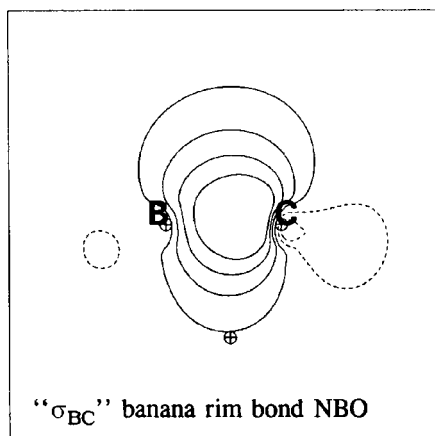


Figure 3.117 The bent “ σ_{BC} ” (“ π_{BC} ”) rim bond (see Eq. (3.269) in the text) in the dicarbollide anion, $C_2B_9H_{11}^{2-}$.

(The structure (3.268a) with two-center $B_1—B_5$ bond has slightly lower non-Lewis density than the alternative structures (3.268b) and (3.268c), but the molecule should be considered a strong resonance hybrid of the near-equivalent structures represented by (3.268).) However, each rim bond is a conspicuously bent *banana bond*, similar to that seen previously when a pair of heavy atoms is bridged by only one of the two usual three-center bonds (cf. Fig. 3.102). Thus, from the viewpoint of a coordinating species approaching the five-membered rim from above, each rim bond appears to be one of the two equivalent strained bonds of a banana-bonded *ethylenic* moiety (or, equivalently, a two-center bond strongly prepared for three-center bonding to an incoming empty orbital). Figure 3.117 depicts one of the strained “ σ_{BC} ” rim NBOs (which might, with equal justification, be labeled a strained “ π_{BC} ” NBO),

$$\text{“}\sigma_{BC}\text{”} = 0.549(sp^{4.09})_B + 0.836(sp^{3.04})_C \quad (3.269)$$

showing the strong bending of the hybrids (by 21.8° at the C end, 14.8° at the B end) from the line of B—C centers (similar to the outward bending for all five rim bonds).

The general similarities of the dicarbollide and cyclopentadienyl (Cp) ions are also evident in the geometry and charge distributions. The dicarbollide five-membered rim bonds are somewhat longer on average than those of Cp (1.658 Å versus 1.414 Å), and the terminal B—H/C—H bonds are bent up $25\text{--}30^\circ$ above the mean plane of the five-membered ring. The dicarbollide ring angles also deviate by $\sim\pm 5^\circ$ from idealized pentagonal values.¹⁶³ The average atomic charge on each

dicarbollide rim atom is $\overline{Q} = -0.332$, which is rather similar to the corresponding value $\overline{Q} = -0.365$ in Cp.¹⁶⁴

τ -Bonding in higher group 13 congeners

Finally, we briefly examine some vertical aspects of three-center bonding for the heavier group 13 elements aluminum and gallium. Both Al and Ga form dinuclear hydrides, Al₂H₆ and Ga₂H₆, that are close analogs of the B₂H₆ structure (Fig. 3.92). The three-center bridge bonds τ_{MHM} (M = Al, Ga) of these species can therefore be directly compared with the corresponding bonds discussed previously for B₂H₆.

Figure 3.118 illustrates the form of the τ_{MHM} bond and antibond NBOs found for M = Al, Ga, for direct comparison with Fig. 3.93. The detailed hybrid compositions of the τ and τ^* NBOs are found to be, for Al,

$$\tau_{\text{AlHAl}} = 0.40(\text{sp}^{7.05})_{\text{Al}} + 0.83(\text{s})_{\text{H}} + 0.40(\text{sp}^{7.05})_{\text{Al}'} \quad (3.270\text{a})$$

$$\tau_{\text{AlHAl}}^{(\Delta)*} = 0.59(\text{sp}^{7.05})_{\text{Al}} - 0.56(\text{s})_{\text{H}} + 0.59(\text{sp}^{7.05})_{\text{Al}'} \quad (3.270\text{b})$$

$$\tau_{\text{AlHAl}}^{(\pi)*} = 0.71(\text{sp}^{7.05})_{\text{Al}} - 0.71(\text{sp}^{7.05})_{\text{Al}'} \quad (3.270\text{c})$$

and for Ga,

$$\tau_{\text{GaHGa}} = 0.42(\text{sp}^{8.50})_{\text{Ga}} + 0.80(\text{s})_{\text{H}} + 0.42(\text{sp}^{8.50})_{\text{Ga}'} \quad (3.271\text{a})$$

$$\tau_{\text{GaHGa}}^{(\Delta)*} = 0.57(\text{sp}^{8.50})_{\text{Ga}} - 0.60(\text{s})_{\text{H}} + 0.57(\text{sp}^{8.50})_{\text{Ga}'} \quad (3.271\text{b})$$

$$\tau_{\text{GaHGa}}^{(\pi)*} = 0.71(\text{sp}^{8.50})_{\text{Ga}} - 0.707(\text{sp}^{8.50})_{\text{Ga}'} \quad (3.271\text{c})$$

which may be compared with the corresponding boron expressions, Eqs. (3.235a)–(3.235c). The general graphical and functional similarities are quite apparent. As for the previous boron case, one can clearly recognize in Fig. 3.118 the two distinct types ($\tau_{\text{MHM}}^{(\Delta)*}$ and $\tau_{\text{MHM}}^{(\pi)*}$) of Al and Ga valence antibonds, with characteristically distinct contributions to electron delocalization. As expected from general electronegativity differences and Bent's rule, the hybrids of Al and Ga gain increasing p character relative to B, and the metal-atom polarization coefficients are reduced compared with those on the more electronegative H. Despite the apparent weakening of hybridization and strengthening of ionic character, the general parallels in the forms of the NBOs suggest that many aspects of three-center bonding in aluminum and gallium compounds should parallel those of boron.

The leading donor–acceptor delocalizations of Al₂H₆ and Ga₂H₆ are compared in Fig. 3.119. With respect to the leading $\tau \rightarrow \tau^{(\Delta)*}$ interaction in B₂H₆ (Fig. 3.94), the corresponding interactions in Al₂H₆ and Ga₂H₆ are evidently strengthened (particularly for Al₂H₆). Moreover, the increased ionic character is manifested in the

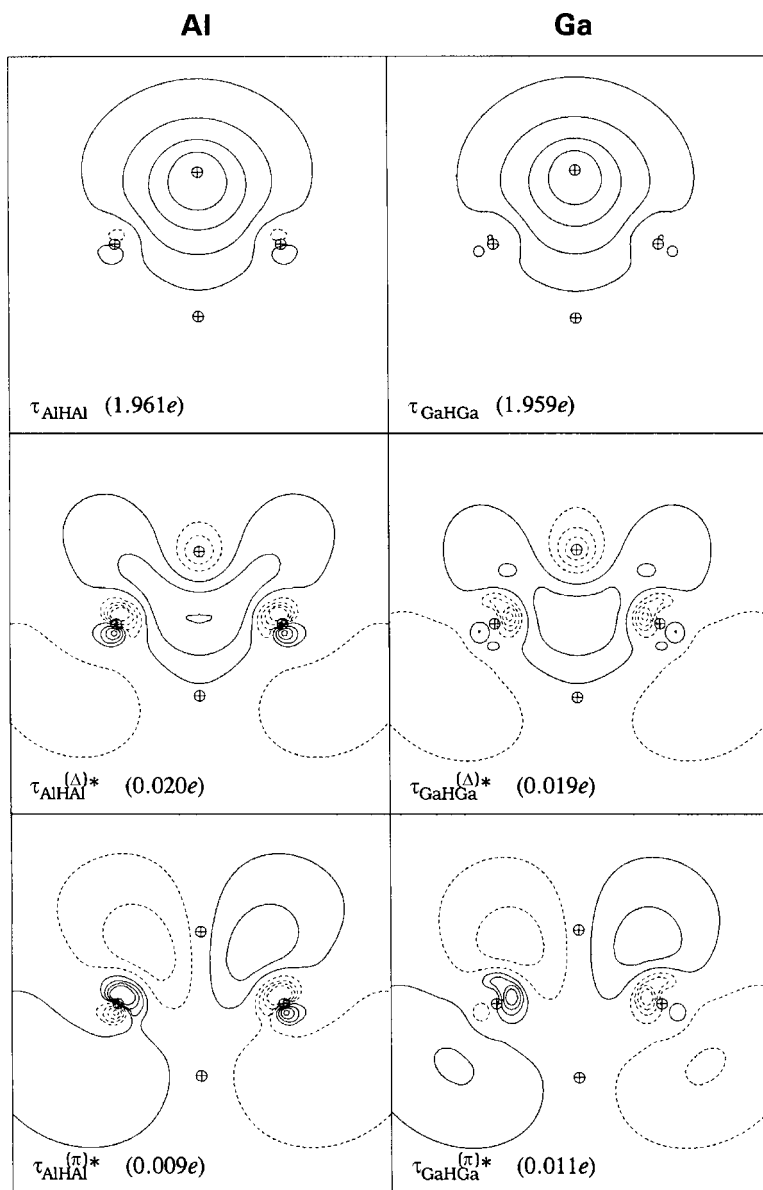


Figure 3.118 Three-center bond (upper row) and antibond (lower two rows) NBOs of Al_2H_6 (left) and Ga_2H_6 (right) (cf. Fig. 3.93 for the corresponding orbitals of B_2H_6).

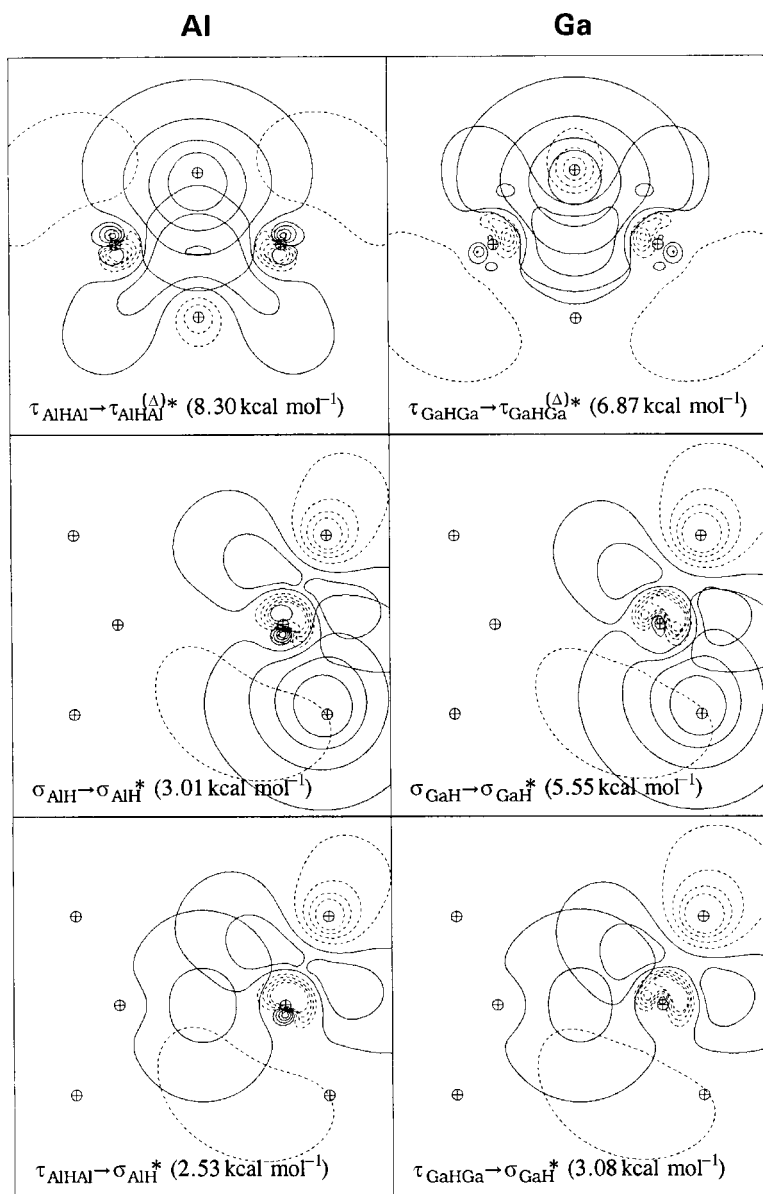


Figure 3.119 Leading donor–acceptor interactions in Al_2H_6 (left) and Ga_2H_6 (right), showing overlap contours in the plane of three-center bridge-bonding (the “pi plane,” top row) and two-center skeletal bonding (the “sigma plane,” bottom two rows), with associated second-order stabilization energies in parentheses.

increased strength of geminal $\sigma_{\text{MH}}-\sigma_{\text{MH}}$ hyperconjugation involving the terminal MH(t) bonds (middle panels of Fig. 3.119), as well as increased delocalization from bridging τ_{MHM} bonds into surrounding $\sigma_{\text{MH(t)}}^*$ orbitals (lower panels of Fig. 3.119). Further aspects of delocalization in Al and Ga compounds are beyond the scope of the present work.

3.7 Summary

Chapter 3 has discussed a wide range of chemical phenomena involving atoms with partially filled s and p shells. Indeed, the chemistry of these elements is so closely tied to the energies and shapes of s/p orbitals (as well as the hybrids, bonds, and antibonds to which they give rise) that we can virtually speak of “s/p-orbital chemistry” as a generic *type* of chemical behavior.

The characteristics of s/p-orbital chemistry are associated, above all, with the atoms H, C, N, and O that dominate organic and biochemical phenomena. Hence, the discussion of bonding in s/p-block elements inevitably carries a “bias” toward organic chemistry, and toward the issues and controversies that continue to animate this most mature and advanced area of chemistry. Indeed, organic chemistry may be considered the “cradle of covalency,” where many principles of chemical bonding were first grasped and exploited.

Before embarking to explore the distinctive chemical phenomena associated with partially filled d shells (Chapter 4), let us summarize the logical steps in a systematic *Aufbau* of chemical bonding concepts (cf. Fig. 3.91), starting from the pure one-center s and p atomic orbitals of isolated atoms and ions. As described in Chapter 2, the interaction of occupied and unoccupied one-center orbitals leads to progressive donor–acceptor delocalization ($1c \rightarrow 1c^*$) that represents the onset of covalency and two-center (shared) character of the occupied orbitals. This regime dominates the “bonding” of molecules which is the principal focus of Chapter 3. Each $1c \rightarrow 1c^*$ pairing underlies an in-phase (2c bond) and out-of-phase ($2c^*$ antibond) orbital that provide the starting point for donor–acceptor interactions at the next higher level of aggregation.

In s-block elements (Section 3.2.1) the formation of two-center bond orbitals is relatively simple, leading only to axially symmetric sigma-type bond functions. However, in p-block elements the $1c \rightarrow 2c$ transition is significantly promoted by *hybridization* and the possibility of forming either σ_{AB} or π_{AB} bonds (or bent bonds not strictly of either pure σ or pure π type; Section 3.2.7). Only in exceptional cases can one neglect the hybridization effects, and in such cases one may even encounter strange “nu bonds” (Section 3.2.9), involving paired $s_{\text{A}}-p_{\text{B}}$ and $p_{\text{A}}-s_{\text{B}}$ interactions that lack the usual symmetries of sigma and pi bonds.

The optimal forms of the bonding hybrids depend on geometry (Section 3.2.3) and relative electronegativity (Bent's rule, Section 3.2.6). Optimal one- and two-center Lewis-structure bonding patterns are commonly those that allow each atom to engage in complementary donor–acceptor interactions that “pair up” the incoming and outgoing delocalizations to minimize formal charge while allowing *each* of the four valence orbitals to share in hosting an electron pair (the maximum permitted by the Pauli exclusion principle). In this manner each p-block element achieves formal valence-shell occupancy consistent with the “rule of 8” (Lewis's octet rule) for the optimal Lewis-structural pattern. As is well known, such simple localized Lewis-structural concepts readily allow one to rationalize the geometry and properties of a vast number of diatomic and polyatomic species, including those involving dative bonding (Section 3.2.10).

Despite the successes of the localized one- and two-center Lewis-structure concept, corrections are necessary for unsaturated pi-bonded molecules in order to account for the delocalization effects of conjugation and aromaticity (Section 3.3) that cannot be adequately described by a single Lewis (resonance) structure. Such corrections can be formally associated with NBO donor–acceptor interactions of $1c \rightarrow 2c^*$ (e.g., $n_A \rightarrow \pi_{BC}^*$) or $2c \rightarrow 2c^*$ (e.g., $\pi_{AB} \rightarrow \pi_{CD}^*$) type, conferring partial three- or four-center character on the occupied orbitals. Related *hyper*-conjugative corrections of similar form (but smaller magnitude) are also necessary in purely saturated molecules (Section 3.4). Particularly important are the vicinal $\sigma_{AB} \rightarrow \sigma_{CD}^*$ delocalizations which contribute to torsion-barrier (Section 3.4.2) and through-bond coupling phenomena (Section 3.4.3). However, neighboring geminal (Section 3.4.4) and remote (Chapter 5) hyperconjugative $n \rightarrow \sigma^*$ and $\sigma \rightarrow \sigma^*$ interactions can also confer a degree of three or four-center character on other bond topologies.

The breakdown of predominant one- and two-center localized behavior results in the need for three-center extension of the Lewis-structure concept. Two important classes of three-center bonding have generally been recognized: (1) the three-center, four-electron (hypervalent ω -bonding) limit of $1c \rightarrow 2c^*$ donor–acceptor interactions (Section 3.5); and (2) the three-center, two-electron (hypovalent τ -bonding) limit of $2c \rightarrow 1c^*$ donor–acceptor interactions (Section 3.6). The former class retains a stronger connection to the parent two-center bonding pattern, because the high-energy $2c^*$ antibond generally cannot compete as an acceptor function with the original empty $1c^*$ valence orbital that led to two-center bond formation. (In fact, for p-block elements, the symmetric three-center geometry is often an unstable transition state connecting the two asymmetric long-range complexes corresponding to distinct two-center bond patterns.) However, the latter (τ) class intrinsically leads to “true” three-center character, because the $1c^*$ acceptor is intrinsically competitive

with each one-center parent of the two-center donor function. The $3c/2e$ τ -bonding limit also leads to more profuse possibilities for *additional* donor–acceptor interactions, due to the favorable 2 : 1 preponderance of the unfilled ($\tau^{(\Delta)*}$ and $\tau^{(\pi)*}$) orbitals that invite further stabilizing delocalizations. As shown in Section 3.6, these delocalizations predominantly involve bridged diamond-shape (butterfly) arrangements giving rise to $\sigma \rightarrow \tau^*$ interactions that somewhat resemble the vicinal $\sigma \rightarrow \sigma^*$ interactions of normal-valent species, but are greatly strengthened by removal of one of the electron pairs (and the associated steric exchange interactions) from the underlying four-atom connectivity pattern.

Although the generalization to localized three-center bonds inevitably involves certain complications, important simplifications of the localized Lewis-structure picture remain. In the case of $3c/4e$ ω -bonding, the corrections can often be adequately described in terms of two-term resonance between alternative two-center bonding patterns. In the case of $3c/2e$ τ -bonding, the resonance-theoretic description (although possible in principle) becomes unwieldy. However, in terms of the single best three-center localized Lewis-structure description (or the resonance mixture of symmetry-equivalent structures), one can still identify specific localized donor–acceptor interactions (e.g., of $\sigma \rightarrow \tau^{(\Delta)*}$ type) that dominate the delocalization corrections. Important localized electronic patterns appear to persist even for such highly delocalized systems as metallic boron.

Notes for Chapter 3

1. W. Heitler and F. London, *Z. Phys.* **44** (1927), 455.
2. L. Pauling, *Chem. Rev.* **5** (1928), 173.
3. H. M. James and A. C. Coolidge, *J. Chem. Phys.* **1** (1933), 825.
4. For a comprehensive bibliography of early work on H_2 and related bonding systems, see A. D. McLean, A. Weiss, and M. Yoshimine, *Rev. Mod. Phys.* **32** (1960), 211; and R. G. Parr, *Quantum Theory of Molecular Electronic Structure* (New York, W. A. Benjamin, 1964).
5. Ø. Burrau, *Konigl. Danske Vid. Selskab.* **7** (1927), 1; D. R. Bates, K. Ledsham, and A. L. Stewart, *Phil. Trans. Roy. Soc. London* **A246** (1953), 215; and H. Wind, *J. Chem. Phys.* **42** (1965), 2371.
6. W. Kolos and L. Wolniewicz, *J. Chem. Phys.* **43** (1965), 2429; W. Kolos and L. Wolniewicz, *J. Chem. Phys.* **49** (1968), 404; and G. Herzberg, *Phys. Rev. Lett.* **23** (1969), 1081.
7. In Hartree–Fock (HF) theory, the energy of a given orbital is lower when the orbital is occupied than when it is vacant (due to the formal self-energy in the former case), and the degeneracy is broken. Thus, perturbative HF expressions such as Eq. (2.7) often have wider numerical validity than would be anticipated in naive MO theory.
8. Of course, in a purely formal manner we could also treat covalent H_2 bond formation in terms of the interaction between H^- and H^+ , but such a two-electron ionic DA model is less accurate (i.e., requires larger perturbative corrections) than the electroneutral model of complementary one-electron DA interactions to be employed in this work.
9. The “spin-charge” $Q_A^{(\alpha)}$ for spin α on atom H_A may be formally defined as

$$Q_A^{(\alpha)} = +Z/2 - n_{1sA}^{(\alpha)}$$

where $Z = 1$ is the nuclear charge and $n_{1s_A}^{(\alpha)}$ is the electronic occupancy of spin-orbital $1s_A^{(\alpha)}$ on A (cf. Fig. 3.3). Noting that

$$n_{1s_A}^{(\alpha)} = 1 - n_{1s_A}^{(\beta)}, \quad n_{1s_B}^{(\alpha)} = 1 - n_{1s_B}^{(\beta)}$$

we find

$$Q_A^{(\alpha)} = -Q_A^{(\beta)}, \quad Q_B^{(\alpha)} = -Q_B^{(\beta)}$$

at all R , and the total atomic charges $Q_A = Q_A^{(\alpha)} + Q_A^{(\beta)}$ and $Q_B = Q_B^{(\alpha)} + Q_B^{(\beta)}$ are therefore identically zero, despite the non-zero spin-charge flow between atoms.

10. Note that Eq. (3.8b) corresponds to a long-range perturbative estimate, whereas Eq. (3.11d) pertains directly to the final MO form, so the latter gives a somewhat more accurate estimate of the actual hybridization.
11. An estimate analogous to (3.11), based on the NAO matrix elements $\langle 2s_A | \hat{F} | 2p_B \rangle = -0.0512$, $\langle 2p_A | \hat{F} | 2p_B \rangle = 0.1084$, leads to the predicted value $\lambda = 0.22$, in good agreement with the actual NHO hybridization.
12. For example, the energy of a pure $2s$ orbital is -0.125 in the neutral H atom ($Z = 1$, $n = 2$ in Eq. (1.12)), but -0.500 in the He^+ monocation ($Z = 2$). To better approximate a homonuclear diatomic cation, we can put $Z = 1.5$ in Eq. (1.12), leading to the estimate $\epsilon_{2s} = -9/32 = -0.281$ a.u. Owing to screening effects, these simple hydrogenic estimates are somewhat lower than the actual ϵ_{2s} values (-0.0868 and -0.2485) found for Li_2 and Li_2^+ at $R = 2.7 \text{ \AA}$. Hybridization further alters these values (e.g., to -0.0766 and -0.2309) but preserves the basic relationship that ϵ is more than *twice* as negative for Li_2^+ as for Li_2 .
13. The general magnitude of F_{AB} can be estimated as follows. If we substitute the optimal λ_{opt} from Eq. (3.16) into Eq. (3.10) for F_{AB} , we obtain

$$F_{AB} = f_{ss'} - \frac{f_{sp'}^2}{f_{pp'}}$$

Using, e.g., the NAO Fock-matrix elements for Li_2^+ quoted in note 11 (together with the corresponding value for $f_{ss'} = \langle 1s_A | \hat{F} | 1s_B \rangle = -0.0668$), we obtain the estimate $F_{AB} \simeq -0.0910$. This somewhat underestimates the magnitude of the actual interaction element (-0.1191), but shows the general direction and strength of the hybridization effect.

14. The classic HLSP-PP-VB (Heitler–London–Slater–Pauling perfect-pairing valence-bond) formalism and its chemical applications are described by L. Pauling, *The Nature of the Chemical Bond*, 3rd edn. (Ithaca, NY, Cornell University Press, 1960; G. W. Wheland, *The Theory of Resonance* (New York, John Wiley, 1944); and H. Eyring, J. Walter, and G. E. Kimball, *Quantum Chemistry* (New York, John Wiley, 1944).
15. L. Pauling and G. W. Wheland, *J. Chem. Phys.* **1** (1933), 362; G. W. Wheland and L. Pauling, *J. Am. Chem. Soc.* **57** (1935), 2086; and Pauling in note 14.
16. Owing to the numerical problems discussed below, various “generalized” valence-bond methods have been developed that allow h_A and h_B to acquire contributions from the opposite center or to be partially delocalized over *all* atoms of a polyatomic molecule. While this mathematical generalization gives increased variational flexibility, the connection to the chemist’s Lewis-structure diagram and Pauling–Slater bonding hybrids is weakened.
17. For example, a characteristic two-electron “resonance integral” of the form

$$K_{AB}(R) = \int h_A^*(1)h_B^*(2)\hat{H}(R)h_B(1)h_A(2)d\tau_1d\tau_2$$

may be replaced by an empirical function $K_{AB}(R)$ chosen to reproduce experimental data that can be related to this integral. Whether the right-hand side of Eq. (3.24) can actually be evaluated and shown to have an R -dependence consistent with the chosen $K_{AB}(R)$ then becomes a matter of secondary importance.

18. R. S. Mulliken, *J. Chem. Phys.* **3** (1935), 573; and R. S. Sanderson, *Polar Covalence* (New York, Academic Press, 1983). The notion of a fundamental dichotomy between ionic and

covalent “types” (espoused by Langmuir, Sidgwick, and Sugden) was opposed by Lewis, Mulliken, and others; for a general historical discussion, see W. B. Jensen, *The Lewis Acid–Base Concepts* (New York, Wiley, 1980), pp. 74–77.

19. L. Pauling, *J. Am. Chem. Soc.* **53** (1931), 1367.
20. J. C. Slater, *Phys. Rev.* **37** (1931), 481.
21. C. A. Coulson, *Valence*, 2nd edn. (London, Oxford University Press, 1952), Chapter 8.
22. For example, for the most discrepant case in Table 3.2, the $sp^{2.37}$ and $sp^{1.44}$ hybrids for ethylene correspond, respectively, to 70% and 59% p character, rather than the expected 66%.
23. However, this small percentage error corresponds to 59.5 kcal mol⁻¹, so the neglected non-Lewis contributions correspond to chemically significant effects.
24. Numerical LMOs of this work are determined by the natural localized-molecular-orbital (NLMO) method: A. E. Reed and F. Weinhold, *J. Chem. Phys.* **83** (1985), 1736. The LMOs determined by other methods (e.g., C. Edmiston and K. Ruedenberg, *Rev. Mod. Phys.* **34** [1963], 457; and J. M. Foster and S. F. Boys, *Rev. Mod. Phys.* **32** [1960], 300) are rather similar, and could be taken as equivalent for present purposes.
25. V. Fock, *Z. Phys.* **61** (1930), 126.
26. The CMOs transform as irreducible representations of the molecular point group, whereas the LMOs form a basis for a reducible representation.
27. $E^{(L)}$ is a strict variational expectation value of the natural Lewis-structure wavefunction $\Psi^{(L)}$, Eq. (1.32), and can be determined with the NOSTAR keyword of the \$DEL keylist.
28. Such four-electron interactions are sometimes considered to be intrinsically *destabilizing* but this is an artifact of performing perturbation theory with a non-Hermitian (unphysical) model $\hat{H}^{(0)}$, as discussed in Section 3.4.2.
29. T. A. Koopmans, *Physica* **1** (1933), 104.
30. These values are uncorrected for zero-point-energy differences and thermal (entropic) effects.
31. See Pauling, note 14, pp. 97ff. Coulson, note 21, p. 141, states “Now there must be some relation between the percentage ionic character and the electronegativity difference $x_B - x_A$. It is of the very essence of the idea of an electronegativity scale that this should be so.”
32. N. B. Hannay and C. P. Smyth, *J. Am. Chem. Soc.* **68** (1946), 171.
33. W. Gordy, *Faraday Soc. Discussions* **19** (1955), 14.
34. L. Pauling and D. M. Yost, *Proc. Nat. Acad. Sci. U.S.A.* **18** (1932), 414; and L. Pauling, *J. Am. Chem. Soc.* **54** (1932), 3570.
35. A. L. Allred and E. G. Rochow, *J. Inorg. Nucl. Chem.* **5** (1958), 264 and 269.
36. As leading references from the extensive literature of atomic, group, and orbital electronegativities, see R. S. Mulliken, *J. Chem. Phys.* **2** (1934), 782; R. S. Mulliken, *J. Chem. Phys.* **3** (1935), 573; W. Gordy, *Phys. Rev.* **69** (1946), 604; R. T. Sanderson, *Science* **114** (1951), 670; A. D. Walsh, *Proc. Roy. Soc. London* **A207** (1951), 13; H. O. Pritchard and H. A. Skinner, *Chem. Rev.* **55** (1955), 745; R. P. Iczkowski and J. L. Margrave, *J. Am. Chem. Soc.* **83** (1961), 3547; J. Hinze and H. H. Jaffé, *J. Am. Chem. Soc.* **84** (1962), 540; *J. Am. Chem. Soc.* **85** (1963), 148; *Can. J. Chem.* **41** (1963), 1315; *J. Phys. Chem.* **67** (1963), 1501; *Fortschr. Chem. Forsch.* **9** (1967), 448; R. Ferreira, *Adv. Chem. Phys.* **13** (1967), 55; J. E. Huheey, *J. Phys. Chem.* **69** (1965), 3284; J. E. Huheey, *J. Phys. Chem.* **70** (1966), 285; *J. Org. Chem.* **36** (1971), 204; and references therein; G. Klopman, *J. Chem. Phys.* **43** (1965), S124; J. K. Wilmshurst, *J. Chem. Phys.* **27** (1957), 1129; A. F. Clifford, *J. Phys. Chem.* **63** (1959), 1227; R. G. Parr and R. F. Borkman, *J. Chem. Phys.* **49** (1968), 1055; R. G. Parr, R. A. Donnelly, M. Levy, and W. E. Palke, *J. Chem. Phys.* **68** (1978), 3801; A. Pasternak, *Chem. Phys.* **26** (1977), 101; and L. C. Allen, *J. Am. Chem. Soc.* **111** (1989), 9003. As pointed out by Hinze, the qualitative concept of “electronegativity” can be traced back to J. J. Berzelius.
37. A simple linear shift of the entire electronegativity scale by -0.56 (i.e., shifting F downward from its arbitrarily chosen value “4.0” on the Pauling scale to new value 3.44) would make $x_{nb}^{(N)} = 0$, the more “obvious” electronegativity of a nonexistent ligand.
38. With regard to his tabulated electronegativity values, Pauling states (note 14, p. 89) “These values are given only to one decimal place on the scale; it is my opinion that this is the limit of their reliability.”

39. As shown in Table 3.8, the actual bond angles sometimes deviate appreciably from the values predicted by Eq. (3.34), reflecting a degree of bond bending. An example is H₂Se, where the NHO hybridization ($\lambda = 7.30$) corresponds to an interhybrid angle of 97.9°, whereas the actual optimized bond angle is 91.3° (~3° bending at each Se—H bond). The deviation in this case can be attributed to the extremely flat character of the bending potential; changing the H—Se—H bond angle from 91° to 99° raises the energy by less than 1 kcal mol⁻¹.
40. H. A. Bent, *Chem. Rev.* **61** (1961), 275.
41. C. A. Coulson and W. E. Moffitt, *Phil. Mag.* **40** (1935), 1; and C. A. Coulson and W. E. Moffitt, *J. Chem. Phys.* **15** (1947), 151.
42. Pauling, note 14, pp. 127ff.
43. W. J. Hehre, L. Radom, P. v. R. Schleyer, and J. A. Pople, *Ab Initio Molecular Orbital Theory* (New York, Wiley, 1986), pp. 265–266.
44. Note that no constraint of the NBO algorithm biases the multiple bonds to be of sigma/pi type rather than, e.g., equivalent “banana bonds” (Pauling, note 14, p. 137) or other possible forms. (The complementary nu-bond pairs of Section 3.2.4 show that quite surprising forms of NBOs are possible.) The nearly universal appearance of NBOs having distinct sigma/pi character is therefore direct numerical evidence that the sigma/pi picture is intrinsically more accurate than that based on banana bonds. For a contrary case in which the banana-bond description is more accurate, see Section 3.4.1 (vinylamine).
45. For example, the MO ϕ_3 of Eq. (3.81) is nearly equivalent to the bonding σ_{NN} NBO ($\phi_3 \simeq 0.941\sigma_{\text{NN}} + \dots$).
46. Usually this notation will not conflict with the other common use of “*”, i.e., to denote an out-of-phase two-center orbital (σ_{AB}^* , etc.), because such “antibonds” are indeed the unfilled orbitals in donor–acceptor interactions.
47. F. Hund, *Z. Phys.* **33** (1925), 345.
48. The ¹CA and promoted configurations are of course exactly degenerate in the limit $\lambda \rightarrow 0$ of weak hybridization.
49. E. A. Ballik and N. F. Ramsey, *Astrophys. J.* **137** (1963), 84.
50. The stable “singlet” solution is found to have $\langle \hat{S}^2 \rangle = 1.0315$, which is indicative of severe spin contamination from states of higher multiplicity. The accuracy of the NBO Lewis description is low ($\rho_{\text{L}} = 98.19\%$) and strong symmetry loss is evident in MOs and NBOs.
51. Pauling, note 14, pp. 352ff.
52. See Jensen, note 18.
53. A. E. Reed and P. v. R. Schleyer, *J. Am. Chem. Soc.* **112** (1990), 1434.
54. D. B. Chestnut, *J. Am. Chem. Soc.* **120** (1998), 10 504.
55. The average sigma-hybridization is sp², but the hybrid toward B is considerably richer in s character (~sp^{1.1}) than are those toward H, in accordance with Bent’s rule.
56. A. E. Reed and F. Weinhold, *J. Chem. Phys.* **83** (1985), 1736.
57. Even for benzene, conjugative effects are found to be an intrinsically small correction ($E^{(\text{L})}(\%) = 99.71$, $\rho^{(\text{L})}(\%) = 97.03$), so a localized $\Psi^{(\text{L})}$ forms a suitable perturbative starting point for describing aromatic conjugation. That is, benzene is certainly *not* “a completely delocalized molecule.”
58. Faraday first extracted benzene (which he called “bicarbonate of hydrogen”) from distillates of whale and codfish oil obtained from Sir Walter Scott, the writer; see M. Miller, *Michael Faraday and the Dynamo* (Philadelphia, Clinton Book Co., 1968), p. 124.
59. Note that a comprehensive mesomeric theory of aromatic structure and reactivity was developed by Robinson, Ingold, and others in the years preceding the quantal resonance formulation of Pauling and Wheland.
60. E. Hückel, *Z. Phys.* **70** (1931), 204; E. Hückel, *Z. Phys.* **76** (1932), 628.
61. $E_{\text{L}}^{(\pi)}$ is obtained by a \$DEL keylist (a standard option of the NBO program) that deletes the possible π – π^* interaction elements from the density matrix and recalculates the SCF energy in the absence of such interactions. For all model \$DEL calculations described in this section we employed the simpler RHF/6-31 + G* level of theory.
62. For both C₆H₆ and C₅H₅ models the ring angles are held constant (at 120° and 108°, respectively), and the C—C bond lengths R of the high-symmetry species are replaced by

partial “single” bonds ($R_s = R + \frac{1}{2} \Delta R$) and “double” bonds ($R_d = R - \frac{1}{2} \Delta R$), differing by the variable distortion variable ΔR .

63. The four leading NRT structures are of approximately equal weighting (17.9%). As seen in Table 3.21, the C—C bond orders are in the range 1.46–1.49 and the N—O bond order is 1.51, which is indicative of strong delocalization in the nitro group as well as in the ring.
64. A. Streitwieser, *Molecular Orbital Theory for Organic Chemists* (New York, Wiley, 1961).
65. A. A. Frost and B. Musulin, *J. Chem. Phys.* **21** (1953), 572.
66. F. A. Cotton, *Chemical Applications of Group Theory* (New York, Wiley, 1963), pp. 125ff.
67. Experimental estimates of $-\beta$ range from 17–20 kcal mol⁻¹ (the “thermochemical value”) to more than 100 kcal mol⁻¹ (“spectroscopic values”). See, e.g., R. S. Mulliken and R. G. Parr, *J. Chem. Phys.* **19** (1951), 1271; and J. R. Platt, *J. Chem. Phys.* **15** (1947), 419.
68. R. S. Mulliken, *J. Chem. Phys.* **7** (1939), 339; and R. S. Mulliken, C. A. Rieke, and W. G. Brown, *J. Am. Chem. Soc.* **63** (1941), 41. A harsh criticism of the hyperconjugation concept and its applications was presented by M. J. S. Dewar, *Hyperconjugation* (New York, Ronald Press Co., 1962). For more modern assessments of hyperconjugative phenomena, see, e.g., U. Salzner and P. v. R. Schleyer, *J. Am. Chem. Soc.* **115** (1993), 10 231; D. Suarez, T. L. Sordo, and J. A. Sordo, *J. Am. Chem. Soc.* **118** (1993), 9850; E. D. Glendening and A. Streitwieser Jr., *J. Chem. Phys.* **100** (1994), 2900; and C. J. Cramer, *J. Mol. Struct. (Theochem)* **370** (1996), 135.
69. See Mulliken, note 68; C. A. Coulson and V. Crawford, *J. Chem. Soc.* **1953** (1953), 2052; and A. Loftus, *J. Am. Chem. Soc.* **79** (1957), 24.
70. E. B. Wilson Jr., *Adv. Chem. Phys.* **2** (1959), 367.
71. T. K. Brunck and F. Weinhold, *J. Am. Chem. Soc.* **101** (1979), 1700. Compare with A. Gavezzotti and L. S. Bartell, *J. Am. Chem. Soc.* **101** (1979), 5142; and A. E. Reed and F. Weinhold, *Isr. J. Chem.* **31** (1991), 277.
72. R. M. Pitzer and W. N. Lipscomb, *J. Chem. Phys.* **39** (1963), 1995; and W. J. Orville-Thomas, *Internal Rotation in Molecules* (New York, Wiley, 1974), pp. 1–18.
73. L. C. Allen, *Theor. Chim. Acta* **24** (1972), 117.
74. Note that Fig. 3.55 is the more exact counterpart of Fig. 4 in Brunck and Weinhold, note 71. Note also that the full potential barrier includes contributions from *gauche*-type interactions at other dihedral angles. In this context, it is interesting that an idealized cosine-like dependence of the $\sigma_{CC}-\sigma_{CH^*}$ overlap (or Fock-matrix element), namely

$$S_{\sigma\sigma^*}(\theta) = A \cos \theta + B$$

would lead to *no* net torsional dependence when summed over all vicinal interactions of a model three-fold rotor. Thus, the fact that the correct angular dependence of torsional stabilization is obtained when all vicinal $\sigma-\sigma^*$ contributions are included (cf. Fig. 3.56) also reflects the fact that the full NBO overlap curve $S_{\sigma\sigma^*}(\theta)$ is *not* simply cosine-like.

75. L. Goodman and H. Gu, *J. Chem. Phys.* **109** (1998), 72; and L. Goodman, H. Gu, and V. Pophristic, *J. Chem. Phys.* **110** (1999), 4268.
76. C. A. Coulson, *Mol. Phys.* **15** (1968), 317.
77. R. F. Hudson, *Angew. Chem., Int. Edn.* **12** (1973), 36; and M. J. S. Dewar and R. C. Dougherty, *The PMO Theory of Organic Chemistry* (New York, Plenum Press, 1975).
78. See, e.g., I. Fleming, *Frontier Orbitals and Organic Chemical Reactions* (New York, Wiley, 1976), pp. 24–27; and T. A. Albright, J. K. Burdett, and M. H. Whangbo, *Orbital Interactions in Chemistry* (New York, Wiley, 1985).
79. This statement follows immediately from the elementary theorem that the eigenfunctions of a Hermitian operator are (or can be taken to be) mutually orthogonal.
80. Note that the choice of non-orthogonal versus orthogonal basis functions has no consequence for the numerical *variational* solutions (cf. Coulson’s treatment of He₂, note 76), but it undermines the possibility of physical “interpretation” in perturbative terms. While a proper Rayleigh–Schrödinger perturbative treatment of the He ··· He interaction can be envisioned, it would not simply truncate at second order as assumed in the PMO analysis of Fig. 3.58. Note also that alternative “perturbation-theory” formulations that make no reference to an

unperturbed $\hat{H}^{(0)}$ can be effective numerical approximation techniques, but they are not “interpretable” in the physical sense of the Rayleigh–Schrödinger formulation.

81. F. Weinhold, *Angew. Chem. Int. Edn.* **42** (2003), 4188.
82. F. Weinhold and J. E. Carpenter, *J. Mol. Struct. (Theochem)* **165** (1988), 189.
83. N. D. Epiotis, *J. Am. Chem. Soc.* **95** (1973), 3087. The original explanation involved the interaction of an out-of-phase combination of fluorine lone pairs with σ_{CC}^* or π_{CC}^* antibonds, but deletion of the latter orbitals is found to have little influence on the *cis* preference.
84. Note that the vicinal $\sigma_{CH}-\sigma_{CH}^*$ stabilization is significantly stronger than that in ethane (Table 3.23), due to the significantly shorter C–C double-bond distance.
85. S. Wolfe, *Acc. Chem. Res.* **5** (1972), 102.
86. A. J. Kirby, *The Anomeric Effect and Related Stereoelectronic Effects at Oxygen* (Berlin, Springer, 1983); G. R. J. Thatcher (ed.), *The Anomeric Effect and Associated Stereoelectronic Effects* (Washington, American Chemical Society, 1993); and E. Juaristi and G. Guevas, *The Anomeric Effect* (Boca Raton, FL, CRC Press, 1994).
87. C. Romers, C. Altona, H. R. Buys, and E. Havinga, *Topics Stereochem.* **4** (1969), 39.
88. C. Scott and F. Grein, *Can. J. Chem.* **72** (1994), 2521.
89. The peroxides are infamously difficult species with severely bent bonds, requiring multiple polarization functions to describe the non-cylindrical character of the bonding. For these species we therefore employed the higher B3LYP/6-311++G(3d,2p) level of theory, with three full polarization sets on each heavy atom and two on hydrogen.
90. Recall that ϕ was defined with respect to the bisector of the H—N—H group. Thus, the formal lp—N—C—F dihedral angle differs from ϕ by 180° .
91. P. A. Petillo and L. E. Lerner, in G. R. J. Thatcher (ed.), *The Anomeric Effect and Associated Stereoelectronic Effects* (Washington American Chemical Society, 1993), pp. 156–175. See also U. Salzner and P. v. R. Schleyer, *J. Org. Chem.* **59** (1994), 2138; and note 88.
92. The small amount of charge transferred in a $\sigma_{AB}-\sigma_{CD}^*$ interaction (about 1% of an electron) is typically a small relative change of occupancy in σ_{AB} , and thus has little effect on the A—B length, but it is a large relative change in σ_{CD}^* antibond occupancy, and thus has a relatively strong effect in lengthening C—D. Any tendency to lengthen donor A—B length is also opposed by the general tendency to maximize σ_{AB} amplitude near the axial atom B. Hence, lengthening of the acceptor C—D bond is generally the most pronounced geometrical effect of strong $\sigma_{AB}-\sigma_{CD}^*$ charge transfer. (Of course, in the $\text{NH}_2\text{CH}_2\text{F}$ example the one-center n_N serves as donor, so there is no A—B “donor bond” to be affected in this case.)
93. T. Nishikawa, T. Itoh, and K. Shimoda, *J. Chem. Phys.* **23** (1955), 1735; and D. R. Lide Jr., *J. Chem. Phys.* **27** (1957), 343.
94. L. M. Pierce and M. Hayashi, *J. Chem. Phys.* **35** (1961), 479.
95. D. C. McKean and I. A. Ellis, *J. Mol. Struct.* **29** (1975), 81.
96. The general role of σ_{CH}^* orbitals and hyperconjugative interactions in methyl tilting was suggested much earlier on qualitative grounds: H. P. Hamlow, S. Okuda, and N. Nakagawa, *Tetrahedron Lett.* **1964** (1964), 2553; and note 141.
97. P. Deslongchamps, *Stereoelectronic Effects in Organic Chemistry* (New York, Pergamon, 1983); P. J. Wagner and B. J. Scheve, *J. Am. Chem. Soc.* **99** (1977), 1858; G. Doddi and G. Ercolani, *J. Org. Chem.* **57** (1992), 4431; and A. L. J. Beckwith and P. J. Duggan, *Tetrahedron* **54** (1998), 6919.
98. The corresponding hyperconjugative interactions in an open-shell singlet description of radical dissociation would similarly promote homolytic bond cleavage.
99. R. Hoffmann, *Acc. Chem. Res.* **4** (1971), 1.
100. G. L. Closs and J. R. Miller, *Science* **240** (1988), 440; N. J. Turro and J. K. Barton, *J. Biol. Inorg. Chem.* **3** (1998), 201; M. Ratner, *Nature* **397** (1999), 480; and B. Giese, *Acc. Chem. Res.* **33** (2000), 631.
101. T. K. Brunck and F. Weinhold, *J. Am. Chem. Soc.* **98** (1976), 3745.
102. K. D. Jordan and M. N. Paddon-Row, *Chem. Rev.* **92** (1992), 395; M. N. Paddon-Row and K. D. Jordan, *J. Am. Chem. Soc.* **115** (1993), 2952; C. Liang and M. D. Newton, *J. Phys. Chem.* **97** (1993), 3199; C. A. Naleway, L. A. Curtiss, and J. R. Miller, *J. Phys. Chem.* **97** (1993), 4050, and references therein.

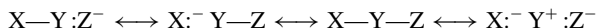
103. H. M. McConnell, *J. Chem. Phys.* **35** (1961), 508.
104. K. D. Jordan and M. N. Paddon-Row, "Electron transfer" in P. v. R. Schleyer (ed.), *Encyclopedia of Computational Chemistry*, Vol. 2 (Chichester, Wiley, 1998), pp. 826–835.
105. J. E. Anderson, A. J. Blockworth, J. Q. Cai, A. G. Davies, and N. A. Tallant, *J. Chem. Soc., Chem. Commun.* **1992** (1992), 1689; and J. E. Anderson, J. Q. Cai, and A. G. Davies, *J. Chem. Soc., Perkin Trans.* **2** (1993), 2633.
106. C. Djerassi, *Optical Rotatory Dispersion: Applications to Organic Chemistry* (New York, McGraw-Hill, 1960); L. Velluz, M. Legrand, and M. Grosjean, *Optical Circular Dichroism, Principles, Measurements, and Applications* (Weinheim, Verlag Chemie, 1965); and G. Snatzke (ed.), *Optical Rotatory Dispersion and Circular Dichroism in Organic Chemistry* (London, Heyden & Son, 1967).
107. L. Rosenfeld, *Z. Phys.* **52** (1928), 161.
108. W. J. Kauzmann, J. E. Walter, and H. Eyring, *Chem. Rev.* **26** (1940), 339; and S. F. Mason, *Mol. Phys.* **5** (1962), 343.
109. W. Moffit, R. B. Woodward, A. Moscovitz, W. Klyne, and C. Djerassi, *J. Am. Chem. Soc.* **83** (1961), 4013.
110. J. P. Jennings, W. Klyne, and P. M. Scopes, *Proc. Chem. Soc.* **1964** (1964), 412.
111. The completely ionic resonance structure in the lower-right-hand panel of Fig. 3.78 might also be depicted as



with high ionic character of the A—C bond.

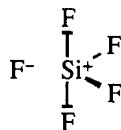
112. M. J. S. Dewar, *J. Am. Chem. Soc.* **106** (1984), 669.
113. R. S. Grev and H. F. Schaefer, *J. Am. Chem. Soc.* **109** (1987) 6569; and note 121.
114. These include MINDO, MNDO, AM1, PM3, and related methods developed by M. J. S. Dewar's group. It should also be noted that such ZDO-based schemes commonly underestimate the vicinal hyperconjugative effects (thereby compensating for neglected two-electron exchange integrals that correspondingly underestimate steric repulsions; see J. Tyrell, R. B. Weinstock, and F. Weinhold, *Int. J. Quant. Chem.* **19** [1981], 781).
115. E. D. Glendenning, unpublished Ph.D. Thesis, University of Wisconsin, Madison (1991).
116. When $F_{\text{gem}}(\theta)$ crosses from positive to negative values at a nodal angle $\theta = \theta_0$, the geminal stabilization (3.174) necessarily vanishes. At lower levels of theory (e.g., RHF/6-31G*), the entire $F_{\text{gem}}(\theta)$ curve for cyclopropane is shifted upward to give such a nodal crossing near $\theta_0 \simeq 70^\circ$. Although the details of the behavior near $F_{\text{gem}}(\theta) \simeq 0$ have little effect on the potential-energy-surface features of greatest interest, it is apparent from the many delicate cancellations entering F_{gem} that geminal delocalization effects (as reflected, e.g., in 2J spin-coupling constants) exhibit unusual sensitivity to theoretical level.
117. For interesting accounts of early developments in the chemistry of small rings and the work of A. Baeyer, see W. H. Perkin, *J. Chem. Soc.* **1929** (1929), 1347; and R. Huisgen, *Angew. Chem. Int. Edn. Engl.* **25** (1986), 297.
118. H. Markownikoff and A. Krestownikoff, *Ann. Chem.* **208** (1881), 333; A. Freund, *Monatsh. Chem.* **3** (1882), 625; W. H. Perkin, *Ber. Deutsch. Chem. Ges.* **16** (1883), 1787; *Ber. Deutsch. Chem. Ges.* **17** (1884), 54.
119. A. Baeyer, *Ber. Deutsch. Chem. Ges.* **18** (1885), 2269.
120. J. W. Knowlton and F. D. Rossini, *J. Res. Natl. Bur. Standards* **43** (1949), 113; J. Coops and S. J. Kaarsemaker, *Rec. Trav. Chim.* **69** (1950), 1364; S. J. Kaarsemaker and J. Coops, *Rec. Trav. Chim.* **71** (1952), 261; and J. D. Cox and G. Pilcher, *Thermochemistry of Organic and Organometallic Compounds* (London, Academic Press, 1970).
121. P. v. R. Schleyer, in H. G. Viehe, R. Janusek, and R. Merenyi (eds.), *Substituent Effects in Radical Chemistry* (Dordrecht, Reidel, 1986), pp. 69–81.
122. P. George, M. Trachtman, C. W. Bock, and A. M. Brett, *Tetrahedron* **32** (1976), 317.
123. J. D. Dill, A. Greenberg, and J. F. Liebman, *J. Am. Chem. Soc.* **101** (1979), 6814; see also note 121.
124. C. A. Coulson and W. E. Moffitt, *Phil. Mag.* **40** (1949), 1.

125. Cremer and Gauss (note 127), Schleyer (note 121), and Glendening (note 115) have estimated the differential rehybridization stabilization of cyclopropane over cyclobutane as 3, 10, and 18 kcal mol⁻¹, respectively.
126. Cremer (note 131), Schleyer (note 121), and Glendening (note 115) have estimated the differential torsional stabilization of cyclopropane over cyclobutane as 12.4, 12, and 11.6 kcal mol⁻¹, respectively.
127. D. Cremer and J. Gauss, *J. Am. Chem. Soc.* **108** (1986), 7467.
128. M. J. S. Dewar and G. P. Ford, *J. Am. Chem. Soc.* **101** (1979), 783, and references therein.
129. As noted above (note 111), geminal NBO delocalizations may be associated with alternative resonance structures related to (3.181). Hence, this structure might better be considered to depict geminal hyperconjugative corrections to the classical single-bonded Lewis structure.
130. R. F. W. Bader, T. S. Slee, D. Cremer, and E. Kraka, *J. Am. Chem. Soc.* **105** (1983), 5061; and R. F. W. Bader, *Acc. Chem. Res.* **18** (1985), 9.
131. D. Cremer, *Tetrahedron* **44** (1988), 7427.
132. J. Musher, *Angew. Chem. Int. Edn.* **8** (1969), 54; and J. L. Musher, *J. Am. Chem. Soc.* **94** (1972), 1370.
133. C. A. Coulson, *J. Chem. Soc.* **1964** (1964), 1442. For early applications of the ionic-resonance model to transition-metal complexes, see M. M. Yakshin, *Compt. Rend. (Dokl.) Acad. Sci. U.R.S.S.* **32** (1941), 555; and Y. K. Syrkin, *Bull. Acad. Sci. U.R.S.S., Classe Sci. Chim.* **1948** (1948), 69.
134. W. Kutzelnigg, *Angew. Chem. Int. Edn. Engl.* **23** (1984), 272.
135. E. Magnusson, *J. Am. Chem. Soc.* **112** (1990), 7940; and note 136.
136. A. E. Reed and F. Weinhold, *J. Am. Chem. Soc.* **108** (1986), 3586.
137. G. C. Pimentel, *J. Chem. Phys.* **19** (1951), 446. Related MO concepts were presented by R. E. Rundle, *J. Chem. Phys.* **17** (1941), 671; R. E. Rundle, *J. Am. Chem. Soc.* **69** (1947), 1327 and 2075; and R. E. Rundle, *Rec. Chem. Prog.* **23** (1962), 194.
138. The symbol “ ω ,” when used to denote a 3c/4e triad (e.g., ω_{ABC}), bond orbital (e.g., $\omega_{AB:C}$) or ligand label (e.g., F_ω), is unlikely to be confused with other common usages such as angular frequency. Its shape has three points and two connecting arcs to suggest three-center character with two connecting electron pairs.
139. N. D. Epiotis, *Deciphering the Chemical Code* (New York, VCH Publishers, 1996).
140. O. Hassell, “Structural Aspects of Interatomic Charge-Transfer Bonding,” *Nobel Lectures: Chemistry 1963–1970* (New York, Elsevier, 1972), pp. 295–331.
141. H. A. Bent, *Chem. Rev.* **68** (1968), 587.
142. A numerical difficulty of the NRT description of the species in Table 3.30 is that the four specified resonance structures



may lead to a type of linear dependence in which the resonance weightings become ill-determined. This indeterminacy arises because each bond of an NRT resonance structure may be arbitrarily *polarized* (i.e., only a single resonance structure is used to describe “covalent–ionic resonance”; Section 1.6) so that, e.g., the single X–Y–Z Lewis structure becomes arbitrarily similar to any of the other three resonance structures. Replacement of X:–Y–Z and X–Y:Z– structures by X–Y–Z and X:–Y+ :Z– structures (as in the most highly ionic FCIF⁻, FClCl⁻, FHF⁻, and HLiH⁻ species) increases the apparent ionic and total valency, but has little effect on covalency.

143. Of course, at a higher level of detail there may also be significant ionic resonance contributions involving *equatorial* ligands. In SiF₅⁻, for example, such contributions correspond to resonance structures of the form



with associated partial ω -bonding among the equatorial F—Si—F triads. While the 120° equilibrium angles render the equatorial $n_F \rightarrow \sigma_{SiF}^*$ interactions somewhat weaker than those corresponding to the optimal 180° axial alignment, the distinction between ω bonds and σ bonds (like that between axial and equatorial) becomes blurred as the bond angles are deformed from ideal trigonal pyramidal values, particularly along a reaction coordinate for axial–equatorial exchange.

144. N. V. Sidgwick and H. M. Powell, *Proc. Roy. Soc.* **A176** (1940), 153; R. J. Gillespie and R. S. Nyholm, *Q. Rev. Chem. Soc.* **11** (1957), 239; and R. J. Gillespie and I. Hargittai, *The VSEPR Model of Molecular Geometry* (Boston, MA, Allyn and Bacon, 1991).
145. N. Bartlett, *Proc. Chem. Soc.* **1962** (1962), 218; N. Bartlett, *Endeavor* **88** (1963), 3; C. L. Chernick, H. H. Claassen, P. R. Fields *et al.*, *Science* **138** (1962), 136; H. H. Claassen, H. Selig, and J. G. Malm, *J. Am. Chem. Soc.* **84** (1962), 3593; and J. L. Weeks, C. L. Chernick, and M. S. Matheson, *J. Am. Chem. Soc.* **84** (1962), 4612.
146. H. H. Hyman (ed.), *Noble-Gas Compounds* (Chicago, IL, University of Chicago Press, 1963).
147. As remarked in Sections 2.3 and 3.2.3, hybridization occurs only in response to chemical bonding. The rare-gas lone pairs are orthogonal to the axes of bonding, hence they remain in unhybridized AOs.
148. L. Pauling, *Proc. Natl. Acad. Sci. U.S.A.* **72** (1975), 4200. As representative examples of recent freshman chemistry textbooks, see D. D. Ebbing and S. D. Gammon, *General Chemistry*, 6th edn. (Boston, Houghton Mifflin, 1999), p. 376; L. Jones and P. Atkins, *Chemistry: Molecules, Matter, and Change*, 4th edn. (New York, W. H. Freeman, 2000), p. 347; and S. S. Zumdahl, *Chemistry*, 5th edn. (Boston, Houghton Mifflin, 2000), p. 389.
149. L. Suidan, J. K. Badenhoop, E. D. Glendening, and F. Weinhold, *J. Chem. Ed.* **72** (1995), 583.
150. W. H. Eberhardt, B. L. Crawford Jr., and W. N. Lipscomb, *J. Chem. Phys.* **22** (1954), 989.
151. W. Dilthey, *Z. Angew. Chem.* **34** (1921), 596.
152. H. C. Longuet-Higgins and R. P. Bell, *J. Chem. Soc.* **1943** (1943), 250; R. P. Bell and H. C. Longuet-Higgins, *Proc. Roy. Soc. London* **A183** (1945), 357; K. S. Pitzer, *J. Am. Chem. Soc.* **67** (1946), 1126; R. S. Mulliken, *Chem. Rev.* **41** (1947), 207; and A. D. Walsh, *J. Chem. Soc.* **1947** (1947), 89.
153. W. C. Price, *J. Chem. Phys.* **15** (1947), 614.
154. W. N. Lipscomb, *Boron Hydrides* (New York, W. A. Benjamin, 1963).
155. K. Wade, *Electron Deficient Compounds, Studies in Modern Chemistry* (London, T. Nelson & Sons, 1971); D. M. P. Mingos, *Acc. Chem. Res.* **17** (1984), 311; and B. K. Teo, H. Zhang, and X. Shi, *Inorg. Chem.* **29** (1990), 2083.
156. K. S. Pitzer and H. S. Gutowsky, *J. Am. Chem. Soc.* **68** (1946), 2204.
157. A. Stock, *Hydrides of Boron and Silicon* (New York, Cornell University Press, 1933).
158. The accuracy of alternative Lewis structures can be assessed by specifying the number and locations of lone pairs and two- and three-center bonds with a \$CHOOSE keylist (a standard option of the NBO program). (The directed \$CHOOSE list replaces the usual NBO search over all possible Lewis structures, but the hybrids and polarization coefficients of \$CHOOSE structures are optimized in the usual way.) The increased non-Lewis density measures the larger error of the \$CHOOSE structure compared with the optimal NBO structure.
159. In the case of many resonance structures of low weighting, for which no dominant “reference” structures can be found by the automatic NRT algorithm, the search for reference structures must be carried out iteratively with an \$NRTSTR keylist, a standard NBO/NRT program option (with syntax similar to a \$CHOOSE keylist) that allows the user to specify reference structures “manually.” Leading NRT structures of an initial pass are input as \$NRTSTR structures for the subsequent pass in an attempt to find a consistent set of reference structures of highest final weighting. Even if this procedure fails to converge to a unique reference set, the NRT bond orders are seen to reach limiting values that are sensibly independent of the chosen reference set (particularly when averaged over symmetry-equivalent bonds). The numerical uncertainties of this procedure are roughly indicated by the reduced precision of entries in Table 3.41(c).
160. W. N. Lipscomb, *Acc. Chem. Res.* **8** (1973), 257.
161. For example, the $C_2B_4H_8$ bond lengths $B_1—B_2$ (1.777 Å), $B_1—B_3$ (1.736 Å), $B_1—C_4$ (1.727 Å), $B_2—B_3$ (1.874 Å), $B_3—C_4$ (1.641 Å), and $C_4—C_5$ (1.491 Å) may be compared with

- corresponding B_6H_{10} values in Table 3.38. The $C_2B_4H_8$ atomic charges for B_1 (-0.077), B_2 (-0.194), B_3 ($+0.008$), and C_4 (-0.369) may be compared with those for B_6H_{10} in Table 3.40.
162. R. G. Adler and M. F. Hawthorne, *J. Am. Chem. Soc.* **92** (1970), 6174; J. A. Long, T. B. Marder, and M. F. Hawthorne, *J. Am. Chem. Soc.* **106** (1984), 3004.
163. Individual dicarbollide bond lengths: 1.7504 Å (7—8, 8—9), 1.6238 Å (9—10, 7—11), 1.5438 Å (10—11). Bond angles: 102.9° (7—8—9), 106.9° (8—9—10, 11—7—8), 111.6° (9—10—11, 10—11—7).
164. Individual dicarbollide rim atomic charges: -0.0841 (7, 9), -0.3387 (8), -0.5764 (10, 11).

4

Molecular bonding in the d-block elements

4.1 Introduction

Given the power of the concept of covalency and the deeper electronic implications that were realized by G. N. Lewis's octet-rule and shared-electron-pair concepts, it is natural to wonder whether these advances are limited to s/p-block elements or apply to the entire periodic table.

Soon after the quantum revolution of the mid 1920s, Linus Pauling and John C. Slater expanded Lewis's localized electronic-structural concepts with the introduction of directed covalency in which bond directionality was achieved by the hybridization of atomic orbitals.¹ For normal and hypovalent molecules, Pauling and Slater proposed that sp^n hybrid orbitals are involved in forming shared-electron-pair bonds. Time has proven this proposal to be remarkably robust, as has been demonstrated by many examples in Chapter 3.

Hypervalent main-group compounds and most transition-metal complexes do not conform to Lewis's octet rule, because they exceed the ideal eight-electron count. Pauling² first addressed this issue for main-group compounds by expanding the available valency of second- and higher-row elements by the addition of valence d orbitals to the set of orbitals that are active in bond formation. By using $sp^n d^m$ hybrid orbitals to form directed covalent bonds and by considering the strong role of resonance among ionic normal-valent structures, Pauling was able to rationalize a large number of hypervalent structures from the p block of the periodic table. However, as we have seen in Section 3.5, modern quantum-mechanical analyses of electron-density distributions downplay the importance of $sp^n d^m$ hybridization in hypervalent p-block compounds, emphasizing instead the importance of ionic resonance and $3c/4e$ bonding interactions.

Pauling further extended the $sp^n d^m$ hybridization approach to the d-block compounds.³ By varying the relative importance of p and d orbitals, Pauling was able to construct hybrid orbitals that rationalized the geometries and magnetic properties of many transition-metal coordination complexes. For example, the square-planar

geometry and diamagnetism exhibited by “d⁸” transition-metal complexes such as PtCl₄²⁻ could be rationalized by making four equivalent σ_{PtCl} electron-pair bonds with sp²d hybrid orbitals at Pt. The eight remaining valence electrons fully occupy the four remaining pure d orbitals on the metal atom, resulting in a diamagnetic (singlet) spin state.

Because the low-energy electronic configurations of d-block elements and their +1 ions are invariably of sd^m form (see Table 2.2, Section 2.8), it is clear that both s and d orbitals will be involved in bond formation at transition-metal centers. What is less clear, a priori, is what role the valence p orbitals will play in bonding of the d-block elements.

This chapter, like the preceding Chapter 3, will examine a wide range of covalent and noncovalent “effects” in the bonding of d-block elements. Section 4.2 addresses the question of the appropriate Lewis-like picture for electron-pair sharing in transition-metal compounds, establishing an idealized normal-valent paradigm for transition-metal bonding. In Section 4.3 we analyze the normal-valent compounds of the d-block elements and discuss the common hybridization motifs associated with single- and multiple-bond formation and the general connections between hybrid-orbital directionality and molecular shape. The inadequacies of the simple Lewis-like picture are described in Section 4.4, with an emphasis on ionicity and donor–acceptor resonance delocalization. Stronger departures from Lewis-like structures are considered in Section 4.5, emphasizing the important role of hypervalency and 3c/4e bonding in transition-metal chemistry. The remaining sections concern a variety of topics in transition-metal bonding, including pi-bonding, hypovalency and catalytic processes, multielectron-bonding ligands, vertical periodic trends, and connections between localized and delocalized bonding models of d-block elements. Throughout this chapter we stress the close parallels to bonding and valency concepts in p-block compounds (Chapter 3), while highlighting the important differences that give rise to the richly distinctive chemistry of the d-block elements.

(A technical note. The 6-311++G** basis set employed elsewhere throughout this book is currently available only for elements H–Kr. For species of the second and third transition series, we have therefore adopted the corresponding ECP basis set of Los Alamos triple-zeta type [comparably augmented and polarized, labeled “LACV3P++**” in the *Jaguar* program system] for the numerical results reported below. However, all numerical examples were first evaluated at lower B3LYP/LANL2DZ level [with the *Gaussian* program system] and subsequently compared with the B3LYP/LACV3P++** results to verify that differences between the two levels are generally small [often affecting numerical table entries in only the third or fourth significant figure]. The close agreement between these theoretical levels gives considerable confidence that the conclusions drawn from the numerical examples are not significantly basis-sensitive.)

4.2 Lewis-like structures for the d-block elements

4.2.1 Common empirical formulas of transition-metal compounds

The development of G. N. Lewis's octet rule for the s/p-block elements was strongly influenced by the stoichiometric ratios of atoms found in the common compounds and elemental forms (CH_4 , CCl_4 , CO_2 , Cl_2 , etc.). Let us therefore begin analogously by examining the *formulas* of the common neutral binary chloride, oxide, and alkyl compounds of transition metals. (Here we substitute alkyl groups for hydrogen because only a small number of binary metal hydrides have been well characterized.)

In many instances several different compositions of the binary oxide and chloride compounds are available. In each case we designate as "most common" the particular compound that is *least expensive and available in the largest quantities* from common suppliers,⁴ as summarized in Table 4.1. Included with each entry is the number (e_u) of unpaired electrons determined from magnetic-susceptibility measurements.

From Table 4.1 a remarkably simple regularity becomes apparent. If G_M denotes the group number, n the stoichiometric ML_n coordination number, V_L the valency of the ligand, and e_u the number of unpaired electrons, one can recognize that the relationship

$$|G_M - 6| + nV_L + e_u = 6 \quad (4.1)$$

is satisfied for an overwhelming majority of common ML_n species.

If we now assume, following Lewis, that each monovalent "bond" coordination is associated with an electron *pair*, we can write the total number (e_{bp}) of valence bond-pair electrons as

$$2nV_L = e_{bp} \quad (4.2a)$$

Furthermore, for $G_M \geq 6$ the maximum possible total number (e_{lp}) of lone-pair electrons is related to G_M by

$$|G_M - 6| = \frac{1}{2}e_{lp} \quad (G_M \geq 6) \quad (4.2b)$$

Thus, for mid-to-late-d-block elements, Eq. (4.1) becomes

$$\frac{1}{2}(e_{lp} + e_{bp}) + e_u = 6 \quad (11 \geq G_M \geq 6) \quad (4.3)$$

Formula (4.3) may be compared with the analogous Lewis-like formula for p-block elements,

$$\frac{1}{2}(e_{lp} + e_{bp}) + e_u = 4 \quad (18 \geq G_M \geq 14) \quad (4.4)$$

Table 4.1. "Most common"^a ML_n compounds (L = chloride, oxide, alkyl) and number of unpaired electrons^b (e_u) for group 3–12 transition metals M; asterisks mark exceptions to Eq. (4.1)

Group	M	Chloride (e_u)	Oxide (e_u)	Alkyl (e_u)
3	Sc	ScCl ₃ (0)	Sc ₂ O ₃ (0)	—
	Y	YCl ₃ (0)	Y ₂ O ₃ (0)	—
	La	LaCl ₃ (0)	La ₂ O ₃ (0)	—
4	Ti	TiCl ₄ (0)	TiO ₂ (0)	Ti(benzyl) ₄ (0)
	Zr	ZrCl ₄ (0)	ZrO ₂ (0)	ZrMe ₄ (0)
	Hf	HfCl ₄ (0)	HfO ₂ (0)	HfMe ₄ (0)
5	V	VCl ₄ (1)	V ₂ O ₅ (0)	V(CH ₂ TMS) ₄ (1)
	Nb	NbCl ₅ (0)	Nb ₂ O ₅ (0)	NbMe ₅ (0)
	Ta	TaCl ₅ (0)	Ta ₂ O ₅ (0)	TaMe ₅ (0)
6	Cr	CrCl ₃ (3)	CrO ₃ (0)	Cr(cyclohexyl) ₄ (2)
	Mo	MoCl ₅ (1)	MoO ₃ (0)	Mo(cyclohexyl) ₄ (2)
	W	WCl ₅ (1)	WO ₃ (0)	WMe ₆ (0)
7	Mn	MnCl ₂ (5)*	MnO (5)*	Mn[C(TMS) ₃] ₂ (5)*
	Tc	TcCl ₄ (1–2)*	Tc ₂ O ₇ (?)	—
	Re	ReCl ₅ (~2)*	Re ₂ O ₇ (0)	ReMe ₆ (1)*
8	Fe	FeCl ₃ (5)*	Fe ₂ O ₃ (5)*	Fe(norbornyl) ₄ (0)
	Ru	RuCl ₃ (0)	RuO ₂ (0)	Ru(mesityl) ₄ (0)
	Os	OsCl ₃ (?)	OsO ₂ (0) ^c	Os(mesityl) ₄ (0)
9	Co	CoCl ₂ (4)*	Co ₃ O ₄ (~4)*	Co(norbornyl) ₄ (1)
	Rh	RhCl ₃ (0)	Rh ₂ O ₃ (0)	Rh(mesityl) ₃ (0)
	Ir	IrCl ₃ (0)	Ir ₂ O ₃ (0)	Ir(mesityl) ₃ (0)
10	Ni	NiCl ₂ (2)*	NiO (4)*	—
	Pd	PdCl ₂ (0)	PdO (?)	—
	Pt	PtCl ₂ (0)	PtO (?)	—
11	Cu	CuCl (0)	Cu ₂ O (0)	Cu(phenyl) (0)
	Ag	AgCl (0)	Ag ₂ O (0)	—
	Au	AuCl (0) ^d	Au ₂ O ₃ (?)	—
12	Zn	ZnCl ₂ (0)	ZnO (0)	ZnMe ₂ (0)
	Cd	CdCl ₂ (0)	CdO (0)	CdMe ₂ (0)
	Hg	HgCl ₂ (0)	HgO (0)	HgMe ₂ (0)

^a According to the cheapness/quantity criterion of note 4.

^b Inferred from magnetic-susceptibility measurements; for a review of methods, see S. K. Sur, *J. Magn. Res.* **82** (1989), 169.

^c OsO₄ (0) is comparable.

^d AuCl₃ (0) is comparable.

which, for closed-shell species ($e_u = 0$), can be written as

$$e_{\ell p} + e_{bp} = 8 \quad (18 \geq G_M \geq 14; e_u = 0) \quad (4.5)$$

the famous “rule of 8” (octet rule). Analogously for d-block elements, Eq. (4.3) can evidently be expressed as

$$e_{\ell p} + e_{bp} = 12 \quad (11 \geq G_M \geq 6; e_u = 0) \quad (4.6)$$

which may be termed the “rule of 12” (duodectet rule) for stable closed-shell transition-metal compounds. The six valence orbitals ($s + 5d$) of the d-block elements therefore appear to underlie the special stability of a Lewis-like duodectet in precisely the same manner as the four valence orbitals ($s + 3p$) of the p-block elements underlie the stability of the usual Lewis octet.

It must be emphasized that the duodectet rule (4.6) initially has no structural connotation, but is based on composition only. Indeed, the compositional regularity expressed by (4.6) encompasses both molecular species (such as the metal alkyls) and extended lattices (such as the oxides and halides) and therefore appears to transcend important structural classifications. Nevertheless, we expect (following Lewis) that such a “rule of 12” may be associated with specific electronic configurations, bond connectivities, and geometrical propensities (perhaps quite different from those of octet-rule-conforming main-group atoms) that provide a useful qualitative model of the chemical and structural properties of transition metals.

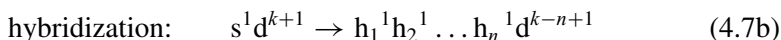
4.2.2 Configurations for localized single and multiple bonding

Following the obvious parallels with p-block hybridization and bonding, the formation of a duodectet-rule-conforming Lewis-like structural formula for an idealized ML_n transition-metal complex⁵ can be pictured as occurring in several steps.

Initially, the central M atom is “promoted” from nominal s^2d^k ground-state configuration to the effective sd^{k+1} configuration for hybridization,



Next, formation of n sigma bonds to the ligands requires formation of n equivalent sd^{n-1} bonding hybrids h_1, h_2, \dots, h_n , leaving $k + 1 - n$ unhybridized singly occupied d spin-orbitals and $9 - k + n$ unoccupied d spin-orbitals,



Finally, for the single-bonded closed-shell case the n monovalent ligands contribute n electrons for σ_{ML} bonding, and the remaining $k - n + 2$ d electrons must

suffice for double occupation of the $5 - (n - 1)$ remaining d orbitals,

$$k - n + 2 = 2[5 - (n - 1)]$$

or

$$n = 10 - k \quad (n \text{ } \sigma \text{ bonds}) \quad (4.8a)$$

This leads to the effective duodectet configuration

$$(\sigma_1)^2 \dots (\sigma_n)^2 d^{12-2n} \quad (n \text{ } \sigma \text{ bonds}) \quad (4.8b)$$

with total number of lone-pair electrons

$$e_{lp} = 12 - 2n = 2k - 8 \quad (4.8c)$$

For the alternative multi-bonded case, the multivalent ligands may be considered to contribute m additional pi-bonding electrons, where

$$m + n = 10 - k \quad (4.9a)$$

This leads to the final duodectet configuration

$$(\sigma_1)^2 \dots (\sigma_n)^2 (\pi_1)^2 \dots (\pi_m)^2 d^{12-2(n+m)} \quad (n \text{ } \sigma \text{ and } m \text{ } \pi \text{ bonds}) \quad (4.9b)$$

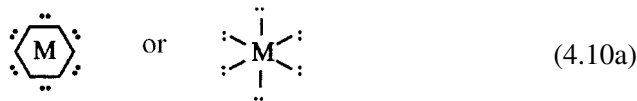
where the total number of lone-pair electrons is again

$$e_{lp} = 12 - 2(n + m) = 2k - 8 \quad (4.9c)$$

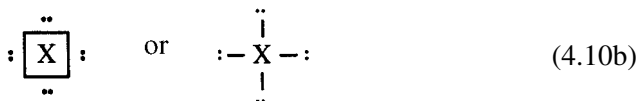
Thus, (4.9a) gives the general condition for an idealized covalently bonded closed-shell Lewis-like duodectet structure (4.9b) with no formal charge on the central metal atom. (The more general conditions for coordinative [dative] ligands and other departures from the idealized Lewis-like formula will be discussed below.)

4.2.3 Lewis-like dot diagrams for transition-metal complexes

The distribution of six electron pairs around a duodectet-rule-conforming transition-metal atom M can be represented with a hexagonally shaped “dot diagram”



analogous to the usual square dot diagram for an octet-rule-conforming main-group element X,



As specified by (4.8) and (4.9), the six valence electron pairs in (4.10a) will generally include n skeletal sigma-bond pairs, m pi-bond pairs, and $e_{lp}/2$ nonbonded pairs.

The general procedure for constructing Lewis-like diagrams for transition-metal species can best be illustrated by representative examples. From Table 4.1 one can recognize that the first transition series (Sc–Zn) includes a disproportionate number of exceptional cases compared with later series, and illustrative examples will therefore be drawn primarily from the third transition series (La–Hg). (The somewhat anomalous behavior of the first transition series and general vertical trends in the d-block elements will be discussed in Section 4.10.)

For tungsten ($k = 4$), for example,⁶ the condition (4.8a) for bonding monovalent ligands (e.g., H, alkyl) requires that $n = 10 - k = 6$, with no remaining lone pairs ($e_{lp} = 0$) according to (4.8b). The appropriate Lewis-like diagram for methyl ligands is therefore that corresponding to hexamethyltungsten (VI),



where each bond stroke denotes a shared electron pair. For divalent ligands⁷ (e.g., O), condition (4.9a) similarly requires that $n = m = (10 - k)/2 = 3$, i.e., for WO_3 (tungsten oxide)



(In each case, we omit lone pairs of the main-group ligand octet.)

Other solutions of (4.9a) can be found for mixed numbers of single and multiple bonds. These include the values $n = 4$, $m = 2$ for two single and two double bonds, for example, for molybdenyl fluoride (MoF_2O_2),



Another possible solution is that ($n = 3$, $m = 3$) corresponding to simultaneous single, double, and triple bonding,



and other possible solutions for mixed single, double, and/or triple bonds can readily be envisioned.

As an example of a late transition metal, let us consider platinum ($k = 8$), for which the only Lewis-like structure with monovalent ligands corresponds to

$n = 10 - k = 2$, $e_{\ell p} = 2k - 8 = 8$. This leads, e.g., for a methyl ligand, to the Lewis-like diagram for $\text{Pt}(\text{CH}_3)_2$,



For the divalent oxygen ligand, the only solution of (4.9) is $n = m = 1$, corresponding to



Further illustrations of such Lewis-like diagrams are given in the examples below.

4.2.4 Saturated metal complexes, oxidation states, and coordination numbers

According to (4.9c), the number of lone pairs ($n_{\ell p}$) in any duodectet-conforming Lewis-like structure is

$$n_{\ell p} = \frac{1}{2} e_{\ell p} = k - 4 \quad (4.17)$$

independent of coordination number. This immediately distinguishes cases with $k \leq 3$ (i.e., groups 3–5), which cannot satisfy (4.17). Elements of these groups can be considered⁸ to be “electron-deficient” or *hypovalent* (in the same sense as group 13 of the p-block elements; Section 3.6) and will hereafter be distinguished from the normal-valent d-block elements (groups 6–11) and the “inert” group 12:

$$\text{hypovalent:} \quad \text{groups 3–5} \quad (k = 1–3) \quad (4.18a)$$

$$\text{normal-valent:} \quad \text{groups 6–11} \quad (k = 4–9) \quad (4.18b)$$

$$\text{inert:} \quad \text{group 12} \quad (k = 10) \quad (4.18c)$$

Thus, in each series the chemistry of “early” transition metals (e.g., hypovalent Sc, Ti, V) is expected to differ appreciably from that of mid to late members (e.g., normal-valent Cr, Mn, Fe, Co, Ni, Cu) and the terminal closed-shell element (e.g., Zn).

Furthermore, according to (4.9a) the *total* number of covalent M—L bonds ($n + m$, both σ_{ML} and π_{ML}) is $10 - k$. Because main-group ligands generally are more electronegative than the central transition-metal atom, each such covalent M—L bond can be termed a formal one-electron oxidation of M. The duodectet-rule-conforming oxidation number (n_{ox}) of M is therefore

$$n_{\text{ox}} = 10 - k \quad (4.19)$$

independently of coordination number. Such formal oxidation corresponds to removing the two *s* electrons and $8 - k$ of the *d* electrons, leaving a formal “*d* count” of d^{2k-8} . According to Eq. (4.8c), the *formal d count of Lewis-like species corresponds precisely to the total number of lone-pair electrons*,

$$d \text{ count} = e_{\ell p} = 2k - 8 \quad (4.20)$$

For example, the saturated Lewis-like oxidation state of chromium ($k = 4$) is expected to be Cr(VI), with formal d^0 count, and that of nickel ($k = 8$) is Ni(II), with formal d^8 count, as in structures (4.11) and (4.16).

Finally, the favored coordination number ($n_{\text{CN}} = n$) of Lewis-like structures must satisfy (4.9a),

$$n_{\text{CN}} = 10 - k - m \quad (4.21a)$$

Highest possible coordination ($n_{\text{CN}}^{\text{max}}$) evidently corresponds to pure single bonding ($m = 0$),

$$n_{\text{CN}}^{\text{max}} = 10 - k \quad (4.21b)$$

whereas lowest possible coordination ($n_{\text{CN}}^{\text{min}}$) corresponds to triple bonding ($m = 2n$),

$$n_{\text{CN}}^{\text{min}} = (10 - k)/3 \quad (4.21c)$$

(Equations (4.21) also identify group 12 [$k = 10$] as the “inert” limit $n_{\text{CN}} = 0$; cf. (4.18c).) For example, the allowed Lewis-like coordination numbers for Cr ($k = 4$) are in the range 2–6, whereas those for Ni ($k = 8$) are restricted to the range 1–2.

Table 4.2 summarizes the Lewis-like oxidation states, *d* count, and coordination numbers for low-spin compounds of all the normal-valent transition metals. While these represent only a subset of the empirically known species, the Lewis-like

Table 4.2. *Lewis-like oxidation numbers (n_{ox}), formal d count, metal electron configuration ($e_{\ell p}$, e_{bp}) and minimum and maximum coordination numbers (n_{CN}) for low-spin normal-valent compounds of group 6–11 transition metals*

Group	k	Oxidation state		Formal <i>d</i> count	Configuration		Coordination	
		n_{ox}	Example		$e_{\ell p}$	e_{bp}	$n_{\text{CN}}^{\text{min}}$	$n_{\text{CN}}^{\text{max}}$
6	4	6	Cr(VI)	d^0	0	12	2	6
7	5	5	Mn(V)	d^2	2	10	2	5
8	6	4	Fe(IV)	d^4	4	8	2	4
9	7	3	Co(III)	d^6	6	6	1	3
10	8	2	Ni(II)	d^8	8	4	1	2
11	9	1	Cu(I)	d^{10}	10	2	1	1

compounds can be taken as a baseline for studying the many possible hypervalent and high-spin modifications of the normal-valent closed-shell parent species.

4.3 Hybridization and molecular shape

4.3.1 General hybrid orbital functions and natural bond angles

Pauling's landmark 1931 paper⁹ established the fundamental principles of the directed covalent bond:

- (1) the bond is formed through the interaction of two singly occupied orbitals, one on each atom; and
- (2) for a given singly occupied bonding orbital, the bond will tend to be formed in the direction in which the orbital amplitude is greatest.

By allowing the mathematical superposition of atomic orbitals, i.e., hybridization, as a mechanism for forming the strongest possible bonds, Pauling derived the set of equivalent and orthogonal hybrids that underlie common Lewis-structural bond patterns. The sp^3 hybrid orbitals point to the corners of a regular tetrahedron, thus providing theoretical justification for the tetrahedral geometry of methane. Similarly, sp^2 hybrids have maxima pointing to the corners of an equilateral triangle and sp hybrids have maxima pointing in opposite directions along a line. The correlation of hybridization with geometry ($sp^3 \simeq$ tetrahedral, $sp^2 \simeq$ trigonal planar, $sp \simeq$ linear) is so powerful and so ingrained in our chemical training that we frequently use hybridization to describe geometry and vice versa (cf. Section 1.6).

We now use a Pauling-like approach to show how hybrid orbitals for a variety of combinations of s, p, and d orbitals may be formulated.¹⁰ We assume that the radial dependences of the s, p, d orbitals are similar so that they can be neglected. The angular parts of the orbital wavefunctions are given by the following expressions (in the usual spherical coordinates θ, ϕ):

$$s = 1 \quad (4.22a)$$

$$p_x = 3^{1/2} \sin \theta \cos \phi \quad (4.22b)$$

$$p_y = 3^{1/2} \sin \theta \sin \phi \quad (4.22c)$$

$$p_z = 3^{1/2} \cos \theta \quad (4.22d)$$

$$d_{z^2} = 5^{1/2}/2(3 \cos^2 \theta - 1) \quad (4.22e)$$

$$d_{x^2-y^2} = (15^{1/2}/2) \sin^2 \theta \cos(2\phi) \quad (4.22f)$$

$$d_{xy} = (15^{1/2}/2) \sin^2 \theta \sin(2\phi) \quad (4.22g)$$

$$d_{xz} = 15^{1/2} \sin \theta \cos \theta \cos \phi \quad (4.22h)$$

$$d_{yz} = 15^{1/2} \sin \theta \cos \theta \sin \phi \quad (4.22i)$$

We shall now construct two “concentrated” spd hybrid orbitals that are equivalent, orthonormal, and have maximum concentration of electron density in their respective bonding directions. We can choose any arbitrary direction for the two bond hybrids that we construct. The judicious choice for the direction of the first bond hybrid is along the z axis, because only one of the five d-orbital functions (d_{z^2}) can contribute to a bond in this direction. The largest value of the angular part of the first hybrid function (i.e., the maximum concentration of electron density) along the z axis for a chosen $sp^\lambda d^\mu$ hybrid orbital h_1 is insured by choosing both the p and d components to lie along the z direction,

$$h_1 = (1 + \lambda + \mu)^{-1/2} (s + \lambda^{1/2} p_z + \mu^{1/2} d_{z^2}) \quad (4.23)$$

The maximum amplitude, $|h_1|_{\max}$, of h_1 along the bonding axis can therefore be evaluated as

$$|h_1|_{\max} = (1 + \lambda + \mu)^{-1/2} [1 + (3\lambda)^{1/2} + (5\mu)^{1/2}] \quad (4.24)$$

for chosen λ and μ . Such concentrated hybrids (with p and d components co-aligned, most focussed possible d component, and largest possible $|h_1|_{\max}$ for given λ and μ) are expected to be variationally optimal for strong covalent bonding.

Example 4.1

Let us evaluate the maximum amplitude $|h_1|_{\max}$ of h_1 for several different hybridizations. Because h_1 lies in the z direction, the maximum amplitude is found by setting $\theta = 0$ ($\phi = \text{anything}$) in the angular expressions (4.22d) and (4.22e). For a pure s orbital ($\lambda = 0, \mu = 0$), this leads to unit amplitude,

$$\text{s orbital:} \quad |h_1|_{\max} = 1$$

Similarly, a pure p hybrid orbital ($\lambda = \infty, \mu = 0$) leads to

$$\text{p orbital:} \quad |h_1|_{\max} = 3^{1/2} = 1.732$$

For an sp^1 hybrid ($\lambda = 1, \mu = 0$), the maximum amplitude is

$$\text{sp}^1 \text{ hybrid:} \quad |h_1|_{\max} = 2^{-1/2} (1 + 3^{1/2}) = 1.932$$

showing that such a hybrid has more concentration of electron density in the z direction than does either a pure s or a p_z orbital. The sp^3 hybrid ($\lambda = 3, \mu = 0$) has a still greater value,

$$\text{sp}^3 \text{ hybrid:} \quad |h_1|_{\max} = 4^{-1/2} (1 + 3^{1/2} 3^{1/2}) = 2.000$$

and it can easily be shown that an sp^3 hybrid has the greatest possible concentration of electron density of any sp^λ hybrid (no d character).

Example 4.2

Problem: Show that the maximum possible hybrid amplitude is $|h_1|_{\max} = 3.000$, corresponding to sp^3d^5 hybridization.

Solution: The mathematical requirement for maximization of $|h_1|_{\max}$, Eq. (4.24), is expressed by the partial derivative conditions

$$\left(\frac{\partial |h_1|_{\max}}{\partial \lambda}\right)_{\mu} = \left(\frac{\partial |h_1|_{\max}}{\partial \mu}\right)_{\lambda} = 0$$

which lead to the equations

$$(3/\lambda)^{1/2} = (5/\mu)^{1/2} = \frac{1 + (3\lambda)^{1/2} + (5\mu)^{1/2}}{1 + \lambda + \mu}$$

The first equality above requires that

$$\mu = 5\lambda/3$$

and the remaining equality then becomes

$$(1 + 8\lambda/3)(3/\lambda)^{1/2} = 1 + (3\lambda)^{1/2} + 5(\lambda/3)^{1/2}$$

One can readily show (by multiplying both sides by $(\lambda/3)^{1/2}$) that the only solution of this equation is $\lambda = 3$. This in turn implies that $\mu = 5\lambda/3 = 5$, corresponding to sp^3d^5 hybridization. Substituting these optimal values into (4.23) leads finally to the maximum possible hybrid amplitude

$$|h_1|_{\max} = 3 \quad (\lambda = 3, \mu = 5)$$

Let us now choose to locate a second equivalent, though not necessarily orthogonal, hybrid orbital h_2 in the $x-z$ plane. The axis of h_2 will be chosen to make the angle α with the axis of h_1 . In order for h_1 and h_2 to be equivalent, the values of the angular parts of the hybrids must be identical in their respective directions. This condition is satisfied for any separation angle α by the following expression for h_2 :

$$h_2 = (1 + \lambda + \mu)^{-1/2} \left[s + \lambda^{1/2}(\cos \alpha p_z + \sin \alpha p_x) + \mu^{1/2} \left(\frac{3 \cos^2 \alpha - 1}{2} d_{z^2} + \frac{3^{1/2} \sin^2 \alpha}{2} d_{x^2-y^2} + 3^{1/2} \sin \alpha \cos \alpha d_{xz} \right) \right] \quad (4.25)$$

(The equation for h_2 can be derived by re-expressing h_1 in a rotated coordinate system, then relating the rotated p and d functions back to those in the original coordinate system.) For h_2 the spherical coordinates have the values $\theta = \alpha$, $\phi = 0$

in the direction of maximum amplitude. With these substitutions, $|h_2|_{\max}$ can be verified to be identical to $|h_1|_{\max}$, Eq. (4.24), for any angle α .

We now have two normalized, equivalent hybrid orbitals, one directed along the z axis and the other making an angle of α with the first. However, these orbitals are not necessarily orthogonal to each other for arbitrary α . The allowed hybrid angles α are those for which the overlap integral $\langle h_1|h_2 \rangle$ vanishes

$$\langle h_1|h_2 \rangle = \frac{1 + \lambda \cos \alpha + \mu \frac{3 \cos^2 \alpha - 1}{2}}{1 + \lambda + \mu} \quad (4.26a)$$

which is equivalent to the condition

$$\frac{3\mu}{2} \cos^2 \alpha + \lambda \cos \alpha + (1 - \mu/2) = 0 \quad (4.26b)$$

The quadratic equation (4.26b) can be readily solved for $\cos \alpha$ to give

$$\cos \alpha = \frac{-\lambda \pm [\lambda^2 - 3\mu(2 - \mu)]^{1/2}}{3\mu} \quad (4.27)$$

Equation (4.27) defines the “natural” bond angles α appropriate for concentrated, equivalent $sp^\lambda d^\mu$ bonding hybrids of chosen λ and μ .¹¹

For the more general case of *inequivalent* spd hybrids, the expressions have to be modified to allow for different hybridization parameters on the two hybrids, namely λ_1 and μ_1 for h_1 and λ_2 and μ_2 for h_2 . The general $\langle h_1|h_2 \rangle$ overlap integral now takes the form

$$\langle h_1|h_2 \rangle = \frac{1 + (\lambda_1 \lambda_2)^{1/2} \cos \alpha + (\mu_1 \mu_2)^{1/2} (3 \cos^2 \alpha - 1)/2}{[(1 + \lambda_1 + \mu_1)(1 + \lambda_2 + \mu_2)]^{1/2}} \quad (4.28a)$$

and the allowed hybrid angles satisfy the orthogonality condition, similar to (4.26b),

$$\frac{3(\mu_1 \mu_2)^{1/2}}{2} \cos^2 \alpha + (\lambda_1 \lambda_2)^{1/2} \cos \alpha + [1 - (\mu_1 \mu_2)^{1/2}/2] = 0 \quad (4.28b)$$

The solution of (4.28b) is

$$\cos \alpha = \frac{-(\lambda_1 \lambda_2)^{1/2} \pm \{[\lambda_1 \lambda_2 - 3(\mu_1 \mu_2)^{1/2} [2 - (\mu_1 \mu_2)^{1/2}]]^{1/2}}{3(\mu_1 \mu_2)^{1/2}} \quad (4.29)$$

which is equivalent to (4.27) with the replacements

$$\lambda = (\lambda_1 \lambda_2)^{1/2}, \quad \mu = (\mu_1 \mu_2)^{1/2} \quad (4.30)$$

i.e., with *geometric-mean* values of the hybridization parameters. Equation (4.29) provides a simple extension of the powerful directionality theorem (3.34) which is valid for general inequivalent spd hybrids.

Example 4.3

Problem: Evaluate the natural bonding angle(s) α for equivalent sp^3d^2 hybrids.

Solution: On putting $\lambda = 3$ and $\mu = 2$ into Eq. (4.27), we obtain

$$\cos \alpha = \frac{-3 \pm [9 - 6(2 - 2)]^{1/2}}{6} = \frac{-3 \pm 3}{6} = 0 \text{ or } -1$$

The two allowed solutions are therefore

$$\begin{aligned}\alpha_1 &= \cos^{-1}(0) = 90^\circ \\ \alpha_2 &= \cos^{-1}(-1) = 180^\circ\end{aligned}$$

corresponding to the bond angles of a regular octahedron.

We can also generalize the “sum rules” (3.37) for a general set of inequivalent $sp^\lambda d^\mu$ hybrids. Each of the nine possible hybrids can be expressed as

$$h_i = (1 + \lambda_i + \mu_i)^{-1/2} (s + \lambda_i^{1/2} \hat{p}_i + \mu_i^{1/2} \hat{d}_i), \quad i = 1-9 \quad (4.31)$$

where \hat{p}_i and \hat{d}_i are the normalized p- and d-type contributions (not necessarily pointing in the same direction) to hybrid h_i . Summation over all hybrids of the squared coefficients (fractional character) of each symmetry type must recover the total number of contributing s, p, and d orbitals,

$$\sum_{i=1}^9 \frac{1}{1 + \lambda_i + \mu_i} = 1 \quad (\text{s-orbital conservation}) \quad (4.32a)$$

$$\sum_{i=1}^9 \frac{\lambda_i}{1 + \lambda_i + \mu_i} = 3 \quad (\text{p-orbital conservation}) \quad (4.32b)$$

$$\sum_{i=1}^9 \frac{\mu_i}{1 + \lambda_i + \mu_i} = 5 \quad (\text{d-orbital conservation}) \quad (4.32c)$$

Only two of these three sum rules are independent.

4.3.2 Idealized sd^μ hybrids and bond angles

Let us now specialize to the case of pure sd hybridization, which underlies the duodectet-rule-conforming Lewis-like structures described in Sections 4.2.2 and 4.2.3. For equivalent sd^μ hybrids, Eq. (4.27) becomes

$$\cos \alpha = \pm \left(\frac{\mu - 2}{3\mu} \right)^{1/2} \quad (\mu \geq 2) \quad (4.33)$$

Table 4.3. Natural bond angles (α_{acute} and α_{obtuse}), percentage *d* character, and hybrid concentration ($|h|_{\text{max}}$) of equivalent sd^μ hybrids

Hybrid	μ	α_{acute} (degrees)	α_{obtuse} (degrees)	% d	$ h _{\text{max}}$
sd^1	1	90.00	90.00	50.00	2.288 ^a
sd^2	2	90.00	90.00	66.67	2.403
sd^3	3	70.53	109.47	75.00	2.436
sd^4	4	65.91	114.09	80.00	2.447
sd^5	5	63.43	116.57	83.33	2.449
sd^{10}	10	58.91	121.09	90.91	2.434
d	∞	54.74	125.26	100.00	2.236

^a Reduced strength in the ligand direction.

and the maximum amplitude (“concentration”) along the axis is

$$|sd^\mu|_{\text{max}} = \frac{1 + (5\mu)^{1/2}}{(1 + \mu)^{1/2}} \quad (4.34)$$

Note from (4.33) that sd^μ hybrids present *two* possible angles of maximum concentration, the acute angle (α_{acute}) and the obtuse angle (α_{obtuse}):

$$\alpha_{\text{acute}} = \cos^{-1} \left[+ \left(\frac{\mu - 2}{3\mu} \right)^{1/2} \right] \quad (4.35a)$$

$$\alpha_{\text{obtuse}} = \cos^{-1} \left[- \left(\frac{\mu - 2}{3\mu} \right)^{1/2} \right] \quad (4.35b)$$

Table 4.3 summarizes the natural bond angles (α_{acute} and α_{obtuse}), percentage *d* character, and concentration ($|h|_{\text{max}}$) for various cases of equivalent sd^μ hybrids (including the sd^1 case to be discussed below).

The natural angles (Table 4.3) for each sd^μ type can be readily visualized from the *shape* of the hybrid orbital, particularly the angles of its nodal surfaces. In effect, two equivalent hybrids can remain orthogonal only if each is oriented approximately along one of the nodal directions of the other. This is illustrated in Fig. 4.1 for the case of an sd^3 orbital, for which the acute (70.53°) and obtuse (109.47°) natural angles are shown nearly to coincide with the nodal angles that separate regions of positive and negative phase. Increasing *s* character tends to shift the two nodal

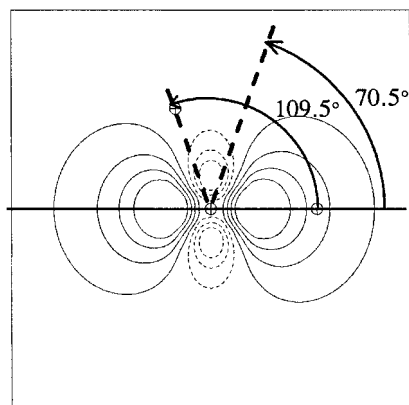


Figure 4.1 A hybrid sd^3 orbital, showing idealized bonding angles $\alpha_{\text{acute}} = 70.53^\circ$ and $\alpha_{\text{obtuse}} = 109.47^\circ$ lying near the nodal “hollows” of the hybrid.

angles closer together, until they coincide at 90° in the limiting case of sd^2 hybrids (33% s character).

The important case $\mu = 1$ (sd^1 -hybridization, ML_2 bonding) requires special treatment. Although two equivalent maximum-strength sd^1 hybrids h_1 and h_2 cannot be orthogonal at any angle α , we recognize from (4.26a) that the overlap $S = \langle h_1 | h_2 \rangle$ is *minimized* (to $S = \frac{1}{4}$) at $\alpha = 90^\circ$ (where $dS/d\alpha = 0$). At this angle the expressions (4.23) and (4.25) for h_1 and h_2 become

$$h_1 = 2^{-1/2}(s + d_{z^2}) \quad (4.36a)$$

$$h_2 = 2^{-1/2}[s - \frac{1}{2}d_{z^2} + (3^{1/2}/2)d_{x^2-y^2}] \quad (4.36b)$$

To restore orthogonality, while preserving as far as possible the desirable features of h_1 and h_2 , we carry out Löwdin's *symmetric orthogonalization* procedure¹²

$$\begin{pmatrix} \bar{h}_1 \\ \bar{h}_2 \end{pmatrix} = \mathbf{S}^{-1/2} \begin{pmatrix} h_1 \\ h_2 \end{pmatrix} \quad (4.37)$$

where $\mathbf{S}^{-1/2}$ is the inverse square root of the 2×2 overlap matrix $(\mathbf{S}_{ij}) = \langle h_i | h_j \rangle$. The Löwdin transformation (4.37) is guaranteed to produce the unique set of orthonormal hybrids \bar{h}_1 and \bar{h}_2 that “resemble” h_1 and h_2 as closely as possible (in the mean-square-deviation sense). For this case the orthogonalized hybrids are found to be

$$\bar{h}_1 = 1.025h_1 - 0.130h_2 \quad (4.38a)$$

$$\bar{h}_2 = -0.130h_1 + 1.025h_2 \quad (4.38b)$$

Example 4.4

Problem: Justify Eqs. (4.38a) and (4.38b).

Solution: It is convenient to rewrite the 2×2 overlap matrix \mathbf{S} in terms of an angle θ such that

$$\mathbf{S} = \begin{pmatrix} 1 & \sin(2\theta) \\ \sin(2\theta) & 1 \end{pmatrix}$$

where

$$S = \sin(2\theta)$$

The inverse-square-root matrix is then

$$\mathbf{S}^{-1/2} = \frac{1}{\cos(2\theta)} \begin{pmatrix} \cos \theta & -\sin \theta \\ -\sin \theta & \cos \theta \end{pmatrix}$$

(as can be verified by matrix multiplication). The desired Löwdin-orthogonalized hybrids are therefore

$$\begin{aligned} \bar{h}_1 &= \frac{1}{\cos(2\theta)} [(\cos \theta)h_1 - (\sin \theta)h_2] \\ \bar{h}_2 &= \frac{1}{\cos(2\theta)} [-(\sin \theta)h_1 + (\cos \theta)h_2] \end{aligned}$$

For the present case ($S = \frac{1}{4}$), the angle θ is

$$\theta = \frac{\sin^{-1}(S)}{2} = 7.239^\circ$$

so

$$\begin{aligned} \bar{h}_1 &= \frac{1}{\cos(14.478^\circ)} [\cos(7.239^\circ)h_1 - \sin(7.239^\circ)h_2] \\ \bar{h}_2 &= \frac{1}{\cos(14.478^\circ)} [-\sin(7.239^\circ)h_1 + \cos(7.239^\circ)h_2] \end{aligned}$$

which are equivalent to Eqs. (4.38a) and (4.38b).

By combining (4.36) and (4.38), we can write the normalized orthogonal hybrids in terms of atomic s and d functions as

$$\bar{h}_1 = 0.632s + 0.790d_{z^2} - 0.112d_{x^2-y^2} \quad (4.39a)$$

$$\bar{h}_2 = 0.633s - 0.451d_{z^2} + 0.627d_{x^2-y^2} \quad (4.39b)$$

The new orthogonal hybrids have 60% d character ($sd^{1.5}$ hybridization) as a result of the Löwdin procedure. However, because these expressions involve *three* atomic orbitals, there must be one other hybrid (in addition to the two bonding hybrids) affected by the orthogonalization transformation. This hybrid, denoted $n^{(h)}$, belongs

to the same subspace as the three atomic orbitals that contribute to \bar{h}_1 and \bar{h}_2 , and so can be written as

$$n^{(h)} = c_1s + c_2d_{z^2} + c_3d_{x^2-y^2} \quad (4.40a)$$

The two orthogonality conditions ($\langle n^{(h)} | \bar{h}_1 \rangle = \langle n^{(h)} | \bar{h}_2 \rangle = 0$) plus the overall normalization condition ($\langle n^{(h)} | n^{(h)} \rangle = 1$) then allow $n^{(h)}$ to be uniquely determined as

$$n^{(h)} = 0.447s - 0.450d_{z^2} + 0.775d_{x^2-y^2} \quad (4.40b)$$

Equation (4.40b) shows that $n^{(h)}$ corresponds to an $sd^{4.00}$ hybrid (80% d character). If the bond hybrids \bar{h}_1 and \bar{h}_2 are directed toward ligands along the x and z axes, then $n^{(h)}$ is oriented in the y direction, perpendicular to the skeletal bonding plane.

The formation of idealized ML_2 skeletal hybrids (90° bond angle) from the initial manifold of s and d orbitals on M can therefore be represented as

$$(s, d_{z^2}, d_{x^2-y^2}, d_{xy}, d_{xz}, d_{yz}) \rightarrow (\bar{h}_1, \bar{h}_2, n^{(h)}, d_{xy}, d_{xz}, d_{yz}) \quad (4.41)$$

where *three* orbitals are affected by hybridization. Although the hybridized $n^{(h)}$ is “d-rich,” it differs appreciably from the unhybridized d_{xy} , d_{xz} , and d_{yz} orbitals in its interactions with other orbitals, particularly in pi-bond formation. Because admixture of s character *reduces* the ability of $n^{(h)}$ to participate in pi-bonding, $n^{(h)}$ will tend to be relegated to nonbonding “lone-pair” status as pi bonds are added to the sigma skeleton. However (as shown in Section 4.4.3 below), the s character of $n^{(h)}$ can be advantageous in *delta*-bonding, leading to a distinctive ML_2 type of “edge-on” δ -bonding involving d_{z^2} orbitals (which in other ML_n cases are fully committed to the sigma skeleton). Thus, the ML_2 (sd^1 -hybridization) bonding motif is unique in several respects.

Example 4.5

Problem: Orthogonal equivalent hybrids for $\mu = 1$ could also be achieved by adding p character ($sp^\lambda d^1$ hybrids). For what minimum λ value is orthogonality achieved? What is the corresponding bond angle α of the $sp^\lambda d^1$ hybrids?

Solution: Real solutions of the orthogonality condition (4.27) are obtained only if

$$\lambda^2 \geq 3\mu(2 - \mu)$$

The p character required in order to restore orthogonality is therefore given by

$$\lambda = [3\mu(2 - \mu)]^{1/2} = 3^{1/2} = 1.732$$

corresponding to $sp^{1.73}d^1$ hybridization, with 26.8% s character, 46.4% p character, and 26.8% d character. According to Eq. (4.27), the corresponding bond angle α satisfies

$\cos \alpha = -3^{-1/2}$, or

$$\alpha = 109.5^\circ$$

However, this hybridization generally seems to be higher in energy for ML_2 systems than the sd^1 ($\alpha = 90^\circ$) hybridization discussed above.

For completeness, let us also briefly summarize the hybrid-conservation sum rules and bond angles for inequivalent sd^μ hybrids. For pure sd^μ hybridization, the sum rules (4.32) reduce to the simplified form

$$\sum_{i=1}^6 \frac{1}{1 + \mu_i} = 1 \quad (\text{s-orbital conservation}) \quad (4.42a)$$

$$\sum_{i=1}^6 \frac{\mu_i}{1 + \mu_i} = 5 \quad (\text{d-orbital conservation}) \quad (4.42b)$$

where only one of these equations is independent. For inequivalent sd^μ hybrids h_1 and h_2 , the idealized interhybrid angle α (4.29) reduces to the simplified form

$$\cos \alpha_{\pm} = \pm \{[1 - 2(\mu_1 \mu_2)^{-1/2}]/3\}^{1/2} \quad (4.43)$$

where α_+ gives the acute angle and α_- the obtuse angle of bonding.

4.3.3 Shapes of idealized Lewis-like structures

To relate the hybrid angles of Table 4.3 to idealized molecular *shapes*, let us now consider a general ML_k species with k monovalent ligands L.¹³ In general, k equivalent sd hybrids of sd^{k-1} composition (i.e., $\mu = k - 1$) are needed to form the sigma skeleton

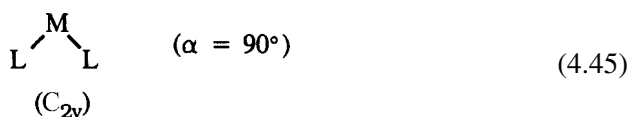
$$h_{\sigma_i} = (sd^{k-1})_i, \quad i = 1, 2, \dots, k \quad (4.44)$$

leaving $6 - k$ unhybridized d orbitals for multiple bonding or lone pairs.

By combining the skeletal hybrid composition (4.44) with the bond angles of Table 4.3, we can recognize the idealized molecular shape(s) corresponding to each ML_k coordination.

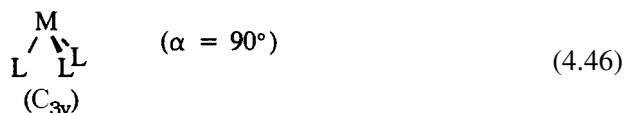
ML_2 (sd^1 -hybridization)

Only less strongly concentrated sd^1 hybrids (4.39) at 90° bond angles are available in this case, leading to strongly bent C_{2v} geometry:

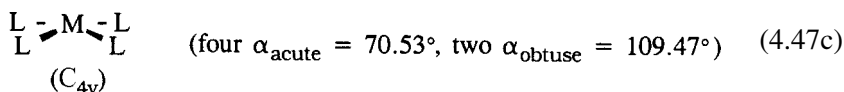
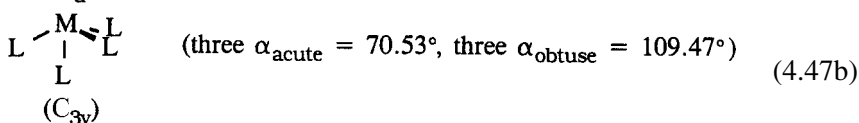
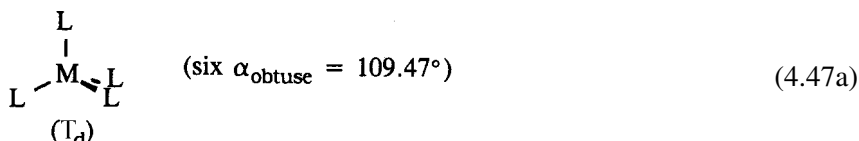


ML_3 (sd^2 -hybridization)

The unique interhybrid angle in this case is 90° ($\alpha_{\text{acute}} = \alpha_{\text{obtuse}}$), leading to a trigonal pyramidal shape of C_{3v} symmetry:


 ML_4 (sd^3 -hybridization)

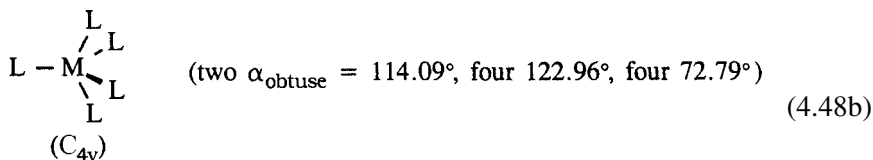
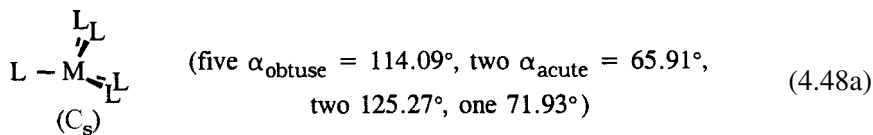
Three distinct isomeric forms (T_d , C_{3v} , C_{4v}) having all bond angles perfectly equal to either $\alpha_{\text{acute}} = 70.53^\circ$ or $\alpha_{\text{obtuse}} = 109.47^\circ$ can be envisioned to derive from equivalent sd^3 hybrids:



Note that “inversion” of one leg of the open T_d form through the opposite trigonal face produces the more cramped C_{3v} form.

 ML_5 (sd^4 -hybridization)

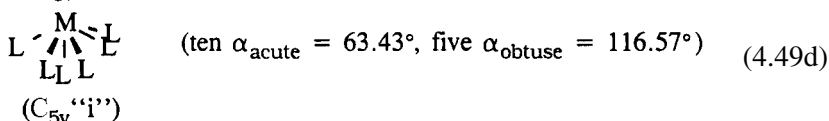
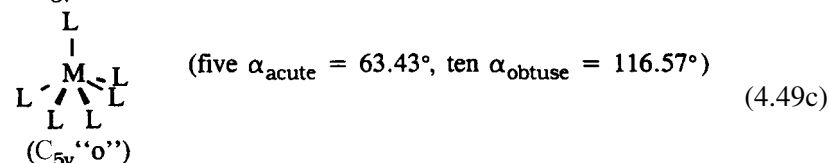
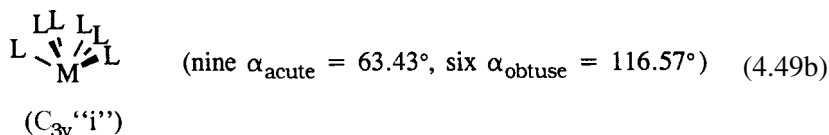
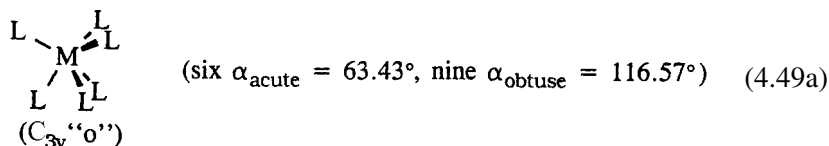
No possible spatial arrangement of five ligands can correspond to the high symmetry of five equivalent sd^4 hybrids. The “best” structures for sd^4 hybridization therefore inevitably involve a degree of mismatching with idealized $\alpha_{\text{acute}} = 65.91^\circ$ and $\alpha_{\text{obtuse}} = 114.09^\circ$ bond angles. Two possible choices (C_s and C_{4v}) are shown schematically:



The actual structures are likely to involve frustrated competition among several such equally unsatisfactory isomeric forms (*none* resembling the D_{3h} trigonal bipyramid).

ML_6 (sd^5 -hybridization)

Four distinct isomeric forms (two each of C_{3v} and C_{5v} symmetry) having all bond angles perfectly equal to either $\alpha_{acute} = 63.43^\circ$ or $\alpha_{obtuse} = 116.57^\circ$ can be envisioned to derive from equivalent sd^5 hybrids:



The second “i” (in, or inverted) form (4.49b) of C_{3v} symmetry can be visualized to arise from the “o” (out, or ordinary) form (4.49a) by inverting the small-angle trigonal pyramid into the middle of the large-angle pyramid. Similarly, the “i” form (4.49d) of C_{5v} symmetry arises upon inverting the stem of the “o” form (4.49c) into the middle of the opposite pentagonal pyramid. Note that none of these structures resembles the octahedral O_h geometry that might be “expected” in six-coordinate compounds.

Figures 4.2–4.5 show accurate perspective ball-and-stick diagrams of the idealized structures in (4.45)–(4.49), in order to aid visualization of the rather unfamiliar shapes associated with equivalent sd^u hybrids. Note that a surprising proportion of these hypothetical sd^u geometries corresponds to placing *all* ligands on one side of a plane through the metal nucleus (see, e.g., Figs. 4.3(b) and (c) and 4.4(b) and (d)), and will thus be disfavored on steric or electrostatic grounds. Hence, the most “reasonable” structures are those shown in Figs. 4.3(a), 4.4(a) and (b), and 4.5(a) and (c), which have fewer cramped α_{acute} angles and fill space more equitably.

The shapes of the idealized Lewis-like sd^u structures can also be visualized in another surprising way,¹⁴ as depicted in Figs. 4.6(a)–(d). For most of these

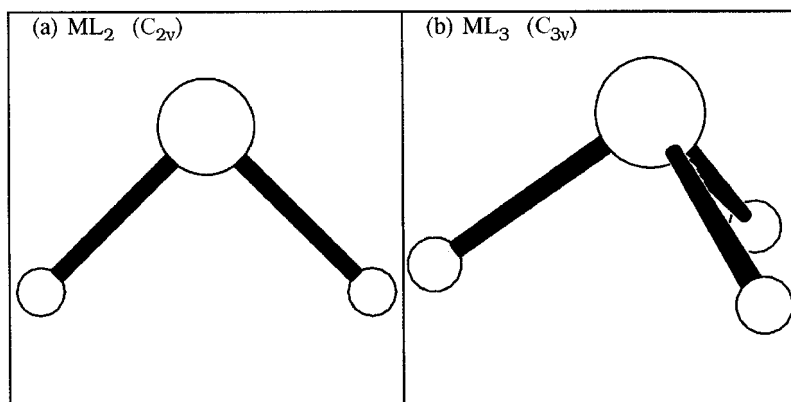


Figure 4.2 Idealized molecular shapes of ML_2 (left, sd) and ML_3 (right, sd^2) Lewis-like species (cf. (4.45) and (4.46) in the text), with optimal L—M—L bond angles $\alpha = 90^\circ$ for all ligands.

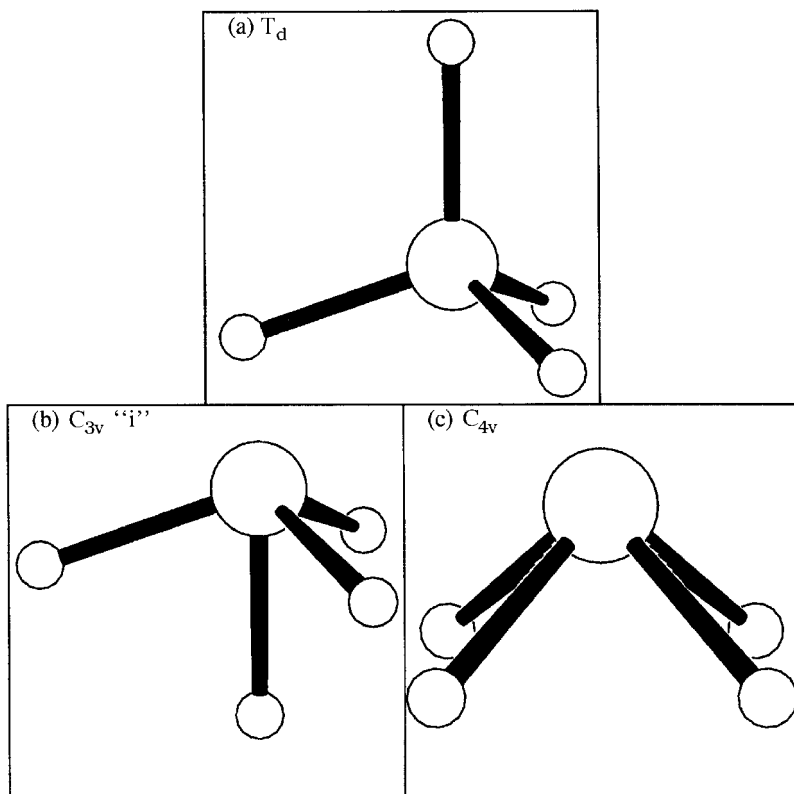


Figure 4.3 Idealized ML_4 molecular shapes for equivalent sd^3 hybridization (cf. (4.47a)–(4.47c) in the text), with optimal L—M—L bond angles $\alpha_{acute} = 70.53^\circ$ or $\alpha_{obtuse} = 109.47^\circ$ for all ligands.

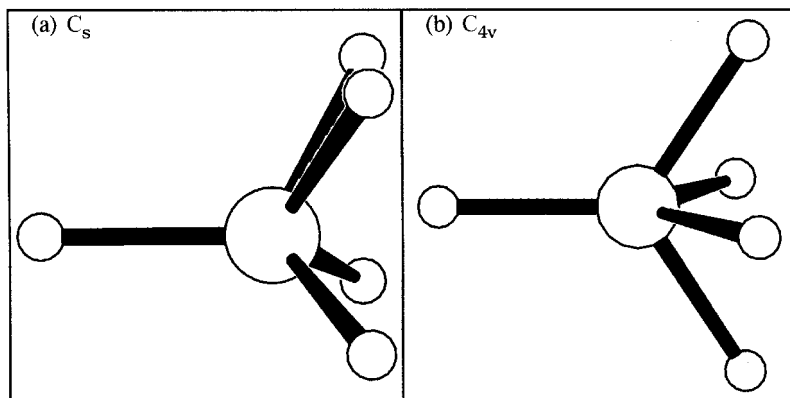


Figure 4.4 Idealized ML_5 molecular shapes having (limited) similarity with optimal $L-M-L$ bond angles $\alpha_{acute} = 65.91^\circ$ and $\alpha_{obtuse} = 114.09^\circ$ of equivalent sd^4 hybridization.

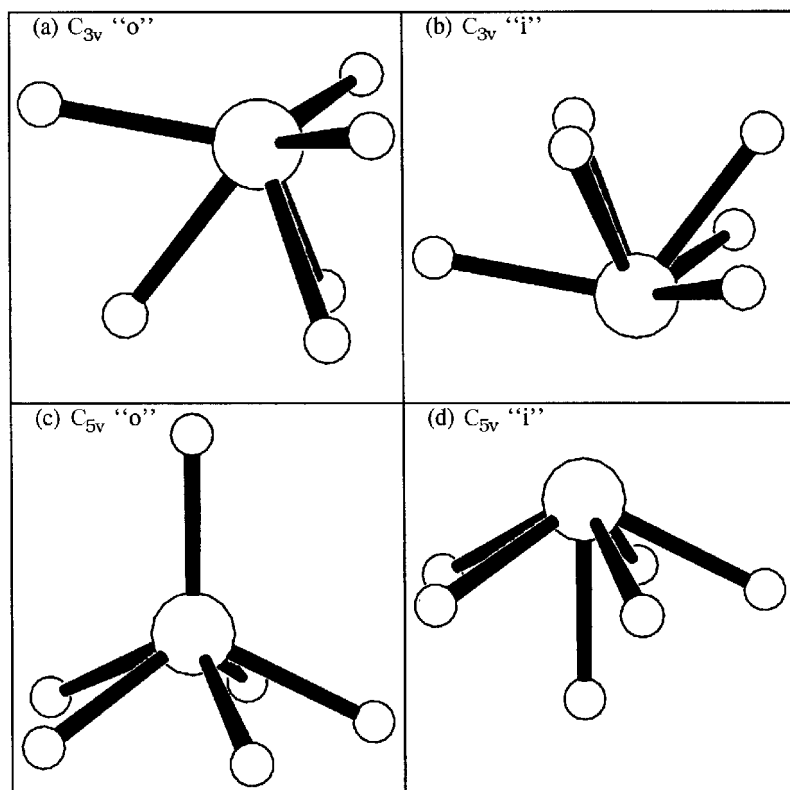


Figure 4.5 Idealized ML_6 molecular shapes for equivalent sd^5 hybridization (cf. (4.49a)–(4.49d) in the text), with optimal $L-M-L$ bond angles $\alpha_{acute} = 63.43^\circ$ or $\alpha_{obtuse} = 116.57^\circ$ for all ligands.

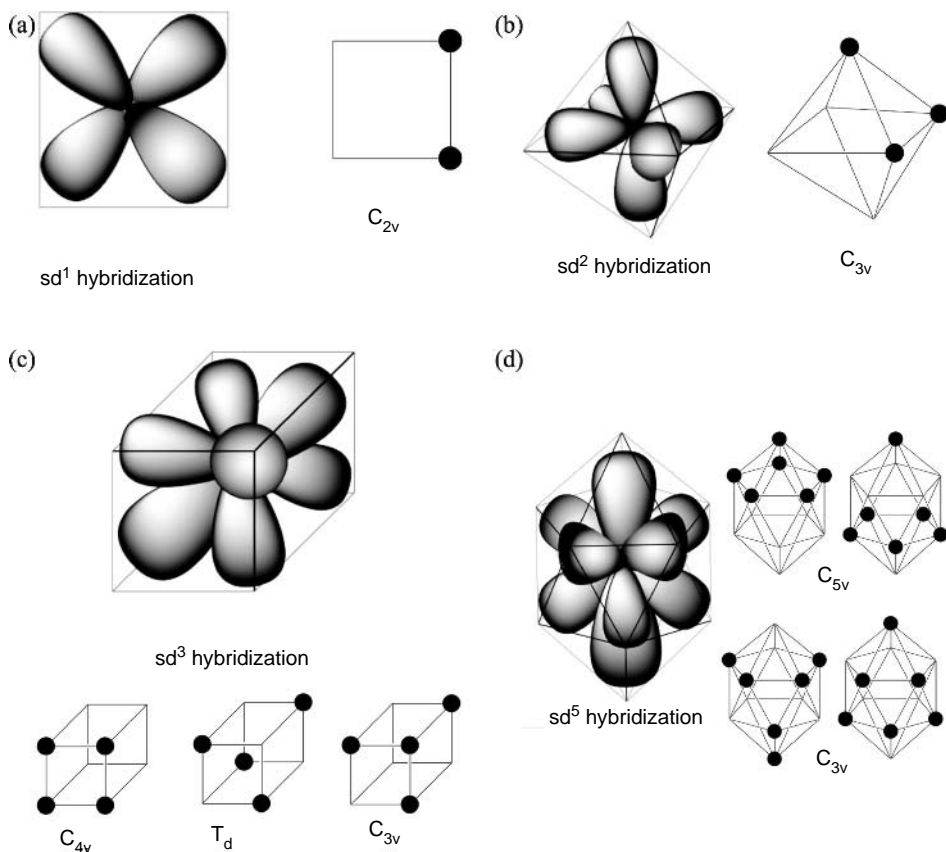


Figure 4.6 Relationships of idealized sd^{n-1} -hybridized ML_n molecular shapes to simple polyhedra. Each panel shows the hybrid-orbital axes in dumbbell “ d_{z^2} ”-like form embedded within the polyhedron, together with the associated allowed (no-*trans*-vertex) dispositions of ligands on the polyhedral vertices (with the unmarked metal atom occupying the polyhedral centroid in each case): (a) sd^1 square, (b) sd^2 octahedron, (c) sd^3 cube, and (d) sd^5 icosahedron.

hybridizations, Eq. (4.43) dictates that the sd^μ orbitals point to the vertices of simple polyhedra. However, due to the centrosymmetric nature of these orbitals, placement of ligands in *trans* positions (i.e., making two M—L bonds with a single hybrid orbital) is strongly disfavored. The n equivalent sd^{n-1} hybrids of an idealized Lewis-like ML_n species can therefore be embedded in a centrosymmetric polyhedron of $2n$ vertices, with M at the center and a single L occupying one or the other of each opposed pair of vertices, as follows.

- (a) In idealized ML_2 bonding, two centrosymmetric sd^1 hybrids have lobes that point to the vertices of a *square*. Each hybrid-orbital axis lies along the diagonal, and one can view the resulting molecular shape (4.45) as a *cis*-divacant square plane, as shown in Fig. 4.6(a).

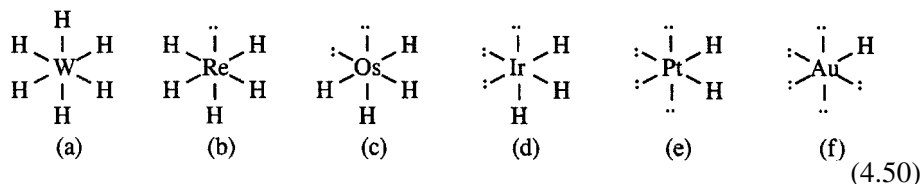
- (b) In idealized ML_3 bonding, the sd^2 -hybrid axes form the body diagonals of an *octahedron*. As shown in Fig. 4.6(b), placement of ligands such that no *trans* vertices are occupied leads (uniquely) to a facially trivacant octahedral molecular shape (4.46) of C_{3v} symmetry.
- (c) In idealized ML_4 bonding, the sd^3 -hybrid axes form body diagonals of a *cube*. However, there are now *three* distinct ways (“colorings”) to distribute the four ligands among the eight vertices without any opposed pair of ligands, leading to the distinct shapes (4.47a)–(4.47c) as shown in Fig. 4.6(c).
- (d) ML_5 bonding is irregular, as noted above. Indeed, no regular ten-vertex polyhedron exists, so in this case there can be no idealized polyhedral shape corresponding to the five equivalent sd^4 -hybrid orbital directions, and only irregular shapes such as (4.48a) and (4.48b) are possible.
- (e) Finally, for idealized ML_6 bonding, the sd^5 hybrids form the body diagonals of the 12-vertex *icosahedron*, with *four* distinct colorings that satisfy the no-*trans*-vertex rule, as shown in Fig. 4.6(d). The four distinct shapes (4.49a)–(4.49d) can be visualized as follows. Perpendicular to the three-fold axis of an icosahedron lies a stack of four parallel triangles. Two opposing trigonal faces of an icosahedron form the two “outer” (smaller) triangles of the stack, while the two “inner” (larger) triangles lie on opposite sides of the icosahedral centroid. Two C_{3v} geometries result from the allowed colorings (no-*trans*-vertex) of triangles. Thus, coloring adjacent inner and outer triangles produces the “i” form (4.49b), whereas the “o” form (4.49a) utilizes non-adjacent inner and outer triangles. Coloring the six vertices of only outer or only inner triangles is not allowed because it results in *trans* ligand dispositions. Similarly, stacking along the five-fold symmetry axis of an icosahedron follows the pattern vertex–pentagon–pentagon–vertex, with the two lone vertices lying on the five-fold axis and the pentagonal planes perpendicular to the axis. Occupation of a lone vertex and either the proximal or the distal pentagon leads to the C_{5v} “i” and “o” structures, respectively.

The idealized Lewis-like shapes are therefore exquisitely adapted to crystallographic packing patterns.

4.4 Covalent and polar-covalent bonding

4.4.1 Metal hydrides and alkyls

Let us begin by considering the duodectet-rule-conforming metal hydrides of the third transition series (W–Au), which have the Lewis-like diagrams



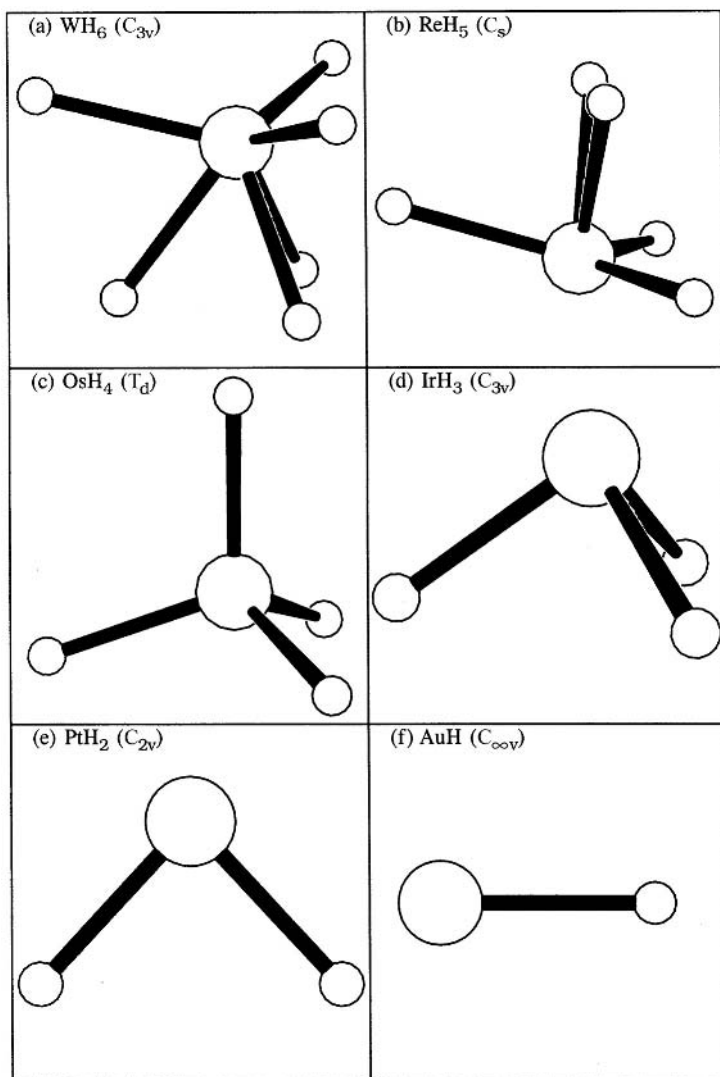


Figure 4.7 Optimized geometries of saturated group 6–11 third series transition-metal hydrides MH_n (see Table 4.4).

As usual, these diagrams depict the atomic connectivity and assignment of bonding and nonbonding electron pairs of the localized Lewis-like wavefunction, but *not* (necessarily) the molecular shape or symmetry.

The actual optimized structures of the MH_n species are shown in Figs. 4.7(a)–(f). From these figures one can immediately recognize the close connection of the optimized geometries to the idealized sd^{μ} shapes discussed in the previous section. For example, the WH_6 structure (Fig. 4.7(a)) closely resembles the idealized ML_6

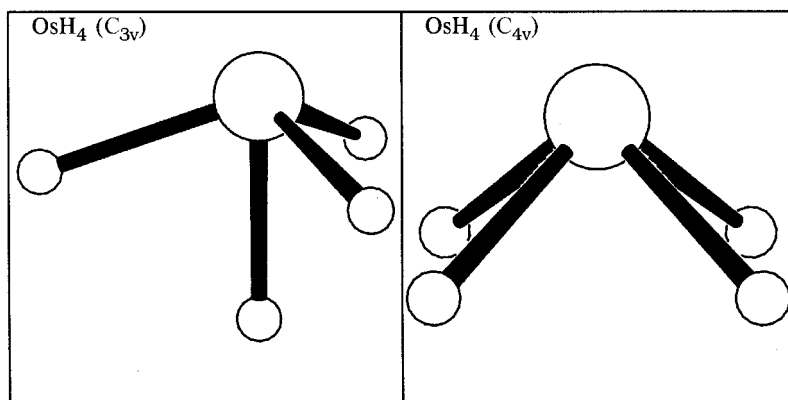


Figure 4.8 Alternative C_{3v} and C_{4v} isomers of OsH_4 , which are calculated (without zero-point-energy correction) to lie 3.51 and 5.16 kcal mol⁻¹, respectively, above the ground T_d form (Fig. 4.7(c)). Note the close resemblance to the respective idealized sd^3 geometries in Figs. 4.3(b) and (c).

C_{3v} “o” shape (Fig. 4.5(a)), ReH_5 (Fig. 4.7(b)) resembles the idealized ML_5 C_s shape (Fig. 4.4(a)), OsH_4 (Fig. 4.7(c)) is the idealized ML_4 T_d shape (Fig. 4.3(a)), and so forth. Thus, the rather unusual hydride geometries immediately suggest the role of sd^u hybridization and covalency, leading to molecular shapes quite unlike those expected from simple ionic or packing (“VSEPR-like”¹⁵) forces.¹⁶

Even the “normal” tetrahedral geometry (Fig. 4.7(c)) of OsH_4 is somewhat misleading with respect to the possible usefulness of VSEPR-like concepts for rationalizing the puzzling metal hydride geometries.¹⁷ Two other isomeric forms of dissimilar shape (C_{3v} and C_{4v}) but similar energy (both within ~ 5 kcal mol⁻¹ of the T_d structure) are shown in Fig. 4.8. These alternative structures are evidently in close correspondence with the corresponding idealized ML_4 structures (Figs. 4.3(b) and (c)), both of which are rather peculiar from a VSEPR viewpoint.

The near-degeneracy of these three isomers is not attributable to any intrinsic “flatness” or lack of structural rigidity of the potential-energy surface, for each isomer appears to be separated by reasonably high kinetic barriers from the others. Figure 4.9 illustrates the adiabatic potential-energy curve connecting the C_{3v} and T_d isomers along the “umbrella” inversion coordinate (θ_{HOsH}), showing the significant barrier (> 8 kcal mol⁻¹) between the two potential wells. More strikingly, the square-planar isomer (D_{4h} symmetry) that could be a transition state between equivalent pyramidal or tetrahedral isomers lies more than 370 kcal mol⁻¹ above the equivalent equilibrium species! Similar remarks apply to comparisons between VSEPR-like and actual geometries of other metal hydrides. For example, compared with the “strange” C_{3v} isomer of WH_6 (Fig. 4.7(a)), the “expected” VSEPR-like octahedral

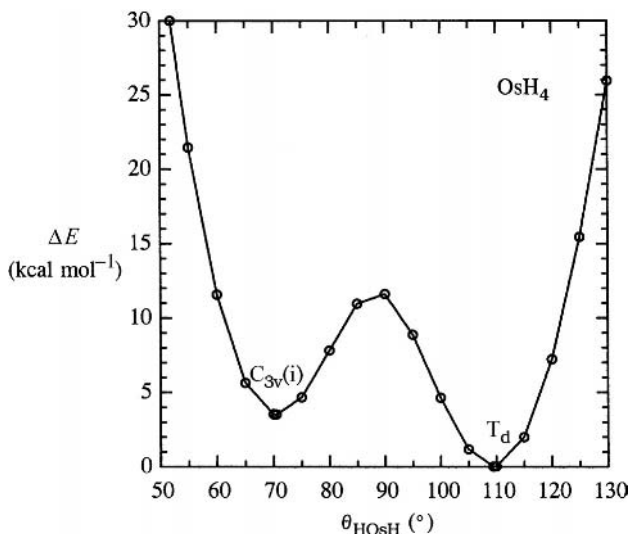


Figure 4.9 The potential for the “umbrella” inversion motion of OsH_4 , showing distinct minima for metastable $C_{3v}(i)$ and stable T_d isomers.

isomer lies about $540 \text{ kcal mol}^{-1}$ higher in energy! Thus, *no useful purpose seems to be served by thinking about these structures in VSEPR-like terms.*

The visual resemblance of optimized (Fig. 4.7) and idealized (Figs. 4.2–4.5) MH_n structures is confirmed by the quantitative geometrical values summarized in Table 4.4. As expected, the optimized bond lengths and angles distort slightly from “equivalency” where permitted by point-group symmetry (for example, the C_{3v} structure of WH_6 has slightly different R_{WH} bond lengths, 1.67 \AA versus 1.71 \AA , in “upper” and “lower” triangular faces). Nevertheless, within these slight distortions the agreement with idealized sd^{μ} hybridization angles is striking. For example, the two acute angles (63.1° and 67.8°) of WH_6 closely resemble the idealized value $\alpha_{\text{acute}} = 63.4^\circ$, and the two obtuse angles (113.6° and 119.9°) are in similarly close agreement with the idealized $\alpha_{\text{obtuse}} = 116.6^\circ$. Similar agreement is seen for all these species (except the ReH_5 case, which is expected to have the highly fluctuational “frustrated” character of sd^4 hybridization). Geometrical parameters of the alternative OsH_4 isomers (Fig. 4.8) are also in quite satisfactory agreement with the “strange” predictions of the sd^{μ} -hybridization picture.

The aptness of the idealized sd^{μ} Lewis-like model is also confirmed by the quantitative NBO descriptors, as summarized in Table 4.5. This table displays the overall accuracy of the Lewis-like description (in terms of $\% \rho_L$, the percentage accuracy of the natural Lewis-like wavefunction for both valence-shell and total electron density) as well as the metal hybridization (h_M), bond polarity toward M ($100c_M^2$), and

Table 4.4. Bond lengths R_{MH} and angles θ_{HMH} of saturated metal hydrides MH_n of the third transition series (see Fig. 4.7)

MH_n	Symmetry	R_{MH} (Å)	Bond angle θ_{HMH} (°)
WH ₆	C _{3v}	1.707(3), 1.668(3)	63.1(3), 67.8(3), 113.6(3), 119.9(6)
ReH ₅	C _s	1.636, 1.623(4)	54.3, 58.9, 62.0, 73.4(3), 103.9, 120.8, 127.4
	C _s	1.656, 1.620(2), 1.644(2)	53.0, 74.2(2), 108.0(2), 119.0(2)
	C _{4v}	1.59, 1.62(4)	61.2(4), 76.5(4), 122.3(2)
	C _{5v}	1.624(5)	62.8(4), 114.7(4)
OsH ₄	T _d	1.601(4)	109.5(6)
	C _{3v}	1.586(3), 1.567	70.8(3), 109.7(3)
	C _{4v}	1.582(4)	72.6(4), 113.8(2)
IrH ₃	C _{3v}	1.548(3)	92.0(3)
PtH ₂	C _{2v}	1.520(2)	86.5
AuH	C _{∞v}	1.542	

Table 4.5. The NBO descriptors of group 6–11 MH_n metal hydrides of the third transition series, showing the percentage accuracy (% ρ_L) of the Lewis-like description (valence shell and total), metal hybrid (h_M), percentage polarization toward M ($100c_M^2$), and occupancy of bonding σ_{MH} NBOs (see Fig. 4.8)

MH_n	% ρ_L		σ_{MH}			(No.)
	Valence	Total	h_M	$100c_M^2$	Occupancy (e)	
WH ₆	97.40	99.56	sd ^{6.35}	49.76	1.9201	(3)
			sd ^{3.98}	42.36	1.9759	(3)
ReH ₅ (C _s)	98.31	99.70	sd ^{3.07}	48.28	1.9876	(1)
			sd ^{4.59}	52.68	1.9140	(2)
			sd ^{3.98}	46.72	1.9856	(2)
OsH ₄ (T _d)	99.93	99.95	sd ^{2.97}	48.56	1.9981	(4)
OsH ₄ (C _{3v})	98.83	99.78	sd ^{2.66}	55.80	1.9191	(4)
			sd ^{3.10}	50.48	1.9808	
IrH ₃	99.41	99.87	sd ^{2.01}	52.68	1.9768	(3)
PtH ₂	99.31	99.87	sd ^{1.21}	54.22	1.9622	(2)
AuH	99.93	99.98	sd ^{0.20}	49.40	2.0000	(1)

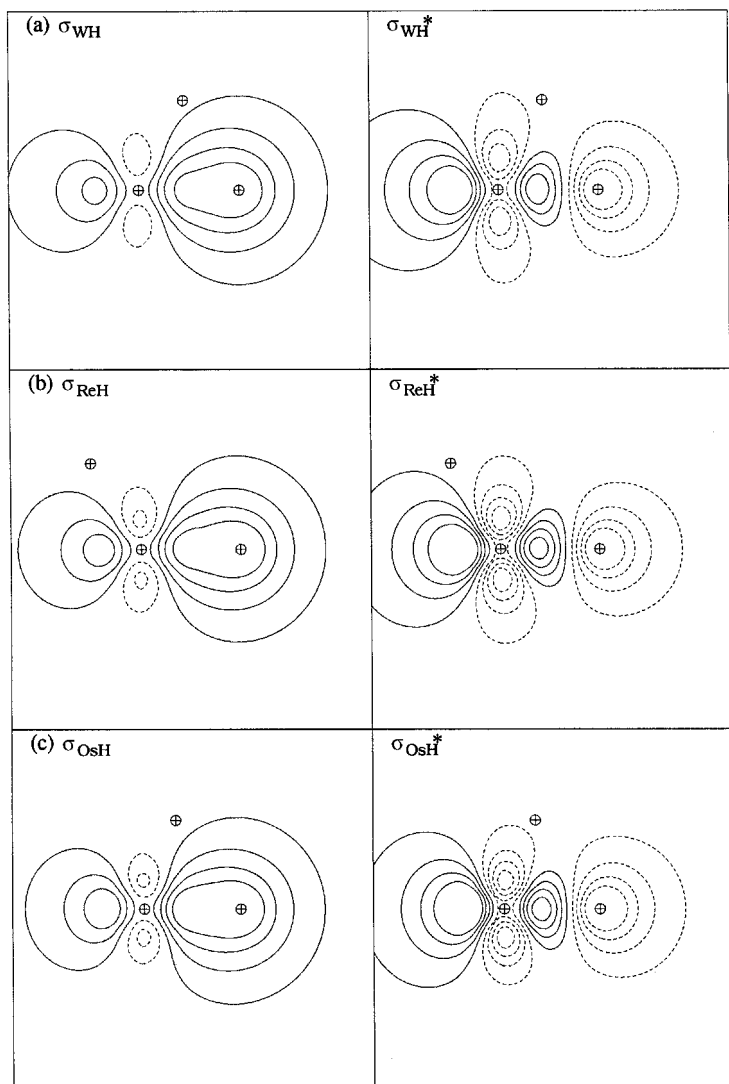


Figure 4.10 Metal hydride bond (σ_{MH}) and antibond (σ_{MH}^*) NBOs of saturated group 6–11 transition-metal hydrides MH_n of the third transition series.

occupancy of each of the metal hydride σ_{MH} NBOs. The accuracy of the Lewis-like description is seen to be quite high ($>97\%$ for valence-shell ρ_{L} , $99.57\%–99.98\%$ for total ρ_{L}), rather comparable to values for common organic species (cf. Tables 3.2 and 3.3). Electron-“pair” occupancies of the localized NBOs are also quite respectable, with all M–H bonds exceeding the standard NBO threshold ($1.90e$) for a well-localized electron pair. The metal hydride bond NBOs are also found to be surprisingly covalent, with bond polarities toward M in the near-50% range ($43\%–56\%$) for all species. Finally, the individual metal NBO hybrid compositions

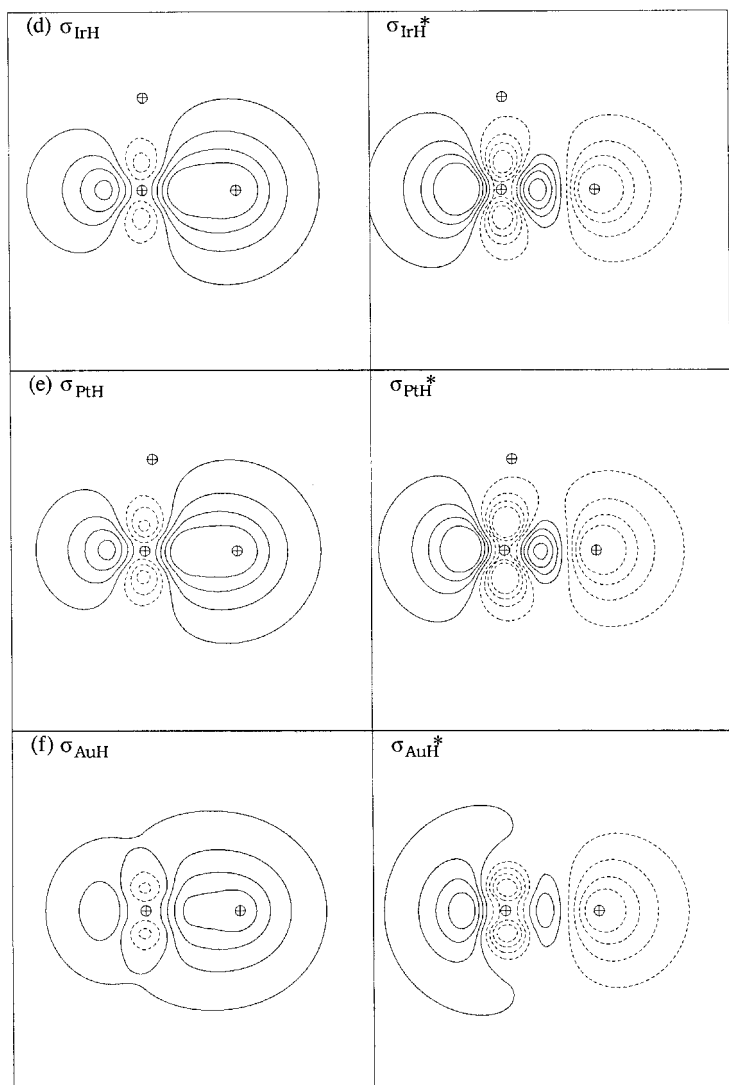


Figure 4.10 (Cont.)

all fall strikingly close to idealized sd^{n-1} values, with average hybridizations $sd^{5.17}$ (versus sd^5), $sd^{4.04}$ (versus sd^4), $sd^{2.97}$ (versus sd^3), $sd^{2.01}$ (versus sd^2), $sd^{1.21}$ (versus sd^1), and $sd^{0.20}$ (versus sd^0) for MH_n hydrides of $n = 6$ through 1, respectively. (Note that the p character of the natural hybrids is found to be negligibly small in all these species.) Thus, the accuracy of a localized Lewis-like model of transition-metal hydrides appears to be fully comparable to that of main-group compounds. A Lewis-like description of OsH_4 is as “perfect” as that of CH_4 !

The recognizability and transferability of localized metal hydride bond and antibond NBOs is also quite high, as demonstrated in Fig. 4.10. The gradual decrease

in d character on going from W ($\sim sd^5$, 83% d) to Pt ($\sim sd$, 50% d) and the relatively constant bond polarity leads to barely perceptible changes in the form of the σ_{MH} and σ_{MH}^* NBOs across the entire span of mid to late (group 6–10) transition metals. However, the abrupt increase of s character at Au ($\sim sd^{0.20}$, 17% d) results in quite distinctive NBO shapes in this case. Simply on the basis of this abrupt change in the form of its localized hybrids and NBOs, the coordination chemistry of gold (or other group 11) hydrides would be expected to differ conspicuously from that of earlier transition-series members.

We can also consider the early (group 3–5) transition-series members in analogous fashion. Whereas groups 6–11 comprise the “normal-valent” members of the d block, the earlier groups 3–5 are formally *hypovalent* (analogous to group 13 of the p block), with 1–3 vacant valence orbitals in their atomic ground-state high-spin configuration. Nevertheless, in the Lewis-like picture the skeletal hydride bonding of hypovalent transition metals is expected to be analogous to that of the normal-valent later members. Thus, the saturated hydrides of the early members of the third transition series are expected to be LaH_3 , HfH_4 , and TaH_5 , corresponding to idealized sd^2 , sd^3 , and sd^4 hybridization, respectively. The optimized geometries conform reasonably to this simple picture, as shown in Fig. 4.11. The NBO hybridizations (averaged if necessary) also agree closely with the expected values, $sd^{3.98}$ (versus sd^4) for TaH_5 and $sd^{2.94}$ (versus sd^3) for HfH_4 .¹⁸ Figure 4.12 shows the (σ_{MH} and σ_{MH}^*) NBOs of hypovalent hafnium and tantalum hydrides to illustrate their similarities to the normal-valent NBOs of Fig. 4.10. Thus, the simple sd^μ -hybridization picture seems to apply well over the entire span of hypovalent (group 3–5) and normal-valent (group 6–11) d-block elements.

Although orbital hybridizations and molecular shapes for hypovalent metal hydrides of the early transition metals and the normal-valent later transition metals are similar, the M—H bonds of the early metals are distinctly more polar. For example, metal-atom natural charges for YH_3 (+1.70), HfH_4 (+1.75), and TaH_5 (+1.23) are all significantly more positive than those (ranging from +0.352 to -0.178) for the homoleptic hydrides from groups 6–10. Indeed, the empirical chemistry of early transition-metal hydrides commonly reveals greater “hydricity” than does that of the later transition-metal hydrides.

A consequence of high ionic characters for early transition-metal hydrides is a tendency toward more symmetric shapes. For LaH_3 the H—M—H bond angles (107.4°) are considerably more open than the idealized 90° angles expected for sd^2 hybridization. One can understand this structural modification by interpolating between the idealized ionic (trigonal planar, 120°) and covalent (90°) C_{3v} extremes. Similar reasoning applies to HfH_4 and TaH_5 , although not so strikingly because the covalent extremes are already quite symmetric.

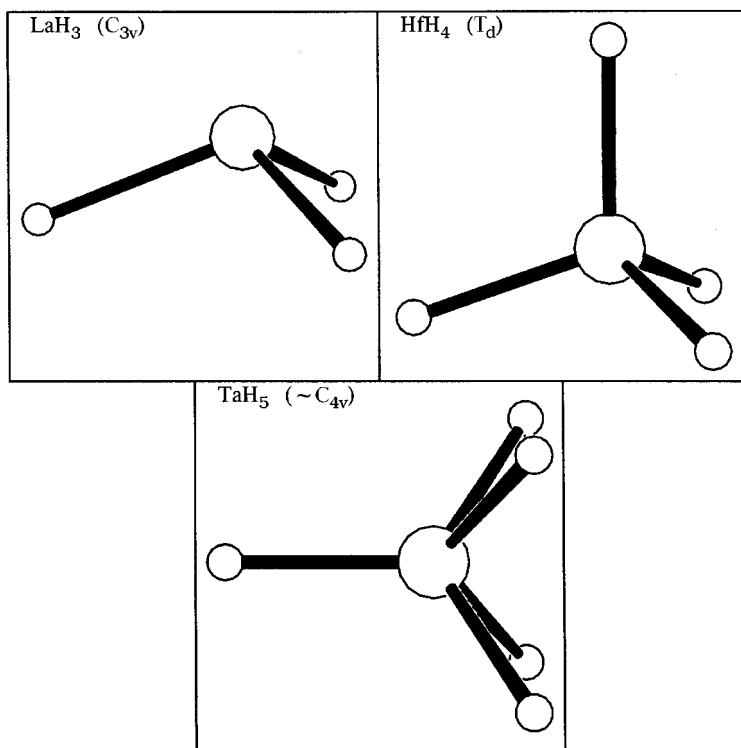


Figure 4.11 Optimized structures and symmetries of the hypovalent group 3–5 hydrides LaH₃, HfH₄, and TaH₅, showing the general resemblance to idealized sd^m geometries (Figs. 4.2(b), 4.3(a), and 4.4(b)).

What shape would an early transition-metal hydride adopt if the ionic component were reduced? Structural analysis of the cation HfH_3^+ (which is isovalent with LaH_3) provides insight. The molecular cation exhibits bond angles (98.1°) that are nearly 10° less than those of LaH_3 , even though the Hf—H bond ionicity ($100c_{\text{Hf}}^2 = 36.35\%$) still deviates appreciably from the covalent limit.

The general correlations of ionicity, d character, and molecular shapes are distinctive features of d-block bonding that warrant further examination. Normal-valent and hypovalent MH_4 molecules cannot adequately illustrate these correlations because tetrahedral shapes are expected both in the ionic and in the covalent bonding extreme. However, strong ionic-versus-covalent differences are expected in MH_2 (180° ionic versus 90° covalent) and MH_3 (120° ionic versus 90° covalent) cases. Table 4.6 summarizes the geometrical and NBO features for all possible simple dihydrides and trihydrides of the third transition series, illustrating how the deviations from idealized covalent geometry vary with metal charge (Q_M). (For open-shell species, the state of highest spin multiplicity has been selected in order to minimize

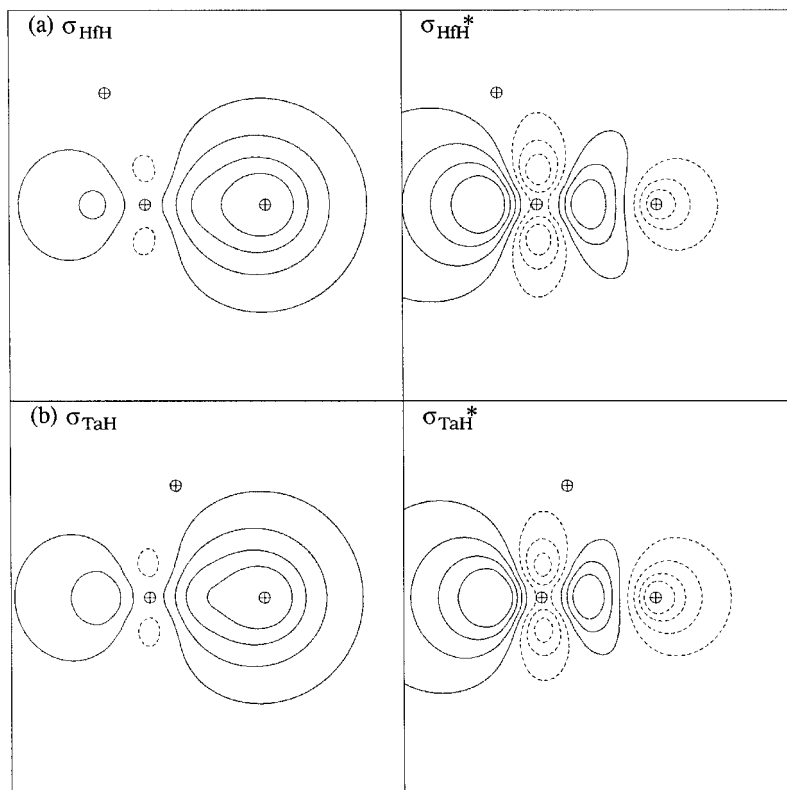


Figure 4.12 Metal hydride bond (σ_{MH}) and antibond (σ_{MH}^*) NBOs for hypovalent $\text{M} = \text{Hf}, \text{Ta}$.

complications arising from multiple near-degenerate configurations.) Table 4.6 displays how increasing ionic character (higher Q_{M}) of $\text{M}-\text{H}$ correlates strongly with increasing deviation of θ_{HMH} from 90° and higher d character in the $\text{M}-\text{H}$ bond hybrids. As we shall see later in this chapter, such correlations are general across the transition series and form the basis of a d-block generalization of Bent's rule.

From the polarities of the maximum-valency MH_n NBOs, one can infer the *natural electronegativity* $x_{\text{M}}^{(\text{N})}$ of each transition metal M , following the procedure outlined in Section 3.2.5. For cases in which two or more inequivalent $\text{M}-\text{H}$ bonds are present (e.g., ReH_5), we employ the average value of c_{M}^2 (or of the bond ionicity i_{MH}) to evaluate $x_{\text{M}}^{(\text{N})}$ from Eq. (3.60). Table 4.7 presents the natural electronegativity values for all three series of the d-block elements.

Finally, let us briefly consider the analogous behavior of MR_n metal alkyl compounds. Tables 4.8 and 4.9 summarize geometrical and NBO data for monomethylated complexes of the form MH_nMe . In agreement with simple Lewis-like pictures

Table 4.6. Geometries and NBO descriptors of MH_2 and MH_3 metal hydrides of the third transition series of various spin multiplicities ($2S + 1$), illustrating the correlations of metal charge (Q_M) with metal hybrid d character (% d , taken as the average of α and β hybrids for open-shell species), bond length (R_{MH}) and angle (θ_{HMH}), and average absolute deviation (Dev. = average $|\theta_{HMH} - 90^\circ|$), from idealized covalent geometry

MH_n	$2S + 1$	R_{MH} (Å)	θ_{HMH} (°)	% d	Dev.	Q_M
HfH ₂	3	1.845	120.1	75.0	30.1	0.994
TaH ₂	4	1.767	116.7	63.2	26.7	0.727
WH ₂	5	1.707	112.0	67.5	22.0	0.516
ReH ₂	4	1.615	72.8	66.3	17.2	0.123
OsH ₂	3	1.602	102.1	62.7	12.2	0.137
IrH ₂	2	1.547	91.9	61.3	1.8	-0.002
PtH ₂	1	1.514	85.6	54.3	4.4	-0.142
HfH ₃	2	1.841	118.7	73.2	28.7	1.447
TaH ₃	3	1.762(2) 1.784	121.8(2) 116.4	73.7	30.0	1.086
WH ₃	4	1.703	111.4	71.6	21.4	0.695
ReH ₃	3	1.626(2) 1.639	110.3(2) 82.8	69.5	15.9	0.271
OsH ₃	2	1.594	104.4	69.1	14.4	0.106
IrH ₃	1	1.541	90.4	66.7	0.4	-0.178

and hybridization schemes, the structures of these normal-valent alkyl complexes bear striking resemblance to the corresponding hydrides, with overall hybridizations closely approximating the predicted sd^n values. However, a significant feature of M—Me versus M—H bonding is the higher polarity of the former, with average $100c_M^2$ values ($\sim 36\%$ for M—Me versus $\sim 45\%$ for M—H) appreciably shifted from the idealized covalent limit (50%). As mentioned previously, increased bond polarity tends to be associated with higher percentage d character of M—Me bond hybrids and greater H—M—Me bond angles. Thus, for methyl metal hydrides the individual bond hybridizations can be viewed as deviations from idealized sd^n values resulting from competition for s character: the more covalent the bond, the higher (more nearly ideal) the s character.

The specific examples of PtHMe and PtMe₂ are illustrative. According to the elementary Lewis-like picture, stable monomethyl and dimethyl platinum analogs of

Table 4.7. Natural electronegativity values $x_M^{(N)}$ ("Pauling units") for d-block (group 3–11) elements of the first three transition series (Sanderson values¹⁹ $x_M^{(S)}$ for the first transition series are given in parentheses)

Group	First series			Second series		Third series	
	M	$x_M^{(N)}$	($x_M^{(S)}$)	M	$x_M^{(N)}$	M	$x_M^{(N)}$
3	Sc	1.16	(1.20)	Y	1.09	La	(1.0) ^a
4	Ti	1.55	(1.32)	Zr	1.43	Hf	1.34
5	V	1.79	(1.45)	Nb	1.67	Ta	1.54
6	Cr	(2.1) ^a	(1.56)	Mo	2.16	W	1.94
7	Mn	(2.0) ^a	(1.60)	Tc	2.25	Re	2.20
8	Fe	2.03	(1.64)	Ru	2.31	Os	2.17
9	Co	1.96	(1.70)	Rh	2.23	Ir	2.22
10	Ni	1.87		Pd	2.04	Pt	2.30
11	Cu	1.47		Ag	1.48	Au	2.01

^a Interpolated (no satisfactory normal-valent hydride is available).

PtH₂ should exist, with dot diagrams such as (4.15) and expected $\sim sd^1$ hybridization leading to strongly bent geometry analogous to that shown in Fig. 4.6(c). These expectations are generally fulfilled, as depicted in the optimized structures shown in Fig. 4.13. The H—Pt—C angle in HPtCH₃ is 93.2°, which is very close to the idealized ML₂ value of 90° (Fig. 4.2(a)). The corresponding C—Pt—C angle in Pt(CH₃)₂ is somewhat larger (102.4°), apparently due to the somewhat higher bond polarity and unfavorable steric interactions. The hybridization is also found to be generally similar to that in PtH₂ ($sd^{1.19}$), but with slightly higher d character in hybrids to carbon ($sd^{1.41}$ in HPtCH₃, $sd^{1.31}$ in Pt(CH₃)₂). The similarities between

Table 4.8. Bond lengths (R_{MC} and R_{MH}) and angles (θ_{CMH} and θ_{HMH}) of saturated metal methylhydrides MH_{*n*}Me of the third transition series

MH _{<i>n</i>} Me	Symmetry	R_{MC} (Å)	R_{MH} (Å)	θ_{CMH} (degrees)	θ_{HMH} (degrees)
WH ₅ Me	$\sim C_{5v}$	2.061	1.682(4)	113.4	65.1(5), 121.4(5)
ReH ₄ Me	$\sim C_s$	2.012	1.672(2), 1.632, 1.637	115.2(2), 119.1(2)	63.9, 75.4, 76.2, 122.9(2)
OsH ₃ Me	$\sim C_{3v}$	2.001	1.598(3)	111.6(3)	107.3(3)
IrH ₂ Me	$\sim C_s$	2.004	1.545(2)	100.1(2)	90.3
PtHMe	$\sim C_s$	2.004	1.518	93.2	
AuMe	$C_{\infty v}$	2.048			

Table 4.9. The NBO descriptors for the species of Table 4.8, showing the percentage accuracies ($\% \rho_L$) of the Lewis-like description (valence shell and total), metal hybrid (h_M), percentage polarization toward M ($100c_M^2$), and occupancy of σ_{MC} and σ_{MH} NBOs

MH_nMe	$\% \rho_L$		σ_{MC}			σ_{MH}		
	Valence	Total	h_M	$100c_M^2$	Occupancy (e)	h_M	$100c_M^2$	Occupancy (e)
WH ₅ Me	97.54	99.44	sd ^{5.06}	31.97	1.998	sd ^{4.98}	48.1	1.935
ReH ₄ Me	98.31	99.62	sd ^{5.72}	37.67	1.996	sd ^{3.20} (2)	49.3	1.973
						sd ^{4.27} (2)	52.2	1.941
OsH ₃ Me	99.23	98.80	sd ^{4.01}	40.92	1.990	sd ^{2.74}	49.9	1.989
IrH ₂ Me	99.68	99.79	sd ^{2.32}	43.40	1.977	sd ^{1.94}	53.0	1.966
PtHMe	99.78	99.82	sd ^{1.41}	46.03	1.962	sd ^{1.09}	53.3	1.952
AuMe	99.85	99.97	sd ^{0.25}	43.30	1.999			

transition-metal hydrides and alkyls therefore appear to parallel closely those in main-group compounds, as the Lewis-like picture would suggest.

4.4.2 Metal alkylidenes and alkylidynes

The Lewis-like picture suggests²⁰ that saturated metal alkylidenes (carbenes) $H_nM=CH_2$ of special stability should correspond to duodectet-rule-conforming

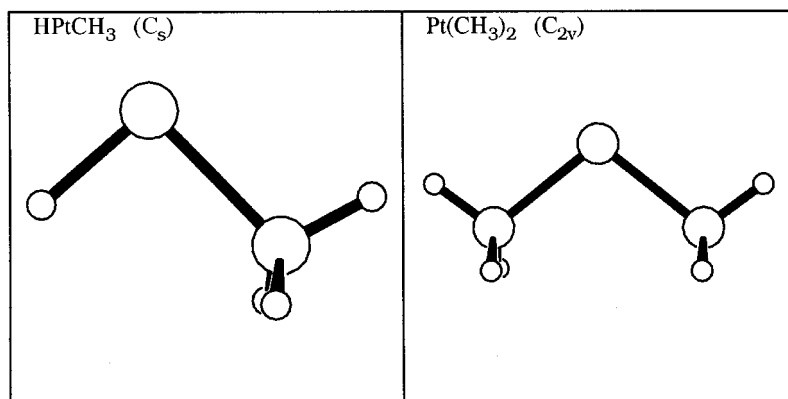
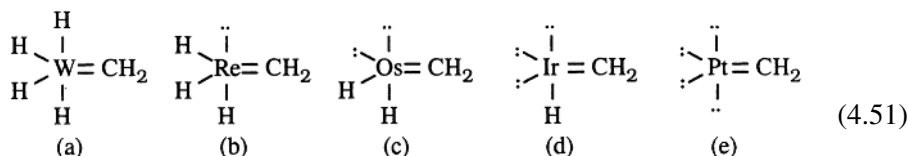


Figure 4.13 Optimized geometries of monomethylplatinum(0) and dimethylplatinum(0) compounds, showing strongly bent structures analogous to PtH₂ (Fig. 4.7(c)).

structures of the form, e.g., for $M = W-Pt$

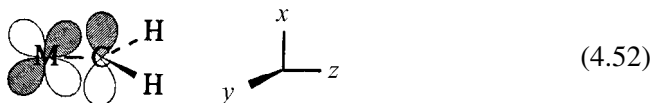


In each case the central metal atom of H_nMCH_2 is expected to form a skeleton of $n + 1$ sigma bonds (n to H, one to C) using approximate sd^n hybridization.

However, the important new feature of metal alkylidenes (4.51) is metal-carbon pi-bonding. As discussed in Section 2.8, pi bonds between transition metals and main-group elements are of $d_\pi-p_\pi$ type, *much* stronger than corresponding $p_\pi-p_\pi$ bonds between heavier main-group elements. Compared with simple metal hydrides and alkyls, metal-carbon pi-bonding in metal alkylidenes affects the selection of metal d orbitals available for hybridization and skeletal bond formation, somewhat altering molecular shapes.

Optimized geometries for the metal alkylidenes (4.51) are shown in Fig. 4.14, and the corresponding bond lengths and angles are summarized in Table 4.10. The role of covalency and hybridization is immediately suggested by the highly unusual metal bond angles, which are certainly “strange” from an electrostatic, steric, or VSEPR perspective. The NBO descriptors of each compound are summarized in Table 4.11, showing the excellent quality of the Lewis-like description in each case (99.6%–99.9% ρ_L). We shall now consider how the shapes of these compounds can be related to details of the sigma and pi NBO compositions.²¹

Construction of the metal-alkylidene sigma skeleton can be visualized in the following manner. Suppose that the M—C bond is taken to lie along the z axis, with the two C—H bonds in the $y-z$ plane,



The metal sigma hybrid to carbon is of standard form,

$$h_\sigma = (1 + \mu)^{-1/2}(s + \mu^{1/2}d_z^2) \quad (4.53a)$$

while the corresponding metal pi-bonding orbital is the pure d_{xz} atomic orbital

$$h_\pi = d_{xz} \quad (4.53b)$$

The remaining metal hybrids to hydrogen (h_σ') must therefore be chosen orthogonal to both h_σ and h_π . The orthogonality constraint $\langle h_\pi | h_\sigma' \rangle = 0$ has no effect on hydride bonds lying in the $y-z$ plane of the methylene group, but it mandates that those lying *out of plane* must lie close to the nodal angle of the d_{xz} orbital, i.e., pointing in the $\pm x$ direction *perpendicular* to the M—C bond axis. Thus, the out-of-plane

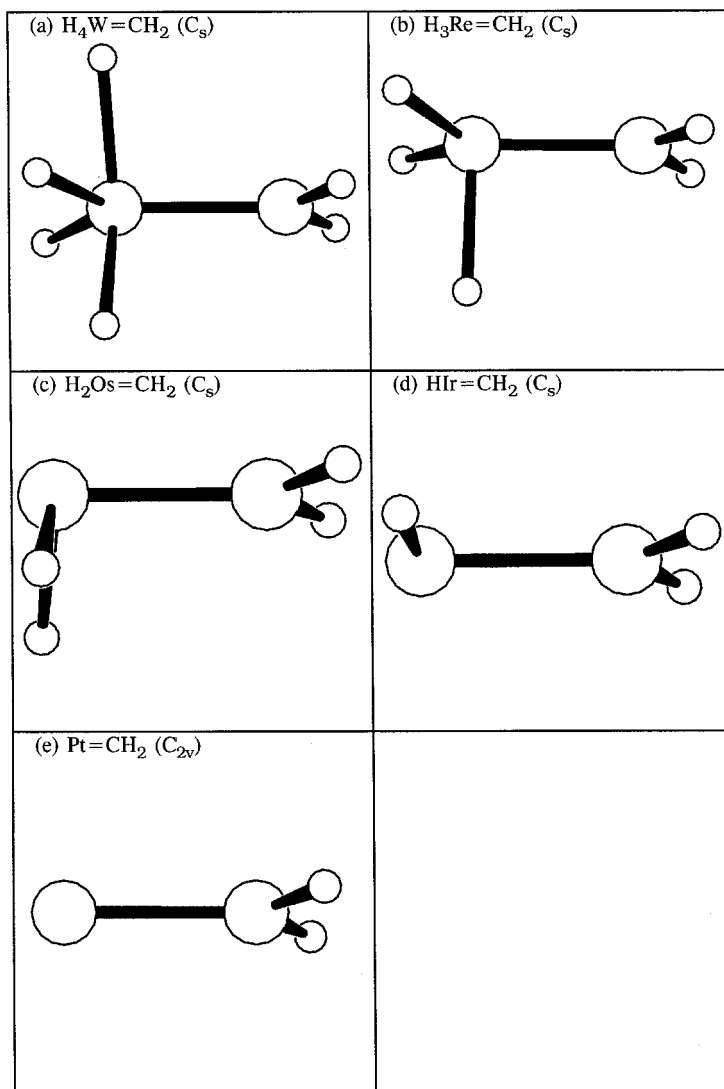


Figure 4.14 Optimized geometries of saturated group 6–10 third-series transition-metal alkylidenes $\text{H}_n\text{M}=\text{CH}_2$ ($\text{M} = \text{W-Pt}$).

hydride bonds should be nearly at right angles to the $\text{M}-\text{C}$ bond, while the in-plane hydride bonds can adopt more nearly ideal angles of equivalent sd^n hybridization.

For $n = 1$ (HIrCH_2) or $n = 2$ (H_2OsCH_2) the idealized sd^n angles are already 90° , so that orthogonality to the π_{MC} bond is achieved automatically. However, for $n = 3$ (H_3ReCH_2) and $n = 4$ (H_4WCH_2) the in-plane hydride bonds can make angles that deviate strongly from perpendicularity, whereas the out-of-plane $\text{M}-\text{H}$ bonds are constrained to lie nearly at right angles ($92-95^\circ$) to the $\text{M}-\text{C}$ axis. Of course, three equivalent in-plane hybrids must make bond angles of 120° , and the

Table 4.10. *Optimized bond lengths R_{MC} and R_{MH} and angles θ_{HMC} and θ_{HMH} of transition-metal alkylidenes $H_nM=CH_2$ in Fig. 4.14. (The subscripts “i” and “o” distinguish H—M—H angles that are respectively “in plane” and “out of plane” with respect to the methylene group.)*

H_nMCH_2	Symmetry	R_{MC} (Å)	R_{MH} (Å)	θ_{HMC} (degrees)	θ_{HMH} (degrees)
H_4WCH_2	C_s	1.872	1.688(2), 1.734 1.687	94.5 (2), 117.8, 118.4	123.8 _i , 125.1 _o , 64.1 (2), 111.1 (2)
H_3ReCH_2	C_s	1.839	1.656 (2), 1.629	92.1, 117.4 (2)	119.4 _i , 100.9 _o
H_2OsCH_2	C_s	1.827	1.599 (2)	95.4 (2)	108.0
$HIrCH_2$	C_s	1.796	1.549	97.4	
$PtCH_2$	C_{2v}	1.796			

values that are actually found ($\theta_{HMC} = 117-118^\circ$, $\theta_{HMH} = 119-124^\circ$) lie close to this limit. Thus, the geometries of Fig. 4.14, although “strange” from a VSEPR-like or main-group perspective, are quite reasonable in the framework of the sd^{μ} Lewis-like picture.

The detailed NBO hybridizations shown in Table 4.11 are in general accord with this picture. The metal hybridization toward C has slightly higher d character than ideal sd^{μ} would suggest (as expected due to the higher polarity of the M—C bonds) whereas hybrids toward in-plane H atoms have correspondingly reduced d character, but the overall pattern of agreement with an idealized sd^{μ} picture is striking. As in the pure hydrides, metal p character appears to play no significant role in the hybridization and bonding of metal alkylidenes.²²

The forms of the localized metal–carbon pi bond and antibond NBOs are again highly recognizable and transferable from species to species. This transferability is

Table 4.11. *The NBO descriptors of the H_nMCH_2 metal alkylidenes in Fig. 4.14, showing the percentage accuracies ($\% \rho_L$) of the Lewis-like description (valence shell and total), metal hybrid (h_M), percentage polarization toward M ($100c_M^2$), and occupancies of bonding σ_{MC} and π_{MC} NBOs*

H_nMCH_2	$\% \rho_L$		h_M	σ_{MC}		π_{MC}	
	Valence	Total		$100c_M^2$	Occupancy (e)	$100c_M^2$	Occupancy (e)
$H_4W=CH_2$	98.24	99.61	$sd^{4.15}$	36.81	1.989	47.66	1.976
$H_3Re=CH_2$	98.94	99.74	$sd^{4.16}$	40.18	1.982	51.59	1.986
$H_2Os=CH_2$	99.11	99.78	$sd^{6.63}$	49.32	1.986	49.37	1.959
$HIr=CH_2$	99.36	99.84	$sd^{1.55}$	43.35	1.979	59.85	2.000
$Pt=CH_2$	99.71	99.93	$sd^{0.51}$	39.93	1.997	68.05	2.000

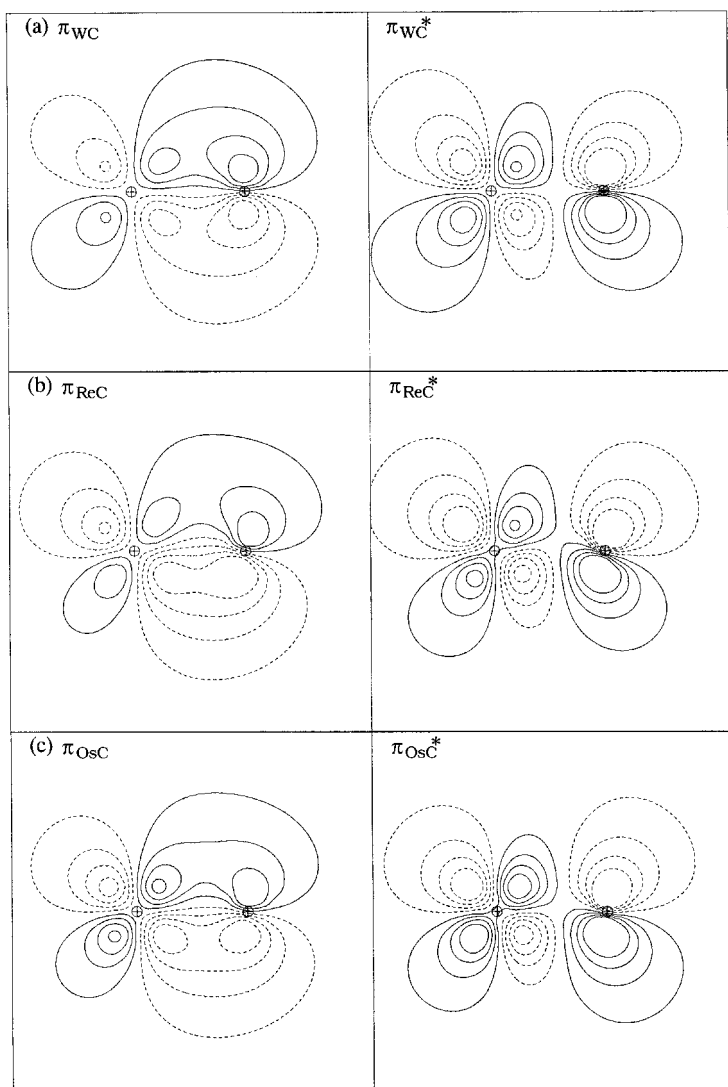


Figure 4.15 Metal–carbon pi-bond (π_{MC}) and antibond (π_{MC}^*) NBOs of saturated group 6–10 transition-metal alkylidenes $H_nM=CH_2$.

exhibited in Fig. 4.15, which shows contour diagrams of π_{MC} and π_{MC}^* NBOs for the entire range $M = W$ –Pt of saturated metal alkylidenes. Some “bond bending” (as discussed below) is evident both in the σ and in the π Re–C bonds, as seen in $H_3Re=CH_2$ (Fig. 4.15(b)), and $H_2Os=CH_2$ (Fig. 4.15(c)), but the effective diatomic “ π ” label of the NBOs is generally descriptive for all these species.

It is noteworthy from Table 4.11 that σ_{MC} and π_{MC} bonds differ in their polarizations, with σ_{MC} polarized slightly more toward carbon and π_{MC} exhibiting either no polarization or a slight preference for the metal. The π_{MC} bond polarization reflects

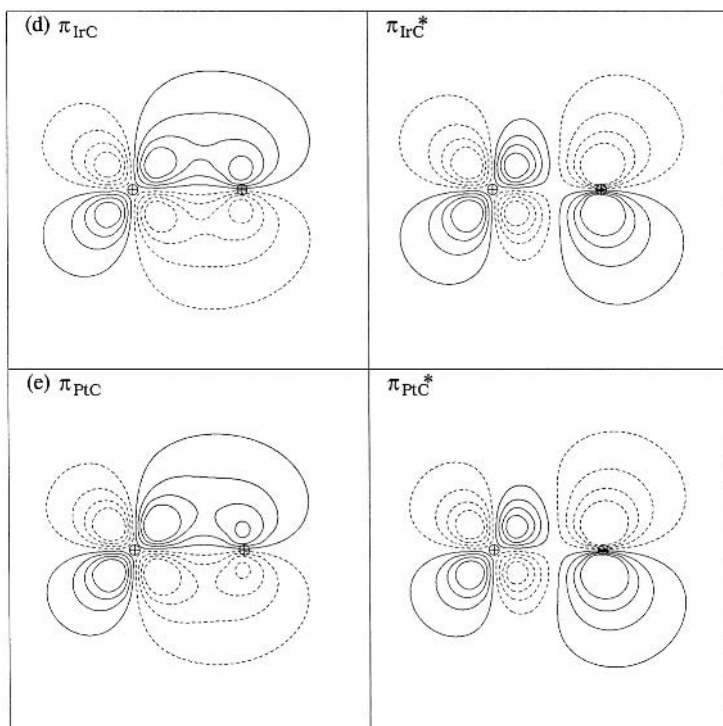


Figure 4.15 (Cont.)

excellent balance between metal d and carbon p orbitals in forming electron-pair pi bonds.

From the pi-bond polarities in Table 4.11 we can readily infer *natural pi electronegativity* values for each metal atom, following the procedure outlined in Section 3.2.8. Numerical values of such pi electronegativities for the first three transition series are presented in Table 4.12.

Comparison of the pi electronegativities in Table 4.12 with the sigma electronegativities of Table 4.6 reveals similar trends but a more constricted range, with a slight tendency toward higher metal electronegativities in forming pi bonds. We have seen in Chapter 3 that p-block elements exhibit similar trends, but the vertical ranges for d-block pi electronegativities are even more compressed.

A corresponding Lewis-like picture can be developed for triply bonded metal alkylidynes (H_nMCH), such as the duodecet-rule-conforming examples

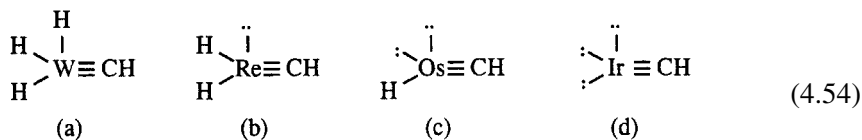


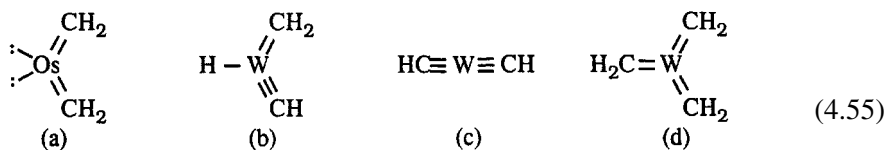
Table 4.12. Natural π electronegativity values ($x_M^{(\pi)}$, “Pauling units”) for the d -block elements (π -bonding elements of groups 3–10) in the first three transition series

Group	First series		Second series		Third series	
	M	$x_M^{(\pi)}$	M	$x_M^{(\pi)}$	M	$x_M^{(\pi)}$
3	Sc	1.89	Y	1.78	La	(1.7) ^a
4	Ti	2.29	Zr	2.11	Hf	1.96
5	V	2.54	Nb	2.32	Ta	2.18
6	Cr	2.42	Mo	2.54	W	2.50
7	Mn	2.34	Tc	2.39	Re	2.53
8	Fe	2.17	Ru	2.19	Os	2.57
9	Co	2.23	Rh	2.03	Ir	2.20
10	Ni	1.97	Pd	1.69	Pt	1.92

^a Extrapolated estimate; no stable La(CH₂)H structure has been found.

Because the two metal–carbon π bonds now extend into *both* dimensions perpendicular to the axis of the metal–carbon bond, the residual metal–hydride bonds are *all* constrained to lie essentially orthogonal to the M–C axis (i.e., in the nodal “hollows” of the π -bonding d_{xz} and d_{yz} orbitals). The optimized structures, as shown in Fig. 4.16, all reveal this common structural tendency, with near-perpendicular (91–96°) H–M–C bond angles in all cases.

Finally, one can readily visualize various duodecet-rule-conforming alkylidene/alkylidyne complexes with more extensive multiple bonding, such as



(Recall that such Lewis-like diagrams are intended to convey only the localized electron-pair assignments about the central hexavalent metal atom, *not* the molecular shape.) Here Os(CH₂)₂ typifies allene-like bonding, while HW(CH₂)(CH), W(CH)₂, and W(CH₂)₃ represent cases of higher central-atom bond order that are unachievable with main-group elements.

The optimized geometries of (4.55a)–(4.55d) are shown in Fig. 4.17 and selected geometrical parameters are summarized in Table 4.13. The molecular shapes and NBO descriptors (not presented) generally agree with the idealized Lewis-like sd^{μ} picture for Os(CH₂)₂, HW(CH₂)(CH), and W(CH₂)₃. However, the C–W–C angle (42°) in the ground state of W(CH)₂ is much smaller than expected for idealized sd^1 geometry, and the optimal NBO description corresponds to a metallacyclopropene,

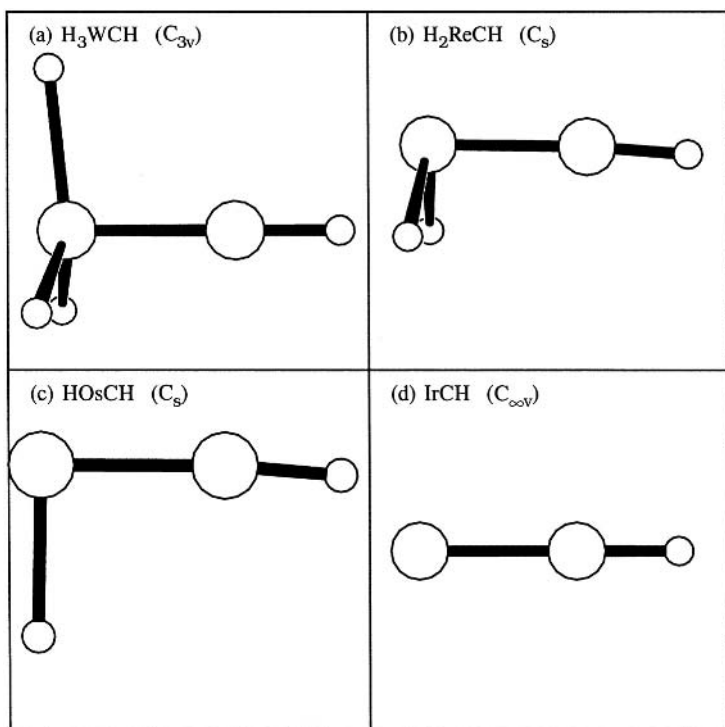


Figure 4.16 Optimized structures of transition-metal alkylidynes H_nMCH ($M = \text{W-Ir}$).

with two W-C single bonds and a C=C double bond rather than the acyclic triple-bonded structure (4.55c); the latter is in this case a metastable species (also a true local minimum) lying about 30 kcal mol^{-1} above the metallacyclopropene isomer.

The failure of $\text{W}(\text{CH}_2)_2$ to achieve “expected” dialkylidyne structure (4.55c) can be readily understood from the number and types of available *d* orbitals. Let us suppose that the CWC skeleton is taken to lie in the x - y plane and that the $d_{x^2-y^2}$ orbital is used to construct perpendicular sd^1 sigma hybrids along the x and y axes. We can then employ d_{xz} and d_{yz} orbitals to construct one out-of-plane pi bond to each ligand, but this leaves only *one* remaining in-plane (d_{xy}) metal orbital for an orthogonal in-plane pi bond, and two full triple bonds are therefore impossible. Thus, the existence of a duodectet-rule-conforming Lewis-like formula may be insufficient to guarantee that the corresponding electronic bonding pattern can actually be achieved within the constraints of sd^u hybridization.

More detailed examination of the structures, orbitals, and energetics of $\text{Ir}(\text{CH}_2)\text{H}$, $\text{Os}(\text{CH}_2)_2$, and $\text{W}(\text{CH}_2)_3$ reveals some unexpected nuances in the nature of σ and π bonds at transition-metal centers. Figure 4.18 illustrates the idealized

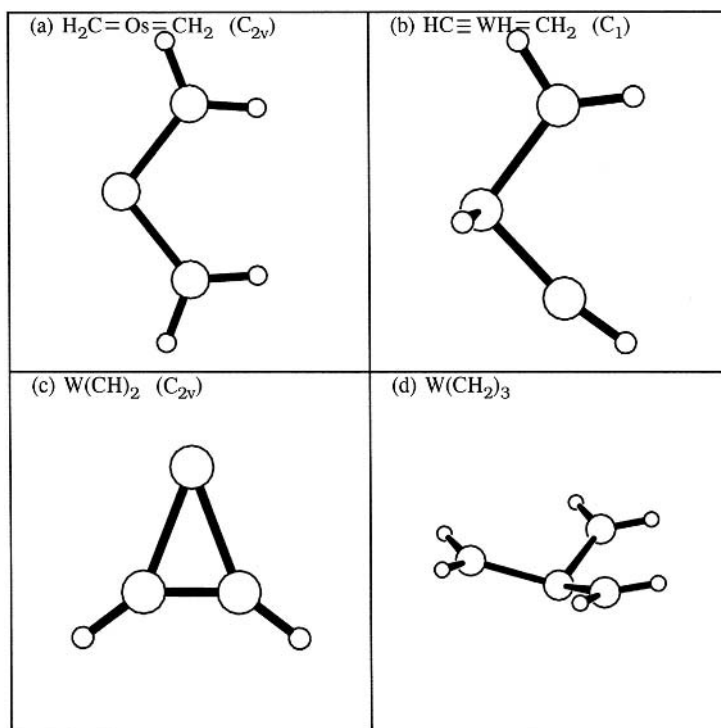


Figure 4.17 Optimized structures of compounds (4.55) with high degrees of multiple bonding (see Table 4.13): (a) $\text{Os}(\text{CH}_2)_2$, (b) $\text{HW}(\text{CH}_2)(\text{CH})$, (c) $\text{W}(\text{CH})_2$, and (d) $\text{W}(\text{CH}_2)_3$.

Table 4.13. Selected geometrical parameters of highly multiple-bonded species (see Fig. 4.17)

Molecule	M	R_{MC} (Å)	θ_{CMC} (degrees)	θ_{MCH} (degrees)	θ_{CMH} (degrees)
$\text{Os}(\text{CH}_2)_2$	Os	1.824	106.4	125.2(2) 120.0(2)	
$\text{HW}(\text{CH}_2)(\text{CH})$	W	1.886 1.750	100.3	136.7 108.6 167.7	95.5 94.3
$\text{W}(\text{CH})_2$	W	1.909	41.7	148.0	
$\text{W}(\text{CH}_2)_3$	W	1.902	109.4	123.2(3) 122.7(3)	

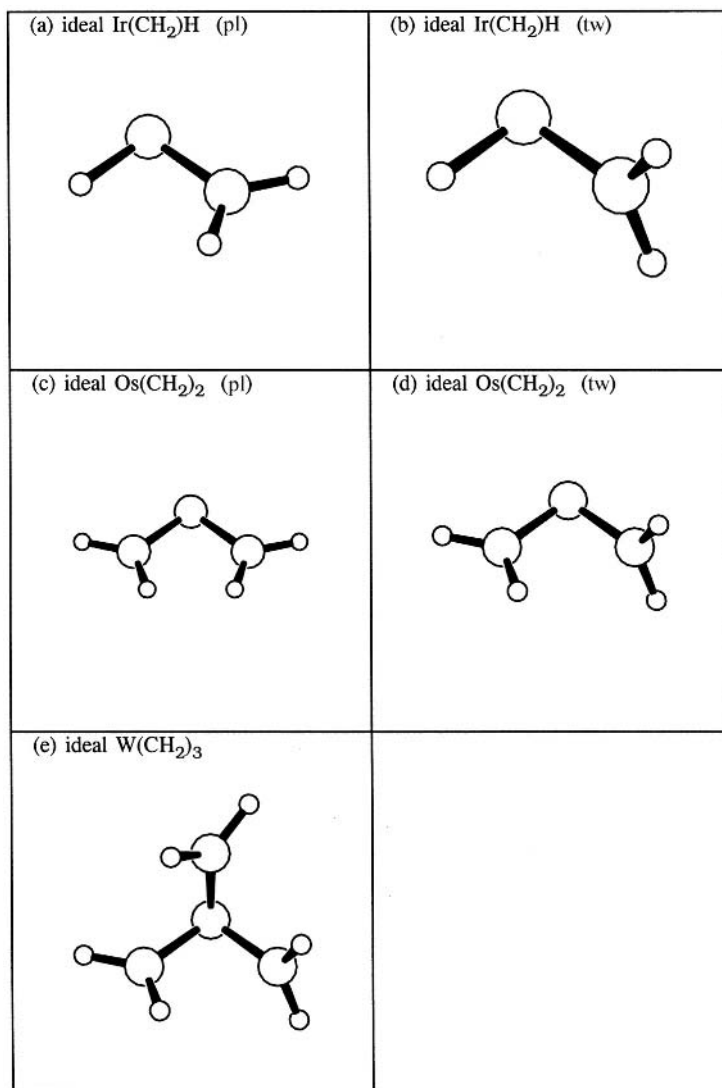


Figure 4.18 Idealized structural isomers of $\text{Ir}(\text{CH}_2)\text{H}$ ((a) pl and (b) tw) and $\text{Os}(\text{CH}_2)_2$ ((c) pl and (d) tw), and $\text{W}(\text{CH}_2)_3$ (e).

structural isomers one might predict for these three species. At the zeroth order of approximation, $\text{Ir}(\text{CH}_2)\text{H}$ and $\text{Os}(\text{CH}_2)_2$ each make two perpendicular σ bonds from metal sd^1 hybrids; due to the higher polarity of $\text{M}-\text{C}$ bonds we actually expect somewhat more d character than sd^1 and some opening of the bond angles. Addition of π bonds, one for the iridium complex and two for the osmium, completes the bonding. Accordingly, both molecules are expected to exhibit bent coordination geometries at the metal with bond angles slightly greater than 90° . Consideration

of idealized orientations of the CH_2 planes leads to two isomers, labeled planar (pl) and twist (tw), of presumably similar energy, for each molecule. As shown in Figs. 4.18(a)–(d), these isomers differ in orientation of the π bonds with respect to the plane defined by the two σ bonds. (Note that a third isomer of $\text{Os}(\text{CH}_2)_2$ with both π bonds lying in the OsC_2 plane is prohibited, since it would require both π bonds to form from the same in-plane d orbital.) Because $\text{W}(\text{CH}_2)_3$ makes three $\text{M}=\text{C}$ double bonds, just one isomer (Fig. 4.18(e)) with $90^\circ \text{C}-\text{W}-\text{C}$ bond angles ($\sim\text{sd}^2$ hybridization) and three π bonds lying in mutually orthogonal planes would be expected.

However, DFT computations demonstrate a significantly different picture. The idealized isomers are *not* near-degenerate (nor even all stable minima!) and the CH_2 planes of the low-energy structures distort *away* from mutual orthogonality, with distinct “banana bonding” (loss of σ/π symmetry) in the case of $\text{W}(\text{CH}_2)_3$. Although the tw structures of $\text{Ir}(\text{CH}_2)\text{H}$ and $\text{Os}(\text{CH}_2)_2$ superficially appear less crowded, they are actually found to be *unstable* transition states (13–16 kcal mol⁻¹ higher in energy, with strong imaginary frequencies for $\text{H}-\text{M}-\text{C}-\text{H}$ torsions: $809i$ for $\text{M} = \text{Ir}$, $601i$ for $\text{M} = \text{Os}$) between the equilibrium pl structures, as shown for $\text{Os}(\text{CH}_2)_2$ in Fig. 4.17(a). Table 4.14 compares energetic and NBO characteristics of the calculated pl/tw isomeric species, showing the expected similarity in NBO descriptions despite the surprising difference in torsional energy. The optimized structure for $\text{W}(\text{CH}_2)_3$, Fig. 4.17(d), also shows strong distortion away from the idealized tri-orthogonal structure depicted in Fig. 4.18(e). Clearly the idealized sigma/pi-bonding picture is inadequate in these cases.

Table 4.14. *Relative energies (E_{rel}) and NBO characteristics of optimized pl and tw isomers of $\text{Ir}(\text{CH}_2)\text{H}$, $\text{Os}(\text{CH}_2)_2$, and $\text{W}(\text{CH}_2)_3$ (see Fig. 4.18), showing Lewis densities (ρ_{L}), hybridizations (h_{M}), and bond polarizations ($100c_{\text{M}}^2$) for each species*

Species	E_{rel} (kcal mol ⁻¹)	ρ_{L} (%)		σ_{MC}		π_{MC}		
		Valence	Total	h_{M}	$100c_{\text{M}}^2$	h_{M}	$100c_{\text{M}}^2$	
$\text{Ir}(\text{CH}_2)\text{H}$	tw	+12.9	98.92	99.77	$\text{sd}^{2.01}$	44.0	$\sim\text{d}$	63.1
	pl	0.0	99.28	99.83	$\text{sd}^{1.55}$	43.4	$\sim\text{d}$	59.8
$\text{Os}(\text{CH}_2)_2$	tw ^a	+16.0	98.86	99.70	$\text{sd}^{2.10}$	42.8	$\sim\text{d}$	53.8
					$\text{sd}^{1.70}$	41.6	$\sim\text{d}$	57.6
	pl	0.0	99.06	99.74	$\text{sd}^{1.71}$	41.9	$\sim\text{d}$	54.7
$\text{W}(\text{CH}_2)_3$			98.44	99.54	$\text{sd}^{2.01}$	35.9	$\sim\text{d}$	46.3

^a For this isomer the two $-\text{CH}_2$ groups are inequivalent due to minor distortion of one of the $\text{M}-\text{C}-\text{H}$ bond angles.

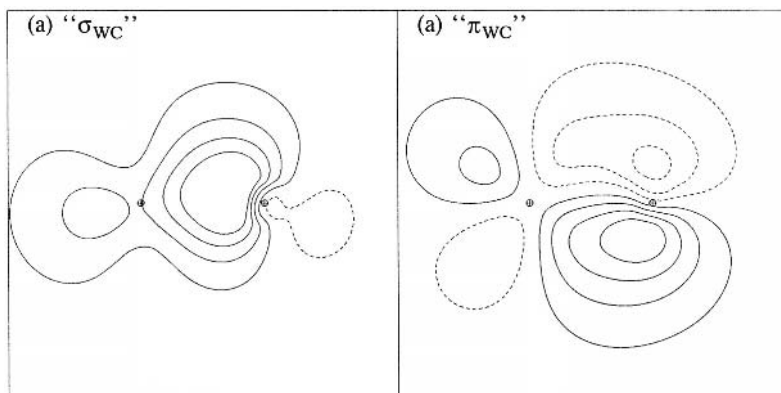


Figure 4.19 The “ σ_{WC} ” (left) and “ π_{WC} ” (right) NBOs of $W(CH_2)_3$, showing significant deviations from idealized σ/π symmetry. The W atom is on the left and the contour plane is perpendicular to the plane of WCH_2 nuclei.

The strongly bent nature of the NBOs of $W(CH_2)_3$ is depicted in Fig. 4.19, confirming the inadequacy of a simple σ/π -bonding picture for this species. Both contour plots are plotted in a plane perpendicular to the CH_2 plane, showing the expected bending of the nominal σ - and π -bond-forming hybrids centered *both* on M and on C in directions above and below the internuclear M—C axis. While the NBOs can still be crudely described with nominal “ σ ” and “ π ” labels, incipient “banana-bond” character is clearly significant.

Why do metal-alkylidene complexes deviate from the idealized structural and energetic expectations of a simple σ/π Lewis-like bonding model? Some factors, such as $>90^\circ$ C—M—C bond angles are attributable to M—C bond polarity and concomitant increase in d character of the sigma hybrids. However, this does not lend insight into the substantial energy differences of pl and tw isomers. (Unlike main-group torsional variations, which are typically of hyperconjugative origin [see Section 3.4.2], the pl/tw energy difference in $Ir(CH_2)H$ and $Os(CH_2)_2$ seems to be strongly established in the idealized Lewis limit, and thus reflects an inherent preference for pl over tw assignments of the primary Lewis-like skeletal hybrids, rather than a secondary delocalization effect.) A significant disadvantage of the tw-like Lewis structure may arise from the fact that the three metal bond pairs (two σ , one π) are forced into a common plane in tw geometry, increasing steric exchange repulsion, whereas π — σ exchange interactions are averted when π_{MC} remains perpendicular to the sigma plane, as in pl geometry. Another factor may involve the odd $n^{(h)}$ hybridized lone pair of sd^1 hybridization (Eqs. (4.36)–(4.41)), which requires still more complex hybrid mixing in order for it to remain orthogonal to the in-plane π_{MC} bond required by the tw isomer, and thus may tend to oppose σ/π coplanarity and promote σ/π breakdown in some unusually strong fashion for the

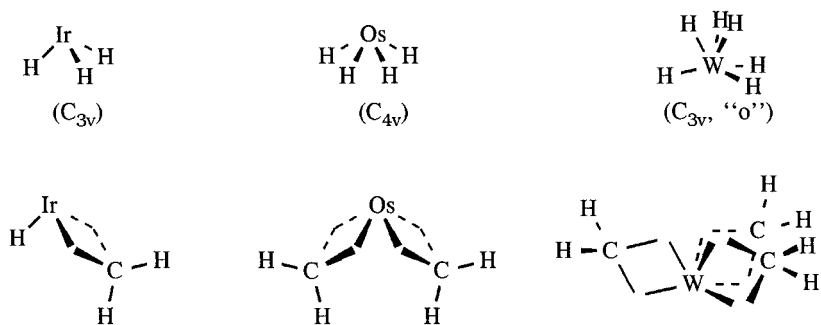


Figure 4.20 A schematic illustration comparing parent hydride and symmetry (above; cf. Figs. 4.2(b), 4.3(c), and 4.5(b)) with the derivative alkylidene (below) in the idealized “banana-bonded” limit for $\text{Ir}(\text{CH}_2)\text{H}$ (left), $\text{Os}(\text{CH}_2)_2$ (center), and $\text{W}(\text{CH}_2)_3$ (right).

sd^1 case. Whatever the proper rationalization for these tendencies, the anomalous character of pi versus banana bonding in transition-metal species should be noted.

Consideration of $\text{M}=\text{C}$ double bonds in the limit of two banana-like single bonds provides intriguing insight into the relative stabilities of the idealized isomers, as depicted schematically in Fig. 4.20 for $\text{Ir}(\text{CH}_2)\text{H}$, $\text{Os}(\text{CH}_2)_2$, and $\text{W}(\text{CH}_2)_3$. In the limit of pure banana-bond character, the orbital picture for $\text{Ir}(\text{CH}_2)\text{H}$ consists of three $\sim\text{sd}^2$ hybrids and three pure d lone pairs at Ir and four $\sim\text{sp}^3$ hybrids at C. Accordingly, the three sd^2 hybrids lie along the Cartesian axes with H on one axis and the M—C line of centers bisecting the other two axes. (The M—C bond hybrids are expected to have somewhat higher d character due to higher M—C bond polarity.) More importantly for our purposes, this picture *requires* that the M—H bond lie in the methylidene plane (pl rotamer), as shown on the left in Fig. 4.20.

Similar reasoning can rationalize the structure of $\text{Os}(\text{CH}_2)_2$. The bent-bond model for $\text{Os}(\text{CH}_2)_2$ prescribes four $\sim\text{sd}^3$ hybrids and two lone pairs at Os. As seen earlier in this chapter, the lobes of four centrosymmetric sd^3 hybrids point to the corners of a cube, yielding three imaginable four-coordinate isomers (T_d , C_{3v} , and C_{4v}). For the present case, the C_{4v} -type motif would appear to be preferred, because it allows each methylidene to make two such bonds at small angles (71°), prevents a strongly disfavored linear C—Os—C arrangement, and maintains equivalency in each of the bonds. The C_{4v} bent-bond motif corresponds to placing the two C atoms at the midpoints of two parallel edges of one face of the cube. Necessarily, the two methylidenes are coplanar and the C—Os—C angle is strongly bent, corresponding to the favored pl structure represented in Fig. 4.20 (middle).

To view $\text{W}(\text{CH}_2)_3$ in the corresponding limit of six sd^5 hybrid banana bonds, begin with the distorted trigonal prismatic C_{3v} isomer. Place the three methylidene carbons midway along the three vertical edges of the prism with the methylidene

planes normal to each edge. The result is a “bowl-shaped” structure closely resembling the calculated structure shown in Fig. 4.17(d) and schematically depicted in Fig. 4.20 (right). In striking contrast to the idealized structure based on perfect σ/π separation (Fig. 4.18(e)), the methyldiene planes are far from orthogonal and the C—W—C bond angles (109.6°) deviate strongly from 90° .

Incorporation of partial bent-bond character into the electronic description of metal alkylidenes helps us to understand preferences among structural isomers, but why should this be a more conspicuous feature of transition-metal–ligand bonding? It is important to recall that some instances of bond-bending were found in the p block, such as the hyperconjugated vinylamine and Ga₂ dimer discussed in Chapter 3. (However, we cannot concur with the conclusion of Messmer and Schultz²³ that bent bonds are *generally* the superior description of multiple-bonding in p-block compounds.) The vinylamine example makes clear how strong π -type interactions (namely $n_N^{(\pi)} \rightarrow \pi_{CC}^*$ hyperconjugation) can alter the expectations of a simple σ -hybridization skeletal model, and we might expect on this basis that the characteristically stronger π -type d_M-p_C interactions in transition-metal complexes would tend to increase the number of such “exceptional” cases in d-group chemistry. However, a more prosaic reason for the “conspicuous” σ/π breakdown in d-block chemistry is that the *consequences* of bond-bending are more readily perceived in this case. Owing to the limited valencies and shapes for p-block elements, there are few structural keys to distinguish the limits of σ/π versus banana-bonding pictures qualitatively; for example, regardless of which model we employ, we predict that H₂CCH₂ and PH(CH₂) will feature coplanarity of all atoms. Only for covalent d-group compounds do the limits of pure banana bonding versus σ/π bonding differ conspicuously.

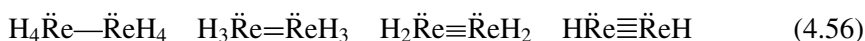
As a further aspect of M=C double bonding, we can briefly mention metal alkylidenes of “Fischer-carbene” type.²⁴ The distinguishing feature of Fischer carbenes is heteroatom substitution at carbon, usually in the form of an alkoxy or amido group (both strong π -type hyperconjugative groups). The reaction chemistry of these carbenes features susceptibility to attack *by* nucleophiles, similar to that expected of activated esters or imides. In contrast, the unsubstituted metal alkylidenes (“Schrock-type carbenes”²⁵) tend to act *as* nucleophiles. The NBO analysis of the model Fischer carbene, Ir(CHO)H, reveals significant differences from the Schrock-carbene analog, IrCH₂H. The geometrical features of the two compounds are rather similar, but the *electronic* structures exhibit telling differences. As expected, heteroatom substitution with an electronegative oxygen atom increases the positive charge at C ($Q_C = +0.212$ versus -0.297), rendering it relatively electrophilic. Relative to the Schrock-type carbene, the M—C sigma bond of the Fischer carbene is therefore more polarized toward carbon, but the π -bond is strongly polarized toward the *metal*, enhancing the expected strong $n_O \rightarrow \pi_{MC}^*$

interaction ($\sim 45 \text{ kcal mol}^{-1}$) of the adjacent oxygen lone pair with the metal–carbon pi antibond. Thus, the vicinal hyperconjugative modifications of $\text{M}=\text{C}$ double bonds appear to parallel those of main-group double bonds in a satisfying manner (cf. Section 4.8).

4.4.3 Metal–metal bonding

Multiple bonding in dinuclear hydrides

Let us first consider metal–metal bonding²⁶ in simple dinuclear hydrides H_nMMH_n . For $\text{M} = \text{Re}$, for example, the four possible duodecet-rule-conforming Lewis-like structures are



corresponding to increasing metal–metal multiple-bonding (up to *quadruply* bonded $\text{HRe}\equiv\text{ReH}$ for $n = 1$) as n decreases. Figure 4.21 displays the optimized geometries of these four species, showing the expected “weird” ReH_n bond angles of sd^{n-1} hybridization at each terminus. However, our present focus is on the nature

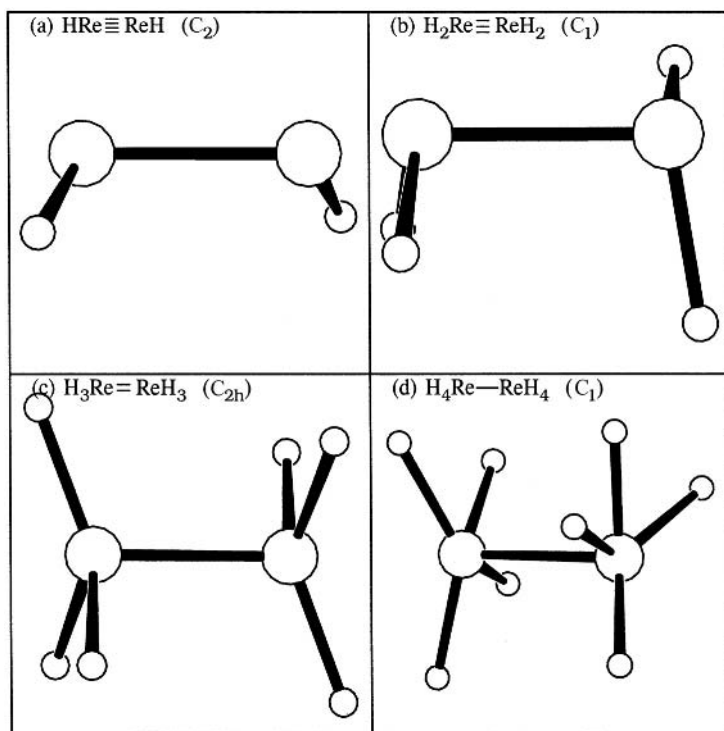


Figure 4.21 Optimized structures of saturated H_nReReH_n , $n = 1-4$.

Table 4.15. Calculated metal–metal (R_{MM}) and average metal–hydride (\bar{R}_{MH}) bond lengths, NBO Lewis-like structures, and percentage accuracies of the localized description ($\% \rho_{\text{L}}$) for saturated H_nMMH_n hydrides (M = Ta–Pt)

H_nMMH_n		R_{MM} (Å)	\bar{R}_{MH} (Å)	Natural Lewis structure	(%)L	
M	n				Valence	Total
Ta	4			(τ = bonded) ^a		
	3	2.648	1.773	$\text{H}_3\text{Ta} = \text{TaH}_3$	98.93	99.85
	2	2.303	1.777	$\text{H}_2\text{Ta} \equiv \text{TaH}_2$	98.27	99.79
	1	2.233	1.842	$\text{HTa} \equiv \text{TaH}$	95.64	99.61
W	5			(dissociated) ^a		
	4	2.389	1.723	$\text{H}_4\text{W} = \text{WH}_4$	96.11	99.46
	3	2.238	1.717	$\text{H}_3\text{W} \equiv \text{WH}_3$	98.05	99.72
	2	2.198	1.708	$\text{H}_2\text{W} \equiv \text{WH}_2$	98.67	99.81
	1	2.098	1.707	$\text{HW} \equiv \text{WH}$	99.11	99.87
Re	4	2.235	1.660	$\text{H}_4\text{Re} - \text{ReH}_4$	89.34	98.47
	3	2.188	1.670	$\text{H}_3\text{Re} = \text{ReH}_3$	90.73	98.73
	2	2.167	1.654	$\text{H}_2\text{Re} \equiv \text{ReH}_2$	98.08	99.73
	1	2.106	1.654	$\text{HRe} \equiv \text{ReH}$	98.28	99.78
Os	3	2.341	1.614	$\text{H}_3\text{Os} - \text{OsH}_3$	97.15	99.56
	2	2.257	1.613	$\text{H}_2\text{Os} = \text{OsH}_2$	97.69	99.68
	1	2.165	1.606	$\text{HOs} \equiv \text{OsH}$	98.63	99.80
Ir	2	2.417	1.553	$\text{H}_2\text{Ir} - \text{IrH}_2$	98.56	99.77
	1	2.233	1.543	$\text{HIr} = \text{IrH}$	99.30	99.89
Pt	1	2.483	1.520	$\text{HPt} - \text{PtH}$	99.17	99.87

^a See the text.

of the 5– n metal–metal bonds that complete the formal valence duodectet about each rhenium atom. Similar metal–metal bonding is expected in dinuclear hydrides of all the normal-valent group 6–10 transition metals, as well as in neighboring hypovalent members of the early transition series.

Table 4.15 summarizes optimized bond lengths and NBO Lewis-like structures for 15 saturated normal-valent H_nMMH_n compounds (M = W–Pt) as well as corresponding hydrides of hypovalent Ta for comparison. The accuracy of the localized Lewis-like description (as measured by $\% \rho_{\text{L}}$) is found to be reasonably high both for normal-valent and for hypovalent species, typically >98% of the valence-shell density and >99.5% of the total density.

However, significantly lower accuracy is found for single-bonded (maximally hydrogenated) members of the series (e.g., $\% \rho_{\text{L}}^{(\text{val})} = 89.3\%$ for $\text{H}_4\text{Re} - \text{ReH}_4$). Furthermore, in two such cases, depicted in Fig. 4.22, the optimized geometry and NBO description do not correspond to the “expected” single-bonded structure.

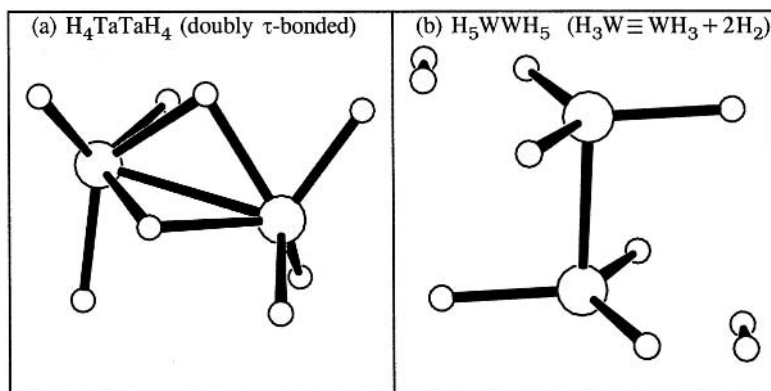


Figure 4.22 Optimized structures of H_4TaTaH_4 and H_5WWH_5 (not conforming to the expected single-bonding picture).

For hypovalent H_4TaTaH_4 , two bridging τ_{TaHTa} bonds are formed in addition to four σ_{TaH} bonds and one σ_{TaTa} bond (Fig. 4.22(a)). For sterically congested H_5WWH_5 , a dihydrogen H_2 moiety is split off at each end to give triple-bonded $\text{H}_3\text{W}\equiv\text{WH}_3 + 2\text{H}_2$ (Fig. 4.22(b)). Thus, fully hydrogenated dimetallic species appear to exhibit stronger delocalization effects than do their formally “unsaturated” (multiply bonded) counterparts.

As in main-group chemistry, hypovalent hydrides of the transition series have pronounced tendencies to form bridging tau bonds. In addition to H_4TaTaH_4 , the multiply bonded species HTaTaH features two symmetrically bridging hydrides. Despite the complexity introduced by such tau bonds, the Ta–Ta interaction clearly has high bond order, as simple Lewis-like structures prescribe.

Figure 4.23 graphically displays the metal–metal bond lengths (cf. Table 4.15) and their dependences on the formal bond order of the Lewis-like formula. These plots all show the expected decrease of R_{MM} with increasing bond order, but with somewhat different rates of decrease for different metal atoms. Thus, the multiple-bonding of the Lewis-like picture readily accounts for the variations of metal–metal bond length in these hydrides.

What is the nature of the multiple metal–metal bonds? Let us consider the specific example of $\text{HW}\equiv\text{WH}$, whose NBO Lewis structure exhibits *five* metal–metal bonds. Figure 4.24 displays the strongly *trans*-bent geometry of $\text{HW}\equiv\text{WH}$ and contour diagrams of the five metal–metal bond NBOs, each drawn in a chosen contour plane (specified in the lower-left-hand corner of the panel) to emphasize its distinguishing characteristics.

Each bond NBO is identified by the usual diatomic symmetry label (σ , π , or δ) to indicate its angular symmetry about the W–W axis.

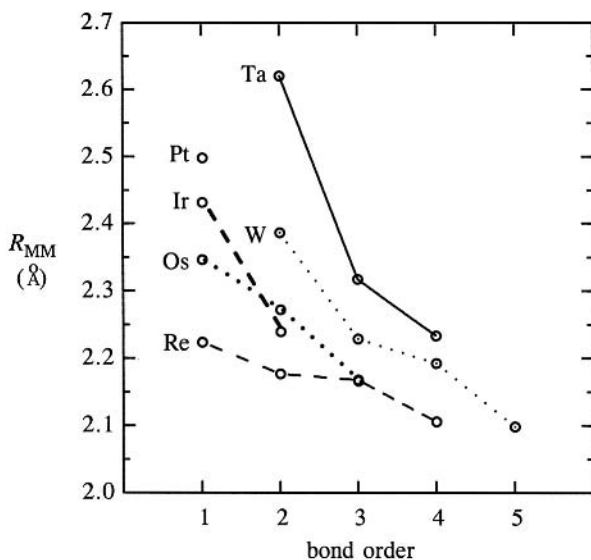


Figure 4.23 Variations of metal–metal bond length with nominal formal “bond order” (the number of bonds in the natural Lewis structure) in duodecet-rule-conforming dinuclear hydrides H_nMMH_n (see Table 4.15).

Sigma: The sigma bond σ_{WW} is isotropic (s-like shape) around the bond axis and has the profile (Fig. 4.24(a)) to be expected from the sd^u hybrids discussed in the preceding section (cf. Fig. 4.9).

Pi: Each pi bond has one axial nodal plane (p-like shape) and the longitudinal profile, (Figs. 4.24(b) and (c)) to be expected from π -type overlap of d orbitals. The two pi bonds are labeled $\pi_W^{(o)}$ (out of plane) or $\pi_{WW}^{(i)}$ (in plane) to distinguish their orientation with respect to the molecular plane.

Delta: Each delta bond has two axial nodal planes (d-like shape) around the bond axis, but they differ according to whether the axial shape is d_{z^2} -like ($\delta_{WW}^{(h)}$, “edge-on” overlap; Fig. 4.24(d)) or d_{xy} -like ($\delta_{WW}^{(u)}$, “face-on” overlap; Fig. 4.24(e)). In the former case the axial nodal planes are at 55° angles, so the participating metal d orbitals can mix (hybridize) with the metal s orbital to form a $\delta_{WW}^{(h)}$ bond of greater strength (which may also be pictured as arising from the one-center $n^{(h)}$ hybrid (4.40b)). In the latter case, the axial nodal planes are mutually perpendicular (preventing s-orbital mixing) and the resulting $\delta_{WW}^{(u)}$ bond therefore involves *unhybridized* d orbitals. Recall that, for a metal making two sd^1 hybridized single bonds, orthogonality requirements lead to two $\sim sd^{1.3}$ bond hybrids and another hybrid with sd^4 hybridization. In this instance σ_{WW} and $\delta_{WW}^{(h)}$ bond hybrids “compete” for the available metal s orbital at each center. Interestingly, and unlike the simple case of PtH_2 , the result of this competition is that the most d-rich hybrid is used to make the second delta bond, leaving the more directed $sd^{3.97}$ hybrid to make the first delta bond.

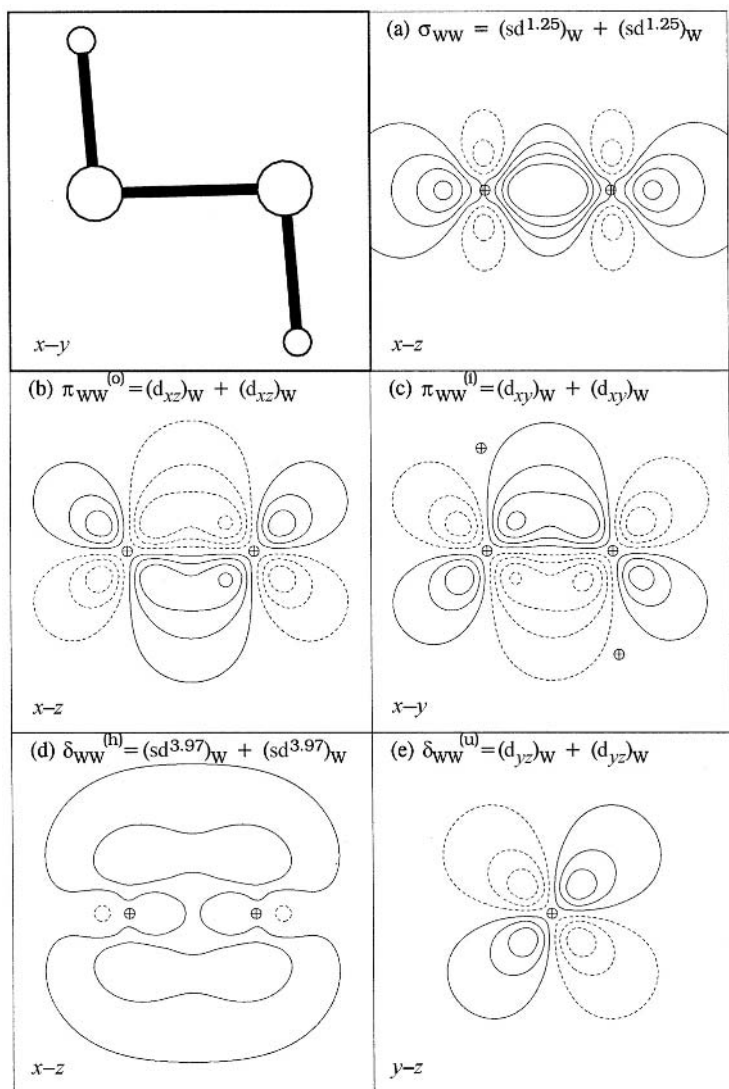


Figure 4.24 Metal–metal bond NBOs of quintuply bonded $\text{HW} \equiv \text{WH}$ ($\rho_{\text{L}} = 99.87\%$), showing the hybrid composition (above) and chosen contour plane (below) for each bond.

Table 4.16 displays the energies and occupancies of the five bond and corresponding antibond NBOs of $\text{HW} \equiv \text{WH}$. Successive metal–metal bonds would be expected to be formed in the order shown in Table 4.16 (i.e., σ before π before δ), on the basis of the spatial range and energy of each overlap type.

Although the classification of metal–metal bonds into distinct σ , π , and δ types is reasonably clear in $\text{HW} \equiv \text{WH}$ ($\text{C}_{2\text{h}}$), such diatomic symmetry labels may become

Table 4.16. *Orbital energies and occupancies of metal–metal bond and antibond NBOs of quintuply bonded HWWH*

Type	Bond		Antibond	
	Energy ^a (a.u.)	Occupancy (<i>e</i>)	Energy ^a (a.u.)	Occupancy (<i>e</i>)
σ_{WW}	−0.3675	1.9944	−0.0667	0.0446
$\pi_{\text{WW}}^{(i)}$	−0.2493	1.9739	−0.0018	0.0096
$\pi_{\text{WW}}^{(o)}$	−0.2478	1.9977	−0.0004	0.0187
$\delta_{\text{WW}}^{(h)}$	−0.2028	1.9840	−0.0676	0.0153
$\delta_{\text{WW}}^{(u)}$	−0.1751	1.9975	−0.0655	0.0023

^a The expectation value of the one-electron Hamiltonian operator.

problematic in species of lower symmetry. This is illustrated in Fig. 4.25 for two of the four metal–metal bonds of $\text{HRe}\equiv\text{ReH}$. In both cases the bonding *d*-type NHOs are seen to be rather strongly tilted with respect to the Re—Re bond axis, so that the designation of “ π -type” overlap (left) or “ δ -type” overlap (right) is only vaguely descriptive. (The remaining two bonds [not shown] are much more recognizably of σ and $\pi^{(i)}$ types.) As has been emphasized elsewhere in this book, the optimal NHOs and NBOs are free to adopt “bent-bond” forms that depart significantly from diatomic-symmetry prototypes, and such departures are likely to become more common in the multiple bonds of low-symmetry *d*-block compounds.

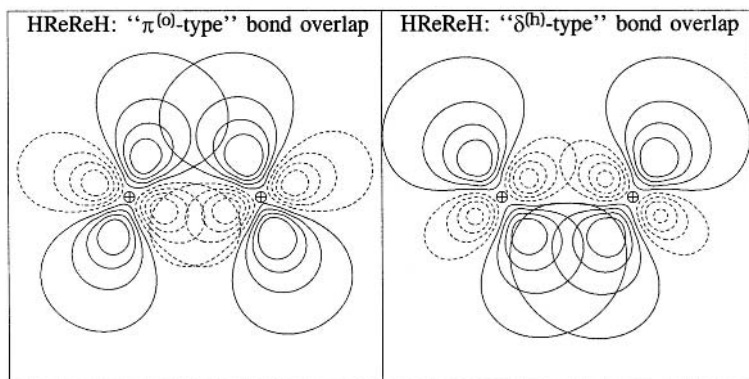


Figure 4.25 Bent “ $\pi^{(o)}$ -like” (left) and “ $\delta^{(h)}$ -like” (right) metal–metal bonding overlap in HReReH , showing tilting of bonding NHOs with respect to the bond axis (the contour plane is perpendicular to one of the two Re—Re—H groups).

Polynuclear metal–metal bonding

Owing to their wide range of valencies (1–6) and unusual sd^h hybrid angles, transition metals of groups 6–11 offer unique structural possibilities beyond those of main-group elements. To illustrate both the similarities and the differences between main-group and transition-metal species, let us compare “analogous” compounds built from formally *isovalent* atoms of the p and d blocks. For this purpose we shall compare compounds of tetravalent osmium with the corresponding well-known compounds of carbon, the prototypical tetravalent building block of organic chemistry.

We have previously seen examples of the carbon-like formulas of mononuclear and dinuclear osmium compounds, namely the “methane-like” tetrahydride (4.50c), “ethylene-like” $H_2Os=CH_2$ (4.51c) and $H_2Os=OsH_2$ (Table 4.15), “acetylene-like” $HOs\equiv CH$ (4.54c) and $HOs\equiv OsH$ (Table 4.15), “allene-like” $H_2C=Os=CH_2$ (4.55a), and so forth. While the coordination numbers and Lewis-like formulas are formally analogous, the actual structures of Os and C species may be quite similar (e.g., the T_d structures of OsH_4 and CH_4) or dissimilar (e.g., the strongly bent C_s structure of $H_2Os=CH_2$ [Fig. 4.13(c)] versus the planar D_{2h} structure of $H_2C=CH_2$).

As further illustrative examples of Os-based carbon-like compounds, we can mention “butadiene-like” Os_4H_6 ($H_2Os=OsH-OsH=OsH_2$), “cyclopropane-like” Os_3H_6 , and “cubane-like” Os_8H_8 . Figure 4.26 displays optimized geometrical structures of these Os-based compounds. All have geometries and NBO Lewis-like descriptions corresponding closely to the analogous C-based compounds, but with the strangely bent, hydride bond angles expected for transition-metal hybridization. Thus, osmium and other group 8 transition metals (perhaps better than Si) appear capable of mimicking many aspects of C-based organic chemistry.

In addition to analogs of known C-based structures, transition metals offer novel bonding possibilities having no known precedents in main-group chemistry. As a variation on the cubane-like cage motif of Fig. 4.26(c) built from tetravalent osmium, we can envision construction of the analogous *naked* metal cage compound Ir_8



of trivalent iridium. Because the expected sd^2 hybrids have natural 90° angles (Fig. 4.2), such a cubic geometry is expected to have *unstrained* skeletal bonds (as displayed in Fig. 4.27) and a well-localized Lewis-like bonding description, as is found.

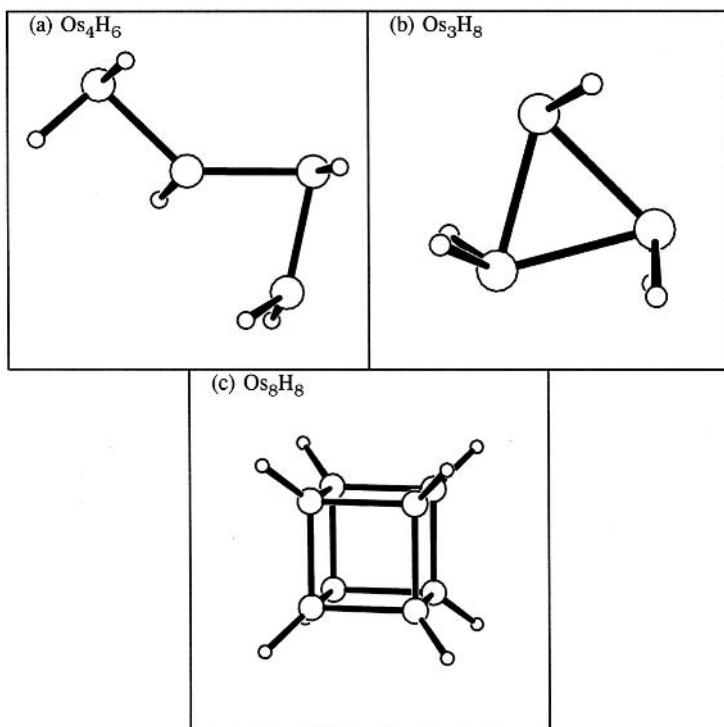


Figure 4.26 Optimized structures of osmium hydride “hydrocarbon-like” compounds: (a) butadiene-like $\text{H}_2\text{Os}=\text{OsH}-\text{OsH}=\text{OsH}_2$; (b) cyclopropane-like Os_3H_6 ; and (c) cubane-like Os_8H_8 .

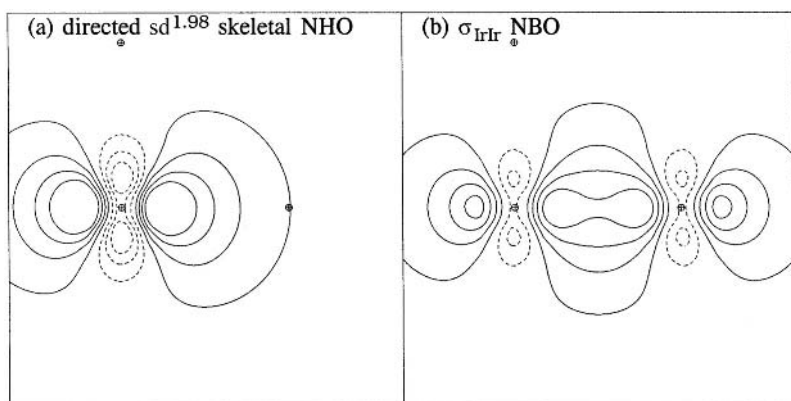


Figure 4.27 The directed $sd^{1.98}$ NHO (a) and the σ_{IrIr} NBO (b) in cubic Ir_8 ($R_{\text{IrIr}} = 2.537 \text{ \AA}$).

4.4.4 Metal halides, oxides, and nitrides: Bent's rule for transition metals

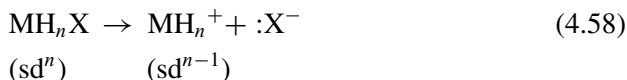
Main-group elements X such as monovalent F, divalent O, and trivalent N are expected to form families of transition-metal compounds MX (M—F fluorides, M=O oxides, M≡N nitrides) that are analogous to the corresponding p-block compounds. In this section we wish to compare the geometries and NBO descriptors of transition-metal halides, oxides, and nitrides briefly with the “isovalent” hydrocarbon species (that is, we compare fluorides with hydrides or alkyls, oxides with alkylidenes, and nitrides with alkylidynes). However, these substitutions also bring in other important electronic variations whose effects will now be considered.

Two main features distinguish MX compounds ($5 \leq G_X \leq 7$) from isovalent MR hydride and alkyl compounds: (i) the higher electronegativity of X, leading to increasingly polar M—X bonds; and (ii) the availability of one or more lone pairs on X, leading to the possibility of dative π -type interactions with low-lying empty metal orbitals.²⁷ The former change may result in changes of metal hybridization and bond angles akin to those expressed by *Bent's rule* (Section 3.2.6) for main-group elements,²⁸ whereas the latter may involve hyperconjugative $n_X \rightarrow n_M^*$ or $n_X \rightarrow \sigma_{MR}^*$ donor–acceptor interactions that also alter an idealized metal-center geometry. We primarily consider Bent's rule-type effects in the present section.

As described in Section 3.2.6, Bent's rule encompasses the relationships between bond polarity (ligand electronegativity) and central-atom geometry through their mutual connection to central-atom hybridization. Such relationships for d-block compounds are expected to differ significantly from those for p-block compounds, due to the quite different idealized angles for sd^{μ} hybridization (Section 4.3.3) as well as the altered way in which s/d hybridization depends on bond polarity. In particular, in ML_n compounds with $n > 3$, two possible angles (α_{acute} and α_{obtuse}) are associated with each idealized hybridization, so the effect of bond polarization on geometry will generally depend on which isomeric angle is considered. Furthermore, for $n > 2$ the d orbitals required for the sd^{n-1} hybrids of the sigma-bond skeleton are essentially disjoint from those remaining for lone pairs or multiple-bond formation (unlike the corresponding situation for main-group lone pairs, which must be involved in hybridization unless they are spatially perpendicular to the entire sigma skeleton). Finally, the relative energies of transition-metal s and d orbitals (which are often reversed by a simple change of configuration or ionization) are no longer so widely separated as to allow rationalization of Bent's rule along the lines originally employed by Bent.

A robust generalization of Bent's rule for d-block compounds can be based on the following simple argument (cf. Section 3.2.6): increased electronegativity of ligand X in an MH_nX compound may be considered equivalent to a higher admixture of

dissociated $\text{MH}_n^+ + \text{:X}^-$ ionic character, the latter requiring only idealized sd^{n-1} (rather than sd^n) hybrids for skeletal bonding:



Thus, increased ionic character of the M—X bond should generally result in *decreased* d character (or increased s character) in the remaining apolar M—H bonds, which corresponds to *increased* d character (decreased s character) in the polar M—X bond itself. We have already seen for simple metal hydrides and alkyls this general correlation: increased d character in hybrids is associated with more polarized bonds.

This general argument may be summarized as follows.

Bent's rule for d-block elements. Increased metal s character tends to go to the M—L bonds of higher covalent character, and increased d character to the bonds of higher ionic character.

Note that the association of higher d character with higher bond ionicity extends to polarity of *either sign*, a subtle but important difference with respect to corresponding Bent's rule statements for p-block elements.²⁹

From the idealized hybrid angles summarized in Table 4.3, we can now draw certain geometrical inferences connected with Bent's-rule-like bond-polarity changes in d-block ML_n compounds. For $n = 2, 3$, little geometrical effect is expected from a change in bond polarity or percentage d character, because the idealized hybrid angles are invariant (90°) for $n = 3$ and $n = 2$. For $n \geq 4$ some geometrical effect is expected, but the change of bond angle with increased d character will be of *opposite* sign depending on whether the isomer with acute (α_{acute}) or obtuse (α_{obtuse}) bond angle is selected. We can summarize the expected geometrical consequences of Bent's rule as follows.

Geometrical consequences of Bent's rule. Relative to idealized ML_n angles, increased d character (increased bond polarity) tends to *decrease* acute angles and *increase* obtuse angles for $n \geq 4$, but has little effect for $n \leq 3$ (near-perpendicular bond angles).

Compared with main-group compounds, one can therefore expect that Bent's rule-like geometrical variations in transition-metal compounds are somewhat muted (or exhibit conflicting patterns of increases and decreases, dependent on the isomer chosen), as the examples below will indicate.

Halides

As a simple example of isovalent replacement of hydride by halide ligands, let us first consider the set of monohalide substitutions on tetrahedral OsH_4 and pyramidal

IrH₃:



Table 4.17 summarizes the optimized bond angles θ_{XMH} and θ_{HMH} and M—X and M—H hybrid and bond-polarity descriptors for these species.

As shown in Table 4.17, the metal hybrids and bond angles do vary in the manner expected from the generalized version of Bent's rule stated above. For the OsH₃X series, the d character of the polar M—X bond increases (to $sd^{5.70}$ for X = F) and that of the less polar Os—H bonds correspondingly decreases as the electronegativity difference between Os and X increases. Compared with idealized tetrahedral bond angles ($\alpha_{\text{obtuse}} = 109.5^\circ$) of sd^3 hybridization, the X—Os—H angles also increase (to 113.4° for X = F) as bond polarity increases, with concomitant reduction in H—Os—H bond angles. In keeping with the ionic/covalent model that underlies the d-block version of Bent's rule, we expect that the IrH₂X series will exhibit constant H—Ir—H bond angles of 90° , because the idealized bond angles for sd^2 (the covalent limit) and sd^1 (the ionic limit) hybridization of the Ir—H bonds are equal. In accordance with this expectation, the IrH₂X structures exhibit only minuscule variations in H—Ir—H angles, whereas the X—Ir—H angles increase significantly (to 105.3° for X = F) with increasing electronegativity of X.

We can estimate the numerical trends more directly from the statement of Bent's rule based on (4.58). Noting that the Os—H bond of OsH₄ is almost perfectly covalent (i.e., 49.6% polarization to Os, $Q_{\text{H}} \simeq 0$ in OsH₄), we can expect for a substituted OsH₃X compound that the charge Q_{X} of a general monovalent X will vary from $Q_{\text{X}} = -1$ in the pure ionic case to $Q_{\text{X}} = 0$ in the pure covalent case. As a crude measure of the fractional weightings f_{ion} and f_{cov} of ionic and covalent forms in (4.58), we can therefore write

$$f_{\text{ion}} = -Q_{\text{X}}, \quad f_{\text{cov}} = 1 - f_{\text{ion}} = 1 + Q_{\text{X}} \quad (4.59)$$

According to these fractional weightings, the percentage d character of each Os—H bond hybrid is therefore expected to vary between 75% (for sd^3 hybrids, the covalent limit) and 66.7% (for sd^2 hybrids, the ionic limit) with changing electronegativity of X:

$$(\%d)_{\text{OsH}} = f_{\text{cov}}(75\%) + f_{\text{ion}}(66.7\%) = 75\% + Q_{\text{X}}(8.3\%) \quad (4.60a)$$

From the sum rule (4.42b) we can furthermore recognize that

$$(\%d)_{\text{OsX}} = 3[100 - (\%d)_{\text{OsH}}] \quad (4.60b)$$

The d-character estimates (4.60a) and (4.60b) can in turn be expressed as μ_{H} and μ_{X} values to estimate bond angles with the help of (4.43), as illustrated in the following example.

Table 4.17. Bond angles and NBO descriptors (atomic charge Q_X , metal hybrid h_M , bond polarization [%pol_M], and occupancy) for σ_{MX} and σ_{MH} bonds of OsH_3X and IrH_2X compounds (X = H, F, Cl, Br, I)

Species	X	θ_{XMH} (degrees)	θ_{HMH} (degrees)	Q_X	σ_{MX}			σ_{MH}		
					h_M	%pol _M	Occupancy (e)	h_M	%pol _M	Occupancy (e)
OsH ₄	H	109.5	109.5	-0.034	—	—	—	sd ^{2.97}	49.9	1.998
OsH ₃ F	F	113.8	104.8	-0.518	sd ^{5.70}	18.6	1.999	sd ^{2.52}	49.6	1.985
OsH ₃ Cl	Cl	110.1	108.8	-0.288	sd ^{3.21}	28.4	1.998	sd ^{2.90}	51.7	1.990
OsH ₃ Br	Br	109.2	109.7	-0.192	sd ^{3.04}	31.1	1.992	sd ^{2.97}	51.9	1.992
OsH ₃ I	I	108.6	110.3	-0.115	sd ^{2.73}	35.3	1.999	sd ^{3.07}	52.0	1.993
IrH ₃	H	90.4	90.4	-0.197	—	—	—	sd ^{2.00}	53.4	1.966
IrH ₂ F	F	105.3	87.5	-0.478	sd ^{3.20}	20.6	1.994	sd ^{1.78}	52.4	1.960
IrH ₂ Cl	Cl	99.9	88.1	-0.191	sd ^{2.20}	30.6	1.988	sd ^{1.96}	54.4	1.962
IrH ₂ Br	Br	98.1	87.9	-0.099	sd ^{2.08}	34.2	1.987	sd ^{1.99}	54.5	1.964
IrH ₂ I	I	97.1	88.2	-0.004	sd ^{1.92}	38.6	1.984	sd ^{2.06}	54.7	1.964

Example 4.6

Problem: Compare the OsH_3X hybridizations and bond angles predicted by the simple Bent's rule estimates (4.59) and (4.60) with the actual values of Table 4.17.

Solution: From (4.60a) and (4.60b), the estimated and actual percentage d characters of the Os—H and Os—X hybrids in each OsH_3X compound are found to be

	%d character of Os—H hybrid				%d character of Os—X hybrid			
	X = F	X = Cl	X = Br	X = I	X = F	X = Cl	X = Br	X = I
Estimated	71.1%	72.6%	73.2%	73.9%	86.7%	82.2%	80.3%	78.2%
Actual	71.5%	73.9%	74.2%	74.8%	83.8%	75.9%	74.1%	72.2%

From the relationship $\%d = \mu/(1 + \mu)$, we can estimate, for example, that the Os—H hybrids in OsH_3F are of $\text{sd}^{2.46}$ type (versus actual $\text{sd}^{2.51}$), leading through (4.43) to an estimated H—Os—H bond angle of 104.5° (versus actual 105.2°). In a similar manner the estimated and actual H—Os—H angles in each OsH_3X compound are found to be

	H—Os—H bond angle (degrees)				
	X = H	X = F	X = Cl	X = Br	X = I
Estimated	109.5	104.5	106.6	107.4	108.2
Formal NHO	109.4	105.1	108.3	109.0	109.8
Actual	109.5	104.8	108.8	109.7	110.3

The qualitative trends are reproduced fairly well by these simple estimates.

One might also consider the effect of halogen substitution on the $\text{C}_{3v}(\text{i})$ “inverted” isomer of OsH_4 (Fig. 4.7(a)). However, it is found that the substituted OsH_3X halide species no longer exhibit this isomeric form as a distinct equilibrium geometry. Instead, the potential surface for umbrella-like deformations exhibits a strong *inflection* feature near the expected $\text{C}_{3v}(\text{i})$ -like geometry, as illustrated for OsH_3F in Fig. 4.28. The IR angular vibrations of OsH_3F and other OsH_3X halides are therefore expected to exhibit anomalous anharmonicity effects corresponding

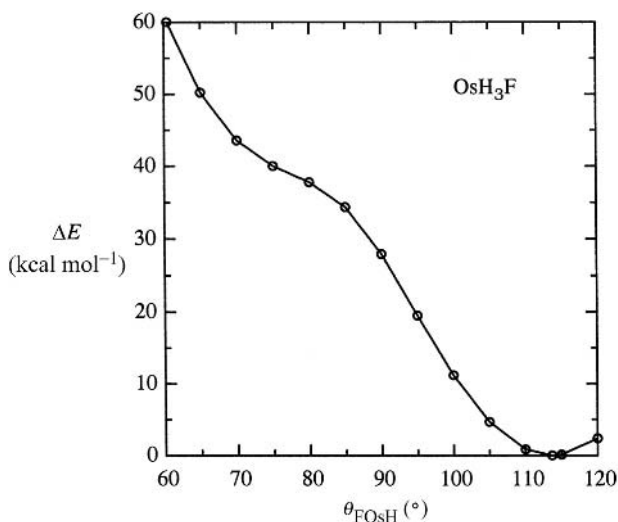


Figure 4.28 The potential for “umbrella” inversion motion of OsH_3F , showing the inflection feature near idealized $C_{3v}(\text{i})$ geometry ($\sim 70^{\circ}$).

to the “missing” inverted $C_{3v}(\text{i})$ isomer, but further aspects of Bent’s rule alteration of hybridization for this isomer cannot be examined directly.

Let us now consider the effects of full substitution with more electronegative fluoride ligands in the saturated third-series metal fluorides MF_n corresponding to hydrides:

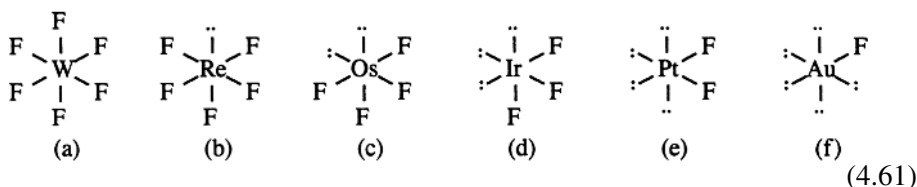


Figure 4.29 and Table 4.18 show the optimized geometries of these fluorides for direct comparison with those of the corresponding hydrides in Fig. 4.6 and Table 4.4.

The visual impression conveyed by comparison of Figs. 4.6 and 4.29 is that fluoride bond angles are “opened up” relative to corresponding hydride angles. This is confirmed by the numerical values in Tables 4.4 and 4.17, showing that the strongly acute hydride bond angles are replaced by more nearly perpendicular or obtuse bond angles in the fluorides (in which only three F—Re—F angles remain significantly acute). Because the idealized hybrids for equivalent ligand bonding would be expected to be the same for H as for F, the increased F—M—F angles

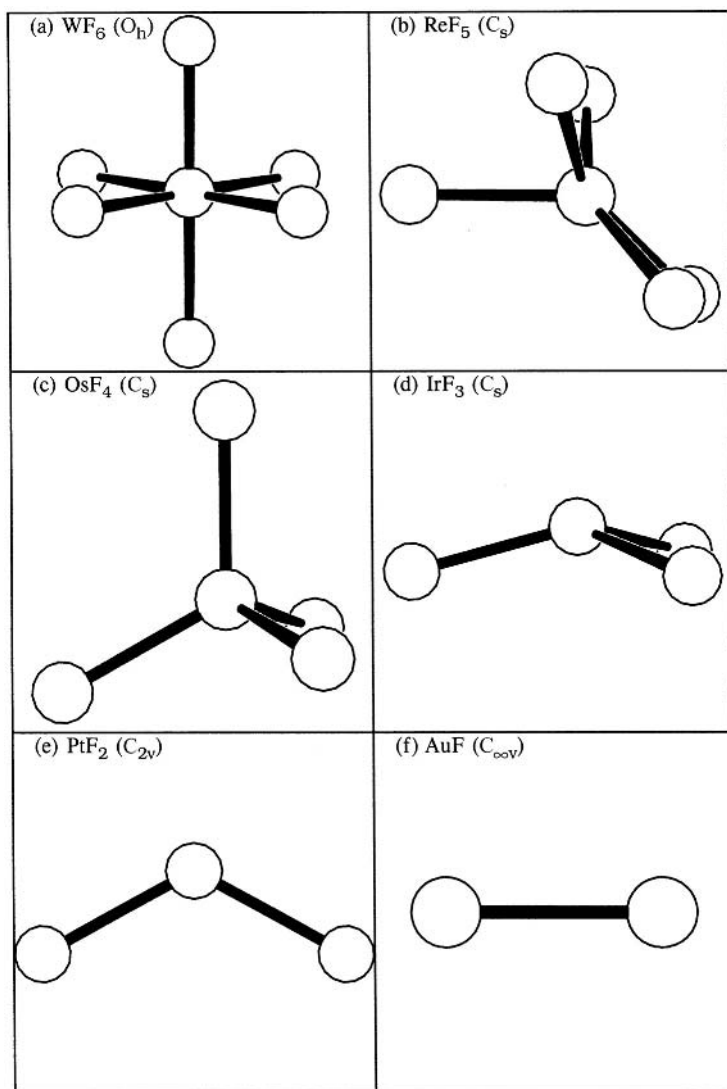


Figure 4.29 Optimized geometries of saturated group 6–11 third series transition-metal fluorides MF_n (see Table 4.18).

presumably reflect the repulsive effects of higher charges and/or steric demands of anionic fluoride ligands. This generalized opening of bond angles is accompanied by a dramatic change of symmetry: tungsten hexafluoride achieves O_h symmetry, versus C_{3v} for WH_6 .

Why is WF_6 octahedral but WH_6 is not? The acute sd^5 -like angles of WH_6 are clearly associated with the strong role of covalency and directional hybridization

Table 4.18. Bond lengths R_{MF} and angles θ_{FMF} of saturated metal fluorides MF_n of the third transition series (see Fig. 4.29)

MF_n	Symmetry	R_{MF} (Å)	Bond angle θ_{FMF} (degrees)
WF_6	O_h	1.866(6)	90.0(12), 180.0(3)
ReF_5	C_s	1.854, 1.870(4)	81.5(2), 79.0, 124.1(2), 84.1(2), 151.5(2), 107.8
OsF_4	T_d	1.90(4)	109.5
IrF_3	C_{3v}	1.871(3)	116.7(3)
PtF_2	C_{2v}	1.886(2)	128.1
AuF	$C_{\infty v}$	1.982	

in the apolar hydrides. For WH_6 , a very good approximation to the electronic structure is that a neutral W atom and six neutral H atoms form six pure covalent bonds. Not surprisingly, such a pure covalent description of W—F bonding is a very *poor* starting point for WF_6 . Natural charges for WF_6 ($Q_W = +2.80$, $Q_F = -0.47$) indicate a better zeroth-order approximation: $WF_3^{3+} + 3F^-$ ions. For now, let us focus on a strictly localized Lewis-like description of the WF_3^{3+} fragment, keeping in mind that resonance and 3c/4e hyperbonding (described in later sections) will be needed to describe the final WF_6 . Hybridization prescriptions suggest $\sim sd^2$ hybridization, and hence 90° bond angles, at the WF_3^{3+} fragment. A duodectet count at the metal can be completed by making each of the W—F interactions a *double* bond. Hence, we can crudely consider the “core” of the WF_6 electronic structure to be represented by the *pyramidal* fragment WF_3^{3+} with Lewis-like structure as shown below:

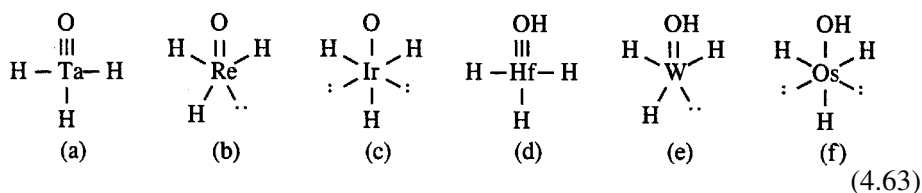


(Geometry optimization of WF_3^{3+} leads to a pyramidal fragment with F—W—F bond angles of 100.9° .) Successive linear 3c/4e F^- hyperbonding additions to each W=F bond of (4.62) then lead to the final resonance-stabilized WF_6 species of O_h symmetry. The overall pattern of comparison between Figs. 4.6 and 4.29 indicates that oversimplified models of bonding (whether of VSEPR/electrostatic or idealized hybrid type) will encounter greater difficulties in rationalizing the structures of transition-metal compounds than they will in rationalizing structures of corresponding main-group compounds.

Oxides and hydroxides

Is the valency of oxygen rigorously, or even commonly, limited to two? For the p-block compounds, few deviations from simple divalency occur, with group V oxides and various oxyacids making notable exceptions. However, with d-block elements the strong driving force to achieve duodectet bonding, combined with the increased bonding opportunities enabled by valence s and d orbitals, results in oxygen valencies varying from one to four.

Consider, for example, the sequences of hydridometal oxides (H_3MO , $\text{M} = \text{Ta}, \text{Re}, \text{Ir}$) and corresponding hydroxides (H_3MOH , $\text{M} = \text{Hf}, \text{W}, \text{Os}$) and their duodectet-rule-conforming Lewis-like structures (noting as usual that such diagrams do not depict geometrical arrangements):



For such series, the fidelity of Lewis-like predictions can be measured readily by monitoring *both* the molecular shapes and the NBO analyses. In each molecule the sigma-bond framework prescribes $\sim\text{sd}^3$ hybridization. Owing to the high electronegativity of oxygen we expect greater d character in the $\text{M}-\text{O}$ metal hybrid and correspondingly less in the $\text{M}-\text{H}$ hybrids. Thus, from the sigma-bonding perspective, we expect C_{3v} symmetry with $\text{O}-\text{M}-\text{H}$ bond angles somewhat greater than 109° . The effects of pi-bonding are readily predicted: a single pi bond lowers the symmetry by forcing one $\text{O}-\text{M}-\text{H}$ angle to a smaller value, whereas two pi bonds restore effective C_3 symmetry but with all $\text{O}-\text{M}-\text{H}$ angles lowered. Furthermore, the hydroxide series is expected to exhibit increasing $\text{M}-\text{O}-\text{H}$ angles as the number of pi bonds is increased, maximizing at 180° for H_3HfOH . As the data in Table 4.19 indicate, all of these expectations are met and the best NBO configuration closely resembles the Lewis-like picture.

Transition-metal oxo complexes are routinely depicted as having $\text{M}=\text{O}$ double bonds, but, as these remarkable series demonstrate, the best single configuration description of the $\text{M}-\text{O}$ bond can vary from a single bond (as in H_3IrO) to a triple bond (as in H_3WO). Examined in detail, the $\text{M}-\text{O}$ bonds are highly polar (8%–41% metal character), and vicinal hyperconjugations contribute appreciable resonance stabilizations beyond the formal Lewis-like structure. Nonetheless, orderly variations in the Lewis-like bonding pattern are revealed compellingly by the changes in molecular shape, spanning variations in formal oxygen valency from one (H_3IrO) to four (H_3HfOH).

Table 4.19. Geometrical and NBO parameters for the series H_3MO ($M = Ta, Re, Ir$) and H_3MOH ($M = Hf, W, Os$), demonstrating regular changes in molecular shape, Lewis-like accuracy ($\% \rho_L$), and bonding descriptors (hybrid h_M and polarization $\%c_M^2$) as formal $M-O$ bond order increases, in accord with Lewis-like structures (4.63)

Species	Symmetry	Angles (degrees)						σ_{MO}		τ_{MO}		σ_{MH}	
		θ_{HMO}	θ_{HMH}	θ_{MOH}	$\% \rho_L$	h_M	$\%c_M^2$	h_M	$\%c_M^2$	h_M	$\%c_M^2$	h_M	$\%c_M^2$
H_3TaO	C_{3v}	103.5	114.7		99.06	$sd^{6.31}$	24.1	$\sim d$	19.4	$sd^{2.47}$	35.2		
H_3ReO	C_s	116.7(2) 94.0	89.8(2) 126.3		97.26	$sd^{7.08}$	29.8	$\sim d$	29.0	$sd^{2.82}$	43.2		
H_3IrO	C_{3v}	115.6	102.3		96.38	$sd^{7.37}$	41.0			$sd^{2.40}$	53.4		
H_3HfOH	C_{3v}	108.8	110.1	180.0	98.98	$sd^{4.16}$	8.6	$\sim d$	5.9	$sd^{2.60}$	25.9		
H_3WOH	C_1	113.8(2) 82.0	116.7 125.0	129.7	98.91	$sd^{6.32}$	16.2	$\sim d$	11.4	$sd^{2.98}$	37.8		
H_3OsOH	C_s	116.6(2) 105.1	103.8(2) 109.1	116.9	98.78	$sd^{5.18}$	23.3			$sd^{2.44}$	42.2		
										$sd^{2.54}$	47.6		
										$sd^{2.64}$	50.2		

Let us briefly make connection with monoxides of the p-block elements. Both in terms of molecular geometry and in terms of valency, H_3IrO (which is a simple model for the fascinating oxygenation catalysts³⁰ based on $(\text{mesityl})_3\text{IrO}$), is a d-block cousin of H_3PO , phosphine oxide. Both complexes can better be depicted as involving polar $\text{M}=\text{O}$ single bonds rather than the double bonds that dominate literature representations.

Even for conventional $\text{M}=\text{O}$ bonding, gradual replacement of two hydride ligands with a single oxide leads to increasingly ionic structures and more complex bonding patterns, such as in the series H_4WO , H_2WO_2 , WO_3 , or H_2OsO and OsO_2 :

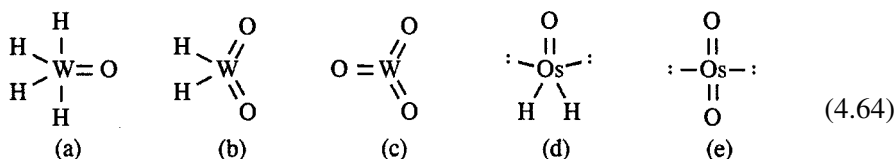


Figure 4.30 displays the equilibrium structures of (4.64a)–(4.64e) and Table 4.20 lists corresponding optimized bond lengths and angles. It is immediately suggested by the strangely acute bond angles in H_4WO (e.g., 62.0° and 69.4° $\text{H}-\text{W}-\text{H}$ angles) that hybridization effects continue to control the monoxide geometry. Similarly, WO_3 and OsO_2 exhibit the respective pyramidal and bent structures that are seen in the corresponding alkylidene complexes. Thus, consistently with the Lewis-like formulas (4.64), substantial covalency and $\text{M}=\text{O}$ double-bond character appears to be a general characteristic of metal–oxide bonding throughout this series.

In contrast with the $\text{M}=\text{C}$ bonds of tungsten and osmium alkylidenes, the oxide $\text{M}=\text{O}$ bonds are significantly more polar and the metal centers acquire substantial positive charge. The NBO analysis generally confirms the Lewis-like $\text{M}-\text{O}$ description of metal–oxide bonding in these species, but substantial delocalization effects are present, which lower the accuracy of a single Lewis-like representation. Delocalization effects will be discussed in later sections, but we can emphasize at this point that deviations from the idealized Lewis-like prescriptions are expected whenever the charge distributions deviate strongly from pure covalency, as in comparing, e.g., WF_6 with WH_6 .

Nitrides and imides

Trends in metal–nitrogen bonding can be illustrated by series of nitrido (H_3MN , $\text{M} = \text{W}, \text{Os}$) and imido (H_3MNH , $\text{M} = \text{Ta}, \text{Re}, \text{Ir}$) complexes, isovalent counterparts

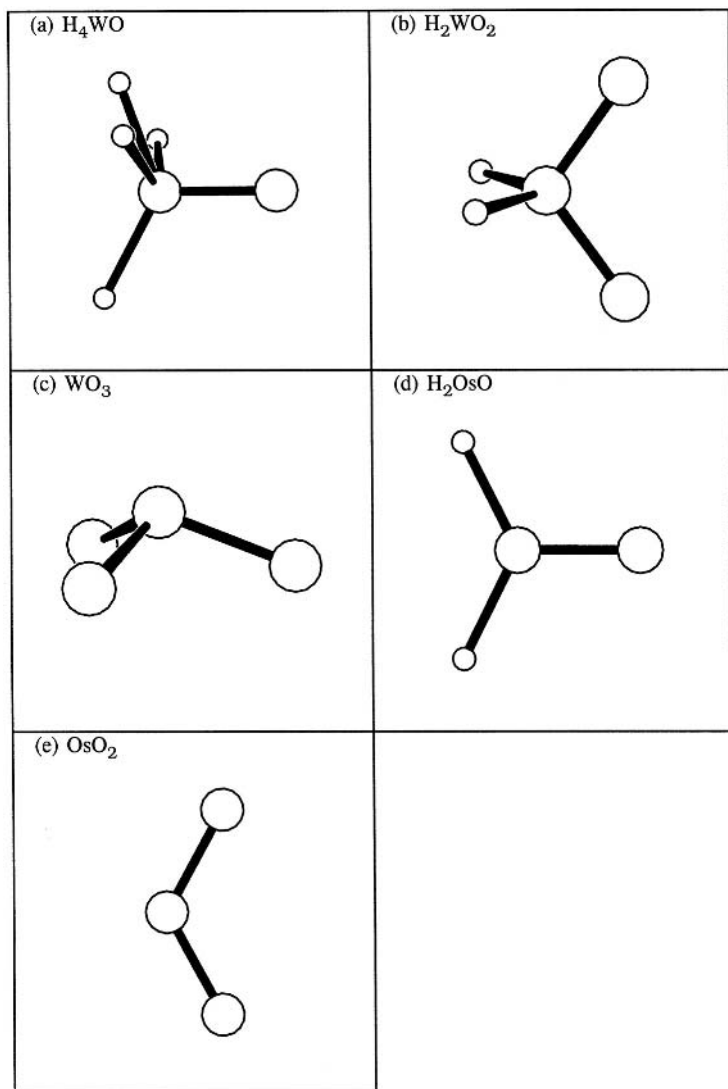
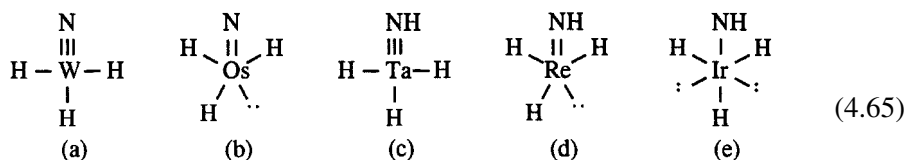


Figure 4.30 Optimized structures of tungsten and osmium oxides (4.64a)–(4.64e).

of corresponding oxide and hydroxide complexes of the previous section:



Optimized structures of these species are shown in Fig. 4.31 and geometrical and NBO descriptors are summarized in Table 4.21. As shown by comparisons with Table 4.19, the geometrical features of the nitride and imide complexes exhibit

Table 4.20. *Optimized geometrical parameters, metal charge (Q_M) and Lewis accuracy ($\% \rho_L$) of tungsten and osmium oxides (4.64a)–(4.64e); see Fig. 4.30*

Species	Symmetry	$R_{MH}(\text{\AA})$	$R_{MO}(\text{\AA})$	θ_{OMO} (degrees)	θ_{HMO} (degrees)	θ_{HMH} (degrees)	Q_M	$\% \rho_L$
H ₄ WO	C ₁	1.683, 1.695, 1.761(2)	1.689		109.7, 118.4 99.1(2)	60.3(2), 120.5, 109.8(2), 131.9	1.195	95.96
H ₂ WO ₂	C _{2v}	1.721	1.708	109.4	106.9	119.8	1.746	94.89
WO ₃	C _{3v}		1.734	107.2			1.980	95.65
H ₂ OsO	C _{2v}	1.632	1.653		116.6	126.7	0.729	97.56
OsO ₂	C _{2v}		1.699	123.2			1.074	95.04

strong parallels with the analogous oxide and hydroxide complexes. The overall symmetry and specific bond angles are in close correspondence to those expected from the Lewis-like picture. Further support is provided by NBO analysis, which indicates reasonably high Lewis accuracies, of the order of 97%–99%, with the exception of two notable outliers. Conspicuously lower Lewis accuracies of 93.7% and 94.4% characterize the complexes H₃OsN and HNIrH₃, respectively, both of which represent the rather unusual N formal charge of -1 (two lone pairs, two bonds). The “best” NBO assignment also differs (by an additional “ π_{MN} ” bond of low occupancy and distorted form) from the idealized Lewis-like representations in (4.65b) and (4.65e), indicating the occurrence of strong resonance delocalization of the anionic N lone pair into adjacent M–H antibonds. Given the rather small differences in electronegativities for Os, Ir, and N, we are led to conclude (in accordance with Pauling’s “electroneutrality principle”) that Lewis structures with excessive formal charge have a diminished probability of describing realistic bonding.

The un-VSEPR-like bond angles in Fig. 4.31 again reflect the strong role of hybridization in controlling nitride geometry. The NBO descriptors in Table 4.21 show the expected similarities to metal–alkylidene bonding, and the variations of hybrid d character and bond polarity are in general accord with the d-block generalization of Bent’s rule as formulated above.

In summary, the Lewis-like model seems to predict the composition, qualitative molecular shape, and general forms of hybrids and bond functions accurately for a wide variety of main-group derivatives of transition metals. The sd-hybridization and duodectet-rule concepts for d-block elements therefore appear to offer an extended “zeroth-order” Lewis-like model of covalent bonding that spans main-group and transition-metal chemistry in a satisfactorily unified manner.

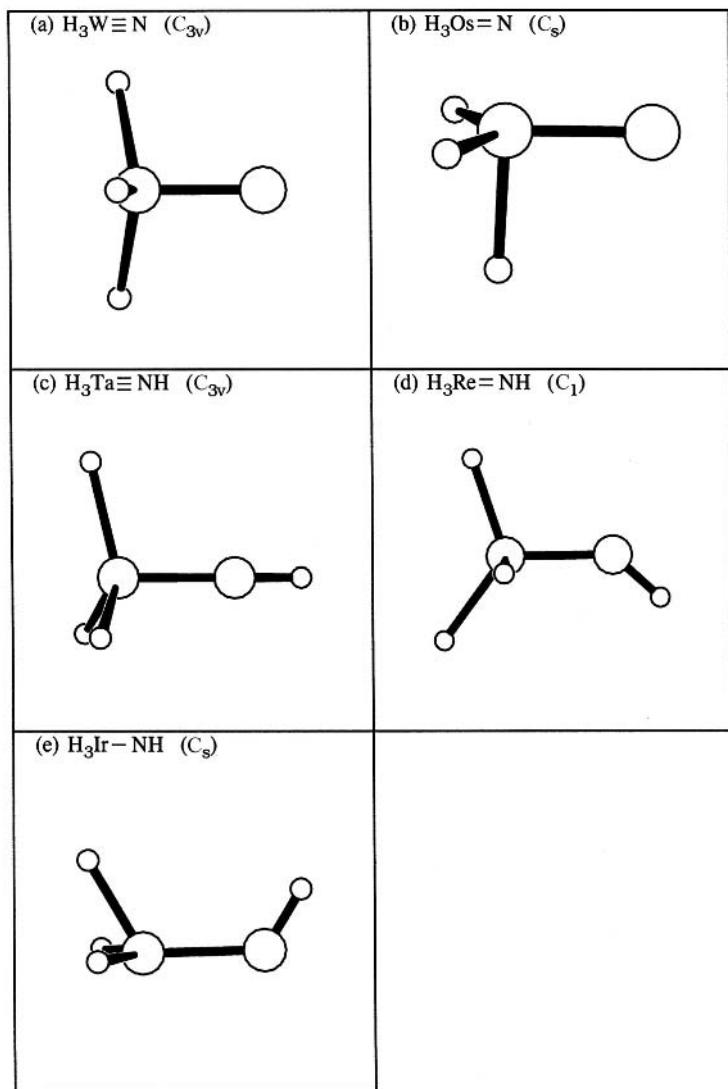


Figure 4.31 Optimized structures of transition-metal nitrides and imides (4.65).

4.5 Coordinative metal–ligand bonding

4.5.1 A preliminary overview of metal–ligand coordination

Werner's model of coordinative bonding

Much confusion in the early history of aqueous transition-metal chemistry stemmed from the inability to distinguish “free” formula ions (serving merely as solvent-separated counterions) from those that remain in direct “coordinated” contact with

Table 4.21. Geometrical and NBO parameters for nitrido and imido complexes (4.65), showing bond angles, valence Lewis accuracy (% ρ_L), and metal bond hybrid (h_M) and polarization (% c_M^2) of σ_{MN} , π_{MN} , and σ_{MH} NBOs

Species	Symmetry	Angles (degrees)				σ_{MN}		π_{MN}		σ_{MH}	
		θ_{HMN}	θ_{HMH}	θ_{MNH}	% ρ_L	h_M	% c_M^2	h_M	% c_M^2	h_M	% c_M^2
H ₃ WN	C _{3v}	98.3	117.9		98.98	sd ^{4.59}	40.7	~d	43.0	sd ^{2.67}	40.3
H ₃ OsN	C _s	111.4(2) 92.6	88.9(2) 137.1		94.36	sd ^{5.26}	45.3	~d	29.0	~d sd ^{1.70}	54.8 30.9
H ₃ TaNH	C _{3v}	102.9	115.1	180.0	99.03	sd ^{4.17}	22.5	~d	24.8	sd ^{2.70}	33.2
H ₃ ReNH	C ₁	91.8 107.9 127.1	87.3 96.8 124.7	137.3	97.39	sd ^{6.18}	34.2	~d	37.8	sd ^{2.06} sd ^{3.26} sd ^{2.21}	49.7 45.8 42.1
H ₃ IrNH	C _s	112.7(2) 118.7	79.5(2) 122.2	122.2	93.72	sd ^{5.80}	45.5			sd ^{1.65} sd ^{2.46}	25.6 43.1



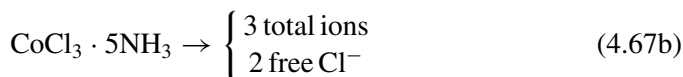
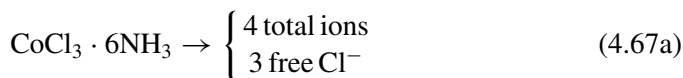
Alfred Werner

the transition metal. A classic case is provided by ammoniated complexes of cobalt(III) chloride, with empirical formulas such as

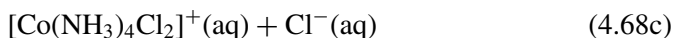
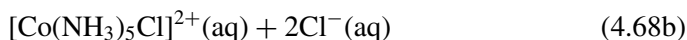
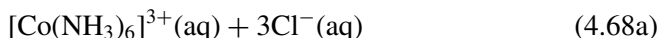


Surprisingly, the compound (4.66c) can be obtained in *two* distinct isomeric forms (of distinct colors, etc.) whereas (4.66a) and (4.66b) each correspond to unique chemical species. Plausible structural formulas for such species presented a great mystery to nineteenth-century chemists.

The structural and formulaic questions concerning compounds such as (4.66a)–(4.66c) were largely resolved by Alfred Werner,³¹ the first inorganic chemist to receive a Nobel Prize (1913). Werner carefully studied the total number of free ions contributing to ionic conductivity, as well as the number of free chloride ions that could be precipitated (exchanged with a more soluble ion) under conditions of excess Ag^+ , namely

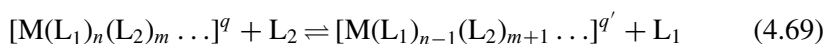


From such evidence, Werner deduced the aqueous forms of these compounds to be



A striking feature of the formulas (4.68a)–(4.68c) is that the “coordination number” (CN) of ligands bonded to Co is *six* (CN = 6) in each case. Werner conjectured that such six-fold coordination corresponds to idealized *octahedral* geometry about the central Co ion, which leads to unique structures for $[\text{Co}(\text{NH}_3)_6]^{3+}$ and $[\text{Co}(\text{NH}_3)_5\text{Cl}]^{2+}$ but distinct *cis* and *trans* isomers for $[\text{Co}(\text{NH}_3)_4\text{Cl}_2]^+$, as observed. X-ray studies subsequently confirmed the accuracy of Werner’s brilliant structural inferences.

These and many similar examples resulted in a highly successful general picture of transition-metal ions M coordinated by closed-shell ligands L (anionic or neutral) to form complex cluster ions $[\text{ML}_n]^q$ in solution. The characteristic coordination shell of each M corresponds to a specific number of sites, with idealized geometry that dictates the possible number of distinct $[\text{M}(\text{L}_1)_n(\text{L}_2)_m \dots]^q$ structural isomers. Each cluster ion is subject to equilibria with other cluster ions or dissociated ligands in solution,



reflecting the relative “lability” (ease of dissociative exchange) of the coordinated ligands. Each complex cluster ion also has distinct magnetic and spectroscopic properties (within the kinetic time scale of ligand-exchange reactions such as (4.69)) that serve as fingerprints of the coordinative environment of M.

Because the low-lying spectroscopic transitions of these species commonly lie in the visible region of the spectrum, coordinated transition metals underlie the colors of many natural and synthetic dyestuffs. Coordinated transition metals are also conspicuous features of the active sites of metalloproteins and play an important role in living systems.

Crystal-field and ligand-field theories of metal–ligand coordination

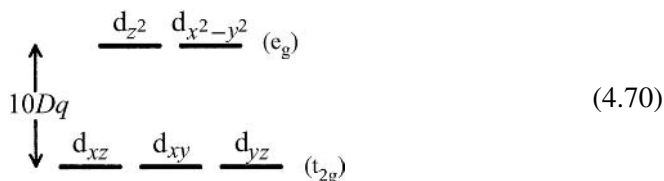
As early as 1929, H. A. Bethe³² constructed a simple perturbative “crystal-field theory” for energy levels and spectroscopic transitions of coordinated transition-metal ions. Bethe’s theory begins from the atomic spectroscopy of the bare transition-metal cation M, perturbed by the electrostatic field of incoming ligands L in the (assumed) geometry of the coordination shell. Each ligand is pictured as an anionic point charge that electrostatically destabilizes proximal metal d orbitals. Metal d



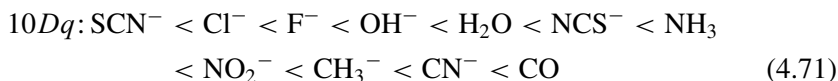
Hans A. Bethe

orbitals pointed *toward* the ligands are thereby raised in energy relative to those directed *between* ligands, splitting the initially degenerate metal d levels into non-degenerate sets.

For example, in the octahedral crystal field of six ligands along the $\pm x$, $\pm y$, and $\pm z$ axes, the d_{z^2} and $d_{x^2-y^2}$ orbitals (the “ e_g ” set) have their lobes pointing directly toward the ligands, and are thus raised in energy relative to the d_{xy} , d_{xz} , and d_{yz} orbitals (the “ t_{2g} ” set) whose lobes point between ligands. This can be represented by the orbital-splitting diagram



As shown in (4.70), the crystal-field splitting energy is labeled “ $10Dq$ ” and can be identified with low-lying experimental spectroscopic transitions between t_{2g} and e_g levels, leading to a characteristic measure of the crystal-field interaction strength of each ligand type. From such measured crystal-field splitting parameters, one can order various common ligands in a “spectrochemical series” of apparent interaction strength,



The spectrochemical series generally predicts the direction of ligand-exchange equilibria such as (4.69), with ligands to the right being more tightly bound (and



John H. Van Vleck

thus less labile with respect to exchange) than those to the left. For each formal d count (>3) the splitting diagram (4.70) also dictates whether metal d electrons remain unpaired in the high-spin configuration that places some electrons in the high-energy e_g set (if $10Dq$ is small), or pair up in the low-spin configuration that maximizes occupancy of the low-energy t_{2g} set (if $10Dq$ is large). Combined with the spectrochemical series (4.71), the crystal-field splitting diagrams (4.70) for various coordination symmetries thereby allow many chemical, magnetic, and spectroscopic properties of transition-metal complexes to be rationalized in a qualitatively satisfactory manner.

However, brief examination of the spectrochemical series (4.71) reveals that the ordered $10Dq$ values are not related in any obvious way to electrostatic properties of the ligands (net charge, dipole moment, etc.). Indeed, the *strongest* crystal-field splitting in (4.71) corresponds to the CO ligand that has neither net charge nor an appreciable dipole moment. Conversely, the ionic F^- ligand (which should best correspond to the “point-charge” assumption of crystal-field theory) is among the *weaker* ligands in this series. Thus, there are obvious chemical inconsistencies with the simple ionic picture that underlies crystal-field theory.

J. H. Van Vleck and others³³ subsequently refined the ionic crystal-field theory to incorporate covalent effects expected from Mulliken’s MO treatment of main-group compounds. The resulting “ligand-field theory” is often taken as synonymous with full MO treatment of the transition-metal complex. Ligand-field theory emphasizes the *mixing* of metal and ligand orbitals that leads to energetic shifts of metal-based MOs (and thus to typical crystal-field splitting patterns) as well as associated changes in ligand-based MOs (such as “ π -backbonding”; see Section 4.5.4 below) that led to overall stabilization and aggregation even in the *absence* of net charge or

strong ionic character. As usual, the full MO description tends to obscure localized aspects of metal–ligand interactions due to symmetry and near-degeneracy mixings in the canonical MOs that exaggerate the apparent “delocalized” character.

The localized Lewis-like picture of metal–ligand coordination: two- versus three-center aspects

From the localized Lewis-like perspective, we can picture coordinative metal–ligand interactions as involving two distinct “types” of localized bonding (which have already been discussed in the context of main-group chemistry; Sections 3.2.11 and 3.5):

- (1) 2c/2e dative bonding (of $n_L \rightarrow d_M^*$ type); and
- (2) 3c/4e hypervalent ω -bonding (of $n_L \rightarrow \sigma_{ML}^*$ or L: M—L \longleftrightarrow L—M :L type).

Given the plethora of unfilled metal d orbitals, one could expect that dative-type interactions with closed-shell Lewis bases would become more common for group 3–12 transition metals than for main-group elements (e.g., B or Al of group 13). However, even more striking is the greater facility of transition metals to participate in hypervalent ω -bonding. In most cases, interaction of M and :L to form a dative M—L bond (of formal $M^-—L^+$ polarity) is accompanied by hypervalent L: + M—L attack by a second :L ligand to form a pair of (near-linear) $\omega_{L:ML}$ and $\omega_{L-M:L}$ prebonds, in accord with the Pimentel–Rundle three-center MO picture (Section 3.5). Thus, formal hypervalency is a ubiquitous feature of transition-metal coordination complexes.

In order to make a formal separation between two- and three-center aspects of coordinative bonding, we shall first consider various aspects of simple two-center dative M—L coordination within the framework of normal-valent transition-metal complexes. Aspects of hypervalent ω -bonding to form higher-coordinate complexes (the more common experimental species) will subsequently be considered in Section 4.5.3.

4.5.2 Sigma coordinative bonding

A transition metal with partially filled d shell can evidently participate either as a Lewis acid or as a Lewis base in 2c/2e dative interactions,



As shown in (4.72a) and (4.72b), such interactions give rise to formal sigma bonds (σ_{MB} or σ_{MA}) that are expected to be oppositely polarized, with atomic charges of opposite sign on the metal atom depending on whether donation is *to* (4.72a) or

Table 4.22. Geometrical and NBO parameters for ammine, phosphine, and carbonyl coordination complexes of Os and Re hydrides, showing bond angles, valence Lewis accuracy ($\% \rho_L$), and metal bond hybrid (h_M) and polarization ($\% c_M^2$) of σ_{ML} and σ_{MH} NBOs

Species	Angles (degrees)			$\% \rho_L$		σ_{ML}		σ_{MH}	
	θ_{HMH}	θ_{LMH}	Q_M	Valence	Total	h_M	$\% c_M^2$	h_M	$\% c_M^2$
OsH ₂ NH ₃	107.7	95.8	−0.046	98.53	99.88	sd ^{3.07}	15.6	sd ^{1.89}	44.8
OsH ₂ PH ₃	102.5	90.9	−0.295	97.80	99.55	sd ^{1.93}	33.7	sd ^{2.12}	47.9
OsH ₂ CO	98.5	90.2	−0.045	96.25	99.13	sd ^{2.30}	34.7	sd ^{1.90}	49.9
ReH ₃ NH ₃	111.2(2)	108.2(2)	0.278	99.53	99.87	sd ^{3.63}	13.5	sd ^{2.81}	41.9
	110.7	107.1						sd ^{2.79}	41.9
ReH ₃ PH ₃	117.0	100.0	0.007	98.01	99.59	sd ^{2.43}	29.3	sd ^{3.20}	43.9
ReH ₃ CO	119.6	93.5	0.272	96.36	99.15	sd ^{2.59}	32.7	sd ^{3.13}	45.5

from (4.72b) the metal atom.³⁴ Of the two types of dative interactions, coordinative bonding of M with a closed-shell Lewis base :L (4.72a) is by far the more important case, and we give primary attention to such bonding in the present section.

As simple examples of (4.72a), let us first consider coordinative additions of three common ligand classes – amines (represented by NH₃), phosphines (represented by PH₃), and carbonyl (CO) – to simple metal fragments to yield OsH₂L and ReH₃L complexes. Owing to the approximate respective isovalency of OsH₂L and ReH₃L with IrH₂X and OsH₃X (X = H or halide), we can compare directly the nature of the Lewis donor–acceptor bonding interaction with that of the covalent bonds discussed previously. Table 4.22 summarizes relevant bond angles, metal charges, and other NBO descriptors for the three ligand classes. Overall hybridizations are seen to follow the Lewis-like formulas with $\sim sd^2$ hybridization for the OsH₂L complexes and $\sim sd^3$ for ReH₃L. As expected for bonds that dissociate in heterolytic fashion, all of the M–L bond polarities shown in Table 4.22 are distinctly polarized toward L ($\% c_M^2 = 15.6\%–34.7\%$).

Do dative bonds for d-block acceptors exhibit the critical attributes we have previously seen for the p block? Figure 4.32 demonstrates clearly that dissociation of NH₃ from the OsH₂ fragment results in “mirror-image” profiles of ΔQ versus distance that are strikingly similar to the dative bond in F₃B:NH₃ (Section 3.2.10). Decreased charge at the metal (acceptor) atom is clearly seen at shorter distances; as the donor ligand is pulled away, charge at the metal increases to yield a net ΔQ of ~ 0.17 at long range.

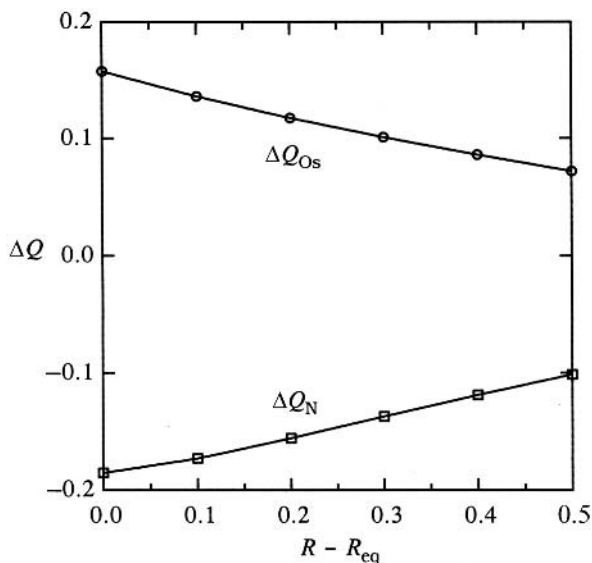
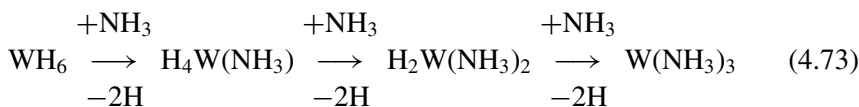


Figure 4.32 “Mirror-image” atomic charge variations $\Delta Q = Q(R) - Q(\infty)$ for Os (circles) and nitrogen (squares) atoms of the σ_{OsN} dative bond ($R_{eq} = 2.087 \text{ \AA}$) of the OsH_2NH_3 coordination complex (see Fig. 3.34).

Also characteristic of dative bonding is substantial deviation of bond ionicity from those calculated according to electronegativity differences. In this regard, the phosphine complex OsH_2PH_3 is illustrative. Because Os ($\chi_{Os} = 2.57$) is *more* electronegative than P ($\chi_P = 2.06$), simple electronegativity considerations predict a bond ionicity $i_{OsP} = 0.205$, polarized 60.2% toward Os. However, as the data in Table 4.22 show, the dative bond is strongly polarized in the *opposite* direction ($\%c_{Os}^2 = 33.7\%$). Nonetheless, the relationship between hybridization and bond polarity follows the expected trend. For the example of OsH_3NH_3 , N ($\chi_N = 3.07$) has high electronegativity relative to H ($\chi_H = 2.10$) and therefore makes bonds with higher metal hybrid d character ($sd^{3.07}$ versus sd^2 ideal). Correspondingly in OsH_3PH_3 , the bonds to the less electronegative P atom have lower d character ($sd^{1.93}$ versus sd^2 ideal).

To illustrate further aspects of the interplay between covalent and coordinate bonding, let us consider the successive coordinative additions of ammonia molecules (ammine ligands, $:NH_3$) to tungsten hydrides in the series $H_{6-2n}W(NH_3)_n$, $n = 1 - 3$,



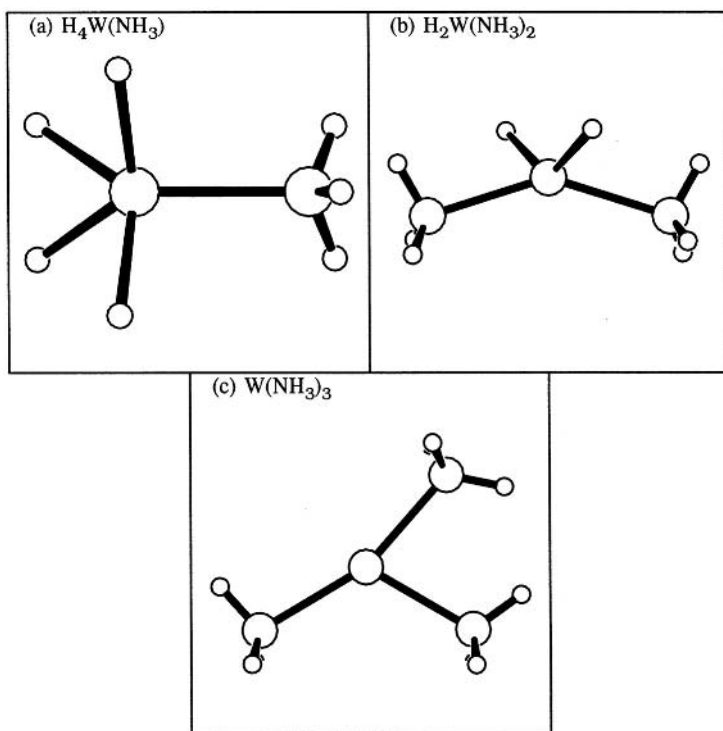
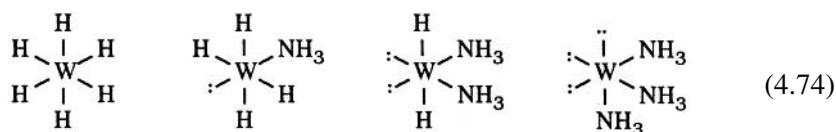


Figure 4.33 Optimized structures of $H_{6-2n}W(NH_3)_n$ coordination complexes: (a) $H_4W(NH_3)$, (b) $H_2W(NH_3)_2$, and (c) $W(NH_3)_3$.

Each coordinated complex in (4.73) is a normal closed-shell duodetecet,



with lone pairs and coordinative $W \leftarrow :N$ donor–acceptor bonds successively replacing pairs of $W-H$ covalent bonds in the closed W valence shell.

Figure 4.33 displays optimized structures of the aminated coordination complexes $H_{6-2n}W(NH_3)_n$, $n = 1 - 3$. Table 4.23 summarizes the metal atomic charges (Q_W) and energies (ΔE_n) of successive coordination reactions in (4.73),

$$\Delta E_n = E[H_{6-2n}W(NH_3)_n] - E[H_{6-2(n-1)}W(NH_3)_{n-1}] - E[NH_3] + E[H_2] \quad (4.75)$$

and the forms of the σ_{WN} dative-bond NBOs in each coordination complex.

As shown in the third column of Table 4.23, replacement of two H radicals by a coordinative ammine ligand becomes successively more endothermic for increasing

Table 4.23. Metal (Q_W) and ligand (Q_L) charges, the energy (ΔE_n) of the coordination reaction (4.75), and the form of the σ_{WL} coordinative bond NBO for $H_{6-2n}WL_n$ complexes, $L = NH_3$ (see Fig. 4.33)

n	Species	ΔE_n (kcal mol ⁻¹)	Q_W	Q_L^a	σ_{WL}
1	$H_4W(NH_3)$	+11.34	+0.424	+0.188	$0.327(sd^{3.99})_W + 0.945(sp^{2.52})_N$
2	$H_2W(NH_3)_2$	+2.42	+0.226	+0.164	$0.323(sd^{5.61})_W + 0.946(sp^{2.37})_N$
3	$W(NH_3)_3$	+37.74	-0.238	+0.079	$(n_N \rightarrow n_W^*)^b$

^a Average value for inequivalent ligands.

^b Strong donor-acceptor interactions (second-order energies: 75–90 kcal mol⁻¹) from nitrogen lone pair ($\sim sp^5$) to unfilled tungsten orbital ($\sim sd^3$).

n (although each species remains a stable equilibrium structure, with all positive frequencies). As expected, each ammine ligand becomes somewhat positively charged and the charge on tungsten shifts toward negative values as n increases, in accordance with the formal charge assignments in (4.72a). However, the progressive difficulty of successive coordinative donations is seen in the decreasing charges on the donor ammine ligands on going from $n = 1$ (+0.19) to $n = 3$ (+0.08). This effect can also be seen in the form of the coordinative σ_{WN} bond, which becomes increasingly polarized toward the ligand until the coordinative interaction is no longer recognized as a formal “bond” (but only a strong $n_N \rightarrow n_W^*$ donor-acceptor interaction) for $n = 3$. Evidently, each dative $L \rightarrow M$ interaction tends to disfavor further interactions of this type (in the expected anticooperative pattern of successive donor-acceptor interactions; cf. Section 2.6), due to the increasingly unfavorable build-up of negative charge on the metal atom.

Figure 4.34 shows the form of the interacting metal and ligand NHOs and the final σ_{WN} NBO for $H_4W(NH_3)$, $n = 1$. (Corresponding plots for $n = 2$ and 3 are very similar.) The complementary “lock-and-key” overlap of the donor and acceptor hybrids is apparent in Fig. 4.34(a). The localized ammine \rightarrow metal ($n_L \rightarrow n_M^*$) interaction depicted in Fig. 4.34(a) is representative of “sigma donation” in a large number of metal-ligand complexes.

Coordination is further promoted by secondary donor-acceptor interactions between orbitals of the metal fragment and the ligand. Representative examples of such interactions are shown in Fig. 4.35 for the special case of $H_2W(NH_3)_2$ (cf. Fig. 4.33(b)).

Leading vicinal interactions of $n_W \rightarrow \sigma_{NH}^*$ and $\sigma_{WH} \rightarrow \sigma_{NH}^*$ type that are characteristic of a single ammine ligand are shown in Figs. 4.35(a) and (b). These

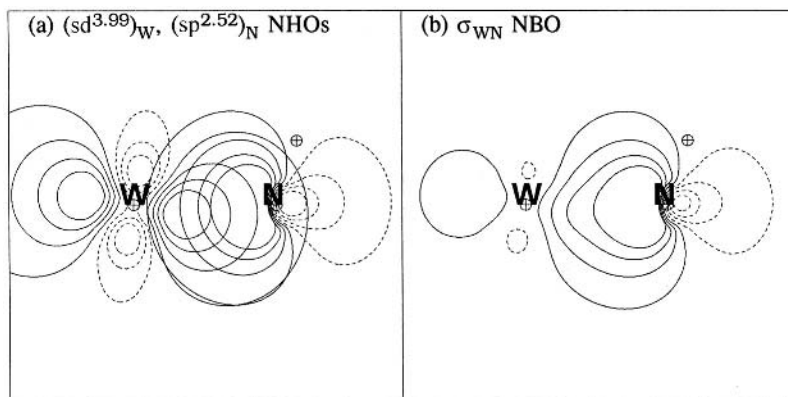


Figure 4.34 The coordinative σ_{WN} bond in $H_4W(NH_3)$ in terms of (a) overlapping NIOs and (b) the final NBO.

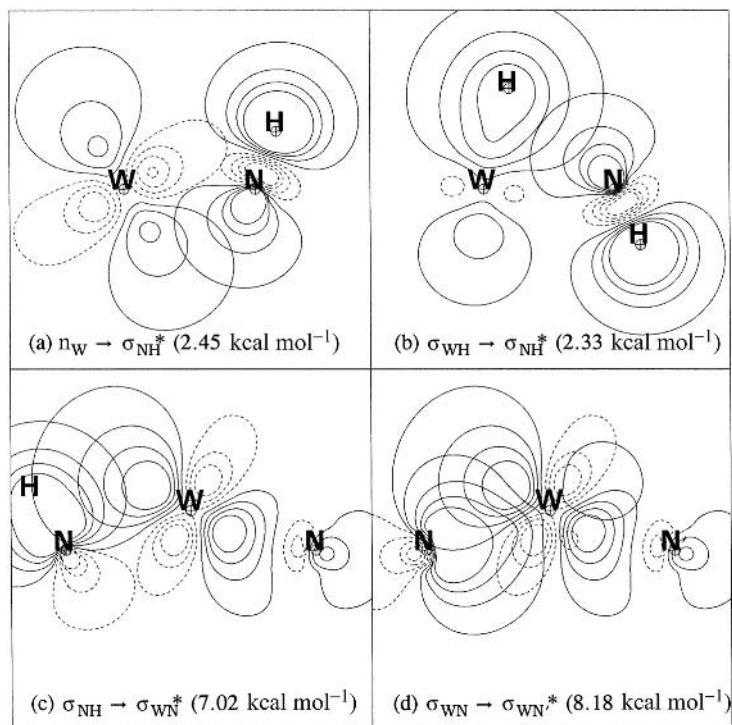


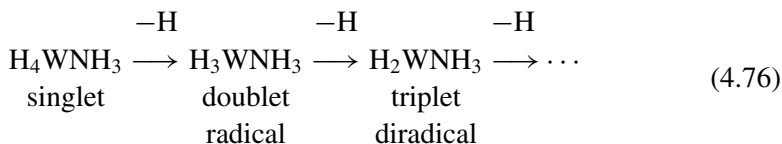
Figure 4.35 Leading hyperconjugative donor–acceptor interactions between amine ligand and amminated metal fragment in $H_2W(NH_3)_2$; cf. Fig. 4.33(b).

interactions are rather analogous (and similar in magnitude) to the hyperconjugative $n \rightarrow \sigma^*$ and $\sigma \rightarrow \sigma^*$ interactions discussed in Section 3.4.2. As shown in Fig. 4.35, these interactions are maximized in coplanar arrangements and evidently contribute to torsional potentials about the metal–ligand bond, as do their main-group analogs. Each $n_W \rightarrow \sigma_{NH}^*$ and $\sigma_{WH} \rightarrow \sigma_{NH}^*$ interaction transfers partial charge from metal to ligand (which is the opposite to the main coordinative $n_N \rightarrow n_W^*$ interaction) and thus constitutes a weak form of “backbonding” to unfilled ligand σ^* orbitals, which are expected to be present in many coordination species.³⁵ In view of their relative weakness and the general similarity to main-group hyperconjugative analogs, such backbonding-type metal–ligand interactions will not be discussed further here.

The strong vicinal $\sigma_{NH} \rightarrow \sigma_{WN'}^*$ interaction that is characteristic of two or more coordinative ligands is shown in Fig. 4.35(c). This interaction is again formally similar to the hyperconjugative main-group interactions discussed in Section 3.4.2, and acts as usual to stabilize conformations in which each $W-N$ coordinative bond is *anti* to a ligand $N-H$ bond. Because the coordinative $\sigma_{WN'}^*$ antibond is strongly (and favorably) polarized toward the metal end of the torsional $N-W$ axis, the $\sigma_{NH} \rightarrow \sigma_{WN'}^*$ interaction is much stronger than in analogous non-coordinate systems, and the effects on geometry (namely the conspicuously closed $H-N-W$ angle to the σ_{NH} donor and open $N-W-N$ angle to the $\sigma_{WN'}^*$ acceptor; cf. Section 3.4.2) are correspondingly more pronounced.

The remaining strong geminal $\sigma_{WN} \rightarrow \sigma_{WN'}^*$ interaction (8.18 kcal mol⁻¹; Fig. 4.35(d)) is closely related to the hypervalent $3c/4e$ ($n_N \rightarrow \sigma_{WN}^*$) interactions to be described in Section 4.6 below. As is evident in Fig. 4.35(d), this interaction is strengthened by more linear $N-W-N'$ alignments and thus contributes to the conspicuously large bond angle ($\theta_{NWN'} = 145.0^\circ$) between ligands in Fig. 4.33(b). The strangely “T-shaped” geometry of the triammine (Fig. 4.33(c)) also reflects the tendency of ligands to “pair up” in near-linear $L-M-L$ arrangements, opposing the expected symmetry of equivalent metal hybrids. Thus, hyperconjugative interactions such as depicted in Fig. 4.35 play an important role in distorting the coordinative geometry away from the “expected” idealized sd^μ -hybrid forms characteristic of covalent organometallic compounds. These interactions are also responsible for the alternating pattern of ΔE_n values in Table 4.23.

Each closed-shell parent species in (4.74) also gives rise to daughter radical species of higher spin by successive removal of hydrogen atoms; that is, starting from the parent tetrahydride,



The specified spin multiplicity in (4.76) is in each case that expected from Hund's rule, with electrons maximally unpaired in remaining orbitals of the tungsten valence shell. Further discussion of daughter radical species is beyond the scope of this work, but certain aspects of open-shell coordination complexes will be considered in Section 4.6.4. below.

4.6 Beyond sigma bonding: transition-metal hyperbonding and pi back/frontbonding

The metal complexes discussed thus far bear little resemblance to the vast majority of common transition-metal complexes. Transition-metal chemistry is dominated by octahedral, square-planar, and tetrahedral coordination geometries, mixed ligand sets, and adherence to the 18-electron rule. The following three sections introduce donor-acceptor interactions that, although not unique to bonding in the d block, make the chemistry of the transition metals so distinctive.

4.6.1 Energetics and geometry of transition-metal hyperbonding

As described in Section 3.5, any polar M—L bond is susceptible to “backside” attack by a Lewis base L' : to form a linear (or near-linear) $3c/4e$ hyperbonded $L' \vdash M \dashv L$ triad, equivalent to strong resonance mixing of the form



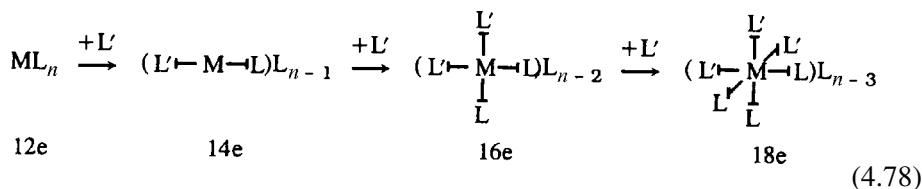
The two “omega prebonds” ($\omega_{L':ML}$ and $\omega_{L'M:L}$) of the triad are distinguishable from ordinary covalent or dative bonds by their high ionicity, strong collinearity, and distinctive spectroscopic signatures (vibrational splitting, ${}^2J_{LL'}$ scalar coupling, and so forth). At the NBO level, such triads are characterized by unusually strong $n_{L'} \rightarrow \sigma_{ML}^*$ (or $n_L \rightarrow \sigma_{ML'}^*$, according to the parent resonance structure selected) donor-acceptor interactions and high NRT weightings of both resonance structures in (4.77). In accordance with the Pimentel–Rundle three-center MO model or Coulson's ionic-covalent resonance picture (Section 3.5), the bonding in (4.77) involves only *valence* orbitals of the central atom M, and hence requires no “expansion of the valence shell” in order to achieve the formal hypervalency (additional two-electron “count”) on M.

Whereas $3c/4e$ hypervalent interactions (4.77) tend to be relatively uncommon and fragile in main-group compounds (often leading to *transition* states for nucleophilic displacement reactions, rather than stable equilibrium species), the corresponding interactions in transition-metal coordination compounds are ubiquitous and robust. The far higher prevalence of hypervalent ω -bonding in transition-metal chemistry may be attributed to three major factors.

- (1) Simple $2c/2e$ bonds to the transition metals commonly are weaker than the corresponding sigma bonds from the p-block elements, resulting in lower-lying acceptor σ_{ML}^* antibonds and increased electronic delocalization.
- (2) The characteristically lower electronegativity of transition metals intrinsically promotes increased polarity of the metal–ligand σ_{ML} bond (which is further accentuated for dative bonds), insuring that the corresponding σ_{ML}^* antibond is polarized toward M, and hence highly exposed to backside $n_{L'} \rightarrow \sigma_{ML}^*$ attack.
- (3) Owing to the *gerade* symmetry of both s and d orbitals, the sd^{μ} metal hybrid h_M is intrinsically *symmetric* between “forward” and “backward” bonding directions (in contrast to the strongly directional character of main-group sp^{λ} hybrids), so bonding to *either* ligand in (4.77) is practically equivalent.

Indeed, the general tendency toward $3c/4e$ bonding in transition-metal complexes is so pronounced that such hypervalency should be considered the *rule*, rather than the exception, in transition-metal chemistry.

As a result of the strong tendency toward $3c/4e$ hypervalent bonding, each M—L coordinative bond of a normal-valent ML_n transition-metal complex will be susceptible to successive ω -additions by other coordinative ligands L' cf. (3.212a):



As shown in (4.78), each ω -addition creates another $L' \leftarrow M \rightarrow L$ linear triad and adds two electrons to the formal “count” at the metal center, increasing the formal hypervalency.

While each member of the sequence (4.78) may be stable as an isolated species, the availability of excess unreacted L' in the reaction vessel normally implies that successive L' ligands will tend to be added (driven by the favorable resonance stabilization in (4.77)), up to the maximum imposed by steric congestion or space-charge limitations. Thus, dependent on the steric bulk or electrostatic charge of the ligands L and L' , stable species of formal 14e, 16e, 18e, or even higher electron count may be obtainable. Because each linear $L' \leftarrow M \rightarrow L$ triad will tend to “block out” one of the three mutually orthogonal spatial directions, the sequence (4.78) must normally terminate after *three* ω -additions (if not before). Thus, from purely three-dimensional spatial considerations, hypervalent transition-metal complexes are typically limited to formal 18e counts (or less). This is evidently the basis for the well-known “18-electron rule” (or “effective-atomic-number” [EAN] rule) which characterizes many observed transition-metal coordination complexes. However, as shown in (4.78), stable coordination complexes satisfying a 12-electron,

14-electron, or 16-electron “rule” may also be expected, as dictated by specific steric or space-charge limits on the ligands.

As prototypical examples of hypervalent coordinative bonding, let us first consider the series of tungsten carbonyls, $W(CO)_n$. The monocarbonyl and dicarbonyl are radicals of higher spin multiplicity (pentuplet and triplet, respectively). The tricarbonyl, $W(CO)_3$, is a duodectet-rule-conforming (12e count) closed-shell singlet, and the higher carbonyls ($n = 4-6$) then correspond to successive ω -additions as in (4.78). Optimized structures for the full sequence $n = 1-6$ are shown in Fig. 4.36, and corresponding geometrical and energetic properties are summarized in Table 4.24.

As shown in Figs. 4.36(a)–(c) and Table 4.24, the normal-valent $n = 1-3$ members have the geometries expected from idealized sd^{n-1} hybridization (Section 4.3.2). The skeletal 90° bond angles of the parent normal-valent $W(CO)_3$ are essentially preserved as carbonyl ligands successively add to form the ω -bonded $OC \leftarrow W \rightarrow CO$ linear triads that are clearly evident in the structures, up to the limit of three orthogonal triads in $W(CO)_6$. As shown in Table 4.24, there is a characteristic elongation by $\sim 0.1 \text{ \AA}$ as each R_{WC} is converted from σ -type to ω -type, and this change occurs practically independently in each of the three orthogonal triads. The strong exothermicity of ω -addition is also remarkably constant from $n = 4$ to 6 ($41.8 \pm 0.5 \text{ kcal mol}^{-1}$), showing that the 3c/4e hypervalent interactions along each orthogonal direction are virtually independent.

Only the octahedral $W(CO)_6$ final product of the ω -addition sequence has a “VSEPR-like” structure (but the three additional lone pairs on W would also lead to a different prediction for this case if strict VSEPR reasoning were applied). The intermediate 12e $W(CO)_3$, 14e $W(CO)_4$, and 16e $W(CO)_5$ molecules are all perfectly stable as isolated species. However, it is clear that, in the presence of excess CO, only the 18e $W(CO)_6$ species will remain as a final product, and the 18e configuration will therefore appear to exhibit “special stability.”

The NBO descriptors of the normal-valent $W(CO)_3$ and hypervalent $W(CO)_n$ ($n = 4-6$) species are summarized in Table 4.25. The carbonyl net charges (Q_{CO}) and metal hybridization (h_W) exhibit the same clear distinction between σ -bonded and ω -bonded ligands as is evident in the geometrical structures (Fig. 4.36). In each case the carbonyl ligands of the ω -bonded triads are noticeably stronger *net* donors to the metal (with ω -bonded carbonyl charges about $0.02e$ more positive than σ -bonded carbonyls, reflecting changes in both sigma- and pi-bonding interactions). The metal hybridization differs systematically, with metal σ hybrids of approximate sd^3 form (showing the persistent connection to idealized sd^{n-1} hybridization of the normal-valent $n = 3$ parent species) and ω -hybrids of sd^2 form in all these species. Note that there is no appreciable involvement of tungsten 6p orbitals in any of these hybrids, so the formal hypervalent extension to 14e, 16e, or

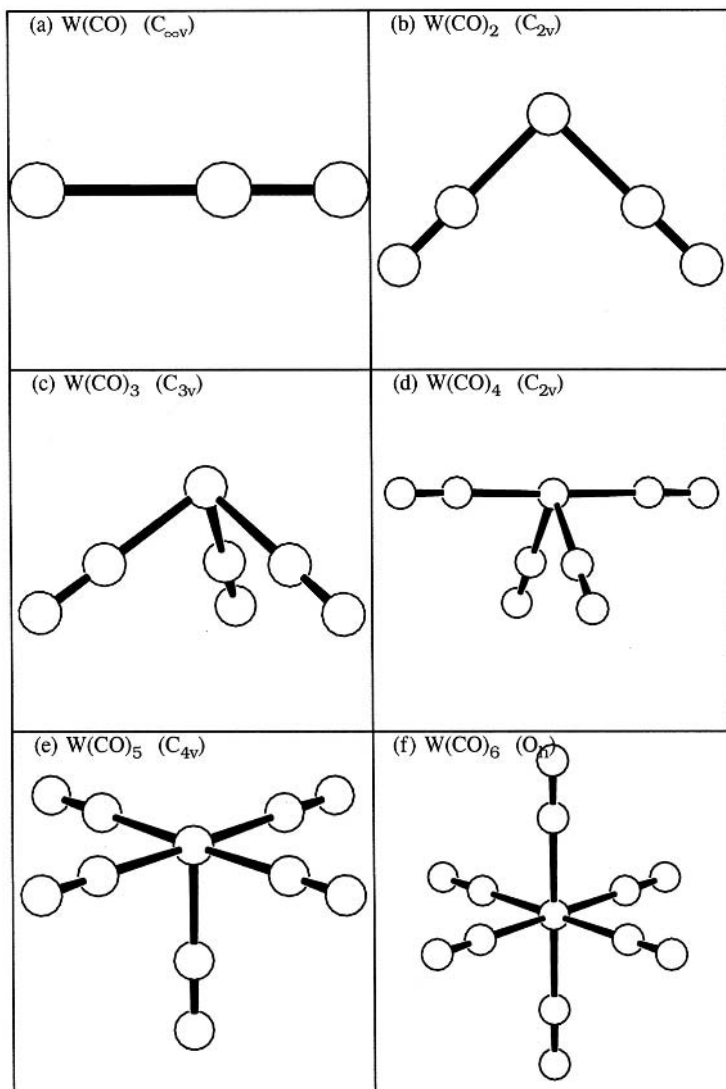


Figure 4.36 Optimized structures of W(CO)_n , $n = 1-6$ (see Table 4.24).

18e count certainly occurs without significant “expansion of the valence shell” to include metal *p* orbitals.

From the above considerations, we can recognize that an “ideal” hypersaturated coordination complex would arise from what may be denoted as a “ $3\omega/3\sigma/3n$ ” metal configuration, with three orthogonal ω bonds (3ω ; one each in the *x*, *y*, and *z* directions) built from three parent sigma bonds (3σ ; from sd^2 hybrids at 90° angles), and with three lone pairs ($3n$; pure *d* orbitals) in the duodectet of the parent

Table 4.24. Bond lengths R_{WC} , angles θ_{CWC} , and incremental CO binding energies $\Delta E(+CO)$ for σ and ω bonds of $W(CO)_n$ complexes (see Fig. 4.36)

Species	R_{WC} (Å)		θ_{CWC} (degrees)			$\Delta E(+CO)$ (kcal mol ⁻¹)
	σ	ω	$\sigma\sigma$	$\sigma\omega$	$\omega\omega$	
W(CO)	1.915	—	—	—	—	—
W(CO) ₂	1.922	—	99.0	—	—	-46.2
W(CO) ₃	1.919	—	89.1	—	—	-66.3
W(CO) ₄	1.938	2.055	89.1	90.5	178.7	-42.4
W(CO) ₅	1.955	2.065	—	90.0	90.7 178.6	-41.6
W(CO) ₆	—	2.070	—	—	90.0 180.0	-41.3

Lewis-like structure. Such an ideal $3\omega/3\sigma/3n$ complex is perforce of formal 18e count and overall six-coordinate octahedral geometry, as is observed to be the most ubiquitous bonding motif in transition-metal chemistry. Only slightly less ideal is the hypersaturated $2\omega/2\sigma/4n$ pattern of a 16e, four-coordinative square-planar geometry, which is again a ubiquitous bonding motif. In this manner we can see (starting from a large number of potential normal-valent Lewis-like “parents”) how exothermic coordinative hyperbonding selects a few “ideal” motifs of maximally hypercoordinated character (within allowed constraints of two- or three-dimensional geometry) that are expected to exhibit exceptional thermodynamic and kinetic stability.

Table 4.25. The NBO descriptors of $W(CO)_n$ complexes ($n = 3-6$), showing carbonyl net charge (Q_{CO}) and tungsten hybridization (h_W) for σ - and ω -bonded carbonyl ligands (see Fig. 4.36)

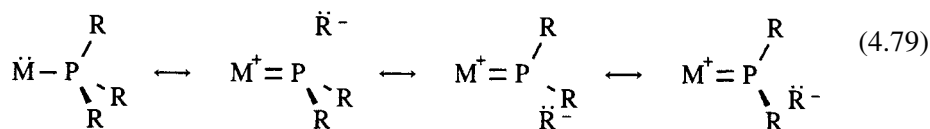
Species	Q_{CO}		h_W	
	σ	ω	σ	ω
W(CO) ₃	-0.044	—	sd ^{2.65}	—
W(CO) ₄	+0.018	+0.041	sd ^{2.63}	sd ^{1.47}
W(CO) ₅	+0.072	+0.103	sd ^{3.18}	sd ^{1.88}
W(CO) ₆	—	+0.155	—	sd ^{2.00}

4.6.2 Pi backbonding

As mentioned in Section 4.5.2, some degree of “backbonding” may be expected in all sigma-coordinated ligands, partially compensating for the dative flow of charge from ligand to metal. However, these backbonding interactions become particularly important for ligands with unfilled π^* orbitals, which are ideally suited for secondary $n_M \rightarrow \pi_L^*$ interactions with filled metal d orbitals. In such a case the ligand acts both as a strong pi acceptor (acid) and as a sigma donor (base), and the net flow of charge between ligand and metal can actually be *reversed* if the former property predominates over the latter. The synergistic interplay between pi backbonding and sigma bonding thereby alleviates the unfavorable build-up of a dipole and greatly strengthens overall coordination.

A closely related synergism exists for ligands bereft of empty π^* orbitals, but instead having low-lying σ^* orbitals that can act as “pi-type” (off-axis) acceptors of electron density from the metal. Consider, for example, the important case of phosphine (PR_3) ligands. Donation of electrons from metal d-orbital lone pairs (n_M) into empty σ_{PR}^* orbitals is favored both by spatial overlap and by the small gap in $n_M - \sigma_{\text{PR}}^*$ orbital energies. Figure 4.37 shows comparison NBO diagrams for $n_{\text{O}_s} \rightarrow \pi_{\text{CO}}^*$ (carbonyl ligand) versus $n_{\text{O}_s} \rightarrow \sigma_{\text{PH}}^*$ (phosphine ligand) interactions in $\text{H}_2\text{Os}:\text{CO}$ versus $\text{H}_2\text{Os}:\text{PH}_3$ coordination complexes, illustrating salient features of the “pi-backbonding” in each species. Figure 4.37(c) also compares the corresponding $n_{\text{O}_s} \rightarrow \sigma_{\text{NH}}^*$ interaction for $\text{H}_2\text{Os}:\text{NH}_3$, showing the significantly weaker pi-type backbonding interactions for ammine compared with phosphine ligands.

Whether of $n_M \rightarrow \pi_L^*$ or $n \rightarrow \sigma_L^*$ (off-axis) type, pi-backbonding interactions correspond to partial inclusion of ionic resonance structures featuring a metal–ligand double bond, as illustrated schematically in (4.79) for phosphine ligands:



We can quantify the tendency of various donor ligands to engage in backbonding by returning to the H_2OsL and H_3ReL ($\text{L} = \text{NH}_3, \text{PH}_3, \text{and CO}$) complexes discussed in Section 4.5.2. Tables 4.26 and 4.27 give key geometrical and NBO metrics for the free ligands (Table 4.26) and the various $n_M \rightarrow \sigma_{\text{NH}}^*$, $n_M \rightarrow \sigma_{\text{PH}}^*$, and $n_M \rightarrow \pi_{\text{CO}}^*$ backbonding interactions in the metal complexes.

Tables 4.26 and 4.27 clearly reveal that the strength of metal-to-ligand pi-backbonding in MH_mXY_n complexes (expressed in terms of either $\Delta E_{\text{M} \rightarrow \text{L}^*}$)⁽²⁾

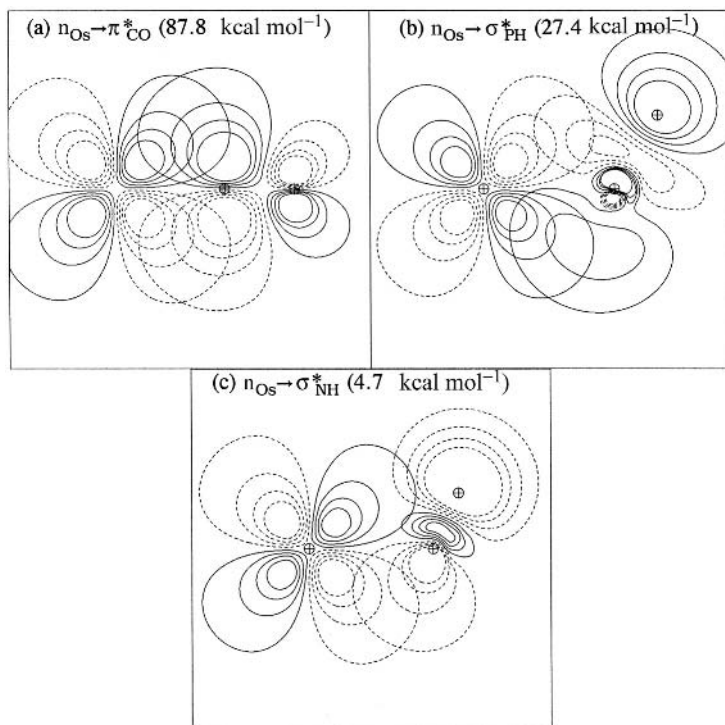


Figure 4.37 Comparisons of pi-type backbonding interactions in $\text{H}_2\text{Os}:\text{L}$ complexes for (a) $\text{L} = \text{CO}$, (b) $\text{L} = \text{PH}_3$, and (c) $\text{L} = \text{NH}_3$.

or ligand antibond occupancy) is maximized when the ligand acceptor orbitals are highly polarized toward X and low in energy. Other features, such as net charge distributions, are affected *both* by the sigma dative interaction of X with the metal (which tends to decrease electron density on the ligand) and by pi-backbonding (which increases electron density on the metal). In accordance with conventional wisdom, the net balance of ligand dative and backbonding interactions with the metals indicates that NH_3 is primarily a σ -donor, CO is a powerful π -acceptor, and PH_3 is both a strong sigma-donor and a good pi-acceptor ligand.

As a prototype for strong $n_{\text{M}} \rightarrow \pi_{\text{L}}^*$ pi-backbonding interactions, let us now consider the carbonyl (CO) ligand in the series of coordinated tungsten complexes $\text{H}_{6-2n}\text{W}(\text{CO})_n$, $n = 1-3$, analogous to (4.71):

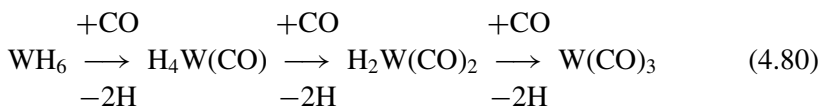


Table 4.26. Geometrical (R_{XY}) and NBO descriptors of XY_n ligands (NH_3 , PH_3 , and CO), illustrating natural atomic charges (Q_Y) and NBO occupancy (Occ^*), polarity ($\%pol = 100c_X^2$), and orbital energy (ϵ^*) of σ_{NH^*} , σ_{PH^*} or π_{CO^*} acceptor orbitals in the free ligands

XY_n	$R_{XY}(\text{\AA})$	Q_Y	Occ^*	$\%pol$	$\epsilon^*(a.u.)$
NH_3	1.015	+0.352	0.000	32.4	0.4360
PH_3	1.423	-0.176	0.003	50.8	0.1838
CO	1.127	-0.480	0.000	76.9	0.0210

Figure 4.38 shows the optimized geometries of these complexes, and Table 4.28 summarizes the successive coordination energies,

$$\Delta E_n = E[H_{6-2n}W(CO)_n] - E[H_{6-2(n-1)}W(CO)_{n-1}] - E[CO] + E[H_2] \quad (4.81)$$

metal and ligand charges, and form of the coordinate σ_{WC} bond NBO in each species. Note the remarkable un-VSEPR-like structure of $H_4W(CO)$ (Fig. 4.38(a)) in which *all* non-metal atoms are found to lie on one side of a plane passing through the metal atom.

In contrast to ammine ligation (Table 4.18), successive coordinations to carbonyl ligands are typically rather exothermic (third column of Table 4.28), with ΔE_n values ranging from $-0.9 \text{ kcal mol}^{-1}$ ($n = 1$) to $-28.9 \text{ kcal mol}^{-1}$ ($n = 3$). Moreover,

Table 4.27. Geometrical (R_{XY}) and NBO descriptors of MH_mXY_n complexes ($MH_m = ReH_3$, OsH_2 ; $XY_n = NH_3$, PH_3 , CO), illustrating ligand charges (Q_L), $M \rightarrow L^*$ delocalization type, occupancy (Occ^*) of respective σ_{NH^*} , σ_{PH^*} , and π_{CO^*} ligand acceptor orbitals, and associated second-order delocalization energies ($\Delta E_{M \rightarrow L^*}^{(2)}$)

Species	$R_{XY}(\text{\AA})$	Q_L	$M \rightarrow L^*$ type	Occ^*	$\Delta E_{M \rightarrow L^*}^{(2)} (\text{kcal mol}^{-1})$
ReH_3NH_3	1.024	+0.219	$n_M \rightarrow \sigma_{NH^*}$	0.052	8.1
ReH_3PH_3	1.426	+0.344	$n_M \rightarrow \sigma_{PH^*}$	0.234	28.6
ReH_3CO	1.127	-0.017	$n_M \rightarrow \pi_{CO^*}$	0.642	122.8
OsH_2NH_3	1.023	+0.212	$n_M \rightarrow \sigma_{NH^*}$	0.045	4.7
OsH_2PH_3	1.423	+0.368	$n_M \rightarrow \sigma_{PH^*}$	0.231	27.4
OsH_2CO	1.165	+0.038	$n_M \rightarrow \pi_{CO^*}$	0.616	87.8

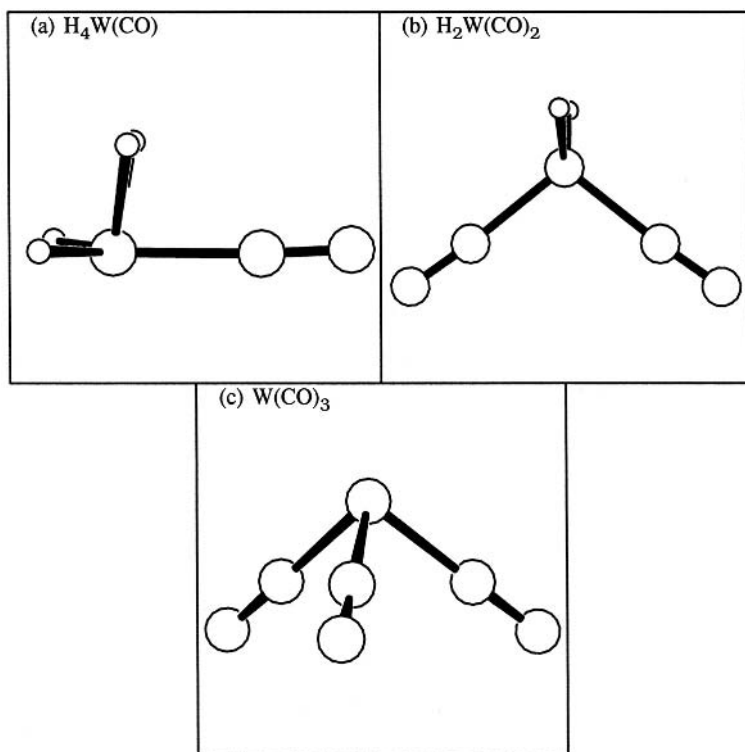


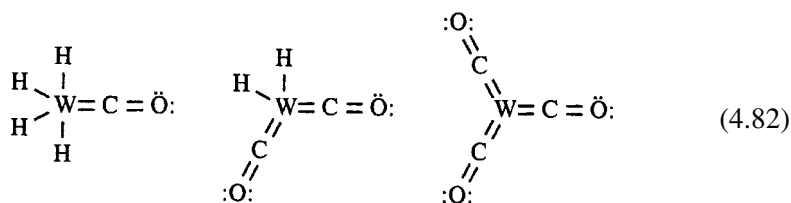
Figure 4.38 Optimized structures of $H_{6-2n}W(CO)_n$ coordination complexes: (a) $H_4W(CO)$, (b) $H_2W(CO)_2$, and (c) $W(CO)_3$.

the net charge of the coordinated CO ligand is seen to be *negative* in all cases, indicating that pi-backbonding (pi acidity) contributes even *more* strongly than does sigma dative bonding (sigma basicity) to coordinative charge displacement in these complexes. The σ_{WC} bond to carbonyl is seen to have appreciably higher covalent character than the corresponding σ_{WC} bond to ammine ligand. Furthermore, the $n_{W \rightarrow \pi_{CO}^*}$ pi-backbonding interaction is so strong that the best Lewis-structure representation for each species contains a formal $W=C$ double bond to each

Table 4.28. Similar to Table 4.23, for $L = CO$ (see Fig. 4.38)

n	Species	ΔE_n (kcal mol ⁻¹)	Q_W	Q_L	σ_{WL}
1	$H_4W(CO)$	-0.9	+0.328	-0.030	$0.548(sd^{2.65})_W + 0.837(sp^{0.59})_C$
2	$H_2W(CO)_2$	-26.6	+0.427	-0.037	$0.506(sd^{3.06})_W + 0.863(sp^{0.57})_C$
3	$W(CO)_3$	-28.9	+0.132	-0.044	$0.496(sd^{3.22})_W + 0.869(sp^{0.57})_C$

ligand,



All these features are consistent with the greater strength of metal–carbonyl coordination and higher ranking of CO in the spectrochemical series (4.69).

Figure 4.39 depicts the coordinative σ_{WC} and π_{WC} metal–carbonyl bonds of $\text{H}_4\text{W}=\text{C}=\text{O}$ both in NBO (right) and in overlapping NHO (left) representations. Although the allene-like ($\text{W}=\text{C}=\text{O}$) representation is the “best” single Lewis structure (in the maximum-density sense; Section 1.5), significant admixtures of single-bonded ($\text{W}-\text{C}\equiv\text{O}$) and nonbonded ($\text{W}:\text{C}\equiv\text{O}$) resonance structures are also

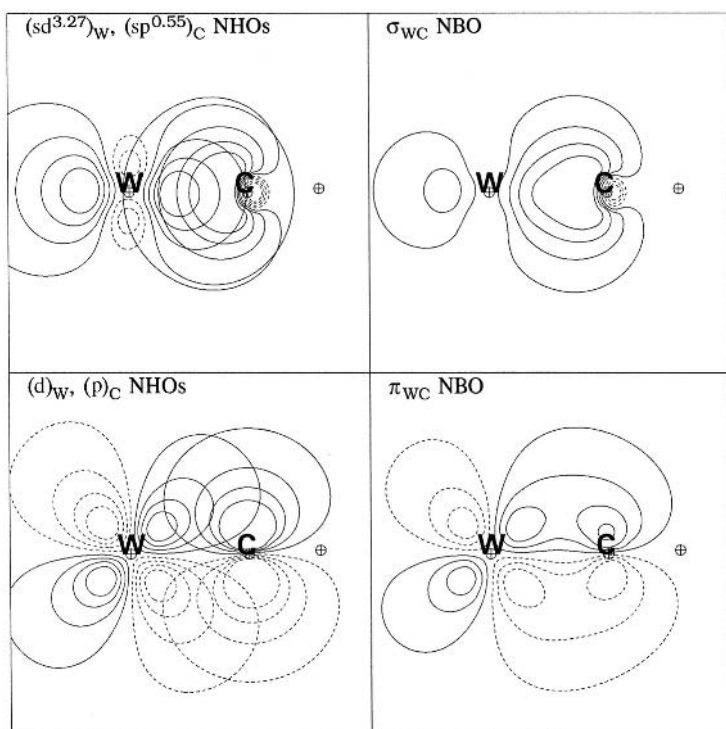
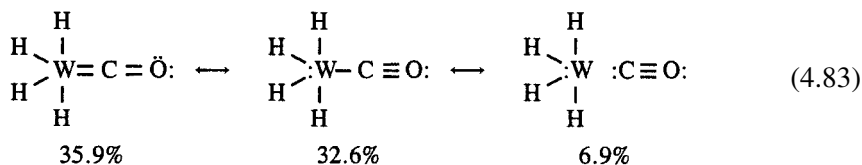


Figure 4.39 Coordinative σ_{WC} (upper) and π_{WC} (lower) bonds in $\text{H}_4\text{W}(\text{CO})$, shown in terms of overlapping NHOs (left) and the final NBO (right).

indicated by the quantitative NRT resonance weightings:



The corresponding NRT bond orders ($b_{\text{WC}} = 1.330$, $b_{\text{CO}} = 2.460$) clearly reflect the significant multiple-bond character of the metal–carbonyl interaction and concomitant weakening of the carbonyl CO bond. The latter is manifested in numerous spectroscopic signatures of bond weakening (e.g., lengthening of R_{CO} , red-shifting of ν_{CO} vibrational frequencies) relative to free carbon monoxide. As the resonance weightings in (4.83) and orbital diagrams in Fig. 4.39 make clear, strong synergistic σ/π covalency reorganization (rather than long-range “crystal-field” electrostatic interaction) is the central electronic phenomenon of metal–carbonyl coordination.

Still other effects of carbonyl coordination are evident on the structure of the metal hydride moiety. As is evident in Fig. 4.38(a), the two “perpendicular” W—H bonds in $\text{H}_4\text{W}(\text{CO})$ ($\theta_{\text{HWC}} = 89.0^\circ$) are strongly inequivalent to the two “trigonal” W—H' bonds ($\theta_{\text{H'WC}} = 121.3^\circ$), with bond angles of both sets deviating significantly from idealized sd^3 or sd^4 hybridization. This inequivalency is largely due to the strong $\sigma_{\text{WH}} \rightarrow \sigma_{\text{WC}}^*$ donor–acceptor interaction depicted in Fig. 4.40, which is by far the largest hyperconjugative stabilization between WH_4 and CO moieties (estimated as $11.6 \text{ kcal mol}^{-1}$ by second-order NBO perturbation theory). As shown in Fig. 4.40, each σ_{WH} interacts principally with the *off-axis* “horse-collar” lobe of the metal d_{z^2} -like NHO, and thus aligns approximately perpendicular to the main

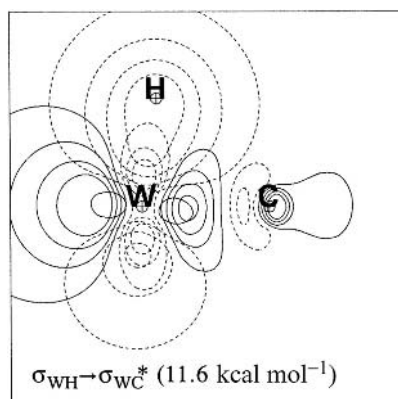


Figure 4.40 Hyperconjugative $\sigma_{\text{WH}} \rightarrow \sigma_{\text{WC}}^*$ interaction in $\text{H}_4\text{W}(\text{CO})$ (cf. Fig. 4.38(a)), with estimated second-order stabilization energy $11.6 \text{ kcal mol}^{-1}$.

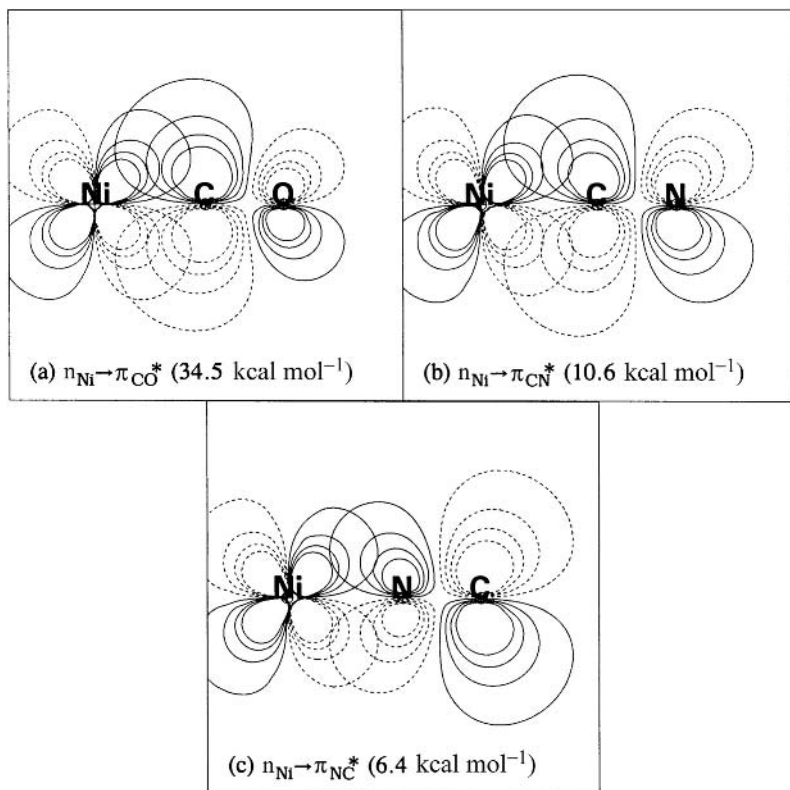


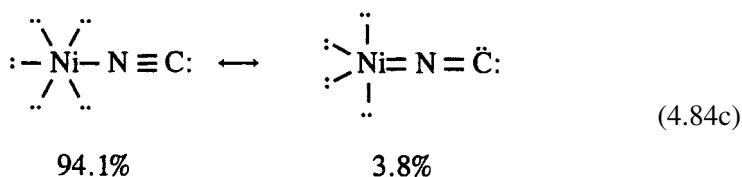
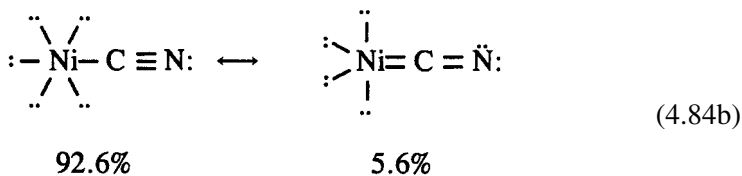
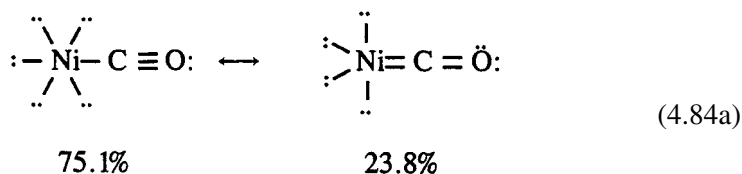
Figure 4.41 Pi-backbonding $n_{\text{Ni}} \rightarrow \pi_{\text{L}}^*$ interactions in NiL complexes: (a) L = CO, (b) L = CN⁻, (c) L = NC⁻.

W—C bonding axis. (Weaker $\sigma_{\text{WH}} \rightarrow \pi_{\text{CO}}^*$ interactions further tilt these bonds slightly toward the adjacent carbonyl moiety.) As a result of such hyperconjugative interactions, each W—H_{perp} has slightly reduced NRT bond order ($b_{\text{WH}} = 0.902$) compared with corresponding W—H_{trig} bonds ($b_{\text{WH}} = 0.954$). Further details of such hyperconjugative interactions (which are clearly secondary to the primary sigma-bonding and pi-backbonding coordinative events discussed above) are beyond the scope of the present treatment.

As a further illustration of the dependence of $n_{\text{M}} \rightarrow \pi_{\text{L}}^*$ pi-backbonding interactions on metal and ligand character, we may compare simple NiL complexes of nickel with carbonyl (CO), cyanide (CN⁻), and isocyanide (NC⁻) ligands, as shown in Fig. 4.41. This figure shows that the $n_{\text{Ni}} \rightarrow \pi_{\text{L}}^*$ pi-backbonding interaction decreases appreciably (from 28.5 kcal mol⁻¹ in NiCO to 6.3 kcal mol⁻¹ in NiNC⁻, estimated by second-order perturbation theory) as the polarity of the π_{L}^* acceptor shifts unfavorably away from the metal donor orbital. The interaction in NiCO is stronger than that in NiCN⁻ partially due to the shorter Ni—C distance in the

former case (1.684 versus 1.775 Å), which is itself evidence of stronger bonding. However, the corresponding difference in geometry between NiCN⁻ and NiNC⁻ is much smaller ($R_{\text{NiC}} = 1.775$ Å versus $R_{\text{NiN}} = 1.772$ Å), and the difference in pi-backbonding is almost entirely due to the unfavorable polarity reversal of the π_{L}^* antibond when n_{Ni} attacks the ion from the “wrong” (N) end.

As one can judge from comparison of Fig. 4.41(a) with Fig. 4.39, the n_{M} donor orbital is more compact for $M = \text{Ni}$ than for $M = \text{W}$, reflecting the general contraction of metal d orbitals along the transition series. Because of this effect, the lobes of the d_{Ni} orbital are somewhat less well “matched” to the size of the carbonyl π_{CO}^* orbital, and general $n_{\text{M}} \rightarrow \pi_{\text{CO}}^*$ interaction strength is correspondingly reduced in the nickel case. The weakened pi-backbonding interactions of Ni are also reflected in the altered ratios of Ni=L versus Ni—L resonance structures in the NRT description of these species (compared, e.g., with corresponding tungsten compounds (4.83)):



Whereas the pi-backbonded $M=L$ form constituted the *leading* resonance structure in (4.83), it becomes only a minor (<5%) feature in the NRT description (4.84c) of NiNC⁻. Thus, pi-backbonding is seen to be a highly variable feature of coordination bonding that can strongly modulate the overall interaction strength, but remains clearly “secondary” to the primary sigma donation (a universal feature of coordinative bonding) in the majority of cases.

4.6.3 Pi-frontbonding

In the previous section we found that metal lone pairs may donate into low-energy ligand antibonding orbitals (either σ^* or π^*) to make backbonds. Can the situation

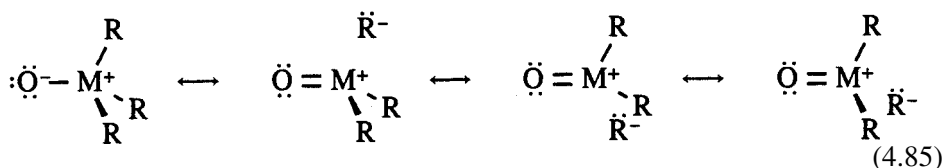
Table 4.29. The NBO characteristics for OIrH_3 and OPH_3 , demonstrating that σ_{MH}^* antibonds have significant coefficients at M ($\% \text{pol}_\text{M} = 100c_\text{M}^2$), low orbital energies (ϵ_{σ^*}), substantial occupancies (Occ_{σ^*}), and strong $n_\text{O} \rightarrow \sigma_{\text{MH}}^*$ delocalizations ($\Delta E_{n \rightarrow \sigma^*}$ ⁽²⁾)

Species	$\% \text{pol}_\text{M}$	ϵ_{σ^*}	Occ_{σ^*}	$\Delta E_{n \rightarrow \sigma^*}$ ⁽²⁾ (kcal mol ⁻¹)
OIrH_3	46.6	0.192	0.576	71.2
OPH_3	51.7	0.120	0.360	64.0

be reversed, i.e., can a ligand lone pair (n_L) delocalize into a metal–ligand antibond? The prescription for such an “inverted” delocalization seems clear: a lone pair on a ligand that is spatially oriented for overlap with metal–ligand antibonds that are appreciably polarized toward the metal. Here we briefly consider such “pi-frontbonding” interactions in the context of OIrH_3 and its chemical cousin OPH_3 .

Recall from Section 4.4.4 that the best single-configuration description of OIrH_3 features an Ir–O *single* bond that is highly polarized toward oxygen. Two of the oxygen lone pairs lie perpendicular to the Ir–O bond in pure p orbitals, whereas the remaining hybridized ($sp^{0.1}$) lone pair is collinear with the Ir–O bond. The Ir–H σ_{IrH} and σ_{IrH}^* orbitals are relatively apolar, with 34.6% of σ_{IrH}^* at Ir. As shown in Table 4.29, the Ir–O interaction exhibits the hallmarks of pi-backbonding seen in metal–phosphine complexes, but now the direction of charge transfer is reversed. Critical NBO properties of OIrH_3 can be seen to include the low energy and high occupancy of σ_{IrH}^* orbitals with substantial metal character. Delocalization energies for the $n_\text{O} \rightarrow \sigma_{\text{IrH}}^*$ frontbonding interactions have magnitudes rather similar to those of normal pi backbonds. Also shown in Table 4.29 are corresponding NBO metrics for phosphine oxide, OPH_3 (cf. Section 3.2.10), which demonstrate the remarkable kinship between simple oxides of iridium and phosphine. Figure 4.42 compares the $n_\text{O} \rightarrow \sigma_{\text{MH}}^*$ NBO interaction diagrams for $\text{M} = \text{Ir}$ and P to illustrate this orbital analogy.

The net consequence of $n_\text{O} \rightarrow \sigma_{\text{MH}}^*$ delocalizations is that OIrH_3 and OPH_3 acquire partial double-bond character due to resonance contributions as shown in (4.85):



The “inverse” relationship to pi-backbonding interactions as shown in (4.79) is apparent.

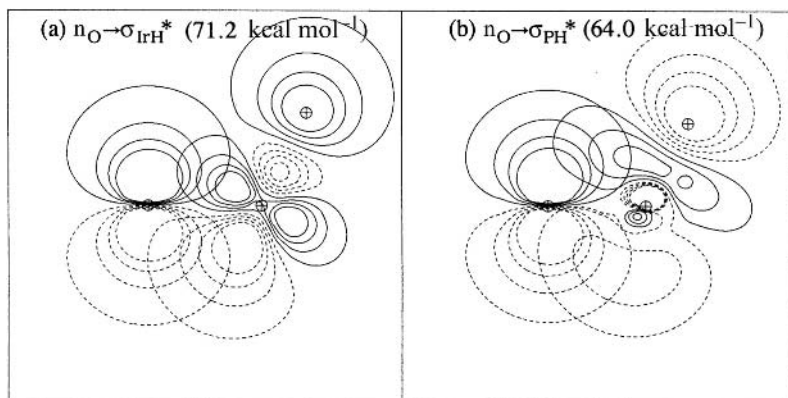


Figure 4.42 A comparison of “pi-frontbonding” interactions of $n_{\text{O}} \rightarrow \sigma_{\text{MH}}^*$ (off-axis) type for (a) OIrH_3 and (b) OPH_3 .

4.6.4 Higher spin states and magnetic properties

While our primary focus has been on stable closed-shell (or low-spin) coordination species in which covalency effects are pronounced, it is also useful to examine the opposite extreme of weak coordinate bonding and “free-atom”-like spin multiplicities, corresponding to the original assumptions of crystal-field theory.

For this purpose, we consider the classic case of the hexaaquamanganese(II) cation $[\text{Mn}(\text{H}_2\text{O})_6]^{2+}$, a prototypical high-spin species of octahedral coordination. The isolated Mn(II) ion is isoelectronic with ferromagnetic Fe(III) and exhibits a similarly high magnetic moment associated with five unpaired electron spins. According to crystal-field theory (Section 4.5.1), the weak-field H_2O ligand lies rather low in the spectrochemical series (4.69), corresponding to a small crystal-field-splitting parameter $10Dq$ in (4.68). In this case the splitting of e_g and t_{2g} levels is insufficient to induce pairing of electrons in the lower t_{2g} orbitals, against the intrinsic preference for unpaired spins expressed by Hund’s rule. The ground-state d-shell configuration of $[\text{Mn}(\text{H}_2\text{O})_6]^{2+}$ is therefore expected to be high-spin (hextuplet) $(d_{xy})^1(d_{xz})^1(d_{yz})^1(d_{x^2-y^2})^1(d_z)^1$ rather than low-spin (doublet) $(d_{xy})^2(d_{xz})^2(d_{yz})^1(d_{x^2-y^2})^0(d_z)^0$. Magnetic measurements are fully consistent with this simple crystal-field picture.

Figure 4.43 shows the optimized structure of $[\text{Mn}(\text{H}_2\text{O})_6]^{2+}$ (hextuplet spin multiplicity). Consistently with the expected weak-field limit, the NBO Lewis structure of $[\text{Mn}(\text{H}_2\text{O})_6]^{2+}$ is found to correspond to an isolated manganese cation and six surrounding H_2O molecules. The charge on the central metal ion is $Q_{\text{Mn}} = +1.691$, corresponding to net transfer of $0.052e$ from each H_2O ligand to the central manganese cation.

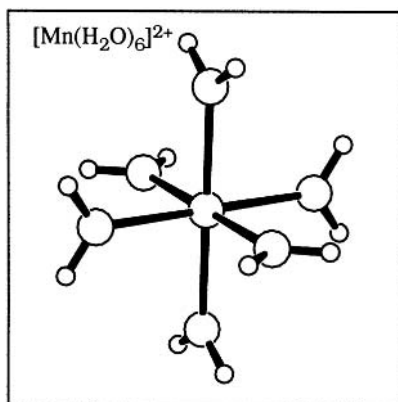
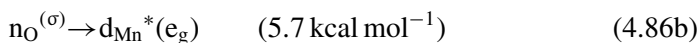
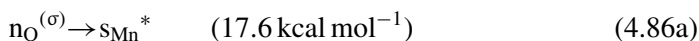


Figure 4.43 The optimized structure of the hexaaquamanganese(II) ion (spin $\frac{5}{2}$, $R_{\text{MnO}} = 2.220 \text{ \AA}$). Note that the bond “sticks” between Mn and O are merely to aid visualization.

The occupancies of metal 4d and 5s orbitals correspond to an overall $s^{0.15}d^{5.15}$ configuration, deviating noticeably from the nominal s^0d^5 assignment. The d spin-orbitals of α spin are essentially completely filled (0.993–0.995), and thus chemically inert. However, the nominally “empty” spin-orbitals of β spin exhibit significant non-zero occupancies (0.063 in each member of the e_g set and 0.017 in each member of the t_{2g} set), and appreciable occupancy of both spins is also found in the 5s orbital (0.088 α , 0.082 β). These “unexpected” occupancies (which would be strictly absent in the isolated ion) can be associated with the leading donor–acceptor interactions, namely



In each case the ligand donor orbital is the in-plane σ -type oxygen lone pair $n_{\text{O}}^{(\sigma)} = (sp^{1.11})_{\text{O}}$ pointing directly toward the metal center. (The corresponding out-of-plane π -type oxygen lone pair $n_{\text{O}}^{(\pi)}$ is relatively uninvolved in coordination, with each $n_{\text{O}}^{(\pi)} \rightarrow d_{\text{Mn}}^*(t_{2g})$ interaction contributing only $1.07 \text{ kcal mol}^{-1}$ to stabilization.) The $d_{\text{Mn}}^*(e_g)$ acceptor orbitals in (4.86b) are the $d_{x^2-y^2}$ and d_{z^2} orbitals that point directly toward the ligand donors, whereas the corresponding t_{2g} orbitals (d_{xy} , d_{xz} , and d_{yz}) can only participate in weaker interactions with donor $n_{\text{O}}^{(\pi)}$ orbitals. Figure 4.44 shows orbital contours of the NBO interactions in (4.86a) and (4.86b), each of which represents a *one*-electron donor–acceptor stabilization of approximately *half* the magnitude that might be expected from a two-electron donor–acceptor interaction of comparable overlap in a closed-shell system.

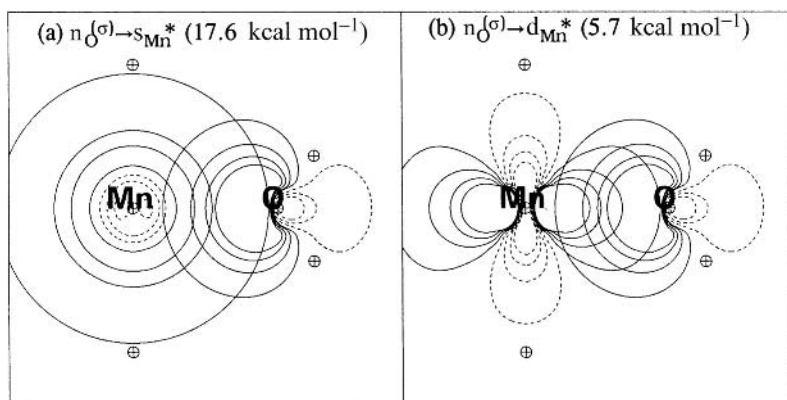


Figure 4.44 Leading donor–acceptor interactions (β spin set) from a sigma-type oxygen lone pair to unfilled manganese valence orbitals of (a) s-type and (b) d-type in $[\text{Mn}(\text{H}_2\text{O})_6]^{2+}$ (cf. Fig. 4.43).

It is evident that the interactions (4.86b) depicted in Fig. 4.44 strongly distinguish the “strong-acceptor” e_g set from the “weak-acceptor” t_{2g} set in $[\text{Mn}(\text{H}_2\text{O})_6]^{2+}$. More generally, it is evident that a metal configuration $(t_{2g})^1(e_g)^0$ will be much more favorably stabilized by donor–acceptor interactions with surrounding octahedral ligands than will a corresponding $(t_{2g})^0(e_g)^1$ configuration, because partial filling of an e_g orbital naturally quenches the stronger $n_L \rightarrow d_M^*(e_g)$ interactions. The energy difference between these two configurations (roughly six times the stabilization energy in (4.86b), minus the corresponding stabilization energies of $n_O^{(\pi)} \rightarrow d_{Mn}^*(t_{2g})$ interactions) corresponds directly to the spectroscopic $t_{2g} \rightarrow e_g$ excitation energy in crystal-field theory, i.e., to the splitting parameter “ $10Dq$ ” in (4.68). The crystal-field $10Dq$ parameter can also be crudely associated with the energy difference between t_{2g} -type and e_g -type metal d natural localized molecular orbitals (NLMOs), which incorporate the weak donor–acceptor mixings with ligands (Section 1.5),

$$\begin{aligned} \Delta\epsilon_{\text{NLMO}} &= \epsilon_{\text{NLMO}}(e_g) - \epsilon_{\text{NLMO}}(t_{2g}) = -0.2438 - (-0.2775) \text{ a.u.} \\ &\simeq 21 \text{ kcal mol}^{-1} \end{aligned} \quad (4.87)$$

Thus, the ligand-stabilized d-orbital splitting pattern is qualitatively consistent with the expectation of crystal-field theory, but the physical origin of this splitting should be attributed to *attractive* donor–acceptor interactions such as (4.86b) rather than to any inherent electrostatic “repulsions” toward the incoming ligands. More accurate treatment of the spectroscopic $10Dq$ value should, of course, be based on separate consideration of the two spectroscopic states.

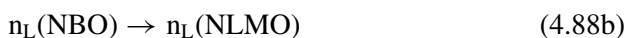
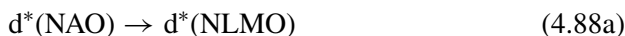
We conclude that the qualitative patterns of e_g-t_{2g} splitting can also be understood from the NBO donor–acceptor viewpoint in the limit of weak-field, high-spin coordination complexes. In such a case the NBOs of the central metal atom retain the essentially one-center character of an isolated ion, sd^{μ} hybridization is negligible, and the effect of the coordination environment is seen in the subtle energetic and occupancy shifts that accompany weak donor–acceptor interactions such as (4.86b). (However, it is noteworthy that the related five-coordinate $Mn(H_2O)_5^{5+}$ and $Cr(H_2O)_5^{3+}$ ions distort significantly from trigonal bipyramidal toward a monovacant octahedral geometry, which is indicative of a structural role of hybridization even in some weak-field, high-spin cases.)

As ligand–metal interaction increases, the energy gain from converting each one-electron donor–acceptor interaction into a corresponding two-electron interaction eventually mandates a configurational change in which metal electrons are paired up in the weak-acceptor t_{2g} orbitals, allowing full two-electron interactions between the strong-acceptor e_g set and the ligand lone pairs. Such a configurational change to low spin can be further promoted by metal sd hybridization, π -backbonding, and other characteristic features of the closed-shell limit of strong covalency. Thus, the NBO donor–acceptor description can smoothly span the entire range of coordinative interactions from weak perturbation of atomic ions to strong covalent reorganization, hybridization, and multiple bonding.

4.6.5 Spectrochemical series and the nephelauxetic effect

A strong focus of the original crystal-field theory (Section 4.5.1) was to rationalize the ligand-induced spectroscopic shifts in metal d-orbital energies. For an octahedral crystal-field-splitting pattern (4.68), the spectroscopic effects of various ligands are summarized in the spectrochemical series (4.69). As remarked in Section 4.5.1, this series has no obvious connection to ionic or dipolar properties of the ligands, and the observed spectroscopic effects may therefore be presumed to involve more covalent aspects of the interaction of metal d orbitals with ligand orbitals.

For simplicity, let us consider the case of mono-ligation to a low-spin metal cation having one empty d orbital. For this purpose we consider the Pt^{2+} cation in its low-spin (singlet) $(d_{xy})^2(d_{xz})^2(d_{yz})^2(d_{x^2-y^2})^2(d_{z^2})^0$ configuration. In the presence of the coordinating ligand, the vacant $d^*(d_{z^2})$ atomic orbital (NAO) of the metal cation mixes covalently with the filled n_L orbital of the ligand, leading to the corresponding semi-localized molecular orbitals (NLMOs)



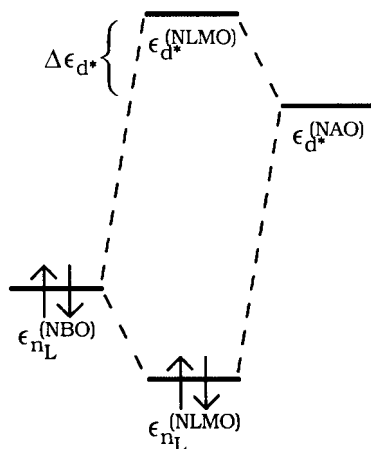


Figure 4.45 A metal–ligand $n_L \rightarrow d^*$ orbital splitting diagram depicting interaction of the metal-atom d^* NAO and ligand n_L NBO to form semi-localized NLMOs of the coordination complex, with splitting energy $\Delta\epsilon_{d^*} = \epsilon_{d^*}^{(NLMO)} - \epsilon_{d^*}^{(NAO)}$.

whose energies are respectively raised and lowered by the interaction, as depicted schematically in Fig. 4.45. The energy splitting $\Delta\epsilon_{d^*}$

$$\Delta\epsilon_{d^*} = \epsilon_{d^*}^{(NLMO)} - \epsilon_{d^*}^{(NAO)} \quad (4.89)$$

may therefore be taken as a measure of the ligand-induced shift of spectroscopic energy when the d^* (d_{z^2}) NAO becomes occupied in an excited configuration.

In effect, filling of the vacant d_{z^2} orbital sacrifices the stabilizing energy of the ground-state $n_L \rightarrow d_{z^2}$ donor–acceptor interaction, so that the ligand increases the spectroscopic transition energy (“raises the energy of the d_{z^2} orbital”) required to populate this orbital in the excited configuration. Thus, the energy shift $\Delta\epsilon_{d^*}$ in (4.89) should be crudely proportional to the “crystal-field-splitting parameter” that governs relative position in the spectrochemical series. Of course, full treatment of the spectroscopic d -orbital energy shifts involves other gains and losses of metal–ligand interaction in each configuration (namely the “pi-backbonding” interactions of a filled d orbital that become unavailable when the orbital is vacated). Nonetheless, the sigma-coordinative term (4.89) should be a leading correlator to the characteristic splitting parameter $10Dq$ for each ligand.

Figure 4.46 displays the $n_L \rightarrow d^*$ orbital contour diagrams and $\Delta\epsilon_{d^*}$ energy splittings for Pt(II)–ligand interactions involving three representative members of the spectrochemical series: F^- , NH_3 , and CO . As seen in Fig. 4.46, the d -orbital shift $\Delta\epsilon_{d^*}$ in the equilibrium geometry is far greater for the “strong-field” carbonyl ligand (0.242 a.u.) than for the “weak-field” fluoride ligand (0.138 a.u.), whereas the

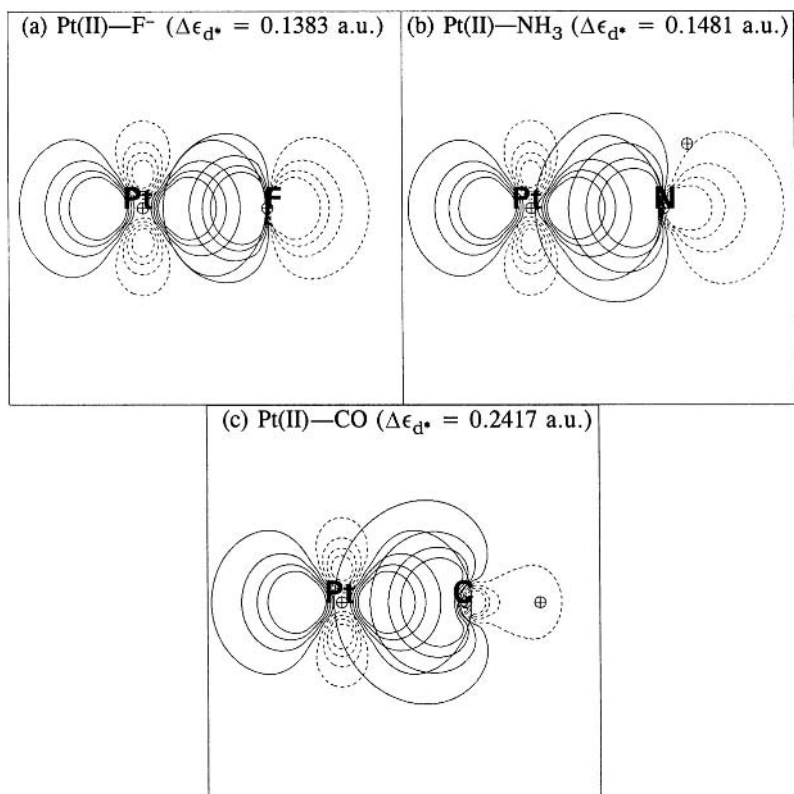


Figure 4.46 Pt(II)–ligand $n_L \rightarrow d_{Pt^*}$ interactions for representative ligands of the spectrochemical series: (a) L = F⁻, (b) L = NH₃, and (c) L = CO. The σ -coordinative d^* -orbital destabilization, $\Delta\epsilon_{d^*} = \epsilon_{d^*}(\text{NLMO}) - \epsilon_{d^*}(\text{NAO})$, is shown in parentheses.

ammine ligand (0.148 a.u.) is intermediate, in accordance with the empirical ordering (4.69).

As a result of metal–ligand coordinations such as depicted in Fig. 4.46, the *sizes* of metal d orbitals are also expected to be altered. The generalized changes in metal d-orbital radii upon coordinating to ligands are often referred to as *nephelauxetic* (literally, “cloud-expanding”) effects.³⁶ One obvious source of orbital expansion is the change of effective nuclear charge on the metal cation, resulting in more diffuse metal orbitals as the cationic character is reduced by ligand coordination. However, d-orbital radii will also be sensitive to detailed shapes and energies of coordinating ligand orbitals. Slight changes of this type are already visible in the d-orbital contours of Fig. 4.46, but further details of nephelauxetic effects in metal–ligand coordination are beyond the scope of this book.

4.6.6 Static Jahn–Teller distortions and lower-symmetry structures

In 1937 Jahn and Teller applied group-theoretical methods to derive a remarkable theorem: nonlinear molecules in orbitally degenerate states are intrinsically unstable with respect to distortions that lower the symmetry and remove the orbital degeneracy.³⁷ Although Jahn–Teller theory can predict neither the degree of distortion nor the final symmetry, it is widely applied in transition-metal chemistry to rationalize observed distortions from an “expected” high-symmetry structure.³⁸ In this section we briefly illustrate the application of Jahn–Teller theory and describe how a localized-bond viewpoint can provide a complementary alternative picture of transition-metal coordination geometries.

The gas-phase structure of MnF_3 in the quintet state³⁹ offers a beautiful illustration of how the Jahn–Teller theory can be used to rationalize molecular-structure distortions. The starting point is to assume a “zeroth-order” molecular structure of high symmetry, e.g., D_{3h} for MnF_3 , which leads to an orbitally degenerate MO pattern. The qualitative canonical MO picture for high-spin MnF_3 in D_{3h} geometry is shown on the left-hand side of Fig. 4.47, with each d-type MO conventionally labeled by its irreducible representation (e'' , a_1' , or e'). The depicted MO configuration $(e'')^2(a_1')^1(e')^1$ leads to doubly degenerate ${}^5E'$ state symmetry, which is subject to Jahn–Teller distortion. In this case, the molecular symmetry can be lowered from D_{3h} to C_{2v} by an in-plane bending mode of e' symmetry, converting the degenerate ${}^5E'$ into the non-degenerate 5A_1 state, as shown on the right-hand side of Fig. 4.47. Lowered energy accompanies this distortion primarily because the degenerate and asymmetrically filled e' orbitals of the D_{3h} point group are split into the low-energy b_2 and high-energy a_1 orbitals of C_{2v} . Thus, Jahn–Teller theory

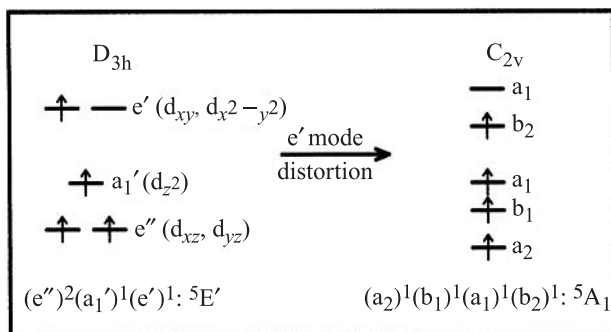


Figure 4.47 A qualitative Jahn–Teller MO diagram (metal d-orbital manifold), depicting lowering of orbital degeneracy (and total energy) through a vibrational distortion (of e' symmetry) from high-symmetry D_{3h} (left) to lower-symmetry C_{2v} (right) geometry of MnF_3 . The MO levels are labeled by conventional symmetry symbols for irreducible representations of the respective point groups.

no distortion from D_{3h} symmetry, which is strongly at odds with the actual structure. (Higher levels of Jahn–Teller theory [known as second-order or pseudo-Jahn–Teller theory] can be used to rationalize structures such as IrH_3 , but unambiguous structural predictions are even more difficult to obtain in this way.)

- (2) Finally, let us consider the singlet and triplet states of the d^2 complex WH_4 . In terms of Lewis-like structures, the triplet (3A_2) state consists of two singly occupied d orbitals for the nonbonded electrons together with four $2c/2e$ bonds of sd^3 -hybridized form (tetrahedral bond angles). However, the singlet states have two possible limiting configurations: (i) a singlet diradical (UHF-like) species, with unpaired electrons in two pure d orbitals, or (ii) a paired (RHF-like) species with one pure d lone pair and one unoccupied d orbital (see Appendix A). However, the two d orbitals involved are equivalent by symmetry, so the resulting states (1E and 1A_1) comprise mixtures of these configurations. Simple localized-bond constructs for this hypovalent molecule predict tetrahedral geometry in both singlet and triplet states, because both have sd^3 skeletal hybridization and the paired or unpaired electrons in pure d orbitals are stereochemically inert. For the triplet state, DFT calculations confirm the non-degenerate configuration and T_d structure. However, for the doubly degenerate 1E state the structure must distort from nominal tetrahedral symmetry in accordance with the Jahn–Teller theorem. Such distortion is indeed found, but its energetic and structural consequences are rather small, leading to average $|\theta_{\text{HWH}}|$ changes of $\sim 5.4^\circ$ and energy lowering by only $\sim 1\text{kcal mol}^{-1}$.

The example of WH_4 illustrates that the Jahn–Teller theorem specifies the necessary conditions for instability of a particular point-group symmetry (whose specific identity must be inferred by other means), but it cannot predict the magnitude of the structural distortions and energy lowering. The localized Lewis-like bonding model is also inadequate in this instance, because the predicted structure is of high symmetry and implies use of *two* symmetry-equivalent d orbitals to accommodate *one* singlet-coupled lone pair. Effectively, the energy is lowered by removing the equivalency of the two d orbitals, allowing the lone pair to become more “localized” in a single d orbital (e.g., to take advantage of specific hyperconjugative interactions in a broken-symmetry structure). One may expect similar distortions to occur whenever the zeroth-order Lewis-like picture requires unequal occupation of symmetry-equivalent lone-pair or singly occupied orbitals.

In summary, the Jahn–Teller theorem brilliantly spells out conditions whereby some distortion *must* occur, but it does not indicate the ultimate geometry or the magnitude of the distortion. Why then is the Jahn–Teller theorem invoked with such frequency? The answer seems to be that an initial “zeroth-order” geometry is often assumed to be of high symmetry, e.g., on the basis of VSEPR-type reasoning. However, the localized Lewis-like picture often provides a much better “zeroth-order” structure (as illustrated by the examples of MnF_3 and IrH_3) in which the electronic origins of the lowered symmetry are already apparent in the optimized pattern

of σ - and ω -bonding interactions. For cases in which the localized Lewis-like picture predicts a high-symmetry degenerate configuration (such as singlet WH_4), Jahn–Teller considerations refine the analysis to account for the effects of localized orbital equivalencies at high-symmetry centers. However, the energetic and structural consequences of such symmetry breaking are often rather insignificant, because the involved electrons are commonly nonbonding lone pairs.

4.6.7 Common coordination motifs of hyperbonded complexes and the “trans influence”

Transition-metal bonding interactions span a broad range. Strong electrostatic interactions and free-ion-like electron configurations characterize highly charged complexes with weak-field dative ligands (e.g., $\text{Mn}(\text{H}_2\text{O})_6^{2+}$), whereas strong covalent bonds involving directional sd^n hybrids typify transition-metal hydrides and alkyls (e.g., $\text{Ir}(\text{mesityl})_3$). The vast majority of transition-metal complexes lie between these two extremes, with ω -bonding playing a leading role. We begin by addressing the distribution of “common” electron counts and bonding motifs for organometallic compounds across the transition series, with specific reference to ω -bonding and its ubiquitous role in the empirical trend known as “trans influence.”

Statistical frequencies for the most “common” electron counts, empirical formulas, and bonding assignments (lone pairs, two-center bonds, ω bonds, formal hybridization) can be extracted⁴⁰ from the *Dictionary of Organometallic Compounds*, as summarized in Table 4.30. We express the empirical formula in Green’s “MLX” nomenclature,⁴¹ where L represents a closed-shell dative ligand (a two-electron donor such as PR_3) and X represents an open-shell “covalent” ligand (a one-electron radical donor such as CH_3 or Cl). The total number of ligands bound to an ML_lX_x compound is given by $l + x$. Assignment of a formal Lewis-like parent structure and the associated hyperbonding pattern permits one to describe any metal complex as a net collection of $1c/2e$ (lone pairs), $2c/2e$ (σ , π , or δ bonds, with formal sd^n hybridization) and $3c/4e$ (ω bond) bonding interactions at the metal center, as shown (with representative examples) in Table 4.30.

As the statistical data in Table 4.30 reveal, organotransition-metal complexes with 18e counts are common, but not to the exclusion of other electron counts; in fact, 18-electron species constitute a statistical majority in only four of the eight groups. Clearly, transition-metal complexes commonly involve hypervalent ω -bonding ($>12e$ count), and a particularly prevalent bonding motif is that for three ω bonds (formed from three parent sd^2 -hybridized σ bonds) and three lone pairs (cf. Section 4.6.1). It is unsurprising that complexes exhibiting this “ideal” bonding pattern (in which all low-lying acceptor orbitals are maximally engaged in donor–acceptor interactions) are (i) invariably octahedral, (ii) often imbued with

Table 4.30. Statistical frequency distributions of electron counts^a, common formulas^a, and localized bonding descriptions (in terms of number of metal-centered lone pairs, 2c/2e bonds, ω bonds, and average sd^n hybridization) for organometallic complexes of groups 3–10

Group	Electron-count frequency (%)			Formula	Examples	Localized bonding			
	14	16	18			l.p.	2c/2e	ω	sd^n
3	27	30	18	ML ₅ X ₃	Cp ₂ YMe(THF)	0	4	2	sd ⁵
				ML ₄ X ₃	Cp ₂ Y- <i>t</i> -Bu	0	5	1	sd ⁵
4	4	55	21	ML ₄ X ₄	Cp ₂ ZrCl ₂	0	4	2	sd ⁵
5	13	15	45	ML ₆ X	CpNb(CO) ₄	2	1	3	sd ³
				ML ₅ X ₃	Cp ₂ Nb(CO)Cl	1	2	3	sd ⁴
6	1	7	82	ML ₅ X ₂	CpMo(CO) ₃ Me	2	1	3	sd ³
				ML ₆	Mo(CO) ₆	3	0	3	sd ²
				ML ₄ X ₄	Cp ₂ MoMeBr	1	2	3	sd ⁴
7	2	2	90	ML ₅ X	Re(CO) ₅ Me	3	0	3	sd ²
				ML ₄ X ₃	CpRe(CO) ₂ Me ₂	2	1	3	sd ³
8	1	1	97	ML ₄ X ₂	Ru(PPh ₃)(CO) ₃ Cl ₂	3	0	3	sd ²
9	1	25	72	ML ₃ X	Rh(PPh ₃) ₂ (CO)Cl	4	0	2	sd ¹
				ML ₃ X ₃	Rh(PMe ₃) ₂ (CO)Cl ₃	3	0	3	sd ²
10	1	70	27	ML ₂ X ₂	Pd(PMe ₃) ₂ (Me)I	4	0	2	sd ¹

^a Data taken from a preliminary survey of compounds in the *Dictionary of Organometallic Compounds*, compiled by G. Parkin and C. Zachmanoglou.

unusual thermodynamic or kinetic stability (e.g., Co(NH₃)₆³⁺), and (iii) well suited to additional pi-backbonding interactions with π -acceptor ligands that can interact strongly with the metal lone pairs.

Let us now explain how the formal MLX and bonding assignments are obtained, using Cp₂Nb(CO)Cl as an example. A niobium atom has five valence electrons. A cyclopentadienyl (Cp) ligand has formal Lewis structure



which can be considered to make one *covalent* electron-pair bond (through the unpaired radical electron) and two *dative* electron-pair bonds (through the two

π bonds), and is hence classified as an “ L_2X ” ligand. The CO ligand is of dative type (L) and the Cl radical is of covalent type (X). (In effect, all assignments of L or X character are based on a *neutral* ligand starting point.) Overall, the formulation is ML_5X_3 , giving a total electron count of 18 electrons (five from Nb, plus three from three X ligands, plus ten from five L ligands). As discussed in Section 4.6.1, each pair of electrons in excess of the duodectet requires one ω bond (three ω bonds in this example). Subtracting the six ligands and 12e involved in ω -bonding from the totals of eight ligands and 18e leaves two ligands to make 2c/2e bonds and one remaining lone pair. The nominal hybridization at Nb will be sd^4 , because the lone pair will occupy one d orbital, thus excluding its participation in bonding. Other entries in Table 4.30 can be worked out in a similar manner, leading in each case to specific structural predictions based on the inferred sd^n hybridization.

Example 4.7

Problem: Rationalize the following geometries:

- (i) $Rh(PPh_3)_3^+$, T-shape;
- (ii) $RuH_2(PPh_3)_2$, seesaw-shape, with *trans* PPh_3 ligands; and
- (iii) $Rh(C_6F_5)_5^{2-}$, monovacant octahedral.

Solution:

- (i) The 14e complex $[Rh(PPh_3)_3]^+$ contains one ω bond, one 2c/2e bond, and four lone pairs, and has overall sd^1 hybridization. Idealized bond angles are 90° for sd^1 hybridization and 180° for ω -bonding, resulting in a T-shaped molecule that bears a strong geometrical and electronic resemblance to ClF_3 .
 - (ii) The 14e complex $RuH_2(PPh_3)_2$ has one ω bond, two 2c/2e bonds, three lone pairs, and overall sd^2 hybridization (90° angles). A seesaw structure enables the 2c/2e bonds to maintain 90° angles with all other ligands while accommodating the 180° preference for the ω -bonded PPh_3 ligands. Strong chemical kinship between SF_4 and $RuH_2(PPh_3)_2$ is revealed by this analysis.
 - (iii) $Rh(C_6F_5)_5^{2-}$ has a 16e count featuring two ω bonds, three lone pairs, and a single 2c/2e bond. A square-pyramidal structure with 90° and 180° bond angles (better described as a monovacant octahedron) neatly satisfies both sd^2 and ω -bonding requirements.
-

Example 4.8

Problem: Devise a bonding description for $(H_2C)RuCl_2(PPh_3)_2$ and predict the structure.

Solution: The electron count is 16e (eight from Ru, two from each phosphine, one from each Cl, and two from methylene, assumed to make a $Ru=C$ double bond). Two ω bonds result, leaving four electrons to make the σ_{RuC} and π_{RuC} bonds and two lone pairs. Skeletal sigma-bonding of the parent Lewis-like structure requires three sd^2 hybrids (90° angles),

whereas the lone pairs and π_{RuC} bond are made with pure d orbitals. The 90° hybrid angles combine with the *trans* preferences for ω bonds to produce a monovacant octahedral geometry with methylene at the unique apex and symmetric Cl-M-Cl and $\text{Ph}_3\text{P-M-PPH}_3$ ω bonds.

Let us now consider certain characteristic structural aspects of ω -bonding, focussing particularly on the “*trans* influence”⁴² that one ligand exerts on the length of a *trans*-disposed metal–ligand bond, a pervasive phenomenon in transition-metal structural chemistry. Localized-bonding considerations provide a particularly simple and attractive description of the electronic features underlying this important structural phenomenon. (Associated energetic aspects of successive ω -additions and possible limits on coordination number and electron count will be considered in Section 4.6.8.)

The *trans* influence can be recognized most directly in the geometry of square-planar complexes, in which any pair of ligands can be described as being in a *cis* ($\sim 90^\circ$) or *trans* ($\sim 180^\circ$) relationship about the metal center. For specificity, let us consider *cis* and *trans* isomers of square-planar platinum diphosphine complexes of the general form $\text{PtHX}(\text{PH}_3)_2$, where $\text{X} = \text{H, F, Cl, Br, or I}$, and where the *cis* or *trans* designation refers to the disposition of the two PH_3 ligands. Table 4.31 summarizes the bond lengths R_{PtH} , R_{PtX} , and R_{PtP} , in each case positioned *trans* to the ligand shown in parentheses. In this series, the *trans* influence of ligand X on R_{PtP} can be seen to follow the approximate ordering

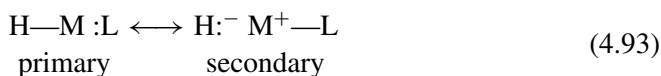
$$\text{H} > \text{I} > \text{Br} \sim \text{Cl} \sim \text{PH}_3 > \text{F} \quad (4.92)$$

Table 4.31. Computed Pt—H, Pt—X, and Pt—PH₃ bond lengths for *cis* and *trans* isomers of $\text{PtHX}(\text{PH}_3)_2$ ($\text{X} = \text{H, F, Cl, Br, I}$), showing marked variations depending on the *trans* ligand (in parentheses)

X	Isomer	R_{PtH} (Å)	R_{PtX} (Å)	R_{PtP} (Å)
H	<i>cis</i>	1.588(P)	1.588(P)	2.368(H)
	<i>trans</i>	1.656(H)	1.656(H)	2.274(P)
F	<i>cis</i>	1.576(P)	2.034(P)	2.436(H), 2.216(F)
	<i>trans</i>	1.565(F)	2.104(H)	2.293(P)
Cl	<i>cis</i>	1.570(P)	2.373(P)	2.442(H), 2.243(Cl)
	<i>trans</i>	1.570(Cl)	2.472(H)	2.297(P)
Br	<i>cis</i>	1.570(P)	2.554(P)	2.433(H), 2.246(Br)
	<i>trans</i>	1.570(Br)	2.649(H)	2.300(P)
I	<i>cis</i>	1.572(P)	2.703(P)	2.427(H), 2.254(I)
	<i>trans</i>	1.576(I)	2.799(H)	2.300(P)

with bond-length variations in the 0.1–0.2 Å range. The order of influence in (4.92) is clearly connected with the natural polarity of the M—X bond and thus with the expected degree of covalency: more covalent M—X bonds exert a larger *trans* influence than polar bonds. Irrespective of whether the bond considered is M—H, M—halide, or M—PH₃, it is always longest when *trans* to H and shortest when *trans* to F.

Because *trans* dispositions commonly result from ω -bonding (the near-linear alignment of the hyperbonding 3c/4e X—M···L triad), it is not surprising that the origin of the *trans* influence can be traced to the resonance nature of ω -bonding. When H is placed *trans* to a halide or PH₃, the dominant resonance structure will be that with a 2c/2e M—H bond and a donor pair of electrons on the halide or phosphine ligand, as depicted on the left in (4.93):



Thus, the M—H bond will be shorter (of higher bond order) while the M—X or M—P bond will be longer (of lower bond order) in the H···M···L resonance hybrid. When two H atoms are placed *trans* to one another, higher weighting of the second resonance structure bearing a pair of electrons localized on H cannot be avoided, and the M—H bonds lengthen. One can expect more generally that those ligands which tend to form apolar bonds with metals (e.g., H and alkyls) will lengthen the bond of any *trans*-disposed ligand.

This same reasoning accounts for the usual site preferences in complexes with mixtures of 2c/2e and ω bonds: ligands making apolar covalent bonds will tend to occupy the 2c/2e bonds. For example, the seesaw-shaped RuH₂(PPh₃)₂ and monovacant-octahedral Ru(CH₂)(PPh₃)₂Cl₂ complexes adopt structures with the H and CH₂ ligands in sites lacking a *trans* ligand.

4.6.8 Steric and electrostatic limits of hyperbonding

To illustrate the dependence of hypervalency on steric and electrostatic factors, let us consider ω -additions of neutral or ionic ligands to [PtF₄]²⁺, a duodectet-rule-conforming Pt(VI) species with Lewis-like formula



(We note that such a species is expected to be a highly reactive oxidant,⁴³ allowing these addition reactions to be safely carried out only in a computer!) As shown in Fig. 4.48, the equilibrium C_s structure of [PtF₄]²⁺ is slightly distorted from

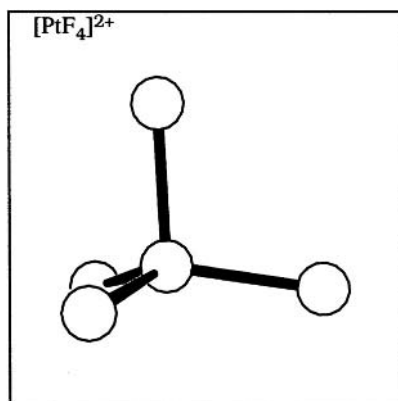
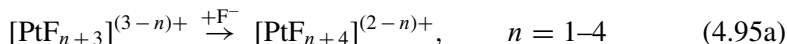


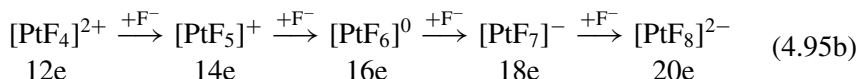
Figure 4.48 The optimized structure of $[\text{PtF}_4]^{2+}$.

idealized sd^3 tetrahedral geometry (by geminal hyperconjugation effects). Each of the four $\text{Pt(VI)}-\text{F}^-$ dative bonds may now be subjected to backside attack by a coordinative ligand L in order to form hypervalent $L-\text{Pt}-\text{F}$ ω bonds, up to the maximum supported by the Pt valence shell.

Starting from the parent $[\text{PtF}_4]^{2+}$ Pt(VI) species of Fig. 4.48, let us now consider the successive additions of fluoride ligands, $L = \text{F}^-$,



corresponding to the series



It is evident from the net charges in (4.95b) that steps $n = 1$ and 2 are strongly favored by Coulombic cation–anion attraction, step $n = 3$ (involving a neutral $[\text{PtF}_6]^0$ precursor) is little affected by ionic forces, and steps $n = 4$ and beyond are strongly opposed by anion–anion repulsion. Thus, the sequence of ω -additions is expected to terminate at $n = 3$ or 4, depending on whether attractive ω -bonding interactions can overcome the repulsive steric and ionic penalties of the $[\text{PtF}_8]^{2-}$ species for $n = 4$. Figure 4.49 shows the optimized structures corresponding to each addition product in (4.95a), and Table 4.32 summarizes some bond lengths, fluoride binding energies, and Pt atomic charges of each species.

From Fig. 4.49(d) and the last row of Table 4.32 one can see that the quadruply hyperbonded $[\text{PtF}_8]^{2-}$ dianion is indeed a (meta)stable local equilibrium species, formally of 20e “count” at the metal atom. Owing to highly unfavorable anion–anion repulsion, the binding of F^- to $[\text{PtF}_7]^-$ is endothermic, but this species is nevertheless a true local equilibrium structure ($R_{\text{PtF}} = 2.04 \text{ \AA}$, all positive frequencies) of O_h

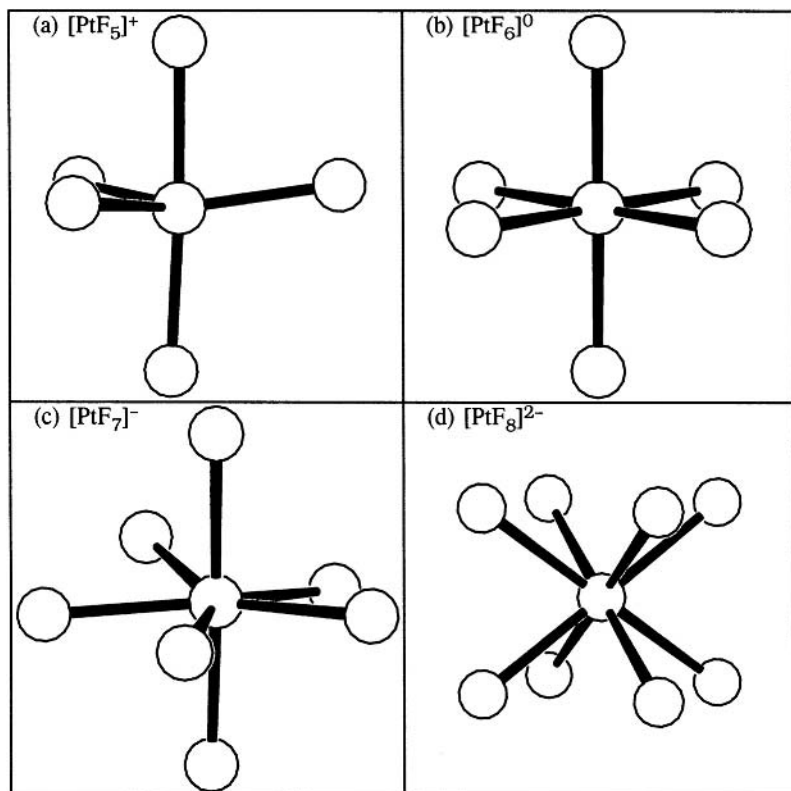


Figure 4.49 Hypervalent complexes resulting from successive additions of fluoride ions to PtF_4^{2+} ; see (4.95a) and (4.95b) in the text.

Table 4.32. Average bond lengths \bar{R}_{PtF} , incremental F^- binding energies $\Delta E(+\text{F}^-)$, and platinum atomic charge Q_{Pt} for $\text{PtF}_n^{(6-n)+}$ complexes (see Fig. 4.49)

Species	\bar{R}_{PtF} (Å)		$\Delta E(+\text{F}^-)$	Q_{Pt}
	σ	ω		
$[\text{PtF}_4]^{2+}$	1.846	—	—	+2.296
$[\text{PtF}_5]^+$	1.864	1.913	-396.4	+2.219
$[\text{PtF}_6]^0$	1.893	1.917	-268.7	+2.175
$[\text{PtF}_7]^-$	1.964	1.973	-97.4	+2.201
$[\text{PtF}_8]^{2-}$	—	2.040	+54.7	+2.137

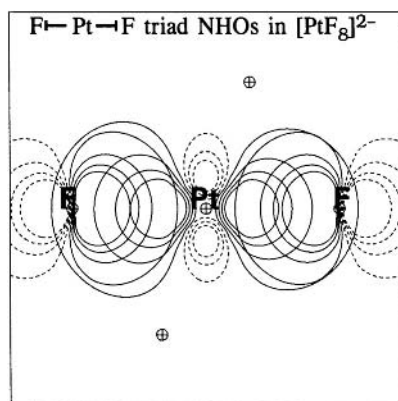


Figure 4.50 Interacting $n_{\text{F}}-h_{\text{Pt}}-n_{\text{F}}$ NHOs of a $\text{F}-\text{Pt}-\text{F}$ hyperbonded triad in $[\text{PtF}_8]^{2-}$.

cubic symmetry. As seen in Fig. 4.49(d), the four $\text{F}-\text{W}-\text{F}$ triads are aligned along the four body diagonals of a cube at tetrahedral (rather than orthogonal 90°) angles. The metal hybrid acceptor NHOs are in each case of $sd^{3.04}$ form, and their overlaps with the two donor n_{F} orbitals are depicted in Fig. 4.50. Evidently the strong $3c/4e$ donor-acceptor interactions depicted in Fig. 4.50 are able to withstand the severe repulsions due to electrostatic space-charge and steric congestion to achieve the final step of (4.95), a metastable molecular dianion of 20e count. The platinum partial charges are similar ($Q_{\text{Pt}} \simeq +2.2$) throughout the hyperbonded series, which is indicative of the shared connection to the $[\text{PtF}_4]^{2+}$ normal-valent parent species.

From the examples shown in Fig. 4.43, we may conclude that the 18e *triply* hyperbonded complexes are often the stable end-products of successive ligand ω -additions to normal-valent parent species, which is consistent with the well-known “18-electron rule.” However, incompletely hyperbonded complexes of 12e, 14e, or 16e count are certainly stable as isolated equilibrium species, and in favorable cases the sequence of ω -additions may also achieve equilibrium configurations *exceeding* the 18e count, as the example of $[\text{PtF}_8]^{2-}$ has demonstrated.⁴⁴

4.6.9 Non-d coordination and hypervalency: hexaamminezinc(II)

Although ligands commonly coordinate to vacant metal d orbitals (i.e., $n_{\text{L}} \rightarrow d_{\text{M}}^*$ interactions), such coordination is also possible with the unfilled metal s orbital (i.e., $n_{\text{L}} \rightarrow s_{\text{M}}^*$ interactions) for metal ions with completely filled d shells. An example is $\text{Zn}^{2+} (d^{10}s^0)$, where the vacant 4s orbital serves as the acceptor orbital for donor-acceptor interactions of $n_{\text{L}} \rightarrow s_{\text{Zn}}^*$ type.

One can expect that $n_{\text{L}} \rightarrow s_{\text{M}}^*$ interactions are typically weaker than corresponding $n_{\text{L}} \rightarrow d_{\text{M}}^*$ interactions, because the isotropic metal s orbital is not “focussed” toward any particular donor ligand n_{L} , whereas a d orbital or sd^{μ} hybrid has strong

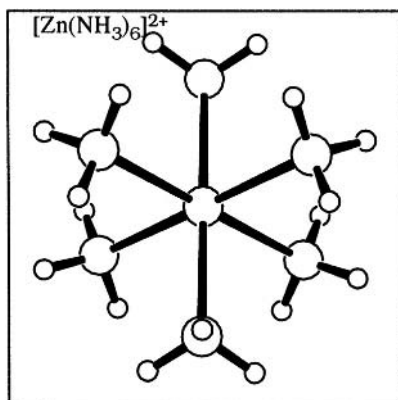


Figure 4.51 The optimized structure of $[\text{Zn}(\text{NH}_3)_6]^{2+}$. (Bond sticks between Zn and N atoms have been added to aid visualization.)

directionality along a particular coordination axis. A second factor is that all available n_L donor orbitals must coordinate to the *single* s_M^* acceptor orbital, with the inevitable anticooperative weakening of competitive $n_L \rightarrow s_M^*$ interactions.

Note that there is no intrinsic restriction on the number of donor n_L orbitals that can interact with a single s_M^* acceptor orbital, as long as the total s_M^* occupancy remains less than the maximum two electrons permitted by the Pauli principle. Thus, the final number of ligands able to participate in $n_L \rightarrow s_M^*$ coordination is essentially limited only by steric congestion, and may commonly extend to the closest-packing limit of *six* when the steric radius of the coordinating ligand atom is not much greater than that of the metal ion. In such a case the metal-atom s orbital occupies the octahedral hole formed by the surrounding six ligands.

As a simple example of non-d coordination, let us consider the hexaamminezinc(II) cation $[\text{Zn}(\text{NH}_3)_6]^{2+}$, whose optimized structure is shown in Fig. 4.51. Each ammine ligand serves as a formal two-electron sigma donor, and the total electron count at Zn therefore corresponds to a 22e system, again violating the “18-electron rule.” Each ammine ligand is bound to the Zn^{2+} cation by about $60.7 \text{ kcal mol}^{-1}$, which is in part attributable to classical electrostatic interactions of ion–dipole type.

However, significant stabilization is also contributed by $n_N \rightarrow s_{\text{Zn}}^*$ donor–acceptor interactions, each with estimated second-order interaction energy $49.4 \text{ kcal mol}^{-1}$, as depicted in Fig. 4.52. Each ammine ligand thereby donates about $0.061e$ to the zinc cation, primarily to the “vacant” 4s orbital which acquires about $0.371e$ total occupancy. As before, the high formal hypervalency at the metal center is achieved *within* the limits of the duodectet rule, i.e., without significant involvement of extravalent metal p orbitals.

As in the examples of Section 4.6.2, one may expect that Zn(II) complexes of lower coordination number also form stable equilibrium species, if considered in

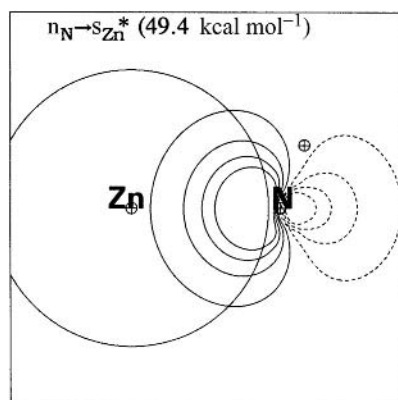


Figure 4.52 The leading donor–acceptor ($n_{\text{N}} \rightarrow s_{\text{Zn}}^*$) interaction between the donor ammine lone pair and the acceptor 4s metal orbital in 22e $[\text{Zn}(\text{NH}_3)_6]^{2+}$ (cf. Fig. 4.51). (Note that the inner nodal structure of the Zn 4s orbital is absent in the “effective-core-potential” representation of the metal atom.)

isolation from excess ligands. Owing to the isotropic s_{Zn}^* orbital that “anchors” the coordinated ligands, the geometry of these species can be expected to conform to the VSEPR-like shapes that minimize ligand steric repulsions. Thus, one can predict that 20e $[\text{Zn}(\text{NH}_3)_5]^{2-}$ (trigonal bipyramidal) is also an apparent exception to the 18-electron rule. However, such incompletely coordinated species will not be considered further in this work.

4.7 Hypovalency, agostic interactions, and related aspects of catalytic activation at metal centers

Like boron and other group 13 semi-metals, transition metals of groups 3–5 are formally “hypovalent” (Section 4.2.4). Such early transition elements are therefore expected to demonstrate parallels to boron chemistry, such as a propensity to form Lewis acid–base adducts with electron-pair donors or to form three-center bridge bonds with other hypovalent species. In the present section we consider representative hypovalent transition-metal species and their interactions with prototype sigma and pi donors to yield Lewis acid–base adducts or other products. Specifically, we examine donor ligands in which electron density is shared between two atomic centers (two-center ligand donors, such as C–H sigma bonds and C=C pi bonds) interacting with a formally vacant one-center orbital at the metal (a $1c^*$ metal acceptor).

It should be noted that the hypovalent Lewis acid–base interactions of the present section are in principle closely related to the general metal–ligand coordination interactions discussed in Section 4.5. However, in normal-valent transition-metal

complexes, the metal ground-state electron configuration typically involves partial or full occupancy of *all* valence orbitals, and formation of a coordination complex therefore requires effective “promotion” from high-spin to low-spin configuration that frees (vacates) a $1c^*$ metal orbital for dative coordination, raising the energetic cost of complexation. Such normal-valent coordination typically requires stronger ligand donors of one-center type, such as the usual lone-pair ligands of the spectrochemical series (4.71). In contrast, “early” (hypovalent) transition-metal species offer the requisite $1c^*$ vacant orbital in their *ground* configuration, and weaker two-center donor ligands are therefore able to coordinate effectively with these metals. In the present section we shall therefore focus primarily on the $2c \rightarrow 1c^*$ donor–acceptor interactions that are a distinctive feature of the coordination chemistry of early transition-metal species.

A characteristic feature of $2c \rightarrow 1c^*$ transition-metal adducts (whether of intramolecular or intermolecular type) is the approximate T-shaped geometry between the two-center donor bond and $1c^*$ metal acceptor orbital. Such arrangements are often identified as “agostic” interactions between the metal center and bond, tending toward bond scission, metal insertion, or metallacycle formation as the interaction strength increases. Thus, the examples below span a range of phenomena pertaining to interactions of hypovalent metal atoms with closed-shell molecular species, touching on many interesting aspects of metal catalysis and reactivity.

4.7.1 Isolated transition-metal Lewis acids

Owing to the inherent reactivity of species containing one or more formally vacant valence orbitals, few such transition-metal species are known as isolable compounds.

One well-known example is the mineral rutile, TiO_2 . We consider the TiO_2 molecular species, which may be approximately formulated as $\text{O}=\text{Ti}=\text{O}$, with sigma and pi bonds of d-rich metal character, as expected for such electronegative ligands. The metal valence shell also includes “vacant” d-type ($n^{(d)*}$) and s-type ($n^{(s)*}$) metal orbitals, as depicted in Fig. 4.54. However, these “vacant” orbitals have significant occupancy ($0.44e$ in $n^{(d)*}$, $0.30e$ in $n^{(s)*}$) associated with partial triple bonding to oxygen (dative interactions with in-plane oxygen lone pairs), and the Lewis-acid character at the metal center is thus strongly attenuated.

Another putative example is TiCl_4 , a distillable Lewis acid. At first glance, one expects an electronic structure comprising four $\text{Ti}-\text{Cl}$ σ bonds (with $\sim sd^3$ hybridization) and two empty Ti valence orbitals. However, closer examination reveals virtually complete filling of the “empty” valence orbitals as a result of strong donation from Cl lone pairs, imparting significant multiple-bond character to the $\text{Ti}-\text{Cl}$ interaction. This example again illustrates how formal vacancies on a central

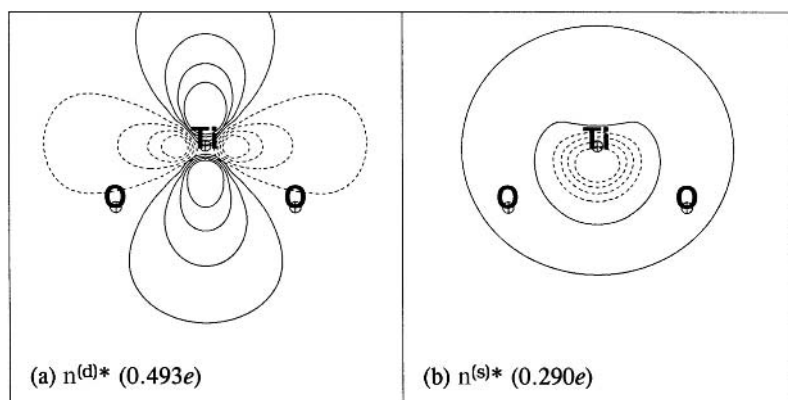


Figure 4.53 “Vacant” d-like ($n(d)^*$) and s-like ($n(s)^*$) Ti nonbonding orbitals of TiO_2 (with actual occupancies in parentheses).

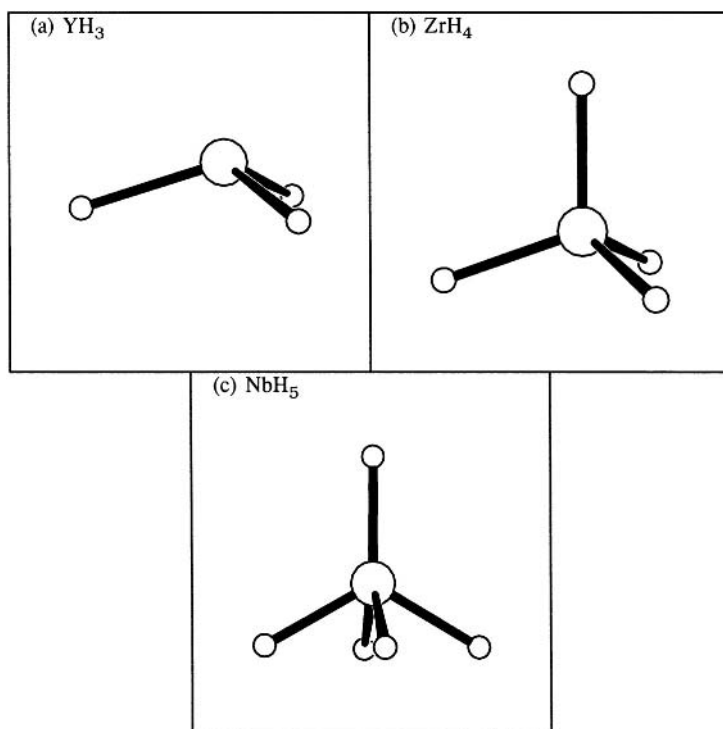


Figure 4.54 Optimized structures of hypovalent metal hydrides: (a) YH_3 , (b) ZrH_4 , and (c) NbH_5 .

Table 4.33. Metal charge (Q_M) and metal bonding (σ_{MH}) and nonbonding (n_M^*) NBOs and occupancies of hypovalent transition-metal hydrides (see Fig. 4.54)

Species	Q_M	Bonding			Nonbonding		
		No.	σ_{MH}	Occupancy	No.	n_M^*	Occupancy
YH ₃	+ 1.723	3	0.46(sd ^{2.41}) _Y + 0.89(s) _H	1.994	1	~pd ^{2.32}	0.002
					1	~pd ^{2.31}	0.000
					1	~pd ^{6.48}	0.000
ZrH ₄	+ 1.572	4	0.61(sd ^{2.99}) _{Zr} + 0.79(s) _H	2.000	2	~pd ^{0.25}	0.000
NbH ₅	+ 1.009	4	0.60(sd ^{4.08}) _{Nb} + 0.80(s) _H	1.998	1	~pd ^{1.69}	0.000
		1	0.64(sd ^{3.89}) _{Nb} + 0.77(s) _H	1.970			

metal atom may be partially filled by lone pairs on adjacent bonded atoms, reducing metal acidity.

As idealized computational models of metal hypovalency, let us therefore consider the early second-series transition-metal hydrides YH₃, ZrH₄, and NbH₅ (avoiding both the complications of lone-pair-bearing ligands and those associated with the lanthanide series). Figure 4.54 shows optimized structures of these species, and Table 4.33 summarizes the bonding (σ_{MH}) and nonbonding (n_M^*) orbitals and occupancies at the metal center.

As indicated in Table 4.33, the optimal Lewis-like description is in good agreement with the expected idealized sd^n hybridization of the sigma framework (sd² for YH₃, sd³ for ZrH₄, sd⁴ for NbH₅). Each structure also has the expected number of vacant n_M^* valence orbitals (three for YH₃, two for ZrH₄, one for NbH₅), with occupancies so small ($\leq 0.002e$) as to be negligible. Thus, these species conform well to the idealized hypovalent Lewis-like description.

On the other hand, replacement of H by other monovalent substituents often leads to a distinct change of electronic character (as is also shown by the example of TiCl₄ noted above). This can be illustrated by the species YF₃ and Y(OH)₃, whose bonding and nonbonding orbitals are summarized in Table 4.34 for direct comparison with YH₃ in Table 4.33. Although some superficial similarities exist, both YF₃ and Y(OH)₃ really fall closer to the pure ionic limit (e.g., Y³⁺(F⁻)₃ and Y³⁺(OH⁻)₃) and the distinction between “bonding” and “nonbonding” metal orbitals becomes problematic. This transition in electronic character is seen most dramatically in Y(OH)₃, which exhibits a planar D_{3h} (!) structure with Y—O single-“bond” NBOs that are of π (not σ !) type, essentially oxygen p π -type lone pairs with slight (<5%) delocalization tails extending into available Y³⁺ orbitals. While the “transition” from covalent to ionic limits is of course mathematically continuous, strong changes in chemical behavior are expected to distinguish hydrides or alkyls

Table 4.34. Metal charge (Q_Y) and metal bonding (σ_{YX}) and nonbonding (n_{Y^*}) NBOs and occupancies of trisubstituted yttrium YX_3 compounds ($X = F, OH$)

Species	Q_Y	Bonding			Nonbonding		
		No.	" σ_{YX} "	Occupancy	No.	n_{Y^*}	Occupancy
YF ₃	+2.296	3	0.24(sd ^{8.01}) _Y	2.000	2	~d	0.103
			+0.97(sp ^{4.21}) _F		1	~pd ^{7.25}	
Y(OH) ₃	+2.273	3	0.19(pd ^{2.00}) _Y	1.988	2	~d	0.268
			+0.98(p _{π}) _O		1	~sd ^{2.75}	

from other substituents. This distinction should be kept in mind in the remainder of this section, which is restricted to hydridic and alkyl species that might not be representative of other "isovalent" substituents.

4.7.2 Agostic interactions and bridge bonding

The characteristic tendency of hypovalent transition metals to interact in a side-on (T-shaped) manner with nearby alkyl C—H bonds has been designated as the "agostic" effect.⁴⁵ Agostic $M \cdots C-H$ interactions can also be identified with general $3c/2e$ donor–acceptor interactions of $2c \rightarrow 1c^*$ type. Availability of suitable $1c^*$ acceptor orbitals is a signature of hypovalent early transition metals.

As an illustration of the agostic effect, let us consider the simple example of $YH_2(C_2H_5)$, the ethyl derivative of the parent YH_3 species (Fig. 4.54(a)). The optimized structure of $YH_2(C_2H_5)$ is shown in Fig. 4.55, exhibiting the distortive

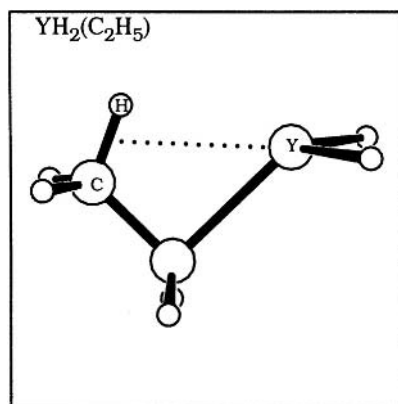


Figure 4.55 The optimized structure of $YH_2(C_2H_5)$, showing the T-shaped geometry of the agostic $Y \cdots C-H$ interaction.

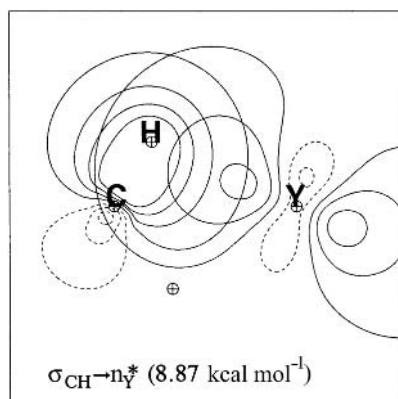


Figure 4.56 The agostic $\sigma_{\text{CH}} \rightarrow n_{\text{Y}}^*$ interaction in $\text{YH}_2(\text{C}_2\text{H}_5)$; cf. Fig. 4.55.

influence of the metal atom on the alkyl radical. This is particularly evident in the abnormally small C—C—Y angle (89.7°), the unusual *eclipsed* conformation of the ethyl moiety, and the conspicuously elongated ($R_{\text{CH}} = 1.093 \text{ \AA}$) and canted ($\theta_{\text{CCH}} = 112.1^\circ$) in-plane C—H bond of the terminal methyl group. As originally characterized,⁴⁶ the agostic $\text{M} \cdots \text{C}—\text{H}$ interaction corresponds to simultaneous partial covalency of the terminal H atom to both M and C atoms, which is evidently related to the three-center H-bridging interactions of carboranes.

The leading $\sigma_{\text{CH}} \rightarrow n_{\text{Y}}^*$ NBO interaction associated with agostic distortions is shown in Fig. 4.56. As indicated, second-order perturbation theory suggests that this interaction stabilizes the structure by $\sim 9 \text{ kcal mol}^{-1}$, easily surmounting the normal $\sim 3 \text{ kcal mol}^{-1}$ barrier to eclipsing. The NBO analysis also shows that the occupancy of the in-plane $\sigma_{\text{CH}(\text{in})}$ bond is noticeably depleted (to $1.948e$, versus $1.989e$ for out-of-plane $\sigma_{\text{CH}(\text{out})}$ bonds), representing a slight formal reduction of bond order. The metal d-type n_{Y}^* orbital correspondingly acquires weak occupancy ($0.044e$), which can be primarily attributed to the single $\sigma_{\text{CH}(\text{in})} \rightarrow n_{\text{Y}}^*$ interaction. Except for the replacement of p-type by d-type metal acceptor orbitals, the agostic $\text{M} \cdots \text{C}—\text{H}$ interactions of transition metals appear quite analogous to those of boron and other main-group hypovalent elements (Section 3.6).

Strong similarities to boron chemistry are also evident in the dimerization reactions



As shown in Fig. 4.57, the hypovalent hydrides YH_3 , ZrH_4 , and NbH_5 (Fig. 4.54) lead to H-bridged species that can be respectively identified as “diyttrane” (Y_2H_6 , Fig. 4.57(a)), “dizirconane” (Zr_2H_8 , Fig. 4.57(b)), and “diniobane” (Nb_2H_{10} , Fig. 4.57(c)) to indicate their obvious structural relationship to diborane (B_2H_6 ,

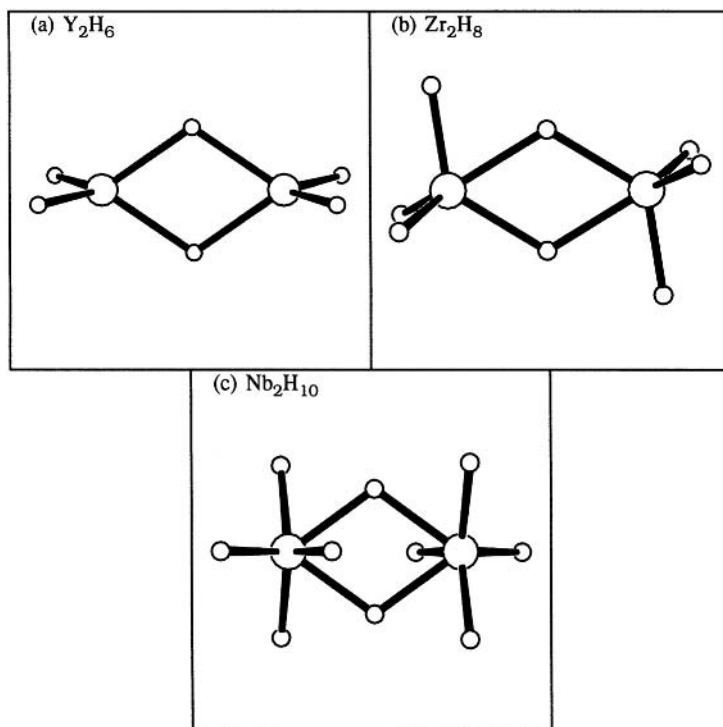


Figure 4.57 Optimized structures of transition-metal diborane analogs: (a) diyttrane, Y_2H_6 ; (b) dizirconane, Zr_2H_8 ; and (c) diniobane, Nb_2H_{10} .

Fig. 3.92). Some geometrical properties of these species are summarized in Table 4.35.

The three-center τ_{MHM} bridge bonds and antibonds of these species display the expected similarities to the diborane NBOs (Fig. 3.93), as illustrated for Y_2H_6 in Fig. 4.58. The two three-center antibond orbitals can again be identified as being of “ Δ -type” ($\tau_{YHY}^{(\Delta)*}$, Fig. 4.58(c)) or “ π -type” ($\tau_{YHY}^{(\pi)*}$, Fig. 4.58(d)) according

Table 4.35. Geometrical bond lengths R and angles of M_2H_{2n} species (see Fig. 4.57)

Species	\bar{R}_{MH} (Å)	$R_{M\dots M}$ (Å)	$R_{M\dots H}$ (Å)	$\theta_{H\dots M\dots H}$ (degrees)	$\theta_{M\dots H\dots M}$ (degrees)
Y_2H_6	1.98	3.53	2.16	70.3	109.7
Zr_2H_8	1.85 ^a	3.39	2.00	63.5	116.5
Nb_2H_{10}	1.75 ^a	3.00	1.85	71.5	108.5

^a Average of inequivalent M—H bonds.

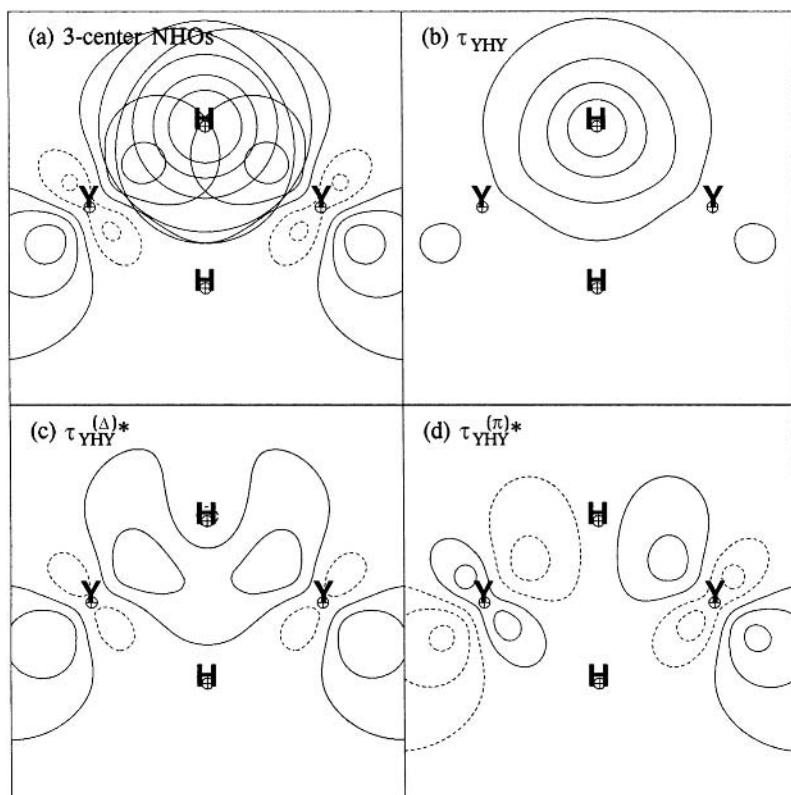


Figure 4.58 The three-center bridge bond of Y_2H_6 , showing (a) overlapping NHOs, (b) the three-center bond τ_{YHY} , and the associated antibonds (c) $\tau_{\text{YHY}}^{(\Delta)*}$ and (d) $\tau_{\text{YHY}}^{(\pi)*}$.

to their symmetric or antisymmetric character with respect to a perpendicular reflection plane through the two bridging atoms. Following the discussion of Section 3.6, these antibonds can be expected to play distinctive roles in aggregation phenomena leading to the formation of larger clusters and extended phases, should one succeed in synthesizing such polyhydrides.

Some comparisons of the NBO descriptors for two-center σ_{MH} and three-center τ_{MHM} bonds of group 1–3 dimetallanes are summarized in Tables 4.36 and 4.37. The accuracy of the τ -bonded natural Lewis-structure description is quite satisfactory in all cases (99.3%–99.8% ρ_{L}). In accord with the electronegativity trend along the series, the metal charge decreases and the polarity of two- and three-center bonds decreases on going from Y to Nb. The three-center τ_{YHY} NBO has particularly high ionic (hydridic) character (as is also apparent in Fig. 4.58(b)), but τ -bond covalency more nearly resembles that of diborane as the series progresses. The occupancies of three-center $\tau_{\text{YHY}}^{(\Delta)*}$ and $\tau_{\text{YHY}}^{(\pi)*}$ antibonds are also seen to increase along the series, in accord with the increasing number of possible $\sigma_{\text{MH}} \rightarrow \tau_{\text{MHM}}^*$

Table 4.36. *The NBO descriptors of M_2H_{2n} species (see Fig. 4.57); namely the accuracy of the natural Lewis structure ($\% \rho_L$), metal charge (Q_M), metal hybrid (h_M), percentage polarization toward metal ($\%_M$), and occupancies (Occ.) of two-center bonds and antibonds*

Species	$\% \rho_L$	Q_M	Two-center σ_{MH}				No.
			h_M	$\%_M$	Occ. (σ)	Occ. (σ^*)	
Y_2H_6	99.87	+1.710	$sd^{2.88}$	22.2	1.984	0.018	
Zr_2H_8	99.77	+1.432	$sd^{2.97}$	31.8	1.994	0.015	2
			$sd^{3.56}$	33.6	1.979	0.029	1
Nb_2H_{10}	99.30	+0.608	$sd^{5.02}$	43.3	1.976	0.041	2
			$sd^{2.94}$	43.2	1.963	0.092	1
			$sd^{6.74}$	45.4	1.902	0.070	1

delocalizations. Further aspects of H-bridged bimetallic and polymetallic structures are beyond the scope of this work.

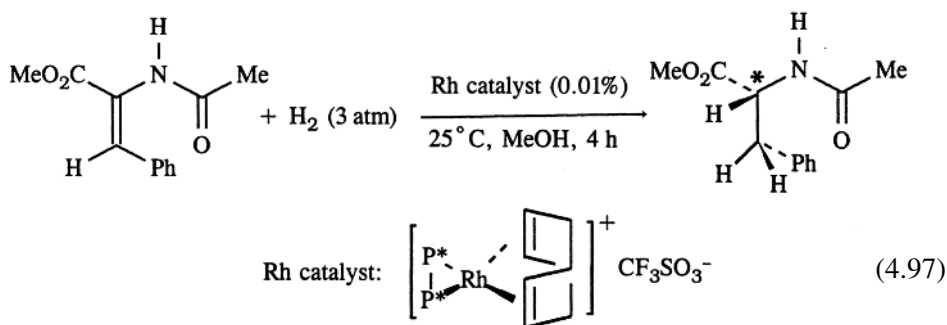
4.7.3 General aspects of catalytic bond activation at transition-metal centers: molecular hydrogen

Underlying the widespread application of transition metals as catalysts for organic transformations is the remarkable ability of transition metals to “activate” normally unreactive bonds, such as carbon–carbon π bonds and the $H_2\sigma$ bond. For example, mixtures of H_2 and simple alkenes can normally coexist without reaction for decades, despite there being a strong thermodynamic driving force toward hydrogenation reactions, but addition of a small amount of an appropriate transition-metal complex catalyzes the reaction to proceed rapidly to its thermodynamic conclusion. In recent decades a wide variety of transition-metal-catalyzed organic transformations⁴⁷ (such as hydroformylation, alkene metathesis, alkene polymerization, alcohol carbonylation, amination, epoxidation, dihydroxylation, allylation, and borylation) have streamlined synthetic procedures for a host of important

Table 4.37. *Similar to Table 4.36, for three-center bonds and antibonds*

Species	Three-center τ_{MHM}				
	h_M	$\%_M$	Occ. (τ)	Occ. ($\tau^{(\Delta)*}$)	Occ. ($\tau^{(\pi)*}$)
Y_2H_6	$sd^{3.96}$	9.3	1.983	0.012	0.009
Zr_2H_8	$sd^{5.66}$	14.6	1.971	0.020	0.011
Nb_2H_{10}	$sd^{6.07}$	21.9	1.913	0.056	0.009

pharmaceutical and commodity chemicals. A spectacular example of transition-metal catalysis is the asymmetric hydrogenation reaction⁴⁸



In this reaction, a rhodium atom complexed to a chiral diphosphine ligand (*P—P*) catalyzes the hydrogenation of a prochiral enamide, with essentially complete enantioselectivity and limiting kinetic rates exceeding hundreds of catalyst “turnovers” per second. While precious metals such as Ru, Rh, and Ir are notably effective for catalysis of hydrogenation reactions, many other transition-metal and lanthanide complexes exhibit similar potency.

Why are transition metals so well suited for catalysis? A complete treatment of this critical question lies well beyond the scope of this book, but we can focus on selected aspects of bond activation and reactivity for dihydrogen and alkene bonds as important special cases. Before discussing specific examples that involve formal metal acidity or hypovalency, it is convenient to sketch a more general localized donor–acceptor overview of catalytic interactions in transition-metal complexes involving dihydrogen⁴⁹ (this section) and alkenes (Section 4.7.4).

General donor–acceptor motifs in metal–dihydrogen interactions

The donor–acceptor viewpoint provides the language and constructs needed for explaining various limiting forms of metal–substrate interactions. Metals have both acceptor capacity – most commonly empty valence nonbonding orbitals (n_M^*) or metal–ligand antibonds (σ_{ML}^*) – and donor capacity – most commonly metal lone pairs (n_M) or metal–ligand bonds (σ_{ML}). The substrate H_2 may donate electrons from the H—H σ bond or accept electrons via the σ^* antibond (ethylene presents similar donor–acceptor possibilities through the π and π^* orbitals). Restricting discussion to non-radical processes, we can identify six distinct M/ H_2 reaction types (A)–(F) and the corresponding donor–acceptor motifs, as summarized in Table 4.38 and described below.

(A) *Dative H_2 coordination.* Metals with empty orbitals can accept charge from the donor σ_{HH} bond of H_2 to yield a simple complex of molecular hydrogen. Alternatively, this

Table 4.38. *Non-radical reaction types for interactions of transition metals (M) with H₂, showing principal donor–acceptor combinations in each case (the symbol □ denotes a vacant valence orbital [formal hypovalency] on the metal atom)*

Schematic reaction	Reaction type	Donor(s)	Acceptor(s)
(A) $M-\square + H_2 \rightarrow M \begin{array}{c} \text{H} \\ \\ \text{H} \end{array}$	Dative H ₂ coordination	σ_{HH}	n_M^* (or σ_{ML}^*)
(B) $M^+-\square + H_2 \rightarrow M-H + H^+$	Electrophilic H ₂ cleavage	σ_{HH}	n_M^* (or σ_{ML}^*)
(C) $\ddot{M}-\square + H_2 \rightarrow \ddot{M} \begin{array}{c} \text{H} \\ \\ \text{H} \end{array}$	Synergistic H ₂ coordination	σ_{HH}/n_M	n_M^* (or σ_{ML}^*)/ σ_{HH}^*
(D) $\ddot{M}-\square + H_2 \rightarrow M \begin{array}{c} \text{H} \\ / \\ \text{H} \end{array}$	“Oxidative addition” (insertion)	σ_{HH}/n_M	n_M^* (or σ_{ML}^*)/ σ_{HH}^*
(E) $R-M-\square + H_2 \rightarrow M-H + R-H$	Sigma-bond metathesis	σ_{HH}/σ_{MR}	n_M^* (or σ_{ML}^*)/ σ_{HH}^*
(F) $M^-: + H_2 \rightarrow M-H + H^-$	Nucleophilic H ₂ cleavage	n_M	σ_{HH}^*

interaction can be termed an agostic (3c/2e) bond between H₂ and a metal. Dihydrogen is a rather poor donor ligand, so this type of coordination is expected to be relatively weak.

- (B) *Electrophilic H₂ cleavage*. If the metal complex has significant positive charge and the M—H bond enthalpy is high, H₂ dative coordination may evolve into a heterolytic cleavage of H₂, yielding H⁺ and a new M—H bond. Additional driving force for this type of dihydrogen activation can be supplied by a base, provided that it cannot outcompete H₂ for binding to the metal.
- (C) *Synergistic H₂ coordination*. When the metal has both donor *and* acceptor orbitals, interaction with the σ_{HH} and σ_{HH}^* orbitals of H₂ can act synergistically (cooperatively) in the Dewar–Chatt–Duncanson mode. Such self-reinforcing charge flow enables a significantly stronger interaction than does simple dative coordination of H₂.
- (D) *“Oxidative addition” (insertion)*. In the limit of strong synergism, the H—H bond can be broken and two new M—H bonds formed. Although termed “oxidative addition,” this reaction does *not* necessarily deplete the metal of electron density (i.e., oxidize the metal). Rather, this reaction is fundamentally an insertion of the metal into the H—H bond. In the process, a lone pair of electrons at the metal and the electron pair of the H—H bond are “uncoupled” and then “recoupled” to form two M—H bonds. Whether synergistic H₂ coordination or insertion prevails depends largely on the relative

strengths of the M—H and H—H bonds. In principle, resonance between the two limits could lead to a variety of structures intermediate between the two extremes, but the H—H bond enthalpy varies so rapidly with distance that most observed structures lie clearly at the “molecular-hydrogen complex” or “metal-dihydride” limit. The reverse reaction, termed “reductive elimination,” can also occur without significant gain or loss of electron density at the metal center.

- (E) *Sigma-bond metathesis.* Dihydrogen is observed to react with transition-metal-alkyl bonds even when the metal lacks lone pairs. In this case the reaction *cannot* be explained in terms of the “oxidative-addition” or “reductive-elimination” motif. Instead, we can view this reaction as a special type of insertion reaction whereby the σ_{MR} bond pair takes the “donor” role of the metal lone pair and donates into the σ_{HH}^* antibond. When the M—R bonds are highly polarized as M^+R^- , the process could also be described as a concerted electrophilic H_2 activation in which R^- acts as the “base” accepting H^+ .
- (F) *Nucleophilic H_2 activation.* Although conceptually possible, this type of reactivity is limited by the relatively low nucleophilicity of metal lone pairs and the high energy of the H^- anion.

With the general framework of Table 4.37 in mind, let us now examine specific examples of the major coordination and reaction motifs resulting from metal- H_2 interaction, with a specific focus on hypovalent metals.

Dative and synergistic complexation of dihydrogen

Direct observation of complexation of molecular H_2 at metal centers is a relatively recent phenomenon. Virtually all such complexes exhibit relatively minor elongation of the H—H bond, indicating that description of these species as “molecular- H_2 complexes” (rather than, e.g., metal dihydrides or some intermediary resonance mixture) is well justified. Experimentally observed molecular H_2 complexes of the “synergistic” type are common, but those of simple “dative” type are not.

Purely dative coordination of H_2 apparently requires a hypovalent metal complex, such as HfH_4 or TaH_5 . Figure 4.59 displays the geometrical structures and leading donor-acceptor interactions resulting from coordination of H_2 to these fragments.

When coordination of dihydrogen is limited to uni-directional dative bonding, as in Fig. 4.59, the metal- H_2 distances are long ($R_{Hf-H_2} = 2.60 \text{ \AA}$, $R_{Ta-H_2} = 2.00 \text{ \AA}$) relative to ordinary M—H distances ($R_{HfH} \simeq 1.82 \text{ \AA}$, $R_{TaH} \simeq 1.75 \text{ \AA}$) and only a small quantity of charge is transferred from H_2 to the metal ($0.05e$ for Hf and $0.12e$ for Ta). In both cases the H—H bond lengths (0.75 \AA for Hf and 0.80 \AA for Ta) elongate slightly relative to that in free H_2 (0.74 \AA). As shown in Fig. 4.59, the $\sigma_{HH} \rightarrow n_M^*$ delocalizations yield estimated stabilizations of 14.8 and 54.7 kcal mol $^{-1}$ for Hf and Ta complexes, respectively. Owing to the more congested structure of $TaH_5(H_2)$, separations between molecular H_2 and Ta—H

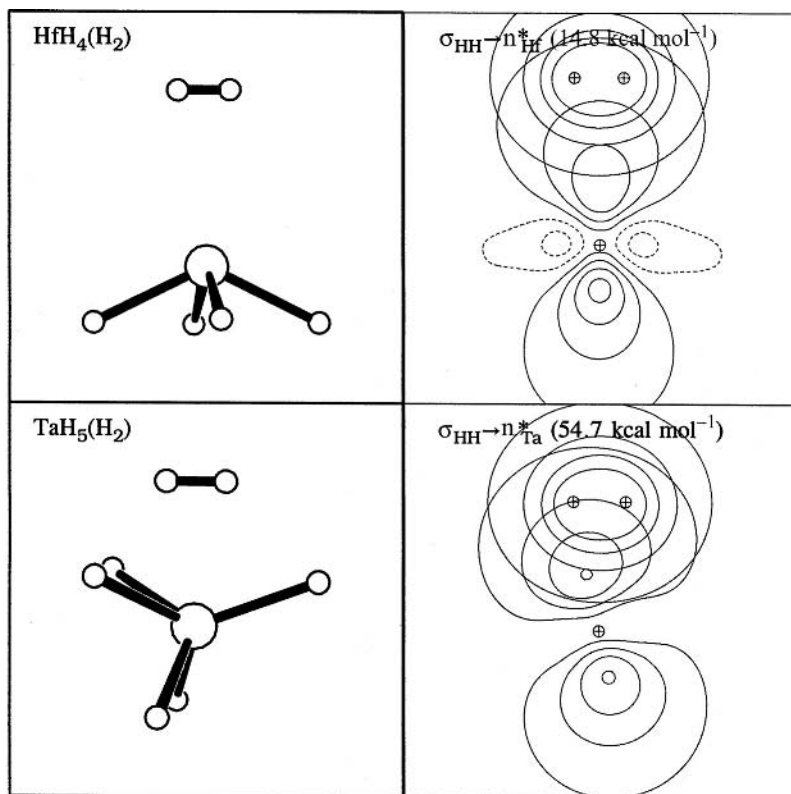


Figure 4.59 The geometry (left) and leading $\sigma_{\text{HH}} \rightarrow n_{\text{M}}^*$ donor–acceptor interaction (right) for molecular-dihydrogen complexes: (a) $\text{HfH}_4 \cdots \text{H}_2$ and (b) $\text{TaH}_5 \cdots \text{H}_2$.

bonds are small. As a result, some backbonding occurs, with charge flowing *from* σ_{TaH} bonds *into* the σ_{HH}^* antibond. These $\sigma \rightarrow \sigma^*$ interactions, which emulate the early stages of the σ -bond-metathesis reaction pathway, contribute $28.5 \text{ kcal mol}^{-1}$ of stabilization as estimated from NBO second-order perturbation theory. Thus, the $\text{TaH}_5(\text{H}_2)$ complex exhibits significant synergism in bonding and appreciably stronger coordination of H_2 . By virtue of these significant donor–acceptor interactions, exchange of hydrogens with H_2 via σ -bond metathesis is an expected pathway for hypovalent hydride complexes.

Let us next examine an interesting molecular- H_2 complex that exhibits synergistic interactions involving a metal σ^* antibond as the acceptor and a filled n_{M} nonbonding orbital as the donor: $[\text{Pt}(\text{PH}_3)_2\text{H}(\text{H}_2)]^+$. By the methods described in Section 4.6.7, this cationic complex can be classified as a $16e \text{ ML}_2\text{X}_2$ species (note that, although H_2 and PH_3 are normally two-electron “L” donors, the net $+1$ charge dictates that one of the “L” ligands be denoted “X” in the MLX scheme). Thus, a square-planar complex is expected, with two ω -bonds originating from

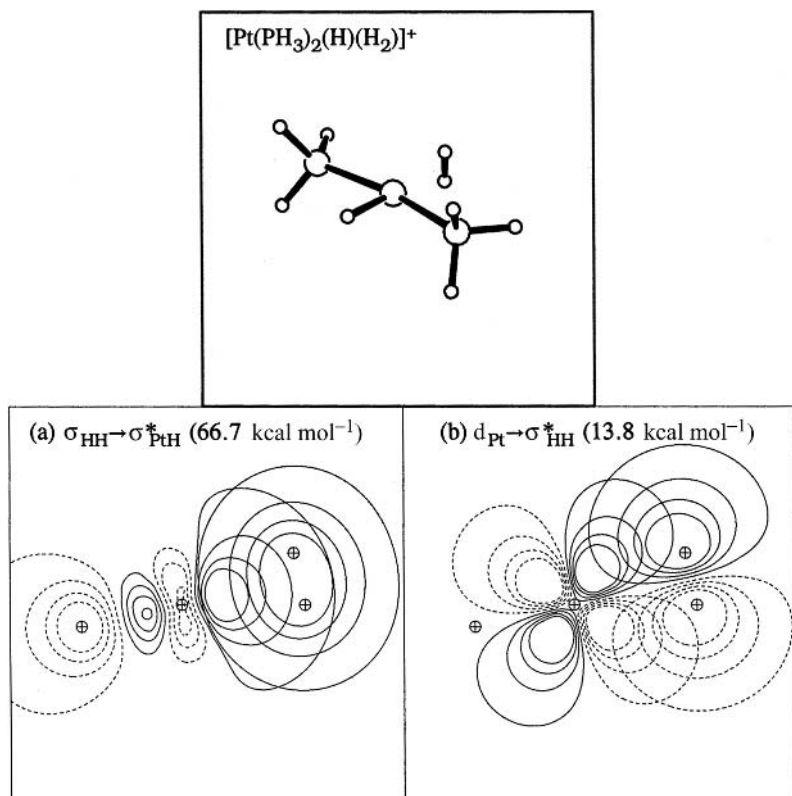


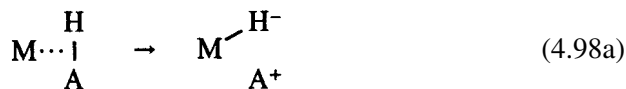
Figure 4.60 Geometry and the primary donor–acceptor interactions of $[\text{Pt}(\text{PH}_3)_2(\text{H})(\text{H}_2)]^+$: (a) from the H_2 σ -bond into the $\text{Pt}-\text{H}$ σ^* antibond and (b) from the d_{Pt} lone pair into the σ_{HH}^* antibond.

the sd^1 -hybridized (90°) $2c/2e$ bonds of the underlying normal-valent species. The optimized structure does indeed exhibit such square-planar geometry, as shown in Fig. 4.60. Key geometrical features include the distances $R_{\text{HH}} = 0.80 \text{ \AA}$, $R_{\text{PtH}} = 1.56 \text{ \AA}$, and $R_{\text{Pt}-\text{H}_2} = 1.87 \text{ \AA}$, which clearly justify the label of “molecular- H_2 complex of a metal hydride” rather than a “metal trihydride.”⁵⁰ Figure 4.60 also illustrates the strong orbital overlaps that facilitate synergistic donation of electron density from the σ_{HH} bond into the in-plane σ_{PtH}^* antibond orbital (estimated $66.7 \text{ kcal mol}^{-1}$ stabilization) and back-donation from the d_{Pt} lone pair into the σ_{HH}^* antibond ($13.8 \text{ kcal mol}^{-1}$ stabilization). It may be noted that the dihydrogen ligand exhibits a slight preference ($\sim 1.2 \text{ kcal mol}^{-1}$) for perpendicular over parallel orientation with respect to the square-planar environment.

Insertion of metals into dihydrogen

If M is hypovalent, $3c/2e$ interactions dominate the initial metal–dihydrogen-bonding picture. One reaction pathway that may result, should M have sufficient

MR donor bonds, is σ -bond metathesis. Alternatively, as the Lewis-acid strength of M increases, the tendency toward agostic or bridging interactions can finally result in H—H bond scission and formal migration of hydride to the metal atom,

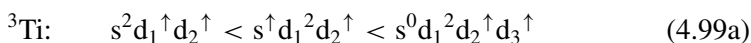


leading to the products of heterolytic fission. However, if M is lone-pair-bearing, the corresponding agostic interaction can either create a stronger coordination of dihydrogen *or* lead to full metal insertion to form neutral products,

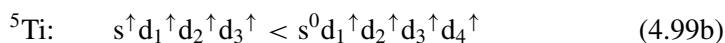


In the latter case, complementary donor–acceptor interactions of $1c \rightarrow 2c^*$ type (e.g., $n_M \rightarrow \sigma_{AH}^*$) can augment the $2c \rightarrow 1c^*$ (e.g., $\sigma_{AH} \rightarrow n_M^*$) interactions described in the previous section. Such complementary pairs of oppositely directed interactions are intrinsically favored compared with single (uni-directional) donor–acceptor interactions, which lead to unfavorable charge separation. Hence, stronger agostic interactions leading to full metal insertion (4.98b) will tend to be associated with transition-metal atoms having favorable donor (n_M) *and* acceptor (n_M^*) capacity.

To illustrate some simple aspects of the insertion of metal atoms into sigma bonds, let us first consider the example of titanium in various spin states inserting into H_2 . The lowest energy configuration of the Ti atom is expected to be of triplet spin multiplicity (spin $S = 1$), with paired electrons filling the low-energy s orbital and the remaining unpaired electrons in the d manifold, whereas higher configurations have a singly occupied or vacant s orbital,



The high-spin quintet states ($S = 2$) can be achieved only in s^1 or s^0 configurations,



while the low-spin singlet states ($S = 0$) correspond to fully paired configurations that are strongly opposed by Hund's rule,



Figure 4.61 displays the potential-energy curves for insertion in the three spin states. All three spin multiplicities lead to local minima at small R , but only the triplet is strongly bound with respect to asymptotic ${}^3\text{Ti} + H_2$ dissociation products, and we focus primarily on this species.

The prominent feature of the triplet curve in the long-range region $R \geq 1.8 \text{ \AA}$ is a double-humped repulsive barrier. This is evidently associated with successive

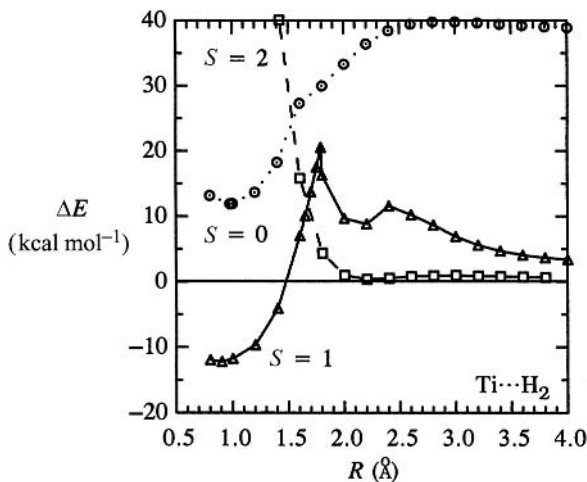


Figure 4.61 Potential-energy curves for reactions inserting singlet (circles), triplet (triangles), and quintet (squares) Ti into H₂. The reaction coordinate *R* is the distance between Ti and the midpoint of H₂, and the zero of energy corresponds to *R* = ∞ for ground-state (triplet) Ti + H₂.

valence promotions from long-range s^2 to short-range $sd^{1.47}$ configurational character, where only the latter configuration allows full insertion to form the deep titanium dihydride well. Such a progression is expected because the final configuration will approximate two $\sim sd^1$ hybridized Ti—H bonds and two singly occupied *d* orbitals. Near $R = 1.8 \text{ \AA}$, the effective Ti configuration has been promoted to $(4s)^{0.83}(3d)^{2.75}$, which is apparently sufficiently low in *s* occupancy to allow the onset of attractive donor–acceptor interactions. (Note that the “cusped” region of the potential curve near $R = 1.8 \text{ \AA}$ has strong multi-configurational character requiring higher levels of theory than employed here, so the details of this region depicted in Fig. 4.61 should be considered to have only qualitative significance.)

Inside $R = 1.8 \text{ \AA}$ the $\text{Ti} \cdots \text{H}_2$ species is strongly stabilized by synergistic $2c \rightarrow 1c^*$ ($\sigma_{\text{HH}} \rightarrow d_{\text{Ti}}$) and $1c \rightarrow 2c^*$ ($d_{\text{Ti}} \rightarrow \sigma_{\text{HH}}^*$) interactions leading to H—H bond breaking and formation of H—Ti—H. Figure 4.62 depicts these interactions at $R = 1.8 \text{ \AA}$. At this distance the “pi-acid” interaction (Fig. 4.62(b)) is stronger than the “sigma-base” interaction (Fig. 4.62(a)), but these two interactions play complementary roles in binding H₂ to the metal atom. At shorter distances, the attractive well eventually results in directed $sd^{1.47}$ hybrids and an effective Ti $(4s)^{0.51}(3d)^{2.55}$ configuration at the equilibrium geometry ($R_e \simeq 0.90 \text{ \AA}$) of the dihydride product species.

From this example one can judge that insertions of metal atoms into sigma bonds may be precluded by unfavorable spin or steric/promotion factors, despite the formal possibility of attractive interactions such as depicted in Fig. 4.62. Long-range s^2 steric/promotion barriers may be expected to block direct insertion of metal atoms

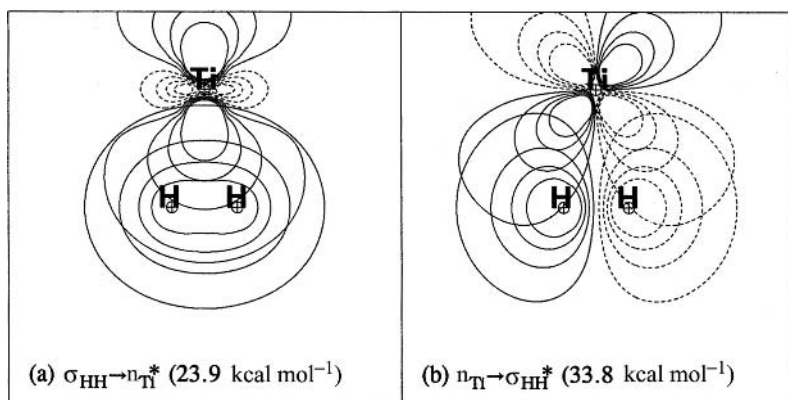
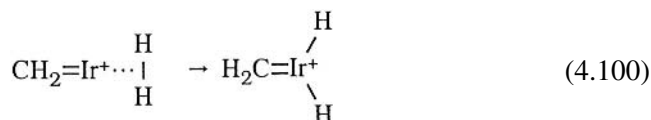


Figure 4.62 $\text{Ti} \cdots \text{H}_2$ donor–acceptor interactions at $R = 1.8 \text{ \AA}$ (with estimated second-order stabilization energies in parentheses): (a) $\sigma_{\text{HH}} \rightarrow n_{\text{Ti}}^*$ (23.9 kcal mol⁻¹) and (b) $n_{\text{Ti}} \rightarrow \sigma_{\text{HH}}^*$ (33.8 kcal mol⁻¹).

into sigma bonds for other early transition-metal species, even if isolated favorable regions of stable H—M—H character exist on the potential-energy surface.

For comparison, let us also consider the experimentally well-documented⁵¹ singlet reactions of H_2 with group 9 metal carbene cations to give metal dihydride insertion products, e.g., for $\text{M} = \text{Ir}$,



The Lewis-like structure of the metallic cation



has a formal unfilled n_{Ir}^* as well as three filled n_{Ir} orbitals. The effective Lewis acidity of the metal is strongly enhanced by cationic net charge, as well as its exposed terminal position in the carbene. Compared with the hypovalent “early” ^3Ti radical discussed above, the Ir cation (4.101) is just two electrons short of a completed valence duodectet, and is expected to exhibit the higher electronegativity associated with “late” transition-metal ions. Furthermore, the singlet CH_2Ir^+ cation configuration ($\sim s^0 d^{8.1}$) will not require extensive promotion of s lone pairs in order to prepare the complex for making two new Ir—H σ bonds.

Figure 4.63 displays the optimized $\text{CH}_2=\text{IrH}_2^+$ product species, and Fig. 4.64 shows the deep attractive well ($>50 \text{ kcal mol}^{-1}$) for bond insertion (4.100), which is of about four times the exothermicity of the corresponding ^3Ti reaction (Fig. 4.61). Figure 4.64 also includes the leading donor–acceptor interactions of

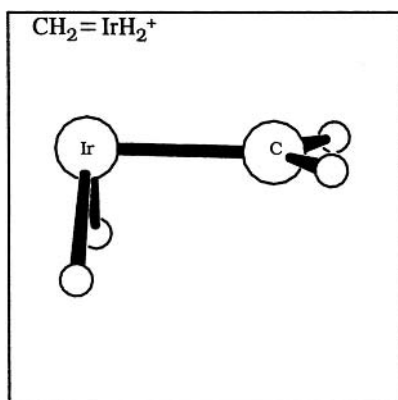


Figure 4.63 The optimized $\text{CH}_2=\text{IrH}_2^+$ product of the insertion reaction (4.100).

$2c \rightarrow 1c^*$ ($\sigma_{\text{HH}} \rightarrow n_{\text{Ir}}^*$) and $1c \rightarrow 2c^*$ ($n_{\text{Ir}} \rightarrow \sigma_{\text{HH}}^*$) types, as estimated by NBO second-order perturbation theory. These short-range attractions become significant near $R \simeq 2.5 \text{ \AA}$, and are evidently instrumental in overcoming the long-range steric barrier that prevails at greater distances.

Figure 4.65 shows contour diagrams of the $\sigma_{\text{HH}} \rightarrow n_{\text{Ir}}^*$ and $n_{\text{Ir}} \rightarrow \sigma_{\text{HH}}^*$ interactions at $R = 1.8 \text{ \AA}$, permitting direct comparisons with Fig. 4.62. In this case the metal acceptor n_{Ir}^* orbital is of high *s* character ($sd^{0.13}$), and the $\sigma_{\text{HH}} \rightarrow n_{\text{Ir}}^*$ interaction

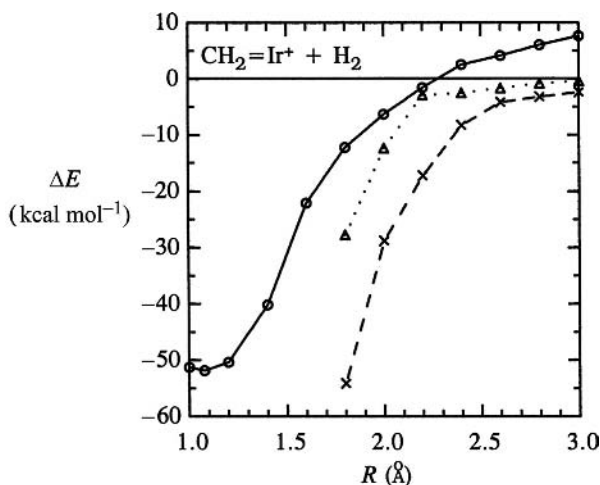


Figure 4.64 The potential energy for the $\text{CH}_2=\text{Ir}^+ + \text{H}_2 \rightarrow \text{CH}_2=\text{IrH}_2^+$ reaction (circles, solid line), with leading long-range donor–acceptor interactions of $n_{\text{Ir}} \rightarrow \sigma_{\text{HH}}^*$ (triangles, dotted line) and $\sigma_{\text{HH}} \rightarrow n_{\text{Ir}}^*$ (crosses, dashed line) types for $R \geq 1.6 \text{ \AA}$ (where the optimal Lewis structure is of reactant form). R is the distance from Ir to the midpoint of H_2 .

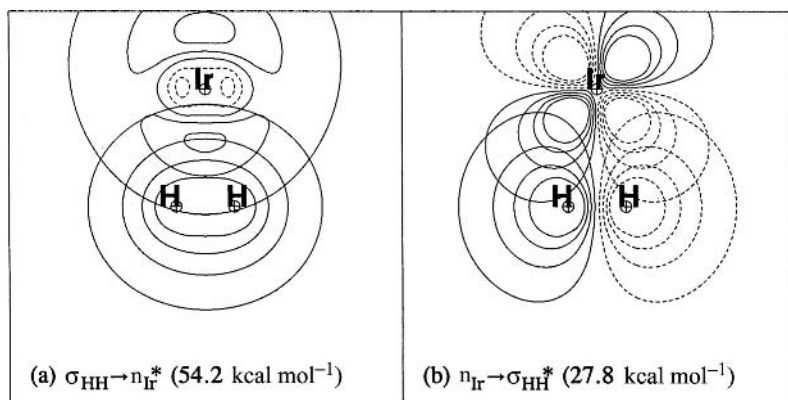


Figure 4.65 Ir · · H₂ donor-acceptor interactions of the insertion reaction (4.100) at $R = 1.8 \text{ \AA}$ (with estimated second-order stabilization energies in parentheses): (a) $\sigma_{\text{HH}} \rightarrow n_{\text{Ir}}^*$ and (b) $n_{\text{Ir}} \rightarrow \sigma_{\text{HH}}^*$.

($\sim 54 \text{ kcal mol}^{-1}$) is significantly stronger than the corresponding Ti interaction in Fig. 4.62(a). The corresponding $n_{\text{Ir}} \rightarrow \sigma_{\text{HH}}^*$ “back-donation” ($\sim 28 \text{ kcal mol}^{-1}$) is nearly identical in form to, but slightly weaker in magnitude than, the analogous Ti interaction in Fig. 4.62(b) which is consistent with the expected difference in electronegativity.

At shorter distances the H—H bond is completely ruptured and replaced by the two Ir—H bonds of the equilibrium product species (Fig. 4.63). The geometry at the metal atom exhibits the expected sd^2 -like geometry (cf. Fig. 4.2(b)), and the final σ_{IrH} NHOs and NBO conform closely to this description, as shown in Fig. 4.66.

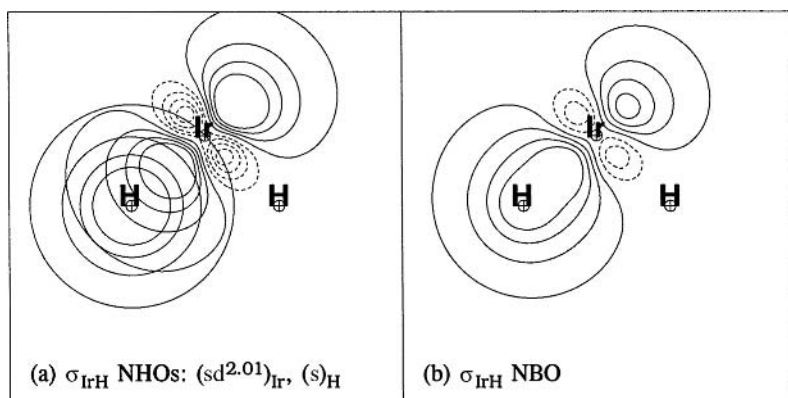


Figure 4.66 The overlapping NHOs (left) and NBO (right) for the σ_{IrH} bond of the product $\text{CH}_2=\text{IrH}_2^+$ (cf. Fig. 4.63).

The conventional nomenclature of “oxidative addition” warrants brief comment in this case. According to the oxidation-state formalism, the addition of H_2 to IrCH_2^+ takes the formal Ir oxidation state from III to V (hence the term “oxidative” addition). However, consideration of natural atomic charges clearly reveals that Ir *gains* electron density over the course of this reaction; insertion of IrCH_2^+ into the H—H bond lowers the charge at Ir from +0.829 to +0.363, making the addition process more “reductive” than “oxidative” for the metal. For the more electronegative late transition metals, particularly those with net positive charge, it is apparent that addition of H_2 will generally tend to have net reductive character. In contrast, addition of H_2 to neutral early-transition-metal complexes will yield M—H bonds that are polarized toward H and hence of net oxidative character (as conventional nomenclature suggests); for example, addition of H_2 to triplet HfH_2 increases the charge on Hf from +0.994 to +1.749. These examples serve as useful reminders that assignment of oxidation state is merely a formalized “bookkeeping” protocol that assists in identifying the number of metal nonbonding d electrons (the d^n count), but is quite misleading if understood in any literal physical sense. Presumed correlations between these assignments and the physical electron-density distribution are spurious and should be avoided in all instances.

In conclusion, the insertion of transition metals into sigma bonds is seen to exhibit a common orbital motif (namely synergistic $2c \rightarrow 1c^*$ and $1c \rightarrow 2c^*$ interactions) both in early (hypovalent) and in late (normal-valent) series members that bear lone pairs. Subtle shifts in electronegativity, orbital shape, and $s \rightarrow d$ promotion energies will alter the magnitudes and “balance” of the two contributing donor–acceptor contributions, affecting the kinetics and thermodynamics of the insertion in important ways. The oxidative addition (insertion) reaction often bears no significant “oxidative” character. Rather, the critical attribute of the insertion reaction is the uncoupling of a lone pair into two electron-pair bonds. As emphasized in the Pross–Shaik two-configuration mixing model,⁵² both the thermodynamics and the kinetics of insertion should correlate with the singlet–triplet gaps of the reactants. Such correlations arise not because the reaction occurs via an actual spin-state change, but because the singlet–triplet gap approximates the “uncoupling” energy needed to prepare from the lone pair the diradical-like character needed to form two new $2c/2e$ bonds.

Sigma-bond metathesis at hypovalent metal centers

Thermodynamically, reaction of H_2 with a metal–carbon bond to produce new C—H and M—H bonds is a favorable process. If the metal has a lone pair available, a viable reaction pathway is initial “oxidative addition” of H_2 to form a metal alkyl dihydride, followed by stepwise “reductive elimination” (the microscopic reverse of oxidative addition) of alkane. On the other hand, hypovalent complexes lack the

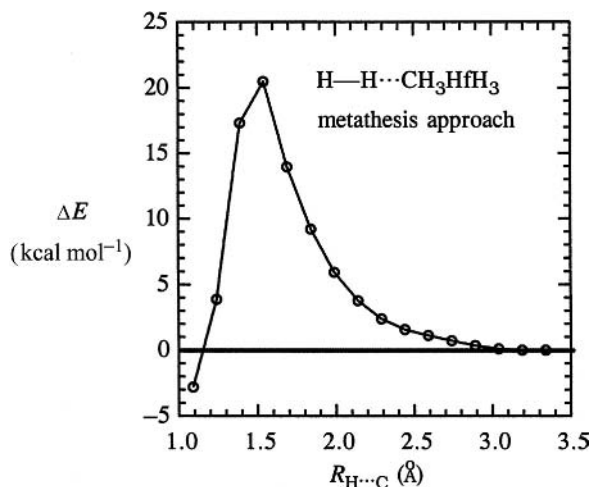


Figure 4.67 The potential-energy profile for the transition-state region of the model σ -metathesis reaction (4.102).

lone pairs required for insertion–elimination sequences and must therefore adopt a different pathway (i.e., different donor–acceptor interactions) in order to proceed. The sigma-bond metathesis reaction, (E) in Table 4.38, is a pathway of considerable importance, particularly as employed industrially to control polyalkene molecular weights by addition of H_2 to a variety of early-transition-metal-catalyzed alkene-polymerization reactions.⁵³

As a simple model for the σ -metathesis pathway, let us examine the key orbital interactions for reaction of H_2 with HfH_3Me to produce HfH_4 and methane:

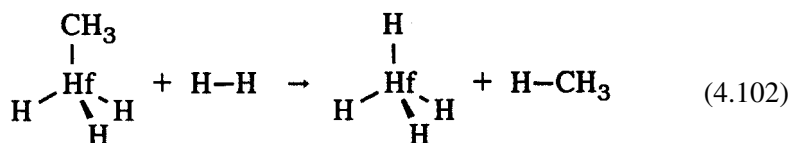


Figure 4.67 depicts the potential-energy curve for reaction (4.102) along an adiabatic reaction coordinate ($R = R_{HMe}$) obtained by stepping along the $H-CH_3$ stretching coordinate with full optimization of geometries at each step. As shown in Fig. 4.67, the reaction exhibits a substantial barrier ($\sim 20.5 \text{ kcal mol}^{-1}$) and overall exothermicity.

As H_2 approaches the methyl group of the Hf complex, electron density is donated from the σ_{HfC} bond into the σ_{HH}^* antibond while the σ_{HH} bond donates into the Hf metal center. Somewhat surprisingly, however, the primary metal acceptor is not an empty metal d orbital but rather a σ_{HfH}^* antibonding orbital. The reason is revealed by the transition-state structure, as displayed in Fig. 4.68. The approach found in this reaction trajectory (which is not necessarily the minimum-energy

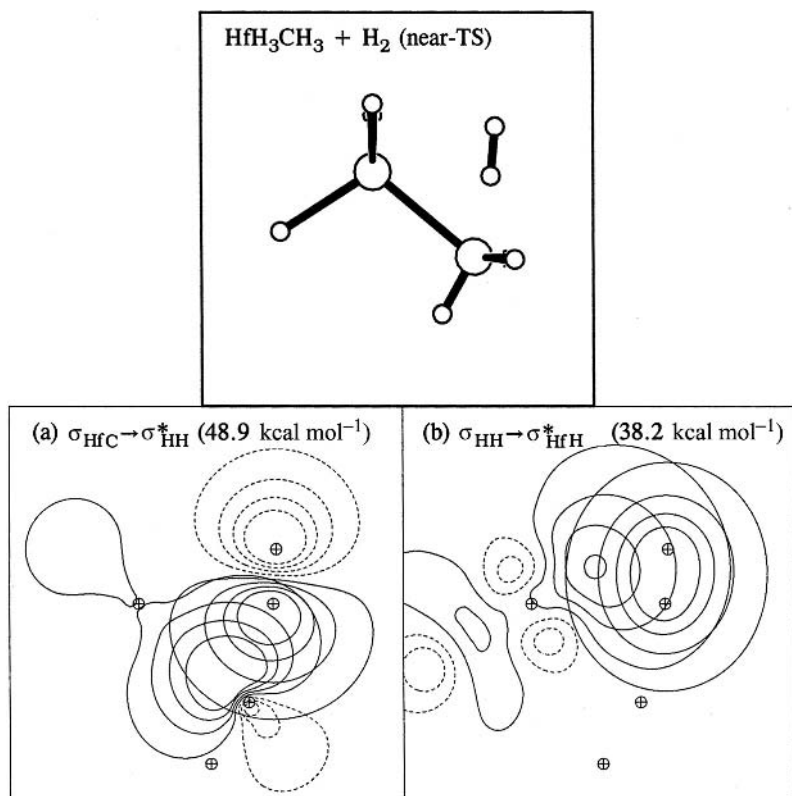


Figure 4.68 The geometry and primary donor–acceptor interactions of the approximate transition state for the model σ -bond-metathesis reaction $\text{HfH}_3\text{CH}_3 + \text{H}_2 \rightarrow \text{HfH}_4 + \text{CH}_4$: (a) from the Hf–C σ bond into the H–H σ^* -antibond and (b) from the H–H bond into the Hf–H antibond.

“intrinsic reaction coordinate” for the reaction) is seen to place the incipient H–Hf bond almost perfectly *trans* to one of the original Hf–H bonds ($\theta_{\text{HHfH}} = 167^\circ$). Therefore, at this geometry the best overlap is found with the Hf–H antibond, emphasizing the importance of metal-centered antibonds as acceptors in reactions at metal centers. Such donor–acceptor interactions are particularly strong when the M–H bonds are polarized toward H (maximal hydridic character), as is the case with the early transition metals. At $R = 1.69 \text{ \AA}$, NBO analysis yields H_2 and HfH_3Me as the dominant Lewis-like configuration (with valence $\rho_{\text{L}} = 97.8\%$). As depicted in Fig. 4.68, strong donation from the σ_{HfC} bond into the σ_{HH}^* orbital yields stabilization of $48.9 \text{ kcal mol}^{-1}$ according to NBO second-order perturbation analysis. Also depicted are the orbitals involved in the $\sigma_{\text{HH}} \rightarrow \sigma_{\text{HfH}}^*$ donor–acceptor interactions, which contribute an additional $38.2 \text{ kcal mol}^{-1}$ stabilization.

Essential to the σ -bond-metathesis reaction is donation of M–R bond density into the H–H antibonding orbital. As a consequence, lower barriers should result

from increasing donor ability of the R group. For example, the more basic secondary and tertiary alkyls of highly polarized (carbanion-like) early-transition-metal alkyls should react faster with H₂ than analogous complexes of methyl or primary alkyls. Recent experimental evidence appears to support this analysis. The significance of this phenomenon for catalytic alkene polymerization is that the responsivity of the relative molecular mass to H₂ as a chain-transfer agent will depend critically on the regioselectivity of the alkene insertion (i.e., whether insertion of alkene into the growing polymer preferentially makes secondary or primary alkyls; C. R. Landis, D. J. Sillars, and J. M. Batterton, unpublished results).

4.7.4 Catalytic activation of alkene bonds

The π bond of an alkene differs significantly from the σ bond of H₂. Most importantly, the π bond is weaker, but, even if it is broken, the two carbon centers cannot separate by more than ~ 0.2 Å due to the residual σ -bonding. In consequence, complete cleavage of the C=C bond (unlike cleavage of the H—H bond) is impractical, and sharp distinctions between limiting reaction types will not be so obvious as for H₂. For example, H₂ binds to transition metals to give either a molecular-dihydrogen complex or a metal dihydride, and the steep dependence of H—H binding energy on bond length dictates that reaction products will tend to fall clearly into one limit or the other, with little resonance mixing except in the immediate region of the transition state. Coordinated alkenes present a dramatically different picture. Most common transition-metal complexes lie somewhere “between” the extremes of limiting reaction types, as depicted in Table 4.39 (cf. Table 4.38 for H₂). In such cases, extensive configurational mixing is expected to complicate the analysis but enrich the chemistry of metal–alkene interactions (relative, e.g., to the simpler metal–H₂ interactions considered in Section 4.7.3). In this section we shall examine coordination modes of alkenes at metal centers and briefly discuss their principal reactivity patterns.

As shown in Table 4.38, three major reaction pathways are available to hypovalent metals in the presence of an alkene: (A) and (C) dative and synergistic coordination; (B) carbocation formation; and (D) and (E) metallacyclic and migratory insertions. The latter types are of particular importance in metal-catalyzed alkene polymerizations and will be given primary attention in the discussion that follows.

Alkene coordination

As a simple example of weak dative coordination of an alkene, we consider the complex formed between C₂H₄ and the C_{4v} structure of hypovalent HfH₄, which is analogous to the HfH₄ ··· H₂ complex discussed in Section 4.7.3. Figure 4.69 displays the optimized structure and leading $\pi_{\text{CC}} \rightarrow n_{\text{Hf}}^*$ NBO interaction of the HfH₄ ··· C₂H₄ complex.

Table 4.39. Non-radical reaction types for interactions of transition metals (M) with alkenes (||), showing principal donor–acceptor combinations in each case (the symbol \square denotes a vacant valence orbital [formal hypovalency] on the metal atom)

Schematic reaction	Reaction type	Donor(s)	Acceptor(s)
(A) $M-\square + \rightarrow M- $	Dative C=C coordination	π_{CC}	n_M^* (or σ_{ML}^*)
(B) $M^+-\square + \rightarrow M-\overset{+}{\text{C}}\text{H}_2$	Carbocation formation	π_{CC}	n_M^* (or σ_{ML}^*)
(C) $\ddot{M}-\square + \rightarrow \ddot{M}- $	Synergistic C=C coordination	π_{CC}/n_M	n_M^* (or σ_{ML}^*)/ π_{CC}^*
(D) $\ddot{M}-\square + \rightarrow M \begin{array}{c} \diagup \\ \diagdown \end{array}$	Metallacyclic insertion	π_{CC}/n_M	n_M^* (or σ_{ML}^*)/ π_{CC}^*
(E) $R-M-\square + \rightarrow M-\text{CH}_2\text{R}$	Migratory insertion	π_{CC}/σ_{MR}	n_M^* (or σ_{ML}^*)/ π_{CC}^*
(F) $M^--\square + \rightarrow M-\overset{-}{\text{C}}\text{H}_2$	Carbanion formation	n_M	π_{CC}^*

As shown in Fig. 4.69, the $\text{HfH}_4 \cdots$ alkene complex exhibits expected parallels with the $\text{HfH}_4 \cdots \text{H}_2$ complex (Fig. 4.59), both in terms of molecular shape and in terms of valence interactions. The characteristic features of such weak dative bonding include long Hf—C distances (2.82 Å), normal C=C bond length (1.34 Å), planar alkene bond angles, and small binding energy (15.1 kcal mol⁻¹).

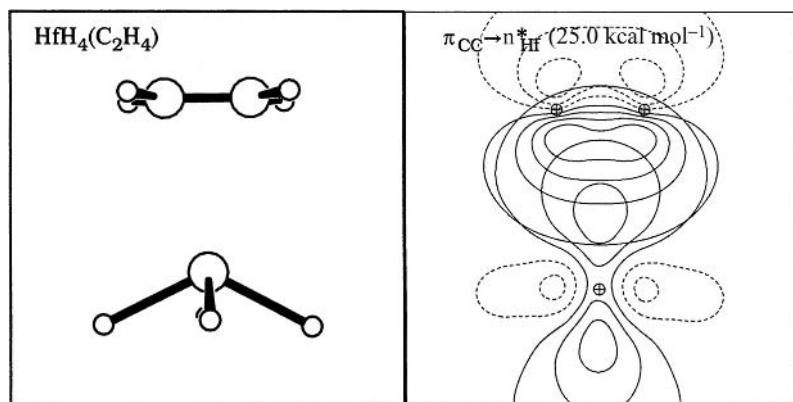


Figure 4.69 The geometry and leading $\pi_{CC} \rightarrow n_M^*$ donor–acceptor interaction for the $\text{HfH}_4 \cdots \text{C}_2\text{H}_4$ dative coordination complex.

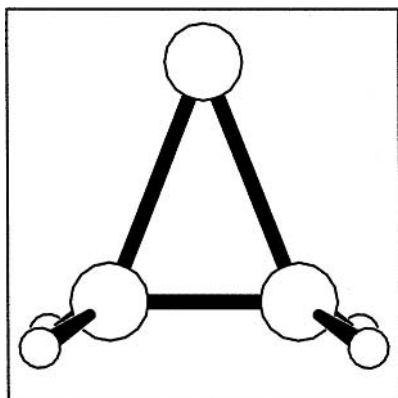
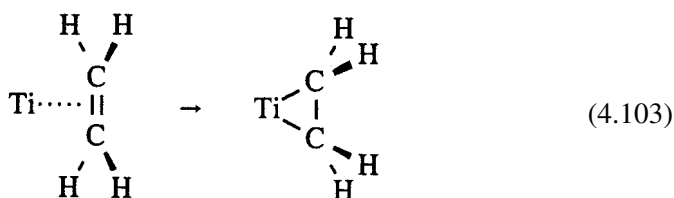


Figure 4.70 The optimized metallacycle product of the $\text{Ti}\cdot + \text{C}_2\text{H}_4$ insertion reaction (4.103).

The NBO analysis characterizes the $\pi_{\text{CC}} \rightarrow n_{\text{Hf}}^*$ interaction as relatively modest ($25.0 \text{ kcal mol}^{-1}$), with $\sim 0.09e$ charge transfer from ethylene to HfH_4 . Accordingly, the coordinated alkene is somewhat activated toward nucleophilic attack, but the chemical effects are minor compared with those for other donor–acceptor motifs to be discussed below.

Metallacyclic pi-bond insertions

In contrast to the severe difficulty of “cracking” a sigma bond, insertion of a transition metal into a pi bond can proceed in facile fashion. This can be illustrated by the attack of Ti on the pi bond of ethylene, which leads to metallacycle formation in the reaction



with the final reaction product as shown in Fig. 4.70. Reactions of this type are commonly rationalized in terms of the Dewar–Chatt–Duncanson model.⁵⁴ Here we describe the mechanism in terms of the NBO donor–acceptor framework.

Figure 4.71 shows the barrierless potential-energy reaction profile for the $\text{Ti}(\text{singlet}) + \text{C}_2\text{H}_4$ insertion reaction (4.103). In parallel with the picture for sigma-bond insertion (Fig. 4.62), the principal donor–acceptor interactions leading to reaction (4.103) are expected to be of synergistic $2c \rightarrow 1c^*$ ($\pi_{\text{CC}} \rightarrow n_{\text{Ti}}^*$) and $1c \rightarrow 2c^*$ ($n_{\text{Ti}} \rightarrow \pi_{\text{CC}}^*$) types. The magnitudes of these stabilizations in the long-range region are included in Fig. 4.71, for comparison with Fig. 4.62. Contour diagrams

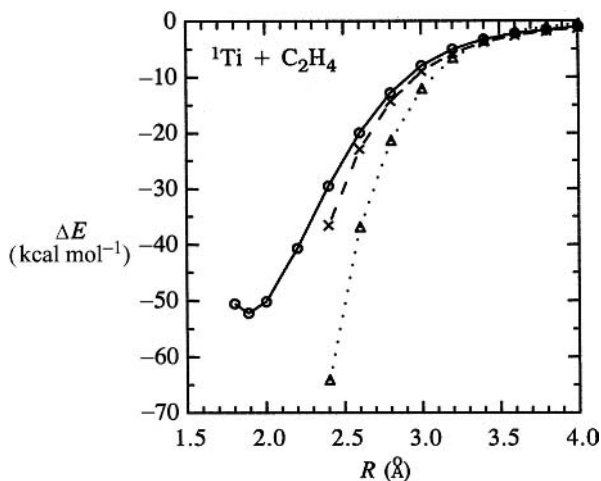


Figure 4.71 The potential-energy curve for the $\text{Ti} \cdots \text{C}_2\text{H}_4$ insertion reaction (4.103) (circles, solid line), with leading long-range donor–acceptor interactions of $n_{\text{Ti}} \rightarrow \pi_{\text{CC}}^*$ (triangles, dotted line) and $\pi_{\text{CC}} \rightarrow n_{\text{Ti}}^*$ (crosses, dashed line) types. (R is the distance from Ti to the midpoint of C_2 .)

of the interacting NBOs at $R = 1.8 \text{ \AA}$ are shown in Fig. 4.72. These exhibit evident similarities to the analogous diagrams (Figs. 4.54 and 4.57) for sigma insertions.

The equilibrium hybrids and NBOs of the final titanacyclopropane ring bonds are shown in Fig. 4.73. Although some bond strain is evident, the degree of bond-bending appears appreciably less than that in cyclopropane (cf. Fig. 3.21). The relatively gentle degree of bending of metal hybrids is particularly noteworthy in

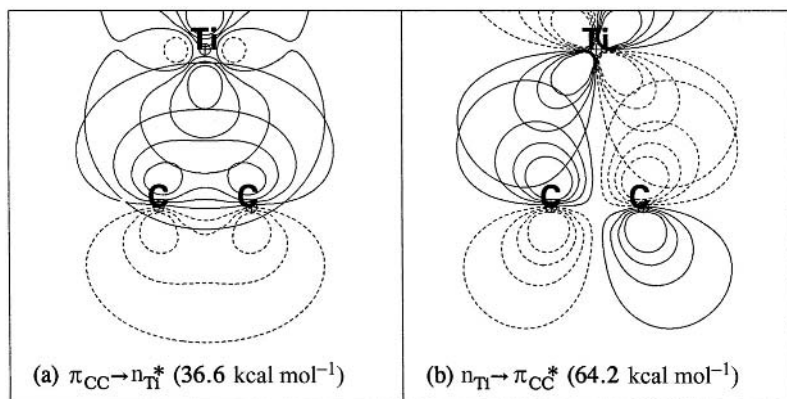


Figure 4.72 The $\text{Ti} \cdots \text{C}_2\text{H}_4$ donor–acceptor interactions of the insertion reaction (4.103) at $R = 2.4 \text{ \AA}$ (with estimated second-order stabilization energies in parentheses): (a) $\pi_{\text{CC}} \rightarrow n_{\text{Ti}}^*$ and (b) $n_{\text{Ti}} \rightarrow \pi_{\text{CC}}^*$.

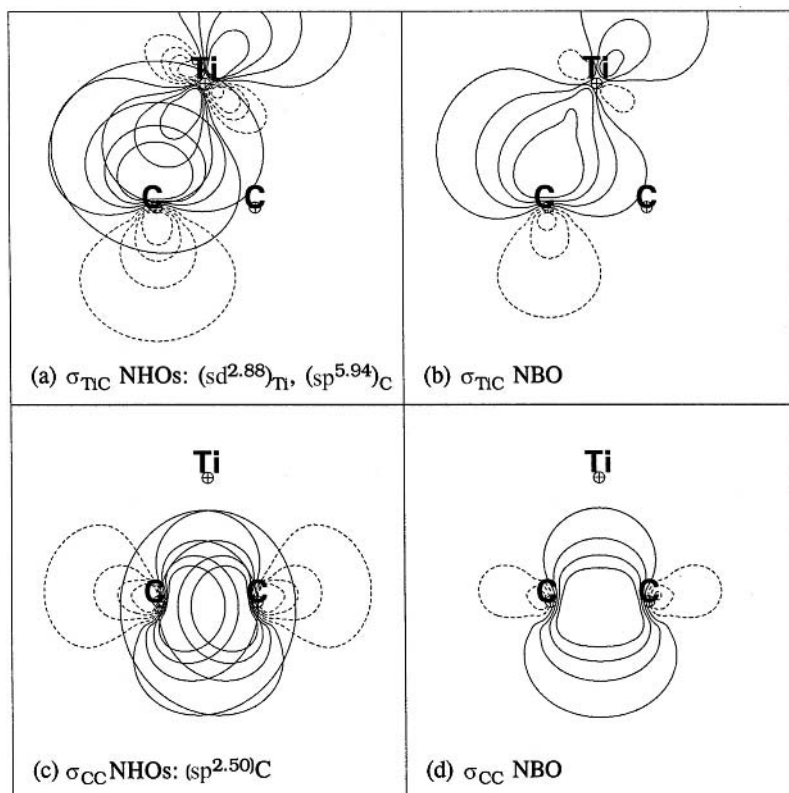


Figure 4.73 The overlapping NHOs (left) and NBO (right) for σ_{TiC} (upper) and σ_{CC} (lower) bonds of the product titanacyclopropane (cf. Fig. 4.70).

view of the small bond angle (43.2°) at the metal apex. This is testimony to the flexibility of metal sd^u hybrids to span a much wider range of bond angles than those of main-group compounds. The net charge at titanium is $Q_{\text{Ti}} = +0.870$, which is indicative of the rather polar character of the σ_{TiC} bonds.

Similarly to the Ti atom, the singlet state of HfH_2 undergoes barrierless coordination of ethylene to make a metallacyclopropane dihydride. Both structural and NBO metrics strongly suggest that we should describe this complex as a simple metallacycle. The characteristics of this class seem to be well represented by the TiC_2H_4 prototype.

Intermediary metal–alkene species

We now consider some simple examples of the more common alkene coordination mode that is intermediate between the limiting extremes of weak dative coordination and strong metallacyclopropane insertion. Our model systems are the simple ethylene adducts of the group 10 metals Ni, Pd, and Pt. Because these metals exhibit

Table 4.40. Key bond lengths R_{MC} and R_{CC} , bond-angle sum about carbon $\sum \theta_C$, metal-atom charge Q_M , and percentage valence Lewis density $\% \rho_L$ for $M-C_2H_4$ adducts of the group 10 metals $M = Ni, Pd, \text{ and } Pt$

M	R_{MC} (Å)	R_{CC} (Å)	$\sum \theta_C$ (degrees)	Q_M	$\% \rho_L$
Ni	1.905	1.425	354.6	+0.260	96.2
Pd	2.137	1.395	356.9	+0.132	97.3
Pt	2.054	1.436	354.1	+0.038	95.0

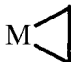
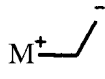
distinct atomic ground-state configurations ($Ni(s^2d^8)$, $Pd(s^0d^{10})$, and $Pt(s^1d^9)$), they are expected to require varying amounts of promotion energy in order to achieve the idealized sd^1 hybridization for metallacyclopropane formation. The Pt complex is expected to form metallacycles with the least amount of promotion energy, whereas both Ni and Pd will require extensive reorganization of the ground-state atomic configuration.

Table 4.40 shows key geometrical and NBO parameters for the three $M-C_2H_4$ adducts, including distances (R_{MC} and R_{CC}), deviations from alkene planarity ($\sum \theta_C = \theta_{HCH} + \theta_{HCC} + \theta_{H'CC}$), metal charge (Q_M), and accuracy of the Lewis-like description (percentage valence Lewis density $\% \rho_L$). The conspicuously low values of $\% \rho_L$ – 96.2% for Ni, 97.3% for Pd, and 95.0% for Pt – indicate that characterization of these adducts as “intermediary” is clearly appropriate. Interestingly, in all cases the coordination with ethylene causes net charge flow from the metal to the alkene, resulting in small positive charges at the metal centers (+0.04 to +0.26). In keeping with electronegativity trends, charge is released in the order $Ni > Pd > Pt$. The Pt complex exhibits the longest C—C distance and greatest deviation from planarity at C, indicating that it has the highest metallacycle character.

Natural resonance theory (Section 1.6) provides a quantitative gauge of the contributions of various resonance structures to the total electronic density. The results are shown in Table 4.41 demonstrating the remarkable “intermediacy” in the nature of metal–alkene interaction relating metallacycle, nonbonded, and carbanion-type resonance forms.

As judged by NRT weightings in Table 4.41, metallacyclic character is strongest for Pt (52.3%), followed by Ni (40.1%) and then Pd (26.8%), whereas nonbonded $M \cdots ||$ character trends in the opposite direction. However, no single bonding description achieves more than a bare majority of the NRT weightings. Perhaps most importantly, the occurrence of multiple resonance structures signals that the density distribution is easily perturbed, thus making available the possibility of many

Table 4.41. The NRT weightings of leading resonance forms (metallacyclic, nonbonded complex, and open carbanion) in intermediary M—C₂H₄ adducts, M = Ni, Pd, and Pt

M	NRT resonance weightings			
	 Cyclic	M Nonbonded	 Carbanion	Others
Ni	40.1%	37.8%	13.7%	8.4%
Pd	26.8%	53.6%	11.4%	8.2%
Pt	52.3%	27.0%	8.0%	12.7%

reaction chemistries, as is observed. More specifically, we expect the reactivity patterns of coordinated alkenes to depend sensitively on coordination geometry, alkene substituents, and other ligands of the metal complex, exhibiting an “intermediary” character quite unlike that of typical M—H₂ adducts.

As a further demonstration of the mutable nature of metal–alkene bonding, consider the hypervalent complex ion, *trans*-[Pt(PH₃)₂H(C₂H₄)]⁺. In contrast with coordination of ethylene to the bare Pt atom, this complex exhibits little elongation of the C=C bond ($R_{CC} = 1.362 \text{ \AA}$), a nearly planar alkene geometry ($\sum \theta_C = 358.5^\circ$), and rather long Pt—C distances ($R_{PtC} = 2.411 \text{ \AA}$). Thus, the dominant resonance structure in this case corresponds to the dative-bonding motif, in Table 4.39(A). Unlike neutral Pt(C₂H₄), this cationic complex exhibits net charge flow of 0.11 *e* from alkene to metal, as expected for dative coordination. Owing to the hypervalent nature of *trans*-[Pt(PH₃)₂H(C₂H₄)]⁺, the best acceptor orbital for π_{CC} electron density is the σ_{PtH}^* antibond; this donor–acceptor interaction generates 59.7 kcal mol⁻¹ of stabilization according to NBO second-order perturbation analysis. The companion $\pi_{CC} \rightarrow n_{Pt}^*$ stabilization is 20.4 kcal mol⁻¹. Overall, these parameters indicate that coordination of ethylene to the cationic Pt fragment yields only slight carbocationic character, with charge flow dominated by the $\pi_{CC} \rightarrow \sigma_{PtC}^*$ dative interaction.

Although steric influences also make some contribution, the geometry of [Pt(PH₃)₂H(C₂H₄)]⁺ appears to be dominated by significant covalency (partial metallacyclopropane character) of the Pt–alkene interaction. Consider the expected structure for pure metallacyclopropane (or more simply, metal dialkyl) bonding. A dialkyl complex [Pt(PH₃)₂HR₂]⁺ of formal ML₂X₃ type has 16e count, corresponding to two ω bonds. The normal-valent parent of this hypervalent molecule is therefore formulated as having two ω prebonds, one ordinary 2c/2e sigma bond, and three pure-d lone pairs, requiring nominal sd² hybridization. The natural 90° bond angles of the parent sd²-hybridized MX₃ and 180° angles of the two ω_{LMX} triads

then dictate a monovacant octahedral coordination geometry, with one of the two R groups perpendicular to the plane of the two ω bonds. For the particular example of the *trans* $[\text{Pt}(\text{PH}_3)_2\text{H}(\text{C}_2\text{H}_4)]^+$ ion, the relatively low metallacyclopropane character and short C—C bond length are insufficient to enforce this idealized asymmetric geometry of the alkene, with one C remaining in the plane (and participating in ω -bonding) and one C approaching the axial position perpendicular to the plane. Nevertheless, the significant preference for the alkene to “twist” with respect to the principal coordination plane can be seen to be an immediate consequence of its partial metallacyclopropane character.

The alkene-orienting phenomenon is quite general and can be stated as follows: transition-metal-coordinated alkenes will tend to adopt geometries that approximate those of the corresponding dialkyls. A striking example of this tendency in the opposite “untwisted” sense is given by coordination of ethylene to $\text{Fe}(\text{CO})_4$. Viewed in the metallacyclopropane or dialkyl limit, the preferred geometry of this ML_4X_2 18e complex is expected to exhibit the octahedral geometry of three ω bonds, with three lone pairs and nominal sd^2 hybridization (90° bond angles). As a result, the preferred orientation⁵⁵ of $\text{Fe}(\text{CO})_4(\text{C}_2\text{H}_4)$ places the C—C bond in plane with two *cis*-disposed CO groups (i.e., in ω -bonding position) rather than parallel to the axis of two *trans*-disposed CO groups. The actual geometry of $\text{Fe}(\text{CO})_4\text{C}_2\text{H}_4$ reflects this tendency of the alkene to orient itself in a plane so that each C lies approximately *trans* to a coplanar CO group, thereby achieving the stabilizing effect of partial M—C covalency and ω_{LMC} bonding, despite the apparently “more crowded” requirement of the octahedral-like (versus trigonal-bipyramidal-like) coordination geometry.

Finally, let us briefly consider the structural consequences of substitution of an alkene by an electron-withdrawing group such as a nitrile. Owing to the unsymmetric nature of acrylonitrile (CH_2CHCN), one expects a distinct asymmetry in the preference of the two vinyl C atoms to occupy the in-plane versus out-of-plane positions in the overall monovacant octahedral coordination pattern – but which way should it occur? The nature of the hypervalent bonding, extrapolated toward the metallacyclopropane limit, provides the essential insight: the carbon atom that is best able to stabilize the partial build-up of negative charge associated with ω -bonding should lie closest to the coordination plane, leaving the other carbon to make a conventional 2c/2e bond in the unique axial position. Accordingly, the CN-substituted carbon atom is expected (and observed) to preempt the in-plane ω -bonding position whenever possible, despite the “more crowded” sterics that seem to be required.

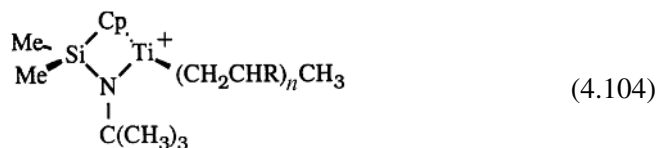
Asymmetry in metal–alkene coordination plays a critical role in asymmetric catalysis, with implications far beyond the scope of the present treatment. An instructive example is provided by catalytic asymmetric hydrogenation of enamides,

in which results of computational studies have recently shown the importance of such asymmetric coordination in determining the sense of enantioselection based on a fascinating “anti-lock-and-key” mechanistic motif.⁵⁶

4.7.5 Catalysis of alkene polymerization

The ability of transition-metal complexes to activate substrates such as alkenes and dihydrogen with respect to low-barrier bond rearrangements underlies a large number of important catalytic transformations, such as hydrogenation and hydroformylation of alkenes. However, activation alone is insufficient if it is indiscriminate. In this section we examine a particularly important class of alkene-polymerization catalysts that exhibit exquisite control of reaction stereoselectivity and regioselectivity as well as extraordinary catalytic power, the foundation for modern industries based on inexpensive tailored polymers.

The chain-carrying catalytic species of alkene-polymerization reactions is commonly a tri-coordinate group 4 transition-metal cation of the general form $L_2M^+P_n$, where P_n is the polyalkene chain. A family of commercially important examples is based on the complex titanium ion⁵⁷



where the Cp (cyclopentadienyl) ring is in sandwich-like coordination with Ti. Starting from the methylated reactant species ($n = 0$), successive $\text{H}_2\text{C}=\text{CHR}$ molecules can be inserted in stereoregular manner under mild conditions, yielding polymeric chains whose length n can be effectively controlled by addition of H_2 to quench chain propagation (via the σ -bond-metathesis pathway discussed in Section 4.7.3). As we shall see in more detail, the critical alkene-activation event is generation of carbocationic character through electrophilic attack by the positively charged metal.

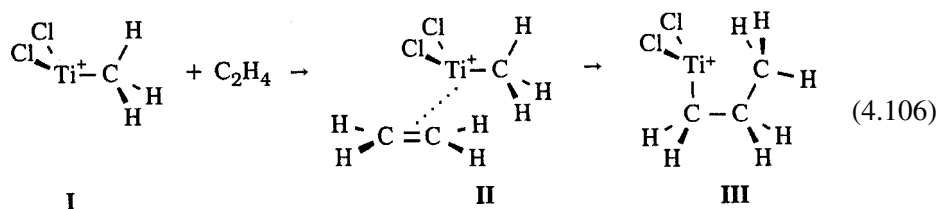
As a simple computational model for the catalysis of alkene polymerization, let us consider some aspects of the general chain-propagation reaction



starting from a methyl precursor reagent ($R = \text{CH}_3$) for polymerization of ethylene ($R' = \text{H}$) with chlorinated titanium cation ($L = \text{Cl}$, $M = \text{Ti}^+$) as the catalytic Lewis acid. We note that the actual polymerization catalysts used in industry exhibit additional features (such as stereoselectivity, pronounced counterion effects, strong variations in relative molecular mass and variable co-monomer-incorporation

proclivities) that such a simple model cannot address. Our focus here lies on the principal orbital interactions that lead to alkene activation and chain growth. (Unlike other examples in this chapter, the present system was treated only at B3LYP/LANL2DZ level.)

According to the general “migratory-insertion” mechanism proposed by Cossee,⁵⁸ chain propagation (4.105) is a two-step process in which the precursor metal reagent (**I**) forms an intermediate alkene complex (**II**) that subsequently rearranges to the insertion product (**III**),



A prominent feature of this mechanism is that the growing polymer chain alternately swings between two *cis*-disposed coordination sites during each monomer insertion. General mechanistic outlines of this reaction have been extensively examined by large-scale computations and confirmed by experimental means.⁵⁹ Our present goal is to clarify the localized donor–acceptor–orbital interactions that underlie (4.106), particularly the nature of the alkyl–alkene complex **II**.

Figure 4.74 shows optimized structures of species **I–III** of the propagation reaction (4.106). All three structures are true equilibrium species (positive frequencies), with intermediate and final product species bound by 39.2 kcal mol⁻¹ (**II**) and 46.9 kcal mol⁻¹ (**III**) with respect to the starting reagents (**I** + C₂H₄). As expected from the elementary *sd*²-hybridization picture (Section 4.3), the trigonal TiRCl₂ geometry is strongly pyramidalized about the metal atom, with a 6.48 kcal mol⁻¹ barrier to inversion. Furthermore, from comparison of Figs. 4.74(a) and 4.74(c) one can recognize that, if the Ti–C bond is held, e.g., in fixed horizontal orientation, the terminal TiCl₂ triangle alternately flips from “up” to “down” orientation as each —CH₂CH₂—segment is inserted into the polymer tail, the so-called chain-swinging (“bell-clapper”) mechanism.

The leading metal–alkene interactions contributing to stabilization of the intermediate complex **II** are depicted in Fig. 4.75. As shown in this figure, *two* vacant Ti orbitals (*n*'_{Ti}* and *n*''_{Ti}*) interact strongly with the π_{CC} bond NBO of the alkene in the expected 2c→1c* manner, holding the alkene in nearly parallel orientation to the metal–carbon bond as it approaches from the “backside” (metal) end of the reactant σ_{TiC} bond (Fig. 4.74(b)). The “backward-canted” *n*''_{Ti}* orbital (Fig. 4.75(b)) can evidently interact with the alkene pi bond at large separation, while the “forward-canted” *n*'_{Ti}* orbital (Fig. 4.75(a)) assists in sliding the alkene forward into nearly

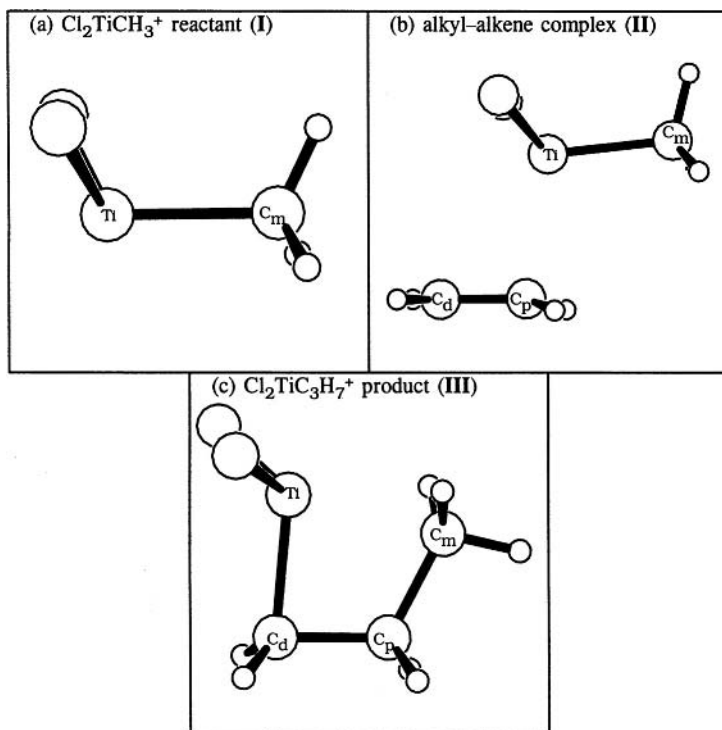


Figure 4.74 Optimized structures of (a) the reactant **I**, (b) the intermediate complex **II**, and (c) the product **III** of the model ethylene-polymerization reaction (4.106), with labeled methyl (C_m), proximal (C_p), and distal (C_d) carbon atoms.

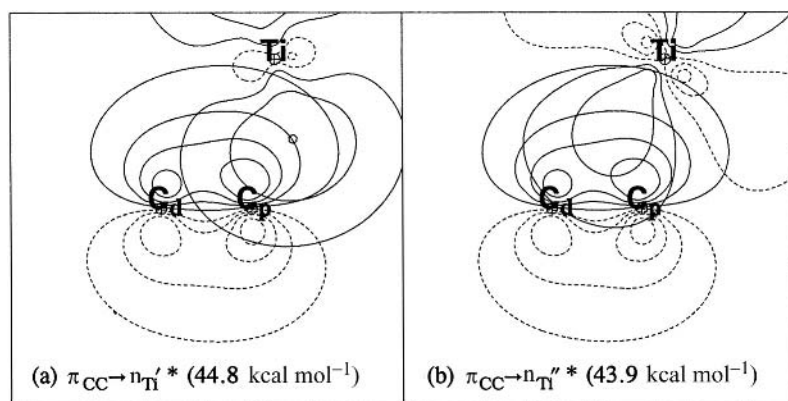


Figure 4.75 The leading donor-acceptor interactions of the $\text{Cl}_2\text{TiCH}_3^+ \cdots \text{C}_2\text{H}_4$ complex (cf. Fig. 4.74(b)), with stabilization energies in parentheses.

Table 4.42. *Skeletal geometries and charges of equilibrium and transition-state species in the model propagation reaction (4.106); cf. Fig. 4.74*

	I	II	II [‡]	III
Distances (Å)				
Ti—C _m	1.975	1.984	2.046	2.233
Ti—C _d	∞	2.862	2.121	1.964
Ti—C _p	∞	2.301	2.506	2.405
C _d —C _p	1.348	1.373	1.419	1.573
C _p —C _m	∞	3.407	2.260	1.612
Angles (degrees)				
C _m —Ti—C _p	—	105.1	58.5	40.5
C _m —Ti—C _d	—	133.2	92.4	81.0
Ti—C _d —C _p	—	52.5	87.8	84.9
Ti—C _p —C _d	—	99.2	57.7	54.4
C _m —C _p —C _d	—	133.2	107.5	118.2
Charges (a.u.)				
Ti	+1.135	+0.877	+0.734	+0.776
C _m	-0.882	-0.881	-0.790	-0.718
C _d	-0.403	-0.147	-0.573	-0.575
C _p	-0.403	-0.604	-0.248	-0.445
Δ <i>E</i> (kcal mol ⁻¹) ^a	(0.0)	-39.2	-32.3	-46.9

^a Relative to separated I + CH₃CH=CH₂.

square alignment with the Ti—C bond to be broken. Thus, the two donor–acceptor (partial τ -bridging) interactions pictured in Fig. 4.75 virtually clamp the alkene into parallel alignment and provide the low-energy pathway to the (approximately square) transition-state geometry in which the precursor π_{CC} and σ_{TiC} bonds can rearrange to form the σ_{TiC} and σ_{CC} bonds of the product polymer tail.

Table 4.42 summarizes some geometrical and charge descriptors of the alkyl–alkene complex II that provide clues as to how the catalytic bond-switching is facilitated. The comparison values for I and III show that the charge distribution and geometry of the intermediate complex II differ markedly from those of the reactant and product species. The two strong donor–acceptor interactions in Fig. 4.75 lead to considerable intermolecular charge flow ($0.305e$) from the incoming alkene to the metal cation, partially neutralizing the cation and creating considerable carbocation character in the alkene. This is particularly true at the distal carbon atom C_d (0.457 less-negative charge than on the proximal C_p), whereas the proximal C_p center (of higher π -bond amplitude) begins to pyramidalize conspicuously as shown in Fig. 4.74(b). The strongly unsymmetric interaction of the ethylene moiety with

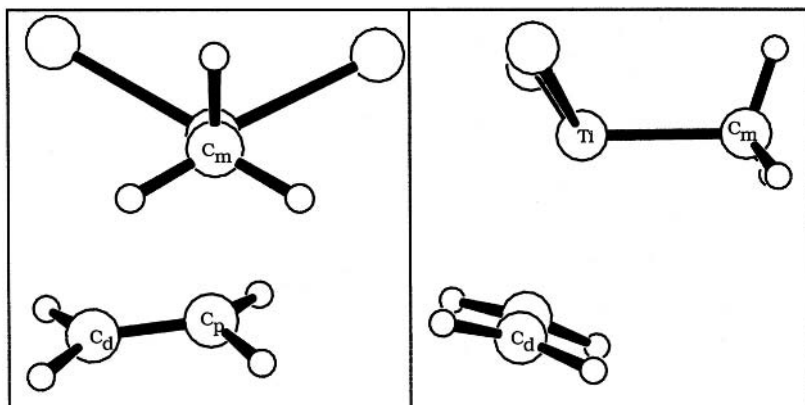


Figure 4.76 Side and end views of the 90° -twisted ethylene complex ($0.5 \text{ kcal mol}^{-1}$ above the untwisted equilibrium complex, Fig. 4.74(b)), showing the interaction of the unsymmetric pi bond with Ti.

Ti is further illustrated in Fig. 4.76, which shows the structure of the 90° -twisted complex (lying about $0.5 \text{ kcal mol}^{-1}$ above the untwisted equilibrium geometry), with significant carbocationic character at the —CH_2 group canted away from the titanium atom. Thus, alkene activation in this species has fundamentally different electronic character from that of, e.g., the titanium insertion complex (4.103) in Section 4.7.4, and corresponds rather to the electrophilic carbocationic formation reaction type of (B) in Table 4.39.

As the alkene continues to approach alignment with the polar metal–carbon bond of the reagent in the untwisted complex, the interaction in Fig. 4.75(b) evolves into the $\sigma_{\text{TiC(d)}}$ bond with the distal alkene carbon (which has switched to become the less cationic alkene center), while the proximal (more cationic) carbon moves closer to the “methide-like”⁶⁰ unit bound to titanium. As the alkene approaches, this methide-like unit can merely reorient its bonding hybrid from the partially cationic metal atom toward the partially cationic C_p to complete the product bond topology. Thus, the flow of charge from alkene to metal that accompanies the donor–acceptor interactions (Fig. 4.75) serves to create the partial cationic vacancy at C_p that eventually induces the CH_3^- moiety to realign its filled n_{C} orbital away from the metal and toward the incoming alkene, completing the carbon–carbon product bond. Because the rearrangement intimately involves all four labeled atoms in Fig. 4.74 (Ti, C_m , C_p , and C_d), the transition state is expected to have pronounced four-center character.

Figure 4.77 displays the transition state (III^\ddagger) between the alkyl–alkene complex **II** and the final product species **III**. In this figure one can see that the methide-like

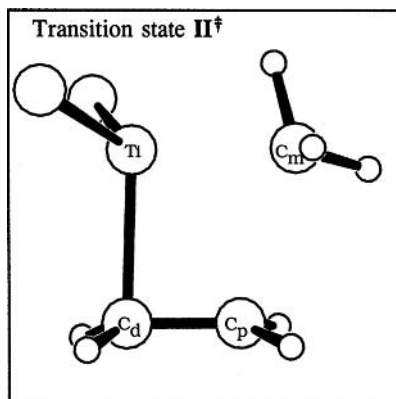


Figure 4.77 The optimized structure of the transition state II^\ddagger for the ethylene-insertion reaction $\text{II} \rightarrow \text{III}$ (4.106), with forward activation energy $\Delta E_f^\ddagger = 6.90$ kcal mol⁻¹ relative to the metal–ethylene complex II .

unit has indeed reoriented itself about half-way between Ti and C_p, directing its bonding hybrid toward the opposite (C_d) apex of the Ti—C_d—C_p—C_m quadrilateral. The natural bond orders of the transition state ($b(\text{Ti}—\text{C}_m) = 0.46$, $b(\text{Ti}—\text{C}_d) = 0.77$, $b(\text{C}_d—\text{C}_p) = 1.14$, $b(\text{C}_p—\text{C}_m) = 0.35$) also indicate that the Ti—C_d—C_p unit is approaching its final (single-bonded) form, while C_m makes approximate “half-bonds” both to Ti and to C_p. The forward activation energy (without zero-point correction) is calculated as 6.90 kcal mol⁻¹, and the entire $\text{II} \rightarrow \text{II}^\ddagger \rightarrow \text{III}$ transition region lies far below the energy of separated reactants ($\text{I} + \text{C}_2\text{H}_4$), so the required activation energy is readily available in the excess energy of the alkyl–alkene complex II . Table 4.42 includes geometrical and charge parameters of the transition state for comparison with those of the equilibrium species.

Figure 4.78 depicts some details of product NBOs and interactions in the product species III . Particularly important are the agostic interactions of Ti with the out-of-plane C—H bonds and the newly formed C—C bond of the terminal methyl group (Figs. 4.78(a) and (b)), which lock the propyl ligand into the highly strained geometry shown in Fig. 4.74(c). The “new” σ_{TiC} bond exhibits strong bending (Fig. 4.78(c)), reflecting the highly activated character of the nascent product species. This high degree of strain in turn helps to surmount the barrier for the ensuing alkene insertion, facilitating further chain propagation.

On the basis of this simple orbital picture, we can also consider the effect of alternative alkene pendant groups R' in the catalytic propagation reaction (4.105). In the case of propylene (R' = CH₃), for example, one can envision two distinct isomers of the alkyl–alkene complex, with either the primary or the secondary alkene carbon atom as the proximal “C_p.” This leads to the alternative primary and

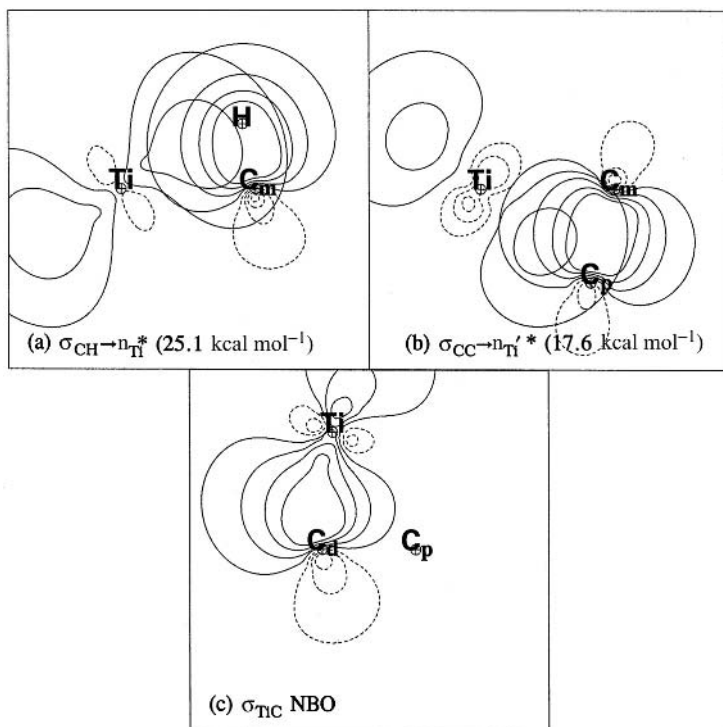
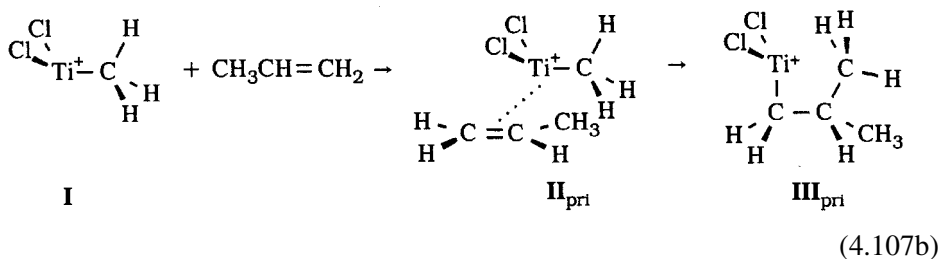
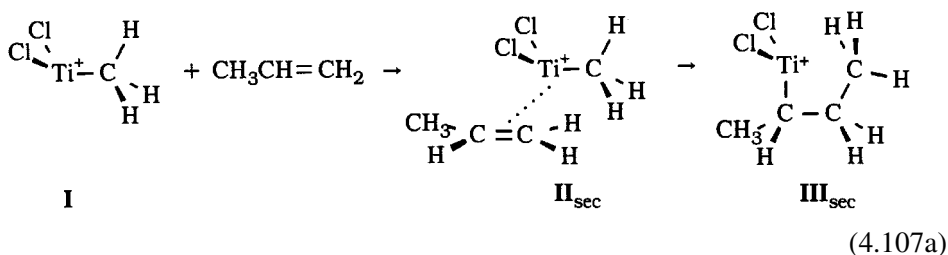


Figure 4.78 Leading agostic interactions involving (a) the C—H bond and (b) the C—C bond of the terminal methyl group, and (c) the bent metal—carbon bond NBO of product **III** (cf. Fig. 4.74(c)).

secondary insertion reactions shown below (analogously to (4.106)):



Understanding the factors controlling primary versus secondary insertion of alkenes is critically important to practical applications, because regioerrors (i.e., occasional secondary insertions in a polymer predominantly formed by primary insertions) can adversely affect relative molecular masses, responsivities to hydrogen, and melting points of polymers.

From the known polarization of the propylene π_{CC} bond *away* from $-\text{CH}_3$ (in accordance with the familiar pi-donor character of methyl substituents), it is easy to predict that $\pi_{CC} \rightarrow n_{\text{Ti}}^*$ interactions will be stronger for II_{sec} than for II_{pri} (because the former has the high-amplitude end of the π_{CC} donor favorably oriented toward the n_{Ti}^* acceptor). In accord with this picture, the leading $\pi_{CC} \rightarrow n_{\text{Ti}}^*$ stabilization (analogously to Fig. 4.75(a)) is $59.3 \text{ kcal mol}^{-1}$ in II_{sec} versus $42.4 \text{ kcal mol}^{-1}$ in II_{pri} . Relative to asymptotic $\text{I} + \text{CH}_3\text{CH}=\text{CH}_2$ reactants, the complex II_{sec} ($-49.2 \text{ kcal mol}^{-1}$) is more than 7 kcal mol^{-1} more stable than II_{pri} ($-42.1 \text{ kcal mol}^{-1}$). The cationic charge of the propylene moiety is also significantly higher in II_{sec} ($+0.364$) than in II_{pri} ($+0.327$), which is consistent with the stronger $\pi_{CC} \rightarrow n_{\text{Ti}}^*$ interactions in the former case.

However, the enhanced stability of II_{sec} is clearly deleterious to formation of the reaction product III_{sec} (relative energy $-47.7 \text{ kcal mol}^{-1}$), because the insertion step (4.107a) is now significantly *endothermic*. In contrast, the primary- C_p reaction (4.107b) to form III_{pri} (relative energy $-45.8 \text{ kcal mol}^{-1}$) remains favorably exothermic. Thus, as is found experimentally, the *primary- C_p* reaction product III_{pri} should be formed in metal-catalyzed polymerization of propylene. (Some catalysts do generate secondary M-alkyls, but the majority of 1-alkene polymerization catalysts appear to bring about propagation by primary insertions.)

Figure 4.79 displays the optimized structures of secondary- C_p (II_{sec}) and primary- C_p (II_{pri}) complexes, and Table 4.43 includes geometrical and charge parameters of these propylene complexes for comparison with those of the corresponding ethylene complex in Table 4.42. The II_{sec} complex can be seen to have smaller Ti- C_p metal-alkene separation (by $\sim 0.1 \text{ \AA}$) and other evidence of tighter metal-alkene binding than that in the II_{pri} complex, in accordance with the donor-acceptor stabilizations discussed above.

Figure 4.80 shows the transition state ($\text{II}_{\text{pri}}^\ddagger$) and final product (III_{pri}) of the actual primary- C_p propylene-insertion reaction (4.107b). Geometrical parameters, charge distributions, and energetics of these species are included in Table 4.43 for comparison with those for the corresponding ethylene reaction in Table 4.42. Compared with the ethylene reaction, reaction with propylene has served to lower the exothermicity (from 7.7 to $3.7 \text{ kcal mol}^{-1}$) and the forward activation energy (from 6.9 to $6.2 \text{ kcal mol}^{-1}$). The propylene transition state (Fig. 4.80(a)) is very similar to the ethylene transition state (Fig. 4.77), except for slight displacement

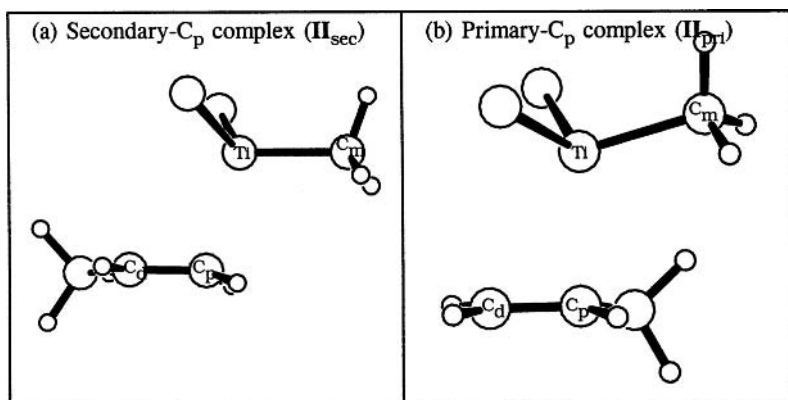


Figure 4.79 Optimized structures of the alternative propylene complexes \mathbf{II}_{sec} and \mathbf{II}_{pri} in insertion reactions (4.107a) and (4.107b).

Table 4.43. *Skeletal geometries and atomic charges of the alternative secondary- C_p (\mathbf{II}_{sec}) and primary- C_p (\mathbf{II}_{pri}) propylene complexes, as well as of the transition state ($\mathbf{II}_{\text{pri}}^\ddagger$) and actual product ($\mathbf{III}_{\text{pri}}$) of the model propylene-polymerization reaction (4.107); cf. Figs. 4.79 and 4.80*

	\mathbf{II}_{sec}	\mathbf{II}_{pri}	$\mathbf{II}_{\text{pri}}^\ddagger$	$\mathbf{III}_{\text{pri}}$
Distance (Å)				
Ti—C _m	1.987	1.994	2.060	2.225
Ti—C _d	2.928	2.732	2.066	1.960
Ti—C _p	2.235	2.336	2.511	2.414
C _d —C _p	1.390	1.374	1.449	1.579
C _p —C _m	3.370	3.487	2.175	1.620
Angle (degrees)				
C _m —Ti—C _p	105.8	107.0	55.8	40.6
C _m —Ti—C _d	132.3	136.1	89.9	80.3
Ti—C _d —C _p	47.4	58.7	89.4	85.3
Ti—C _p —C _d	105.4	91.1	55.4	54.0
C _m —C _p —C _d	138.9	123.2	105.3	115.6
Charge (a.u.)				
Ti	+0.888	+0.835	+0.750	+0.772
C _m	−0.892	−0.877	−0.792	−0.722
C _d	+0.092	−0.244	−0.603	−0.578
C _p	−0.666	−0.319	−0.052	−0.228
ΔE (kcal mol ^{−1}) ^a	−49.2	−42.1	−35.9	−45.8

^a Relative to separated $\mathbf{I} + \text{CH}_3\text{CH}=\text{CH}_2$.

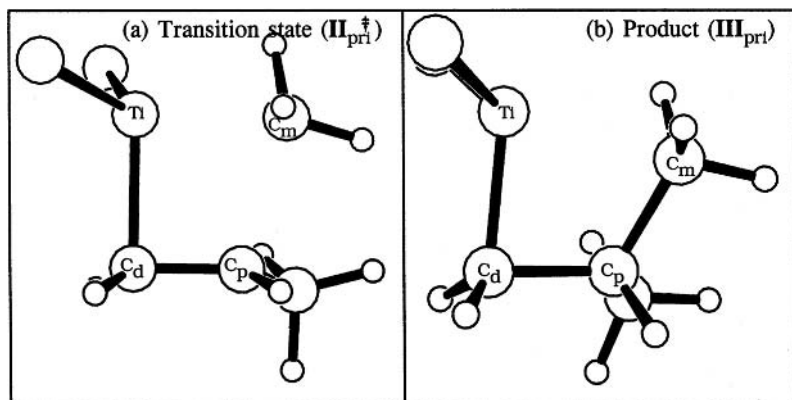


Figure 4.80 Optimized structures of (a) the transition state ($\text{II}_{\text{pri}}^\ddagger$) and (b) the product (III_{pri}) of the model propylene-insertion reaction (4.107b).

of C_m out of the $\text{Ti}-\text{C}-\text{C}_p$ plane (apparently due to steric pressure of the methyl substituent). Thus, the pronounced effect of methyl substitution on the initial carbocationic alkene complex is followed by rather modest changes in the remainder of the potential-energy profile.

In summary, transition-metal-catalyzed alkene-polymerization reactions highlight the metal-induced electrophilic activation of $\text{C}-\text{C}$ π bonds to form carbocation-like alkene complexes. Considerations involving substituent pi-donor or pi-acceptor strength (i.e., tendency toward carbocation formation) will be useful in similarly rationalizing polymerization reactions (4.105) for more general alkenes.

Computations and experimental kinetic isotope effects suggest that the polymerization occurs in two discrete steps:⁶¹ (1) alkene binding to form carbocationic intermediates, followed by (2) migration of an alkide-like group. However, the distinction between this stepwise process and a concerted migratory insertion is subtle. The actual mechanism of catalytic polymerization will depend on the nature of the ligands, counterion, solvent, and other variables. Irrespective of whether the insertion is concerted or stepwise, the orbital interactions are essentially unchanged.

Why are transition metals well suited for catalysis of this process? Certainly the electrophilicity of cationic metal centers is important, as is the relative weakness of transition-metal-carbon bonds. However, similar electrophilicities and bond strengths could be found among main-group cations as well. A key to the effectiveness of Ti catalysts is the presence of *two* metal-based acceptor orbitals. In effect, two such orbitals are needed to choreograph the reversal of net charge flow at the two alkene carbons as the intermediate alkene complex moves through the transition state toward the final product.

4.8 Hyperconjugative effects

Although certain formal parallels between transition-metal hydrides and the “analogous” hydrocarbon species (see, e.g., the discussion surrounding Fig. 4.23) have been noted, it is also important to recognize the profound *differences* between corresponding M_nH_m and C_nH_m compounds. These differences are particularly apparent with reference to hyperconjugative delocalization effects, which have entirely different strengths and patterns (as well as increased basis sensitivity) in transition-metal compared with hydrocarbon species. A small selection of these effects will now be examined.

The strikingly different characteristics of transition-metal hyperconjugative interactions are particularly apparent in their influence on internal rotation barriers. To illustrate, let us first consider “ethane-like” Os_2H_6 , whose optimized staggered and eclipsed conformations (displaying conspicuous deviations from those of ethane) are shown in Fig. 4.81.

While the energy difference between staggered and eclipsed conformers ($15.1 \text{ kcal mol}^{-1}$) is about five *times* that of ethane, Os_2H_6 exhibits the “expected” preference for staggered geometry. One might therefore assume that this preference originates in vicinal $\sigma_{OsH}-\sigma_{OsH}^*$ delocalizations analogous to those in ethane-like molecules (Section 3.4.2), but such interactions are found to be rather *negligible* in Os_2H_6 . Instead, the leading barrier-determining interactions are those depicted in Fig. 4.82, involving vicinal $n_{Os} \rightarrow \sigma_{OsH}^*$ delocalization of metal *lone pairs* into adjacent antibonds. In fact, these interactions are so strong that the geometries are significantly distorted from the idealized ethane-like structure. Furthermore, in the eclipsed geometry the optimal NBO structure actually includes a formal $Os=Os$ double bond! Even in the staggered geometry, which the single best NBO structure depicts as having a single bond between the two Os centers, NRT analysis yields

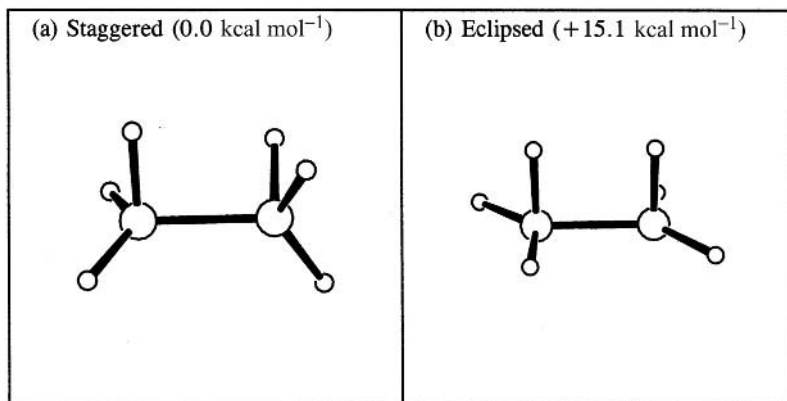


Figure 4.81 Staggered and eclipsed conformers of “ethane-like” Os_2H_6 .

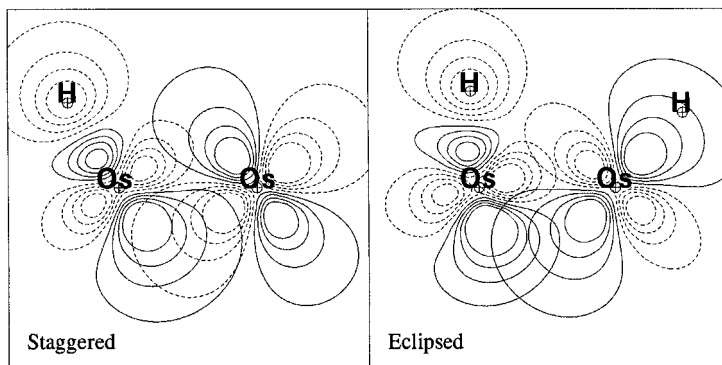


Figure 4.82 Leading vicinal $n_{\text{Os}} \rightarrow \sigma_{\text{OsH}}^*$ donor–acceptor interactions of Os_2H_6 in (a) staggered and (b) eclipsed conformations.

an Os—Os bond order of 1.38. Thus, while vicinal hyperconjugative interactions are indeed responsible for torsional barriers both in ethane (Fig. 3.55) and in Os_2H_6 (Fig. 4.82), the donor–acceptor stabilization in the latter case is *much* stronger due to the unique d-type donor orbitals available to metal atoms.

A still more dramatic example is given by the saturated decahydride of ditungsten, H_5WWH_5 , which has the formal Lewis-like structure



This species contains no valence lone pairs, and so may be considered a “purer” example for comparison with $\text{H}_3\text{C}-\text{CH}_3$. However, an attempt to twist the $-\text{WH}_5$ group about the tungsten–tungsten single bond incurs a torsion barrier of more than 60 kcal mol^{-1} , comparable to the energy of breaking covalent bonds! In this case, the staggered and eclipsed forms are *both* found to be of much higher energy (36.1 and $61.0 \text{ kcal mol}^{-1}$, respectively) than an equilibrium twisted form with reference H—W—W—H dihedral angle $\phi = 76.1^\circ$, as shown in Fig. 4.83.

From the structures in Fig. 4.83 one can readily see that the $-\text{WH}_5$ groups undergo strong rearrangements under “internal rotation,” with varying numbers of hydride bonds that make unusually acute W—W—H bond angles: four in the equilibrium geometry of Fig. 4.83(c), two in the staggered geometry of Fig. 4.83(a), none in the eclipsed geometry of Fig. 4.83(b). Each such acutely bent hydride bond is able to enter into strong $\sigma_{\text{WH}}-\sigma_{\text{WH}}^*$ hyperconjugative interaction with an approximately coplanar obtusely bent hydride antibond, as depicted in Fig. 4.84. As seen in Fig. 4.84, such acutely bent $\sigma_{\text{WH}}-\sigma_{\text{WH}}^*$ interactions are extremely strong (corresponding to partial τ_{HWH} -bridging in the alternative resonance structure

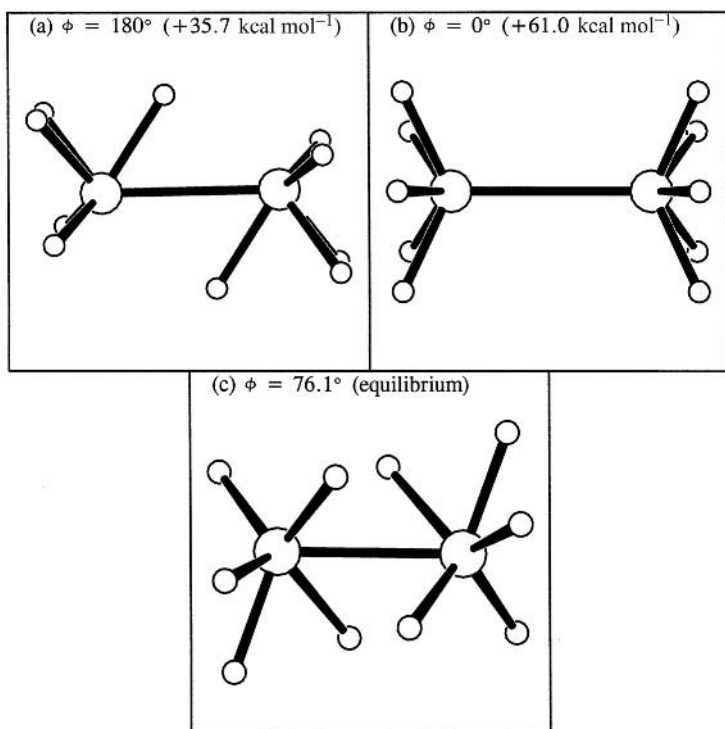


Figure 4.83 Optimized “conformers” of W_2H_{10} , showing (a) staggered ($\phi = 180^\circ$), (b) eclipsed ($\phi = 0^\circ$), and (c) equilibrium ($\phi = 76.1^\circ$) isomers (ϕ is a particular H—W—W—H torsional angle). Note the severe hydride rearrangements that accompany internal rotation.

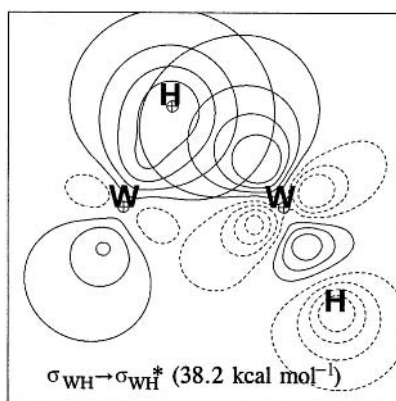


Figure 4.84 The leading vicinal $\sigma_{\text{WH}} - \sigma_{\text{WH}}^*$ interaction in equilibrium W_2H_{10} (Fig. 4.83(c)), involving an acutely bent σ_{WH} bond with an obtusely oriented vicinal σ_{WH}^* antibond in approximately coplanar alignment.

representation), with stabilization energies in the 35–40 kcal mol⁻¹ range. Only in the high-energy eclipsed arrangement (Fig. 4.83(b)) are such acute $\sigma_{\text{WH}}-\sigma_{\text{WH}}^*$ interactions fully prevented by steric repulsions. Indeed, due to the highly distortive strength of acute $\sigma_{\text{WH}}-\sigma_{\text{WH}}^*$ interactions, the concept of a pure “internal rotation” mode (involving more-or-less-fixed —WH₅ torsional groups) becomes problematic, and true parallels with main-group torsional phenomena cannot be drawn.

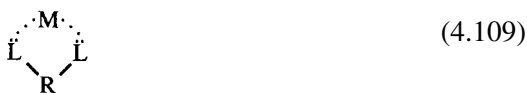
As a general conclusion, we can say that vicinal hyperconjugative interactions in transition-metal species tend to be *much* stronger than those in main-group compounds. Torsional degrees of freedom are therefore much more strongly hindered in metallic species, and the notion of “pure” torsional motion of simple rigid-rotor form lacks physical relevance in this limit.

The differences in hyperconjugative interactions are evidently related to characteristic mechanical properties of metallic versus non-metallic materials. Whereas organic materials typically have soft torsional modes that can accommodate deformations while preserving covalent-bond angles, the corresponding saturated metal hydrides incur strong distortions of skeletal bond angles when metal–metal bonds are twisted. Thus, the latter materials exhibit a tendency toward fractures and brittleness under applied stresses, instead of the rubbery elasticity that is characteristic of organic polymers. However, further discussion of these differences is beyond the scope of this book.

4.9 Multielectron coordination

4.9.1 Polydentate coordination and the chelate effect

The discussion of coordinative metal–ligand bonding in Section 4.5 was implicitly restricted to the simplest type of electron-pair-donor ligand L:, namely a monodentate (two-electron) Lewis base. However, numerous ligands are known to donate multiple electron pairs to a Lewis acid, and hence can participate in polydentate coordination to a transition-metal atom. In the extreme case, such higher-order ligands (termed “chelates”) may coordinate to multiple sites around a metal atom (up to *eight* sites for the ethylenediaminetetraacetate [EDTA] ion), enveloping and sequestering the atom in a complex of high stability. In the present section, we examine simple aspects of bidentate (two-pair) :L—R—L: ligation in metal complexes of the form



Such bidentate chelation is found to be favored over monodentate complexation in many cases, this being the so-called “chelate effect.”

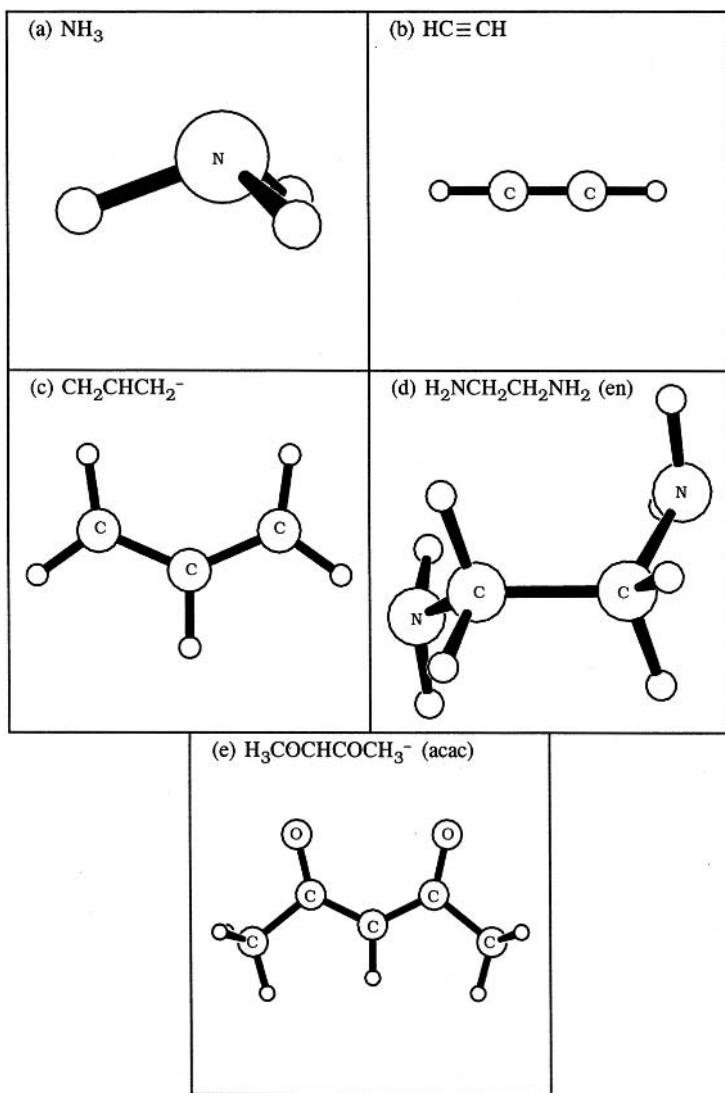


Figure 4.85 (a) Monodentate and (b)–(e) bidentate ligands for $\text{M}(\text{ligand})^+$ complexes.

Figure 4.85 illustrates a variety of the free ligands to be discussed below. The chosen ligands include monodentate ammine (Fig. 4.85(a)) and a variety of neutral and anionic bidentate donors: acetylene (Fig. 4.85(b)), the allyl anion (Fig. 4.85(c)), ethylenediamine (“en”, Fig. 4.85(d)), and the acetylacetonate anion (“acac”, Fig. 4.85(e)). We shall examine these bidentate ligands in complexes with transition-metal ions having one or two vacant valence orbitals, comparing these species with corresponding $\text{M}(\text{NH}_3)_2^+$ diammine species of two free monodentate ligands.

Iridium monocation complexes

Let us first consider the eight-electron Ir^+ ion as a prototype “two-pair-acceptor” species, forming $12e \text{IrL}_2^+$ complexes. Optimized $\text{Ir}(\text{ligand})^+$ structures for the monodentate and bidentate ligands of Fig. 4.85 are shown in Fig. 4.86. As shown

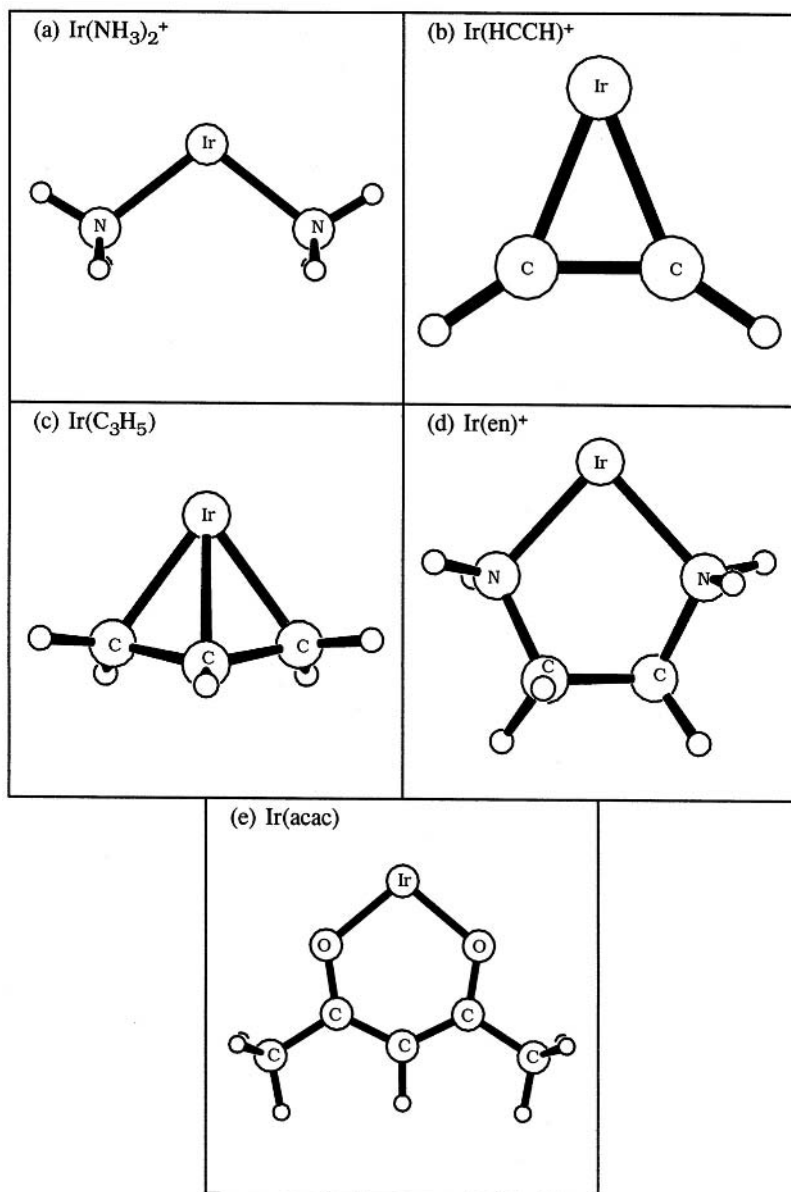


Figure 4.86 Some Ir^+ complexes (see Tables 4.44 and 4.45).

Table 4.44. *Properties of bicoordinate metal–ligand complexes for M = Ir⁺ (see Fig. 4.86): binding energy ΔE and geometrical parameters (bond length R_{ML} and valence angle \angle_{LML})*

	Ligand(s)	Cycle	Symmetry	ΔE (kcal mol ⁻¹)	R_{ML} (Å)	\angle_{LML} (degrees)
(a)	Ammine	—	C _{2v}	159.2	2.032	101.3
(b)	Acetylene	3	C _{2v}	125.4	1.854	43.3
(c)	Allyl anion ^a	4	C _s	362.8	2.036 (2.060)	72.3 (41.5)
(d)	en	5	C ₂	166.9	2.026	84.1
(e)	acac Anion	6	C _{2v}	259.6	1.935	100.0

^a Parenthesized values refer to the middle C atom in the symmetry plane.

in Fig. 4.86, the chosen ligands lead to successively increasing ring sizes with the Ir⁺ ion on going from the three-membered Ir-alkyne (Fig. 4.86(b)) to the six-membered Ir-acac (Fig. 4.86(e)). Some energetic, geometrical, and NBO descriptors of these Ir⁺ complexes are summarized in Tables 4.44 and 4.45. For each complex, Table 4.44 shows the total binding energy (ΔE) (with respect to singlet Ir⁺ and free ligand(s)), point-group symmetry, and metal–ligand coordinative bond length (R_{ML}) and angle (ϕ_{LML}), while Table 4.45 summarizes various NBO descriptors of the complexes, including the metal charge (Q_M), metal hybridization (h_M) and polarization ($\%pol_M$) of the σ_{ML} bond, and the NRT bond order (b_{ML}). These tables provide the basis for overall comparisons of the complexes to be discussed individually below.

Table 4.45. *Properties of bicoordinate metal–ligand complexes for M = Ir⁺ (see Fig. 4.86): metal charge Q_M , bonding hybrid h_M , percentage polarization toward the metal atom ($\%pol_M$), and NRT bond order b_{ML} of the σ_{ML} NBO*

	Ligand(s)	Q_M	h_M	$\%pol_M$	b_{ML}
(a)	Diammine	0.281	sd ^{1.58}	19.9	0.989
(b)	Acetylene	0.568	sd ^{1.26}	45.2	0.906
(c)	Allyl anion ^a	0.056	sd ^{2.52} (sd ^{2.49})	49.1 (53.1)	0.889 (0.783)
(d)	en	0.250	sd ^{1.62}	20.9	0.775
(e)	acac Anion	0.409	sd ^{1.77}	18.9	1.009

^a Parenthesized values refer to the middle C atom in the symmetry plane.

If we consider the “ideal” interhybrid angle for a divalent metal to be 90° (as expected for sd^1 hybridization; Section 4.3.2), we can recognize from the values in Table 4.44 that the \angle_{LML} angles are too small for three- and four-membered rings, about right for five-membered rings, and too large for six-membered rings. (The extremely small \angle_{LML} angle in smaller rings is virtually dictated by the much larger covalent radius of the metal atom.) Thus, on the basis of the hybridization picture we can expect that five-membered rings will tend to be favored relative to other sizes of metal-chelating ring.

By comparing the similar binding energies (159.2 and 166.9 kcal mol⁻¹) for the acyclic diammine (Fig. 4.86(a)) and the corresponding cyclic chelate complex (Fig. 4.86(d)), we can recognize that there is little enthalpic advantage in the chelated complex. Thus, the chelate effect (the strong thermodynamic tendency to favor chelated over non-chelated complexes) is primarily entropic in origin.⁶² In the case of $Ir(en)^+$ chelate, the ligand evidently overcomes an unfavorable torsional barrier to achieve the eclipsed equilibrium chelate geometry. This disadvantage is offset by the favorable (electron-releasing) effect of the alkyl bridging group, which enhances the Lewis-base donor strength of secondary (Fig. 4.86(d)) versus primary (Fig. 4.86(a)) amine groups, as one can judge from the relative metal charges in the two complexes.

The binding energies in Table 4.44 show the expected strong preference for anionic over neutral ligands in complexes of the metal cation. However, the geometries and other properties of these complexes reflect strong *covalency* effects (albeit enhanced by net ionic attraction) that will principally be considered.

Particularly striking in this respect is the evidence in Table 4.44 for strong charge reorganization that accompanies metal–ligand complexation. Compared with the bare ion, Q_M is sharply reduced by transfer of 43%–94% of the metal “cation” charge onto the ligand. This charge transfer is expected to alter the chemical properties of the ligands profoundly, tending to diminish their usual reactivity toward electrophiles but instead increase the vulnerability to nucleophilic attack (the so-called “*Umpolung* effect.”⁶³ Other chemical changes in ligand properties induced by metal complexation will be detailed below.

Gold monocation complexes

For comparison, let us also consider the ten-electron $M(\text{ligand})^+$ complexes for $M^+ = Au^+$ as a prototype “one-pair-acceptor” species. (For convenience, we refer to these species as formal “ Au^+ complexes,” but it should be understood that the actual bonding is far more covalent than the ionic label “ Au^+ ” might seem to suggest.) Optimized structures for the AuL_2^+ complexes are shown in Fig. 4.87 for direct comparison with the Ir^+ complexes in Fig. 4.86. Similarly, the energetic, geometrical, and NBO descriptors of these Au^+ complexes are summarized in

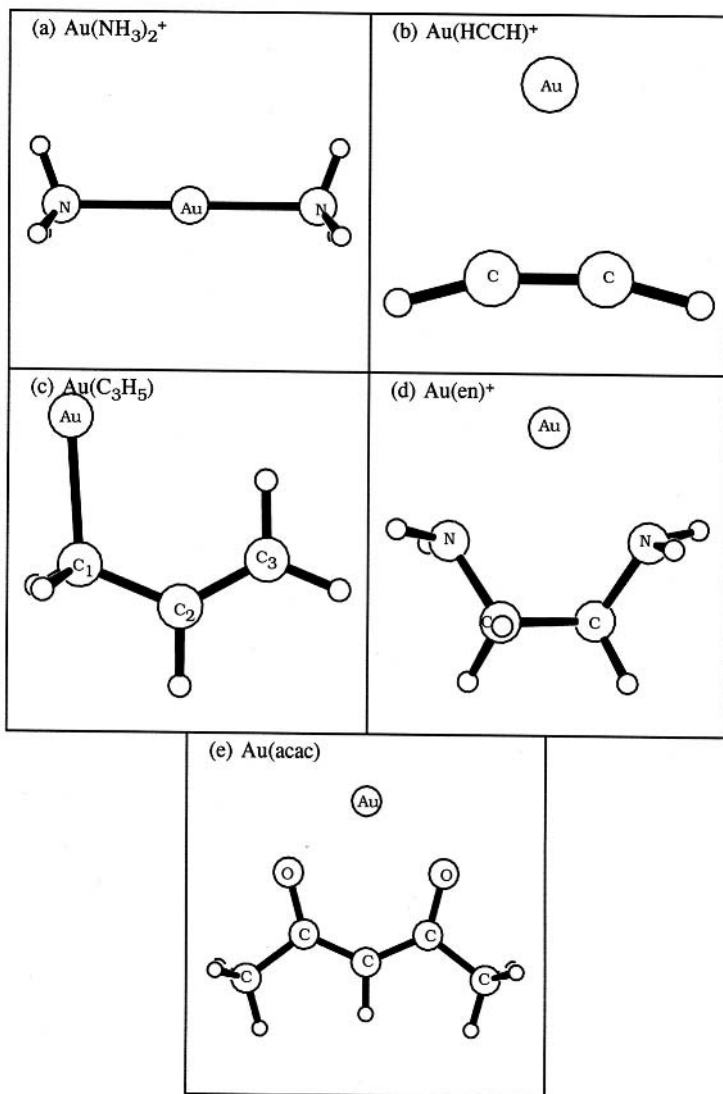


Figure 4.87 Some Au^+ complexes (see Tables 4.46 and 4.47).

Tables 4.46 and 4.47 for direct comparison with the Ir^+ complexes in Tables 4.44 and 4.45.

Comparison of the binding energies ΔE for Ir^+ and Au^+ species shows that the latter are *much* more weakly bound (by roughly 60–80 kcal mol⁻¹) for all the bidentate ligands. This large difference merely reflects the fact that a two-pair donor interacts more effectively with a two-pair acceptor (e.g., Ir^+) than with a one-pair acceptor (e.g., Au^+), a simple consequence of the chemical donor–acceptor

Table 4.46. Similar to Table 4.44, for $M = Au^+$ (see Fig. 4.87)

	Ligand(s)	Cycle	symmetry	$\Delta E(\text{kcal mol}^{-1})$	$R_{ML}(\text{\AA})$	$\angle_{LML}(\text{^\circ})$
(a)	ammine	—	D_{3h}	132.4	2.092	180.0
(b)	Acetylene	3	C_{2v}	53.4	2.184	32.9
(c)	Allyl anion	4	C_s	292.7	2.059 (3.042) (3.370)	(49.2) ^a (26.0) ^b (49.2) ^a
(d)	en	5	C_2	92.8	2.321	80.5
(e)	acac Anion	6	C_{2v}	185.4	2.196	97.5

^a The angle between the bonded and the outermost C atom.

^b The angle between the bonded and the middle C atom.

character of the interaction, thus providing a striking example of the thermodynamic consequence of exceeding the duodectet configuration.

As expected, the weaker binding to Au^+ is also reflected in the geometry and charge distribution of the bidentate complexes. Thus, except for the allyl case (to be discussed below), the metal–ligand distances R_{ML} are $\sim 0.3 \text{ \AA}$ longer for Au^+ than for corresponding Ir^+ complexes. Similarly, the charge transfer from donor to acceptor is considerably less in the weaker Au^+ complexes, an effect that is particularly conspicuous for the ethylenediamine ligand ($\sim 0.4e$ difference in Q_M).

Against this backdrop of weakened bidentate complexation to Au^+ , the relative strength of the $Au(NH_3)_2^+$ diammine complex is quite remarkable. While $Au(NH_3)_2^+$ is indeed somewhat less strongly bound than $Ir(NH_3)_2^+$, the reduction is only about 10%–15%, far less than the corresponding reduction ($\sim 40\%$) for the “analogous” ethylenediamine bidentate ligand. Thus, in this case there is a strong enthalpic *anti-chelate* effect that favors the unchelated $Au(NH_3)_2^+$ over the $Au(en)^+$ chelate complex, opposing the intrinsic entropic advantage of the latter.

Table 4.47. Similar to Table 4.45, for $M = Au^+$ (see Fig. 4.87)

	Ligand(s)	Q_M	h_M	$\%pol_M$	b_{ML}
(a)	Diammine	0.482	(sd ^{0.28})	(16.4)	(0.503) ^a
(b)	Acetylene	0.796	($\sim s$)	(0.0)	(0.13) ^b
(c)	Allyl anion	0.128	sd ^{0.26}	44.6	0.850
(d)	en	0.674	($\sim s$)	(9.3)	(0.39) ^c
(e)	acac Anion	0.710	($\sim s$)	(8.2)	(0.60) ^c

^a 3c/4e N—Au—N hyperbond.

^b No M—L bonds in the leading NBO structure.

^c One M—L bond in the leading NBO structure.

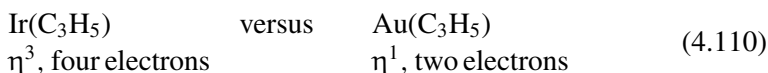
The explanation for this enthalpic anti-chelate effect is apparent from examination of the NBOs. The $\text{Au}(\text{NH}_3)_2^+$ complex exhibits a classic $3c/4e$ ω -bond interaction motif, described in resonance terms as $\text{H}_3\text{N}:\text{M}^+ - \text{NH}_3 \longleftrightarrow \text{H}_3\text{N} - \text{M}^+ : \text{NH}_3$, or in NBO terms as a strong $n_{\text{N}} \rightarrow \sigma_{\text{AuN}}^*$ interaction. The interacting NHOs correspond closely to the Pimentel–Rundle three-center MO picture (Section 3.5) of hypervalent bonding, based on an s-type valence hybrid on gold and the two p-type AOs on nitrogen. As discussed in Sections 3.5 and 4.6, such $n_{\text{N}} \rightarrow \sigma_{\text{AuN}}^*$ stabilizations are characteristically maximized in *linear* arrangements, but this favorable geometry is not achievable in the chelated complex (with $\angle_{\text{NAuN}} = 83^\circ$). Thus, the acyclic diammine can be strongly stabilized by hypervalent ($3c/4e$) resonance, whereas the corresponding stabilization is quenched in the chelate geometry.

4.9.2 Hapticity

The geometries in Figs. 4.86 and 4.87 suggest an important distinction in the multi-center “hapticity” character of ligand attachment to the metal atom. Hapticity refers to the number of atoms in a ligand that are coordinated to the metal. In the Ir^+ diammine complex (Fig. 4.86(a)), the metal attaches to each of two n_{N} donor lone pairs in simple monohapto (one-center, η^1) fashion. However, in the Ir^+ complexes with HCCH or C_3H_5^- the metal attaches to the face of the pi bond or three-center allylic pi system in dihapto (two-center, η^2) or trihapto (three-center, η^3) fashion, respectively. The hapticity label “ η ” therefore conveniently denotes the delocalized n -center character of the donated electron pair(s) and the geometry of the resulting coordination complex.

It is useful to consider the possible formulations of alkyne and allyl bonding to metals in terms of Green’s MLX formalism.⁶⁴ Coordination of an alkyne in a simple dative two-electron fashion is denoted ML, whereas the limit of metallacyclobutene formation is denoted MX_2 . For the allyl ligand, three imaginable coordinations are possible: simple η^1 coordination is denoted MX, but η^3 coordination can encompass both MLX (one σ bond plus a dative alkene coordination) and MX_3 (three M—C σ bonds).

The effects of altered hapticity can be seen by comparing the η^3 , four-electron allyl complex of Ir^+ (Fig. 4.86(c)) with the corresponding complex of Au^+ (Fig. 4.87(c)). Because Au^+ requires only two electrons to complete its formal duodectet, the metal–allyl complexation now involves only the anionic n_{C} center of a *localized* allylic $\text{H}_2\ddot{\text{C}}-\text{CH}=\text{CH}_2$ moiety, and the hapticity “slips” from η^3 to η^1 :



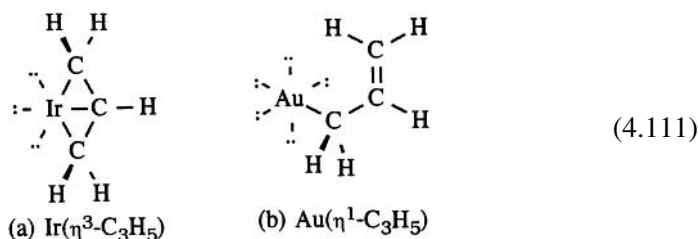
The resulting change in electronic character of the η^3 versus η^1 ligand is reflected in the altered symmetry, bond lengths, and NRT bond orders of allylic C—C bonds,

Table 4.48. Comparison bond lengths R_{AB} and bond orders b_{AB} in η^3 , four-electron ($M = Ir^+$) versus η^1 , two-electron ($M = Au^+$) metal–allyl complexes (see Figs. 4.85(c) and 4.86)

Atoms		M = Ir ⁺ (η^3)		M = Au ⁺ (η^1)	
A	B	R_{AB} (Å)	b_{AB}	R_{AB} (Å)	b_{AB}
C ₁	C ₂	1.451	1.118	1.495	1.044
C ₂	C ₃	1.451	1.118	1.330	1.951
M	C ₁	2.060	0.899	2.059	0.850
M	C ₂	2.036	0.783	3.042	0.001
M	C ₃	2.060	0.899	3.370	0.041

as summarized in Table 4.48. In particular, the NRT bond orders of Au(C₃H₅) correspond closely to the completely localized Au—CH₂—CH=CH₂ description of the η^1 complex.

The leading NBO Lewis structures for the two allyl complexes are



and the corresponding metal–carbon-bond NBOs of each structure are displayed in Fig. 4.88. As indicated, the η^3 -bonded structure (4.111a) has *three* metal–carbon single bonds, two “edge” bonds (Fig. 4.88(a))

$$\sigma_{IrC}(\text{edge}) = 0.70(\text{sd}^{2.52})_{Ir} + 0.71(\text{sp}^{6.73})_C \quad (4.112a)$$

and a central bridge bond (Fig. 4.88(b))

$$\sigma_{IrC}(\text{middle}) = 0.73(\text{sd}^{2.49})_{Ir} + 0.72(\text{sp}^{5.64})_C \quad (4.112b)$$

The C—C bonds are close to being ordinary single bonds ($b_{CC} \simeq 1.12$, $R_{CC} = 1.45$ Å), showing that little vestige of allylic resonance remains (as the geometry in Fig. 4.86(c) makes apparent), and the η^3 species (4.111a) is therefore better characterized as a metallabicyclobutane. For the η^1 complex (4.111b), the single σ_{AuC} bond (Fig. 4.87(c)) has the approximate composition

$$\sigma_{AuC} = 0.67(\text{sd}^{0.26})_{Au} + 0.74(\text{sp}^{5.64})_C \quad (4.112c)$$

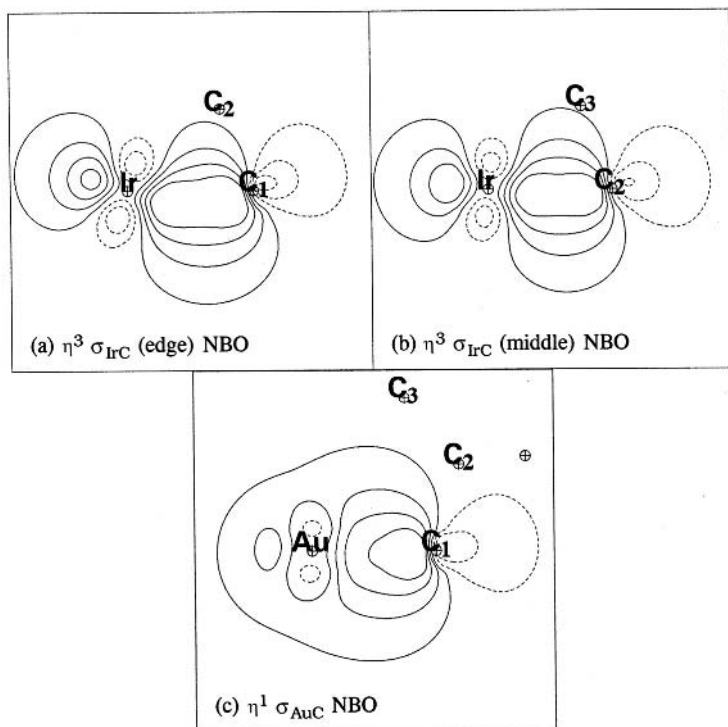


Figure 4.88 Metal–carbon bond NBOs in $M(\text{allyl})$ complexes for (a) edge σ_{IrC} and (b) middle σ_{IrC} bonds of $\text{Ir}(\eta^3\text{-C}_3\text{H}_5)$, and (c) the σ_{AuC} bond of $\text{Au}(\eta^1\text{-C}_3\text{H}_5)$; cf. Fig. 4.87.

In other words, the gold complex is of formal MX type. Thus, the NBO description of the bonding goes considerably beyond the hapticity labels in (4.110) and suggests that only a severely distorted and reorganized form of the “allyl anion” exists in either of these complexes.

Because the localized $\text{H}_2\ddot{\text{C}}\text{—CH=CH}_2$ form of the ligand has the carbanionic n_{C} coordinated directly to the metal acceptor orbital, the η^1 coordination is expected to be strongest on a per-electron-pair basis. The metal charges ($Q_{\text{M}} = +0.126$ [Ir] versus $+0.157$ [Au]) and metal–ligand binding energies ($\Delta E = -312.1$ kcal mol $^{-1}$ [Ir] versus -253.9 kcal mol $^{-1}$ [Au]) also indicate that the *per-pair* donor–acceptor interaction is significantly stronger in the η^1 than in the η^3 allyl complex.

4.9.3 Two- versus four-electron coordination of alkynes

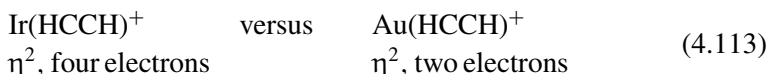
Whereas changes in hapticity are normally required for changes in the number of coordinated electron pairs, acetylene and other triple-bonded ligands exhibit the

Table 4.49. Comparison bond lengths R , angles, and C—C bond orders b_{CC} of $M(\text{HCCH})^+$ complexes ($M = \text{Ir}, \text{Au}$) and free ligand (cf. Figs. 4.86(b) and 4.87(b))

M	R_{MC} (Å)	R_{CC} (Å)	\angle_{HCC} (degrees)	\angle_{CMC} (degrees)	b_{CC}
Ir	1.854	1.367	147.0	43.3	1.43
Au	2.184	1.236	166.4	32.9	2.75
—	—	1.199	180.0	—	3.00

interesting ability of being able to serve as either two- or four-electron donors *without* change in hapticity.⁶⁵

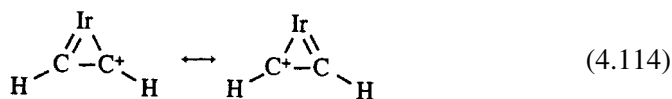
To see the effects of alteration in number of alkyne electron-pair donations, let us compare the four-electron ML_2 $\text{Ir}(\text{HCCH})^+$ complex in Fig. 4.86(b) with the corresponding two-electron ML $\text{Au}(\text{HCCH})^+$ complex,



as shown in Fig. 4.87(c). The gold complex is found to exhibit a triangular η^2 -type structure rather similar to that of the iridium complex, but with significantly greater metal–ligand separation (2.184 versus 1.854 Å), weaker binding (53.4 versus 125.4 kcal mol⁻¹), and diminished ligand→metal charge transfer (0.205*e* versus 0.432*e*). Table 4.49 compares some geometrical features of these complexes, confirming the “less perturbed” character of the HCCH ligand in the η^2 , two-electron Au^+ complex.

The leading NBO Lewis structure of the less strongly bound $\text{Au}(\text{HCCH})^+$ complex does indeed correspond to separated $\text{Au}^+ \cdots \text{HCCH}$ reactants. Figure 4.89 illustrates the principal NBO donor–acceptor interactions for the $\text{Au}(\text{HC}\equiv\text{CH})^+$ complex, which are seen to be rather similar to those for the long-range $\text{Ti}(\text{H}_2\text{C}=\text{CH}_2)$ complex (Fig. 4.72). Thus, for a transition metal with only one vacant valence orbital, acetylene and ethylene π_{CC} bonds function rather similarly as two-electron donors, and the “ η^2 , two-electron complex” description is apt.

However, for the “ η^2 , four-electron” $\text{Ir}(\text{HCCH})^+$ complex, the metal–ligand interactions are so strong that a better NBO description corresponds to either of the two following equivalent metallacyclopropene insertion products:⁶⁶



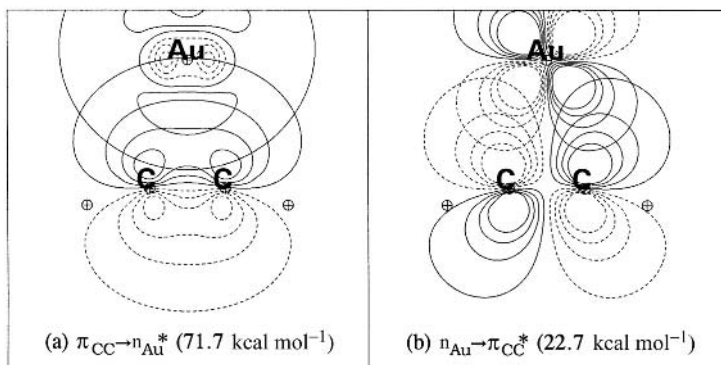


Figure 4.89 The leading NBO donor–acceptor interactions of $[Au \cdots HCCH]^+$ arising from η^2 , two-electron complexation (with stabilization energies in parentheses).

The σ_{IrC} and π_{IrC} bonds of the equilibrium metallacyclopropene have the approximate compositions

$$\sigma_{IrC} = 0.67(sd^{1.26})_{Ir} + 0.74(sp^{3.47})_C \quad (4.115a)$$

$$\pi_{IrC} = 0.94(d)_{Ir} + 0.35(p)_C \quad (4.115b)$$

The overlapping hybrids of the NBOs (4.115) are shown in Fig. 4.90, exhibiting the strong “bond bending” of the sigma skeletal framework.

In summary, the detailed electronic character of dihapto metal–acetylene complexes depends strongly on the Lewis-acceptor capacity of the metal. Formal two-versus four-electron η^2 ligation to a transition metal can lead to breaking of one or both π bonds, dramatically altering the structure and reactivity of the alkynyl

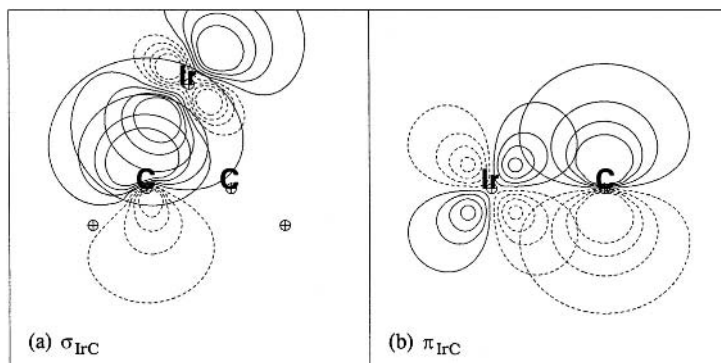
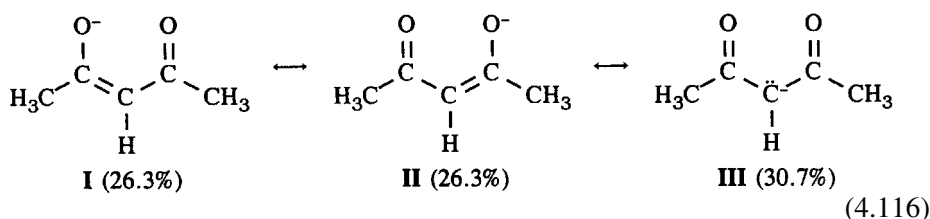


Figure 4.90 Overlapping hybrids for the σ_{IrC} and π_{IrC} NBOs of the $Ir(HCCH)^+$ metallacyclopropene (“ η^2 , four-electron-complex”) species (4.112).

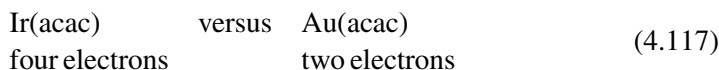
moiety. The Ir^+ complex with acetylene clearly lies toward the MX_2 extreme, whereas the Au^+ complex is best formulated as ML. (Given the strong $\text{M}=\text{C}$ character of $\text{Ir}(\text{HCCH})^+$, afficiandos of the Green labeling scheme would be well justified in classifying the complex as “ MX_3Z ,” with X’s representing the two σ_{MC} bonds and one π_{MC} bond, and Z representing the carbenium ion.) Thus, an oversimplified “ η^2 , four-electron” label fails to do justice to the rich chemistry that can be expected on the basis of the more complete NBO description.

4.9.4 Resonance enhancement

We now turn to the acetylacetonate (acac) ligand, for which resonance of the form



is expected (oxygen lone pairs are not shown), with actual NRT weightings as shown in parentheses. The bidentate $\text{ML}_2\text{Ir}(\text{acac})$ complex in Fig. 4.86(e) can be compared with the corresponding Au^+ complex,



whose optimized structure is shown in Fig. 4.87(e). Comparison geometrical, charge, and bond-order values for free and complexed acetylacetonate ligands are summarized in Table 4.50.

Table 4.50. Comparison bond lengths R , atomic charges Q_{A} , and NRT bond orders b_{AB} of $\text{M}(\text{acac})$ complexes ($\text{M} = \text{Ir}, \text{Au}$) and free acetylacetonate ligand (cf. Figs. 4.86(e) and 4.87(e)); “C(m)” denotes the central methyne carbon atom

M	$R_{\text{CC}(\text{m})}$ (Å)	R_{CO} (Å)	$Q_{\text{C}(\text{m})}$	Q_{O}	$b_{\text{CC}(\text{m})}$	b_{CO}
Ir	1.404	1.293	-0.449	-0.578	1.389	1.465
Au	1.414	1.275	-0.475	-0.724	1.390	1.496
—	1.424	1.242	-0.562	-0.677	1.316	1.696

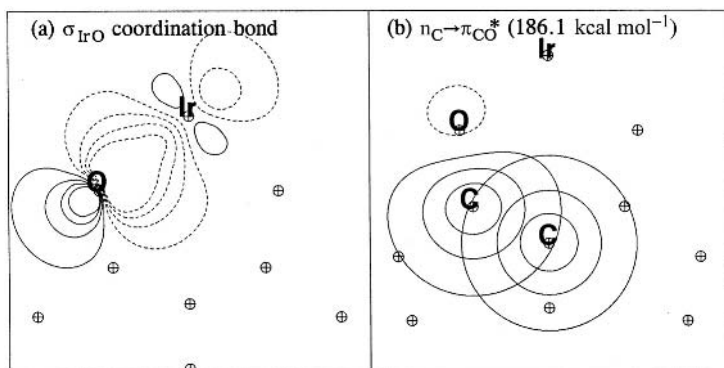
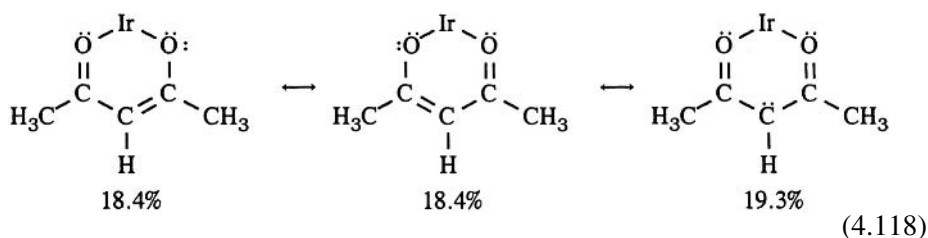


Figure 4.91 Principal NBO interactions in the Ir(acac) complex (cf. Fig. 4.86(e)), showing (a) the sigma-type Ir—O coordination bond ($h_{\text{Ir}} = sd^{1.77}$) and (b) powerful pi-type $n_{\text{C}} \rightarrow \pi_{\text{CO}^*}$ interactions (in a contour plane 1.0 Å above the skeletal sigma plane), with associated second-order stabilization energies shown in parentheses.

As shown in (4.118), the leading resonance structure for the Ir(acac) resonance hybrid,



corresponds to structure **III** of the free ligand (4.116), with the addition of two σ_{IrO} bonds formed by in-plane O lone pairs and Ir $sd^{1.77}$ hybrid orbitals, illustrated in Fig. 4.91(a). Because these bonding interactions lie within the skeletal sigma plane, they do not directly compete with the pi-type acac resonance interactions. The resonance shift from leading **III**-type structure to **I**- and **II**-type structures corresponds to very strong pi-type $n_{\text{C}} \rightarrow \pi_{\text{CO}^*}$ donations, as shown for the metal–ligand complex in Fig. 4.91(b) (essentially similar to the corresponding interaction of the free ligand). In contrast to the allyl anion (Section 4.9.2), for which pi-type resonance is essentially quenched by metal complexation, acac resonance delocalization is geometrically and electronically compatible with complexation to a metal atom. Put simply, acac interacts with Ir in essentially pure sigma fashion, averting destructive interference with the resonance-stabilized pi system.

Indeed, it is evident that acac resonance can shift to *promote* metal–ligand coordination. Thus, by giving increased weight to **I** and **II** at the expense of **III**, the system readjusts to give higher anionic character at each oxygen, thereby increasing the Lewis basicity of the ligand and strengthening metal–ligand coordination. The

numerical values in Table 4.50 show the trend toward increased anionic charge Q_O at oxygen (and reduced anionic character at carbon) that accompanies metal complexation. The NRT bond orders b_{CO} and b_{CC} exhibit the corresponding increase in C—O single-bond character and C=C double-bond character associated with the **III** \rightarrow **I**, **II** resonance shift. The corresponding changes in bond lengths R_{CO} and R_{CC} are also consistent with these bond-order shifts.

One can recognize that such resonance enhancement of donor–acceptor bonding is a rather general phenomenon. Indeed, one can generally expect intramolecular resonance shifts to be strongly *coupled* to intermolecular complexation in such a way that metal coordination promotes ligand resonance shifts (and accompanying structural and charge rearrangements) and vice versa. Such cooperative coupling of intramolecular and intermolecular delocalization is virtually dictated by the overall variational stabilization of the metal–ligand complex.

Even the allyl anion can be seen as an example of resonance-enhanced coordination. As shown in Section 4.9.2, $\eta^1\text{-C}_3\text{H}_5^-$ complexation is accompanied by a shift toward the localized $\text{H}_2\ddot{\text{C}}^- \text{—CH=CH}_2$ resonance structure that places maximum anionic character at the metal-coordinated carbon atom. In effect, the carbanionic lone pair n_C is “shared” between intramolecular $n_C \rightarrow \pi_{CC}^*$ (allylic resonance) and intermolecular $n_C \rightarrow n_M^*$ (metal coordination) delocalizations, and the former can be diminished to promote the latter, if greater overall stabilization of the metal–ligand complex is achieved thereby.

4.9.5 Sandwich complexes

Among the most remarkable examples of higher coordination and hapticity are the metallocene “sandwich complexes” for which E. O. Fischer and G. Wilkinson received the Nobel Prize in 1973.⁶⁷ Well-known prototypes include ferrocene, $\text{Fe}(\text{C}_5\text{H}_5)_2$, and nickelocene, $\text{Ni}(\text{C}_5\text{H}_5)_2$, whose optimized singlet structures are shown in Fig. 4.92. However, analogous “double-decker” and “triple-decker” metal sandwich compounds are known for a variety of transition metals and aromatic ring sizes (C_nH_n , $n = 4\text{–}8$), indicating the great generality of metallocene formation. In particular, $\text{M}(\text{C}_5\text{H}_5)_n$ cyclopentadienyl (Cp) derivatives are now known for *every* main-group and d-block transition metal, as well as for many of the f-block metals.⁶⁸ Thus, the electronic origins of metallocene formation must be manifested in very general features of metal–alkene coordination.

The $\text{Fe}(\text{Cp})_2$ and $\text{Ni}(\text{Cp})_2$ structures in Fig. 4.92 illustrate the important variation in hapticity that often distinguishes $\text{M}(\text{Cp})_2$ complexes for metal atoms of different acceptor characters. Thus, high-symmetry ferrocene (S_{10}) corresponds to highest η^5 hapticity, whereas singlet nickelocene (lowered C_{2v} symmetry) exhibits lower η^3 coordination to each Cp ring. (The crystallographic structure of triplet nickelocene

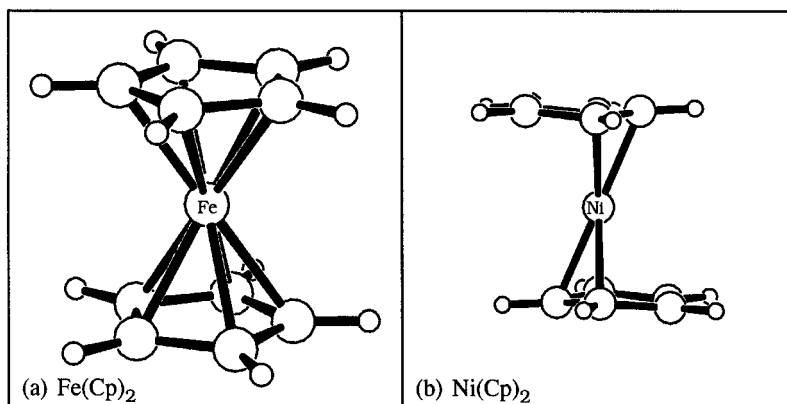
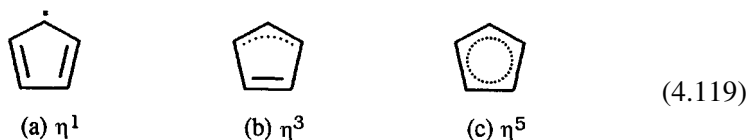


Figure 4.92 $M(\text{cyclopentadienyl})_2$ sandwich complexes for (a) $M = \text{Fe}$ and (b) $M = \text{Ni}$ in their singlet states; see Table 4.51. (Metal-carbon bond sticks have been drawn to assist visualization.)

exhibits a similar, though less pronounced, shift toward η^3 coordination, as will be discussed below.) The change in hapticity evidently reflects strong differences in the electronic and geometrical characteristics of the Cp ring. As shown in Table 4.51, $\text{Fe}(\eta^5\text{-C}_5\text{H}_5)_2$ corresponds to fully delocalized high-symmetry (D_{5h}) aromatic-ring geometry, whereas $\text{Ni}(\eta^3\text{-C}_5\text{H}_5)_2$ corresponds to low-symmetry *localized* Cp geometry, with strong bond alternation and nonplanar *puckering* (by $\sim 8^\circ$) of the uncoordinated C_2H_2 relative to the coordinated allylic C_3H_3 portion of each Cp ring. The dependence of the hapticity and delocalization of Cp on the acceptor character of the coordinated metal somewhat parallels the corresponding situation for allyl ligands discussed in Section 4.9.2.

As a simple conceptual model, let us initially formulate $M(\text{Cp})_2$ with the metal and Cp ligand in their neutral forms: an idealized transition-metal diradical complexed to two cyclopentadienyl radicals. The NBO analysis strongly suggests the accuracy of such a neutral-Cp starting picture, with virtually negligible net charge (e.g., -0.085 in the ferrocene case) on each Cp ring. Each Cp ligand can be visualized in three progressively delocalized forms:



These idealized depictions may be considered as resonance hybrids of (a) one, (b) two, and (c) all five of the equivalent localized structures corresponding to (4.119a). We shall now consider the possible interactions of these distinct “versions” of the Cp ligand with Fe, Ni, and other metal acceptors.

Table 4.51. Comparison geometrical parameters of $M(\text{Cp})_2$ sandwich complexes, $M = {}^1\text{Fe}, {}^{1,3}\text{Ni}$ (see Fig. 4.92)

Parameter	$M = \text{Fe}$	$M = {}^1\text{Ni}$	$M = {}^3\text{Ni}$ (exp. ^c)
Point group	S_{10}	C_2	$\sim S_{10}$
Distances (Å)			
M–ring ^a	1.682	1.784	1.817
M—C	2.074(5)	2.052(1) 2.115(2) 2.460(2)	2.164(1) 2.171(1) 2.191(1) 2.192(1) 2.174(1)
C—C	1.426(5)	1.459(2) 1.422(2) 1.375(1)	1.414(1) 1.417(1) 1.407(1) 1.411(1) 1.415(1)
Angles (degrees)			
\angle_{ccc}	108.0(5)	106.1(1) 107.9(2) 108.4(2)	$108 \pm 0.3(5)$
Ring pucker ^b	0.0	8.0	0.0

^a The shortest distance to the ring: ring midpoint (for Fe and ³Ni) or allyl C···C midpoint (for ¹Ni).

^b The angle between the allyl plane and the residual Cp ring plane.

^c P. Seiler and J. D. Dunitz, *Acta Crystallogr.* **B36**, (1980), 2255.

Green's MLX notation is useful for classifying the three idealized resonance hybrids bound to a metal: (a) $\eta^1 = \text{MX}$; (b) $\eta^3 = \text{MLX}$; and (c) $\eta^5 = \text{ML}_2\text{X}$. Thus, ferrocene can be immediately classified as an 18e ML_4X_2 complex featuring three ω bonds, three lone pairs, and overall sd^2 hybridization, the ω -saturated "ideal pattern" (cf. Section 4.6.1) expected to be of highest possible stability. In contrast, 16e nickelocene is formulated as ML_2X_2 , with two ω bonds, four lone pairs, and nominal sd^1 hybridization, again a highly favored (ω -saturated) pattern for the underlying 12e (MX_2) Lewis-like structure. For both metals, these two MLX formulations are very common. As a further contrast, we may also consider the highly reactive 16e tungstocene, whose analogous formulation is ML_4X_2 with two ω bonds, two ordinary $2c/2e$ bonds, and two lone pairs, corresponding to nominal sd^3 hybridization. Representative examples of such localized metallocene MLX and Lewis-like assignments (including spin multiplicity, formal d count, ω/σ bonds, and nominal hybridization) are shown in Table 4.52.

Table 4.52. A synopsis of localized electronic structures for simple metallocenes in terms of MLX formulation, spin-state multiplicity, nonbonding d electrons (d count) and orbitals (n_d), ordinary ($2c/2e$) and ω ($3c/4e$) bonds, and nominal sd^n hybridization

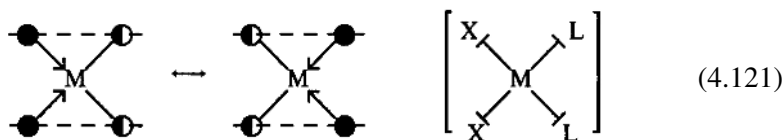
Metallocene	MLX	Spin-state multiplicity	d Count	n_d	Bonds		
					$2c/2e$	ω	sd^n
HfCp ₂	ML ₄ X ₂	1	2	1	4	1	sd ⁴
		3	2	2	2	2	sd ³
WCp ₂	ML ₄ X ₂	1	4	2	2	2	sd ³
		3	4	3	0	3	sd ²
FeCp ₂	ML ₄ X ₂	1	6	3	0	3	sd ²
NiCp ₂	ML ₂ X ₂	1	8	4	0	2	sd ¹
	MLX	3	8	5	0	1	~s

Nickelocenes

As anticipated by its ML₂X₂ formulation (Table 4.52), the computed structure of singlet nickelocene approximates a square-planar di-allylic coordination mode. We can deconstruct each η^3 -Cp to Ni interaction into an electron-pair bond (M—X) with the “radical” carbon and a dative interaction (M—L) with the π_{CC} bond, symbolized as shown below with a half-filled circle (\odot) to represent the radical site and a filled circle (\bullet) to represent the dative π -bond site:



In turn, each M—X bond engages in $3c/4e$ ω bonds with the opposite L donor of the other η^3 -Cp ring. Thus, the following resonance structures summarize the primary bonding pattern, which can be compactly described as two ω bonds:



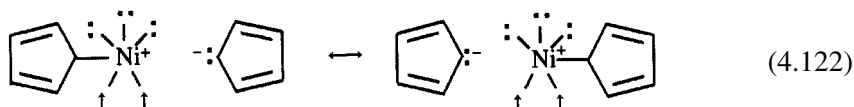
In the resonance representation (4.121), each Cp ring is seen from the edge (dashed lines), with the characteristic L: M—X \longleftrightarrow L—M:X resonance interactions forming the two ω -bonded triads that link the sandwich fragments.

Examined in detail, we expect some deviation from this idealized localized-bonding description. In particular, the allylic LX groups of Cp cannot span the full

90° bond angles of a nominal sd^1 square-planar geometry as depicted in (4.121). As a result, the ω bonds are strained toward a more rectangular geometry, and the bonding hybrids acquire greater d character than the nominal sd^1 hybridization in order to alleviate bond strain.

It should be emphasized that each resonance structure in (4.121) represents only one localized aspect of the complex resonance hybrid. Each ω bond is equivalent to two distinct resonance forms, and the specific Cp depicted in (4.120) is only one of five equivalent resonance forms that could be enumerated for a particular ω_{LMX} triad, rendering a complete NRT resonance description impractical. Although the lowest-energy structure of nickelocene exhibits strong asymmetry in Ni—C distances and a pronounced shift toward η^3 coordination, one can expect the resonance hybrid to exhibit a highly fluxional potential-energy surface. Because the idealized square-planar structure is already strained away from 180° ω_{CNiC} triads and 90° bond angles, the additional strain needed to swap Ni—C bonding interactions among all five carbons should be minimal. Such plasticity likely will result in disordered structures of singlet nickelocene that depend strongly on the environment.

For nickelocene in the triplet state, a very different bonding picture can be expected (Table 4.52). The two unpaired electrons now require *two* nonbonding d orbitals (beyond the three filled d orbitals for the remaining six electrons), so that only a valence s orbital remains for $2c/2e$ bonding. This leads to formal $M-Cp^+$ and nonbonded Cp^- fragments at the $1c/2e$ Lewis-like level, which naturally interact with strong three-center ω -bonding resonance of the form



In terms of the Green formalism, this bonding might be considered as being of “ η^1 -MLX” type (see Table 4.52). This description seems apt to describe the majority-spin (α) electrons and the single remaining ω bond (or “half-bond,” since only α electrons are restricted to the single three-center resonance motif depicted in (4.122)). However, in the minority-spin (β) subset, the bonding motif now corresponds to the “ideal pattern” of three occupied n_d , three Lewis-like two-center coordination bonds, and *three* three-center ω -interactions, a formal ferrocene-like bonding pattern (as discussed below) that can apparently more than compensate for the formal loss of one three-center ω -bonding interaction in the α subset. Thus, a more descriptive Green-like labeling might be formulated as “ $M(LX)_\alpha(L_4X_2)_\beta$,” to indicate that the overall properties of the “spin hybrid” should be intermediate between formal η^1 -MLX(α) and η^5 -ML₄X₂(β) bonding patterns, with the latter “ideal” pattern expected to dominate structurally and energetically. Qualitatively,

one can thereby understand the tendency of triplet nickelocene to adopt a more ferrocene-like (S_{10}) geometry than singlet nickelocene, and, indeed, to become the energetically *preferred* spin multiplicity (due both to increased ω -bonding and to favorable exchange interactions). Further discussion is beyond the scope of this work.

Ferrocene

Ferrocene has long been put forth as a prime example of the general superiority of the delocalized (symmetry-based) MO viewpoint over localized bonding models. Indeed, a complete accounting of all formal resonance structures is cumbersome at best; for example, Pauling presented a valence-bond model of ferrocene that invoked over 500 resonance configurations, a depiction that has been described as “repulsive.”⁶⁹ However, as we shall show, a semi-localized Lewis-like formulation built from lone pairs, ω bonds, and sd^2 bonding hybrids provides a compact and compelling description of the electronic structure of ferrocene that accounts naturally for its extraordinary properties, without recourse to assumptions of a particular symmetry or geometry.

Whereas d^8 Ni selects the rectangular di-allylic hyperbonding pattern in (4.121), d^6 Fe of ferrocene offers an additional vacant d orbital and hence opens up new geometrical possibilities of an additional ω bond. In concert with the three ω bonds and nominal sd^2 (90°) hybridization (Table 4.52), the two Cp ligands are naturally expected to coordinate in η^5 (L_2X) fashion to occupy the six octahedrally arrayed coordination sites of the metal. Visualization of this coordination mode is aided by considering the possible patterns of L-type (filled circles; π_{CC}) and X-type (half-filled circles; radical) sites of L_2X Cp

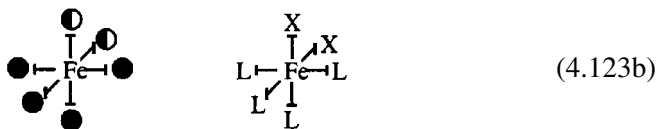


The effective FeL_4X_2 topology is simply an octahedral array of ligands, where each Cp provides the three ligands for one of a pair of parallel triangular faces. The downward view toward one of the octahedron's triangular faces is depicted in (4.123a), showing one possible disposition of L and X apices:



Alternatively, this pattern is shown in two forms in (4.123b) as an orthogonal ω -bonded structure, which can be viewed from the upper left to see the projection

shown in (4.123a):



The pattern shown is only one of a large number of distinct ways of choosing the L/X labels in (4.122) and (4.123), corresponding to the large number of equivalent resonance structures that could be written. However, such an exercise adds little value to the simple picture of ferrocene bonding provided by the localized bonding units.

The hallmark features of ferrocene – parallel Cp rings, η^5 coordination, and extraordinary stability – arise from the general stability and geometrical requirements of transition metals with three ω bonds, three lone pairs, and sd^2 hybridization. At first glance, this topological description of ferrocene may suggest that special stability is associated with the staggered arrangement of the Cp rings, but a more detailed examination reveals that near-linear ω bonds are equally possible in the eclipsed geometry due to the five different arrangements of L/X sites on each Cp ring. Thus, ferrocene exhibits only a modest barrier to rotation of the parallel rings.

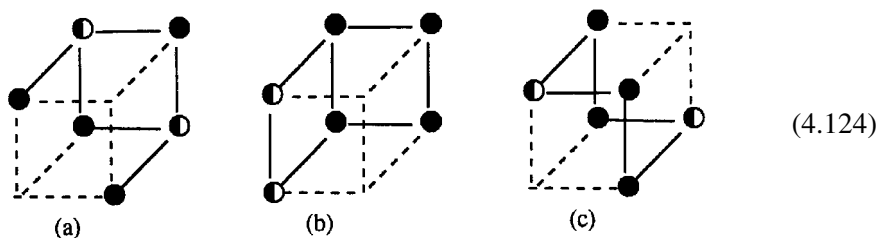
In contrast with ring rotation, deformation of the ferrocene Cp rings from the parallel arrangement must be accompanied by rather steep increases in energy. Owing to the rigid framework of three reinforcing ω -bond axes spanning the body diagonals of the octahedron, bending the rings away from parallel must weaken all $3c/4e$ bonds. Thus, crystallographic structures of ferrocene and its derivatives should exhibit little deviation from parallel ring orientation. In similar spirit, strapping the two rings together with short hydrocarbon or silyl chains to make *ansa* ferrocenes should result in substantial strain.

Tungstenocene

Unlike ferrocene, tungstenocene has only a fleeting existence before inserting into an alkane C—H bond to make the bent metallocene, $Cp_2W(R)H$.⁷⁰ It is therefore instructive to consider how the change from ferrocene to tungstenocene (including changes in spin state) can significantly alter metallocene geometry and reactivity.

Whereas the removal of two valence d electrons on going from nickelocene to ferrocene enables both an increase in ω -bonding and a change in hybridization from sd^1 to sd^2 , the corresponding loss of valence-electron count on going from ferrocene to tungstenocene results in a *decrease* in the number of ω bonds (to two) and a further change in hybridization (to sd^3), as shown in Table 4.52. Therefore $W(\eta^5-Cp)_2$ in its closed-shell singlet state is formulated as ML_4X_2 and comprises two ω bonds, two $2c/2e$ bonds, two lone pairs, and sd^3 hybrids.

We recall (Section 4.3.3) that the lobes of sd^3 hybrids point toward the vertices of a cube. The effective bonding topology of closed-shell singlet tungstenocene can therefore be constructed by considering arrangements of six ligands (two L_2X sets) at the cube corners, leaving two corners vacant. The three possible distinct arrangements are shown in (4.124a)–(4.124c), with the top and bottom faces representing the two Cp rings, and with dashed lines marking vacant vertices:



Of the three structures shown above, the one with three *trans* pairs, namely (4.124c), should be most disfavored, because it has more *trans* arrangements than ω bonds. The two remaining structures both provide two *trans* pairs for the two ω bonds, but (4.124b) requires a distorted Cp geometry (with, e.g., one X—L distance exceeding the other). Thus, only structure (4.124a) is suited to accommodate the electronic requirements of singlet WCp_2 . However, it is easy to recognize that (4.124a) requires the metallocene to be *bent*. (Only the least-favored structure (4.124c) can give linear Cp—W—Cp geometry for the singlet.) Indeed, results of DFT computations of singlet tungstenocenes typically give bent structures with Cp—W—Cp angles near 150° , in reasonable agreement with the idealized sd^3 bonding geometry (Exercise 4.9).

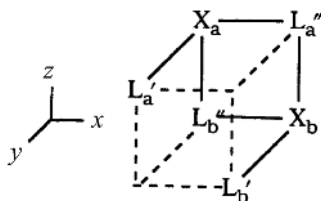
Tungstenocene in the triplet state (and presumably in the diradical singlet state as well) presents a different bonding configuration. Construction of triplet tungstenocene from a closed-shell starting point involves uncoupling one lone pair, thus making one fewer d orbital available for bonding. As a result, triplet tungstenocene must make three ω bonds with sd^2 hybridization, leaving four nonbonding electrons in three d orbitals. Other than the distribution of nonbonding electrons, this bonding description is identical to that of ferrocene. Thus, one expects a strong preference for a “linear” structure for 3WCp_2 . If the molecular axis of the linear structure is taken to be the z axis, the four nonbonding electrons are distributed among the d_{z^2} , d_{xy} , and $d_{x^2-y^2}$ orbitals (the d_{xy} and $d_{x^2-y^2}$ orbitals are essentially equivalent). As we have seen in Section 4.6.6, this electronic situation is subject to Jahn–Teller distortion. However, such distortion should be rather small, due to the strong driving force for maximization of ω -bonding and the nonbonding character of the partially occupied orbitals. In accord with the above expectations, DFT computations of triplet tungstenocene give a linear structure.

In summary, the localized-bond viewpoint provides sophisticated insight into the progression of metallocene structures from η^3 -nickelocene to linear η^5 -ferrocene to linear (triplet) or softly bent (singlet) η^5 -tungstenocene. The localized-bonding formulation is useful despite the obviously high level of delocalization (and daunting number of resonance structures) in these compounds. In contrast with the symmetry-based canonical MO viewpoint, the localized-bond model does not require assumption of an initial structure or symmetry. Instead, the electronic structure and molecular geometry are built from elementary one-center (lone pair), two-center (ordinary σ or π bonds), and three-center (ω bond) orbitals formed from the requisite sd^n hybrids. When it is combined with classification schemes such as Green's MLX categorization, a particularly pleasing, portable, and compact description of transition-metal complexes that is based on general bonding principles that apply equally well to the rest of the periodic table can be achieved.

Example 4.9

Problem: Estimate the θ_{CpWCp} bending angle of singlet tungstenocene from the idealized sd^3 cubic bonding diagram in (4.124a).

Solution: If the two Cp rings are labeled "a" and "b," the disposition of radical (X) and dative (L' and L'') coordination sites may be assigned to the oriented sd^3 cube (4.124a) as shown in the diagram below, with Cp_a as the upper face (+z direction) and Cp_b the lower face (-z direction):



From the central metal atom as the origin, we can construct oriented (unnormalized) vectors pointing toward each occupied corner of the cube with Cartesian (x, y, z) coordinates as shown below:

Apex	x	y	z
\vec{X}_a	-1	-1	+1
\vec{L}'_a	-1	+1	+1
\vec{L}''_a	+1	-1	+1
\vec{X}_b	+1	-1	-1
\vec{L}'_b	+1	+1	-1
\vec{L}''_b	-1	-1	-1

The centroids \vec{a} and \vec{b} of Cp_a and Cp_b rings can therefore be associated with the vectors

$$\begin{aligned}\vec{a} &= \frac{1}{3}(\vec{X}_a + \vec{L}'_a + \vec{L}''_a) = \left(-\frac{1}{3}, -\frac{1}{3}, +1\right) \\ \vec{b} &= \frac{1}{3}(\vec{X}_b + \vec{L}'_b + \vec{L}''_b) = \left(+\frac{1}{3}, -\frac{1}{3}, -1\right)\end{aligned}$$

The angle θ_{ab} between these vectors is determined by the geometrical formula

$$\cos(\theta_{ab}) = \frac{\vec{a} \cdot \vec{b}}{|\vec{a}||\vec{b}|}$$

with $\vec{a} \cdot \vec{b} = -1$, $|\vec{a}| = |\vec{b}| = (11/9)^{1/2}$, leading to

$$\cos(\theta_{ab}) = -9/11 = -0.818$$

or

$$\theta_{ab} = 144.9^\circ$$

Because a Cp ring cannot fully span the three idealized cubic coordination sites, the cube is expected to elongate along the z axis to accommodate the resulting strain. The final Cp—W—Cp angle is therefore expected to be a little greater than this idealized value, in good agreement with observed values ($\sim 150^\circ$).

4.10 Vertical trends in transition-metal bonding

4.10.1 Relativistic effects on hybrids and bonding

The d-block elements span a wide range of atomic numbers from $Z = 21$ (Sc) in the first transition series to $Z = 80$ (Hg) in the third series. Because Z (the number of units of positive charge at the nucleus) governs the kinetic and potential energy of the electrons, high- Z elements are associated with high electronic kinetic energies, corresponding eventually to velocities that approach the speed of light (c). In this limit the non-relativistic Schrödinger equation (Section 1.1) is no longer adequate, but must be corrected for the effects of special relativity (i.e., with Dirac-like treatment). Vertical trends in transition-metal chemistry are therefore intimately related to relativistic corrections to the standard low- Z solutions of the Schrödinger equation.

A convenient measure of the importance of relativistic corrections is given by the ratio ξ_{rel} of Z to the “fine-structure constant” ($e^2/(\hbar c) \simeq 137$, a dimensionless ratio of fundamental physical constants)

$$\xi_{\text{rel}} = \frac{Z}{e^2/(\hbar c)} \simeq \frac{Z}{137} \quad (4.125)$$

For the lighter elements ξ_{rel} is much less than unity (e.g., $\xi_{\text{rel}} = 0.15$ for Sc) and the relativistic corrections are small. However, these corrections become much larger for heavier elements (e.g., $\xi_{\text{rel}} = 0.58$ for Hg, about *four times* larger than for Sc) and the perturbative correction procedure breaks down completely as ξ_{rel} approaches unity. Thus, while relativistic corrections are largely ignorable for the first transition series, these corrections become of dominant chemical importance in later series, particularly after filling of the lanthanide f shell.

Two of the leading relativistic effects can be summarized in physical terms as follows.

- (1) (R1) As a result of the relativistic “speed limit,” inner-shell s electrons (those most exposed to the large nuclear charge) fall into tighter orbits about the nucleus (much as a satellite falls into a lower orbit as its speed is reduced). Relativistic core electrons therefore occupy 1s orbitals of smaller average radius than their non-relativistic counterparts, and higher s orbitals can accordingly contract and lower their energy while still maintaining orthogonality to the shrunken s core.
- (2) (R2) As a result of the inner-s contraction (R1), valence d electrons (occupying “less-penetrating” orbitals of higher angular momentum) are better screened from the nuclear charge. The reduced effective nuclear charge will therefore lead to relativistic valence d orbitals of higher energy and greater diffuseness than their non-relativistic counterparts.

(The relativistic effects (R1) and (R2) can be simulated by adjusting the sizes of *basis functions* used in a standard variational treatment. This adjustment is usually combined with an “effective-core-potential” [ECP] approximation in which inner-shell electrons are replaced by an effective [pseudo] potential of chosen radius. The calculations of this chapter were carried out with such ECP basis sets in order to achieve approximate incorporation of the leading relativistic effects.)

Because the valence s orbital governs apparent atomic size, the relativistic effect (R1) is responsible for the well-known “lanthanide contraction” that sharply alters vertical periodic trends in density, bond lengths, and related properties of post-lanthanide third-series elements, compared with those of the first and second series. The relativistic shifts (R2) in orbital energies and sizes of valence s and d levels also lead to numerous post-lanthanide anomalies in ionization energy and associated electrical, optical, and chemical properties (the high reflectivity of gold, liquidity of mercury, and so forth).⁷¹ In the transition series, the lanthanide contraction most noticeably serves to make third- and second-row elements more *similar* in terms of bond lengths and strengths than would be predicted from the large changes in such properties on going from the first to the second row.

Figure 4.93 illustrates some aspects of the “break” in the vertical trend of atomic orbital energies ϵ_s and ϵ_d for early, middle, and late transition elements, showing the contrasting behavior of third-series versus first- and second-series elements. The

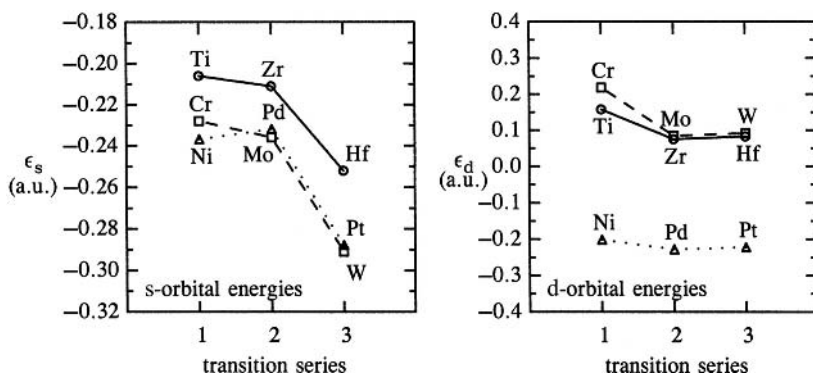


Figure 4.93 Orbital energies for s-type (left) and d-type (right) valence NAOs of group 4 (circles; solid line), group 6 (squares; dashed line), and group 10 (triangles; dotted line) elements of the first three transition series.

solid lines show the vertical trends for the early elements of group 4 (Ti, Zr, Hf) while the dashed lines show corresponding trends for the elements of group 6 (Cr, Mo, W) and the dotted lines represent the late transition elements of group 10 (Ni, Pd, Pt).⁷² Relativistic effects associated with the lanthanide contraction clearly emerge in the large decrease of valence s-orbital energies on moving from the second to the third transition series of all groups. Naturally such effects maximize at the right-hand end of the transition series due to the increase in nuclear charge. The “promotion-energy” gap between s- and d-orbital energies ($\epsilon_s - \epsilon_d$) systematically decreases on moving from the first to the second transition series.⁷³ Thus, s–d promotion and hybridization are much more favored for the second- and third-row transition metals.

Figure 4.94 similarly exhibits the vertical trend in orbital sizes of valence s and d orbitals for group 4 (left), group 6 (middle), and group 10 (right) elements. One can see that the valence d-orbital radius tends to lie well inside that of the valence s orbital for the first two members of the group (this is particularly apparent in Group 10), whereas the d orbital *expands* somewhat in the third member to “match” the s-orbital radius better. This improved match of s- and d-orbital radii naturally tends to favor sd hybridization in the post-lanthanide third series compared with the first two series. Thus, as was already apparent from purely empirical considerations (Section 4.2.1), the chemistry of the third transition series better conforms to the simple Lewis-like hybridization picture than does that of the first two series. Nevertheless, one can judge from Figs. 4.93 and 4.94 that the vertical shifts in s- and d-orbital energies and radii are rather subtle (often less dramatic than corresponding *horizontal* shifts in the same transition series), and relativistic and nuclear-charge effects therefore serve mainly to *modulate* general sd-hybridization tendencies that are present throughout the d block.

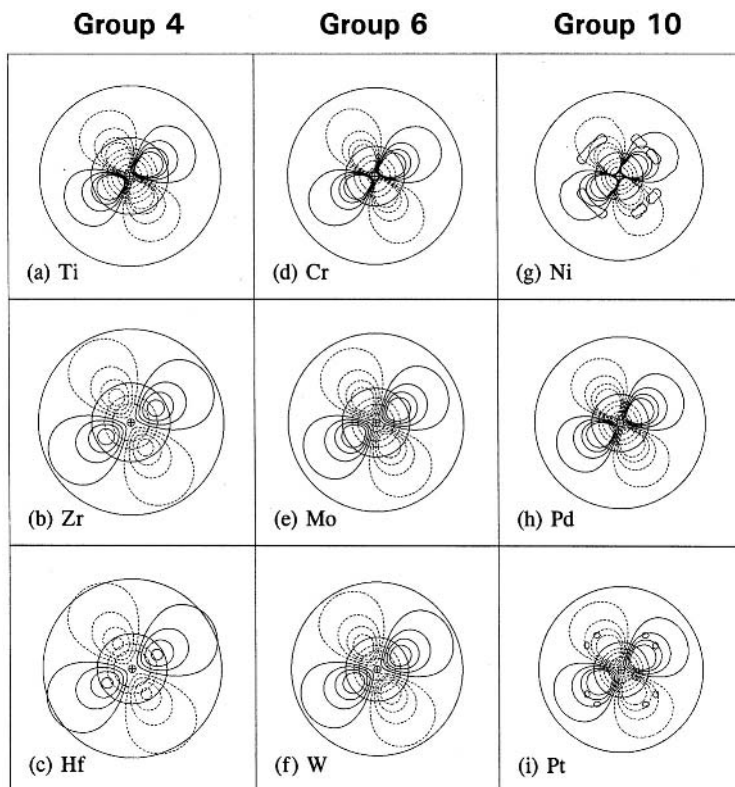


Figure 4.94 Valence *s* and *d* NAOs for series 1–3 transition metals of group 4 (Ti, Zr, Hf), group 6 (Cr, Mo, W), and group 10 (Ni, Pd, Pt).

4.10.2 Vertical trends in covalent bonding

Metal–hydride and metal–alkyl bonding

As prototypes of covalent bonding, let us first consider the σ_{MH} bonds of saturated metal hydrides MH_n for the group 4, 6, and 10 metals considered above. Figure 4.95 illustrates optimized structures of the saturated (but hypovalent) MH_4 tetrahydrides of group 4 (left), the saturated MH_6 hexahydrides of group 6 (middle), and the MH_2 dihydrides of group 10 (right). (Note, however, that CrH_6 is unstable with respect to formation of the molecular- H_2 complex; the structure used here was therefore frozen at the H—M—H bond angles of MoH_6 and the M—H bond lengths [only] were adjusted to reach the lowest energy.) The structural similarities down a column allow the lighter hydrides of each group to be compared with the corresponding third-series hydrides, as previously discussed in Section 4.4.1. Table 4.53 presents numerical comparisons of bond lengths and bond angles in these species. The numerical values verify the strong visual impression from Fig. 4.95

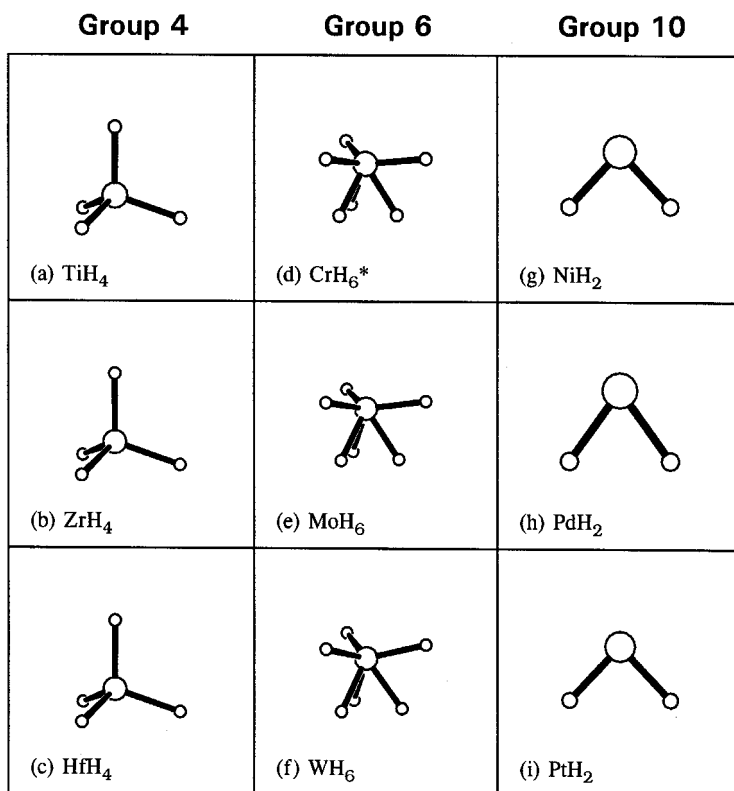


Figure 4.95 Vertical trends in geometry of saturated MH_n hydrides of group 4 (Ti, Zr, Hf), group 6 (Cr, Mo, W), and group 10 (Ni, Pd, Pt). (Note that CrH_6 was optimized with MoH_6 -like angular geometry to prevent formation of the $\text{Cr}(\text{H}_2)_3$ dihydrogen complex.)

of the pronounced vertical similarities within each group (except for CrH_6). Thus (with this exception), the structures in Fig. 4.95 suggest that electronic patterns of hybridization and covalency are qualitatively similar within each group, and that the vertical modulations due to relativistic and other effects are rather subtle.

The computational bond-length variations in Table 4.53 exhibit the expected periodic trends. Most noticeably, third- and second-series elements for groups 4, 6, and 10 exhibit similar bond lengths, i.e., the post-lanthanide “contraction” with respect to the ordinary increase of atomic size with increasing Z .

Subtle variations in relative M—H bond lengths of second- versus third-row transition metals can be traced to anomalies in ground electronic configurations for the metal atoms (Appendix B). Consider group 4, for which all members have s^2d^2 ground electronic configurations, as a reference point. The M—H bond lengths of this group order as $\text{Ti} < \text{Hf} < \text{Zr}$, which is consistent with a strong lanthanide-contraction effect that makes the apparent bonding radius of Hf smaller than that

Table 4.53. Comparison bond lengths R_{MH} and angles θ_{HMH} for saturated metal hydrides of groups 4, 6, and 10 (H' and H'' denote inequivalent short and long hydride bonds in MH_6 compounds)

Species	$R_{MH'}$ (Å)	$R_{MH''}$ (Å)	$\theta_{H'MH'}$ (degrees)	$\theta_{H'MH''}^a$ (degrees)	$\theta_{H''MH''}$ (degrees)
Group 4					
TiH ₄	1.688		109.5		
ZrH ₄	1.850		109.5		
HfH ₄	1.832		109.5		
Group 6					
CrH ₆ ^b	1.516	1.568	61.4	64.1	116.8
MoH ₆	1.642	1.690	61.4	64.1	116.8
WH ₆	1.662	1.707	63.1	67.8	113.5
Group 10					
NiH ₂	1.417		85.4		
PdH ₂	1.522		71.3		
PtH ₂	1.520		86.6		

^a The angle between the closest (“eclipsed”) H' and H'' .

^b Optimized with H—M—H bond angles identical to those of MoH₆ (see the text).

of Zr. In contrast, the MH_6 hydrides of group 6 exhibit a slightly longer computed bond length for the third-row element (W) than for the second-row element (Mo). The failure of the W—H bond to “contract” in the expected way can be understood as a vestige of the underlying s^2d^4 configuration of elemental W versus the s^1d^5 configuration of Mo. Apparently, the added promotional energy needed to create six sd^5 hybrid orbitals at W (which is not required for the s^1d^5 configuration at Mo) results in an “uncontracted” bond. This does not mean that the relativistic effects associated with the transition from the second to third transition series are absent; rather it indicates that the effects act to increase the W bond length by favoring the s^2d^4 configuration over the s^1d^5 configuration. (Other expected consequences of the lanthanide contraction are clearly apparent in elemental properties of W and Mo such as the larger ionization energy of W.)

Similarly, the molecular shapes of group 10 dihydrides exhibit strong perturbations that correlate with atomic ground-state configurations. Among this collection of MH_2 dihydrides, PdH₂ clearly is the outlier with its strongly acute H—M—H angle. This structural deviation of the Pd complex correlates with the d^{10} atomic ground-state configuration of Pd, which is “unpromoted” relative to the Ni (s^2d^8) and Pt (s^1d^9) ground states.

Further details of vertical hybridization and covalency trends are presented in the NBO descriptors of Table 4.54. Ignoring for the moment the exceptional case

Table 4.54. The NBO descriptors of group 4, 6, and 10 metal hydrides, showing percentage accuracies of NBO Lewis structures ($\% \rho_L$), metal charges (Q_M), and metal hybrids (h_M) and percentage polarization ($\% \text{pol}_M$) of σ_{MH} NBOs (primes denote longer M—H bonds)

Species	$\% \rho_L$	Q_M	h_M	$\% \text{pol}_M$	h_M'	$\% \text{pol}_M'$
Group 4						
TiH ₄	99.71	+1.232	sd ^{2.96}	34.7	—	—
ZrH ₄	99.97	+1.571	sd ^{2.95}	30.5	—	—
HfH ₄	99.64	+1.789	sd ^{2.93}	27.6	—	—
Group 6						
CrH ₆ ^a	93.01	-0.106	sd ^{5.56}	54.6	sd ^{4.44}	48.2
MoH ₆	99.02	+0.047	sd ^{5.37}	53.3	sd ^{4.65}	46.6
WH ₆	99.56	+0.481	sd ^{6.26}	49.8	sd ^{4.08}	42.4
Group 10						
NiH ₂	99.87	+0.211	sd ^{1.07}	44.6	—	—
PdH ₂	99.47	+0.049	sd ^{1.07}	49.1	—	—
PtH ₂	99.88	-0.143	sd ^{1.21}	54.2	—	—

^a Optimized with H—M—H bond angles identical to those of MoH₆ (see the text).

of CrH₆, we can recognize that all these species are well described ($>99\% \rho_L$) by the idealized Lewis-like picture, but the third series is indeed “best” in this respect. The average hybridization conforms closely to the expected sd^{n-1} for all the MH_n species, and the average covalency is uniformly high (within $\pm 5\%$ of idealized $50\% \text{pol}_M$ for non-hypovalent species). Thus, the idealized Lewis-like picture of covalent metal–hydride bonding retains its general accuracy throughout the vertical group, *enhanced* (if anything) by lanthanide contraction.

The most striking vertical trend concerns the metal–hydride bond strengths, as summarized in Table 4.55. We define the first M—H bond strength ($\Delta E_{MH(1)}$) for each species as the energy needed to break the first M—H bond:

$$\Delta E_{MH(1)} = |E(\text{MH}_n) - [E(\text{MH}_{n-1}) + E(\text{H})]| \quad (4.126)$$

As shown in Table 4.55, this quantity *increases* going down the periodic column in each group, a trend that is known to hold generally throughout the d-block elements. This d-block trend is in contrast to the corresponding main-group trend for bond strengths to *diminish* down a periodic column.

The vertical trend in d-block bond energies can be rationalized in terms of the relative sizes of s and d valence orbitals. As shown in Fig. 4.94, the d orbitals typically are contracted to lie *inside* the valence s orbital, but this disparity diminishes on going down a column as the d orbitals grow in size. This growth is physically

Table 4.55. First M—H bond dissociation energies $\Delta E_{\text{MH}(1)}$ for group 4, 6, and 10 metal hydrides

Series	Group 4		Group 6		Group 10	
	M	$\Delta E_{\text{MH}(1)}$	M	$\Delta E_{\text{MH}(1)}$	M	$\Delta E_{\text{MH}(1)}$
1	Ti	62.3	Cr	48.0 ^a	Ni	51.4
2	Zr	74.3	Mo	65.4	Pd	64.2
3	Hf	81.6	W	67.7	Pt	81.0

^a CrH₆ and CrH₅ were optimized at the H—M—H bond angles of MoH₆ and MoH₅ (see the text).

attributable to (1) d-core steric repulsion, which sharply increases the radius of 4d and higher *nd* shells relative to the initial 3d shell; and (2) the relativistic screening effect (Section 4.10.1), which further expands *nd* relative to the (*n* + 1)*s* radius for higher *n*.

As a result of this vertical d-shell expansion, the outer lobe of the metal $h_{\text{M}}(sd^{n-1})$ hybrid extends to greater radial distance from the core boundary (roughly, the first negative contour of the *s* orbital in Fig. 4.94), and therefore more effectively overlaps with the incoming h_{H} orbital. Figure 4.96 shows contour (left) and radial-profile (right) plots of the interactions of h_{M} and h_{H} for each σ_{MH} of the group 10 dihydrides. A convenient measure of the “effectiveness” of the interaction is given by the off-diagonal $\langle h_{\text{M}} | \hat{F} | h_{\text{H}} \rangle$ Fock-matrix element between the hybrids,⁷⁴ as shown in Fig. 4.96. As the radial profiles in Fig. 4.96 show most clearly, the bonding lobe of the h_{M} hybrid for Ni is too contracted to match that of the incoming h_{H} orbital (which is prevented from penetrating into the metal core region) effectively. However, the metal bonding lobe gradually spreads to larger radial distance for Pd and Pt, and the two hybrid maxima come into improved congruence, as reflected in the increased magnitude of $\langle h_{\text{M}} | \hat{F} | h_{\text{H}} \rangle$. Because the size-mismatch between the *sd* and *sp* angular components of bonding hybrids has the *opposite* sense for d-block and p-block elements, the general vertical trend in bonding effectiveness is also opposite in the two blocks.

The influences of ground-state *atomic* configurations and promotional effects are again brought to light in the bond-dissociation-energy trends. Recall (Appendix B) that W has s^2d^4 whereas Mo has s^1d^9 atomic configuration. The built-in promotional-energy penalty of WH₆ results in an unexpectedly weak W—H bond dissociation energy, which is nearly equal to that of MoH₆ rather than following the trend of group 4 and being significantly stronger. For the group 10 dihydrides, the bond dissociation energy of Pd (d^{10} atomic configuration) is also weakened by ~ 17 kcal mol⁻¹ compared with that of Pt (s^1d^9 configuration).

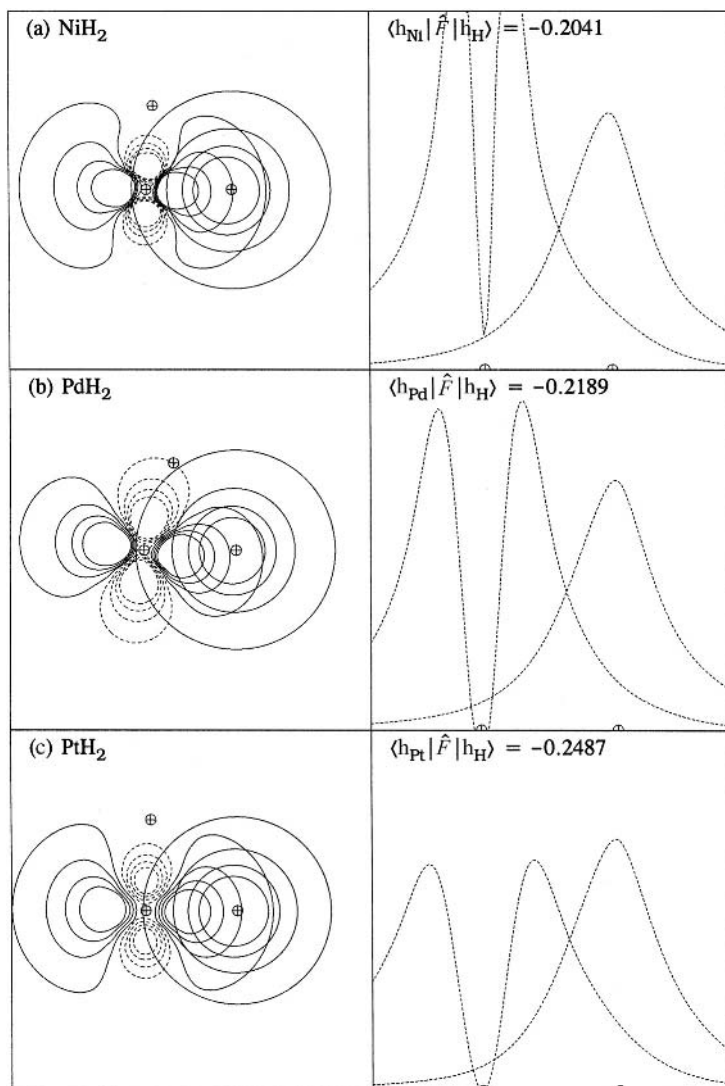


Figure 4.96 Contour plots (left) and radial-profile plots (right) of overlapping h_M and h_H NHOs of σ_{MH} bonds for group 10 dihydrides (NiH_2 , PdH_2 , and PtH_2). Numerical $\langle h_M | \hat{F} | h_H \rangle$ Fock-matrix interaction elements are shown for each case.

For comparison, we can consider the corresponding metal–methyl (M–Me) bond energies in analogous MH_nMe species as representative of general metal–alkyl bonding trends. Table 4.56 summarizes the statistical distributions (means and standard deviations) of bond dissociation energies (BDEs) for M–H and M–Me bonds throughout the three transition-metal series. As shown in Table 4.56, M–Me bond energies tend to track the corresponding M–H values. Although

Table 4.56. *Statistical means and standard deviations (SD) for bond dissociation energies (BDEs) of M—H and M—Me bonds of saturated MH_nX (X = H, Me) transition-metal complexes from the first three series of the d block*

Series	M—H BDE (kcal mol ⁻¹)		M—Me BDE (kcal mol ⁻¹)	
	Mean	SD	Mean	SD
1 (Sc—Cu)	54.2	8.6	49.7	8.2
2 (Y—Ag)	66.0	6.9	57.1	9.3
3 (La—Au)	72.8	7.4	67.0	7.0

the BDEs exhibit a degree of overall similarity, the statistical variations appear too large to justify any presumed “constant-BDE” value. Salient features of Table 4.56 include (1) the uniformly high bond energies associated with the third transition series, (2) conspicuously lower bond energies for the first transition series, and (3) generally greater strengths of M—H bonds compared with M—Me bonds. The last feature is in agreement with available empirical values. However, experimental bond-dissociation enthalpies for transition-metal species are rather sparse and difficult to obtain. In the future it is likely that computed bond energies such as those summarized in Table 4.56 will play a prominent role in developing a more fundamental understanding of metal–ligand interactions.

Within the overall statistical comparisons between series, as summarized in Table 4.56, the individual BDEs reflect significant variations along each periodic row, as shown both for M—Me and for M—H bonds in Fig. 4.97. It can be seen that bonds to the earlier transition metals tend to be stronger than those to the later transition metals (particularly for the first two rows), due to the higher ionic character in the M—H and M—Me bonds. Prominent features of the M—H bond energies discussed above (e.g., Tables 4.53–4.55 and surrounding text) are mirrored in the corresponding M—Me values. For example, compared with the general trendline in Fig. 4.97, the Pd—Me bond is found to be conspicuously weak. This effect can be traced to the d¹⁰ ground configuration of Pd; as bonds are removed from divalent Pd complexes, the original “cost” of promotion from the atomic d¹⁰ to the molecular s¹d⁹ configuration is “recovered,” thus lessening the energy required to break the bond.

One can see more generally that irregular behavior in Fig. 4.97 tends to be concentrated near groups 5 and 6, a region where configurational anomalies (s¹dⁿ versus s²dⁿ⁻¹) are rather common. However, an additional complication of this region arises from the occurrence of sd⁴ hybridization, in either the pre- or the post-dissociation complex; recall (Section 4.3.3) that *no* molecular geometry can

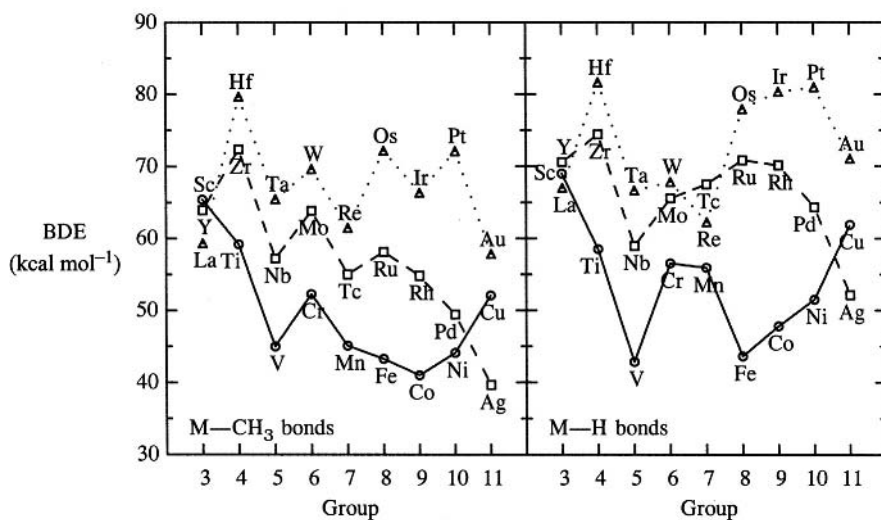


Figure 4.97 Periodic trends in bond dissociation energies (BDE) for M—CH₃ bonds (left) and M—H bonds (right) of saturated MH_nX (X = CH₃, H) compounds of row 1 (circles, solid line), row 2 (squares, dashed line), and row 3 (triangles, dotted line) of the d block. (For these comparisons [only], all calculations were carried out at lower B3LYP/LANL2DZ level.)

strainlessly accommodate the idealized bond angles of sd^4 hybridization. As a result, the structures of this region tend to be rather plastic, making the location of the global minimum structure difficult to establish, and possibly leading to unusual environmental sensitivity or disorder in experimental structures.

Metal–metal bonding

Whereas M—H bonds closely approximate the limit of idealized metal sigma bonding (due to the extreme simplicity of H as a bonding partner), corresponding metal–metal bonds often exhibit bewildering complexity, due to the much greater variety of donor–acceptor interactions available to each metal atom. Thus, the idealized Lewis-like picture often breaks down (or is only one of many alternative resonance structures contributing to the electronic distribution) and vertical trends in metal–metal bonding become increasingly “irregular” compared with those for metal–hydride bonding. In the present section we examine a few representative vertical bonding trends in metal–metal single- and multiple-bonding of group 6 and 10 transition metals for comparison with the corresponding metal–hydride bonding patterns discussed above.

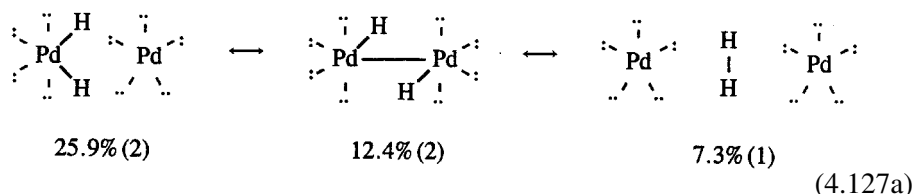
Table 4.57 summarizes geometrical and NBO descriptors of multiple-bonded HMMH compounds of groups 6 and 10 for ensuing discussion. These include metal–metal bond lengths (R_{MM}) and M—M—H angles (θ_{MMH}), metal charge

Table 4.57. Geometrical and NBO descriptors of multiple-bonded HMMH compounds of groups 6 and 10 (see Fig. 4.98)

Species	R_{MM} (Å)	θ_{MMH} (degrees)	Q_M	$\% \rho_L$	b_{MM}	NEC	DE_{MM} (kcal mol ⁻¹)
Group 6							
HCrCrH	1.642	88.6	+0.376	99.16	4.96	$s^{0.60}d^{5.03}$	-58.5
HMoMoH	2.025	90.8	+0.260	99.65	4.92	$s^{0.70}d^{5.06}$	51.3
HWWH	2.098	92.9	+0.229	99.87	4.96	$s^{0.87}d^{4.91}$	80.1
Group 10							
HNiNiH	2.186	84.2	+0.222	98.61	0.92	$s^{0.59}d^{9.18}$	12.9
HPdPdH	2.737	35.4	+0.146	98.85	0.53	$s^{0.23}d^{9.62}$	52.3
HPtPtH	1.592	94.9	-0.056	99.17	0.96	$s^{0.90}d^{9.15}$	49.3

(Q_M), percentage accuracy of the leading NBO Lewis structure ($\% \rho_L$), NRT metal–metal bond order (b_{MM}), NAO valence-electron configuration of the metal centers (natural electron configuration, NEC), and the energy (DE_{MM}) required to dissociate the metal–metal bonding into two MH fragments (of sextet multiplicity for group 6 or doublet multiplicity for group 10).

Vertical irregularities in metal–metal bonding are already apparent in the simplest “single-bonded” HMMH dihydrides of group 10 dimetallic species. Figure 4.98 displays optimized structures for the three M_2H_2 species ($M = Ni, Pd, Pt$; right-hand panels), showing that particularly the Pd member differs significantly from the Pt member previously considered (Table 4.54). Whereas the HNiNiH and HPtPtH structures are structurally analogous and show evidence of only slight distortions from idealized sd^1 hybrid forms (namely the slightly acute M–M–H angles of HNiNiH and the twisted 107° dihedral angle of HPtPtH, due to secondary geminal and vicinal interactions), the structure of Pd_2H_2 is radically different. The di-bridged C_{2v} structure is slightly folded (dihedral HPdPdH = 168.4°) and highly delocalized. The “expected” H–Pd–Pd–H single-bonded form is only a minor resonance structure of the full NRT description, which has leading contributions such as



The resonance-averaged NRT bond orders are

$$b_{PdPd} = 0.53, \quad b_{PdH} = 0.59, \quad b_{HH} = 0.27 \quad (4.127b)$$

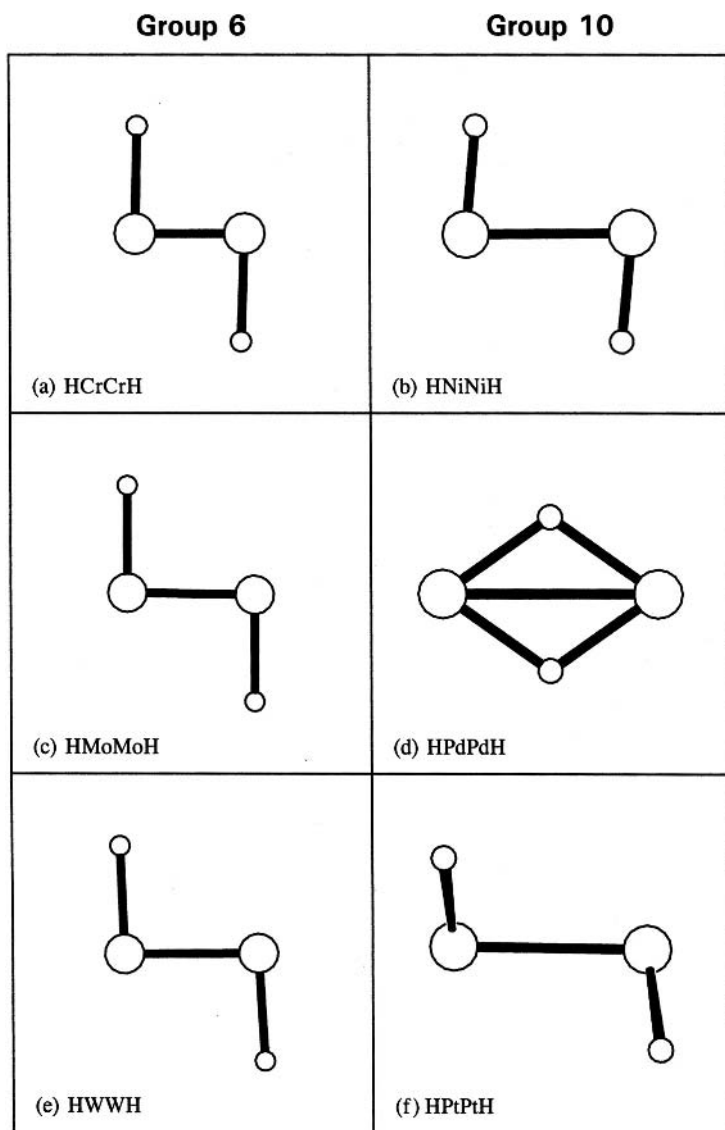


Figure 4.98 Optimized structures of M_2H_2 compounds of group 6 (Cr, Mo, W) and group 10 (Ni, Pd, Pt) transition metals.

showing that a substantial amount of Pd—Pd + H_2 bonding character is also present in this species, despite the 1.95-Å separation of the two H atoms.

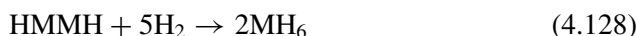
The distinction between Pd compounds and those of Ni and Pt is also evident in the NAO valence configurations of metal atoms in the three final HMMH species of Table 4.57. The values show that Ni and Pt have more nearly the promoted s^1d^9 configuration for hybridized bonding, whereas Pd is more nearly the unhybridized

s^0d^{10} configuration.⁷⁵ As we have seen before, the weakened role of sd hybridization in HPdPdH is evident in the atomic ground-state d^{10} configuration of Pd. The irregular vertical trend in bonding could thus be attributed to the periodic effects on the s–d promotion gap for group 10 metals.

We can also consider the opposite limit of high multiple metal–metal bonding in the HMMH compounds of group 6. Optimized structures of these species are shown in Fig. 4.98 (left-hand panels) and selected geometrical and NBO descriptors are summarized in the first three rows of Table 4.57. As can be seen, the structures and NBO descriptors of group 6 HMMH species are fairly uniform and follow expected periodic trends. Both Cr–Cr and Mo–Mo interactions exhibit the expected quintuply bonded structure; as shown in Fig. 4.99, the σ_{MM} , π_{MM} , and δ_{MM} bonds are quite analogous to those of HWWH (Fig. 4.24). The much shorter Cr–Cr distance, compared with Mo–Mo and W–W distances, largely follows the trends seen in M–H bond lengths. Nuances attributable to periodic effects of metal-atom configuration are also apparent, giving rise to slightly longer bonds at W and higher s character in the NAO metal-atom valence configuration.

The energy (DE_{MM}) for dissociating each of the M–M quintuple bonds into sextet MH fragments is a somewhat misleading measure of “bond strength,” for although the apparent vertical M–M dissociation energy tends to increase with increasing atomic number, dissociation of HCrCrH is computed to be highly exothermic! The origin of this behavior lies in the very strong exchange interactions of the MH sextet fragments. Exchange interactions among the five aligned spins of each MH fragment create substantial stabilization relative to the completely coupled state of the HMMH dimer, particularly for the compacted 3d orbitals of Cr. Combined with the expected weaker bonds of a first-row metal, this leads to a net thermodynamic driving force toward dissociation of the five Cr–Cr bonds. Nevertheless, the quintuply bonded HCrCrH species is indeed computed to be a metastable local equilibrium species.

As an improved metric of M–M quintuple-bond strength, let us instead consider the energetics of hydrogenation of HMMH to form two MH_6 metal hydrides,



an “isodesmic” reaction that removes the strong dependence on differential exchange interactions. For group 6 metals we calculate the heats of hydrogenation in (4.128) to be + 62.5 kcal mol^{−1} for Cr, +1.7 kcal mol^{−1} for Mo, and −52.5 kcal mol^{−1} for W. Thus, relative to making ten M–H bonds, the formation of M–M quintuple bonds is *most* favorable for Cr, the metal with shortest M–M distance and weakest M–H bonds (note, however, that these estimates are

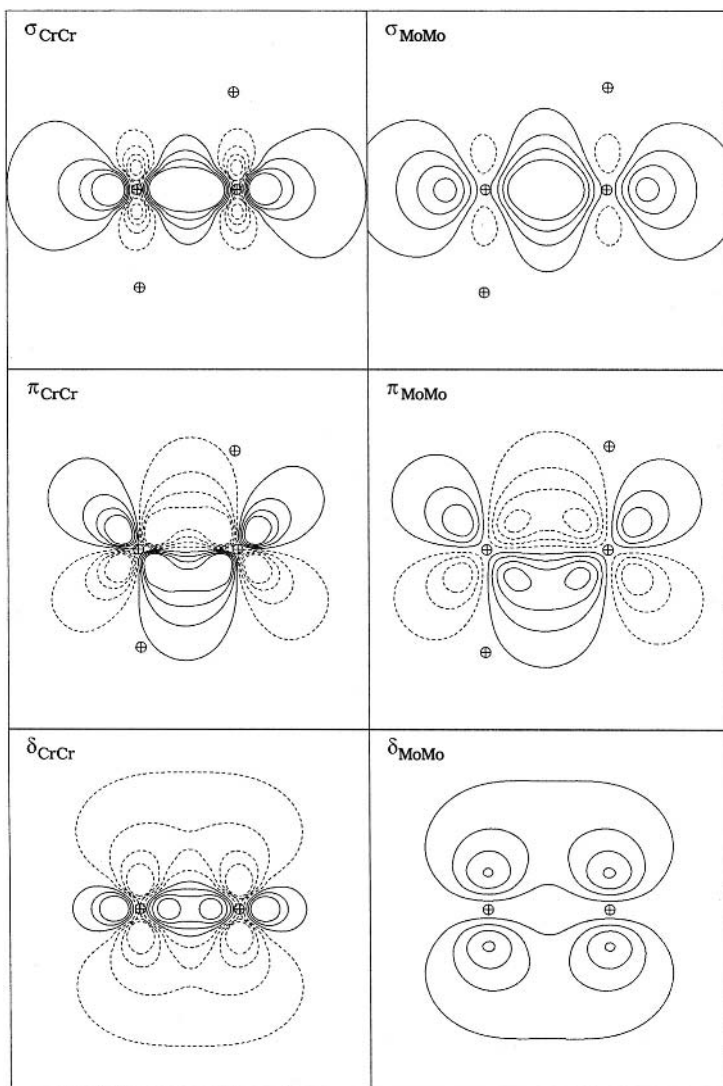


Figure 4.99 Representative σ_{MM} , π_{MM} , and δ_{MM} NBOs from quintuply bonded HCrCrH (left) and HMoMoH (right), for comparison with HWWH (Fig. 4.24).

based on CrH_6 adopting the molecular shape of MoH_6). Thus, the interpretation of M—M bonding strength depends strongly on the reference point chosen. In particular, this analysis illustrates the very large contribution of exchange energies to the computation of homolytic bond dissociation energies for electron-pair bonds at metal centers.

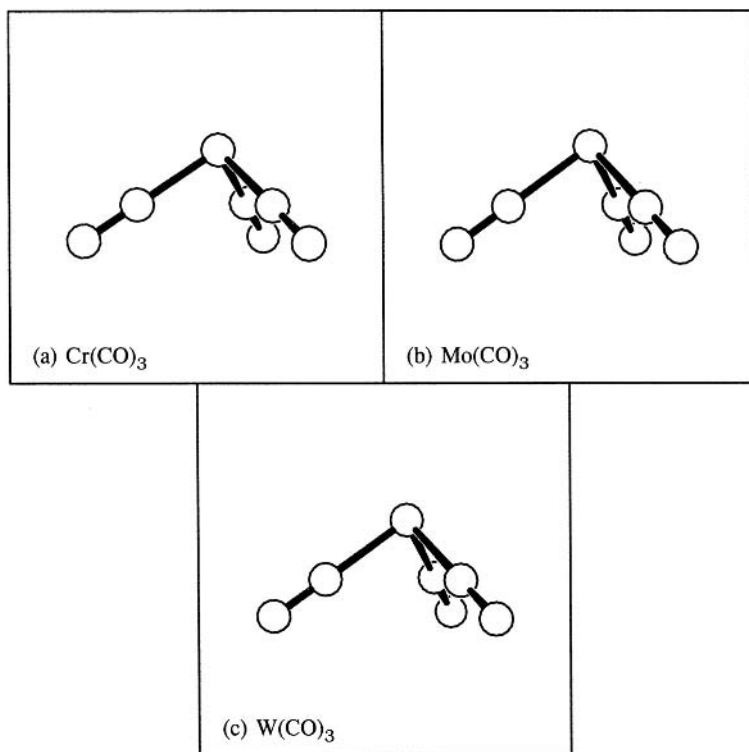


Figure 4.100 $M(\text{CO})_3$ structures of group 6 transition metals (Cr, Mo, W).

4.10.3 Vertical trends in coordinate bonding and hyperbonding

As illustrative examples of vertical trends in coordination bonding and hyperbonding, let us consider the carbonyl complexes of group 6 transition metals: $M(\text{CO})_n$ ($M = \text{Cr, Mo, W}$; $n = 1-6$). These complexes exhibit a high degree of structural homology, as illustrated for the normal-valent C_{3v} tricarbonyl complexes in Fig. 4.100. Analogous structural similarity characterizes the hypervalent ($n = 4-6$) higher members of the sequence. Hence, the vertical variations in dative and hypervalent coordinate bonding correspond to subtle variations in bond lengths and bond energies, against a backdrop of strong overall similarity to the picture sketched in Sections 4.5 and 4.6.

Figure 4.101 displays the subtle variations in metal–carbonyl bond lengths in the group 6 $M(\text{CO})_n$ complexes. In each case one can clearly distinguish the coordinate σ_{MC} bonds (solid lines) from the hypervalent ω_{MC} prebonds (dashed lines). The latter are about 0.1\AA longer, but exhibit a similar vertical variation within the group.

The general order of metal–carbonyl bond lengths is found to be $\text{Cr} \ll \text{W} < \text{Mo}$, similar to what is seen for other $M-X$ bond lengths, except that W and Mo bond lengths are usually similar, with bonds at W being slightly longer (a feature

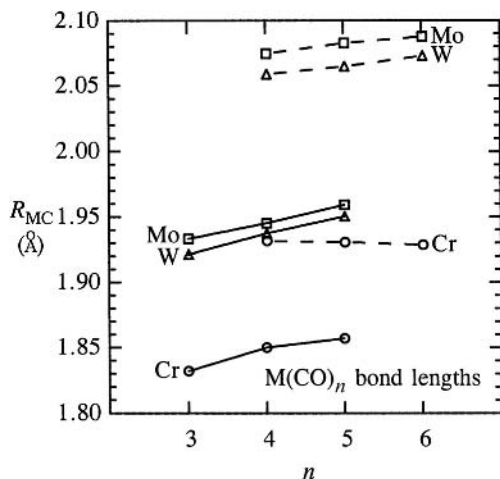


Figure 4.101 Metal–carbon bond lengths R_{MC} for dative σ_{MC} (solid line) or hypervalent ω_{MC} prebonds (dashed line) in $M(\text{CO})_n$ compounds of group 6 metals Cr (circles), Mo (squares), and W (triangles).

that is attributable to the underlying s^2d^4 ground-state configuration). However, the R_{MC} distance is also modulated by the strength of π -backbonding (which pulls the ligand into closer binding), and such $n_M \rightarrow \pi_{\text{CO}}^*$ backbonding interactions become significantly stronger for W than for Mo, due to the relativistically induced diffuseness and higher energy of the metal d-type donor orbital. The π -backbonding in the post-lanthanide series is further enhanced by the relativistic core contraction, which permits closer approach of the ligand to the metal. Thus, stronger π -backbonding and reduced core size are both factors in the apparent “lanthanide contraction” of W– versus Mo–carbonyl bond lengths.

Figure 4.102 displays vertical comparisons of the overlapping NHOs for σ_{MC} coordination (left) as well as the $n_M \rightarrow \pi_{\text{CO}}^*$ pi-backbonding interactions (right) in the three $M(\text{CO})_3$ species. In this figure, one can see the improved NBO overlap and strengthened stabilization energy (in parentheses) of $n_M \rightarrow \pi_{\text{CO}}^*$ pi-backbonding interactions on moving down the periodic column. The slightly closer approach of the carbonyl lone pair to the Cr nucleus (Fig. 4.102(a)) is also discernible.

We can also examine the energetics of carbonyl bonding in the successive binding energies ΔE_n for CO addition;

$$\Delta E_n(+\text{CO}) = |E[M(\text{CO})_n] - \{E[M(\text{CO})_{n-1}] + E[\text{CO}]\}| \quad (4.129)$$

Vertical trends in carbonyl binding energies are displayed graphically in Fig. 4.103. As seen in this figure, the strengths of the initial σ_{MC} bonds ($n = 3$) are appreciably greater than those of subsequent ω_{MC} prebonds ($n = 4-6$). Because the energetics of carbonyl coordination is dominated by π -backbonding (Section 4.5), ΔE_3

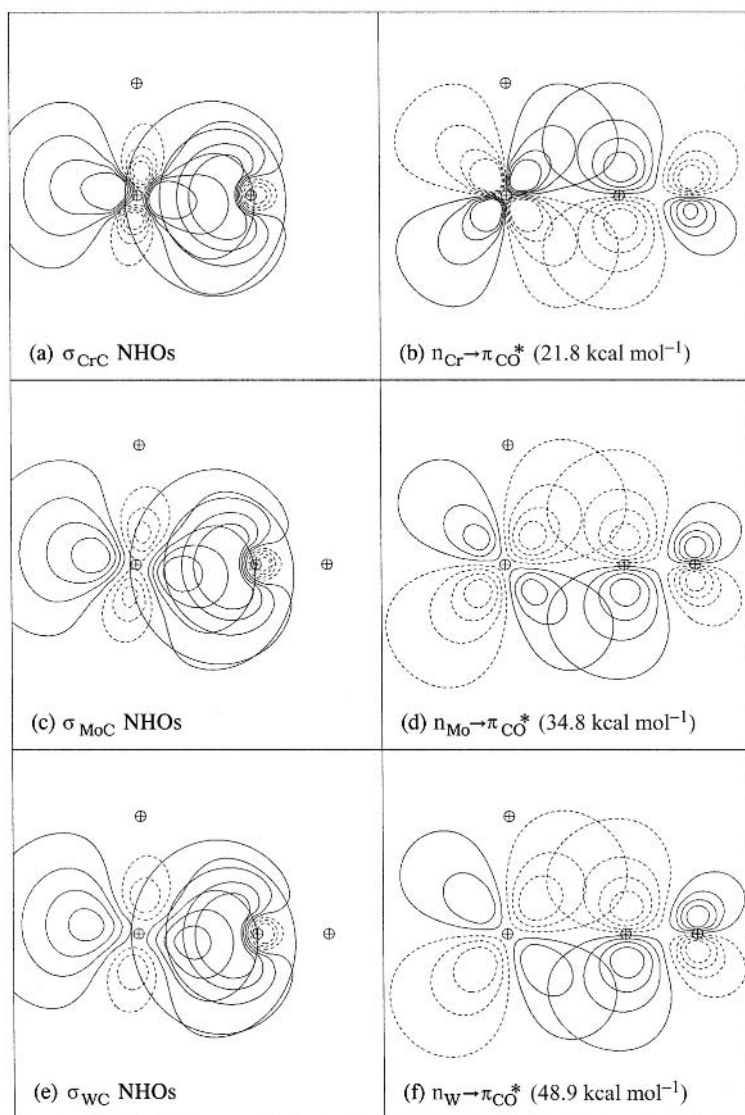


Figure 4.102 A comparison of coordinative σ_{MC} hybrids (left) and $n_{\text{M}} \rightarrow \pi_{\text{CO}}^*$ pi-backbonding interactions (right) for $M(\text{CO})_3$ compounds of group 6.

increases steadily with the relative size of metal *d* orbitals (Fig. 4.96): $\text{W} > \text{Mo} \sim \text{Cr}$. As hypervalent triads are created by the addition of CO to $M(\text{CO})_3$ fragments, delocalized bonds are formed both in the σ - and in the π -bonding framework. Within the σ framework, $3c/4e$ ω bonds are formed, which share four electrons (three from each CO) among the metal and two ligands. In contrast, the π -bonding framework involves *hypovalent* $3c/2e$ (τ_π) bonding, with the two electrons formally originating

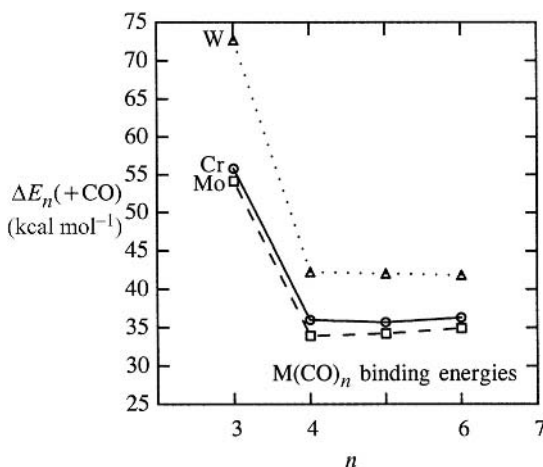


Figure 4.103 Incremental CO binding energies, Eq. (4.129), for $M(\text{CO})_n$ complexes of group 6 metals: Cr (circles), Mo (squares), and W (triangles). For $n = 3$, the quantity plotted is the average energy of dissociating all three carbonyls from $M(\text{CO})_3$.

from a metal lone pair that interacts with two ligand π_{CO}^* orbitals. The net result is that, on a per-ligand basis, σ -donation and π -backbonding interactions are weakened for hypervalent complexes relative to the parent $M(\text{CO})_3$ duodectet species. Note that, because hypervalent additions involve mutually orthogonal triads (and are therefore virtually independent), the hyperbond energies ΔE_n for $n = 4-6$ are nearly constant for all three metals.

In summary, bonding of metals to carbonyls has a strong π -backbonding component in addition to the usual σ -donation contribution. The resulting periodic variations in bond lengths and energies represent the composite effect, with π -backbonding overlap increasing down a column, but with closer ligand approach permitted for the first-row element. For group 6, the net result is that M—CO bond energies for Cr and Mo are similar, despite the fact that their M—C bond lengths are very different. Although M—H and M—Me bond energies for Mo and W are quite similar, the significantly greater strength of W—CO bonds relative to Mo—CO bonds arises from the substantially greater π -backbonding for the tungsten carbonyls.

4.11 Localized versus delocalized descriptions of transition-metal bonding and hyperbonding

The NBO-based “VB-like” description of localized transition-metal bonding and hyperbonding (as espoused throughout this chapter) differs significantly from more familiar descriptions of transition-metal complexes in delocalized MO terms. In this

concluding section, we wish to highlight some of these differences in terms of a simple representative example (PtH_4^{2-}) that illustrates how the localized NBO-type and delocalized MO-type descriptions are related. This example can also serve to address other common questions arising from the NBO Lewis-like description, such as the role of p orbitals and the validity of Pauling-type hybridization schemes (i.e., the classic dsp^2 hybrids for square-planar $\text{D}_{4\text{h}}$ complexes such as PtH_4^{2-}).

Qualitative splitting and nodal patterns for a simplified three-center MO model

Let us first characterize the localized σ - and ω -bonding in PtH_4^{2-} , using the analogy to the simple three-center MO model of hyperbonding in rare-gas compounds (Section 3.5). Figure 4.104 illustrates the analogy for a hypothetical single ω bond of XeH_2 (left-hand panels) or two mutually perpendicular ω bonds of XeH_4 (center panels), where each atom contributes *one* valence AO (s_{H} , p_{Xe} , and $s_{\text{H}'}$) to the three-center MOs. The left-hand panels show XeH_2 ($\text{D}_{\infty\text{h}}$ point group), in which the three-center mixing leads to bonding (ϕ_{b} , lower: σ_{u}^+), nonbonding (ϕ_{n} , middle: σ_{g}^+), and antibonding (ϕ_{a} , upper: σ_{u}^+) MOs along the chosen axis,

$$\phi_{\text{b}} \simeq \eta(s_{\text{H}} + p_{\text{Xe}} + s_{\text{H}'}) \quad (4.130\text{a})$$

$$\phi_{\text{n}} \simeq \eta(s_{\text{H}} + s_{\text{H}'}) \quad (4.130\text{b})$$

$$\phi_{\text{a}} \simeq \eta(s_{\text{H}} - p_{\text{Xe}} + s_{\text{H}'}) \quad (4.130\text{c})$$

with $\text{D}_{\infty\text{h}}$ symmetry label, nodal pattern, and electronic occupancy as shown in each panel. If p_x lies along the chosen bonding axis, then the orthogonal (p_y and p_z) orbitals remain as “unused” (but fully occupied) nonbonding levels of π_{u} symmetry (shown in lighter gray to indicate their passive role in skeletal bonding). The center panels show the corresponding *two* orthogonal three-center MOs and $\text{D}_{4\text{h}}$ symmetry labels for square-planar XeH_4 , in which only a single filled p_z orbital ($a_{2\text{u}}$) remains “unused” in bonding. Finally, the right-hand panels show the analogous levels, symmetries, and nodal patterns for PtH_4^{2-} , where the only complication is that the central Pt now uses sd hybrids (one of d_{z^2} and one of $d_{x^2-y^2}$ character) to make the three-center MO combinations. If we neglect the central-atom orbitals which are passive (gray-colored), the following trend emerges: for n $3\text{c}/4\text{e}$ bonding interactions, there will be n filled bonding orbitals and n filled ligand-based orbitals. Thus, one can see how the complex PtH_4^{2-} MO pattern on the right evolves rather simply from such localized three-center “building blocks,” a representative example of how localized-bonding concepts can assist intelligent analysis of a complex MO energy-level diagram.

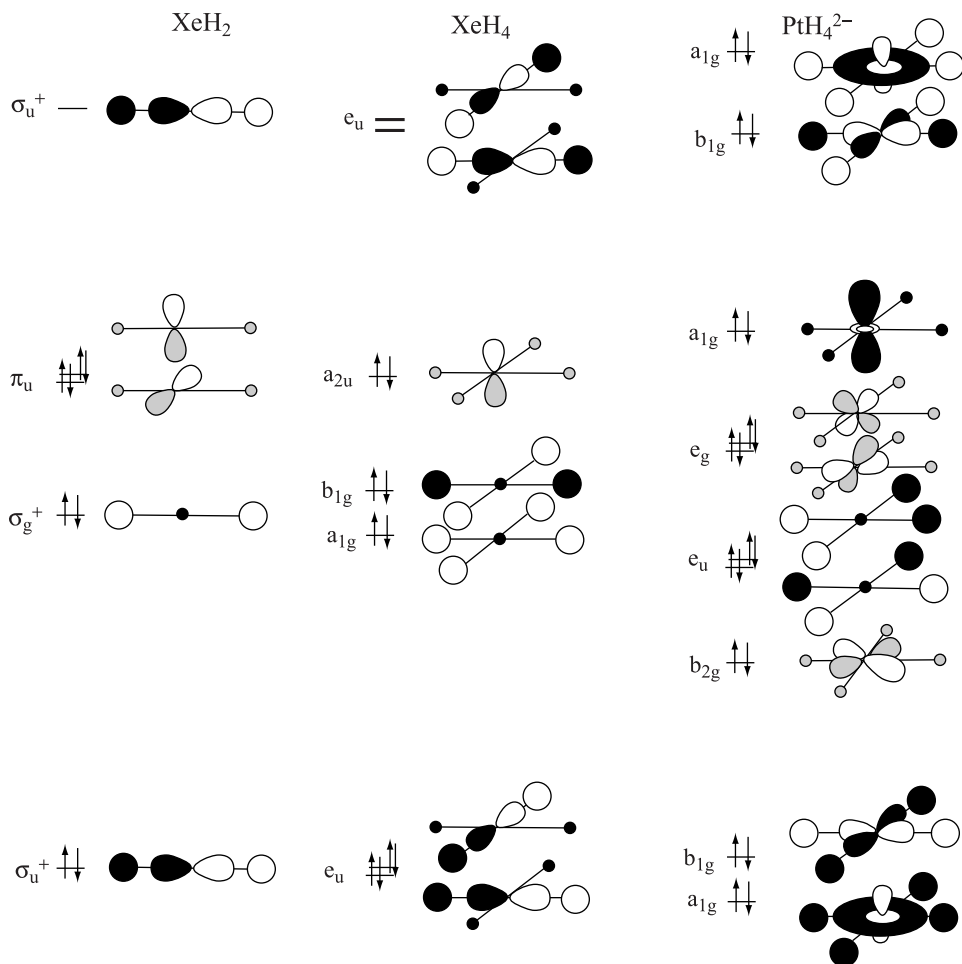


Figure 4.104 Model MO diagrams for XeH_2 , XeH_4 , and PtH_4^{2-} . Light-gray coloration indicates atom-centered orbitals that are not involved in bonding.

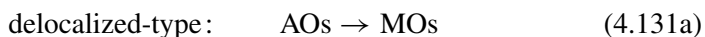
Molecular-orbital- versus valence-bond-type descriptions

Let us now examine the connection between localized and delocalized descriptions in somewhat more formal terms, using the actual numerical energy levels of PtH_4^{2-} to illustrate the formal connections. Inevitably, this discussion entails somewhat more technical detail concerning computational MO methodology than required elsewhere in this book, and we assume a general familiarity with Sections 1.4 and 1.5, Appendix A, and other sections mentioned below.

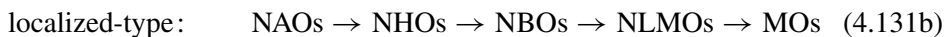
It is important first to recall that the distinctions drawn here between localized “VB(NBO)-type” and delocalized “MO-type” descriptions are essentially *independent* of the actual *ab initio* or DFT computational method on which the analysis

happens to be based. The computational examples examined throughout this book are in fact all based on MO-like hybrid density-functional (B3LYP) calculations (leading to familiar LCAO-MO expansions of the Kohn–Sham MOs in terms of AO basis functions), but the details of the NBO-based Lewis-like description would be essentially identical for *any* computational method that achieves comparable accuracy in describing the chemical phenomena. Furthermore, if the wavefunction were *not* calculated in some type of MO framework (as is the nearly universal practice today), one could readily envision its analysis in terms of the delocalized multi-center natural orbitals (NOs; see Section 1.5) to obtain an “MO-like” description that is essentially parallel to that for actual MO-based wavefunctions. It is also important to recall (Section 3.2.2) that the “VB-like” localized NBOs have mathematical forms that are fundamentally *different* from those envisioned in the classic Heitler–London–Slater–Pauling formulation of valence-bond theory; see Section 3.2.4 for other aspects of the general comparison between localized and delocalized MO descriptions.

In order to contrast the MO-type and VB-type descriptions, we may say that the former attempts to describe the MOs (or NOs) in terms of *general* mixings of AO basis functions (LCAO-MO description),



whereas the latter attempts to interpolate the intermediate steps of localized hybrid and bond formation, culminating in a set of (semi-)localized molecular orbitals (LMOs) that are mathematically equivalent to the symmetry-adapted canonical molecular orbitals, but are considerably simpler to understand in perturbative terms. In the NBO framework, the sequential steps leading from initial atomic orbitals (NAOs) to final localized molecular orbitals (NLMOs) (or delocalized canonical MOs) can be represented by the successive basis transformations



involving intermediate localized hybrid (NHO) and bond (NBO) orbitals. The localized description therefore attempts to break down the “straight-shot” LCAO-MO description (4.131a) into a succession of smaller steps (4.131b) that can be individually comprehended in simple perturbative terms.

Figure 4.105 depicts overall aspects of the localized versus delocalized analysis of MOs of PtH_4^{2-} (B3LYP/LANL2DZ level), showing (on a consistent vertical energy scale) the basis AOs (left), occupied valence MOs (center), and NAOs (right) for each type of analysis. As shown by the connecting tie-lines in the left-hand half of the diagram, nearly all the 30 basis AOs of the LANL2DZ set make appreciable (>5%) contributions to one or more of the 12 occupied valence MOs (corresponding to non-negligible “perturbations” for the delocalized LCAO-MO analysis (4.131a)),

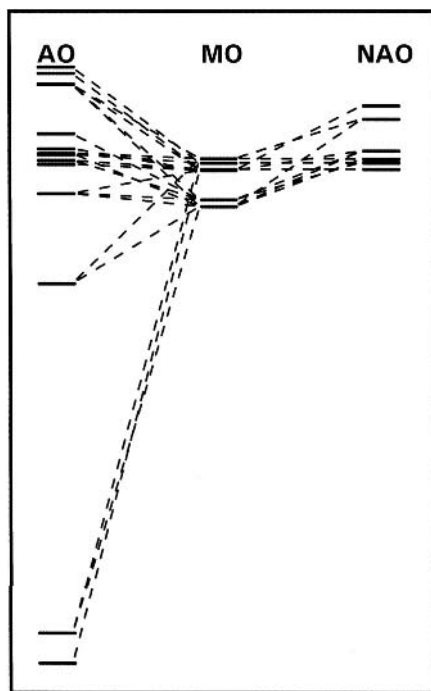


Figure 4.105 A schematic “perturbative-analysis” diagram for occupied valence MOs (center) of PtH_4^{2-} (B3LYP/LANL2DZ level), showing tie-lines for analysis in terms of AO basis functions (left) versus NAOs (right). (A tie-line is shown when the AO or NAO contributes at least 5% to the connected MO.) Note the much smaller number of contributing orbitals, the sparser tie-line patterns, and the more realistic physical range of atomic orbital energies for NAOs than for standard Gaussian-basis AOs.

whereas a much smaller number of tie-lines is needed in the right-hand half to depict the overall LCAO-MO analysis (4.131b). It is immediately apparent from Fig. 4.105 that the contributing basis “AOs” span an unphysically large energy range, virtually squeezing the entire band of occupied MOs and NAOs into unrecognizably narrowed form when shown on a common energy scale. Indeed, it would be a Herculean task to provide a “perturbative MO” analysis of the AO→MO tie-lines on the left, because (i) the required “perturbative shifts” are *orders of magnitude* greater than the actual MO energy splittings (or, indeed, the entire range of MO energies!), and (ii) a *large* number of such perturbative tie-lines would be required in order to achieve any reasonably complete LCAO-MO description. (The situation in the more accurate augmented triple-zeta AO basis set would be vastly worse than that depicted in Fig. 4.105.)

In fact, the artificially large span of “AO energies” in Fig. 4.105 is entirely an artifact of the unphysical nature of the basis “AOs” themselves. Basis AOs are

commonly chosen (purely for computational convenience) as non-orthogonal Gaussian- or Slater-type functions, radially *nodeless* and thus unable to incorporate even qualitative aspects of Pauli core repulsion and other exchange-repulsion phenomena in a variationally consistent manner. The “AO energies” that underlie the LCAO-MO tie-lines are therefore essentially *unrelated* to physical energy levels of the constituent atoms at *any* distance (unlike the NAO energies, which correctly evolve to the proper free-atom values as the atoms separate to infinity). Thus, we give no further attention to analysis based on these AOs.

Let us now focus instead on the localized sequence (4.131b) for the NAO→MO tie-lines on the right-hand side of Fig. 4.105. Figure 4.106 shows this portion of the energy-level diagram on an expanded scale, which allows key features of the successive localized transformations (4.131b) to be clearly recognized. Selected orbitals are marked with conventional NAO, NHO, NBO, NLMO, or MO labels to assist identification, and only those perturbative tie-lines involving significant (>5%) orbital mixing are included. In particular, four of the five metal d orbitals merely “pass through” the diagram from left to right as nonbonding orbitals of essentially unaltered form and need not be considered further (5d_{xz} and 5d_{yz} become e_g MOs, 5d_{xy} becomes b_{2g}, and 5d_{z²} becomes a_{1g}; cf. Fig. 4.103). Note that the relevant orbital energies ε₁ (a.u.) all occur at *positive* values in the PtH₄²⁻ dianion.

It can be seen from Fig. 4.106 that only a few significant interaction tie-lines are involved in the localized transformations (a) NAO → NHO, (b) NHO → NBO, and (c) NBO → NLMO. Figure 4.107 depicts each of these interactions as a perturbation diagram, showing how precursor orbitals evolve to form successor orbitals in the localized sequence (4.131b). Each diagram has a simple physical interpretation. Figure 4.107(a) depicts formation of the metal hybrid (~sd^{1.24}) from constituent 6s and 5d_{x²-y²} NAOs, qualitatively

$$h_{\text{Pt}} \simeq 2^{-1/2}(s + d_{x^2-y^2}) \quad (4.132a)$$

or, more quantitatively,

$$h_{\text{Pt}} = 0.650(6s) + 0.697(5d_{x^2-y^2}) + \dots \quad (4.132b)$$

Figure 4.107(b) depicts formation of two-center bonding and antibonding (σ_{PtH} and σ_{PtH}^{*}) NBOs from the constituent hybrids h_{Pt} and h_H:

$$\sigma_{\text{PtH}} = 0.645(sd^{1.24})_{\text{Pt}} + 0.765(s)_{\text{H}} \quad (4.133a)$$

$$\sigma_{\text{PtH}}^* = 0.765(sd^{1.24})_{\text{Pt}} - 0.645(s)_{\text{H}} \quad (4.133b)$$

Finally, Fig. 4.107(c) depicts the n_H→σ_{PtH}^{*} interaction that results in the three-center ω_{H:PtH} NLMO (as well as the corresponding virtual ω^{*} NLMO),

$$\omega_{\text{H:PtH}} = 0.820n_{\text{H}} + 0.476\sigma_{\text{PtH}}^* + \dots \quad (4.134)$$

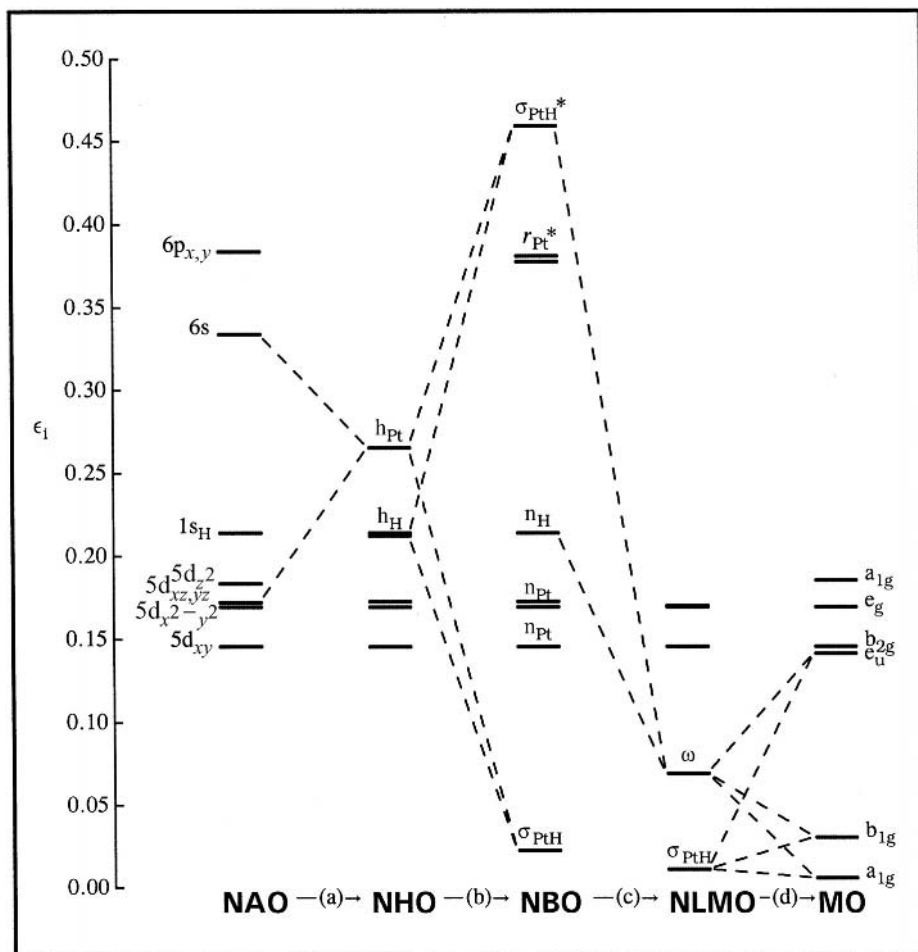


Figure 4.106 Valence orbital energy-level diagrams for PtH_4^{2-} relating atomic NAOs to molecular MOs through intermediate localized NHO, NBO, and NLMO steps, with final occupied NLMOs and MOs (cf. Fig. 4.104) shown on the right of the diagram. Dashed tie-lines represent all significant ($>5\%$) mixing coefficients in the successive transformations: (a) NAO \rightarrow NHO, (b) NHO \rightarrow NBO, (c) NBO \rightarrow NLMO, and (d) NLMO \rightarrow MO. The metal 6p orbitals are shown for the NAO and NBO steps (in the latter case, identified as Rydberg r_{Pt}^*), but these orbitals make no significant contribution to occupied NBOs, NLMOs, or MOs.

As illustrated elsewhere in this book, each of the interactions (a)–(c) can be well approximated by low-order perturbation theory.

The remaining step (d) in Fig. 4.106 (NLMO \rightarrow MO) involves more complex tie-line patterns, but fortunately these are all *superfluous* and can be ignored as having no physical consequence! This remark follows from the general (unitary) equivalence of MO determinantal wavefunctions formed either from NLMOs or

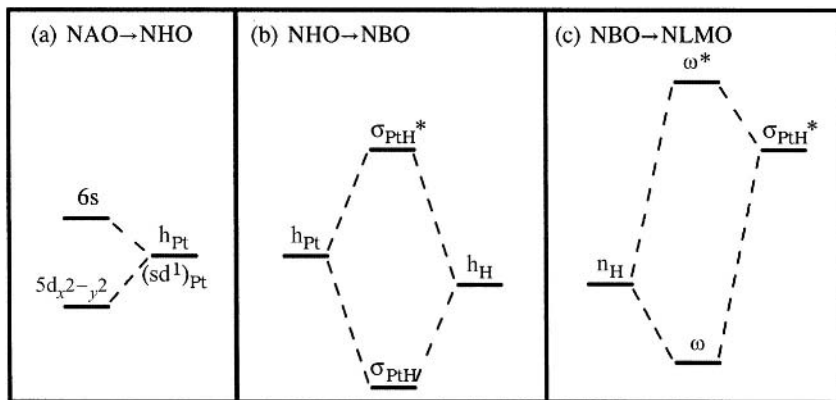


Figure 4.107 Perturbative interaction diagrams (on a common vertical energy scale; cf. Fig. 4.106) depicting significant localized bonding interactions for PtH₄²⁻: (a) metal hybrid formation (NAO→NHO), (b) interaction of bonding hybrids to form bonding (σ) and antibonding (σ^*) NBOs (NHO→NBO), and (c) $n_{\text{H}} \rightarrow \sigma_{\text{PtH}}^*$ interaction to form the $\omega_{\text{H:PtH}}$ three-center NLMO (NBO→NLMO).

from MOs (Section 3.2.4), which implies that the replacement of MOs by NLMOs in the MO wavefunction cannot affect the energy, density, or any other observable property. Therefore, *no* physical insights are lost (and considerable simplicity is gained) by focussing on the easy construction of localized NLMOs, rather than delocalized canonical MOs.

For completeness, Fig. 4.108 displays orbital contour diagrams to compare the forms of the localized NBOs (left) and delocalized MOs (right) of PtH₄²⁻. As shown by their symmetry labels, the high-symmetry MOs transform as irreducible representations of the D_{4h} point group, but their forms are very sensitive to slight geometrical distortions or other chemical perturbations. In contrast, the lower-symmetry NBOs (which form a basis for *reducible* representation of D_{4h}) have robust and transferable forms that are highly recognizable even in strongly altered chemical environments. Thus, the localized NBOs offer considerable advantages as conceptual “building blocks” for visualizing the persistent features of chemical fragments under chemical transformations.

p-Orbital participation?

A persistent feature of qualitative models of transition-metal bonding is the supposed importance of p orbitals in the skeletal hybridization.⁷⁶ Pauling originally envisioned dsp² hybrids for square-planar or d²sp³ hybrids for octahedral bonding, both of 50% p character. Moreover, the “18-electron rule” for transition-metal complexes seems to require participation of *nine* metal orbitals, presumably the five d, one s, and three p orbitals of the outermost [(n - 1)d]⁵[ns]¹[np]³ quantum shell.

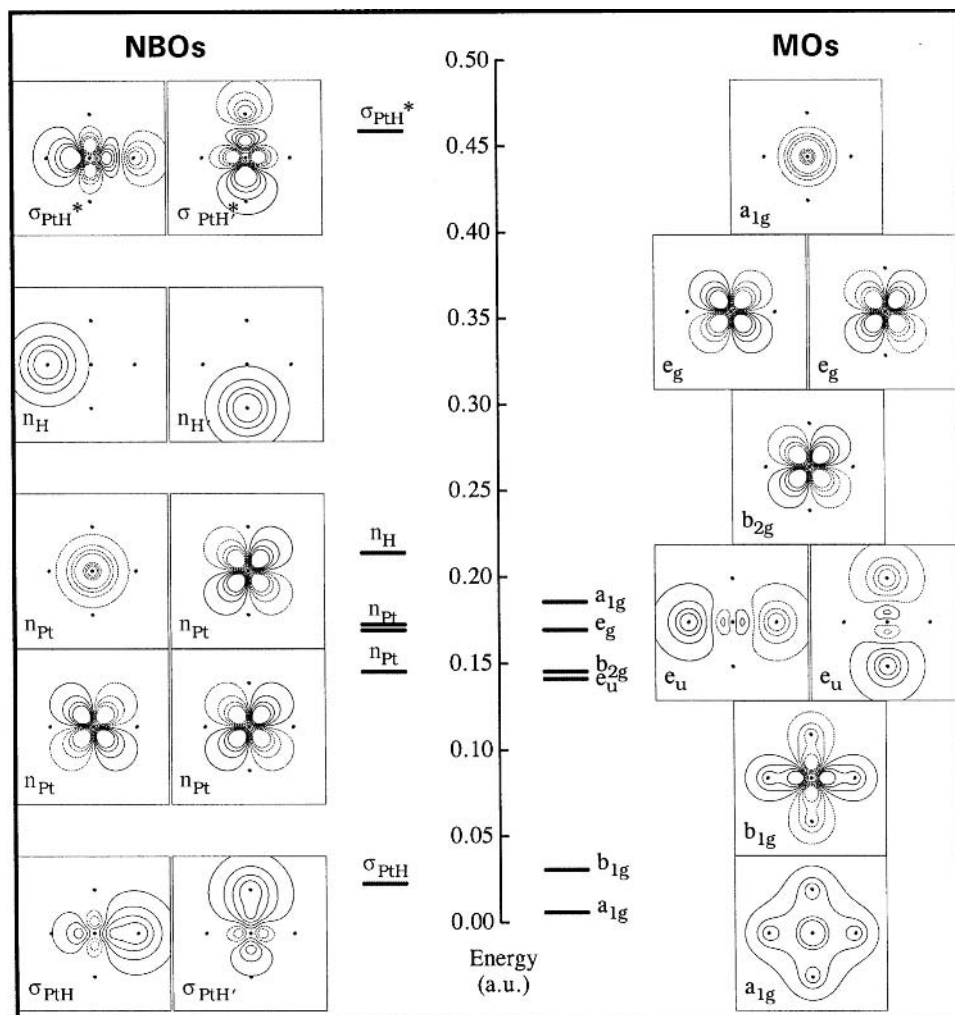


Figure 4.108 Contour plots of principal valence NBOs (left) and MOs (right) of PtH_4^{2-} (B3LYP/LANL2DZ level).

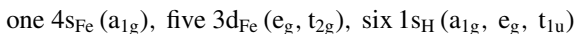
However, we have shown how the 18-electron rule is commonly satisfied in the *absence* of any significant p-orbital participation, on the basis of hypervalent $3c/4e$ ω -bonding interactions wholly *within* the framework of normal-valent sd^n hybridization. Results of NBO and Mulliken analyses of high-level wavefunctions for transition-metal complexes commonly exhibit only paltry occupation of the outer p orbitals (comparable in this respect to the weak contributions of d-type “polarization functions” in main-group bonding).

The square-planar PtH_4^{2-} species presents an optimal opportunity for high covalency (to overcome the massive electrostatic disadvantage of doubly anionic charge)

and high p character (to achieve the “expected” dsp^2 skeletal hybridization). However, the Pt 6p orbitals are found to be rather high in energy (Fig. 4.106) and to make only minor contributions to skeletal hybrids. The quantitative form of the h_{Pt} valence hybrid, Eq. (4.132b), does indeed reveal slight p-orbital contributions (totalling about 5.5%), but these are far smaller than the dominant contributions shown in (4.132b), which are clearly of sd^1 -like, rather than dsp^2 -like, character. None of the significant tie-lines in Fig. 4.106 involves p-orbital participation, and it is clear that a near-quantitative description of the NLMO bonding pattern (Fig. 4.107) can be achieved within the framework of primary metal 6s/5d hybridization, with only a secondary “polarization” role of the 6p orbitals. As in the analogous case of “d-orbital participation” in hypervalent main-group compounds (Section 3.5), it seems that the issue of significant “p-orbital participation” in hypervalent d-block compounds can be safely dismissed for all known species. Hypervalent complexes of square-planar or octahedral geometry (Example 4.10) can generally be described quite well by localized sd^n hybridization and ω -bonding models that invoke no significant contribution of outer p orbitals.

Example 4.10

Problem: Give a comparable sd^n -based localized 2c/2e and 3c/4e description of octahedral FeH_6^{4-} (which, like PtH_4^{2-} , is an experimentally synthesized and characterized species) and compare it with the delocalized MO description. For the latter, assume O_h symmetry and employ the 15 AOs spanning the irreducible representations shown below:

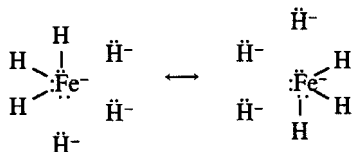


Identify the overall pattern of occupation of bonding and nonbonding orbitals in the approximate MO diagram, and associate this (if possible) with the corresponding number of 3c/4e interactions determined by application of the Lewis-like model.

Solution: The total electron count is

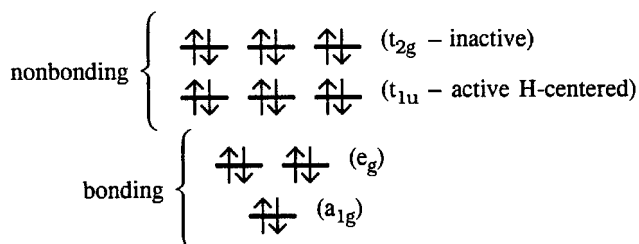
$$8 (\text{from Fe}) + 6 (\text{from six H}) + 4 (\text{net charge}) = 18$$

As previously recognized (e.g., Table 4.52), this corresponds to the “ideal pattern” of three ω bonds, three lone pairs, and sd^2 (90°) hybridization, locking in a rigid octahedral structure. On the basis of the formally duodectet-rule-consistent parent species FeH_3^- , the overall ω -bonding is compactly described by the two resonance structures



which summarize the localized description.

For the delocalized MO description, symmetry considerations (in *assumed* O_h geometry) indicate that three bonding MOs arise from the interaction of Fe a_{1g} (4s) and doubly degenerate e_g (3d) orbitals with symmetry-adapted linear combinations of H 1s orbitals. This leaves the triply degenerate Fe t_{2g} and ligand t_{1u} sets to form nonbonding orbitals. The Fe t_{2g} set corresponds to “inactive” lone pairs, by virtue of their orthogonality to bonding Fe—H orbitals (analogously to the distinction made for PtH_4^{2-}). Thus, the filled “active” MOs are three bonding (a_{1g} and e_g) and three nonbonding (t_{1u} , ligand-based) orbitals, while the antibonding a_{1g} and e_g orbitals are unoccupied. As seen previously for PtH_4^{2-} (Fig. 4.104), this conforms well to the three-center MO description of 3c/4e ω -bonding, wherein three filled bonding and three (ligand-based) nonbonding orbitals lead to three ω bonds. The qualitative MO diagram is shown below:



4.12 Summary

The present chapter has provided but an outline of the broad, fascinating domain of the d-block elements. Because theoretical understanding and synthetic control of transition metals has lagged behind that of main-group elements, much of d-block chemistry remains a scientific frontier area, rich with the prospects of future chemical discoveries.

Practically every topic addressed in this chapter bears witness to the remarkable prescience of the localized-bonding concepts introduced by G. N. Lewis. Indeed, Lewis’s two most celebrated concepts – the shared-pair electron-dot diagrams of molecular structure and the electron-pair donor–acceptor picture of acid–base reactions – find productive and symbiotic unification in virtually every aspect of transition-metal chemistry. Enhanced with the quantum mechanical concepts of hybridization and resonance, the familiar Lewis–Pauling–Bent picture of localized chemical bonding exhibits the numerous relationships between d-group and main-group chemistries, allowing the phenomena of covalency, hypovalency, and hypervalency to be addressed in quite parallel terms.

Yet, despite the numerous parallels, the *specifics* of the localized Lewis-like picture of transition-metal bonding differ so remarkably from those of bonding in main groups as to create the impression of a bizarre wonderland of new chemical

structures and phenomena, unprecedented in main-group chemistry. Thus, while dot diagrams, hybrids, two- and three-center bonding, Bent's rule, resonance, and general Lewis-acid–base donor–acceptor concepts generalize immediately to transition-metal chemistry, these concepts acquire decidedly “weird” and unfamiliar characteristics compared with their main-group analogs.

- (1) The “rule of 12” replaces the “rule of eight” as the guiding principle of Lewis-like dot diagrams.
- (2) Idealized sd-hybrids replace sp-hybrids for skeletal hybridization, with resulting weird (non-VSEPR) bond angles.
- (3) Higher-order bonding motifs appear, with quadruple or higher metal–metal bond orders.
- (4) The relative strengths of conjugative and hyperconjugative interactions are sharply altered, and general delocalization phenomena become *much* more pronounced near transition metals, where the abundance of low-lying unfilled valence orbitals provides many new pathways for donor–acceptor stabilization.
- (5) The possibilities for coordinative bonding and related types of “acid:base adduct” association with closed-shell species are *strongly* increased, leading to an enhanced tendency toward intermolecular aggregation and condensation.
- (6) Hypervalent 3c/4e bonding becomes a *ubiquitous* feature of transition-metal bonding (to the extent that normal-valent coordination complexes may appear the “exceptional” case!).
- (7) The abundance of accessible donor and acceptor orbitals in common transition-metal complexes facilitates low-energy bond rearrangements such as insertion (“oxidative-addition”) reactions, thus enabling the critically important catalytic potential of metals.

Thus, while numerous parallels between main-group and transition-metal chemistries can be identified, the actual structural and reactivity patterns of transition-metal compounds differ in richly distinctive ways from those familiar in main-group organic and inorganic chemistry. For example, as a consequence of the strong role of 3c/4e ω -bonding in transition-metal complexes, the specific nature of the ligands and their geometrical arrangement *strongly* modulate metal reactivity. Chemical exploitation of such sensitivities is well advanced in the biological domain, where metalloenzymes perform spectacular chemical transformations of crucial importance to life processes. Future advances in industrial applications of catalysis will also rely heavily on constructing new inner- and outer-coordination-sphere environments in order to enable novel latent reactivities to emerge.

Although rich with distinctive chemical possibilities, bonding at transition metals makes use of localized-bond “building blocks” that are familiar to main-group inorganic and organic chemists. Importantly, these building blocks are consistent with the best electron-density distributions that are currently available. Commonality of bonding concepts across the periodic table and consistency with high-level electronic-structure computations should be reassuring qualities to thoughtful

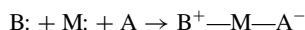
students of chemistry, for they obviate the need for radical conceptual changes (such as crystal-field theory) in passing from p-block to d-block elements, and they suggest the enduring significance of conceptual constructs that survive rigorous *ab initio* scrutiny. The strong connection between bonding in the main group and in transition series even suggests that some of the “unique” features of transition metals, including their catalytic potential, might be realized in the main group with proper “tweaking” of the coordination environment.

Full understanding and control of transition-metal species in biotic and abiotic processes is still in its relative infancy. In the ongoing twenty-first-century exploration of this fascinating domain, *ab initio* theory can be expected to play an increasingly important role.

Notes for Chapter 4

1. L. Pauling, *J. Am. Chem. Soc.* **53** (1931), 1367; L. Pauling, *The Nature of the Chemical Bond* (Ithaca, NY, Cornell University Press, 1st edn. 1939, 3rd edn. 1960); and J. C. Slater, *Phys. Rev.* **38** (1931), 255, 481 and 1109.
2. L. Pauling, *The Nature of the Chemical Bond* (Ithaca, NY, Cornell University Press, 3rd edn. 1960), pp. 144–146 and 177–182.
3. L. Pauling, Z. S. Herman, and B. J. Kamb, *Proc. Nat. Acad. Sci. U.S.A.* **1982** (1982), 1361; and L. Pauling, *Proc. Nat. Acad. Sci. U.S.A.* **72** (1975), 4200.
4. F. Weinhold and C. R. Landis, *Chem. Educ. Res. Pract. Eur.* **2** (2001), 91.
5. C. R. Landis, T. Cleveland, and T. K. Firman, *J. Am. Chem. Soc.* **117** (1995), 1859.
6. C. R. Landis, T. Cleveland, and T. K. Firman, *J. Am. Chem. Soc.* **117** (1995), 1859; C. R. Landis, T. Cleveland, and T. K. Firman, *Science* **272** (1996), 179; C. R. Landis, T. K. Firman, D. M. Root, and T. Cleveland, *J. Am. Chem. Soc.* **120** (1998), 1842; T. Cleveland, T. K. Firman, and C. R. Landis, *J. Am. Chem. Soc.* **120** (1998), 2641; C. R. Landis, *NATO Advanced Workshop on Molecular Modeling and Dynamics of Biological Molecules Containing Metal Ions, Pisa, Italy, March 16–21, 1997* (New York, Kluwer, 1997), pp. 49–76.
7. T. K. Firman and C. R. Landis, *J. Am. Chem. Soc.* **123** (2001), 11 728.
8. C. R. Landis, T. Cleveland, and T. K. Firman, *J. Am. Chem. Soc.* **117** (1995), 1859.
9. L. Pauling, *J. Am. Chem. Soc.* **53** (1931), 1367.
10. C. R. Landis, T. K. Firman, D. M. Root, and T. Cleveland, *J. Am. Chem. Soc.* **120** (1998), 1842. For a group-theoretical approach to hybrid-orbital formulation, see D. M. P. Mingos and L. Zhenyang, *Struct. Bonding* **72** (1990), 73.
11. By suitable limiting procedures one can verify that this formula reduces properly to the corresponding Eq. (3.34) for equivalent sp^x hybrids in the special case $\mu = 0$.
12. P. -O. Löwdin, *J. Chem. Phys.* **18** (1950), 365; and P. -O. Löwdin, *Adv. Quantum Chem.* **5** (1970), 185.
13. For symmetry-based qualitative molecular-orbital analyses of molecular shapes in the limit of strong metal s- and d-orbital participation in bonding, see R. B. King, *Inorg. Chem.* **37** (1998), 3057; and C. A. Bayse and M. B. Hall, *J. Am. Chem. Soc.* **121** (1999), 1348.
14. T. K. Firman and C. R. Landis, *J. Am. Chem. Soc.* **120** (1998), 12 650.
15. R. J. Gillespie and I. Hargittai, *The VSEPR Model of Molecular Geometry* (Boston, MA, Allyn & Bacon, Boston, 1991).
16. For recent reviews of bonding at metal centers, see F. Maseras, A. Lledos, E. Clot, and O. Eisenstein, *Chem. Rev.* **100** (2000) 601; G. Frenking and N. Frohlich, *Chem. Rev.* **100** (2000), 717; and M. Kaupp, *Angew. Chem. Int. Edn. Engl.* **40** (2001), 3534.
17. Of course, since OsH_4 contains two valence lone pairs in addition to the four bond pairs, the high-symmetry T_d structure is not predicted by VSEPR, unless the lone pairs are arbitrarily

- considered to be “sterically inactive.” The sawhorse-like C_{2v} geometry predicted by nominal VSEPR concepts appears to lie *much* higher in energy, and this geometry is probably not even a local minimum on the OsH_4 potential-energy surface.
18. In the HfH_4 case the hybrids also contain slightly larger contributions (1.39%) of p character. Note that the anomalous ground-state configuration of La is not handled properly in the NBO program, so further information on the NBO compositions is not available for LaH_3 .
 19. R. T. Sanderson, *J. Chem. Educ.* **65** (1988), 112.
 20. For a general review of metal–ligand multiple bonds, see W. A. Nugent and J. M. Mayer, *Metal–Ligand Multiple Bonds: The Chemistry of Transition Metal Complexes Containing Oxo, Nitrido, Imido, Alkylidene, or Alkylidyne Ligands* (New York, Wiley, 1988).
 21. T. K. Firman and C. R. Landis, *J. Am. Chem. Soc.* **123** (2001), 11 728.
 22. Very slight p character (<1%) occurs in the pi bond, where a slight admixture of p_z can slightly polarize the metal d_{xz} toward the adjacent methylene.
 23. P. A. Schultz and R. P. Messmer, *J. Am. Chem. Soc.* **115** (1993), 10925.
 24. For a review, see F. A. Cotton and C. M. Lukehart, *Prog. Inorg. Chem.* **16** (1972), 243.
 25. R. R. Schrock, *Acc. Chem. Res.* **12** (1979), 98.
 26. For a comprehensive review of metal–metal bonding, see F. A. Cotton and R. A. Walton, *Multiple Bonds Between Metal Atoms* (New York, Wiley, 1982) and note 16.
 27. For a lucid description of both electronegativity and pi-donation effects on M–X bonding, see M. Kaupp, *Chem. Eur. J.* **5** (1999), 3632.
 28. H. Bent, *Chem. Rev.* **61** (1961), 275.
 29. In p-block elements, a central-atom lone pair is visualized as the limit of bonding to a “ligand of lowest possible electronegativity,” and thus acquires high s character. In d-block elements, a central-atom lone pair is of essentially pure d character (except for the special $n^{(h)}$ hybrid of ML_2 coordination) and s character is essentially reserved for the covalent sigma skeletal bonds.
 30. J. Muldoon and S. N. Brown, *Inorg. Chem.* **41**(2002), 4815.
 31. A. Werner, *Z. Anorg. Chem.* **3** (1893), 267; and G. B. Kauffman, *J. Chem. Educ.* **36** (1959), 521.
 32. H. Bethe, *Ann. Phys.* **3** (1929), 135.
 33. J. H. Van Vleck, *J. Chem. Phys.* **3** (1935), 803 and 807. For an historical overview of subsequent developments, see C. J. Ballhausen, *J. Chem. Educ.* **56** (1979), 194, 215 and 357.
 34. One can also envision the simultaneous dative interactions of M with a Lewis base *and* a Lewis acid,

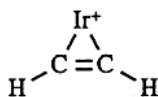


corresponding to net donation from B: to A while leaving the bridging metal atom formally electroneutral. In this case the metal atom serves as a “wire” to mediate the formal electron transfer from B: to A without itself being oxidized or reduced. Such interactions are beyond the scope of this book.

35. Such off-axis “pi-type” interactions are expected to depend sensitively on polarization shifts of the ligand acceptor σ^* orbitals. Thus, the electronegativity of P being lower than that of N makes these backbonding interactions significantly stronger in PH_3 (due to the more favorable polarization of σ_{PH}^* antibonds), putting PH_3 higher than NH_3 in the spectrochemical series. The σ -backbonding effects, even though they are weaker than π -backbonding effects to be discussed below, are found to be of chemically appreciable significance in many cases, but a more complete discussion is beyond the scope of the present work.
36. M. H. L. Pryce and W. A. Runciman, *Disc. Faraday Soc.* **26** (1958), 34.
37. H. A. Jahn and E. Teller, *Proc. R. Soc. London* **A161** (1937), 220.
38. For a detailed review of chemical applications of Jahn–Teller theory, see I. B. Bersuker, *Chem. Rev.* **101** (2001), 1067.
39. M. Hargittai, B. Réffy, M. Kolonits, C. J. Marsden, and J. -L. Heully, *J. Am. Chem. Soc.* **119** (1997), 9042.
40. We thank Professor G. Parkin and C. Zachmanoglou for providing the MLX program and database of transition-metal organometallic compounds taken from the *Dictionary of Organometallic Compounds*, 2nd edn. (London, Chapman and Hall, 1995).

41. M. L. H. Green, *J. Organomet. Chem.* **500** (1983), 127. The Green method is also called the “Covalent-Bond-Classification” (CBC) method.
42. A. Pidcock, R. E. Richards, and L. M. Venanzi, *J. Chem. Soc. A* **1966** (1966), 1707; B. Olgemoeller and W. Beck, *Inorg. Chem.* **22** (1983), 997; F. R. Hartley, *Chem. Soc. Rev.* **2** (1973), 163; R. P. Hughes, M. A. Meyer, M. D. Tawa *et al.*, *Inorg. Chem.* **43** (2004), 747; and C. R. Landis, T. K. Firman, D. M. Root, and T. Cleveland, *J. Am. Chem. Soc.* **120** (1998), 1842.
43. PtF_4^{2+} can be considered the “core” structure of hypervalent PtF_6 , a powerful oxidant used to oxidize O_2 and Xe: see N. Bartlett, *Endeavour* **88** (1963), 3.
44. A closely related complex anion, $\text{Pt}(\text{CN})_8^{2-}$, also can be “made” in the computer and adopts the analogous cubic coordination geometry. We note that experimentally characterized eight-coordinate anions of the early transition series such as $\text{W}(\text{CN})_8^{4-}$ are *not* cubic; cubic structures would not be expected due to the lower number of lone pairs at the metal and the higher d character in the bonding hybrids. Rather, D_{4d} or D_{2d} structures are found. The localized-bond analysis of $18e \text{W}(\text{CN})_8^{4-}$ gives three ω bonds, sd^4 hybridization, one lone pair, and formal charge of -1 at W.
45. M. Brookhart and M. L. H. Green, *J. Organomet. Chem.* **250** (1983), 395; and M. Brookhart, M. L. H. Green, and L. -L. Wong, *Prog. Inorg. Chem.* **36** (1988), 1. The underlying Greek word $\alpha\gamma\omicron\sigma\tau\acute{o}\varsigma$ is translated “to clasp, to draw towards, to hold to oneself.”
46. M. L. H. Green, *J. Organomet. Chem.* **500** (1983), 127.
47. G. W. Parshall and S. D. Ittel, *Homogeneous Catalysis: The Applications and Chemistry of Catalysis by Soluble Transition Metal Complexes*, 2nd edn. (New York, Wiley, 1992); and E. N. Jacobsen, A. Pfaltz, and H. Yamamoto (eds.), *Comprehensive Asymmetric Catalysis* (Berlin, Springer, 1999).
48. For a related complex, see W. V. Konze, B. L. Scott, and G. J. Kubas, *J. Am. Chem. Soc.* **124** (2002), 12 550; Bill Knowles shared the 2001 Nobel Prize (with Barry Sharpless and Ryoji Noyori) for his development of catalytic asymmetric hydrogenation.
49. C. R. Landis and J. Halpern, *J. Am. Chem. Soc.* **109** (1987), 1746.
50. For an overview of complexation of molecular dihydrogen to metals, see G. J. Kubas, *Metal Dihydrogen and Sigma-Bond Complexes: Structure, Theory, and Reactivity* (New York, Kluwer Academic, 2001).
51. Y. G. Abashkin, S. K. Burt, and N. Russo, *J. Phys. Chem. A* **101** (1997), 8085.
52. A. Pross and S. Shaik, *Acc. Chem. Res.* **16** (1983), 363; and M. -D. Su, *Inorg. Chem.* **34** (1995), 3829.
53. For comprehensive reviews of transition-metal-catalyzed alkene polymerization, see *Chem. Rev.* **100** (2000), issue 4; and J. Scheirs and W. Kaminsky (eds.), *Metallocene-Based Polyolefins: Preparation, Properties, and Technology*, Vol. 2 (London, John Wiley & Sons, 1999). See also W. J. Evans, D. M. DeCoster, and J. Greaves, *Macromolecules* **28** (1995), 7929.
54. M. J. S. Dewar, *Bull. Soc. Chim. Fr.* **C71** (1951), 18; and J. Chatt and L. A. Duncanson, *J. Chem. Soc.* **1953** (1953), 2939.
55. T. A. Albright, J. K. Burdett, and M. -H. Whangbo, *Orbital Interactions in Chemistry* (New York, Wiley, 1985), p. 322.
56. C. R. Landis and S. Feldgus, *Organometallics*, **20** (2001), 2374.
57. J. C. Stevens, in J. W. Hightower, W. Delglass, E. Iglesia, and A. T. Bell (eds.), *Studies in Surface Science and Catalysis*, Vol. 101 (Amsterdam, Elsevier, 1996), pp. 11–20; and the first two references in note 53.
58. P. Cossee, *J. Catal.* **3** (1964), 80; and E. J. Arlman and P. Cossee, *J. Catal.* **3** (1964), 99.
59. J. P. Collman, L. S. Hegedus, J. R. Norton, and R. G. Finke, *Principles and Applications of Organotransition Metal Chemistry* (Mill Valley, CA, University Science Books, 1987), pp. 580ff; and the first two references in note 53.
60. This term is meant to convey *relative* charge on C_m rather than truly ionic limiting character. Thus, as shown in Table 4.28, C_m is more negative by 0.734 charge units than the adjacent C_p .
61. C. R. Landis, K. A. Rosaen, and J. Uddin, *J. Am. Chem. Soc.* **124** (2002), 12 062.
62. R. D. Hancock and A. E. Martell, *Comments Inorg. Chem.* **6** (1988), 237.
63. R. H. Crabtree, *The Organometallic Chemistry of the Transition Metals* (New York, Wiley, 1988), p. 91.

64. M. L. H. Green, *J. Organomet. Chem.* **500** (1983), 127.
 65. M. E. Bos, W. D. Wulff, R. A. Miller, S. Chamberlin, and T. A. Brandvold, *J. Am. Chem. Soc.* **113** (1991), 9293.
 66. The full NBO/NRT description corresponds to about 30% contribution from each resonance structure in (4.107), 19% from



(see F. A. Cotton and M. Shang, *Inorg. Chem.* **29** [1990], 508) and the remainder from many minor structures, with overall NRT bond orders $b_{\text{IrC}} = 1.29$ and $b_{\text{CC}} = 1.35$.

67. G. Wilkinson, *J. Organomet. Chem.* **100** (1975), 273.
 68. T. J. Marks, *Prog. Inorg. Chem.* **25** (1979), 223; R. Poli, *Chem. Rev.* **91** (1991), 509; and B. E. Bursten and R. J. Strittmatter, *Angew. Chem. Int. Edn. Engl.* **30** (1991), 1069.
 69. R. Hoffmann, S. Shaik, and P. C. Hiberty, *Acc. Chem. Res.* **36** (2003), 750.
 70. See J. C. Green, *Chem. Soc. Rev.* **27** (1998), 263; and J. C. Green, J. N. Harvey, and R. Poli, *J. Chem. Soc., Dalton Trans.* **2002** (2002), 1861 and references cited therein.
 71. P. Pyykkö and J. -P. Desclaux, *Acc. Chem. Res.* **12** (1979), 276; and K. S. Pitzer, *Acc. Chem. Res.* **12** (1979), 271. For further discussion of the shapes of relativistic orbitals and the relationship to total angular momentum and magnetic quantum numbers, see R. E. Powell, *J. Chem. Educ.* **45** (1968), 558; and D. R. McKelvey, *J. Chem. Educ.* **60** (1983), 112.
 72. For these comparisons, each atom was chosen in nominal s^1d^{n-1} high-spin configuration. Note that the ground state of Pd (unlike those of Ni and Pt) is low-spin s^0d^{10} , so the relative tendency of Pd to form sd hybrids is, if anything, even *lower* than suggested by the large s-d splitting in Fig. 4.89.
 73. The corresponding energies ϵ_p of the (unoccupied) p orbitals lie at much higher (positive) values, out of the plotting range in Fig. 4.93.
 74. This matrix element corresponds to the Hückel β -parameter, and its magnitude would be directly proportional to the bond energy in a simple Hückel-like picture.
 75. Because the metal atom becomes slightly more negative down the column ($Q_{\text{Ni}} = +0.201$, $Q_{\text{Pd}} = +0.097$, $Q_{\text{Pt}} = -0.071$), the sum of valence occupancies does not “add up” to the expected nominal total for an isolated atom. The occupancy of the low-lying p shell is negligible ($\approx 0.01e$) in all cases.
 76. C. A. Bayse and M. B. Hall, *J. Am. Chem. Soc.* **121** (1999), 1348.

5

Supramolecular bonding

5.1 An introductory overview of intermolecular forces

5.1.1 Molecular and supramolecular units

The firm establishment of John Dalton's atomic theory in the early nineteenth century ushered in a long period of preoccupation with the nature of molecules¹ and the bond types responsible for molecule formation. By the mid twentieth century, a molecule was commonly defined² in operational terms as “the smallest part of a chemical substance that can exist free in the gaseous state, with retention of the composition and chemical properties that are possessed by the gaseous material in bulk,” or in more theoretical terms as “an aggregate of atoms which is held together by relatively strong (valence) forces, and which therefore acts as a unit.”

Let us first seek to give a more rigorous and operational *ab initio* characterization of such “units.” The important physical idea underlying the above definitions is that of the connecting covalent bonds that link the nuclei. One can therefore recognize that a molecular unit is equivalently defined by the *covalent-bond network* that contiguously links the nuclei included in the unit. We can re-state the definition of a “molecular unit” in a way that emphasizes the *electronic* origin of molecular connectivity.

(D1) *A molecular unit is an aggregate of atoms that is linked by a topologically connected network of covalent bonds; equivalently, an electronic distribution that links a collection of nuclei by a contiguous network of covalent bonds.*

Because the electronic distribution of a system is determined by $|\psi|^2$ for a specific solution of Schrödinger's equation, definition (D1) allows us to determine “molecular” character directly from the form of the system's wavefunction ψ , corresponding to some definite point on the Born–Oppenheimer potential-energy surface.³

If we now understand “covalent bond” to correspond to a specific form of two-center (or three-center) NBO in the optimal localized description of the electron

distribution $|\psi|^2$, we can give a fully operational NBO procedure for determining molecular units. Specifically, for a general N -electron system we may use the NBO procedure to search $|\psi(\vec{r}_1, \vec{r}_2, \dots, \vec{r}_N)|^2$ for the optimal localized NBO description (Section 1.5) that determines the linkages of nuclei into molecular units. Each molecular unit is thereby associated with the number of electrons required to fill the idealized Lewis-structure pattern of localized bonded and nonbonded NBOs. This leads to a composite set of nuclei and electrons that may be neutral or ionic, with either open- or closed-shell character, according to the numbers and types of occupied α and β spin NBOs. The definition (D1) therefore implicitly includes such species as H_2^+ , B_2H_6 , NO, and numerous other open- and closed-shell neutral and ionic aggregates that would properly be considered “molecular” species (in their near-equilibrium geometry) from the modern theoretical viewpoint. Note that this procedure can in principle be applied equally to $|\psi|^2$ for an isolated molecule or a system of many molecules.⁴

Already in the early twentieth century it was realized that definitions such as (D1) do not adequately cover all “units” of interest in chemistry. Thus, by 1902 Werner had demonstrated (Section 4.5.1) that numerous covalently saturated “ligand” (L) species (L = CO, NH_3 , H_2O , etc.) could exist both as free molecular species and in coordinated form as components of transition-metal complexes ML_n with open-shell metals M,



By 1920 it had also become apparent that weak associations existed between closed-shell hydride-bearing molecules (AH) and lone-pair-bearing bases (:B), leading to “hydrogen-bonded”⁵ species of the form

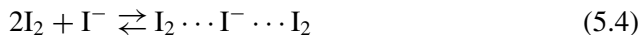


which can even persist strongly into the high-temperature vapor phase (e.g., formic acid⁶). A particularly striking example is the bifluoride ion ($\text{FH} \cdots \text{F}^-$), which exhibits *symmetric* $\text{F} \cdots \text{H}$ distances that obliterate any perceived distinction between “H-bond” and “covalent bond.” In the 1950s, Mulliken⁷ noted the appearance of characteristic spectroscopic lines in solutions of I_2 in benzene (and many related solution pairs) that could not be attributed to either pure component, but instead reflect the presence of weakly linked “charge-transfer complexes”



In the 1960s, Hassel⁸ studied the structures of many mixed crystals whose unit cells correspond to noncovalently linked “donor–acceptor complexes,” such as the

V-shaped I_5^- ion that can be formulated as



Each of the examples (5.1)–(5.4) illustrates the linking of molecules into *supramolecular* species that constitute new “units” of liquid, gaseous, or solid phases. Other provocative examples of supramolecular aggregation include the allotropic phases of sulfur (composed of a variety of linear and cyclic polymeric chains)⁹ and the remarkable Zintl salts (with anions composed of variable metal clusters).¹⁰

Let us, for the moment, simply refer to each dotted linkage in (5.1)–(5.4) as a “noncovalent bond,” without prejudice to a particular physical interpretation. In parallel to (D1) we can therefore make the following definition:

(D2) *a supramolecular unit is an aggregate of molecular units that is linked by a topologically connected network of noncovalent bonds; equivalently, an electronic distribution that links a collection of molecular units by a contiguous network of noncovalent bonds.*

Here, the concept of linkage implies only that each intermolecular noncovalent bond is sufficiently large compared with kT to withstand ambient thermal collisions. Thus, for near-standard-state conditions (where $kT \simeq 0.6 \text{ kcal mol}^{-1}$), even weak noncovalent interactions of $1\text{--}2 \text{ kcal mol}^{-1}$ may be adequate to yield supramolecular complexes with stable equilibrium populations, thereby becoming true constituent units of the phase of lowest free energy.

As in the molecular case (D1), the definition (D2) allows the supramolecular unit(s) to be determined by an operational NBO search of a given electron distribution $|\psi(\vec{r}_1, \vec{r}_2, \dots, \vec{r}_N)|^2$. Given the NBO molecular units of the distribution, we can search the intermolecular interactions (e.g., the table of perturbative donor–acceptor stabilizations) to determine the connecting noncovalent bonds that satisfy the required thermal threshold, and thereby determine the contiguously bonded supramolecular unit(s) by (D2).

Supramolecular aggregations are commonly referred to by a variety of terms, including “adduct,” “complex,” and “van der Waals molecule.” In this chapter we shall primarily employ the more neutral term “cluster,” which may, if desired, be qualified with the type of intermolecular interaction leading to clustering (e.g., “H-bonded cluster”). General and specific “types” of intermolecular forces are discussed in the following sections.

As defined above, the viability of a supramolecular cluster is temperature-dependent. This is also true for molecular species, but the strength of covalent bonds is so great compared with ambient thermal energies that we can normally ignore this dependence except at extremely high temperatures. The strength of intermolecular binding determines whether a given cluster has appreciable equilibrium

population at a given temperature, and thus should be considered a significant “unit” of the equilibrium phase at that temperature. For example, a weakly bound He_2 dimer is a physically significant component of the gaseous helium phase only at extremely low temperatures ($\ll 1$ K), whereas H-bonded $(\text{H}_2\text{O})_n$ clusters dominate both solid and liquid phases of water and aqueous solutions up to much higher temperatures. Our primary focus will therefore be on stronger forms of molecular association that lead to significant clustering in equilibrium phases under standard-state conditions.¹¹ Because terrestrial chemical and biological processes usually occur in aqueous solutions, where H-bonding and other forms of molecular association are ubiquitous, supramolecular clustering plays a critical role in a vast range of chemical and biochemical phenomena.

It is scarcely necessary to remark that a stable equilibrium population of clusters does *not* imply an infinite (or even very long) lifetime of an individual cluster. Indeed, even in the case of “stable” molecules in equilibrium, NMR evidence clearly demonstrates that individual atoms are often in rapid exchange with the surroundings, and the analogous dynamical exchange (or other reactive) processes in clusters are expected to be still more facile. The temporal history of any individual atom or molecular fragment may therefore reflect frequent shuttling between clusters, as well as dynamical rearrangements within clusters. Just as the lifetime of an organization may transcend that of its individual members, the persistence of a supramolecular cluster will often exceed that of individual atomic or molecular fragments of which it is composed.

On the experimental side, the characteristic “floppiness” and dynamical exchange rates of supramolecular clusters present a strong challenge to determination of their structures and abundancies. The useful structural information provided by any particular spectroscopic technique is sharply limited by how the intrinsic measurement time scale compares with the rates of dynamical exchange and rearrangement processes. Under these circumstances, *ab initio* theory provides a powerful source of information concerning the structures, energetics, and thermodynamic abundancies of supramolecular clusters.¹² Future progress in understanding supramolecular clustering is likely to depend on ever more determined use of *ab initio* theory as a primary structural tool, as well as development of creative new spectroscopic techniques to address the unique structural questions presented by clusters.

5.1.2 Conceptual and perturbative models of supramolecular bonding

The nature of the noncovalent bonds that link molecules into supramolecular clusters has inspired discussion and speculation throughout the history of valence theory. Werner’s transition-metal studies originally led to the concept of “near-valence”

(*Nebenvalenz*) to describe the chemical forces underlying formation of “inner complexes,” and G. N. Lewis’s general concept of the Lewis-acid–base adduct allowed many types of coordinate bonding to be recognized as simple extensions of Lewis-like covalent concepts.

The nature of the H-bonding linkage in Eq. (5.2) has been particularly controversial. Latimer and Rodebush¹³ stated that “The hydrogen nucleus held by two octets constitutes a weak bond.” G. N. Lewis¹⁴ wrote, in a section with the provocative title “Bivalent hydrogen,”

It seems to me that the most important addition to my theory of valence lies in the suggestion of what has become known as the hydrogen bond . . . This suggestion is that an atom of hydrogen may at times be attached to two electron pairs of two different atoms, thus acting as a loose bond between these atoms.

However, in his early papers on H-bonding¹⁵ Pauling argued that¹⁶

A hydrogen atom, with only one stable orbital, cannot form more than one pure covalent bond, and the attraction of two atoms observed in hydrogen-bond formation must be due to ionic forces.

These contrary views set the stage for a protracted battle between proponents of the “partial-covalency” and “electrostatic” explanations of H-bonding.¹⁷ In its most extreme form (expressed in practically all elementary chemistry textbooks), the electrostatic viewpoint emphasizes the importance of dipole-dipole and other long-range Coulombic forces of purely *classical* origin, with no appreciable resonance-type contributions. However, the recent discoveries of long-range quantum-mechanical phase coherence¹⁸ and NMR *J*-couplings¹⁹ across hydrogen bonds have provided powerful new evidence for the conclusion that “the electrostatic model does not account for all of the phenomena associated with H-bond formation.”²⁰

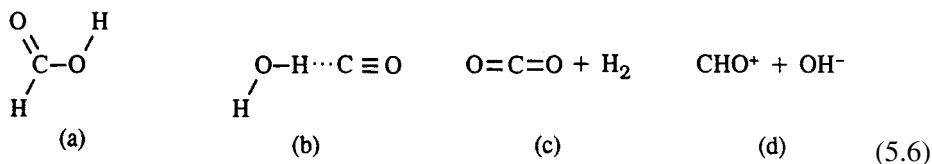
Let us attempt to pose the question of the chemical units and their interactions in a more rigorous mathematical manner. We start from the exact Hamiltonian \hat{H} for a system composed of N electrons (coordinates $\{\vec{r}_i\}$) and ν nuclei (coordinates $\{\vec{R}_A\}$),

$$\hat{H} = \hat{H}(\vec{r}_1, \vec{r}_2, \dots, \vec{r}_N; \vec{R}_A, \vec{R}_B, \dots) \quad (5.5)$$

At this (non-Born–Oppenheimer) level, all equivalent nuclei (like all electrons) appear in a completely *symmetric* manner, and the concept of “chemical structure” is absent.

As a specific example, let us suppose that the system is composed of 24 electrons, one carbon, two oxygen, and two hydrogen nuclei. To the chemist, this system might

correspond to any of the following Lewis structures:



However, the form of \hat{H} does not allow us to distinguish one structure from another; neither can we distinguish “ionizable H” from “non-ionizable H” in (5.6a) (any more than we can distinguish one electron from another). Thus, the exact Hamiltonian alone gives no help in choosing which (if any) structure is “correct” in the chemical sense, because \hat{H} is *identical* for all the species in (5.6).

Nevertheless, very-long-lived quasi-stationary-state solutions of Schrödinger’s equation can be found for each of the chemical structures shown in (5.6a)–(5.6d). These are virtually stationary on the time scale of chemical experiments, and are therefore in better correspondence with laboratory samples than are the true stationary eigenstates of \hat{H} .²¹ Each quasi-stationary solution corresponds (to an excellent approximation) to a distinct minimum on the Born–Oppenheimer potential-energy surface. In turn, each quasi-stationary solution can be used to construct an alternative *model* unperturbed Hamiltonian $\hat{H}^{(0)}$ and perturbative interaction $\hat{V}^{(\text{int})}$,

$$\hat{H} = \hat{H}_a^{(0)} + \hat{V}_a^{(\text{int})} = \hat{H}_b^{(0)} + \hat{V}_b^{(\text{int})} = \hat{H}_c^{(0)} + \hat{V}_c^{(\text{int})} = \hat{H}_d^{(0)} + \hat{V}_d^{(\text{int})} \quad (5.7)$$

In any given region of the Born–Oppenheimer potential-energy surface, we can judge which structure of (5.6a)–(5.6d) is *best* by determining which perturbative decomposition in (5.7) is numerically most rapidly convergent.

More generally, for any chosen assignment of chemical units we can rewrite \hat{H} as

$$\hat{H} = \hat{H}_{\text{units}}^{(0)} + \hat{V}_{\text{units}}^{(\text{int})} \quad (5.8)$$

The best choice of $\hat{H}_{\text{units}}^{(0)}$ in turn determines the form of the interaction $\hat{V}_{\text{units}}^{(\text{int})}$ between units. For example, if the best model is $\hat{H}_b^{(0)}$, corresponding to the H-bonded complex (5.6b), the corresponding $\hat{V}_b^{(\text{int})}$ is characteristic of hydrogen bonding, whereas if $\hat{H}_d^{(0)}$ is best, the corresponding $\hat{V}_d^{(\text{int})}$ is characteristic of an ionic interaction.²² Thus, by using the fact that a general *variational* model can be reformulated as a perturbative $\hat{H}^{(0)}$ (Section 1.1), we can use the machinery of perturbation theory both (i) to determine the optimal molecular (or supramolecular) units describing a particular region of the potential-energy surface, and (ii) to identify rigorously the corresponding interaction $\hat{V}_{\text{units}}^{(\text{int})}$ between these units. The NBO technique permits one to determine the optimal $\psi_{\text{units}}^{(\text{NBO})}$ and $\hat{H}_{\text{units}}^{(0)}$ for such a

perturbative description of the interactions between molecular or supramolecular units in a very general fashion (most commonly within the framework of the Born–Oppenheimer approximation).

Note that, in contrast to other forms of intermolecular perturbation theory to be considered below, the NBO-based decomposition (5.8) is based on a full matrix representation of the supermolecule Hamiltonian \hat{H} . All terms in (5.8) are therefore fully consistent with the Pauli principle, and both $\hat{H}_{\text{units}}^{(0)}$ and $\hat{V}_{\text{units}}^{(\text{int})}$ are properly Hermitian (and thus, physically interpretable) at all separations.

5.1.3 Classical and non-classical intermolecular bonding forces

London's perturbation theory of long-range intermolecular forces and its limits

The standard classification of “types” of intermolecular forces goes back to London's perturbation theory of the 1930s.²³ Before introducing these types, we briefly review the premises and terminology of London's theory, particularly the fundamental distinction between short-range and long-range forces.

The starting point for London's treatment is a partitioning of the N electrons and ν nuclei of a composite Hamiltonian \hat{H} into two subunits (distinguished by prime and double-prime symbols) associated with respective Hamiltonian operators \hat{H}' and \hat{H}'' ,

Units	\hat{H}'	\hat{H}''	
Electrons (i)	$1, 2, \dots, j$	$j + 1, \dots, N$	(5.9)
Nuclei (α)	$1, 2, \dots, \lambda$	$\lambda + 1, \dots, \nu$	

As indicated, we shall denote electrons and nuclei with Roman (i) and Greek (α) indices, respectively. In terms of kinetic-energy operators for electrons (\hat{t}_e) and nuclei (\hat{T}_N) and the Coulombic potential-energy interactions of electron–electron (\hat{v}_{ee}), nuclear–nuclear (\hat{V}_{NN}), and nuclear–electron (\hat{V}_{Ne}) type, we can write the supermolecule Hamiltonian as

$$\hat{H} = \hat{H}' + \hat{H}'' + \hat{V}_{\text{int}} \quad (5.10)$$

where, for example, the Hamiltonian \hat{H}' is

$$\hat{H}' = \hat{t}_e + \hat{T}_N + \hat{v}_{e'e'} + \hat{V}_{N'N'} + \hat{V}_{N'e'} \quad (5.11a)$$

and the interaction \hat{V}_{int} is

$$\hat{V}_{\text{int}} = \hat{v}_{e'e''} + \hat{V}_{N'N''} + \hat{V}_{N'e''} + \hat{V}_{N''e'} \quad (5.11b)$$



Fritz London

In terms of electronic (\vec{r}_i) and nuclear (\vec{R}_α) coordinates, the first three terms of (5.11b) are

$$\hat{v}_{e'e''} = \sum_{i'} \sum_{j''} \frac{e^2}{|\vec{r}_{i'} - \vec{r}_{j''}|} \quad (5.12a)$$

$$\hat{V}_{N'N''} = \sum_{\alpha'} \sum_{\beta''} \frac{(Z_{\alpha'}e)(Z_{\beta''}e)}{|\vec{R}_{\alpha'} - \vec{R}_{\beta''}|} \quad (5.12b)$$

$$\hat{V}_{N'e''} = \sum_{\alpha'} \sum_{i''} \frac{(Z_{\alpha'}e)(-e)}{|\vec{R}_{\alpha'} - \vec{r}_{i''}|} \quad (5.12c)$$

and the remaining term is written analogously.

Now let the centers of mass of each unit be denoted \vec{R}_c' and \vec{R}_c'' , respectively, and write the Hamiltonian (5.10) in standard perturbative form

$$\hat{H} = \hat{H}^{(0)} + \hat{V}_{\text{int}} \quad (5.13)$$

Then, in the long-range limit

$$R = |\vec{R}_c' - \vec{R}_c''| \rightarrow \infty \quad (5.14)$$

the unperturbed operator and eigenfunction are assumed to be

$$\hat{H}^{(0)} = \hat{H}'(\vec{R}_c') + \hat{H}''(\vec{R}_c'') \quad (5.15a)$$

$$\psi^{(0)} = \psi'(\vec{R}_c') \cdot \psi''(\vec{R}_c'') \quad (5.15b)$$

where

$$\hat{H}'\psi' = E'\psi' \quad (5.16a)$$

$$\hat{H}''\psi'' = E''\psi'' \quad (5.16b)$$

From this starting point, London employed standard techniques of Rayleigh–Schrödinger perturbation theory to evaluate the leading effects of the intermolecular \hat{V}_{int} on the non-interacting molecules described by $\hat{H}^{(0)}$.

Equation (5.15b) is the fundamental assumption underlying London’s theory, which is *essential* both for numerical evaluation and for physical interpretation of the perturbative expressions. Whereas short-range *intramolecular* interactions in (5.16a) and (5.16b) must be described with properly antisymmetric eigenfunctions satisfying

$$\hat{A}\psi' = \psi', \quad \hat{A}\psi'' = \psi'' \quad (5.17a)$$

London assumed that the unperturbed system $\hat{H}^{(0)}$ of (5.15a) can be adequately approximated by the *non*-antisymmetric $\psi^{(0)}$ of (5.15b):

$$\hat{A}\psi^{(0)} \neq \psi^{(0)} \quad (5.17b)$$

The neglect of intermolecular exchange effects in (5.15b) greatly simplifies the numerical evaluation of the first-order correction

$$E^{(1)} = \langle \psi^{(0)} | \hat{V}_{\text{int}} | \psi^{(0)} \rangle \quad (5.18)$$

(as well as higher perturbative corrections) and leads to an appealing *classical* interpretation of contributions to $E^{(1)}$ (see below). Because “exchange effects” are purely quantum mechanical in nature, associated with mathematical terms that grow *exponentially* as intermolecular distance diminishes, the approximation (5.15b) is only tenable in the long-range limit (5.14).

London introduced a second approximation by expanding \hat{V}_{int} as a “multipole” power series in $1/R$ (inverse intermolecular separation)

$$\hat{V}_{\text{int}} = \sum_n \frac{V^{(n)}}{R^n} \quad (5.19)$$

whose successive terms depend on permanent multipoles (dipole, quadrupole, . . .) of the separated species. The multipole expansion (5.19) is valid (convergent) only if the intermolecular separation is much greater than the effective molecular radii (e.g., empirical van der Waals radii)

$$R \gg \langle |\vec{R}_c' - \vec{r}_i'| \rangle_{\text{max}} + \langle |\vec{R}_c'' - \vec{r}_j''| \rangle_{\text{max}} \quad (5.20)$$

Like (5.15b), the multipole approximation (5.19) is dependent on the long-range assumption (5.14); *both* approximations fail (for different reasons) if the molecular wavefunctions ψ' and ψ'' overlap appreciably.

Note that failure to satisfy (5.20) has far more serious theoretical consequences than mere failure of convergence of the multipole series (5.19). This can be seen by examining excited-state solutions $\psi_{i'}$ and $\psi_{j''}$ of (5.16a) and (5.16b), the higher “unperturbed eigenfunctions” of $\hat{H}^{(0)}$:

$$\psi_{ij}^{(0)} = \psi_{i'}(\vec{R}_c') \cdot \psi_{j''}(\vec{R}_c'') \quad (5.21)$$

In the overlap region these “unperturbed eigenfunctions” can no longer remain mutually orthogonal,

$$\langle \psi_{ij}^{(0)} | \psi_{kl}^{(0)} \rangle \neq \delta_{ik} \delta_{jl} \quad (5.22a)$$

and the corresponding “unperturbed Hamiltonian” $\hat{H}^{(0)}$ therefore *cannot* be a Hermitian operator,²⁴

$$\hat{H}^{(0)} \neq \hat{H}^{(0)\dagger} \quad (5.22b)$$

Thus, attempts to extend the London theory to distances at which (5.20) is violated must lead to unphysical (non-Hermitian) “perturbation corrections,” with increasingly severe mathematical and physical contradictions. These difficulties are in contrast to the corresponding NBO-based decomposition (5.8), which remains Pauli-compliant and Hermitian at all distances.

From the beginning, London’s theory was recognized as an expedient, but somewhat arbitrary, device to simplify numerical evaluations and recover quasi-classical interpretations of selected “long-range contributions” to the total intermolecular interaction; in the words of a classic text,²⁵

It is convenient, although artificial to divide intermolecular forces into two types – long-range (van der Waals) forces and short-range (valence or chemical) forces.

It is remarkable that London’s approximate treatment allowed the “long-range forces” to be described with considerable accuracy some three or four decades before the short-range “chemical” forces became comparably tractable. Before proceeding to the description of the short-range valence or chemical forces (with which this book is principally concerned), we briefly review the leading London long-range types.

London identified three major types of long-range forces: (LR-1) electrostatic, (LR-2) induction, and (LR-3) dispersion. (A fourth [“degeneracy” or “resonance”] type occurs only in specialized cases involving identical molecules, one of which is in a degenerate excited state,²⁶ and will not be considered further.) Of these, (LR-1)

and (LR-2) have direct classical counterparts and occur in the first-order correction (5.18), whereas (LR-3) is a higher-order correction that is intrinsically quantum mechanical in nature. We now briefly describe each force type in turn.

(LR-1) electrostatic forces

The multipole expansion (5.19) includes a potentially infinite number of terms depending on net charges (C_a, C_b), dipole moments (μ_a, μ_b), quadrupole moments (Q_a, Q_b), and higher electric multipole moments of the isolated molecules a and b. The leading term of each type can be written in terms of an R -dependent coefficient and an angular factor (typically of order unity in the most favorable orientation). We summarize below the multipoles and radial dependences of the leading few terms, neglecting details of the angular factors (which are given in standard references²⁷):

$$\text{ionic:} \quad C_a C_b / R \quad (5.23a)$$

$$\text{ion-dipole:} \quad C_a \mu_b(\text{angular}) / R^2 \quad (5.23b)$$

$$\text{ion-quadrupole:} \quad C_a Q_b(\text{angular}) / R^3 \quad (5.23c)$$

$$\text{dipole-dipole:} \quad \mu_a \mu_b(\text{angular}) / R^3 \quad (5.23d)$$

$$\text{dipole-quadrupole:} \quad \mu_a Q_b(\text{angular}) / R^4 \quad (5.23e)$$

$$\text{quadrupole-quadrupole:} \quad Q_a Q_b(\text{angular}) / R^5 \quad (5.23f)$$

Note that *two* distinct types of interactions (ion-quadrupole and dipole-dipole) contribute to an overall R^{-3} dependence, and the number of distinct multipole types having similar R^{-n} dependences continues to increase with increasing n . For uncharged systems, the dipole-dipole interaction (5.23d) is expected to dominate, with an angular term that favors parallel alignment of the two dipoles.

(LR-2) induction forces

For polarizable charge distributions, additional classical-type interactions arise from the *induced* dipole, quadrupole, and higher moments on each monomer, which are proportional to the fields created by the asymmetric charge distribution on the other monomer. The proportionality constants for each multipole field are the monomer *polarizabilities* α_a and α_b ($\alpha^{(\mu)}$ for dipole fields, $\alpha^{(Q)}$ for quadrupole fields, etc.). The leading two induction interactions are:

$$\text{ion-induced dipole:} \quad -\frac{1}{2} C_a^2 \alpha_b / R^4 \quad (5.24a)$$

$$\text{dipole-induced dipole:} \quad -\mu_a^2 \alpha_b(\text{angular}) / R^6 \quad (5.24b)$$

Whereas the electrostatic forces arising from permanent moments can be attractive or repulsive (depending on orientation), the induction forces are intrinsically attractive. In the large- R limit, these interactions are generally negligible (i.e., of

the same order as neglected terms in the *permanent* multipole series (5.23)) unless lower-order permanent moments are absent. Thus, if (5.19) and (5.20) are valid for neutral species, the leading induction term (of dipole-induced-dipole type) should be negligible compared with leading permanent-moment terms in (5.23).

(LR-3) dispersion forces

The most celebrated result of London's theory is the dispersion interaction

$$\text{dispersion:} \quad -D_{ab}/R^6 \quad (5.25)$$

so named because the coefficient D_{ab} can be expressed in terms of the same oscillator strengths and spectral energy differences as those that appear in the theory of the dispersion of light. The London dispersion force is also called the "van der Waals force" (and D_{ab} the "van der Waals force constant") because its R^{-6} dependence is consistent with the attractive term in the well-known van der Waals equation of state for gases. The dispersion interaction affects even the most spherically symmetric charge distributions (i.e., those of rare-gas atoms) and hence leads to aggregation and condensation of *all* matter at sufficiently low temperature.

The physical origin of the dispersion interaction is often described in terms of a quasi-classical induced-dipole–induced-dipole picture. The quantum-mechanical fluctuations of the electronic distribution about its spherically symmetric average can be pictured as leading to an instantaneous (snapshot) dipole $\mu_a^{(\text{inst})}$ on monomer a, which in turn induces an instantaneous dipole $\mu_b^{(\text{inst})}$ on b. Thus, if the dipole fluctuations of the two monomers are properly *correlated*, a net attraction of the form (5.25) results. As remarked by Hirschfelder *et al.*²⁸

The classical explanation of the dispersion forces between two atoms . . . seems qualitatively correct and quite plausible. This mechanism, however, is not apparent from the quantum mechanical derivations. On this account, it is best if we do not stress the classical significance of these forces.

Casimir and Polder²⁹ later showed that the dispersion interaction constant D_{ab} can be expressed in the surprising form

$$D_{ab} = \frac{3}{\pi} \int_0^\infty \alpha_a(i\omega)\alpha_b(i\omega)d\omega \quad (5.26)$$

where $\alpha_a(i\omega)$ is the dynamical (frequency-dependent) electric polarizability of monomer a at *imaginary* frequency $i\omega$. The deep quantum-electrodynamical reasoning that underlies this remarkable expression is beyond the scope of this book.

Casimir and Polder also showed that, at *very* long range (i.e., separations greater than a characteristic distance R_0 of a few hundred ångström units), the dispersion interaction takes the modified asymptotic form

$$\text{very-long-range dispersion:} \quad -D_{\text{ab}}^{(\text{rel})}/R^7 \quad (5.27)$$

weakened by a factor $1/R$ as a result of relativistic retardation. Qualitatively, this effect can be attributed to the finite speed of light and resulting slight time delay for an initial $\mu_{\text{a}}^{(\text{inst})}$ on a to make its presence felt as an induced fluctuation $\mu_{\text{b}}^{(\text{inst})}$ on b; retardation allows the dipole fluctuations to “wobble” out of perfect alignment, weakening the dispersion interaction with respect to its non-relativistic form (5.26). The relativistic weakening of dispersion interactions has important effects on the stability of colloids³⁰ and demonstrates that the range of validity of an R^{-6} -type dispersion contribution is limited both at large *and* at small R .

Summing up, we can say that the underlying assumptions (5.15b) and (5.17b) of London’s theory are valid only in the long-range region where quantum-mechanical exchange effects are truly negligible. Just as it would be meaningless to employ (5.27) as the “dispersion contribution” for $R < R_0$ (because there is *no* such physical interaction of this mathematical form at shorter distances), it is similarly unjustified to assume that classical-type expressions (5.23) retain validity in the short-range region where quantum exchange effects are significant. While such quasi-classical extrapolations are sorely tempting,³¹ they necessarily lead to unphysical violations of Hermiticity and antisymmetry (sterics) as noted in (5.22b). For this reason, we make no attempt to separate quasi-classical London-like terms from the full quantum expressions, but instead adopt the NBO-based perturbative decomposition (5.8) that is inherently fully quantal and applicable at *all* distances. As shown by Glendening and coworkers using the natural-energy-decomposition-analysis (NEDA) method,³² one can indeed define NBO-based “electrostatic” and “polarization” components that reduce properly to the expected classical asymptotic forms in the long-range limit. However, the equilibrium geometries of important supramolecular complexes lie well *inside* the distance of van der Waals contact,³³ where exchange effects are certainly non-negligible, i.e., where *exponential* quantal exchange effects supplant the benign power-law behavior of the classical long-range limit.

The short-range valence or chemical forces: “resonance bonding”

Virtually by definition, the forces *between* molecules cannot be ascribed to “covalent bonds” such as those that link atoms *within* molecules. Hence, such forces may be (and often are) tautologically labeled as “noncovalent” to distinguish them from the strongest $2c/2e$ “covalent” bonds that underlie the formation of molecules. (Nearly as uninformative is the designation “weak bonding,” which

is supposed to be contrasted with the “strong bonding” of conventional 2c/2e covalency.)

A rather impoverished view of chemical valency and bonding interactions might suggest that standard 2c/2e covalent bonds exhaust the possibilities of quantal exchange phenomena, and that remaining intermolecular interactions should be considered to be of classical long-range type (as described above). However, even chemists of the pre-quantum era recognized the necessity of generalizing the simplest 2c/2e bonding picture to accommodate the effects of “electromerism” or “resonance,” schematically represented as a kind of *averaging* between distinct bonding patterns, e.g.,



The essence of the resonance concept is *partial* (non-integer) bond order, *intermediate* between, e.g., the idealized single- and double-bond patterns in (5.28a).

A similar resonance concept may be envisioned in cases in which a bond linking A, B, and C is *lacking* in one or the other resonance structure,



Still other resonance possibilities refer to molecular fragments that are completely disconnected (though in different ways) in *both* resonance structures,



Such “disconnected” resonance structures correspond to *intermolecular* resonance, i.e., to *partial* bond orders between distinct “molecular units.” Resonance diagrams such as (5.28b) and (5.28c) suggest that the distinction between “intramolecular” and “intermolecular” partial bonding must be, at most, a matter of *degree*.

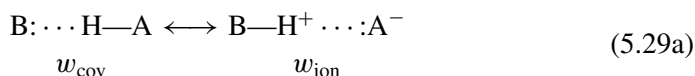
Resonance such as (5.28a)–(5.28c) is inherently a quantal phenomenon, with no classical counterpart. In NBO language, each of the resonance interactions (5.28a)–(5.28c) corresponds to a donor–acceptor interaction between a nominally filled (donor; Lewis-type) and unfilled (acceptor; non-Lewis-type) orbital, the orbital counterpart of G. N. Lewis’s general acid–base concept. As mentioned above, Lewis and Werner (among others) had well recognized the presence of such valence-like forces in the dative or coordinative binding of free molecular species. Thus, the advent of quantum mechanics and Pauling’s resonance theory served to secure and justify chemical concepts that had previously been established on the basis of compelling chemical evidence.

Because the resonance-type interactions (5.28b) and (5.28c) that lead to partial bond order *between* molecular species are essentially similar to those *within*

molecules (5.28a), it is clear that the term “noncovalent bonding” is seriously inadequate and misleading with respect to the underlying covalent (or partially covalent) nature of these interactions. Instead, we suggest that such interactions are better characterized as “resonance forces” to indicate clearly their close association with other chemical bonding and resonance phenomena. In this chapter we describe the most important intermolecular forces of this type, emphasizing the close relationship of intermolecular resonance forces to other NBO donor–acceptor phenomena studied throughout this book.

5.2 Hydrogen bonding

As remarked in Section 5.1.2, the discovery of hydrogen bonding provoked ongoing controversy between proponents of a “partial covalency” and advocates of an “electrostatic” picture of H-bond formation. The former group emphasized the importance of resonance-type *chemical* forces of quantum-mechanical origin that could be represented as



whereas the latter emphasized the importance of dipole–dipole and other electrostatic forces of classical origin.

The persistent and seductive appeal of classical electrostatic models is in part attributable to the fact that the simplest Coulombic approximation (with plausible atomic charges and the given H-bonded geometry) leads to binding energies of the correct order of magnitude (see Example 5.1). Commenting on this fortuitous agreement, Coulson wrote,³⁴

It is tempting to argue that in view of the close agreement between this electrostatic energy and the hydrogen bond energy, a true account has been obtained of the most important factors involved. But this is not so.

Coulson concluded that the most important contribution to H-bonding is “ionic resonance” (5.29a). However, generations of empirical modelers have found it convenient to employ simple pairwise-additive Coulombic formulas with empirically fitted point charges to model H-bonds, and such empirical models have tended to encourage uncritical belief in the adequacy of a classical electrostatic picture of H-bonding.

Example 5.1

Problem: Given the monomer natural charges (Q_i) and the equilibrium Cartesian coordinates (x_i, y_i, z_i) of the water dimer, $\text{H}_2\text{O} \cdots \text{H}_2\text{O}$

Atom i	Q_i	x_i (Å)	y_i (Å)	z_i (Å)
O	-0.916	-0.006 183	1.525 447	0.000 000
H	+0.458	0.036 726	0.556 520	0.000 000
H	+0.458	0.909 465	1.817 564	0.000 000
O	-0.916	-0.006 183	-1.376 675	0.000 000
H	+0.458	-0.423 629	-1.782 131	0.767 110
H	+0.458	-0.423 629	-1.782 131	-0.767 110

evaluate the apparent electrostatic binding energy from the classical Coulomb formula

$$\Delta E_{\text{Coulomb}} = \sum_{i=1}^3 \sum_{j=4}^6 \frac{Q_i Q_j}{|\vec{R}_i - \vec{R}_j|}$$

Solution: $\Delta E_{\text{Coulomb}} = -8.2 \text{ kcal mol}^{-1}$. (The actual H-bond energy is $\Delta E_{\text{H-bond}} = -5.8 \text{ kcal mol}^{-1}$.)

In NBO language, the resonance hybrid (5.29a) corresponds to a two-electron intermolecular donor–acceptor interaction of the form



in which electron density from the lone pair n_{B} of the Lewis base B: delocalizes into the unfilled σ_{AH}^* hydride antibonding orbital of the Lewis acid AH. Such intermolecular delocalization also corresponds to partial *charge transfer* (CT) from the Lewis base to the Lewis acid, conferring partial positive charge on the former and negative charge on the latter, as depicted in the right-hand resonance structure in (5.29a). Stronger $n_{\text{B}} \rightarrow \sigma_{\text{AH}}^*$ delocalization therefore leads to increased weighting of the ionic resonance form (w_{ion}) in the resonance hybrid (5.29a).

Hydrogen bonds may be considered special types of 3c/4e interactions, closely related to other forms of hypervalency in main-group (Section 3.5) and d-block (Section 4.6) compounds. However, the fundamental $n_{\text{B}} \rightarrow \sigma_{\text{AH}}^*$ interaction of $\text{B} \cdots \text{HA}$ hydrogen bonding displays unusual characteristics compared with other “three-center MO” phenomena, due mainly to the unique properties of the H atom, whose valence shell contains only the isotropic 1s orbital for construction of σ_{AH} and σ_{AH}^* NBOs.

On the basis of known shapes of hydride bonds and antibond NBOs (Section 3.2.6) and their dependence on the relative electronegativity of A and H, we can predict certain geometrical, energetic, and dielectric features of B:···HA hydrogen bonding, all related to the strength of $n_B \rightarrow \sigma_{AH}^*$ charge-transfer delocalization.

- (1) Hydrogen-bonded complexes will tend to adopt the near-linear geometry corresponding to *strongest* $n_B \rightarrow \sigma_{AH}^*$ interaction (“maximum $n_B - \sigma_{AH}^*$ overlap”), i.e.,

$$|\langle n_B | \hat{F} | \sigma_{AH}^* \rangle| = \text{maximum} \quad (5.30a)$$

for the highest-energy, most diffuse lone pair n_B and the lowest-energy, most polar hydride antibond σ_{AH}^* .

- (2) Owing to the increased occupancy of the σ_{AH}^* antibond, the covalent A—H bond will be lengthened and weakened (stretching frequency ν_{AH} red-shifted):

$$\Delta R_{AH} > 0 \quad (5.30b)$$

$$\Delta \nu_{AH} < 0 \quad (5.30c)$$

- (3) To maximize $n_B - \sigma_{AH}^*$ overlap, the σ_{AH} bond will repolarize to *withdraw* electron density from H (increasing ionicity i_{AH}), thereby *increasing* the amplitude of σ_{AH}^* on H,

$$\Delta i_{AH} > 0 \quad (5.30d)$$

- (4) The monomer AH becomes slightly *anionic* and B becomes slightly *cationic* as a result of the $n_B \rightarrow \sigma_{AH}^*$ intermolecular charge transfer, with resultant net charge transfer $Q_{CT} = Q_B - Q_{AH}$ from Lewis base to Lewis acid:

$$Q_{AH} < 0, \quad Q_B > 0 \quad (Q_{CT} > 0) \quad (5.30e)$$

The simple $n_B - \sigma_{AH}^*$ predictions (5.30a)–(5.30e) can be tested and compared with expectations of classical electrostatic models for each of the H-bonded complexes to be discussed below.

Note that the repolarization effect (5.30d) can lead to a paradox (Example 5.2), namely, that net electron density is *diminished* around the H-bonded proton, even though slight electron population is *added* to AH in H-bond formation. Combined with the loss of occupancy from B, this has the consequence that an electron-density-difference map will usually show net *reduction* (not “pile-up”) of electronic charge in the B···H region. The resolution of this paradox can be expressed by saying that the charge transfer is into the σ_{AH}^* antibond, whose induced repolarization often shifts a *larger* quantity of charge in σ_{AH} away from the proton.

Example 5.2

Problem: In a certain $B \cdots HA$ hydrogen bond, the σ_{AH} bond repolarizes by 1% from its free form

$$\sigma_{AH(f)} = (0.60)^{1/2}h_A + (0.40)^{1/2}h_H$$

to its H-bonded form

$$\sigma_{AH(b)} = (0.61)^{1/2}h_A + (0.39)^{1/2}h_H$$

and $0.030e$ of charge is transferred from n_B to $\sigma_{AH(b)}^*$. In this process, does the formal electron population at H increase or decrease?

Solution: Assuming double occupancy of σ_{AH} , the 1%-repolarization effect reduces the electron population at H by

$$(0.40 - 0.39)(2e) = 0.020e$$

whereas the $0.030e$ added occupancy of the antibond $\sigma_{AH(b)}^* = (0.39)^{1/2}h_A - (0.61)^{1/2}h_H$ increases the electron population at H by

$$0.61(0.030e) = 0.018e$$

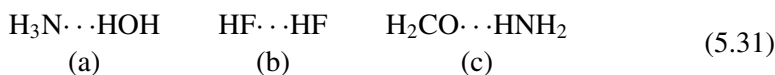
Thus, the net electron population on H is reduced (by $0.002e$), even though AH becomes more *anionic* overall.

Although (1)–(4) involve “polarization” and other terms that are reminiscent of a classical dipole–dipole picture, it must be re-emphasized that the n_B – σ_{AH}^* picture is formulated entirely in the *quantal* framework (including full consistency with the Pauli exclusion principle). Thus, while vague connections to concepts of classical electrostatics can be drawn, the NBO donor–acceptor picture of H-bonding is essentially based on overlap-type “ionic resonance” (5.29a), not on “ionic forces” (or the like) of classical type.

5.2.1 Binary H-bonds

Prototype H-bonded complexes

As simple prototypes of hydrogen bonds, let us first consider the three binary complexes



as shown in Fig. 5.1. The $\text{H}_3\text{N} \cdots \text{H}_2\text{O}$ complex (Fig. 5.1(a)) serves as a prototype of the hydrogen bond of amine bases in aqueous solution, where the phenomenon of H-bonding was first clearly recognized.³⁵ The $\text{HF} \cdots \text{HF}$ dimer (Fig. 5.1(b)) is

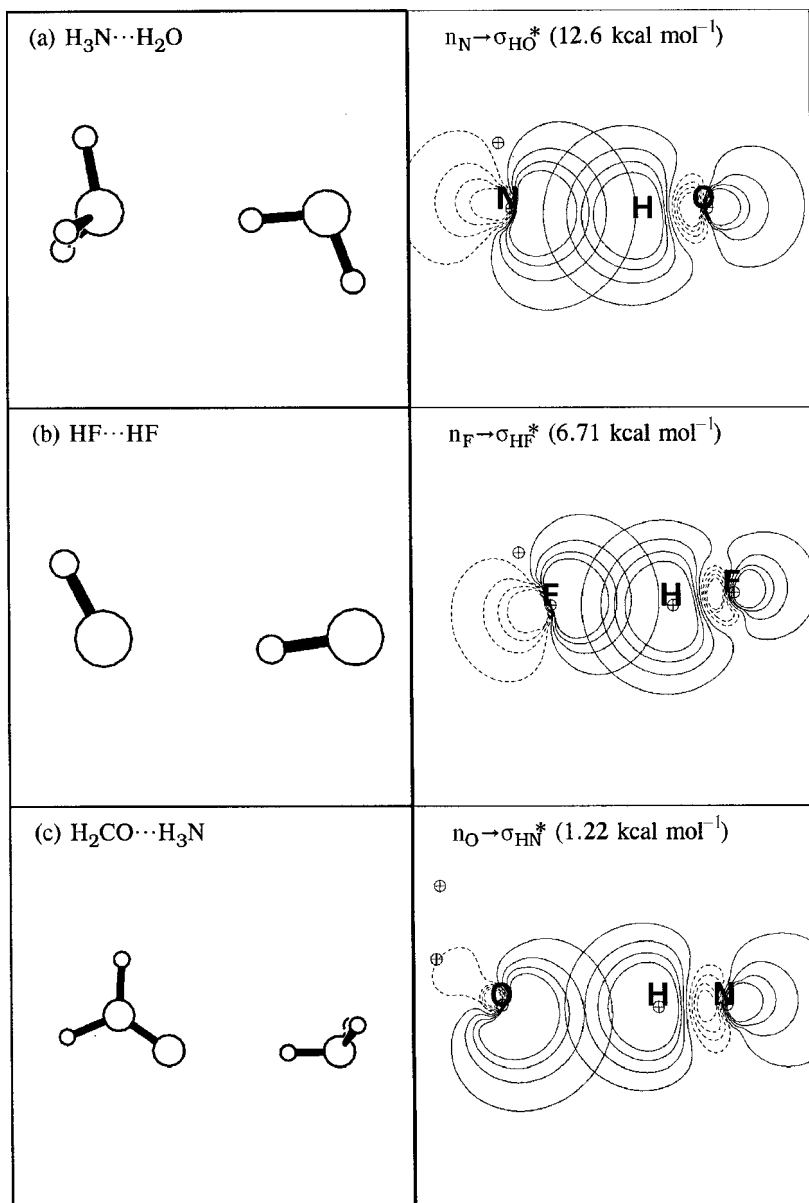


Figure 5.1 Hydrogen-bonded $\text{B}\cdots\text{HA}$ binary complexes (left) and leading $n_{\text{B}} \rightarrow \sigma_{\text{HA}}^*$ donor-acceptor interactions (right), with second-order stabilization energies in parentheses (cf. Table 5.1). (Note that the H atom falls slightly out of the contour plane in the upper-right panel, so that the cross-hairs symbol for this nucleus is absent.)

Table 5.1. *Properties of binary B:⋯⋅HA hydrogen-bonded complexes (see Fig. 5.1), showing the H-bond energy $\Delta E_{B\cdots H}$, H-bond length $R_{B\cdots H}$, van der Waals contact distance $R_{B\cdots H}^{(vdW)}$, and covalent-bond elongation ΔR_{AH} (relative to isolated monomer)*

Species	$\Delta E_{B\cdots H}$ (kcal mol ⁻¹)	$R_{B\cdots H}$ (Å)	$R_{B\cdots H}^{(vdW)}$ (Å)	ΔR_{AH} (Å)
H ₃ N⋯⋅HOH	7.27	1.96	3.05	0.0149
HF⋯⋅HF	5.05	1.83	2.69	0.0069
H ₂ CO⋯⋅HNH ₂	1.41	2.35	2.88	0.0018

noteworthy for the simplicity of its component monomers, each a simple diatomic of high polarity that approximates an ideal dipole. The H₂CO⋯⋅H₃N complex (Fig. 5.1(c)) serves as a prototype of the C=O⋯⋅H—N hydrogen bond that is ubiquitous in proteins, and hence critical to life processes. Table 5.1 summarizes some structural and energetic parameters for these species.

All three species in Fig. 5.1 exhibit equilibrium structures that are distinctly peculiar from a classical electrostatic viewpoint. Each monomer has a pronounced dipole,

$$\mu_{\text{NH}_3} = 1.69 \text{ D} \quad (5.32a)$$

$$\mu_{\text{H}_2\text{O}} = 2.16 \text{ D} \quad (5.32b)$$

$$\mu_{\text{HF}} = 1.98 \text{ D} \quad (5.32c)$$

$$\mu_{\text{H}_2\text{CO}} = 2.45 \text{ D} \quad (5.32d)$$

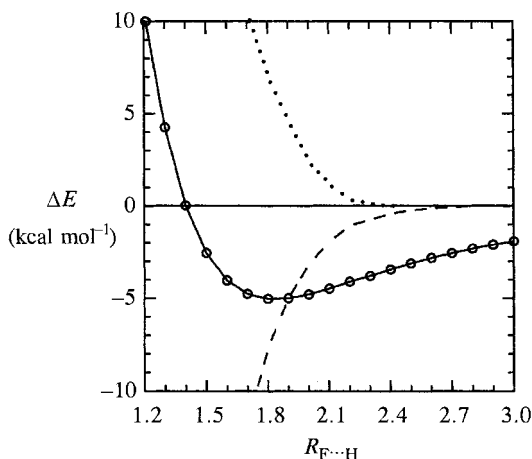
directed, in each case, along the principal rotation axis (with the negative pole toward the electronegative heavy atom and the positive pole toward the hydrogens). Yet even in the “ideal-dipole” HF-dimer case, one monomer is strongly canted out of collinearity, nearly *perpendicular* to the direction that would maximize dipole–dipole attraction. In H₂CO⋯⋅H₃N the two monomer–dipole orientations (although roughly parallel) are displaced far from the expected collinearity, and in H₃N⋯⋅H₂O the relative orientation of dipoles is again far (>50°) from that expected to maximize dipole–dipole attraction. Thus, a classical dipole–dipole picture gives little or no useful guidance as to the actual structures assumed by these H-bonded complexes. Neither do the magnitudes of monomer dipoles (all within ~20% of $\bar{\mu} = 2.1$ D) correlate in any obvious manner with H-bond strengths (which vary by more than a factor of *five*).

The reason for the failure of a long-range electrostatic picture is evident from comparison of the actual $R_{B\dots H}$ H-bond distance (second column of Table 5.1) with the corresponding sum of van der Waals radii $R_{B\dots H}^{(vdW)}$ (third column). As this comparison shows (cf. note 33), the actual monomer separations are far *inside* van der Waals contacts, by distances ranging from 0.5 Å to more than 1.1 Å! Hence, the condition (5.20) for the validity of the London long-range approximation is grossly violated, and it is not surprising that the resulting classical-like electrostatic formulas have little relevance for the actual equilibrium region of H-bonded species.

The importance of overlap-type interactions is also apparent from the $n_B \rightarrow \sigma_{AH}^*$ NBO contour diagrams shown in the right-hand panels of Fig. 5.1. These interactions lead to stabilizations of 1–12 kcal mol⁻¹, sufficient to overcome the significant steric barrier that must be present at such short equilibrium distances. In each case the observed geometry is close to that expected (cf. (5.30a)) from *maximizing* the intermolecular overlap of the donor lone pair n_B and the acceptor antibond σ_{AH}^* orbitals.³⁶ Thus, the simple $n_B \rightarrow \sigma_{AH}^*$ picture predicts a qualitatively correct H-bonding geometry, on the basis of general overlap principles similar to those employed for other donor–acceptor interactions surveyed throughout this book.

Example 5.3

Let us examine the balance between steric and donor–acceptor forces in greater detail for the case of HF···HF. The graph below plots the adiabatic potential-energy curve for H-bond formation (solid line, circles), as well as the steric repulsion energy³⁷ ΔE_{steric} (dotted line) and $n \rightarrow \sigma^*$ donor–acceptor attraction energy $\Delta E_{n \rightarrow \sigma^*}$ ⁽²⁾ (dashed line) at each $R_{F\dots H}$.



As shown in the figure, the valence-type interactions ΔE_{steric} and $\Delta E_{\text{n} \rightarrow \sigma^* (2)}$ are rather negligible beyond $\sim 2.5 \text{ \AA}$, and the longer-range attraction may be attributed primarily to classical dipole–dipole forces. However, the steric repulsions and $\text{n} \rightarrow \sigma^*$ attraction both grow rapidly at shorter distances, until, at $R_{\text{F} \cdots \text{H}} = 1.8 \text{ \AA}$,

$$\begin{aligned}\Delta E_{\text{steric}} &= +6.7 \text{ kcal mol}^{-1} \\ \Delta E_{\text{n} \rightarrow \sigma^* (2)} &= -7.6 \text{ kcal mol}^{-1} \\ \Delta E_{\text{rem}} &= -4.1 \text{ kcal mol}^{-1}\end{aligned}$$

where ΔE_{rem} is the remainder that may be ascribed to residual classical electrostatic interactions. (Note that this quantity is again fortuitously close to the net H-bond energy, as though steric and donor–acceptor contributions were absent.) Thus, the donor–acceptor (ionic-resonance) interaction $\Delta E_{\text{n} \rightarrow \sigma^* (2)}$ is found to be the largest contribution to net binding at equilibrium. This analysis for $(\text{HF})_2$ is also consistent with the early conclusion of Coulson concerning the sources of binding in the water dimer.

Table 5.2 presents further details of the interacting n_{B} and σ_{AH^*} NBOs and their diagonal (ϵ_{n} and ϵ_{σ^*}) and off-diagonal ($F_{\text{n}\sigma^*}$) matrix elements, and Table 5.3 summarizes the charge transfer ($\Delta Q_{\text{B} \rightarrow \text{A}}$), A–H-bond ionicity (i_{AH}), and (P)NBO overlap integrals ($S_{\text{n}\sigma}$ and $S_{\text{n}\sigma^*}$) in the H-bonding region. The entries of Table 5.2 allow one to estimate the $\text{n}_{\text{B}} \rightarrow \sigma_{\text{AH}^*}$ interaction strengths, as shown in the right-hand panels of Fig. 5.1.

Table 5.2. *The NBOs n_{B} and σ_{AH^*} and associated orbital energies (ϵ_{n} and ϵ_{σ^*}) of binary $\text{B} \cdots \text{HA}$ H-bonded complexes (cf. Fig. 5.1), with $F_{\text{n}\sigma^*} = \langle \text{n}_{\text{B}} | \hat{F} | \sigma_{\text{AH}^*} \rangle$ interaction matrix element (note that two oxygen lone pairs contribute to H-bonding in $\text{H}_2\text{CO} \cdots \text{H}_3\text{N}$)*

Complex	Donor		Acceptor		$F_{\text{n}\sigma^*}$
	n_{B}	ϵ_{n} (a.u.)	σ_{AH^*}	ϵ_{σ^*} (a.u.)	
$\text{H}_3\text{N} \cdots \text{HOH}$	$(\text{sp}^{3.44})_{\text{N}}$	−0.3717	$0.49(\text{sp}^{2.67})_{\text{O}} - 0.87(\text{s})_{\text{H}}$	+0.4746	−0.0924
$\text{HF} \cdots \text{HF}$	$(\text{sp}^{4.61})_{\text{F}}$	−0.6363	$0.46(\text{sp}^{3.44})_{\text{F}} - 0.89(\text{s})_{\text{H}}$	+0.4239	−0.0753
$\text{H}_2\text{CO} \cdots \text{HNH}_2$	$(\text{sp}^{0.68})_{\text{O}}$ $(\text{p})_{\text{O}}$	−0.7441 −0.3082	$0.56(\text{sp}^{2.67})_{\text{N}} - 0.83(\text{s})_{\text{H}}$	+0.4733	−0.0239 −0.0206

Table 5.3. The NBO descriptors of binary $B \cdots HA$ H-bonded complexes (see Fig. 5.1), showing net intermolecular charge transfer $\Delta Q_{B \rightarrow A}$, σ_{AH} bond ionicity i_{AH} , and PNBO overlap integrals for attractive $n_B - \sigma_{AH}^*$ ($S_{n\sigma^*}$) and repulsive $n_B - \sigma_{AH}$ ($S_{n\sigma}$) interactions

Complex	$\Delta Q_{B \rightarrow A}$	i_{AH}	$S_{n\sigma^*}$	$S_{n\sigma}$	$(S_{n\sigma^*}/S_{n\sigma})^2$
$H_3N \cdots HOH$	0.0269	0.5102	0.2922	0.1534	3.63
$HF \cdots HF$	0.0124	0.5744	0.2022	0.1050	3.71
$H_2CO \cdots HNH_2$	0.0026	0.3744	0.0692	0.0684	1.02
			0.0576	0.0448	1.65

Example 5.4

Problem: Use the data in Table 5.2 to verify the values given in Fig. 5.1 for the stabilization associated with each $n_B \rightarrow \sigma_{AH}^*$ interaction.

Solution: According to the general second-order perturbation theory presented in Section 1.4 (cf. Fig. 1.3), we can rewrite Eq. (1.24) for the present case ($\phi_i^{(0)} = n_B$, $\phi_j^{*(0)} = \sigma_{AH}^*$) as

$$E_{n \rightarrow \sigma^*}^{(2)} = -2 \frac{F_{n\sigma^*}^2}{\epsilon_{\sigma^*} - \epsilon_n}$$

From the entries in Table 5.2 we obtain

$$\begin{aligned} H_3N \cdots HOH: \quad E_{n \rightarrow \sigma^*}^{(2)} &= -2 \frac{(-0.0924)^2}{0.4746 - (-0.3717)} = -0.0202 \text{ a.u.} \\ HF \cdots HF: \quad E_{n \rightarrow \sigma^*}^{(2)} &= -2 \frac{(-0.0753)^2}{0.4239 - (-0.6363)} = -0.0107 \text{ a.u.} \\ H_2CO \cdots HNH_2: \quad E_{n \rightarrow \sigma^*}^{(2)} &= -2 \frac{(-0.0239)^2}{0.4733 - (-0.7441)} = -9.384 \times 10^{-4} \text{ a.u.} \\ &E_{n' \rightarrow \sigma}^{(2)} = -2 \frac{(-0.0206)^2}{0.4733 - (-0.3082)} = -1.086 \times 10^{-3} \text{ a.u.} \end{aligned}$$

With the conversion factor $1 \text{ a.u.} = 627.5 \text{ kcal mol}^{-1}$, these values correspond to the stabilizations given in Fig. 5.1 (in the last case, the summed contribution for two oxygen lone pairs).

Consistently with (5.30b)–(5.30e), the intermolecular charge transfer $\Delta Q_{B \rightarrow A}$ (Table 5.3, first column) clearly correlates with the strength of $n_B \rightarrow \sigma_{AH}^*$ interactions (Fig. 5.1), the $\Delta E_{B \cdots H}$ binding energy (Table 5.1, first column), and the (inverse) $R_{B \cdots H}$ distance (Table 5.1, second column). Furthermore, the transferred

charge (of the order of 1% of an electron) appears as increased occupancy of the antibonding σ_{AH}^* orbital, which is correlated in the expected manner with the covalent-bond elongation ΔR_{AH} (Table 5.1, fourth column).

The charge transfer is in turn strongly correlated with the *overlap* $S_{\text{n}\sigma^*}$ of n_{B} and σ_{AH}^* orbitals. Columns 3 and 4 of Table 5.3 compare the values of the attractive donor–acceptor ($S_{\text{n}\sigma^*}$) and repulsive donor–donor ($S_{\text{n}\sigma}$) overlaps (the latter of which is related to the steric repulsions between filled n_{B} and σ_{AH} NBOs). The ratio $(S_{\text{n}\sigma^*}/S_{\text{n}\sigma})^2$, shown in the final column of Table 5.3, gives a rough measure of the energetic balance between attractive and repulsive terms in the equilibrium geometry. When *both* $S_{\text{n}\sigma^*}$ and $(S_{\text{n}\sigma^*}/S_{\text{n}\sigma})^2$ are favorable, the shortest and strongest H-bonds result. The ratio $(S_{\text{n}\sigma^*}/S_{\text{n}\sigma})^2$ depends most strongly on acceptor *polarity* (i.e., the ionicity factor i_{AH} in Table 5.3, second column), and is therefore most favorable for σ_{HF}^* . However, as shown in Example 5.4, the n_{F} of electronegative fluorine is too low in energy to be a favorable donor. The $\text{HF} \cdots \text{HF}$ H-bond is therefore weaker than that of $\text{H}_3\text{N} \cdots \text{H}_2\text{O}$, which has slightly less favorable acceptor polarity $(S_{\text{n}\sigma^*}/S_{\text{n}\sigma})^2$ but a *much* more favorable donor energy ϵ_{n} . In this manner, finer details of the net H-bond strength can be related to details of the key n_{B} , σ_{AH} and σ_{AH}^* NBOs of the H-bonding region. The patterns exhibited by these three complexes are broadly representative of those found for a much larger number of H-bonded systems that have been examined by NBO analysis.³⁸

Further evidence of the importance of intermolecular donor–acceptor interactions can be obtained by *deleting* these interactions from the variational calculation, and recalculating the optimized geometries with charge transfer (CT) *omitted*. The structures resulting from such CT-deleted species are shown in Fig. 5.2. Energetic and structural properties of CT-deleted species are summarized in Table 5.4 for direct comparison with the actual H-bonded species in Table 5.1.

As a glance at Fig. 5.2 makes clear, the CT-deleted structures bear almost no recognizable relationship to the true H-bonded structures (Fig. 5.1). It should be stressed that deleting the intermolecular donor–acceptor interactions corresponds to an almost imperceptible change ($<0.05\%$) in the monomer charge densities, so *all* significant steric and electrostatic properties of the monomers remain essentially unaltered. All three CT-deleted complexes take the geometries that might be expected in a simple dipole–dipole model, but the net binding energies are virtually *negligible* ($<1 \text{ kcal mol}^{-1}$, of the order of ambient thermal energies kT) and the distance $R_{\text{B}\cdots\text{H}}$ elongates to *large* separations beyond van der Waals contact. Thus, the CT-deleted species bear almost no resemblance to H-bonded species, though they conform well to the expectations of a London long-range picture. While the London-like terms are always present in the full calculation, their influence appears to be very *weak* compared with that of covalent-type donor–acceptor interactions in the near-equilibrium region of H-bonded species. Further examples of the

Table 5.4. Properties of “CT-deleted” $B \cdots HA$ complexes (see Fig. 5.2), showing binding energies $\Delta E_{B \cdots A}$ and intermolecular bond distances $R_{B \cdots H}$ and $R_{B \cdots A}$, compared with van der Waals contact distances $R_{B \cdots A}^{(vdW)}$ for heavy atoms A and B (note that optimum intermolecular separations are imprecisely determined on the extremely flat potential-energy surface)

Species	$\Delta E_{B \cdots A}$ (kcal mol ⁻¹)	$R_{B \cdots H}$ (Å)	$R_{B \cdots A}$ (Å)	$R_{B \cdots A}^{(vdW)}$ (Å)
$H_3N \cdots H_2O$	0.16	5.80	6.09	3.09
$HF \cdots HF$	0.84	3.65	4.57	2.54
$H_2CO \cdots H_3N$	0.14	6.72	7.02	3.09

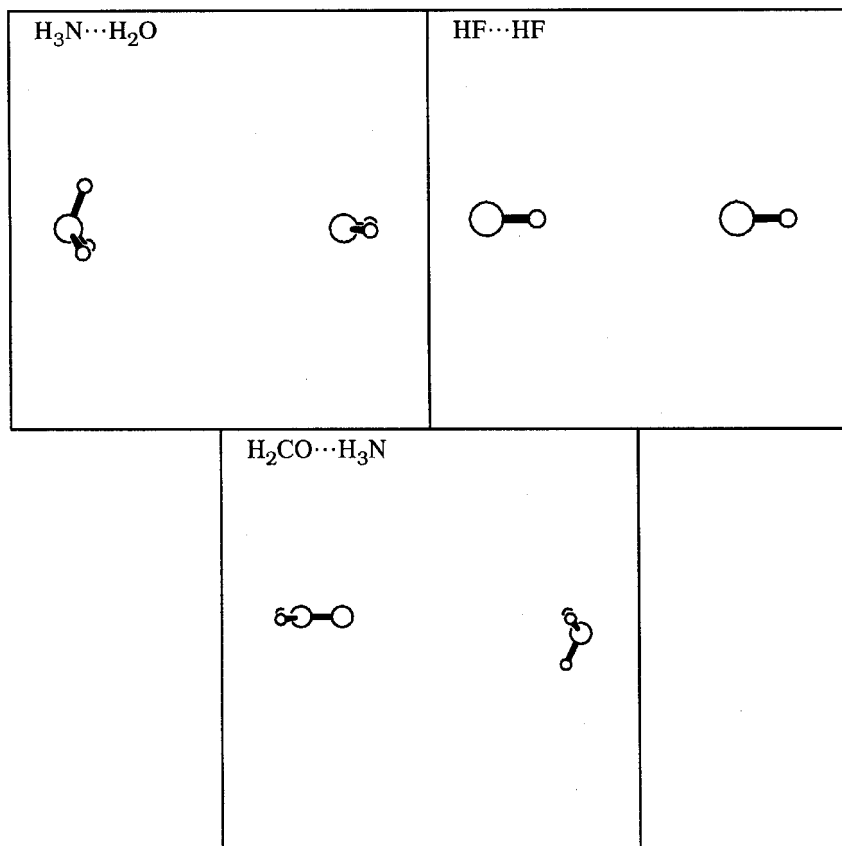


Figure 5.2 Optimized structures of “CT-deleted” complexes, with all intermolecular donor–acceptor interactions removed.

relative *unimportance* of classical dipole–dipole interactions to H-bond structure and energetics will be given below.

Hydrogen-bond isomerization

Lewis bases having two or more lone-pair-bearing atoms can exhibit a form of isomerism in H-bonding. This can be illustrated most simply with carbon monoxide, which has sigma-type lone pairs both on C and on O, and thus is expected to form $n \rightarrow \sigma^*$ H-bonds of either $\text{OC} \cdots \text{HA}$ or $\text{CO} \cdots \text{HA}$ type with a hydride-bearing Lewis acid. For example, complexation of CO with HF gives rise to distinct $\text{OC} \cdots \text{HF}$ or $\text{CO} \cdots \text{HF}$ complexes.³⁹ The two possible isomeric forms are shown in Fig. 5.3, *both* bound by rather typical H-bond energies:

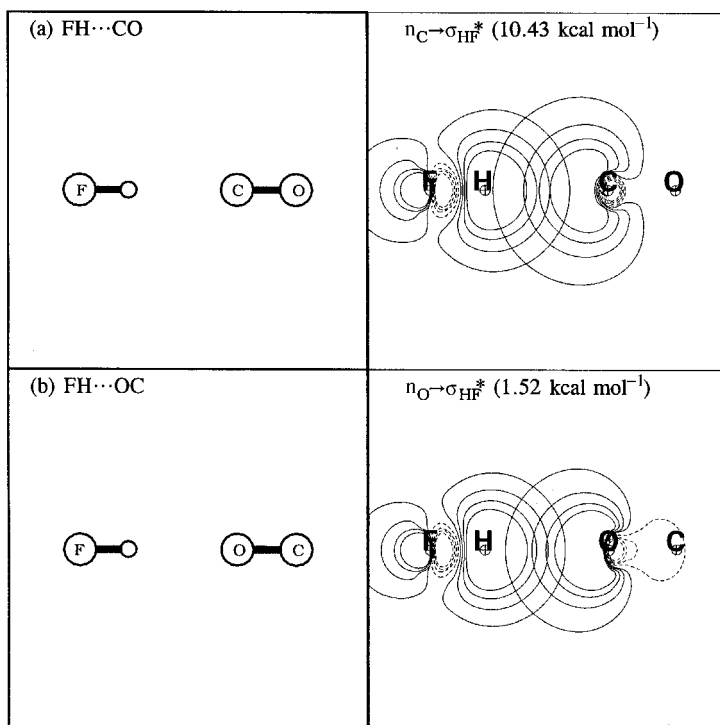
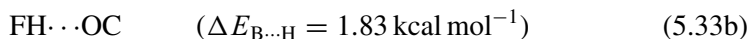
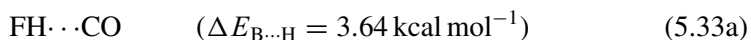


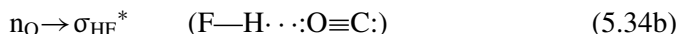
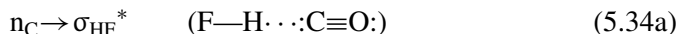
Figure 5.3 Isomeric $\text{FH} \cdots \text{CO}$ and $\text{FH} \cdots \text{OC}$ complexes (left) and leading donor–acceptor interactions (right), with estimated second-order stabilization energies in parentheses.

Table 5.5. Hydrogen-bond energies $\Delta E_{B\cdots H}$, HF monomer net charge Q_{HF} , H-bond lengths $R_{B\cdots H}$, and covalent-bond stretchings ΔR_{AH} for $CO\cdots HF$ and $OC\cdots HF$ isomers (see Fig. 5.3)

$B\cdots HA$	$\Delta E_{B\cdots H}$ (kcal mol ⁻¹)	Q_{HF}	$R_{B\cdots H}$ (Å)	ΔR_{AH} (Å)
$OC\cdots HF$	3.64	-0.0280	2.06	0.0078
$CO\cdots HF$	1.83	-0.0028	2.07	0.0022

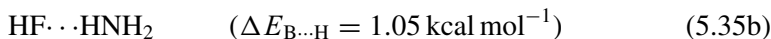
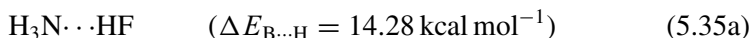
Both species exhibit the expected linear geometry that maximizes the dominant $n \rightarrow \sigma^*$ interaction. However, these isomers are rather perplexing from a dipole-dipole viewpoint. The dipole moment of CO is known to be rather small (calculated $\mu_{CO} = 0.072$ D), with relative polarity C^-O^+ .⁴⁰ While the linear equilibrium structure(s) may appear to suggest a dipole-dipole complex, robust H-bonds are formed *regardless* of which end of the CO dipole moment points toward HF! This isomeric indifference to dipole directionality shows clearly that classical dipole-dipole interactions have at most a secondary influence on the formation of a hydrogen bond.

The right-hand panels of Fig. 5.3 show the two strong $n \rightarrow \sigma^*$ donor-acceptor interactions responsible for H-bonding,



As expected, the n_C lone pair on electropositive carbon is a better donor than that on electronegative oxygen, so the $FH \cdots CO$ isomer is more strongly bound. Table 5.5 summarizes some energetic, structural, and charge properties of these isomers that clearly demonstrate the stronger intermolecular charge transfer in (5.33a). Thus, the stronger $n_C \rightarrow \sigma_{HF}^*$ interaction in $OC \cdots HF$ is seen to lead to about ten times higher anionic character on HF, a shorter H-bond length (despite the larger van der Waals radius of C), and significantly greater lengthening (and weakening) of the covalent H—F bond than in the $CO \cdots HF$ isomer.

We can also examine isomeric pairs of H-bonded complexes in which the roles of electron-pair donor and acceptor are *reversed*, and the mutual dipole orientations are therefore fundamentally altered. As an example, Fig. 5.4 shows the isomeric pair of complexes between ammonia and hydrogen fluoride,



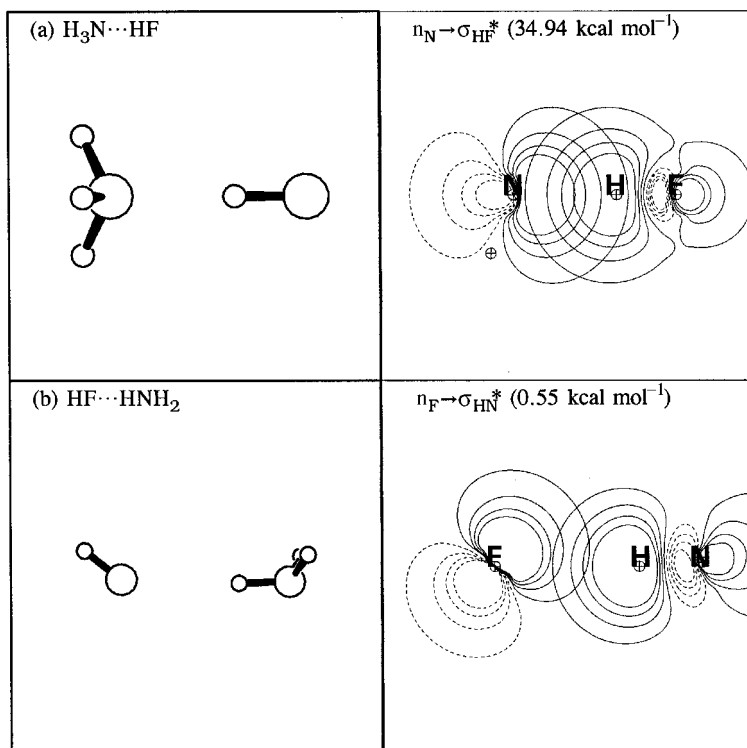


Figure 5.4 Isomers of the $\text{NH}_3 \cdots \text{HF}$ complex (left) and leading donor–acceptor interactions (right), with estimated second-order stabilization energies in parentheses. (Note that a second $n_{\text{F}}' \rightarrow \sigma_{\text{HN}}^*$ stabilization [with orthogonal n_{F}' directed along the H—F axis] competes with that shown in (b) to control the $\text{HF} \cdots \text{HNH}_2$ geometry.)

which illustrate such donor–acceptor reversal. The right-hand panels of Fig. 5.4 show the respective $n \rightarrow \sigma^*$ interactions that dictate the direction of charge transfer in each complex. Table 5.6 summarizes energetic, structural, and charge characteristics of these isomers.

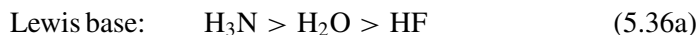
As shown in Table 5.6, the directions of charge flow in the two complexes are opposite, making HF significantly *anionic* in the strong $\text{H}_3\text{N} \cdots \text{HF}$ isomer

Table 5.6. *Similar to Table 5.5, for $\text{H}_3\text{N} \cdots \text{HF}$ and $\text{HF} \cdots \text{H}_3\text{N}$ isomers (see Fig. 5.4)*

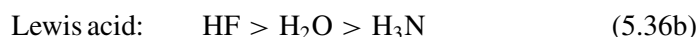
$\text{B} \cdots \text{HA}$	$\Delta E_{\text{B} \cdots \text{H}} \text{ (kcal mol}^{-1}\text{)}$	Q_{HF}	$R_{\text{B} \cdots \text{H}} \text{ (Å)}$	$\Delta R_{\text{AH}} \text{ (Å)}$
$\text{H}_3\text{N} \cdots \text{HF}$	14.28	−0.0721	1.67	0.0392
$\text{HF} \cdots \text{HNH}_2$	1.05	+0.0012	2.34	0.0007

but slightly *cationic* in the weak $\text{HF} \cdots \text{H}_2\text{N}-\text{H}$ isomer. The geometrical parameters also indicate the much stronger effect of delocalization in the $\text{H}_3\text{N} \cdots \text{HF}$ isomer, including the extremely short $\text{N} \cdots \text{H}$ bond length ($\sim 1.4 \text{ \AA}$ inside van der Waals contact) and the significantly elongated covalent HF bond ($\sim 0.04 \text{ \AA}$ longer than in isolated HF). These changes are all in accord with the expected greater weighting of the alternative proton/charge-transferred resonance structure in (5.29a).

On the basis of relative electronegativities (Section 3.2.5), the order of *donor* (n_{A}) strengths of group 5–7 AH_n hydrides is expected to be



whereas the corresponding order of *acceptor* (σ_{AH^*}) strengths is expected to be



Thus, among possible binary complexes that can be formed from these monomers, the $\text{H}_3\text{N} \cdots \text{HF}$ (best donor, best acceptor) complex is expected to be *strongest*, whereas the “inverted” $\text{HF} \cdots \text{H}_2\text{N}-\text{H}$ (worst donor, worst acceptor) complex should be *weakest*. These extreme differences in donor–acceptor strength are consistent with the wide disparity in H-bond energies (5.35a) and (5.35b).

The examples cited above are only two of the many possible cases of H-bond isomerization. Because of the low kinetic barriers separating these species, equilibration of H-bonded isomer populations to limiting thermodynamic values is generally expected to be much faster than for covalent isomers. Methods of quantum statistical thermodynamics can be used to calculate partition functions and equilibrium population distributions for H-bonded isomers,⁴¹ just as in the parallel case for covalent isomers and conformers.

Hydrogen-bonding to water

Hydrogen bonds to water are of special importance because of their pervasive role in aqueous solution phenomena. Some general trends in H-bonding to water can be illustrated by the series of binary H-bonded complexes



involving first-row hydride molecules. Figure 5.5 displays optimized structures and the leading $n \rightarrow \sigma^*$ interaction for each complex, and Table 5.7 compares the energetics, geometries, and charge distributions of these species.

The H-bonded species in Fig. 5.5 exhibit smooth variations of H-bond length and strength with respect to position in the periodic table, in a manner consistent with the expected ordering (5.36b) of Lewis-acid strengths. In each case the intermolecular interaction is dominated by the $n_{\text{O}} \rightarrow \sigma_{\text{AH}^*}$ donor–acceptor stabilization shown in the right-hand panel. Energetic, geometrical, and vibrational properties of

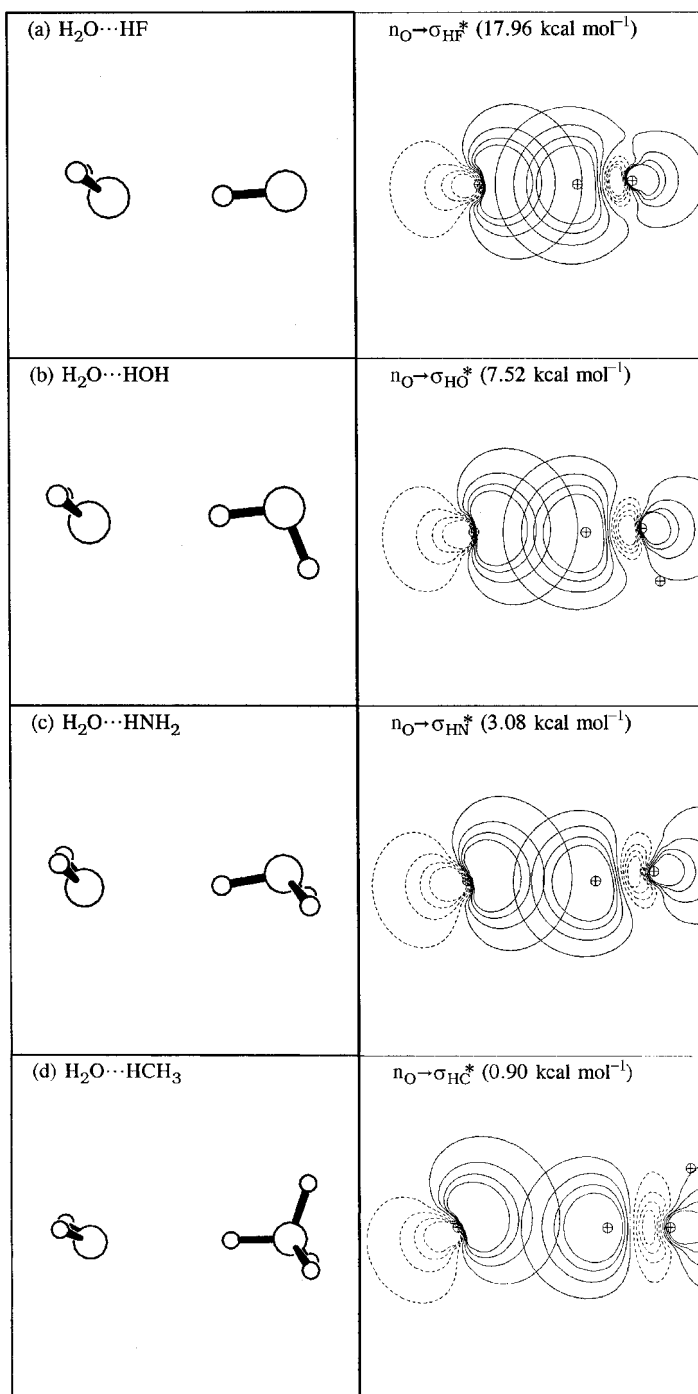


Figure 5.5 Optimized structures (left) and leading $n\rightarrow\sigma^*$ donor–acceptor interactions (right) for H_2O complexes (5.37).

Table 5.7. Hydrogen-bond energies $\Delta E_{O\cdots H}$, bond lengths $R_{O\cdots H}$ and R_{AH} , covalent-bond stretching ΔR_{AH} , and frequency change $\Delta\nu_{AH}$ for $H_2O\cdots HA$ complexes

$H_2O\cdots HA$	$\Delta E_{O\cdots H}$ (kcal mol ⁻¹)	$R_{O\cdots H}$ (Å)	R_{AH} (Å)	ΔR_{AH} (Å)	$\Delta\nu_{AH}$ (cm ⁻¹)
$H_2O\cdots HF$	10.10	1.704	0.942	0.0194	-426
$H_2O\cdots HOH$	5.83	1.934	0.970	0.0078	-162
$H_2O\cdots HNH_2$	2.66	2.212	1.018	0.0034	-48
$H_2O\cdots HCH_3$	0.41	2.586	1.091	-0.0001	+31

the complexes are all found to vary in a smooth and physically reasonable manner with the strength of this interaction, as shown in Fig. 5.6. Thus, the increase in $n-\sigma^*$ interaction strength (and associated charge transfer) leads in the manner predicted by (5.30b)–(5.30e) to increased H-bond strength (Fig. 5.6(a)), decreased H-bond

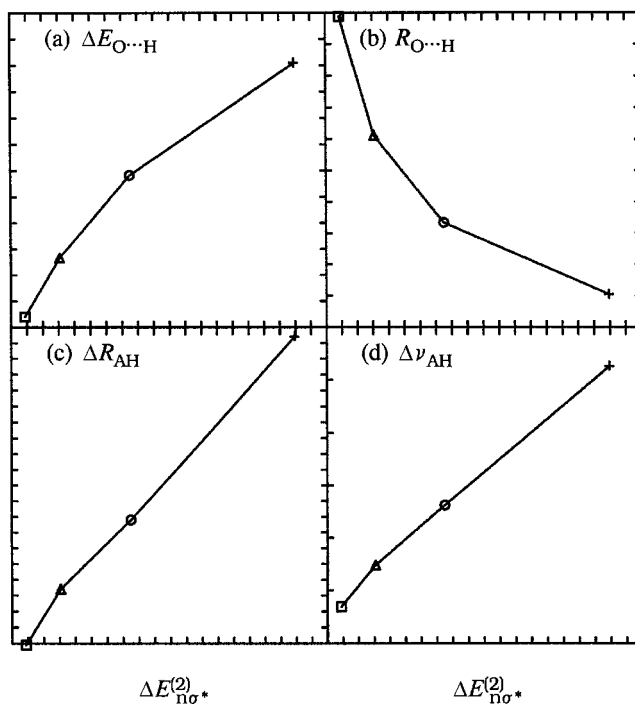


Figure 5.6 Correlated variations of energetic ($\Delta E_{O\cdots H}$), geometrical ($R_{O\cdots H}$ and ΔR_{AH}), and vibrational ($\Delta\nu_{AH}$) properties of H-bonded water complexes ($H_2O\cdots HA$, A = F [crosses], OH [circles], NH_2 [triangles], and CH_3 [squares]) with respect to donor-acceptor interaction $\Delta E_{n\sigma^*}^{(2)}$ (abscissa, 1 kcal mol⁻¹ tick marks). Vertical tick marks in each panel correspond to the quantity being plotted: (a) $\Delta E_{O\cdots H}$, 1 kcal mol⁻¹; (b) $R_{O\cdots H}$, 0.1 Å; (c) ΔR_{AH} , 0.001 Å; and (d) $\Delta\nu_{AH}$, 100 cm⁻¹. (See Table 5.7 for numerical values.)

length (Fig. 5.6(b)), lengthened A—H covalent bond (Fig. 5.6(c)), and red-shifted ν_{AH} stretching frequency (Fig. 5.6(d)). Dependences such as shown in Fig. 5.6 are typical of those found in a wide variety of H-bonded complexes,⁴² demonstrating that the characteristic features of H-bonding arise from, and are strongly coupled to, the *single* strong $\langle n | \hat{F} | \sigma^* \rangle$ matrix element.

It is noteworthy that CH_4 falls in line with the trends shown by other $\text{H}_2\text{O} \cdots \text{H}_n\text{A}$ complexes. The formation of this complex is doubly perplexing from an electrostatic viewpoint, because CH_4 *lacks* an overall dipole moment (or other large multipole moments) as well as any significant bond dipole⁴³ for electrostatic bonding. While the H-bonding to methane is quite weak ($\sim 0.4 \text{ kcal mol}^{-1}$), CH_4 possesses antibonding σ_{CH}^* orbitals that allow it to act as a (weak) Lewis acid. From the donor–acceptor viewpoint, therefore, the formation of a weak $\text{CH} \cdots \text{O}$ hydrogen bond is to be expected.

An exceptional feature of $\text{CH} \cdots \text{O}$ hydrogen bonding, contrary to expectations (5.30b) and (5.30c), is evident in the ΔR_{AH} and $\Delta \nu_{\text{AH}}$ values of Table 5.7. Whereas H-bonding typically leads to lengthening and vibrational red-shifting of the covalent bond (due to increased occupancy of σ^*), the H-bonded CH bond of $\text{H}_2\text{O} \cdots \text{HCH}_3$ is instead slightly *shortened* and *blue*-shifted with respect to isolated CH_4 . The bond-length difference is even more apparent within the complex, where the H-bonded $R_{\text{CH(b)}}$ (1.0908 Å) is shortened by 0.0008 Å relative to the three free $R_{\text{CH(f)}}$ values. Certain spectroscopic tests that are sometimes considered to be diagnostic signatures of H-bonding will therefore fail for $\text{CH} \cdots \text{O}$ bonds.

The H-bond-induced asymmetries in C—H bonds are also apparent in the forms of the NBOs:

$$\sigma_{\text{CH(b)}} = 0.783(\text{sp}^{2.87})_{\text{C}} + 0.622(\text{s})_{\text{H}} \quad (5.38\text{a})$$

$$\sigma_{\text{CH(f)}} = 0.774(\text{sp}^{3.04})_{\text{C}} + 0.634(\text{s})_{\text{H}} \quad (5.38\text{b})$$

While the $\sigma_{\text{CH(b)}}^*$ antibond has the expected higher occupancy (0.0022e, versus 0.0004e for $\sigma_{\text{CH(f)}}^*$), other induced changes in the *form* of the σ_{CH} and σ_{CH}^* NBOs apparently act in such a way as to shorten the CH(b) bond. The physical origin of this shortening can be explained as follows.

The relative apolarity of C—H bonds makes the degrees of overlap of an incoming n_{O} donor orbital with σ_{CH}^* and σ_{CH} NBOs rather comparable, so $n_{\text{O}}-\sigma_{\text{CH}}^*$ attraction tends to be offset by comparable $n_{\text{O}}-\sigma_{\text{CH}}$ steric repulsion, with little net bonding. However, by increasing the s character of the C—H(b) hybrid (to $\text{sp}^{2.87}$, versus $\text{sp}^{3.04}$ for free CH), the electronegativity of carbon is effectively increased, and the $\sigma_{\text{CH(b)}}$ NBO repolarizes to expose $\sigma_{\text{CH(b)}}^*$ more to attack by n_{O} . However, the slight increase of s character (in accord with Bent's rule) is accompanied by a slight reduction in size of the carbon hybrid (because valence s orbitals have smaller average radius than p orbitals), so that the C—H(b) bond *contracts* slightly

Table 5.8. The NBO descriptors of H-bonded water complexes $\text{H}_2\text{O} \cdots \text{HA}$, showing the net intermolecular charge transfer from Lewis base to Lewis acid (Q_{CT}), change in covalent-bond polarity (Δi_{AH}), and (P)NBO overlaps ($S_{\text{n}\sigma^*}$, $S_{\text{n}\sigma}$) of n_O with antibond σ_{AH}^* and σ_{AH} orbitals

$\text{H}_2\text{O} \cdots \text{HA}$	Q_{CT}	Δi_{AH}	$S_{\text{n}\sigma^*}$	$S_{\text{n}\sigma}$
$\text{H}_2\text{O} \cdots \text{HF}$	0.0339	+0.0406	0.3564	0.1833
$\text{H}_2\text{O} \cdots \text{HOH}$	0.0138	+0.0356	0.2516	0.1486
$\text{H}_2\text{O} \cdots \text{HNH}_2$	0.0034	+0.0274	0.1474	0.1266
$\text{H}_2\text{O} \cdots \text{HCH}_3$	0.0020	+0.0242	0.0849	0.0722

as it repolarizes. The repolarization-induced contraction apparently overcomes the effect of increased antibond occupancy, leading to a slight net shortening $\sigma_{\text{CH(b)}}$ even as the occupancy of $\sigma_{\text{CH(b)}}^*$ increases.⁴⁴

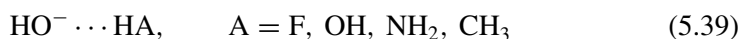
Table 5.8 summarizes the NBO descriptors of the net charge transfer from Lewis base to Lewis acid (Q_{CT}), change in covalent-bond polarization (Δi_{AH}), and (P)NBO overlap of n_O with bond ($S_{\text{n}\sigma}$) and antibond ($S_{\text{n}\sigma^*}$) orbitals of the Lewis acid. The entries in Table 5.8 show the unfavorable diminution of $|S_{\text{n}\sigma^*}/S_{\text{n}\sigma}|$ and reduced charge transfer as the Lewis acid changes from polar HF to apolar CH_4 . These NBO descriptors can also be closely correlated with quantities in Table 5.7, showing their mutual dependence on the strength of $\text{n}-\sigma^*$ donor–acceptor interaction.

5.2.2 Charge-assisted ($\pm\text{CAHB}$) H-bonds

The strength of the $\text{n}_\text{B}-\sigma_{\text{AH}}^*$ donor–acceptor interaction is expected to be greatly enhanced if the Lewis base is an anion and/or the Lewis acid is a cation. Anionic character of B increases the diffuseness (average orbital radius) and raises the energy of the n_B donor orbital, while cationic character of AH increases the polarity and lowers the energy of the σ_{AH}^* acceptor orbital. All these effects act to strengthen $\Delta E_{\text{n}\sigma^*}$ ⁽²⁾ stabilization. Thus, H-bonding is expected to be strongly “assisted” when the donor or acceptor monomers acquire net charge. Gilli *et al.*⁴⁵ have labeled such positively or negatively charge-assisted H-bonds as being of “ $\pm\text{CAHB}$ ” type, and have identified many experimental examples of the distinctive structures and chemistry of charged hydrogen bonds.

Anion-assisted H-bonds: hydroxide complexes

As simple examples of anion-assisted H-bonds, let us consider the complexes formed between the hydroxide ion and the series of first-row Lewis acid acceptors considered in the previous subsection,



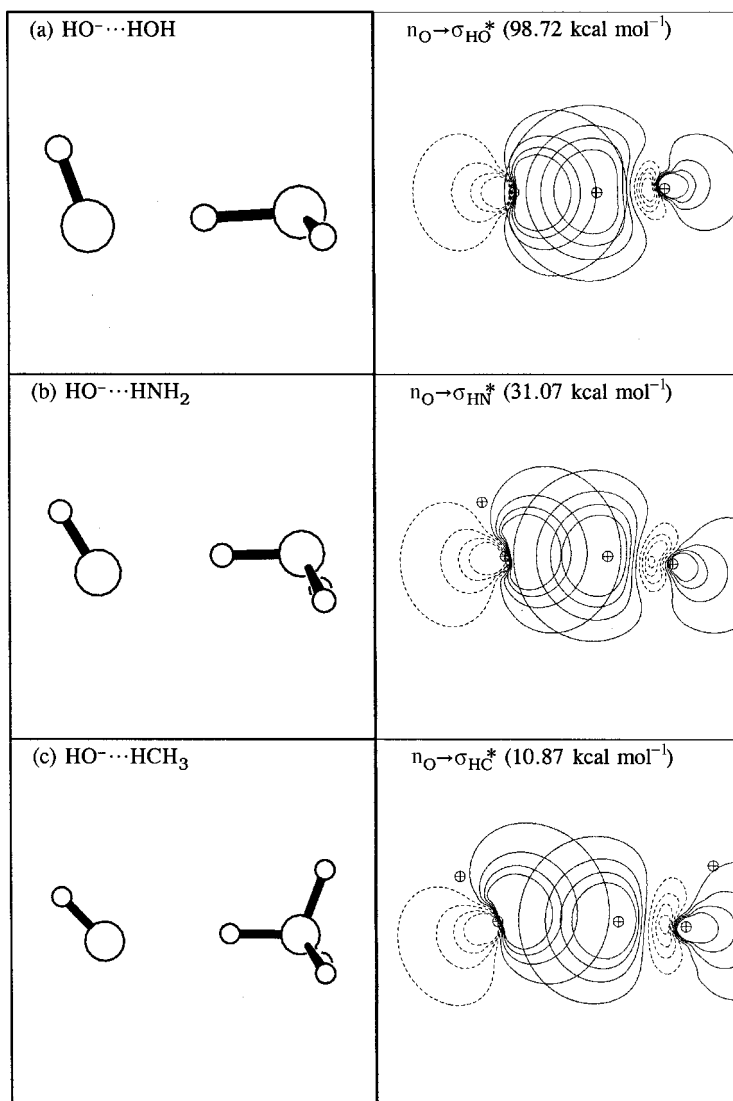


Figure 5.7 Optimized structures (left) and leading $n \rightarrow \sigma^*$ donor-acceptor interactions (right) for $\text{HO}^- \cdots \text{HA}$ complexes (A = OH, NH_2 , CH_3). (Note that the hypothetical complex “ $\text{HO}^- \cdots \text{HF}$ ” is not shown, because this species undergoes proton transfer to form $\text{HOH} \cdots \text{F}^-$.)

In the case of A = F, there is apparently no local minimum corresponding to the $\text{HO}^- \cdots \text{HF}$ isomer, and instead the proton transfers to form $\text{HOH} \cdots \text{F}^-$ as the only stable equilibrium species. However, in the case of the weaker HA Lewis acids, stable $\text{HO}^- \cdots \text{HA}$ structures are found. Figure 5.7 displays optimized structures of these complexes and the dominant $n-\sigma^*$ interaction in each case, while Table 5.9 summarizes energetic and structural properties of these complexes for

Table 5.9. *Similar to Table 5.7, for HO⁻ ··· HA complexes (see Fig. 5.7)*

HO ⁻ ··· HA	$\Delta E_{\text{O}\cdots\text{H}}$ (kcal mol ⁻¹)	$R_{\text{O}\cdots\text{H}}$ (Å)	R_{AH} (Å)	ΔR_{AH} (Å)	$\Delta \nu_{\text{AH}}$ (cm ⁻¹)
(HO ⁻ ··· HF) ^a	(52.18) ^b	(1.058)	(1.401)	—	—
HO ⁻ ··· HOH	29.39	1.363	1.117	0.1547	-2201
HO ⁻ ··· HNH ₂	17.09	1.685	1.073	0.0585	-969
HO ⁻ ··· HCH ₃	6.48	1.979	1.112	0.0211	-245

^a The actual species corresponds to proton-transferred HOH ··· F⁻.

^b Binding energy with respect to OH⁻ + HF monomers; the corresponding energy with respect to H₂O + F⁻ is 28.71 kcal mol⁻¹.

direct comparison with the corresponding neutral complexes in Table 5.7. The trends in Table 5.9 are all consistent with the expected order (5.36a) of Lewis-acid strength, and strikingly *inconsistent* with the ordering of monomer dipole moments (5.32).

The structures of anionic HO⁻ ··· HA complexes are conspicuously similar to those of the isoelectronic HF ··· HA complexes (cf., e.g., Figs. 5.4(b) and 5.7(b)), but the H-bonding is evidently *much* stronger in the anionic case. Judging from comparison of net binding energies, covalent-bond stretching ΔR_{AH} , second-order stabilization $\Delta E_{\text{n}\sigma^*}$ ⁽²⁾, charge transfer, or other measures of intermolecular n- σ^* interaction strength, one can say that the anionic H-bonds are very roughly an *order of magnitude* stronger than those of corresponding neutral complexes. Thus, if we compare neutral H₂O ··· HNH₂ with anionic HO⁻ ··· HNH₂, we can see that the H-bond energy increases by a factor of 6.4 (from 2.66 to 17.09 kcal mol⁻¹), A—H elongation by a factor of 17.2 (from 0.0034 to 0.0585 Å), and $\Delta E_{\text{n}\sigma^*}$ ⁽²⁾ stabilization by a factor of 10.1 (from 3.08 to 31.07 kcal mol⁻¹). Even the weak Lewis acid CH₄ makes an anionic HO⁻ ··· HCH₃ H-bond with roughly the same strength as that of the H₂O ··· H₂O complex (6.48 versus 5.83 kcal mol⁻¹).

While strong ion-dipole forces are present in these species, it is apparent from the structures in Fig. 5.7 that valence-type forces must still be playing a leading role. This can again be confirmed by *deleting* all intermolecular NBO interactions and reoptimizing the CT-deleted structures, as shown in Fig. 5.8. The CT-deleted structures conform well to the expectations of the classical ion-dipole picture, but they are *far* from the actual H-bonded structures. As shown in Table 5.10, the binding energies of CT-deleted ion-dipole complexes are less than 20% of the true H-bond energies, and the intermolecular distances are far (~ 1 Å) beyond those of the actual H-bonded complexes. The actual anionic H-bonded species involve increasing violations of the London long-range assumption (5.20) (or even chemical-bond rearrangements in the case of HO⁻ ··· HF), so empirical models or rationalizations based on classical electrostatics and induction become increasingly unrealistic.

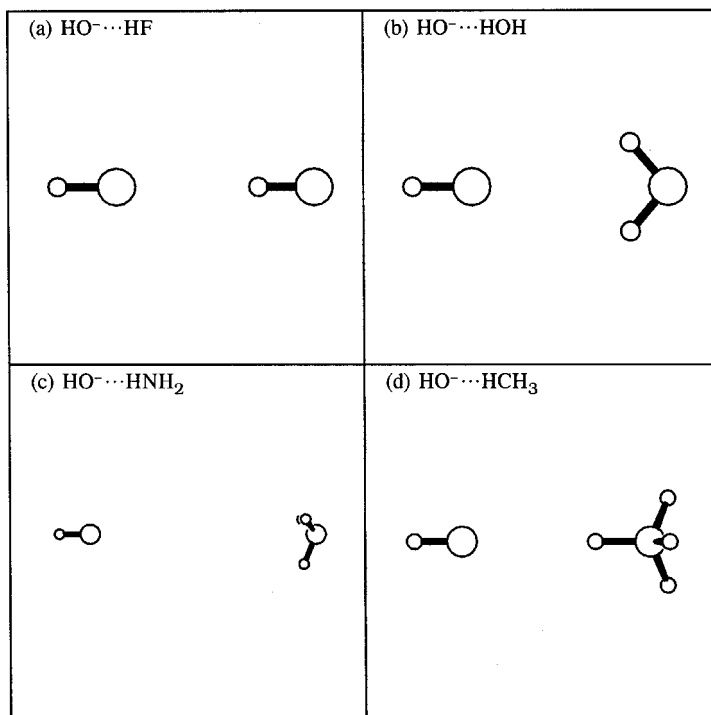


Figure 5.8 Optimized structures of CT-deleted “ion–dipole complexes” $\text{HO}^- \cdots \text{HA}$ ($\text{A} = \text{F}, \text{OH}, \text{NH}_2, \text{CH}_3$).

The trends in charge transfer, increase in polarity of AH, and $n\text{-}\sigma$ versus $n\text{-}\sigma^*$ (P)NBO overlaps are all rather parallel in $\text{HO}^- \cdots \text{HA}$ and $\text{H}_2\text{O} \cdots \text{HA}$ complexes, except for the proportionally greater strength of the anionic H-bonds. Table 5.11 summarizes these NBO descriptors for anionic $\text{HO}^- \cdots \text{HA}$ complexes in a form that allows direct comparison with Table 5.8. Note that the overlap integrals $S_{n\sigma^*}$ and $S_{n\sigma}$ increase to ever larger values ($>0.5!$), which is grossly inconsistent with classical models based on neglect of exchange-type interactions.

Table 5.10. *Similar to Table 5.4, for CT-deleted hydroxide complexes*
 $\text{HO}^- \cdots \text{HA}$ ($\text{A} = \text{F}, \text{OH}, \text{NH}_2, \text{CH}_3$)

Species	$\Delta E_{\text{complex}}$ (kcal mol ⁻¹)	$R_{\text{O}\cdots\text{H}}$ (Å)	$R_{\text{O}\cdots\text{A}}$ (Å)	$R_{\text{O}\cdots\text{A}}^{(\text{vdW})}$ (Å)
$\text{HO}^- \cdots \text{HF}$	12.5	2.32	3.24	2.73
$\text{HO}^- \cdots \text{HOH}$	5.5	2.68	3.19	2.92
$\text{HO}^- \cdots \text{HNH}_2$	1.6	6.76	7.08	3.09
$\text{HO}^- \cdots \text{HCH}_3$	0.2	2.71	3.81	3.08

Table 5.11. *Similar to Table 5.8, for hydroxide-ion complexes*

$\text{OH}^- \cdots \text{HA}$	Q_{CT}	Δi_{AH}	$S_{\text{n}\sigma^*}$	$S_{\text{n}\sigma}$
$\text{OH}^- \cdots \text{HOH}$	0.1886	+0.1786	0.5959	0.3416
$\text{OH}^- \cdots \text{HNH}_2$	0.0859	+0.1422	0.4375	0.2884
$\text{OH}^- \cdots \text{HCH}_3$	0.0400	+0.1350	0.2987	0.2064

All the above comparisons lead to the common conclusion that the anion-assisted H-bonds involve $\text{n}-\sigma^*$ interactions that are different in quantity, but not in quality, from those of corresponding neutral H-bonds. Classical electrostatic models (e.g., of ion–dipole type) are even *less* able to treat anionic H-bonds than neutral H-bonds, because the former tend to be *closer* to the chemical limit of full charge transfer to the isomeric proton-transferred species. Neutral and anionic-assisted H-bonds therefore appear to represent different (overlapping) ranges from a *continuum* of H-bond strengths, all sharing common $\text{n}-\sigma^*$ characteristics. The donor–acceptor description applies consistently from the weakest neutral H-bonded species, in which “H-bond” and “covalent bond” are clearly distinct (e.g., $\text{H}_2\text{O} \cdots \text{H}_4\text{C}$, in which $R_{\text{O}\cdots\text{H}} - R_{\text{CH}} \simeq 1.6 \text{ \AA}$) to the strong anion-assisted limit, where the difference between H-bonds and covalent bonds becomes increasingly blurred (e.g., $\text{HO}^- \cdots \text{H}_2\text{O}$, in which $R_{\text{O}\cdots\text{H}} - R_{\text{OH}} \simeq 0.2 \text{ \AA}$). Thus, *no sharp distinction* should be drawn between the weakest H-bonds and those for which proton transfer is complete, except with reference to the *strength* of the $\text{n}-\sigma^*$ interactions (or the relative weightings of resonance structures in (5.29a)) that underlie the full range of H-bonding phenomena.

Example 5.5

Problem: Use the data in Tables 5.7 and 5.8 and Figs. 5.5 and 5.7 to estimate the relative importance of donor–acceptor interactions in neutral versus ionic H-bond complexes.

Solution: If we compare the ratio of estimated donor–acceptor interaction ($\Delta E_{\text{n}\sigma^*}^{(2)}$) with the full H-bond energy (ΔE_{full}) for ionic $\text{HO}^- \cdots \text{HA}$ versus neutral $\text{H}_2\text{O} \cdots \text{HA}$ complexes, we find the following values:

$$\text{HA} = \text{H}_2\text{O}: \Delta E_{\text{n}\sigma^*}^{(2)}/\Delta E_{\text{full}} = 98.7/29.4 = 3.4 \text{ (ionic) versus } 7.5/5.8 = 1.3 \text{ (neutral)}$$

$$\text{HA} = \text{H}_3\text{N}: \Delta E_{\text{n}\sigma^*}^{(2)}/\Delta E_{\text{full}} = 31.1/17.1 = 1.8 \text{ (ionic) versus } 3.1/2.7 = 1.1 \text{ (neutral)}$$

$$\text{HA} = \text{H}_4\text{C}: \Delta E_{\text{n}\sigma^*}^{(2)}/\Delta E_{\text{full}} = 10.9/6.5 = 1.7 \text{ (ionic) versus } 0.9/0.4 = 2.3 \text{ (neutral)}$$

Thus, with the exception of the weak neutral methane complex, it appears that the ratio $\Delta E_{\text{n}\sigma^*}^{(2)}/\Delta E_{\text{full}}$ increases with H-bond strength, and the relative importance of $\Delta E_{\text{n}\sigma^*}^{(2)}$ tends to be *higher* in ionic than in neutral complexes.

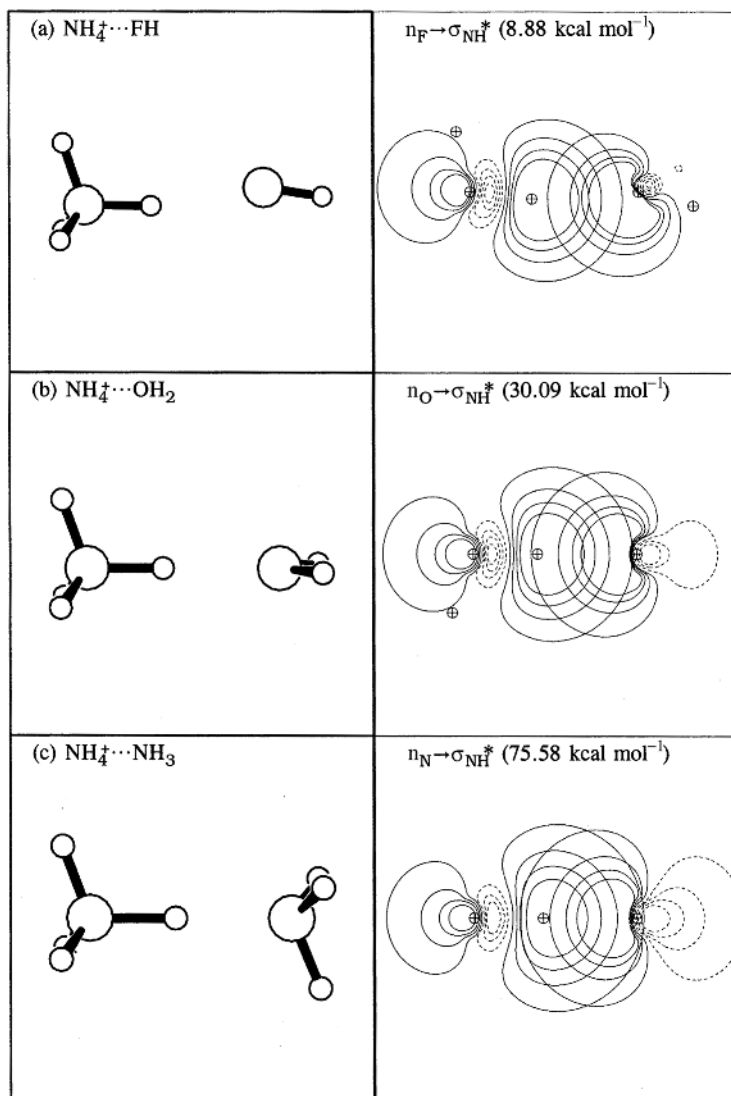


Figure 5.9 Structures (left) and leading $n_{\text{B}} \rightarrow \sigma_{\text{NH}}^*$ donor–acceptor interactions (right) for $\text{NH}_4^+ \cdots \text{B}$ complexes ($\text{B} = \text{FH}, \text{OH}_2, \text{NH}_3$).

Cation-assisted H-bonds: ammonium complexes

The effect of cationic charge on the Lewis acid can be similarly illustrated for the case of NH_4^+ H-bonded to various first-row hydride Lewis bases,



Figure 5.9 displays the equilibrium structures assumed by these cation-assisted H-bond complexes, and Table 5.12 summarizes energetic and structural properties

Table 5.12. *Similar to Table 5.7, for NH₄⁺ ⋯ B complexes (see Fig. 5.9)*

NH ₄ ⁺ ⋯ B	$\Delta E_{\text{H}\cdots\text{B}}$ (kcal mol ⁻¹)	$R_{\text{H}\cdots\text{B}}$ (Å)	R_{NH} (Å)	ΔR_{NH} (Å)	$\Delta \nu_{\text{NH}}$ (cm ⁻¹)
NH ₄ ⁺ ⋯ FH	12.90	1.766	1.035	0.0087	-158
NH ₄ ⁺ ⋯ OH ₂	22.01	1.637	1.064	0.0373	-642
NH ₄ ⁺ ⋯ NH ₃	28.23	1.550	1.143	0.1168	-1748

of the complexes for comparison with those of corresponding neutral (Table 5.7) and anionic complexes (Table 5.9). Table 5.13 similarly displays various NBO descriptors (charge transfer, change in polarity, and n- σ and n- σ^* overlaps) of the ammonium complexes that can be directly compared with those of corresponding neutral (Table 5.8) and anionic (Table 5.11) complexes.

As expected, the properties of the ammonium complexes vary smoothly with the relative strength (5.36a) of the Lewis base (rather than, e.g., with dipole-moment ordering). While the order of enhancement of magnitude of H-bond strength with net charge is similar to that in the anion-assisted case, the patterns of this enhancement are somewhat different in the cation-assisted case. In particular, the hydride bond of the ammonium cation is more strongly polarized than that of the neutral NH₃ monomer, so that the ratio $(S_{\text{n}\sigma^*}/S_{\text{n}\sigma})^2$ is more favorable for weak as well as strong H-bonds. As a result, the *net* H-bond energy for given $\Delta E_{\text{n}\sigma^*}$ ⁽²⁾ donor-acceptor stabilization is generally higher for cationic than for anionic H-bonds. Because of the higher bond polarity that is already present in the monomer, the H-bond-induced increase Δi_{NH} is somewhat weaker in the ammonium complexes. The shorter N—H bond of ammonium also allows somewhat closer approach and greater charge transfer in the cation-assisted case. In general, however, the overall picture is that adding net positive charge to the Lewis acid or negative charge to the Lewis base will *both* powerfully strengthen the n- σ^* H-bonding interaction.

To facilitate comparison of \pm CAHB complexes, we tabulate some properties of the N—H ⋯ O hydrogen bond of the cation-assisted NH₄⁺ ⋯ OH₂ complex (Fig. 5.9(b)) for direct comparison with those of analogous neutral and

Table 5.13. *Similar to Table 5.8, for ammonium-ion complexes*

NH ₄ ⁺ ⋯ B	Q_{CT}	Δi_{NH}	$S_{\text{n}\sigma^*}$	$S_{\text{n}\sigma}$
NH ₄ ⁺ ⋯ FH	0.0198	0.0304	0.2431	0.1270
NH ₄ ⁺ ⋯ OH ₂	0.0644	0.0650	0.4449	0.2457
NH ₄ ⁺ ⋯ NH ₃	0.1691	0.1140	0.5939	0.3399

Table 5.14. Comparisons of N—H···O hydrogen bonds in cation-assisted, neutral, and anion-assisted complexes

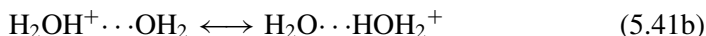
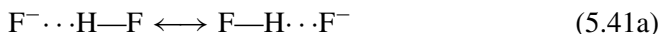
Complex	Type	$\Delta E_{\text{H}\cdots\text{O}}$ (kcal mol ⁻¹)	$R_{\text{H}\cdots\text{O}}$ (Å)	R_{NH} (Å)	ΔR_{NH} (Å)	Q_{CT}	$\Delta E_{\text{n}\sigma^*}$ ⁽²⁾ (kcal mol ⁻¹)
NH ₄ ⁺ ···OH ₂	+CAHB	22.01	1.637	1.064	0.0373	0.1691	30.09
NH ₃ ···OH ₂	Neutral	2.66	2.212	1.018	0.0034	0.0034	3.08
NH ₃ ···OH ⁻	-CAHB	17.09	1.685	1.073	0.0585	0.0589	31.07

anion-assisted NH₃ complexes (Figs. 5.5(c) and 5.7(b)) in Table 5.14. These comparisons may be taken as representative of a wide variety of \pm CAHB complexes.

Symmetric no-barrier H-bonds

The bifluoride ion (F⁻···HF) and H₅O₂⁺ hydronium ion (H₃O⁺···OH₂) both merit special attention as examples of strong, symmetric ionic H-bonds. The bifluoride ion played an important role in historical recognition of the H-bonding phenomenon⁴⁶ and is widely recognized as the strongest known example (>40 kcal mol⁻¹) of H-bonding. The H₅O₂⁺ ion appears to be an important species in aqueous acid solutions, and hence (together with hydrated complexes of OH⁻) plays a leading role in aqueous acid–base chemistry.

Figure 5.10 displays optimized structures of FHF⁻ and H₅O₂⁺ (left), together with the leading n- σ^* interaction from a single localized Lewis-structure representation (i.e., F⁻···HF or H₂OH⁺···OH₂). As can be seen in Fig. 5.10, each species adopts a *symmetric* structure in which any possible distinction between the “H-bond” and the “covalent bond” is *obliterated*, corresponding to *equal* weighting of proton/charge-transferred resonance structures



Each n- σ^* donor–acceptor interaction pictured in Fig. 5.10 is therefore completely equivalent to the interaction for the alternative Lewis structure. This resonance description is in perfect correspondence with the Pimentel–Rundle three-center MO picture of hypervalent bonding (Section 3.4). The H-bonded complexes HF₂⁻ and H₅O₂⁺ are also obvious analogs of the hypervalent transition-metal complexes discussed in Section 4.6.

Because FHF⁻ epitomizes the limit of strong hydrogen bonding in a particularly simple geometrical form, let us examine some further aspects of its potential-energy surface. The triatomic species can generally be described in terms of three variables,

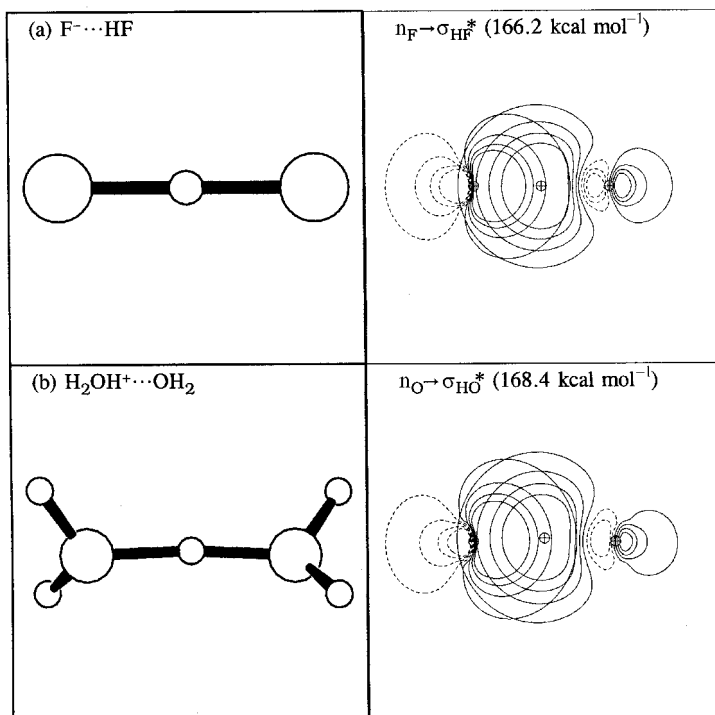


Figure 5.10 Optimized structures (left) and leading $n \rightarrow \sigma^*$ interactions (right) of symmetric (a) $F^- \cdots HF$ and (b) $H_2OH^+ \cdots OH_2$ ions. The “H-bond” distances are (a) 1.147 Å and (b) 1.198 Å, only ~ 0.2 Å beyond normal covalent distances in the isolated monomers.

the covalent bond r_{HF} (shorter), the H-bond $R_{F \cdots H}$ (longer), and the bending angle θ_{FHF} . Adiabatic one-dimensional potential-energy profiles can be obtained for each coordinate by optimizing the two remaining coordinates along the adiabatic path.

Figure 5.11 depicts the conventional H-bonding potential-energy curve for approach of F^- to HF (solid curve, circles). This figure also displays the $n_F \rightarrow \sigma_{HF}^*$ attractive donor–acceptor interaction $\Delta E_{n \rightarrow \sigma^*}$ ⁽²⁾ (dashed curve) and the steric repulsion energy (Section 1.7; dotted curve) at each $R_{F \cdots H}$. As seen in Fig. 5.11, there is a strong attractive interaction that extends far beyond the distance of appreciable steric or donor–acceptor interaction (> 2.5 Å). This evidently corresponds to the expected ion–dipole interaction in the long-range limit of classical electrostatics (Section 5.1.3).⁴⁷ However, the “real” H-bond may be considered to correspond to the *incremental* binding that begins with the onset of strong valence-type steric and donor–acceptor interactions near $R_{F \cdots H} \simeq 2.5$ Å, i.e., the contributions that *distinguish* FHF^- from ordinary ion–dipole complexes. Against the exponentially growing steric repulsions, the attractive donor–acceptor interactions are

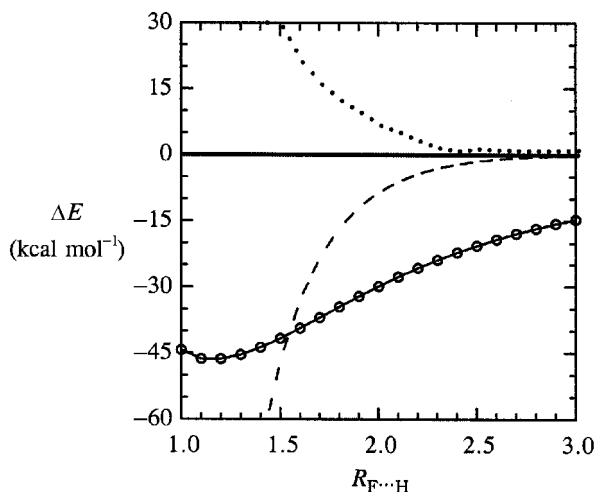


Figure 5.11 The adiabatic potential-energy curve for $F^- \cdots HF$ hydrogen-bond formation (solid line, circles), with the steric repulsion energy (dotted line) and estimated $n_F-\sigma_{HF}^*$ donor-acceptor attraction (dashed line) included for comparison.

able to bring the closed-shell species into remarkably short equilibrium separation ($R_{F\cdots H} \simeq 1.15 \text{ \AA}$), far inside that expected for a classical ion-dipole complex.

Figure 5.12 depicts the corresponding adiabatic one-dimensional potential for the covalent r_{HF} proton-transfer coordinate, showing the barrierless switch-over at equilibrium between $FH \cdots F^-$ and $F^- \cdots HF$ bond patterns. The potential well is seen to be extremely flat in the neighborhood of equilibrium, corresponding to the extremely low IR frequency of the proton-transfer mode (1299 cm^{-1} , red-shifted

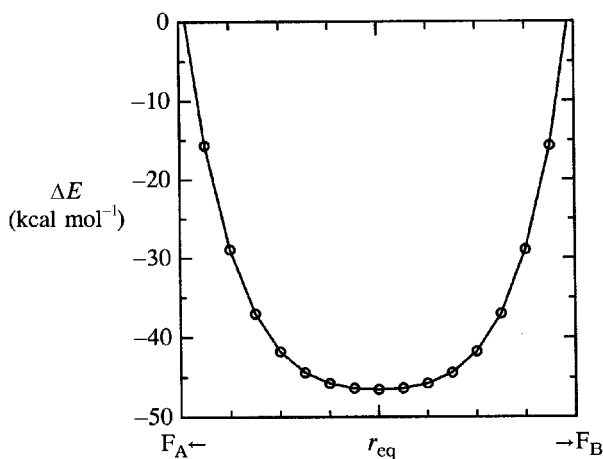


Figure 5.12 The adiabatic proton-transfer potential for r_{HF} displacements from equilibrium toward one or the other F in $F \cdots H \cdots F$ (the tick-mark separation is 0.1 \AA).

by 2800 cm^{-1} from ν_{HF} in isolated HF). The calculated proton chemical shielding at equilibrium, 15.93 ppm, also corresponds to strong downfield displacement (by more than 14 ppm) from the corresponding shielding in isolated HF. This no-barrier limit of H-bonding therefore leads to a highly unusual regime of proton-transfer dynamics and shielding with many interesting aspects that are beyond the scope of the present book.⁴⁸

Finally, Fig. 5.13 shows the adiabatic bending potential for nonlinear deformations. The angular dependence appears similar to a cosine-like (or dipole–dipole) behavior near equilibrium, but departs conspicuously from this mathematical form at larger deformation angles. The potential shows the strong propensity for linear $\text{F}\cdots\text{H}\cdots\text{F}$ H-bonding arrangements consistent with maximization of $n\text{-}\sigma^*$ donor–acceptor overlap.

It is evident that charged no-barrier H-bonds such as those in HF_2^- and H_5O_2^+ provide an extremely facile pathway for proton-exchange reactions and accompanying charge “switching” (formal electron transfer) between protonated species. Such processes are essential features of aqueous acid–base chemistry, electrochemistry, and many important biological functions. The species (5.41a) and (5.41b) vividly illustrate that H-bonding is essentially a partial proton/charge-transfer reaction whose limiting form indeed corresponds to symmetric proton/charge *sharing* between the competing Lewis bases.

The resonance description of charged and uncharged H-bonds

To gain a more comprehensive overview of the full range of H-bond strengths, let us compare all 19 neutral and charged $\text{B}\cdots\text{HA}$ complexes considered previously in

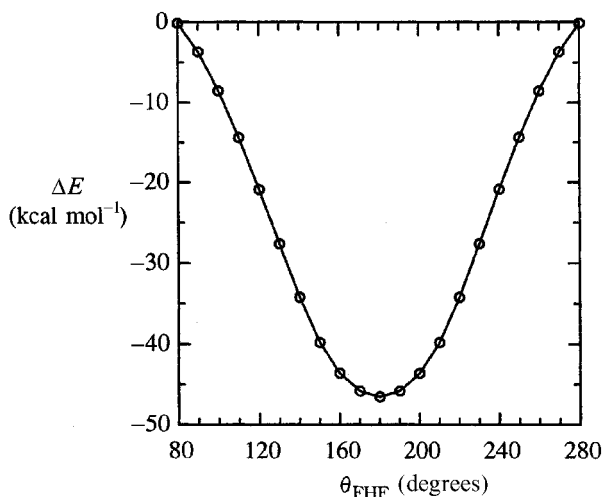


Figure 5.13 The adiabatic bending potential for the $\text{F}^-\cdots\text{HF}$ ion.

Table 5.15. *A comparison of neutral and charged H-bond complexes B...HA from Sections 5.2.1 and 5.2.2 (ordered by H-bond strength), showing net H-bond energy ΔE_{HB} , leading $n \rightarrow \sigma^*$ stabilization $\Delta E_{n \rightarrow \sigma^*}$ ⁽²⁾, net charge transfer $Q_{\text{B} \rightarrow \text{AH}}$, and NRT bond orders $b_{\text{A}-\text{H}}$ and $b_{\text{B} \dots \text{H}}$*

No.	Lewis base/acid		Charge	Energy (kcal mol ⁻¹)			Bond orders	
	B	HA		ΔE_{HB}	$\Delta E_{n \rightarrow \sigma^*}$ ⁽²⁾	$Q_{\text{B} \rightarrow \text{AH}}$ (e)	$b_{\text{A}-\text{H}}$	$b_{\text{B} \dots \text{H}}$
1.	H ₂ O	HCH ₃	0	0.4	0.9	0.0020	0.999	0.001
2.	HF	HNH ₂	0	1.1	0.6	0.0012	1.000	0.000
3.	H ₂ CO	HNH ₂	0	1.4	1.2	0.0026	0.921	0.071
4.	CO	HF	0	1.8	1.5	0.0280	0.988	0.009
5.	H ₂ O	HNH ₂	0	2.7	3.1	0.0034	0.990	0.008
6.	OC	HF	0	3.6	10.4	0.0280	0.941	0.059
7.	HF	HF	0	5.1	6.7	0.0124	0.967	0.026
8.	H ₂ O	HOH	0	5.8	7.5	0.0138	0.969	0.030
9.	HO ⁻	HCH ₃	-	6.5	10.9	0.0400	0.957	0.043
10.	H ₃ N	HOH	0	7.3	12.6	0.0269	0.951	0.049
11.	H ₂ O	HF	0	10.1	18.0	0.0339	0.902	0.074
12.	HF	HNH ₃ ⁺	+	12.9	8.9	0.0198	0.957	0.034
13.	H ₃ N	HF	0	14.3	34.9	0.0721	0.826	0.164
14.	OH ⁻	HNH ₂	-	17.1	31.1	0.0859	0.856	0.143
15.	H ₂ O	HNH ₃ ⁺	+	22.0	30.1	0.0644	0.868	0.117
16.	H ₃ N	HNH ₃ ⁺	+	28.2	75.6	0.1691	0.685	0.306
17.	HO ⁻	HOH	-	29.4	63.4	0.1886	0.634	0.365
18.	H ₂ O	HOH ₂ ⁺	+	36.7	168.4	0.2365	0.500	0.500
19.	F ⁻	HF	-	46.5	166.2	0.2336	0.500	0.500

this chapter. In addition to the NBO descriptors presented previously, it is useful to compare the relative NRT weightings w_{cov} and w_{ion} of covalent and ionic resonance contributions (5.29a). Equivalently, we can examine the formal covalent ($b_{\text{A}-\text{H}}$) and H-bonded ($b_{\text{B} \dots \text{H}}$) NRT bond orders, which are closely related to covalent/ionic resonance weights through the approximate expressions

$$b_{\text{A}-\text{H}} \simeq \frac{w_{\text{cov}}}{w_{\text{cov}} + w_{\text{ion}}} \quad (5.42a)$$

$$b_{\text{B} \dots \text{H}} \simeq \frac{w_{\text{ion}}}{w_{\text{cov}} + w_{\text{ion}}} \quad (5.42b)$$

Overall trends in covalent/ionic resonance will be compared with net charge transfer and other descriptors previously correlated with H-bond strength.

Table 5.15 compares the neutral and charged H-bonded complexes of Sections 5.2.1 and 5.2.2, ordered by H-bond strength from weakest (H₂O...H₄C) to strongest (F...H...F⁻). For each B...AH complex, the table shows the total charge, the energy of the H-bond (ΔE_{HB}) and the leading $n \rightarrow \sigma^*$ stabilization ($\Delta E_{n \rightarrow \sigma^*}$ ⁽²⁾),

the net charge transfer from Lewis base to Lewis acid ($Q_{B \rightarrow AH}$), and the calculated NRT bond orders for covalent (b_{A-H}) and H-bond ($b_{B \cdots H}$) linkages.

It is clear from Table 5.15 that neutral and ionic H-bonds fall on a *continuum* of H-bond strengths, ranging from <1 kcal mol⁻¹ to >40 kcal mol⁻¹. While it is true that the weakest H-bonded complexes 1–8 are all neutral, and the strongest complexes 14–19 are all charged, the middle group of complexes 9–13 includes a mix of charged and uncharged H-bonds of comparable strengths (≈ 6 – 15 kcal mol⁻¹). Other properties of these H-bonded complexes also vary rather uniformly over a wide range of values, with broadly overlapping ranges for neutral and ionic complexes. From this viewpoint there is neither any sharp distinction to be drawn between neutral and \pm CAHB H-bonds, nor any apparent discontinuity in the mechanism of H-bonding up to the strongest known cases. Because substantial charge transfer *must* be present in the bifluoride ion, the overall continuity of properties in Table 5.15 strongly suggests the role of charge transfer *throughout* this series.

The overall increase in H-bond energies (by about two orders of magnitude) is mirrored by increases of comparable magnitude in the charge transfer (from 0.2% to $>20\%$ of an electron), $n \rightarrow \sigma^*$ stabilization (from 1 to >100 kcal mol⁻¹), and $b_{B \cdots H}$ bond order (from 0.001 to 0.500). The general trends of the data in Table 5.15 can be more clearly displayed in graphical form. Figure 5.14 shows how the energies ΔE_{HB} and $\Delta E_{n \rightarrow \sigma^* (2)}$ vary in a highly correlated manner with $Q_{B \rightarrow AH}$. The increasing gap between $\Delta E_{n \rightarrow \sigma^* (2)}$ and net ΔE_{HB} can be attributed to the ever

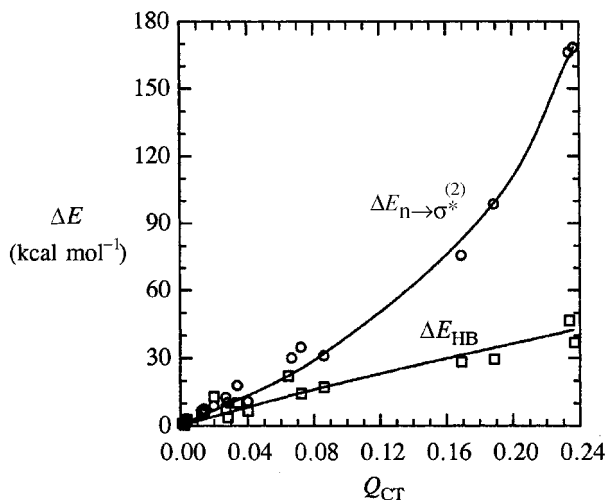


Figure 5.14 Correlation of net H-bond energy (ΔE_{HB} , squares) and principal $n \rightarrow \sigma^*$ stabilization energy ($\Delta E_{n \rightarrow \sigma^* (2)}$, circles) with intermolecular charge transfer (Q_{CT}); cf. Table 5.15. (Approximate trend-lines are shown for each quantity to aid visualization.)

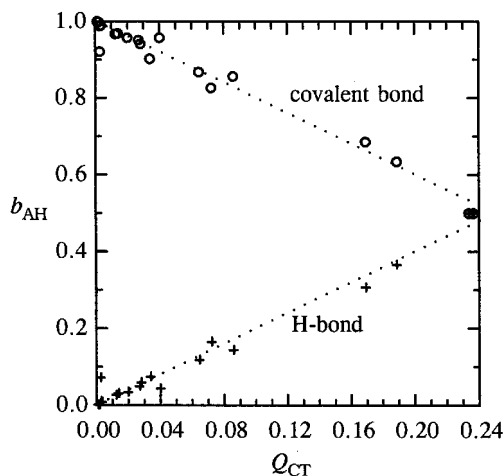


Figure 5.15 The correlation of NRT bond orders b_{AH} of covalent bonds (circles) and H-bonds (plus signs) with intermolecular charge transfer (Q_{CT}); cf. Table 5.15. (Approximate trend-lines are shown to aid visualization.)

increasing steric repulsion that must be overcome in the shortest, strongest forms of H-bonding.

Figure 5.15 shows the corresponding correlation of Q_{CT} with H-bond and covalent-bond orders. The progressive strengthening of covalent/ionic resonance (and the associated shifts in bond lengths and frequencies) can be seen to be directly proportional to the increase in net charge transfer, as the covalent/ionic-resonance picture suggests. Intermolecular charge transfer therefore appears as a convenient single order parameter that underlies the strong correlations among numerous properties of H-bonded complexes.

In summary, the covalent/ionic-resonance picture can be used to describe the entire range of neutral and charged H-bonding phenomena. The NRT resonance weights (w_{cov} and w_{ion}) and bond orders (b_{A-H} and $b_{B...H}$) are correlated in the expected manner with bond lengths, IR frequencies, intermolecular charge transfer, and other properties.

Dihydrogen bonds

A novel form of $Y \cdots HX$ hydrogen bonding⁴⁹ results when the Lewis base Y is itself a hydride ion (H^-). Because the electron affinity of a hydrogen atom is extremely weak (21 kcal mol^{-1}), the H^- ion is among the most weakly bound and diffuse anionic species known, and hence a powerful Lewis base. In this case, the $H^- \cdots HX$ complex can be referred to as a “dihydrogen bond”⁵⁰ to denote the unusual H-bonding between hydrogen atoms. A water complex of this type was

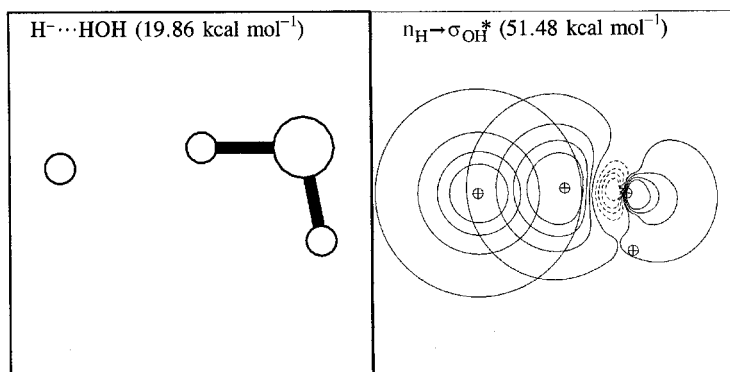


Figure 5.16 The optimized structure and leading $n \rightarrow \sigma^*$ donor–acceptor interaction in $\text{H}^- \cdots \text{HOH}$. The geometrical parameters are $R_{\text{H}\cdots\text{H}} = 1.446 \text{ \AA}$, $r_{\text{OH}(\text{b})} = 1.031 \text{ \AA}$, $r_{\text{OH}(\text{f})} = 0.963 \text{ \AA}$, $\theta_{\text{H}\cdots\text{HO}} = 171.8^\circ$, and $\theta_{\text{HOH}} = 100.6^\circ$.

first characterized by Lineberger and coworkers,⁵¹ and can be formulated as



Ionic or semi-ionic $\text{Y}-\text{H}$ bonds of sufficient hydridic character ($\text{Y}^+ - \text{H}^-$) can also be expected to make dihydrogen bonds of the form



in which the Lewis-base donor orbital is formally a two-center σ_{YH} bond (rather than the usual one-center n_{Y} lone pair). Complexes of the form (5.43b) have now become rather widely recognized.⁵² In the present section we examine some prototype examples of anionic dihydrogen bonding involving both one-center (n_{H}) and two-center (σ_{YH}) hydridic donor orbitals.

Let us first consider the aqueous H_3O^- species (5.43a), which is found to be bound by $19.86 \text{ kcal mol}^{-1}$ (relative to $\text{H}^- + \text{H}_2\text{O}$). Figure 5.16 shows the optimized structure of this species together with the leading $n_{\text{H}} \rightarrow \sigma_{\text{OH}}^*$ donor–acceptor interaction. As seen in Fig. 5.16, the hydridic s-type lone pair n_{H} has an extremely large radius and complete lack of directionality, leading to the strong interaction ($\Delta E_{n \rightarrow \sigma^*}^{(2)} = -51.48 \text{ kcal mol}^{-1}$) with the proximal σ_{OH}^* of the water molecule. Because the electron affinity of H^- is so weak and the energy of the donor orbital so high ($\epsilon_{\text{n}} = +0.05545 \text{ a.u.}$), the charge transfer to the Lewis base is unusually large ($Q_{\text{CT}} = 0.2172$) for the given degree of $n-\sigma^*$ overlap. Thus, the $\text{H}^- \cdots \text{H}-\text{O}$ dihydrogen bond exhibits certain anomalies because of the unusual properties of the s-type n_{H} donor orbital, but it conforms in general respects to the $n-\sigma^*$ picture.

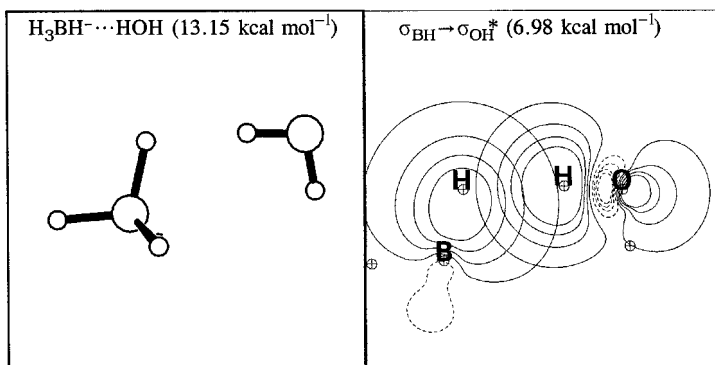


Figure 5.17 The optimized structure and leading $\sigma \rightarrow \sigma^*$ donor–acceptor interaction in $\text{H}_3\text{BH}^- \cdots \text{HOH}$. The geometrical parameters are $R_{\text{H}\cdots\text{H}} = 1.704 \text{ \AA}$, $r_{\text{OH}(\text{b})} = 0.981 \text{ \AA}$, $r_{\text{OH}(\text{f})} = 0.962 \text{ \AA}$, $r_{\text{BH}(\text{b})} = 1.244 \text{ \AA}$, $r_{\text{BH}(\text{f})} = 1.230 \text{ \AA}$, $\theta_{\text{H}\cdots\text{HO}} = 174.6^\circ$, $\theta_{\text{BH}\cdots\text{H}} = 107.4^\circ$, and $\theta_{\text{HOH}} = 100.6^\circ$.

As a second example of dihydrogen bonding, let us consider the borohydride anion (BH_4^-) in complexation with water (as analyzed by Jackson⁵³),



In this case the formal donor orbital is the two-center σ_{BH} , so the complex is formally of type (5.43b). The optimized structure of $\text{BH}_4^- \cdots \text{HOH}$ is shown in Fig. 5.17, together with the dominant $\sigma_{\text{BH}} \rightarrow \sigma_{\text{OH}^*}$ donor–acceptor interaction.

As seen in Fig. 5.17, the σ_{BH} donor makes a sideways (rather than end-on) approach to the acceptor σ_{OH^*} orbital, approaching the T-shaped geometry that is common in agostic interactions (Sections 3.6 and 4.7) involving a σ -bond donor. However, the greater orbital amplitude of σ_{BH} is at the hydride end (rather than the midpoint of the bond), so the resulting geometry is more nearly L-shaped. As usual, the dihydrogen bond is nearly in linear alignment ($\theta_{\text{H}\cdots\text{HO}} = 174.6^\circ$) with the coordinated O—H bond, which is lengthened and weakened in the expected manner. The coordinated B—H donor bond of the Lewis base is *also* somewhat lengthened compared with free B—H bonds. As expected, the donor and acceptor NBOs have opposite polarities,

$$\sigma_{\text{BH}(\text{b})} = 0.67(\text{sp}^{3.17})_{\text{B}} + 0.75(\text{s})_{\text{H}} \quad (5.45\text{a})$$

$$\sigma_{\text{OH}(\text{b})} = 0.87(\text{sp}^{2.73})_{\text{O}} + 0.49(\text{s})_{\text{H}} \quad (5.45\text{b})$$

and the natural charges of the donor and acceptor hydrogen-bridge atoms reflect the strongly zwitterionic ($\text{BH}^- \cdots \text{H}^+\text{O}$) character of the charge distribution

$$Q_{\text{H}}(\text{BH}) = -0.1025, \quad Q_{\text{H}}(\text{OH}) = +0.5053 \quad (5.46)$$

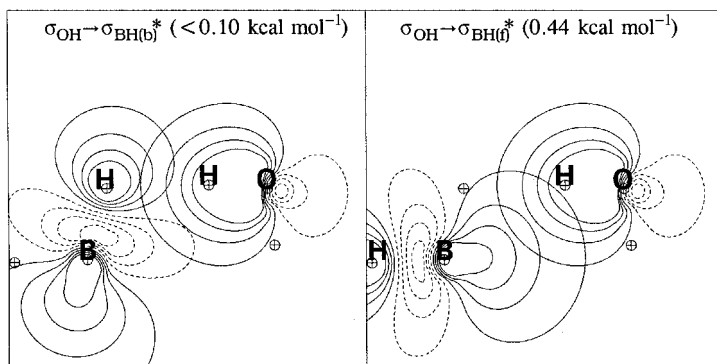


Figure 5.18 Weak $\sigma_{\text{OH}} \rightarrow \sigma_{\text{BH}}^*$ back-transfer involving (left) H-bonded and (right) free B—H antibonds of the borohydride ion. Note that the nodal plane of the $\sigma_{\text{BH(b)}}^*$ precludes significant net overlap with σ_{OH} in the L-shaped geometry.

The net charge transfer from Lewis base to Lewis acid is $Q_{\text{CT}} = 0.0208e$, about an order of magnitude weaker than the corresponding charge transfer in $\text{H}^- \cdots \text{HOH}$. Other measures of H-bond strength are proportionately weaker in the $\sigma - \sigma^*$ complex (5.44) than in the $n - \sigma^*$ complex (5.43a). As in other anionic complexes, there is a large background attraction that can be attributed to classical ion–dipole forces.

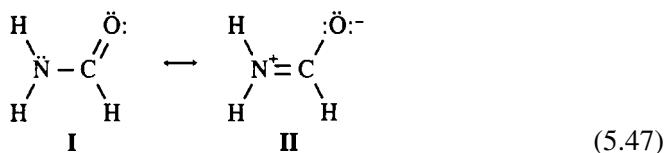
It is interesting to note the slight back-transfer of $\sigma_{\text{OH}} \rightarrow \sigma_{\text{BH}}^*$ type from H_2O to BH_4^- . Such reciprocal CT interactions might well be expected from the inherent symmetry of the $\text{BH} \cdots \text{HO}$ dihydrogen bridge. However, this weak back-transfer (estimated stabilization $0.44 \text{ kcal mol}^{-1}$) involves *not* the directly bonded $\sigma_{\text{BH(b)}}^*$, but rather the free B—H(f) oriented *anti* to the dihydrogen bond. Figure 5.18 depicts both these interactions, showing the unfavorable overlap with the proximal $\sigma_{\text{BH(f)}}^*$ as well as the somewhat more favorable overlap with the backside lobe of the distal $\sigma_{\text{BH(f)}}^*$.

5.2.3 Resonance-assisted H-bonds (RAHBs)

As pointed out by Gilli *et al.*,⁵⁴ $\text{B} \cdots \text{HA}$ hydrogen bonding appears to be systematically enhanced whenever the individual monomers B and HA exhibit strong resonance delocalization, leading to what are termed “resonance-assisted” H-bonds (RAHBs). This interesting effect appears to be of special importance in the biological domain, where resonance delocalization is a conspicuous feature of H-bonding moieties such as the amide groups of proteins, the purine and pyrimidine bases of DNA, and the histidine and glutamate residues that often play a key role in the active sites of enzymes. Thus, it appears that the RAHB phenomenon is manifested by the most fundamental H-bonds of molecular biology.

Resonance-assisted amide complexes

The RAHB effect may be illustrated by the ubiquitous $\text{C}=\text{O} \cdots \text{H}-\text{N}$ hydrogen bond of protein chemistry. As shown in Section 5.2.2, the simplest non-RAHB “prototype” for such bonding, the formaldehyde–ammonia complex (5.31c), has only a feeble H-bond ($1.41 \text{ kcal mol}^{-1}$). However, when the carbonyl and amine moieties are combined in the resonating amide group of, e.g., formamide, with strong contributions of covalent (**I**) and ionic (**II**) resonance structures,



the strength of the resulting amide \cdots amide H-bond is enhanced by more than a factor of *four* (to $6.19 \text{ kcal mol}^{-1}$). Figure 5.19 depicts the optimized structure of

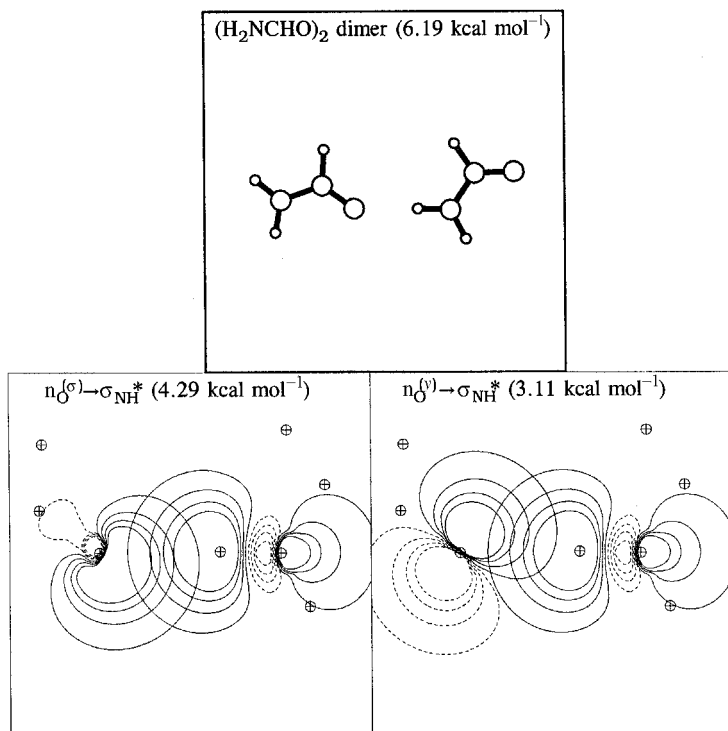


Figure 5.19 The optimized structure of the linear formamide dimer and leading $n_{\text{O}} \rightarrow \sigma_{\text{NH}}^*$ interactions with distinct σ -type $n_{\text{O}}^{(\sigma)}$ and in-plane p -type $n_{\text{O}}^{(y)}$ lone pairs.

the formamide dimer $(\text{H}_2\text{NCHO})_2$, together with the two main $n_{\text{O}} \rightarrow \sigma_{\text{HN}}^*$ donor–acceptor interactions, for direct comparison with the corresponding non-RAHB interaction in Fig. 5.1(c). The in-plane p-type oxygen lone pair is labeled $n_{\text{O}}^{(\nu)}$ to distinguish it from the σ -type $n_{\text{O}}^{(\sigma)}$ along the bond axis.

The electronic origin of RAHB enhancement can be readily judged from the resonance diagrams (5.47). To the extent that the resonance hybrid has significant weighting of **II**, the n_{O} donor acquires *anionic* character and the σ_{NH}^* acceptor acquires *cationic* character. Thus, significant resonance weighting w_{II} implies that H-bonding will automatically be enhanced through the \pm CAHB effect discussed in the previous section.

However, the coupling between intramolecular resonance (5.47) and the strength of H-bonding goes beyond a static picture of the resonance hybrid (5.47). Because \pm CAHB character strongly promotes the strength of bonding, one can expect that the resonance weightings (5.47) will be *shifted* toward higher w_{II} by H-bond formation. Conversely, perturbations of the amide moiety that affect resonance delocalization (substituent effects, changes in geometry, formation of another H-bond, etc.) must also be expected to affect the strength of H-bonding. In other words, the intermolecular and intramolecular resonance hybrid weightings in (5.29a) and (5.47) are expected to be *coupled* in a mutually reinforcing (cooperative) manner. Because each resonance structure in (5.29a) and (5.47) corresponds to distinct structural, IR, and charge properties, the concept of intra/intermolecular resonance coupling (i.e., of resonance-assisted H-bonding, *or* equivalently, H-bond-assisted resonance shifts) has immediate implications for geometrical, dynamical, and dielectric changes associated with H-bonding.

Consistently with this picture, the relative NRT weighting of the ionic resonance structure **II** is found to be significantly higher in both members of the H-bonded complex. Such weighting is reflected in increased b_{CN} bond order (from 1.303 to 1.339) and decreased b_{CO} bond order (from 1.744 to 1.703) in the Lewis base. Consistently with these bond-order shifts, the CO bond is found to be slightly elongated (by 0.006 Å) and the CN bond slightly shortened (by 0.008 Å) relative to the free monomer, whereas other bonds are much less affected. Although these small changes in geometry would be difficult to detect directly, the corresponding vibrational red-shift of ν_{CO} ($\sim 25 \text{ cm}^{-1}$) is a well-known signature of H-bond formation.

Further synergistic enhancement of amide resonance and H-bonding occurs when both monomers can participate in *two* complementary H-bonds, once as a Lewis base and once as a Lewis acid. Such concerted (cooperative) pairs of H-bonds occur in the cyclic formamide dimer, as illustrated in Fig. 5.20. In this case the strength of each H-bond is further enhanced (to $6.61 \text{ kcal mol}^{-1}$, about 4.7 times that of the “prototype” (5.31c)), the bond orders b_{CN} and b_{CO} are further shifted (to 1.384 and 1.655, respectively), and the bond lengths undergo further shifts in the

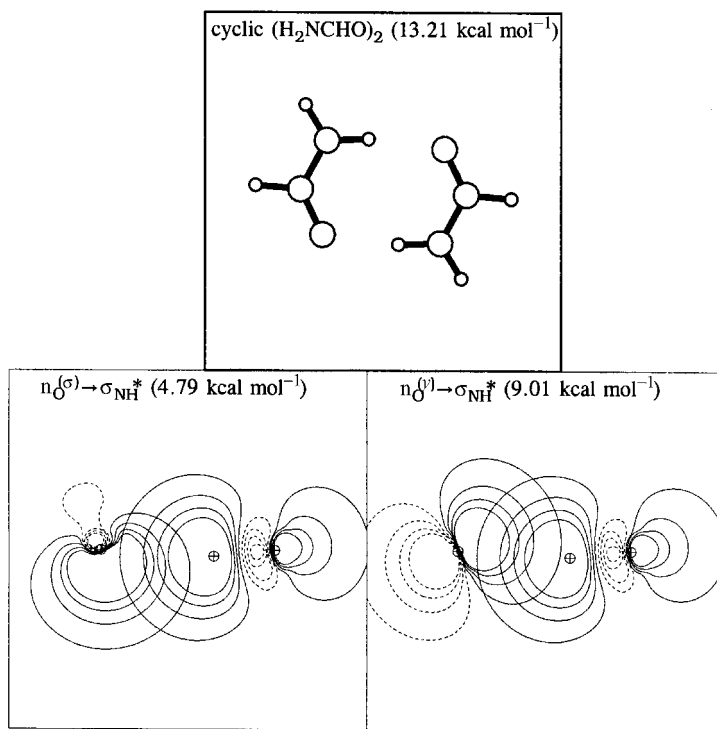


Figure 5.20 Similar to Fig. 5.19, for the cyclic formamide dimer.

direction suggested by increased weighting of **II**. The H-bond properties also shift in the manner expected with increased $n-\sigma^*$ interaction strength; the H-bond $R_{\text{O}\cdots\text{H}}$ shortens from 1.987 to 1.886 Å while the covalent $r_{\text{NH}(b)}$ bond lengthens from 1.015 to 1.026 Å.

Table 5.16 summarizes the H-bond energies and NRT bond orders for $\text{C}=\text{O}\cdots\text{H}-\text{N}$ hydrogen bonds in a variety of binary formamide complexes, including those shown in Figs. 5.19 and 5.20 as well as the “half-RAHB” species $\text{H}_2\text{NCHO}\cdots\text{HNH}_2$ and $\text{H}_2\text{CO}\cdots\text{HNHCHO}$ in which only *one* member of the complex is strongly resonance-stabilized. The species in Table 5.16 all exhibit the clear trend toward increased $\text{O}\cdots\text{H}-\text{N}$ bond strength (with increased $b_{\text{O}\cdots\text{H}}$ and decreased b_{NH}) as the $\text{N}-\text{C}=\text{O} \longleftrightarrow \text{N}=\text{C}-\text{O}$ resonance delocalization increases in either monomer (with increased b_{CN} and decreased b_{CO}). Thus, the b_{CO} bond orders of the half-RAHB complexes are decreased to values (1.723 and 1.726) intermediate between those of isolated formamide (1.744) and the cyclic dimer (1.655), while the b_{CN} bond orders are correspondingly increased to values (1.320 and 1.322) intermediate between those for the monomer (1.303) and cyclic dimer (1.384).

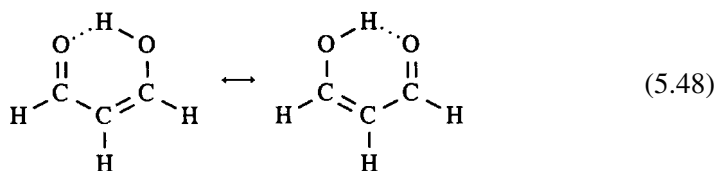
Table 5.16. A comparison of H-bond energy (ΔE_{HB}) and NRT bond orders (b_{AB}) for $\text{C}=\text{O} \cdots \text{H}-\text{N}$ hydrogen bonds in binary formamide complexes

Complex ^a	ΔE_{HB} (kcal mol ⁻¹)	Lewis base		Lewis acid		$b_{\text{O}\cdots\text{H}}$	b_{NH}
		b_{CO}	b_{CN}	b_{CO}	b_{CN}		
$\text{H}_2\text{NCHO} \cdots \text{H}_3\text{N}$	3.81	1.723	1.320	—	—	0.005	0.993
$\text{H}_2\text{CO} \cdots \text{H}_2\text{NCHO}$	4.17	2.058	—	1.726	1.322	0.007	0.987
$\text{H}_2\text{NCHO} \cdots \text{H}_2\text{NCHO}$	6.19	1.703	1.339	1.716	1.331	0.010	0.983
Cyclic $(\text{H}_2\text{NCHO})_2$	2(6.61)	1.655	1.384	1.655	1.384	0.012	0.974

^a The bond orders of isolated H_2NCHO are $b_{\text{CO}} = 1.744$, $b_{\text{CN}} = 1.303$, and $b_{\text{NH}} = 0.993$.

Intramolecular RAHB coupling

As a further illustration of the phenomenon of H-bond resonance coupling let us consider the *intramolecular* H-bond of β -hydroxyacrolein ($\text{O}=\text{CHCH}=\text{CHOH}$), a prototypical “enolone” (2-en-3-ol-1-one, or enol isomer of β -diketone).⁵⁵ This molecule may be envisioned as existing in two distinct isomeric forms, according to the position of the proton in the $\text{O} \cdots \text{H}-\text{O}$ hydrogen bond:



If the $\text{O} \cdots \text{H} \cdots \text{O}$ bridging were symmetric (as in the C_{2v} transition state between the inequivalent $\text{O} \cdots \text{H}-\text{O}$ and $\text{O}-\text{H} \cdots \text{O}$ isomers), the two Lewis structures in (5.48) would contribute equivalently to the resonance hybrid. However, in the actual equilibrium structures, the proton is in a double-well potential lying closer to one or the other oxygen, and the resonance structures in (5.48) make *inequivalent* contributions to the resonance hybrid in either isomer. Thus, proton transfer in the $\text{O} \cdots \text{H}-\text{O}$ moiety is expected to be strongly coupled to keto–enol resonance in the conjugated backbone, providing for strong RAHB enhancement.

The cyclic H-bonded form (5.48) may be compared with the open conformer (5.49) in which the hydroxyl group is twisted away from the favorable H-bonding geometry.



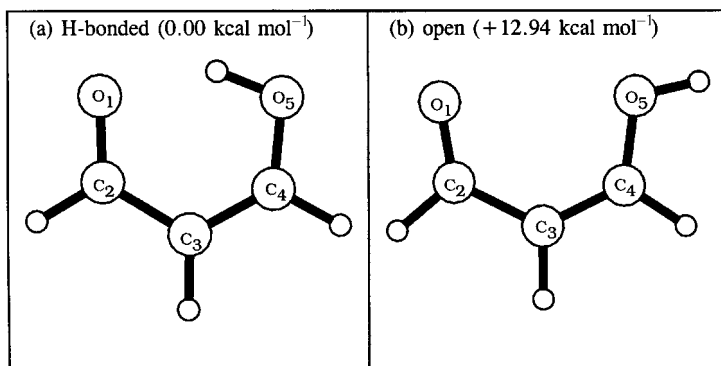


Figure 5.21 Optimized structures of β -hydroxyacrolein in its H-bonded (left) and “open” (right) conformers.

In this case, resonance delocalization along the conjugated backbone is expected to be reduced, due to loss of the synergistic RAHB coupling to H-bond formation. The optimized structures of β -hydroxyacrolein conformers are depicted in Fig. 5.21, and Table 5.17 compares bond lengths and NRT bond orders of the two conformers. Despite the conspicuously bent H-bonding geometry in Fig. 5.21(a), the H-bonded conformer is found to be favored by almost 13 kcal mol^{-1} (an unusually strong example of neutral $\text{O} \cdots \text{H} - \text{O}$ bonding).

As shown in Table 5.17, the unusually robust intramolecular H-bond in Fig. 5.21(a) is accompanied by pronounced bond-length and bond-order shifts along the enolone backbone, which is consistent with the greater weighting of the right-hand (proton-transferred) resonance structure in (5.48). Thus, the nominal C_2O_1 “double” bond is elongated by more than 0.02 \AA in the H-bonded form (consistently with the reduction of NRT bond order by 0.06), while the adjacent $\text{C}_2 - \text{C}_3$ “single”

Table 5.17. Comparison bond lengths R_{AB} and NRT bond orders b_{AB} for H-bonded and open forms of β -hydroxyacrolein (see Fig. 5.21 for atom numberings)

A—B	H-bonded		Open	
	R_{AB} (Å)	b_{AB}	R_{AB} (Å)	b_{AB}
$\text{O}_1 - \text{C}_2$	1.238	1.932	1.214	1.990
$\text{C}_2 - \text{C}_3$	1.439	1.092	1.465	1.044
$\text{C}_3 - \text{C}_4$	1.364	1.638	1.347	1.745
$\text{C}_4 - \text{O}_5$	1.320	1.297	1.343	1.205
$\text{O}_5 - \text{H}$	0.997	0.961	0.962	0.991
$\text{O}_1 \cdots \text{H}$	1.700	0.022	3.850	0.000

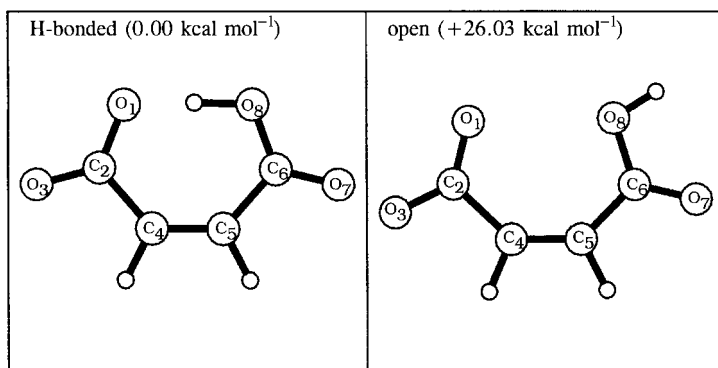
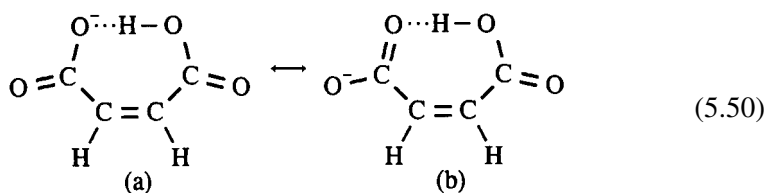


Figure 5.22 Optimized structures of H-bonded (left) and “open” (right) conformers of the maleate anion (see Table 5.18).

bond is correspondingly shortened and strengthened, and so on (in alternating fashion) around the enolone backbone. cursory examination of the pattern of skeletal geometry reveals the pronounced sensitivity of enolone resonance to H-bond formation, and the conjugative resonance shift evidently underlies the unusually strong H-bonding in this system.

An even stronger case of intramolecular RAHB coupling is provided by the maleate ion ($\text{HOOCCH}=\text{CHCOO}^-$), whose H-bonded and open conformers are shown in Fig. 5.22. Skeletal bond lengths and bond orders of these conformers are compared in Table 5.18. As shown in Fig. 5.22, the H-bonded conformer is favored in this case by more than 26 kcal mol^{-1} , which is indicative of a powerful intramolecular $n_{\text{O}} \rightarrow \sigma_{\text{OH}}^*$ interaction (estimated second-order stabilization $104 \text{ kcal mol}^{-1}$) that is sufficient to overcome the severe steric repulsion of the extremely short $\text{H} \cdots \text{O}$ nonbonded distance ($\sim 1.3 \text{ \AA}$).⁵⁶

In this case, the principal resonance delocalization accompanying H-bond formation involves only the two alternative forms of the terminal carboxylate moiety,



The favored structure (5.50a) evidently places higher anionic character on the Lewis base O, thus conferring higher $\text{O}^- \cdots \text{H} - \text{O}$ (anion-assisted) character. In effect, a shift of the maleate resonance hybrid toward the localized structure

Table 5.18. *Similar to Table 5.17, for the maleate anion (see Fig. 5.22 for atom numberings)*

A—B	H-bonded		Open	
	R_{AB} (Å)	b_{AB}	R_{AB} (Å)	b_{AB}
O ₁ —C ₂	1.283	1.398	1.243	1.468
C ₂ —O ₃	1.238	1.618	1.243	1.574
C ₂ —C ₄	1.521	0.978	1.552	0.952
C ₄ —C ₅	1.344	1.935	1.349	1.927
C ₅ —C ₆	1.506	0.996	1.474	1.026
C ₆ —O ₇	1.228	1.675	1.226	1.736
C ₆ —O ₈	1.307	1.323	1.344	1.229
O ₈ —H	1.099	0.895	0.969	0.987
O ₁ ···H	1.328	0.071	3.676	0.000

(5.50a) concentrates negative charge where it is most effective in promoting strong $n_O \rightarrow \sigma_{OH}^*$ donor–acceptor interaction.

Consistently with this picture, the net charge at O₁ in the H-bonded conformer is appreciably more negative (−0.755 versus −0.736) and the C₂—O₁ bond order is appreciably smaller (1.398 versus 1.468) than in the open conformer. Correspondingly, at the opposite H—O₈ (Lewis-acid) end of the H-bond, charge and bond-order shifts of the *opposite* sign accompany the partial proton transfer. The combined resonance shifts in the two carboxylate groups thus synergistically promote H-bond strength and partial proton transfer. The bond lengths in Table 5.18 are also consistent with this overall pattern of NRT bond-order shifts.

In contrast, resonance delocalization and bond alternation in the C—C=C—C backbone are only slightly affected by H-bond formation (namely, the C₄—C₅ bond order varies by only 0.008 between H-bonded and open conformers), because such resonance shifts do not intrinsically alter the charge distribution in the H-bonded O···H—O triad. This example illustrates the principle that H-bonding is not generally coupled to resonance per se, but only to such resonance as leads to effective \pm CAHB enhancement (Section 5.2.2).

Gilli and coworkers⁵⁷ have recognized many other examples of the RAHB phenomenon from the Cambridge Structural Database, documenting the structural correlations that strongly support the hypothesis of the covalent nature of these H-bonds. The computational examples presented in this section are fully consistent with their RAHB model, and similar NBO/NRT patterns would be expected to characterize the many interesting classes of compounds that were considered by these workers, but are beyond the scope of the present work.

5.2.4 Cooperativity and non-transferability in H-bonded clusters

Non-additive cooperative effects are among the most distinctive signatures of quantum donor–acceptor interactions. Whereas Coulomb’s law of classical electrostatics (Section 2.6) epitomizes a potential-energy function of pairwise-additive (non-cooperative) form, the quantum-mechanical interactions of the short-range exchange region are known to exhibit significant non-additivity. For covalent bonds, this non-additivity is often a fairly small percentage ($\sim 5\%$) of the total molecular binding energy, and a “sum-of-bond-energies” approximation can then give a qualitatively useful estimate of thermochemical properties.⁵⁸ For H-bonds, however, we shall see that the corresponding non-additivity errors tend to be significantly *larger*, and a pairwise-additive model of H-bonding (e.g., of simple-point-charge [SPC] type⁵⁹) fails to give an adequate description of H-bonding energetics.⁶⁰

The assumption of additivity that underlies many empirical intermolecular potentials can be stated more formally as follows. Suppose that A, B, C, . . . represent chosen molecules in a given spatial configuration. The potential-energy function $\mathcal{V}(A, B, C, \dots)$ (relative to isolated molecules⁶¹) will be said to be “pairwise additive” (and denoted \mathcal{V}_{PW}) if

$$\mathcal{V}_{\text{PW}}(A, B, C, \dots) = \mathcal{V}(A, B) + \mathcal{V}(A, C) + \mathcal{V}(B, C) + \dots \quad (\text{all pairwise terms}) \quad (5.51)$$

where $\mathcal{V}(A, B)$, etc. are the corresponding potentials for pairs of molecules. The non-pairwise-additive percentage error (%npw) of the approximation (5.51) for the chosen configuration can be expressed as

$$\% \text{npw} = \frac{\mathcal{V}_{\text{PW}}(A, B, C, \dots) - \mathcal{V}(A, B, C, \dots)}{\mathcal{V}_{\text{PW}}(A, B, C, \dots)} \times 100 \quad (5.52)$$

The interactions will be described as “cooperative” or “anticooperative” (for the chosen configuration) according to whether the deviations are positive or negative,

$$\% \text{npw} > 0 \quad (\text{“cooperative”}) \quad (5.53a)$$

$$\% \text{npw} < 0 \quad (\text{“anticooperative”}) \quad (5.53b)$$

i.e., according to whether \mathcal{V}_{PW} *underestimates* or *overestimates* the true binding energy $\mathcal{V}_{\text{true}} = \mathcal{V}(A, B, C, \dots)$. Familiar examples of pairwise-additive potentials (5.51) include SPC, Lennard-Jones,⁶² and many similar forms composed of point-charge and atom–atom interaction terms.

A special case of pairwise additivity (for sufficiently short-range potentials) is the limit of pair (“bond”) *transferability* or *constancy* from one environment to another. As mentioned above, such transferability is found to hold rather well for covalent bonds, but the corresponding transferability of H-bonds cannot be assumed without further justification. Such H-bond-additivity or -transferability assumptions often

lie at the heart of disagreements concerning the energetics of H-bonded clusters. In the ensuing discussion we shall therefore focus on *non-additivity of H-bond energies* (or non-transferability of a given H-bond from one environment to another) as the central chemical issue,⁶³ making use of clusters built from simple HF, H₂NCHO, and H₂O monomers.

HF clusters: tests of pairwise-additive models

Let us first consider higher clusters (HF)_{*n*} of the prototype “ideal-dipole” HF molecule, whose dimer was described in Section 5.2.1. Figure 5.23 displays the geometries of a number of open and cyclic (HF)_{*n*} clusters (*n* = 3–5) that may be compared with that of the dimer (cf. Fig. 5.1(b) and Table 5.1).

The geometries of the open (HF)_{*n*} clusters in Figs. 5.23(a)–(c) were chosen to mimic (and extend) the bent structure of the dimer in the manner that might be expected from a simple dipole–dipole picture. In these species the $\theta_{\text{HF}\dots\text{F}}$ angle was constrained to be the *same* for each monomer, thus creating a zig-zag one-dimensional *chain* of an extended herringbone pattern (but with $\theta_{\text{HF}\dots\text{F}}$ and all other

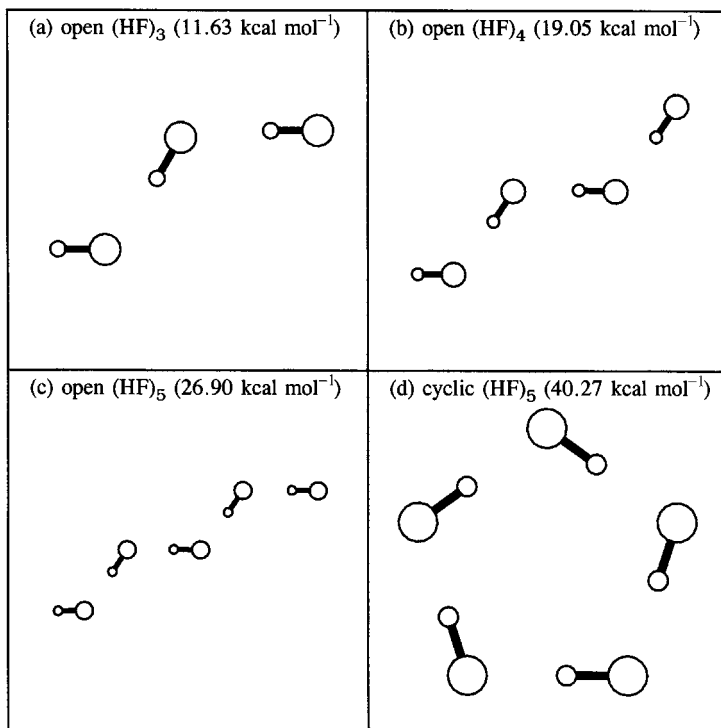


Figure 5.23 Model (HF)_{*n*} clusters (*n* = 3–5), with calculated net binding energies in parentheses. Only the cyclic pentamer (d) is a true equilibrium structure (see the text).

geometrical variables optimized for each species). Such model chains correspond to the simplest dipole-aligned configurations that still preserve (approximately) the characteristic canted geometry of each adjacent dimer pair; cf. Fig. 5.1(b). However, such dipole-aligned chains (although cooperatively stabilized relative to the dimer; see below) are *unstable* structures, which, upon relaxation of the constraint, will spontaneously rearrange to the more stable *cyclic* geometry (such as the cyclic pentamer shown in Fig. 5.23(d)).⁶⁴ Thus, the model chain clusters (Figs. 5.23(a)–(c)) allow us to sample spatial configurations that are of interest with respect to the expectations of a dipole–dipole model, but are otherwise unrealistically high in energy, corresponding to quite unimportant regions of the potential-energy surface.⁶⁵

By simply expressing the net binding energy of each $(\text{HF})_n$ in terms of the nominal number of H-bonds in each species, namely

$$(\text{HF})_2, \quad 5.05 \text{ kcal mol}^{-1} \quad (5.54\text{a})$$

$$\text{open } (\text{HF})_3, \quad 2(5.82 \text{ kcal mol}^{-1}) \quad (5.54\text{b})$$

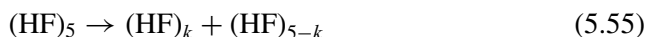
$$\text{open } (\text{HF})_4, \quad 3(6.35 \text{ kcal mol}^{-1}) \quad (5.54\text{c})$$

$$\text{open } (\text{HF})_5, \quad 4(6.73 \text{ kcal mol}^{-1}) \quad (5.54\text{d})$$

$$\text{cyclic } (\text{HF})_5, \quad 5(8.05 \text{ kcal mol}^{-1}) \quad (5.54\text{e})$$

one can recognize that the binding energy on a per-H-bond basis is increasing in a conspicuously non-additive fashion, so a “sum-of-bond-energies” scheme for H-bonds will have far greater errors than in the covalent-bond case. The error is rather modest ($\sim 15\%$) for the open trimer, but grows to about 60% for the cyclic pentamer.

The values in (5.54a)–(5.54e) reflect cooperative increases in *average* H-bond strength (for complete fragmentation to monomers), but the energies required to break *particular* H-bonds are still larger. Thus, while the average H-bond strength in the $(\text{HF})_5$ chain is only $6.73 \text{ kcal mol}^{-1}$ (enhanced by 33.3%), the energy of breaking a single H-bond



is $7.85 \text{ kcal mol}^{-1}$ (55.4%) for separation into monomer plus tetramer ($k = 1$), or $10.22 \text{ kcal mol}^{-1}$ (102.4%) for separation into dimer plus trimer ($k = 2$). Cooperativity-induced enhancements of H-bond strength can therefore be of the order of 100% even in the weaker chain isomers. As shown by comparison of (5.54d) and (5.54e), these enhancements become still larger in cyclic topologies.

However, comparisons such as (5.54a)–(5.54e) cannot yet be used for direct estimation of the formal non-additivity (5.52), because they neglect the contributions of *non-adjacent* pairs in (5.51). Table 5.19 summarizes details of the individual $\mathcal{V}(\text{A}, \text{B})$ contributions and non-pairwise errors ($\% \text{npw}$) for two of these cases: the

Table 5.19. Energies of single monomers (E_{mon}) and dimer pairs (E_{pair}) leading to evaluation of $\mathcal{V}(\text{pair})$, \mathcal{V}_{PW} , and %npw (Eqs. (5.51) and (5.52)) for the open trimer and cyclic pentamer of HF (note [see note 61] that, for these comparisons, $\mathcal{V}(\text{pair})$, $\mathcal{V}_{\text{true}}$, and \mathcal{V}_{PW} are all expressed with respect to the energies of monomers frozen in the geometry of the complex)

Monomer	E_{mon} (a.u.)	Pair	No.	E_{pair} (a.u.)	$\mathcal{V}(\text{pair})$ (kcal mol ⁻¹)
Open trimer					
(Fig. 5.23(a))					
A	-100.482 366 1	A, B	1	-200.972 578 0	-5.02
B	-100.482 204 2	A, C	1	-200.965 739 4	-0.68
C	-100.482 294 6	B, C	1	-200.972 582 0	-5.07
					-10.77
					-11.81
					+9.7%
Cyclic pentamer					
(Fig. 5.23(d))					
A	-100.481 274 4	A, B	5	-200.968 683 9	-3.85(5)
		A, C	5	-200.964 376 0	-1.15(5)
					-25.00
					-43.75
					+75.0%

open trimer (5.54b) and cyclic pentamer (5.54e). From these entries one can see that %npw is about 10% in the former case and 75% in the latter case, slightly different from (but of the same general magnitude as) the percentage errors that would be inferred from the simpler comparisons in (5.54a)–(5.54e). Thus, by either criterion, the deviations from pairwise additivity tend to be *far* greater in the H-bonding than in the covalent-bonding case.

The values of %npw in Table 5.19 give inherent limits on the errors due to non-pairwise-additive effects, regardless of the form of $\mathcal{V}(\text{pair})$. However, it is also useful to examine the specific errors of a simple electrostatic potential $\mathcal{V}_{\text{Coul}}$, which is inherently of pairwise-additive form. For this purpose we assume that each monomer is characterized by point charge q ,

$$q = q_{\text{H}} = -q_{\text{F}} \quad (5.56a)$$

and that $\mathcal{V}_{\text{Coul}}$ simply includes all intermolecular Coulombic interactions between these point charges,

$$\mathcal{V}_{\text{Coul}} = \sum_{i < j}^{\text{inter}} \frac{q_i q_j}{R_{ij}} \quad (5.56b)$$

where R_{ij} is the distance between charges i and j . In this case, the charge q appears quadratically in each term on the right-hand side of Eq. (5.56b). The q^2 -dependence may be factored out to give

$$\mathcal{V}_{\text{Coul}} = q^2 \sum_{i < j}^{\text{inter}} \frac{\pm 1}{R_{ij}} \quad (5.56c)$$

where the summation includes only geometrical factors for charges of like (+) or unlike (−) sign.

It is clear from (5.56c) that q can be chosen to give $\mathcal{V}_{\text{Coul}}$ any desired value, i.e., to make (5.56c) “work” for a chosen cluster species. Thus, it is meaningful only to compare how a single value of q fits two or more different clusters, in order to assess how well $\mathcal{V}_{\text{Coul}}$ describes $\mathcal{V}_{\text{true}}$.

For simplicity, let us focus on the HF dimer (dim) and cyclic pentamer (5c). If we choose q to fit the dimer exactly, namely

$$q = q_{\text{dim}} = 0.442 \quad (5.57a)$$

then the corresponding Coulombic point charge for the cyclic pentamer is underestimated:

$$\mathcal{V}_{\text{Coul}}(5c) = 35.7 \text{ kcal mol}^{-1} \text{ versus } \mathcal{V}_{\text{true}} = 40.3 \text{ kcal mol}^{-1} \text{ (12.9\% too low)} \quad (5.57b)$$

Conversely, if we choose q to fit the cyclic pentamer, namely

$$q = q_{5c} = 0.469 \quad (5.58a)$$

then the dimer binding energy is correspondingly overestimated:

$$\mathcal{V}_{\text{Coul}}(\text{dim}) = 5.7 \text{ kcal mol}^{-1} \text{ versus } \mathcal{V}_{\text{true}} = 5.1 \text{ kcal mol}^{-1} \quad (5.58b)$$

(The actual natural charge in the cyclic pentamer is $q_{\text{nat}} = 0.570$, which makes the Coulombic point-charge estimate entirely unrealistic.) Thus, no matter how q is chosen, a simple Coulombic point-charge model will give >10% errors for one or the other of these clusters.

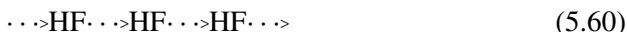
Errors of this magnitude obviously have an important effect on calculated equilibrium distributions. For example, under ambient conditions the Coulombic point-charge binding energy (5.57a) would underestimate the Boltzmann factor for the cyclic pentamer by two or three orders of magnitude, relative to the actual equilibrium population. Of course, q could also be chosen to make the equilibrium averages “come out right,” but this would still lead to significant errors in the individual cluster populations.

In contrast to a classical dipole–dipole or point-charge picture, the quantal donor–acceptor picture readily accounts for the observed cooperativity. Each HF···HF

hydrogen bond corresponds to intermolecular $n_F \rightarrow \sigma_{HF}^*$ CT delocalization that confers slight *cationic* character on one monomer and slight *anionic* character on the other. The directionality of charge transfer in each bond can be conveniently denoted by an arrow depicting the direction of charge flow,



similar to the vector-like symbols employed for the other donor–acceptor interactions throughout this book. Such CT-dipolar character prepares the cationic monomer as an enhanced Lewis acid, and the anionic monomer as an enhanced Lewis base, for extension of the chain of H-bonds in either direction:



In this manner one can see that the terminal monomers of the chain acquire net *ionic* character (because they can participate in CT only in a single direction), whereas interior monomers remain relatively *electroneutral* (due to there being equal numbers of CT interactions “in” and “out”).

The concerted charge transfers in (5.60) lead to a distinctive pattern of monomer charges along the chain, as displayed in Fig. 5.24. The trend-lines for terminal monomers (circles) suggest that the net monomer charge (Q_{HF}) at each end of the chain approaches an asymptotic value of 2%–3% of an electron as the chain length n increases. The energy employed to “charge up” the chain can of course be

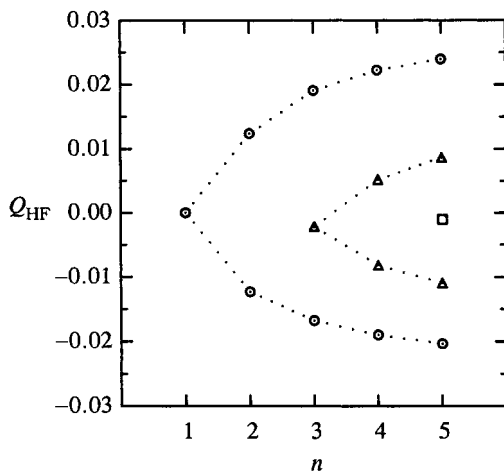


Figure 5.24 Monomer charges (Q_{HF}) in model $(HF)_n$ chain clusters (Figs. 5.23(a)–(c)). For each n , distinct symbols identify monomers at the end (circle), second from end (triangle), and third from end (square) positions of the chain, with connecting dotted lines to aid visualization. Note the strong CT-polarization pattern from the cationic to the anionic end of chain.

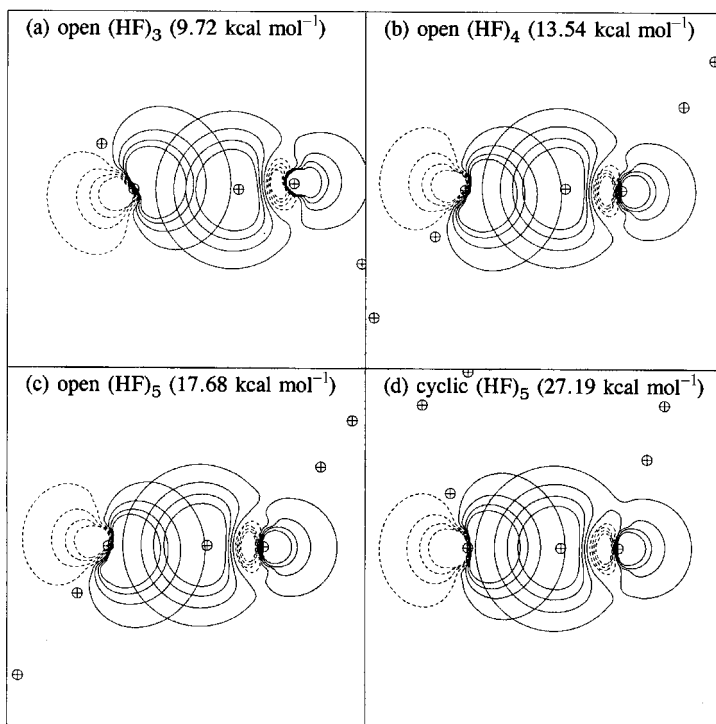


Figure 5.25 The strongest (innermost) $n_F \rightarrow \sigma_{HF}^*$ interactions in $(HF)_n$ chain (a)–(c) and cyclic (d) clusters (cf. Fig. 5.23), with estimated second-order stabilization energies in parentheses. These innermost interactions best approximate the limiting case of an infinite cyclic structure.

recovered by bringing the chain ends together to form a cyclic cluster, leading to the strong stabilization observed on going from (5.54d) to (5.54e).

Charge-transfer delocalization thereby provides a powerful mechanism for stabilizing cluster topologies in which a maximal number of monomers achieve closed-CT character (Section 2.6). Particularly favored are H-bonded cycles in which each monomer participates equally as a Lewis base and as a Lewis acid in a concerted *pair* of CT delocalizations. In general, the favored patterns such as (5.60) correspond to matching CT arrows in and out of each monomer, with each such balanced extension further strengthening CT delocalization in the interior monomers. Figure 5.25 displays the innermost (and strongest) $n_F \rightarrow \sigma_{HF}^*$ interaction in each $(HF)_n$ cluster, showing the progressive strengthening of this interaction, particularly in the cyclic topology (Fig. 5.25(d)).

In contrast to cooperative CT patterns such as (5.60), one may also consider *anticooperative* patterns in which two or more CT delocalizations are put into

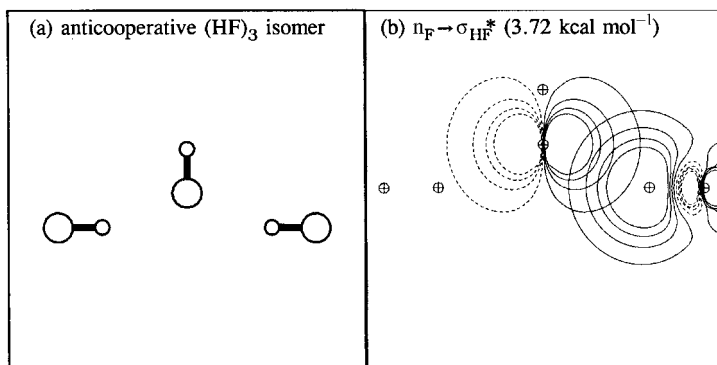
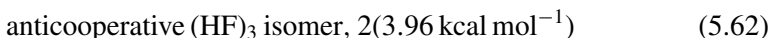


Figure 5.26 (a) The isomeric “anticooperative” open $(\text{HF})_3$ structure (fully optimized), and (b) the leading $n_{\text{F}} \rightarrow \sigma_{\text{HF}}^*$ interaction with one of the two equivalent Lewis-acid monomers (with the second-order stabilization energy in parentheses). The net binding energy is $7.92 \text{ kcal mol}^{-1}$.

antagonistic competition. A simple example is the isomeric $\text{FH} \cdot \cdot \cdot \text{F}(\text{H}) \cdot \cdot \cdot \text{HF}$ trimer



in which the central monomer serves *twice* as a Lewis base. Figure 5.26 displays the optimized structure of this isomer, together with one of the two equivalent $n_{\text{F}} \rightarrow \sigma_{\text{HF}}^*$ NBO delocalizations from the central monomer to a terminal monomer. Compared with the cooperative structures (5.54a)–(5.54e), the H-bonds in this isomer are appreciably weakened,



by about 21.6% with respect to the dimer value (5.54a). (Again, the value in (5.62) is only an *average* for complete cluster dissociation; to break a single H-bond of (5.61) requires only $2.87 \text{ kcal mol}^{-1}$, about 43% less than required to dissociate the dimer.)

From the examples given above, it becomes apparent that, by suitably altering the pattern of surrounding H-bonds in cooperative or anticooperative fashion, the strength of a given $\text{HF} \cdot \cdot \cdot \text{HF}$ hydrogen bond can be modulated over a wide range of values. Thus, it hardly makes sense to speak of “the H-bond energy” in the absence of knowledge about the surrounding network of H-bonds, because the cooperative or anticooperative modulating effect of the environment may be of the same order as the intrinsic strength of the isolated H-bond itself! Cooperativity effects, far from being a small perturbation, will often be found to be the *dominant* feature of the H-bond energy landscape.

Example 5.6

Problem: From the table of interatomic distances (in atomic units; 1 a.u. = 0.529 Å) for the linear (HF)₃ trimer (Fig. 5.23),

	H ₂	H ₃	F ₁	F ₂	F ₃
H ₁	4.5380	9.0614		6.1903	10.6319
H ₂		4.5796	3.2957		6.2386
H ₃			7.5951	3.3471	
F ₁				5.0566	9.0804
F ₂					5.1040

estimate the binding energy from the simple-point-charge approximation, using the estimated charge ($q = 0.469$) that “fits” the cyclic pentamer. Compare your result with the actual value.

Solution: From the Coulombic point-charge formula

$$\Delta E_{\text{Coul}} = \sum_{i < j} \frac{q_i q_j}{R_{ij}}$$

and the R_{ij} values of the table, we obtain

$$\begin{aligned} \Delta E_{\text{Coul}} &= +q^2 \left(\frac{1}{4.5380} + \frac{1}{9.0614} + \frac{1}{4.5796} + \frac{1}{5.0566} + \frac{1}{9.0804} + \frac{1}{5.1040} \right) \\ &\quad - q^2 \left(\frac{1}{6.1903} + \frac{1}{10.6319} + \frac{1}{6.2386} + \frac{1}{3.2957} + \frac{1}{7.5951} + \frac{1}{3.3471} \right) \\ &= (0.469)^2 (-0.0968) = -0.0213 \text{ a.u.} \\ &= -13.4 \text{ kcal mol}^{-1} \end{aligned}$$

which is about 15% larger than the actual binding energy (11.6 kcal mol⁻¹).

Linear formamide clusters

The energetics of H-bonding is perhaps nowhere more important than in protein chemistry. The characteristic secondary structures of proteins, such as α helices and β sheets, are characterized by repetitive patterns of C=O · · · HN hydrogen bonds between the skeletal amide groups of extended polypeptide chains. The structure and function of biological enzymes appear to be critically dependent on the H-bonds gained and lost as the polypeptide chain sheds solvent molecules to fold into the unique native conformation in which it is biologically active. The ubiquitous role of amide moieties as H-bonding connectors for complex biological structures emphasizes the importance of accurately understanding the cooperative energetics of extended amide · · · amide H-bonded chains.

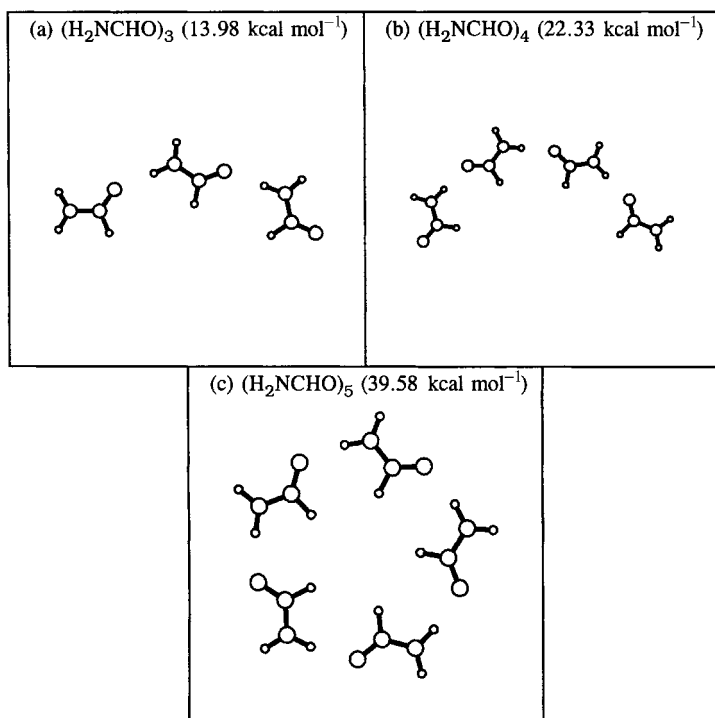
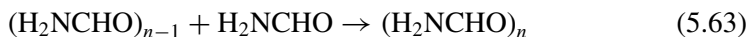


Figure 5.27 Formamide clusters (with net binding energies in parentheses).

As a simple prototype of extended amide···amide H-bonded chains, let us consider the series of linear formamide clusters, $(\text{H}_2\text{NCHO})_n$, extending the linear dimer (Fig. 5.19) that was previously considered. As noted in Section 5.2.3, it is critical that the $\text{C}=\text{O} \cdots \text{HN}$ hydrogen bonds be modeled with resonance-stabilized amide moieties (rather than, e.g., with unconjugated carbonyl and amine moieties), due to the important role of RAHB coupling. We examine the cooperative increases in the binding energy (ΔE_n) for successively extending the H-bonded amide chain by a single unit,



which is critical for the initiation and propagation of the folding sequence toward the proper secondary structure of a polypeptide.

Figure 5.27 depicts the next three members ($n = 3-5$) of the extended formamide sequence, showing the spontaneous cyclization that occurs at $n = 5$ (with further cooperative H-bond strengthening). Table 5.20 compares various energetic, structural, and charge properties of the $n = 2-4$ linear clusters. This table immediately displays the strong non-additivity of amide H-bonding, including progressive shifts

Table 5.20. Cooperative (n -dependent) properties of linear formamide chains (see Figs. 5.19 and 5.27), showing the incremental binding energy ΔE_n , average H-bonded $\bar{R}_{O\cdots H}$ and \bar{R}_{NH} distances, and partial charges Q_1 and Q_n on terminal monomers of the $(H_2NCHO)_n$ chain (for comparison, the cyclic pentamer in Fig. 5.27(c) has $\bar{R}_{O\cdots H} = 1.879 \text{ \AA}$, $\bar{R}_{NH} = 1.024 \text{ \AA}$, and average H-bond energy $7.92 \text{ kcal mol}^{-1}$)

n	ΔE_n (kcal mol $^{-1}$)	$\bar{R}_{O\cdots H}$ (Å)	\bar{R}_{NH} (Å)	Q_1	Q_n
2	6.19	1.987	1.0146	+0.0141	-0.0141
3	7.79	1.939	1.0169	+0.0173	-0.0194
4	8.34	1.911	1.0186	+0.0181	-0.0214

in intramolecular and intermolecular bond lengths, charge distribution, and H-bond energies that will now be considered.

Figure 5.28 displays the cooperative (n -dependent) increase in binding energy ΔE_n for the chain-propagation reaction (5.63). As the dotted trend-line shows, each chain step makes successive additions increasingly exothermic, strongly promoting chain growth at the expense of shorter segments. For example, the H-bond that results from joining two dimers to form a tetramer is about 61% stronger than that which results from joining two monomers to form a dimer. Under ambient conditions, this energetic difference converts into a large Boltzmann factor favoring

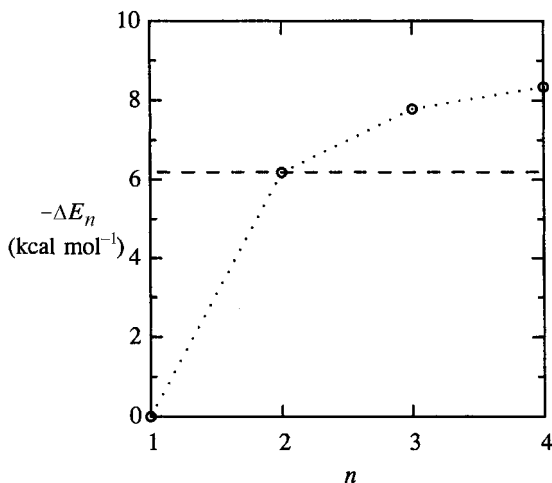


Figure 5.28 Cooperative increases in binding energy ($-\Delta E_n$) for successive extensions of the linear formamide chain (5.63). (The horizontal dashed line marks the “reference” dimer value.)

the tetramer over two dimers. Thus, the cooperativity of amide H-bonding has significant implications for the spontaneous formation of extended H-bonded chains at the expense of shorter fragments.

From Table 5.20 one can also see that the terminal monomers become increasingly cationic or anionic (bearing charges of about $\pm 2\% e$) as the chain extends. This net ionic character at each end gives rise to a longer-range ion-dipole Coulombic interaction with nearby monomers, tending to reorient them for attachment to the growing chain. It must be emphasized that this growing CT-dipolar character is *in addition to* the ordinary vector sum of monomer dipole moments. Thus, the macroscopic dipole of the H-bonded amide chain is itself cooperatively enhanced with each addition to the chain, further facilitating the proper orientation and addition of monomers at each end.

Table 5.20 shows that the structural parameters of individual monomers are also shifted by enhanced H-bonding in longer chains. Thus, in each $\text{NH}\cdots\text{O}$ region the covalent R_{NH} bond is progressively lengthened (and weakened) while the $R_{\text{O}\cdots\text{H}}$ H-bond is correspondingly shortened, in the manner expected for stronger H-bonding. The NRT bond orders (not shown) are also shifted in the manner expected for enhanced RAHB coupling, with associated small changes in geometry, vibrational frequency, chemical shielding, and other spectroscopic properties within each monomer. While Table 5.20 shows the *average* changes in R_{NH} and $R_{\text{O}\cdots\text{H}}$ for all monomers of the chain, it should be noted that the effects are strongest on the most *interior* monomers, and tend to diminish toward the chain ends. Thus, each amide monomer virtually carries a signature of its location within the chain, as well as the overall length of the chain in which it resides. As Ludwig has shown,⁶⁶ these cooperativity-induced positional shifts of spectroscopic properties of each amide moiety are often comparable to the substituent effects of varying amino-acid residues. Thus, a spectroscopic method that is sufficiently sensitive to distinguish, e.g., a valine from a serine residue in an α -helical segment may also give useful information about the overall length of the segment and the serial position of each residue along the helical axis.

Further aspects of the fascinating properties of H-bonded clusters in biomolecules⁶⁷ are beyond the scope of the present work.

Water clusters

Liquid water is an essential component of most terrestrial chemical processes, including those of living organisms. The cooperativity of H-bonding in water clusters is therefore of primary importance for understanding the structure and dynamics of pure water, as well as a vast spectrum of aqueous solvation phenomena in biotic and abiotic systems. In the present section we examine cooperativity effects for a

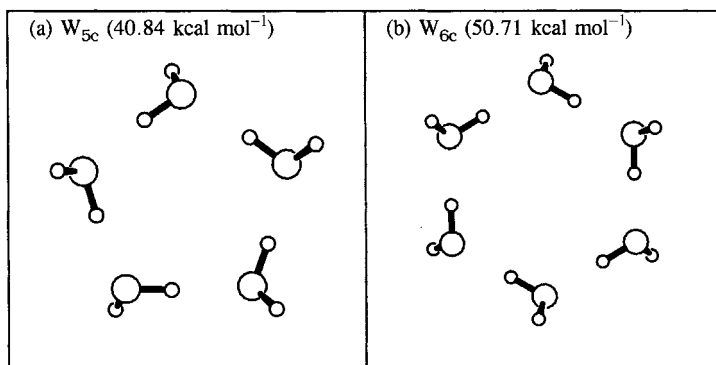


Figure 5.29 Fully cooperative cyclic water clusters (with net binding energies in parentheses).

variety of water clusters, illustrating both enthalpic and entropic consequences of alternative H-bond connectivity patterns.

Two of the water clusters that appear to exhibit particular thermodynamic stability under ambient conditions of the liquid phase are shown in Fig. 5.29: a cyclic pentamer (W_{5c}) and a cyclic hexamer (W_{6c}). The characteristic factors (F1)–(F3) that distinguish these clusters from other possible isomeric forms can be identified as follows:

- (F1) *cooperative closed-CT proton ordering*, with H-bonds arranged to make complementary pairs of $n_O \rightarrow \sigma_{OH}^*$ donor–acceptor interactions emanating from each monomer (i.e., with each monomer serving an equal number of times as a donor and an acceptor);
- (F2) *two-coordinate cyclic topology*, employing two of the four possible H-bond coordination sites at each monomer; and
- (F3) *unstrained H-bonds*, with near-linear $O \cdots H—O$ alignments at each monomer.

The enthalpic and entropic advantages associated with each of these factors will now be discussed in comparison with alternative isomeric forms of lower thermodynamic stability.

Three alternative pentameric isomers (W_{dacc} , W_{dcacc} , and W_{dadac}) that lack the cooperative closed-CT factor (F1), but satisfy (F2) and (F3), are shown in Figs. 5.30(a)–(c) (these are representative near-stationary configurations, but not true equilibrium species; see the figure caption). All three retain two-coordinate cyclic topology, but each exhibits two or more open-CT monomers having unbalanced double-donor (d) or double-acceptor (a) character, as labeled in the figure. Thus, “ W_{dacc} ” denotes the isomer with monomer 1 as a double-donor, monomer 2 a double-acceptor, and the remaining monomers 3–5 of closed-CT (c) character (with monomers numbered clockwise from the top of the figure). The W_{dacc} and W_{dcacc} isomers have two open-CT monomers (near-neighbor or non-near-neighbor,

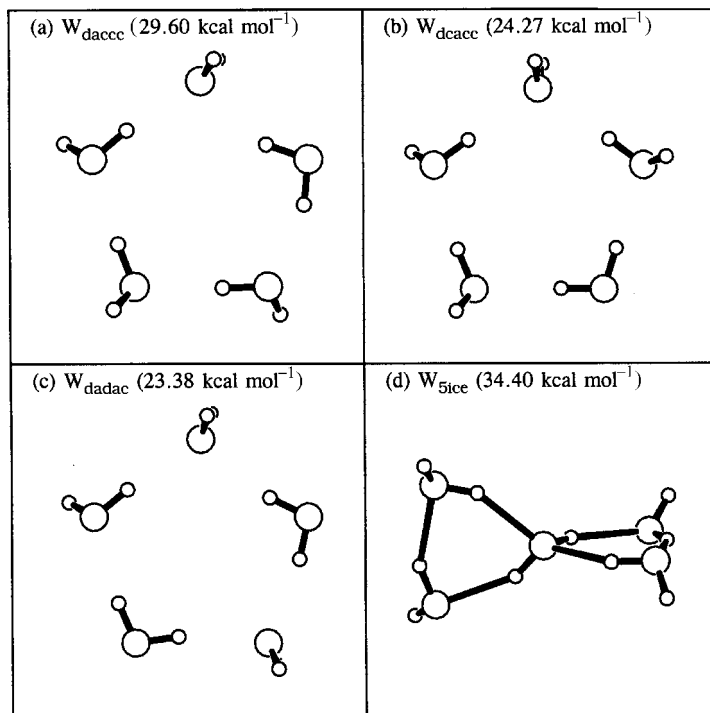


Figure 5.30 Alternative water pentamer isomers having partial anticoooperativity, (a)–(c), or higher coordination and ring strain, (d). Labels in (a)–(c) correspond to clockwise monomer numbering from the top (see the text). (Species (a)–(c) have been optimized under the constraint of planar equilateral skeletal geometry to prevent rearrangement to W_{5c} [Fig. 5.29(a)] and are therefore only near-stationary points on the potential-energy surface.)

respectively), while W_{dadac} has four alternating open-CT monomers. As shown in Figs. 5.30(a)–(c), the net binding energies of these isomers are sharply reduced (by $\sim 25\%$ – 45%) as the cooperative proton ordering is progressively reduced. Thus, the unique (fully cooperative) proton ordering in Fig. 5.29(a) is seen to have a significant enthalpic advantage over alternative cyclic pentamers that might seem equivalent in a pairwise-additive approximation.

The alternative pentamer W_{5ice} in Fig. 5.30(d) contains only closed-CT monomers, but exhibits ice-like four-coordinate topology at the central monomer. This isomer may be pictured as two corner-sharing cyclic trimers (*spiro* topology), but it results from any starting geometry with four-coordinate central monomer. Although the bicyclic W_{5ice} isomer has *six* H-bonds (instead of the usual five in monocyclic isomers), each H-bond is seen to be badly strained from linearity in the small 3-ring geometry. This isomer therefore satisfies (F1), but fails to satisfy (F2) and (F3), and is again seen to be enthalpically inferior (by 16%) to the W_{5c} isomer.

While the pentameric W_{5ice} has two short cooperative 3-cycles attached to the central monomer, one can recognize that contiguous four-coordinate sites lead to increasing frustration of cyclic cooperative proton-ordering patterns. In the fully four-coordinate structure of crystalline ice-I, it is recognized⁶⁸ that there is *no* net long-range proton-ordering, so that cooperative and non-cooperative connectivities of adjacent H-bond sites become equally likely. Although four-coordinate monomers enjoy an obvious enthalpic advantage in having four H-bonds rather than two, this advantage is considerably offset by the inherent loss of cooperativity in a proton-disordered tetrahedral lattice.

While the advantage of W_{5c} over alternative pentamers in Figs. 5.30(a)–(d) is primarily enthalpic, there is an additional *entropic* (and thus, *T*-dependent) advantage over W_{5ice} and related isomers that lack (F2) and (F3). This advantage stems from the favorable vibrational flexibility of W_{5c} , particularly the low-frequency “torsional” modes that dominate the vibrational contribution to the cluster partition function. Because each H-bond has high axial symmetry, and, thus, little resistance to torsional motions, the energy required in order to twist a monomer of W_{5c} about a *pair* of connecting H-bonds is quite small, corresponding to extremely soft vibrational frequencies in the 10–20-cm⁻¹ range. However, this mode becomes strongly hindered when the monomer forms additional H-bonds, corresponding to higher-dimensional three- or four-coordinate connectivity. Thus, the librational modes of the central monomer in W_{5ice} are greatly raised in frequency (>100 cm⁻¹), appreciably lowering the vibrational entropy compared with W_{5c} . Torsional motions in the remaining monomers of W_{5ice} are also significantly hindered by H-bond bending that lowers cylindrical symmetry. Thus, both because of its higher-dimensional connectivity and because it contains highly strained H-bonds, the ice-like W_{5ice} cluster is strongly disfavored entropically compared with W_{5c} . Similar entropic disadvantages oppose other high-coordinate cluster patterns, except at low temperature.

Owing to the aforementioned enthalpic and entropic advantages, cooperatively ordered ring and chain clusters may be expected to win out over four-coordinate polyhedral clusters as principal constituents of a stable equilibrium phase within a limited temperature range. It appears highly likely that this unique domain of stability of proton-ordered rings and chains can be identified with the liquid phase. The essential topological continuity of such a phase to a monomeric gaseous limit, as well as its essential *discontinuity* from the solid tetrahedral-lattice limit, give credence to this identification, which is supported by recent experiments.⁶⁹

Intermediate between the extended four-coordinate connectivities that dominate the low-*T* solid phase and the two-coordinate ring/chain connectivities that dominate at higher *T* are certain *three*-coordinate polyhedral structures that retain a degree of cooperative proton ordering. Two examples of such trigonally coordinated “buckyball” clusters, a 24-mer and a 28-mer, are shown in Fig. 5.31. The

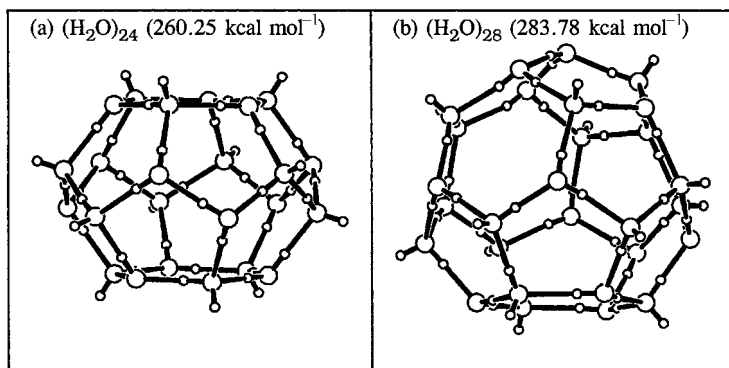


Figure 5.31 Water “buckyball” clusters (with net binding energies in parentheses). (Geometries were optimized at lower 6-31+G* (24-mer) or 6-31G* (28-mer) basis level, with quoted energetics evaluated at full B3LYP/6-311+ + G** level. Hence, the actual binding energies and H-bond strengths are, if anything, *stronger* than those quoted in the text.)

buckyball structures are closely related to the clathrate cages found for many crystalline hydrates,⁷⁰ the basis for Pauling’s clathrate model of liquid water.⁷¹

Closed buckyball polyhedra are known to be composed of cyclic pentameric and hexameric faces (see Fig. 5.29), with exactly *twelve* pentamers and variable numbers of hexamers (n_6). Because each vertex is shared by three faces, the total number of vertices (n_{vertex}) must satisfy the topological constraint

$$3n_{\text{vertex}} = 5 \times 12 + 6n_6 \quad (5.64)$$

where $n_6 = 1, 2, \dots$. Thus, the buckyball clusters in Fig. 5.31 with (a) $n_{\text{vertex}} = 24$ and (b) $n_{\text{vertex}} = 28$ vertices correspond to $n_6 = 2$ and $n_6 = 4$ hexamers, respectively. The two hexameric faces of $(\text{H}_2\text{O})_{24}$ appear at the top and bottom in Fig. 5.31(a), while the four hexameric faces of $(\text{H}_2\text{O})_{28}$ are distributed in a tetrahedral pattern (each surrounded by six pentagons) in Fig. 5.31(b).

Each vertex of a buckyball cluster is attached by *three* H-bonds, and hence must have net donor (2D1A) or acceptor (1D2A) character that seems to preclude significant cooperativity. However, by suitably *pairing* each donor and acceptor monomer, one may produce connected dimers that are each of effective 3D3A pseudo-closed-CT character. Such cooperative dimer units may then be joined in proton-ordered fashion to form closed polyhedra that retain a high degree of cooperative stabilization.

Both clusters in Fig. 5.31 exhibit considerable cooperative proton-ordering that distinguishes them from many alternative proton-disordered (and destabilized) isomeric forms that could be imagined. For example, the 24-mer (Fig. 5.31(a)) has two fully cooperative W_{6c} -like “caps” as well as a fully cooperative 12-ring “girdle,”

joined together by H-bonds (shared pentamer edges) of *alternating* CT direction, such that the two connecting hemispheres have complementary CT character at every juncture. The 36 H-bonds of the 24-mer have an average bond strength of $7.23 \text{ kcal mol}^{-1}$, and the 42 H-bonds of the 28-mer have an average strength of $6.76 \text{ kcal mol}^{-1}$, both significantly enhanced (by 24% and 16%, respectively) by the cooperative ordering.

The average binding energy *per monomer* is actually greater for the 24-mer ($10.84 \text{ kcal mol}^{-1}$) and the 28-mer ($10.14 \text{ kcal mol}^{-1}$) of Fig. 5.31 than for W_{5c} ($8.17 \text{ kcal mol}^{-1}$) or W_{6c} ($8.45 \text{ kcal mol}^{-1}$). Thus, the large buckyball cage clusters will compete with smaller ring clusters at sufficiently low temperatures; although the cage clusters are not present in significant concentrations under standard state conditions, they begin to appear as a minor (1%–2%) constituent near the lower end of the liquid range.⁷² Similar icosahedral clusters are also known to occur as basic structural units of alternative ice phases (such as ice-VI) that are only slightly less stable than ice-I. Thus, the three-coordinate cage structure appears to compete both with the two-coordinate W_{5c} and W_{6c} ring structures and with extended four-coordinate lattice structures near the ice point. The surprising ability of proton-ordered three-coordinate cages to compete thermodynamically with four-coordinate lattices again reflects the strong enthalpic role of cooperativity and the fact that “not all H-bonds are created equal.”

Owing to the relative rigidity and large excluded inner cavity of a buckyball, the average entropy (on a per-monomer basis) and density are appreciably lower than in W_{5c} and W_{6c} ring structures. Thus, even a small percentage of buckyball clusters in the low- T liquid distribution will tend to decrease the density and entropy near the freezing point. While the reduction of entropy at lower T is not unusual, the corresponding decrease in density below $\sim 5^\circ\text{C}$ is one of the well-known anomalies of liquid water.

An interesting feature of cage structures is their ability to encapsulate small molecules or molecular fragments, removing them from competition for H-bonding sites (which are all directed *outward* from the cage). This is particularly advantageous in the case of hydrophobic alkyl fragments that are otherwise highly disruptive of effective H-bonding. Figure 5.32 illustrates this possibility for the case of a stable mixed ethanol–water cluster $(\text{H}_2\text{O})_{23}\text{HOC}_2\text{H}_5$, in which one equatorial vertex of the 24-mer (Fig. 5.31(a)) has been replaced by amphiphilic $\text{C}_2\text{H}_5\text{OH}$. In this case the polar —OH head group of the amphiphile participates in skeletal H-bonding, while the hydrophobic tail is sequestered within the cage.

Such “hydrophobic H-bonding” naturally leads to an appreciable reduction in volume, and is therefore increasingly favored at higher pressures. Similarly, in the spirit of LeChâtelier’s principle, one may expect that the presence of a hydrophobic solute *promotes* formation of cage structures, i.e., tends to shift the cluster

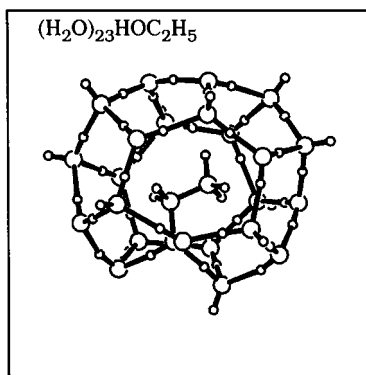
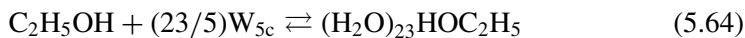


Figure 5.32 The mixed $(\text{H}_2\text{O})_{23}\text{HOC}_2\text{H}_5$ buckyball cluster (cf. Fig. 5.30(a)), showing the encapsulation of the hydrophobic alkyl group.

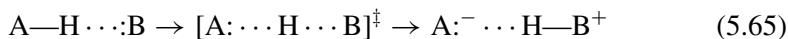
equilibrium



to the *right*. In this shift, high-entropy ring structures are converted into low-entropy cage structures, accompanied by the strong enthalpy release of the associated ring \rightarrow cage conversion. Both the volume reduction and the anomalous entropy–enthalpy changes (evoking the imagery of “flickering clusters”⁷³) are well-known features of hydrophobic solvation. However, further discussion of this interesting phenomenon is beyond the scope of the present work.

5.2.5 Proton transfer

Hydrogen-bonding is essentially a partial proton-transfer reaction. Thus, the ionic-resonance mnemonic (5.29a), which expresses the partial covalency of H-bonding, suggests an immediate relationship to the “degree of completion” of the actual proton-transfer reaction



The two H-bonded species in (5.65) can be visualized as points along an intrinsic *reaction coordinate* that connects reactant and product species through the transition state (‡). In this manner we can gain a more global perspective on how each H-bonded species is related to overall progress along the chemical reaction pathway.

For simplicity (and to avoid strong net change in dipolar character), we examine the simple proton-transfer reaction between two strong *anionic* Lewis bases, H^-

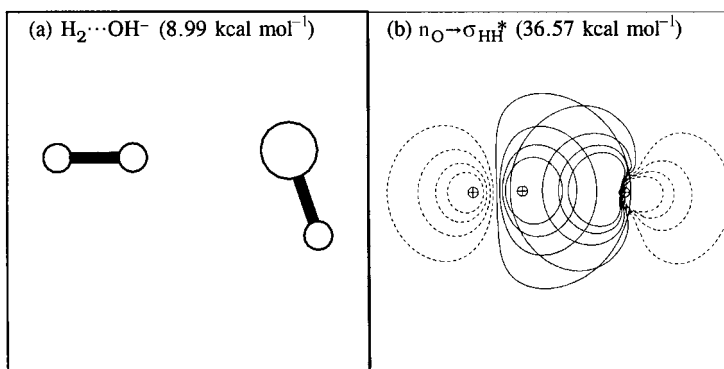
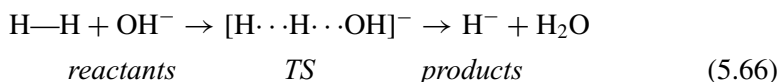


Figure 5.33 The optimized structure and leading $n \rightarrow \sigma^*$ donor–acceptor interaction of $\text{H}_2 \cdots \text{OH}^-$. The geometrical parameters are $r_{\text{HH}} = 0.821 \text{ \AA}$, $R_{\text{O} \cdots \text{H}} = 1.689 \text{ \AA}$, $r_{\text{OH}} = 0.966 \text{ \AA}$, $\theta_{\text{HH} \cdots \text{O}} = 177.8^\circ$, and $\theta_{\text{H} \cdots \text{OH}} = 106.4^\circ$.

and OH^- ,



The H-bonded $\text{H}^- \cdots \text{HOH}$ product species was previously depicted in Fig. 5.16, while the structure and leading $n \rightarrow \sigma^*$ interaction for the corresponding $\text{H}_2 \cdots \text{OH}^-$ reactant species are shown in Fig. 5.33. Figure 5.34 similarly depicts the structure of the transition-state species and principal $n \rightarrow \sigma^*$ interaction for the reactant-like Lewis structure that better describes the resonance hybrid (see below).

Figure 5.35 displays a schematic energy-level diagram for each stationary species along the proton-transfer reaction coordinate. Although Pauling bond strengths

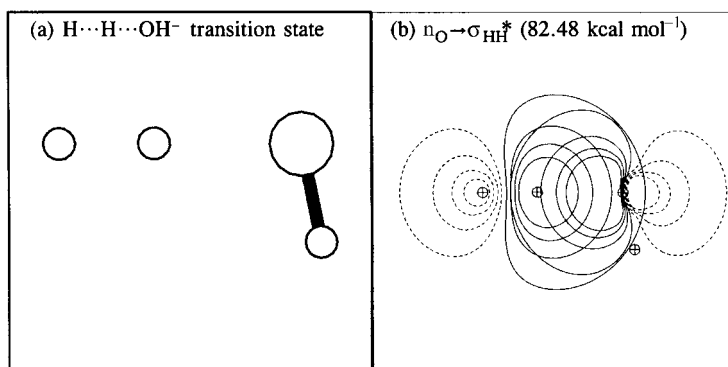


Figure 5.34 The optimized structure and leading $n \rightarrow \sigma^*$ donor–acceptor interaction of the $[\text{H} \cdots \text{H} \cdots \text{OH}]^-$ transition state. The geometrical parameters are $R_{\text{H} \cdots \text{H}} = 0.910 \text{ \AA}$, $R_{\text{O} \cdots \text{H}} = 1.417 \text{ \AA}$, $r_{\text{OH}} = 0.966 \text{ \AA}$, $\theta_{\text{H} \cdots \text{H} \cdots \text{O}} = 179.5^\circ$, and $\theta_{\text{H} \cdots \text{OH}} = 101.3^\circ$.

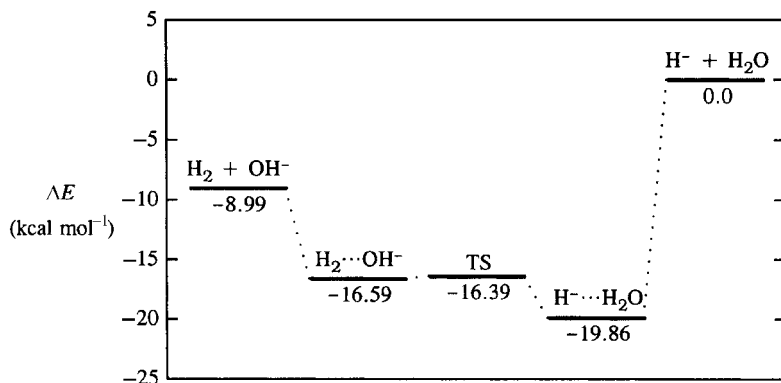


Figure 5.35 A schematic energy-level diagram for key stationary points along the $\text{H}_2 + \text{HO}^- \rightarrow \text{H}^- + \text{HOH}$ proton-transfer reaction coordinate.

both for the reactant H—H and for the product H—O bond are quite large (>100 kcal mol^{-1}), the H-bond-catalyzed proton-transfer process (5.66) is seen to occur with very *small* activation energy (<4 kcal mol^{-1}) in either the forward (ΔE_f^\ddagger) or the reverse (ΔE_r^\ddagger) direction:

$$\Delta E_f^\ddagger = 0.2 \text{ kcal mol}^{-1}, \quad \Delta E_r^\ddagger = 3.5 \text{ kcal mol}^{-1} \quad (5.67)$$

Thus, only a gentle perturbation (much weaker than the strength of H-bonding itself) is sufficient to transfer the proton from one well to the other, interchanging the identities of the formal covalent bond and hydrogen bond.⁷⁴

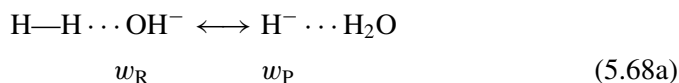
Table 5.21 presents details of the binding-energy profile (ΔE , relative to asymptotic $\text{H}^- + \text{H}_2\text{O}$), the net charge (Q_{H}) transferred to the product hydride ion, and the $\text{H} \cdots \text{H} \cdots \text{O}$ bond lengths (R_{HH} and R_{OH}) and NRT bond orders (b_{HH} and b_{OH}) along the reaction coordinate. All these entries support the idea that both $\text{H}^- \cdots \text{HOH}$ and $\text{H}_2 \cdots \text{OH}^-$ are electronically closer to the half-transferred TS^\ddagger limit than to dissociated reactants or products. Thus, the charge at the terminal H in $\text{H}_2 \cdots \text{OH}^-$ is already 35% of its final value (-1), and the b_{HH} bond order (0.825) is *closer* to the TS^\ddagger value (0.733) than to its nominal value (1.00) in isolated reactants. Similar comparisons can be made for the product-like $\text{H}^- \cdots \text{HOH}$ complex at the opposite end of the reaction coordinate. Thus, as suggested by the energy profile in Fig. 5.35, proton transfer (and the associated charge and bond-order transfer) is already well advanced in either of the H-bonded complexes.

Figure 5.36 displays the global behavior of bond orders and charge transfer along a segment of the reaction coordinate s , showing the relatively smooth progression from reactant-like to product-like values. The fractional weightings of the leading

Table 5.21. Variations of binding energy ΔE , charge transferred to terminal hydrogen Q_H , bond lengths R_{HH} and R_{OH} , and NRT bond orders b_{HH} and b_{OH} along the intrinsic reaction coordinate in proton-transfer reaction (5.66)

Reaction coordinate	Binding ΔE (kcal mol ⁻¹)	CT Q_H (e)	Bond length (Å)		Bond order	
			R_{HH}	R_{OH}	b_{HH}	b_{OH}
$H_2 + OH^-$	-8.99	0.000	0.744	∞	1.000	0.000
$H_2 \cdots OH^-$	-16.59	-0.277	0.821	1.689	0.849	0.138
-0.2	-16.46	-0.352	0.868	1.513	0.825	0.175
-0.1	-16.41	-0.376	0.886	1.467	0.805	0.195
0.0	-16.39	-0.406	0.910	1.417	0.733	0.250
0.1	-16.43	-0.442	0.943	1.363	0.702	0.275
0.2	-16.58	-0.483	0.986	1.311	0.686	0.312
0.3	-16.92	-0.527	1.032	1.257	0.629	0.354
0.4	-17.49	-0.576	1.087	1.203	0.587	0.396
0.5	-18.23	-0.626	1.148	1.150	0.571	0.429
0.6	-18.95	-0.675	1.215	1.100	0.508	0.492
$H^- \cdots H_2O$	-19.86	-0.783	1.446	1.031	0.381	0.617
$H^- + H_2O$	0.00	-1.000	∞	0.962	0.000	1.000

resonance structures



are approximately related to the bond orders by

$$b_{H \cdots H} \simeq w_R, \quad b_{O \cdots H} \simeq w_P \quad (5.68b)$$

As shown in Fig. 5.36, w_R and w_P become equal near $s \simeq 0.6$, whereas the charge transfer is half-complete near $s \simeq 0.3$, and the energetic TS is at $s = 0$. Different criteria therefore lead to different estimates of the progress of reaction, but by all criteria the shifts of partial charge and covalency are quite pronounced in the H-bonded complexes. The net charge transfer Q_H to the evolving hydride Lewis base is seen to parallel b_{OH} closely, as the resonance picture (5.68a) suggests.

Finally, Fig. 5.37 displays the bond-order–bond-length relationship for $O \cdots H$ and $H \cdots H$ bonds over the entire range of the proton-transfer reaction. Both curves display nonlinear dependences tending to $R_{AB} \rightarrow \infty$ as $b_{AB} \rightarrow 0$, and to the standard single-bond distance as $b_{AB} \rightarrow 1$. The points for the H-bonded complexes (those at largest R and smallest b) evidently join smoothly to the more global behavior.

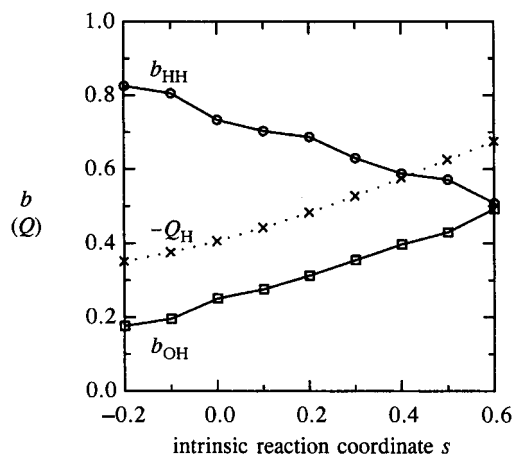


Figure 5.36 The NRT bond orders b_{HH} (circles) and b_{OH} (squares) and terminal-hydrogen charge Q_{H} (crosses) along the intrinsic reaction coordinate for the $\text{H}_2 \cdots \text{OH}^- \rightarrow \text{H}^- \cdots \text{HOH}$ proton-transfer reaction.

Thus, by virtue of the continuity of the bond-order–bond-length relationship across the entire proton-transfer region, the interpretation of the H-bonded complexes in terms of partial proton transfer (with associated charge and covalent-bond transfer) can hardly be avoided. (Additional discussion of the properties of transition-state species in relation to the associated reactant and product species will be presented in Section 5.4.)

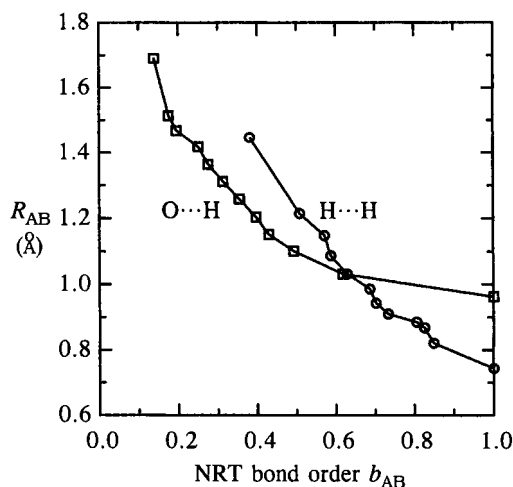


Figure 5.37 The NRT bond-order–bond-length relationships for O—H (squares) and H—H (circles) bonds along the $\text{H} \cdots \text{H} \cdots \text{O}$ intrinsic reaction coordinate of the $\text{H}_2 + \text{OH}^- \rightarrow \text{H}^- + \text{HOH}$ proton-transfer reaction (cf. Fig. 5.36).

In summary, we may say that the NBO/NRT description of partial proton transfer in the equilibrium H-bonded complex(es) is fully consistent with the observed behavior along the *entire* proton-transfer coordinate, including the transition state. At the transition state the importance of partial covalency and bond shifts can hardly be doubted. Yet the isomeric H-bonded complexes may approach the TS limit quite closely (within $0.2 \text{ kcal mol}^{-1}$ in the present example) or even *merge* to form a single barrierless reaction profile (as in FHF^- or H_5O_2^+). Hence, the adiabatic continuity that connects isomeric H-bond complexes to the proton-transfer transition state suggests once more the essential futility of attempting to describe such deeply chemical events in terms of classical electrostatics.

5.2.6 Hydrogen-bonding to transition metals

Although transition metals M are not considered as standard hydrogen-bonding partners, they exhibit a number of properties that favor H-bond complexation to suitable Lewis acids or bases, namely



Because of their low intrinsic electronegativities, neutral late transition metals (bearing an abundance of lone pairs) can serve as good donors in $n_{\text{M}} \rightarrow \sigma_{\text{AH}}^*$ interactions of the form (5.69a). Furthermore, transition-metal-hydride bonds (Section 4.4.1) often display sufficient covalency or polar-covalency (particularly in transition-metal *cations*) to serve as good acceptors in $n_{\text{B}} \rightarrow \sigma_{\text{MH}}^*$ interactions of the form (5.69b). In the present section we shall briefly examine the simple example of platinum dihydride (PtH_2) as a “water-mimic” in binary H-bonded complexes with H_2O ,



as well as with another PtH_2 ,



Figure 5.38 displays the optimized structure and primary $n_{\text{Pt}} \rightarrow \sigma_{\text{OH}}^*$ donor-acceptor interaction of the complex (5.70a) in which PtH_2 serves as the Lewis-base donor. The qualitative similarity to the water dimer structure (Fig. 5.5(b)) is immediately apparent, including the short $\text{Pt} \cdots \text{H}$ distance (2.47 \AA , more than 0.5 \AA inside van der Waals contact), the roughly linear $\text{Pt} \cdots \text{H} - \text{O}$ angle (161°), and the characteristic elongation of the H-bonded versus free $\text{O} - \text{H}$ bond of the water monomer (by 0.01 \AA). The leading $n_{\text{Pt}} \rightarrow \sigma_{\text{OH}}^*$ donor-acceptor interaction in Fig. 5.38(b) is

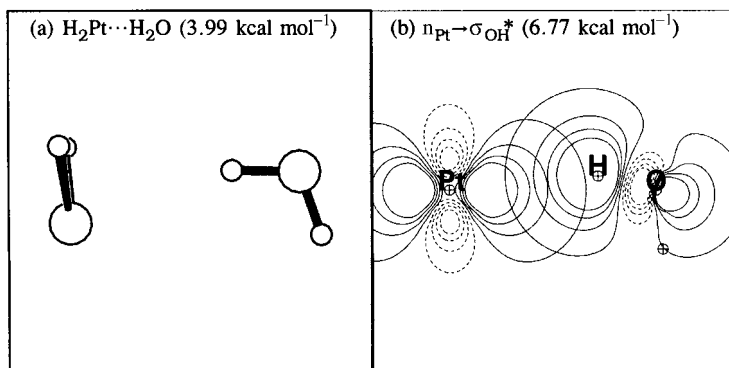


Figure 5.38 The optimized structure and leading $n \rightarrow \sigma^*$ donor–acceptor interaction in the H-bonded $\text{H}_2\text{Pt} \cdots \text{HOH}$ complex.

primarily responsible for the net charge transfer $Q_{\text{CT}} = 0.019e$ from PtH_2 to H_2O . (However, two additional weak $\sigma_{\text{PtH}} \rightarrow \sigma_{\text{OH}}^*$ interactions also contribute to stabilization [each contributes $1.49 \text{ kcal mol}^{-1}$], leading to the curiously bent $n_{\text{Pt}} \rightarrow \sigma_{\text{OH}}^*$ overlap and $\text{Pt} \cdots \text{O} \cdots \text{H}$ bond angle in Fig. 5.38.) In most respects, PtH_2 is a surprisingly faithful water-mimic as the Lewis base in H-bonding interactions with water.

Figure 5.39 displays the corresponding complex (5.70b) in which PtH_2 serves as the Lewis acid. Again, the general similarity to $(\text{H}_2\text{O})_2$ is apparent, except for the 180° torsion about the H-bond (a very-low-energy deformation mode in both $\text{H}_2\text{O} \cdots \text{HOH}$ and $\text{H}_2\text{Pt} \cdots \text{HOH}$). The characteristic short $\text{O} \cdots \text{H}$ distance (1.95 \AA), near-linear $\text{O} \cdots \text{H} \cdots \text{Pt}$ bond angle (175°), and relative elongation of the H-bonded versus free $\text{Pt} \cdots \text{H}$ bond (by 0.01 \AA) are all rather typical signatures of H-bonding. The stronger $n_{\text{O}} \rightarrow \sigma_{\text{PtH}}^*$ interaction in Fig. 5.39(b) also leads to stronger charge transfer ($Q_{\text{CT}} = 0.045e$) than in (5.70a). Despite the stronger charge transfer, the net

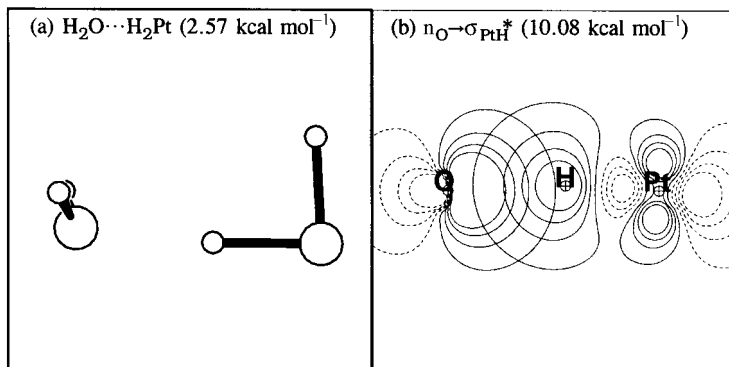


Figure 5.39 The optimized structure and leading $n \rightarrow \sigma^*$ donor–acceptor interaction of the H-bonded $\text{H}_2\text{O} \cdots \text{HPtH}$ complex.

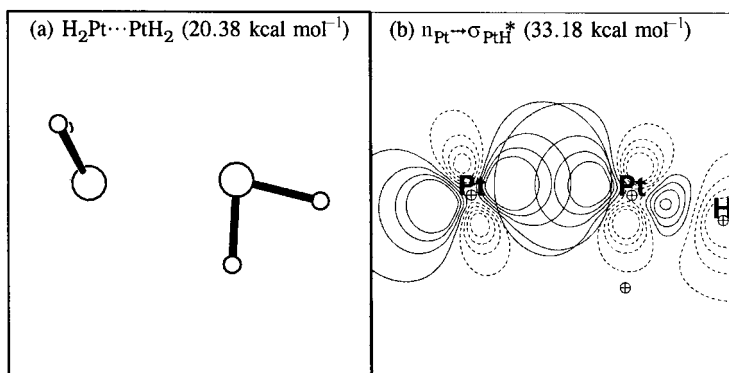


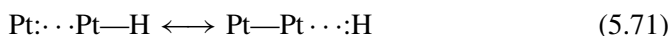
Figure 5.40 The optimized structure and leading $n \rightarrow \sigma^*$ donor–acceptor interaction of the “anti-H-bonded” $\text{H}_2\text{Pt}\cdots\text{PtH}_2$ complex.

H-bond energy is weaker in (5.70b) than in (5.70a), apparently due to weaker steric repulsions in the geometry of Fig. 5.38(a). Overall, PtH_2 again serves surprisingly well as a mimic for H_2O in the role of Lewis acid.

Finally, Figure 5.40 displays the surprising structure of the $(\text{PtH}_2)_2$ dimer, an “anti-H-bond” $n-\sigma^*$ donor–acceptor complex. As expected, the leading NBO donor–acceptor interaction is of $n_{\text{Pt}} \rightarrow \sigma_{\text{PtH}}^*$ type, but the attack by n_{Pt} is now on the *backside* of the σ_{PtH}^* NBO, leading to unusual $\text{Pt}\cdots\text{Pt}-\text{H}$ coordination to the hydride antibond as depicted in Fig. 5.40b.

The rather surprising geometry of the $(\text{PtH}_2)_2$ complex can be readily understood from the NBO interaction diagram in Fig. 5.40(b). Because of the similar electronegativity of Pt relative to H, the σ_{PtH} bond is not polarized toward H nor the σ_{PtH}^* antibond toward the metal atom, which is unfavorable for normal $\text{Pt}\cdots\text{H}-\text{Pt}$ coordination to H. Moreover, the d-rich hybrid on Pt has no strong directionality in the bonding direction, so backside attack on the metal end of the σ_{PtH}^* antibond becomes strongly favored. The strong ($\sim 33 \text{ kcal mol}^{-1}$) stabilization associated with this backside $n_{\text{Pt}} \rightarrow \sigma_{\text{PtH}}^*$ interaction results in the “backward” H-bond in (5.70c) being much stronger than either of the H-bonds in (5.70a) and (5.70b). The charge transfer, $Q_{\text{CT}} = 0.092e$, is also significantly higher in the homodimer. Other aspects of the anti-H-bond in Fig. 5.40(a) are rather typical, including the anomalously short $\text{Pt}\cdots\text{Pt}$ distance (2.66 \AA), the near-linear $\text{Pt}\cdots\text{Pt}-\text{H}$ angle (165°), and the differential elongation (by 0.03 \AA) of the anti-H-bonded versus free $\text{Pt}-\text{H}$ bond.

The $\text{Pt}\cdots\text{Pt}-\text{H}$ anti-H-bond linkage can also be viewed as a hypervalent $3c, 4e$ (ω -bond) resonance hybrid of the form



In this form, the bonding is analogous to many similar examples of $\text{X}\cdots\text{M}-\text{Y} \longleftrightarrow \text{X}-\text{M}\cdots\text{Y}$ hypervalency studied in Section 4.6. The accessible M^+H^-

character of transition-metal bonds allows the hydride ligand to effectively serve as the Lewis base in such three-center combinations. Thus, the geometry of the $(\text{PtH}_2)_2$ dimer, although somewhat anomalous, conforms in all essential respects to that expected for strong $n-\sigma^*$ donor-acceptor interaction.

5.2.7 Summary: the uniqueness of hydrogen-bonding

The examples of Section 5.2 can be summarized by saying that H-bonds are an unusually strong form of $n-\sigma^*$ donor-acceptor interaction exhibiting the expected strong cooperative effects associated with intermolecular charge transfer.

However, the question "What makes hydrogen *unique* in forming such bonds?" remains to be answered. More specifically, what makes A—H bonds (and antibonds) so distinctively suitable for strong $\text{A—H} \cdots \text{B}$ interactions with general lone-pair-bearing atoms B? We now briefly address this question in the context of examples cited above.

It is clear that A—H bonds make no claim to having distinctively large dipole moments or other electrostatic properties that would account for their unique chemical behavior from a classical electrostatic viewpoint. Indeed, numerous examples cited above illustrate the rather striking *indifference* of H-bonding to the magnitude (or even the *orientation*) of monomer dipoles.

Nevertheless, there is an evident advantage in choosing A of high electronegativity, so as to polarize the σ_{AH} bond toward A and the σ_{AH}^* antibond toward H. Such A—H bond polarity has two significant quantum-mechanical advantages: (i) it *reduces* steric exchange repulsions as the filled n_{B} approaches the H terminus of the filled σ_{AH} ; and (ii) it *increases* attractive $n-\sigma_{\text{AH}}^*$ interaction by increasing the amplitude of the σ_{AH}^* acceptor orbital near H for favorable overlap with the incoming n_{B} donor orbital. While a large A—H-bond dipole is therefore *conducive* to $\text{B} \cdots \text{H—A}$ hydrogen-bonding, it is not a necessary prerequisite for H-bond formation (as, e.g., the example of $\text{H}_2 \cdots \text{OH}^-$ makes clear). Thus, bond-polarity factors are of only secondary importance in explaining why hydride A—H bonds lead to distinctively strong $n_{\text{B}}-\sigma_{\text{AH}}^*$ interactions.

Of much greater importance are two quantum-mechanical features that are unique to the hydrogen-atom valence shell:

- (H1) the only available hydrogen valence orbital is an isotropic s-type orbital with *no angular nodes*; and,
- (H2) because the H atom has no electronic core underlying the valence shell, its valence orbital also has *no radial nodes*.

The hydrogenic 1s orbital is therefore unique in presenting *no* strong angular or radial barriers toward approaching atoms.⁷⁵

The unique absence of angular and radial nodes in the H-atom valence orbital has two important consequences for the efficacy of $n_B-\sigma_{AH}^*$ interaction at the H-terminus.

- (H1') The H-terminus of the σ_{AH}^* antibond presents a spherical, nodeless, high-amplitude lobe for favorably overlapping the incoming n_B donor orbital in a broad range of directions around the A—H axis. At the opposite (A) end of the antibond, the backside lobe of the sp^n hybrid is of weak amplitude, and is surrounded by a conical nodal surface (within $\sim 70^\circ$ of the A—H axis) that adversely limits high overlap with an incoming donor orbital along this direction.
- (H2') Because the H-end of the σ_{AH}^* antibond encloses no electronic core, the incoming n_B donor orbital can overlap with *practically the entire hydride end of the antibond*, rather than merely the outer annular region that lies beyond the nodal boundary of the core region.

Of these factors, (H1) (or (H1')) is shared to some degree with other alkali metals, and indeed, analogous “lithium bonding” is known to exhibit some characteristics of hydrogen bonding.⁷⁶ However, factor (H2) (or (H2')) is unique to the hydrogen atom and is by far the more important factor allowing high $n-\sigma^*$ overlap and donor–acceptor stabilization. (A similar factor was found [Section 3.2] to be responsible for the *covalent* bonding in Li_2 being relatively weak compared with that in H_2 .)

In summary, we can say that, because of the unique absence of angular and radial nodes in the H-atom valence shell, the hydride σ_{AH}^* orbital is uniquely suited to strong $n-\sigma^*$ donor–acceptor interactions with Lewis bases. In turn, the unique energetic and angular features of $n_B-\sigma_{AH}^*$ interactions (or equivalently, of $B: H-A \longleftrightarrow B-H^+:A^-$ covalent–ionic resonance) can be directly associated with the distinctive structural and spectroscopic properties of $B:\cdots H-A$ hydrogen bonding.

5.3 Charge-transfer complexes

5.3.1 Mulliken charge-transfer complexes

The general concept of a “charge-transfer complex” was introduced by Mulliken⁷⁷ to describe a form of association between donor (D) and acceptor (A) molecules that could be represented in resonance language as



The key distinguishing feature of charge-transfer (CT) complexation is that the partial admixture of ionic D^+A^- character in the resonance hybrid (5.72) confers a tendency toward association that is *absent* in the purely covalent $D\cdots A$ limit, i.e., in the absence of covalent–ionic resonance. The mechanism of CT binding is

therefore wholly quantum mechanical in nature, acting even in species such as the 1 : 1 benzene : halogen complexes



where the isolated monomers have *no* net charge or dipole moment that would be expected to lead to complex formation. As expressed by Herzberg,⁷⁸ “the resonance supplies the whole of the binding energy.”

The spectroscopic signature of CT-complex formation is the appearance of intense spectral features (“charge-transfer bands,” near 3000 Å for benzene : iodine and other arene : halogen complexes) that are *not* present in the pure monomers. These bands thus reflect the presence in solution of associated $\text{D} \cdots \text{A}$ species whose electronic properties differ from those of isolated D and A. Because of the remarkable intensity of the CT bands and their appearance against a null background, conspicuous color changes can result from even the loosest forms of $\text{D} \cdots \text{A}$ association. Charge-transfer spectroscopy therefore provides a highly sensitive probe for subtle microstructural clustering features of the liquid. Mulliken adduced further experimental evidence for specific donor–acceptor associations from the fixed stoichiometric compositions and curiously oriented $\text{D} \cdots \text{A}$ arrangements in crystalline solids.

Mulliken recognized that the essential feature of CT-complex formation is the complementary (electron) donor and acceptor characters of the two monomers. From the starting point of G. N. Lewis’s broad acid–base conception in terms of electron pairs,⁷⁹ Mulliken chose to adopt Sidgwick’s⁸⁰ more general and descriptive terminology of “donors” and “acceptors” (of electrons) for Lewis bases and acids, respectively. Mulliken also recognized the close connection to Ingold’s categorization of “nucleophilic” and “electrophilic” reagents⁸¹ in organic chemistry, but he sought to remove certain restrictions implicit in the older terminology that might tend to inhibit “fullest or freest use of the inherent possibilities of the donor–acceptor concept.”⁸²

Mulliken emphasized particularly “the nature of *partial* electron transfer” (his emphasis) that is implied by the resonance description. For this purpose he introduced a heuristic “charge-transfer coordinate,” with values varying from 0 to 1 to represent the range from charge-localized precursors to complete intermolecular charge transfer. Mulliken employed this coordinate to depict schematic potential-energy diagrams for a wide variety of CT phenomena, including “inner,” “outer,” and activated complexes on the pathway from neutral reactants to heterolytic dissociation products. On the basis of such diagrams, Mulliken also proposed an elaborate classification of CT complexes (using special prefixes, superscripts, and subscripts for each D and A, somewhat resembling spectroscopic labels), but this has not found wide usage.⁸³

Despite strong similarities to Mulliken's basic donor–acceptor framework, the NBO description of CT complexes differs in several respects from Mulliken's theory. The important NBO donor–acceptor interactions are determined by an *ab initio* procedure, rather than inferred from empirical ionization properties of monomers or the geometry of the complex. Contributing NBO interactions may include synergistic donation and *back*-donation through different orbital pairings between monomers, as well as background contributions of classical electrostatic type.⁸⁴ The forms of donor and acceptor NBOs are intrinsically free to vary continuously along a chosen reaction coordinate (including deviations from idealized σ - or π -bond symmetry), thus blurring the distinction between Mulliken's distinct "types" of CT complexes. Furthermore, the Mulliken resonance description (5.72) suggests partial ion *radical* (open-shell D^+A^-) character, whereas the two-electron NBO donor–acceptor stabilization is better described in resonance terms as



involving purely *closed*-shell species (similar to general coordinate bonding). Nevertheless, in cases where NBOs of clear n , σ , or π symmetry participate in a *single* dominant donor–acceptor stabilization, the qualitative agreement with Mulliken's description can be recognized.

It is also apparent that intermolecular charge transfer confers partial $D^+ \cdots A^-$ zwitterionic character, leading to *long*-range Coulombic attractions of classical type. Thus, the covalent–ionic resonance in (5.74) leads both to covalent short-range and to ionic long-range attractive forces that contribute to binding. A characteristic feature of Mulliken-type CT complexes is that valence donor–acceptor interactions are *inadequate* to account for the total binding, and the role of (CT-induced) electrostatic interactions therefore becomes relatively more important. Numerical evidence for long-range Coulombic attractions in CT complexes will be presented below.

As an example of Mulliken CT complexation, let us consider the benzene:bromine complex, whose optimized structure and leading intermolecular NBO interaction are displayed in Fig. 5.41. NBO charge analysis of the $C_6H_6 \cdots Br_2$ complex reveals the presence of slight CT ($0.0021e$) from C_6H_6 to Br_2 , which is consistent with the Mulliken description. Both monomers are altered by complex formation, with the Br—Br bond NBO becoming noticeably polarized away from the benzene ring,

$$\sigma_{BrBr} = 0.702(p)_{Br(near)} + 0.712(p)_{Br(far)} \quad (5.75)$$

thereby polarizing the σ_{BrBr}^* antibond orbital favorably toward the ring donor orbitals. Given the weakness of the binding (of the order of standard-state kT), it

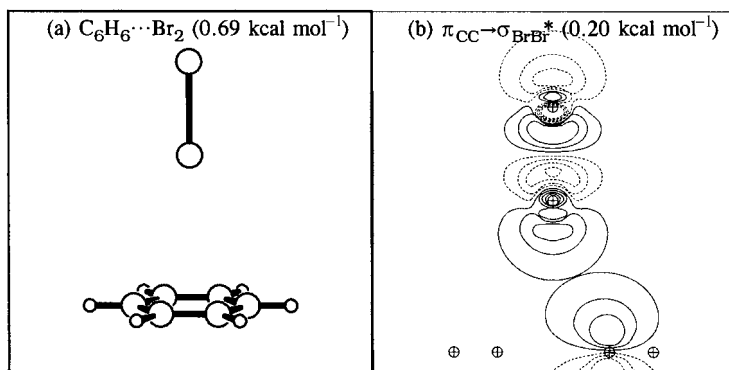


Figure 5.41 The optimized structure and one of three equivalent leading $\pi \rightarrow \sigma^*$ donor–acceptor interactions of the $\text{C}_6\text{H}_6 \cdots \text{Br}_2$ charge-transfer complex. (The scale in (b) is 9 \AA along each edge, 50% larger than in other such plots in this book.)

is remarkable that the optical properties of benzene : halogen binary pairs allowed these species to become recognized as prototypes of Mulliken CT complexation.

The principal intermolecular donor–acceptor interactions of this weakly bound complex are found to be of $\pi_{\text{CC}}-\sigma_{\text{BrBr}}^*$ form ($3 \times 0.20 \text{ kcal mol}^{-1}$), as illustrated in Fig. 5.41(b). A prominent feature of Br_2 (and other heavy halogens) is the nearly pure-p character of the bromine bonding hybrid, resulting in a conspicuous backside lobe on the σ_{BrBr}^* antibond (see Fig. 5.41(b)) that is effective in end-on complexation to the pi-donor face of benzene. The unusually small energy separation between donor and acceptor NBOs,

$$\epsilon_{\sigma^*(\text{BrBr})} - \epsilon_{\pi(\text{CC})} = 0.15 \text{ a.u.} \quad (5.76)$$

also contributes to effective CT stabilization. The $\text{C}_6\text{H}_6 \cdots \text{Br}_2$ complex may therefore be categorized as being of $\pi-\sigma^*$ type, which is consistent with the NBO $\pi_{\text{CC}}-\sigma_{\text{BrBr}}^*$ donor–acceptor interaction (Fig. 5.41(b)) corresponding to the resonance description in (5.74).

In principle, related CT complexes are possible for donor NBOs of n, σ , or π type, and for acceptor NBOs of n^* , σ^* , or π^* type. Table 5.22 cites examples of such CT complexes for various types of donor (rows) and acceptor (columns) NBOs, including species to be discussed below.

Charge-transfer complexes involving one-center n^* acceptor orbitals ($n-n^*$, $\sigma-n^*$, and $\pi-n^*$ Lewis-base–Lewis-acid adducts) have been discussed in Sections 3.2.10 and 3.6. Many CT complexes involving σ^* acceptors have been illustrated for H-bonds ($n-\sigma^*$) and dihydrogen bonds ($\sigma-\sigma^*$), as well as for the $\text{C}_6\text{H}_6 \cdots \text{Br}_2$ ($\pi-\sigma^*$) example above. In the remainder of this section we shall therefore focus on CT

Table 5.22. "Types" of donor–acceptor complexes, tabulating prototype examples (and text references) for n-, σ -, and π -type donor (vertical) and acceptor (horizontal) orbitals

	n*	σ^*	π^*
n	F ₃ N···BH ₃ (n _N –n _B *) Fig. 3.33	H-bonds (n– σ^*) Section 5.2	H ₃ N···NO ⁺ (n _N – π_{NO} *) Fig. 5.42
σ	H ₂ ···BH ₃ (σ_{HH} –n _B *) Fig. 3.98	Dihydrogen bonds (σ – σ^*) Fig. 5.17	H ₂ ···NO ⁺ (σ_{HH} – π_{NO} *) Fig. 5.44
π	C ₂ H ₄ ···BH ₃ (π_{CC} –n _B *) Fig. 3.99	C ₆ H ₆ ···Br ₂ (π_{CC} – σ_{BrBr} *) Fig. 5.41	C ₂ H ₄ ···NO ⁺ (π_{CC} – π_{NO} *) Fig. 5.45

complexes involving π^* acceptor orbitals (n– π^* , σ – π^* , or π – π^*), using the strong π -acid NO⁺ (the nitrosyl cation) as an illustrative acceptor monomer.⁸⁵

5.3.2 n– π^* Complexation

Figure 5.42 displays an example of n– π^* CT complexation in the H₃N···NO⁺ complex. The strong binding of this complex (~ 44 kcal mol^{–1}) is partially attributable to long-range ion–ion and ion–dipole attraction, but the NBOs of Fig. 5.42(b) exhibit the strong influence of n– π^* donor–acceptor stabilization. As expected, NO⁺ has a triple-bonded Lewis structure, with both σ and π bonds polarized toward electronegative oxygen. The low-energy π_{NO} acceptor orbitals are therefore oppositely polarized to place large amplitude lobes at the nitrogen end. Favorable overlap of the ammonia lone pair n_N with one of these π_{NO} lobes therefore requires a canted N···NO geometry, with $\theta_{\text{N}\cdots\text{NO}} = 112^\circ$, as depicted in Fig. 5.42(a). While such canted geometry is strange from the classical ion–dipole perspective, it is clearly optimal for effective n– π^* overlap and may be taken as a characteristic geometrical signature of the participation of a π^* acceptor.

In parallel to the properties of H-bonded complexes (Section 5.2), the monomer properties in the CT complex of Fig. 5.42 are strongly altered by n– π^* stabilization. Tables 5.23 and 5.24 summarize geometrical and NBO descriptors of the H₃N···NO⁺ complex that illustrate these changes.

As seen in Table 5.23, nearly 40% of an electronic charge is formally transferred from ammonia to NO⁺, and the resulting increase in π_{NO} antibond density leads to elongation of R_{NO} by 0.035 Å (relative to the isolated monomer), which is quite

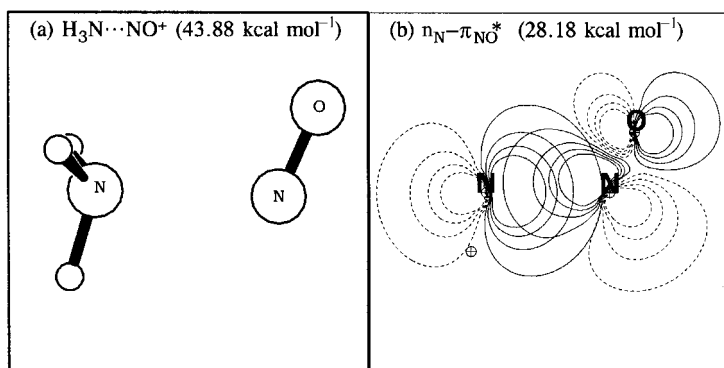


Figure 5.42 The optimized structure (a) and leading $n_{\text{N}}-\pi_{\text{NO}^*}$ donor-acceptor interaction (b) of the $\text{H}_3\text{N}\cdots\text{NO}^+$ charge-transfer complex.

substantial⁸⁶ considering the high bond order and large stretching force constant. The π_{NO^*} acceptor NBO becomes increasingly polarized toward the n_{N} donor NBO in the complex (increasing its acceptor strength). The lone pair of the complexed ammonia monomer also acquires significantly higher p character (increasing its donor strength) and becomes distinctly less pyramidal, effectively *reducing* the dipole moment of the monomer (contrary to the expectations of an ion-dipole model). Consistently with the resonance description (5.74), the $b_{\text{N}\cdots\text{N}}$ bond order becomes appreciable (0.45), and the short $R_{\text{N}\cdots\text{N}}$ distance (2.06 Å) is well inside van der Waals contact. The geometrical and charge properties of the complex are therefore well accounted for in terms of a simple $n_{\text{N}}-\pi_{\text{NO}^*}$ CT-interaction picture.

The importance of $n-\pi^*$ CT delocalization can also be assessed by deleting these interactions (with the \$DEL option) and reoptimizing the structure, as shown in Fig. 5.43. For this purpose we deleted all three valence antibonds of NO^+ (σ_{NO^*} and two π_{NO^*} NBOs) to suppress the leading possible valence CT delocalizations from Lewis base to Lewis acid. Note that these three NBOs have *zero* occupancy

Table 5.23. Comparative geometrical properties of $\text{H}_3\text{N}\cdots\text{NO}^+$ (Fig. 5.42(a)) and isolated H_3N and NO^+ monomers

Species	Bond length (Å)			Bond angle (degrees)	
	R_{NH}	R_{NO}	$R_{\text{N}\cdots\text{N}}$	$\bar{\theta}_{\text{HNH}}$	$\theta_{\text{N}\cdots\text{NO}}$
$\text{H}_3\text{N}\cdots\text{NO}^+$	1.021	1.095	2.057	110.1	112.4
Monomers	1.015	1.060	∞	107.9	—

Table 5.24. Comparative NBO/NRT properties of $\text{H}_3\text{N}\cdots\text{NO}^+$ (Fig. 5.42(a)) and isolated H_3N and NO^+ monomers

	Q_{NO}	$b_{\text{N}\cdots\text{N}}$	n_{N}	π_{NO^*}
$\text{H}_3\text{N}\cdots\text{NO}^+$	+0.603	0.450	$\text{sp}^{11.5}$	$0.58(\text{sp}^{7.8})_{\text{N}} + 0.81(\text{sp}^{14.0})_{\text{O}}$
Monomers	+1.000	0.000	$\text{sp}^{3.65}$	$0.60(\text{p})_{\text{N}} + 0.80(\text{p})_{\text{O}}$

in isolated NO^+ , so the CT-deleted potential-energy surface becomes identical to the full surface in the long-range limit.

As shown in Fig. 5.43, the CT-deleted species differs dramatically from the true $\text{H}_3\text{N}\cdots\text{NO}^+$ $n-\pi^*$ complex in Fig. 5.42. The CT-deleted binding energy is reduced to $20.4 \text{ kcal mol}^{-1}$, which is rather typical of the value expected for an ion-dipole complex but less than *half* the true value. In the CT-deleted structure, the characteristic canted $\text{N}\cdots\text{NO}$ geometry is lost, the intermolecular separation increases by almost 1 \AA (to $R_{\text{N}\cdots\text{N}} = 3.11 \text{ \AA}$, $R_{\text{N}\cdots\text{O}} = 2.99 \text{ \AA}$), and the monomer geometries revert essentially to their long-range limits, without the characteristic distortions (NH_3 flattening, NO^+ elongation) of the actual complex (Table 5.23). Thus, although ion-dipole forces of classical type provide important background attraction, the signature energetic and geometrical features of the $\text{H}_3\text{N}\cdots\text{NO}^+$ complex appear to be uniquely associated with the $n-\pi^*$ interaction depicted in Fig. 5.42(b).

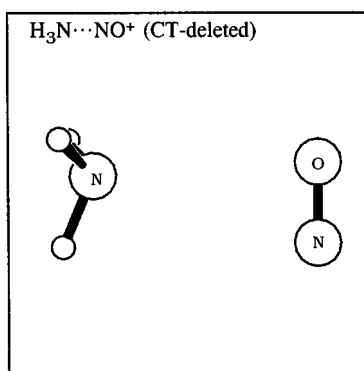


Figure 5.43 The optimized structure of CT-deleted $\text{H}_3\text{N}\cdots\text{NO}^+$ (with valence antibonds of NO^+ deleted to suppress intermolecular $n_{\text{N}}-\pi_{\text{NO}^*}$ delocalization). The shortest intermolecular $\text{N}\cdots\text{O}$ and $\text{N}\cdots\text{N}$ distances are 2.99 and 3.11 \AA , respectively, and the net binding energy is $20.4 \text{ kcal mol}^{-1}$ (cf. Fig. 5.42 and Table 5.23).

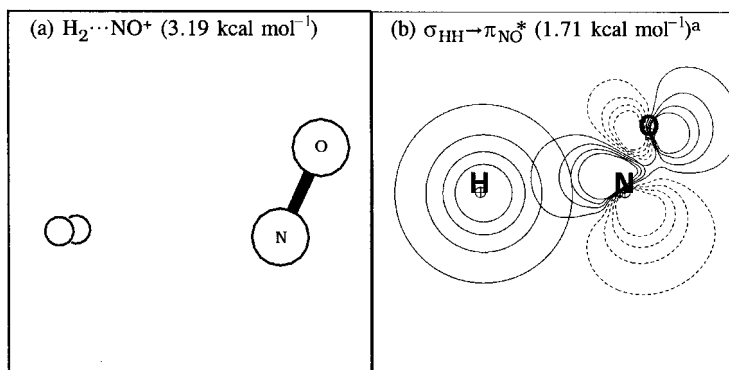


Figure 5.44 The optimized structure and leading $\sigma_{\text{HH}} \rightarrow \pi_{\text{NO}}^*$ donor–acceptor interaction of the $\text{H}_2 \cdots \text{NO}^+$ complex. (^a The sum of two near-equivalent interactions, $0.85 \text{ kcal mol}^{-1}$ each.)

5.3.3 $\sigma - \pi^*$ Complexation

Figure 5.44 displays a simple example of $\sigma - \pi^*$ complexation in the $\text{H}_2 \cdots \text{NO}^+$ complex. The canted geometry of the optimized complex again suggests the important role of the π_{NO}^* acceptor orbital, as shown in the donor–acceptor interaction of Fig. 5.44(b). Owing to the much weaker donor strength of σ_{HH} compared with the amine lone pair, the overall strength of $\sigma - \pi^*$ binding ($\sim 3 \text{ kcal mol}^{-1}$) and charge transfer from H_2 to nitrosyl ($Q_{\text{CT}} = 0.063e$) are considerably weaker than in the $\text{H}_3\text{N} \cdots \text{NO}^+$ case. The changes in monomer properties (not tabulated) are similar in direction but weaker in magnitude than those discussed above for $\text{H}_3\text{N} \cdots \text{NO}^+$.

The relative weakness of $\sigma - \pi^*$ compared with $n - \pi^*$ complexation can be rationalized as follows. The general second-order estimate of donor–acceptor stabilization in the $\sigma - \pi^*$ case is

$$\Delta E_{\sigma\pi^*}^{(2)} = -2 \frac{\langle \sigma | \hat{F} | \pi^* \rangle^2}{\epsilon_{\pi^*} - \epsilon_{\sigma}} \quad (5.77a)$$

whereas that for $n - \pi^*$ stabilization is

$$\Delta E_{n\pi^*}^{(2)} = -2 \frac{\langle n | \hat{F} | \pi^* \rangle^2}{\epsilon_{\pi^*} - \epsilon_n} \quad (5.77b)$$

Two general differences are apparent. The Fock-matrix element $\langle \sigma | \hat{F} | \pi^* \rangle$ involving the two-center σ donor is generally weaker than the corresponding $\langle n | \hat{F} | \pi^* \rangle$ for the one-center n donor, because of the general reduction of σ -orbital amplitude at each center (by the normalization factor $2^{-1/2}$) as well as the more directed p-rich character of n compared with σ . For the present comparison this results in a difference

$$\langle \sigma | \hat{F} | \pi^* \rangle \simeq 0.021 \text{ a.u.}, \quad \langle n | \hat{F} | \pi^* \rangle \simeq 0.093 \text{ a.u.} \quad (5.78a)$$

which strongly increases the numerator in (5.77b) compared with (5.77a). Furthermore, the energy (ϵ_σ) of a sigma bonding orbital is lowered compared with that (ϵ_n) of a lone-pair orbital, so the energy denominator in (5.77b) is greatly reduced compared with that in (5.77a),

$$\epsilon_{\pi^*} - \epsilon_\sigma \simeq 0.65 \text{ a.u.}, \quad \epsilon_{\pi^*} - \epsilon_n \simeq 0.37 \text{ a.u.} \quad (5.78b)$$

The combined effect is a strong decrease in the magnitude of $\epsilon_{\pi^*} - \epsilon_\sigma$ compared with $\epsilon_{\pi^*} - \epsilon_n$, and thus a weakening of the bonding in $\text{H}_2 \cdot \cdot \text{NO}^+$ compared with that in $\text{H}_3\text{N} \cdot \cdot \text{NO}^+$.

The smaller energy denominator, $\Delta\epsilon = \epsilon_{\pi^*} - \epsilon_n$, also leads to an altered proportionality between the donor–acceptor stabilization energy and the quantity of charge transferred (Q_{CT}), as discussed in Chapter 2 (see the discussion surrounding Eq. (2.18)). From the general proportionality

$$Q_{\text{CT}} \simeq \Delta\epsilon \Delta E_{\text{CT}}^{(2)} \quad (5.79)$$

one can recognize that, for $n-\pi^*$ delocalizations, a given Q_{CT} corresponds to weakened stabilization (or a given stabilization to increased charge transfer) compared with $\sigma-\pi^*$ delocalizations.

5.3.4 $\pi-\pi^*$ Complexation

Alkene $\pi-\pi^$ complexes*

Let us begin by considering ethylene (C_2H_4) as a prototypical localized pi donor and the nitrosyl cation as the Lewis pi acceptor. Figure 5.45 illustrates the interesting structure of the ethylene–nitrosyl $\pi-\pi^*$ CT complex. As shown in Fig. 5.45(a), the optimized complex (C_s symmetry) exhibits the characteristic $x \cdot \cdot \text{NO}$ canted geometry (x is the midpoint of the C—C bond) that is expected to bring the nitrosyl π_{NO}^* acceptor NBO into favorable overlap with the π_{CC} donor NBO, as shown in Fig. 5.45(b).

The short intermolecular distance ($R_{\text{XN}} = 2.445 \text{ \AA}$), the tilt angle ($\theta_{x \cdot \cdot \text{NO}} = 115.4^\circ$), and the elongation of NO (by 0.031 \AA) largely reflect the influence of the dominant $\pi_{\text{CC}}-\pi_{\text{NO}}^*$ donor–acceptor delocalization depicted in Fig. 5.45(b). The large intermolecular charge transfer from C_2H_4 to NO^+ ($Q_{\text{CT}} = 0.374e$) is also consistent with the expected enhancement (cf. Eq. (5.79)) due to the small energy denominator for this case

$$\Delta\epsilon = \epsilon_{\pi^*} - \epsilon_\pi \simeq 0.34 \text{ a.u.} \quad (5.80)$$

Thus, the energetic, structural, and charge properties of this species are aptly summarized by the designation as a “ $\pi-\pi^*$ CT complex.”

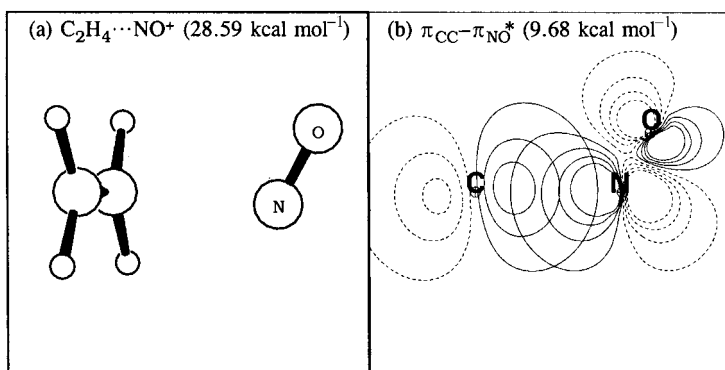


Figure 5.45 The optimized structure and leading intermolecular $\pi \rightarrow \pi^*$ donor–acceptor interaction of the $C_2H_4 \cdots NO^+$ complex.

However, the important role of long-range Coulombic forces is also indicated by the fact that the net binding ($28.6 \text{ kcal mol}^{-1}$) far exceeds the leading valence $\pi_{CC} - \pi_{NO}^*$ stabilization ($9.7 \text{ kcal mol}^{-1}$). At the equilibrium $C \cdots N$ intermolecular separation of $\sim 2.4 \text{ \AA}$, the CT-induced net monomer charge ($\pm 0.37e$) corresponds to long-range Coulombic attraction of $\sim 20 \text{ kcal mol}^{-1}$, which is sufficient to account for this deficit. Of course, this “classical” electrostatic interaction is itself a consequence of quantal intermolecular charge transfer, which has no classical counterpart.

The strong substituent effect of adjacent alkyl groups on the ethylenic pi bond can be seen by comparison with the corresponding propylene : nitrosyl complex, as shown in Fig. 5.46. In this case, the charge transfer ($Q_{CT} = 0.475e$) and binding energy ($37.56 \text{ kcal mol}^{-1}$) are significantly increased, relative to bare ethylene donor.

In the $CH_3CH=CH_2 \cdots NO^+$ complex, the nitrosyl cation retains the characteristic canted geometry indicative of strong $\pi_{CC} - \pi_{NO}^*$ interaction (Fig. 5.46(c)). However, the electrophilic attack shifts toward the terminal C of the pi bond, *away* from the methyl substituent. Such anti-Markovnikov complexation is, of course, to be expected from the relative polarization of the propylene pi bond toward the terminal C (so that the π_{CC}^* antibond is polarized toward the alkyl pi-donor).

However, as NO moves away from the plane between the pi-bonded C atoms (the nodal plane of the π_{CC}^* antibond), a complementary $n_N - \pi_{CC}^*$ “back-donation” becomes appreciable, as depicted in Fig. 5.46(d). Thus, both monomers act synergistically as *both* donors and acceptors in this complex (in distinct pairs of conjugated donor and acceptor orbitals). The *net* donation is from alkene to nitrosyl, and the clear dominance of the interaction in Fig. 5.46(c) justifies the designation of $C_3H_6 \cdots NO^+$ as a “ $\pi_{CC} \rightarrow \pi_{NO}^*$ CT complex.”

Owing to the compensating back-donation (Fig. 5.46(d)) that arises as nitrosyl is displaced from the midpoint of $C=C$ (where the donor amplitude tends to be

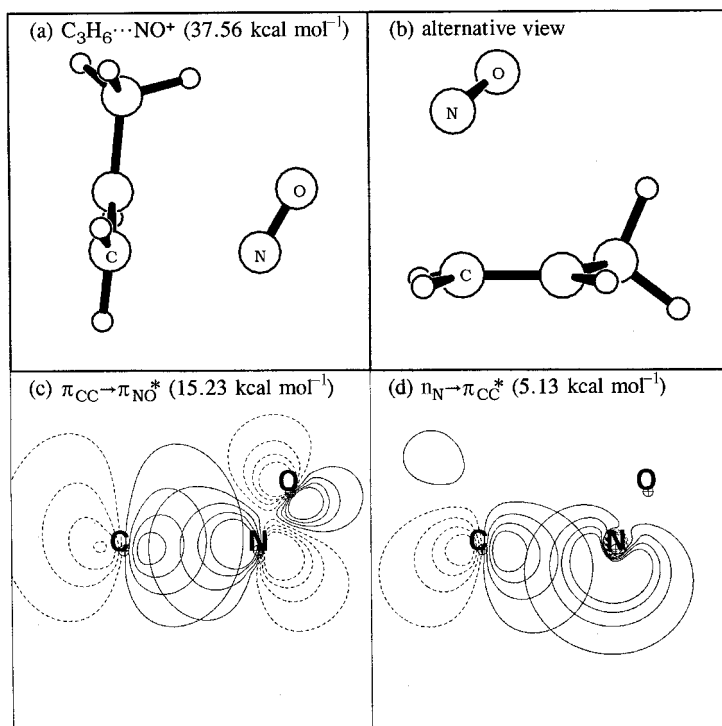


Figure 5.46 Optimized structure views, (a) and (b), and leading donor–acceptor interactions, (c) and (d), in the $\text{C}_3\text{H}_6 \cdots \text{NO}^+$ charge-transfer complex. The contour plane of (c) and (d) corresponds approximately to view (a).

highest), little energy is required to shift NO^+ from one end of the π_{CC} bond to the other. The nitrosyl moiety can therefore migrate readily from one end of the pi bond to the other (dependent on the relative pi-donor strength and electronegativity of substituent(s) on the pi bond), even though the $\theta_{\text{C}\cdots\text{NO}}$ tilt angle and $R_{\text{N}\cdots\text{C}}$ separation remain rather tightly constrained. Further aspects of this interesting pi-migratory mobility are beyond the scope of the present work.

Table 5.25 compares some energetic, structural, and NBO electronic properties of the nitrosyl $\pi-\pi^*$ complexes (including those to be discussed below). The binding energies, charge transfers, and monomer distortions are all seen to be significantly enhanced in $\text{CH}_3\text{CHCH}_2 \cdots \text{NO}^+$ compared with $\text{C}_2\text{H}_4 \cdots \text{NO}^+$, which is consistent with the trend in $\pi-\pi^*$ donor–acceptor interaction strength. The increasing Q_{CT} values ($\sim 0.5e$) also correspond to increasing long-range Coulombic attractions ($\sim 30\text{--}40 \text{ kcal mol}^{-1}$) in these species.

We can also illustrate the interesting non-additivity of *multiple* donor–acceptor interactions involving the same monomer. For this purpose we consider the ternary $\text{NO}^+(\text{C}_2\text{H}_4)_2$ complex in which *two* ethylene molecules donate to the same

Table 5.25. Comparative binding energies ΔE , intermolecular charge transfer Q_{CT} , bond lengths, and $\theta_{C\dots NO}$ angle of nitrosyl $\pi-\pi^*$ CT complexes

Species	ΔE	$Q_{CT}^a(e)$	R_{NO} (Å)	$R_{C\dots N}$ (Å)	$\theta_{C\dots NO}$ (degrees)
NO^+	—	—	1.060	—	—
$C_2H_4 \cdots NO^+$	28.6	0.374	1.091	2.445 ^b	115.4 ^b
$CH_3CHCH_2 \cdots NO^+$	37.6	0.475	1.102	2.234	119.4
$(C_2H_4)_2 \cdots NO^+$	41.4	0.509	1.102	2.500	112.5
$C_6H_6 \cdots NO^+$	47.8	0.537	1.101	2.385 ^b	135.0 ^b

^a $Q_{CT} = 1 - Q_{NO}$.

^b Referred to the midpoint of the nearest C=C bond.

nitrosyl acceptor. As seen in numerous other examples in this book (e.g., Sections 2.6, 3.3.1, and 5.2.4), such an open-CT donor-acceptor pattern is expected to result in *anticooperative* weakening of each $ON^+ \cdots C_2H_4$ coordination. Figure 5.47 displays the optimized structure, (a) and (b), and weakened $\pi_{CC} \rightarrow \pi_{NO}^*$ interaction (c) of the ternary complex, while the entries of Table 5.25 show that each $\pi_{CC} \cdots \pi_{NO}^*$ donor-acceptor bond lengthens by about 0.06 Å, the average bond strength weakens by about 28%, and the charge transfer is reduced by about 32%, relative to the binary $NO^+(C_2H_4)$ complex. Two weak $n_N - \pi_{CC}^*$ back-donations (not shown) are also present, each with estimated stabilization 1.36 kcal mol⁻¹, but the complex clearly warrants designation as a $\pi-\pi^*$ CT complex.

As shown most clearly in Fig. 5.47(b), the mutual coordination to nitrosyl brings the two ethylene ligands into conspicuously close proximity ($R_{C\dots C} = 3.41$ Å). The canted angle between the two pi bonds ($\theta_{C\dots C=C} = 110.9^\circ$) is also favorable for two weak $\pi_{CC} - \pi_{CC}^*$ interactions between the C_2H_4 units (estimated second-order stabilization 0.20 kcal mol⁻¹ each) that also contribute marginally to the overall stability of the complex (Fig. 5.47(d)). Thus, the nitrosyl CT complex appears to pin the two coordinated ethylenic units into a mutual arrangement that may be conducive to chemical reactivity, but further study of the interesting potential-energy surface of this species is beyond the scope of the present work.

Aromatic $\pi-\pi^*$ complexes

Nitrosyl CT interaction with pi bonds is further strengthened in the interesting complexes with benzene and other aromatic species. Figure 5.48 shows the equilibrium structure and leading intermolecular NBO interaction for the $C_6H_6 \cdots NO^+$ complex, and Table 5.25 includes geometrical and charge properties of this species. The aptness of the term “charge-transfer complex” is evident from the fact that *more*

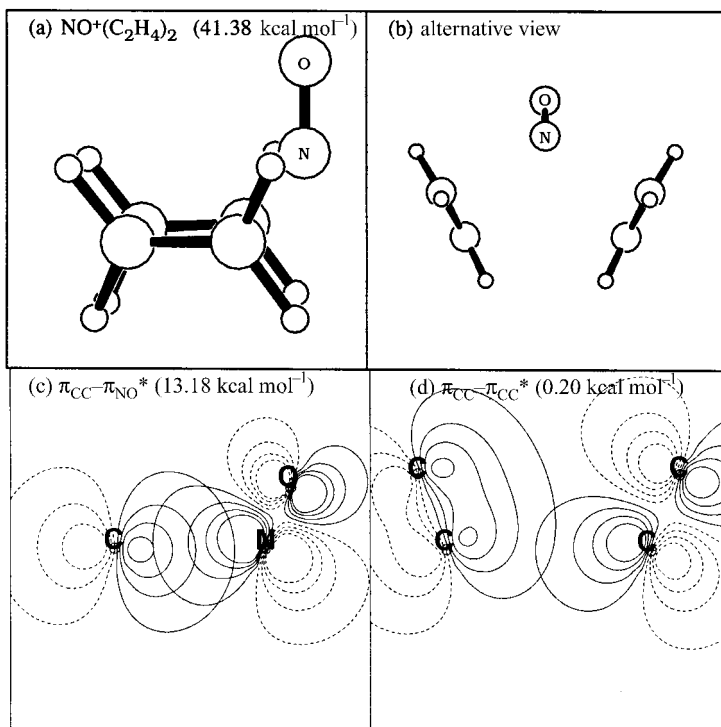


Figure 5.47 Optimized-structure views, (a) and (b), and donor–acceptor interactions, (c) and (d), in $\text{NO}^+(\text{C}_2\text{H}_4)_2$.

than half of the net cationic charge resides on the *benzene* moiety, continuing the trend found in weaker $\pi-\pi^*$ CT complexes.

Kochi and coworkers⁸⁷ succeeded in characterizing $\text{C}_6\text{H}_6 \cdots \text{NO}^+$ and many other nitrosyl–arene complexes by X-ray crystallography as well as optical and vibrational spectroscopy. The experimentally determined properties of these species – including the canted geometry of the nitrosyl over the edge of the benzene ring, the benzene-ring distortions (to be described below), and the strong charge transfer from nitrosyl to arene – are in accord with the theoretical characterization presented in Fig. 5.48 and Table 5.25.

As shown in Figs. 5.48(c) and (d), the nitrosyl accepts electron density in each of the two orthogonal π_{NO}^* NBOs. The π_{NO}^* protruding out of the plane of Fig. 5.48(b) accepts electron density primarily from the proximal $\text{C}=\text{C}$ pi bond beneath NO (Fig. 5.48(d)), while that lying in the plane has two equivalent interactions (Fig. 5.48(c)) with the two remaining distal π_{CC} NBOs. Thus, the charge-donation pattern corresponds to the lower symmetry of a particular localized Kekulé structure rather than the D_{6h} -symmetric pi cloud of the entire ring.

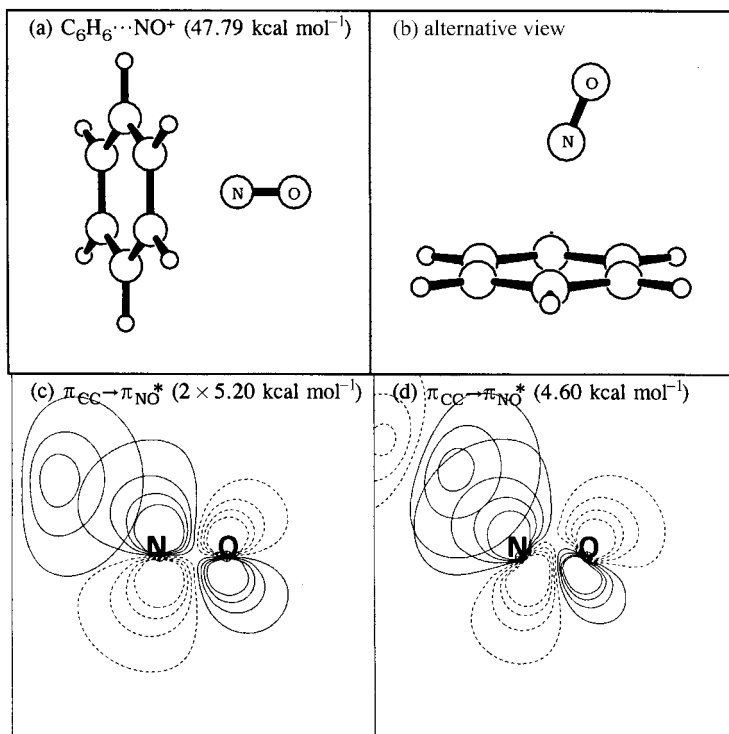


Figure 5.48 Optimized-structure views, (a) and (b), and leading $\pi_{CC} \rightarrow \pi_{NO}^*$ donor–acceptor interactions, (c) and (d), in the $C_6H_6 \cdots NO^+$ charge-transfer complex. The contour planes of (c) and (d) correspond, respectively, to in-plane and orthogonal out-of-plane cuts through the NO moiety in view (a).

The CT interaction is manifested not only in pronounced lengthening of the nitrosyl bond (Table 5.25) but also in more subtle structural changes in the benzene ring. In the distorted C_{2v} ring geometry, the proximal C=C bond beneath NO is appreciably elongated (1.406 \AA) relative to the opposite C=C bond (1.399 \AA), while the two remaining pairs of C=C bonds exhibit intermediate distortions (1.404 and 1.401 \AA), according to their proximity to the nitrosyl moiety.

These structural distortions are also mirrored in the asymmetric charge distribution around the benzene ring. Thus, the total valence pi occupancy (the sum of π_{CC} and π_{CC}^* occupancies) is slightly lower in the two distal C=C bonds ($1.8166e$) than in the proximal C=C bond ($1.8262e$), in accordance with the relative strengths of donor–acceptor interactions shown in Figs. 5.48(c) and (d) and the R_{CC} variations quoted above. The polarization coefficients of the three π_{CC} NBOs and total natural charges of each C also reflect the lowered symmetry of donor–acceptor interactions with nitrosyl. This example again illustrates how a localized NBO description of benzene (cf. Section 3.3.2) provides certain advantages over the canonical MO

description in elucidating details of π interactions with specific substituents or complexing agents.

5.3.5 Other charge-transfer complexes

Let us briefly mention some other binary $A \cdots B$ charge-transfer complexes involving neutral monomers A and B chosen rather arbitrarily from the large number of possible species of this type. These examples serve to illustrate interesting aspects of the general CT phenomenon and exhibit the strong commonality with donor–acceptor interactions considered elsewhere in this book.

In analogy to its complexes with nitrosyl cation (as described above), benzene can form donor–acceptor adducts with a variety of metallic and non-metallic Lewis acids. These lead to materials with novel optical and electrical properties that can be tuned through substituents on the aromatic ring.

Benzene–tricarbonylchromium

A simple example of aromatic CT complexation to transition metals is illustrated in the $\text{Cr}(\text{CO})_3 \cdots \text{C}_6\text{H}_6$ complex shown in Fig. 5.49. In the geometry of this complex, each of the three polar σ_{CrC} acceptor orbitals of $\text{Cr}(\text{CO})_3$ is oriented to point the d-type metal hybrid lobe toward one of the benzene $\text{C}=\text{C}$ bonds, somewhat analogous to the nitrosyl positioning shown in Fig. 5.48(b).

Owing to the $\pi_{\text{CC}}-\sigma_{\text{CrC}}$ CT interactions, the usual equivalence between the two Kekulé structures of benzene is broken and the ring distorts strongly to D_{3h} symmetry, with pronounced alternation (by 0.02 \AA) of $\text{C}=\text{C}$ bond lengths. Complexes of this type are evidently closely related to the metallocene sandwich compounds discussed elsewhere in this book (Section 4.9.5), with the benzene molecule described as a “tridentate ligand” in the language of metal coordination chemistry.

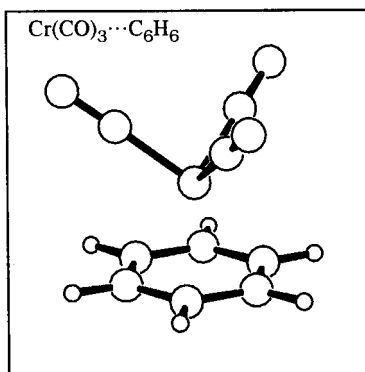


Figure 5.49 The structure of the benzene–chromiumtricarbonyl CT complex (C_{3v} symmetry).

Owing to the close connection with other metal–ligand coordination phenomena discussed in Sections 4.5–4.9, we do not consider this example further.

Benzene–TCNE

A well-known example of benzene coordination to a non-metallic neutral Lewis acid is given by the binary CT complex with tetracyanoethylene (TCNE),⁸⁸



as shown in Fig. 5.50. The optimized geometry places the cyano π_{CN}^* antibonds in favorable orientation for weak $\pi_{\text{CC}}-\pi_{\text{CN}}^*$ interactions with the benzene π_{CC} bonds, as depicted in Fig. 5.50(b). Table 5.26 summarizes geometrical and charge characteristics of the benzene–TCNE complex.

Despite the relatively weak net attraction, characteristic CT-induced shifts of geometry and charge distribution are apparent in both monomers. As shown in Table 5.26, the benzene ring distorts slightly in quinoid-like fashion, and each C–H bond polarizes to put increased anionic charge at C, thereby increasing the Lewis-base strength. On the TCNE monomer, each C≡N bond also repolarizes to give increased π_{CN}^* acceptor strength. In addition, however, each cyano group *bends* out of planarity by 1–2° (giving the bowl-shaped concavity in the view of Fig. 5.50(a)) to emulate slightly the canted geometry of other $\pi-\pi^*$ complexes. All these changes are in the direction expected to strengthen the valence $\pi_{\text{CC}}-\pi_{\text{CN}}^*$ CT interaction of Fig. 5.50(b).

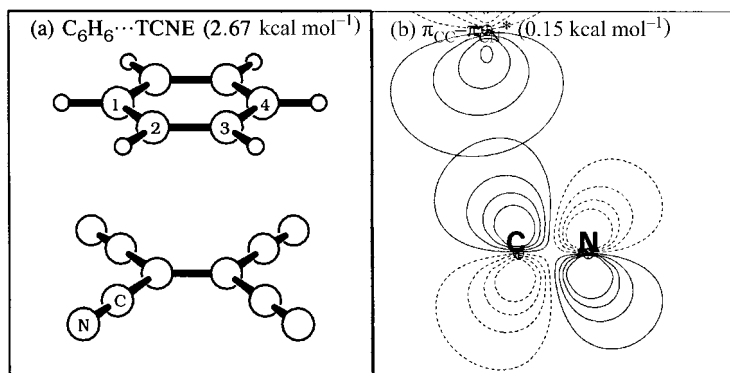


Figure 5.50 The optimized structure (a) and leading $\pi_{\text{CC}}-\pi_{\text{CN}}^*$ donor–acceptor interaction (b) of the benzene–tetracyanoethylene (TCNE) charge-transfer complex. (The contours of $\pi_{\text{C}_1\text{C}_2}-\pi_{\text{CN}}^*$ interaction in panel (b) are in the plane of benzene C_2 and the marked C and N atoms of TCNE shown in (a).) The intermolecular separation is 3.63 Å and the net charge transfer from benzene to TCNE is 0.0179e.

Table 5.26. Selected geometrical parameters (bond length R , valence angle θ , and dihedral angle ϕ) and atomic charges Q (for atoms involved in the $\pi_{\text{CC}}-\pi_{\text{CN}}^*$ interaction) of the benzene \cdots TCNE complex compared with isolated monomers; see Fig. 5.50

Variable	Complex	Isolated
Benzene		
$R_{\text{C}_1\text{C}_2}$ (Å)	1.396	1.398
$R_{\text{C}_2\text{C}_3}$ (Å)	1.395	1.398
$\theta_{\text{HC}_1\text{C}_4}$ (degrees)	179.6	180.0
Q_{C_1}	-0.211	-0.205
Q_{C_2}	-0.209	-0.205
TCNE		
$R_{\text{C}=\text{C}}$ (Å)	1.367	1.368
θ_{CCN} (degrees)	178.5	180.0
$\phi_{\text{NC}=\text{CN}(\text{t})}$ (degrees)	177.3	180.0
Q_{C}	+0.262	+0.253
Q_{N}	-0.201	-0.188

He-BeO

A quite different type of CT complex is the linear He \cdots BeO species shown in Fig. 5.51. This is one of an interesting series of complexes between rare-gas atoms and beryllium oxide that were first discovered computationally by Koch and coworkers.⁸⁹

As shown by NBO analysis, the BeO molecule is highly ionic (roughly $\text{Be}^{+1.6}\text{O}^{-1.6}$), making the beryllium end a powerful Lewis acid. The filled σ_{BeO} NBO is strongly polarized toward oxygen, so the unfilled σ_{BeO}^* antibond is virtually entirely composed of the sp hybrid on beryllium. Both the backside of this σ_{BeO}^* antibond and the vacant n_{Be}^* orbital (the oppositely directed sp hybrid on Be) can interact strongly with the filled n_{He} orbital, as shown in Figs. 5.51(b) and (c). Despite the strong steric repulsions that are present at the close He \cdots Be approach distance (1.51 Å), the complex is bound by a healthy 6.4 kcal mol⁻¹.

The backside $n_{\text{He}}-\sigma_{\text{BeO}}^*$ donor-acceptor interaction in Fig. 5.51(c) is particularly noteworthy. This interaction displays the *advantage* of the compact n_{He} radius (which is normally a strong deterrent to effective Lewis basicity) in overlapping with the contracted backside lobe of σ_{BeO}^* while avoiding the surrounding angular nodes (and resulting loss of overlap). This example illustrates that the “donor” or “acceptor” character of a monomer involves *specific orbital pairings* of the two monomers, rather than, e.g., a generic property of the monomer that is independent of the identity of the other monomer. Thus, while the He atom is well known to

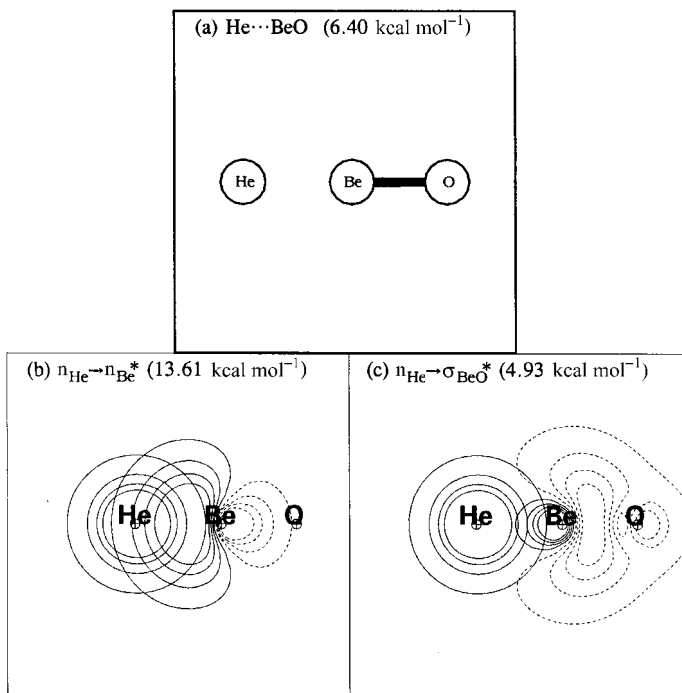


Figure 5.51 The optimized structure (a) and leading donor–acceptor interactions, (b) and (c), of the He...BeO charge-transfer complex ($R_{\text{He}\cdots\text{Be}} = 1.506 \text{ \AA}$, $R_{\text{BeO}} = 1.320 \text{ \AA}$, $Q_{\text{CT}} = 0.039e$).

be “inert” with respect to most Lewis acids, its compact size is a clear asset with respect to effective CT interactions with the contracted Be 2s and 2p orbitals of BeO. Whether He can appear chemically active to serve as an effective Lewis base evidently depends critically on whether suitable *matching* orbitals can be found on the Lewis acid.

More generally, we can recognize that an acceptor orbital of unusual size or shape may demand an “unusual” Lewis base to offer a suitable matching donor orbital. The CT complexes formed by a monomer therefore provide a direct reflection of the shapes, sizes, and energies of its filled and unfilled valence orbitals. The rich diversity of donor–acceptor chemistry can be largely attributed to the richly variegated forms of donor and acceptor *orbitals*, which is consistent with the strongly quantum-mechanical character of donor–acceptor phenomena.

5.4 Transition-state species

5.4.1 Chemical reactions and transition-state complexes

According to Eyring’s reaction-rate theory,⁹⁰ the elementary bimolecular chemical reaction between reactant species A and B proceeds through a *transition-state*



Henry Eyring

complex $A \cdots B^\ddagger$ along the reaction path leading to product species P:



The transition-state (TS) complex $A \cdots B^\ddagger$ is considered to correspond to a topological *saddle-point* along the minimum-energy pathway (intrinsic reaction coordinate s) that connects the reactant and product equilibrium minima on the potential-energy surface. Alternatively, $A \cdots B^\ddagger$ corresponds to a *maximum* on the one-dimensional (Arrhenius-like) reaction profile that connects reactant and product minima (Fig. 5.52). Just as vacationers at Winter Park must make the difficult climb over Berthoud Pass before descending to Denver, so must chemical travelers A and B on the potential-energy landscape climb over the high-energy TS pass before descending to the low-energy valley of final products.

Like other supramolecular complexes, a TS complex $A \cdots B^\ddagger$ is a true stationary point on the potential-energy surface, with vanishing forces at every nucleus. However, unlike other complexes discussed above, a TS complex sits atop a repulsive hill rather than at the bottom of an attractive energy well of the potential-energy surface. In the $A \cdots B^\ddagger$ case, intermolecular donor–acceptor stabilizations serve to *soften the repulsions* between A and B, rather than create an energy well (or deepen an existing well) relative to asymptotically separated systems A and B at rest. In other respects the donor–acceptor stabilizations of an $A \cdots B^\ddagger$ species are fully analogous to those of an $A \cdots B$ equilibrium species in counteracting the repulsive forces that may otherwise be present at the chosen configuration.

Donor–acceptor stabilizations of a TS $A \cdots B^\ddagger$ complex are intimately related to the general theory of catalysis. Reduction of the repulsive TS barrier between

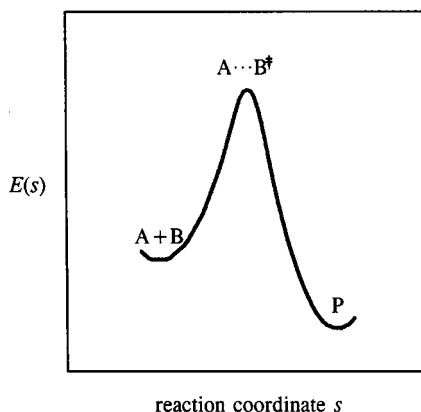


Figure 5.52 A schematic reaction energy profile for the bimolecular elementary reaction (5.82).

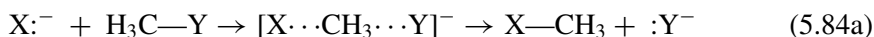
reactants and products reduces the activation energy of reaction in both forward and reverse directions:

$$E_a^f = E(\text{A} \cdots \text{B}^\ddagger) - E(\text{reactants}) \quad (5.83a)$$

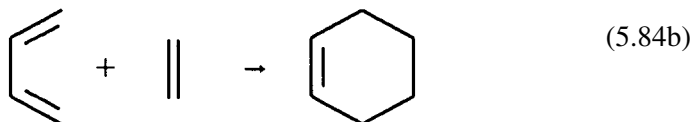
$$E_a^r = E(\text{A} \cdots \text{B}^\ddagger) - E(\text{products}) \quad (5.83b)$$

thereby accelerating (catalyzing) the reaction rate relative to the unstabilized TS barrier. The general catalytic influence of a TS-stabilizing interaction refers both to this net energy lowering at TS geometry (an enthalpic effect) and to general softening of the potential with respect to vibrational displacements (an entropic effect). Both influences contribute to the reduction of the Gibbs free energy of activation (ΔG^\ddagger) that accelerates the reaction rate.

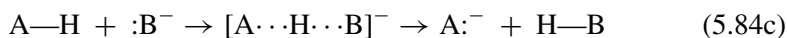
In accord with general Eyring TS theory, we may consider every elementary chemical reaction to be associated with a unique $\text{A} \cdots \text{B}^\ddagger$ supramolecular complex that dictates the reaction rate. In the present section we examine representative TS complexes from two well-known classes of chemical reactions: $\text{S}_{\text{N}}2$ nucleophilic displacement reactions



and Diels–Alder 4 + 2 cycloaddition reactions



The TS complex for an illustrative proton transfer reaction,



was previously described in Section 5.2.5, and that for a model olefin-polymerization reaction was described in Section 4.7.5.

Consistently with the discussion in Section 4.7.5, we can describe the entire reaction profile from reactant (R) to product (P) species,



in terms of NRT weightings and bond orders along the intrinsic reaction coordinate⁹¹ (IRC) s . Near the reactant limit ($s \simeq s_{\text{R}}$) the weighting w_{R} of reactant-like resonance structure is near unity, while that (w_{P}) of product-like resonance structure is negligible,

$$s \simeq s_{\text{R}}: \quad w_{\text{R}} \simeq 1, \quad w_{\text{P}} \simeq 0 \quad (5.86a)$$

and at the opposite product limit these relative weightings are reversed,

$$s \simeq s_{\text{P}}: \quad w_{\text{R}} \simeq 0, \quad w_{\text{P}} \simeq 1 \quad (5.86b)$$

As $w_{\text{R}}(s)$ and $w_{\text{P}}(s)$ vary between these limits, they necessarily cross in the neighborhood of the transition state. The TS^\ddagger complex therefore corresponds to a resonance hybrid of nearly *equal* reactant-like and product-like contributions,⁹²

$$w_{\text{R}}(s) \simeq w_{\text{P}}(s) \quad \text{at } s = s^\ddagger \quad (5.86c)$$

Equation (5.86c) also expresses the chemically reasonable condition that nascent product bonds are approximately half-formed and reactant bonds half-broken (NRT bond order $\simeq \frac{1}{2}$) at $s = s^\ddagger$.

The NRT description of TS complexes is closely related to the general two-state valence bond model of Shaik and Pross.⁹³ This model emphasizes the coupled changes in two adiabatic states that evolve from distinct diabatic valence-bond (VB) configurations ϕ_{R} and ϕ_{P} in the neighborhood of a degeneracy. As the non-interacting VB states cross in energy at $s = s^\ddagger$,

$$E_{\text{R}}(s) = E_{\text{P}}(s) \quad \text{at } s = s^\ddagger \quad (5.87a)$$

the VB interaction element

$$\Delta_{\text{RP}} = \langle \phi_{\text{R}} | \hat{H} | \phi_{\text{P}} \rangle \quad (5.87b)$$

leads to an *avoided* crossing in the corresponding adiabatic states $E_{\pm}(s)$

$$E_{\pm}(s) \simeq \frac{E_{\text{R}} + E_{\text{P}}}{2} \pm |\Delta_{\text{RP}}| \quad (5.87c)$$

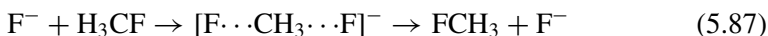
such that the lower (ground) state $E_{-}(s)$ passes through a *maximum* and the upper (excited) state $E_{+}(s)$ through a *minimum* at $s = s^\ddagger$. The NRT description (5.86) of the ground-state TS complex is consistent with (but does not require) such

mirror-like behavior in the potential-energy surfaces of the coupled states. Only the behavior of the ground-state surface will be examined in the following examples.

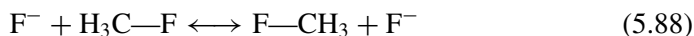
The NRT formalism will be used to describe the interacting species along the entire reaction coordinate. Such a continuous representation allows the TS complex to be related both to asymptotic reactant and product species and to other equilibrium bonding motifs (e.g., 3c/4e hypervalent bonding; Section 3.5). A TS complex can thereby be visualized as intermediate between two distinct chemical bonding arrangements, emphasizing the relationship between supramolecular complexation and partial chemical reaction.

5.4.2 S_N2 Reactions

As a simple prototype of nucleophilic displacement reactions (5.84a), let us consider the symmetric case $X = Y = F$,



for fluoride exchange with methyl fluoride. In this case the TS complex is the trigonal-bipyramidal (D_{3h} -symmetric) species shown in Fig. 5.53(a), exhibiting strong resonance delocalization that can be clearly attributed to 3c/4e hypervalent ω -bonding (the Pimentel–Rundle three-center MO picture; Sections 3.5 and 4.6). Such bonding is expressible in resonance terms as



or in NBO terms as a strong intermolecular $n_F-\sigma_{CF}^*$ donor–acceptor delocalization (Fig. 5.53(b)).

In the $[F \cdots CH_3 \cdots F]^-$ TS complex there is evidently a perfectly symmetric relationship between the two outer p_F orbitals and the central p_C orbital that form

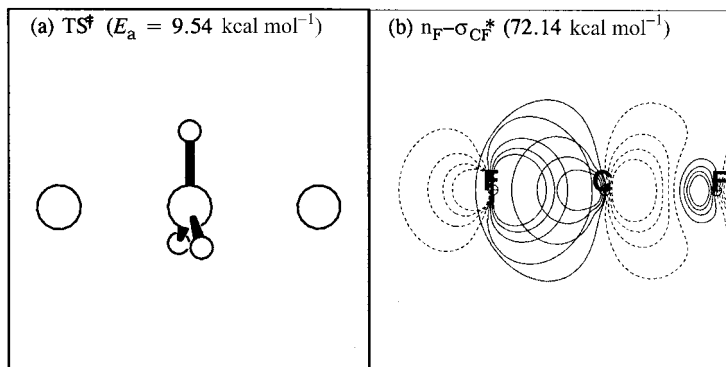


Figure 5.53 The transition-state complex for the $F^- + CH_3F$ fluoride-exchange reaction (5.87): (a) the optimized structure and (b) the leading $n_F-\sigma_{CF}^*$ donor–acceptor interaction.

the three-center bonding MO. The $3c/4e$ interaction is also representable as an $\omega_{\text{F:CF}} = \omega_{\text{FC:F}}$ hyperbond in a structural formula of the form



As previously described (see, e.g., the discussion surrounding Fig. 3.86), there is an intimate connection between certain *equilibrium* hyperbonded species (e.g., FMH_3F , $\text{M} = \text{Si}, \text{Ge}, \dots$) and the corresponding transition species (e.g., FMH_3F , $\text{M} = \text{C}$) in isovalent systems. Only a slight strengthening (by $\sim 10 \text{ kcal mol}^{-1}$) of the $n_{\text{F}} - \sigma_{\text{CF}}^*$ interaction in Fig. 5.52(b) would suffice to convert (5.89) from a supramolecular TS “complex” into a stable “molecule.” This viewpoint allows one to see the essential electronic *continuity* that unites many molecular and supermolecular species. The NBO donor–acceptor interactions that contribute to stable species are also expected to be present in isovalent unstable species of corresponding geometry.

Figure 5.54 displays the IRC reaction profile for the fluoride-exchange reaction (5.87). Because the reaction coordinate is the IRC rather than R_{FC} , the barrier profile differs somewhat from that shown in Fig. 3.86. The activation energy is calculated to be $9.54 \text{ kcal mol}^{-1}$ (without zero-point-energy correction), corresponding to an appreciable rate of chemical exchange under ambient thermal conditions.

The stabilizing effect of the intermolecular $n_{\text{F}} - \sigma_{\text{CF}}^*$ interaction (Fig. 5.53(b)) can also be assessed by *deleting* the $\langle n_{\text{F}} | \hat{F} | \sigma_{\text{CF}}^* \rangle$ interaction-matrix element and recalculating the potential-energy surface $E_{\text{del}}(s)$ in the absence of this interaction.

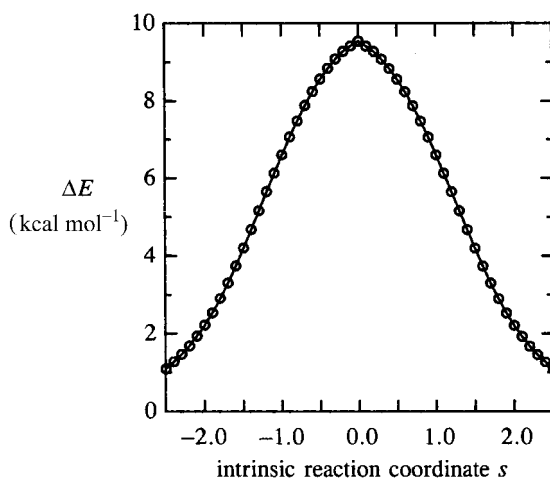


Figure 5.54 The potential-energy reaction profile (along the IRC) for the $\text{F}^- + \text{H}_3\text{CF} \rightarrow \text{FCH}_3 + \text{F}^-$ reaction.

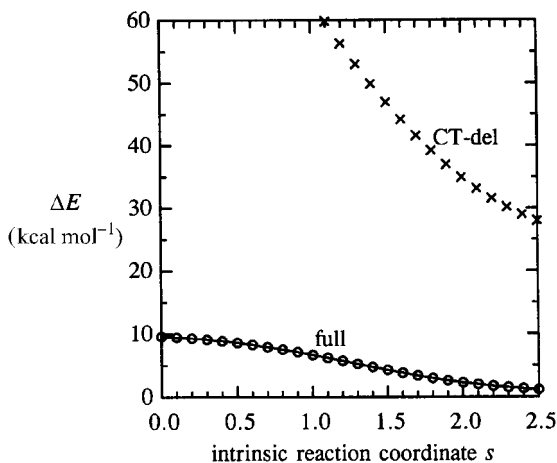


Figure 5.55 A comparison of the reaction energy profiles for the full calculation (circles) and the CT-deleted calculation (crosses), with the $n_{\text{F}}-\sigma_{\text{CF}}^*$ NBO interaction deleted in the latter case.

Figure 5.55 illustrates the strong difference between the CT-deleted E_{del} (crosses) and the actual potential-energy values for the full calculation (circles) on the product side of the IRC. Clearly, a low-energy TS pass from reactant to product species is possible only when the intermolecular $n_{\text{F}}-\sigma_{\text{CF}}^*$ stabilization is included. Even in the far wing of the reaction profile at $s = 2.5$, the synergistic geometrical and electronic distortions of the evolving TS complex are seen to be so pronounced that the simple second-order estimate of $n_{\text{F}}-\sigma_{\text{CF}}^*$ interaction strength (Fig. 5.53(b)) is quite inadequate to represent the actual numerical magnitude of the intermolecular stabilization.

Figure 5.56 illustrates the variation of NRT bond orders b_{CF} for reactant and product C—F bonds along the reaction coordinate, and Fig. 5.57 illustrates the corresponding variations of natural atomic charge on the two F atoms. Despite the numerical scatter, one can see in Fig. 5.56 that the reactant (b_{CF}) and product ($b_{\text{CF}'}$) bond orders respectively diminish and increase while preserving approximately *constant* total bond order in the shifting $\omega_{\text{F:CF}}$ hyperbond,

$$b_{\text{CF}} + b_{\text{CF}'} \simeq 1 \quad (5.90)$$

paralleling the behavior in H-bonded proton-transfer complexes (cf. Fig. 5.36). The charge transfer also progresses in the expected manner from the TS complex (where $Q_{\text{F}} = Q_{\text{F}'} = -0.708$) toward dissociated products ($Q_{\text{F}} \rightarrow -1$, $Q_{\text{F}'} \rightarrow -0.395$), as depicted in Fig. 5.57. Note particularly that the supramolecular complex displays *continuous* variation of charge transfer along the reaction coordinate (rather than, e.g., discontinuous electron “hopping”), which is consistent with Mulliken’s concept of using a charge-transfer coordinate to track the progress of electron transfer.

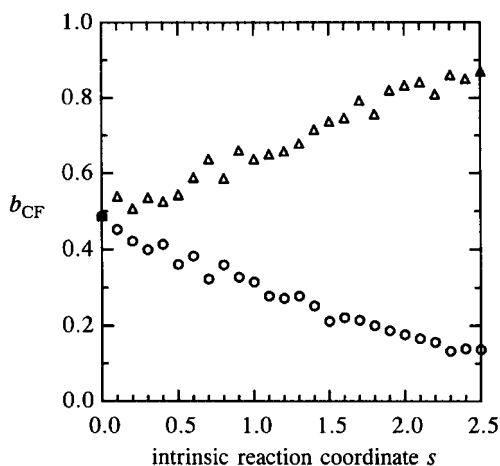


Figure 5.56 Variations of reactant (circles) and product (triangles) C—F bond orders b_{CF} on going from the TS complex ($s = 0$) toward the final product.

The results above confirm that a TS supramolecular complex exhibits particularly strong chemical-exchange effects, but is recognizably related by electronic continuity to other types of complexes and stable molecules. Against the steeply repulsive forces of steric interactions, NBO donor-acceptor interactions are evidently responsible for opening a gateway pass through a repulsive barrier region into a new valley of chemical stability. Thus, even more important than their role in stabilizing equilibrium species is the fact that donor-acceptor interactions serve to soften repulsive regions and open up low-lying reactive pathways that serve to channel and guide chemical species toward productive chemical rearrangements on the potential-energy surface.

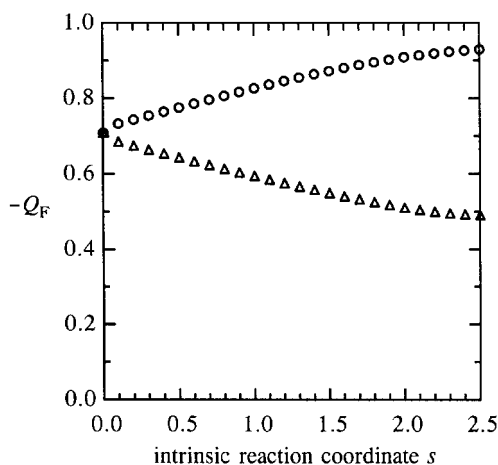


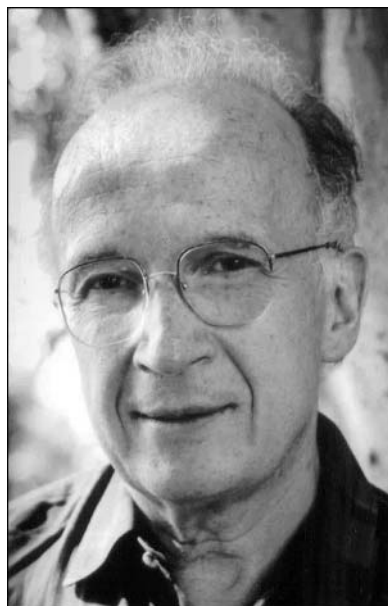
Figure 5.57 Variations of fluorine atomic charge Q_F on going from the TS complex ($s = 0$) toward the final product for initially bonded (circles) and free (triangles) F.

5.4.3 Diels–Alder reactions and Woodward–Hoffmann rules

Since its recognition and systematic exploration by Otto Diels and Kurt Alder in the 1920s, the Diels–Alder reaction motif (5.84b) has provided one of the most powerful tools of organic synthesis. The Diels–Alder reaction led directly to the dramatic pre-World War II development of the chemical industry for production of synthetic rubber and other polymeric materials. Today, the commercial impact of Diels–Alder methods extends to virtually all areas of agricultural, pharmaceutical, and natural-products chemistry.

Elucidation of the mechanism of Diels–Alder and related pericyclic reactions was also associated with noteworthy advances in bonding theory. These advances⁹⁴ culminated in the remarkable “selection rules” formulated by Robert B. Woodward and Roald Hoffmann in the 1960s.⁹⁵ The Woodward–Hoffmann rules provide a unified framework for assessing favorable (“allowed”) and unfavorable (“forbidden”) MO phase patterns in a cyclic transition state of the type that governs Diels–Alder cycloaddition and related electrocyclic and sigmatropic reactions. General recognition of the importance of the conservation of orbital symmetry in organic reaction mechanisms constituted one of the most dramatic paradigm shifts in twentieth-century chemical thinking.

As shown in (5.84b), the characteristic feature of the Diels–Alder reaction is the addition of an ethylenic double bond (dienophile) across the 1, 4-positions of a conjugated diene to give a cyclohexene ring product. The ethylenic bond is usually



Roald Hoffmann



Robert B. Woodward

activated by adjacent carbonyl, carboxyl, cyano, or nitro groups, and many substituents also serve to activate the diene. Although the simplest butadiene + ethylene reaction is immeasurably slow under ambient conditions, this limiting prototype provides a suitable model system for examining general features of the Diels–Alder transition state, as well as a baseline for discussing substituent effects.

Figure 5.58 depicts two views of the Diels–Alder TS complex, which lies about $25.5 \text{ kcal mol}^{-1}$ above isolated butadiene + ethylene reactants (or $54.1 \text{ kcal mol}^{-1}$ above the cyclohexene product). Figure 5.58b shows clearly the strong departures from planarity that signal reorganization from trigonal sp^2 to tetrahedral sp^3 bonding in the TS complex.

Figures 5.58(c) and (d) display the leading strong donor–acceptor stabilizations of the TS complex in terms of reactant NBOs (each panel depicting one of two equivalent interactions). As shown in Fig. 5.58(c), each pi bond (π_{12} and π_{34}) of the diene delocalizes strongly into the ethylenic pi antibond (π_{56}^*), with estimated 34 kcal mol^{-1} total stabilization. Figure 5.58(b) shows how each butadiene terminal —CH_2 group twists to orient its p_π orbital toward the corner lobe of the ethylene π_{eth}^* antibond (as also shown by the canted π_{buta} orbital in Fig. 5.58(c)). However, strong synergistic CT delocalization in the *opposite* direction (with estimated total 23 kcal mol^{-1} stabilization) is provided by the two strong $\pi_{\text{eth}} \rightarrow \pi_{\text{buta}}^*$ interactions shown in Fig. 5.58(d). The net result of this closed-CT pattern of π – π^* donor–acceptor interactions is therefore to stabilize the TS complex by more than 57 kcal mol^{-1} , providing the relatively low-energy TS pass between reactant and product valleys with little *net* accumulation of charge on either monomer.

To achieve the strong delocalizations shown in Fig. 5.58(c), it is obviously crucial that the two π_{buta} donor NBOs are free to adopt *opposite* overall phases (as is

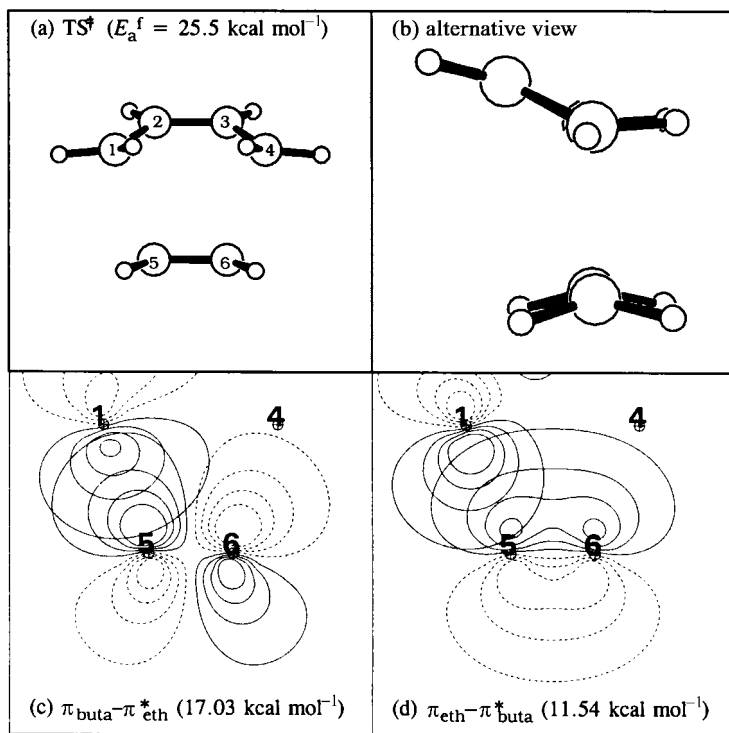


Figure 5.58 Views of the model Diels–Alder transition state, (a) and (b), and leading donor–acceptor interactions, (c) and (d), in reactant-type NBOs (one of the two equivalent interactions of each type).

always possible for two distinct pi bonds), so that each can overlap constructively with oppositely phased lobes of the ethylene π_{eth}^* antibond. Similarly, in Fig. 5.58(d), it is crucial that the two π_{buta}^* antibonds can orient lobes of the *same* phase toward the π_{eth} donor NBO. Thus, if the upper C₁ and C₄ atoms in Figs. 5.58(c) and (d) were *directly* bonded by π_{14} and π_{14}^* NBOs (as in the analogous 2 + 2 cycloaddition reaction), the corresponding $\pi_{14} \rightarrow \pi_{56}^*$ and $\pi_{56} \rightarrow \pi_{14}^*$ stabilizations would be strictly *vanishing*, as in the cyclobutadiene example of Section 3.3.2. This simple consequence of localized $\pi-\pi^*$ interaction patterns is the localized NBO analog of the Woodward–Hoffmann rules.

Alternatively, we can also analyze the TS complex with respect to NBOs of the product-like Lewis structure (by using the standard \$CHOOSE option of the NBO program). Figure 5.59(a) depicts an alternative view of the TS geometry, with bond sticks drawn to emphasize the relationship to the product cyclohexene molecule. Figures 5.59(b)–(d) depict the leading donor–acceptor stabilizations in the product NBO Lewis structure.

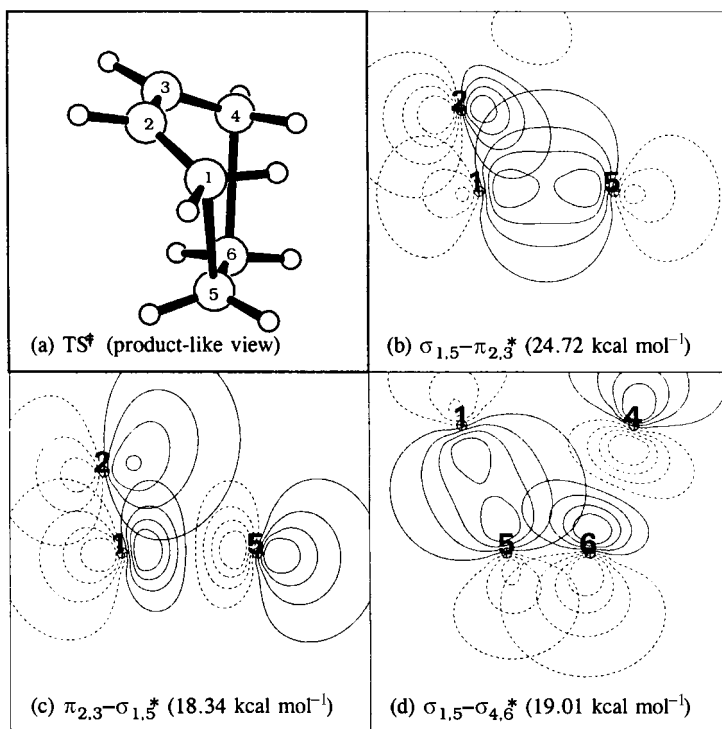


Figure 5.59 A view of the model Diels–Alder transition state (a) and leading donor–acceptor interactions (b)–(d) in product-type NBOs.

The principal hyperconjugative delocalizations are from the two nascent sigma bonds ($\sigma_{1,5}$ and $\sigma_{4,6}$) to the cyclohexene $\pi_{2,3}^*$ antibond, each contributing $24.7 \text{ kcal mol}^{-1}$ (Fig. 5.59(b)). Synergistically, the cyclohexene pi bond $\pi_{2,3}$ back-donates to the new antibonds $\sigma_{1,5}^*$ and $\sigma_{4,6}^*$, giving strong stabilization (Fig. 5.59(c)) and a closed-CT delocalization pattern. Finally, the two coplanar nascent sigma bonds hyperconjugate strongly with one another, each such $\sigma-\sigma^*$ interaction contributing $19.0 \text{ kcal mol}^{-1}$ stabilization (Fig. 5.59(d)). Overall, the TS complex is stabilized (relative to a perfectly localized cyclohexene Lewis structure of distorted TS geometry) by more than $120 \text{ kcal mol}^{-1}$ due to the strong valence $\pi\rightarrow\sigma^*$, $\sigma\rightarrow\pi^*$, and $\sigma\rightarrow\sigma^*$ delocalizations depicted in Figs. 5.59(b)–(d).

It is again clear from these diagrams that the $\sigma_{1,5}$ and $\sigma_{4,6}$ skeletal sigma bonds are “allowed” to adopt *opposite* phases for favorable $\sigma_{1,5}-\pi_{2,3}^*$ and $\sigma_{4,6}-\pi_{2,3}^*$ overlap with the oppositely phased lobes of $\pi_{2,3}^*$ (and similarly for the two complementary $\pi_{2,3}\rightarrow\sigma_{1,5}^*$ and $\pi_{2,3}\rightarrow\sigma_{4,6}^*$ interactions). In contrast, the corresponding interactions with a bridging $\sigma_{1,4}$ bond (if present) would be “forbidden” to benefit from such stabilization.

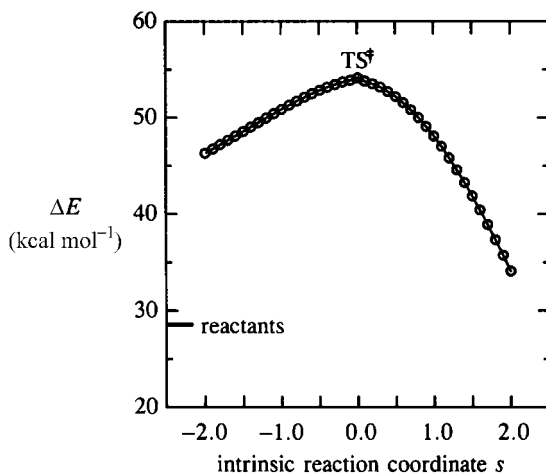


Figure 5.60 The transition-state region of the reaction profile (along the IRC) for the model butadiene + ethylene Diels–Alder reaction. (The zero of energy corresponds to the cyclohexene product.)

The localized product-NBO view also makes clear the importance of the *non-planarity* of the TS in achieving favorable hyperconjugative stabilizations, because interactions of $\pi\text{-}\sigma^*$ and $\sigma\text{-}\pi^*$ type necessarily *vanish* in planar geometry. Indeed, one can see that favorable vicinal $\pi\text{-}\sigma^*$ or $\sigma\text{-}\pi^*$ overlap should primarily involve *one end* (hybrid) of each NBO, oriented, if possible, in the *anti* conformation for maximum stabilization. This viewpoint allows one to recognize the importance of *angular* and *orientational* factors that would not be evident in a purely topological framework.

Figure 5.60 displays a portion of the Diels–Alder reaction profile in the neighborhood of the TS complex. In this case the IRC profile is rather unsymmetric around $s = 0$, ascending slowly from the reactant side toward the TS summit, then plummeting rapidly toward the product cyclohexene limit, which lies about 29 kcal mol^{-1} below the reactants (and 54 kcal mol^{-1} below the TS).

Figure 5.61 displays the variations of NRT carbon–carbon bond orders (b_{CC}) along the reaction coordinate (with the atom numberings shown in Fig. 5.59(a)). As shown in Fig 5.61, the strengths of the reactant pi bonds $\pi_{1,2}$, $\pi_{3,4}$, and $\pi_{5,6}$ are steadily diminishing, while those of the product $\pi_{2,3}$, $\sigma_{1,5}$, and $\sigma_{4,6}$ bonds are steadily increasing through the TS region. The variation of $b_{5,6}$ closely parallels that of $b_{1,2}$ (or $b_{3,4}$), showing that the dissolution of the three reactant π_{CC} bonds is highly synchronous. The crossing point $b_{1,2} = b_{2,3}$ (where the $w_R = w_P$ degeneracy condition (5.86c) is satisfied) occurs at $s = +0.1$, very close to the actual transition state.

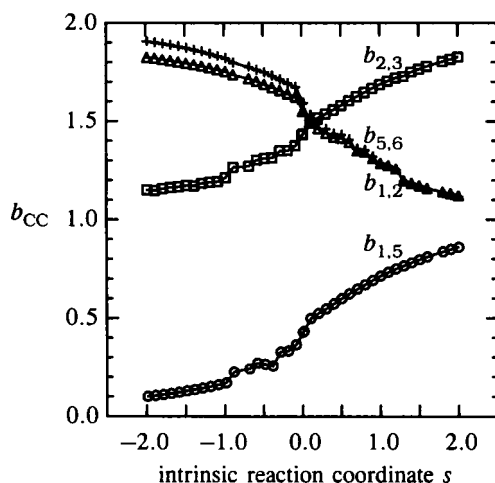


Figure 5.61 Variations of NRT C—C bond orders $b_{1,2}$ (triangles), $b_{2,3}$ (squares), $b_{1,5}$ (circles), and $b_{5,6}$ (plus signs) along the IRC for the model Diels–Alder reaction (see Fig. 5.59(a) for the atom numbering).

In accord with general resonance-theory concepts, we may expect that each bond order in Fig. 5.61 can be approximated in terms of an effective product-like weighting w_P by

$$b_{2,3} \simeq 1 + w_P \quad (5.91a)$$

$$b_{1,2} \simeq b_{5,6} \simeq 2 - w_P \quad (5.91b)$$

$$b_{1,5} \simeq w_P \quad (5.91c)$$

corresponding to idealized single ($b_{2,3} = 1$) and double ($b_{1,2} = b_{5,6}$) reactant bonds when $w_P = 0$. Furthermore, the product weighting w_P should vary from zero to unity at $s = -\infty$ to $s = \infty$, a behavior that is approximately described by the simple trigonometric function

$$w_P(s) \simeq \frac{1}{2} + \frac{1}{\pi} \tan^{-1}(s) \quad (5.92)$$

(where the arctangent function is evaluated in radians). Figure 5.62 plots these approximations for comparison with the calculated NRT bond orders in Fig. 5.61, showing that the simple estimate (5.92) well describes the actual bond-order variations.

Finally, Fig. 5.63 plots the NRT bond-order–bond-length relationship for all C—C bond variations in the IRC range ($-2 \leq s \leq 2$) of Fig. 5.60. The b_{CC} – R_{CC} curve is approximately *linear* in the region $1 \leq b_{CC} \leq 2$,

$$R_{CC} \simeq -0.20b_{CC} + 1.71 \quad (b_{CC} = 1.5 \pm 0.4 \text{ \AA}) \quad (5.93a)$$

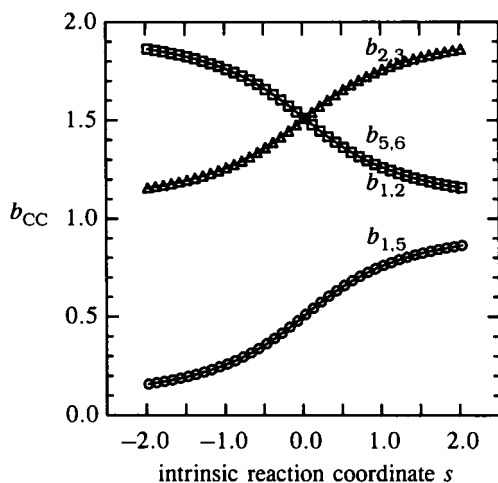


Figure 5.62 Similar to Fig. 5.61, as estimated from Eqs. (5.91) and (5.92).

and, with a different slope, in the region around $b_{CC} \simeq 0.5$,

$$R_{CC} \simeq -0.61b_{CC} + 2.51 \quad (b_{CC} = 0.5 \pm 0.3 \text{ \AA}) \quad (5.93b)$$

These crude approximations allow the C—C skeletal geometry variations to be simply estimated from the bond-order variations in Figs. 5.61 and 5.62.

Example 5.7 (below) illustrates how the variations in Figs. 5.61–5.63 can be related through the approximate relationship (5.92) that expresses the composition

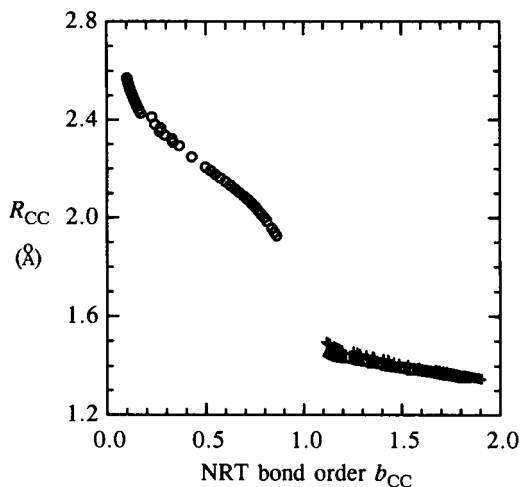


Figure 5.63 The NRT bond-order–bond-length correlations for C₁—C₂ (triangles), C₂—C₃ (squares), C₁—C₅ (circles), and C₅—C₆ (plus signs) bonds in the model Diels–Alder reaction (see Fig. 5.59(a) for the atom numbering).

of the resonance hybrid along the IRC. Together with a picture of the interacting reactant-like and product-like NBOs (Figs. 5.58 and 5.59), these combined approximations lead to a useful qualitative description of key bond lengths and angles that govern transition-state stabilization and “allowed” passage along the IRC.

Example 5.7

Problem: Use the approximations (5.91)–(5.93) to estimate the Diels–Alder R_{CC} bond lengths at $s = 0.5$.

Solution: From the estimate (5.92) we obtain

$$w_P(s = 0.5) = 0.5 + \frac{\tan^{-1}(0.5)}{\pi} = 0.5 + \frac{0.4636}{3.1416} = 0.65$$

From Eqs. (5.91a)–(5.91c), the corresponding bond orders are

$$\begin{aligned} b_{1,2} &= 1.35 \\ b_{2,3} &= b_{5,6} = 1.65 \\ b_{1,5} &= b_{4,6} = 0.65 \end{aligned}$$

The bond-order–bond-length relations (5.93a) and (5.93b) therefore predict

$$\begin{aligned} R_{1,2} &= 1.38 \text{ \AA} && (\text{actual: } 1.38 \text{ \AA}) \\ R_{2,3} &= R_{5,6} = 1.44 \text{ \AA} && (\text{actual } R_{2,3} = 1.41 \text{ \AA}, R_{5,6} = 1.42 \text{ \AA}) \\ R_{1,5} &= R_{4,6} = 2.11 \text{ \AA} && (\text{actual: } 2.15 \text{ \AA}) \end{aligned}$$

The simple approximations (5.91)–(5.93) give a reasonable qualitative description of Diels–Alder bond orders and bond lengths over the range of IRC values shown in Fig. 5.60, showing that the changes in geometry leading to the transition-state complex are effectively governed by a *single* resonance-hybrid composition parameter w_P .

5.5 Coupling of intramolecular and intermolecular interactions

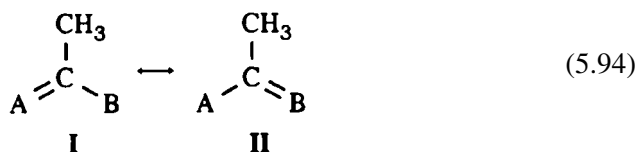
5.5.1 The theory of resonance-assisted coupling of H-bonding and torsions

The preceding Section 5.4 dealt with limiting transition-state complexes in which interacting monomers are severely distorted and electronically rearranged from their isolated forms. Nevertheless, in stable equilibrium complexes the perturbation of monomer properties due to intermolecular interactions is often considered to be negligible (as is explicitly assumed, e.g., in the London long-range theory; Section 5.1.3). Authors of earlier studies (Sections 5.2 and 5.3) therefore tended to ignore intramolecular effects of supramolecular complexation, except those involving monomer bonds whose NBOs are most active participants in intermolecular

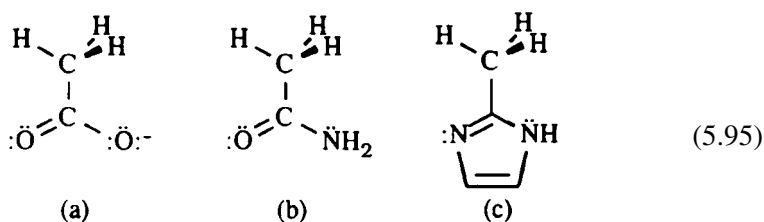
charge delocalization. In the present section we discuss some surprising effects of supramolecular complexation on monomer properties that might appear to be well insulated from such perturbations.

As described in Section 3.4.2, the intramolecular couplings between torsions and vibrations are principally due to hyperconjugative NBO donor–acceptor interactions that are conveniently expressed in the language of resonance theory. The intermolecular donor–acceptor interactions of H-bonding can also be formulated in resonance language (see, e.g., (5.29a) or (5.72)). Thus, couplings between intramolecular and intermolecular interaction modes should also be describable in resonance-theoretic terms, with increased strength for monomers exhibiting increased resonance delocalization.

A particularly interesting sensitivity to intermolecular interactions occurs when a torsional group (e.g., R = CH₃) is attached to the central atom of a resonance-stabilized allylic-like system,

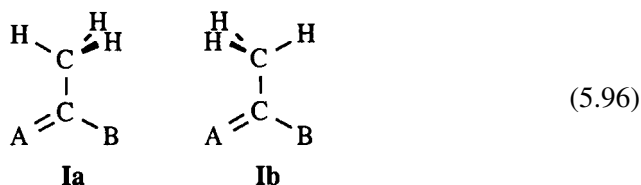


Examples of this motif include the carboxylate, amide, and imidazole derivatives shown below:

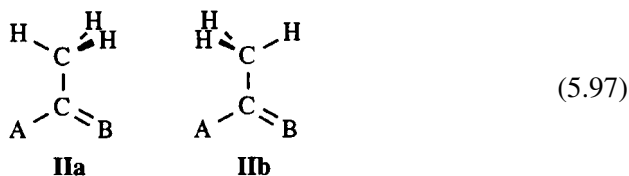


These moieties (particularly (5.95b)) are prominent in protein chemistry, and mechanisms for controlling their torsional stiffness have obvious potential implications for protein-folding processes.

As described in Section 3.4.2, hyperconjugative donor–acceptor stabilizations favor conformers in which one of the rotor C—H bonds eclipses an adjacent double bond. (This is equivalent to an ethane-like *staggered* preference if the double bond is pictured in terms of two bent “banana bonds.”) Hence, in the case of a perfectly localized Lewis structure **I**, the methyl group would be expected to adopt the preferred “pseudo-*cis*” conformation **Ia** (with in-plane C—H *syn* to A=C),



whereas localized structure **II** would prefer the “pseudo-*trans*” conformation **IIb**,



The rotation barrier ($\Delta E_{\text{rb}}^{(\text{I})}$) for structure **I**,

$$\Delta E_{\text{rb}}^{(\text{I})} = E(\text{Ib}) - E(\text{Ia}) \quad (5.98)$$

and that ($\Delta E_{\text{rb}}^{(\text{II})}$) for structure **II**,

$$\Delta E_{\text{rb}}^{(\text{II})} = E(\text{IIa}) - E(\text{IIb}) \quad (5.99)$$

might both be expected to be similar to those (1–2 kcal mol⁻¹) of the propene derivatives discussed in Section 3.4.1.

However, in the limit of equal resonance weights ($w_{\text{I}} = w_{\text{II}}$) in the resonance hybrid (5.94), the rotameric forms **Ia** and **IIa** or **Ib** and **IIb** become *equivalent*, and the rotation barrier ($\Delta E_{\text{rb}}^{(\text{hyb})}$) of the resonance hybrid is expected to vanish,⁹⁶

$$\Delta E_{\text{rb}}^{(\text{hyb})} \simeq 0 \quad (5.100)$$

More generally, for unequal weightings ($w_{\text{I}} \neq w_{\text{II}}$) we may expect the rotation barrier to be approximated by

$$\Delta E_{\text{rb}}^{(\text{hyb})}(w_{\text{I}}, w_{\text{II}}) \simeq |w_{\text{I}} - w_{\text{II}}|(w_{\text{I}} \Delta E_{\text{rb}}^{(\text{I})} + w_{\text{II}} \Delta E_{\text{rb}}^{(\text{II})}) \quad (5.101a)$$

or, equivalently,

$$\Delta E_{\text{rb}}^{(\text{hyb})}(w_{\text{I}}, w_{\text{II}}) \simeq \Delta b \Delta E_{\text{rb}}^{(\text{av})} \quad (5.101b)$$

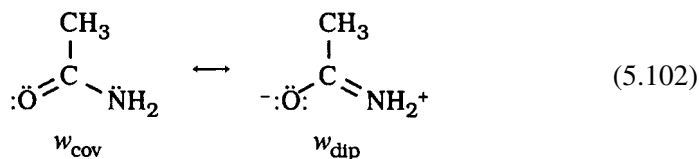
where $\Delta b = |b_{\text{AC}} - b_{\text{BC}}| \simeq |w_{\text{I}} - w_{\text{II}}|$ is the (absolute) difference in NRT bond orders and $\Delta E_{\text{rb}}^{(\text{av})}$ is the resonance-average of barriers of the two localized structures.

According to (5.101) the rotation barrier varies linearly with the shift in resonance weights (or bond orders) on going from one resonance form to the other. Thus, resonance hybrids with particular sensitivity to intermolecular interactions (such as resonance-assisted H-bonds, Section 5.2.3) can be expected to exhibit strong

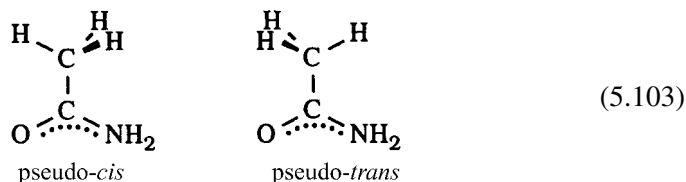
variations in the stiffness of adjacent torsional bonds with changes of solvation or complexation. (Of course, H-bonding will also alter bond lengths and charges in the resonating $A=C-B \longleftrightarrow A-C=B$ moiety, but the more distant couplings to torsional groups are of primary interest in this section.)

5.5.2 Hydrogen-bond modulation of torsion barriers in amides

As a simple example of the influence of H-bonding on torsions, let us consider the methyl torsions in the acetamide molecule (5.95b). By bringing various H-bonding species into complexation with the carbonyl oxygen and/or amine group of the amide moiety, we can alter the relative weightings of covalent (w_{cov}) versus dipolar (w_{dip}) amide resonance forms,



and thereby raise or lower the barrier ΔE_{rb} to torsions of the methyl group (or other alkyl substituents at the C_α position). In fact, by sufficiently *reversing* the relative weightings w_{cov} and w_{dip} , we expect to reverse the *preference* of the methyl rotor for the pseudo-*cis* or pseudo-*trans* conformation,



To be specific, let us define

$$\Delta E_{\text{rb}} \equiv E(\text{pseudo-trans}) - E(\text{pseudo-cis}) \quad (5.104)$$

With this definition, the switch in conformational preference is reflected in the sign of ΔE_{rb} :

$$\Delta E_{\text{rb}} > 0 \quad \text{for } w_{\text{cov}} \gg w_{\text{dip}} \quad (5.105a)$$

$$\Delta E_{\text{rb}} < 0 \quad \text{for } w_{\text{cov}} \ll w_{\text{dip}} \quad (5.105b)$$

Figure 5.64 displays optimized structures for a variety of acetamide $\cdots X$ complexes, with X chosen from common ionic ($X = \text{H}^+$, OH^- , NH_4^+) and neutral ($X = \text{H}_2\text{O}$ monomer and dimer, HCOOH , acetamide) complexing agents. Distinct isomers are possible in several cases, such as those for O-protonation (Fig. 5.64(a))

or N-protonation (Fig. 5.64(k)), and those for H_2O acting as a Lewis base (Fig. 5.64(h)) or as a Lewis acid toward O (Fig. 5.64(f)) or N (Fig. 5.64(j)). In the case of the hypothetical “acetamide $\cdots \text{OH}^-$ ” complex (Fig. 5.64(b)), an amide proton spontaneously transfers to OH^- to form a water \cdots imide complex, but this retains the fundamental allylic-like resonance motif “seen” by the methyl rotor. Only in the case of N-protonated acetamide (Fig. 5.64(k)) is this motif fully quenched by removal of the n_{N} from conjugation with π_{CO}^* .

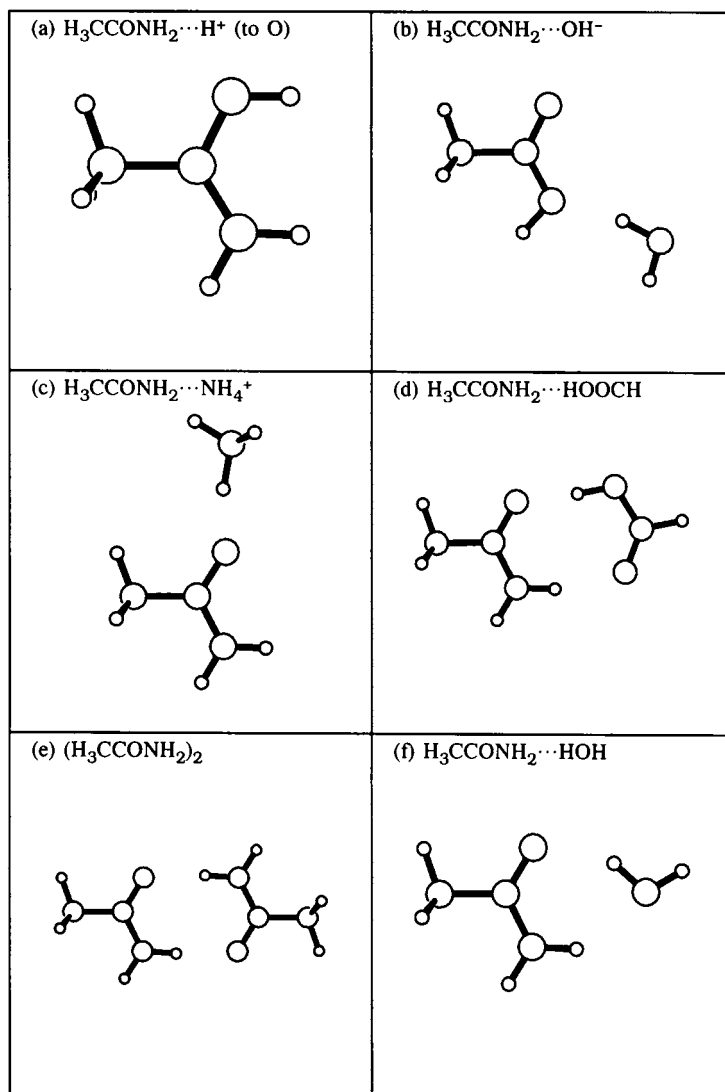


Figure 5.64 Hydrogen-bonded and fully protonated acetamide complexes, showing the optimized pseudo-*cis* conformer for each species.

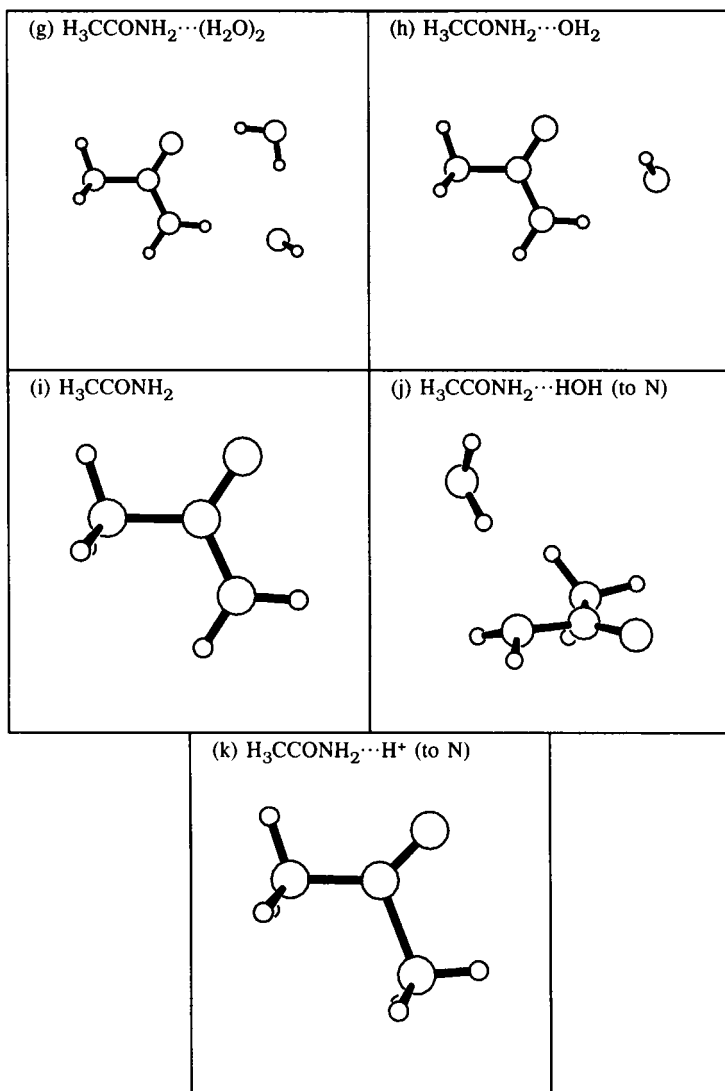


Figure 5.64 (Cont.)

Each complex in Fig. 5.64 is shown with the methyl rotor in the pseudo-*cis* (PC) conformation; the corresponding pseudo-*trans* (PT) conformers have similar appearance, except for the 60° methyl rotation. The displayed PC conformer represents a top-of-barrier transition state for complexes (a)–(i) in Fig. 5.64, but is the stable equilibrium geometry for complexes (j) and (k).⁹⁷

The complexes in Figs. 5.64(a)–(i) are ordered according to the algebraic value of ΔE_{rb} , as shown in Table 5.27 (with values expressed in wavenumbers; $1 \text{ kcal mol}^{-1} = 350 \text{ cm}^{-1}$). Table 5.27 also includes the amide CO/CN bond lengths

Table 5.27. Methyl rotation barriers ΔE_{rb} for various H-bonded and protonated acetamide $\cdots X$ complexes (cf. Fig. 5.64), with comparison NRT bond orders b_{CO} and b_{CN} and bond lengths R_{CO} and R_{CN} of the amide moiety in each complex

	X	ΔE_{rb} (cm ⁻¹)	b_{CO}	b_{CN}	R_{CO} (Å)	R_{CN} (Å)
(a)	H ⁺ (to O)	-418	1.397	1.580	1.298	1.310
(b)	OH ⁻	-232	1.531	1.506	1.250	1.330
(c)	NH ₄ ⁺	-183	1.555	1.445	1.248	1.337
(d)	HCOOH	-140	1.595	1.412	1.237	1.347
(e)	OC(CH ₃)NH ₂	-129	1.611	1.400	1.233	1.351
(f)	HOH	-111	1.654	1.357	1.229	1.357
(g)	(H ₂ O) ₂	-97	1.677	1.336	1.223	1.362
(h)	OH ₂	-95	1.680	1.334	1.225	1.362
(i)	(free)	-65	1.715	1.301	1.218	1.369
(j)	HOH (to N)	+72	1.745	1.264	1.214	1.390
(k)	H ⁺ (to N)	+235	2.283	0.682	1.167	1.652

and NRT bond orders for all complexes. The barriers are seen to vary over a total range of about 650 cm⁻¹ (~2.7 times kT under normal ambient conditions) from the most PT-favored to PC-favored species. However, for PT-favored complexes alone, the barrier height increases from the low value for free acetamide (65 cm⁻¹) to about 230 cm⁻¹ for the OH⁻ complex, corresponding to an overall H-bond-induced increase in barrier height of about 170 cm⁻¹ for this conformer. The H-bond interactions are accompanied by variations of ~0.2 in individual CO/CN bond orders, in accord with the RAHB phenomenon discussed in Section 5.2.3.

The intimate connection between methyl torsional stiffening and the variation in amide CO/CN bond orders is illustrated in Fig. 5.65. This plot shows that the methyl rotation barrier ΔE_{rb} varies roughly *linearly* with the difference Δb in CO/CN bond orders,

$$\Delta E_{\text{rb}} (\text{cm}^{-1}) = 360 \Delta b - 230 \quad (5.106)$$

in accordance with Eq. (5.101b). The slope of this line (360 cm⁻¹ per bond) corresponds approximately to the barrier height in the limit of ideally localized C=O/C—N or C—O/C=N amide bonds.

Figure 5.65 provides theoretical evidence that resonance-assisted H-bonding can serve as an effective mechanism for *switching* a methyl rotor from one preferred conformation to another, or for controlling the stiffness of torsional motions in alkylated amides. In particular, the torsional potentials of proteins (more specifically, the Ramachandran ψ angle at C_α) should be sensitive to N—H \cdots O and related H-bonding interactions involving the amide backbone. In principle, this electronic

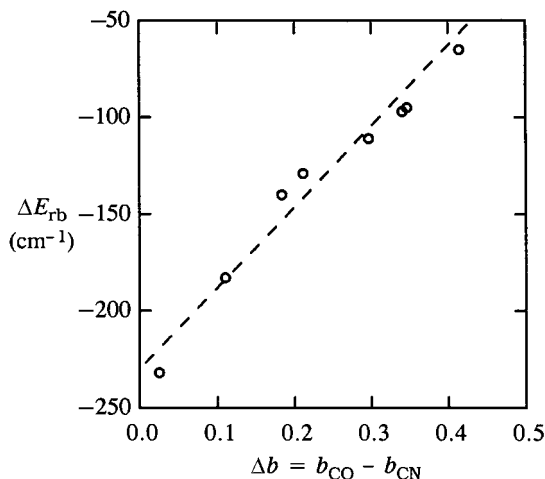


Figure 5.65 The dependence of the acetamide methyl-rotation barrier (ΔE_{rb}) on NRT bond-order differences in the amide group ($\Delta b = b_{CO} - b_{CN}$) for various H-bonded complexes of the pseudo-*cis* ($\phi_{OCCH(in)} = 0^\circ$) rotamer (see Table 5.27). The dashed line (of slope 360 cm^{-1} per bond) shows the approximate trend of the data points.

effect allows protein-backbone torsions to be “steered” by local H-bond patterns toward successful folding shapes, which is possibly an important mechanistic feature of complex protein-folding pathways. Direct experimental evidence for (or against) this interesting coupling effect would be highly desirable.

Further evidence for H-bond-induced resonance shifts and NRT bond-order–bond-length correlations is presented in Fig. 5.66. As shown in this figure, the calculated bond orders b_{CO} and b_{CN} are highly correlated with corresponding optimized values of R_{CO} and R_{CN} in all the H-bonded acetamide $\cdots X$ complexes. For all the H-bonded complexes (b)–(j) these correlations are rather accurately expressed by the linear equations

$$R_{CO} = -0.168b_{CO} + 1.508 \quad (5.107a)$$

$$R_{CN} = -0.211b_{CN} + 1.644 \quad (5.107b)$$

Furthermore, the sum of amide bond orders b_{CO} and b_{CN} is essentially *constant* (to within better than 1%),

$$b_{CO} + b_{CN} \simeq 3.00 \quad (5.108)$$

as would be expected from their mutual dependence on the relative weighting of resonance structures in (5.102). Thus, the changes in amide geometry and C_α torsional variations in acetamide $\cdots X$ complexes seem to be very satisfactorily described with a *single* measure of the amide resonance weighting in (5.102), which in turn depends on the strength of RAHB coupling as described in Section 5.2.3.

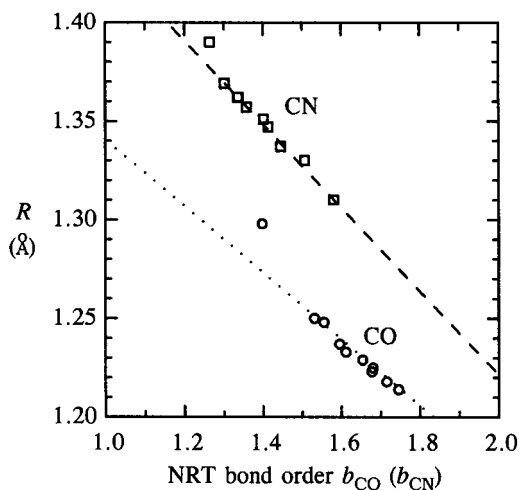


Figure 5.66 Bond-order–bond-length correlations for amide CO (circles) and CN (squares) bonds in the acetamide $\cdots X$ complexes of Fig. 5.64 (see Table 5.27). The dotted and dashed lines correspond to Eqs. (5.107a) and (5.107b), respectively.

Example 5.8

Problem: What is the critical weighting w_{dip} of the alternative dipolar amide resonance structure in (5.102) that would *reverse* the preference for pseudo-*cis* over pseudo-*trans* geometry at C_α ? What are the corresponding bond lengths R_{CO} and R_{CN} at this critical resonance weighting?

Solution: According to Eq. (5.106), ΔE_{rb} changes sign (vanishes) when

$$\Delta b = 230/360 = 0.639$$

which can be related to w_{dip} through the equation

$$\Delta b = b_{\text{CO}} - b_{\text{CN}} = w_{\text{cov}} - w_{\text{dip}} = 1 - 2w_{\text{dip}}$$

The critical resonance weighting is therefore

$$w_{\text{dip}} = (1 - \Delta b)/2 = 0.361/2 = 0.181$$

From general bond-order concepts we can also write

$$b_{\text{CO}} = 2w_{\text{cov}} + w_{\text{dip}} = 2(1 - w_{\text{dip}}) + w_{\text{dip}} = 1.819$$

$$b_{\text{CN}} = w_{\text{cov}} + 2w_{\text{dip}} = (1 - w_{\text{dip}}) + 2w_{\text{dip}} = 1.181$$

From the bond-order–bond-length correlations (5.107), we obtain finally

$$R_{\text{CO}} = -0.168(1.819) + 1.508 = 1.202 \text{ \AA}$$

$$R_{\text{CN}} = -0.211(1.181) + 1.644 = 1.395 \text{ \AA}$$

In the foregoing we have emphasized the role of H-bonding in modulating or switching the amide C—C $_{\alpha}$ torsion barrier. However, a similar effect can be achieved by any perturbation that shifts the relative weighting of resonance forms w_{cov} and w_{dip} in (5.102). In particular, pyramidalization or twisting of the —NH₂ group out of coplanarity with C=O will sharply diminish $n_{\text{N}} \rightarrow \pi_{\text{CO}}^*$ delocalization, increasing w_{cov} relative to w_{dip} and driving C—C $_{\alpha}$ torsions toward the pseudo-*cis* geometry (cf. Example 5.8). Such nonplanar distortions of the amide moiety might result from a steric or other geometrical constraint (e.g., buckling of a proline ring) as well as H-bonding to n_{N} . Thus, opportunities for controlling torsional (folding) processes through remote electronic or structural influences are realized to an extravagant degree in amides.

The resonance-mediated coupling mechanisms described above involve subtle quantal intramolecular/intermolecular donor–acceptor effects that tend to be inadequately described by current-generation empirical potentials. “Simulations” based on these potentials are therefore likely to be inherently defective for describing realistic folding processes in proteins. However, approximations such as those illustrated in Example 5.8 may ultimately make it feasible to incorporate additional resonance-mediated effects into empirical force fields of tractable form.

5.6 Summary

The concept of the molecule as primary building block of matter is deeply imbued in chemists, who often define their discipline as “the study of molecules.” Yet the existence of reactant, product, and other molecular isomeric forms on the *same* potential-energy surface warns that the molecular concept must have fuzzy boundaries at the quantum-mechanical level. Only in the London long-range limit of negligible exchange interactions can a rigid distinction between “intramolecular” and “intermolecular” regimes be upheld.

At shorter distances, particularly those characteristic of H-bonded and other charge-transfer complexes, the concepts of partial covalency, resonance, and “chemical” forces must be extended to *supramolecular* species. In such cases the distinction between, e.g., the “covalent bond” and the “H-bond” may become completely arbitrary. The concept of supramolecular clusters as fundamental chemical units presents challenges both to theory and to standard methods of structural characterization. Fortunately, the quantal theory of donor–acceptor interactions follows parallel lines for intramolecular and intermolecular cases, allowing seamless description of molecular and supramolecular bonding in a unified conceptual framework. In this sense, supramolecular aggregation under ambient thermal conditions should be considered a true chemical phenomenon.

Because of its pervasive influence in solution-phase and biophysical phenomena, *hydrogen-bonding* plays a particularly important role in the theory of supramolecular aggregation. Compared with fully formed covalent bonds, H-bonds exhibit a lower degree of transferability and bond-energy additivity, and, thus, higher sensitivity to environmental influences such as the pattern of surrounding H-bonds. Such non-additive cooperative or anticooperative aspects of H-bonded clusters confer the capacity for *nonlinear* responses that are strikingly more complex than those of single molecules. The complex nonlinearities of H-bonded clusters doubtless underlie their pervasive role in life processes.

Mulliken's general concept of *charge-transfer complexes* can be given explicit and quantitative reformulation in the NBO framework. This allows one to recognize the essential electronic continuity that relates CT complexes of different "types," including H-bonded species ($n-\sigma^*$ CT complexes). Particular attention was paid to the interesting $\pi-\pi^*$ CT complexes of NO^+ and related pi-acids, which exemplify the distinctive quantal dependence on the shapes of donor and acceptor orbitals.

The unique intermediate character of *transition-state complexes* allows these species to be analyzed as cases of supramolecular bonding for *two distinct* limiting sets of molecular units (reactant-like or product-like). In either limit, stabilizing donor-acceptor interactions of the transition-state complex can be related to selection rules (of Woodward-Hoffmann type) for successful low-energy passage-ways from reactant to product channels on the adiabatic potential-energy surface. Topological *and* geometrical criteria for optimal NBO donor-acceptor interactions provide a localized extension of the conventional Woodward-Hoffmann rules for pericyclic reactions.

The close relationship between intramolecular and intermolecular donor-acceptor interactions, as well as their convenient mutual description in resonance terms, allows one to identify possible resonance-assisted *coupling* mechanisms that enable intramolecular structure and dynamics to be controlled by intermolecular coordination (and vice versa). A particularly interesting example involves H-bond *switching* of the equilibrium $\text{C}-\text{C}_\alpha$ (ψ) rotation angle of peptides, as well as H-bond control of the rotation-barrier height for either conformer. Such H-bond-induced switching mechanisms may underlie the complex folding pathways of biological proteins.

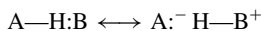
The examples cited in this chapter are but a rather small and arbitrary selection from the richly varied possibilities for supramolecular bonding. Recognition of the intrinsic *chemical* (partially covalent, exchange-type) character of supramolecular interactions leads inevitably to an extended definition of "chemistry" that includes many aspects of nanoscale aggregation, structure, and function in the biophysical and material-science domains. From this viewpoint, the molecule is seen to be

but one plateau in a hierarchy of chemical units leading from isolated atoms to aggregated clusters and superclusters at mesoscopic and macroscopic scales.

Notes for Chapter 5

1. According to the *Oxford English Dictionary*, the word “molecule” seems to have arisen in the seventeenth century in the discussions initiated by the physical speculations of Descartes. Early formal definitions described a molecule as “a group of atoms mechanically indivisible” (H. E. Roscoe, *Elementary Chemistry* [1871], p. 169) or “a group of atoms drawn and held together by what chemists call affinity” (J. Tyndall, *Longm. Mag.* **1** [1882], 30).
2. *Encyclopedia Britannica* (1949 edition), entry for “molecule.”
3. For a general non-adiabatic wavefunction, the average (expectation) values of nuclear coordinates can similarly serve to define the “point” on the “surface.”
4. In the latter case, the calculated net charge of each molecular unit need not be an integer. However, each molecular unit can still be assigned *idealized* integer charge corresponding to full integer occupancy of each NBO, i.e., to the localized $|\psi_{\text{NBO}}|^2$ natural-Lewis-structure description (Section 1.5).
5. The term “hydrogen bond” was used by Pauling in 1931 to describe the FHF^- species, replacing the earlier term “hydrogen bridging” for this general phenomenon. See the interesting historical discussion in G. A. Jeffrey, *An Introduction to Hydrogen Bonding* (New York, Oxford University Press, 1997), pp. 2–6.
6. A. S. Coolidge, *J. Am. Chem. Soc.* **50** (1928), 2166; J. W. Stout and L. H. Fisher, *J. Chem. Phys.* **9** (1941), 163; R. C. Millikan and K. S. Pitzer, *J. Am. Chem. Soc.* **80** (1958), 3515; J. E. Bertie and K. H. Michaelian, *J. Chem. Phys.* **76** (1982), 886; and M. A. Wendt, T. C. Farrar, and F. Weinhold, *J. Chem. Phys.* **109** (1998), 5945.
7. R. S. Mulliken and W. B. Person, *Molecular Complexes. A Lecture and Reprint Volume* (New York, Wiley, 1969).
8. O. Hassell, “Structural aspects of interatomic charge-transfer bonding,” in *Nobel Lectures: Chemistry 1963–1970* (New York, Elsevier, 1972), pp. 295–331.
9. R. Steudel, *Angew. Chem.* **24** (1985), 59; *Z. Naturf.* **B43** (1988), 581; “Elemental sulfur and related homocyclic compounds” in *Studies in Inorganic Chemistry*, Vol. 5 (New York, Elsevier, 1984), pp. 3–37.
10. J. D. Corbett, S. C. Crichtlow, and R. C. Burns, *Rings, Clusters, and Polymers of the Main Group Elements* (Washington, American Chemical Society, 1983), p. 95; and J. D. Corbett, *Chem. Rev.* **85** (1985), 383.
11. At lower temperatures, weaker intercluster interactions may lead to further aggregation into *superclusters* (clusters of clusters). In this manner the “unit” at one temperature becomes the subunit at a lower temperature, leading to a hierarchy of organizational levels. Clusters and superclusters may underlie the properties of many amorphous solids and glasses, but such materials are beyond the scope of the present work.
12. F. Weinhold, *J. Chem. Phys.* **109** (1998), 367 and 373.
13. W. M. Latimer and W. H. Rodebush, *J. Am. Chem. Soc.* **42** (1920), 1419. This paper is often cited as the discovery of H-bonding (but see Jeffrey, note 5). Its title, “Polarity and ionization from the standpoint of the Lewis theory of valence,” reflects the strong influence of G. N. Lewis on all aspects of the early development of H-bond theory.
14. G. N. Lewis, *Valence and the Structure of Atoms and Molecules* (New York, Chemical Catalog Co., 1923).
15. L. Pauling, *Proc. Nat. Acad. Sci. U.S.A.* **14** (1928), 359; and L. Pauling, *J. Am. Chem. Soc.* **53** (1931), 1367.
16. L. Pauling, *Nature of the Chemical Bond*, 2nd edn. (Ithaca, Cornell University Press, NY, 1948), p. 284.

17. Pauling later expressed the view that partial covalency or “ionic–covalent-resonance” contributions of the form



are indeed important. This should be contrasted to the more primitive electrostatic picture that attributes H-bonding to the dipole–dipole (and higher-multipole) interactions between *neutral* monomers, without significant charge-transfer ($A:^- H-B^+$) character.

18. E. D. Isaacs, A. Shukla, P. M. Platzman *et al.*, *Phys. Rev. Lett.* **82** (1999), 600; and *Science* **283** (29 January 1999).
19. I. G. Shenderovich, S. N. Smirnov, G. S. Denisov *et al.*, *Ber. Bunsenges. Phys. Chem.* **102** (1998), 422; M. F. Summers, *J. Am. Chem. Soc.* **114** (1992), 4931; K. Wütrich, *Proc. Natl. Acad. Sci. U.S.A.* **95** (1998), 14 147; G. Cornilescu, J.-S. Hu, and A. Bax, *J. Am. Chem. Soc.* **121** (1999), 2949; and Y.-X. Wang, J. Jacob, F. Cordier *et al.*, *J. Biomol. NMR* **14** (1999), 181.
20. G. C. Pimentel and A. L. McClellan, *The Hydrogen Bond* (San Francisco, CA, W. H. Freeman, 1960).
21. Formic acid is notorious for decomposing, so a laboratory sample prepared as pure (5.6a) will, on a fairly short time scale, show evidence of other “decomposition products” (5.6b)–(5.6d) that contribute to the stationary eigenstate of (5.5).
22. Because classical electrostatic effects are incorporated in $\hat{H}^{(0)}$, the quantal $V^{(\text{int})}$ (representing delocalization between units) may be zero in this case.
23. F. London, *Z. Physik. Chem.* **B11** (1930), 222; R. Eisenschitz and F. London, *Z. Phys.* **60** (1930), 491; and F. London, *Trans. Faraday Soc.* **33** (1937), 8.
24. This follows from the elementary theorem that the eigenfunctions of any Hermitian operator are (or can be taken to be) orthogonal. For a more complete discussion of the pathologies associated with non-orthogonality and neglect of exchange interactions, see F. Weinhold and J. E. Carpenter, *J. Mol. Struct. (Theochem)* **165** (1988), 189. See also the discussion of PMO theory surrounding Examples 3.17 and 3.18 in Section 3.4.2.
25. J. O. Hirschfelder, C. F. Curtiss, and R. B. Bird, *Molecular Theory of Gases and Liquids* (New York, Wiley, 1954; corrected printing 1964).
26. Note 25, p. 993.
27. See note 25.
28. See note 25.
29. H. B. G. Casimir and D. Polder, *Phys. Rev.* **73** (1948), 360.
30. E. J. W. Verwey, J. T. G. Overbeek, and K. van Nee, *Theory of Stability of Lyophobic Colloids* (Amsterdam, Elsevier, 1948).
31. Of course, from an empirical viewpoint there is an unlimited number of multipole and polarizability fitting parameters that can make such short-range continuations of (5.23)–(5.26) appear to “work” for a restricted set of properties and range of R .
32. E. D. Glendening and A. Streitwieser Jr., *J. Chem. Phys.* **100** (1994), 2900; and E. D. Glendening, *J. Am. Chem. Soc.* **188** (1996), 2473.
33. W. C. Hamilton and J. A. Ibers, *Hydrogen Bonding in Solids* (New York, W. A. Benjamin, 1968), p. 16.
34. C. A. Coulson, *Research* **10** (1957), 149.
35. W. M. Latimer and W. H. Rodebush, *J. Am. Chem. Soc.* **42** (1920), 1419.
36. Of course, the n_B , σ_{AH} , and σ_{AH}^* NBOs of the H-bonding region are important contributors to the dipole, quadrupole, and higher-multipole moments of the monomers. Thus, certain multipoles may appear to “explain” the geometry through their close connections to these NBOs, but this is not an incisive way to describe the physical situation.
37. As calculated by natural steric analysis (Section 1.7), ΔE_{steric} declines from its long-range asymptotic limit to make a weak oscillation inside 3.0 Å, ending in a weak minimum at ~ 2.4 Å before the final steep exponential growth. For present purposes, this minimum was set to be the “zero” for plotting ΔE_{steric} , and only the shorter-range behavior is plotted in the figure.
38. A. E. Reed, F. Weinhold, L. A. Curtiss, and D. Pochatko, *J. Chem. Phys.* **84** (1986), 5687.

39. L. A. Curtiss, D. J. Pochatko, A. E. Reed, and F. Weinhold, *J. Chem. Phys.* **82** (1985), 2679. For experimental studies of $\text{FH} \cdots \text{CO}$, see A. C. Legon, P. D. Soper, and W. H. Flygare, *J. Chem. Phys.* **74** (1981), 4944.
40. The curious reversal from the C^+O^- polarity expected on electronegativity grounds may be attributed to the formal charges (C^- and O^+) that are associated with the usual triple-bonded Lewis-structure formula.
41. F. Weinhold, *J. Chem. Phys.* **109** (1998), 367 and 373.
42. A. E. Reed, F. Weinhold, L. A. Curtiss, and D. Pochatko, *J. Chem. Phys.* **84** (1986), 5687.
43. The C—H bond is generally regarded as a prototype apolar bond, and even the *sign* of the C—H bond dipole moment is a subject of considerable controversy: K. B. Wiberg and J. J. Wendolski, *J. Comput. Chem.* **2** (1981), 53; K. B. Wiberg and J. J. Wendolski, *J. Phys. Chem.* **88** (1984), 586; and A. E. Reed and F. Weinhold, *J. Chem. Phys.* **84** (1986), 2428.
44. For a more complete discussion of the phenomenon of blue-shifting, see I. V. Alabugin, M. Manoharan, S. Peabody, and F. Weinhold, *J. Am. Chem. Soc.* **125** (2003), 5973 and references therein.
45. G. F. Gilli, V. Belluci, V. Ferretti, and V. Bertolasi, *J. Am. Chem. Soc.* **111** (1989), 1023; and P. Gilli, V. Verretti, V. Bertolasi, and G. Gilli, *Adv. Mol. Struct. Res.* **2** (1995), 67.
46. See notes 5 and 13–15.
47. When the σ_{HF}^* acceptor NBO is removed from the variational calculation (by the \$DEL option), the $\text{F}^- \cdots \text{HF}$ species reoptimizes to a highly unsymmetric ($R_{\text{F}\cdots\text{H}} = 2.918 \text{ \AA}$, $r_{\text{HF}} = 0.907 \text{ \AA}$) ion–dipole complex that is bound by only 6.63 kcal mol⁻¹.
48. W. W. Cleland, *Biochemistry* **31** (1992), 317; W. W. Cleland and M. M. Kreevoy, *Science* **264** (1994), 1887; J. A. Gerlt and P. G. Gassman, *J. Am. Chem. Soc.* **115** (1993), 11 552; and P. A. Frey, S. A. Whitt, and J. B. Tobin, *Science* **264** (1994), 1927. For the contrary view based on classical electrostatics, see A. Warshel, A. Papazyan, and P. Kollman, *Science* **269** (1995), 102.
49. Because boron (B) atoms occur in formulas of this section, we employ the symbol “Y” (not yttrium!) for a generic Lewis base and “X” for a generic Lewis acid.
50. R. H. Crabtree, *Science* **282** (2000), 5396.
51. E. Debeer, E. H. Kim, D. M. Neumark, R. F. Gunion, and W. C. Lineberger, *J. Phys. Chem.* **99** (1995), 13 627.
52. R. S. Stevens, R. Bau, R. Milstein, O. Blum, and T. F. Koetzle, *J. Chem. Soc. Dalton Trans.* **1990** (1990), 1429; L. S. Van der Sluys, J. Eckert, O. Eisenstein *et al.*, *J. Am. Chem. Soc.* **112** (1990), 4831; A. J. Lough, S. Park, R. Ramachandran, and R. H. Morris, *J. Am. Chem. Soc.* **116** (1994), 8356; and R. H. Crabtree, P. E. M. Siegbahn, O. Eisenstein, A. L. Rheingold, and T. F. Koetzle, *Acc. Chem. Res.* **29** (1996), 348.
53. R. Custelcean and J. E. Jackson, *J. Am. Chem. Soc.* **120** (1998), 12 935.
54. See note 45.
55. J. Emsley, *Struct. Bonding* **57** (1984), 147.
56. In fact, the barrier for proton transfer in the maleate anion appears to lie *below* the zero-point vibrational energy level (W. M. Westler, private communication). Thus, vibrationally averaged properties of the maleate anion will correspond to a symmetrically bridged C_{2v} transition-state structure rather than to either of the asymmetrically bridged equilibrium structures in Fig. 5.22. For present purposes this interesting feature of the potential surface can be ignored.
57. See note 45.
58. Pauling, note 16, p. 85.
59. H. J. C. Berendsen, J. R. Grigera, and T. P. Straatsma, *J. Phys. Chem.* **91** (1987), 6269. This potential also includes a Lennard-Jones contribution (which mainly provides a repulsive core to prevent unphysical collapse), and so cannot be compared directly with the Coulombic point-charge potential in Eq. (5.56b).
60. Of course, the empirical point charges of an SPC-type model can always be chosen to make one or a few selected H-bonded clusters “come out right.” We therefore emphasize the *overall* quality of the description of H-bonded clusters of various sizes and topologies.
61. For this purpose we freeze each monomer in its geometry in the complex, so that only changes in *intermolecular* potential energy are involved. The “binding energies” $\mathcal{V}(\text{A}, \text{B})$ thus differ slightly from those with respect to fully relaxed monomers.

62. J. E. Lennard-Jones, *Proc. Roy. Soc.* **A106** (1924), 463; and note 25, p. 32.
63. Note that, due to their infinite-range character, pure Coulombic potentials can actually lead to significant bond non-additivity for any proposed separation into bonded and nonbonded units. This reflects the fact that classical electrostatics is oblivious to any perceived separation into chemical units, because *all* Coulombic pairings (whether in the “same” or “separate” units) make long-range contributions to the total interaction energy.
64. In fact, in the preferred cyclic geometry of Fig. 5.23(d) the orientation of adjacent dipoles is close ($<20^\circ$) to the perpendicular angle at which dipole–dipole forces are *vanishing*. The strong preference for cyclic clusters is thus quite perplexing from a classical dipole–dipole viewpoint.
65. On enthalpic grounds alone, under ambient conditions the Boltzmann factor for the chain pentamer would be reduced by about 10^{10} relative to that for the cyclic pentamer, showing that the former topology contributes negligibly to the equilibrium population distribution.
66. R. Ludwig, unpublished *Habilitationsschrift*, Universität Dortmund (1998), Chapter 8.
67. F. Weinhold, *J. Mol. Struct. (Theochem)*, WATOC 1996 Symposium Issue, **398–399** (1997), 181.
68. This essential absence of longer-range proton order in tetrahedral H-bond networks is the origin of the famous zero-point entropy of ice: L. Pauling, *J. Am. Chem. Soc.* **57** (1935), 2680; and L. Pauling, note 16, pp. 466–468.
69. A distribution of linearly coordinated ring and chain clusters can evidently shift incrementally (through elementary scission reactions of single H-bonds) from larger 5- and 6-rings (Fig. 5.29) to dimers (Fig. 5.5(b)), and finally to monomers. The latter limit is necessarily identified as the “gaseous” phase, which can thereby be connected to the “liquid” limit by a continuous set of incremental changes (above the gas–liquid critical point). However, no similar incremental changes could convert linearly coordinated clusters satisfying (F1)–(F3) into the disordered high-coordinate extended lattice that is characteristic of the ice-I solid phase. Thus, consistent with experiment, no solid–fluid critical point should exist beyond which the transition between these distinct cluster topologies could be continuous. Results of experiments strongly support the picture of proton-ordered, two-coordinate cluster structure in liquid water: P. Wernet, D. Nordlund, U. Bergmann *et al. Science* **304** (2004), 995.
70. G. A. Jeffrey and R. K. McMullan, *Prog. Inorg. Chem.* **8** (1967), 43; and G. A. Jeffrey, note 5, pp. 160–173. Studies of clathrate hydrates date to Davy and Faraday in the early nineteenth century: H. Davy, *Phil. Trans. Roy. Soc. London* **101** (1811), 155; and M. Faraday, *Quart. J. Sci.* **15** (1823), 71.
71. L. Pauling and R. E. Marsh, *Proc. Nat. Acad. Sci. U.S.A.* **36** (1952), 112; and L. Pauling, note 16, p. 473.
72. R. Ludwig and F. Weinhold, *J. Chem. Phys.* **1190** (1999), 508.
73. H. S. Frank and W.-Y. Wen, *Disc. Faraday Soc.* **24** (1957), 133; H. S. Frank, *Proc. Roy. Soc.* **A247** (1958), 481; and H. S. Frank and A. S. Quist, *J. Chem. Phys.* **34** (1961), 605.
74. As seen in Fig. 5.35, the highest TS barrier to proton transfer along the reaction coordinate lies significantly (>7 kcal mol $^{-1}$) below the energy of either reactant or product asymptote. Thus, unless trapped in the deep $\text{H}^- \cdots \text{H}_2\text{O}$ well, an H^- ion impinging on a water molecule will undergo spontaneous proton transfer to form $\text{H}_2 + \text{OH}^-$, without an apparent barrier.
75. The hydrogen 1s orbital encloses a positively charged nucleus that repels other nuclei by a Coulombic R^{-1} potential. However, such a Coulombic “barrier” between nuclei is much weaker than the steric repulsion between electronic cores, which varies *exponentially* with distance.
76. M. M. Szczesniak, Z. Latajka, P. Piechuch *et al.*, *Chem. Phys.* **94** (1985), 55; A. M. Sapse and P. v. R. Schleyer (eds.), *Lithium Chemistry* (New York, Wiley, 1995).
77. R. S. Mulliken, *J. Am. Chem. Soc.* **72** (1950), 600; R. S. Mulliken, *J. Am. Chem. Soc.* **74** (1952), 811; R. S. Mulliken, *J. Phys. Chem.* **56** (1952), 801; R. S. Mulliken, *J. Chem. Phys.* **23** (1955), 397; E. K. Plyler and R. S. Mulliken, *J. Am. Chem. Soc.* **81** (1959), 823; L. E. Orgel, *Quart. Rev. Chem. Soc.* **8** (1954), 422; and note 7.
78. G. Herzberg, *Molecular Spectra and Molecular Structure. III. Electronic Spectra and Electronic Structure of Polyatomic Molecules* (New York, Van Nostrand Reinhold, 1966), p. 427.
79. W. B. Jensen, *The Lewis Acid–Base Concepts: An Overview* (New York, John Wiley, 1980).
80. N. V. Sidgwick, *The Electronic Theory of Valency* (London, Oxford University Press, 1929), p. 116.

81. C. K. Ingold, *J. Chem. Soc.* **1933** (1933), 1120; and C. K. Ingold, *Chem. Rev.* **15** (1934), 225.
82. R. S. Mulliken, *J. Chem. Phys.* **56** (1952), 801. See also the appended discussion with H. C. Brown (pp. 821–822).
83. See the critical comments of H. C. Brown in note 82.
84. In particular, Mulliken wished to classify H-bonded species as “primarily electrostatic” (and thus not of the same type as $n-\sigma^*$ CT complexes) and his classification scheme often seems to suggest distinct electronic mechanisms for distinct “types” of CT complexes. In contrast, NBO analysis shows that H-bonded species fall clearly within the category of $n-\sigma^*$ CT complexes and suggests the unifying *commonality* of donor–acceptor types (though with varying background contributions of electrostatic or steric origin). The NBO viewpoint is therefore much closer to that expressed by Brown (see note 82) or Herzberg (note 78).
85. For other computational and experimental studies of NO^+ complexation, see K. Raghavachari, W. D. Reents Jr., and R. C. Haddon, *J. Comput. Chem.* **7** (1986), 265; N. V. Zyk, E. E. Nesterov, A. N. Khlobystov *et al.*, *J. Org. Chem.* **64** (1999), 7121; J. H. Atherton, R. B. Moodie, and D. R. Noble, *J. Chem. Soc. Perkin Trans. 2* (2000), 229; and G. Borodkin, I. R. Elanov, V. A. Podryvanov, and M. M. Shakirov, *J. Am. Chem. Soc.* **117** (1995), 12 863.
86. It should be noted that DFT methods such as B3LYP appear to be quantitatively less reliable in describing the unusual charge reorganizations of strong π^* complexes (compared, e.g., with *ab initio* MP2 description). However, the HF, MP2, and DFT descriptions of the π^* complexes are in satisfactory qualitative agreement for the main structural features discussed below. We therefore continue to employ the B3LYP/6-311 ++G** description for consistency with the other numerical examples of this book.
87. E. K. Kim, and J. K. Kochi, *J. Am. Chem. Soc.* **113** (1991), 4962; E. Bosch and J. K. Kochi, *Res. Chem. Intermed.* **22** (1996), 209.
88. T. L. Cairns, R. A. Carboni, D. D. Coffman *et al.*, *J. Am. Chem. Soc.* **80** (1958), 2775; M. L. Smith and J. L. McHale, *J. Phys. Chem.* **89** (1985), 4002; Y. Kimura, Y. Takebayashi, and N. Hirota, *Chem. Phys. Lett.* **257** (1996), 429; F. Markel, N. S. Ferris, I. R. Gould, and A. B. Myers, *J. Am. Chem. Soc.* **114** (1992), 6208; W. Jarzaba, S. Murata, and M. Tachiya, *Chem. Phys. Lett.* **301** (1999), 347; K. Wynne, G. D. Reid, and R. M. Hochstrasser, *J. Chem. Phys.* **105** (1996), 2287; T. Kim, H. Sarker, and N. L. Bauld, *J. Chem. Soc. Perkin Trans. 2* (1995), 557; and R. B. King, M. K. Johnson, D. M. Kurtz *et al.*, *Electron Transfer in Biology and the Solid State* (London, Oxford University Press, 2000).
89. Note that the complexes in Figs. 5.64(a)–(i) have a plane of symmetry that makes it easy to locate both PC and PT stationary points. In contrast, the rotameric transition states for low-symmetry complexes involving the nitrogen lone pair (such as Fig. 5.64(j)) are often challenging. W. Koch, G. Frenking, J. Gauss, D. Cremer, and J. R. Collins, *J. Am. Chem. Soc.* **109** (1987), 5917.
90. H. Eyring, *J. Chem. Phys.* **3** (1935), 107; and S. Glasstone, K. J. Laidler, and H. Eyring, *Theory of Rate Processes* (New York, McGraw-Hill, 1941).
91. The IRC in mass-weighted internal coordinates ($\text{amu}^{1/2}$ bohr) is determined by the method of C. Gonzalez and H. B. Schlegel, *J. Phys. Chem.* **94** (1990), 5523.
92. Equation (5.86c), written as a strict equality, may also be taken to define the “NRT transition state” as an alternative to (and slightly different from) the usual definitions based on energetic, saddle-point-curvature, or density-of-states criteria. Note that this NRT alternative definition can be employed for non-IRC choices of reaction coordinate, and remains valid even in the case of *barrierless* processes (such as many ion–molecule or radical-recombination reactions) for which the reaction profile does not exhibit an energy maximum as in Fig. 5.52. The NRT definition is practically identical to the usual saddle-point definition of the transition state in the present examples.
93. A. Pross and S. S. Shaik, *Acc. Chem. Res.* **16** (1983), 363; and S. Shaik and A. Shurki, *Angew. Chem. Int. Edn. Engl.* **38** (1999), 586.
94. The Woodward–Hoffmann rules have intellectual roots that can be traced back to Wigner–Witmer correlation rules (E. Wigner and E. E. Witmer, *Z. Phys.* **51** [1928], 859) and general correlation-diagram concepts (R. S. Mulliken, *Rev. Mod. Phys.* **4** [1932], 1) as employed, e.g., by K. F. Herzfeld, *Rev. Mod. Phys.* **41** (1949), 527. Alternative MO

- formulations or rationalizations for Woodward–Hoffmann rules and favored phase patterns in pericyclic transition states were presented by (among others) H. C. Longuet-Higgins and E. W. Abrahamson, *J. Am. Chem. Soc.* **87** (1965), 2045; H. E. Zimmerman, *J. Am. Chem. Soc.* **88** (1966), 1563 and 1566 (“Hückel versus Möbius” TS); and M. J. S. Dewar, *Tetrahedron Suppl.* **8** (1966), 75 (“aromatic versus antiaromatic” TS). Closely related are the general concepts of donor–acceptor orbital interactions and phase matching (the “overlap-orientation principle”) as developed by R. S. Mulliken (Section 5.3.1) and subsequently extended into the language of “frontier-orbital” HOMO–LUMO interactions by K. Fukui (K. Fukui, in P.-O. Löwdin and B. Pullman, *Molecular Orbitals in Chemistry, Physics and Biology* [New York, Academic Press, 1964], p. 513; and *Tetrahedron Lett.* **1965** [1965], 2009 and 2427).
95. R. B. Woodward and R. Hoffmann, *J. Am. Chem. Soc.* **87** (1965), 395 and 2511; R. Hoffmann and R. B. Woodward, *J. Am. Chem. Soc.* **87** (1965), 2046; and R. B. Woodward and R. Hoffmann, *The Conservation of Orbital Symmetry* (Weinheim, Verlag Chemie, 1970).
96. Properly speaking, the V_3 (three-fold symmetry component) of the barrier is absent, but weak V_6 and higher components may be present. (The quoted barrier in (5.72) refers to this weak residual angular dependence.) See K.-T. Lu, F. Weinhold, and J. C. Weisshaar, *J. Chem. Phys.* **102** (1995), 6787; A.-Q. Zhao, C. S. Parmenter, D. B. Moss *et al.*, *J. Chem. Phys.* **96** (1992), 6362; and K. Takazawa, M. Fujii, and M. Ito, *J. Chem. Phys.* **99** (1993), 3205.

Appendix A. Methods and basis sets

A quantum-mechanical calculational model can be uniquely specified by identifying (i) the method of approximation and (ii) the orbital basis set that underlies the model. The model is conventionally specified by a keyword label of the form *method/basis*, where *method* and *basis* are suitable identifying abbreviations or acronyms. Simple examples are “RHF/6-31G**” (for the RHF restricted Hartree–Fock method and the 6-31G* basis set) or “B3LYP/6-311++G**” (for the B3LYP hybrid density functional method and the 6-311++G** basis set). In this appendix we briefly describe the principal method and basis types that are now well established in the literature,¹ particularly as implemented in the *Gaussian* program.² Consult notes 1 and 2 for background information and original references.

Methods

Quantum-mechanical approximation methods can be classified into three generic types: (1) variational, (2) perturbative, and (3) density functional. The first two can be systematically improved toward exactness, but a systematic correction procedure is generally lacking in the third case.

Variational methods

Variational approximation methods are identified by the form of the variational trial function, particularly by the number and types of Slater determinants.

The simplest approximation corresponds to a single-determinant wavefunction. The best possible approximation of this type is the Hartree–Fock (HF) molecular-orbital determinant. The HF wavefunction is constructed from the minimal number of occupied MOs (i.e., $N/2$ for an N -electron closed-shell system), each approximated as a variational linear combination of the chosen set of basis functions (*vide infra*).

To distinguish between closed-shell and open-shell configurations (and determinants), one may generally include a prefix to specify whether the starting HF wavefunction is of restricted closed-shell (R), restricted open-shell (RO), or unrestricted (U) form. (The restricted forms are total \hat{S}^2 spin eigenfunctions, but the unrestricted form need not be.) Thus, the abbreviations RHF, ROHF, and UHF refer to the spin-restricted closed-shell, spin-restricted open-shell, and unrestricted HF methods, respectively.

More accurate multi-determinant “configuration-interaction” (CI) wavefunctions are described by specifying the types of substitutions (“excitations”) from the starting HF

determinant, replacing sets of occupied MOs with corresponding virtual MOs. The substitutions may include all singles (S), doubles (D), triples (T), or quadruples (Q), leading to designations such as CIS (inclusion of all single excitations), CISD (all single and double excitations), and so forth. Such wavefunctions are termed “single-reference” type, because all allowed substitutions originate from the starting HF configuration using MOs optimized for this configuration. The spin restrictions on these CI wavefunctions can be specified by prefixes analogous to those for the reference HF configuration; for example, the abbreviations RCISD, ROCISD, and UCISD specify restricted closed-shell, restricted open-shell, and unrestricted CISD, respectively.

“Multi-reference” wavefunctions can be formed by choosing two or more reference configurations and allowing the MOs to reoptimize self-consistently for the multi-configuration form. An important special case is the CASSCF (complete active-space self-consistent-field) method, in which the set of reference configurations is generated by including all excitations from a chosen “active space” of occupied and virtual MOs. Another special case is the GVB (generalized valence-bond) method, in which reference configurations are selected to match the spin-pairing pattern of a chosen valence-bond structure. Further aspects of multi-reference variational wavefunctions are beyond the scope of this appendix.

Quadratic CI (QCI) and coupled cluster (CC) exemplify more complex methods that are not strictly variational in character, but include physical corrections similar to those of higher-order perturbation theory. Keywords for these methods also include a specification of substitutions from the reference HF configuration, such as QCISD or CCSD, respectively, for QCI or CC methods with all single and double substitutions. More complete descriptions of these methods are beyond the scope of this appendix.

Perturbative methods

Perturbative approximation methods are usually based on the Møller–Plesset (MP) perturbation theory for correcting the HF wavefunction. Energetic corrections may be calculated to second (MP2), third (MP3), or higher order. As usual, the open- versus closed-shell character of the wavefunction can be specified by an appropriate prefix, such as ROMP2 or UMP2 for restricted open-shell or unrestricted MP2, respectively.

An important advantage of MP2 and higher-order perturbation methods is their size-consistency at every order. This is in contrast to many variational CI methods, for which the calculated energy of two identical non-interacting systems might *not* be equal to twice that of an individual system. Size-consistent scaling is also characteristic of QCI and CC methods, which are therefore preferable to standard CI-type variational methods for many applications.

Density-functional methods

Density-functional methods are based on approximating the HF exchange operator and post-HF correlation corrections by certain functionals $\mathcal{E}_x[\rho]$, $\mathcal{E}_c[\rho]$ of the electron density ρ (and possibly its gradient). A density-functional method is uniquely identified by its exchange and correlation functionals. Examples of the former include the original Becke (B), Becke one-term (B1), Becke three-term (B3), Perdew–Wang (PW), and modified one-term Perdew–Wang (mPW1) exchange functionals. Examples of the latter include the Lee–Yang–Parr (LYP) and Perdew–Wang (PW) correlation functionals.

(Note that several $\mathcal{E}_x[\rho]$ “functionals” [such as the popular Becke three-term approximation B3] include an admixture of the true HF exchange operator with the usual

functional of electron density. Such methods are referred to as “hybrid density-functional methods” to indicate their closer connection to *ab initio* methods.)

The keyword for a given density-functional method is formed by concatenating the symbols for its exchange and correlation functionals. For example, combining the Becke three-term (B3) exchange functional with the Lee–Yang–Parr (LYP) correlation functional leads to the popular B3LYP density functional method.

As usual, a density-functional method (such as B3LYP) can be further specified as being of restricted closed-shell (RB3LYP), restricted open-shell (ROB3LYP), or unrestricted (UB3LYP) form.

Basis sets

Contemporary basis sets are usually formed from atomic-orbital basis functions \mathcal{X}_μ of “contracted Gaussian” form,

$$\mathcal{X}_\mu = \sum_{i=1}^r a_{\mu i} g_i$$

where the g_i ’s are “primitive” Gaussian-type orbitals, the $a_{\mu i}$ ’s are fixed contraction coefficients, and r is the length of the contraction. An r -term-contracted Gaussian-type orbital (CGTO) is often denoted in the form “ rG ” (e.g., “3G” for a three-term contraction).

Each CGTO \mathcal{X}_μ can be considered as an approximation to a single Slater-type orbital (STO) with effective nuclear charge ζ (zeta). The composition of the basis set can therefore be described in terms of the number of such effective zeta values (or STOs) for each electron. A “double-zeta” (DZ) basis includes *twice* as many effective STOs per electron as a single-zeta “minimal basis” (MB) set, a “triple-zeta” (TZ) basis *three* times as many, and so forth. A popular choice, of so-called “split-valence” type, is to describe core electrons with a minimal set and valence electrons with a more flexible DZ (or higher) set.

Pople-style basis sets

The keyword label of a standard Pople-style split-valence basis specifies the sp sets (groups of CGTOs of s and p symmetry) with distinct zeta values for each atomic shell, as well as the contraction length of each CGTO. The keyword contains the following syntactical components:

- (1) the contraction length n_c of the core-level set;
- (2) (after a hyphen) the contraction lengths n_v' , n_v'' , n_v''' , ... of valence-level sp sets for each distinct zeta value;
- (3) (preceding the character “G”) a “+” if a *diffuse* sp set is added to each heavy (non-H) atom, or “++” if also a diffuse s function is added to each H; and
- (4) (following the “G”) a “**” if *polarization* functions are added to each heavy atom, or “***” if they are added also to H.

(“Diffuse” functions refer to extra-valent Rydberg-like functions of very small effective ζ , which are suitable for describing anions or the very-long-range tails of electronic distributions. “Polarization” functions refer to components of higher angular momentum than required in the atomic ground configuration, e.g., an added set of five d orbitals on each C, or three p orbitals on each H.)

The generic symbol to represent a Pople-style basis set is of the form

$$n_c - n_v' n_v'' \dots (++)G(**)$$

where parenthesized (diffuse and polarization) extensions are optional. Some examples of this notation are given below, with a corresponding verbal description of the basis composition:

3-21G minimal 3G ($n_c = 3$) core and double-zeta 2G ($n_v' = 2$), 1G ($n_v'' = 1$) valence sp sets, with no diffuse or polarization functions

6-31G* minimal 6G ($n_c = 6$) core and triple-zeta 3G ($n_v' = 3$), 1G ($n_v'' = 1$) valence sp sets, with polarization functions on heavy atoms

6-311++G** minimal 6G ($n_c = 6$) core and triple-zeta 3G ($n_v' = 3$), 1G ($n_v'' = 1$), 1G ($n_v''' = 1$) valence sp sets, with diffuse and polarization functions on all atoms

Higher polarization functions can also be specified by replacing “***” by a parenthesized list of polarization sets for heavy atoms and (after a comma) for hydrogen. For example, “(2d1f,2p)” would specify two additional d sets and one additional f set on each heavy atom, as well as two additional p sets on each H.

Some exceptions to this general syntax may be noted.

- (1) The label “STO-3G” (equivalent to 3-3G in the notation described above) denotes a minimal basis 3G set for both core and valence shells ($n_c = 3$, $n_v = 3$).
- (2) The label “3-21G(*)” denotes a 3-21G set for atoms up to neon ($Z = 10$), but inclusion of a d set for heavier atoms.
- (3) Polarization functions may be optionally chosen to be of “pure” or “Cartesian” form (by another keyword). In the former case, one includes the expected number of angular-momentum components (i.e., five d orbitals, seven f orbitals, etc.), whereas in the latter case some additional component(s) of lower angular momentum are included (e.g., a Cartesian “d set” includes five d orbitals plus one s orbital, a Cartesian “f set” includes seven f orbitals plus three p orbitals, and so forth).

Effective-core-potential (ECP) basis sets

The ECP basis sets include basis functions only for the outermost one or two shells, whereas the remaining inner core electrons are replaced by an “effective core” or “pseudopotential.” The ECP basis keyword consists of a source identifier (such as LANL for “Los Alamos National Laboratory”), the number of outer shells retained (1 or 2), and a conventional label for the number of ζ sets for each shell (MB, DZ, TZ, . . .). For example, “LANL1MB” denotes the minimal LANL basis with minimal basis functions for the outermost shell only, whereas “LANL2DZ” is the set with double-zeta functions for each of the two outermost shells. The ECP basis set employed throughout Chapter 4 (denoted “LACV3P” in Jaguar terminology) is also of Los Alamos type, but with full triple-zeta valence flexibility and polarization and diffuse functions on all atoms (comparable to the 6-311++G** all-electron basis used elsewhere in this book).

An important advantage of ECP basis sets is their ability to incorporate approximately the physical effects of relativistic core contraction and associated changes in screening on valence orbitals, by suitable adjustments of the radius of the effective core potential. Thus, the ECP valence atomic orbitals can approximately mimic those of a fully relativistic (spinor) atomic calculation, rather than the non-relativistic all-electron orbitals they are nominally serving to replace. The partial inclusion of relativistic effects is an important physical correction for heavier atoms, particularly of the second transition series and beyond. Thus, an ECP-like treatment of heavy atoms is necessary in the non-relativistic framework of standard electronic-structure packages, even if the reduction in number of

basis orbitals obtained through neglect of atomic core electrons were of no practical importance. For this reason, all-electron basis sets (such as 6-311G and its extensions) are commonly unavailable for atoms beyond the first transition series.

Correlation-consistent basis sets

Dunning has developed a series of “correlation-consistent” polarized valence n -zeta basis sets (denoted “cc-pVnZ”) in which polarization functions are systematically added to *all* atoms with each increase in n . (Corresponding diffuse sets are also added for each n if the prefix “aug-” is included.) These sets are optimized for use in correlated calculations and are chosen to insure a smooth and rapid (exponential-like) convergence pattern with increasing n . For example, the keyword label “aug-cc-pVDZ” denotes a valence double-zeta set with polarization and diffuse functions on all atoms (approximately equivalent to the 6-311++G** set), whereas “aug-cc-pVQZ” is the corresponding quadruple-zeta basis which includes (3d2f1g,2p1d) polarization sets.

Related basis sets in common usage include the original Dunning full and valence double-zeta sets, denoted D95 and D95V, respectively (built from nine s-type and five p-type primitives). These sets may be augmented in the usual way with diffuse and/or polarization functions, as in the example “D95++**” (diffuse and first-polarization sets on all atoms).

Notes for Appendix A

1. W. J. Hehre, L. Radom, P. v. R. Schleyer, and J. A. Pople, *Ab Initio Molecular Orbital Theory* (New York, Wiley, 1986).
2. J. B. Foresman and A. Frisch, *Exploring Electronic Structure Calculations*, 2nd edn. (Pittsburgh, PA, Gaussian, Inc., 1998).

Appendix B. Chemical periodicity

Introduction

Figure B.1 depicts the periodic table of the elements in the current IUPAC-approved form, with US-style assignments of group numbers as used throughout this book. This standard textbook table (STT) provides an accepted common vocabulary for the “row” (period) and “column” (group) assignments of each chemical element, and is thus an asset to clear pedagogical communication.

However, the STT somewhat muddles the natural groupings into s block, p block, d block, and f block of filling valence shells, which, from a fundamental perspective, is the most important feature of elemental electron configuration. The STT evolved from Mendeleev’s original conception¹ of serially ordering the elements in periodic tabular repeat patterns to reflect conspicuous *chemical* groupings (such as maximum oxidation number, physical state under standard-state conditions, and the like), long before the discovery of quantum theory and realization of the close associations between chemical and spectroscopic behavior. The STT chemical groupings reflect subtle biases toward ambient thermal conditions or the ambiguities arising from selected chemical criteria or the current extent of chemical knowledge. For theoretical purposes, certain alternative representations of chemical periodicity may therefore be advantageous in depicting the fundamental valence-electron occupancy patterns that underlie both chemistry and spectroscopy.²

The theory of periodicity in electronic *Aufbau* of atomic configurations

According to the general Sturm–Liouville theory,³ the eigenvalues of any one-dimensional Schrödinger-type eigenvalue equation can be monotonically ordered according to the number of *nodes* (oscillations between negative and positive values) in the corresponding eigenfunctions. This result corresponds to the expected physical association of wave energy with the oscillatory curvature or “choppiness” of the waveform. The energy–node relationship is also implicit in Bohr’s general quantum relationship $E = h\nu$ between energy and oscillation frequency ν . The number of oscillatory nodes is therefore a strict “quantum number” for arranging the numerical sequence of one-dimensional eigenstates into monotonically increasing energetic order.

In a molecular-orbital-type (Hartree–Fock or Kohn–Sham density-functional) treatment of a three-dimensional atomic system, the field-free eigenfunctions $\psi_{n\ell}$ can be rigorously separated into radial (r) and angular (θ) components, governed by respective quantum numbers n and ℓ . In accordance with Sturm–Liouville theory, each increase of n (for

Periodic Table of the Elements (IUPAC-Approved STT)

		1	2	3	4	5	6	7	8	9	10	11	12	13	14	15	16	17	18
H 1																			He 2
Li 3	Be 4													B 5	C 6	N 7	O 8	F 9	Ne 10
Na 11	Mg 12													Al 13	Si 14	P 15	S 16	Cl 17	Ar 18
K 19	Ca 20	Sc 21	Ti 22	V 23	Cr 24	Mn 25	Fe 26	Co 27	Ni 28	Cu 29	Zn 30	Ga 31	Ge 32	As 33	Se 34	Br 35	Kr 36		
Rb 37	Sr 38	Y 39	Zr 40	Nb 41	Mo 42	Tc 43	Ru 44	Rh 45	Pd 46	Ag 47	Cd 48	In 49	Sn 50	Sb 51	Te 52	I 53	Xe 54		
Cs 55	Ba 56	La [†] 57	Hf [†] 72	Ta [†] 73	W [†] 74	Re [†] 75	Os [†] 76	Ir [†] 77	Pt [†] 78	Au [†] 79	Hg [†] 80	Tl [†] 81	Pb [†] 82	Bi [†] 83	Po [†] 84	At [†] 85	Rn [†] 86		
Fr 87	Ra 88	Ac [†] 89	Rf [†] 104	Db [†] 105	Sg [†] 106	Bh [†] 107	Hs [†] 108	Ir [†] 109	110	111	112	113	114	115	116	117	118		
Lanthanides *		Pr 58	Nd 59	Pm 60	Sm 61	Eu 62	Gd 63	Tb 64	Dy 65	Ho 66	Er 67	Tm 68	Yb 69	Lu 70					
Actinides **		Pa 90	U 91	Np 92	Pu 93	Am 94	Cm 95	Bk 96	Cf 97	Es 98	Fm 99	Md 100	No 101	Lr 102					

Figure B.1 The periodic table of the elements in IUPAC-approved standard textbook-table (STT) form, showing the US-style labeling of group number 1–18.

fixed ℓ) is associated with an additional radial node and an increase of radial energy. Similarly, each increase in ℓ (for fixed n) is associated with an additional angular node and an increase in angular energy. Therefore, one can generally expect that the total (radial + angular) energy varies monotonically with the total number of nodes, and hence with $n + \ell$ (the total number of radial and angular modes, including that at infinity). This is the essential physical and mathematical basis of the “ $n + \ell$ rule” (Madelung rule)⁴ that governs the order of orbital energy *Aufbau* in many-electron systems.

A highly exceptional limit occurs for the single-electron hydrogenic atom, where the potential energy is of pure Kepler-like $1/r$ form. In this case (only), the ℓ variations lead to energetic degeneracy, which can be attributed to Fock’s dynamical symmetry.⁵ However, *any* deviation from the Kepler-like, potential symmetry (due, e.g., to interactions with other electrons) restores the expected Sturm–Liouville variation of energy with $n + \ell$. Many-electron atoms therefore exhibit the expected variation of energy with ℓ (e.g., $\epsilon_{3s} < \epsilon_{3p} < \epsilon_{3d}$) rather than the degenerate pattern of the one-electron hydrogen atom ($\epsilon_{3s} = \epsilon_{3p} = \epsilon_{3d}$).

Within each $(n + \ell)$ manifold, the dependence on n (or ℓ) can also be readily understood. The hydrogen-like tendency toward near-degeneracy of ℓ values, but strong dependence on n , tends to persist even in many-electron atoms. As a result, the orbital energies continue to depend much more strongly on n than on ℓ . The lowest-energy orbital of the $(n + \ell)$ manifold is therefore that of lowest n (or, equivalently, highest ℓ), e.g.,

$$\epsilon_{nd} < \epsilon_{(n+1)p} < \epsilon_{(n+2)d}$$

This is equivalent to saying that the smaller number of *radial* nodes (rather than angular nodes) tends to dictate the favored low-energy orbital in orbital *Aufbau*, i.e., the orbital of

Left-Step Table of the Elements

																		← s →																	
																		H	He																
																		Li	Be																
																		← p →																	
																		B	C	N	O	F	Ne	Na	Mg										
																		Al	Si	P	S	Cl	Ar	K	Ca										
																		← d →																	
																		Sc	Ti	V	Cr	Mn	Fe	Co	Ni	Cu	Zn	Ga	Ge	As	Se	Br	Kr	Rb	Sr
																		Y	Zr	Nb	Mo	Tc	Ru	Rh	Pd	Ag	Cd	In	Sn	Sb	Te	I	Xe	Cs	Ba
																		← f →																	
La	Ce	Pr	Nd	Pm	Sm	Eu	Gd	Tb	Dy	Ho	Er	Tm	Yb	Lu	Hf	Ta	W	Re	Os	Ir	Pt	Au	Hg	Tl	Pb	Bi	Po	At	Rn	Fr	Ra				
57	58	59	60	61	62	63	64	65	66	67	68	69	70	71	72	73	74	75	76	77	78	79	80	81	82	83	84	85	86	87	88				
Ac	Th	Pa	U	Np	Pu	Am	Cm	Bk	Cf	Es	Fm	Md	No	Lr	Rf	Dd	Sg	Bh	Hs	Mt	Ds														
89	90	91	92	93	94	95	96	97	98	99	100	101	102	103	104	105	106	107	108	109	110	111	112	113	114	115	116	117	118	119	120				

Figure B.2 The left-step table (LST) of the chemical elements.

highest ℓ (or lowest n) will be of lowest energy in a given $(n + \ell)$ manifold. This leads to the familiar “lowest $n + \ell$; highest ℓ ” rule for building the electron-configuration sequence that underlies the periodic table.

The left-step table

Figure B.2 displays the alternative left-step table (LST) of the elements, as first suggested by Janet⁶ and strongly advocated (among others) by Mazurs and Bent.⁷ Because the rows of the LST are labeled by $n + \ell$ and the columns by ℓ blocks, this form of table automatically gives the correct “highest $n + \ell$, highest ℓ ” sequence of configurational orbital filling when read in the standard left-to-right, top-to-bottom order. The LST is therefore optimal for visualizing an element’s correct valence-electron configuration (up to the usual near-degenerate exceptions discussed below).

As emphasized by Bent, the LST properly places H and He with the s block and realigns the ℓ shells into the actual sequence of configurational orbital filling. The LST therefore avoids the curious STT-based implication that the d-block elements ($\ell = 2$) are somehow the “transition” between the s block ($\ell = 0$) and p block ($\ell = 1$).

The LST also allows one to achieve a better recognition of the pattern of dissimilarities that characteristically separate the first from the second (and successive) congeners of a given ℓ block. These are most dramatic in the case of 1s versus 2s (i.e., H versus Li, or He versus Be), but they remain conspicuous for 2p versus 3p (e.g., C versus Si, or N versus P) and even for 3d versus 4d (as discussed, e.g., in Sections 2.8, 3.2.1, 3.2.9, 4.10, and 5.2.7). The abrupt changes between the first and later fillings of a given ℓ shell can be generally attributed to the core-exclusion effect, i.e., the dramatic difference in “inner-core pressure” (due to the Pauli principle) that prevents the valence shell from shrinking into the region of its own nucleus, or making deep-penetrating bonding overlap into the nuclear region of another similar valence shell, when there exists a deeper core shell of the same ℓ symmetry.

Although the LST presents many attractive features, its row/column rearrangements inevitably invite “period” and “group-number” designations that are inconsistent with either US or UK STT-based conventions. The LST and STT representations therefore tend to promote confrontational rather than complementary usage among their proponents, somewhat negating the beneficial contribution of the LST to chemical understanding.⁸

The ascending periodic helix

The monotonically ascending periodic progression of orbital energy filling can be alternatively exhibited by arranging the elements along a continuous *band* that wraps in spiraling fashion onto a three-dimensional cylindrical surface (as shown in cut-out planarized form in Fig. B.3). In this manner the “table” of elements acquires the topology of a three-dimensional *helix*, with “turns” replacing “periods” and a continuous spiraling ascent replacing the discrete rows and “carriage returns” of a planar tabular display.⁹ The periodicities of such a helical display appear in the circular repeat patterns that align parallel to the helical axis. The close conceptual kinship to a tabular LST representation is clearly evident, but the quasi-continuous nature of the *Aufbau* progression is emphasized by the fact that successive ℓ blocks are encountered along a continuously spiraling pathway, where successive (n, ℓ) subshells automatically appear in proper sequence ($\dots 3d \dots 4p \dots 5s \dots 4f \dots$), without abrupt vertical shifts or dislocations. We refer to this variant as the *ascending periodic helix* (APH), to emphasize its distinctive features with respect to the STT and LST forms.

The three-dimensional APH display may be conveniently chosen to map onto a simple cylindrical surface (e.g., a coffee cup) by adding blank filling space to each helical turn in order to maintain a constant radius of curvature. Figure B.3 provides a simple planar template that one can cut and paste to form the APH cylindrical display.

Alternatively, each loop of the APH design may be constructed with variable radius to connect continuously (with no filling space) into an ascending “Guggenheim-staircase” pattern. In this construction the APH arcs upward from H ($Z = 1$) in ever-increasing energetic and atomic-number spirals, to the as-yet undiscovered realm at the head of the staircase.

In either construction, each element of the APH can be assigned a unique *turn* (t)¹⁰ and *angular step* ($\ell - n$) along the helical pathway, measured from the s-block origin that forms the natural “spine” of the spiral pattern (the heavy vertical line in Fig. B.3). For example, the element chromium (Cr) can be denoted as the “t5/d4” element, to locate it at the “d4” angular step (the fourth element of the d block) on the “t5” tier of the helix. In this manner, the distinctive form, topology, and orientation of the APH effectively complement

Ascending Periodic Helix of the Elements

Ac 89	Th 90	Pa 91	U 92	Np 93	Pu 94	Am 95	Cm 96	Bk 97	Cf 98	Es 99	Fm 100	Md 101	No 102	Lr 103	Rf 104	Dd 105	Sg 106	Bh 107	Hs 108	Mt 109	Ds 110	111	112	113	114	115	116	117	118	119	120		
La 57	Ce 58	Pr 59	Nd 60	Pm 61	Sm 62	Eu 63	Gd 64	Tb 65	Dy 66	Ho 67	Er 68	Tm 69	Yb 70	Lu 71	Hf 72	Ta 73	W 74	Re 75	Os 76	Ir 77	Pt 78	Au 79	Hg 80	Tl 81	Pb 82	Bi 83	Po 84	At 85	Rn 86	Fr 87	Ra 88		
														Y 39	Zr 40	Nb 41	Mo 42	Tc 43	Ru 44	Rh 45	Pd 46	Ag 47	Cd 48	In 49	Sn 50	Sb 51	Te 52	I 53	Xe 54	Cs 55	Ba 56		
														Sc 21	Ti 22	V 23	Cr 24	Mn 25	Fe 26	Co 27	Ni 28	Cu 29	Zn 30	Ga 31	Ge 32	As 33	Se 34	Br 35	Kr 36	Rb 37	Sr 38		
																										Al 13	Si 14	P 15	S 16	Cl 17	Ar 18	K 19	Ca 20
																										B 5	C 6	N 7	O 8	F 9	Ne 10	Na 11	Mg 12
																												Li 3	Be 4				
																												H 1	He 2				
																														S			

Figure B.3 The ascending periodic helix (APH) of the chemical elements, showing the evident relationship to the LST form (Fig. B.2). The heavy vertical line marks the start of each new turn. The diagram can be pasted onto a smooth cylindrical surface by joining element 88 with element 89 and element 56 with element 57 at the cylindrical seam.

standard STT-based concepts and terminology, while displaying periodic relationships in a fresh and stimulating visual image to students of chemistry.

Table B.1 summarizes the ground-state electron configuration and formal APH indices (turn number t , angular number $\ell-n$) for each known element, together with atomic number (Z) and relative atomic mass). As shown by the asterisks in the final column, 20 elements exhibit anomalous electron configurations (including two that are doubly anomalous – Pd and Th), compared with idealized $t/\ell-n$ APH descriptors. These are particularly concentrated in the first d-block series, as well as among the early actinides. Such anomalies are indicative of configurational near-degeneracies that may require sophisticated multi-reference approximation methods for accurate description.

It is noteworthy that He is the natural turn-terminator for $t = 1$, the level which is expected to exhibit *greatest* energetic separation from higher t levels in any Schrödinger-type eigenvalue problem. Helium therefore *retains* its traditional role (together with Ne, Ar, . . .) as the terminus of a filling cycle, exhibiting the expected closed-shell stability just prior to entering a new cycle. The relocation of He to the s block (which appears somewhat heretical from the STT viewpoint) therefore *promotes* recognition that He, Ne, Ar, . . . are true chemical congeners, and indeed that helium is the “noblest of the noble” in this respect.

Table B.1. *The currently known chemical elements, showing atomic number (Z), chemical symbol, name, relative atomic mass, ground-state electron configuration, and APH indices ($t =$ turn number; $\ell-n =$ angular number); asterisks (*, **) symbolize “anomalous” (APH non-conforming) ground-state electronic configurations, which are indicative of configurational near-degeneracy*

Z	Symbol	Name	Relative atomic mass (amu)	Electron configuration	APH
					$t \ell-n$
1	H	Hydrogen	1.008	(1s) ¹	1 s1
2	He	Helium	4.003	(1s) ² = [He]	1 s2
3	Li	Lithium	6.941	[He](2s) ¹	2 s1
4	Be	Beryllium	9.012	[He](2s) ²	2 s2
5	B	Boron	10.81	[He](2s) ² (2p) ¹	2 p1
6	C	Carbon	12.011	[He](2s) ² (2p) ²	2 p2
7	N	Nitrogen	14.007	[He](2s) ² (2p) ³	2 p3
8	O	Oxygen	15.999	[He](2s) ² (2p) ⁴	2 p4
9	F	Fluorine	18.998	[He](2s) ² (2p) ⁵	2 p5
10	Ne	Neon	20.179	[He](2s) ² (2p) ⁶ = [Ne]	2 p6
11	Na	Sodium	22.990	[Ne](3s) ¹	3 s1
12	Mg	Magnesium	24.305	[Ne](3s) ²	3 s2
13	Al	Aluminum	26.982	[Ne](3s) ² (3p) ¹	3 p1
14	Si	Silicon	28.086	[Ne](3s) ² (3p) ²	3 p2
15	P	Phosphorus	30.974	[Ne](3s) ² (3p) ³	3 p3
16	S	Sulfur	32.06	[Ne](3s) ² (3p) ⁴	3 p4
17	Cl	Chlorine	35.453	[Ne](3s) ² (3p) ⁵	3 p5
18	Ar	Argon	39.948	[Ne](3s) ² (3p) ⁶ = [Ar]	3 p6
19	K	Potassium	39.098	[Ar](4s) ¹	4 s1
20	Ca	Calcium	40.08	[Ar](4s) ²	4 s2
21	Sc	Scandium	44.956	[Ar](4s) ² (3d) ¹	4 d1

Cont.

Table B.1. (Cont.)

Z	Symbol	Name	Relative atomic mass (amu)	Electron configuration	APH <i>t l-n</i>
22	Ti	Titanium	47.9	[Ar](4s) ² (3d) ²	4 d2
23	V	Vanadium	50.942	[Ar](4s) ² (3d) ³	4 d3
24	Cr	Chromium	51.996	[Ar](4s) ¹ (3d) ⁵	4 d4*
25	Mn	Manganese	54.938	[Ar](4s) ² (3d) ⁵	4 d5
26	Fe	Iron	55.847	[Ar](4s) ² (3d) ⁶	4 d6
27	Co	Cobalt	58.933	[Ar](4s) ² (3d) ⁷	4 d7
28	Ni	Nickel	58.7	[Ar](4s) ² (3d) ⁸	4 d8
29	Cu	Copper	63.546	[Ar](4s) ¹ (3d) ¹⁰	4 d9*
30	Zn	Zinc	65.38	[Ar](4s) ² (3d) ¹⁰	4 d10
31	Ga	Gallium	69.72	[Ar](4s) ² (3d) ¹⁰ (4p) ¹	4 p1
32	Ge	Germanium	72.59	[Ar](4s) ² (3d) ¹⁰ (4p) ²	4 p2
33	As	Arsenic	74.922	[Ar](4s) ² (3d) ¹⁰ (4p) ³	4 p3
34	Se	Selenium	78.96	[Ar](4s) ² (3d) ¹⁰ (4p) ⁴	4 p4
35	Br	Bromine	79.904	[Ar](4s) ² (3d) ¹⁰ (4p) ⁵	4 p5
36	Kr	Krypton	83.8	[Ar](4s) ² (3d) ¹⁰ (4p) ⁶ = [Kr]	4 p6
37	Rb	Rubidium	85.468	[Kr](5s) ¹	5 s1
38	Sr	Strontium	87.62	[Kr](5s) ²	5 s2
39	Y	Yttrium	88.906	[Kr](5s) ² (4d) ¹	5 d1
40	Zr	Zirconium	91.22	[Kr](5s) ¹ (4d) ³	5 d2*
41	Nb	Niobium	92.906	[Kr](5s) ¹ (4d) ⁴	5 d3*
42	Mo	Molybdenum	95.94	[Kr](5s) ¹ (4d) ⁵	5 d4*
43	Tc	Technetium	98.	[Kr](5s) ² (4d) ⁵	5 d5
44	Ru	Ruthenium	101.07	[Kr](5s) ¹ (4d) ⁷	5 d6*
45	Rh	Rhodium	102.906	[Kr](5s) ¹ (4d) ⁸	5 d7*
46	Pd	Palladium	106.4	[Kr](4d) ¹⁰	5 d8**
47	Ag	Silver	107.868	[Kr](5s) ¹ (4d) ¹⁰	5 d9*
48	Cd	Cadmium	112.41	[Kr](5s) ² (4d) ¹⁰	5 d10
49	In	Indium	114.82	[Kr](5s) ² (4d) ¹⁰ (5p) ¹	5 p1
50	Sn	Tin	118.69	[Kr](5s) ² (4d) ¹⁰ (5p) ²	5 p2
51	Sb	Antimony	121.75	[Kr](5s) ² (4d) ¹⁰ (5p) ³	5 p3
52	Te	Tellurium	127.6	[Kr](5s) ² (4d) ¹⁰ (5p) ⁴	5 p4
53	I	Iodine	126.905	[Kr](5s) ² (4d) ¹⁰ (5p) ⁵	5 p5
54	Xe	Xenon	131.3	[Kr](5s) ² (4d) ¹⁰ (5p) ⁶ = [Xe]	5 p6
55	Cs	Cesium	132.905	[Xe](6s) ¹	6 s1
56	Ba	Barium	137.33	[Xe](6s) ²	6 s2
57	La	Lanthanum	138.906	[Xe](6s) ² (5d) ¹	6 f1*
58	Ce	Cerium	140.12	[Xe](6s) ² (5d) ¹ (4f) ¹	6 f2*
59	Pr	Praseodymium	140.908	[Xe](6s) ² (4f) ³	6 f3
60	Nd	Neodymium	144.24	[Xe](6s) ² (4f) ⁴	6 f4
61	Pm	Promethium	145.	[Xe](6s) ² (4f) ⁵	6 f5
62	Sm	Samarium	150.4	[Xe](6s) ² (4f) ⁶	6 f6
63	Eu	Europium	151.96	[Xe](6s) ² (4f) ⁷	6 f7
64	Gd	Gadolinium	157.25	[Xe](6s) ² (4f) ⁷ (5d) ¹	6 f8*
65	Tb	Terbium	158.925	[Xe](6s) ² (4f) ⁹	6 f9
66	Dy	Dysprosium	162.5	[Xe](6s) ² (4f) ¹⁰	6 f10
67	Ho	Holmium	164.930	[Xe](6s) ² (4f) ¹¹	6 f11
68	Er	Erbium	167.26	[Xe](6s) ² (4f) ¹²	6 f12
69	Tm	Thulium	168.934	[Xe](6s) ² (4f) ¹³	6 f13
70	Yb	Ytterbium	173.04	[Xe](6s) ² (4f) ¹⁴	6 f14

Table B.1. (Cont.)

Z	Symbol	Name	Relative atomic mass (amu)	Electron configuration	APH $t \ell - n$
71	Lu	Lutetium	174.967	[Xe](6s) ² (4f) ¹⁴ (5d) ¹	6 d1
72	Hf	Hafnium	178.49	[Xe](6s) ² (4f) ¹⁴ (5d) ²	6 d2
73	Ta	Tantalum	180.948	[Xe](6s) ² (4f) ¹⁴ (5d) ³	6 d3
74	W	Tungsten	183.85	[Xe](6s) ² (4f) ¹⁴ (5d) ⁴	6 d4
75	Re	Rhenium	186.207	[Xe](6s) ² (4f) ¹⁴ (5d) ⁵	6 d5
76	Os	Osmium	190.2	[Xe](6s) ² (4f) ¹⁴ (5d) ⁶	6 d6
77	Ir	Iridium	192.22	[Xe](6s) ² (4f) ¹⁴ (5d) ⁷	6 d7
78	Pt	Platinum	195.09	[Xe](6s) ¹ (4f) ¹⁴ (5d) ⁹	6 d8*
79	Au	Gold	196.967	[Xe](6s) ¹ (4f) ¹⁴ (5d) ¹⁰	6 d9*
80	Hg	Mercury	200.59	[Xe](6s) ² (4f) ¹⁴ (5d) ¹⁰	6 d10
81	Tl	Thallium	204.37	[Xe](6s) ² (4f) ¹⁴ (5d) ¹⁰ (6p) ¹	6 p1
82	Pb	Lead	207.2	[Xe](6s) ² (4f) ¹⁴ (5d) ¹⁰ (6p) ²	6 p2
83	Bi	Bismuth	208.980	[Xe](6s) ² (4f) ¹⁴ (5d) ¹⁰ (6p) ³	6 p3
84	Po	Polonium	209.	[Xe](6s) ² (4f) ¹⁴ (5d) ¹⁰ (6p) ⁴	6 p4
85	At	Astatine	210.	[Xe](6s) ² (4f) ¹⁴ (5d) ¹⁰ (6p) ⁵	6 p5
86	Rn	Radon	222.	[Xe](6s) ² (4f) ¹⁴ (5d) ¹⁰ (6p) ⁶ = [Rn]	6 p6
87	Fr	Francium	223.020	[Rn](7s) ¹	7 s1
88	Ra	Radium	226.025	[Rn](7s) ²	7 s2
89	Ac	Actinium	227.028	[Rn](7s) ² (6d) ¹	7 f1*
90	Th	Thorium	232.038	[Rn](7s) ² (6d) ²	7 f2**
91	Pa	Protactinium	231.036	[Rn](7s) ² (5f) ² (6d) ¹	7 f3*
92	U	Uranium	238.029	[Rn](7s) ² (5f) ³ (6d) ¹	7 f4*
93	Np	Neptunium	237.048	[Rn](7s) ² (5f) ⁴ (6d) ¹	7 f5*
94	Pu	Plutonium	244.	[Rn](7s) ² (5f) ⁶	7 f6
95	Am	Americium	243.	[Rn](7s) ² (5f) ⁷	7 f7
96	Cm	Curium	247.	[Rn](7s) ² (5f) ⁷ (6d) ¹	7 f8*
97	Bk	Berkelium	247.	[Rn](7s) ² (5f) ⁹	7 f9
98	Cf	Californium	251.	[Rn](7s) ² (5f) ¹⁰	7 f10
99	Es	Einsteinium	252.	[Rn](7s) ² (5f) ¹¹	7 f11
100	Fm	Fermium	257.	[Rn](7s) ² (5f) ¹²	7 f12
101	Md	Mendelevium	258.	[Rn](7s) ² (5f) ¹³	7 f13
102	No	Nobelium	259.	[Rn](7s) ² (5f) ¹⁴	7 f14
103	Lr	Lawrencium	260.	[Rn](7s) ² (5f) ¹⁴ (6d) ¹	7 d1
104	Rf	Rutherfordium	261.	[Rn](7s) ² (5f) ¹⁴ (6d) ²	7 d2
105	Dd	Dubnium	262.	[Rn](7s) ² (5f) ¹⁴ (6d) ³	7 d3
106	Sg	Seaborgium	263.	[Rn](7s) ² (5f) ¹⁴ (6d) ⁴	7 d4
107	Bh	Bohrium	262.	[Rn](7s) ² (5f) ¹⁴ (6d) ⁵	7 d5
108	Hs	Hassium	265.	[Rn](7s) ² (5f) ¹⁴ (6d) ⁶	7 d6
109	Mt	Meitnerium	266.	[Rn](7s) ² (5f) ¹⁴ (6d) ⁷	7 d7
110	Ds	Darmstadtium	271.	[Rn](7s) ² (5f) ¹⁴ (6d) ⁸	7 d8

Notes for Appendix B

1. D. I. Mendeleev (translation), *J. Chem. Soc. (London)* **55** (1889), 634.
2. E. G. Mazurs, *Graphic Representations of the Periodic System During One Hundred Years*, 2nd edn. (Tuscaloosa, AL, University of Alabama Press, 1974). Mazurs identifies 146 distinct graphical representations of chemical periodicity that have appeared in the literature.

3. P. M. Morse and H. Feshbach, *Methods of Theoretical Physics*, Part I (New York, McGraw-Hill, 1953), pp. 721–724.
4. E. Madelung, *Die mathematische Hilfsmittel des Physikers*, 3rd. edn. (Berlin, Springer-Verlag, 1936).
5. V. Fock, *Z. Phys.* **98** (1935), 145.
6. C. Janet, *Chem. News* **138** (1929), 372 and 388; for a text of Janet’s original paper, see www.periodic-table.net.
7. E. G. Mazurs, *Graphic Representations of the Periodic System During One Hundred Years*, 2nd edn. (Tuscaloosa, AL, University of Alabama Press, 1974); and H. A. Bent, “Following in the footsteps of Mendeleev: the left step periodic table.” We thank Professor Bent for kindly providing a preprint of this manuscript.
8. For example, E. G. Mazurs (note 2, p. 105) expresses the discord as follows: “The periodicity of atomic structure must be accepted as a Natural Law. Therefore, scientists have to change their minds, get away from the conservatism that accepts only Mendeleev’s chemical table as right, and adjust the other phenomena to this phenomenon; that is, derive the chemical and physical properties of the elements from the electronic structure of the atoms.”
9. Helix-based displays of chemical periodicity have many precedents, going back to Mendeleev himself; see, e.g., B. K. Emerson, *Am. Chem. J.* **45** (1911), 160; B. K. Emerson, *Science* **34**, (1911), 640; H. Stintzing, *Z. Physik. Chem.* **91** (1916), 500; and E. G. Mazurs, note 2, pp. 52–54.
10. Usage of the “tier” or “turn” index t ($t = n + \ell$) also has many precedents; see, e.g., W. J. Wiswesser, *J. Chem. Educ.* **22** (1945), 314; Y. Ta, *Ann. Phys. (Paris)* **1** (1946), 88; and E. G. Mazurs, note 2, pp. 99–100.

Appendix C. Units

A physical *unit system* is implicitly defined by the choice of three underlying *base units*, which suffice to determine dimensionally consistent units for other measurable physical quantities. (Why *three* such base units are required is as yet an unanswered physical question.) Although the choice of units may superficially appear arbitrary, it was recognized by Gibbs (in his first scientific communication)¹ that one can rationally address the question of the “conditions which it is most necessary for these units to fulfil for the convenience both of men of science and of the multitude.”

Gibbs noted that “in causing a constant factor (or divisor) to disappear, the solution of mechanical problems is simplified by the choice of appropriate units.” Accordingly, one should select appropriate units that “greatly simplify the relations of the numerical representatives of the quantities and expedite the calculation.” We can paraphrase this viewpoint by stating that a criterion for selecting the most appropriate system of units is to simplify the most fundamental theorems and equations underlying the given area of scientific inquiry. For chemical purposes, the Gibbs criterion can be extended to include the electrical phenomena that underlie the electronic structure of atoms and molecules.

We can apply this criterion to two unit systems in common usage. Among electronic structure theorists, pervasive use is made of *atomic units* (a.u.), for which the three base units are

$$m_e = \text{base unit of } \textit{mass} = \text{mass of the electron}^2 \quad (\text{C.1a})$$

$$e = \text{base unit of } \textit{charge} = \text{charge of the electron} \quad (\text{C.1b})$$

$$\hbar = \text{base unit of } \textit{angular momentum} = \text{Planck's constant}/(2\pi) \quad (\text{C.1c})$$

Because its base units directly underlie the quantum theory of electrons (i.e., the mass, charge, and angular momentum of the electron itself), the atomic units naturally simplify the fundamental Schrödinger equation for electronic interactions. (Indeed, with the choice $m_e = e = \hbar = 1$, the Schrödinger equation reduces to pure numbers, and the solutions of this equation can be determined, once and for all, in a mathematical form that is *independent* of any subsequent re-measurement of e , m_e , and \hbar in chosen practical units.) In contrast, textbooks commonly employ the *Système International d'Unités* (SI), whose base units were originally chosen without reference to atomic phenomena:

$$\text{kilogram (kg)} = \text{base unit of } \textit{mass} = \text{a platinum–iridium bar (kept in a guarded chateau near Paris}^3) \quad (\text{C.2a})$$

Table C.1. Conversion factors from atomic to SI units

Atomic unit (base units)	SI value	Name (symbol)
Mass (m_e)	9.10939(−31) kg	Mass of the electron
Charge (e)	1.602188(−19) C	Electronic charge
Angular momentum (\hbar)	1.05457(−34) J s rad ^{−1}	Planck's constant/ 2π
Energy ($m_e c^4 / \hbar^2$)	4.35975(−18) J	Hartree (H)
Length ($\hbar^2 / (m_e e^2)$)	5.29177(−11) m	Bohr; Bohr radius (a_0)
Time ($\hbar^3 / (m_e e^4)$)	2.41888(−17) s	Jiffy
Electric dipole moment ($\hbar^2 / (m_e e)$)	8.47836(−30) C m	2.541 765 D (Debye units)
Magnetic dipole moment ($e\hbar / (2m_e)$)	9.27402(−24) J T ^{−1}	Bohr magneton (μ_B)

Table C.2. An energy-conversion table for non-SI units

Unit	Value in non-SI units					
	a.u.	kcal mol ^{−1}	eV	cm ^{−1}	Hz	K
a.u.	1	6.27510(2)	2.72114(1)	2.19475(5)	6.57968(15)	3.15773(5)
kcal mol ^{−1}	1.59360(−3)	1	4.33641(−2)	3.49755(2)	1.04854(13)	5.03217(2)
eV	3.67493(−2)	2.30605(1)	1	8.06554(3)	2.41799(14)	1.16044(4)
cm ^{−1}	4.55634(−6)	2.85914(−3)	1.23984(−4)	1	2.99792(10)	1.43877
Hz	1.51983(−16)	9.53708(−14)	4.13567(−15)	3.33564(−11)	1	4.79922(−11)
K	3.16683(−6)	1.98722(−3)	8.61739(−5)	6.95039(−1)	2.08367(10)	1

Table C.3. Fundamental constants, in atomic and SI units

Physical constant	Symbol	Value (a.u.)	Value (SI)
Rydberg constant	R_∞	2.29253(2)	1.09737(−23) m ^{−1}
Planck constant	h	6.28319(= 2π)	6.62608(−34) J s
Speed of light	c	1.37036(2)	2.99792(8) m s ^{−1}
Proton mass	m_p	1.83615(3)	1.67262(−27) kg
Atomic mass unit	amu	1.82289(3)	1.66054(−27) kg
Fine-structure constant	α	7.29735(−3)	7.29735(−3)

Table C.4. Other constants and conversion factors

Quantity (symbol)	SI value or equivalent
Avogadro's number (N_0)	6.022 14(23) mol ^{−1}
Kilocalorie (kcal)	4.184 00(3) J
Kelvin (K)	°C + 273.15
Boltzmann constant (k)	1.380 66(−23) J K ^{−1}
Faraday constant (\mathcal{F})	9.648 53(4) C mol ^{−1}

- meter (m) = base unit of *length* = originally, a metal stick whose length represented the King's arm or a certain fraction of the Earth's circumference (now redefined in terms of atomic constants) (C.2b)
- second (s) = base unit of *time* = originally, a certain fraction of a day (now redefined in terms of atomic constants) (C.2c)

Two of the three SI base units have in the meantime acquired redefinitions in atomic terms (e.g., the "second" is now defined as 9 192 631 770 hyperfine oscillations of a cesium atom). However, the definitions (C.2a)–(C.2c) conceal another unfortunate aspect of SI units that cannot be overcome merely by atomic redefinitions. In the theory of classical or quantal electrical interactions, the most fundamental equation is Coulomb's law, which expresses the potential energy \mathcal{V} of two charged particles of charge q_1 and q_2 at separation R as

$$\mathcal{V} = c_{\text{units}} \frac{q_1 q_2}{R} \quad (\text{C.3})$$

where c_{units} depends on the choice of units. Adoption of atomic units causes this constant factor to "disappear" ($c_{\text{a.u.}} = 1$), giving Coulomb's law its simplest possible form, whereas adoption of SI units leads irreducibly to an appendage ($c_{\text{SI}} = 1/(4\pi\epsilon_0)$), where the SI "permittivity of a vacuum" $\epsilon_0 = 8.854 \dots \times 10^{-12}$ unnecessarily complicates Coulomb's law. In this sense, atomic units better satisfy the Gibbs criterion for description of fundamental electronic phenomena.

Tables C.1–C.4 provide conversion factors from a.u. to SI units and a variety of practical (thermochemical, crystallographic, spectroscopic) non-SI units in common usage. Numerical values are quoted to six-digit precision (though many are known to higher accuracy) in an abbreviated exponential notation, whereby 6.022 14(23) means $6.022\ 14 \times 10^{23}$. In this book we follow a current tendency of the quantum chemical literature by expressing relative energies in thermochemical units (kcal mol^{-1}), structural parameters in crystallographic ångström units (Å), vibrational frequencies in common spectroscopic units (cm^{-1}), and so forth. These choices, although "inconsistent" according to SI orthodoxy, seem better able to serve effective communication between theoreticians and experimentalists.

Notes for Appendix C

1. J. W. Gibbs, "The proper magnitude of the units of length and of other quantities used in mechanics," read before the Connecticut Academy of Sciences, March 21, 1866; reprinted in Appendix II of L. P. Wheeler, *Josiah Willard Gibbs: The History of a Great Mind* (Hambden, CT, Archon Books, 1970).
2. Properly speaking, m_e should be the *reduced* mass for the specific nuclear mass of the system. The values given in Table C.1 for m_e and R_∞ pertain to the infinite-mass limit, which suffices for practical purposes (and can be easily corrected, if necessary).
3. *New York Times* (May 27, 2003): "Scientists Struggling to Make the Kilogram Right Again: For mysterious reasons, a platinum–iridium cylinder that defines the kilogram has been losing weight. So scientists are looking for other ways to set the standard."

Chemical-species index

(Common organic or laboratory species are alphabetically listed in the Common names index, whereas remaining species/reactions are listed in the following Chemical formula index, grouped (rather arbitrarily) by the “main” element of the species. The indexed species (with few exceptions) are those for which explicit computational results are provided in the text, whereas species merely mentioned in passing are generally excluded.)

Common names

acetamide (CH_3CONH_2)

rotation barrier modulation, 696–702

complexes, 697–699

acetylacetonate anion (acac; $\text{H}_3\text{COCHCOCH}_3^-$)

as bidentate ligand, 523–526

resonance, 534–536

acetylene (HCCH)

localization, 110

hybrids, 112, 114

as bidentate ligand, 523–526, 531–534

acrylonitrile (CH_2CHCN), 508

allene ($\text{H}_2\text{C}=\text{C}=\text{CH}_2$), 186

allyl (CH_2CHCH_2)

anion, 20

Lewis structure, 29–30

resonance, 33–34

valencies, 35

as bidentate ligand, 523–526, 536

conjugation, 186

hapticity, 529

amine oxide (H_3NO), 179–181

ammine (NH_3) ligand, 440–446, 454–455

ammonia (NH_3)

adduct with BF_3 , 177–179

dimer, 254

complexes, 596, 607, 611, 630, 665–667

as monodentate ligand, 523–526

ammonium cation (NH_4^+), 616

complexes, 616

aniline ($\text{C}_6\text{H}_5\text{NH}_2$), 198, 206–208

benzene (C_6H_6)

complexes, 580, 663, 672–675

discovery, 196

hybrids, 112

localization, 108

π – π^* interactions, 198

β -hydroxyacrolein ($\text{O}=\text{CHCH}=\text{CHOH}$), 631

bifluoride anion (FHF^-), 280, 286, 580, 618, 657

borazine ($\text{B}_3\text{N}_3\text{H}_6$), 198, 204–205

butadiene ($\text{H}_2\text{C}=\text{CHCH}=\text{CH}_2$), 186, 209–210

carbonate anion (CO_3^{2-}), 302–306

carbonyl (CO) ligand, 440–446, 453–458

carbon monoxide (CO), 604

complexes with HF , 601

complexes with Li^+ , 71–72

CMO versus LMO description, 116–118

cyanide ($:\text{CN}^-$) ligand, 458–459

cyclobutadiene (C_4H_4), 196, 200–202

cyclobutane (C_4H_8), 270–273

cyclohexene (C_6H_{10}), 680, 686–693

cyclopentadienyl (C_5H_5), 198, 203–204

compared to dicarbollide, 345–348

as polydentate ligand, 471–472

in alkene polymerization catalyst, 509

in sandwich complexes, 536–545

cyclopropane (C_3H_6)

Coulson–Moffitt picture, 146

Dewar picture, 264

decapentaene ($\text{CH}_2=\text{CH}(\text{CH}=\text{CH})_3\text{CH}=\text{CH}_2$), 186

diaminoalkanes $\text{H}_2\text{N}(\text{CH}_2)_n\text{NH}_2$, $n = 1$ –4, 253–259

- diazabicyclooctane (DABCO; $\text{N}(\text{CH}_2\text{CH}_2)_3\text{N}$), 253
 dicarbollide anion ($\text{C}_2\text{B}_9\text{H}_{11}^{2-}$), 345–348
 difluoroethane ($\text{CH}_2\text{FCH}_2\text{F}$), 241–242
 difluoroethylene, 238–240
- ethane (H_3CCH_3), 227–231
 ethylene/ethene ($\text{H}_2\text{C}=\text{CH}_2$), 108, 110, 112–114
 complexes, 669–672
 protonated, 313–316
 reactions, 501–509, 680–682, 686–693
 ethylenediamine (en; $\text{H}_2\text{NCH}_2\text{CH}_2\text{NH}_2$), 523–526
 ethylenediaminetetraacetate (EDTA) ion, 522
- ferrocene ($\text{Fe}(\text{C}_5\text{H}_5)_2$), 536, 541–542
 fluoropropene ($\text{CH}_2=\text{CHCH}_2\text{F}$), 216, 220–223
 formaldehyde ($\text{H}_2\text{C}=\text{O}$), 596, 630
 formamide (H_2NCHO), 628
 dimer, 628
 complexes, 630
 clusters, 643–646
- glyoxal ($\text{O}=\text{CHCH}=\text{O}$), 186
 guanidinium (triaminomethyl) fluoride ($\text{C}(\text{NH}_2)_3\text{F}$), 249–252
- hexadiene ($\text{H}_2\text{C}=\text{CHCH}_2\text{CH}_2\text{CH}=\text{CH}_2$), 186
 hexatriene ($\text{H}_2\text{C}=\text{CHCH}=\text{CHCH}=\text{CH}_2$), 186
 hydrazine (N_2H_4), 241
 hydrogen peroxide (HOOH), 240–241
 hydronium cation ($\text{H}_3\text{O}^+\cdot\cdot\text{OH}_2$), 618, 657
 hydroxide anion (OH^-), 611, 653
 complexes, 611, 653, 697–699
- isocyanide ($:\text{NC}^-$) ligand, 458–459
- maleate anion ($\text{HOOCCH}=\text{CHCOO}^-$), 633
 methane (CH_4), 610, 108, 112, 114, 116–118
 complexes, 607, 611
 cation (CH_4^+), 120–122, 125
 geminal delocalizations, 267
 methanediol (dihydroxymethane, $\text{CH}_2(\text{OH})_2$), 243
 methide (CH_3^-), 513
 methylamine (CH_3NH_2), 234–236, 247–248
 methylene (CH_2), 137
- nickelocene ($\text{Ni}(\text{C}_5\text{H}_5)_2$), 536, 539–541
 nitrate anion (NO_3^-), 302–306
 nitrite anion (NO_2^-), 302–306
 nitrobenzene ($\text{C}_6\text{H}_5\text{NO}_2$), 198, 206–208
 nitrosyl (nitrosonium) cation (NO^+), 665–675
- octatetraene ($\text{H}_2\text{C}=\text{CH}(\text{CH}=\text{CH})_2\text{CH}=\text{CH}_2$), 186
- perchlorate anion (ClO_4^-), 302–306
 propane (C_3H_8), 270–273
- propylene/propene ($\text{CH}_3\text{CH}=\text{CH}_2$), 216
 complexes, 670–672
 polymerization reaction, 514–518
- quinone ($\text{C}_6\text{H}_4\text{O}_2$), 198, 205–206
- sulfate anion (SO_4^{2-}), 302–306
- tetracyanoethylene (TCNE, $\text{C}(\text{CN})_2=\text{C}(\text{CN})_2$), 676–677
 tungstenocene ($\text{W}(\text{C}_5\text{H}_5)_2$), 538, 542–545
- vinylamine ($\text{H}_2\text{C}=\text{CHNH}_2$), 216, 219–220
- water (H_2O), 116–118, 649
 cation (H_2O^+), 120–122, 125
 complexes, 596, 607, 616, 625–626, 653, 657, 697–699
 clusters, 646–652

Chemical formula

- Al
 Al_2 , 170–172
 Al_2H_6 (dialuminane), 348–351
 As
 As_2 , 172–173
 H_3AsO (arsine oxide), 179–181
 Au
 AuH , 387–397
 AuF , 426–428
 $\text{Au}(\text{CH}_3)$, 396–399
 $\text{Au}(\text{acac})$, 526–529, 534–536
 $\text{Au}(\text{C}_3\text{H}_5)$, 526–534
 $\text{Au}(\text{en})^+$, 526–529
 $\text{Au}(\text{HCCH})^+$, 526–529
 $\text{Au}(\text{NH}_3)_2^+$, 526–529
 Ar
 ArF_n , $n = 1, 2, 4, 6$, 299–302
- B
 B_2 , 158, 163–167, 170
 BF_3 , 177–179
 BH_4^- (borohydride anion), 626
 B_2H_6 (diborane), 308–313
 compared with protonated ethylene, 313–317
 analogs, 348–351, 483–487
 BH_2AsH_3 , 182
 BH_2PH_2 , 182
 B_4H_{10} (tetraborane), 319–327
 B_5H_9 , 319–324, 327–332
 B_5H_{11} , 319–324, 332–335
 B_6H_{10} , 319–324, 336–338, 344–346
 $\text{B}_{12}\text{H}_{12}^-$, 338–344
 Be

- BeF₂, 74–76
 HeBeO, 677
 Br
 Br₂, 172–173, 663–664
 Br₃[−] (tribromide anion), 286

 C, 48
 C₂, 158, 164–165, 167–168
 CH₂=X (X=CH₂, SiH₂, GeH₂, NH, PH, AsH, O, S, Se), 152–155
 CH₂=CHBHCH=CH₂, 186
 CH₂=CHC(=CH₂)CH=CH₂, 186
 CHONHCHO, 186
 CH₂=NCH=O, 186
 CHF(OH)PH₂, 145–146
 CH₂FNH₂, 242–247, 250
 CH₃COCH₂CH₂NH₂, 260–263
 CH₃F₂[−], 290
 C₂B₄H₈, 344–346
 C₂H₄⋯BH₃, 314–317
 Cl
 Cl₂, 172–173, 175–177
 ClF, 293
 Cl₃[−] (trichloride anion), 286
 ClFCl[−], 286
 ClF₅, 293
 ClF₃, 293
 Co, 77–78
 CoF, 79–81
 Cr, 77–78, 548
 CrF, 79–81
 CrF₆, 85–86
 CrH₆, 549–553
 Cr(CO)₃, 560–563
 complex with benzene, 675–676
 Cr₂H₂, 555–560
 Cu, 77–78
 CuF, 79–81

 F
 F₂, 104–105, 158, 164–165, 170, 175–177
 F₃[−] (trifluoride anion), 280, 286
 FCIF[−], 286
 FCICl[−], 286
 FFCl[−], 286
 HF (hydrogen fluoride), 27–31
 dimer 596
 clusters, 636–643
 complexes, 601, 607, 611, 616
 F[−] compounds
 AF, A = F, Cl, Br, H, Li, 101–102
 of transition metals, 79–86
 Fe, 77–81
 FeF₂, 85–86
 FeF₃, 85–86

 FeH₆^{4−}, 572–573
 Fe(CO)₄(C₂H₄), 508
 Fe(C₅H₅)₂ (ferrocene), 536, 541–542

 Ga
 Ga₂, 171–174
 Ge
 Ge₂, 172–173
 H₃GeGeH₃ (digermane), 237–238, 348–351

 H, 8–10, 23–24
 H[−], 625, 653
 H₂, 25–26, 90–96
 complexes, 668–669
 metal reactions, 498–501
 H₂⁺, 90–92
 H₃⁺, 314–316
 H₃[−] (trihydride anion), 286
 He, 38
 He₂, 38, 582
 HeBeO, 677
 HeH⁺, 233–234
 Hf, 548
 HfH₂, 397
 HfH₃, 397
³HfH₂ + H₂ reaction, 498
 HfH₃(CH₃) + H₂ reaction, 499–501
 HfH₃(OH), 429–430
 HfH₄, 549–553
 HfH₄(H₂), 490–491
 HfH₄ + C₂H₄ reaction, 501–503

 I
 I₂, 580
 I₃[−] (triiodide anion), 278, 280, 286
 Ir
 Ir(acac), 524–529, 534–536
 IrH₂, 397
 Ir(CH), 404, 406
 IrH(CH₂), 400, 406–412
 IrH₂(CH₃), 396–399
 IrH₂X, X = F, Cl, Br, I, 423–426
 IrF₃, 426–428
 IrH₃, 387–397, 468–469
 H₃Ir(NH), 431–434
 H₃IrO, 429–430, 460–461
 (H₂C)Ir + H₂ insertion reaction, 495–497
 Ir(C₃H₅), 524–534
 Ir(en)⁺, 524–529
 Ir(HCCH)⁺, 524–529
 Ir(NH₃)₂⁺, 524–529
 H₂IrIrH_n, n = 1, 2, 413–418
 Ir₈, 419–420

 Kr, 10–12

- Li, 4–5, 17–18, 47–48, 53–56
 Li⁺, 71–73
 Li₂, 90–91, 99–100
 Li₂⁺, 90–91, 99–100
 LiF, 49–64, 86
 LiF · · Li⁺, 65–66
 (Li⁺)_n(F⁻)_m clusters, 66–71
 HLiH⁻, 286, 288
- Mn, 77–78
 MnF, 79–81, 83–84
 MnF₃, 467–468
 Mn(H₂O)₆²⁺, 461–464
 Mo, 548
 MoH₆, 549–553
 Mo(CO)₃, 560–563
 MoO₂F₂, 369
 HMoMoH, 555–560
- N
 N₂, 116–118, 158, 164–165, 168–169
 N₂⁺, 120–124
 Nb
 NbH₅, 481–483
 Nb₂H₁₀ (diniobane), 484–487
 CpNb(CO)Cl, 471–472
 Ni, 77–78, 548
 NiF, 79–81, 83–84
 NiH₂, 549–553
 HNiNiH, 555–560
 Ni + C₂H₄ reaction, 505–509
 Ni(CN), 458–459
 Ni(CO), 458–459
 Ni(NC), 458–459
 Ni(C₅H₅)₂ (nickelocene), 536, 539–541
- O
 O₂, 158, 164–165, 169
 Os
 OsH₂, 397
 OsH₃, 397
 OsH₄, 387–397, 419
 OsH₃(CH₃), 396–399
 Os(CH₂)₂, 405–412, 419
 OsO₂, 431–432
 OsHCH, 404, 406, 419
 H₂OsO, 431–432
 H₂Os(CO), 441–442, 452–453
 H₂Os(NH₃), 441–442, 452–453
 H₂Os(PH₃), 441–442, 452–453
 H₃OsN, 431–434
 H₃Os(OH), 429–430
 H₃OsX, X = F, Cl, Br, I, 423–426
 OsF₄, 426–428
- H_nOsOsH_n, *n* = 1, 3, 413–419, 519–520
 Os₃H₆, 419–420
 Os₄H₆, 419–420
 Os₈H₈, 419–420
- P
 P₂, 172–173
 PF₃, 293
 PF₅, 277–278, 293
 :PH₃ (phosphine ligand), 440–446, 452, 454
 H₃PO (phosphine oxide), 179–181, 460
 Pd, 548
 PdH₂, 549–553
 Pd + C₂H₄ reaction, 505–509
 HPdPdH, 555–560
 Pt, 548
 PtH₂, 387–397, 549–553, 416
 dimer and complexes, 657–660
 PtH₄²⁻, 564–573
 Pt(CH₂), 400
 Pt(CH₃)₂, 370, 398–399
 PtH(CH₃), 396–399
 PtO, 370
 PtF₂, 426–428
 [Pt(CO)]²⁺, 465–466
 [PtF]⁺, 465–466
 [PtF_{4+n}]⁽ⁿ⁻²⁾⁻, *n* = 0–4, 474–477
 PtCl₄²⁻, 364
 [Pt(NH₃)]²⁺, 465–466
 PtH(PH₃)₂X, X = H, F, Cl, Br, I, 473–474
 [PtH(PH₃)₂(H₂)]⁺, 491–492
 [PtH(PH₃)₂(C₂H₄)]⁺, 507–509
 HPtPtH, 413–418, 555–560
 Pt + C₂H₄ reaction, 505–509
- Re
 ReH₂, 397
 ReH₃, 397
 ReH₅, 387–397
 H₂Re(CH), 404, 406
 H₂Re(CH₂), 400
 H₃Re(NH), 431–434
 H₃Re(NH₃), 441–442, 452–453
 H₃ReO, 429–430
 H₃Re(CO), 441–442, 452–453
 H₃Re(PH₃), 441–442, 452–453
 H₄Re(CH₃), 396–399
 ReF₅, 426–428
 H_nReReH_n, *n* = 1–4, 413–418
- Rh
 [Rh(C₆F₅)₅]²⁻, 472
 [Rh(PPh₃)₃]⁺, 472
 H₂Ru(PPh₃)₂, 472
 Ru(CH₂)Cl₂(PPh₃)₂, 472–474

- S
 S₂, 172–173
 HSSH, 240–241
 Sc, 77–78
 ScF, 79–81
 Se
 Se₂, 172–173
 Si
 Si₂, 172–173
 SiH₃F₂⁻, 290
 SiH₄ (silane), 267
 SiH₅⁻, 290
 SiF₅⁻, 290
 H₃SiSiH₃ (disilane), 237–238
 Si₃H₈ (trisilane), 270–273
 Si₃H₆ (cyclotrisilane), 268–273
 Si₄H₈ (cyclo-tetrasilane), 270–273
 Sr
 SrF₂, 73–76
 S
 SF₂, 293
 SF₄, 293
 SF₆, 293
 Ta
 TaH₂, 397
 TaH₃, 397
 H₃Ta(NH), 431–434
 H₃TaO, 429–430
 TaH₅(H₂), 490–491
 H_nTaTaH_n, *n* = 1–4, 413–418
 Ti, 77–81, 83–84, 548
 TiH₄, 549–553
 TiCl₄, 480
 TiO₂ (rutile), 480
 Ti + H₂ insertion reaction, 493–495
 Ti + C₂H₄ insertion reaction, 503–505, 532
 Cl₂TiCH₃ + C₂H₄ polymerization reaction, 509–518
 Cl₂TiCH₃ + CH₃CHCH₂ polymerization reaction,
 514–518
 V, 77–81
 VF, 79–81
 W, 548
 WH₂, 397
 WH₃, 397
 WH₄, 469–470
 WH₆, 387–397, 549–553
 W(CH₃)₆, 369
 H₅W(CH₃), 396–399
 HWNO, 369
 H₂WO₂
 H₃W(OH), 429–430
 H₃W(CH), 404, 406
 H₃W(CH₂), 400
 H₃WN, 431–434
 H₄WO, 431–432
 W(CH)₂, 405–407, 406
 W(CH₂)₃, 405–407, 406–412
 W(CO)₃, 560–563
 W(CO)_n, *n* = 1–6, 449–451
 WO₃, 369, 431–432
 HW(CH)(CH₂), 405–407
 WH_{6–2n}(CO)_n, *n* = 1–3, 453–458
 WH_{6–2n}(NH₃)_n, *n* = 1–3, 442–446
 WF₃³⁺, 428
 WF₆, 431, 426–428
 HWWH, 555–560
 H₅WWH₅, 520–522
 H_nWWH_n, *n* = 1–5, 413–418
 W(C₅H₅)₂ (tungstenocene), 538,
 542–545
 Xe
 XeH₂, 564
 XeH₄, 564
 Y
 YH₃, 481–483
 H₂Y(C₂H₅), 483–484
 YF₃, 482–483
 Y(OH)₃, 482–483
 Y₂H₆ (diyttrane), 484–487
 Zn, 77–78
 ZnF, 79–81
 Zn(NH₃)₆²⁺, 477–479
 Zr, 548
 ZrH₄, 481–483, 549–553
 Zr₂H₈ (dizirconane), 484–487

Author index

(Entries are of the form page(note), so that, e.g., “495(51)” refers to note 51 on page 495.)

- Abashkin, Y. G., 495(51)
Abrahamson, E. W., 686(94)
Adler, R. G., 345(162)
Alabugin, I. V., 611(44)
Albright, T. A., 230(78), 508(55)
Allavena, M., 73(16)
Allen, L. C., 130(36), 227(73)
Allinger, N., 25(43)
Allred, A. L., 130(35)
Altona, C., 240(87)
Anderson, J. E., 259(105)
Arlman, E. J., 510(58)
Atherton, J. H., 665(85)
Atkins, P., 302(148)
- Badenhoop, J. K., 25(44), 32(53), 37(57), 40(58),
62(9), 303(149)
Bader, R. F. W., 11(26), 274(130)
Baeyer, A., 269(117), 269(119)
Ballhausen, C. J., 439(33)
Ballik, E. A., 167(49)
Barbiellini, B., 583(18)
Barnhurst, L. A., 665(85)
Barrante, J. R., 3(6)
Bartell, L. S., 227(71)
Bartlett, N., 299(145), 474(43)
Barton, J. K., 253(100)
Bates, D. R., 90(5)
Bau, R., 625(52)
Bauld, N. L., 676(88)
Bax, A., 583(19)
Bayse, C. A., 381(13), 570(76)
Beck, W., 473(42)
Becke, A., 16(34)
Beckwith, A. L. J., 248(97)
Bell, A. T., 509(57)
- Bell, R. P., 308(152)
Belluci, V., 611(45), 627(54), 634(57)
Bent, H. A., 138(40), 286(141), 421(28), 717(7)
Berendsen, H. J. C., 635(59)
Berg, R. A., 73(16)
Bergmann, U., 649(69)
Bersuker, I. B., 467(38)
Bertie, J. E., 580(6)
Bertolasi, V., 611(45), 627(54), 634(57)
Berzelius, J. J., 130(36)
Bethe, H. A., 6(14), 437(32)
Bird, R. B. 47(2), 588(25), 588(26), 589(27), 590(28),
635(62)
Blockworth, A. J., 259(105)
Blum, O., 625(52)
Bock, C. W., 270(122)
Bohmann, J. A., 25(44)
Borkman, R. F., 130(36)
Born, M., 6(13)
Borodkin, G., 665(85)
Bos, M. W., 532(65)
Bosch, E., 673(87)
Boys, S. F., 115(24)
Bradley, A. J., 695(96)
Brandvold, T. A., 532(65)
Brett, A. M., 270(122)
Brookhard, M., 483(45)
Brown, H. C., 662(82), 662(83), 663(84)
Brown, S. N., 431(30)
Brown, W. G., 215(68)
Brunck, T. K., 227(71), 227(74), 254(101)
Büchler, A., 73(16)
Burdett, J. K., 230(78), 508(55)
Burns, R. C., 581(10)
Burrau, Ø, 90(5)
Bursten, B. E., 536(68)

- Burt, S. K., 495(51)
 Buys, H. R., 240(87)
 Byers Brown, W., 3(7)
- Cade, P. E., 11(26)
 Cai, J. Q., 259(105)
 Cairns, T. L., 676(88)
 Calder, V., 73(16)
 Carboni, R. A., 676(88)
 Carpenter, J. E. 25(44), 234(82), 588(24)
 Casimir, H. B. G., 590(29)
 Caulton, K. G., 625(52)
 Cavalleri, M., 649(69)
 Chamberlin, S., 532(65)
 Charkin, O. P., 73(17)
 Chatt, J., 503(54)
 Chernick, C. L., 299(145)
 Chestnut, D. B., 181(54)
 Claassen, H. H., 299(145)
 Clark, T., 25(43)
 Cleland, W. W., 621(48)
 Cleveland, T., 367(5), 369(6), 370(8), 372(10),
 473(42)
 Clifford, A. F., 130(36)
 Closs, G. L., 253(100)
 Clot, E., 389(16)
 Coffman, D. D. 676(88)
 Collins, J. R., 677(89)
 Collman, J. P., 510(59)
 Coolidge, A. S., 90(3), 580(6)
 Coops, J., 270(120)
 Corbett, J. D., 581(10)
 Cordier, F., 583(19)
 Cornilescu, G., 583(19)
 Cossee, P., 510(58)
 Cotton, F. A., 210(66), 412(24), 413(26), 532(66)
 Coulson, C. A., 26(47), 106(21), 129(31), 146(41),
 227(69), 230(76), 230(80), 272(124), 277(133),
 593(34)
 Cox, J. D., 270(120)
 Crabtree, R. H., 526(63), 624(50), 625(52)
 Cramer, C. J., 215(68)
 Crawford, B. L. Jr., 307(150)
 Crawford, V., 227(69)
 Cremer, D., 272(125), 272(126), 272(127), 274(130),
 274(131), 677(89)
 Critchlow, S. C., 581(10)
 Curtiss, C. F., 47(2), 588(25), 588(26), 589(27),
 590(28), 635(62)
 Curtiss, L. A. 8(22), 255(102), 602(38), 604(39),
 610(42)
 Custelcean, R., 626(53)
- Davidson, E. R., 22(37)
 Davidson, N., 6(11)
- Davies, A. G., 259(105)
 Davy, H., 650(70)
 DeCoster, D. M., 499(53)
 Debeer, E., 625(51)
 Delglass, W., 509(57)
 Denisov, G. S., 583(19)
 Desclaux, J.-P., 546(71)
 Deslongchamps, P., 248(97)
 Dewar, M. J. S., 215(68), 230(77), 264(112),
 264(114), 274(128), 503(54), 686(94)
 Dill, J. D., 270(123)
 Dilthey, W., 308(151)
 Dirac, P. A. M., 1(1)
 Djerassi, C., 260(106), 260(109)
 Doddi, G., 248(97)
 Donnelly, R. A., 130(36)
 Dougherty, R. C., 230(77)
 Duggan, P. J., 248(97)
 Duncanson, L. A., 503(54)
 Dunger, A., 583(19)
- Ebbing, D. D., 302(148)
 Eberhardt, W. H., 307(150)
 Eckert, J., 625(52)
 Edmiston, C., 115(24)
 Eisenschitz, R., 585(23)
 Eisenstein, O., 389(16), 625(52)
 Elanov, I. R., 665(85)
 Ellis, I. A., 247(95)
 Emerson, B. K., 718(9)
 Emsley, J., 631(55)
 Engelhardt, V. A., 676(88)
 Epiotis, N. D., 238(83), 283(139)
 Epstein, S. T., 3(7), 7(16)
 Ercolani, G., 248(97)
 Evans, W. J., 499(53)
 Eyring, H., 1(2), 102(14), 260(108), 678(90)
- Faraday, M., 196(58), 650(70)
 Farrar, T. C., 580(6)
 Feldgus, S., 509(56)
 Ferreira, R., 130(36)
 Ferretti, V., 611(45), 627(54), 634(57)
 Ferris, N. S., 676(88)
 Feshbach, H., 715(3)
 Fields, P. R., 299(145)
 Finke, R. G., 510(59)
 Firman, T. K., 367(5), 369(6), 369(7), 370(8),
 372(10), 383(14), 400(21), 473(42)
 Fischer, E. O., 536(67)
 Fisher, L. H., 580(6)
 Fleming, I., 230(78)
 Flygare, W. H., 604(39)
 Fock, V., 14(28), 105(25), 716(5)
 Ford, G. P., 274(128)

- Foresman, J. B., 8(21), 710(2),
 Foster, J. M., 115(24)
 Foster, J. P., 25(42)
 Frank, H. S., 652(73)
 Frenking, G., 389(16), 677(89)
 Freund, A., 269(118)
 Frey, P. A., 621(48)
 Frisch, A., 8(21), 710(2)
 Frohlich, N., 389(16)
 Frost, A. A., 210(65)
 Fujii, M., 695(96)
 Fukui, K., 686(94)
- Gammon, S. D., 302(148)
 Gassman, P. G., 621(48)
 Gauss, J., 272(125), 272(126), 272(127),
 677(89)
 Gavezzotti, A., 227(71)
 George, P., 270(122)
 Gerlt, J. A., 621(48)
 Gessespie, R. J., 389(15)
 Gibbs, J. W., 8(20), 723(1)
 Giese, B., 253(100)
 Gigli, G., 73(19)
 Gillespie, R. J., 293(144)
 Gilli, G. F., 611(45), 627(54), 634(57)
 Gilli, G., (45), 627(54)
 Gilli, P., (45), 627(54)
 Gindin, V. A., 583(19)
 Glasstone, S., 678(90)
 Glatzel, P., 649(69)
 Glendening, E. D., 25(44), 32(53), 216(68), 265(115),
 303(149), 591(32)
 Gole, J. L., 73(17)
 Golubev, N. S., 583(19)
 Gonzalez, C., 681(91)
 Goodman, L., 228(75)
 Gordy, W., 130(33), 130(36)
 Gould, I. R., 676(88)
 Gray, C. W., 303(Fig. 3.90)
 Greaves, J., 499(53)
 Green, J. C., 542(70)
 Green, M. L. H., 470(41), 483(45), 484(46),
 529(64)
 Greenberg, A., 270(123)
 Grein, F., 240(88)
 Grev, R. S., 264(113)
 Grigera, J. R., 635(59)
 Grosjean, M., 260(106)
 Grzesiek, S., 583(19)
 Gu, H., 228(75)
 Guevas, G., 240(86)
 Guido, M., 73(19)
 Gunion, R. F., 625(51)
 Gutowsky, H. S., 313(156)
- Haddon, R. C., 665(85)
 Hall, J. H., 625(52)
 Hall, M. B., 381(13), 570(76)
 Halpern, J., 488(49)
 Hamann, D. R., 583(18)
 Hamilton, W. C., 591(33)
 Hamlow, H. P., 247(96)
 Hancock, R. D., 526(62)
 Hanna, H. J., 303(Fig. 3.90)
 Hannay, N. B., 130(32)
 Hargittai, I., 293(144), 389(15)
 Hargittai, M., 467(39)
 Hartley, F. R., 473(42)
 Hartree, D. R., 14(28)
 Harvey, J. N., 542(70)
 Hassell, O., 286(140), 580(8)
 Hassett, D. M., 73(17)
 Havinga, E., 240(87)
 Hawthorne, M. F., 345(162)
 Hayashi, M., 247(94)
 Hayes, E. F., 73(17), 73(18)
 Heckert, R. E., 676(88)
 Hegedus, L. S., 510(59)
 Hehre, W. J., 7(19), 151(43), 710(1)
 Heitler, W., 90(1)
 Helmholtz, L., 31(49)
 Henneker, W. H., 11(26)
 Herman, Z. S., 363(3)
 Herzberg, G., 90(6), 158(Table 3.13), 662(78),
 663(84)
 Herzfeld, K. F., 686(94)
 Heully, J.-L., 467(39)
 Hiberty, P. C., 541(69)
 Hightower, J. W., 509(57)
 Hinze, J., 130(36)
 Hirota, N., 676(88)
 Hirsch, T. K., 649(69)
 Hirschfelder, J. O., 3(7), 47(2), 588(25), 588(26),
 589(27), 590(28), 635(62)
 Hochstrasser, R. M., 676(88)
 Hoffmann, R., 31(49), 253(99), 541(69), 686(95)
 Hohenberg, P., 16(32)
 Hu, J.-S., 583(19)
 Huber, K. P., 158(Table 3.13)
 Hudson, R. F., 230(77)
 Hückel, E., 197(60)
 Huffman, J. C., 625(52)
 Hughes, R. P., 473(42)
 Huheey, J. E., 130(36)
 Huisgen, R., 269(117)
 Hund, F., 166(47)
 Hunt, W. J., 73(17)
 Husimi, K., 22(37)
 Hylleraas, E. A., 3(8), (30)
 Hyman, H. H., 299(145), 299(146)

- Ibers, J. A., 591(33)
 Iczkowski, R. P., 130(36)
 Ingold, C. K., 196(59), 662(81)
 Isaacs, E. D., 583(18)
 Ito, M., 695(96)
 Itoh, T., 247(93)
 Ittel, S. D., 487(47)
- Jackson, J. E., 626(53)
 Jackson, S. A., 625(52)
 Jacob, J., 583(19)
 Jacobsen, E. N., 487(47)
 Jaffé, H. H., 130(36)
 Jahn, H. A., 467(37)
 James, H. M., 90(3)
 Janet, C., 717(6)
 Janusek, R., 270(121)
 Jarzeba, W., 676(88)
 Jeffrey, G. A., 580(5), 650(70)
 Jennings, J. P., 260(110)
 Jensen, W. B., 105(18), 177(52), 662(79)
 Johnson, M. K., 676(88)
 Jones, L., 302(148)
 Jordan, K., 255(102), 255(104)
 Juaristi, E., 240(86)
- Kaarsemaker, S. J., 270(120)
 Kamb, B. J., 363(3)
 Kaminsky, W., 499(53)
 Kauffman, G. B., 436(31)
 Kaupp, M., 73(17), 389(16), 421(27)
 Kauzmann, W. J., 260(108)
 Khlbystov, A. N., 665(85)
 Kim, E. H., 625(51)
 Kim, E. K., 673(87)
 Kim, T., 676(88)
 Kimball, G. E., 1(2), 102(14)
 Kimura, Y., 676(88)
 King, R. B., 381(13), 676(88)
 Kirby, A. J., 240(86)
 Kirpekar, S., 583(19)
 Klemperer, W., 73(16)
 Klimenko, N. M., 73(17)
 Klopman, G., 130(36)
 Klyne, W., 260(109), 260(110)
 Knight, A. E. W., 695(96)
 Knowles, W. S., 488(48)
 Knowlton, J. W., 270(120)
 Koch, W., 677(89)
 Kochi, J. K., 673(87)
 Koetzle, T. F., 625(52)
 Kohn, W., 16(32), 16(33)
 Kollman, P., 621(48)
 Kolonits, M., 467(39)
 Kolos, W., 90(6)
- Konze, W. V., 488(48)
 Koopmans, T. A., 119(29)
 Kraka, E., 274(130)
 Kreevoy, M. M., 621(48)
 Krestownikoff, A., 269(118)
 Kubas, G. J., 488(48), 492(50), 625(52)
 Kurtz, E. M., 676(88)
 Kutadeladze, A. G., 665(85)
 Kutal, C., 676(88)
 Kutzelnigg, W., 277(134)
- Laidler, K. J., 678(90)
 Landis, C. R., 365(4), 367(5), 369(6), 369(7), 370(8),
 373(10), 383(14), 400(21), 488(49), 509(56),
 518(61), 473(42)
 Langmuir, I., 105(18)
 Latajka, Z., 661(76)
 Latimer, W. M., 583(13), 596(35)
 Ledsham, K., 90(5)
 Lee, C., 16(34)
 Lee-Huang, S., 583(19)
 Legon, A. C., 604(39)
 Legrand, M., 260(106)
 Lennard-Jones, J. E., 635(62)
 Lerner, L., 243(91)
 Lesiecki, M. L., 73(16)
 Levine, I. N., 3(6)
 Levy, M., 130(36)
 Lewis, G. N., 26(46), 105(18), 583(13), 583(14)
 Liang, C., 255(102)
 Lide, D. R. Jr., 247(93)
 Lierman, J. F., 270(123)
 Limbach, H.-H., 583(19)
 Lineberger, W. C., 625(51)
 Lipscomb, W. N., 227(72), 307(150), 309(154),
 329(160)
 Little, E. L., 676(88)
 Lledos, A., 389(16)
 Löwdin, P.-O., 7(17), 15(31), 23(40), 378(12),
 686(94)
 Loftus, A., 227(69)
 London, F., 90(1), 585(23)
 Long, J. A., 345(162)
 Longuet-Higgins, H. C., 308(152), 686(94)
 Lough, A. J., 625(52)
 Lu, K.-T., 695(96)
 Ludwig, R., 646(66), 651(72)
 Lukehart, C. M., 412(24)
- Madelung, E., 716(4)
 Magnusson, E., 277(135)
 Malkina, O. L., 583(19)
 Malm, J. G., 299(145)
 Mann, D. E., 73(16)
 Manning, W. M., 299(145)

- Manoharan, M., 611(44)
 Marder, T. B., 345(162)
 Margrave, J. L., 130(36)
 Markel, F., 676(88)
 Markownikoff, H., 269(118)
 Marks, T. J., 536(68)
 Marsden, C. J., 73(17), 467(39)
 Marsh, R. E., 650(71)
 Martell, A. E., 526(62)
 Maseras, F., 389(16)
 Mason, S. F., 260(108)
 Matheson, M. S., 299(145)
 Mayer, J. M., 39(20)
 Mazurs, E. G., 715(2)
 Mazurs, E. G., 717(7), 717(8), 718(9),
 718(10)
 McClellan, A. L., 583(20)
 McConnell, H. M., 255(103)
 McGeer, E. G., 676(88)
 McHale, J. L., 676(88)
 McKean, D. C., 247(95)
 McKelvey, D. R., 546(71)
 McKusik, B. C., 676(88)
 McLean, A. D. 90(4)
 McMullan, R. K., 650(70)
 Mendeleev, D. I., 715(1), 718(9)
 Merenyi, R., 270(121)
 Messmer, R. P., 412(23)
 Meyer, M. A., 473(42)
 Michaelian, K. H., 580(6)
 Middleton, W. J., 676(88)
 Miller, J. R., 253(100), 255(102)
 Miller, M., 196(58)
 Miller, R. A., 532(65)
 Millikan, R. C., 580(6)
 Milstein, R., 625(52)
 Mingos, D. M. P., 309(155), 372(10)
 Moffitt, W. E., 146(41), 260(109), 272(124)
 Møller, C., 14(29)
 Moodie, R. B., 665(85)
 Moore, C. E., 77(Table 2.2)
 Morales, C. M., 25(44)
 Morris, R. H., 625(52)
 Morse, P. M., 715(3)
 Moscowitz, A., 260(109)
 Moss, D. B., 695(96)
 Muldoon, J., 431(30)
 Mulliken, R. S., 31(49), 105(18), 130(36), 212(67),
 215(68), 227(69), 308(152), 580(7), 661(77),
 662(82), 663(84), 686(94)
 Murata, S., 676(88)
 Musaev, D. G., 73(17)
 Musher, J., 276(132)
 Musulin, B., 210(65)
 Myers, A. B., 676(88)
 Nakagawa, N. 247(96)
 Naleway, C. A., 255(102)
 Näslund, L. A., 649(69)
 Nesterov, E. E., 665(85)
 Neumark, D. M., 625(51)
 Newton, M. D., 255(102)
 Nibler, J. W., 73(16)
 Nilsson, A., 649(69)
 Nishikawa, T., 247(93)
 Noble, D. R., 665(85)
 Nordlund, D., 649(69)
 Norton, J. R., 510(59)
 Norton, M. L., 676(88)
 Noyori, R., 488(48)
 Nugent, W. A., 399(20)
 Nyholm, R. S., 293(144)

 Odelius, M., 649(69)
 Ogasawara, H., 649(69)
 Ojamäe, L., 649(69)
 Okuda, S., 247(96)
 Olgemoeller, B., 473(42)
 Oppenheimer, J. R., 6(13)
 Orgel, L. E., 661(77)
 Orville-Thomas, W. J., 227(72), 661(76)
 Overbeek, J. T. G., 591(30)
 Owens, K. G., 695(96)

 Paddon-Row, M. N., 255(102), 255(104)
 Palke, W. E., 130(36)
 Papazyan, A., 621(48)
 Park, S., 625(52)
 Parkin, G., 470(40)
 Parmenter, C. S., 695(96)
 Parr, R. G., 14(30), 16(34), 90(4), 130(36), 212(67)
 Parshall, G. W., 487(47)
 Partington, J. R., 45(1)
 Pasternak, A., 130(36)
 Pauli, W., 6(15)
 Pauling, L., 26(47), 31(50), 32(51), 102(14), 102(15),
 106(19), 129(31), 130(34), 132(38), 151(42),
 151(44), 169(51), 196(59), 302(148), 363(1),
 363(2), 363(3), 372(9), 580(5), 583(15), 635(58),
 649(68), 650(71), 90(2)
 Peabody, S., 611(44)
 Perkin, W. H., 269(117), 269(118)
 Person, W. B., 580(7)
 Petillo, P., 243(91)
 Pettersson, L. G. M., 649(69)
 Pfaltz, A., 487(47)
 Pidcock, A., 473(42)
 Piechuch, P., 661(76)
 Pierce, L. M., 247(94)
 Pilcher, G., 270(120)
 Pimentel, G. C., 278(137), 583(20)

- Pitzer, K. S., 227(72), 308(152), 313(156), 546(71), 580(6)
- Platt, J. R., 212(67)
- Platzman, P. M., 583(18)
- Plesset, M. S., 14(29)
- Plyler, E. K., 661(77)
- Pochatko, D., 602(38), 604(39), 610(42)
- Podryvanov, V. A., 665(85)
- Polder, D., 590(29)
- Poli, R., 536(68), 542(70)
- Pophristic, V., 228(75)
- Pople, J. A., 7(19), 151(43), 710(1)
- Powell, H. M., 293(144)
- Powell, R. E., 546(71)
- Preuss, H., 73(17)
- Price, W. C., 308(153)
- Pritchard, H. O., 130(36)
- Pross, A., 498(52), 681(93)
- Pryce, M. H. L., 466(36)
- Pullman, B., 686(94)
- Pyykkö, P., 546(71)
- Quarterman, L. A., 299(145)
- Quist, A. S., 652(73)
- Radom, L., 7(19), 151(43), 710(1)
- Raghavachari, K., 665(85)
- Ramachandran, R., 625(52)
- Ramsey, N. F., 167(49)
- Rao, C. N. R., 661(76)
- Ratajczak, H., 661(76)
- Ratner, M., 253(100)
- Rayleigh (Lord), 3(5)
- Reed, A. E., 8(22), 25(41), 25(44), 30(48), 115(24), 180(53), 183(56), 227(71), 278(136), 602(38), 604(39), 610(42), 610(43)
- Reents, W. D. Jr., 665(85)
- Réffy, B., 467(39)
- Reibke, R., 583(19)
- Reid, G. D., 676(88)
- Rheingold, A. L., 473(42), 625(52)
- Richards, R. E., 473(42)
- Rieke, C. A., 215(68)
- Robinson, Sir R., 196(59)
- Rochow, E. G., 130(35)
- Rodebush, W. H., 583(13), 596(35)
- Romers, C., 240(87)
- Root, D. M., 369(6), 372(10), 473(42)
- Roothaan, C. C. J., 14(28)
- Rosaaen, K. A., 518(61)
- Roscoe, H. E., 579(1)
- Rosenfeld, L., 260(107)
- Rossini, F. D., 270(120)
- Ruedenberg, K., 115(24)
- Runciman, W. A., 466(36)
- Rundle, R. E., 278(137)
- Russo, N., 495(51)
- Salpeter, E. E., 6(14)
- Salzner, U., 73(17), 215(68), 243(91)
- Sanderson, R. S., 105(18), 130(36), 398(19)
- Sandifur, C. W., 303(Fig. 3.90)
- Sapse, A. M., 661(76)
- Sarker, H., 676(88)
- Saurez, D., 215(68)
- Schaefer, H. F., 73(117), 264(113)
- Scheirs, J., 499(53)
- Scheve, B. J., 248(97)
- Schlegel, H. B., 681(91)
- Schleyer, P. v. R., 7(19), 8(22), 25(43), 73(17), 151(43), 180(53), 215(68), 243(91), 255(104), 270(121), 272(125), 272(126), 661(76), 710(1)
- Schnatzke, G., 260(106)
- Schrödinger, E., 3(5), 8(23)
- Schreiner, F., 299(145)
- Schrock, R. R., 412(25)
- Schultz, P. A., 412(23)
- Schwerdtfeger, P., 73(20)
- Scopes, P. M., 260(110)
- Scott, (Sir) W., 196(58)
- Scott, B. L., 488(48)
- Scott, C., 240(88)
- Scott, R. A., 676(88)
- Scribner, R. M., 676(88)
- Selig, H. H., 299(145), 299(145)
- Shaik, S., 498(52), 541(69), 681(93)
- Shakirov, M. M., 665(85)
- Sham, L. J., 16(33)
- Shang, M., 532(66)
- Sharpless, K. B., 488(48)
- Sheft, I., 299(145)
- Shenderovich, I. G., 583(19)
- Sheshardri, K. S., 73(16)
- Shi, X., 309(155)
- Shimoda, K., 247(93)
- Shukla, A., 583(18)
- Shurki, A., 681(93)
- Sidgwick, N. V., 105(18), 293(144), 662(80)
- Siegbahn, P. E. M., 625(52)
- Siegel, S., 299(145)
- Siu, A. K. Q., 73(17)
- Skinner, H. A., 130(36)
- Slater, J. C., 14(28), 106(20), 363(1)
- Slee, T. S., 274(130)
- Sloth, E. N., 299(145)
- Smirnov, S. N., 583(19)
- Smith, M. L., 676(88)
- Smyth, C. P., 130(32)
- Soper, P. D., 604(39)
- Sordo, J. A., 215(68)

- Sordo, T. L., 215(68)
 Stahl, S. J., 583(19)
 Stauffer, J. L., 73(16)
 Stein, L., 299(145)
 Steudel, R., 581(9)
 Stevens, J. C., 509(57)
 Stevens, R. S., 625(52)
 Stewart, A. L., 90(5)
 Stinzing, H., 718(9),
 Stock, A., 319(157)
 Stoll, H., 73(17)
 Stout, J. W., 580(6)
 Straatsma, T. P., 635(59)
 Streitwieser, A. Jr., 209(64), 215(68), 536(68),
 591(32)
 Studier, M. H., 299(145)
 Su, M.-D., 498(52)
 Sugden, T. M., 105(18),
 Suidan, L., 303(149)
 Summers, M. F., 583(19)
 Sur, S. K., 366(Table 4.1)
 Syrkin, Y. K., 277(133)
 Szczesniak, M. M., 661(76)
 Szentpaly, L. v., 73(20)
- Tachiya, M., 676(88)
 Takazawa, K., 695(96)
 Takebayashi, Y., 676(88)
 Tallant, N. A., 259(105)
 Tawa, M. D., 473(42)
 Taylor, G. R., 14(30)
 Teller, E., 467(37)
 Teo, B. K., 309(155)
 Thatcher, G. R. J., 240(86), 243(91)
 Theobald, C. W., 676(88)
 Tobin, J. B., 621(48)
 Trachtman, M., 270(122)
 Tulk, C. A., 583(18)
 Turro, N. J., 253(100)
 Tyndall, J., 579(1)
 Tyrrell, J., 264(114)
- Uddin, J., 518(61)
- Van Nees, K., 591(30)
 Van Vleck, J. H., 439(33)
 Van der Sluys, L. S., 625(52)
 Velluz, L., 260(106)
 Venanzi, L. M., 473(42)
 Vergarnini, P. J., 625(52)
 Verwey, E. J. W., 591(30)
 Viehe, H. G., 270(121)
- Walsh, A. D., 130(36), 308(152)
 Walter, J. E., 260(108)
 Walter, J., 1(2), 102(14)
 Walton, R. A., 413(26)
 Wang, Y.-X., 583(19)
 Ward, A. J., 473(42)
 Warshel, A., 621(48)
 Weeks, J. L., 299(145)
 Weinhold, F., 8(22), 25(41), 25(42), 25(43), 25(44),
 30(48), 32(53), 37(57), 40(58), 62(9), 115(24),
 183(56), 227(71), 227(74), 231(81), 234(82),
 254(101), 264(114), 278(136), 303(149), 365(4),
 580(6), 582(12), 588(24), 602(38), 604(39),
 607(41), 610(42), 610(43), 611(44), 646(67),
 651(72), 695(96)
 Weinstock, R. B., 25(41), 30(48), 264(114)
 Weiss, A., 90(4)
 Weisshaar, J. C., 695(96)
 Weisskopf, V. F., 37(56), 63(10)
 Wen, W.-Y., 652(73)
 Wendolski, J. J., 610(43)
 Wendt, M. A., 580(6)
 Werner, A., 436(31)
 Wernet, P., 649(69)
 Whangbo, M. H., 230(78), 508(55)
 Wharton, L., 73(16)
 Wheeler, L. P., (1), 8(20)
 Wheland, G. W., 32(51), 102(14), 102(15),
 196(59)
 White, D., 73(16)
 Whitt, S. A., 621(48)
 Wiberg, K. B., 610(43)
 Wigner, E., 686(94)
 Wilcox, C. H. 7(17)
 Wilkinson, G., 536(67)
 Williamson, A., 473(42)
 Wilmshurst, J. K., 130(36)
 Wilson, E. B. Jr., 227(70)
 Wind, H., 90(5)
 Windberg, H. E., 676(88)
 Wingfield, P., 583(19)
 Wiswesser, W. J., 718(10)
 Witmer, E. E., 686(94)
 Wolfe, S., 240(85)
 Wolfsberg, M., 31(49)
 Wolniewicz, L., 90(6)
 Wong, L.-L., 483(45)
 Woodward, R. B., 260(109), 686(95)
 Wulff, W. D., 532(65)
 Wütrich, K., 583(19)
 Wynne, K., 676(88)
- Yakshin, M. M., 277(133)
 Yamamoto, H., 487(47)
 Yang, W., 16(34)

Yarkony, D. R., 73(17)
Yoshimine, M., 90(4)
Yost, D. M., 130(34)

Zachmanoglou, C., 470(40)
Zakharov, L. N., 473(42)
Zefirov, N. S., 665(85)

Zhang, H., 309(155)
Zhao, A.-Q., 695(96)
Zhenyang, L., 372(10)
Zimmerman, H. E., 686(94)
Zirin, M. H., 299(145)
Zum Dahl, S. S., 302(148)
Zyk, N. V., 665(85)

Subject index

(Italic page numbers are for locations of photographs.)

- acceptor (Lewis acid)
 - relative strengths, 607
 - see* donor–acceptor interaction
- agostic interaction, 317–319, 480, 483–487
- Alder, K., 686
- alkaline earth
 - bent ionic MX_2 , 73–76, 87
- “alkene-orienting” effect, 508
- alpha helix, 646
- anomeric effect, 240–243
- antiaromaticity, 196–205
 - see* cyclobutadiene
- anti-H-bond, 659
- anticooperativity, 642–643
- antiperiplanar influence
 - see* stereoelectronic effect
- antisymmetry, 587
- aromaticity, 196–205
- asymmetric catalysis, 508–509
- asymmetric hydrogenation, 488
- atomic
 - ground-state electron configuration, 719–721
 - units, 723–725
 - (Rutherford) model, 89
- Aufbau* principle
 - atomic configuration, 719–721
 - homonuclear diatomic molecules
 - MO, 158–159
 - NBO, 160–172
 - multi-center, 306–313, 351
- B3LYP
 - see* density functional
- Baeyer ring-strain theory, 269–273
- banana bond, 351, 694
 - idealized, in double bond, 223, 409, 411–412
 - in cyclopropane, 274
 - in dicarbollide, 347
 - in Ga_2 , 171, 174
 - in HReReH , 418
 - in vinylamine, 219–220, 226
 - in $\text{W}(\text{CH}_2)_3$, 409
- Bartlett, N., 299
- basis set, 712–714
 - correlation consistent, 714
 - Dunning style, 714
 - ECP, 713–714
 - LACV3P++, 364
 - Pople-style, 712–713
- Bent, H. A., 138, 286, 573
- Bent’s rule, 352, 574, 610
 - in boron hydrides, 326
 - for d-block species, 421–434
 - ionicity, d character, and shape, 395–396
 - restated form, 421–422
 - for s/p-block species, 138–146
 - NBO extension, 140–146
 - in C_3H_6 , 147
 - in geminal delocalization, 265
 - in hypervalency, 293
 - in N_2^+ , 121
 - in torsion–vibration coupling, 246
 - R-dependent, 151
- Berzelius, J. J., 45–46
- Bethe, H. A., 437, 438
- blue-shifting hydrogen bonds, 610
- Bohr, N., 8–9
- bond
 - covalent, 579, 591
 - coordinate covalent/dative, 177–182, 440

- hypovalent (3c/2e), 306–351
 hypervalent (3c/4e), 282–306, 440, 447–451, 594, 618, 683
 ionic, 45–88
 one-electron, 91–92
 resonance (“weak,” “noncovalent”) 591, 593
 three-electron, 169
 bond bending
 NBO description 146–151, 351
 in C₃H₆, 146–147
 in CH₂FNH₂, 147
 in NH₃, PH₃ umbrella motion, 147–151
 bond dissociation energy (BDE)
 in hypervalent SF_n species, 298–299
 in group 4, 6, 10 compounds
 metal–hydride, 551–555
 metal–methyl, 553–555
 metal–metal, 558–559
 bond order
 see natural resonance theory (NRT), resonance
 bond-order–bond-length relation
 amide complexes, 700–701
 Diels–Alder, 691–693
 stereoelectronic effect, 251
 dinuclear transition metal hydrides, 416
 altered hapticity, 530
 Born–Oppenheimer approximation, 579, 583–585
 and molecular structure concept, 6
 for H₂⁺, 90
 boron hydrides, 319–344
 d-block analogs, 483–487
 boron polymorphs, 341
 bridge-bonding
 see hypovalency, tau-bond
 Brunck, T. K., 227, 240
 buckyball (H₂O)_n, 649–652

 carbenes
 transition metal, 399–413
 Fischer- and Schrock-type, 413
 carbocation
 in alkene polymerization, 509–518
 stereoelectronic stabilization, 251–252
 carboranes, 344–351
 Casimir, H. G., 590–591
 catalysis
 by hypovalent transition metals, 487–518
 metal–H₂ reactions, 488–501
 metal–alkene reactions, 501–509
 chelation, 522–529
 anti-chelate effect, 528–529
 chelate effect, 522
 entropic nature, 526
 hapticity, 529–534
 resonance enhancement, 534–536
 cluster (“van der Waals molecule”), 581, 602
 charge “leakage,” 86–87
 in LiF, 51–52
 charge transfer (CT), 595, 623–624, 640, 665–675
 complex, 580–581, 594, 661–678
 CT-deleted (*see* \$DEL)
 in dative bonding, 178–179
 in ionic bonding, 58–60
 open- versus closed-CT networks, 71, 87, 193–196
 \$CHOOSE (select Lewis structure) procedure, 688
 colloid stability, 591
 complete active space (CAS), 711
 configuration interaction (CI), 710–711
 conjugation
 s/p-block, 182–214
 and resonance concept, 182–196
 cooperativity, 629, 635–646
 in benzene, 197–200
 in chelation, 536
 in ionic compounds, 87
 in (Li⁺)_n(F⁻)_m clusters, 66–71
 in pi networks, 193–196
 coordinate metal–ligand bonding
 crystal field and ligand field theory, 437–440
 localized Lewis-like picture, 440
 pi-backbonding, 452–459
 pi-frontbonding, 459–461
 sigma coordinative bonding, 440–446
 Werner picture, 434–437
 coordination number (CN), 370–372, 437
 core orbitals
 effect on bonding overlap, 96–99
 effect on vertical trends, 551–552
 role in alkaline earth MX₂ bending, 73
 correlation energy, 14
 Cossee, P., 510
 Coulomb’s law
 discovery, 45
 in Schrödinger equation, 6
 model, 594
 units, 46, 725
 Coulson, C. A., 106, 107, 110, 593
 Coulson–Moffitt picture of C₃H₆, 146, 273–275
 hybrid directionality theorem, 110
 hypervalent ionic resonance, 277, 447
 covalency, 89
 NRT definition, 35
 one- and two-electron, 90–96
 organic chemistry origins, 351
 covalent wavefunction, 102
 contrast with NBO description, 104–105
 see Heitler–London model
 Crawford, B., 307
 Cremer, D., 272

- crystal field theory, 437–439
 splitting energy (10Dq), 438, 461, 463, 464–466
- crystallographic packing shapes, 386–387
- cycloaddition (*see* reaction)
- d-block compounds
 covalent and coordinate bonding, 363–575
 donor–acceptor interactions, 82–85
 ionic bonding, 76–86
 ubiquity of hyperbonding, 447–448
- d-count, 371
 and Green's MLX classification, 470–471
 and omega-bonding, 470–473
 in crystal field splitting, 439
 in sandwich complexes, 539
- d-orbital participation
 in bent alkaline earth dihalides, 73
 in hypervalency, 276, 288, 572
 in main-group oxyacids, 302–306
- Dalton, J., 579
- dative (coordinate covalent) bonding, 177–182
 in transition metal chemistry, 440–446
 NBO characteristics, 178, 441
 pi-bonds, 181–182
- dative coordination reaction (*see* reaction)
- Davy, H., 45
- ΔDEL (deletion) procedure, 273, 602, 613, 666–667, 683–684
- delta bonding, 415–418
- density functional
 B3LYP, 16
 methods, 16, 711–712
- density operator, 21–23
 first-order, 21, 41
 kernel, 21–22
 matrix elements, 22
- Dewar, M. J. S., 264–265, 273–275
- Diels, O., 686
- Diels–Alder reaction (*see* reaction)
- dihydrogen bonds, 624
- dipole moment, 598, 605
 macroscopic, 646
 see multipole
- Dirac, P. A. M., 1
 bra-ket notation, 3
 equation, 6, 545
- dispersion force, 588, 590
 retarded (Casimir–Polder), 591
 unimportance in torsion barriers, 227
- donor (Lewis base)
 relative strengths, 607
 see donor–acceptor interaction
- donor–acceptor interaction
 absence in cyclobutadiene, 200–202
 comparison with MO description, 94–96
 geminal, 263–264
 in hyperbonding, 281–289
 in hypovalency, 306–351
 in ionic transition metal compounds, 82–85
 in metal–H₂ interaction, 488–490
 in transition metal–ligand coordination, 440–446
 multi-center *Aufbau*, 306
 one-electron, 91, 462
 orientational versus energetic dependence, 185–190
 perturbation theory, 16–19
 relative strengths, 236
 stabilization, 19–20
 symmetry-allowed in homonuclear diatomics, 162
 two-electron, 92–93
 vicinal versus non-vicinal, 193
- duodectet rule (“rule of 12”), 365–367, 574
- e_g orbital (octahedral), 438, 461–464
- early transition metals (*see* hypovalency)
- Earnshaw's theorem, 46, 65
- Eberhardt, W., 307
- effective atomic number (EAN, “18-electron”) rule, 448
 and p-orbital participation, 570
 statistical frequency, 470–471
 violation, 474, 477–478
- effective core potential (ECP), 713–714
 basis set, 364
 in alkaline-earth dihalide bending, 74
- electron
 configuration, 719–721
 in d-block atoms and ions, 76–78
 singlet complementary atoms (¹CA), 166
 correlation, 14
 correlation-consistent basis sets, 714
 effect on orbital shape, 15
 left–right (bond) type, 103
 discovery, 45
 density, 9, 14
 spin and antisymmetry, 36–37
- electron affinity
 of fluorine, 78
 of first-row transition metal atoms, 76–77
- “electron-deficient” compounds (*see* hypovalency)
- electronegativity
 Allred–Rochow, 130, 132–134
 and hybridization, 134–137
 and ionic character, 80–81, 442
 natural, 127 (tables, 133, 155, 398, 405)
 of transition metals, 396–398, 404–405
 orbital versus atomic property, 157
 pi-type, 151–157
 Pauling, 129–133

- electroneutrality principle
 main-group oxyacids, 302
 versus high formal charge, 433
 electrophilic cleavage reaction (*see* reaction)
 electrophilic displacement reaction (*see* reaction)
 electrophilic substitution reaction (*see* reaction)
 electrostatics (classical)
 in crystal field theory, 437–439
 multipoles, 587–525
 torsion barrier effects, 327
 view of H-bonding, 583, 593, 615, 636
 electrovalency, 35
 enolones, 631
 entropic factors (H-bonding), 649
 Epiotis, N., 283
 excited states
 $^3n \rightarrow \pi^*$ ketone excitation, 260–263
 primary hyperconjugation in $^3\pi \rightarrow \pi^*$ excitation,
 223–226
 spin excitation in transition metals, 461–464
 Eyring, H., 678, 679

 Faraday, M., 45, 196
 fine-structure constant, 545
 Fischer, E. O., 536
 “flickering clusters,” 652
 Fock, V.
 dynamical symmetry, 716
 invariance theorem, 115
 operator, 115
 force
 ionic, 596, 611, 615
 steric/exchange, 37–38
 “four-electron-destabilizing” interactions,
 229–234
 Frankland, E., 45
 Franklin, B., 45

 Galvani, L., 45
gauche effect, 240–243
 Gauss, J., 272
 Gaussian
 basis function 568, 712
 program, 364
 generalized valence bond (GVB) method,
 711
 Gilli, G. F., 611, 627, 634
 Gibbs, J. W., 8, 723–725
 Glendening, E. D., 591, 264
 Green’s MLX classification, 470–472
 and hapticity, 529–531
 in sandwich complexes, 538–545
 for $\text{Fe}(\text{CO})_4\text{C}_2\text{H}_4$, 508
 for $[\text{Pt}(\text{PH}_3)_2\text{HR}_2]^+$, 507
 for $[\text{Pt}(\text{PH}_3)_2\text{H}(\text{H}_2)]^+$, 491–492

 Hamiltonian operator, 1, 9, 36, 584
 hapticity, 539–534
 and Green’s MLX formalism, 529
 in sandwich complexes, 536–545
 Hartree–Fock (HF) model, 13–14, 41, 710
 perturbation theory, 17–19
 Hassel, O., 286, 580–581
 Havinga, E., 240
 Hermitian property, 585, 588
 Heitler–London wavefunction for H_2 , 90, 102–105
 Herzberg, G., 662
 Hirschfelder, J. O., 590
 helium
 dimer, 38, 582
 $\text{He} \cdots \text{BeO}$, 677–678
 Hoffmann, R., 686
 through-bond coupling, 253–256
 see Woodward–Hoffmann rules
 homonuclear diatomic molecules, 157–172
 NBO *Aufbau* principles, 166
 hydrogen bonding, 580, 593–660
 charge-assisted ($\pm\text{CAHB}$), 611
 cooperativity, 635
 coupling with torsions, 693–702
 entropic factors, 649
 isomerization, 604–611
 low-barrier, 618
 resonance nature, 621
 resonance-assisted (RAHB), 627
 strength, 607
 transition metal, 657–660
 uniqueness, 594, 660–661
 Hückel MO theory
 ab initio α , β parameters, 212–214
 comparison with NBO description, 208–214
 $4n + 2$ rule, 197
 Frost–Musulin mnemonic, 210–212
 Hund’s rule, 166, 170
 Husimi, K., 22
 hybrid following, 147–151
 hybridization
 and bond orbitals, 26
 and directionality, 107–111
 and electronegativity, 134–137
 see Bent’s rule
 and structure concepts, 35–36
 in $\text{CHF}(\text{OH})\text{PH}_2$, 145–146
 in d block, 81–82, 372–387
 in group 13–17 hydrides, 125–127
 in H_2 , 95–96
 in ionic bonding, 49–60
 in Li_2^+ , 99–100
 in NH_3 , H_2O , HF, 135
 in s/p block, 106–115
 R-dependence, 172–175

- hybridization (*Continued*)
 sum rules, 111–112
 theory, 52–60, 372–387
see natural hybrid orbital (NHO)
- hydrophobic effect, 651–652
- hyperbonding (3c/4e)
 in ionic transition metal complexes, 86
 in chelate effect, 529
see omega bond
- hyperconjugation
 primary, 215–226
 spectroscopic effects, 223, 226
 stabilization, 216–220
 torsional effects, 220–223
 secondary, 223, 226–252
 ethane-like barriers and torsion–vibration coupling, 227–247
 geminal
 angular dependence, 268–269
 Dewar model, 273–275
 hybrid decomposition, 264–268
 resonance description, 263–264
 ring strain, 269–273
 in d-block elements, 519–522, 574
 methyl tilt, 247–248
 stereoelectronic reactivity effects, 248–252
 summary, 352
 through-bond coupling effects, 252–269
 W-effect and octant-rule interactions, 259–263
- hypervalency, 275–306
 absence in main-group oxyacids, 302–306
 definition 276
 NBO description, 282–306
 non-d coordination, 477–479
 rare-gas compounds, 299–302
 three-center MO model, 277–281
 ubiquity in transition metal species, 447–448, 574
see omega bonding
- hypovalency, 306–353
 agostic interactions, 317–319, 483–487
 catalytic bond activation, 487–515
 in boron hydrides, 319–344
 in carboranes, 344–348
 in groups 3–5, 479–483
 in other group-13 compounds, 348–351
 isolable Lewis acids, 480, 483
 NBO 3c/2e *Aufbau* picture, 306–313
 protonated pi-bond model, 313–317
 tau bonds and antibonds, 309–311
 unpromoted 1c* orbitals, 479–480
see tau bonding
- ice-like clusters, 648, 651
- induction, 581–583
- Ingold, K., 662
- internal rotation barrier
 anomeric effect, 240–243
 ethane-like molecules, 234–238
 “4e-destabilization” rationale, 229–234
gauche effect, 240–243
 H-bond modulation, 693–702
 in C₂H₆, 227–229
 in “ethane-like” Os₂H₆, 519–520
 in ferrocene
 in W₂H₁₀
 primary hyperconjugation, 220–223
 secondary hyperconjugation, 227–251
- intramolecular vibrational relaxation (IVR), 244
- inversion (umbrella) barrier, 148–151
- ionic bonding
 in d-block elements, 76–86
 steric effects, 62–64
 clusters and lattices, 65–71
 crystal field theory, 437–439, 464
 model breakdown, 60–62, 87
 model of hypervalency, 277–278
 orbitals, 47–48
- ionicity/ionic character
 and electronegativity, 127–134
 anomalous values in dative bonding, 178, 443
 definition, 101
 Hannay–Smyth equation, 130
 in Heitler–London model, 102–105
 in hypervalent species, 282–289
 in hypovalent species, 394, 482
 in pi-bonding, 191–193
- ionic-covalent transition
 short-range, 52, 60–62, 80, 86, 91
 long-range, 60
- ionic wavefunction
 contrast with NBO description, 104–105
see Heitler–London wavefunction
- ionization potential
 Koopmans versus NBO picture, 119–125
 of CO, N₂, H₂O, CH₄, 120–125
 of transition metal atoms, 77–78
- Jaguar* program, 364
- Jahn–Teller theorem, 467–470
 in tungstenocene, 543
 pseudo (second-order), 469
 versus localized description, 468–470
- James–Coolidge wavefunction, 90
- Kekulé, A., 45, 196
- kinetic isotope effect, 518
- Klemperer, W., 73
- Koch, W., 677
- Kochi, J., 673
- Kolos, W., 90

- Koopmans' theorem, 119
 failure in through-bond-coupling phenomena, 255–259
 MO versus NBO picture, 119–125
- lanthanide contraction, 546
see vertical trends
- Latimer, W., 583
- Lennard-Jones potential, 635
- Lewis, G. N., 27, 89, 177, 302–306, 363, 573, 583, 592
 octet rule, 352, 363, 367
- Lewis acid–base adduct, 177
- Lewis structure, 105, 584
 of main-group oxyacids, 302–306
 for d-block elements, 365–372
- “Lewis-like” transition metal bonding
 anomalies in multiple pi-bonds, 406–412
 comparison with ligand-field/MO picture, 563–573
 comparison with main-group Lewis picture, 573–575
- dot diagrams, 368–370
- duodectet rule, 365–367
- hybrids, directionality, and molecular shape, 372–387
- limitations in metal–metal bonding, 555
 oxidation state, coordination number, and d-count, 370–372
 promoted configurations, 367–368
- ligand field theory, 439–440
- Lipscomb, W. N., 307, 309, 319, 323, 336
- lithium bonding (analog of H-bonding), 661
- localized versus delocalized description
 of ionization phenomena, 115–125
 of Jahn–Teller distortion, 468–470
 of sandwich complexes, 544
 of transition-metal bonding and hyperbonding, 563–573
- London, F., 90, 585, 586
 theory of long-range forces, 585–591
- long-range forces, 585–591
- Löwdin, P.-O., 23
 orthogonalization method, 231
- Ludwig, R. L., 646
- Madelung rule (*see* periodic table)
- magnetic properties, 461–464
- metal–alkene bonding, 501–509
- metal–H₂ bonding, 498–501
- metal–metal bonding, 413–420
 dinuclear hydrides, 413–418
 multiple bonds, 415–418
 polynuclear species, 419–420
 vertical trends, 555–560
- metallacycle formation (*see* reaction, insertion)
- metallic versus non-metallic mechanical properties, 522
- metallocenes (*see* sandwich complexes)
- metathesis reaction (*see* reaction)
- methyl tilt, 247–248
- migratory insertion, 510
- model chemistry, 584
 and concepts, 5–7
 and perturbation theory, 2–5
 and variation theory, 7–8
 Hartree–Fock, 13–14, 41
 ionic, 45
 breakdown
 Lewis, 29
 reality, 40–41
- molecule/molecular unit, 579–581, 592
 structure, 5–6, 105
- molecular orbital (MO) theory
 and ligand field theory, 439
 versus localized MO description, 115–125
see Hartree–Fock method
- Møller–Plesset (MP) method, 711
- Mulliken, R. S., 215
 approximation, 31, 58, 188, 231, 265
 charge-transfer complex, 580, 661–663, 684, 703
 hyperconjugation, 215, 227
 MO theory, 439
 population analysis, 571
- multiple bonds
 d-group, 413–418, 555–560
 main-group, 112–115
 absence in H₃NO, H₃PO, H₃AsO, 179–181
see quadruple and quintuple bond
- multipoles (electric), 587–590
 ion–dipole, 64
 quantal corrections, 65
 model of hypervalency, 288
 dipole–dipole, 65
- naked metal cluster, 419
- natural atomic orbital (NAO)
 description, 24–25
 for group 4, 6, 10 metals, 548
 pre-orthogonal (PNAO), 30–32
 variation with charge/configuration, 47–48
- natural bond orbital (NBO)
Aufbau in homonuclear diatomics, 165–166
 compared with Heitler–London wavefunction, 102–105
 description, 25
 for group 6–11 transition metal hydrides, 391–393
 for group 13–17 hydrides, 125–127
 for pi-bonds of group 6–10 metal carbenes, 402–404
 for pi-bonds of group 14–16 CH₂X, 152–155

- natural bond orbital (NBO) (*Continued*)
Lewis and non-Lewis, 26–27
polyene, 180–196
pre-orthogonal (PNBO), 30–32
program, 27–28
vicinal versus non-vicinal interactions, 193
- natural energy decomposition analysis (NEDA), 591
- natural hybrid orbital (NHO)
angular strain and bond bending, 146, 151
bent, 150–151
comparison, 35–36
composition (sp^λ), 52, 54–55
definition, 26
in ionic transition-metal bonding, 82–85
see hybridization
- natural Lewis structure
accuracy, 112, 117, 187, 324, 327, 340–341, 392, 400–402, 414, 433
definition, 26–30
model, 29, 41
- natural localized molecular orbital (NLMO)
hyperconjugatively modified, 223–224
in conjugated systems, 183, 188
in spectroscopic excitation, 260–262
to estimate crystal field splitting, 463, 464–466
versus canonical MO, 115–125, 468–470, 568–570
- natural minimal basis (NMB)
accuracy, 108
definition, 25
dynamical character, 48–49
- natural orbital
definition, 15–16, 23–24
- natural resonance theory (NRT), 32–36
variational criterion, 32–34
bond order, 34
valency, 34–35
of amine oxides and related species, 181
of boron hydrides, 325–344
of hyperconjugation, 225, 250–251
of polyenes, 185–196
see resonance
- natural steric analysis
description, 37–40
- near-valence (*Nebervalenz*), 582–583
- nephelauxetic effect, 464–466
- non-bonding (lone pair)
anomalous $n^{(h)}$ of sd^1 bonding, 379–380, 410
in delta-bonding, 416
 π -interactions, 190–191
- normal-valency of d-block elements, 370
- nuclear magnetic resonance (NMR)
exchange processes, 582
 J -couplings, 282, 291–292, 583
shielding, 621
- nucleophilic cleavage reaction (*see* reaction)
- nu-bonds, 123–124, 351
- open-shell, 710–711
d-block atoms, 76
daughter radicals of parent normal-valent species, 446–447
excited states, 260–263
homonuclear diatomics, 157–173
in $W(CO)_2$, $W(CO)_2$, 449
in MnF_3
- octant rule, 259–263
- omega bonding ($3c/4e$), 282–306
and d-count, 470–473
and *trans* influence, 473–474
characteristics, 286–288, 447
“ideal” $3\omega/3\sigma/3n$ motif, 450–451, 470, 540, 542
in metal alkenes, 507–508
in nucleophilic displacement reactions, 289–293
omega-additions, 294
omega-prebond, 282, 447
steric/electrostatic limits, 448, 474–477
ubiquity in d-block species, 447–448
with transition metal s-orbitals, 477–479
see hypervalency and Pimentel–Rundle three-center MO model
- optical rotatory dispersion (ORD), 260
- overlap, 602, 614
and steric forces, 37–40
concept, 30–32
in PMO theory, 230–234
relation to hybridization, 55
visualization, 58, 188
- oxidation state
of d-block elements, 370–372
- “oxidative addition,” 498
- p-orbital participation
in transition-metal hybrids, 82, 363–364, 449, 478, 590–573
- Pauli exclusion principle, 6, 352, 596
and orbital occupancy, 13
and steric repulsion, 36–40
- Pauling, L., 106, 363, 372, 573, 583, 592
description of B_2H_6 , 312–313
description of ferrocene, 541
electronegativity, 129–134
 H_2^+ , 90
hybrids for transition metal bonding, 363–364, 570
Pauling–Wheland resonance theory, 32, 35, 102
 $3e$ π -bonds in O_2 , 169
valence-bond model, 105
- periodic table(s)
theory of periodic *Aufbau*, 715–717
standard (STT) form, 716

- left-step (LST) form, 717
- ascending periodic helix (APH) form, 718–719
- perturbation theory
 - Møller–Plesset, 16–18, 711
 - and models, 2–5, 584
 - first-order, 3, 18
 - Rayleigh–Schrödinger, 3
 - second-order, 3, 18–19
 - role of vacant orbitals, 13
 - donor–acceptor interactions, 16–19
 - London, 585–591
 - of relativistic corrections, 545–546
 - of AO-MO versus NAO-MO interactions, 566–567
- “perturbative molecular orbital” (PMO) theory
 - criticism, 230–234
- pi-backbonding, 446, 452–459
- pi-complex model (*see* sigma aromaticity)
- pi-frontbonding, 459–461
- Pimentel, G. C., 279
 - Pimentel–Rundle 3c-MO model, 278–281, 440, 447
- pi-migration, 670–671
- pi-star acceptors, 665–675
- polarization, 595–596, 610
- polarization coefficients, 101–102
- polarization functions, 151, 712
- polar bonding
 - NBO versus VB description, 100–104
- Polder, D., 590–591
- polydentate binding (*see* chelation)
- Pople, J. A., 7
 - model chemistry, 2–3
- Priestley, J., 45
- promotion energy, 139–140, 547, 558
- protein folding, 699–701
- proton ordering (in H-bonding), 647
- proton transfer, 652–657
- quadruple bond
 - in HReReH, 413
 - in H₂WWH₂, 414
 - in HTaTaH, 414
 - vertical trend, 555–560
- quantum-mechanical resonance energy (QMRE), 194–195
- quantum numbers, 9–10, 719–721
- quasi-stationary states (*see* time-scale)
- quintuple bond
 - in HWWH, 415–418
 - vertical trend, 558–559
- rare-gas compounds, 299–302
- reaction
 - alkene polymerization, 499, 501, 509–518
 - dative coordination
 - of H₂, 488–492
 - of alkenes, 501–503, 505–509
 - Diels–Alder, 680–682, 686–693
 - electrophilic cleavage, 489
 - electrophilic displacement, 317–319
 - insertion (“oxidative addition”)
 - into H₂, 489–490, 492–498, 574
 - into alkenes, 503–505
 - nucleophilic cleavage, 490
 - nucleophilic displacement (S_N2), 289–293, 682–685
 - “reductive elimination,” 498
 - sigma-bond metathesis, 490–491, 498–501
 - synergistic coordination, 488–492
- reaction coordinate, 500, 655–657, 680
- regioselectivity, 501, 514–518
- relativistic effects
 - and vertical trends, 545–563
 - description, 6
 - with ECP basis sets, 713–714
- resonance, 592, 628
 - enhancement of chelation, 534–536
 - enhancement of H-bonding, 627–634
 - force, 593
 - in amide groups, 191
 - in aromatic and antiaromatic systems, 196–208
 - in B₂H₆
 - in conjugated systems, 182–196
 - in Diels–Alder reaction, 690–693
 - in geminal hyperconjugation, 263–264
 - cyclopropane, 275
 - in H-bonding, 621, 628, 654–657
 - in main-group oxyacids, 302–306
 - in metallacyclic character, 505–509
 - in omega-bonding, 474
 - in pi-backbonding, 452, 457–459
 - in S_N2 reactions, 291
 - in sandwich complexes, 537
 - in torsion–vibration coupling, 694–702
 - in transition-state species, 681–682
 - ionic (3c/4e hypervalency), 277, 281–2, 286
 - Pauling–Wheland, 32, 102
 - see* natural resonance theory (NRT)
- ring pucker, 273
- Rodebush, W. H., 583
- Rosenfeld, L., 260
- rotation barrier (*see* internal rotation barrier)
- Rundle, R. E., 279
 - Pimentel–Rundle 3c-MO model, 278–281, 440, 447
- Rutherford model of the atom, 89
- s-block elements
 - bonding, 90–100
 - alkaline-earth fluorides, 73–76

- sd^4 hybrids
 idealized angles, 376–381
 mathematical form, 372–374
 molecular shapes, 381–387
- S_N2 (*see* reaction)
- sandwich complexes, 536–545
- Schleyer, P. v. R., 270
- Schrödinger, E., 2
 equation, 1, 8
 Rayleigh–Schrödinger perturbation theory, 3
- Schwerdtfeger, P., 73
- Shaik–Pross VB model, 498, 681
- short-range forces, 588, 591–593
 see resonance force
- Sidgwick, N. V., 662
- “sigma-aromaticity” concept, 264, 273–275
- sigma–pi breakdown (*see* banana bond)
- simple point charge (SPC) potential, 594, 635, 643
- singlet complementary atom (1CA) configuration, 166
- size-consistency, 711
- Slater, J. C., 106, 363
 Slater-type orbitals, 568
- spectrochemical series, 438
 and nephelauxetic effect, 464–466
 and transition metal promotion, 480
 CO position, 456
 H₂O position, 461–463
- spin (electron)
 and Jahn–Teller theorem, 467–470
 and magnetic properties, 461–464
 as relativistic effect, 6
 high- versus low-spin configuration, 439
 in 1CA configuration of homonuclear diatomics, 166
 in daughter radicals of normal-valent species, 446–447
 in W(CO), W(CO)₂, 449
 in metal–H₂ insertion reactions, 493–495, 498
 properties of first-row transition metals, 76–77
- spin-charge
 in H₂, 93
 in homonuclear diatomics, 166
- spin hybrid, 540
- stationary state (*see* time-scale)
- stereoelectronic effects
 on chemical reactivity, 248–252
 on ionization phenomena, 252–259
 on spectroscopic excitation, 259–263
- “steric attraction,” 238–240
- steric effects
 and Pauli principle, 36–38
 in ionic bonding, 62–64
 in torsion barriers, 227, 238
 in methyl tilt, 248
 versus stereoelectronic effects, 252
 in rare-gas compounds, 301
 in multiple pi-bonds of transition metals, 410
 in H₃WWH₅, 415
 counteracting donor–acceptor attraction, 599–600, 685
 see natural steric analysis
- Stock, A., 319
- Stoney, J., 45
- stylx* code, 321
- “superexchange,” 255
- superposition principle, 9
- supramolecular unit, 581
 bonding, 579–709
- synergistic coordination reaction (*see* reaction)
- Szentpaly, L., 73
- t_{2g} orbital (octahedral), 438, 461–464
- tau-bonding (3c/2e)
 central type, 329–331
 Δ -type antibonds, 307, 310–315
 in H₄TaTaH₄, HTaTaH, 415
 in group 3–5 hydrides, 485–487
 open type, 330–331
 π -type antibonds, 307, 310, 313–315
 see hypovalency
- temperature-dependence, 581–582
- theoretical strain energy (TSE), 270
- Thomson, J. J., 45
- three-center bonding, 352–353
 see hypovalency, hypervalency, tau-bond, and omega-bond
- three-center MO model (*see* Pimentel–Rundle model)
- through-bond (TB) coupling
 in diaminoalkanes, 252–255
 and ionization phenomena, 255–259
 other stereoelectronic effects, 259–263
- through-space (TS) coupling, 252–254
- tight-binding approximation, 213
 see Hückel MO theory
- time-scale, 582, 584
- torsion barriers (*see* internal rotation barriers)
- torsion–vibration coupling, 243–247
 geometrical flexing effects, 245–246
 NBO compositional changes, 246–247
- trans* influence, 473–474
- transition metal (TM) bonding, 363–575
 coordinate metal–ligand bonding, 434–479
 hyperbonding, 447–451
 pi-backbonding, 452–459
 pi-frontbonding, 459–461
 spin and magnetic properties, 461–464
 covalent and polar covalent bonding, 387–434
 alkylidenes and alkylidyne, 399–413
 halides, oxides, hydroxides, nitrides, imides, 421–435

- hydrides and alkyls, 387–399
 - metal–metal bonds, 413–420
- hybridization and molecular shape, 372–387
- Lewis-like structures, 365–372
- transition state (TS), 653–657
 - complex, 678–685
 - for alkene–polymerization reaction, 509–518
 - for Diels–Alder reaction, 687–690
 - for S_N2 reaction, 682–683
- trigonal bipyramidal geometry, 289–293
 - and S_N2 reactivity, 292
- Umpolung* effect, 526
- units, 723–725
- valence bond (VB) theory
 - comparison with NBO description, 102–105
 - see* localized versus delocalized *and* Heitler–London wavefunction
- valence-shell electron-pair repulsions (VSEPR) model
 - and Jahn–Teller theorem, 469
 - and Lewis structure, 36
 - comparison with 3c/4e NBO model, 293–299
 - failure, 389–390, 400, 402, 428, 433, 449, 454, 574
 - for ArF_6 , 301
 - in MX_2 bonding, 73
 - in hypervalency, 278
- valence-shell expansion, 447, 449–450
 - see* p-orbital participation *and* d-orbital participation
- valency
 - covalency, 35
 - discovery, 45, 105
 - electrovalency, 35
 - NRT definition, 34–35
- van der Waals force (*see* dispersion)
- van der Waals molecule (*see* cluster *and* supramolecular unit)
- van der Waals radius, 587, 591, 599, 602
 - and limit of classical picture, 47
 - natural (table), 40
- van Vleck, J. H., 439
- variational method, 710–711
- vertical trends
 - in main-group hypovalency, 348–351
 - in transition metal bonding, 545–563
 - coordination and hyperbonding, 560–563
 - metal–hydride and metal–alkyl, 548–555
 - metal–metal, 555–560
- vibration
 - frequency shift, 282, 291, 609–610, 620, 629
 - coupling to torsion, 245–247
- W-effect, 259–263
- Weinhold, F., 227, 240
- Weisskopf, V. W., 37
- Werner, A., 436, 580, 582, 592
- Wilkinson, G., 536
- Wolniewicz, L., 90
- Woodward, R. B., 687
- Woodward–Hoffmann rules, 686, 703
 - localized extension, 687–690
- Zintl salts, 581